Bioconjugate Chemistry

Review

pubs.acs.org/bc

Targeting the Estrogen Receptor using Steroid–Therapeutic Drug Conjugates (Hybrids)

Kinh-Luan Dao and Robert N. Hanson*

Department of Chemistry and Chemical Biology Department, Northeastern University, 360 Huntington Avenue, Boston Massachusetts 02115-50000

ABSTRACT: The estrogen receptor (ER) is a potentially useful biological target for diagnosis and therapy in hormonally responsive human breast cancer. This protein is often overexpressed both on the membrane and on the nuclear compartment of breast cancer cells and therefore provides a mechanism for targeted drug delivery. Over the past 30 years, many research groups have attempted to exploit the high affinity and receptor selectivity of steroidal estrogens to deliver cytotoxic agents that by themselves lack selectivity. In this review, we describe the strategies and methods employed by those investigators in their efforts to develop steroid–drug conjugates with the goals of enhanced antiproliferative activity and ER-selectivity. In particular, the choices of steroid scaffolds and sites for drug conjugation have evolved as the understanding of role of ER in cell function has expanded. Present knowledge of the mechanism of action for estrogens and antiestrogens helps explain the failure of most efforts to achieve their stated objectives. The review culminates in the description of our program, which has produced the first conjugate that clearly has achieved those goals and provides an approach for developing new agents for future clinical use.

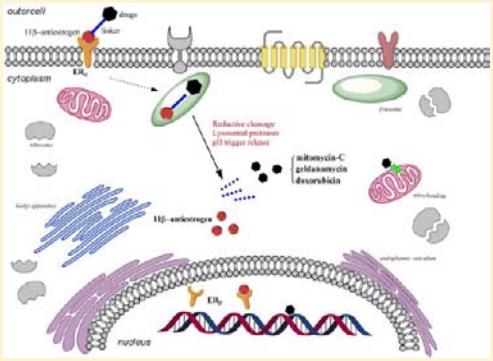

INTRODUCTION

One of the major challenges in cancer chemotherapy involves delivery of potent drugs selectively to the pathological cells without exposing the toxic effects of the drugs to the normal tissue. Because few cytotoxic drugs used today possess such inherent selectivity for the disease, an entire field of targeted drug delivery has developed. The aim of this discipline is to devise methods by which nonselective, but highly active, agents can be modified such that they will recognize cancer cells in preference to normal cells. Among the many strategies devised, one that has received significant attention is the preparation of targeting group–drug conjugates. In this approach, the drug is covalently attached (ligated) to another molecule which possesses the requisite cancer cell recognition properties. The criteria that the resultant conjugate must meet are several—the modification must not alter significantly the recognition properties of the targeting moiety; the modification does not modify the therapeutic properties of the drug; and the entire conjugate demonstrates the biological properties regarding efficacy, potency, and selectivity. In addition, the compounds must be chemically and biologically stable, and be prepared in as few steps as possible.

Achieving this goal for most cancers remains to be demonstrated; however, a number of studies in this regard have been undertaken for hormone (estrogen) responsive breast cancer. This form of breast cancer provides an excellent example, as it possesses a well-characterized targeting mechanism (estrogen receptor) as well as many potentially useful therapeutic agents. Although this biological target has been the subject of research for over 30 years, few reviews have evaluated the strategies for targeted drug delivery.[1−3] In this review, we provide the therapeutic context for targeted drug delivery, a rationale for targeting the estrogen receptor, a survey of past approaches to estrogen receptor targeted drug delivery conjugates using the steroidal derivatives, and our current efforts, which have resulted in the identification a potential estrogen receptor-based drug delivery system.

DIAGNOSIS AND THERAPY OF BREAST CANCER

Breast Cancer. Breast cancer is the most common cancer among women in the United States, with an estimate that 1 in 8 women will develop breast cancer in their lifetime.[4] It is still the most common cause of death in women between 35 and 55 years of age, and worldwide, it is considered the most common cause of cancer death.[4−6] Currently, the mortality rates due to breast cancer have decreased in many industrialized countries, including the United States. Two possible explanations for this decline in breast cancer mortality are (1) more effective early detection due to widespread screening efforts and (2) advances in adjuvant systemic therapy. In early-stage breast cancer without distant metastases, cure rates of up to 70% seem possible. However, even with currently available therapeutics, recurrent or metastatic breast cancer is still considered incurable.[5,7]

Received: July 9, 2012
Revised: September 19, 2012
Published: October 5, 2012

 © 2012 American Chemical Society

Diagnostic Imaging Breast Cancer. Early detection is a major factor that improves the chances of survival in all forms of cancers, and breast cancer has one of the more mature screening and detection regimes.[8,9] Mammography is still the most common method for early detection, often detecting cancer before physical symptoms appear. This technique uses X-rays to noninvasively visualize an abnormal anatomical structure, such as nonhomogeneous tissue density within the breast. The diagnostic mammogram typically is more accurate in postmenopausal compared to premenopausal women.[10] Ultrasonography is another diagnostic modality that is used to discriminate between fluid-filled and solid tissue structures. Ultrasound is typically used to evaluate a limited region of the breast, but not as a screening test of the entire breast. The third imaging modality is breast magnetic resonance imaging (MRI), which uses a magnetic field to create a detailed anatomical image. In order to enhance resolution, this method requires injection of a spin contrast agent, such as a gadolinium complex, to improve the quality of the images, as heterogeneity in the density of the breast tissue can be problematic. MRI is not recommended for screening cancer in most women, because it is not as reliable as mammography for certain breast conditions, such as ductal carcinoma in situ (a type of noninvasive or early breast cancer). In addition, MRI testing is more likely to identify suspicious regions that turn out not to be cancerous (false positives). All of these methods are noninvasive and, in combination with clinical and self-breast exams, represent the basis for breast cancer detection. However, these procedures only provide anatomical information for tissue abnormalities which may or may not be cancerous, and therefore, a biopsy is required to confirm if the abnormal tissue is a carcinoma.[11]

Treatment of Breast Cancer. Breast cancer therapy can be "personalized", based on a variety of factors, including the stages of the disease and biopsy (histological) results. Localized disease is treated primarily with surgery, either a lumpectomy or mastectomy, to remove the gross cancerous tissue. Radiation and chemotherapy may be used prior to surgery (neoadjuvant setting) to reduce the tumor mass. Surgery is usually followed (adjuvant setting) by radiation therapy to kill any remaining cancerous cells. Advanced stage breast cancer is considered a systemic disease, and therefore, adjuvant systemic therapy (endocrine therapy, chemotherapy and/or trastuzumab) is administered in addition to loco-regional treatment.[12] Adjuvant chemotherapy is usually given for 3 to 6 months after radiation and typically consists of a combination or "cocktail" of drugs. Such combinations are normally more effective than single drug therapy for breast cancer treatment, as each component imparts its benefit through a different mechanism. Most chemotherapeutic approaches are prone to significant systemic side effects due to their high toxicity and lack of cancerous tissue specificity. As a result, significant efforts have been directed toward the development of new therapeutic strategies with greater specificity and enhanced therapeutic efficacy and/or bioavailability.[8,11,13−15]

■ ESTROGEN RECEPTORS AS TARGETS OF STEROID−DRUG CONJUGATES

Role of Estrogen and Estrogen Receptor (ER) in Breast Cancer. The underlying molecular mechanism by which estrogens increase the risk of breast cancer is still not fully understood. However, estrogen metabolites are known to bind to DNA and induce mutations. For example, estradiol (the endogenous parent estrogen) undergoes hydroxylation (oxidation) by the cytochrome P450 system to form catechol estrogens, which are further oxidized to the corresponding quinones and/or semiquinones. The quinone derivative of catechol estrogen can subsequently bind to DNA, forming DNA adducts. Furthermore, the semiquinones generate free radicals that can react with oxygen, forming superoxide radicals (reactive oxygen species-ROS), which can also attack and alter DNA. In addition, direct estrogen stimulation of the breast epithelial cell proliferation is another increased breast cancer risk factor. Enhanced cell replication resulting from estrogen exposure results in the propagation of genetic errors, and the mutagenesis increases the risk of genetic alteration. Although estrogens enhance the growth of certain types of breast cancer cells in cell culture, the detailed mechanisms by which the steroids promote growth *in vivo* are still not completely clear.[16−20]

A discussion of estrogen receptors (ER), predominately the alpha (α)-subtype, is required to appreciate the role of estrogens in breast cancer. In general, the α-subtype estrogen receptors (ERα) are the more dominant form in ER-positive (ER+) breast cancer cells undergoing proliferation than in normal cells, suggesting that paracrine factors, such as secreted growth factors, proteases, and growth receptors, mediate the mitotic effects of estrogen. In addition, the dissociation between cell proliferation and the presence of ERα in normal epithelial cells, proliferating breast cancer cells expressing ERα, suggests that estrogen can directly stimulate the growth of breast cancer cells. More recent data has indicated that ERα and ERβ may have different roles in the formation and/or progression of breast cancer. For breast (ER+) tumor cells, estrogens can stimulate growth only if ERα is present. By comparison, estrogen interactions with ERβ inhibited cell proliferation and prevented tumor formation. Further studies have shown that ERα is the subtype that is generally up-regulated during the conversion from normal mammary epithelial into carcinoma, whereas the β-form is usually decreased. For example, Rao et al. used immunohistochemistry(IHC) to demonstrate the higher level of ER$_\beta$-positive cells in normal mammary gland than in abnormal, but nonproliferating benign breast tissue. In contrast, ERα levels increased during progression from normal to abnormal tissue. Therefore, the ERα/ERβ ratio appears to change during breast cancer carcinogenesis; however, whether this relationship is a cause for malignant transformation is still unclear.[21]

Review of Structure and Function of Estrogen Receptors. The estrogen receptors (ER) are members of the nuclear hormone (NR) receptor, ligand-controlled transcriptional factor superfamily. These proteins mainly function as activators or repressors of transcription but can also mediate nongenomic pathways, such as signaling cascades or ion channels.[22,23] As mentioned in the previous section, there are two major isoforms of ER, ERα and ERβ, possessing similar affinities for 17β-estradiol (E2). ERα is predominately located in breast and uterus tissue, while ERβ is mainly found in central nervous system, cardiovascular, and bone tissues.[21,24−28] The two isoforms share modest sequence identity but are structurally homologous, maintaining conserved structural and functional distinct domains.[29−31]

The current understanding of the cellular uptake and distribution of 17β-estradiol, as well as the other endogenous estrogens, is more complex than previously described.[29,32,33] In addition to passive diffusion through the outer cellular

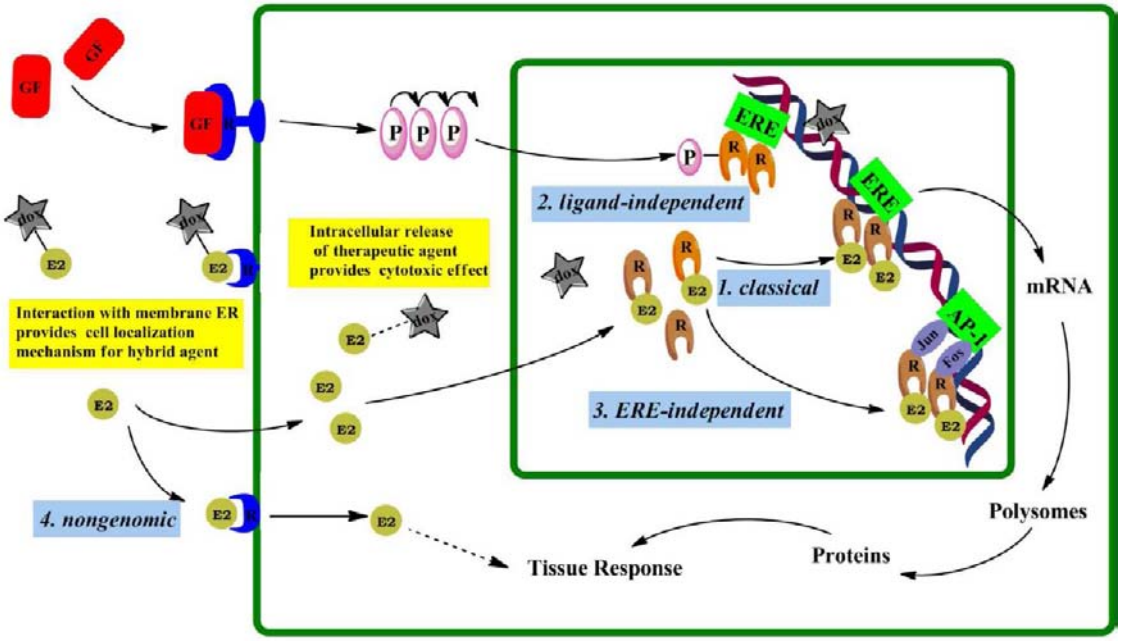

Figure 1. Multifaceted mechanisms of estradiol and estrogen receptor signaling.

membrane, estrogens may also bind to cognate estrogen receptors embedded within the cell membrane (mER). These membrane estrogen receptors arise from the same genes as the nuclear receptors and are chemically identical. Interaction of estrogens with mER results in endosome formation, leading to an alternate entry and signaling pathway.[18] Once within the cell, via either route of entry, free estrogen binds to the ligand binding domain (LBD) of the ER as part of the ER-Hsp90 chaperone complex. Upon ligand binding, ER undergoes a conformational change, causing dissociation of Hsp90 and permitting subsequent estrogen receptor dimerization. The conformational changes induced by the ligand−ERα interaction subsequently drive the transcriptional responses. For the endogenous ligands, the formation of the ligand−ERα complexes promotes the recruitment of coactivator proteins and association with the corresponding estrogen response elements (ERE) within the DNA. Completion of transcriptional complex leads to the downstream RNA and protein responses typically associated with the steroidal estrogens.[1,23]

For synthetic ligands that target the estrogen receptor, the process for uptake, binding, coregulator recruitment, and transcriptional activity may be significantly altered. Depending upon physicochemical properties or ER-binding affinity of the compound, the balance between passive diffusion and membrane ER-endosomal uptake may vary widely. Within the cell, affinity for the ER-LBD can affect the rate and efficacy of ER-HSP dissociation and resultant ER dimerization process. More importantly, the conformational changes induced with ER-LBD by the synthetic ligand give rise to complexes with ER that may not resemble those formed with the endogenous ligands. Ligand-ER complexes similar to those formed by estradiol will tend to recruit a similar (but not necessarily identical) set of coregulatory proteins and generate similar, but not identical, transcriptional responses. Such compounds are called estrogen agonists.[29] At the opposite extreme are ligands that bind within the same site as estradiol but produce different conformational changes. Such complexes fail to recruit the same set of coregulatory proteins or recruit coregulatory proteins that block the transcriptional responses. These compounds are called antagonists or antiestrogens (AE). Most synthetic ligands for the ER have properties that fall between these two extremes, and these variations in properties must be taken into consideration when using the ligands for targeting the ER.[24,29,30,34−36] The specific structure−activity relationships (SAR) for ER are well-described and therefore will not be reviewed here.[37−43]

Biological (Downstream) Consequences of Agonists/Antagonist with Estrogen Receptors. The agonist hormone 17β-estradiol (E2) is a key regulator of growth, differentiation, and function in a wide array of target tissues, including the male and female reproductive tracts, mammary gland, and skeletal and cardiovascular systems.[33,36] The biological effects of estradiol (E2) are mediated through at least four different ER pathways as shown in Figure 1.[44] The classical ligand-dependent **1** is the pathway in which E2-ER complexes bind to estrogen-responsive elements (EREs) in target promoters leading to an up- or down-regulation of gene transcription and subsequently leading to tissue responses. In the ligand-independent pathway **2**, the growth factors (GF) or cyclic adenosine monophosphate activate intracellular kinase pathways, leading to phosphorylation (P) and activation of ER at ERE-containing sites. Pathway **3** is ERE-independent in which E2-ER complexes alter transcription of genes containing alternative response elements, such as AP-1. Through their association with other DNA-bound transcription factors (Fos/Jun), which tether the activated ER to DNA, this results in an up- or down-regulation of gene expression. And finally, pathway **4** is cell-surface (nongenomic) signaling, in which E2 activates a putative membrane binding site, possibly an isoform of ER, linked to intracellular signal transduction pathways that are associated with rapid tissue responses.[44−46] Although all of the E2-ER dependent pathways induce both up- and down-regulation of ER gene expression, pathway **3** probably has the most significant impact on gene regulation, as it also alters other transcription factor pathways. As indicated previously, modification of the structure of the ER ligand would be

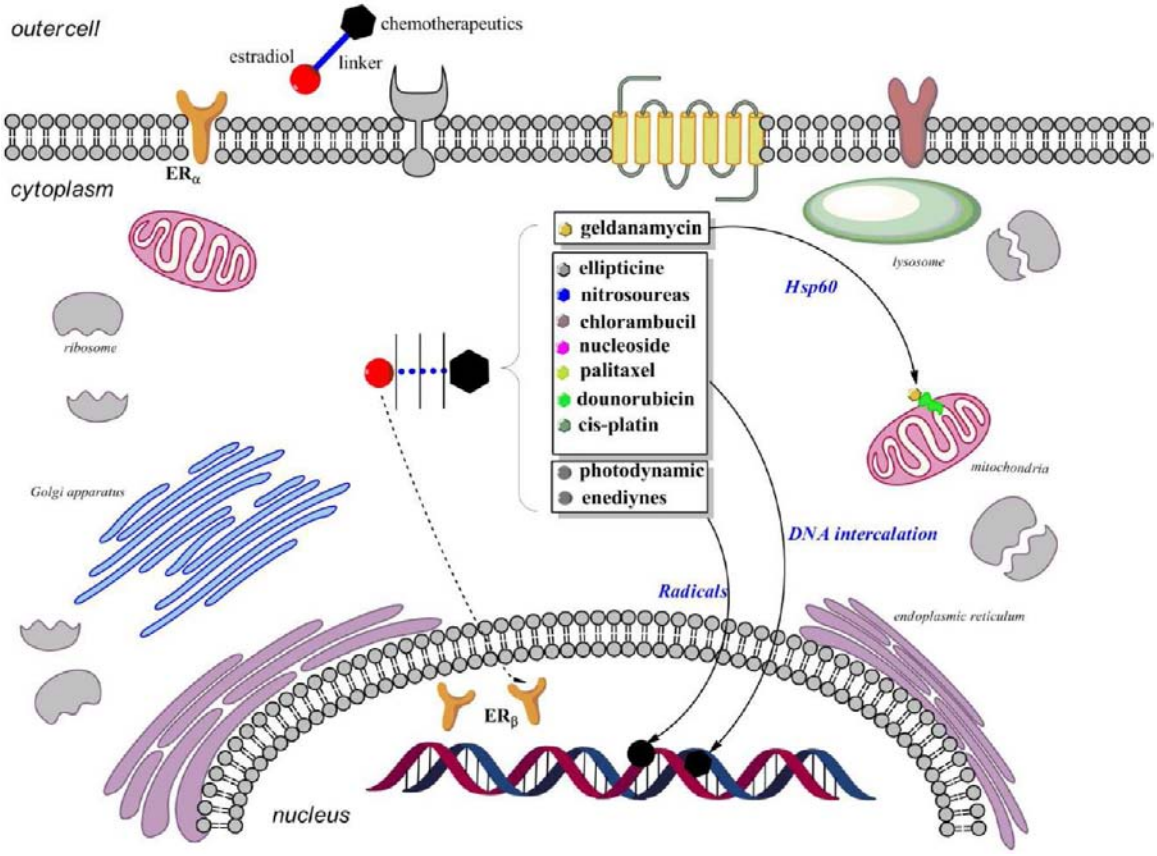

Figure 2. Targets of chemotherapeutic agents.

expected to generate alterations in each of these pathways, leading to a different overall biological response.

Concepts of Using Steroidal Estrogens to Target ER. Steroidal estrogens, such as E2 and its substituted derivatives, are attractive vectors for targeted drug delivery because they have been shown to localize in tissues that overexpress ER.[2,47−49] Although steroidal estrogens may freely penetrate non ER-expressing tissues, they are not retained within them. Such observations provide the basis for developing estrogen conjugates for therapeutic drugs that lack inherent breast cancer cell selectivity. The core structure of E2 provides a scaffold for incorporating functional groups, large or small, that can impart additional biological activity. The challenge is how to transform E2 into a targeting molecule for drug delivery without significantly disrupting its inherent binding properties for the ER.[50−52]

A review of this field can essentially be divided into two distinct eras. The first era was pre-1990 when such agents were primarily based on the known structure−activity relationship (SAR) for ER agonists and antagonists. The second era began after 1990 when E2 conjugates could be designed based on the crystal structures of agonist or antagonist ligands complexed with the ER-LBD.[53−55] The pre-1990 SAR studies emphasized both the necessity of free 3,17β-OH groups on estradiol and for small substituents on the aromatic "A" ring, as well as at the 6, 7, 11, 16, and 17 positions. Large substituents at those sites as well as the other positions on E2-scaffold were detrimental to ER-binding. The advent of the ligand-ER LBD crystal structures rationalized the observations, and it was clear that the phenolic-3-OH was oriented toward the inner core of LBD, an interaction with Glu and Arg residues, as well as a water molecule. The 17β-OH formed hydrogen bonds with a specific His-524 located in helix 12. The remainder of the E2 structure is bounded by a predominantly hydrophobic surface. The crystal structures of complexes with simple ER ligands do not provide insights into adaptive responses of ER compared to complexes with more highly modified steroidal structures. 17α-substituted phenylvinyl E2 derivatives, for example, induce a pocket in ER-LBD not previously observed; however, the pocket can accommodate high-affinity ligands which are potent agonist or low-affinity compounds that are essentially inactive. Substituents at the equivalent of 11β-position of E2 can be accommodated within the ER-LBD, with larger groups (beyond 3−9 atoms) resulting in a conformational change in which the Helix-12 of the ER assumes an antagonist pose. The dialkylaminoethoxyphenyl groups found in many nonsteroidal antiestrogens occupy this space. For 7α-substituted E2 derivatives having large groups (3−4 atoms), the steroidal scaffold appears to rotate around the 3−17β axis, and projects the 7α-substituent into the 11β-pocket. Therefore, E2-drug conjugate development must consider these observations in the overall design process.

Roles of Chemotherapeutic Agents. Most of the conventional chemotherapeutic agents that have been used were selected for their ability to target one of the six hallmarks associated with human cancer cells. As formulated by Hanahan and Wienberg et al., these include limitless proliferative potential; self-sufficiency in growth signaling; insensitivity to antigrowth signals; evasion of apoptosis; sustained angiogenesis; and tissue invasion and metastasis. The majority of the anticancer compounds used for conjugation with estradiol are endowed with intrinsic immunosuppressive properties owing to

the fact that they preferentially target rapidly proliferating cells.[56] As shown below, Figure 2 illustrates the functional targeting of anticancer reagents that have been used in estradiol–anticancer drug conjugates. In general, the drugs were chosen because they demonstrated chemotherapeutic effects against breast cancer; however, they were nonselective with respect to the breast cancer tissue, and therefore produced serious systemic toxic side effects. These side effects led many research groups to couple the chemotherapeutic drugs with a high-affinity targeting agent, such as estradiol, to make a conjugate that would be more selective to the disease and yet retain the potency of the original drug, thereby alleviating the off-target toxicity.

EVOLUTION OF ANTIESTROGEN–DRUG CONJUGATES

General Concepts of Antiestrogen–Drug Conjugates.

Targeted therapeutic drug conjugates are designed to synergize the two independent functionalities. The aim is to make a single entity that has therapeutic efficacy of the therapeutic compound and the selectivity of the targeting compound. The conjugates should possess better pharmacokinetics, and enhanced pharmacological properties such as specificity, cellular uptake, and/or retention.[57−59] Considering the many roles that ERs play in normal and abnormal physiology, the list of potential therapeutic groups which could be attached to ER-targeting steroids becomes quite extensive. Nevertheless, because the ultimate objective in each substance is essentially the same, i.e., developing therapeutic group intracellular to an ER responsive cell, the overall criteria for each conjugate will remain the same. As with all drug-conjugates, the compound must be chemically and biologically stable—at least during circulation *in vivo*. The ER-targeting moiety should retain high affinity for ER, with a relative binding affinity (RBA) ≥ 10% compared to that of estradiol. The conjugate should be capable of achieving an intracellular concentration, either by active uptake or passive diffusion, sufficient to promote the therapeutic effect. The conjugate should provide a mechanism by which the therapeutic component is effectively available to its site of action. That effect should occur at levels below those at which toxicity is generated in normal cells, or non ER-selective cells. The targeting component should not interfere with the therapeutic responses.[1,2,47,59−61] The process by which ER-targeted conjugates should be screened was described in excellent detail by Katzenellenbogen et al.[62] These methods include an initial screening through a series of assays to demonstrate its effectiveness as a ligand with high binding affinity for ER, potent efficacy in an appropriate assay, selective activity in ER-dependent but not ER-negative breast cancer cells, that is reversible by exposure to estradiol.

In the following section, we will review examples of efforts to develop steroid (steroidal)-based ER targeted drug delivery systems. Most of the therapeutic targets are associated with cancer; however, some are directed toward the other hormone related disorders. In each example, we will evaluate the choice of estradiol derivative, the therapeutic moiety, and the linker as contributing to the observed biological effects. The first set of examples focuses on agonist-like estradiol derivatives, i.e., those with 3, 6, 7, 16, and 17-substitution patterns. The subsequent examples will look at the steroidal antiestrogens, beginning with the 7α-substituted estradiols and ending with a summary of our work which resulted in a highly active 11β-substituted estradiol derivative.

The evolution of conjugating chemotherapeutic agents to a steroid E2 scaffold is represented in the schematic in Figure 3. This review will discuss details with each case, where R could be a specific design of a functional linker/tether that is attached to a specific anticancer reagent.

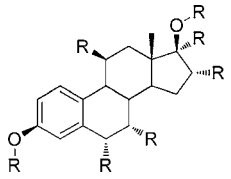

Figure 3. Generic E2–drug conjugates.

E2–Ellipticine Conjugates. Ellipticine is a DNA intercalating agent that has been evaluated as a breast cancer chemotherapeutic agent; however, its lack of selectivity and severe side effects negated its clinical utility. Two sets of 17α-substituted estradiol–ellipticine conjugates were prepared with the objective of enhancing breast cancer cell selectivity and cytotoxicity (Figure 4A,B). Delbarre et al. used estradiol

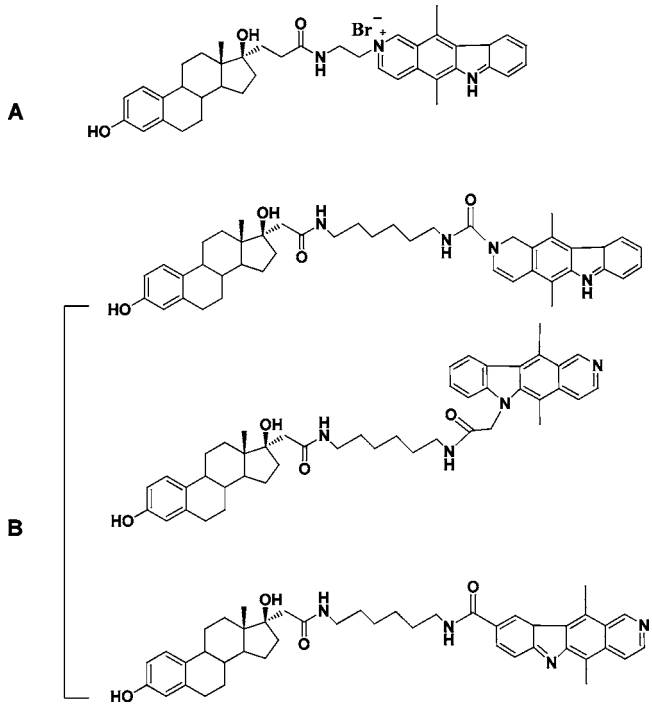

Figure 4. E2–Ellipticine Conjugates: (A) E2-Ellipticine short linker;[63] (B) E2-Ellipticine long linker[64].

modified at the 17α-position with a propionic acid residue to conjugate ellipticine as its quaternary salt (Figure 4A). Conjugation of the estradiol derivative had no significant effect on enhancing cytotoxicity in ER-positive (ER+) MCF-7 breast cancer cells when compared with untargeted ellipticine (control) alone. This effect was explained by the low binding affinity of the conjugate to the ER receptors. As it is now, appreciated from the crystal structure of 17α substituted estradiol-ER-LBD complexes, large substituents such as the ellipticine moiety cannot be well-accommodated within the binding pocket and would dramatically reduce binding affinity. The interactions of the E2–ellipticine conjugate with DNA remained similar to those of ellipticine modified with

dx.doi.org/10.1021/bc300378e | *Bioconjugate Chem.* 2012, 23, 2139–2158

triarylethylene (nonsteroidal antiestrogen) derivatives, suggesting that the steroidal group did not significantly interfere with DNA intercalation.[63] Cytotoxicity studies with assay of MCF-7 in the presence and absence of ^{3}H-estradiol indicated that the E2−ellipticine conjugate exerted both cytostatic and cytotoxic effects, which was primarily due to the pyridocarbazole moiety. The cellular uptake of the conjugate appeared to be independent of interactions with the estrogen receptors; therefore, this was an example in which steroidal targeting and therapeutic effects were not synergistic. [63]

Cushman et al. synthesized a series of E2−ellipticine conjugates with the longer linkers and neutral ellipticine derivatives (Figure 4B). The purpose of these modifications was to position the ellipticine nucleus further from the 17β-hydroxyl group of E2, since SAR of the estrogens indicated that the most crucial units required for binding were the free 3-OH and 17β-OH groups. Besides varying the chain length of the linkers, the authors investigated the point of linker attachment on different regions of the ellipticine ring system. The summary of biological results showed that linker chain length had a major effect on the E2−ellipticine conjugates, with longer linkers having better ER binding properties compared to the shorter linker. Those derivatives assembled with longer linker in group B had RBA values of approximately 0.001% to 0.003%, while the derivative with a shorter linker (Figure A) had RBA of 0.005 (E2 = 100).[63,64] The studies also indicated that attaching E2 to the 2-position of ellipticine promoted the enhancement of potency and DNA binding affinity when compared to the 6- and the 9-positional derivatives of the ellipticine. However, the E2−2-ellipticine conjugate displayed no selectivity toward the ER+ breast cancer cells, suggesting that conjugation did not impart significant ER recognition properties. Again, the most logical explanation for the observed effects is that the linker-ellipticine moiety cannot be readily accommodated in the inducible 17-α binding pocket, thereby compromising the ER-binding capacity. The uptake into the cell and distribution to the nucleus would be passive, assisted perhaps, by the physicochemical properties of the estradiol moiety.[64]

Estradiol−Nitrosoureas Conjugate. The 2-chloroethylnitrosourea (CNU) is highly reactive component found in many antineoplastic chemotherapeutic agents.[67,68] The clinical use of such agents is often limited by the nonselective mechanism of cytotoxicity, and therefore, there have been numerous efforts to develop new compounds with greater target tissue selectivity and lower systemic toxicity.[68] Eisenbrand et al. prepared a series of 2-chloroethylnitrosourea-alanyl (CNU-ala)-estradiol hybrids, in which the point of ligation was via a 3/17-O ether linkage, or at 6α-position (Figure 5).[65] The results showed that, compared with parent CNU-ala, E2-CNU conjugates had 3-fold longer terminal plasma half-life, probably due to the higher lipophilicity of conjugates. Moreover, it was found that the CNU-E2 amino acid esters were also inhibitors of serum esterase, which may have contributed to the longer half-life.[65]

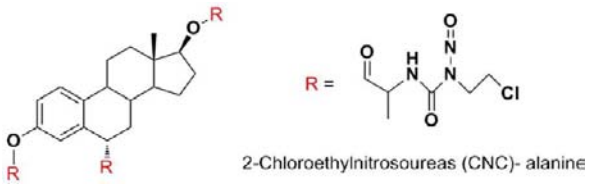

Figure 5. CNU-alanine-estradiol-3, 6α, or 17-ester (**CNU-E2**).[65,66]

The experimental evidence suggested that relative binding affinity to ER by the designed conjugates of CNU-E2 may have played a role in its anticancer activity in hormone-dependent tumors; however, the reported RBA values were relative low for all CNU-E2 conjugates compared to E2 by itself (E2-CNU-3-ester = 4.7; E2-CNU-6α-ester 0.28; E2-CNU-17α-ester.8 and E2-CNU-3 and 17 esters 0.05; comparing to E2 = 100; K_d = 0.09−0.23nM[69,70]). It was noted that E2-CNU-6α-ester had the lowest affinity, even though the 3-OH and 17-OH groups, relevant for ER interaction, were left free. This was due to the fact that the parent 6-hydroxyl estradiol has low RBA itself (6.3%). The RBA value of the 3-ester was the highest in the series, contrary to the greater importance of the 3-OH for ER binding affinity; however, the reported value resulted from rapid cleavage of phenolic ester bond under the incubation condition. This process led to the liberated E2 while it competes for the ER binding sites, causing higher RBA value.[65]

Although the E2-CNU-17 ester had the lowest RBA values (0.8%) compared to other ester conjugates, its biological results indicated that it was the most active antineoplastic agent. The E2-CNU-3-ester displayed lower potency and the 6-ester was essentially inactive. The lack of antineoplastic activity of the latter two compounds (3,6-esters) may correlate with their lower RBA values, and no evidence was provided to show that the conjugates acted via ER. The results showed that E2-CNU−17-ester conjugate had enhanced cytotoxicity and antineoplastic potency compared to the parent CNU-alanine; however, the conjugate was not evaluated in ER(+)-cancer cells. Therefore, an association with ER, for either selective uptake or cytotoxicity, was not conclusively demonstrated.[66]

E2-Geldanamycin Conjugates. Geldanamycin (GDA) is an ansamycin benzoquinone antibiotic that has a well-established role in cancer chemotherapy, including breast cancer.[72] It has been shown that replacement of the 7-methoxy group with an allylamino moiety (7-allylaminogeldanamycin-AAG) improves the in vivo pharmacokinetic properties. Geldanamycin exerts its antineoplastic effect by binding to chaperone-heat shock proteins (HSPs) of cancer cells, leading to degradation of the Hsp90 complex in this case, and therapeutic response. As with most cancer therapeutic agents, its efficacy is limited by lack of target tissue selectivity and systemic toxicity.[73−75] Danishefski et al. prepared a series of 7-*N*-geldanamycin derivatives, linked through the 16α position of estradiol, in an effort to impart ER-selectivity. The linkers were alkyl groups that varied in length, some of which contained an embedded alkene group. The investigators reported that the 2-butenyl-linked E2-GDA conjugate demonstrated the highest ER-binding affinity, but even this value was very low compared to that of E2. The investigators reasoned, based on SAR studies, that substitution at 16α would allow retention of activity for both components—estradiol and Geldanamycin.[71]

The initial biological results of the conjugate with the butanyl linkage demonstrated significant inhibition of proliferation in ER-overexpressed cancer cells. The E2-GDA conjugate showed no effect on IGF1R and reduced activity against Raf-1, suggesting some degree of selectivity for ER vs non ER responses. Nevertheless, the overall cytotoxic activity of the conjugate was less than that of GDA alone, and the biological effects were not blocked by coadministration of E2. Therefore, although the conjugates could be readily prepared, they did not achieve their therapeutic objectives. Neither conjugate has a synergistic ER-mediated effect.

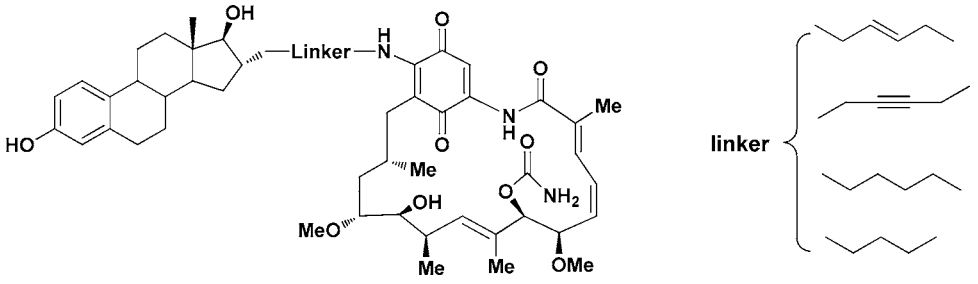

Figure 6. Geldanamycin-Estradiol at 16α (**GDM-E2**).[71]

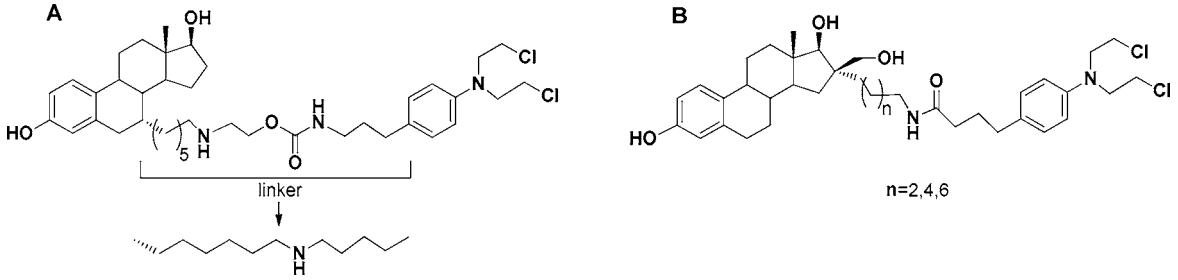

Figure 7. Estradiol–Chlorambucil conjugates (A) 7α (**Chlor-E2**)[76] and (B) 16α (**Chlor-E2**).[77]

E2-Chlorambucil Conjugates. Chlorambucil is an orally active nitrogen mustard, typically used in the treatment of chronic lymphocytic leukemia. Its mechanism of reaction involves cross-linking DNA, leading ultimately to cell death. Although highly effective against certain cancers, the non-selectivity of its mechanism of action limits its use against breast cancer. As a results, several efforts have been made to conjugate this drug to estradiol in order to impart the requisite selectivity while retaining efficacy.[78,79]

In the first approach, described by Essigmann et al., chlorambucil was attached to estradiol at the 7α-position via a series of linkers (Figure 7A). Evaluation of the products indicated that the carbamylated and the amino conjugates retained the highest ER affinity, RBA = 46% and 40%, respectively. The high ER affinity was attributed to having the conjugate adopt a binding mode similar to that observed for the antiestrogenic 7α-undecylamine estradiol derivative, ICI 164,384.[80] For this derivative, the 7α side chain is extended through the 11β-binding pocket, at the surface of which the lipophilic chain undergoes 90° flexion. The conformational adaptation enables the linker to track closely with the surface contours of the LBD, and in the case of the conjugate would make the terminal chlorambucil group available for reaction with the DNA. The studies indicated that the most potent conjugate interacted initially with the DNA, with the recruitment of ER occurring later. The result was that the treated cells were less likely to repair the defects caused by alkylation with the chlorambucil moiety in the presence of ER, lending to enhanced cell death.[76] In this case, the ER–conjugate interaction enhanced the alkylation responses rather than providing a true targeting effect.[76,81] Conjugates with linkers containing other groups, such as amido-, amino-, or guanidine-, between the hexanyl-substituted estradiol and the carboxyl group chlorambucil had lower RBA values.[76] As would be expected, these E2–chlorambucil conjugates demonstrated low cytotoxicity against ER(−)-breast cancer cells.[76,80,81]

In the second approach, described by Gupta et al., chlorambucil was attached at the 16α-position of E2 with alkyl linker groups of varying lengths (Figure 7B).[77] Theoretically, this approach would allow the estradiol moiety to retain the free 3,17β-OH group required for high ER binding; however, as previously noted substitution at the 16α-position with the sterically demanding group generally is detrimental to ER binding and tends to impart other biological properties. This had been observed previously such as with the 16α-Geldanamycin substitution. In this series evaluated, the conjugate with a four-carbon spacer was found to be more active in hormone-independent ER(−) cell lines, e.g., MDA-MB-486, while the conjugate with a six-carbon spacer was more active toward ER-dependent MCF-7 cancer cells. ER binding data were not provided and, because the studies were done without coincubation with estradiol, an ER-targeting effect could not be demonstrated.

In these two series of E2-chlorambucil conjugates, one can see the influence of experimental design. Although both series retain the capacity to alkylate the DNA, only 7α-substituted estradiol derivative retained significant ER binding affinity and, therefore, demonstrable *in vitro* ER-related selective cytotoxicity. The 16α-substituted E2-conjugates were readily accessible in a few steps, whereas the more effective 7α-compounds required a more extensive synthetic scheme.[77]

E2-Nucleoside Conjugates. Nucleosides, their derivatives, and analogues constitute one of the most important therapeutic classes for the treatment of neoplastic disease. As in the case with most anticancer drugs, they are most effective against highly proliferative cells and therefore display no inherent selectivity for hormone responsive tissue. Because the 5-substituted uracils constitute one of the major classes of anticancer nucleosides,[83,84] it was logical to develop an E2–nucleoside conjugate to impart tissue selectivity. Van Lier et al. prepared a series of estradiol–nucleoside conjugates using a palladium catalyzed cross-coupling reaction to ligate the 17α-terminally alkynylated estrogen derivatives with 5-halo-nucleosides (Figure 8).[85] The RBA values of these conjugates were extremely low. Changing the alkyl spacer from two to eight carbons resulted in a modest increase in RBA values from 0.07% to 2.9%. Substitution at the N-1-position of pyrimidine with either a ribose or deoxyribose residue substantially

dx.doi.org/10.1021/bc300378e | *Bioconjugate Chem.* 2012, 23, 2139–2158

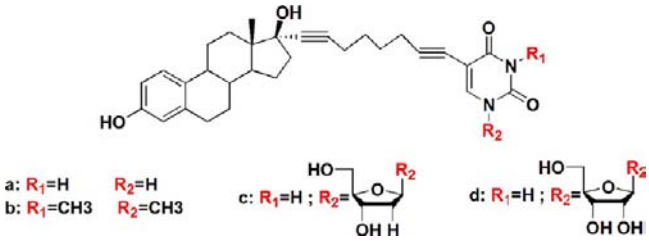

Figure 8. E2–Nucleoside conjugates.[82]

decreased RBA values. As previously described, the 17α binding pocket has a limited capacity for sterically demanding substituents, and the addition of bulky, hydrophobic groups probably cannot be accommodated.[1,23,24,30] Evaluation of these conjugates against ER(−)- and ER(+)-breast cancer cell lines indicated that the compounds showed neither significant enhancement of cytotoxicity nor ER-related selectivity.[82,85,86]

Therapeutic E2–Daunorubicin Conjugates. Daunorubicin is a member of the anthracycline antibiotics family and frequently used for the treatment of advanced breast cancer.[89] In spite of cumulative dose-related cardiotoxicity, the anthracycline antibiotics are still the preferred chemotherapeutic agents for metastatic breast cancer.[90] Because of their beneficial effects, many significant efforts have been undertaken to enhance the target tissue selectivity of these compounds and thereby reduce the undesired cardiotoxicity. Two examples of E2–anthracycline conjugates reflect this effort. In the first study by Hartman et al., the E2–anthracycline conjugate was linked via a 17-oxime (Figure 9A). This conjugate demonstrated

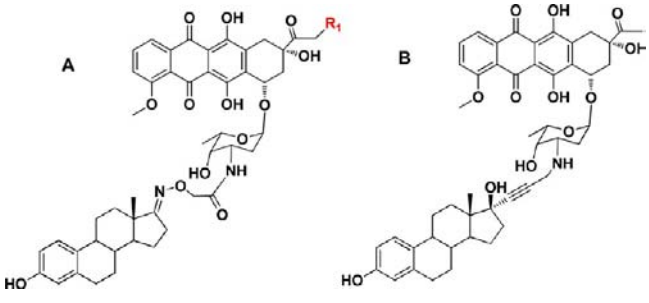

Figure 9. E2–Daunorubicin: (A) 17-imine;[87] (B) 17α-aminopropynyl.[88]

negligible ER binding affinity and no ER-responsive cancer selectivity. As previously noted, loss of 17β-OH group and the additional presence of a bulky substituent at the 17-position are detrimental to ER binding affinity.[87]

In the second approach, the estradiol was conjugated through an 17α-aminopropynyl group to the sugar moiety of the anthracycline.[88] Although more rational than the previous approach, this ligation strategy resulted in a loss of ER binding affinity and reduced cytotoxicity. The conjugate had an RBA value of <1% that of E2 and was significantly less active than daunorubicin in both ER(+)- and ER(−)-breast cancer cell lines. Although the conjugate could be easily synthesized, the approach generated neither ER-related selectivity nor enhanced cytotoxicity. In these examples, the choice of ligation sites on the estradiol component and the chemotherapeutic agent resulted in the loss of biological properties.

E2–Paclitaxel (Taxol) Conjugates. Paclitaxel (Taxol) is a potent antimitotic cancer drug,[92−95] and because the mechanism of action is different from that of most agents, it has become a valuable component in combination therapy. In particular, it has established a major role in the treatment of recurrent, metastatic breast cancer.[96,97] Unfortunately, its solubility characteristics and inherent toxicity compromise its usefulness in the treatment of cancer patients. One approach to improve Taxol selectivity and efficacy for breast cancer, as well as improving its formulation properties, involved its conjugation to estradiol. Kingston et al. described the preparation of a series of E2–paclitaxel conjugates in which the site of attachment moiety occurred at either the 11β or 16α positions of the estradiol and at the 2′, 7′, or 10-hydroxyls of the paclitaxel group (Figure 10). SAR for steroidal estrogens would suggest that substitution at the 11-positions would be tolerated, providing certain conditions were met, but that the 16-position substitution would be detrimental to ER binding (previously discussed in the case of E2-Geldanamycin and E2-Chlorambucil). On the other hand, ester conjugation of paclitaxel at its 2′, 7′, or 10-positions should not affect the drug activity, providing the ester bond underwent hydrolysis at that site to release the free drug within the cell.[98,99]

One of the objectives in the synthesis of the conjugates was not only to improve the formulation properties of paclitaxel because it had poor aqueous solubility, but also to enhance the drug target selectivity. The use of the 2′-hemisuccinate or 7-hemisuccinate ester group was intended to improve the conjugate solubility. The results indicated that the 2′-substituted Taxol conjugates with either the 11β- or 16α-substituted estradiol were less active than Taxol, and demonstrated no significant selectivity for ER(+) MCF-7 cells as compared to the ER(−)MDA-MB-231 cells.[91] Similar results were observed for the conjugates in which paclitaxel was linked to the 11β- or 16α-positions of E2. All conjugates had low ER binding affinity and were less active in the cell assays than paclitaxel. The conjugate of 10-substituted paclitaxel and the 11β-substituted estradiol was 3-fold more active against the ER(+)-MCF-7 cells than the ER(−)-MDA-MB-231 cells, but less potent than paclitaxel alone in either cell line. In summary, the investigators demonstrated the ability to prepare a variety of E2–paclitaxel conjugates, designed to explore the contributions of different attachment sites and linker properties, but were unsuccessful in achieving enhanced potency and/or ER-related cytotoxicity.[91,98,99]

E2–Photodynamic Therapy (PDT) Conjugates. Photodynamic therapy (PDT) is a form of cancer treatment that relies upon the accumulation of a photosentisizer into cancerous tissues followed by localized irradiation. Irradiation excites the photosentisizer to generate radicals, leading to reactive oxygen species (ROS) that cause damage to cellular components, ultimately leading to cell death (apoptosis). This effect is typically achieved through the use of metalated porphyrin derivatives, or less frequently through chemically reactive species that, upon appropriate activation, lead to the generation of radicals. One of the first E2-PDT approaches was developed by van Lier et al., in which estradiol was modified with a alkynyl linker at the 17α position and then conjugated with a photosentisizing porphyrin or phthalocyanine derivatives (Figure 11A). Although the synthesis of the conjugate using spacers of different lengths was successful, the RBA values of the conjugate were dependent on the specific structure of the spacer. The highest RBA values were reported by those lipophilic E2-PDT conjugates via using the aliphatic alkynyl and benzylic linkers. The RBA increased with increased spacer length, for example, 17α-(2-propynyl)estradiol-PDT RBA =

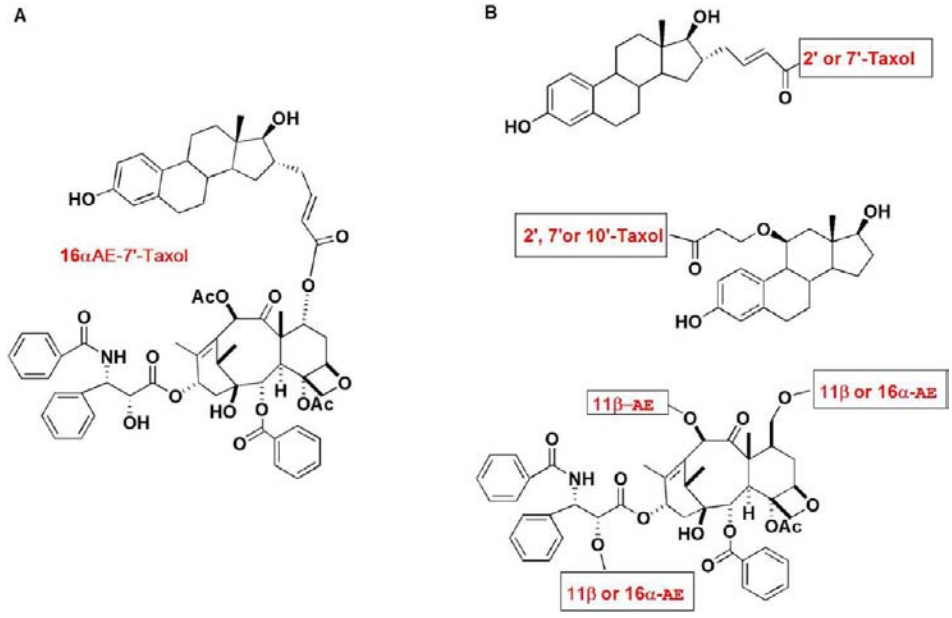

Figure 10. E2−Paclitaxel (Taxol) Conjugates:[91] (A) 16α-E2 ether linkage at 7′-O-Taxol; (B) derivatives of E2−Paclitaxel conjugates.

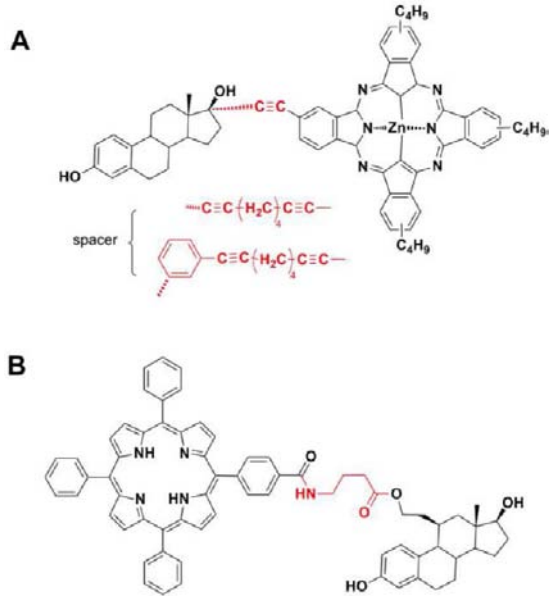

Figure 11. E2−Photodynamic therapy (PDT) conjugates: (A) 17α;[100] (B) 11β.[101]

1.35%; 17α-(2-buta-1,7-diynyl)estradiol-PDT has RBA = 3.08%; and 17α-phenyl-(3-buta-1,7-diynyl)estradiol has RBA = 8.54% (Figure 11A). Although the RBA values were also slightly dependent on the attachment position at phthalocyanines, the overall ER binding of these derivatives were relatively poor (<0.2%). As a consequence, the biological evaluation of the conjugates indicated that there was no synergy between the steroidal group and PDT component.[102,103]

In the second approach, Ray et al. conjugated the PDT component to an established, high-affinity 11β-substituted estradiol derivative.[104] Evaluation of the binding properties of the E2−PDT conjugate indicated that most of the ER binding affinity was lost (RBA = 0.4%). The conjugate was evaluated in ER(+)-MCF-7 cells as well as in other cancer cells that overexpress ER, but the results demonstrated no pattern of ER-dependency. An analysis of the results based upon the current knowledge of the ER ligand binding pocket suggests that the linker between the PDT component and the 11-β position of estradiol was too short to be readily accommodated. As a result, the properties of the PDT component dominated the biological responses.[105,106]

An alternate approach to generating radicals and the reactant ROS in situ is via the Bergman cyclization of ene-diyne moiety. This mechanism is presumed to be the operant mode by which the ene-diyne-containing antibiotics, such as Calicheamicin and Neocarzinostatin, exert their cytotoxic effects. While extremely potent, lack of tissue activity severely limits their clinical utility. Conjugation to tissue-selective monoclonal antibodies, e.g., MyloTarg, has been one successful method for limiting off-target toxicity. Jones et al. have explored simpler ene-diyne derivatives, as shown in Figure 12, as an approach to developing selective radical-generating therapeutics. Introduction of thermoreactive ene-diyne ester and ether derivatives at the 3-

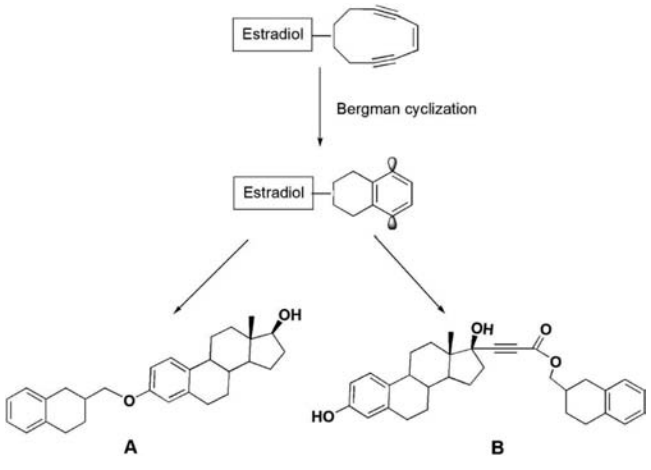

Figure 12. E2−Enediyne conjugates as substrates for Bergman cycloaromatization:[107] (A) 3-ether; (B) 17α-alkynyl.

dx.doi.org/10.1021/bc300378e | *Bioconjugate Chem.* 2012, 23, 2139−2158

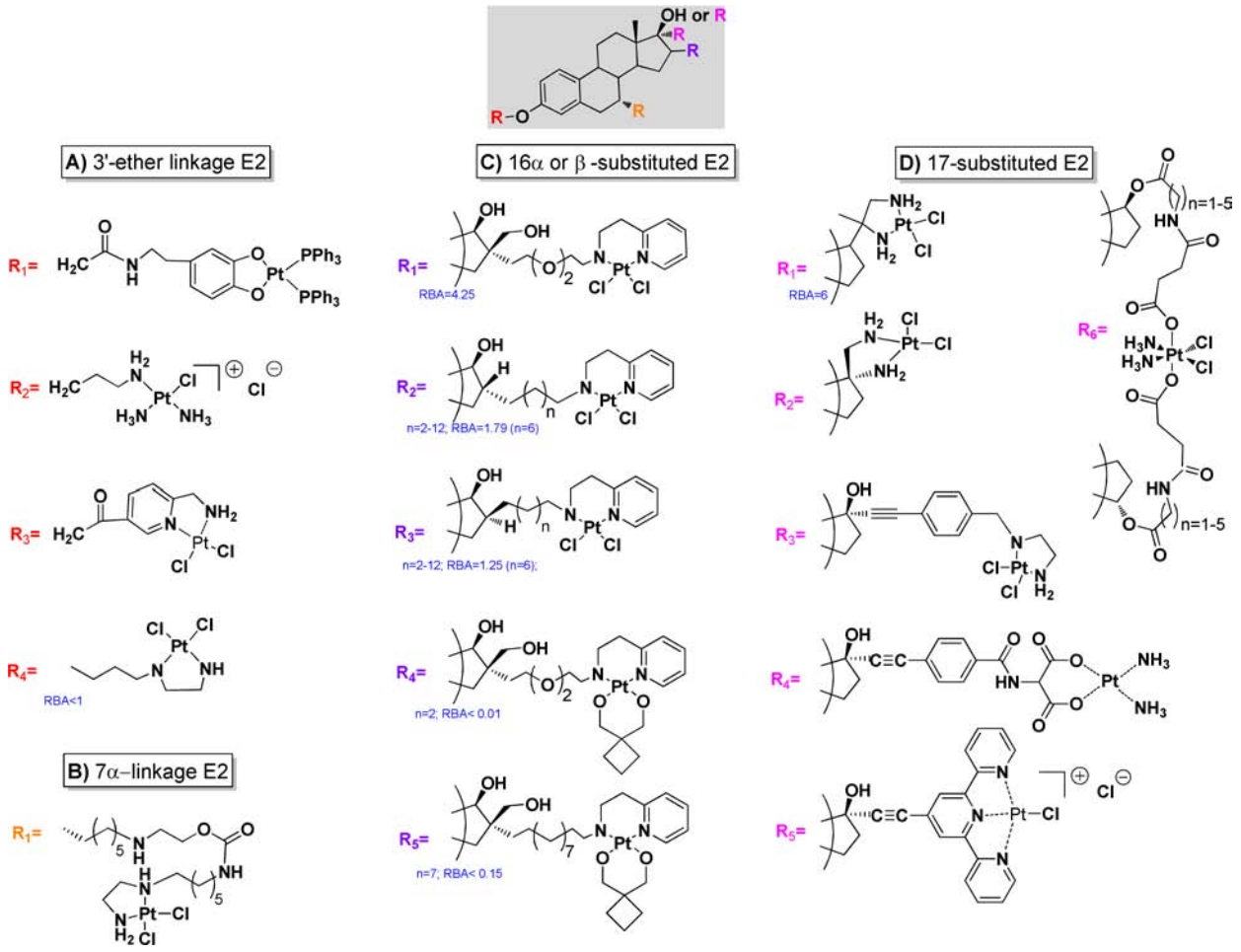

Figure 13. Cisplatin–E2 conjugates: (A) 3′O-AE-$\mathbf{R}_1$,[111] -$\mathbf{R}_2$,[112] -$\mathbf{R}_3$,[2] and -$\mathbf{R}_4$;[113] (B) 7αAE-$\mathbf{R}_1$;[114] (C) 16′AE-$\mathbf{R}_1$,[115] -$\mathbf{R}_2$,[116,117] -$\mathbf{R}_3$,[113,118] -$\mathbf{R}_4$,[119] and-$\mathbf{R}_5$;[117,119,120] (D)17α AE-$\mathbf{R}_1$,[121,122] -$\mathbf{R}_2$,[113,123] -$\mathbf{R}_3$,[124] -$\mathbf{R}_4$,[124] -$\mathbf{R}_5$,[122] and -$\mathbf{R}_6$.[125–127]

and 17α-positions of estradiol was accomplished in good overall yields.[107–110]

As anticipated, based upon the estrogen SAR, the observed RBA values were extremely low—the ether-linked conjugate (Figure 12A) had RBA = 0.003%, and the 17α-alkynyl conjugate (Figure 12B) RBA = 0.5%. Therefore, lack of selectivity for ER(+)-breast cancer cells was not unexpected.[107]

E2–Platin Conjugates. The discovery of cis-platin as an agent for the treatment neoplastic disease represents one of the remarkable developments in cancer chemotherapy. This compound and its derivatives now comprise a major component in the treatment regimens for many forms of cancer, including breast cancer. In spite of its inherent activity, its usefulness is limited, like many anticancer drugs, by its lack of tissue selectivity and systemic toxicity. In the field of breast cancer research, a number of efforts have been undertaken to develop E2–platin conjugates that would retain the anticancer activity of cis-platin but demonstrate the ER-selectivity of estradiol. A recent review specifically described the metalated-estrogen conjugates,[2] and therefore, only the relevant findings will be summarized here.

As shown in Figure 13, a substantial number of E2–platin conjugates have been prepared and evaluated as potential therapeutic agents. Conjugates in which the substituent was ligated at the 3- or 17β-position typically demonstrated very low ER-binding affinity. Although significant cytotoxic activity was retained with these derivatives, such effects could not be attributed to specific ER targeting events. Even the novel Pt(IV) complex prepared by Lippard et al. failed to demonstrate significant ER(+) selectivity. Substitution at the 16α-position, as reported by Berbube et al. generated a novel series of conjugates. These compounds were active in several cancer cell lines, but demonstrated little ER-based selectivity. The absence of an ER-related response was not surprising given the low ER-binding affinity of the E2–platin conjugates.

The more interesting E2-platin-estradiol conjugates were those in which the metal-containing group was attached at either the 7α- or 17α-position, as these substitution patterns are known to be more sterically tolerant. As with the mono and terpyridyl ethynyl estradiols, the steric interference with the ER-binding pocket was much greater with the bulkier substituent; thus, the RBA of the monopyridyl E2–platin conjugate is 10-fold higher compared to that of the terpynydyls derivative. However, these conjugates displayed little cytotoxic activity or ER-based selectivity.

Essigmann et al. described the synthesis of (E-en)Pt(II)Cl_{2n}, a bifunctional cisplatin conjugate consisting of ethylendiamine dichlororidoplatinum (II) tethered to the 7-position of estradiol (Figure 13B).[114] The investigators suggested that, following internalization of the conjugate, hydrolysis of the carbamate group in the linker would release the biologically active cis-platin moiety. This E2–platin conjugate retained significant ER-binding affinity (RBA = unreported) and demonstrated enhanced cytotoxicity in ER(+) breast cancer cell lines as

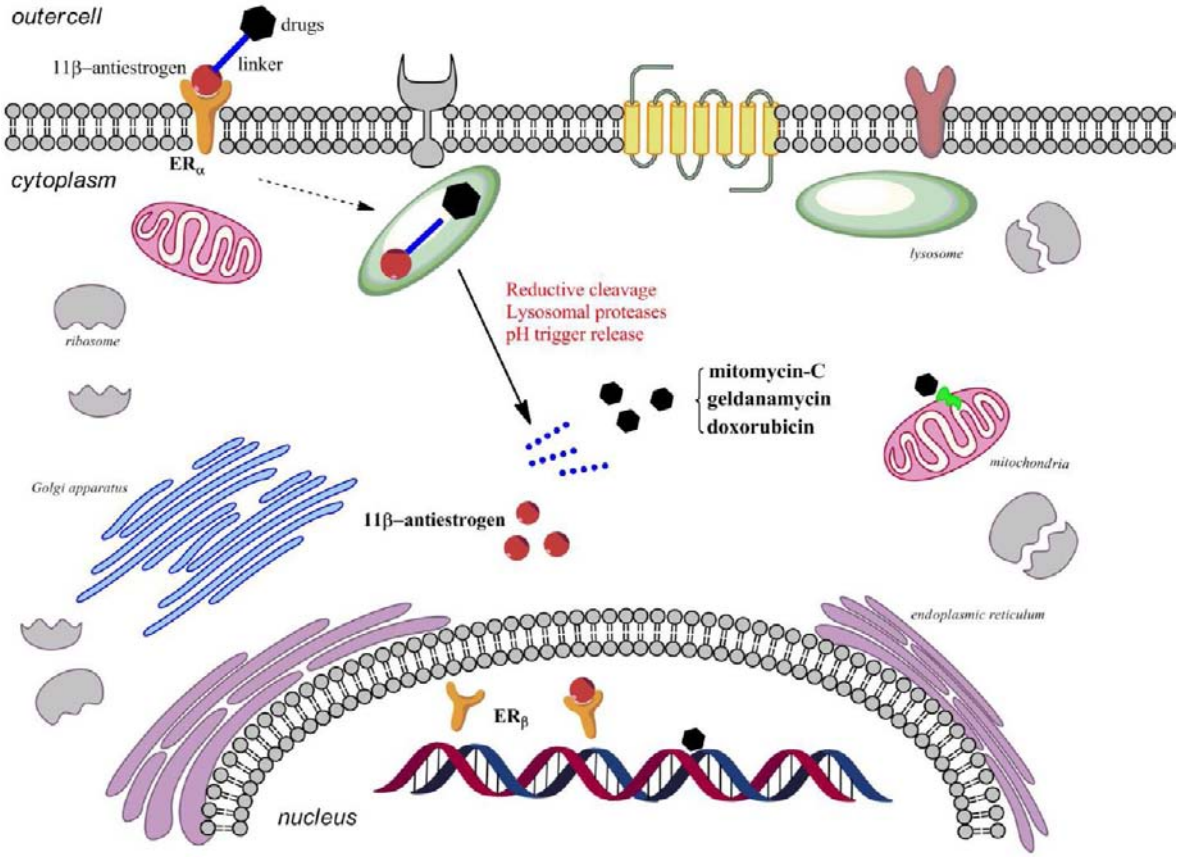

Figure 14. Therapeutic strategy of estradiol–drug conjugate ligated through 11β-position with modular linkers. (*Note: there was initially not any attempt to anticipate the need for dissociation of E2 and drug components.*)

compared to cis-platin alone. The study did not compare the efficacy of the conjugate in ER(−)-breast cancer cells, and therefore, target cell selectivity was indeterminate. Nevertheless, this constituted one of the first studies in which efforts to impart ER-selectivity to inherently nonselective anticancer agents were moderately successful. Unfortunately, there have been no subsequent published studies following these preliminary results.

Miscellaneous E2 Drug Conjugates. Most of the examples described so far in this review have employed a well-recognized cancer chemotherapeutic agent, e.g., antibiotic, DNA intercalator, antimitotic, as the conjugate partner for estradiol. Other recent examples have used therapeutic components with noncancer targets, in which bioactivity or selectivity may be enhanced through ER-based targeting. Kim et al. evaluated the effects of E2-conjugates containing a proteasome degrading peptide.[121] Peptides that contain an E2 regulator motif promote ubiquitination of proteins, leading to their degradation. In this study, the active pentapeptide was ligated directly to the 17β-OH using esterification, while introduction of the pentapeptide at the 16α- or 7α-position of estradiol required a 10–12-step synthesis to yield the target E2–pentapeptide conjugate. All of the derivatives demonstrated retention of protosomal degradation activity indicating that the presence of the steroid did not interfere with the action of the peptide. However, only the 7α-substituted estradiol-based conjugate demonstrated significant ER-binding affinity and therefore was selected for subsequent optimization studies.[128]

Katzenellenbogen et al. reproted the preparation and evaluation of an E2 conjugate in which the second component would recruit FKBP, an abundant intracellular protein. The strategy was based on the premise that the estradiol component would initially target the ER, whereupon the second component would recruit FKBP rather than the usual coregulatory protein.[129] The peptidomimetic SLF moiety was conjugated at the 17α-position of estradiol using both short and long linker groups. The RBA value for the conjugate with the short linker was 1.5%, while no value was provided for the longer linker variant. Although initial studies indicated that the E2 conjugate was capable of simultaneous binding to both ER and FKBP, it was unable to disrupt the formation of ER–coactivator complexes *in vitro*.[129]

■ DEVELOPMENT OF DRUG–ESTRADIOL CONJUGATES LINKED THROUGH THE 11β-POSITION

Having conducted this review of existing estradiol (E2)–drug conjugates, we determined that none yet satisfied the criteria needed to establish their potential as therapeutic agents. We undertook to develop our own approach to develop such an agent. We had prior experience in the design, preparation, and evaluation of high-affinity estrogens as potential imaging agents for breast cancer, which required many of the same concerns as targeted drug delivery. Our extensive work with 17α-(substituted vinyl) estradiol, both published and unpublished, demonstrated the limitations imposed by substituents at that position.[55,130,131] Therefore, we focused our efforts on the 11β-position of estradiol, a site that had received significantly less

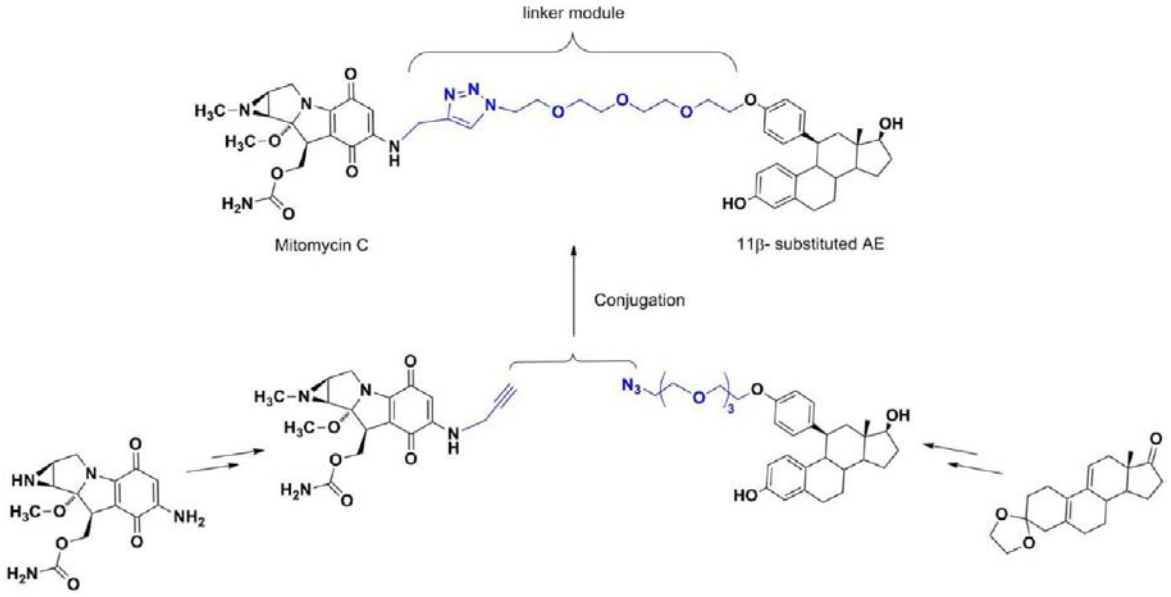

Figure 15. Mitomycin–antiestrogen conjugate ligated at 11β position.

attention. SAR for steroidal estrogens indicated that small substituents at that site conferred agonist activity, usually with an increase of binding affinity. Alkyl or heteroalkyl groups beyond 3–4 atoms in length imparted ER antagonist properties, often without a significant loss of binding affinity.[131,132] Unsubstituted aromatic groups at the 11β-position also were agonists, while more highly substituted derivatives expressed antagonist properties. Although publications described the synthesis and favorable biological properties of these 11β-substituted estradiol derivatives (RU39411 and RU58668), they were not translated into clinical use.[133] The more demanding chemical syntheses needed to prepare these compounds made them less competitive commercially, and therefore, nonsteroidal antiestrogens, such as tamoxifen and raloxifene, or the simpler steroidal antagonist, faslodex, gained established roles in endocrine therapy.[54,55,133,134]

In our program to develop new E2–drug conjugates, the 11β-aryl estradiol-based antiestrogens (AE) possessed several advantages. We established our criteria that the final conjugate would need to retain high ER affinity, express ER antagonist properties, have enhanced anticancer activity compared to the parent drug, show selectivity for ER-expressing cancer cells, and have a linker that improved pharmaceutical properties.

The choice of the 11β-aryl substituent would permit the parent estradiol scaffold to occupy the default ligand binding pocket. Previous SAR studies indicated that the 11β-aryl group occupies a secondary pocket that extends to the surface of the receptor.[55,133] In the antagonist conformation, the 4′-position of the aryl group would access the solvent-exposed space and therefore should permit further conjugation without loss of affinity or loss of efficacy. We would then be able to prepare derivatives of therapeutic agents that could be conjugated to the 11β-aryl estradiols through the 4′-position of the aryl group. Our actual strategy called for the modular assembly of the ultimate conjugate by using convergent synthesis. We would prepare specifically functionalized 11β-aryl estradiol derivatives and functionalized therapeutic agents and then ligate them, using "click" chemistry to form the final drug–estradiol conjugate.[135]

In our first study in this program, we developed the synthetic strategy for the estradiol component of the conjugate. Starting from the estra-4,9-diene-3,17-dione monoethylene glycol ketal precursor, we prepared a series of 11β-(4-substituted phenyl)-estradiols in good overall yields. Evaluation of the products for ERα- and ERβ-LBD binding affinity indicated that the compounds demonstrated high binding affinity (RBA = 20–80%) compared to estradiol and that they were ER subtype nonselective. The studies also indicated that 4-substituents on the phenyl ring that were larger than methoxy were ER antagonists. Ligation of a prototypical quinone derivative using "click" chemistry also proceeded in high yield to give a product that retained high affinity and antagonist properties. Therefore, our hypothesis that we could use the 11β-aryl estradiol scaffold as the basis for developing the proposed drug–estradiol conjugates appeared to be valid.[54,55,134,135]

E2–Mitomycin C Conjugate. The first target was the preparation of an E2–mitomycin C conjugate. We chose mitomycin C as the bioactive component based on its clinical use for the treatment of advanced breast cancer and its potential reactivity through the quinone group.[136–138] We realized that although E2–mitomycin C conjugates had been explored previously, lack of success was largely due to factors we believed were surmountable.[139] Mitomycin C belongs to the class of compounds that require metabolic activation, i.e., quinone reduction, prior to alkylation of the DNA,[140] and it also displays a degree of sequence selectivity based upon its molecular structure.[141] Structural modifications at the 7-amino group also display potent anticancer and DNA alkylating activity, suggesting that incorporation of a pendant group at that position would be tolerated.[142,143] As a result, we selected as an initial conjugate, a compound (Figure 12) which would incorporate all of the structural features essential for targeted activity—the antiestrogenic 11β-(4-alkoxyaryl) estradiol for ER binding, the alkylamino mitomycin C for DNA binding, and the hydrophilic, biologically compatible tri(ethylene glycol) linker to span the two functional groups.[144] The target conjugate was successfully prepared using a convergent synthesis.

The antiestrogen (AE)-Mit C competitively displaced estradiol from ERα-LBD with RBA value of 7 ± 1%. The

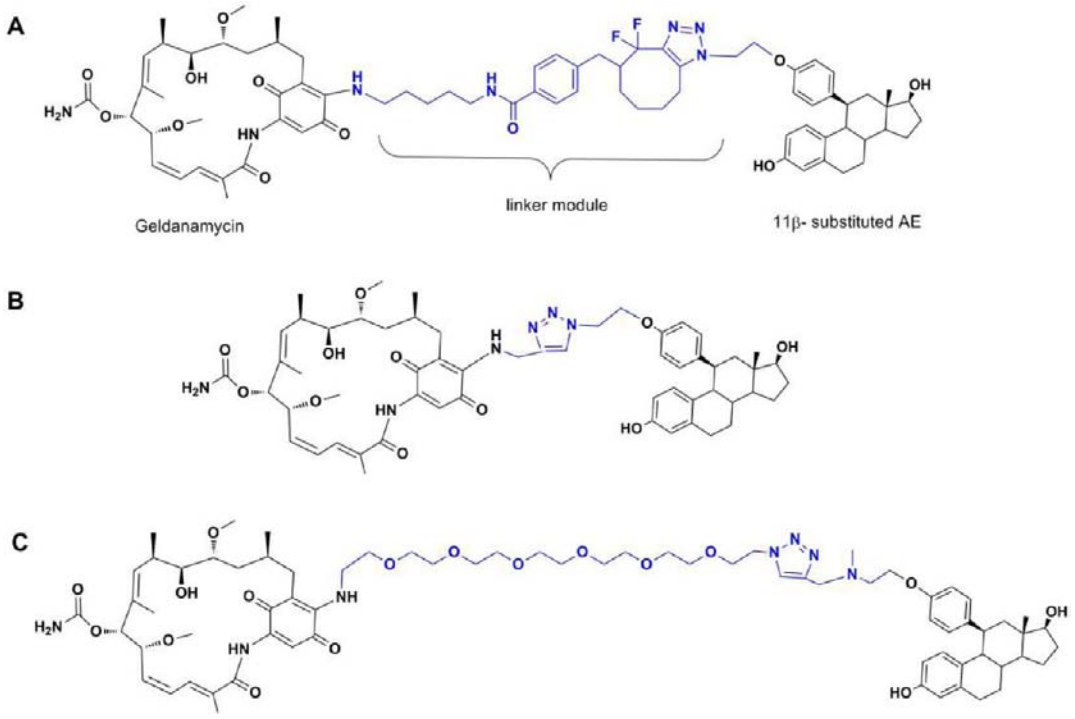

Figure 16. Antiestrogen (AE)−Geldanamycin conjugates, ligated at 11β position of E2.

azido-estradiol intermediate, in the same assay system, had an RBA = 26 ± 9%, indicating that the presence of the additional mitomycin C group at the terminus of the linker did not have an adverse effect on overall ER-LBD binding.[145−147] The hybrid agent did not stimulate the production of alkaline phosphatase, an efficacy assay, at any dose level; however, the compound potently blocked the stimulation caused by 1 nM estradiol. Again, the results demonstrated that the presence of the mitomycin C moiety did not interfere with the receptor binding or transcriptional response. The N-propargyl-porfiromycin component (Mit C, Figure 15), as expected, had negligible binding affinity to the ERα-LBD (RBA = 0.3 ± 0.2%), and low levels of inhibition in the alkaline phosphatase assay. Assays evaluating the effect of the conjugate on cell proliferation ER(+)- MCF-7 and ER(−)-MDA-231 breast cancer cell lines indicated that the cytotoxicity activity was comparable to that of mytomicin C alone. Therefore, the conjugate met the criteria of retaining ER high affinity and antiestrogen efficacy, but it did not enhance the cytotoxicity effect, nor did it demonstrate selectivity for ER-expressing cells.

Steroidal Antiestrogen−Geldanamycin Conjugates. The objective for our second study was a series of conjugates comprising of the steroidal antiestrogen linked to the quinone-containing drug, geldanamycin. Although the previous E2−geldanamycin conjugates had been unsuccessful, the failure was largely due to the position on estradiol to which the geldanamycin moiety had been appended. Geldanamycin is a quinone-containing antibiotic which can undergo modifications on the quinone ring without loss of activity. Because further modification with a linker group appeared to be well-tolerated, we proposed to employ different linkers ligated to the 11-β steroidal antiestrogen and evaluate the biological responses.[148,149]

The AE-GDA hybrids were assembled with our modular methodology using three different linkers (Figure 16). Two variations of the steroidal antiestrogen were also prepared. The first variation used the 11β-(4 azidoethoxyphenyl) group that we had previously synthesized. For the second, we introduced the propargylaminoethoxyphenyl group to more closely mimic the side chain found in the steroidal antiestrogen RU39411. The geldanamycin compounds were prepared by displacement of the methoxy group on the quinone moiety using the appropriately substituted amine (propargyl, ω-azido-oligo-ethylene glycolyl) or in two steps using the diamine followed by acylation with the gem difluoro-activated cyclooctynol. The normal or "copperless click" ligation reaction gave the AE−geldanamycin conjugates in good overall yields.

These conjugates were tested for cytotoxicity against two cell lines, the ER(+)-MCF-7 and the ER(−)-SKBR3, which also overexpresses HER-2. The preliminary results indicated that the conjugates demonstrated no significant selectivity in cytotoxicity between the two cell lines; for example, the IC_{50} of compound **13B** was 1.2 ± 0.09 μM in MCF-7 cells, comparable to that for SKBR3 cells,(IC_{50} = 0.71 ± 0.16 μM). The IC_{50} values were also not better than geldanamycin alone in any of the cell lines tested. Nevertheless, the conjugates retained cytotoxic activity and the results provided insights on the influence of the linker group, as there appeared to be a relationship on the distance between the two components and the activity of the conjugate. The results suggested that the longer tether was better.

The results from these two studies provided several important contributions to the design of future conjugates. First, the use of the steroid 11β-substituted phenyl estradiol scaffold tolerated substitution without loss of antiestrogen activity; however, it was not translated into ER-related selectivity. Second, rational substitution of linking groups onto the therapeutic agents did not significantly modify their cytotoxic effects; however, addition of the steroidal unit did not increase activity. Third, intermediate to long linkers were more effective in retaining activity for both components; however, no synergy between the two has been obtained. Therefore, our

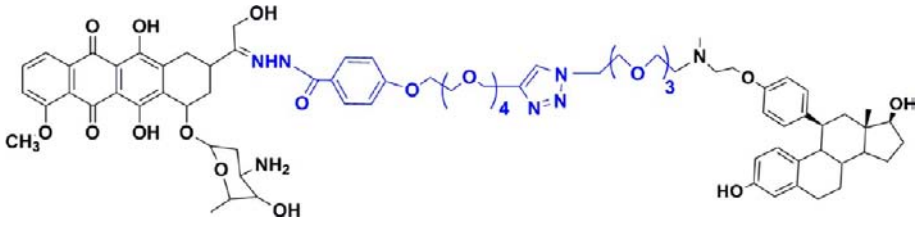

Figure 17. AE−Dox conjugate substituted at 11β position of E2.

solution to the problem would involve discrete alterations in each aspect of the overall process. As the following example will demonstrate, the most significant change would involve the use of a dissociative linker which would allow each terminal component to act independently within the cell. In this regard, our initial choice of a steroidal antiestrogen was critical, as steroidal agonists at the concentrations used in these studies would tend to promote cell proliferation, while antagonists were cytostatic agents.

AE−Doxorubicin Conjugate. Our subsequent study was undertaken to resolve two issues that we had observed with the previous conjugates. Central to this approach was the selection of a potent anticancer drug for which dissociation-release mechanisms had previously been used. We selected doxorubicin, not only because it has been widely used for treatment of advanced breast cancer. Although it had been used in other conjugation studies, those ligation studies had focused on the daunosamine moiety and not on the ketone moiety. Schally et al. had shown that hormone peptide−doxorubicin conjugates ligated through the ketone demonstrated intracellular release following endosomal uptake. Therefore, we chose to use a variation of the pH-sensitive, hydrazone approach as the basis for designing our antiestrogen (AE)−doxorubicin (Dox) conjugate.[150,151]

In the design AE−Dox conjugate, we selected the steroidal antagonist RU39411 as our ER targeting component, as we had shown previously that *N*-oligoethylene glycolated derivatives of the parent compound retained high ER affinity and were potent, nonselective ER antagonists.[152,153] Although the concept of doxorubicin hydrazones is well-documented,[154−157] we still needed to develop a specific oilgoethylene glycol derivative to form the requisite hydrazone. Our use of half-linkers to functionalize and ligate the targeting and therapeutic termini had been developed in the earlier mitomycin C and geldanamycin and was modified to accommodate the pH-sensitive hydrazone moiety. In this approach (Figure 17), we predicted that the resultant AE−Dox conjugate would retain antiproliferative effects comparable to doxorubicin in all cancer cell lines, but demonstrate enhanced antiproliferative effects in cell lines that overexpress ER.

The synthesis of the individual half-linkers and the antiestrogen component proceeded in high yields as did the subsequent preparation of the intermediate doxorubicin−hydrazone, and the azido OEG antiestrogen also proceeded well together with required modified agents. Final ligation using "click" chemistry gave the pure AE−Dox conjugate in 80% yield for biological studies. The results of biological assay are summarized in Table 1. As can be seen, the AE−Dox conjugate showed a significant enhancement of cytotoxicity (approximately 70-fold) in ER(+)-MCF-7 cells compared to doxorubicin alone or the doxorubicin−hydrazone. The IC_{50} for the AE−Dox conjugate was 0.011 μM compared to 0.602 μM and 0.597 μM for the free Dox and the linker−Dox, respectively.

Table 1. Inhibition Concentration, IC_{50}[a] (nM), of Various Dox Compounds[135]

compounds	MCF-7	MDA-MB-231	MCF-7 (+E2)
Dox	602 ± 20	89 ± 7	585 ± 30
Dox-Linker	597 ± 20	86 ± 5	594 ± 20
AE-Dox	11 ± 6	90 ± 8	589 ± 3

[a]The IC_{50} was estimated by using *GraphPad* 3-parameters curve fitting for 24 h drug exposure data points. All values represented here were evaluated in a duplicate of a triplicate count. Standard deviation was measured from the mean of six wells for each compound.

Although coincubation with estradiol (E2) had no effect on either Dox or Dox-hydrazone, E2 reduced the IC_{50} of the AE−Dox conjugate to Dox levels, clearly indicating the participation of ER-mediated event in the cytotoxicity process. For the ER(−)-MDA-MB-231 cell line, there were no differences among the three doxorubicin formulations, and coincubation with estradiol had no effect on this cell line (not shown); therefore, cytotoxicity in this cell line was an ER-independent process. The antiestrogen and the antiestrogen half-linker had no cytotoxic effects on either cell line at concentrations less than 50 μM (results not shown).

To characterize the activity of the AE−Dox conjugate further, we evaluated the conjugate using fluorescent activated cell sorting (FACS), in both the presence and absence of E2 (Figure 18). The AE−Dox conjugate demonstrated enhanced cell binding compared to Dox in ER(+)-MCF-7 cells as in the presence of E2; cell binding was similar to that of Dox alone. With ER(−)-MDA-MB-231 cells, there were no significant differences in cell binding between Dox and AE−Dox, and the binding was unaffected by incubation with E2. The results demonstrated the marked targeting effect imparted by the presence of the steroidal antiestrogen component in the conjugate and were consistent with a selective interaction between the membrane ER and the conjugate.

We subsequently examined the intracellular localization of the AE−Dox conjugate using the fluorescent property of the doxorubicin moiety. The results (Figure 19) support the concept that ER targeting enhanced uptake of the AE−Dox conjugate in ER-positive breast cancer cells. The cellular localization AE−Dox and Dox was evaluated in ER(+)-MCF-7 cells in the presence and absence of ES. The low level of fluorescence in cells treated with Dox alone (Panel B) is associated primarily with the nucleus, as doxorubicin is a known DNA intercalating agent. AE−Dox (Panel C) shows a significantly enhanced uptake within the ER(+)-MCF-7 cells, compared to Dox alone (Panel B), showing the extent to which the AE component of the conjugate facilitated uptake. The coincubation of the cells E2 (Panel D) decreased the uptake of the AE−Dox (Panel B), confirming that uptake is an ER-mediated process. These results provide a basis for interpreting the initial cytoxicity data. ER-facilitated uptake of the AE−Dox

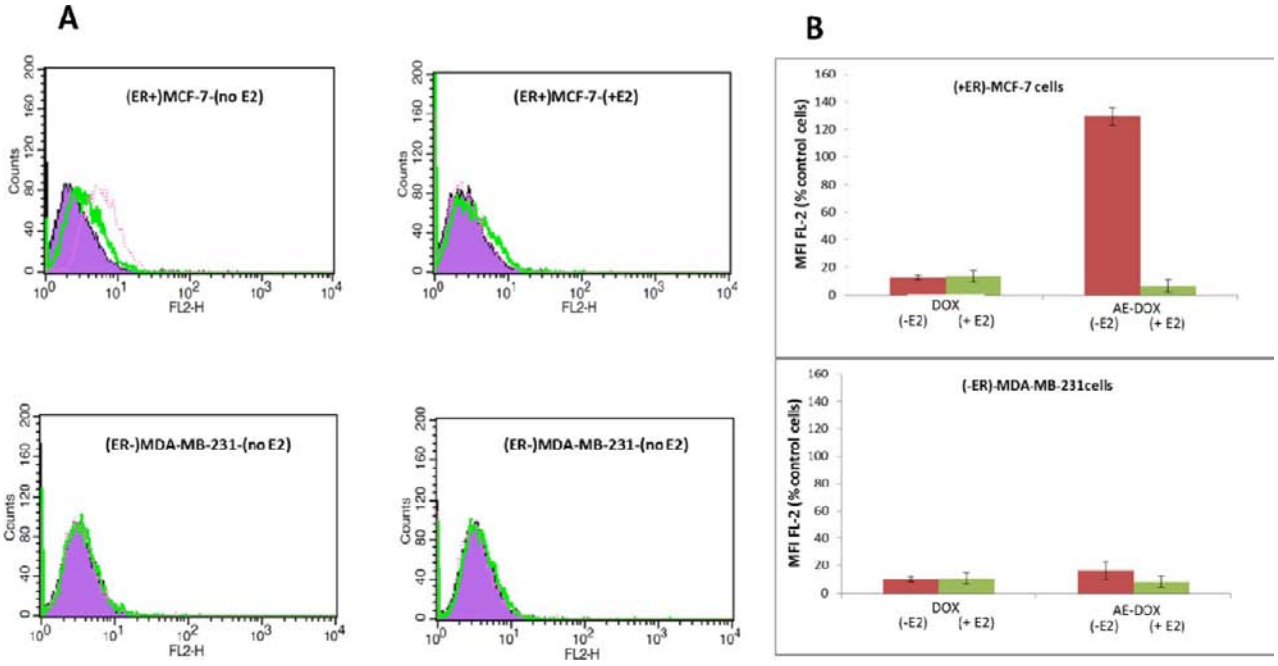

Figure 18. FACS analysis of ER(+)MCF-7 and ER(−)MDA-MB-231 cells. (A) Histogram analysis of cells treated with 0.1 μM of Dox and AE−Dox with and without ES; (purple) cells only (green) Dox treated cells and (red) AE-Dox treated cells. (B) Percentage of Dox-positive cells in ER(+)MCF-7 and ER(−)MDA-MB-231cells; *P < 0.01 (Dox vs AE-DOX (-E2)); §P < 0.01 (AE-Dox (-E2) vs AE-Dox(+E2).[135]

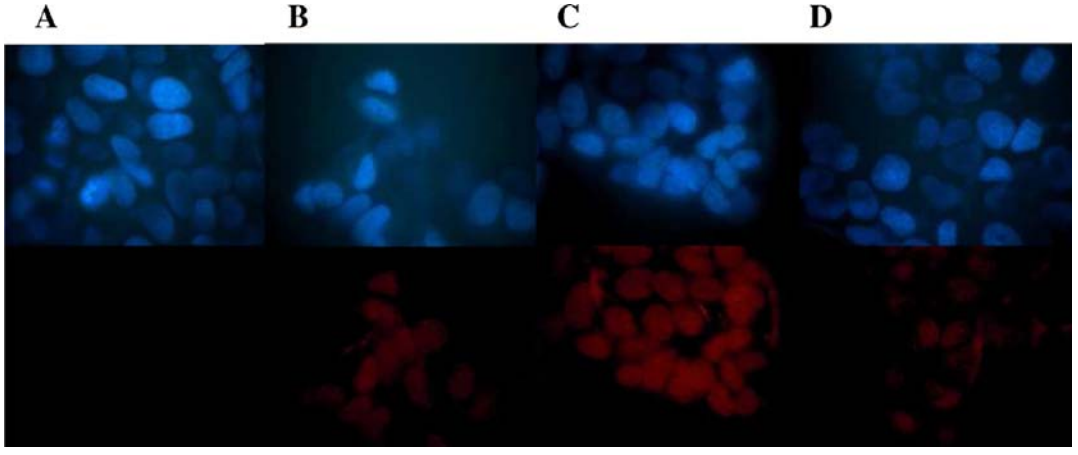

Figure 19. Fluorescence microscopy images ER(+)MCF-7 cells treated for 1 h with 0.1 μM of (B) Dox; (C) AE−Dox; (D) AE−Dox after pretreatment with 50 μM estradiol; and (A) untreated cell: Hoechst fluorescent (upper panel), Red fluorescence (lower panel).

conjugate would generate a higher intracellular concentration, leading to greater Dox release and therefore more rapid cell death.[135]

In summary, the AE−Dox conjugate provides the most impressive illustration of synergy between a ER-targeting components and a therapeutic agent to date. The cytotoxicity data indicated the AE−Dox conjugate was 70-fold more potent than Dox alone in ER(+)-MCF-7 cells, an effect that was blocked by the presence of estradiol. FACS studies on both cell lines supported the contention that the initial interaction was with the membrane ER. Subsequent studies using fluorescence microscopy in MCF-7 cells further supported the hypothesis that the uptake proceeded via a membrane ER-mediated effect, leading to an enhanced intracellular accumulation of Dox. Within the cell, the pH-sensitive hydrazone release mechanism led to elevated levels of free Dox, thereby eliciting the observed cytotoxicity. The results have generated additional studies designed to characterize the individual steps of the process.

■ CONCLUSIONS

This review has described the process of targeted drug delivery using the evolution of steroid−drug conjugates in breast cancer. As an example, the key points involve the recognition that successful agents require much more than just chemical ligation of a targeting group to a therapeutic drug. In the case of ER-targeted agents, the recognition of the role of membrane ER provided not only an explanation for earlier failures, but also a strategy for ultimate success. All efforts to use binding to the agonist conformation of ER resulted in failure because investigators were unable to introduce linking groups onto the estradiol scaffold without seriously compromising binding affinity. As a result, uptake into cells proceeded via passive diffusion and provided little or no selectivity between ER-

expressing and ER-negative cell lines. Only the 7-α and 11-β-substituted antiestrogenic steroids retained sufficiently high ER affinity to bind to the mER and be taken up via endocytotic processes. Even with high-affinity steroidal antiestrogens, ER-selective responses were not always observed, suggesting that physicochemical properties of the overall conjugate, which may favor passive diffusion vs receptor-mediated uptake, remain to be evaluated. Linking strategies also played an important role. Most of the approaches described in the review used relatively simple, chemically stable linear linkers to ligate the two components. Unfortunately, once within the cell, the conjugates underwent a competition over which terminus would predominate as a more active terminal. The ER-seeking group, as previously indicated, no longer had a high affinity for ER (nuclear or cytoplasmic) but in some cases could be recognized by other steroid binding protein, such as those involved with estrogen metabolism (e.g., sulfotransferase, oxidases, reductases). The therapeutic component would be recognized by its binding site(s); however, its effectiveness would be moderated by the attached linker and steroidal component. While many of the conjugates retained significant activity compared to the parent therapeutic drug, cellular responses due to the steroidal component were rarely reported. The most promising results were obtained when the conjugate incorporated a mechanism for dissociation, an approach suggested by other drug-targeting strategies. This approach would allow the two components, and particularly the therapeutic component, to exert an independent effect. As our study demonstrated, incorporation of all these features, using a carefully developed research design, gave a conjugate that recognized the membrane ER, underwent endocytosis to provide an acidic environment that promoted hydrolysis of a hydrazone, and released free doxorubicin at a level capable of causing cytotoxicity to breast cancer cells. Future studies to demonstrate the in vivo efficacy and to translate this approach to other drugs and other cancer cell lines are in progress.

AUTHOR INFORMATION

Corresponding Author

*E-mail: r.hanson@neu.edu.

Notes

The authors declare no competing financial interest.

ACKNOWLEDGMENTS

We acknowledge the financial support from the Department of Defense Congressional Directed Medical Research Programs (W81XWH-10-1-0262[K.-L.D.] and W81XWH-06-0551[RNH]), Department of Energy (DE-SC0001781[RNH]), and Susan G Komen Foundation (BCTR0600659[RNH]).

REFERENCES

(1) Jordan, V. C., and Brodie, A. M. H. (2007) Development and evolution of therapies targeted to the estrogen receptor for the treatment and prevention of breast cancer. *Steroids 72*, 7−25.

(2) Biersack, B., and Schobert, R. (2009)) Metallodrug conjugates with steroids and selective estrogen receptor modulators (SERM). *Curr. Med. Chem. 16*, 2324−2337.

(3) Oakman, C., Bessi, S., Zafarana, E., Galardi, F., Biganzoli, L., and Di, L. A. (2009) Recent advances in systemic therapy. New diagnostics and biological predictors of outcome in early breast cancer. *Breast Cancer Res.*, DOI: 10.1186/ber2238.

(4) Siegel, R., Ward, E., Brawley, O., and Jemal, A. (2011) Cancer statistics, 2011. *CA Cancer J. Clin. 61*, 212−236.

(5) Pickle, L. W., Hao, Y., Jemal, A., Zou, Z., Tiwari, R. C., Ward, E., Hachey, M., Howe, H. L., and Feuer, E. J. (2007) A new method of estimating United States and state-level cancer incidence counts for the current calendar year. *CA Cancer J. Clin. 57*, 30−42.

(6) Breen, N., Gentleman, J. F., and Schiller, J. S. (2011) Update on mammography trends. *Cancer 117*, 2209−2218.

(7) Kiefe, C. I. (2002) Race/ethnicity and cancer survival. *JAMA 287*, 2138−2139.

(8) Tabar, L., Yen, M.-F., Vitak, B., Chen, H.-H. T., Smith, R. A., and Duffy, S. W. (2003) Mammography service screening and mortality in breast cancer patients: 20-year follow-up before and after introduction of screening. *Lancet 361*, 1405−10.

(9) Duffy, S. W., Tabar, L., Chen, H.-H., Holmqvist, M., Yen, M.-F., Abdsalah, S., Epstein, B., Frodis, E., Ljungberg, E., Hedborg-Melander, C., Sundbom, A., Tholin, M., Wiege, M., Akerlund, A., Wu, H.-M., Tung, T.-S., Chiu, Y.-H., Chiu, C.-P., Huang, C.-C., Smith, R. A., Rosen, M., Stenbeck, M., and Holmberg, L. (2002) The impact of organized mammography service screening on breast carcinoma mortality in seven Swedish counties. *Cancer 95*, 458−69.

(10) Tiwari, R. C., Ghosh, K., Jemal, A., Hachey, M., Ward, E., Thun, M. J., and Feuer, E. J. (2004) A new method of predicting US and state-level cancer mortality counts for the current calendar year. *CA Cancer J. Clin. 54*, 30−40.

(11) Saslow, D., Boetes, C., Burke, W., Harms, S., Leach, M. O., Lehman, C. D., Morris, E., Pisano, E., Schnall, M., Sener, S., Smith, R. A., Warner, E., Yaffe, M., Andrews, K. S., and Russell, C. A. (2007) American Cancer Society guidelines for breast screening with MRI as an adjunct to mammography. *CA Cancer J. Clin. 57*, 75−89.

(12) Hortobagyi, G. N. (1998) Treatment of breast cancer. *N. Engl. J. Med. 339*, 974−984.

(13) Hinestrosa, M. C., Dickersin, K., Klein, P., Mayer, M., Noss, K., Slamon, D., Sledge, G., and Visco, F. M. (2007) Shaping the future of biomarker research in breast cancer to ensure clinical relevance. *Nat. Rev. Cancer 7*, 309−315.

(14) Bundred, N., and Howell, A. (2002) Fulvestrant (Faslodex): current status in the therapy of breast cancer. *Exp. Rev. Anti. Ther. 2*, 151−60.

(15) Ravdin, P. M., Cronin, K. A., Howlader, N., Berg, C. D., Chlebowski, R. T., Feuer, E. J., Edwards, B. K., and Berry, D. A. (2007) The decrease in breast-cancer incidence in 2003 in the United States. *NEJM 356*, 1670−1674.

(16) Eroles, P., Bosch, A., Alejandro, P.-F. J., and Lluch, A. (2012) Molecular biology in breast cancer: Intrinsic subtypes and signaling pathways. *Can. Treat. Rev. 38*, 698−707.

(17) Li, D.-M., and Feng, Y.-M. (2011) Signaling mechanism of cell adhesion molecules in breast cancer metastasis: potential therapeutic targets. *Breast Can. Res. Treat. 128*, 7−21.

(18) Miller, W. R. (2011) Molecular endocrinology and breast cancer - A reed before the wind lives on (a tribute to Professor Mike Reed). *Steroids 76*, 745−749.

(19) Perez, E. A. (2011) New treatment strategies in the management of breast cancer. *EJC Suppl. 9*, 22−29.

(20) Perou, C. M., and Boeresen-Dale, A.-L. (2011) Systems biology and genomics of breast cancer. *Cold Spring Harbor Perspect. Biol. 3*, a003293.

(21) Rao, J., Jiang, X., Wang, Y., and Chen, B. (2011) Advances in the understanding of the structure and function of ER-α36,a novel variant of human estrogen receptor-alpha. *J. Steroid Biochem. Mol. Biol. 127*, 231−237.

(22) Katzenellenbogen, B. S., and Katzenellenbogen, J. A. (2000) Estrogen receptor transcription and transactivation. Estrogen receptor alpha and estrogen receptor beta. Regulation by selective estrogen receptor modulators and importance in breast cancer. *Breast Cancer Res. 2*, 335−344.

(23) Jordan, V. C. (2003) Antiestrogens and selective estrogen receptor modulators as multifunctional medicines. 1. receptor interactions. *J. Med. Chem. 46*, 883−908.

(24) Katzenellenbogen, B. S., Miller, M. A., Eckert, R. L., and Sudo, K. (1983) Antiestrogen pharmacology and mechanism of action. *J. Steroid Biochem. 19*, 59−68.
(25) Meegan, M. J., and Lloyd, D. G. (2003) Advances in the science of estrogen receptor modulation. *Curr. Med. Chem. 10*, 181−210.
(26) Iwase, H., Yutaka, Y., and Zhang, Z. (2007) Estrogen receptor structure and function in breast cancer pathogenesis. *Res. Signpost*, 121−134.
(27) Marino, M., and Ascenzi, P. (2006) Estrogen receptor-α: plasma membrane localization and functions. *Immunol., Endocr. Metab. Agents Med. Chem. 6*, 281−289.
(28) Teng, C. T. (2002) Estrogen receptor-related receptor α: biological roles. *Recent Res. Dev. Endocrinol. 3*, 389−400.
(29) Schultz-Norton, J. R., Ziegler, Y. S., and Nardulli, A. M. ERα-associated protein networks. *Trends Endocrinol. Metab. 22*, 124−129.
(30) Katzenellenbogen, B. S., Sun, J., Harrington, W. R., Kraichely, D. M., Ganessunker, D., and Katzenellenbogen, J. A. (2001) Structure-function relationships in estrogen receptors and the characterization of novel selective estrogen receptor modulators with unique pharmacological profiles. *Ann. N. Y. Acad. Sci. 949*, 6−15.
(31) Kuiper, G. G., Carlsson, B., Grandien, K., Enmark, E., Haeggblad, J., Nilsson, S., and Gustafsson, J.-A. Comparison of the ligand binding specificity and transcript tissue distribution of estrogen receptors α and β. *Endocrinology 138*, 863−870.
(32) Lin, H.-m., Zhao, L., and Cheng, S.-y. (2002) Cyclin D1 is a ligand-independent co-repressor for thyroid hormone receptors. *J. Biol. Chem. 277*, 28733−28741.
(33) Levin, E. R. (2009) Hormone action and breast cancer. *Cancer Treat. Res. 147*, 37−46.
(34) Bryant, H. U., and Dere, W. H. (1998) Selective estrogen receptor modulators: an alternative to hormone replacement therapy. *Proc. Soc. Exp. Biol. Med. 217*, 45−52.
(35) Montano, M. M., Ekena, K., Delage-Mourroux, R., Chang, W., Martini, P., and Katzenellenbogen, B. S. An estrogen receptor-selective coregulator that potentiates the effectiveness of antiestrogens and represses the activity of estrogens. *Proc. Natl. Acad. Sci. U. S. A. 96*, 6947−6952.
(36) Howell, A. (2001) Future use of selective estrogen receptor modulators and aromatase inhibitors. *Clin. Cancer Res. 7*, 4402S−4410S.
(37) Keely, N. O., and Meegan, M. J. (2009) Selective estrogen receptor modulators: recent developments in design, structural studies and clinical applications. *Curr. Trends Med. Chem. 6*, 1−17.
(38) Lin, S.-X., Chen, J., Mazumdar, M., Poirier, D., Wang, C., Azzi, A., and Zhou, M. (2010) Molecular therapy of breast cancer: progress and future directions. *Nat. Rev. Endocrinol. 6*, 485−493.
(39) McDonnell, D. P., and Wardell, S. E. (2010) The molecular mechanisms underlying the pharmacological actions of ER modulators: implications for new drug discovery in breast cancer. *Curr. Opin. Pharmacol. 10*, 620−628.
(40) Pickar, J. H., MacNeil, T., and Ohleth, K. (2010) SERMs: Progress and future perspectives. *Maturitas 67*, 129−138.
(41) Shanle, E. K., and Xu, W. (2011) Endocrine disrupting chemicals targeting estrogen receptor signaling: identification and mechanisms of action. *Chem. Res. Toxicol. 24*, 6−19.
(42) Gennari, L., Merlotti, D., and Nuti, R. (2010) Selective estrogen receptor modulator (SERM) for the treatment of osteoporosis in postmenopausal women: focus on lasofoxifene. *Clin. Interventions Aging 5*, 19−29.
(43) Gennari, L., Merlotti, D., Valleggi, F., Martini, G., and Nuti, R. (2007) Selective estrogen receptor modulators for postmenopausal osteoporosis: current state of development. *Drugs Aging 24*, 361−379.
(44) Hall, J. M., Couse, J. F., and Korach, K. S. (2001) The multifaceted mechanisms of estradiol and estrogen receptor signaling. *J. Biol. Chem. 276*, 36869−36872.
(45) Katzenellenbogen, B. S., Bhakoo, H. S., Ferguson, E. R., Lan, N. C., Tatee, T., Tsai, T.-L. S., and Katzenellenbogen, J. A. (1979) Estrogen and antiestrogen action in reproductive tissues and tumors. *Recent Prog. Horm. Res. 35*, 259−300.
(46) Katzenellenbogen, B. S., Montano, M. M., Ediger, T. R., Sun, J., Ekena, K., Lazennec, G., Martini, P. G., McInerney, E. M., Delage-Mourroux, R., Weis, K., and Katzenellenbogen, J. A. (2000) Estrogen receptors: selective ligands, partners, and distinctive pharmacology. *Recent Prog. Horm. Res. 55*, 163−93.
(47) Ameller, T., Legrand, P., Marsaud, V., and Renoir, J.-M. (2004) Drug delivery systems for oestrogenic hormones and antagonists: the need for selective targeting in estradiol-dependent cancers. *J. Steroid Biochem. Mol. Biol. 92*, 1−18.
(48) Curigliano, G. (2012) New drugs for breast cancer subtypes: Targeting driver pathways to overcome resistance. *Cancer Treat. Rev. 38*, 303−310.
(49) Harbeck, N., Salem, M., Nitz, U., Gluz, O., and Liedtke, C. (2010) Personalized treatment of early-stage breast cancer: Present concepts and future directions. *Cancer Treat. Rev. 36*, 584−594.
(50) Ameller, T., Legrand, P., Marsaud, V., and Renoir, J.-M. (2004) Drug delivery systems for oestrogenic hormones and antagonists: the need for selective targeting in estradiol-dependent cancers. *J. Steroid Biochem. Mol. Biol. 92*, 1−18.
(51) Bodor, N., and Buchwald, P. (2006) Brain-targeted delivery of estradiol: therapeutic potential and results obtained with a chemical delivery system approach. *Am. J. Drug Delivery 4*, 161−175.
(52) Sharma, R., and Sharma, C. L. (2008) Macromolecular drugs: novel strategy in target specific drug delivery. *J. Clin. Diagn. Res. 2*, 1020−1023.
(53) Tedesco, R., Katzenellenbogen, J. A., and Napolitano, E. (1997) 7α,11β-Disubstituted estrogens: probes for the shape of the ligand binding pocket in the estrogen receptor. *Bioorg. Med. Chem. Lett. 7*, 2919−2924.
(54) Hanson, R. N., Napolitano, E., and Fiaschi, R. (1990) Synthesis and estrogen receptor binding of novel 11 beta-substituted estra-1,3,5(10)-triene-3,17 beta-diols. *J. Med. Chem. 33*, 3155−60.
(55) Hanson, R. N., Tongcharoensirikul, P., Dilis, R., Hughes, A., and DeSombre, E. R. (2007) Synthesis and evaluation of isomeric (17α,20E)-11β-methoxy-21-(trifluoromethylphenyl)-19-norpregna-1,3,5(10),20-tetraene-3,17β-diols as ERα-hormone binding domain ligands: effect of the methoxy group on receptor binding and uterotrophic growth. *J. Med. Chem. 50*, 472−479.
(56) Hanahan, D., and Weinberg, R. A. (2000) The hallmarks of cancer. *Cell 100*, 57−70.
(57) Decker, M. (2011) Hybrid molecules incorporating natural products: applications in cancer therapy, neurodegenerative disorders and beyond. *Curr. Med. Chem. 18*, 1464−1475.
(58) Muregi, F. W., Kirira, P. G., and Ishih, A. (2011) Novel rational drug design strategies with potential to revolutionize malaria chemotherapy. *Curr. Med. Chem. 18*, 113−143.
(59) Meunier, B. (2008) Hybrid molecules with a dual mode of action: dream or reality? *Acc. Chem. Res. 41*, 69−77.
(60) Hanson, R. N., Kirss, R., McCaskill, E., Hua, E., Tongcharoensirikul, P., Olmsted, S. L., Labaree, D., and Hochberg, R. B. (2012) Targeting the estrogen receptor with metal-carbonyl derivatives of estradiol. *Bioorg. Med. Chem. Lett. 22*, 1670−1673.
(61) Knox, A. J. S., Meegan, M. J., Sobolev, V., Frost, D., Zisterer, D. M., Williams, D. C., and Lloyd, D. G. (2007) Target specific virtual screening: optimization of an estrogen receptor screening platform. *J. Med. Chem. 50*, 5301−5310.
(62) Katzenellenbogen, J. A.; Zablocki, J. A. (1987) Cytotoxic Oestrogen and Antiestrogens: Concepts, Progress, and Evaluation. In *Pharmacology and Clinical Uses of Inhibitors of Hormone Secretion and Action* (Wakeling, B. J. A. F. A. E., Ed.) pp 41−5, Bailliere Tindall, London.
(63) Delbarre, A., Oberlin, R., Roques, B. P., Borgna, J. L., Rochefort, H., Le, P. J. B., and Jacquemin-Sablon, A. (1985) Ellipticine derivatives with an affinity to the estrogen receptor. An approach to develop intercalating drugs with a specific effect on the hormone-dependent breast cancer. *J. Med. Chem. 28*, 752−61.
(64) Devraj, R., Barrett, J. F., Fernandez, J. A., Katzenellenbogen, J. A., and Cushman, M. (1996) Design, Synthesis, and Biological

Evaluation of Ellipticine−Estradiol Conjugates. *J. Med. Chem. 39*, 3367−3374.
(65) Eisenbrand, G., Berger, M. R., Fischer, J., Schneider, M. R., Tang, W., and Zeller, W. J. (1998) Development of more selective anticancer nitrosoureas. *Anti-Can. Drug Dev. 2*, 351−9.
(66) Betsch, B., Berger, M. R., Spiegelhalder, B., Schmahl, D., and Eisenbrand, G. (1990) An estradiol-linked nitrosourea and site-directed chemotherapy in mammary carcinoma. *Eur. J. Cancer 26*, 895−8.
(67) Glassner, B. J., Weeda, G., Allan, J. M., Broekhof, J. L. M., Carls, N. H. E., Donker, I., Engelward, B. P., Hampson, R. J., Hersmus, R., Hickman, M. J., Roth, R. B., Warren, H. B., Wu, M. M., Hoeijmakers, J. H. J., and Samson, L. D. (1999) DNA repair methyltransferase (Mgmt) knockout mice are sensitive to the lethal effects of chemotherapeutic alkylating agents. *Mutagenesis 14*, 339−347.
(68) Tsubura, A., Lai, Y.-C., Miki, H., Sasaki, T., Uehara, N., Yuri, T., and Yoshizawa, K. (2011) Animal models of N-methyl-N-nitrosourea-induced mammary cancer and retinal degeneration with special emphasis on therapeutic trials. *In Vivo 25*, 11−22.
(69) Thorpe, S. M., and Rose, C. (1988) Biological and clinical relevance of Kd values for estradiol binding in primary breast cancer tumors. *Eur. J. Cancer Clin. Oncol. 24*, 1163−70.
(70) Katzenellenbogen, B. S., Pavlik, E. J., Robertson, D. W., and Katzenellenbogen, J. A. (1981) Interaction of a high affinity anti-estrogen (α-[4-pyrrolidinoethoxy]phenyl-4-hydroxy-α′-nitrostilbene, CI628M) with uterine estrogen receptors. *J. Biol. Chem. 256*, 2908−15.
(71) Kuduk, S. D., Zheng, F. F., Sepp-Lorenzino, L., Rosen, N., and Danishefsky, S. J. (1999) Synthesis and evaluation of geldanamycin-estradiol hybrids. *Bioorg. Med. Chem. Lett. 9*, 1233−1238.
(72) Prodromou, C., Roe, S. M., Piper, P. W., and Pearl, L. H. (1997) A molecular clamp in the crystal structure of the N-terminal domain of the yeast Hsp90 chaperone. *Nat. Struct. Biol. 4*, 477−482.
(73) Annamalai, B., Liu, X., Gopal, U., and Isaacs, J. S. (2009) Hsp90 is an essential regulator of EphA2 receptor stability and signaling: implications for cancer cell migration and metastasis. *Mol. Cancer. Res. 7*, 1021−32.
(74) Moser, C., Lang, S. A., and Stoeltzing, O. (2009) Heat-shock protein 90 (Hsp90) as a molecular target for therapy of gastrointestinal cancer. *Anticancer Res. 29*, 2031−2042.
(75) Uehara, Y., Hori, M., Takeuchi, T., and Umezawa, H. (1985) Screening of agents which convert 'transformed morphology' of Rous sarcoma virus-infected rat kidney cells to 'normal morphology': identification of an active agent as herbimycin and its inhibition of intracellular src kinase. *Jpn. J. Cancer Res. (GANN) 76*, 672−5.
(76) Sharma, U., Marquis, J., Nicole Dinaut, A., Hillier, S. M., Fedeles, B., Rye, P. T., Essigmann, J. M., and Croy, R. G. (2004) Design, synthesis, and evaluation of estradiol-linked genotoxicants as anti-cancer agents. *Bioorg. Med. Chem. Lett. 14*, 3829−3833.
(77) Gupta, A., Saha, P., Descoteaux, C., Leblanc, V., Asselin, E., and Berube, G. (2010) Design, synthesis and biological evaluation of estradiol-chlorambucil hybrids as anticancer agents. *Bioorg. Med. Chem. Lett. 20*, 1614−1618.
(78) Fonseca, S. B., Pereira, M. P., Mourtada, R., Gronda, M., Horton, K. L., Hurren, R., Minden, M. D., Schimmer, A. D., and Kelley, S. O. (2011) Rerouting chlorambucil to mitochondria combats drug deactivation and resistance in cancer cells. *Chem. Biol. 18*, 445−453.
(79) Drablos, F., Feyzi, E., Aas, P. A., Vaagbo, C. B., Kavli, B., Bratlie, M. S., Pena-Diaz, J., Otterlei, M., Slupphaug, G., and Krokan, H. E. (2004) Alkylation damage in DNA and RNA-repair mechanisms and medical significance. *DNA Repair 3*, 1389−1407.
(80) Mitra, K., Marquis, J. C., Hillier, S. M., Rye, P. T., Zayas, B., Lee, A. S., Essigmann, J. M., and Croy, R. G. (2002) A rationally designed genotoxin that selectively destroys estrogen receptor-positive breast cancer cells. *J. Am. Chem. Soc. 124*, 1862−1863.
(81) Rink, S. M., Yarema, K. J., Solomon, M. S., Paige, L. A., Tadayoni-Rebek, B. M., Essigmann, J. M., and Croy, R. G. (1996) Synthesis and biological activity of DNA-damaging agents that form decoy binding sites for the estrogen receptor. *Proc. Natl. Acad. Sci. U. S. A. 93*, 15063−15068.
(82) Ali, H., Ahmed, N., Tessier, G., and van Lier, J. E. (2006) Synthesis and biological activities of nucleoside−estradiol conjugates. *Bioorg. Med. Chem. Lett. 16*, 317−319.
(83) Sagi, G., Otvos, L., Ikeda, S., Andrei, G., Snoeck, R., and De, C. E. (1994) Synthesis and antiviral activities of 8-alkynyl-, 8-alkenyl-, and 8-alkyl-2′-deoxyadenosine analogs. *J. Med. Chem. 37*, 1307−11.
(84) De, C. E., Descamps, J., Balzarini, J., Giziewicz, J., Barr, P. J., and Robins, M. J. (1983) Nucleic acid related compounds. Synthesis and biological activities of 5-alkynyluracil nucleosides. *J. Med. Chem. 26*, 661−6.
(85) Van, L. J. E., Kan, G., Autenrieth, D., and Hulsinga, E. (1978) Steroid-nucleosides. *Cancer Treat. Rep. 62*, 1251−3.
(86) Van, L. J. E., Kan, G., Autenrieth, D., and Nigam, V. N. (1977) Steroid-nucleosides possible novel agents for cancer chemotherapy. *Nature 267*, 522−3.
(87) Hartman, N. G., Patterson, L. H., Workman, P., Suarato, A., and Angelucci, F. (1990) Doxorubicin-3′-NH-estrone-17-oxime-ethyl-carbonyl, a doxorubicin-estrone conjugate that does not redox cycle in rat liver microsomes. *Biochem. Pharmacol. 40*, 1164−7.
(88) Kasiotis, K. M., Magiatis, P., Pratsinis, H., Skaltsounis, A.-L., Abadji, V., Charalambous, A., Moutsatsou, P., and Haroutounian, S. A. (2001) Synthesis and biological evaluation of novel daunorubicin-estrogen conjugates. *Steroids 66*, 785−791.
(89) Al-Omar, A., Abdou, S., De, R. L., Marsura, A., and Finance, C. (1999) Complexation study and anticellular activity enhancement by Doxorubicin-cyclodextrin complexes on a multidrug-resistant adeno-carcinoma cell line. *Bioorg. Med. Chem. Lett. 9*, 1115−1120.
(90) Gianni, L., Corden, B. J., and Myers, C. E. (1983) The biochemical basis of anthracycline toxicity and antitumor activity. *Rev. Biochem. Toxicol. 5*, 1−82.
(91) Liu, C., Strobl, J. S., Bane, S., Schilling, J. K., McCracken, M., Chatterjee, S. K., Rahim-Bata, R., and Kingston, D. G. I. (2004) Design, synthesis, and bioactivities of steroid-linked taxol analogues as potential targeted drugs for prostate and breast cancer. *J. Nat. Prod. 67*, 152−159.
(92) Rowinsky, E. K., Burke, P. J., Karp, J. E., Tucker, R. W., Ettinger, D. S., and Donehower, R. C. (1989) Phase I and pharmacodynamic study of taxol in refractory acute leukemias. *Cancer Res. 49*, 4640−7.
(93) Kalbakis, K., Pappas, P., Kouroussis, C., Vamvakas, L., Kalykaki, A., Vardakis, N., Nikolaidou, M., Marselos, M., Georgoulias, V., and Mavroudis, D. (2008) A dose escalation and pharmacokinetic study of biweekly pegylated liposomal doxorubicin, paclitaxel and oxaliplatin in patients with advanced solid tumors. *Cancer Chem. Pharm. 62*, 449−456.
(94) Matsuda, G., Kunisaki, C., Makino, H., Fukahori, M., Kimura, J., Sato, T., Oshima, T., Nagano, Y., Fuii, S., Takagawa, R., Kosaka, T., Ono, H. A., Akiyama, H., and Ichikawa, Y. (2009) Phase II study of weekly paclitaxel as a second-line treatment for S-1-refractory advanced gastric cancer. *Anticancer Res. 29*, 2863−2868.
(95) Sissung, T. M., Mross, K., Steinberg, S. M., Behringer, D., Figg, W. D., Sparreboom, A., and Mielke, S. (2006) Association of ABCB1 genotypes with paclitaxel-mediated peripheral neuropathy and neutropenia. *Eur. J. Cancer 42*, 2893−2896.
(96) Levin, M. (2001) The role of taxanes in breast cancer treatment. *Drugs Today 37*, 57−65.
(97) Gueritte, F. (2001) General and recent aspects of the chemistry and structure-activity relationships of taxoids. *Curr. Pharm. Des. 7*, 1229−49.
(98) He, L., Jagtap, P. G., Kingston, D. G., Shen, H. J., Orr, G. A., and Horwitz, S. B. (2000) A common pharmacophore for Taxol and the epothilones based on the biological activity of a taxane molecule lacking a C-13 side chain. *Biochemistry 39*, 3972−8.
(99) Kingston, D. G. (2000) Recent advances in the chemistry of taxol. *J. Nat. Prod. 63*, 726−34.
(100) Khan, E. H., Ali, H., Tian, H., Rousseau, J., Tessier, G., Shafiullah, and van Lier, J. E. (2003) Synthesis and biological activities

of phthalocyanine−estradiol conjugates. *Bioorg. Med. Chem. Lett. 13*, 1287−1290.
(101) James, D. A., Swamy, N., Paz, N., Hanson, R. N., and Ray, R. (1999) Synthesis and estrogen receptor binding affinity of a porphyrin-estradiol conjugate for targeted photodynamic therapy of cancer. *Bioorg. Med. Chem. Lett. 9*, 2379−2384.
(102) Khan, E. H., Ali, H., Tian, H., Rousseau, J., Tessier, G., Shafiullah, and van, L. J. E. (2003) Synthesis and biological activities of phthalocyanine-estradiol conjugates. *Bioorg. Med. Chem. Lett. 13*, 1287−1290.
(103) Tsumura, K., Suzuki, A., Tsuzuki, T., Tanimoto, S., Kaneko, H., Matsumura, S., Imoto, M., Umezawa, K., Takahashi, D., and Toshima, K. (2011) Molecular design, chemical synthesis, and biological evaluation of agents that selectively photo-degrade the transcription factor estrogen receptor-α. *Org. Biomol. Chem. 9*, 6357−6366.
(104) James, D. A., Swamy, N., Paz, N., Hanson, R. N., and Ray, R. (1999) Synthesis and estrogen receptor binding affinity of a porphyrin-estradiol conjugate for targeted photodynamic therapy of cancer. *Bioorg. Med. Chem. Lett. 9*, 2379−2384.
(105) Brzozowski, A. M., Pike, A. C. W., Dauter, Z., Hubbard, R. E., Bonn, T., Engstrom, O., Ohman, L., Greene, G. L., Gustafsson, J.-A., and Carlquist, M. (1997) Molecular basis of agonism and antagonism in the estrogen receptor. *Nature 389*, 753−758.
(106) Tanenbaum, D. M., Wang, Y., Williams, S. P., and Sigler, P. B. (1989) Crystallographic comparison of the estrogen and progesterone receptor's ligand binding domains. *Proc. Natl. Acad. Sci. U. S. A. 95*, 5998−6003.
(107) Jones, G. B., Hynd, G., Wright, J. M., Purohit, A., Plourde, G. W., Huber, R. S., Mathews, J. E., Li, A., Kilgore, M. W., Bubley, G. J., Yancisin, M., and Brown, M. A. (2001) Target-directed enediynes: designed estramycins. *J. Org. Chem. 66*, 3688−3695.
(108) Nicolaou, K. C., Smith, A. L., and Yue, E. W. (1993) Chemistry and biology of natural and designed enediynes. *Proc. Natl. Acad. Sci. U. S. A. 90*, 5881−8.
(109) Nicolaou, K. C., and Dai, W. M. (1991) Chemistry and biology of enediyne-cytostatic antibiotics. *Angew. Chem., Int. Ed. Engl. 30*, 1387−1416.
(110) Nicolaou, K. C., Sorensen, E. J., Discordia, R., Hwang, C. K., Minto, R. E., Bharucha, K. N., and Bergman, R. G. (1992) Ten-membered cyclic enediynes with remarkable chemical and biological properties. *Angew. Chem., Int. Ed. Engl. 31*, 1044−6.
(111) Gandolfi, O., Blum, J., and Mandelbaum-Shavit, F. (1984) Antitumor steroidal-cis-platinum(II)-o-catecholato conjugates: preliminary evaluation on breast cancer MCF-7 cells. *Inorg. Chim. Acta 91*, 257−61.
(112) Altman, J., Castrillo, T., Beck, W., Bernhardt, G., and Schoenenberger, H. (1991) Metal complexes with biologically important ligands. 62. Platinum(II) complexes of 3-(2-aminoethoxy)-estrone and -estradiol. *Inorg. Chem. 30*, 4085−8.
(113) Perron, V., Rabouin, D., Asselin, E., Parent, S., C.-Gaudreault, R., and Berube, G. (2005) Synthesis of 17β-estradiol-linked platinum-(II) complexes and their cytotoxic activity on estrogen-dependent and -independent breast tumor cells. *Bioorg. Chem. 33*, 1−15.
(114) Kim, E., Croy, R. G., and Essigmann, J. M. (2007) Design of programmable platinum antitumor agents for breast and ovarian cancers. *J. Biol. Inorg. Chem. 12* (Suppl1), S36.
(115) Provencher-Mandeville, J., Debnath, C., Mandal, S. K., Leblanc, V., Parent, S., Asselin, E., and Berube, G. (2011) Design, synthesis and biological evaluation of estradiol-PEG-linked platinum(II) hybrid molecules: Comparative molecular modeling study of three distinct families of hybrids. *Steroids 76*, 94−103.
(116) Descoteaux, C., Provencher-Mandeville, J., Mathieu, I., Perron, V., Mandal, S. K., Asselin, E., and Berube, G. (2003) Synthesis of 17β-estradiol platinum(II) complexes: biological evaluation on breast cancer cell lines. *Bioorg. Med. Chem. Lett. 13*, 3927−3931.
(117) Gagnon, V., St-Germain, M.-È., Descôteaux, C., Provencher-Mandeville, J., Parent, S., Mandal, S. K., Asselin, E., and Berube, G. (2004) Biological evaluation of novel estrogen-platinum(II) hybrid molecules on uterine and ovarian cancers—molecular modeling studies. *Bioorg. Med. Chem. Lett. 14*, 5919−5924.
(118) Descoteaux, C., Leblanc, V., Belanger, G., Parent, S., Asselin, E., and Berube, G. (2008) Improved synthesis of unique estradiol-linked platinum(II) complexes showing potent cytocidal activity and affinity for the estrogen receptor alpha and beta. *Steroids 73*, 1077−1089.
(119) Saha, P., Descoteaux, C., Brasseur, K., Fortin, S., Leblanc, V., Parent, S., Asselin, E., and Berube, G. (2012) Synthesis, antiproliferative activity and estrogen receptor α affinity of novel estradiol-linked platinum(II) complex analogs to carboplatin and oxaliplatin. Potential vector complexes to target estrogen-dependent tissues. *Eur. J. Med. Chem. 48*, 385−390.
(120) Provencher-Mandeville, J., Descoteaux, C., Mandal, S. K., Leblanc, V., Asselin, E., and Berube, G. (2008) Synthesis of 17β-estradiol-platinum(II) hybrid molecules showing cytotoxic activity on breast cancer cell lines. *Biorg. Med. Chem. Let. 18*, 2282−2287.
(121) Georgiadis, M. P., Haroutounian, S. A., and Chondros, K. P. (1987) Synthesis and biological studies of steroidal cis-platinum(II) complexes. *Inorg. Chim. Acta 138*, 249−52.
(122) Hannon, M. J., Green, P. S., Fisher, D. M., Derrick, P. J., Beck, J. L., Watt, S. J., Ralph, S. F., Sheil, M. M., Barker, P. R., Alcock, N. W., Price, R. J., Sanders, K. J., Pither, R., Davis, J., and Rodger, A. (2006) An estrogen−platinum terpyridine conjugate: DNA and protein binding and cellular delivery. *J. Eur. Chem. A 12*, 8000−8013.
(123) Gabano, E., Cassino, C., Bonetti, S., Prandi, C., Colangelo, D., Ghiglia, A., and Osella, D. (2005) Synthesis and characterisation of estrogenic carriers for cytotoxic Pt(II) fragments: biological activity of the resulting complexes. *Org. Biomol. Chem. 3*, 3531−3539.
(124) Gabano, E., Cassino, C., Bonetti, S., Prandi, C., Colangelo, D., Ghiglia, A., and Osella, D. (2005) Synthesis and characterisation of estrogenic carriers for cytotoxic Pt(II) fragments: biological activity of the resulting complexes. *Org. Biomol. Chem. 3*, 3531−3539.
(125) Barnes, K. R., Kutikov, A., and Lippard, S. J. (2004) Synthesis, characterization, and cytotoxicity of a series of estrogen-tethered platinum(IV) complexes. *Chem. Biol. 11*, 557−564.
(126) Huang, J.-C., Zamble, D. B., Reardon, J. T., Lippard, S. J., and Sancar, A. (1994) HMG-domain proteins specifically inhibit the repair of the major DNA adduct of the anticancer drug cisplatin by human excision nuclease. *Proc. Natl. Acad. Sci. U. S. A. 91*, 10394−8.
(127) He, Q., Liang, C. H., and Lippard, S. J. (2000) Steroid hormones induce HMG1 overexpression and sensitize breast cancer cells to cisplatin and carboplatin. *Proc. Natl. Acad. Sci. U. S. A. 97*, 5768−5772.
(128) Cyrus, K., Wehenkel, M., Choi, E.-Y., Lee, H., Swanson, H., and Kim, K.-B. (2010) Jostling for position: optimizing linker location in the design of estrogen receptor-targeting PROTACs. *Chem. Med. Chem. 5*, 979−985.
(129) Moore, T. W., Gunther, J. R., and Katzenellenbogen, J. A. (2010) Probing the the topol. tolerance of multimeric protein interactions: evaluation of an estrogen/synthetic ligand for FK506 binding protein conjugate. *Bioconjugate Chem. 21*, 1880−1889.
(130) Agoston, G. E., Shah, J. H., Suwandi, L., Hanson, A. D., Zhan, X., LaVallee, T. M., Pribluda, V., and Treston, A. M. (2009) Synthesis, antiproliferative, and pharmacokinetic properties of 3- and 17-double-modified analogs of 2-methoxyestradiol. *Bioorg. Med. Chem. Lett. 19*, 6241−4.
(131) Hanson, R. N., McCaskill, E., Tongcharoensirikul, P., Dilis, R., Labaree, D., and Hochberg, R. B. (2012) Synthesis and evaluation of 17α-(dimethylphenyl)vinyl estradiols as probes of the estrogen receptor-α ligand binding domain. *Steroids 77*, 471−476.
(132) Olmsted, S. L., Tongcharoensirikul, P., McCaskill, E., Gandiaga, K., Labaree, D., Hochberg, R. B., and Hanson, R. N. (2012) Synthesis and evaluation of 17α-E-20-(heteroaryl)norpregn-1,3,5(10),20 tetraene-3,17β-diols [17α-(heteroaryl)vinyl estradiols] as ligands for the estrogen receptor-α ligand binding domain (ERα-LBD). *Bioorg. Med. Chem. Lett. 22*, 977−979.
(133) Hanson, R. N., Hua, E., Adam, H. J., Labaree, D., and Hochberg, R. B. (2012) Synthesis and evaluation of 11β-(4-

Substituted phenyl) estradiol analogs: Transition from estrogen receptor agonists to antagonists. *Bioorg. Med. Chem. 20*, 3768−80.
(134) Hanson, R. N., Napolitano, E., Fiaschi, R., and Onan, K. D. (1990) Synthesis and estrogen receptor binding of novel 11β-substituted estra-1,3,5(10)-triene-3,17β-diols. *J. Med. Chem. 33*, 3155−60.
(135) Dao, K.-L., Sawant, R. R., Hendricks, J. A., Ronga, V., Torchilin, V. P., and Hanson, R. N. (2012) Design, synthesis, and initial biological evaluation of a steroidal anti-estrogen-doxorubicin bioconjugate for targeting estrogen receptor-positive breast cancer cells. *Bioconjugate Chem. 23*, 785−795.
(136) Loibl, S., von, M. G., Schwedler, K., Schmidt, K. A., Hoeper, D., Kaufmann, M., and Costa, S. D. (2004) Mitomycin C, 5-fluorouracil and folinic acid (Mi-Fu-Fo) as salvage chemotherapy in breast cancer patients with liver metastases and impaired hepatic function: a phase II study. *Anti-Cancer Drugs 15*, 719−724.
(137) Massacesi, C., La, C. A., Marcucci, F., Pilone, A., Rocchi, M. B. L., Zepponi, L., Santini, D., Tonini, G., and Burattini, L. (2006) Capecitabine and mitomycin C is an effective combination for anthracycline- and taxane-resistant metastatic breast cancer. *Oncology 70*, 294−300.
(138) Bradner, W. T. (2001) Mitomycin C: A clinical update. *Cancer Treat. Rev. 27*, 35−50.
(139) Ishiki, N., Onishi, H., and Machida, Y. (1998) In vivo properties of the conjugates of mitomycin C with estradiol benzoate and estradiol: pharmacokinetics and antitumor characteristics against P388 leukemia and sarcoma 180. *Biol. Pharm. Bull. 21*, 1180−6.
(140) Wolkenberg, S. E., and Boger, D. L. (2002) Mechanisms of in situ activation for DNA-targeting antitumor agents. *Chem Rev 102*, 2477−95.
(141) Tomasz, M., Das, A., Tang, K. S., Ford, M. G. J., Minnock, A., Musser, S. M., and Waring, M. J. (1998) The purine 2-amino group as the critical recognition element for sequence-specific alkylation and crosslinking of DNA by Mitomycin C. *J. Am. Chem. Soc. 120*, 11581−11593.
(142) Lee, S. H., and Kohn, H. (2005) 7-N,7′-N′-(1″,2″-Dithianyl-3″,6″-dimethylenyl)bismitomycin C: synthesis and nucleophilic activation of a dimeric mitomycin. *Org. Biomol. Chem. 3*, 471−482.
(143) Paz, M. M., Kumar, G. S., Glover, M., Waring, M. J., and Tomasz, M. (2004) Mitomycin dimers: polyfunctional cross-linkers of DNA. *J. Med. Chem. 47*, 3308−3319.
(144) Sami, S. M., Iyengar, B. S., Tarnow, S. E., Remers, W. A., Bradner, W. T., and Schurig, J. E. (1984) Mitomycin C analogs with aryl substituents on the 7-amino group. *J. Med. Chem. 27*, 701−8.
(145) Lewis, W. G., Green, L. G., Grynszpan, F., Radic, Z., Carlier, P. R., Taylor, P., Finn, M. G., and Sharpless, K. B. (2002) Click chemistry in situ: Acetylcholinesterase as a reaction vessel for the selective assembly of a femtomolar inhibitor from an array of building blocks. *Angew. Chem., Int. Ed. 41*, 1053−1057.
(146) Rostovtsev, V. V., Green, L. G., Fokin, V. V., and Sharpless, K. B. (2002) A stepwise Huisgen cycloaddition process: copper(I)-catalyzed regioselective "ligation" of azides and terminal alkynes. *Angew. Chem., Int. Ed. 41*, 2596−2599.
(147) Wang, Q., Chan, T. R., Hilgraf, R., Fokin, V. V., Sharpless, K. B., and Finn, M. G. (2003) Bioconjugation by copper(I)-catalyzed azide-alkyne [3 + 2] cycloaddition. *J. Am. Chem. Soc. 125*, 3192−3193.
(148) Mandler, R., Kobayashi, H., Hinson, E. R., Brechbiel, M. W., and Waldmann, T. A. (2004) Herceptin-geldanamycin immunoconjugates: pharmacokinetics, biodistribution, and enhanced antitumor activity. *Cancer Res. 64*, 1460−1467.
(149) Xiao, L., Lu, X., and Ruden, D. M. (2006) Effectiveness of Hsp90 inhibitors as anti-cancer drugs. *Mini-Rev. Med. Chem. 6*, 1137−1143.
(150) Markman, M. (2007) New, expanded, and modified use of approved antineoplastic agents in ovarian cancer. *Oncology 12*, 186−190.
(151) Tejada-Berges, T., Granai, C. O., Gordinier, M., and Gajewski, W. (2002) Caelyx/Doxil for the treatment of metastatic ovarian and breast cancer. *Expert Rev. Anticancer Ther. 2*, 143−150.
(152) Prat, D., Benedetti, F., Nait, B. L., and Girard, G. F. (2004) Recent developments in the synthesis of 11β-aryl-estrone derivatives. *Tetrahedron Lett. 45*, 765−768.
(153) Nique, F., Van, d. V. P., Bremaud, J., Hardy, M., Philibert, D., and Teutsch, G. (1994) 11β-Amidoalkoxyphenyl estradiols, a new series of pure antiestrogens. *J. Steroid Biochem. Mol. Biol. 50*, 21−9.
(154) Aryal, S., Grailer, J. J., Pilla, S., Steeber, D. A., and Gong, S. (2009) Doxorubicin conjugated gold nanoparticles as water-soluble and pH-responsive anticancer drug nanocarriers. *J. Mater. Chem. 19*, 7879−7884.
(155) Lee, C. C., Cramer, A. T., Szoka, F. C., and Frechet, J. M. J. (2006) An intramolecular cyclization reaction is responsible for the in vivo inefficacy and apparent pH insensitive hydrolysis kinetics of hydrazone carboxylate derivatives of doxorubicin. *Bioconjugate Chem. 17*, 1364−1368.
(156) Torchilin, V. P. (2006) Multifunctional nanocarriers. *Adv. Drug. Delivery Rev. 58*, 1532−55.
(157) Prabaharan, M., Grailer, J. J., Pilla, S., Steeber, D. A., and Gong, S. (2009) Amphiphilic multi-arm-block copolymer conjugated with doxorubicin via pH-sensitive hydrazone bond for tumor-targeted drug delivery. *Biomaterials 30*, 5757−5766.

Bioconjugate Chemistry

Communication

pubs.acs.org/bc

Radioactive Smart Probe for Potential Corrected Matrix Metalloproteinase Imaging

Chiun-Wei Huang, Zibo Li,* and Peter S. Conti

Molecular Imaging Center, Department of Radiology, University of Southern California, Los Angeles, California 90033, United States

Supporting Information

ABSTRACT: Although various activatable optical probes have been developed to visualize metalloproteinase (MMP) activities in vivo, precise quantification of the enzyme activity is limited due to the inherent scattering and attenuation (limited depth penetration) properties of optical imaging. In this investigation, a novel activatable peptide probe ^{64}Cu-BBQ650-PLGVR-K(Cy5.5)-E-K(DOTA)-OH was constructed to detect tumor MMP activity in vivo. This agent is optically quenched in its native form, but releases strong fluorescence upon cleavage by selected enzymes. MMP specificity was confirmed both in vitro and in vivo by fluorescent imaging studies. The use of a single modality to image biomarkers/processes may lead to erroneous interpretation of imaging data. The introduction of a quantitative imaging modality, such as PET, would make it feasible to correct the enzyme activity determined from optical imaging. In this proof of principle report, we demonstrated the feasibility of correcting the activatable optical imaging data through the PET signal. This approach provides an attractive new strategy for accurate imaging of MMP activity, which may also be applied for other protease imaging.

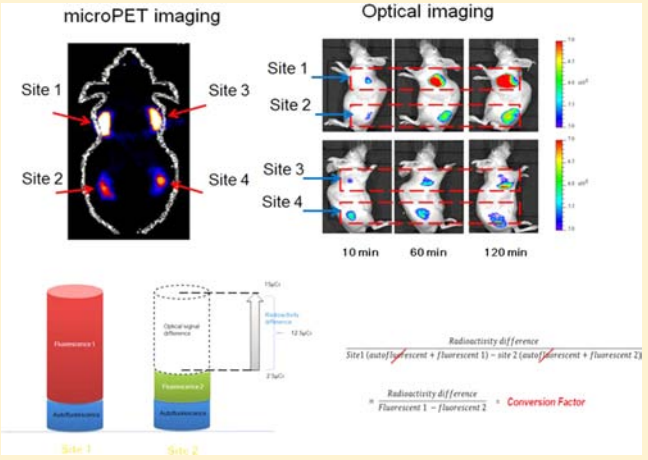

INTRODUCTION

Advances in molecular imaging offer strategies for noninvasive, quantitative, and repetitive imaging of targeted macromolecules and biological processes in living organisms, which could provide an efficient early diagnosis, predict disease course, and finally lead to personalized medicine.[1−4] Optical imaging with fluorescent probes has recently been proven to be a powerful tool with the advantages of lower cost, portability, and real-time capabilities.[5−9] A unique feature of fluorescence is that optical probes can be designed so that they will emit light ("turning on") only in the presence of a targeted enzyme or upon internalization. These activatable or "smart" agents could have low to no background signal and generate signal only after being exposed to the specific molecular target/process.

The matrix metalloproteinase (MMP) family are important extracellular matrix remodeling proteases whose activity has been implicated in a number of key normal and pathologic processes.[10−13] The latter include tumor growth, progression, metastasis, and dysregulated angiogenesis associated with these events.[12,14−18] In fact, MMPs have come to represent important therapeutic and diagnostic targets for the treatment and detection of human cancers.[19,20] For example, up-regulation of MMPs has been found to play an important role in tumor invasiveness, metastasis, and angiogenesis. Although the use of activatable probes seems to be a popular method to monitor enzyme activity, very limited platforms are available to clearly image protease activity in vivo after systemic administration. The majority of the reported systems were tested as proof-of-concept examples in in vitro or ex vivo conditions, such as after intratumoral injection in tumor models.[21−23] For in vivo imaging, we believe one limitation of activatable probes is the lack of quantitative information. For example, if we assume two tumors, tumor-1 and tumor-2, with the same enzyme activity, when more probes are localized in tumor-1 due to better blood supply, we will observe higher optical signal in tumor-1 compared with tumor-2. This result if solely determined from absolute optical signal would be misleading, since tumor-2 has the same level of enzyme activity as tumor-1.

Positron emission tomography (PET) is a noninvasive functional imaging technique with millimeter resolution and high sensitivity. An important advantage of PET is the quantitative information obtained with this imaging modality. In order to take advantage of the strengths of each imaging modality, we developed an activatable dual modality (PET/fluorescent) imaging agent that could more accurately detect tumor MMP activity in vivo. This novel MMP activatable "smart" probe could be divided into three parts: the MMP cleavable peptide sequence, a pair of dye/quencher (activatable

Received: April 9, 2012
Revised: September 30, 2012
Published: October 2, 2012

 © 2012 American Chemical Society dx.doi.org/10.1021/bc3001968 | Bioconjugate Chem. 2012, 23, 2159−2167

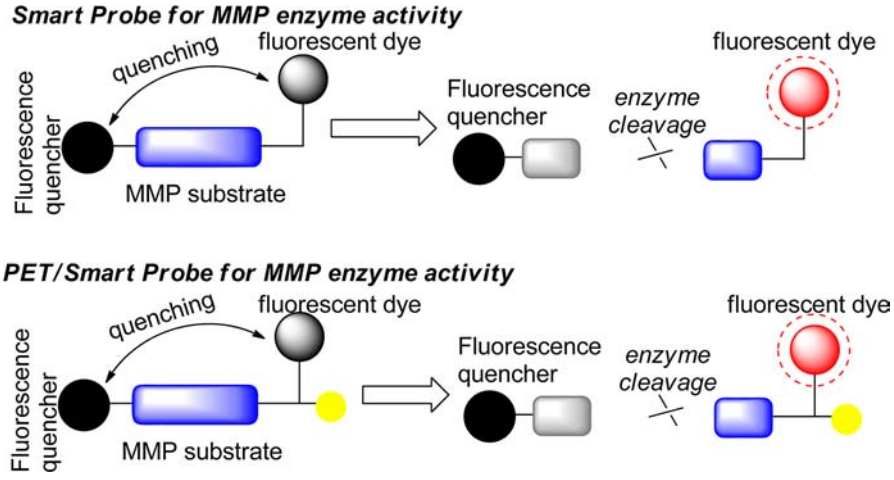

Figure 1. (a) The limitation of a fluorogenic probe is that the amount of probe cannot be accurately determined in tumor regions. Although two tumors may have the same enzyme activity, one may have higher optical signal if more probe is localized in the tumor region, which will result in misleading information. (b) A radioactive motif would allow us to more accurately determine how much probe is localized in a tumor region through quantitative PET imaging. This use of a multimodality imaging probe may provide corrected enzyme activity through the measurement of total probe concentration (from PET) and the cleavage rate (from optical).

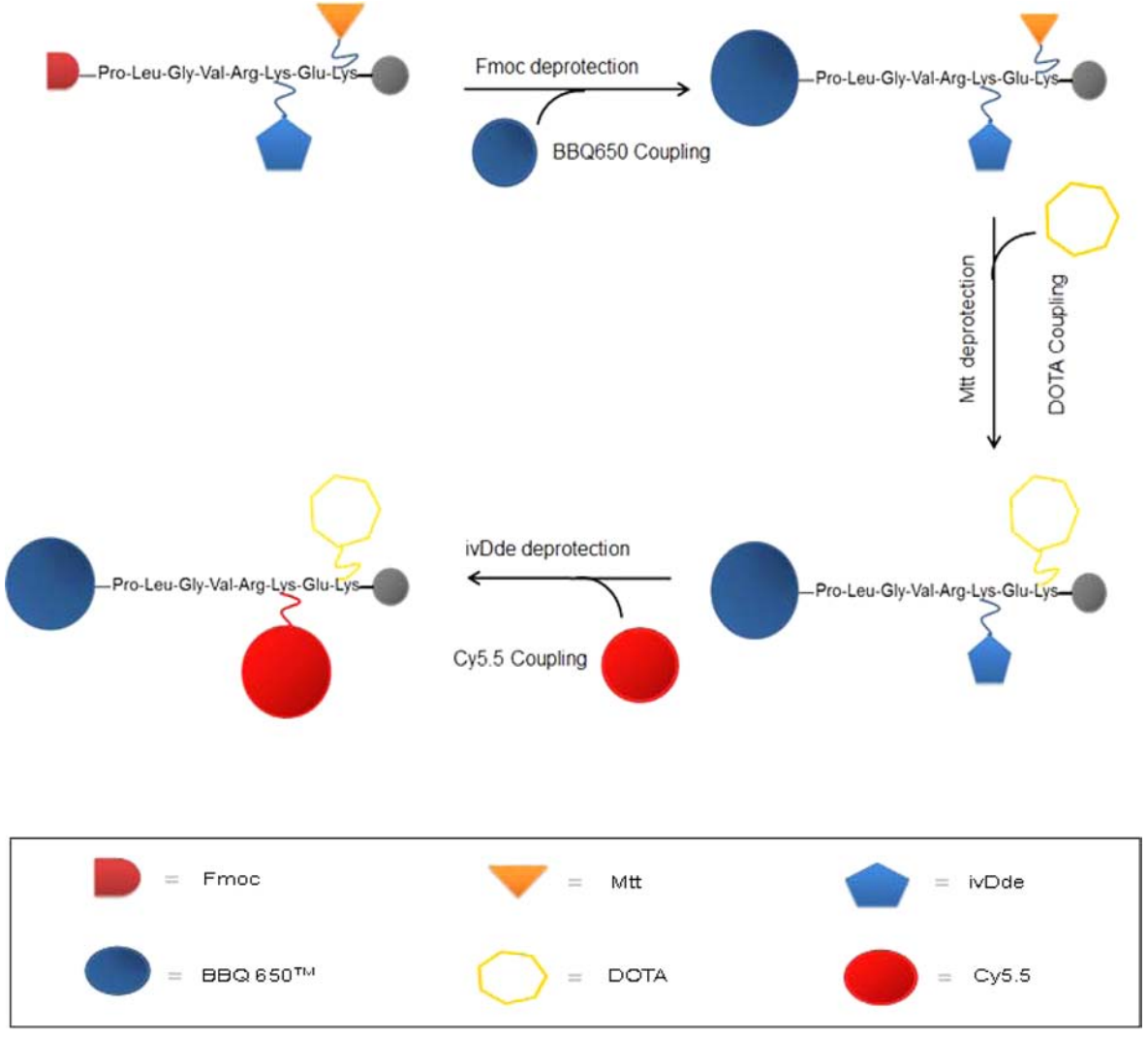

Figure 2. Synthetic scheme of a MMP activatable probe.

dx.doi.org/10.1021/bc3001968 | *Bioconjugate Chem.* 2012, 23, 2159–2167

component), and the bifunctional chelator for radiometal labeling (Figure 2). The MMP-cleavable sequence PLGVR is preferentially cleaved by MMP-7, -9, -12, and-13. The quencher, BBQ650, is nonfluorescent, thus contributing no background fluorescence upon release. The imaging agent is optically quenched in its native form, but provides strong near-infrared fluorescence signal (700−900 nm) upon cleavage by selected MMP enzymes such as MMP-13. The latter has been shown to be highly expressed in various aggressive phenotypes of tumors,[24−26] making MMP-13 a potential prognostic marker between benign and malignant tumors. Although most peptide-based activatable probes provide their fluorescence signal through the release of their near-infrared dyes, in this study, all of the activated fluorescence remains closely conjugated with the radiometal labeled segments, which would allow us to track both dissociated and quenched probe with PET imaging. We expect that the enzyme activity determined from optical imaging could be corrected through PET imaging. The basic principle is illustrated in Figure 1.

EXPERIMENTAL PROCEDURES

General. All commercially available chemical reagents and solvents were purchased from Sigma-Aldrich (St. Louis, MO) and used without further purification. 9-Fluorenylmethyloxycarbonyl (Fmoc)-protected amino acids and Rink amide resin were purchased from either Novabiochem (San Diego, CA) or Bachem (Torrance, CA). DOTA(OBu-t)3-NHS(1,4,7,10-tetraazacyclododecane-1-(*N*-hydroxysuccinimi-deacetate)-4,7,10-tris(*tert*-butyl acetate)) was purchased from Macrocyclics Inc. (Dallas, TX). Human recombinant MMP enzymes were purchased from R&D Systems (Minneapolis, MN). The enzymes were activated according to the vendor's protocols, if necessary. The broad-spectrum MMP inhibitor III was obtain from EMD Chemicals (San Diego, CA). $^{64}CuCl_2$ solution was purchased from University of Wisconsin (Madison, WI). Water was purified using a Milli-Q ultrapure water system from Millipore (Milford, MA, USA), followed by passage through a Chelex 100 resin before bioconjugation and radiolabeling. The purification of the crude product was carried out on an analytical reversed-phase high-performance liquid chromatography (HPLC) system equipped with a Waters 2487 dual UV absorbance detector (Waters, Milford, MA) using a Phenomenex C18 RP (250 × 4.6 mm 5 μm) column. The flow rate was 1 mL/min using a gradient mobile phase from 98% solvent A (0.1% TFA in water) and 5% solvent B (0.1% TFA in acetonitrile) (0−2 min) to a mobile phase of 40% solvent A and 65% solvent B at 32 min. The radioactivity was detected with a Ludlum 2200 single-channel radiation detector.

Synthesis of BBQ650-PLGVR-K(Cy5.5)-E-K(DOTA)-OH Probe. BBQ650-PLGVR-K(Cy5.5)-EK(DOTA)-OH was synthesized based on the procedure illustrated in Figure 2. In brief, peptides were synthesized though a standard Fmoc solid-phase peptide synthesis method with 4-fold excess amounts of benzotriazole-1-yl-oxy-tris-pyrrolidino-phosphonium hexafluorophosphate (PyBOP), 1-hydroxybenzotriazole (HOBt), and 8-fold molar excess of diisopropylethylamine (DIPEA). Acylation was carried out for 60 min and completion of the conjugation was confirmed by the trinitrobenezene sulfonic acid test (TNBS). Removal of the Fmoc protective group on the α-amino group was achieved with 20% piperidine in dimethylformamide (DMF) (v/v). DMF was used to wash the resin between each acylation and deprotection step. The synthesis of BBQ650-PLGVR-K(ivDde)-E-K(Mtt)-resin was achieved through the conjugation of BBQ650 NHS ester with the N-terminal amino group after the Fmoc protecting group removal. BBQ650 NHS ester (3 equiv dissolved in DMF) was added to the fully protected peptide (1 equiv still on the resin) in the presence of 10 equiv DIPEA. The reaction mixture was stirred overnight in the dark at room temperature and washed thoroughly with DMF (5×). The DOTA conjugates were achieved through the conjugation of DOTA-mono-NHS-tris (t-Bu) ester with BBQ650-PLGVR-K(ivDde)-E-K(NH_2)-Wang resins after the removal of Mtt protecting group with 2% of TFA in DCM (3 min × 10). The DOTA-mono-NHS-tris (t-Bu) ester (3 equiv) dissolved in DMF was added to the BBQ650 conjugated peptide containing resins (1 equiv), in the presence of 10 equiv DIPEA. The reaction mixture was stirred in the dark for 3 h at room temperature. Unreacted DOTA chelator was removed by washing the resins with DMF thoroughly. Through a similar procedure as the BBQ650 conjugation, the fluorescence dye Cy5.5 was introduced to the partially deprotected peptide by coupling onto the exposed lysine amino group after the ivDde protecting group was regioselectively removed with 2% of hydrazine monohydrate in DMF. The conjugated peptides were cleaved from the resin and side chain protecting groups were simultaneously removed by treating with the cleavage solution (95% TFA, and 5% water) for 3 h. Peptide-containing supernatants were separated from the solid support by filtration and concentrated under a stream of nitrogen. Crude peptide was precipitated out and washed twice with ice-cold diethyl ether, which was then dissolved in 10% acetic acid in water before lyophilization. The desired products were purified and characterized by HPLC. The purity of conjugated peptides was greater than 95%, based on analytical HPLC. Fractions containing desired conjugates were collected, lyophilized, characterized by LTQ Orbitrap Hybrid mass spectrometer, and stored in the dark at −20 °C.

Enzyme Cleavage Assay. At 37 °C, 1 μM peptide probe was incubated in triplicate with 5 nM human-recombinant MMP-13 using an assay buffer of 50 mM Tris, 150 mM NaCl, 10 mM $CaCl_2$, and 0.05% Brij-35 (w/v) at pH 7.5 with 500 rpm. Fluorescence intensity was monitored (excitation at 675, emission at 690 nm) at sequential time points (0 min, 10 min, 30 min, 60 min, and 120 min). Recombinant human MMP-13 was added to the peptide probe solution to test cleavage specificity and stability of the amino acid sequence. Formation of the hydrolyzed peptide domains was monitored by HPLC and compared with uncleaved peptide.

Cell Lines. The human glioblastoma cell line, U87MG, was obtained from American Type Culture Collection (Manassas, VA) and maintained at 37 °C in a humidified atmosphere containing 5% CO_2 in DMEM (Mediatech, Inc.) and 10% fetal bovine serum (Life Technologies, Inc., Grand island, NY). The U87MG cell line was chosen in this study for its high expression of a variety of MMPs, including MMP-2, MMP-9, and MMP-13.[27,28]

Tumor Xenografts. Animal procedures were performed according to an approved protocol by the University of Southern California Institutional Animal Care and Use Committee. Female athymic nude mice (BALB/c *nu/nu*) were obtained from Harlan (Indianapolis, IN) at 4 to 6 weeks of age and injected subcutaneously in the right shoulder with 5 × 10^6 of U87MG human glioblastoma cells suspended in 100 μL of PBS. When tumors reached 0.4 to 0.6 cm in diameter (28 days after implant), the tumor-bearing mice were subjected to in vivo fluorescence imaging studies.

dx.doi.org/10.1021/bc3001968 | *Bioconjugate Chem.* 2012, 23, 2159−2167

In Vivo NIR Imaging Evaluation of MMP Activation. In vivo fluorescence imaging was performed with an IVIS Lumina (Xenogen, Alameda, CA) equipped with 21 emission filter sets that can be used to image optical signals from green to near-infrared. In vivo imaging of activatable peptide probes were performed to evaluate activation specificity. Blocking studies were performed with the broad-spectrum MMP inhibitor III (EMD Bioscience) (0.4 mM; 50 μL) through intratumor injection 30 min before the injection of imaging probes. Scans were performed with U87MG xenograft mice (n = 3) after intratumor injection of activatable peptide probes (2 nmol) with and without MMP inhibitor at serial time points (5 min,10 min, 15 min, 30 min, 60 min, and 90 min). Identical illumination settings (lamp voltage, filters, f/stop, field of views, binning) were used for acquisition of all images, and fluorescence emission scans were normalized to photons per second per centimeter squared per steradian (p/s/cm^2/sr). Images were analyzed using the *Living Image* software (Xenogen, Alameda, CA) with spectral unmixing to reduce tissue autofluorescence. Mean activated fluorescent intensities and corresponding standard deviation were calculated for each group of animals.

^{64}Cu Labeling. BBQ650-PLGVR-K(Cy5.5)-E-K(DOTA)-OH was radiolabeled with $^{64}Cu^{2+}$ according to our previously reported method.[29,30] Briefly, $^{64}CuCl_2$ was added to DOTA conjugated peptides in 0.1 M sodium acetate buffer (pH 5.5) and incubated at 40 °C for 1 h. The radiochemical purity of the final product was >95% as confirmed by radio-HPLC. The radioactive peak containing the desired product was collected and rotary-evaporated to remove solvent. The HPLC-purified product was then reconstituted in phosphate-buffered saline to 1 mCi/mL and passed through a 0.22 mm Millipore filter into a sterile multidose vial for in vitro and in vivo experiments.

In Vitro Stability Assay. The in vitro stability of ^{64}Cu-BBQ650-PLGVR-K(Cy5.5)-E-K(DOTA)-OH was studied at different time points. Briefly, 3.7 MBq of labeled peptide was pipetted into 1 mL of PBS and mouse serum (1:1). After incubation at 37 °C for 4, 12, and 24 h, an aliquot of the mixture was removed from the PBS solution and the radiochemical purity was determined with radio-HPLC. For the stability test in serum, aliquots were added to 100 μL of PBS with 50% TFA. After centrifugation, the supernatant solution was removed and filtered for radio-HPLC analysis.

Proof of Concept in Vivo Multimodality Imaging Studies. Mice (n = 3) were subcutaneously injected with ^{64}Cu-BBQ650-PLGVR-K(Cy5.5)-E-K(DOTA)-OH (15 μCi (0.13 nmol) at sites 1 and 3, and 2.5 μCi (0.022 nmol) at sites 2 and 4, respectively) and the same amount of MMP-13 enzyme (sites 1−4) with or without the MMP inhibitor III (Table 1). Mice were anesthetized with 2% isoflurane and imaged with static scans at sequential time points (10 min, 60 min, 120 min, and 180 min). For each optical imaging scan, regions of interest (ROIs) were drawn over each injection site to measure optical signal. Small-animal PET imaging was performed on a microPET R4 rodent model system (Concorde Microsystems, Knoxville, TN). Images were acquired after each optical imaging scan and reconstructed by a two-dimensional ordered subsets expectation maximum (2D-OSEM) algorithm. Regions of interest (ROI) were drawn over injected sites on decay-corrected whole-body coronal images. The average radioactivity concentration was obtained from mean pixel values within three-dimensional ROI volumes. The accuracy of noninvasive microPET imaging was used to assist the quantification of optical signals.

Table 1. In Vivo Proof-of-Concept Quantification Correction Study Layout of PET/Optical Probe, MMP-13 Enzyme and Inhibitor

	site 1	site 2	site 3	site 4
PET/optical probe	15 μCi	2.5 μCi	15 μCi	2.5 μCi
MMP-13 enzyme	10 ng	10 ng	10 ng	10 ng
MMP inhibitor	-	-	20 nM	20 nM

Data Processing and Statistics. All data were measured in mean ± SD using three independent measurements. Statistical analysis was performed using the Student's t test. Statistical significance was assigned for P values less than 0.05.

RESULTS

Chemistry and Radiolabeling. The MMP sensitive peptide probe BBQ650-PLGVR-K(Cy5.5)-E-K(DOTA)-OH was synthesized in high purity (>98%) by solid-phase peptide synthesis. In this design, resonance energy transfer occurs between a donor group (NIR Cy5.5 dye) and a fluorescence quencher group (BQQ-650). The chemical structure of BBQ650-PLGVR-K(Cy5.5)-E-K(DOTA)-OH and activation mechanism are shown in Figure 3. The identity of peptide probe was confirmed by HPLC and electrospray ionization (ESI-MS) mass spectra. The HPLC retention time was (R_t) = 25.3 min and mass was m/z: $[M+3H]^+$ = 937.06 (calculated: 937.14) (Figure S1). The ^{64}Cu-labeled BBQ650-PLGVR-K(Cy5.5)-E-K(^{64}Cu-DOTA)-OH was achieved in more than 95% decay-corrected yield with >98% radiochemical purity. The specific activity of ^{64}Cu-BBQ650-PLGVR-K(Cy5.5)-E-K(DOTA)-OH was around 4.2×10^{15} Bq/mol.

In Vitro Stability. The in vitro stability of ^{64}Cu labeled probe was studied in PBS (pH 7.4) and mouse serum at physiological temperature (37 °C). The purpose of these studies was to demonstrate that the ^{64}Cu radiotracer remains intact before being injected into the mice. The stability was presented as the percentage of intact peptide probe on the basis of the radio-HPLC analysis. As shown in Figure S2, after 24 h of incubation, more than 97% of imaging agent remained intact in PBS, and more than 80% of peptide remained intact in mouse serum. It is clear that the radiotracer has reasonable stability for in vivo imaging.

In Vitro Studies. In order to verify that the DOTA motif has no major effect on the "smart probe" property, the newly synthesized BBQ650-PLGVR-K(Cy5.5)-E-K(DOTA)-OH was tested for its cleavage specificity by MMP-13 enzyme in vitro. In our design, the MMP enzyme would cleave the peptide substrate that bridged a fluorescent dye and quencher, and release of the quencher will provide the fluorescence from the probe. Specific hydrolysis of peptides by MMPs was evaluated and characterized. The cleavage specificity of fluorescent probes was assessed in triplicate by optical imaging with the IVIS Lumina scanner. As shown in Figure 3c, fluorescent intensity was time dependent; the signal has an 8.2-fold increase from 0 to120 min, which can be blocked in the presence of MMP inhibitors. In addition, the HPLC profile also demonstrated two peptide fragments after the enzymatic cleavage (Figure 3b). These results showed that modification of the cleavage site with additional amino acids, fluorescence compounds, and DOTA chelator did not affect the MMP enzyme cleavage reaction.

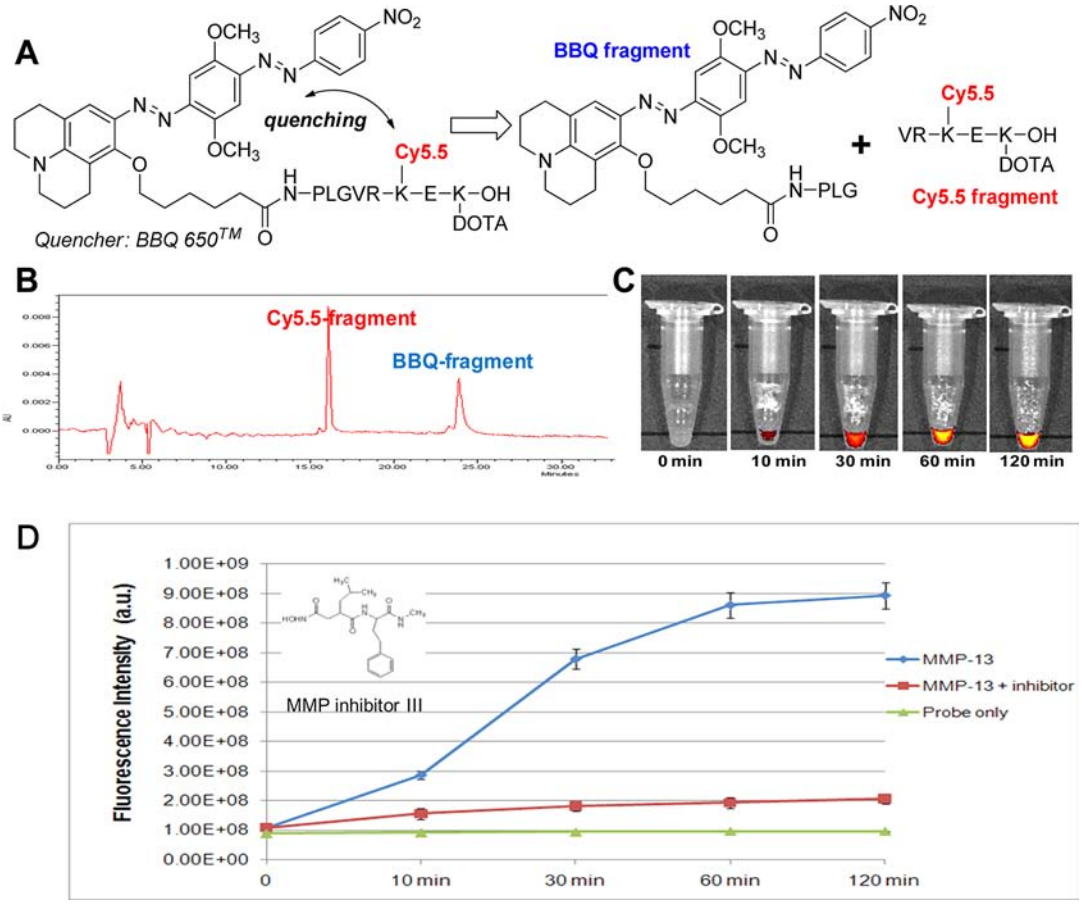

Figure 3. Cleavage of BBQ650TM-PLGVR-K(Cy5.5)-E-K(DOTA)-OH by MMP-13: (a) Reaction scheme. (b) HPLC analysis of the crude reaction mixture. (c) Reaction was followed by optical imaging at different time points. (0 min, 10 min, 30 min, 60 min, and 120 min). (d) Quantification plot of the fluorescence intensity of MMP-13 with and without a broad spectrum MMP inhibitor III.

In Vivo Evaluation of MMP Activation. In vivo MMP activation of BBQ650-PLGVR-K(Cy5.5)-E-K(DOTA)-OH was evaluated in nude mice bearing U87MG human glioma xenograft tumors (n = 3) at sequential time points with the IVIS Lumina small animal optical imaging system. Representative images at different time points were shown in Figure 4. The probes demonstrated an instant positive fluorescent signal upon injection, which could be attributed to the MMP enzymes secreted from the tumor. The U87MG tumor was clearly visualized with high tumor-to-background contrast and steady increase in fluorescent intensity during the time course of scans. On the contrary, the control group (preinjected with MMP inhibitor) showed dramatically lower intensity at the tumor area at all time points and confirmed the cleavage specificity of the peptide probe.

Proof of Concept In Vivo Multimodality Imaging Studies. As the enhanced optical signal may depend on both MMP enzyme activity and the amount of "smart" imaging probes localized in tumor region, we expect that the introduction of PET could assist in the correction of enzyme activity determined from optical imaging. In order to support our assumption, we injected the same amount of MMP-13 enzyme with different amounts of substrate (^{64}Cu-BBQ650-PLGVR-K(Cy5.5)-E-K(DOTA)-OH) under the mouse skin. As shown in Figure 5, the optical signal reached a plateau at sites 1, 2, 3, and 4, which was 1.08×10^4, 6.47×10^3, 6.66×10^3, and 5.78×10^3 (a.u.), respectively. Comparison of sites 1 and 2 simulates one scenario where results may vary due to substrate delivery. Although sites 1 and 2 have the same MMP activity, site 1 gave much higher optical signal than site 2 due to the larger amount of substrate. Based on optical imaging alone, one may conclude that the enzyme activity at site 1 is higher than site 2 since increased optical signal was observed (1.08×10^4 v 6.47×10^3 (a.u.)). In contrast, the substrate difference was clearly reflected in PET imaging, which would warrant the correction of the observed optical signal with PET imaging. Additional confusion came from the blocking study with the MMP inhibitors. The same amount of substrate was localized at the injection sites 1 and 3 (or 2 and 4, also reflected in PET imaging). As expected, we did not observe prominent optical signal at the sites 3 and 4 due to the inhibition of the MMP enzyme activity. However, as shown in Figure 5, the blocking effect of MMP inhibitor of each pair calculated from the optical signal values was 38.33% (site 1 v site 3) and 10.66% (site 2 v site 4), respectively. It seems that the pair of sites 1 and 3 demonstrated greater than 3-fold higher inhibition compared with the pair of sites 2 and 4. Since we injected the same amount of MMP enzyme and inhibitor at both sites, the discrepancy of the blocking efficiency obtained from the optical data is quite confusing and misleading, which may limit the measurement of MMP activity by activatable optical probes.

Introduction of PET imaging provided an opportunity to coregister the optical signal with the PET signal. In order to perform these corrections, we made the following assumptions: (1) For site 1 and site 2, activatable peptide probes had been completely hydrolyzed by MMP-13 at 180 min postinjection.

dx.doi.org/10.1021/bc3001968 | Bioconjugate Chem. 2012, 23, 2159–2167

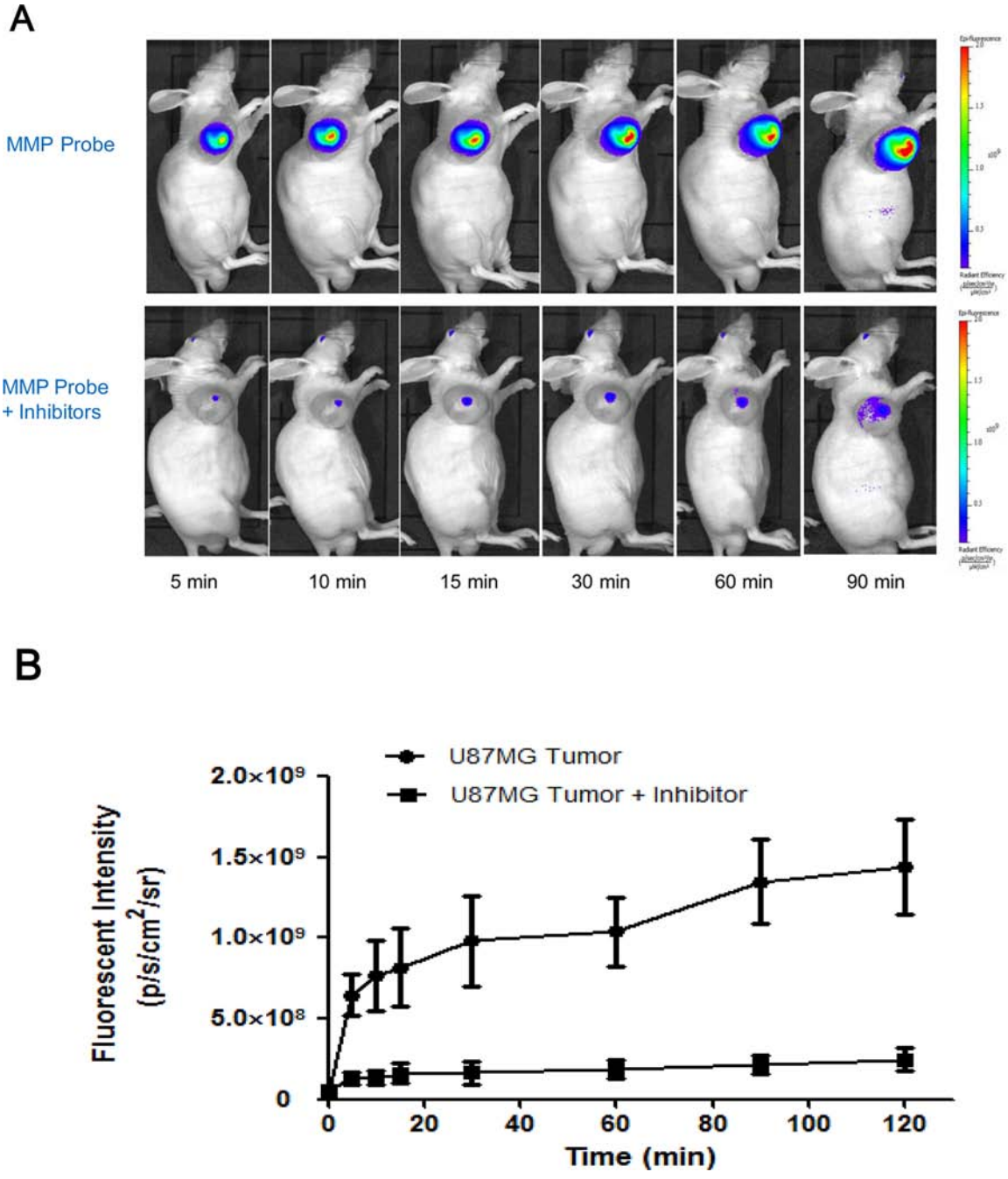

Figure 4. (a) Representative NIR fluorescence images of MMP-positive U87MG tumor-bearing mice after intratumoral injection of the probe without or with MMP inhibitor. (b) Quantification analysis of NIR fluorescence intensity of U87MG tumor in vivo.

(2) The optical signal of each site composed of autofluorescence and MMP probe fluorescence. (3) Autofluorescent background was similar at all sites. With these assumptions in mind, we determined the increased fluorescent signal (4.33×10^3 (a.u.)) at site 1 compared to site 2 was caused by probes corresponding to 12.5 μCi activity, as determined with PET. The normalized fluorescence signal (a.u.) per unit of radioactivity (μCi) can be calculated to be 346.4 (a.u./μCi) (Figure 6). Skin autofluorescence can be estimated by subtracting the converted fluorescent signal with acquired fluorescent signal (1.08×10^4 to 5.19×10^3) as 5.6×10^3 (a.u.). Therefore, the "real" fluorescent signal coming from the hydrolysis of substrate would only be 5.19×10^3 (a.u.) as determined from site 1 with 15 μCi. Using this autofluorescent value as a quantification baseline, the MMP activity can be further validated more precisely.

This conversion factor allowed recalculation of the inhibition effect at site 3 (or 4) by converting the radioactivity value to equivalent optical signal. For example, the real fluorescent signal at inhibition site can be calculated as the following: [(the fluorescent signal at site 3 (or 4) − autofluorescent signal)/PET activity × 346.4]. The inhibition percentage was calculated at site 3 and site 4 to be 79.6% and 79.7%, respectively. The blocking efficacy was more precisely quantified after the coregistration of PET/fluorescence signals. These results demonstrated the advantage of our smart-optical/PET design.

dx.doi.org/10.1021/bc3001968 | *Bioconjugate Chem.* 2012, 23, 2159−2167

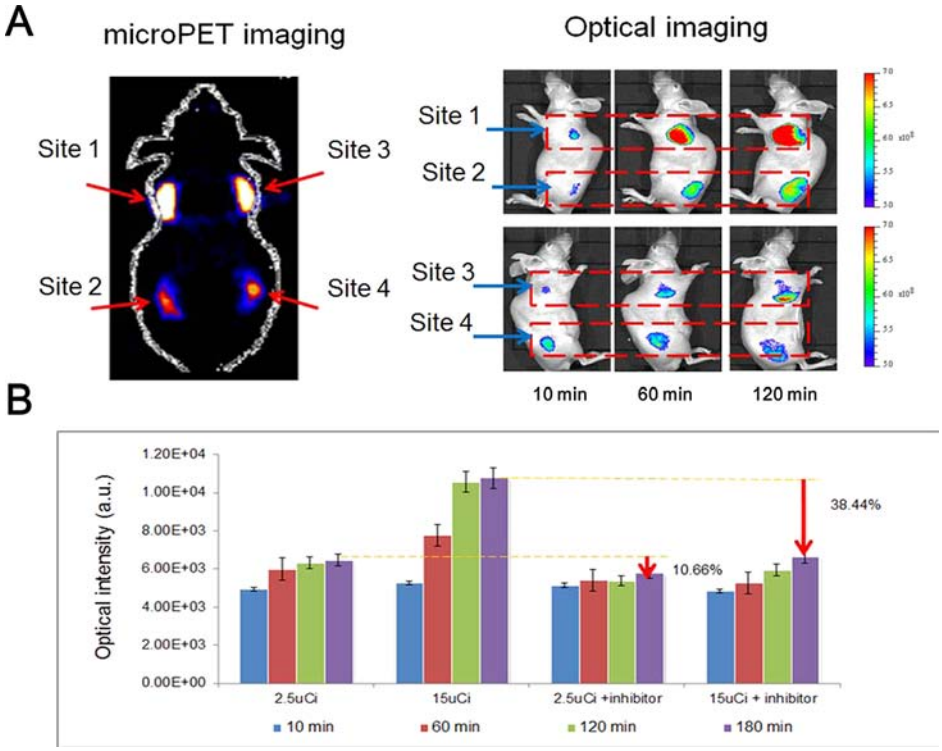

Figure 5. In vivo multimodality imaging studies. (a) Representative PET/NIR images of mice injected subcutaneously with ^{64}Cu-BBQ650-PLG VR-K(Cy5.5)-E-K(DOTA)-OH probes (15 μCi and 2.5 μCi at sites 1 and 3 and 2 and 4, respectively) and the same amount of MMP-13 without (sites 1 and 2) or with (sites 3 and 4) the MMP inhibitor. (b) Inhibition analysis of MMP inhibitor based on NIR fluorescence results in vivo.

DISCUSSION

Matrix metalloproteinases (MMPs) have been identified as a key modulators in extracellular matrix remodeling and shown to play a pivotal role in promoting various stages of tumor invasion and metastasis. The recognition of MMPs as disease biomarkers stimulated the development of imaging strategies targeting these proteases for improved diagnosis and staging of tumors.[31−33] Although various activatable optical probes have been developed to visualize the MMP activities in vivo, precise quantification of the enzyme activity is limited due to the inherent scattering and attenuation (limited depth penetration) properties of optical imaging. We hoped this challenge could be solved at least in part by introducing a secondary imaging modality: PET. The positron signal from the radioisotope can help determine the total amount of probes located in a tumor region (both quenched and unquenched), which could be used to correct the enzyme activity determined from optical imaging. Thus, measurement of PET signal will yield information about the precise distribution of the agent, while measurement of the optical signal will yield information about the MMP activity. This coincident measurement technique using both PET and activatable optical imaging will help us draw a correlation involving the distribution pattern of agents and activity level of MMP enzymes simultaneously. In addition, this method can be performed in the same animal at similar time points, thus eliminating problems that may occur when trying to compare across animals or time points.

In this study, the designed probe BBQ650-PLGVR-K(Cy5.5)-E-K(DOTA)-OH was obtained though solid-phase peptide synthesis in high purity (>98%). In our proof-of-concept study, we first tested the enzyme sensitivity of this probe through in vitro cleavage assays and in vivo intratumoral injection imaging. It was demonstrated that the MMP enzyme sensitivity was maintained after the introduction of additional amino acids and DOTA chelator to the PLGVR sequence. In addition, cleavage was effectively blocked with MMP inhibitor both in vitro and in vivo.

To demonstrate the important role of PET on correcting the enzyme activity determined from optical imaging, we injected the same amount of MMP-13 enzyme with different amounts of substrate (^{64}Cu-BBQ650 -PLGVR-K(Cy5.5)-E-K(DOTA)-OH) under the mouse skin. Although injection sites 1 and 2 have the same level of MMP enzyme, site 1 gave much higher optical signal simply due to the increased localization of imaging probe. However, the substrate difference was clearly reflected in PET imaging. By using PET signal as a converting baseline, we can correct the optical signal from enzyme activities and eliminate the autofluorescence signal from mouse skin. On the basis of the optical/PET signal conversion, the inhibition ratio between site 1 and site 3 (or site 2 and site 4) can also be appropriately corrected. These experiments demonstrated the advantage of our *smart-optical/PET* design. We would also like to point out that there are many other issues that need to be addressed in order to obtain a translatable probe for in vivo imaging of MMP activity through systemic administration: short half-life, poor pharmacokinetic profiles, instability, and high background induced by a nonspecific degradation of fluorogenic substrates. A targeting ligand may efficiently increase the retention time of the probe in the target region, minimize nonspecific accumulation caused by global MMP activity, and enhance tumor-to-background signal. In our followup studies, a potent targeting structure will be introduced to the MMP probe design to avoid the fast clearance of activated imaging fragments from tumor lesions. The targeting ligand not only can provide an anchoring capability of probes in tumor lesions, but also will produce the

dx.doi.org/10.1021/bc3001968 | *Bioconjugate Chem.* 2012, 23, 2159−2167

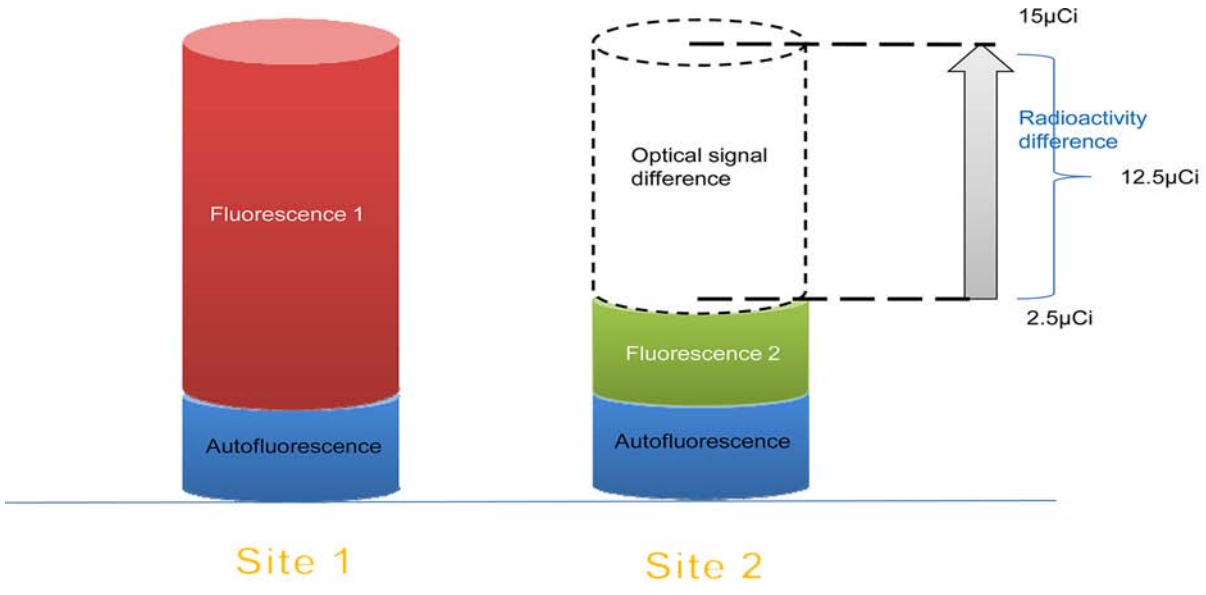

$$\frac{Site\ 1\ (autofluorescence + fluorescence\ 1) - Site\ 2\ (autofluorescence + fluorescence\ 2)}{Radioactivity\ 1\ (15\mu Ci) - Radioactivity\ 2(2.5\mu Ci)}$$

$$= \frac{Fluorescence\ 1 - Fluorescence\ 2}{Radioactivity\ difference\ (12.5\mu Ci)} = \frac{1.08x10^4 - 6.47\ x\ 10^3\ (a.u.)}{12.5\ (\mu Ci)} = 346.4\ (a.u./\mu Ci)$$

Figure 6. Diagram for the normalization of fluorescence signal (a.u.) based on radioactivity (μCi). Assuming that the autofluorescent signals are similar at all sites, thus, the conversion factor can be gained by dividing the difference of the acquired optical signals with the radioactivity difference, which is 346.4 (a.u./μCi).

quantification of selected receptors. Previously, Ogawa et al (2009) had synthesized a dual labeled anti-HER1 (or -HER2) antibody for dual-modality tumor targeting imaging.[34] In that study, an activatable fluorescent property of ICG dye was used to introduce additional information in addition to the "on" signal from the ^{111}indium radionuclide. The nuclear imaging successfully provided the quantification data in detail to compensate the attenuation of fluorescent signal. However, antibody based probes generally accumulate in tumor regions slowly and circulate in the blood pool for a relatively long time. For an MMP targeted probe, the effect of global MMP activity needs to be carefully considered. Therefore, a peptide-based targeting unit may be preferred due to its quick accumulation in tumors and fast clearance from the blood. Currently, we are improving our probe design through development of targeted radioactive MMP probes.

CONCLUSIONS

The use of a single modality, such as optical imaging, to image biomarkers/processes may lack detail and even be misleading in many cases. A coincident measurement technique using an additional imaging modality could be advantageous. In this proof of principle report, we demonstrated the feasibility of correcting the optical imaging data through PET imaging. This approach stands as an attractive new strategy for accurate measurement of MMP activity, which can also be applied for other protease imaging.

ASSOCIATED CONTENT

Supporting Information

ESI-MS of BBQ650-PLGVR-K(Cy5.5)-E-K(DOTA)-OH, in vitro stability curve of ^{64}Cu-BBQ650-PLGVR-K(Cy5.5)-E-K(DOTA)-OH in PBS (pH = 7.4) or mouse serum. This material is available free of charge via the Internet at http://pubs.acs.org.

AUTHOR INFORMATION

Corresponding Author

*Telephone: 323-442-3252; Fax: 323-442-3253; e-mail: ziboli@usc.edu.

Notes

The authors declare no competing financial interest.

ACKNOWLEDGMENTS

This study was supported by the USC Molecular Imaging Center, the Department of Energy (DE-SC0002353), and the American Cancer Society (121991-MRSG-12-034-01-CCE). We would also like to thank Mr. Ryan Park for proofreading the manuscript.

REFERENCES

(1) Richmond, T. D. (2008) The current status and future potential of personalized diagnostics: Streamlining a customized process. *Biotechnol. Annu. Rev. 14*, 411−422.

(2) Walk, E. E. (2010) Improving the power of diagnostics in the era of targeted therapy and personalized healthcare. *Curr. Opin. Drug Discovery Devel. 13*, 226−234.
(3) Massoud, T. F., and Gambhir, S. S. (2007) Integrating noninvasive molecular imaging into molecular medicine: an evolving paradigm. *Trends Mol. Med. 13*, 183−191.
(4) Gross, S., and Piwnica-Worms, D. (2006) Molecular imaging strategies for drug discovery and development. *Curr. Opin. Chem. Biol. 10*, 334−342.
(5) Hilderbrand, S. A., and Weissleder, R. (2010) Near-infrared fluorescence: application to in vivo molecular imaging. *Curr. Opin. Chem. Biol. 14*, 71−79.
(6) Mahmood, U., and Weissleder, R. (2003) Near-infrared optical imaging of proteases in cancer. *Mol. Cancer Ther. 2*, 489−496.
(7) Rao, J., Dragulescu-Andrasi, A., and Yao, H. (2007) Fluorescence imaging in vivo: recent advances. *Curr. Opin. Biotechnol. 18*, 17−25.
(8) Kosaka, N., Ogawa, M., Choyke, P. L., and Kobayashi, H. (2009) Clinical implications of near-infrared fluorescence imaging in cancer. *Future Oncol. 5*, 1501−1511.
(9) Ntziachristos, V., Bremer, C., and Weissleder, R. (2003) Fluorescence imaging with near-infrared light: new technological advances that enable in vivo molecular imaging. *Eur. Radiol. 13*, 195−208.
(10) Sbardella, D., Fasciglione, G. F., Gioia, M., Ciaccio, C., Tundo, G. R., Marini, S., and Coletta, M. (2011) Human matrix metalloproteinases: An ubiquitarian class of enzymes involved in several pathological processes. *Molecular Aspects of Medicine.,*.
(11) Malemud, C. J. (2006) Matrix metalloproteinases (MMPs) in health and disease: an overview. *Front. Biosci. 11*, 1696−1701.
(12) Deryugina, E. I., and Quigley, J. P. (2010) Pleiotropic roles of matrix metalloproteinases in tumor angiogenesis: contrasting, overlapping and compensatory functions. *Biochim. Biophys. Acta 1803*, 103−120.
(13) Candelario-Jalil, E., Yang, Y., and Rosenberg, G. A. (2009) Diverse roles of matrix metalloproteinases and tissue inhibitors of metalloproteinases in neuroinflammation and cerebral ischemia. *Neuroscience 158*, 983−994.
(14) Pellikainen, J. M., Ropponen, K. M., Kataja, V. V., Kellokoski, J. K., Eskelinen, M. J., and Kosma, V. M. (2004) Expression of matrix metalloproteinase (MMP)-2 and MMP-9 in breast cancer with a special reference to activator protein-2, HER2, and prognosis. *Clin. Cancer Res. 10*, 7621−7628.
(15) Deryugina, E. I., and Quigley, J. P. (2006) Matrix metalloproteinases and tumor metastasis. *Cancer Metastasis Rev. 25*, 9−34.
(16) Davis, G. E., Stratman, A. N., Sacharidou, A., and Koh, W. (2011) Molecular basis for endothelial lumen formation and tubulogenesis during vasculogenesis and angiogenic sprouting. *Int. Rev. Cell Mol. Biol. 288*, 101−165.
(17) Yoon, S. O., Park, S. J., Yun, C. H., and Chung, A. S. (2003) Roles of matrix metalloproteinases in tumor metastasis and angiogenesis. *J. Biochem. Mol. Biol. 36*, 128−137.
(18) Zhang, B., Cao, X., Liu, Y., Cao, W., Zhang, F., Zhang, S., Li, H., Ning, L., Fu, L., Niu, Y., Niu, R., Sun, B., and Hao, X. (2008) Tumor-derived matrix metalloproteinase-13 (MMP-13) correlates with poor prognoses of invasive breast cancer. *BMC Cancer 8*, 83.
(19) Coussens, L. M., Fingleton, B., and Matrisian, L. M. (2002) Matrix metalloproteinase inhibitors and cancer: trials and tribulations. *Science 295*, 2387−2392.
(20) Chetty, C., Rao, J. S., and Lakka, S. S. (2011) Matrix metalloproteinase pharmacogenomics in non-small-cell lung carcinoma. *Pharmacogenomics 12*, 535−546.
(21) Kamiya, M., Kobayashi, H., Hama, Y., Koyama, Y., Bernardo, M., Nagano, T., Choyke, P. L., and Urano, Y. (2007) An enzymatically activated fluorescence probe for targeted tumor imaging. *J. Am. Chem. Soc. 129*, 3918−3929.
(22) Ogawa, M., Kosaka, N., Longmire, M. R., Urano, Y., Choyke, P. L., and Kobayashi, H. (2009) Fluorophore-quencher based activatable targeted optical probes for detecting in vivo cancer metastases. *Mol. Pharmaceutics 6*, 386−395.
(23) Deguchi, J. O., Aikawa, M., Tung, C. H., Aikawa, E., Kim, D. E., Ntziachristos, V., Weissleder, R., and Libby, P. (2006) Inflammation in atherosclerosis: visualizing matrix metalloproteinase action in macrophages in vivo. *Circulation 114*, 55−62.
(24) Johansson, N., Vaalamo, M., Grénman, S., Hietanen, S., Klemi, P., Saarialho-Kere, U., and Kähäri, V. M. (1999) Collagenase-3 (MMP-13) is expressed by tumor cells in invasive vulvar squamous cell carcinomas. *Am. J. Pathol. 154*, 469−480.
(25) Nannuru, K. C., Futakuchi., M., Varney, M. L., Vincent, T. M., Marcusson, E. G., and Singh, R. K. (2010) Matrix metalloproteinase (MMP)-13 regulates mammary tumor-induced osteolysis by activating MMP9 and transforming growth factor-beta signaling at the tumor-boneinterface. *Cancer Res. 70*, 3494−3504.
(26) Hsu, C. P., Shen., G. H., and Ko, J. L. (2006) Matrix metalloproteinase-13 expression is associated with bone marrow microinvolvement and prognosis in non-small cell lung cancer. *Lung Cancer 52*, 349−357.
(27) Komatsu, K., Nakanishi, Y., Nemoto, N., Hori, T., Sawada, T., and Kobayashi, M. (2004) Expression and quantitative analysis of matrix metalloproteinase-2 and-9 in human gliomas. *Brain Tumor Pathology 21*, 105−112.
(28) Gessi, S., Sacchetto, V., Fogli, E., Merighi, S., Varani, K., Baraldi, P. G., Tabrizi, M. A., Leung, E., Maclennan, S., and Borea, P. A. (2010) Modulation of metalloproteinase-9 in U87MG glioblastoma cells by A3 adenosine receptors. *Biochem. Pharmacol. 79*, 1483−1495.
(29) Huang, C. W., Li, Z., Cai, H., Shahinian, T., and Conti, P. S. (2011) Biological stability evaluation of the $\alpha 2\beta 1$ receptor imaging agents: diamsar and DOTA conjugated DGEA peptide. *Bioconjugate Chem. 22*, 256−263.
(30) Huang, C. W., Li, Z., Cai, H., Chen, K., Shahinian, T., and Conti, P. S. (2011) Design, synthesis and validation of integrin $\alpha 2\beta 1$-targeted probe for microPET imaging of prostate cancer. *Eur. J. Nucl. Med. Mol. Imaging 38*, 1313−1322.
(31) Bremer, C., Bredow, S., Mahmood, U., Weissleder, R., and Tung, C. H. (2001) Optical imaging of matrix metalloproteinase-2 activity in tumors: feasibility study in a mouse model. *Radiology 221*, 523−529.
(32) Zhu, L., Xie, J., Swierczewska, M., Zhang, F., Quan, Q., Ma, Y., Fang, X., Kim, K., Lee, S., and Chen, X. (2011) Real-time video imaging of protease expression in vivo. *Theranostics 1*, 18−27.
(33) Sheth, R. A., Maricevich, M., and Mahmood, U. (2010) In vivo optical molecular imaging of matrix metalloproteinase activity in abdominal aortic aneurysms correlates with treatment effects on growth rate. *Atherosclerosis 212*, 181−187.
(34) Ogawa, M., Regino, C. A., Seidel, J., Green, M. V., Xi, W., Williams, M., Kosaka, N., Choyke, P. L., and Kobayashi, H. (2009) Dual-modality molecular imaging using antibodies labeled with activatable fluorescence and a radionuclide for specific and quantitative targeted cancer detection. *Bioconjugate Chem. 20*, 2177−2184.

Supplemental material:

Radioactive Smart Probe for Potential Corrected Matrix Metalloproteinase Imaging

Chiun-Wei Huang, Zibo Li*, Peter S Conti

Molecular Imaging Center, Department of Radiology, University of Southern California, Los Angeles, CA 90033, USA

Correspondence: Zibo Li, Ph.D., Department of Radiology, University of Southern California, 2250 Alcazar St, CSC 103, Los Angeles, California 90033, USA. Telephone: 323-442-3252; Fax: 323-442-3253; e-mail: ziboli@usc.edu

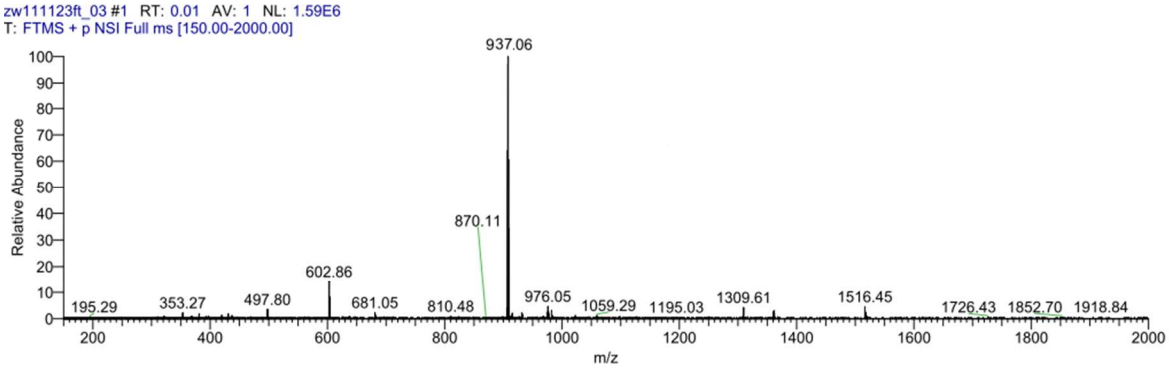

Figure S1.ESI-MS m/z spectrum of BBQ650^{IM}-PLGVR-K(Cy5.5)-E-K(DOTA)-OH.

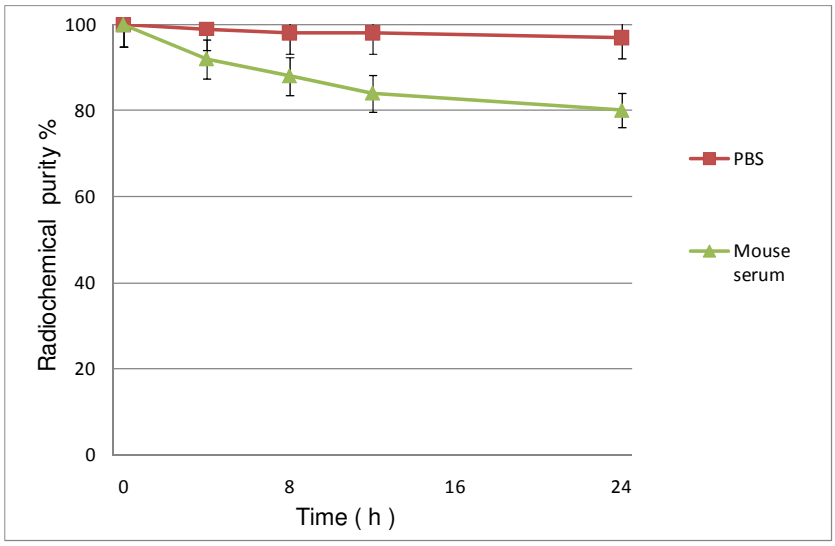

Figure S2. The *in vitro* stability curve of ^{64}Cu-BBQ650^{TM}-PLGVR-K(Cy5.5)-E -K(DOTA)-OH after incubation in PBS (pH=7.4) or mouse serum at 37℃.

Bioconjugate Chemistry

Communication

pubs.acs.org/bc

Enhanced Photodynamic Efficacy of Zinc Phthalocyanine by Conjugating to Heptalysine

Linsen Li,[†,‡,§] Zhipu Luo,[†,‡,§] Zhuo Chen,*[,†,‡,§] Jincan Chen,[†,‡,§] Shanyong Zhou,[†,‡] Peng Xu,[†,‡,§] Ping Hu,[†,‡] Jundong Wang,[∥] Naisheng Chen,[∥] Jinling Huang,[∥] and Mingdong Huang*[,†,‡,§]

[†]State Key Laboratory of Structural Chemistry, Fujian Institute of Research on the Structure of Matter, Chinese Academy of Sciences, Fuzhou, China

[‡]Danish-Chinese Centre for Proteases and Cancer (http://www.proteaseandcancer.org)

[§]Graduate University of Chinese Academy of Sciences, 19 Yuquan Road, Beijing 100049, China

[∥]College of Chemistry and Chemical Engineering, Fuzhou University, Fujian, China

Supporting Information

ABSTRACT: Zinc phthalocyanine (ZnPc) is a promising photosensitizer for photodynamic therapy, but faces some challenges: ZnPc is insoluble in water and thus requires either special formulation of ZnPc by, e.g., liposome or Cremophor EL, or chemical modification of *Pc* ring to enhance its bioavailability and photodynamic efficacy. Here, we conjugated monosubstituted ZnPc-COOH with a series of oligolysine moieties with different numbers of lysine residues (ZnPc-$(Lys)_n$ (n = 1, 3, 5, 7, 9) to improve the water solubility of the ZnPc conjugates. We measured the photosensitizing efficacies and the cellular uptakes of this series of conjugates on a normal and a cancerous cell line. In addition, we developed a sensitive *in situ* method to distinguish the difference in photodynamic efficacy among conjugates. Our results showed that ZnPc-$(Lys)_7$ has the highest photodynamic efficacy compared to the other conjugates investigated.

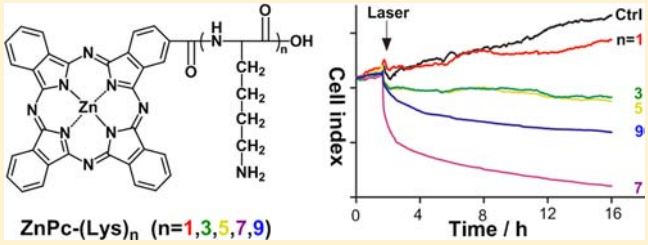

Photodynamic therapy (PDT) is a therapeutic procedure utilizing singlet oxygen and other reactive oxygen species generated by a photosensitizer through visible light irradiation to create cytotoxicity. It has been used for treatment in various therapeutic areas, including urology (bladder cancer[1,2]), gastroenterology (stomach and esophageal cancer[3]), respiratory medicine (lung cancer[4,5]), and ophthalmology (age-related macular degeneration[6]), as well as dermatology (acne[7,8]). Zinc phthalocyanine (ZnPc) is a promising class of photosensitizers for PDT[9−14] due to its relatively high photodynamic efficacy and high molar absorption coefficient in the infrared spectral region (around 670 nm). However, ZnPc is hydrophobic and insoluble in water, which hinders its systemic administration and restricts its clinical application. Special formulation is needed to increase its bioavailability and improve therapeutic outcomes. Such formulation methods include usages of liposomes or biodegradable polymeric nanoparticles.[15−18] Besides the formulation method, another strategy to enhance aqueous solubility is chemical modifications of the *Pc* core by attaching hydrophilic substituent to the core. This approach has been used in several ZnPc-based photosensitizers, including photocyanine (disulfonated diphthalimidomethyl phthalocyanine zinc)[19,20] and RLP068 (an amphiphilic tetracationic derivative of ZnPc).[21]

We previously reported a ZnPc-based photosensitizer by conjugating a pentalysine moiety to ZnPc core to enhance water solubility. This conjugate, β-carbonylphthalocyanine zinc (ZnPc-$(Lys)_5$), showed excellent *in vitro* photodynamic efficacy and significant tumor inhibition in *in vivo* studies.[22,23] The use of a five lysines to conjugate to ZnPc was an arbitrary choice. The optimal number of lysine needed for highest photodynamic efficacy is unknown, and is the subject of this study. We synthesized a series of ZnPc derivatives, ZnPc-$(Lys)_n$ (n = 1, 3, 5, 7, 9), by coupling ZnPc-COOH[24] with oligolysine peptides. Each compound was characterized by ESI-MS and UV/vis absorption spectrum (shown in Figure S1 and S2, Supporting Information) and purified to >95% purity on a semipreparative C_{18} HPLC column (Figure 1). The retentions time of these ZnPc compounds were observed to be inversely proportional to the number of lysine moieties attached (Figure 1 inset). Retention time of ZnPc-$(Lys)_n$ decreased with the increasing number of lysines, reflecting the increasing water solubility of the conjugates.

ZnPc is insoluble in water, while conjugation with only one lysine residue to ZnPc rendered slight water solubility. With more lysine residues linked to ZnPc, the conjugates ZnPc-$(Lys)_n$ showed increased solubility in water (>1 mM). Such water solubility is important for these photosensitizers to avoid

Received: June 16, 2012
Revised: September 22, 2012
Published: October 12, 2012

ACS Publications © 2012 American Chemical Society

dx.doi.org/10.1021/bc3002997 | *Bioconjugate Chem.* 2012, 23, 2168−2172

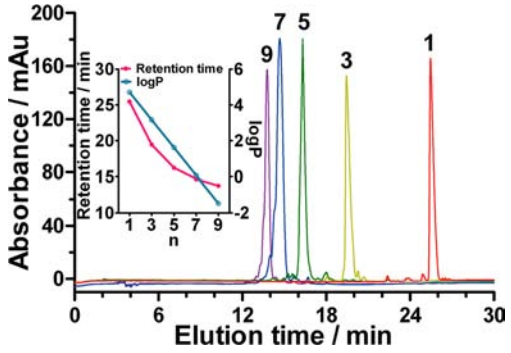

Figure 1. ZnPc-$(Lys)_n$ (n = 1, 3, 5, 7, 9) were synthesized and purified to >95% purity on a C_{18} reversed-phase HPLC column. The inset shows the relationships of the number of lysines coupled to ZnPc vs retention time and logP (logarithm of the partition coeffficient between octanol and water).

the use of surfactant, e.g., Cremophor EL, which is typically used to enhance the aqueous solubility of hydrophobic photosensitizer[25] but could cause undesired side effects.[26] We also observed that more hydrophilic conjugates aggregated less in aqueous solution, consistent with a previous study.[27]

The singlet oxygen ($^1O_2$) quantum yields of ZnPc-$(Lys)_n$ (n = 1, 3, 5, 7, 9) were measured, giving the values as follows: 0.70 ± 0.08 for ZnPc-(Lys), 0.60 ± 0.02 for ZnPc-$(Lys)_3$, 0.63 ± 0.02 for ZnPc-$(Lys)_5$, 0.74 ± 0.04 for ZnPc-$(Lys)_7$, and 0.74 ± 0.02 for ZnPc-$(Lys)_9$. These values are comparable to those of ZnPc or other ZnPcs derivatized at beta position of *Pc* ring,[28] indicating that coupling of oligolysine to ZnPc does not change the photochemical or photophysical properties of ZnPc.

Furthermore, we evaluated cellular uptakes of ZnPc-$(Lys)_n$ (n = 1, 3, 5, 7, 9) toward two human cell lines: a carcinoma cell line (stomach adenocarcinoma cell, BGC-823) and a non-cancerous fibroblast cell line (embryo lung fibroblasts, HELF). The cells were incubated with ZnPc-$(Lys)_n$ (n = 1, 3, 5, 7, 9) for 2 h, and then washed to get rid of the unbound photosensitizers. This 2 h incubation time was determined from the results of a series of kinetic cell uptake experiments on BGC-823 with different incubation times (Figure 2). Our results showed that BGC-823 absorbed ZnPc-$(Lys)_n$ (n = 1, 3, 5, 7, 9) rapidly and reached plateaus after ~2 h. As shown in Figure 3, cellular uptakes of ZnPc-$(Lys)_n$ (n = 1, 3, 5, 7, 9) in both adenocarcinoma BGC-823 and HELF were dose-dependent, with higher concentrations of the ZnPc compounds leading

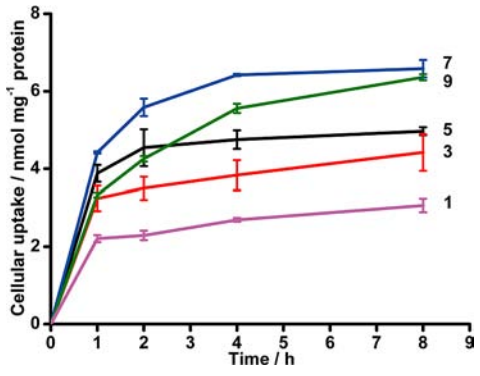

Figure 2. Kinetics of cellular uptake of ZnPc-$(Lys)_n$ (1 μM, n = 1, 3, 5, 7, 9) into BGC-823 cells shows that the uptake reaches a plateau after 2 h incubation.

to greater cellular uptakes. It is notable that cellular uptakes of ZnPc-$(Lys)_n$ (n = 1, 3, 5, 7, 9) in BGC-823 were significantly higher (about 10 times) than that in HELF, indicating that the oligolysine group enhances ZnPc's selectivity toward tumor cells. This can be partly due to the ionic interactions between the cationic charges on oligolysine under physiological pH condition and the higher anionic charges on tumor cell surfaces derived from poly(sialic acid) residues compared to normal cells.[29] Among the photosensitizer conjugates with different number of lysine groups, the differences in cellular uptakes to BGC-823 were small but noticeable and larger than the experimental errors, especially at a higher concentration (>$10^{-6.5}$ M). The cellular uptake of ZnPc-$(Lys)_n$ (n = 1, 3, 5, 7, 9) is not linearly proportional to the number of lysines attached to ZnPc. ZnPc-$(Lys)_1$ turned out to have the lowest cellular uptakes than the other conjugates. The overall order of cellular uptake with 2 h incubation is as follows: ZnPc-$(Lys)_5$ > ZnPc-$(Lys)_3$ > ZnPc-$(Lys)_7$ > ZnPc-$(Lys)_9$ > ZnPc-$(Lys)_1$. We would like to point out that the differences in cellular uptakes among ZnPc-$(Lys)_n$ (n = 3, 5, 7, 9) are not large. Nevertheless, these results show that the number of lysine residues conjugated to ZnPc is not the only structural factor determining the cellular uptake of these photosensitizers to either BGC-823 or HELF cells.

Photosensitizers were thought to enter into cells through the following mechanisms:[30] (1) pinocytosis, where photosensitizers are trapped on ruffled area on cell surface, which then pinches off into the cell to form a vesicle and subsequently fuse with lysosomes or endosomes (such mechanism is typically nonspecific and has low efficiency, and is the main mechanism for the hydrophilic photosensitizers like tetrasulfonated zinc phthalocyanine); (2) adsorptive endocytosis, where photosensitizers are incorporated into the outer leaflet of the plasma membrane and consequently move laterally to the endocytic vesicles to enter into cells (amphiphilic photosensitizers, e.g., disulfonated zinc phthalocyanine, were thought to adopt such a mechanism); (3) receptor-mediated endocytosis, where the photosensitizers have affinity toward a surface membrane receptor and the photosensitizers are internalized by the inward budding of the region of plasma membrane containing the receptor (clathrin plays an important role in receptor-mediated endocytosis by assisting the formation of entry vesicles, but is then uncoated once inside cells to allow the vesicle to fuse with other membranes to form the endosomes). The ZnPc-nK photosensitizers are amphipathic and likely enter cells through the adsorptive endocytosis pathway. However, other endocytosis mechanisms may also be involved depending on the degree of lysine conjugation. It will be interesting to further study the cellular uptake and endocytosis mechanism of this series of photosensitizers to understand the details of endocytosis mechanism.

In this study, we investigated the subcellular localizations of ZnPc-$(Lys)_n$ (n = 3 and 9) in BGC-823 using organelle-specific fluorescent probes (Mito-tracker Green for mitochondria and Lyso-tracker Red for lysosomes) and a confocal microscope. Both ZnPc-$(Lys)_3$ and ZnPc-$(Lys)_9$ were observed mainly localized in cytosol, most likely in lysosomes and mitochondria based on the costaining results with the organelle tracking dyes (as shown in SI Figure S3 and S4). The current confocal microscopy method does not have sensitivity or resolution high enough to find differences between two conjugates in their subcellular localizations. However, it is clear that neither of the conjugates was observed to localize in the nucleus. This is

dx.doi.org/10.1021/bc3002997 | *Bioconjugate Chem.* 2012, 23, 2168–2172

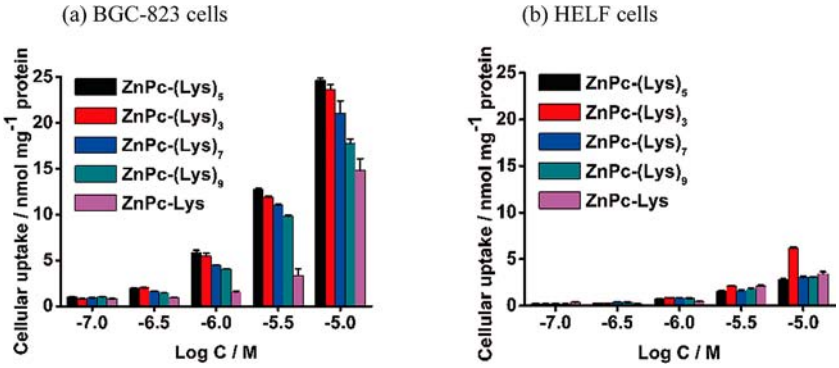

Figure 3. Dose-dependent cellular uptake of ZnPc-$(Lys)_n$ after 2 h incubation with BGC-823 (a) or HELF (b). Both panels are on the same *Y* axes for easy comparison.

important because compounds with large aromatic rings like ZnPc may be able to intercalate into the major groove of DNA, which is not preferred for normal cells because it may cause DNA mutations or saturate the genome repair capability, and thus may lead to genome instability of normal cells.

We further evaluated the phototoxicities of these ZnPc-$(Lys)_n$. Cells were first incubated with ZnPc-$(Lys)_n$ for 2 h, then washed by culture medium to get rid of the unbound photosensitizer, followed by exposure to 670 nm light at a low dosage of 1.5 J/cm^2. The surviving cells were quantitated using the conventional AlamarBlue assay. In the absence of light, all ZnPc-$(Lys)_n$ exhibited low toxicity (IC_{50} > 100 μM) toward both BGC-823 cells and HELF cells (right panels in Figure 4).

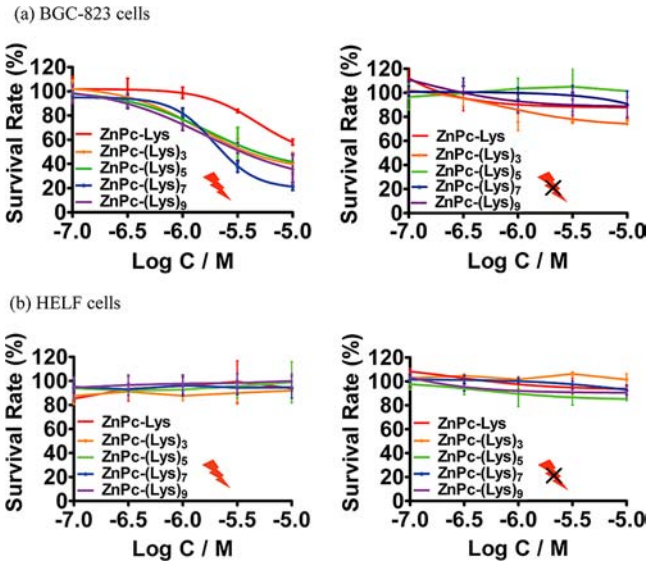

Figure 4. Phototoxicity (left panels, with a light dosage of 1.5 J/cm^2 at 670 nm) and dark toxicity (right panels) of ZnPc-$(Lys)_n$ in BGC-823 (a) and HELF (b) measured by AlamarBlue fluorometric cell viability assay. Data represent the mean ± SEM of three independent experiments, each performed in quadruplicate.

In contrast, ZnPc-$(Lys)_n$ showed significant phototoxicity to BGC-823 in the presence of light (left panels in Figure 4a) but not to HELF cells (left panels in Figure 4b), indicating their phototoxic selectivity to cancer cells. Such selectivity is consistent with results from their cellular uptakes (Figure 3). Among all ZnPc-$(Lys)_n$ investigated, ZnPc-$(Lys)_7$ is the most potent photosensitizer, killing 80% of cells at 10 μM concentration, yielding an IC_{50} of 1.9 μM.

It appears that the differences of photodynamic efficacy among ZnPc-$(Lys)_n$ were not very large (Figure 3); we thus developed a sensitive and *in situ* method to monitor, in real time, their phototoxicities. This method is based on an electric cell-substrate impedance sensing (ECIS) technique which is a label-free approach to follow the cytotoxic response of adherent cells in real-time, and it is based on electric impedance of cells grown on gold-film electrodes. Dead cells detached from gold electrode shall not contribute to impedance. Adherent cell were grown on plates with gold mesh electrodes in the bottom of wells. The electric impedance value measured is proportional to the number of cells attached to the gold electrode.[31] This is a label-free approach to follow the cytotoxic response of adherent cells in real time. As shown in Figure 5, the impedance of HELF did not change significantly upon treatment of 1 μM ZnPc-$(Lys)_n$ followed by irradiation at a dosage of 1.5 J/cm^2, whereas the impedance of BGC-823 decreased rapidly compared to that of the untreated group upon the same treatment. In BGC-823 cells, ZnPc-$(Lys)_7$ exhibited the most efficient photodynamic efficacy, while ZnPc-Lys was the least efficient photosensitizer among all ZnPc-$(Lys)_n$ studied. These results are consistent with the cytotoxicity assay shown in Figure 4. Together, our experiments demonstrated the presence of an optimal degree of amphiphilicity on photosensitizer for the best phototoxicity. The presence of such an optimal degree of amphiphilicity on ZnPc photosensitizers for photodynamic efficacy was also observed by Cauchon et al. on their series of photosensitizers, alkynyl-substituted trisulfonated ZnPc ($ZnPcS_3R$), where the highest cellular uptake and phototoxicity were observed in the nonynyl derivative with a chain length of nine carbon atoms.[27]

The advantage of this impedance-based method is not only its high sensitivity to distinguish the difference in phototoxicity efficacy among the ZnPc-$(Lys)_n$ photosensitizers, but also the possibility for real-time measurement. It is worthwhile to note that phototoxicity was induced rapidly upon light irradiation: a large proportion of cells were killed in less than 0.5 h. Our microscopy examination after light irradiation also confirmed the finding that BGC-823 cells were fragmented and lost cell membrane integrity upon treatment of 1 μM ZnPc-$(Lys)_n$ followed by irradiation at a dosage of 1.5 J/cm^2 (see Figure S5, Supporting Information). Again, these images showed that ZnPc-$(Lys)_7$ is the best photosensitizer in this series of conjugates.

dx.doi.org/10.1021/bc3002997 | *Bioconjugate Chem.* 2012, 23, 2168–2172

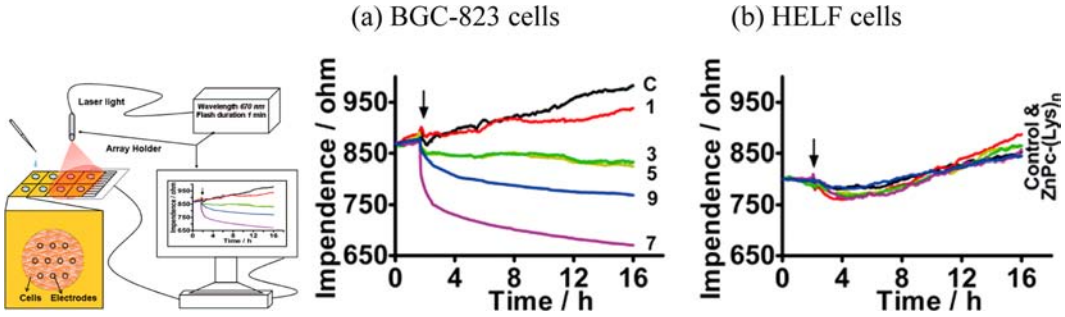

Figure 5. Schematic of photodynamic efficacy measurement based on ECIS method (left panel). The right panel shows the real-time phototoxicity of ZnPc-$(Lys)_n$ (n = 1, 3, 5, 7, 9) on BGC-823 and HELF. Cells were preincubated without (C: Control) or with 1 μM of ZnPc-$(Lys)_n$ for 2 h, followed by irradiation (at the time point indicated with an arrow) with 670 nm laser for 1 min.

It is well-known that ZnPc-based photosensitizers have a strong tendency to aggregate in aqueous solution, presumably through the $\pi-\pi$ stacking interaction of the *Pc* aromatic ring. Such aggregation quenches ZnPc fluorescence and dramatically reduces singlet oxygen quantum yield and their photodynamic activity. Is it possible that oligolysine moieties on ZnPc-$(Lys)_n$ compounds interfere with the aggregation behavior of these compounds, and thus their cellular uptake and phototoxicity behaviors on cell surface? To rule out this possibility, we incubated BGC-823 with ZnPc-$(Lys)_n$ and measured the UV/vis spectra of ZnPc-$(Lys)_n$ bound to the cell surface. Considering the limited amount of the compounds adsorbed onto the cells, we used a diffusion reflectance method to enhance the signals (Figure S6). The results showed the absence of bands corresponding to the aggregated ZnPc-$(Lys)_n$ but the presence of Q bands (670 nm, monomeric ZnPc) in all ZnPc-$(Lys)_n$ compounds, even though the signal (peak height of 670 nm band) was not particularly strong to allow for further quantitative assessment. Our results indicated that ZnPc-$(Lys)_n$ oligomerization in aqueous solution can be broken up by lipid bilayers on the cell surface into monomer. Even though the photosensitizer can also oligomerize upon entering into cytosol, it can become monomeric again upon contact with cellular organelles like mitochondria or lysosomes. Thus, this observation explains the effectiveness of phototoxicity of our photosensitizers despite their aggregation in aqueous solution.

In summary, we synthesized a series of ZnPc-based photosensitizers conjugated with different numbers of lysine residues. The potential of these compounds as photodynamic therapy photosensitizers was assessed using human stomach adenocarcinoma cells (BGC-823) and human embryo lung fibroblasts (HELF), based on their photophysical and photochemical properties, quantitative cellular uptakes, intracellular localization and phototoxicity measurements. These photosensitizers showed selective phototoxicities to carcinoma cells, but minimal toxicities to fibroblast cells along with low dark toxicities to both cells. A real-time impedance-based assay was developed to distinguish the difference of phototoxicities among them, unambiguously identifying that ZnPc-$(Lys)_7$ is the most potent compound for photodynamic effect. This study determined the optimal degree of amphiphilicity on ZnPc-based photosensitizer for maximal cellular phototoxicity and can be valuable to guide future design of photosensitizers. Meanwhile, ECIS-based phototoxicity assay opens up a new way to evaluate photodynamic efficacy of photosensitizers on adherent cells.

■ ASSOCIATED CONTENT

Ⓢ Supporting Information

Experimental details and characterization data. This material is available free of charge via the Internet at http://pubs.acs.org.

■ AUTHOR INFORMATION

Corresponding Author

*E-mail: zchen@fjirsm.ac.cn (ZC) and mhuang@fjirsm.ac.cn (MH). Tel: (+86)0591-83704996, Fax: (+86)0591-83714946.

Notes

The authors declare no competing financial interest.

■ ACKNOWLEDGMENTS

We thank National Natural Science Foundation (30973567, 81171634 and 31161130356) for financial support.

■ REFERENCES

(1) Pinthus, J. H., Bogaards, A., Weersink, R., Wilson, B. C., and Trachtenberg, J. (2006) Photodynamic therapy for urological malignancies: past to current approaches. *J. Urol. 175*, 1201−7.

(2) Juarranz, A., Jaen, P., Sanz-Rodriguez, F., Cuevas, J., and Gonzalez, S. (2008) Photodynamic therapy of cancer. Basic principles and applications. *Clin. Transl. Oncol. 10*, 148−54.

(3) Wiedmann, M. W., and Caca, K. (2004) General principles of photodynamic therapy (PDT) and gastrointestinal applications. *Curr. Pharm. Biotechnol. 5*, 397−408.

(4) Ost, D. (2003) Photodynamic therapy in lung cancer. A review. *Methods Mol. Med. 75*, 507−26.

(5) Usuda, J., Kato, H., Okunaka, T., Furukawa, K., Tsutsui, H., Yamada, K., Suga, Y., Honda, H., Nagatsuka, Y., Ohira, T., Tsuboi, M., and Hirano, T. (2006) Photodynamic therapy (PDT) for lung cancers. *J. Thorac. Oncol. 1*, 489−93.

(6) Mittra, R. A., and Singerman, L. J. (2002) Recent advances in the management of age-related macular degeneration. *Optom. Vis. Sci. 79*, 218−24.

(7) Elsaie, M. L., and Choudhary, S. (2010) Photodynamic therapy in the management of acne: an update. *J. Cosmet. Dermatol. 9*, 211−7.

(8) Riddle, C. C., Terrell, S. N., Menser, M. B., Aires, D. J., and Schweiger, E. S. (2009) A review of photodynamic therapy (PDT) for the treatment of acne vulgaris. *J. Drugs Dermatol. 8*, 1010−1019.

(9) Liu, J. Y., Lo, P. C., Fong, W. P., and Ng, D. K. (2009) Effects of the number and position of the substituents on the in vitro photodynamic activities of glucosylated zinc(II) phthalocyanines. *Org. Biomol. Chem. 7*, 1583−91.

(10) Liu, J. Y., Jiang, X. J., Fong, W. P., and Ng, D. K. (2008) Highly photocytotoxic 1,4-dipegylated zinc(II) phthalocyanines. Effects of the chain length on the in vitro photodynamic activities. *Org. Biomol. Chem. 6*, 4560−6.

(11) Milla, L. N., Yslas, E. I., Cabral, A., Durantini, E. N., Romanini, S., Rivarola, V., and Bertuzzi, M. (2009) Pharmacokinetic, toxicological

and phototherapeutic studies of phthalocyanine ZnPcCF3. *Biomed. Pharmacother. 63*, 209−15.
(12) Duan, W., Lo, P. C., Duan, L., Fong, W. P., and Ng, D. K. (2010) Preparation and in vitro photodynamic activity of amphiphilic zinc(II) phthalocyanines substituted with 2-(dimethylamino)ethylthio moieties and their N-alkylated derivatives. *Bioorg. Med. Chem. 18*, 2672−7.
(13) Machado, A. H. A., Moraes, K. C. M., Soares, C. P., Beltrame, M., and da Silva, N. S. (2010) Cellular changes after photodynamic therapy on HEp-2 cells using the new ZnPcBr8 phthalocyanine. *Photomed. Laser Surg. 28*, S143−S149.
(14) Bai, M., Lo, P. C., Ye, J., Wu, C., Fong, W. P., and Ng, D. K. (2011) Facile synthesis of pegylated zinc(II) phthalocyanines via transesterification and their in vitro photodynamic activities. *Org. Biomol. Chem. 9*, 7028−32.
(15) Ricci-Junior, E., and Marchetti, J. M. (2006) Preparation, characterization, photocytotoxicity assay of PLGA nanoparticles containing zinc (II) phthalocyanine for photodynamic therapy use. *J. Microencapsul. 23*, 523−38.
(16) Chatterjee, D. K., Fong, L. S., and Zhang, Y. (2008) Nanoparticles in photodynamic therapy: an emerging paradigm. *Adv. Drug Delivery Rev. 60*, 1627−37.
(17) Fadel, M., Kassab, K., and Fadeel, D. A. (2010) Zinc phthalocyanine-loaded PLGA biodegradable nanoparticles for photodynamic therapy in tumor-bearing mice. *Lasers Med. Sci. 25*, 283−72.
(18) da Volta Soares, M., Oliveira, M. R., Dos Santos, E. P., de Brito Gitirana, L., Barbosa, G. M., Quaresma, C. H., and Ricci-Junior, E. (2011) Nanostructured delivery system for zinc phthalocyanine: preparation, characterization, and phototoxicity study against human lung adenocarcinoma A549 cells. *Int. J. Nanomed. 6*, 227−38.
(19) Xie, B. G., Huang, H. F., Huang, J. D., Chen, N. S., and Huang, J. L. (2004) Determination and pharmacokinetics of photosensitizer ZnPcS2P2 uptaken by K562 cells. *Guang Pu Xue Yu Guang Pu Fen Xi 24*, 1415−8.
(20) Huang, Z. (2008) An update on the regulatory status of PDT photosensitizers in China. *Photodiagnosis Photodyn. Ther. 5*, 285−287.
(21) Fabris, C., Soncin, M., Mazzon, E., Calzavara-Pinton, P., Lia, F., Giacomo, C., Dei, D., Tampucci, S., Roncucci, G., and Jori, G. (2005) A novel tetracationic phthalocyanine as a potential skin phototherapeutic agent. *Exp. Dermatol. 14*, 675−83.
(22) Singh, K. P., Brown, M., Murphy, M. E., and Gillespie, S. H. (2012) Moxifloxacin for tuberculosis. *Lancet Infect. Dis. 12*, 176 author reply 177−8..
(23) Chen, Z., Zhou, S., Chen, J., Deng, Y., Luo, Z., Chen, H., Hamblin, M. R., and Huang, M. (2010) Pentalysine beta-carbonylphthalocyanine zinc: an effective tumor-targeting photosensitizer for photodynamic therapy. *ChemMedChem 5*, 890−898.
(24) Chen, J., Chen, N., Huang, J., Wang, J., and Huang, M. (2006) Derivatizable phthalocyanine with single carboxyl group: Synthesis and purification. *Inorg. Chem. Commun. 9*, 313−315.
(25) Konan, Y. N., Gurny, R., and Allemann, E. (2002) State of the art in the delivery of photosensitizers for photodynamic therapy. *J. Photochem. Photobiol., B 66*, 89−106.
(26) Yamaguchi, J. Y., Nishimura, Y., Kanada, A., Kobayashi, M., Mishima, K., Tatsuishi, T., Iwase, K., and Oyama, Y. (2005) Cremophor EL, a non-ionic surfactant, promotes Ca(2+)-dependent process of cell death in rat thymocytes. *Toxicology 211*, 179−86.
(27) Cauchon, N., Tian, H., Langlois, R., La Madeleine, C., Martin, S., Ali, H., Hunting, D., and van Lier, J. E. (2005) Structure-photodynamic activity relationships of substituted zinc trisulfophthalocyanines. *Bioconjugate Chem. 16*, 80−89.
(28) Ogunsipe, A., Chen, J.-Y., and Nyokong, T. (2004) Photophysical and photochemical studies of zinc(ii) phthalocyanine derivatives?effects of substituents and solvents. *New J. Chem. 28*, 822−827.
(29) Kornguth, S. E., Kalinke, T., Robins, H. I., Cohen, J. D., and Turski, P. (1989) Preferential binding of radiolabeled poly-L-lysines to C6 and U87 MG glioblastomas compared with endothelial cells in vitro. *Cancer Res. 49*, 6390−6395.
(30) Norum, O. J., Selbo, P. K., Weyergang, A., Giercksky, K. E., and Berg, K. (2009) Photochemical internalization (PCI) in cancer therapy: from bench towards bedside medicine. *J. Photochem. Photobiol., B 96*, 83−92.
(31) Giaever, I., and Keese, C. R. (1993) A morphological biosensor for mammalian cells. *Nature 366*, 591−2.

Enhanced Photodynamic Efficacy of Zinc Phthalocyanine by Conjugating to Heptalysine

- Supporting Information

Linsen Li,[†,‡,§] Zhipu Luo,[†,‡,§] Zhuo Chen,*[,†,‡,§] Jincan Chen,[†,‡,§] Shanyong Zhou,[†,‡] Peng Xu,[†,‡,§] Ping Hu,[†,‡] Jundong Wang,[¶] Naisheng Chen,[¶] Jinling Huang,[¶] and Mingdong Huang*[,†,‡,§]

[†] State Key Laboratory of Structural Chemistry, Fujian Institute of Research on the Structure of Matter, Chinese Academy of Sciences, China

[‡] Danish-Chinese Centre for Proteases and Cancer

[§] Graduate University of Chinese Academy of Sciences, 19 Yuquan Road, Shijingshan District, Beijing 100049, China

[¶] Institute of Functional Materials, College of Chemistry and Chemical Engineering, Fuzhou University, Fujian, China

* Corresponding author, E-mail: zchen@fjirsm.ac.cn (ZC) and mhuang@fjirsm.ac.cn (MH).

Contents	Page
Synthesis of ZnPc-$(Lys)_n$ (n=1, 3, 5, 7, 9)	**S3**
Characterization of ZnPc-$(Lys)_n$ (n=1, 3, 5, 7, 9)	**S5**
Cells and culture conditions	**S8**
Cytotoxicity assay	**S8**
Optimization of cell-photosensitizer incubation time for phototoxicity experiments	**S9**
Cellular uptake	**S9**
Subcellular localization	**S10**
Cellular phototoxicity by impedance measurements	**S12**
Diffuse reflectance measurement on cell surface	**S13**
Statistics	**S14**

Synthesis of ZnPc-$(Lys)_n$ (n=1, 3, 5, 7, 9)

As shown in **Scheme 1**, monosubstituted β-carboxyphthalocyanine zinc (ZnPc-COOH) was first synthesized according to our published protocol. [1] Polylysine ZnPc conjugates of varying charges (ZnPc-$(Lys)_n$) (n=1, 3, 5, 7, 9) were then prepared by coupling ZnPc-COOH prepared as above with tBoc-protected polylysine on Wang resin ($(Lys)_n$-Wang resin, n = 1, 3, 5, 7, 9; Shanghai Biotech Bioscience and Technology Co. Ltd., China). Typically, 500 mg of ZnPc-COOH (0.8 mmol) was dissolved in N,N-dimethylformamide (DMF, 25 ml) with 5% pyridine, and was incubated in the dark with a peptide coupling agent N,N'-dicyclohexylcarbodiimide (DCC, 330mg, 1.6 mmol) and an activating reagent 1-hydroxybenzotriazole (HOBt, 215 mg, 1.59 mmol) for 30 min at room temperature. This solution was then mixed with filtered $(Lys)_n$-Wang resin solution (n = 1, 3, 5, 7, 9) which was prepared as follows: 375 mg of $(Lys)_n$-Wang resin (n = 1, 3, 5, 7, 9; parity grade: 0.3 - 0.8 mmol/g) was added into DMF (6 ml) and the solution was kept at room temperature for 30 min before being filtered. After adding another 4 ml of DMF with 5% pyridine, the mixed solution was kept stirring overnight to allow the reaction to reach completion. The Wang resin was washed with DMF until becoming colorless and then washed with dichloromethane and methanol before dried under vacuum. To cleave the coupled product from the resin and to cleave tBoc protecting groups from lysine residues, the resin was allowed to react with 95% trifluoroacetic acid for 3 h. ZnPc-$(Lys)_n$ (n=1, 3, 5, 7, 9) was then precipitated out by cooled anhydrous ethyl ether. These final products were dried under vacuum and further purified by preparative HPLC (Dalian Elite Analytical Instruments Co. Ltd., Dalian, China) with a Fuji C_{18} column (250×30 mm, 10 μm, Beijing Chuangxin Tongheng Science & Technology Co. Ltd., Beijing, China), eluting with a linear gradient of 50→100% mixed solvent CH_3OH/CH_3CN (1:1 v/v) under a flow rate 10 ml/min within 20 min. The final

yields of ZnPc-$(Lys)_n$ (n=1, 3, 5, 7, 9) were calculated as 66.1%, 53.1%, 38.6%, 21.6% and 38.5% respectively based on compound ZnPc-COOH.

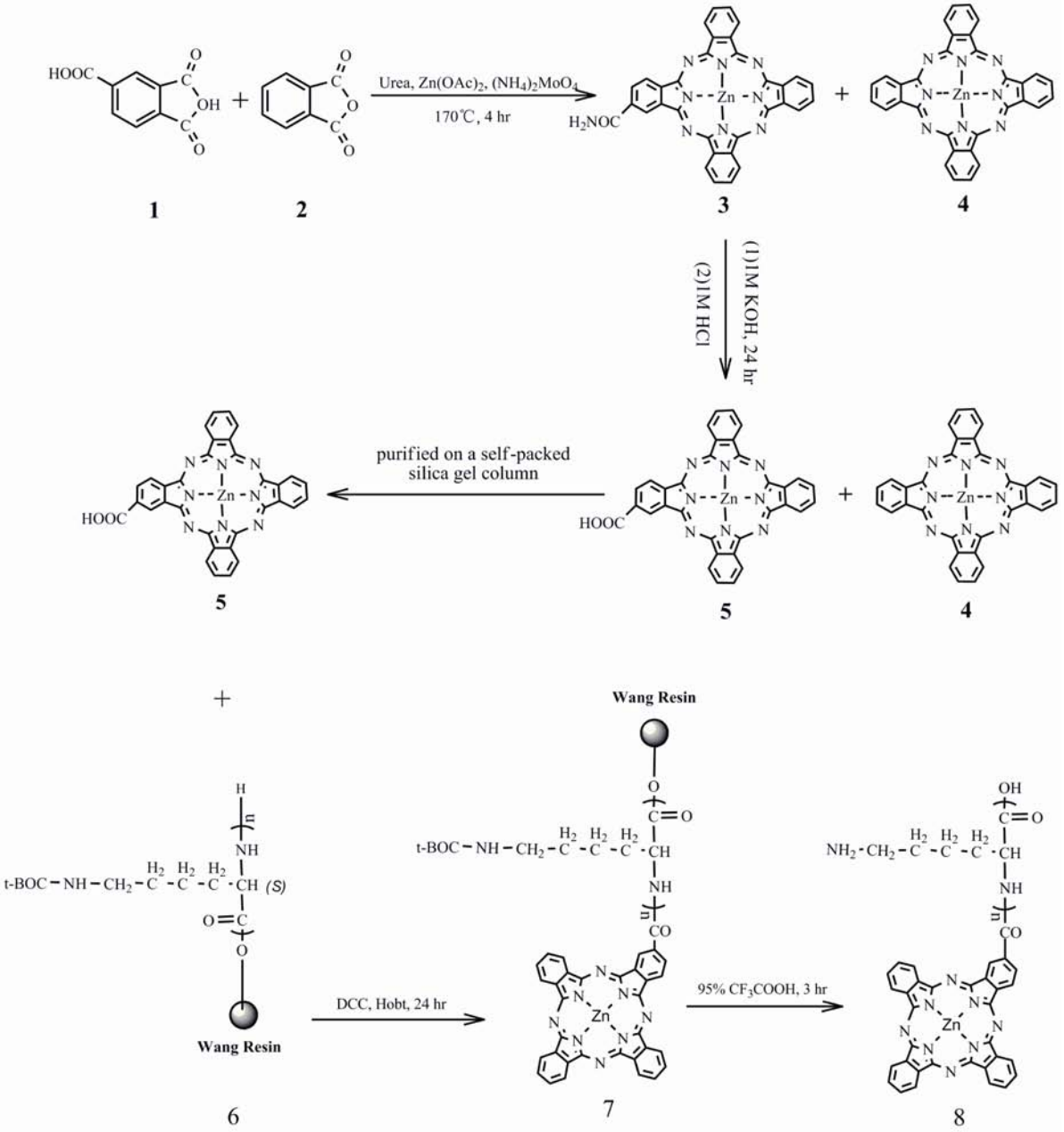

Scheme 1 Synthetic route and chemical structures of ZnPc-$(Lys)_n$ (n=1, 3, 5, 7, 9)

Characterization of ZnPc-$(Lys)_n$ (n=1, 3, 5, 7, 9)

As shown in **Figure S1**, ZnPc-$(Lys)_n$ (n=1, 3, 5, 7, 9) were confirmed by mass spectrometry with ESI MS (DECAX-30000 LCQ Deca XP) as follows: ZnPc-Lys: m/z $[M+H]^+$ calcd for $C_{39}H_{28}N_{10}O_3Zn$: 751.1, found: 751.4; m/z $[2M+H]^+$ calcd for $C_{39}H_{28}N_{10}O_3Zn$: 1501.2, found: 1501.3; ZnPc-$(Lys)_3$: m/z $[M+H]^+$ calcd for $C_{51}H_{52}N_{14}O_5Zn$: 1007.4, found: 1007.7; ZnPc-$(Lys)_5$: m/z $[M+H]^+$ calcd for $C_{63}H_{76}N_{18}O_7Zn$: 1263.8, found: 1264.2, m/z $[M+2H]^{2+}$ calcd for $C_{63}H_{76}N_{18}O_7Zn$: 632.4, found: 633.2; ZnPc-$(Lys)_7$: m/z $[M+H]^+$ calcd for $C_{75}H_{100}N_{22}O_9Zn$: 1520.1, found: 1519.9, m/z $[M+2H]^{2+}$ calcd for $C_{75}H_{100}N_{22}O_9Zn$: 760.6, found: 760.7; ZnPc-$(Lys)_9$: m/z $[M+H]^+$ calcd for $C_{87}H_{124}N_{26}O_{11}Zn$: 1776.5, found: 1775.9, m/z $[M+2H]^{2+}$ calcd for $C_{87}H_{124}N_{26}O_{11}Zn$: 888.7, found: 888.2. All above data confirm the molecular structures of ZnPc-$(Lys)_n$ (n=1, 3, 5, 7, 9).

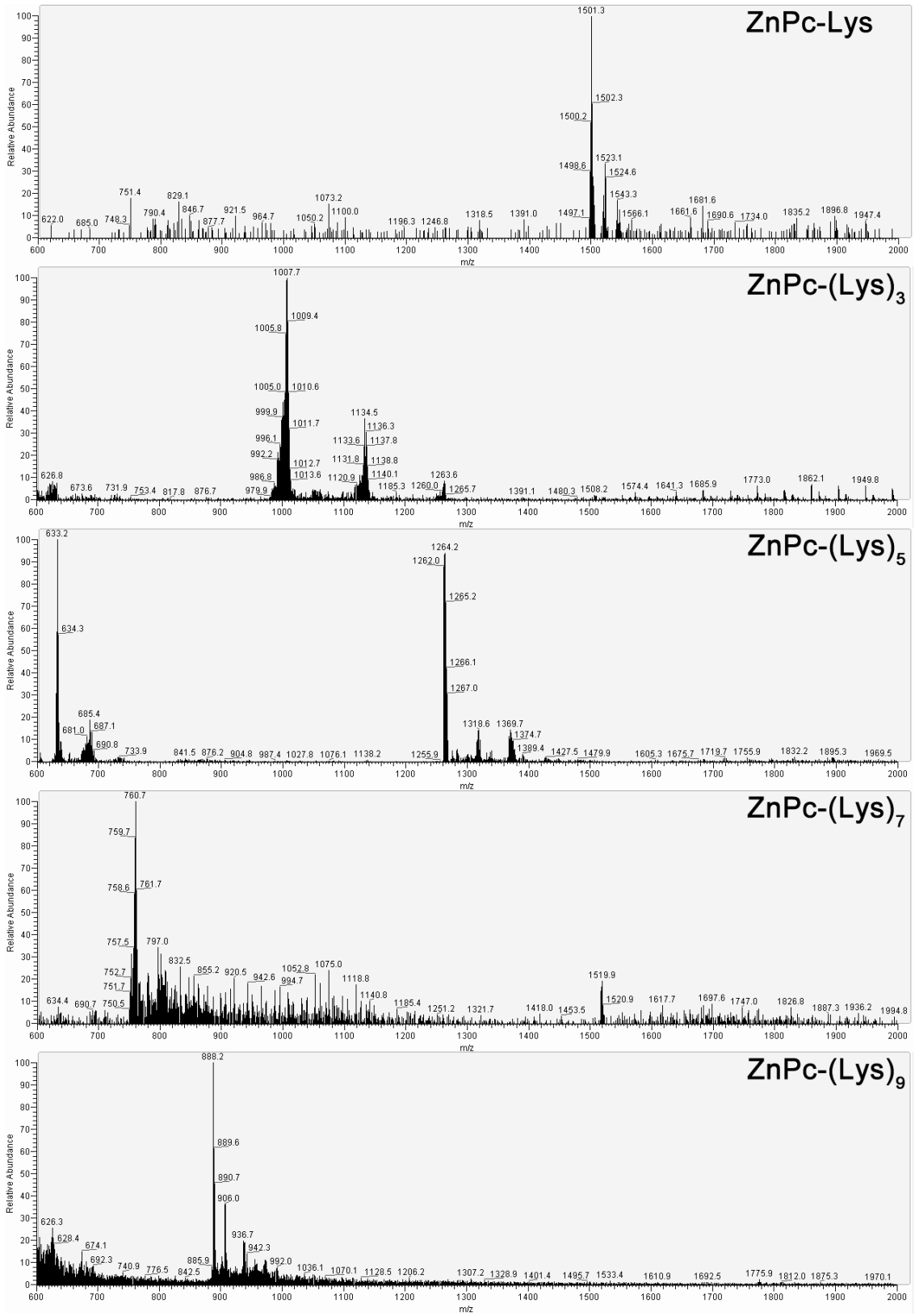

Figure S1 Mass spectrum of ZnPc-$(Lys)_n$ (n=1, 3, 5, 7, 9) in DMSO

The UV/Vis absorption spectrum of ZnPc-$(Lys)_n$ in DMSO were recorded from 300 to 800 nm by multi-mode microplate reader (Synergy 4, BioTek Instruments) (as shown in **Figure S2**). Furthermore, an analytical HPLC was carried out on a C_{18} RP HPLC system (Dalian Elite Analytical Instruments Co. Ltd., Dalian, China; column: SinoChrom ODS-BP, 250×20mm, 10μm) using a linear gradient of 50→100% CH_3OH/CH_3CN (1:1 v/v) at a flow rate of 1 ml/min for 20 min. The purity of ZnPc-$(Lys)_n$ (n=1, 3, 5, 7, 9) were determined by a reversed-phase HPLC as 100%, 98%, 100%, 95% and 100%, respectively.

The UV/Vis absorption spectra of above ZnPc compounds in DMSO showed weak absorptions in sun-light spectrum regions, with a weak band centered at 343 nm which is desirable in reducing their potential dark toxicities. In addition, all these compounds exhibit a Q band at 678 nm ($\varepsilon_{678\ nm} \approx 1.2 \times 10^5$ L mol^{-1} cm^{-1}) along with a weak band at 610 nm (Supporting Information), which is attributed to oligomer (especially dimer) of ZnPc. Only a minimal degree of aggregation was observed in ZnPc compounds in DMSO. However, obvious aggregation existed for all ZnPc-$(Lys)_n$ compounds in aqueous buffer, including water and phosphate buffer saline, or in fetal bovine serum containing cell culture medium.

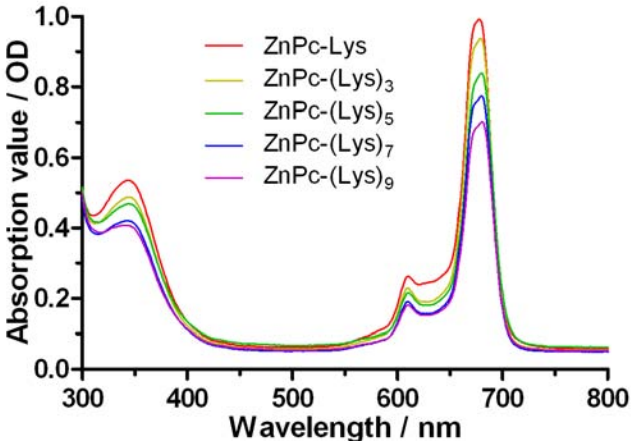

Figure S2 The UV-Vis absorption spectrum of ZnPc-$(Lys)_n$ (n=1, 3, 5, 7, 9) in DMSO.

Cells and culture conditions

The cell lines we used in the study were human stomach adenocarcinoma (BGC-823) and human embryo lung fibroblasts (HELF). They were purchased from Shanghai Institute of Cell Biology, Chinese Academy of Sciences, China and were routinely maintained in RPMI-1640 (GIBCO BRL), supplemented with 10% (v/v) heat-inactivated fetal calf serum (FCS), penicillin (100 UmL^{-1}), and streptomycin (100 μgmL^{-1}) at 37°C under humidified air containing 5% CO_2. Both cells are adherent cells and thus need to be detached by treatment with a trypsin-EDTA solution before cell counting and dilution to 96-well plates in preparation for photodynamic assays. Cells were maintained in logarithmic phase with viability >95%.

Cytotoxicity assay

Cells at a density of 2 x 10^5 cells per ml at a volume of 200 μl per well were placed in 96-multiwell plates and incubated overnight at 37°C under 5% CO_2. One column of wells did not receive cells to serve as a blank. The cells were incubated with ZnPc compounds at various concentrations (10^{-7}, $10^{-6.5}$, 10^{-6}, $10^{-5.5}$and 10^{-5} M) for a period of 2 h. One control column in the plate was filled with conjugate-free culture medium only. The cells were then washed twice with sterile PBS before fresh medium was added. The plates were illuminated with a light dosage of 1.5 J/cm^2 (at a fluence of 100 mW/cm^2 for 1 min) using a 670 nm SAS-DL3 medical laser (Beijing Shou'anshan Electronic Technology Co. Ltd., China) before keeping in the incubator for 14 h; dark toxicity was measured in parallel. Cell viability was determined 14 h after irradiation on a multi-mode microplate reader (Synergy 4, BioTek Instruments) using the AlamarBlue™ fluorometric cell viability assay (BioSource International Inc., Camarillo, CA, USA) with λ_{ex} 530 nm and λ_{em} 590 nm. The average fluorescence reading of the blank wells was subtracted from the readings of the wells containing cells. Four replicates were run per drug dose in each

cell line, and all experiments were repeated three times. The cell phototoxicity curves were plotted as a function of the conjugate dose.

Optimization of cell-photosensitizer incubation time for phototoxicity experiments

Cells were trypsinized in the exponential growth phase and counted using a hemocytometer. Aliquots of cells (~ 2×10^5 per 1 ml growth medium with 10% FCS) were seeded into wells of 96-multiwell culture plates (Falcon). These were returned to the incubator and kept at 37°C to allow cells to attach and resume exponential growth. Then the medium was removed and replaced with growth medium with 10% FCS with a final concentration of the ZnPc-$(Lys)_n$ conjugates at 10^{-6} M in quadruplicates and again kept at 37°C. At all times the plates were protected from light by wrapping with aluminum foil. After several different incubation periods (0 h, 1 h, 2 h, 4 h or 8 h), the drug solution was aspirated from the wells. The cells were washed three times with sterile PBS and then dissolved in 0.1 M NaOH / l% SDS for 1 h to give a homogenous solution. The fluorescence of the cell extract was measured on a multi-mode microplate reader (Synergy 4, BioTek Instruments) with λ_{ex} 610 nm and λ_{em} 680 nm. The protein content of the entire cell extract was determined by BCA protein assay. Standard curves were made with cell lysates treated as above with known added amounts of bovine serum albumin. Results were expressed as nmol of ZnPc per mg cell protein.

Cellular uptake

With the same procedure described above, cells (~ 2×10^5 per 1 ml growth medium with 10% FCS) were seeded into wells of 96-multiwell culture plates (Falcon) and treated with various concentrations of conjugates (10^{-7}, $10^{-6.5}$, 10^{-6}, $10^{-5.5}$and 10^{-5}M final concentration in medium) in quadruplicates. At all times the plates were protected from light by wrapping with aluminum foil.

After 2 h incubation, the drug solution was aspirated from the wells. The cells were washed three times with sterile PBS and then dissolved in 0.1 M NaOH / l% SDS for at least 1 h to give a homogenous solution. The fluorescence of the cell extract was measured on a multi-mode microplate reader (Synergy 4, BioTek Instruments) with λ_{ex} 610 nm and λ_{em} 680 nm. The protein content of the entire cell extract was determined by BCA protein assay kit. Standard curves were made with cell lysates treated as above with known added amounts of bovine serum albumin. Results were expressed as nmol of ZnPc per mg cell protein.

Subcellular localization

Cell suspensions (~ 1×10^5 cells per 1 ml growth medium with 10% FCS) were plated onto glass cover slips and incubated for overnight at 37°C, 5% CO_2 to allow cell adhesion. The medium was removed, and the attached cells were washed three times with PBS, and then overlaid with 1 ml of culture medium containing 1% FCS, before being exposed to 10 μM of ZnPc-$(Lys)_n$ for 2 h at 37°C. For this co-localization, the cells were incubated for 30 min with Mito-Tracker Green (20 nM, Beyotime Institute of Biotechnology) and Lyso-Tracker Red (50 nM, Beyotime Institute of Biotechnology), which were used as organelle markers for the mitochondria and lysosomes, respectively. The unbound dye was then removed by washing three times with PBS and twice more with low-phosphate buffer (HBSS/HEPES) prior to the cells imaging with confocal laser scanning microscope (Olympus FluoView 1000). Specimens were excited by He-Ne laser light (λ 633 nm) and the emission wavelength was at 650-800nm. The emitted fluorescence was filtered using a barrier filter (670/40 nm band pass). Laser line intensity, photometric gain, PMT setting, and filter attenuation were kept constant throughout the experiments.

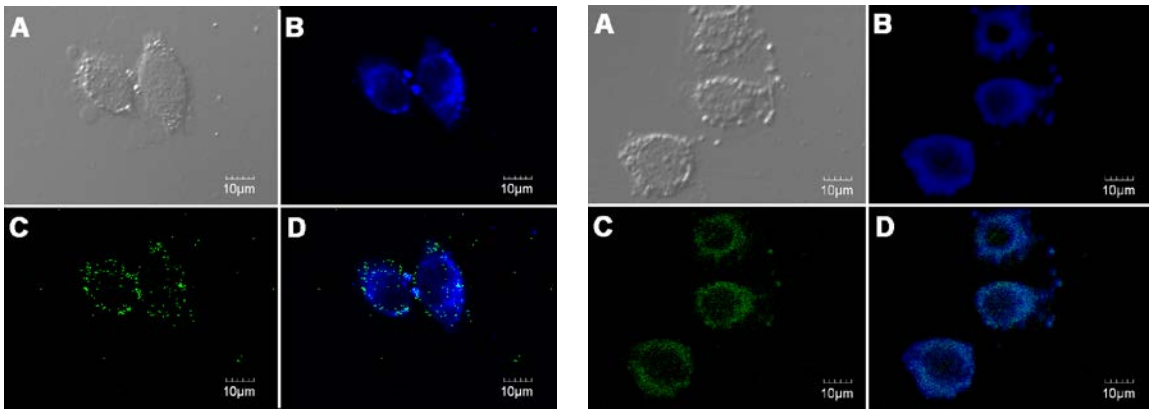

10 μM of ZnPc-$(Lys)_3$ 10 μM of ZnPc-$(Lys)_9$

Figure S3 Subcellular localizations of conjugates ZnPc-$(Lys)_3$ and ZnPc-$(Lys)_9$ in BGC-823 cells at 10 μM for 2 h. A) Phase contrast, B) ZnPc-$(Lys)_3$ or ZnPc-$(Lys)_9$ fluorescence, C) Mito-Tracker Green fluorescence, D) overlay of Mito-Tracker Green with ZnPc-$(Lys)_3$ or ZnPc-$(Lys)_9$ fluorescence.

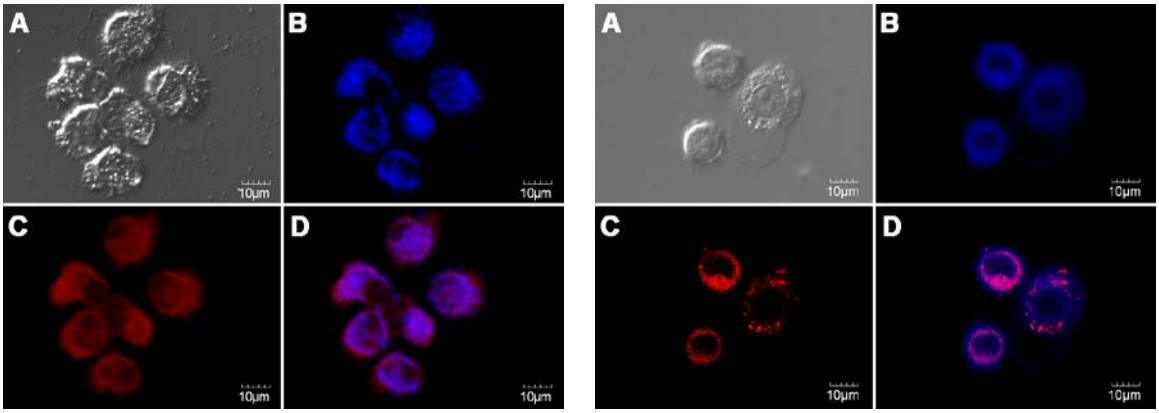

10 μM of ZnPc-$(Lys)_3$ 10 μM of ZnPc-$(Lys)_9$

Figure S4 Subcellular localizations of conjugates ZnPc-$(Lys)_3$ and ZnPc-$(Lys)_9$ in BGC-823 cells at 10 μM for 2 h. A) Phase contrast, B) ZnPc-$(Lys)_3$ or ZnPc-$(Lys)_9$ fluorescence, C) Lyso-Tracker Red fluorescence, D) overlay of Lyso-Tracker Red with ZnPc-$(Lys)_3$ or ZnPc-$(Lys)_9$ fluorescence.

Cellular phototoxicity by electric impedance measurements

An 8 well plate 8W10E (Applied Biophysics, NY) was used in this assay. Each well has a surface area of 0.8 cm^2 and holds 600 μl culture medium. Each well contains ten individual interdigitated gold microelectrodes (250 μm diameter) to measure electric current flow through the medium. These individual electrodes are connected to an ECIS Z system (Applied Biophysics, Inc., NY, USA). The frequency of electric impedance response for each cell type was optimized with of multi-frequency optimization run with a 60 sec sampling interval. In a typical ECIS experiment, the 8W10E plates were equilibrated with cell medium in an incubator (37°C, 100% humidity and 5% CO_2) for at least 2 h before the cells (2×10^5) were seeded into each well of the array plates with fresh medium (200 μl). The plates were then connected to ECIS instrument and put back into the incubator. The cells were allowed to attach to the plates for 5 h when the electric impedance response of cells on the plates was stabilized and became a straight line. The ECIS measurement was paused and the culture medium of wells in the 8W10E plates was replaced with just fresh medium (as a control) or the medium containing ZnPc conjugates (at a final concentration of 1 μM). After 2 h incubation, the cells were washed with fresh culture medium without photosensitizer to remove the unbound photosensitizer. The 670 nm laser light was applied to the selected wells to a light dosage of 1.5 J/cm^2 using a SAS-DL3 medical laser instrument. The electric impedance data collection was continued throughout the incubation and extended for 16 h after the light illumination.

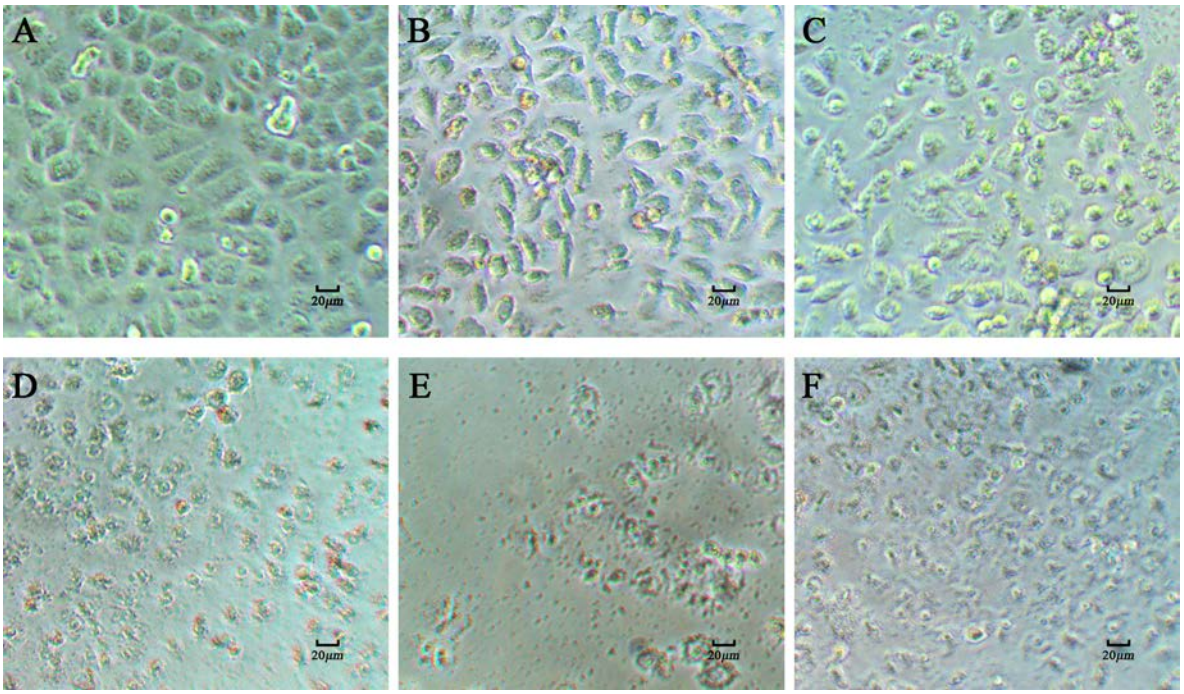

Figure S5 Microscopic images of the BGC-823 cells after incubation without (control, A) or with 1 μM of photosensitizer ZnPc-$(Lys)_n$ [n=1 (B), n=3 (C), n=5 (D), n=7 (E), n=9 (F)] for 2 h, washed out the photosensitizer, and irradiated by an 670 nm laser light at a dosage of 1.5 J/cm^2. These images were taken around 14h after the laser light irradiation.

Diffuse reflectance measurement on cell surface

We determined the diffusion reflectance of above ZnPc compounds on cell surface by using a Lamda 900 UV/VIS spectrometer equipped with inexpensive standard accessory cell-space integrating spheres. Typically, BGC-823 cells at a density of 4 x 10^5 cells per ml at a volume of 2 ml per well were placed in 6-multiwell plates with a 22×22 mm cover glass on the bottom of each well. Cells were allowed to incubate at 37°C under 5% CO_2 for a period of 8 h before adding ZnPc conjugates to get a final concentration of 10 μM. After 5 h incubation, cells were washed gently with PBS twice. The glass cover with cells was then taken out and was allowed to dry at room temperature before the diffuse reflectance spectra were measured using a Lamda 900

UV/VIS spectrometer in the wavelength region between 550 and 750 nm. A $BaSO_4$ plate was applied as a blank.

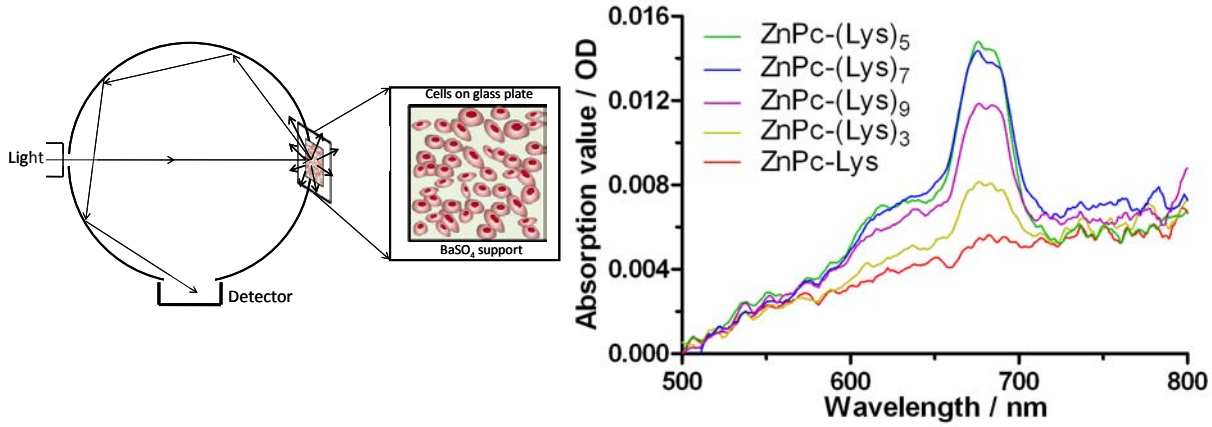

Figure S6 Schematics of the diffusion reflectance measurement (left panel) and the diffusion reflectance spectra of ZnPc-$(Lys)_n$ conjugates on BGC-823 cell surface (right panel)

Statistics

Statistical computations were performed using GraphPad Prism, version 4.0 (GraphPad Software Inc. San Diego, CA) & SigmaPlot, version 11.0 (Systat Software, Inc., Chicago, USA). Quantitative data were expressed as mean ± standard error (SE) from at least three independent experiments and assessed using a one-way ANOVA and a Newman-Keuls test. A probability value of $p<0.05$ was considered statistically significant.

Reference

1. Chen, J.; Chen, N.; Huang, J.; Wang, J.; Huang, M. *Inorg Chem Commun* **2006,** *9* (3), 313-315.

Bioconjugate Chemistry

Article

pubs.acs.org/bc

Development of Chitosan Oligosaccharide-Modified Gold Nanorods for in Vivo Targeted Delivery and Noninvasive Imaging by NIR Irradiation

Shobhit Charan,[†,‡,§] Kumar Sanjiv,[∥] Narendra Singh,[†] Fan-Ching Chien,[†] Yi-Fan Chen,[⊥] Navchtsetseg Navchaa Nergui,[†,‡,§] Shih-Hsin Huang,[†] Chiung Wen Kuo,*[,†] Te-Chang Lee,[⊥] and Peilin Chen*[,†]

[†]Research Center for Applied Sciences, [§]Taiwan International Graduate Program, Nanoscience and Technology Program, [∥]TIGP Molecular Medicine Program, and [⊥]Institute of Biomedical Sciences, Academia Sinica, Taipei 115, Taiwan

[‡]Department of Chemistry, National Taiwan University, Taipei 106, Taiwan

Supporting Information

ABSTRACT: In the present study, we demonstrate the synthesis and applications of multifunctional gold nanorod-based probes for specific targeting and noninvasive imaging based on localized heating generated by gold nanorods after NIR irradiation. The structural design of the probe consists of MUA (11-mercaptoundecanoic acid)-capped gold nanorods covalently linked with low-molecular-weight chitosan oligosaccharide (M_w ~5000) via carbodiimide (EDC) coupling agent. This surface modification is performed for complete replacement of toxic CTAB (hexadecyltrimethyl-ammonium chloride) and acid-responsive delivery of gold nanorods in acidic environment as known to be present at tumor surrounding areas. The resulting chitosan oligosaccharide-modified gold nanorods (CO-GNRs) were further conjugated with tumor targeting monoclonal antibody against EGFR (epidermal growth factor receptor) to provide localized targeting functionality owing to the overexpression of EGFR in human oral adenosquamous carcinoma cell line CAL 27. Initial in vitro and in vivo toxicity assessments indicated that CO-GNRs did not induce any significant toxicity and are thus suitable for biological applications. Furthermore, selective targeting and accumulation of CO-GNRs were observed in vitro via two-photon luminescence imaging studies in CAL 27, which was also observed through in vivo targeting studies performed via NIR (near-infrared) laser irradiation in CAL 27 xenografts of BALB/c nude mice. Hence, the CO-GNRs that we have developed are biocompatible and nontoxic and can be a potential candidate for in vivo targeted delivery, noninvasive imaging based on localized hyperthermia, and photothermal-related therapies.

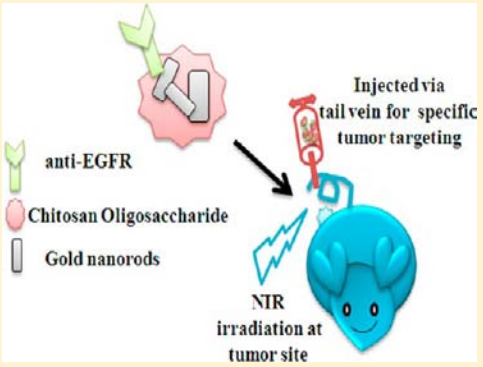

INTRODUCTION

In recent years, the development of new optical materials in the near-infrared (NIR) region (700−950 nm) has attracted a great deal of research interest due to the ability of light in this spectral region to penetrate more deeply into tissues in contrast with visible light.[1] In addition, the absorbance and autofluorescence from biological tissues are minimal in the NIR region. Therefore, there is great potential for the development of noninvasive in vivo applications using NIR radiation.[1,2] In the past few years, a growing number of studies have reported the synthesis of NIR fluorescent dyes and other tunable nanoparticles such as quantum dots for in vivo imaging.

However, NIR fluorescent dyes suffer from photobleaching, while quantum dots are known to exert a cytotoxic effect, thus limiting their applications. Hence, a nontoxic and more robust NIR material is required for in vivo imaging. Gold nanorods have recently been identified as potential candidates for in vivo imaging because of their robustness and unique optical properties in the NIR region. In principle, gold nanorods have two plasmon resonance peaks in their absorption spectra, the longitudinal surface plasmon peak (SPR) and the transverse surface plasmon peak. This longitudinal SPR peak can be tuned to the NIR region by changing the aspect ratio and diameter of the nanorods.[2] When these nanorods are excited at NIR wavelengths, they can simultaneously behave as optical contrast agents and photothermal transducers.[3−5] In addition, the simple synthesis,[6−8] tunability, good biocompatibility, and relative ease of conjugation with antibodies and other targeting moieties of gold nanorods make them excellent candidates for noninvasive imaging and image-guided therapies based on localized hyperthermia.[3,5,9−15] However, in vivo targeted delivery of gold nanorods is the key obstacle in obtaining high-contrast images and more efficient photothermal treatment. To achieve targeted delivery using gold nanorods, many

Received: March 15, 2012
Revised: October 2, 2012
Published: October 3, 2012

 © 2012 American Chemical Society

surface modification schemes have been used to replace CTAB, but they often suffer from poor biocompatibility, increased particle size, and a low capacity for loading additional moieties to enable multifunctional applications. Most of these modified particles have only improved targeting and photothermal effect in in vitro cancer cells.[10,16,17] Among these modifications, PEGylated gold nanorods have shown the best performance in terms of toxicity and photothermal effect both in vitro and in vivo, but they do suffer from rapid excretion (half-life ~1 h).[18] To solve this rapid excretion problem, chitosan has been introduced recently to extend the circulation time.[18] Chitosan is biodegradable, biocompatible, and water-soluble.[19−23] The presence of primary amine groups also enables bioconjugation with a variety of molecules and permits the introduction of other functional groups such as carboxyl or acetylene groups. Furthermore, it maintains its structure in a neutral environment, although it becomes soluble and degrades in an acidic environment, which indicates that chitosan can act as an acid-responsive drug delivery carrier by degrading and releasing the drug in the desired environment.[24] However, the high molecular weight of chitosan limits its performance in biological applications due to limited water solubility and particle−particle cross-linking.[25] Therefore, low-molecular-weight chitosan or chitosan oligosaccharide (~5000 Da) is a better choice for in vivo applications. Most of the methods reported for the in vitro/in vivo application of chitosan have used photopolymerization of acrylated chitosan[18] or thiol and oleic anhydride modification of chitosan[25−30] to replace the CTAB on the surface of the gold nanorods. However, these reported methods require the attachment of functionalized chitosan directly onto the surface of the gold nanorods, which may lead to aggregation and limit its performance for in vivo applications. Therefore, covalent conjugation of chitosan to the gold nanorods is highly desired to provide additional stability for in vivo applications. Hence, our aim is to develop a multifunctional probe, which utilizes the unique properties endowed by gold nanorods as photothermal transducers when excited at near-infrared wavelength and its covalent linkage with chitosan oligosaccharide for a successful acid-responsive delivery of the nanorods. The synthesized probes will be further decorated with cancer-specific antibody to enhance the localization of the probe which was subsequently used for specific targeting and noninvasive imaging based on localized hyperthermia after NIR irradiation.

Herein, we report the systematic functionalization of CTAB-capped gold nanorods to construct the multifunctional probe. The first step involves the simple replacement of CTAB with MUA (11-mercaptoundecanoic acid) on the nanorod surface with PEG (poly(ethylene glycol)) as an intermediate layer for stability.[31] The next step involves the covalent linkage of MUA-coated gold nanorods with low-molecular-weight chitosan oligosaccharide (~5000) using EDC chemistry[32] to produce CO-GNRs (chitosan oligosaccharide-modified gold nanorods). EDC facilitates the formation of a covalent amide bond between the amine groups present on chitosan oligosaccharide and the carboxyl groups on the nanorod surface generated from the MUA treatment. The final step deals with the conjugation of CO-GNRs with monoclonal antibody against EGFR (epidermal growth factor receptor) to achieve tumor targeting functionality due to overexpression of EGFR in CAL 27 cells.[33] Before in vivo tumor targeting application, we have also evaluated the toxicity of the CO-GNRs both in vitro and in vivo and quantified the cellular uptake by ICP-MS (inductively coupled plasma mass spectrometer). To test the potential of multifunctional gold nanorod-based probe, two-photon luminescence imaging was performed over CAL 27 cultured cells. Later on, in vivo studies performed via NIR laser irradiation at tumor sites in CAL 27 xenografts (CAL27 cells injected in living mice to obtain tumor) on BALB/c nude mice as the model further confirm the localized targeting as observed by elevated temperature at the tumor site. These results have confirmed that these functionalized gold nanorods can serve as a biocompatible, nontoxic, and cancer-specific probe to be utilized in targeted delivery and can be helpful in photothermal-related therapies.

EXPERIMENTAL SECTION

Materials. $HAuCl_4$ (hydrogen tetrachloroaurate (III) hydrate), CTAB (hexadecyltrimethylammonium chloride), NaCl (sodium chloride), $NaBH_4$ (sodium borohydride), ascorbic acid, PAA (poly(acrylic acid) , M_w ~15 000g/mol), PSS (poly(sodium-4-styrenesulfonate), M_w ~70 000g/mol), HCl (hydrochloric acid), EDC (carbodiimide), chitosan oligosaccharide lactate (M_w ~5000), and anti-EGFR monoclonal antibody were purchased from Sigma-Aldrich (E2760), mPEG-SH from Nektor, M_w ca. 5000, and MTT assay kit purchased from Sigma. All chemicals were analytical grade and were used without further purification.

Instrumentation. UV−visible spectra of gold nanorod solutions were measured in a UV−visible spectrophotometer (JASCO V-570) using quartz cuvettes with a 1 cm path length. For transmission electron microscopy (TEM)/EDAX, nanorod solutions were dried on a carbon-coated film and imaged at 100 kV (JEM 2010, JEOL). Zeta potential of the nanoparticles was measured using a Brookhaven Instruments BI-90 plus particle size analyzer and zeta potential analyzer. FT-IR spectra were recorded as attenuated total reflectance (ATR) on a Perkin-Elmer spectrum between 400 and 4000 cm^{-1}.

Preparation of the Au Seed Solution. The seed solution was prepared by mixing 9.75 mL of 0.1 M CTAB solution with 0.25 μL of 0.1 M $HAuCl_4$. To the stirred solution, 0.6 mL ice-cold 0.01 M $NaBH_4$ was added, which resulted in the formation of a bright brownish-yellow solution. Vigorous stirring of the seed solution was continued for 2 min, and then the solution was stored at 30 °C without further stirring.

Preparation of the Growth Solution and Nanorods. The growth solution was prepared by mixing 9.5 mL of the CTAB solution at 0.1 M to 0.5 mL of 0.01 M $HAuCl_4$, which resulted in the dark yellow color of the growth solution. A total of 100 μL of 0.01 M $AgNO_3$ solution was added to the solution at 25 °C. After gentle mixing, 80 μL of 0.1 M freshly prepared ascorbic acid solution was added to the test tube. The addition of an additive such as HCl (0.1 M) just before the injection of the seed solution tuned the longitudinal surface plasmon peak from 680 to 850 nm. Further addition of Na_2S allowed the red shift of the longitudinal surface plasmon peak to 1050 nm. The nanorod solutions were centrifuged twice at 7000 rpm for 20 min and redispersed in double-distilled water to remove excess CTAB molecules.

Surface Modification of CTAB-Capped Gold Nanorods. *MUA−Chitosan Modification.* Before 11-mercaptoundecanoic acid (MUA) modification to generate carboxyl groups over CTAB-stabilized gold nanorods, we introduced PEG to provide steric stability to the nanorods. Excess PEG molecules were removed by centrifugation at 8500 rpm for 15 min, and the PEGylated rods were resuspended in H_2O. To this

solution, 0.5 mL of a 20 mM solution of 11-mercaptoundecanoic acid (MUA, Sigma-Aldrich) in ethanol was added into 5 mL of the gold nanorod solution and sonicated at room temperature followed by raising the temperature till 50 °C for 2 h and then stirred mildly for 24 h at room temperature for ligand exchange process. Nanorods were then collected by centrifugation at 7000 rpm for 15 min and resuspended in PBS buffer solution. The zeta potential measured for MUA-capped gold nanorods is −35 ± 3 and particle size by DLS is found be around 82 ± 4.3.[34] For covalent binding, EDC 0.04 g was simultaneously added with chitosan oligosaccharide lactate (average M_w ~5000 dissolved in a mixture of acetic acid and water (1%)) to 5 mL of a MUA-coated gold nanorod solution. The solution was mixed, stirred overnight, centrifuged at 7000 rpm for 15 min, and resuspended in PBS (pH 3.4). The zeta potential measured for chitosan-capped gold nanorods (CO-GNRs) is −35 ± 3 and particle size by DLS is found be around 82 ± 4.3.

PSS-Coated Gold Nanorods. To the purified CTAB capped GNR solution (1 mL) was added to 200 μL of PSS (10 mg/mL prepared in 1 mM NaCl) and NaCl (100 μL, 1 mM) simultaneously. The resulting solution was stirred vigorously for 30 minutes, and the process is repeated again for layer-by-layer approach. Surface-modified GNRs with PSS solution were centrifuged twice at 10 000 rpm to remove excess polyelectrolyte and redispersed in 1× PBS (pH = 7.4).

PAA-Coated Gold Nanorods. To the purified CTAB-capped GNR solution (1 mL) was added 200 μL of PAA (10 mg/mL prepared in 6 mM NaCl) and NaCl (100 μL, 6 mM) simultaneously. The resulting solution was mixed gently for 3 h for complete polymer coating. To remove excess PAA polymer, the solution was centrifuged for 3 min at 14 000 rpm. The pellet was redispersed in 1× PBS (pH = 7.4).

Pegylated Gold Nanorods. CTAB-coated gold nanorod solution was centrifuged at 14 000 rpm for 10 min, decanted, and resuspended in water to remove excess CTAB. A thiol-terminated PEG solution (200 μL, 5 mM) was added to the gold nanorod solution (1 mL, 1 mM). The mixed solution was stirred for 24 h at room temperature, dialyzed for 3 days, and redispersed in 1× PBS (pH = 7.4).

Preparation of anti-EGFR Conjugated CO-GNRs. The CO-GNR-capped nanorods were then mixed with an antibody solution (5 μL/mL) that was diluted in PBS and allowed to react for 30 min. The antibodies are presumed to be bound to the CO-GNRs surface by electrostatic physisorption interaction.[35] The nanorods conjugated with anti-EGFR monoclonal antibodies (Sigma) were centrifuged and redispersed into PBS (pH 7.4) to form a stock solution with an optical density of approximately 0.5 at 786 nm. The anti-EGFR/nanorod conjugates were stable at 4 °C for several days. The binding efficiency was estimated by BCA assay kit (Pierce).

Stability of anti-EGFR Conjugated CO-GNRs. To investigate the leakage of anti-EGFR from CO-GNR probe in 24 h, anti-EGFR conjugated CO-GNR and CO-GNR without anti-EGFR were suspended in 300 μL PBS in a 1.5 mL microtube and incubated for 24 h at 37 °C with 100 rpm shaking. After incubation, the solutions were centrifuged and the resulting supernatant was used to quantify the protein using Micro BCA assay kit (Pierce) following the manufacturer's protocol. Protein concentration were computed against a standard curve, and values for CO-GNR without anti-EGFR were subtracted from the values for anti-EGFR conjugated CO-GNR to reduce the background from the GNR, since GNR alone also absorbs light at the wavelength used for the protein assay (560 nm). After computation, it was found that about that ~88% of EGFR antibodies remain attached in the CO-GNR probe even after 24 h of shaking at 100 rpm at 37 °C.

Determination of Number of Antibody per Nanoparticles Using MicroBCA Assay Kit (Pierce). Protein concentrations of the antibody-conjugated nanorod solutions were measured with the bicinchoninic acid (BCA) assay (Pierce) following manufacturer's protocol. Supernatant from the gold nanorod solution (without antibody, 200 μL gold nanorod in PBS), antibody-conjugated nanorod (5 μL antibody + 200 μL gold nanorod in PBS, wherein the supernatant contains unbound antibody) and antibody alone (5 μL antibody + 200 μL PBS to represent total antibody added) were measured and computed against a standard curve composed of serial dilution of known concentration of bovine serum albumin diluted in PBS. Aside from subtracting a reagent blank, the no-antibody gold nanorod supernatant was also subtracted from the antibody-conjugated gold nanorod supernatant measurements to eliminate background from unreacted gold nanorods. The binding efficiency was then calculated based on this forumula

$$\{[\mu g \text{ protein of total antibody added} - (\mu g \text{ protein of unboound antibody} - \mu g \text{ protein[background] nanorod only})]/\mu g \text{ protein of total antibody added}]\} \times 100$$

The reaction and the assay were done more than three times with comparable results. The binding efficiency was estimated to be about 80% by BCA assay kit and 20 ± 5 antibody per nanoparticles is calculated by no. of antibodies/no. of Au atoms per nanoparticle.

Cytotoxicity Assay. The cytotoxicity of the GNRs was analyzed using the CAL 27 oral adenosquamous carcinoma cell line. Cells were seeded in 96-well plates at a density of 5×10^3 cells per well and incubated for 24 h at 37 °C in a humidified incubator. CAL 27 cells were treated with the indicated concentrations (1−200 μg/mL in terms of gold nanorods) of surface-modified gold nanorods and incubated for 72 h. Cell viability was measured by MTT assay kit (Sigma) by following manufacturer's protocol. Typically, PBS solution containing 10 μL of 5 mg/mL of 3-[4,5-dimethylthiazol-2-yl]-2,5-diphenyltetrazoliumbromide (MTT) solution was added to each well and incubated for an additional 4 h. After mixing, 90 μL of MTT solubilization solution was added to each well. The stain was aspirated and purple-colored crystals were dissolved with acidic isopropyl alcohol. The optical density (OD) of the solvent was measured at 570 nm using a microplate reader (Molecular devices Spectra Max M_2^e spectrophotometer). All experiments were carried out three times.

Cellular Uptake. The cellular uptake of gold nanorods was investigated in terms of Au^{3+} concentration using ICP-MS analysis. The cells were incubated with surface modified gold nanorods at 37 °C for 4 h. After 4 h of incubation, the cells suspension was removed and the attached cells were washed with phosphate-buffered saline solution (pH 7.4) to ensure complete removal of unbound gold nanorods. Microwave-assisted digestion was adopted for 90 min to dissolve Au out of the cells using aqua regia. Later, 0.1 mL of treated solution was diluted to 50 mL volumetric flask. The signal of dissolved Au solution was measured by ICP-MS, and the concentration was

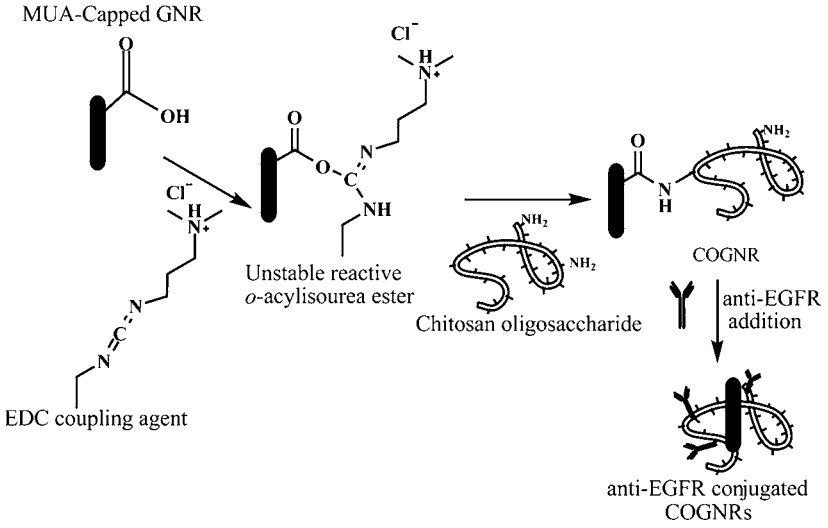

Figure 1. Schematic representation of applied strategy used for bioconjugation.

calculated using the calibration method. ICP-MS (inductively coupled plasma mass spectrometer) (Thermo−II) was used with direct nebulization in normal mode using optimized conditions consisting of an Xs skimmer cone with a platinum sampler cone. The extraction voltage was typically −573 V, the R_f power 1250 W, focus voltage was 17.5 V, and the nebulizer gas flow rate was 0.91 L/min. Dwell times were 10 ms for Au; 100 sweeps were required per replicate and 10 replicates per sample.

$$\text{Formula used for Au NR per cell} = \frac{\text{Wt. of single Au atoms/Wt. of single Au NR}}{\text{Number of cells}}$$

Western Blot. Protein was extracted with RIPA buffer with protease inhibitors (150 mM NaCl, 50 mM Tris pH 7.2, 0.1% SDS, 1% Triton X-100, 1% deoxycholate). Later, 30 μg protein lysates from either CAL27 or from mouse liver were loaded per lane of 8% SDS-PAGE gel, transferred in PVDF membrane (Millipore), followed by incubating overnight with antibody, 1:3000 dilution in 1% nonfat milk in 0.05% PBST. Upper half of the blot with antibody was run against EGFR (Cell Signaling), and the lower half with β-actin (Abcam). The blot was then washed with 1× PBST for 30 min, incubated with HRP-labeled antibody against rabbit (Abcam) for 1 h at RT and again washed for 30 min. The washed blot was then visualized by incubating it for 1 min with ECL substrate (T-Pro Lumifast Plus Chemiluminsescent substrate).

Toxicity Evaluation of CO-GNRs in BALB/C Mice. Use of the mouse model for toxicity studies was approved by and conducted according to the guidelines of the Academia Sinica Institutional Animal Care and Utilization Committee. Male 6-week-old BALB/c nude mice were obtained from the breeding stock of the Institute of Biomedical Sciences (IBMS), Academia Sinica, Taipei, Taiwan. The animals were housed in a specific pathogen-free environment under controlled conditions of light and humidity and were given sterilized food and water ad libitum. Hematological and biochemical parameters and the histopathology of the liver, kidney, lung, and spleen in mice treated with CO-GNRs (100 μg in terms of GNR amount) were examined at the Pathology Core of the Institute of Biomedical Sciences, Academia Sinica, and Taiwan Mouse Clinic. After the seventh day following the intravenous injection of CO-GNRs, blood was drawn from the heart, and animals were sacrificed to obtain the organs for histopathology studies. Blood parameters were analyzed with an Abbott Cell-Dyn 3700 machine, and biochemical parameters were analyzed with a Fuji Dri-Chem Clinical Chemistry Analyzer FDC 3500.

Biodistribution and in Vivo Imaging. To induce a solid tumor, CAL 27 cells (10×10^6 in 100 μL PBS) were injected subcutaneously into both the left and right rear flank areas of male BALB/c nude mice with ages from 6 to 7 weeks. When the tumors grew to approximately 50 mm^3 in diameter, anti-EFGR-conjugated CO-GNRs (100 μg in terms of GNR amount) suspended in 0.85% saline solution (100 μL) were either injected intravenously through the tail vein (4 mg/kg) or directly at the xenograft site. Saline solution was used as control. Biodistribution of CO-GNRs and anti-EGFR conjugated CO-GNRs was performed after 24 h after intravenous injection. The major organs including tumors were lysed with HNO_3 and the amount of Au was calculated by ICP-MS. Next, the thermal images were obtained by irradiating the mice by NIR light which were collected by FLIR A320 infrared camera at the indicated time after intravenous or direct injection.

Statistical Analysis. All the statistical analysis was carried out using two-tailed Student's t test, with $P < 0.05$ considered to be statistically different.

RESULTS AND DISCUSSION

Characterization of CTAB-Capped Gold Nanorods. We first synthesized the tunable CTAB-stabilized gold nanorods by a modified additive-controlled method,[36] which were later characterized by TEM for various aspect ratio, elemental analysis using EDS and FT-IR (characterization details are provided in the Supporting Information Figures S1 and S2). The gold nanorods used in the in vitro and in vivo experiments had a length of 47 ± 3 nm and a diameter of 11 ± 1.8 nm (an aspect ratio of 4.2 as measured from the TEM image shown in Figure 2a) and exhibit longitudinal SPR absorption at 780 nm as shown in Figure 2b.

Surface Modification of CTAB-Capped Gold Nanorods. Due to the toxicity issues associated with the CTAB-capped gold nanorods, by convention, its surface has to be further modified for its possible use in biological application. We have used 11-mercapto-undecanoic acid (MUA) mod-

dx.doi.org/10.1021/bc3001276 | Bioconjugate Chem. 2012, 23, 2173−2182

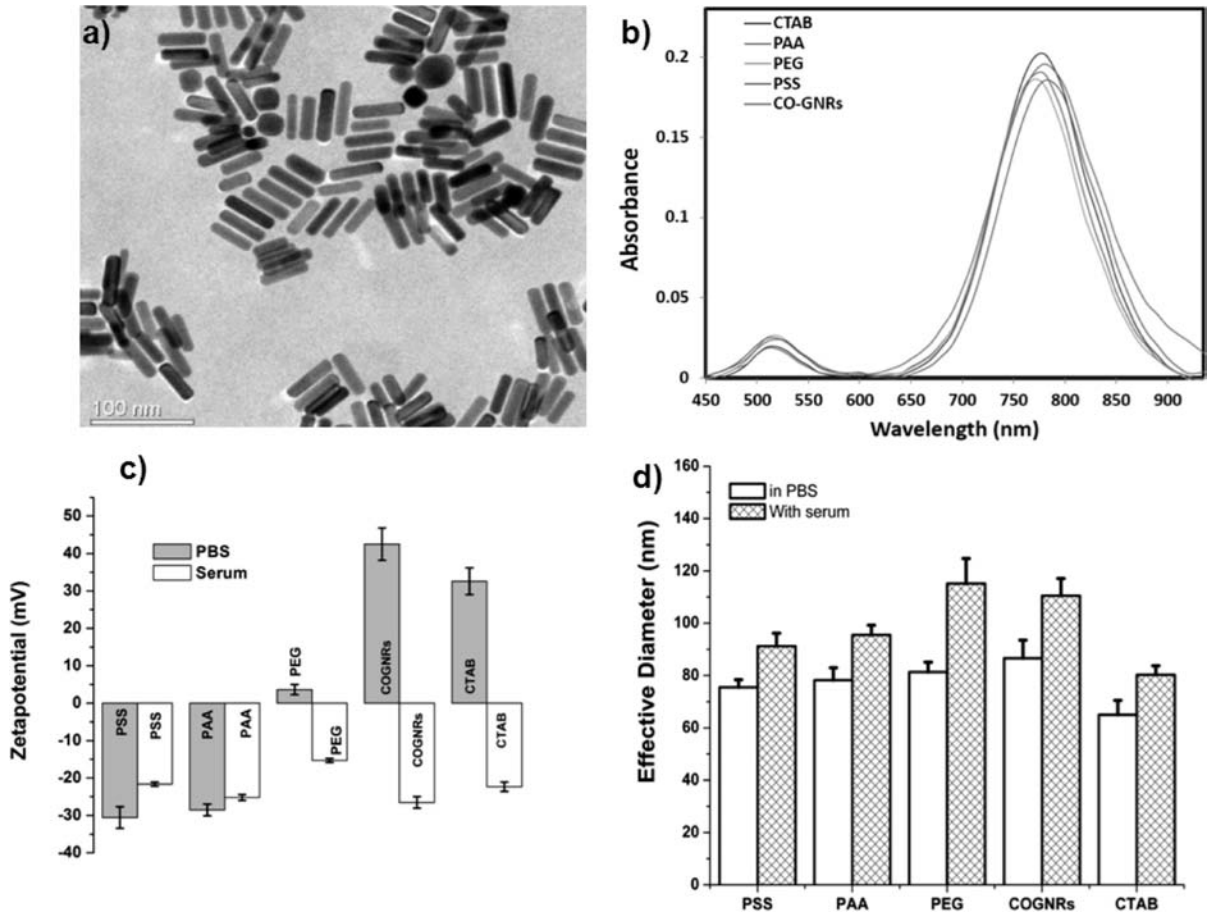

Figure 2. (a) TEM image of 780 nm gold nanorods. (b) UV−vis−NIR extinction spectra of surface-modified and CTAB-capped gold nanorods with a 780 nm peak. (c) Zeta potential measurements of various surface-modified gold nanorods before (in PBS) and after treatment with serum. (d) Particle size measurement by DLS before (in PBS) and after treatment with serum for 8 h. n = 3 for DLS and zeta potential measurements.

ification to generate carboxylic groups over CTAB-stabilized gold nanorods, which was later covalently linked with chitosan and used for further experiments (see Supporting Information Figures S3, S4, and S5). The chemical mechanism of the reaction of coupling between MUA and chitosan involves activating the carboxyl group of MUA with EDC to form an unstable reactive *o*-acylisourea ester and subsequently allowed to react with the amine groups present over the surface of chitosan to form a stable amide bond (Figure 1). Aside from surface modification with low-molecular-weight chitosan oligosaccharide (M_w ~5000), we have also used various polyelectrolytes such as PSS (poly(sodium-4-styrenesulfonate), PAA (poly(acrylic acid)), and biocompatible/biodegradable polymers, i.e., mPEG-SH (poly(ethylene glycol)) to replace cytotoxic CTAB for biological experiments. Surface modification with PSS, PAA, PEG, and chitosan oligosaccharide produced a negligible shift within 10 nm in the longitudinal SPR peak (Figure 2b), indicating that these surface modifications did not significantly change the optical properties of the nanorods. Figure 2c shows the zeta potential measurement to evaluate the stability for all surface-modified gold nanorods in PBS and after treatment with culture medium containing 10% FBS (fetal bovine serum) for 8 h at pH = 7.4. The zeta (ζ) potential of gold nanorods serves as a criterion for inspecting surface charge changes on the nanoparticles, as well as a measure of their stability followed by various surface coating. In addition, the size determination by dynamic light scattering (DLS) showed increased particle size after treatment with cell culture media containing 10% fetal bovine serum (FBS) in Figure 2d. This may be due to possible binding of serum proteins over the nanorod surface, as it can bind to many different surface charges due to its differently charged domains.[37] However, for biological applications, biocompatibility and cytotoxicity are still the primary concerns.

Cytotoxicity. To test the biocompatibility, we evaluated in vitro cell viability at different concentration of various surface-modified gold nanorods by using MTT Assay using CAL 27 oral cancer cells at a seeding density of 5 × 10^3 cells/well. Figure 3 displays the result of the cytotoxicity measurement 72 h after the addition of the surface-functionalized gold nanorods at various concentrations. CTAB-stabilized gold nanorods exert a concentration-dependent loss of viability (between 50% and 96%), whereas no significant cytotoxicity was observed for all other surface-modified gold nanorods. By comparison of all the surface-modified nanorods tested in this study, both PEG and chitosan modification exhibited the least toxicity. However, we chose to use chitosan in the subsequent experiments due to the inherent limitation of rapid excretion of PEG (half-life ~1 h).[18]

Cellular Uptake. Furthermore, the cellular uptake of gold nanorods was quantified by inductively coupled plasma mass spectrometry (ICP-MS) 4 h after the addition of 0.1 μg gold nanorod solution. The results demonstrate a clear effect of the surface modification on the uptake of gold nanorods by CAL 27 cells (Figure 4a). CTAB-coated gold nanorods exhibited the

dx.doi.org/10.1021/bc3001276 | *Bioconjugate Chem.* 2012, 23, 2173−2182

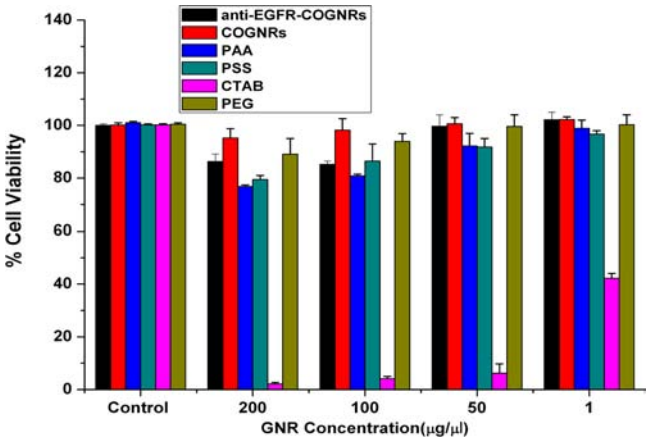

Figure 3. MTT proliferation assay of CAL 27 cells treated at different concentrations of surface-modified gold nanorods.

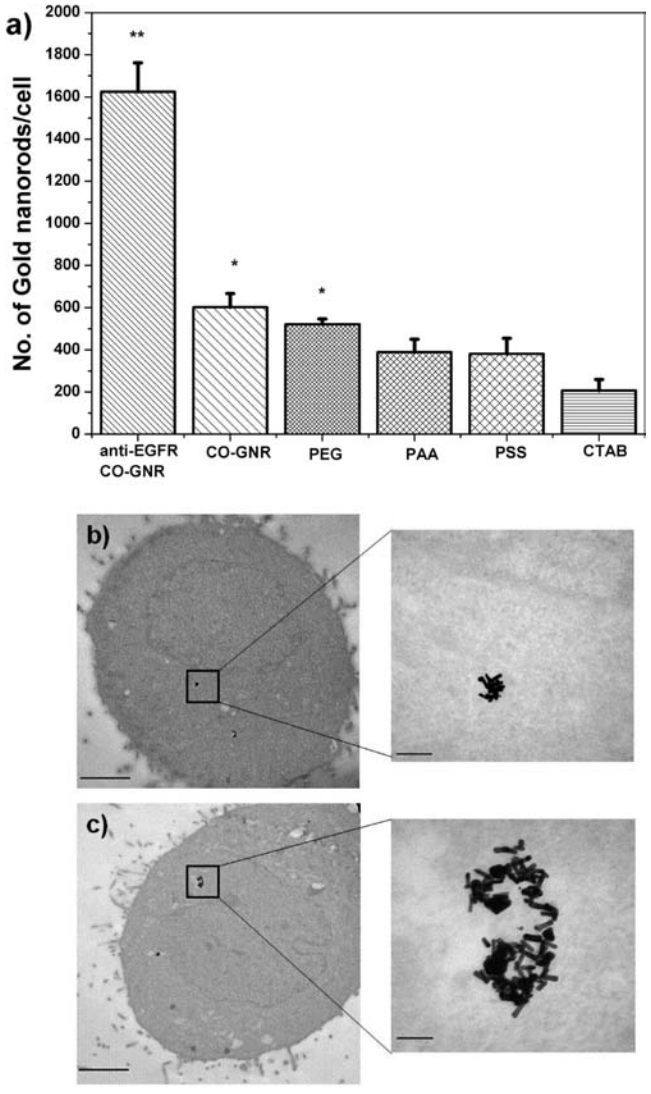

Figure 4. (a) Cellular uptake of CTAB and surface-modified gold nanorods as measured by ICP-MS (n = 3). *P value obtained by comparison with CTAB; error bars represent 1 standard deviation. (b) TEM images of CTAB-stabilized gold nanorods and (c) anti-EGFR conjugated CO-GNRs; Scale bar: 2 μm and 100 nm for inset.

lowest uptake, while the gold nanorods modified with chitosan exhibited the highest uptake among all the other surface modifications. With both viability and cell uptake taken into account, chitosan appeared to be the best choice for surface modification, and thus, chitosan was used for the antibody conjugation for further experiments. Zeta potential of anti-EGFR conjugated CO-GNRs was found to be -18 ± 2.86 mV, and size distribution by DLS measurement was observed around 104.5 $\pm$ 5.28 nm.[38] The UV–visible measurement showed the red shift in the longitudinal surface plasmon peak after conjugation of anti-EGFR with CO-GNRs indicating successful bioconjugation[39] (Supporting Information S6). Anti-EGFR-conjugated CO-GNRs showed an enhanced cellular uptake compared to CO-GNRs as indicated statistically. In addition, the distribution of CTAB-stabilized gold nanorods and anti-EGFR conjugated CO-GNRs was also visualized by transmission electron microscopy (TEM), which clearly showed that the nanorods were trapped inside the vesicles of the cells (Figure 4b,c, respectively).

Two-Photon Luminescence Imaging. Gold nanorods are known to exhibit strong two-photon fluorescence. Therefore, the distribution of gold nanorods among CAL 27 cells were further investigated with two-photon luminescence imaging using a Ti:sapphire laser (100 fs, 80 MHz laser pulse and laser power of 3.6mW) with an excitation wavelength of 780 nm.[9] Consistent with the cellular uptake measured by ICP-MS, anti-EGFR-conjugated CO-GNRs were observed to be enriched inside the cells compared to CO-GNRs alone (Figure 5). Furthermore, no two-photon signal was observed from control cells without gold nanorods. To check the specificity of the CO-GNRs, we used Chinese hamster ovary cells (CHO cells) because of its nonexpression of epidermal growth factor receptor (EGFR), which makes them an ideal negative control in our investigation for targeted delivery of gold nanorods. The results clearly indicate that CHO cells which do not express EGFR receptors showed negligible cellular uptake with anti-EGFR conjugated CO-GNRs in contrast with Cal27 cells, thus confirming the specific targeting potential of CO-GNRs. Furthermore, we also used IgG-modified COGNRs as a negative control to demonstrate the selectivity of anti-EGFR-conjugated COGNRs in cal27 cells (Supporting Information Figure S7).

In Vivo Toxicity. Based on the in vitro toxicity and cellular uptake results, the in vivo toxicity of gold nanrods (i.e., CO-GNRs and anti-EGFR conjugated COGNRs) was also analyzed. To test the in vivo toxicity, an intravenous tail vein injection containing (100 μg in terms of GNR amount) suspended in PBS (100 μL) at pH 7.4 was administered in the BALB/c nude mice model. The toxicity was evaluated 7 days after injection using hematological, clinical biochemistry and histological analysis. Both surface-modified gold nanorods showed no significant difference in WBC (white blood cell) count in comparison with the control group. However, a slight toxic effect on the bone marrow was observed indicated by a slight reduction in RBC (red blood cell) count and Hgb (hemoglobin) concentration (Supporting Information Table S1). The rest of the blood parameters of the surface-modified gold nanorod treated mice are shown in Table S2 (Supporting Information) and presented no significant changes. The biochemical profile of mice treated with surface-modified gold nanorods (CO-GNRs and anti-EGFR conjugated COGNRs) was also examined in this study. In general, drugs administered to the body of an animal pass through the liver for metabolism.

dx.doi.org/10.1021/bc3001276 | Bioconjugate Chem. 2012, 23, 2173–2182

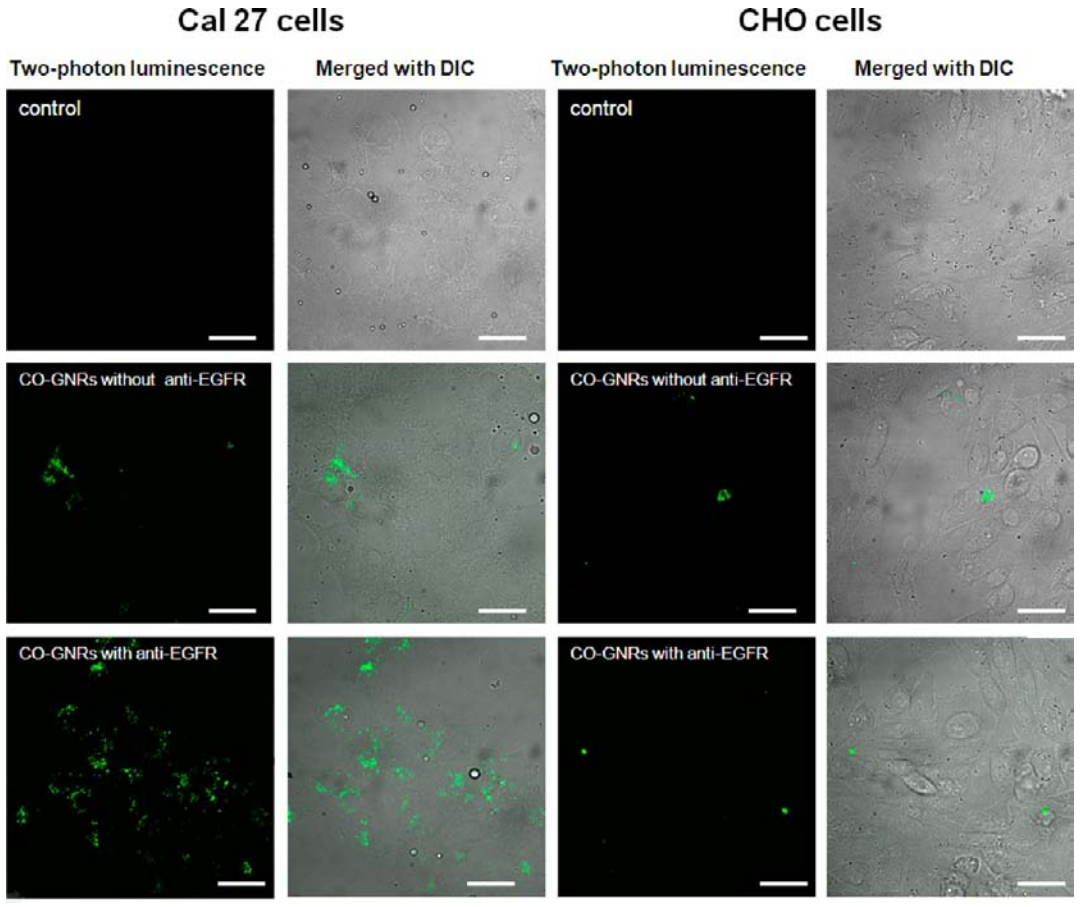

Figure 5. Two-photon luminescence and merged image with DIC of CO-GNRs with and without anti-EGFR conjugation in Cal 27, CHO cells were used as a negative control for CO-GNRs. Cells were incubated with 0.1 μg gold nanorods for 4 h. Scale bar, 10 μm.

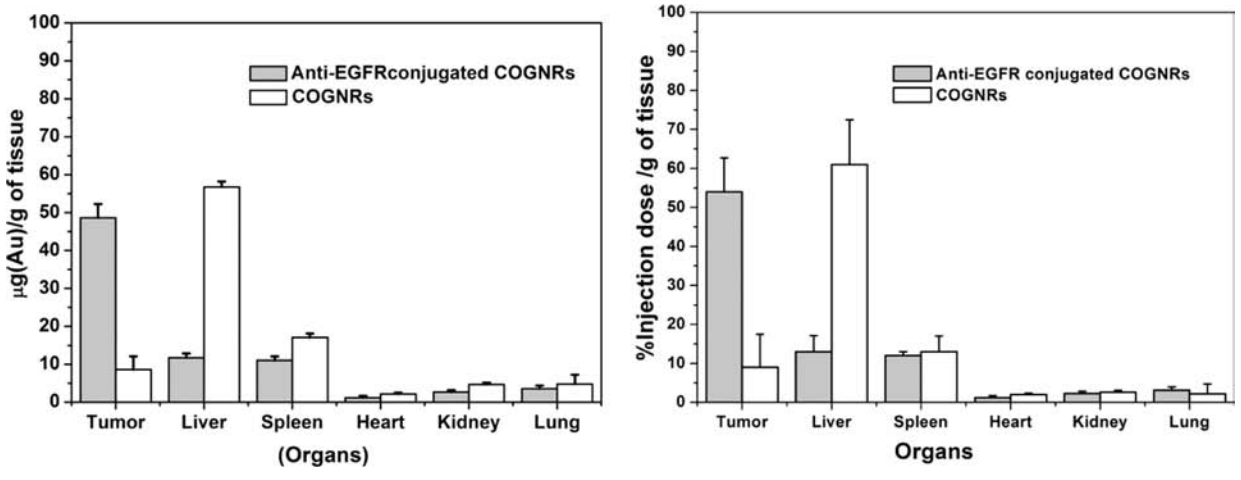

Figure 6. Biodistribution of gold nanorods in nude BALB/c mice at 24 h after intravenous (tail vein) injection. The gold amounts in tissue samples were measured by ICP-MS (n = 3).

However, no significant changes in the AST (aspartate aminotransferase), ALT (alanine transaminase), CRE (creatinine), BUN (blood urine nitrogen), or GLU (glucose) levels were observed in COGNRs in contrast with slightly higher values observed in AST and ALT levels of anti-EGFR conjugated COGNRs (Supporting Information Table S3). Furthermore, histopathological assessment of major organs (kidney, heart, spleen, lung, and liver) was also conducted 7 days after the administration of both the gold nanorod groups (SI Figure S8). Only the liver exhibited a significant difference between the control and CO-GNR, anti-EGFR conjugated COGNR cases. The liver section shows a few minor spots of vacuolar degeneration, a reversible type of change. This reversible change observed in the liver was well-correlated with the increase in the AST level. However, all the measured factors were within the normal range, and no statistically significant difference was observed in renal function parameters such as blood urea nitrogen and creatine levels. These results

dx.doi.org/10.1021/bc3001276 | Bioconjugate Chem. 2012, 23, 2173−2182

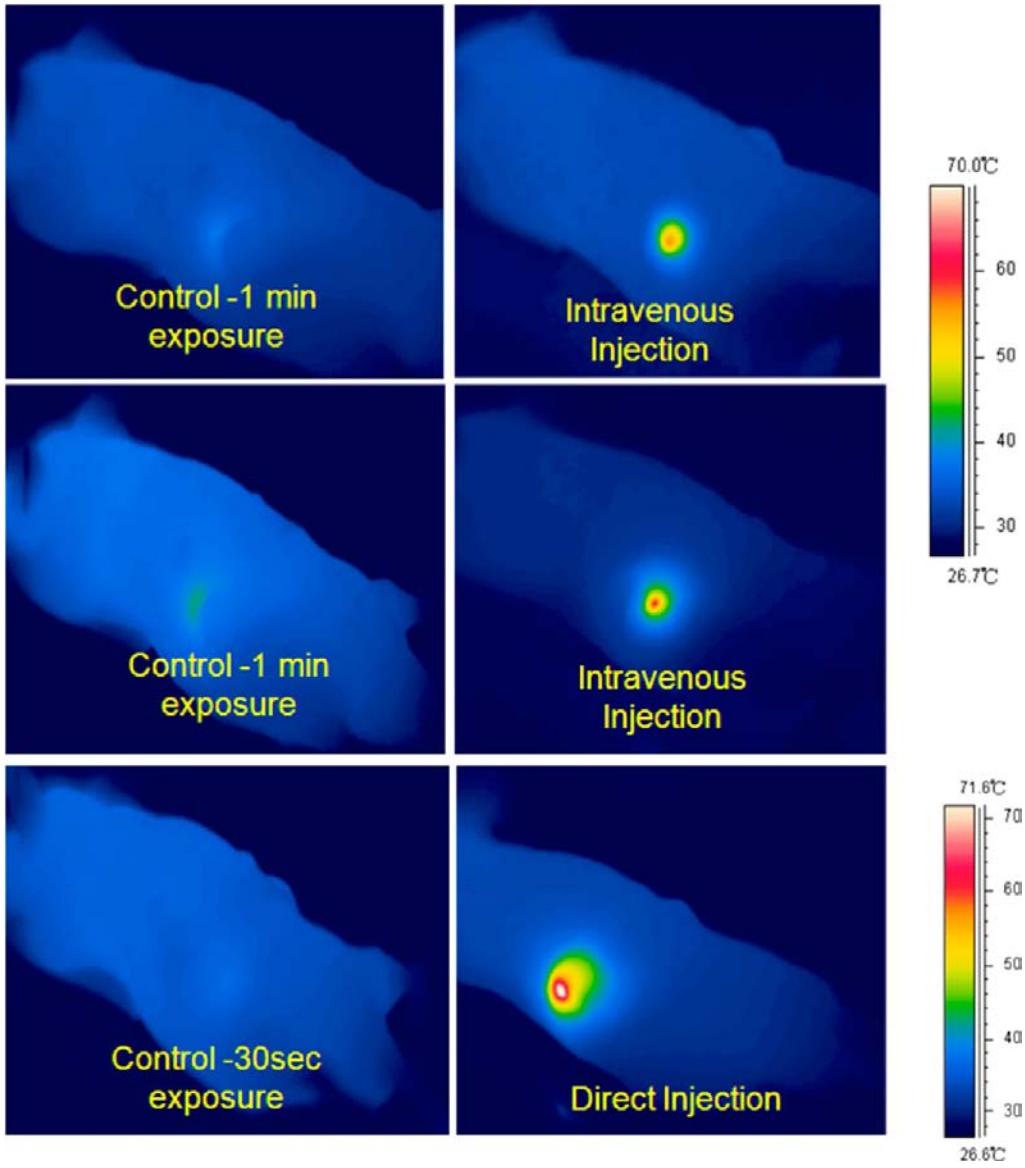

Figure 7. NIR thermal imaging of tumor in CAL 27 xenografts after (a) 1 min laser irradiation (780 nm, 3 W/cm^2), (b) 2 min laser irradiation 24 h after tail vein injection, and (c) 30 s laser irradiation 1 h after direct injection at tumor site. Control mice were administered via saline.

suggested that there was no significant toxicity of the surface-modified gold nanorods. Based on the hematological, clinical biochemistry analysis and histopathological examination, both CO-GNRs and anti-EGFR conjugated COGNRs do not exert statistically significant toxicity at the concentration (100 μg in terms of GNR amount) tested here.

Biodistribution and Photothermal Imaging. To further investigate the localization of CO-GNRs in an animal model with solid tumors, the anti-EGFR conjugated CO-GNRs were intravenously injected (100 μg in terms of GNR amount suspended in 100 μL of PBS, pH = 7.4) into the tail vein of BALB/c nude mice bearing bilateral CAL 27 tumors. Major organs including tumors were excised 24 h after intravenous injection to determine the biodistribution of the gold nanorods. ICP-MS was used to quantify the amount of gold nanorods in various organs. Figure 6 clearly shows the higher uptake of anti-EGFR conjugated CO-GNRs in the tumor and low liver uptake, indicating efficient targeting in contrast with CO-GNRs alone (also confirmed by Western blot of comparison between overexpression of EGFR in CAL 27 and BALB/c mice liver; see Figure S10). Knowing that the anti-EGFR conjugated CO-GNRs (100 μg in terms of GNR amount suspended in 100 μL of PBS, pH = 7.4) concentrated in the tumor site and that the gold nanorod exhibited large plasmonic resonance in the NIR region, we then conducted selective NIR laser irradiation in an animal model with solid tumors. Anti-EGFR conjugated CO-GNRs were intravenously injected, and 24 h after administration, the mice were exposed to NIR laser irradiation (780 nm, 3 W/cm^2, 2 mm beam diameter) for 2 min. As shown in Figure 7, the elevation in temperature at the tumor site during laser exposure confirmed targeted delivery of CO-GNR. Anti-EGFR conjugated CO-GNRs (100 μg in terms of GNR amount suspended in 100 μL of PBS, pH = 7.4) were also injected directly into the tumor site to observe any thermal changes associated with this different injection protocol. One hour after administration, laser irradiation at the tumor site yielded a temperature increase up to ~71 °C in only 30 s compared with intravenous injection, which took 2 min at the same power density (in vitro heating profile of GNR in culture media with increasing laser irradiation time experiment was also carried out

dx.doi.org/10.1021/bc3001276 | *Bioconjugate Chem.* 2012, 23, 2173−2182

to compare in vivo results; see Figure S9). This observation could be explained by the decreased amount of gold nanorods reaching the tumor site for systemic injection compared with direct injection. Although EGFR was used to enhance the specificity of the delivery to the tumor site, the circulating blood delivers the CO-GNRs to other body parts, and EGFR is present in other organs although at lower levels than in the tumor. Nonetheless, the evidence still shows the enrichment in the tumor and the specific delivery of the CO-GNRs to the tumor site.

CONCLUSION

In conclusion, we have demonstrated the systematic functionalization and characterization of multifunctional gold nanorod-based probes for specific targeting and noninvasive imaging applications. Our results suggest that anti-EGFR-conjugated CO-GNRs showed no significant toxicity either in vitro or in vivo. Additionally, cellular uptake and biodistribution were analyzed quantitatively for Au content with ICP-MS, which revealed successful localization of anti-EGFR-conjugated CO-GNRs in the tumor area. More importantly, two photon optical images clearly demonstrate the internalization and selectivity of anti-EGFR-conjugated CO-GNRs for CAL 27 human tongue oral cancer cells overexpressing EGFR. This observation was perfectly correlated with the localized temperature shift at the tumor site after irradiation with NIR laser of the BALB/c mice with CAL27 xenografts. Based on these results, functionalized CO-GNRs can be a promising probes for biosensing, drug delivery, noninvasive imaging based on localized hyperthermia generated by gold nanorods and other photothermal-based applications.

ASSOCIATED CONTENT

Supporting Information

Additional figures and tables as described in the text. This material is available free of charge via the Internet at http://pubs.acs.org.

AUTHOR INFORMATION

Corresponding Author

*E-mail: kuo55@gate.sinica.edu.tw, peilin@gate.sinica.edu.tw.

Author Contributions

S. Charan synthesized multifunctional gold nanorod-based probes and performed experiments, analyzed data and wrote the paper. S. Charan and K. Sanjiv prepared BALB/c nude mice bearing CAL27 xenografts and prepared cultured cells. K. Sanjiv and Yi-Fan Chen perform in vivo toxicity. S. Charan and F. C. Chien performed experiment for two-photon luminescence imaging and NIR based in vivo studies. N. N. Nergui helped during synthesis and surface modification of gold nanorods. S. H. Huang prepared TEM samples of cell sectioning. N. Singh and C. W. Kuo supervised the experiments for surface modification and cellular uptake studies. T. C. Lee provided reagents and materials for in vitro and in vivo experiments. C. W. Kuo and P. Chen designed experiments, analyzed data, and wrote the paper.

Notes

The authors declare no competing financial interest.

ACKNOWLEDGMENTS

This research is supported, in part, by National Science Council, Taiwan, under contract NSC 100-2113-M-001-027-MY3, NSC 101-212-M-001-011, and Academia Sinica Research Project on Nanoscience and Technology.

REFERENCES

(1) Zaheer, A., Lenkinski, R. E., Mahmood, A., Jones, A. G., Cantley, L. C., and Frangioni, J. V. (2001) In vivo near-infrared fluorescence imaging of osteoblastic activity. *Nat. Biotechnol. 19*, 1148−1154.

(2) Chun, A. L. (2009) Gold nanorods: Delivering the message. *Nat. Nano.*, DOI: 10.1038/nnano.2009.109.

(3) Maltzahn, G. v., Centrone, A., Park, J.-H., Ramanathan, R., Sailor, M. J., Hatton, T. A., and Bhatia, S. N. (2009) SERS-coded gold nanorods as a multifunctional platform for densely multiplexed near-infrared imaging and photothermal heating. *Adv. Mater. 21*, 3175−3180.

(4) Niidome, T. (2010) Development of functional gold nanorods for bioimaging and photothermal therapy. *Journal of Physics: Conference Series 232*, 012011.

(5) Niidome, T., Akiyama, Y., Shimoda, K., Kawano, T., Mori, T., Katayama, Y., and Niidome, Y. (2008) In vivo monitoring of intravenously injected gold nanorods using near-infrared light. *Small 4*, 1001−1007.

(6) Nikoobakht, B., and El-Sayed, M. A. (2003) Preparation and growth mechanism of gold nanorods (NRs) using seed-mediated growth method. *Chem. Mater. 15*, 1957−1962.

(7) Jana, N. R., Gearheart, L., and Murphy, C. J. (2001) Wet chemical synthesis of high aspect ratio cylindrical gold nanorods. *J. Phys. Chem. B 105*, 4065−4067.

(8) Gole, A., and Murphy, C. J. (2004) Seed-mediated synthesis of gold nanorods: role of the size and nature of the seed. *Chem. Mater. 16*, 3633−3640.

(9) Huang, X., El-Sayed, I. H., Qian, W., and El-Sayed, M. A. (2006) Cancer cell imaging and photothermal therapy in the near-infrared region by using gold nanorods. *J. Am. Chem. Soc. 128*, 2115−2120.

(10) Li, Z., Huang, P., Zhang, X., Lin, J., Yang, S., Liu, B., Gao, F., Xi, P., Ren, Q., and Cui, D. (2009) RGD-conjugated dendrimer-modified gold nanorods for in vivo tumor targeting and photothermal therapy. *Mol. Pharmaceutics 7*, 94−104.

(11) von Maltzahn, G., Centrone, A., Park, J.-H., Ramanathan, R., Sailor, M. J., Hatton, T. A., and Bhatia, S. N. (2009) SERS-coded gold nanorods as a multifunctional platform for densely multiplexed near-infrared imaging and photothermal heating. *Adv. Mater. 21*, 3175−3180.

(12) von Maltzahn, G., Park, J.-H., Agrawal, A., Bandaru, N. K., Das, S. K., Sailor, M. J., and Bhatia, S. N. (2009) Computationally guided photothermal tumor therapy using long-circulating gold nanorod antennas. *Cancer Res. 69*, 3892−3900.

(13) Wang, L., Liu, Y., Li, W., Jiang, X., Ji, Y., Wu, X., Xu, L., Qiu, Y., Zhao, K., Wei, T., Li, Y., Zhao, Y., and Chen, C. (2010) Selective targeting of gold nanorods at the mitochondria of cancer cells: implications for cancer therapy. *Nano Lett. 11*, 772−780.

(14) Kuo, C. W., Lai, J. J., Wei, K. H., and Chen, P. (2007) Studies of surface-modified gold nanowires inside living cells. *Adv. Funct. Mater. 17*, 3707−3714.

(15) Kuo, C.-W., et al. (2008) Surface modified gold nanowires for mammalian cell transfection. *Nanotechnology 19*, 025103.

(16) Huff, T. B., Tong, L., Zhao, Y., Hansen, M. N., Cheng, J.-X., and Wei, A. (2007) Hyperthermic effects of gold nanorods on tumor cells. *Nanomedicine 2*, 125−132.

(17) Huang, Y.-F., Sefah, K., Bamrungsap, S., Chang, H.-T., and Tan, W. (2008) Selective photothermal therapy for mixed cancer cells using aptamer-conjugated nanorods. *Langmuir 24*, 11860−11865.

(18) Choi, W. I., Kim, J.-Y., Kang, C., Byeon, C. C., Kim, Y. H., and Tae, G. (2011) Tumor regression in vivo by photothermal therapy based on gold-nanorod-loaded, functional nanocarriers. *ACS Nano 5*, 1995−2003.

(19) Chang, C.-W., Wang, C.-H., and Peng, C.-A. (2009) Gold Nanorods Modified with Chitosan As Photothermal Agents, in *13th International Conference on Biomedical Engineering* (Lim, C. T., and Goh, J. C. H., Eds.) pp 874−877, Springer, Berlin.

(20) Guo, R., Zhang, L., Zhu, Z., and Jiang, X. (2008) Direct facile approach to the fabrication of chitosan−gold hybrid nanospheres. *Langmuir 24*, 3459−3464.
(21) Matteini, P., Ratto, F., Rossi, F., Centi, S., Dei, L., and Pini, R. (2010) Chitosan films doped with gold nanorods as laser-activatable hybrid bioadhesives. *Adv. Mater. 22*, 4313−4316.
(22) Wang, C.-H., Chang, C.-W., and Peng, C.-A. (2010) Gold nanorod stabilized by thiolated chitosan as photothermal absorber for cancer cell treatment. *J. Nanopart. Res.*, 1−10.
(23) Amidi, M., Mastrobattista, E., Jiskoot, W., and Hennink, W. E. (2010) Chitosan-based delivery systems for protein therapeutics and antigens. *Adv. Drug Delivery Rev. 62*, 59−82.
(24) Agnihotri, S. A., Mallikarjuna, N. N., and Aminabhavi, T. M. (2004) Recent advances on chitosan-based micro- and nanoparticles in drug delivery. *J. Controlled Release 100*, 5−28.
(25) Nandanan, E., Jana, N. R., and Ying, J. Y. (2008) Functionalization of gold nanospheres and nanorods by chitosan oligosaccharide derivatives. *Adv. Mater. 20*, 2068−2073.
(26) Kafedjiiski, K., Hoffer, M., Werle, M., and Bernkop-Schnürch, A. (2006) Improved synthesis and in vitro characterization of chitosan-thioethylamidine conjugate. *Biomaterials 27*, 127−135.
(27) Kafedjiiski, K., Krauland, A. H., Hoffer, M. H., and Bernkop-Schnürch, A. (2005) Synthesis and in vitro evaluation of a novel thiolated chitosan. *Biomaterials 26*, 819−826.
(28) Kim, T.-H., Jiang, H.-L., Jere, D., Park, I.-K., Cho, M.-H., Nah, J.-W., Choi, Y.-J., Akaike, T., and Cho, C.-S. (2007) Chemical modification of chitosan as a gene carrier in vitro and in vivo. *Prog. Polym. Sci. 32*, 726−753.
(29) Lee, D., Zhang, W., Shirley, S., Kong, X., Hellermann, G., Lockey, R., and Mohapatra, S. (2007) Thiolated chitosan/DNA nanocomplexes exhibit enhanced and sustained gene delivery. *Pharm. Res. 24*, 157−167.
(30) Roldo, M., Hornof, M., Caliceti, P., and Bernkop-Schnürch, A. (2004) Mucoadhesive thiolated chitosans as platforms for oral controlled drug delivery: synthesis and in vitro evaluation. *Eur. J. Pharm. Biopharm. 57*, 115−121.
(31) Thierry, B., Ng, J., Krieg, T., and Griesser, H. J. (2009) A robust procedure for the functionalization of gold nanorods and noble metal nanoparticles. *Chem. Commun.*, 1724−1726.
(32) Lopez-Cruz, A., Barrera, C., Calero-DdelC, V. L., and Rinaldi, C. (2009) Water dispersible iron oxide nanoparticles coated with covalently linked chitosan. *J. Mater. Chem. 19*, 6870−6876.
(33) Sakaguchi, M., Kuroda, Y., and Hirose, M. (2006) The antiproliferative effect of lidocaine on human tongue cancer cells with inhibition of the activity of epidermal growth factor receptor. *Anesth. Analg. (Hagerstown, MD, U. S.) 102*, 1103−1107.
(34) Dougherty, G. M., Rose, K. A., Tok, J. B. H., Pannu, S. S., Chuang, F. Y. S., Sha, M. Y., Chakarova, G., and Penn, S. G. (2008) The zeta potential of surface-functionalized metallic nanorod particles in aqueous solution. *Electrophoresis 29*, 1131−1139.
(35) Sokolov, K., Follen, M., Aaron, J., Pavlova, I., Malpica, A., Lotan, R., and Richards-Kortum, R. (2003) Real-time vital optical imaging of precancer using anti-epidermal growth factor receptor antibodies conjugated to gold nanoparticles. *Cancer Res. 63*, 1999−2004.
(36) Jing, Z., et al. (2010) Additive controlled synthesis of gold nanorods (GNRs) for two-photon luminescence imaging of cancer cells. *Nanotechnology 21*, 285106.
(37) Alkilany, A. M., Nagaria, P. K., Hexel, C. R., Shaw, T. J., Murphy, C. J., and Wyatt, M. D. (2009) Cellular uptake and cytotoxicity of gold nanorods: molecular origin of cytotoxicity and surface effects. *Small 5*, 701−708.
(38) Huang, X., Peng, X., Wang, Y., Wang, Y., Shin, D. M., El-Sayed, M. A., and Nie, S. (2010) A reexamination of active and passive tumor targeting by using rod-shaped gold nanocrystals and covalently conjugated peptide ligands. *ACS Nano 4*, 5887−5896.
(39) Rayavarapu, R. G., Petersen, W., Ungureanu, C., Post, J. N., van Leeuwen, T. G., and Manohar, S. (2007) Synthesis and bioconjugation of gold nanoparticles as potential molecular probes for light-based imaging techniques. *Int. J. Biomed. Imaging 2007*, 29817.

Supporting Information

Development of Chitosan Oligosaccharide-Modified Gold Nanorods for *In vivo* Targeted Delivery and Non-Invasive Imaging by NIR Irradiation

Shobhit Charan[†,$,#], Kumar Sanjiv[±] , Narendra Singh[†], Fan-Ching Chien[†] , Yi-Fan Chen[§], Navchtsetseg Navchaa Nergui[†,$,#], Shih-Hsin Huang[†] , Chiung Wen Kuo[†*] , Te-Chang Lee[§] and Peilin Chen[†*]

[†] Research Center for Applied Sciences, Academia Sinica, Taipei 115, Taiwan.

[$]Department of Chemistry, National Taiwan University, Taipei 106, Taiwan

[#]Taiwan International Graduate Program, Nanoscience and Technology Program, Academia Sinica, Taipei 115

[±] TIGP Molecular Medicine Program, Academia Sinica, Taiwan

[§]Institute of Biomedical Sciences, Academia Sinica, Taipei- 115, Taiwan

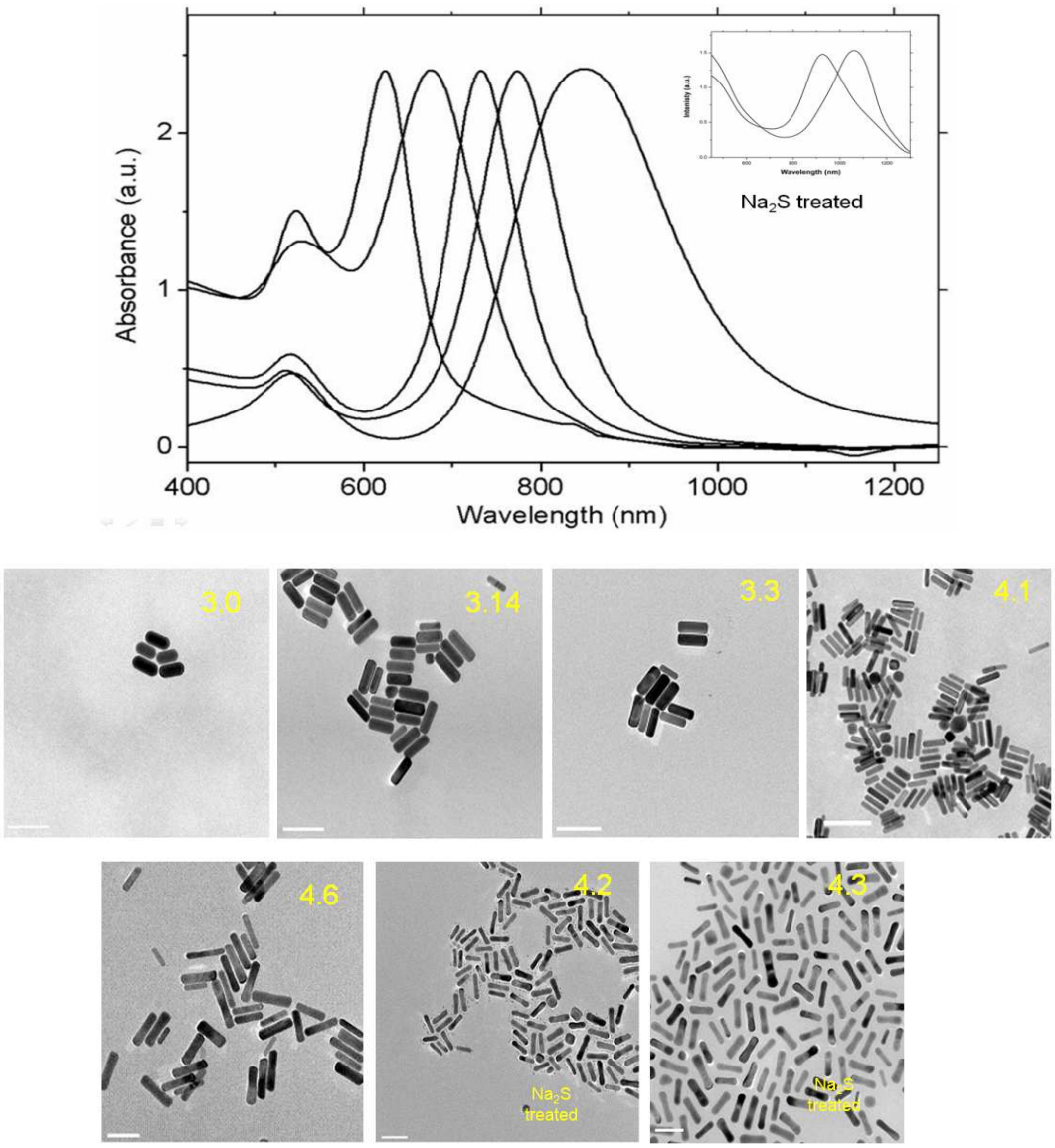

Figure S1.displays a) the UV-vis-NIR extinction spectra of tunable gold nanorods by additive controlled method (HCl and Na_2S) b) TEM image of various aspect ratio of CTAB coated gold nanorod ; Above scale bar-100nm and below 50nm

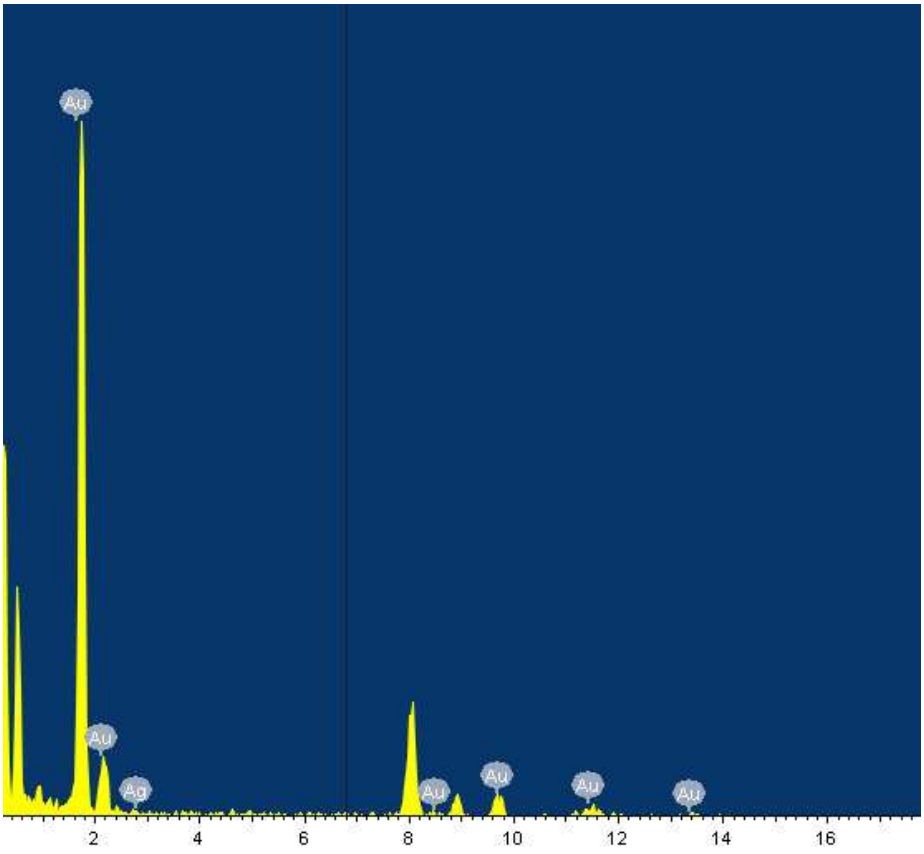

Element	Weight%	Atomic%
Ag L	-0.61	-1.13
Au L	100.61	101.13
Totals	100.00	

Figure S2. displays the EDS analysis of CTAB coated gold nanorod

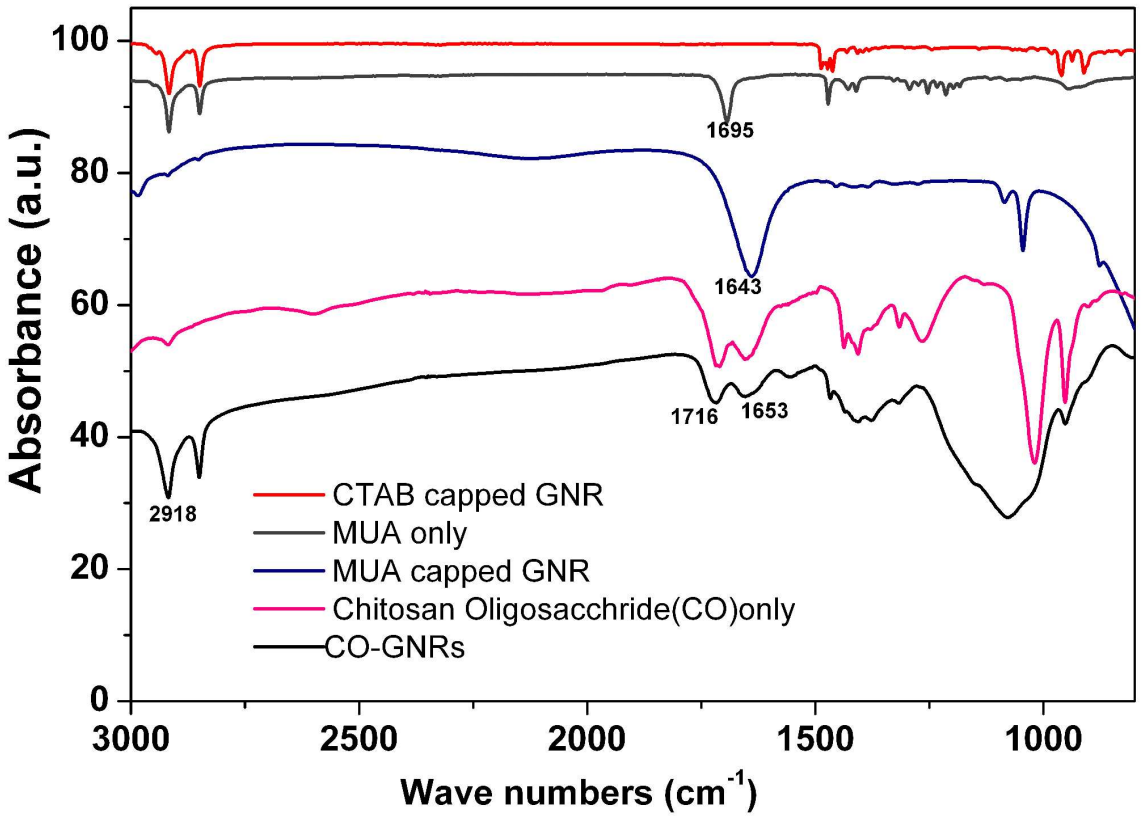

Figure S3 displaying the FT-IR spectrum of chitosan modified gold nanorods (CO-GNRs), The major peak detected in mercaptoundecanoic acid (MUA) capped GNR is ~1643cm^{-1} for >C=O group and for water soluble chitosan modified gold nanorods (CO-GNRs) could be observed around ~2,920/cm (>C-H stretching), ~1,653/cm (>C=O for amide stretching), C=O stretching vibrations at 1716 cm^{-1}, indicating the presence of lactate groups in the chitosan structure.

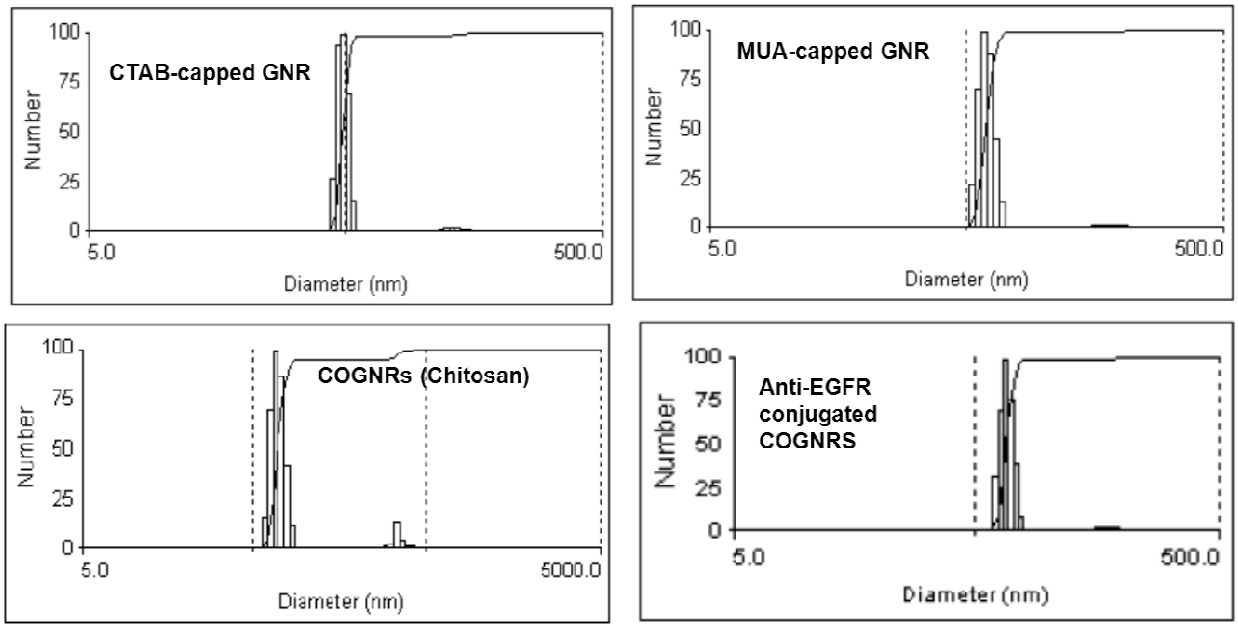

Figure S4. Step-by-step particle size analysis of surface-modified gold nanorods

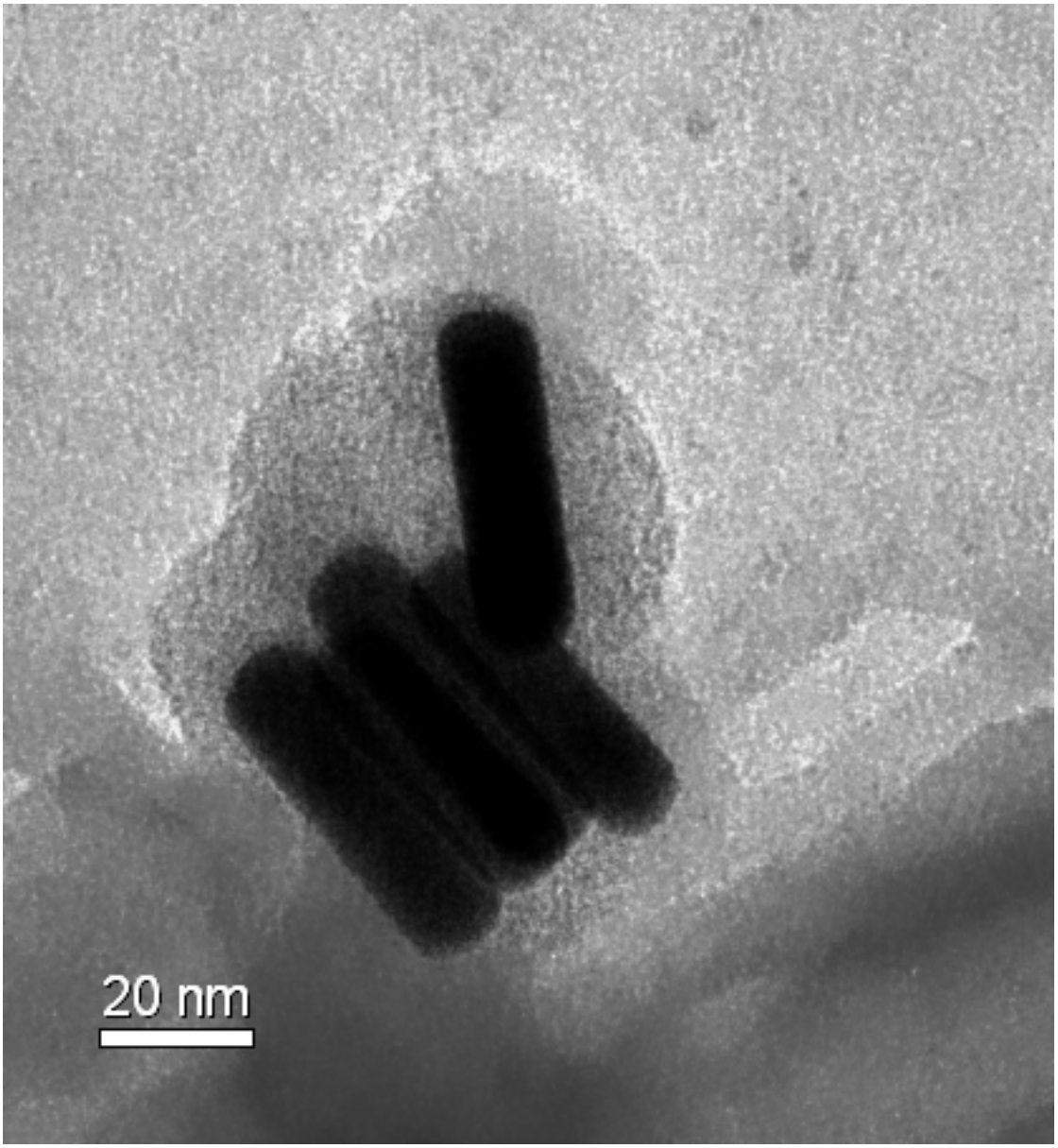

Figure S5 . TEM image of Chitosan modified gold nanorods(CO-GNRs)

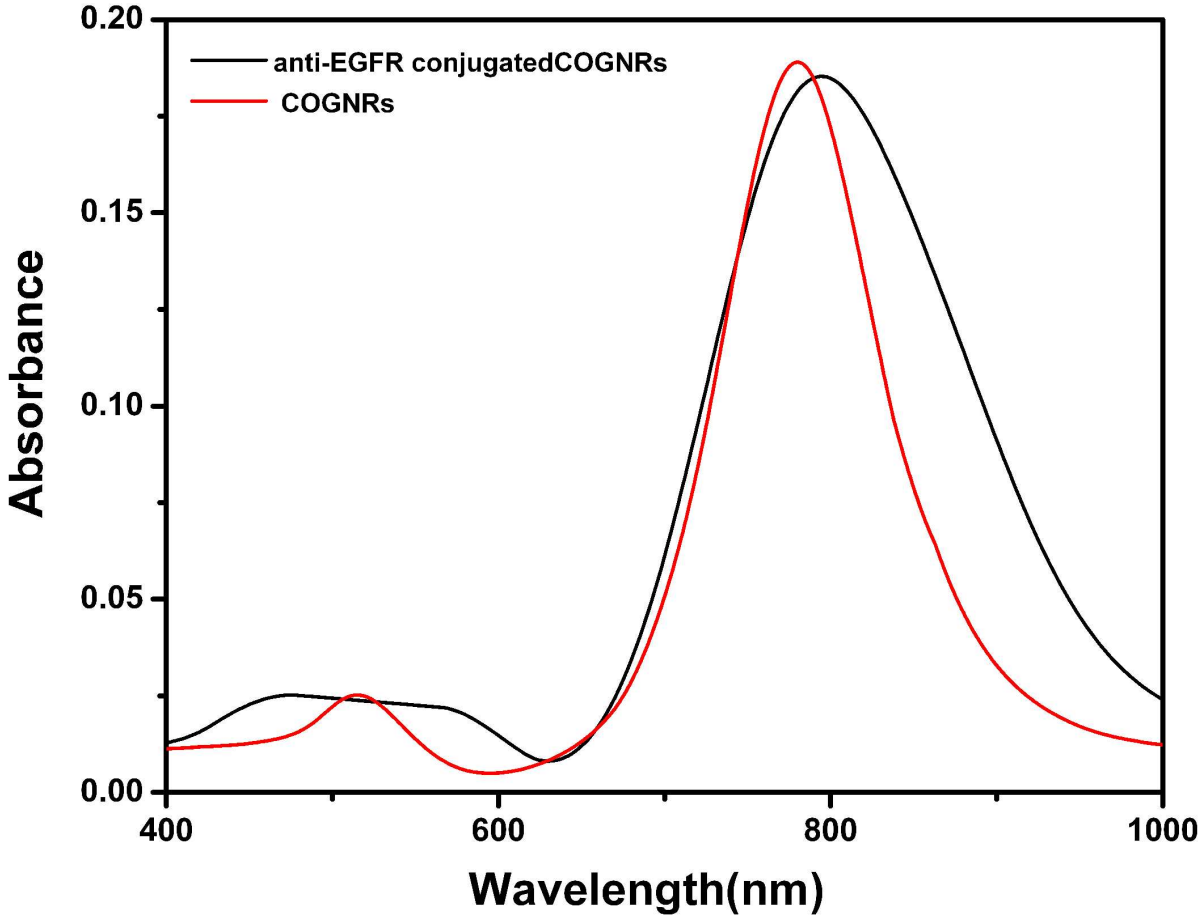

Figure S6. Absorption spectrum of CO-GNRs at 782nm and red shifted LSPR peak at 793 nm for anti-EGFR conjugated CO-GNRs.

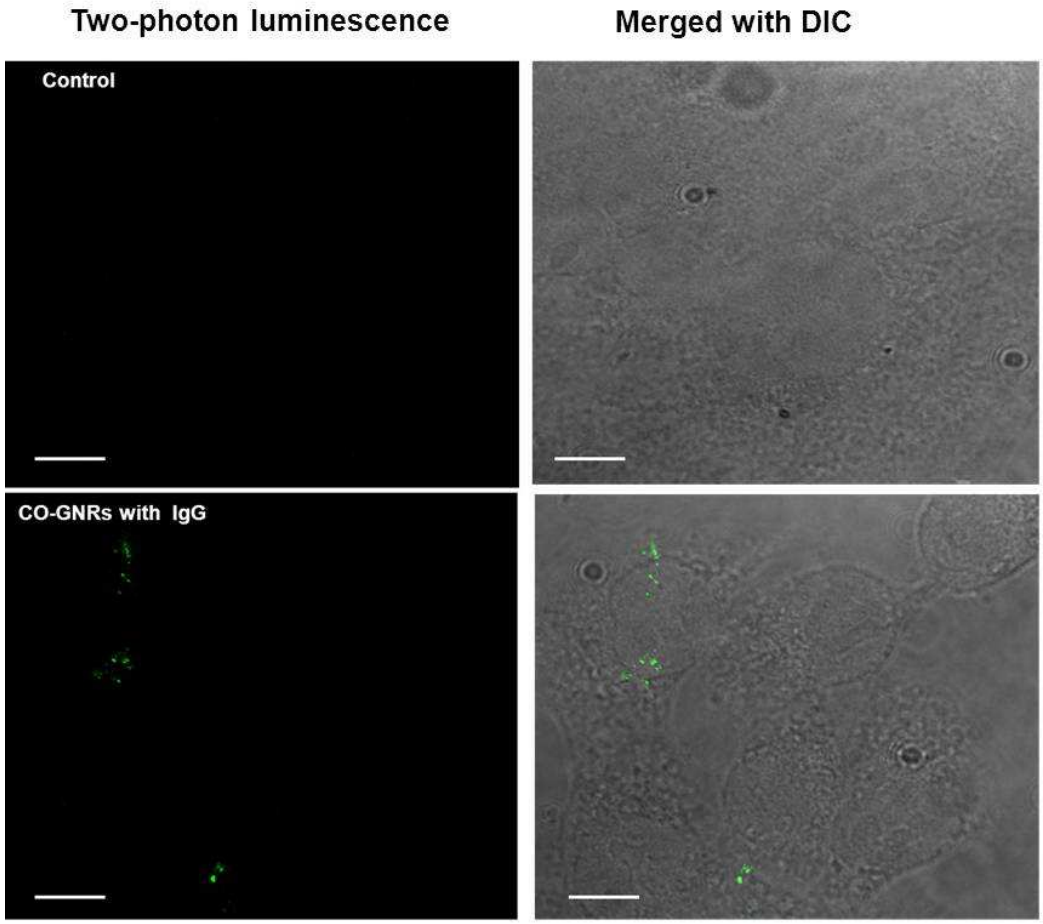

Figure S7 Two-photon luminescence and merged image with DIC of IgG-modified CO-GNRs in Cal 27 as a negative control for CO-GNRs to show the selectivity of anti-EGFRs conjugated COGNRs. Cells were incubated with 0.1μg gold nanorods for 4 hours. Scale bar, 10 μm

Table S1. Blood profile in BALB/C mice treated with COGNRs and anti-EGFR conjugated COGNRs. Various blood parameters were measured in the blood of BALB/C mice on the 7th day after the end of treatment. Data are means of three mice

Blood parameter	Normal range	Control	COGNRs	Anti-EGFR conjugated COGNRs
RBC count (10^9/l)	5.0–13.7	8.66 ± 1.45	6.40 ± 0.99	7.07±1.33
WBC count (10^9/l)	7.9–10.1	3.71 ± 1.88	5.05 ± 2.2	5.31±1.80
Hgb value (g/dl)	10.2–16.6	13.63 ± 1.45	10.82 ± 1.07	13.9±0.78

Table S2. Other Blood profile parameters in BALB/C mice treated with COGNRs and anti-EGFR conjugated COGNRs.

Blood parameter	unit	Control	COGNR	anti-EGFR conjugated COGNR
WBC count	10^9/L	3.71 ± 1.88	5.05 ± 2.2	5.31±1.80
NEU count	10^9/L	1.55 ± 0.78	2.21 ± 0.59	1.16±0.23
LYM count	10^9/L	2.01 ± 1.28	2.61 ± 2.49	3.34±1.48
MONO count	10^9/L	0.06 ± 0.01	0.09 ± 0.04	0.356±0.19
EOS count	10^9/L	0.04 ± 0.01	0.04 ± 0.01	0.23±0.04
BASO count	10^9/L	0.04 ± 0.01	0.07 ± 0.02	0.21±0.14
RBC count	10^{12}/L	8.66 ± 1.45	6.40 ± 0.99	9.07±0.33
HGB value	g/ dL	13.63 ± 1.45	10.82 ± 1.07	13.9±0.78
HCT value	%	46.16 ± 5.96	37.3 ± 2.98	48.06±1.9
MCV value	fL	53.56 ± 2.47	58.83 ± 4.49	52.93±0.15
MCH value	pg	15.8 ± 0.63	17 ± 1.25	15.33±0.37
MCHC value	g/ dL	29.5 ± 0.45	28.9 ± 0.58	28.933±0.66

Table S3. Biochemical profiles of plasma in mice treated with COGNRs and anti-EGFR conjugated COGNRs. Various biochemical enzyme parameters were measured in the blood of BALB/c nude mice 7 days after administration

Enzymes	Normal range	Control	CO-GNRs	Anti-EGFR conjugated COGNRs
AST(U/l)	17-77	51 ± 5	71.35 ±8.99	78.33 ± 7.8
ALT(U/l)	54-298	29.5 ± 3.5	38.3 ± 10.3	46.66 ± 6.4
CRE-P(mg/dl)	0.20-0.90	0.27 ± 0.02	0.30 ± 0.01	0.13 ± 1.1
BUN-P(mg/dl)	9.0-33	27.5 ± 3.05	29.9± 3.47	22.16 ± 2.65
GLU-P(mg/dl)	140-263	187 ± 9	174 ± 19.30	162.66 ± 2.1

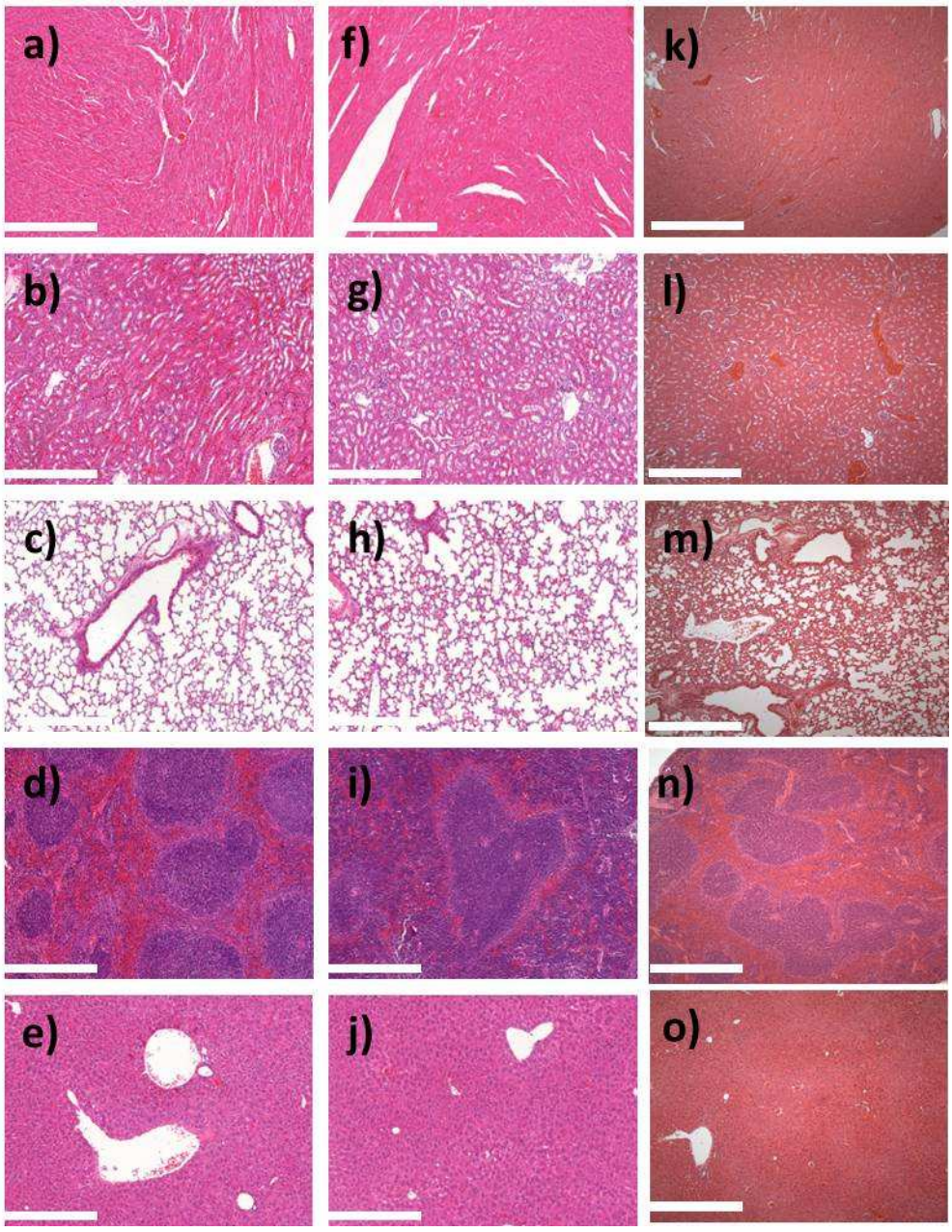

Figure S8. Toxicity of chitosan-modified gold nanorods in various organs in BALB/c nude mice. Different organs were harvested from mice 7 days after CO-GNR administration. (a-e) control with PBS , (f-j) treatment with CO-GNRs, (k-o)treatment with anti-EGFR conjugated COGNRs with PBS (a)(f)heart, (b)(g) kidney (c)(h) lung (d)(i) spleen (e)(j) liver Histological sections were stained with H&E and scanned. Magnification: 5×; Scale bar 500 μm

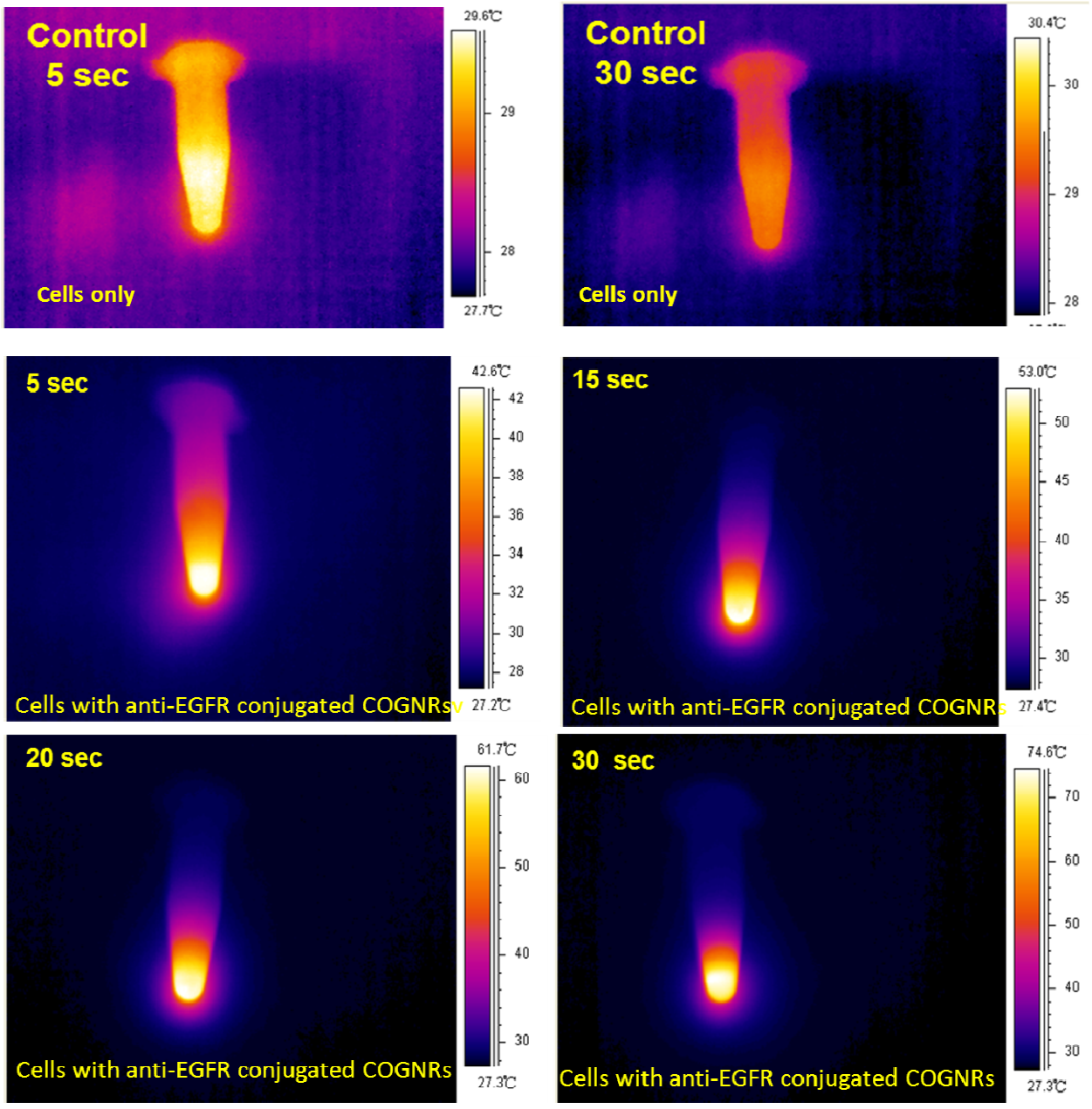

Figure S9 in vitro NIR thermal imaging of anti-EGFR conjugated COGNRs (100µg in terms of gold nanorods) in CAL 27 cells after different laser irradiation time suspended in 100µl of PBS 7.4

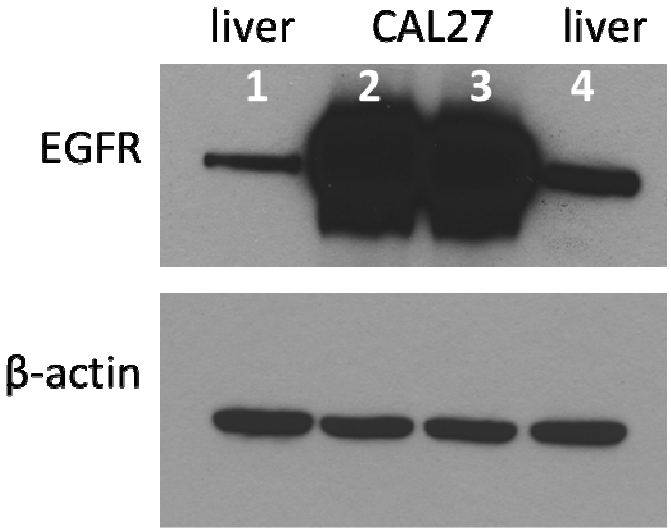

Figure S10 western blot analysis displaying the EGFR overexpression in CAL 27 cells (1)B6 mice liver (2)CAL 27 100% confluency (3) CAL 27 80% confluency and (4) BALB/C nude mice liver

Bioconjugate Chemistry

Article

pubs.acs.org/bc

Synthesis of Steroid–Oligonucleotide Conjugates for a DNA Site-Encoded SPR Immunosensor

Nuria Tort,[†,⊥] J.-Pablo Salvador,[†,⊥] Anna Aviñó,[‡,⊥,#] Ramón Eritja,[*,‡,⊥,#] Jordi Comelles,[§,⊥] Elena Martínez,[§,⊥] Josep Samitier,[§,∥,⊥] and M.-Pilar Marco[†,⊥]

[†]Applied Molecular Receptors Group (AMRg) and [‡]Nucleic Acids Chemistry Group. Chemical and Biomolecular Nanotechnology Department. IQAC–CSIC. Jordi Girona, 18-26, 08034-Barcelona, Spain

[§]Nanobioengineering Group, Institute for Bioengineering of Catalonia (IBEC), Baldiri Reixac, 10-12, 08028 Barcelona, Spain

[∥]Department of Electronics, University of Barcelona, Martí i Franquès, 1, 08028 Barcelona, Spain

[⊥]CIBER de Bioingenieria, Biomateriales y Nanomedicina (CIBER-BBN)

[#]Institute for Research in Biomedicine, Baldiri Reixac 19, E-08028 Barcelona, Spain

Supporting Information

ABSTRACT: The excellent self-assembling properties of DNA and the excellent specificity of the antibodies to detect analytes of small molecular weight under competitive conditions have been combined in this study. Three oligonucleotide sequences (N_1up, N_2up, and N_3up) have been covalently attached to three steroidal haptens (8, hG, and 13) of three anabolic-androgenic steroids (AAS), stanozolol (ST), tetrahydrogestrinone (THG), and boldenone (B), respectively. The synthesis of steroid–oligonucleotide conjugates has been performed by the reaction of oligonucleotides carrying amino groups with carboxyl acid derivatives of steroidal haptens. Due to the chemical nature of the steroid derivatives, two methods for coupling the haptens and the ssDNA have been studied: a solid-phase coupling strategy and a solution-phase coupling strategy. Specific antibodies against ST, THG, and B have been used in this study to asses the possibility of using the self-assembling properties of the DNA to prepare biofunctional SPR gold chips based on the immobilization of haptens, by hybridization with the complementary oligonucleotide strands possessing SH groups previously immobilized. The capture of the steroid–oligonucleotide conjugates and subsequent binding of the specific antibodies can be monitored on the sensogram due to variations produced on the refractive index on top of the gold chip. The resulting steroid–oligonucleotide conjugates retain the hybridization and specific binding properties of oligonucleotides and haptens as demonstrated by thermal denaturation experiments and surface plasmon resonance (SPR).

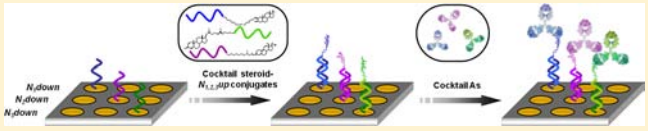

INTRODUCTION

The food safety, biomedical research, and environmental monitoring areas require methods of screening with the ability to detect, rapidly and sensitively, trace amount of small targets (<1000 Da). As an example, anabolic androgenic steroids (AAS) are completely prohibited substances by the WADA (World Antidoping Agency) [1] and the European Community,[2] for their respective use to improve athletic performance and to increase meat production in the agro-alimentary field, due to the associated adverse health effects. Immunosensors based on the surface plasmon resonance (SPR) principle provide a rapid and convenient analytical alternative for monitoring (bio)-chemical substances in a label-free way.[3−9] Several strategies have been used to anchor the immunoreagents onto gold chips to develop SPR biosensors to detect small molecules under competitive immunochemical configurations. In indirect formats, usually a protein functionalized with the hapten is immobilized on the surface of the transducer;[10−12] however, alternative methods to avoid the use of a carrier protein have been described. For example, an oligo(ethyleneglycol) (OEG) linker was used on a SPR biosensor to detect 2,4,6-trinitrotoluene (TNT)[13] and testosterone.[14] In direct detection formats, the antibody can be immobilized directly through a self-assembled layer (SAM) of heterobifunctional linkers possessing a thiol group, although alternative methods to appropriately orientate the antibody molecule have also been described. Thus, the immobilization of antibodies by affinity interaction has been reported with a layer of protein A previously immobilized on the gold substrate.[15] Moreover, the use of DNA–protein conjugates has also been reported on nanoscale immunosensors microstructured biochips.[16] Hence, a protein G-DNA conjugate has been employed to ensure controlled immobilization of antibodies to intended areas of a chip surface or to particles.[17] The DNA-directed immobilization (DDI) strategy provides a chemically mild process for the simultaneous binding of multiple proteins to a solid support using DNA surfaces as immobilization matrices. It consists of tagging biomolecules with oligonucleotide chains that are complementary to ssDNA previously linked on the surface. An additional advantage of this strategy is the possibility of

Received: March 21, 2012
Revised: September 26, 2012
Published: October 29, 2012

ACS Publications © 2012 American Chemical Society

dx.doi.org/10.1021/bc300138p | *Bioconjugate Chem.* 2012, 23, 2183–2191

Table 1. Oligonucleotide Sequences and Chemical Structures of the Steroidal Haptens Used in This Study

Name	Sequence
N_1down-SH	5' HS-$(CH_2)_6$-CAGGACAATATCGTTGCGTG 3'
8-*N_1up*	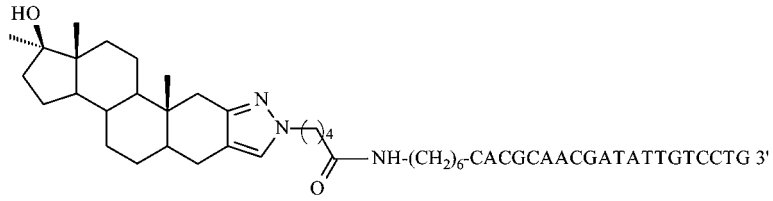
N_2down-SH	5' HS-$(CH_2)_6$-CGGAGGTACATTCGACTTGA 3'
hG-*N_2up*	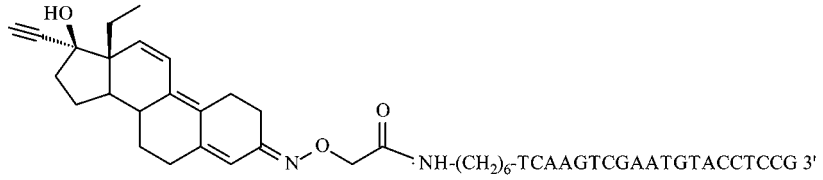
N_3down-SH	5' HS-$(CH_2)_6$-CGGATAGAGCACTACGTTGT 3'
13-*N_3up*	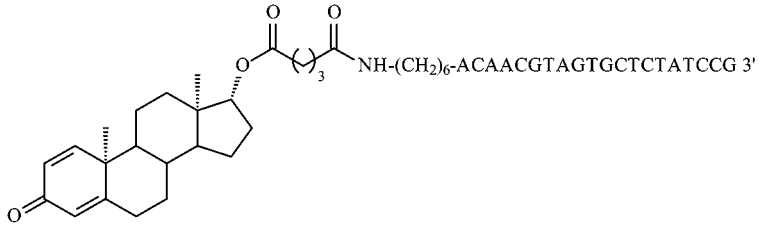

producing regenerable sensor surfaces due to the reversible nature of the DNA hybridization reaction. This strategy has been used to immobilize antibodies covalently linked to ssDNA onto a SPR surface where the complementary strands have been previously immobilized, to detect three fertility hormones in a direct competitive format.[18,19] However, this approach has been rarely used to immobilize haptens on a SPR gold chip. Previously, we demonstrated the possibility of using DDI to create hapten microarrays for fluorescent detection.[20] This time, our objective has been to demonstrate the biofunctionality of steroid−oligonucleotide bioconjugates synthesized and characterized to use them on a SPR biosensor and to assess the possibility of developing multiplexed SPR immunosensors for small organic molecules by directly immobilizing the haptens on the gold chip through a DDI approach.[12,22−27]

EXPERIMENTAL PROCEDURES

Chemicals, Reagents, and Buffers. *General.* Phosphoramidites and ancillary reagents used during oligonucleotide synthesis were from Applied Biosystems (PE Biosystems Hispania S.A., Spain), Link Technologies (Link Technologies Ltd., Scotland), and Glen Research (Glen Research Inc.., USA). The rest of the chemicals were purchased from Aldrich, Sigma, or Fluka (Sigma-Aldrich Química S.A., Spain). NAP-10 columns (Sephadex G-25) were purchased from Pharmacia Biotech. The preparation of the stanozolol (ST), tetrahydrogestrinone (THG), and boldenone (B) haptens (8, hG, and 13, respectively) and the production of the antiserums (As147, As170, and As138, respectively) has been described previously.[28−30] *N,N′*-Dicyclohexylcarbodiimide 99% (DCC) was purchased from Aldrich and the *N*-hydroxysuccinimide (NHS) from Fluka. Benzotriazol-1-yl-oxytripyrrolidinophosphonium hexafluorophosphate (PyBOP) was from Bachem (Bachem, Switzerland). Long-chain alkylamine controlled pore glass (LCAA-CPG) was from CPG (CPG Inc., New Jersey, USA).

Instrumentation. Oligonucleotide sequences were synthesized on an Applied Biosystems DNA synthesizer model 3400 (Applied Biosystems, USA). Mass spectra (matrix-assisted laser desorption ionization time-of-flight, MALDI-TOF) were provided by the mass spectrometry service of the University of Barcelona. UV−vis spectra were recorded on a Shimadzu UV-2101PC spectrophotometer. HPLC (SHIMADZU-9A) with manual injector volume of 150 μL, bomb LC-9A, and detector SPD-M6A UV−vis.

Commercial SPR chips with bare gold surface, SPRchip and spotReady (GWC Technologies, USA) substrates, were used for all the experiments. Imaging SPR measurements were collected with a GWC Technologies SPR Imager II instrument (GWC Technologies, USA). Measurements were performed at

dx.doi.org/10.1021/bc300138p | *Bioconjugate Chem.* 2012, 23, 2183−2191

Scheme 1. Synthesis of Steroid–Oligonucleotide Conjugates[a]

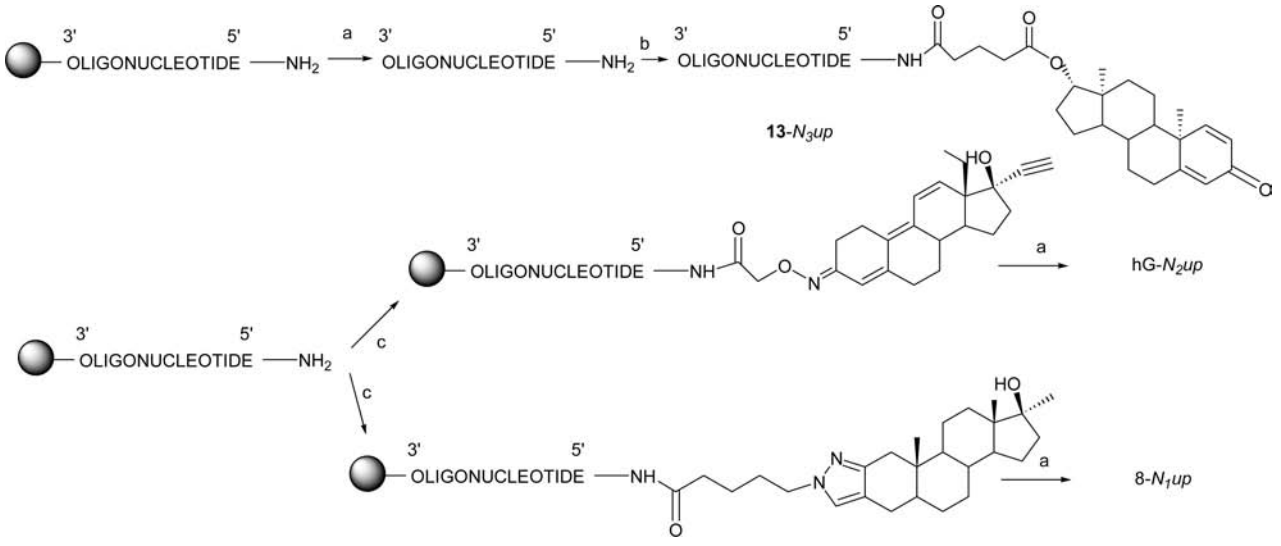

[a](a) ammonia treatment, (b) hapten coupling using DCC and NHS, and (c) hapten coupling using PyBOP and DIPEA.

a fixed angle of incidence collecting the changes on the reflected light intensity through imaging the SPR chip with a CCD camera. The spotReady chips contain an array of gold spots where positive and negative controls can be included and measured simultaneously. Individual chips were index-matched to the prism and fitted with a 20 μL flow cell connected to a peristaltic pump from Ismatec (Glattbrugg, Switzerland). A total volume of 0.5 mL was needed to completely fill the tubing and flow cell with buffer or analyte. The SPR images were collected and analyzed using V^{+2} software (Digital Optics, New Zeland).

Synthesis and Purification of Oligonucleotides and Steroid–Oligonucleotide Conjugates. Three pairs of oligonucleotide complementary sequences were designed (see Table 1). Three oligonucleotides were prepared with an amino group at the 5′-end (N_1up, N_2up, and N_3up) and the three complementary sequences contained a thiol group at 5′-end (N_1down, N_2down, and N_3down). Oligonucleotide sequences carrying an amino and thiol group at the 5′-end were assembled on a 1 μmol scale. The benzoyl (Bz) group was used for the protection of the amino group of C and A, and the isobutyryl (ibu) group for the protection of G. The phosphoramidite derivative of 6-aminohexanol carrying the monomethoxytrityl (MMT) group (Glen Research and Link Technologies)[31] was used for the introduction of the amino group at the 5′-end. The thiol group at the 5′-end was introduced using the phosphoramidite derivative of 6-hydroxyhexyldisulfide protected with the dimethoxytrityl (DMT) group (5′-thiol modifier C6 S–S CE phosphoramidite, Link Technologies, Inc., Scotland). Coupling yields were >98%. After the assembly of the sequences, the resulting solid supports (except for N_1up and N_2up) were treated with concentrated ammonia for 6 h at 50 °C. Oligonucleotides carrying thiol groups were deprotected with concentrated ammonia carrying 0.1 M dithiotreitol (DTT). The resulting $N_{1-3}down\text{-}SH$ oligonucletides were stored in presence of DTT to prevent the disulfide formation. Prior to immobilization, thiol-oligonucleotides were desalted with Sephadex G-25 (NAP-10 columns, GE Healthcare) eluted with water to remove the excess of DTT.

The corresponding $N_{1-3}up\text{-}NH_2$ oligonucleotides have been conjugated with the steroids (8, hG, and 13, respectively). For the preparation of these conjugates, we have used two different approaches: (1) the active ester method in aqueous solution (solution-phase strategy), which consists of the activation of the acid of the steroidal haptens using DCC and NHS, and (2) the solid-phase strategy, using PyBOP as activating agent and diisopropylethylamine (DIPEA).

1. Synthesis of Oligonucleotides Carrying Steroids Using the Solution-Phase Coupling Protocol (Scheme 1). The resulting solid support obtained after the assembly of the oligonucleotide sequence ($N_3up\text{-}NH_2$), and removal of the last MMT group, was treated with concentrated ammonia for 6 h at 50 °C. The mixture was filtered and the ammonia solution concentrated to dryness. The residue was passed over a Dowex 50 × 4 (Na^+ form) column to exchange ammonium for sodium ions. The resulting amino-oligonucleotide was dissolved in 0.2 mL of water and mixed with 0.1 mL of an aqueous buffer. We tried three different aqueous buffers: (1) 1 M sodium carbonate, pH 9.0; (2) 50 mM Tris pH 8.5; and (3) 0.2 M sodium borate pH 8.6. In a separate container, the steroidal hapten with the carboxylic acid group (13, 10 molar excess) was dissolved in 0.1 mL of DMF and mixed with NHS (25 molar excess) and DCC (50 molar excess). The mixture was left with magnetic stirring for 3 h at room temperature, until the solution became opaque due to the precipitation of the urea. Then, we centrifuged (10 000 rpm for 15 min) to remove the precipitate and the supernatant was added to the aqueous solution of the amino-oligonucleotide. The reaction mixture was kept at 37 °C with magnetic stirring overnight. The mixture was concentrated to dryness, and the residue was dissolved in water and passed through a NAP-10 column. Finally, the oligonucleotide fractions were analyzed by reverse-phase HPLC-UV. HPLC solutions were solvent A, 5% ACN in 100 mM triethylammonium acetate (TEAA) pH 6.5, and solvent B, 70% ACN in 100 mM triethylammonium acetate pH 6.5. Column: PRP-1 (Hamilton), 350 × 8 mm. Flow rate: 3 mL/min. A 20 min lineal gradient from 5% to 35% ACN was used. The desired oligonucleotide conjugate carrying the steroid eluted at around 11 min, while the unreacted amino-oligonucleotide eluted at

dx.doi.org/10.1021/bc300138p | Bioconjugate Chem. 2012, 23, 2183–2191

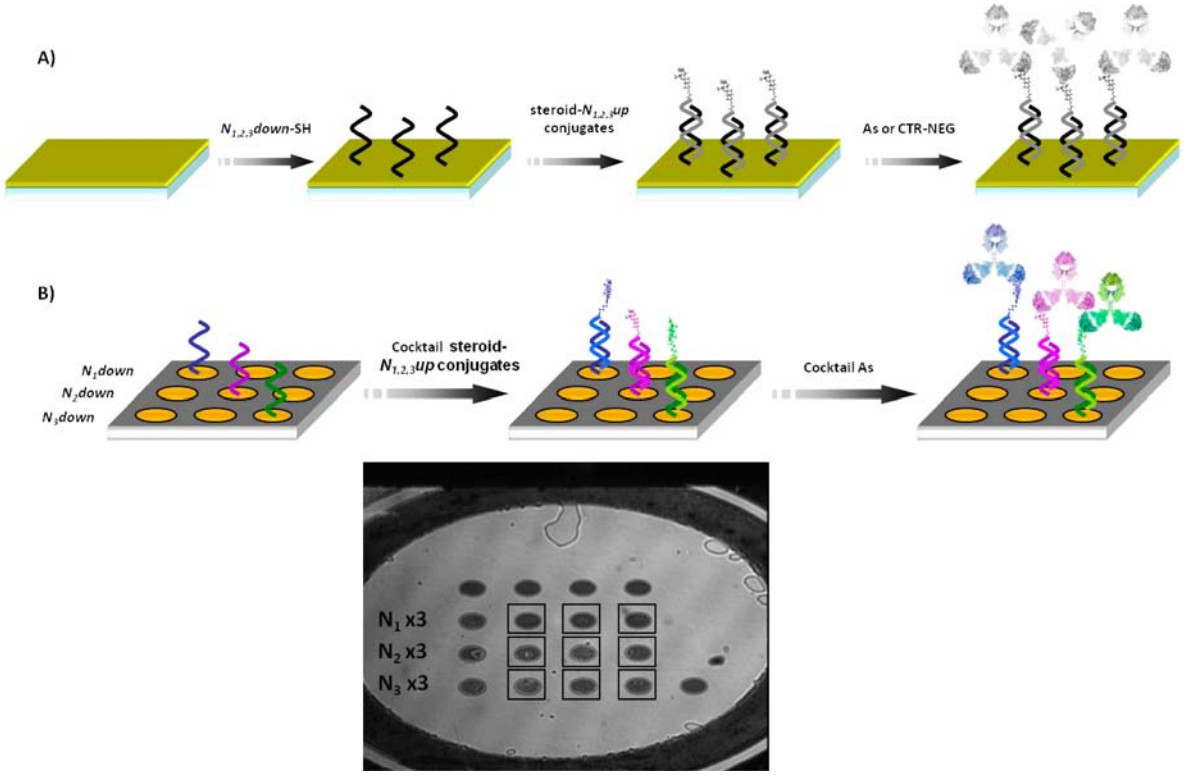

Figure 1. Schematic representation of the experimental procedure employed to assess the steroid−oligonucleotide bioconjugate biofunctionality by SPR. ssDNA biofunctionalized chips are used to immobilize the haptens through hybridization with the corresponding steroid−oligonucleotide bioconjugates. Subsequently, biofunctionality is assessed by exposing the chips to specific antibodies. (A) Evaluation of the biofunctionality of each steroid−oligonucleotide conjugate (8-N_1up, hG-N_2up, and 13-N_3up) using the individual SPR procedure. (B) Evaluation of the DNA site-encoded applicability of these conjugates for the development of a multiplexed SPR immunosensor.

around 2−5 min. The desired product was characterized by UV-spectra and mass spectrometry (MALDI-TOF), with a global yield for 13-N_3up of 20% (carbonate buffer) to 30% (Tris, borate buffers). MALDI-TOF m/z (negative mode) 13-N_3up, calc 6639, found 6400 (M-239) corresponding to the fragmentation of the ester linkage of the hapten during the acquisition of MALDI spectra. Electrospray m/z (negative mode) 13-N_3up, calc 6639, found 6639. Increasing the molar excess of active ester from 10× to 30× excess allows the conversion of the amino-oligonucleotide to the desired conjugate to 45%.

2. Synthesis of Oligonucleotides Carrying Steroids Using the Solid-Phase Coupling Protocol. The oligonucleotide sequences carrying an amino group at the 5′-end were prepared as described above ($N_{1,2}up$-NH_2). The resulting solid supports were treated with 3% trichloroacetic acid/CH_2Cl_2 to eliminate the MMT group, washed with ACN, and reacted with the carboxylic acid derivatives of the steroids as follows. A mixture containing 10 molar excess of the hapten (hG or 8), 20 molar excess of *N*,*N*-diisopropylethylamine (DIEA), and 10 molar excess of PyBOP was prepared in dry DMF (0.2 mL). The mixture was left for 10 min at room temperature and added to the support. After 30 min at room temperature, the mixture was filtered and washed with DMF and ACN. The support was dried, and concentrated ammonia (1 mL) was added. The ammonia solution was left for 6 h at 50 °C. The mixture was filtered and the ammonia solution was concentrated to dryness. The fractions containing oligonucleotide were analyzed by HPLC-UV as described above. The desired steroid−oligonucleotide conjugates eluted at around 11 min, and were obtained with global yields of 52% for 8-N_1up and 40% for hG-N_2up. Finally, the conjugates were characterized by UV and mass spectrometry (MALDI-TOF). MALDI-TOF m/z (negative mode) 8-N_1up, calc 6668, found 6672; hG-N_2up, calc 6619, found 6614. In this last compound, we also observed a second peak at 6333 m/z corresponding to the hapten fragmentation at the oxime bond.

DNA Site-Encoded SPR Immunosensor. *General Considerations.* All the SPR experiments began with a buffer baseline (10 mM PBS with 100 mM NaCl, assay buffer), and the same buffer was used to wash between each step and to prepare all the solutions of the bioreagents. All the solutions were flowed at a rate of 3 $\mu L \cdot s^{-1}$. Solutions carrying the thiolated oligonucleotides ($N_{1,2,3}$ *down-SH*) and the steroid−oligonucleotide conjugates (8-N_1up, hG-N_2up, and 13-N_3up) were prepared at 150 $\mu g \cdot mL^{-1}$ and 60 $\mu g \cdot mL^{-1}$, respectively, in the assay buffer. Nonspecific adsorption of proteins was avoided by using a blocking solution of 2% of bovine serum albumine (BSA). Antisera for ST (As147), THG (As170), and B (As138) and for negative controls (CTR-NEG, preimmune serum) were diluted 250 times in the assay buffer.

Individual SPR Procedure. (Figure 1A) Biofunctionalization of the SPRchip was accomplished by flowing a solution of the thiolated oligonucleotides down ($N_{1,2,3}$*down-SH*) for 15 min. A solution containing the corresponding steroid−oligonucleotide conjugate (8-N_1up/hG-N_2up/13-N_3up) in the assay buffer was flowed to the cell for about 20 min, until a steady-state was reached. Afterward, the chip was washed (10 min), and the blocking solution was passed (15 min). After a new washing step, the solution of the specific antisera (As147/As170/As138,

dx.doi.org/10.1021/bc300138p | *Bioconjugate Chem.* 2012, 23, 2183−2191

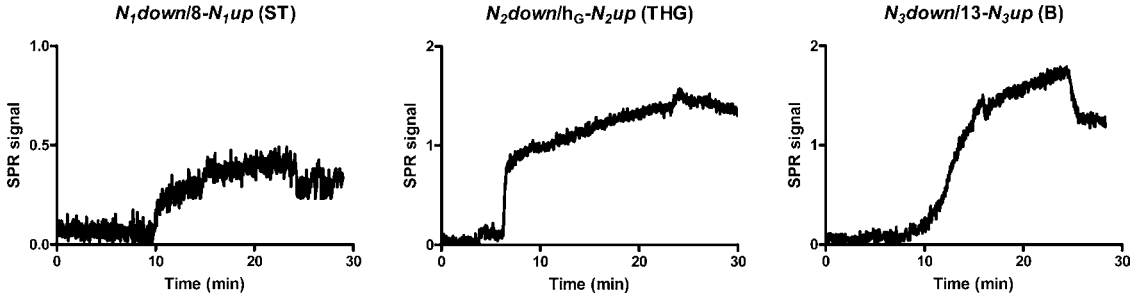

Figure 2. SPR sensograms recorded on the hybridization step between the steroid−oligonucleotide conjugates and the oligonucleotides *down* previously immobilized on the chip surface.

1/250 dilution) was flowed for about 20 min until the signal reached the maximum, and then washed again with the assay buffer. At the end of the cycle, the chips were regenerated by flowing a solution of 0.3 M NaOH for about 15 min. The regeneration step provided gold chips with the *Nxdown*-SH oligonucleotides immobilized. Absence of nonspecific binding was assessed by passing a solution of a preimmune serum.

Multiplexed SPR Procedure. (Figure 1B) For this experiment, a spotReady substrate with 16 gold spots per chip, with a spot diameter of 1 mm, was used, and the solutions of *Nxdown*-SH oligonucleotides (150 $\mu g \cdot mL^{-1}$ in the assay buffer) were deposited (0.5 μL/spot) per triplicate for 1 h at room temperature. Then, with the chip inside the SPR setup, a solution containing a mixture of the three steroid−oligonucleotide conjugates (8-N_1up/hG-N_2up/13-N_3up) was flowed to the cell for about 20 min, until a steady state was reached. Afterward, the chip was washed (10 min), and the blocking solution was passed (10 min). After a new washing step, a solution with a mixture of the three specific antisera (As147/As170/As138, called cocktail As), was flowed for about 25 min until the signal reached the maximum, and then washed again with buffer. The existence of no cross-hybridization between the different oligonucleotides pairs and the affinity of each antibody for the different steroid−oligonucleotide conjugates had been previously studied.[20]

RESULTS AND DISCUSSION

Synthesis and Purification of Steroid−Oligonucleotide Conjugates. A set of three complementary pairs of ssDNA (N_1, N_2, and N_3, *up* and *down*) were synthesized. These sequences have 50% G/C content (purines/pyrimidines) and have the same composition but different sequences. In this way, it is expected that the three resulting duplexes will have similar hybridization properties. The sequences should display high hybridization efficiency for maximum hapten density at the surface after immobilization. The specificity of the hybridization of these sequences has been previously studied in our group in a microarray multiplexed competitive format,[20] and the results indicated hardly any cross-hybridization between the three sequences.

Once a complete set of oligonucleotides sequences were chosen, the steroid−oligonucleotide conjugates were prepared. The synthesis of oligonucleotides carrying steroids such as cholesterol,[32,33] hydroxyprogesterone,[34] dexamethasone,[35] digoxigenin,[36] cholic,[37] lithocholic,[38] and bile acids[39] have been described in order to obtain hydrophobic derivatives of oligonucleotides for antisense, triplex, and RNA interference studies.[40] Most of these compounds are synthesized by conjugation of carboxylic acid derivatives to oligonucleotide carrying amino groups, although the direct incorporation to oligonucleotides using the corresponding phosphoramidites have also been described for compounds that can be prepared in large amounts.[32−34] In our case, the amount of carboxylic acid derivatives available was low, so postsynthetic methods were selected. Thus, ST, THG, and B steroid−oligonucleotides conjugates were prepared through the formation of amide bonds (see Table 1). The steroidal haptens used in these conjugations have been previously used to develop enzyme-linked immunosorbent assays (ELISAs) to detect AAS in real samples.[28−30]

The conjugation of boldenone hapten[13] to amino-oligonucleotide N_3up was performed with the unprotected amino-oligonucleotide in aqueous solution. The hapten 13 has an ester group, which in basic medium could be hydrolyzed. For this reason, conjugation was not possible before ammonia deprotection. Therefore, we used the solution-phase coupling to obtain the desired conjugate 13-N_3up (B) in 20−30% yield (Figure S2, Supporting Information). The NHS-ester of 13 was prepared by reaction of the carboxylate moiety with NHS using DCC.[41] Increasing the molar excess of active ester from 10× to 30× excess allows the conversion of the amino-oligonucleotide to the desired conjugate to 45% (Figure S2, Supporting Information).. The mass obtained for this conjugated was 6400 m/z, while the mass expected was 6639 m/z. We attribute this difference to the fact that during MALDI-TOF analysis fragmentation can occur as a result of heating (laser ionization) in the acidic environment (the matrix) and then what we could observe is the oligonucleotide with the steroid attached hydrolyzed at the ester point. This was confirmed by using electrospray MS analysis. The softer ionization conditions provided the expected mass (13-N_3up, calc 6639, found 6639).

On the other hand, it had been also reported that solid-phase synthesis may be advantageous to the standard synthesis in solution,[42] since it allows forming the amide bond in organic solvent in which the steroidal haptens have better solubility. Thus, the conjugates 8-N_1up (ST) and hG-N_2up (THG) (Table 1) were obtained in higher yields (52−40%), demonstrating that the conjugation reaction is clearly advantageous using the solid-phase coupling protocol. Both conjugates were characterized with MALDI-TOF mass spectrometry (8-N_1up, calc 6668, found 6672; hG-N_2up, calc 6619, found 6614).

In order to assess the influence of the steroids in the duplex structure, denaturation curves were analyzed. Table S1 (Supporting Information) shows the melting temperatures of duplexes carrying the steroids stanozolol,[8] tetrahydrogestrinone (hG), and boldenone.[13] As expected, the presence of the steroid at the 5′-end of the duplex has very little effect on the stability of the duplex.

dx.doi.org/10.1021/bc300138p | *Bioconjugate Chem.* 2012, 23, 2183−2191

The recognition of the oligonucleotide−steroid conjugates by specific antibodies was analyzed by immobilization of the duplex DNA carrying steroids on glass surfaces followed by incubation with the specific antisera and the visualization of the antigen−antibody interaction with a fluorescently labeled antirabbit secondary antibody as described previously.[20] The presence of the oligonucleotides chain does not affect to the recognition of antigen antibody, as can be observed in the detectability parameters (LOD and IC_{50}) in Table S2 in the Supporting Information.

Evaluation by SPR of the Biofunctionality of the Steroid−Oligonucleotide Conjugates. *Hybridization.* The specificity of the hybridization step was assessed by SPR by flowing the solutions of the steroid-$N_{1-3}up$ conjugates into a cell containing the $N_{1-3}down$ functionalized chips and recording the SPR signal (see Figure 2). The DNA double helix is stabilized by hydrogen bonds between the bases of the two strands. The strength of the double-stranded formation depends on (a) the number of matching bases in a sequence, (b) the number and loci of mismatches, and (c) the base composition. The prevailing DNA architecture, the double helix, has well-stacked nearly parallel bases with overlapping π-electron systems. Such π-electron systems may be good candidates for long-distance and one-dimensional (linear) charge transport.[43] Yoo et al.[44,45] demonstrated differences in conductivity due to variation in the base pair sequence. Poly(dG).Poly(dC) showed a conductivity of 40 S/cm, whereas that for Poly(dA).Poly(dT) was about 0.1 S/cm. This fact could be an explanation to the different behavior in the hybridization between the three hapten−oligonucleotide conjugates, because as it can be observed in Figure 2, the N_1down/N_1up-*8* pair has a lower change in the SPR signal than the N_2down/N_2up-*hG* and N_3down/N_3up-*13* pairs. In Table 1, the sequence of the oligonucleotide N_1down at the 5′-end has CAG, whereas the sequences N_2down and N_3down have CGG. Therefore, changes in the conductometric properties of the double helix could affect the refractive index and influence in the SPR signal.[46,47]

Immunochemical Recognition. Three specific antisera (As147, As170, and As138, 1/250 dilution) and a nonspecific serum (CTR-NEG) were used to test whether, after the conjugation of the steroids with the oligonucleotides chains, the antibodies could still recognize their corresponding steroidal haptens. The features of these antibodies have been previously described.[28−30] Results presented in Figure 3 and Figure S1 (Supporting Information) show the change in the SPR signal recorded as a result of three consecutive cycles in different chips for each system (ST, THG, and B). The first cycle shows the specific antibody binding to each steroid−oligonucleotide conjugate (steroid-N_{1-3}up) hybridized on the surface of the sensor. On each graph, the absence of nonspecific signal can also be observed when the CTR-NEG serum was injected, after regenerating the surface. Similarly, subsequent injection of the specific antiserum on systems ST and THG allows recovering the same signal again. In the case of the B system, the signal of the third cycle is lower than the signal obtained in the first cycle, but both first and third cycles are clearly much higher than the nonspecific (CTR-NEG) second cycle. The difference between the first and third cycles for the B system (N_3down-N_3up-13/As138) could be attributed to the low S/N ratio obtained or to a small loss of the binding response. The differences observed in the maximum of the signal and in the slope of the binding step, among the three systems N_1, N_2, and N_3 (see Figure 3) are due to the distinct antisera affinity for the corresponding steroid−oligonucleotide conjugates. Another remarkable fact is the complete regeneration of the surface with a simple washing step with diluted NaOH solution, which offers the possibility that the chips can be reused.

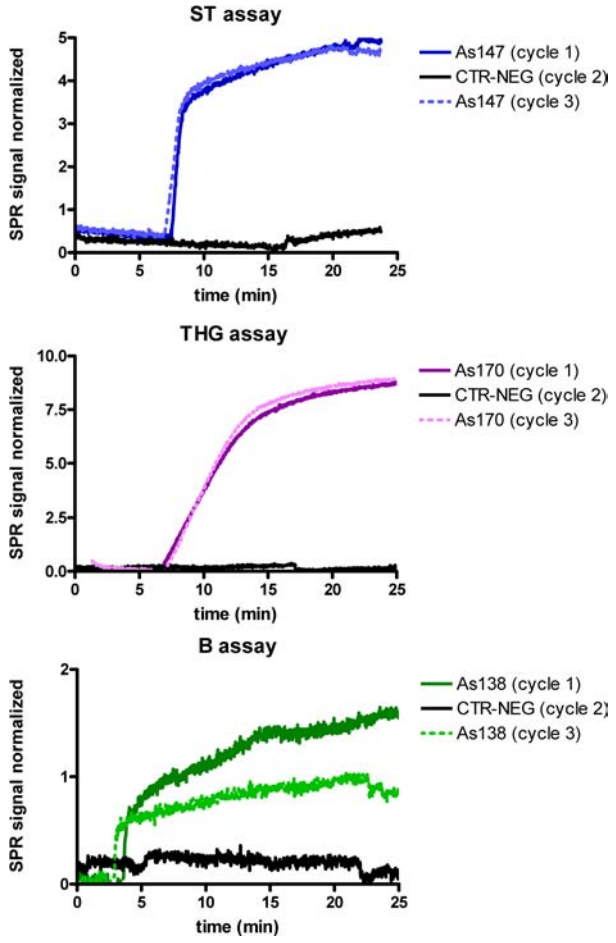

Figure 3. SPR sensograms recorded on the antibody binding step: ST (top), THG (middle), and B (bottom). Each graph shows the response of three consecutive cycles, after regeneration of the surface at the end of each cycle: (a) first cycle, specific antibody; (b) second cycle, preimmune serum; (c) third cycle, specific antibody.

Finally, as a proof of concept, the possibility of developing a multiplexed SPR immunosensor was demonstrated. In this experiment, the DNA-directed immobilization of a cocktail of steroid−oligonucleotide conjugates was used to detect the three AAS simultaneously, under competitive conditions (see Figure 4). The DNA biofunctionalized chip was prepared using a spotReady substrate with 16 gold spots per chip in which the oligonucleotides *N1down*-SH, *N2down*-SH, and *N3down*-SH were deposited per triplicate spots. Then, with the chip placed inside the SPR setup, the assay was performed as described in the Experimental Procedures by flowing a solution containing a mixture of the three steroid−oligonucleotide conjugates (8-N_1up/hG-N_2up/13-N_3up) (Figure 4 left), followed by the cocktail As (Figure 4 right). As can be observed, the change in the refractive index produced in the hybridization step and as result of the antibody binding is recorded as an SPR signal on each respective spot demonstrating the possibility of using DDI to prepare hapten-biofunctionalized SPR chips responding simultaneously to the presence of the corresponding specific antibodies.

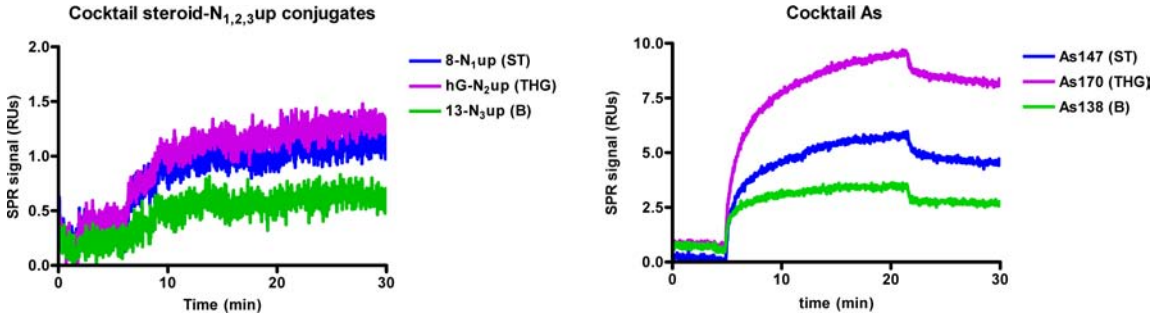

Figure 4. Sensograms recorded in the DNA-directed SPR immunosensor: on the left, the specific hybridization of the steroid−oligonucleotide conjugates with their complementary strands previously immobilized on the gold chip; on the right, the immunochemical recognition of each specific antibody for the corresponding steroid.

CONCLUSIONS

Immunochemical methods show great potential for detection of small targets for a large number of applications. In spite of the powerful analytical tools that are being developed, one of the important issues is the efficient immobilization of analytes to the sensing sufaces. The present work demonstrates the potential of oligonucleotide−steroid conjugates for DNA-directed immobilization of haptens on sensor surfaces. To this end, we have demonstrated that three different steroids can be conjugated to oligonucleotides using the same steroid derivatives used for the obtention of protein-conjugates needed for immunization. Moreover, the results show that coupling of the hapten to the oligonucleotides preserves the antibody recognition properties allowing the construction of a biosensor for the specific detection of steroids. The presence of the steroid does not affect the hybridization properties of the oligonucleotides. The immobilization of the conjugates to the gold sensing surface is performed by immobilization of the complementary strand carrying a thiol group followed by hybridization. The DNA-directed immobilization strategy presents the advantage of the possibility of reusing the same sensor chip for multiple measurements after an easy dehybridization step. Moreover, consecutive measurement cycles addressed to detect other molecules could be performed on the same DNA-chip, by just binding distinct haptens, proteins, or antibodies, to the complementary oligonucleotide strands. The strategy presented here shows a valuable approach for small organic molecule detection on biosensors. The coupling of the hapten to the oligonucleotide has been demonstrated to preserve the antibody recognition properties allowing the construction of a biosensor for the specific detection of esteroids. For these reasons, the use of the DNA-direct immobilization strategy opens the way to get a multiplexed imaging SPR immunosensor by easily immobilizing distinct haptens on different spots of the ssDNA biofunctionalized chip. This methodology opens the possibility to detect a large number of analytes simultaneously using a DNA site-encoded chip in multichannel SPR devices[12,22] and SPR-imaging biosensors,[23−27] or in the future, using encoded nanoparticles biofunctionalized with the specific antibodies for multiplex-localized surface plasmon resonance (LSPR) sensing. Finally, the methodology described for the preparation of the steroid−oligonucleotide conjugates may be useful for the generation of potential nucleic acid drugs.

ASSOCIATED CONTENT

Supporting Information

Examples of complete SPR sensograms obtained for each system, stanozolol (ST, 8), tetrahydrogestrinone (THG, hG), and boldenone (B, 13). HPLC analysis and mass spectra of oligonucleotide conjugate 13-N_3*up*. Melting temperatures of duplexes carrying steroids and analysis of the recognition of the conjugates with specific antisera. This material is available free of charge via the Internet at http://pubs.acs.org.

AUTHOR INFORMATION

Corresponding Author

*Phone 34-934039942; E-mail recgma@cid.csic.es.

Notes

The authors declare no competing financial interest.

ACKNOWLEDGMENTS

This work was supported by grants from the Ministry of Science and Innovation, MICINN (MAT2011-29335-C03-01 and CTQ2010-20541-C03-01), CCEE (FUNMOL, FP7-NMP-213382-2), Generalitat de Catalunya (2009/SGR/1343, 2009/SGR/208), and CIBER-BBN. CIBER-BBN is an initiative funded by the VI National R&D&i Plan 2008-2011, Iniciativa Ingenio 2010, Consolider Program, CIBER Actions, and financed by the Instituto de Salud Carlos III with assistance from the European Regional Development Fund. Núria Tort has a FI_B fellowship from the AGAUR (Agència de Gestió d'Ajuts Universitaris i de Recerca) of the (Generalitat de Catalunya) Government of Catalonia.

REFERENCES

(1) WADA (2010) The 2010 prohibited list. http://www.wada-ama.org/documents/world_anti-doping_program/wadp-prohibited-list/wada_prohibited_list_2010_en.pdf.

(2) EECC (1996) Directive 96/23/EC. *Off. J. Eur. Commun. L 125*, 3.

(3) Mullett, W. M., Lai, E. P. C., and Yeung, J. M. (2000) Surface plasmon resonance-based immunoassays. *Methods 22*, 77−91.

(4) Shankaran, D. R., Gobi, K. V., and Miura, N. (2007) Recent advancements in surface plasmon resonance immunosensors for detection of small molecules of biomedical, food and environmental interest. *Sens. Actuators, B 121*, 158−177.

(5) Hoa, X. D., Kirk, A. G., and Tabrizian, M. (2007) Towards integrated and sensitive surface plasmon resonance biosensors: A review of recent progress. *Biosens. Bioelectron. 23*, 151−160.

(6) Ricci, F., Volpe, G., Micheli, L., and Palleschi, G. (2007) A review on novel developments and applications of immunosensors in food analysis. *Anal. Chim. Acta 605*, 111−129.

(7) Campbell, C. T., and Kim, G. (2007) SPR microscopy and its applications to high-throughput analyses of biomolecular binding events and their kinetics. *Biomaterials 28*, 2380−2392.
(8) Cooper, M. (2003) Label-free screening of bio-molecular interactions. *Anal. Bioanal. Chem. 377*, 834−842.
(9) Boozer, C., Kim, G., Cong, S., Guan, H., and Londergan, T. (2006) Looking towards label-free biomolecular interaction analysis in a high-throughput format: a review of new surface plasmon resonance technologies. *Curr. Opin. Biotechnol. 17*, 400−405.
(10) Yuan, J., Oliver, R., Aguilar, M.-I., and Wu, Y. (2008) Surface plasmon resonance assay for chloramphenicol. *Anal. Chem. 80*, 8329−8333.
(11) Yuan, J., Oliver, R., Li, J., Lee, J., Aguilar, M., and Wu, Y. (2007) Sensitivity enhancement of SPR assay of progesterone based on mixed self-assembled monolayers using nanogold particles. *Biosens. Bioelectron. 23*, 144−148.
(12) Fernández, F., Hegnerová, K., Piliarik, M., Sanchez-Baeza, F., Homola, J., and Marco, M. P. (2010) A label-free and portable multichannel surface plasmon resonance immunosensor for on site analysis of antibiotics in milk samples. *Biosens. Bioelectron. 26*, 1231−1238.
(13) Mizuta, Y., Onodera, T., Singh, P., Matsumoto, K., Miura, N., and Toko, K. (2008) Development of an oligo(ethylene glycol)-based SPR immunosensor for TNT detection. *Biosens. Bioelectron. 24*, 191−197.
(14) Mitchell, J. S., and Lowe, T. E. (2009) Ultrasensitive detection of testosterone using conjugate linker technology in a nanoparticle-enhanced surface plasmon resonance biosensor. *Biosens. Bioelectron. 24*, 2177−2183.
(15) Lee, W., Oh, B. K., Min Bae, Y., Paek, S. H., Hong Lee, W., and Choi, J. W. (2003) Fabrication of self-assembled protein A monolayer and its application as an immunosensor. *Biosens. Bioelectron. 19*, 185−192.
(16) Niemeyer, C. M. (2002) The developments of semisynthetic DNA-protein conjugates. *Trends Biotechnol. 20*, 395−401.
(17) Jung, Y., Lee, J. M., Jung, H., and Chung, B. H. (2007) Self-directed and self-oriented immobilization of antibody by protein G-DNA Conjugate. *Anal. Chem. 79*, 6534−6541.
(18) Boozer, C., Ladd, J., Chen, S., and Jiang, S. (2006) DNA-Directed protein immobilization for simultaneous detection of multiple analytes by surface plasmon resonance biosensor. *Anal. Chem. 78*, 1515−1519.
(19) Boozer, C., Ladd, J., Chen, S., Yu, Q., Homola, J., and Jiang, S. (2004) DNA directed protein immobilization on mixed ssDNA/oligo(ethyleneglycol) self-assembled monolayers for sensitive biosensors. *Anal. Chem. 76*, 6967−6972.
(20) Tort, N., Salvador, J. P., Eritja, R., Poch, M., Martínez, E., Samitier, J., and Marco, M. P. (2009) Fluorescence site-encoded DNA addressable hapten microarray for anabolic androgenic steroids. *TrAC Trends Anal. Chem. 28*, 718−728.
(21) Bier, F. F., Kleinjung, F., Ehrentreich-Förster, E., and Scheller, F. W. (1999) Changing functionality of surfaces by directed self-assembly using oligonucleotides—The oligo-tag. *BioTechniques 27*, 752−760.
(22) Homola, J., Vaisocherová, H., Dostálek, J., and Piliarik, M. (2005) Multi-analyte surface plasmon resonance biosensing. *Methods 37*, 26−36.
(23) Kanda, V., Kariuki, J. K., Harrison, D. J., and McDermott, M. T. (2004) Label-free reading of microarray-based immunoassays with surface plasmon resonance imaging. *Anal. Chem. 76*, 7257−7262.
(24) Ladd, J., Taylor, A. D., Piliarik, M., Homola, J., and Jiang, S. (2008) Hybrid surface platform for the simultaneous detection of proteins and DNAs using a surface plasmon resonance imaging sensor. *Anal. Chem. 80*, 4231−4236.
(25) Rebe Raz, S., Bremer, M. G. E. G., Haasnoot, W., and Norde, W. (2009) Label-free and multiplex detection of antibiotic residues in milk using imaging surface plasmon resonance-based immunosensor. *Anal. Chem. 81*, 7743−7749.
(26) Kanoh, N., Kyo, M., Inamori, K., Ando, A., Asami, A., Nakao, A., and Osada, H. (2006) SPR Imaging of photo-cross-linked small-molecule arrays on gold. *Anal. Chem. 78*, 2226−2230.
(27) Lee, H. J., Nedelkov, D., and Corn, R. M. (2006) Surface plasmon resonance imaging measurements of antibody arrays for the multiplexed detection of low molecular weight protein biomarkers. *Anal. Chem. 78*, 6504−6510.
(28) Salvador, J.-P., Sanchez-Baeza, F., and Marco, M.-P. (2007) Preparation of antibodies for the designer steroid tetrahydrogestrinone and development of an enzyme-linked immunosorbent assay for human urine analysis. *Anal. Chem. 79*, 3734−3740.
(29) Salvador, J. P., Sánchez-Baeza, F., and Marco, M. P. (2008) Simultaneous immunochemical detection of stanozolol and the main human metabolite, 3′-hydroxy-stanozolol, in urine and serum samples. *Anal. Biochem. 376*, 221−228.
(30) Kramer, K., Hubauer, A., Lausterer, R., Salvador, J. P., and Marco, M. P. (2007) Production of antibodies for the quantitative detection of the anabolically active Androgens 17β-boldenone and methylboldenone. *Anal. Lett. 40*, 1461−1472.
(31) Connolly, B. A. (1987) The synthesis of oligonucleotides containing a primary amino group at the 5′-terminus. *Nucleic Acids Res. 15*, 3131−3139.
(32) LeDoan, T., Etore, F., Tenu, J. P., Letourneux, Y., and Agrawal, S. (1999) Cell binding, uptake and cytosolic partition of HIV anti-gag phosphodiester oligonucleotides 3′-linked to cholesterol derivatives in macrophages. *Bioorg. Med. Chem. 7*, 2263−2269.
(33) Letsinger, R. L., and Chaturvedi, S. (1998) Tailored hydrophobic cavities in oligonucleotide-steroid conjugates. *Bioconjugate Chem. 9*, 826−830.
(34) Ketola, J., Hurskainen, P., and Hovinen, J. (2009) Derivatization of 11-hydroxyprogesterone using phosphoramidite chemistry. *Bioconjugate Chem. 20*, 625−628.
(35) Acedo, M., Tarrason, G., Piulats, J., Mann, M., Wilm, M., and Eritja, R. (1995) Preparation of oligonucleotide-dexamethasone conjugates. *Bioorg. Med. Chem. Lett. 5*, 1577−1580.
(36) Escarceller, M., Rodriguez-Frias, F., Jardi, R., San Segundo, B., and Eritja, R. (1992) Detection of hepatitis B virus DNA in human serum samples: Use of digoxigenin-labeled oligonucleotides as modified primers for the polymerase chain reaction. *Anal. Biochem. 206*, 36−42.
(37) Bhatia, D., Yue-Ming, L., and Ganesh, K. N. (1999) Steroid-DNA conjugates: improved triplex formation with 5-amido-(7-deoxycholic acid)-dU incorporated oligonucleotides. *Bioorg. Med. Chem. Lett. 9*, 1789−94.
(38) Rump, E. T., de Vrueh, R. L. A., Sliedregt, L. A. J. M., Biessen, E. A. L., van Berkel, T. J. C., and Bijsterbosch, M. K. (1998) Preparation of conjugates of oligodeoxynucleotides and lipid structures and their interaction with low-density lipoprotein. *Bioconjugate Chem. 9*, 341−349.
(39) Starke, D., Lischka, K., Pagels, P., Uhlmann, E., Kramer, W., Wess, G., and Petzinger, E. (2001) Bile acid-oligodeoxynucleotide conjugates: synthesis and liver excretion in rats. *Bioorg. Med. Chem. Lett. 11*, 945−949.
(40) de Fougerolles, A., Vornlocher, H. P., Maraganore, J., and Lieberman, J. (2007) Interfering with disease: a progress report on siRNA-based therapeutics. *Nat. Rev. Drug Discovery 6*, 443−453.
(41) Thompson, S. (2003) Small-molecule-protein conjugation procedures. In *Molecular Diagnosis of Infectious Diseases*, Decker, J., Reische, U., Eds.; pp 255−265, Chapter 17, Springer Protocols Vol 94, Humana Press, Springer Science, Heidelberg.
(42) Merrifield, B. (1986) Solid phase synthesis. *Science 232*, 341−347.
(43) Odom, D. T., Dill, E. A., and Barton, J. K. (2000) Robust charge transport in DNA double crossover assemblies. *Chem. Biol. 7*, 475−481.
(44) Yoo, K. H., Ha, D. H., Lee, J. O., Park, J. W., Kim, J., Kim, J. J., Lee, H. Y., Kawai, T., and Choi, H. Y. (2001) Electrical conduction through poly(dA)-poly(dT) and poly(dG)-poly(dC) DNA molecules. *Phys. Rev. Lett. 87*, 198102.

(45) Taniguchi, M., and Kawai, T. (2005) Electron-molecular-vibration coupling for small polarons in DNAs. *Phys. Rev. E 72*, 061909.
(46) Georgiadis, R., Peterlinz, K. A., Rahn, J. R., Peterson, A. W., and Grassi, J. H. (2000) Surface plasmon resonance spectroscopy as a probe of in-plane polymerization in monolayer organic conducting films. *Langmuir 16*, 6759−6762.
(47) Kang, X., Cheng, G., and Dong, S. (2001) A novel electrochemical SPR biosensor. *Electrochem. Commun. 3*, 489−493.

Synthesis of steroid-oligonucleotide conjugates for a DNA site-encoded SPR immunosensor

Nuria Tort[1,5], J.-Pablo Salvador[5,1], Anna Aviñó[2,5,6], Ramón Eritja[2,5,6,], Jordi Comelles[4,5], Elena Martínez[4,5], Josep Samitier[3,4,5], M.-Pilar Marco[1,5]*

[1] Applied Molecular Receptors Group (AMRg) and [2] Nucleic Acids Chemistry Group. Chemical and Biomolecular Nanotechnology Department. IQAC-CSIC. Jordi Girona, 18-26, 08034-Barcelona, Spain

[3] Nanobioengineering Group, Institute for Bioengineering of Catalonia (IBEC), Balidri Reixac, 10-12, 08028 Barcelona, Spain

[4] Department of Electronics, University of Barcelona, Martí i Franquès, 1, 08028 Barcelona, Spain

[5] CIBER de Bioingenieria, Biomateriales y Nanomedicina (CIBER-BBN)

[6] Institute for Research in Biomedicine, Baldiri Reixac 19, E-08028 Barcelona

SUPPORTING INFORMATION:

Pages 2-3. Figure S1. Examples of complete SPR sensograms obtained for each system, stanozolol (ST, 8), tetrahydrogestrinone (THG, hG) and boldenone (B, 13)
Pages 3-5: Figure S2. HPLC analysis and mass spectra of oligonucleotide conjugate 13-N_3*up*
Page 6: Melting temperatures of duplexes carrying steroids.
Page 7: Analysis of the recognition of the conjugates with specific antisera

Figure S1. Examples of complete SPR sensograms obtained for each system, stanozolol (ST, 8), tetrahydrogestrinone (THG, hG) and boldenone (B, 13).

ST system

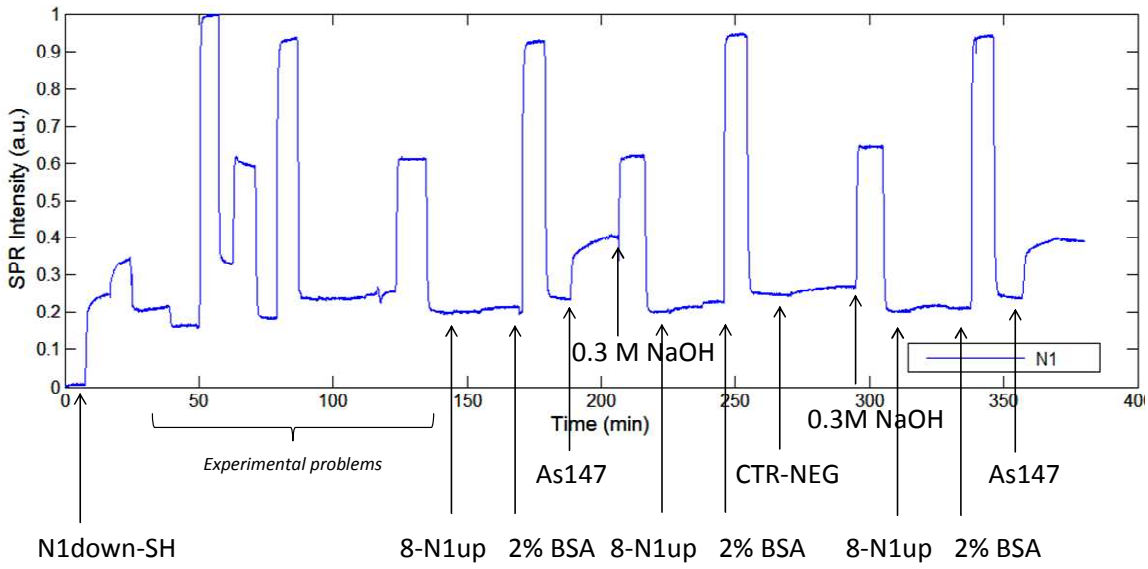

THG system

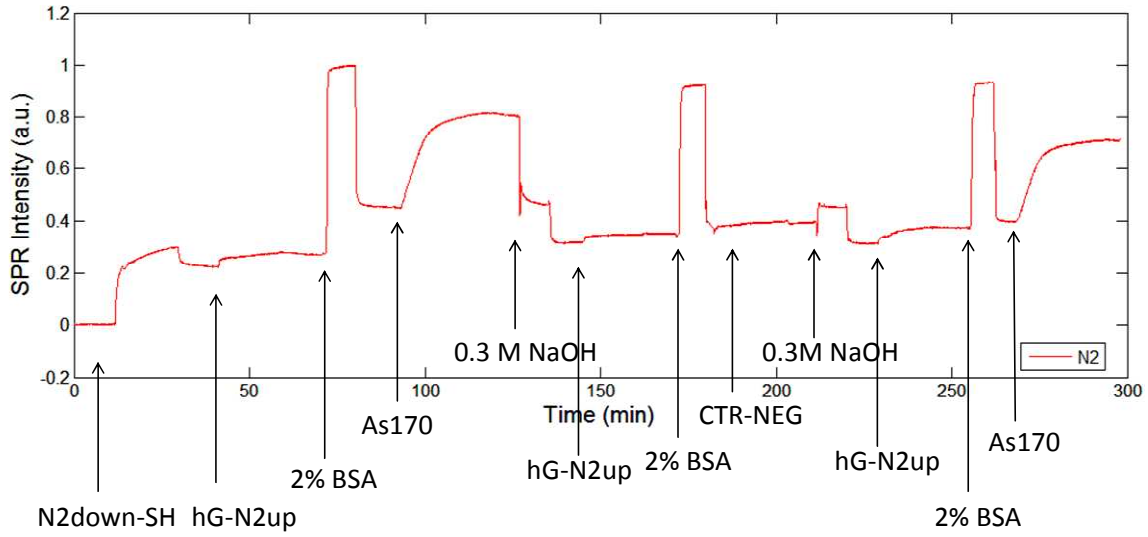

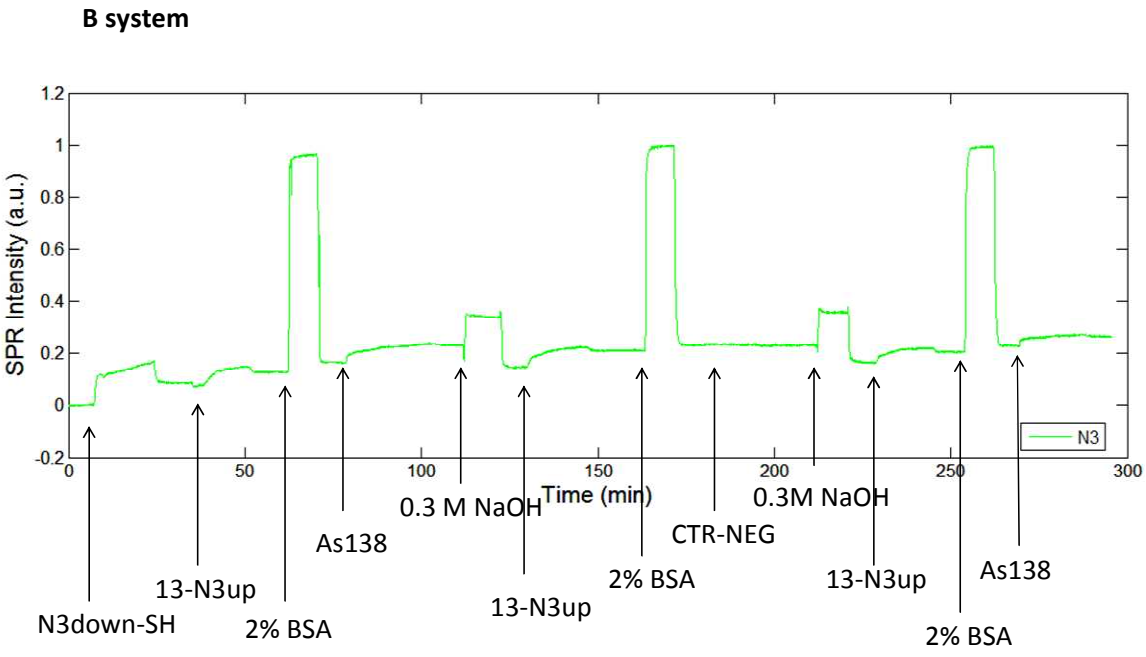

Figure S2. HPLC analysis of oligonucleotide conjugate 13-N_3*up*.

A) Reaction mixture resulting from the reaction of NH_2- N_3*up* and 10 eq of the active ester of 13 in Tris buffer after overnight treatment at room temperature. The peak at retention time 5-6 min corresponds to unreacted NH_2- N_3*up*. The peak at retention time 12-14 min corresponds to the expected conjugate 13-N_3*up*.

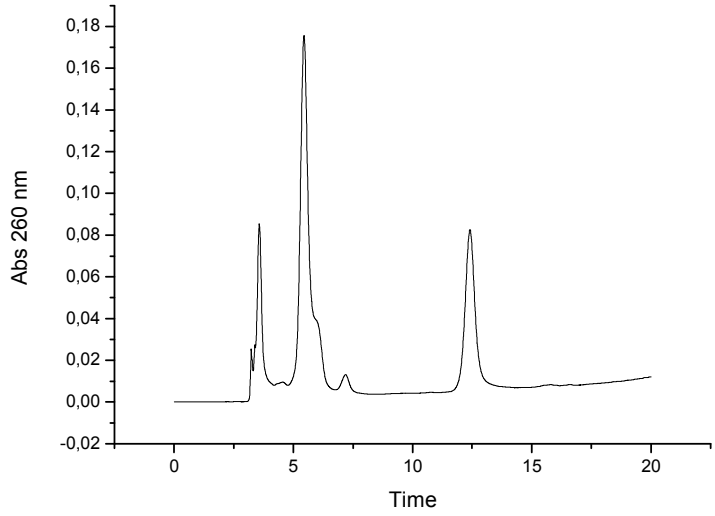

B) Reaction mixture resulting from the reaction of NH_2- N_3*up* and 10 eq of the active ester of 13 in borate buffer after overnight treatment at room temperature.

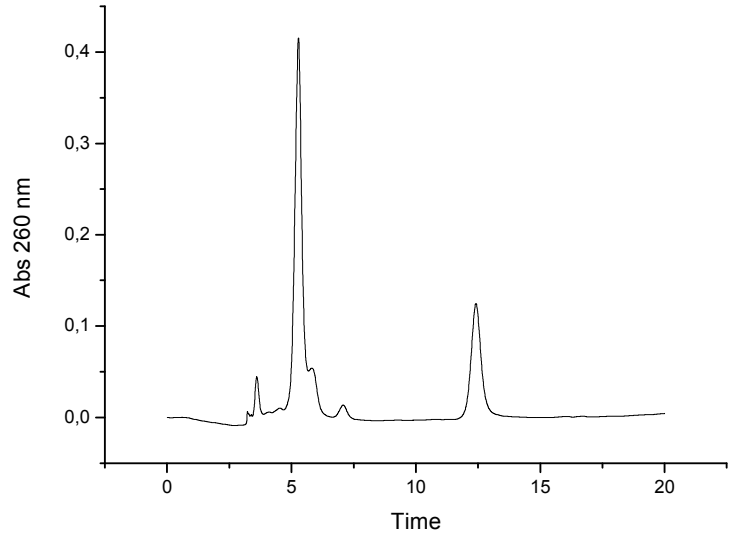

C) Reaction mixture resulting from the reaction of NH_2- N_3*up* and 10 eq of the active ester of 13 in carbonate buffer after overnight treatment at room temperature.

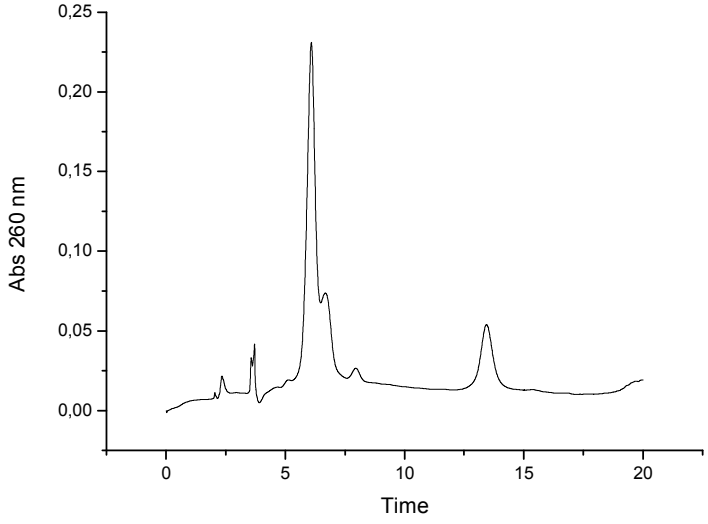

D) Reaction mixture resulting from the reaction of NH_2- N_3up and 30 eq of the active ester of 13 in borate buffer after overnight treatment at room temperature.

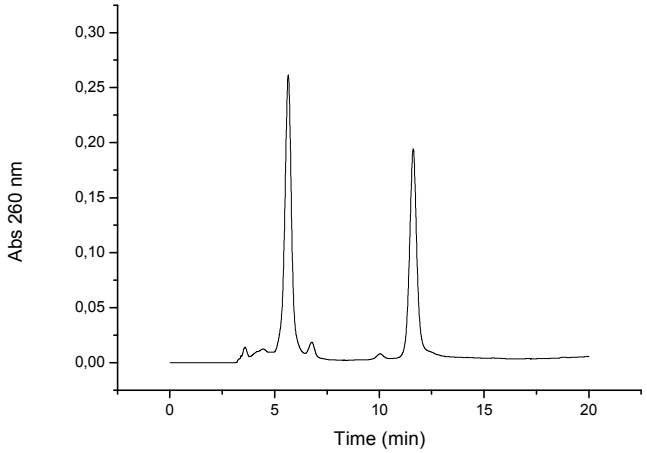

E) Electrospray deconvoluted mass spectra of oligonucleotide conjugate 13-N_3up.

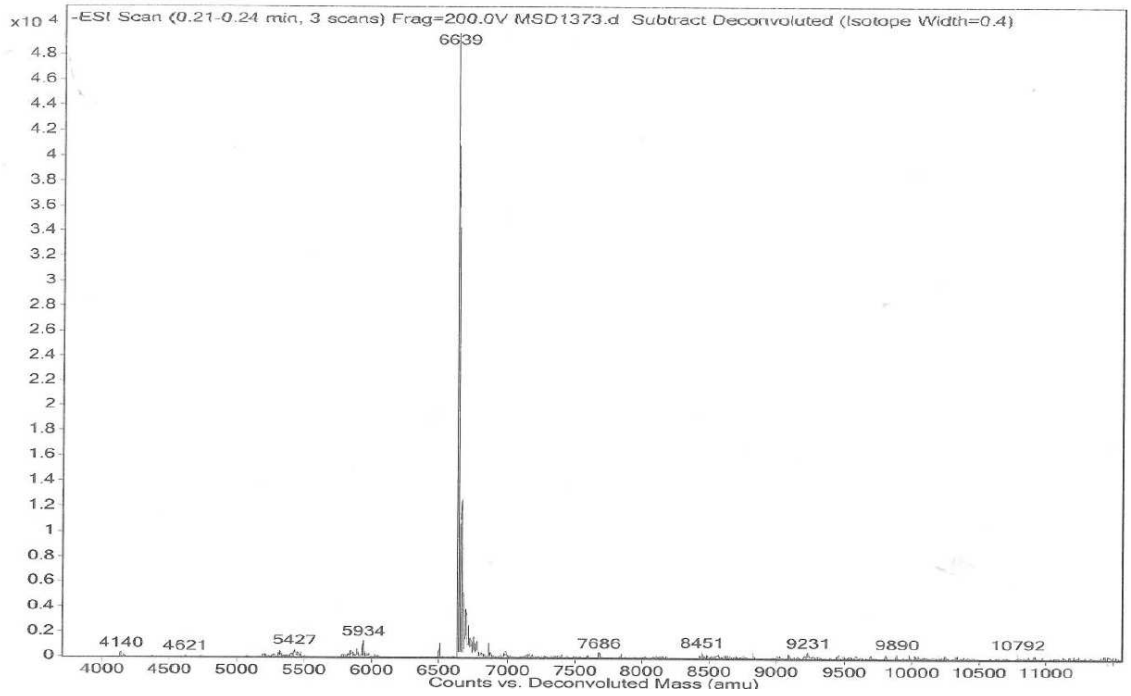

Table S1. Melting temperatures of duplexes carrying steroids.

DUPLEX	T_m (ºC)	ΔT_m (ºC)
N_1down / *N_1up*	68.3	--
N_1down / 8-*N_1up*	67.0	-1.3
N_2down / *N_2up*	65.6	--
N_2down / hG-*N_2up*	65.8	+0.2
N_3down / *N_3up*	64.5	--
N_3down / 13-*N_3up*	65.6	+1.1

Conditions: 50 mM NaCl, 0.1 M phosphate buffer pH 7.0. ΔT_m is the difference between the melting temperatures of modified duplex minus the melting temperatures of the corresponding unmodified duplex

Denaturation studies. Oligonucleotide duplexes (Table S1) were dissolved in 0.1 M sodium phosphate buffer, 50 mM NaCl (pH=7.0). The samples were heated at 90 ºC for 5 min, allowed to cool slowly to room temperature to induce annealing and then kept overnight in a refrigerator (4 ºC). The melting curves were recorded by heating the samples with a temperature controller from 10 to 80 ºC at a constant rate of 1 ºC/min when monitoring the absorbance at 260 nm. The absorption spectra and melting experiments (absorbance vs. temperature) were recorded in 1 cm path-length cells. Melting curves were performed at 3-4 μM duplex concentration. The T_m values were calculated with the *Meltwin 3.2* software.

Table S2. Analytical parameters for the detection of ST, THG and B in ELISA[1], FLISA and microarray[2] format.

	ST			THG			B		
	ELISA	**FLISA**	**Microarray**	**ELISA**	**FLISA**	**Microarray**	**ELISA**	**FLISA**	**Microarray**
IC_{50} /mg·L^{-1}	0.16	0.46	1.72	0.14	0.46	1.14	5.90	2.77	7.37
LOD /mg·L^{-1}	0.02	0.05	0.32	0.04	0.08	0.14	0.23	0.14	0.48
Slope	-1.07	-1.19	-1.35	-0.96	-1.41	-1.28	-0.80	-0.90	-0.77
Max_{signal}	1.04[a]	1436[b]	9292[b]	0.88[a]	1191[b]	9160[b]	1.45[a]	1021[b]	5446[b]
Min_{signal}	0.02[a]	-15[b]	926[b]	0.03[a]	8[b]	1123[b]	0.01[a]	29[b]	261[b]

[a], absorbance units
[b], relative fluorescences units

(1) Tort, N.; Salvador, J. P.; Marco, M. P. *Analytical and Bioanalytical Chemistry* **2012**, *403*, 1361.
(2) Tort, N.; Salvador, J.-P.; Eritja, R.; Poch, M.; Martínez, E.; Samitier, J.; Marco, M.-P. *TrAC Trends in Analytical Chemistry* **2009**, *28*, 718.

Fluorencence linked immunosorbent assay (FLISA) for AAS.

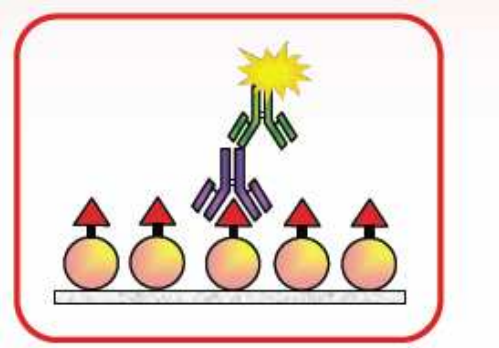

Experimental part. The concentrations of all of the immunoreagents are summarized in Table S3. Microtiter plates were coated with the haptenized protein conjugate (AT) at the appropriate concentration in coating buffer (100µL/well) overnight at 4 °C. The following day, the plates were washed four times with PBST. The different standard solutions or samples were diluted in PBST and added to the microtiter plates (50µL/well), followed by the corresponding solution of the antiserum in PBST (50µL/well), and incubated for 30 min at RT. The plates were washed again as before, and a solution of anti-IgG-FITC (20 µg/mL in PBST) was added (100µL/well) and incubated for 30 min more at RT. After a new washing step, a solution of 30% of glicerine in carbonate buffer was added (100µL/well) and incubated 5 min at room temperature. The microplate were washed againg and the fluorescence were read at 494 nm of excitation and 529 nm of emission. The standard curves were fitted to a four-parameter equation according to the following formula: $Y=[(A - B)/1 - (x/C)^{D}]+B$, where A is the maximal fluorescence signal, B is the minimum fluorescence signal, C is the concentration that yields an absorbance that is 50 % of the maximum fluorescence signal (i.e., it is the IC_{50}), and D is the slope at the inflection point of the sigmoid curve. The limit of detection (LOD) is defined as the concentration that produces 90 % of the maximum fluorescence signal (IC_{90}).

Table S3: Immunoreagents concentration for FLISA.

AT/As	[AT][a]	[As]	[AntiIgG-FITC]
8-BSA/As147	0.15625	1/6400	
13-BSA/As138	0.15625	1/16000	20[a]
hG-BSA/As170	0.3125	1/2000	

a) Concentration in μg/mL.

Bioconjugate Chemistry

Article

pubs.acs.org/bc

^{99m}Tc-MAG3-Aptamer for Imaging Human Tumors Associated with High Level of Matrix Metalloprotease-9

Sonia Da Rocha Gomes,[†,‡,▽,●] Julie Miguel,[■,▽] Laurent Azéma,[†,‡] Sandrine Eimer,[‡,#] Colette Ries,[‡,§] Eric Dausse,[†,‡] Hugues Loiseau,[‡,⊥] Michèle Allard,[‡,§,∥,¶] and Jean-Jacques Toulmé*[,†,‡]

[†]INSERM U869, ARNA, Institut Européen de Chimie et Biologie, 33607 Pessac, France

[‡]Université de Bordeaux, 33076 Bordeaux, France

[§]CNRS, INCIA, UMR 5287, 33400 Talence, France

[∥]Pôle d'imagerie, [⊥]Département de Neurochirurgie, [#]Département de Pathologie, CHU de Bordeaux, 33076 Bordeaux, France

[¶]Ecole Pratique des Hautes Etudes, Bordeaux, France

[■]Pôle des Produits de Santé, CHU de Bordeaux, Pessac, France

Supporting Information

ABSTRACT: The human matrix metalloprotease 9 (hMMP-9) is involved in many physiological processes such as tissue remodeling. Its overexpression in tumors promotes the release of cancer cells thus contributing to tumor metastasis. It is a relevant marker of malignant tumors. We selected an RNA aptamer containing 2′-fluoro, pyrimidine ribonucleosides, that exhibits a strong affinity for hMMP-9 (K_d = 20 nM) and that discriminates other human MMPs: no binding was detected to either hMMP-2 or -7. Investigating the binding properties of different MMP-9 aptamer variants by surface plasmon resonance allowed the determination of recognition elements. As a result, a truncated aptamer, 36 nucleotides long, was made fully resistant to nuclease following the substitution of every purine ribonucleoside residue by 2′-*O*-methyl analogues and was conjugated to *S*-acetylmercaptoacetyltriglycine for imaging purposes. The resulting modified aptamer retained the binding properties of the originally selected sequence. Following ^{99m}Tc labeling, this aptamer was used for ex vivo imaging slices of human brain tumors. We were able to specifically detect the presence of hMMP-9 in such tissues.

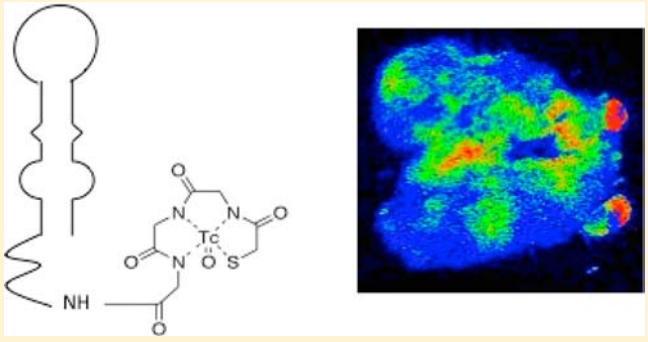

INTRODUCTION

Primary brain tumors can be classified in various ways: topographic (i.e., extraparenchymal or intraparenchymal), neuropathologic (according to cell type),[1] and prognostic (benign, unpredictable behavior or malignant). For the latter, few gliomas are benign tumors (pilocytic astrocytoma), but the vast majority of gliomas are malignant and infiltrative tumors and present poor treatment results (grade 3 or anaplastic astrocytoma and grade 4 or glioblastoma). Unfortunately, lower-grade gliomas can transform into glioblastoma.[2] The transformation to a more malignant phenotype involves a multistep process including tissue invasion, resulting from tumor cell ability to migrate in brain parenchyma.[3]

Uncontrolled cellular proliferation is a cardinal feature of neoplasia. The ability to measure the proliferation rate in tumors in patients in vivo will help with tumor grading and staging, and assessing the effect of therapy. Today, modern imaging techniques enable the investigation of pathological changes within tumors themselves in vivo, exploiting the increased cellular metabolism in these cells using positon emission tomography (PET) imaging of 3′-deoxy-3′-[^{18}F]-fluorothymidine (FLT), [^{11}C]-methionine or *O*-2-[^{18}F]-fluoroethyl-tyrosine (FET). New imaging modalities are required for a better monitoring of tumor malignancy associated with extracellular damage in surrounding brain tissue, especially functional imaging reflecting intimate biological mechanisms of tumor cell proliferation.

One of the possible mechanisms involved in surrounding tissue invasion is the overexpression of matrix metalloproteinases (MMPs) capable of degrading extracellular matrix components, permitting cell migration.[4,5] An alternative approach for imaging tumors would be to follow MMPs expression as a surrogate marker of malignant tumor cell invasion within brain parenchyma.[6] Tumor cells form mass lesions in the central nervous system, and enzymatic degradation of extracellular matrix by MMPs is necessary for the malignant tumor cells to migrate into normal brain tissue. Indeed, MMP inhibitors constitute attractive potential anti-

Received: March 21, 2012
Revised: October 8, 2012
Published: October 8, 2012

ACS Publications © 2012 American Chemical Society

dx.doi.org/10.1021/bc300146c | *Bioconjugate Chem.* 2012, 23, 2192−2200

cancer agents.[7,8] hMMP-2 and hMMP-9 constitute a subgroup of MMPs called gelatinases that degrade the basal lamina around capillaries, and enable angiogenesis and neurogenesis, participating in extracellular matrix degradation and facilitating tumor cells migration in brain parenchyma.[9] Because changes in extracellular matrix surrounding a brain tumor can occur before a change in magnetic resonance imaging (MRI) data of the tumor itself, it can be postulated that hMMP-9 PET or SPECT (single photon emission computed tomography) molecular imaging would be an accurate means for monitoring therapy in grade 2 glioma or diffuse astrocytoma.

Aptamers were developed in the early 1990s.[10−12] These structured DNA, RNA, or modified oligonucleotides are identified after iterative cycles of selection/amplification through a process named SELEX (systematic evolution of ligands by exponential enrichment) from a random oligonucleotide library. Aptamers were successfully selected for a wide range of targets (proteins, nucleic acids, peptides, small molecules, cells, etc.) and were shown to display both high affinity and specificity.[13,14] Aptamer-based tools were designed for diagnostic or therapeutic applications over the past decade and are a promising alternative to monoclonal antibodies in many applications[15,16] including molecular imaging.[17] Aptamers can be modified to make them resistant to nucleases and conjugated to fluorescent tags or radioelements. The first aptamer for in vivo imaging was developed in 1997 for the detection of human neutrophil elastase in a rat model of inflammation.[18] Since these encouraging results, aptamers have been successfully applied to target tumor cells for detection or real-time imaging.[19−26] Most aptamer imaging probes have been selected against cells for cancer detection particularly with aptamer-conjugated nanoparticles.[22,27−29] Recently, an antibody-like nanostructure composed of two aptamers and a dendrimer was developed with temperature-dependent binding to cancer cells.[30] Histological analyses have been carried out with fluorescent or biotinylated aptamers.[31−35] A new strategy based on activable aptamer showed less fluorescence background with specific tumor retention.[36]

In this work, a specific aptamer directed against the human MMP-9 protein has been identified and converted into a ^{99m}Tc-labeled hMMP-9 probe following truncation, backbone modification, and end functionalization. We characterized the binding properties of this aptamer and evaluated its potential for in vitro imaging brain tumors by assessing the intensity of radiotracer labeling and detectability of various primary tumor slices and compared these with immunohistochemistry analysis.

MATERIALS AND METHODS

Materials. Aptamer Production and Analysis. *SELEX Conditions.* The oligonucleotide library was obtained by transcription from a DNA library, synthesized by Proligo, containing 30 random nucleotides (N30) flanked by invariant primer annealing sites: 5′-GTGTGACCGACCGTGGTGC-N30-GCAGTGAAGGCTGGTAACC-3′. Two different primers P20 5′GTGTGACCGACCGTGGTGC and 3′SL 5′TAATACGACTCACTATAGGTTACCAGCCTTCACTGC containing the T7 transcription promoter (underlined), were used for PCR amplification. The modified 2′-fluoropyrimidine RNA library used for the selection and aptamer F3 were obtained by transcription (DuraScribe T7 transcription kit from Epicenter Technologies containing 2′-F-CTP and 2′-F-UTP). The mutant T7 RNA polymerase Y639F[37] was also used.

The in vitro selection against hMMP-9 protein (Calbiochem) was performed at 23 °C in SP buffer (50 mM Tris HCl, pH 7.4, 50 mM NaCl, 100 mM KCl, 5 mM $CaCl_2$, 1 mM magnesium acetate) using the filter retention technique (HAWP 0.45 μM, Millipore).[38] Filters were pretreated with alkali as described by McEntee et al. [39] in order to reduce nonspecific adsorption of nucleic acids. The library was first incubated with the alkali-treated filters for 20 min then with hMMP-9 protein for 20 min. The mixture was filtered and filters washed with SP buffer. Candidates bound to the protein were eluted with 500 μL phenol/urea 7 M for 20 min at 65 °C and reverse transcribed with 200 U M-MLV reverse transcriptase RNase H$^-$ Point Mutant (Promega): 1 μL was used for 25 cycles of PCR at 63 °C with 1 U of AmpliTaq Gold DNA polymerase (Applied Biosystems) and the two P20 and 3′SL primers. 2′-F-RNA candidates were obtained by in vitro transcription of the PCR products with the DuraScribe T7 transcription kit (Epicenter Technologies). During the successive in vitro selection rounds, candidates and protein concentrations were progressively decreased, whereas the number of washes, used to eliminate weak binders, was increased. This resulted in a tougher competition between the candidates for binding as evolution proceeded. Monitoring the evolution of the binding properties of the selected population after every cycle indicated an increase in binding efficiency of the candidates up to round 15. After 14 selection cycles against the hMMP-9 protein, selected candidates were cloned using the TOPO TA cloning kit (Invitrogen) and sequenced (Genome Express Company).

Oligonucleotide Synthesis. The truncated variants F3B, F3C1, and F3C2 of the aptamer F3, the 2′-*O*-methyl purine/2′-fluoropyrimidine F3B (F3Bomf) derivative, the 3′-end biotinylated aptamers (F3B, F3Bomf), the control sequence 5′ UGCCAAACGCGUCCCCUUUGCCCGGC-CUCCGCCGCA 3′ and the mutants F3BΔ and F3BA were chemically synthesized on an Expedite 8909 in our laboratory according to standard procedures. All oligonucleotides were purified by electrophoresis on denaturing 20% polyacrylamide, 7 M urea gels. Secondary structure prediction of aptamers was determined using the mfold web server (http://mfold.rna.albany.edu/?q=mfold).

NMR Analysis of F3B Variant. ^{1}H NMR spectra were recorded at pH 6.4 and 5.5, in 10 mM sodium phosphate buffer containing 90/10 H_2O/D_2O. Imino protons were assigned based on the analysis of NOESY spectra recorded at 4 and 15 °C.

Oligonucleotide Conjugation. Oligonucleotides F3Bomf and the control sequence, bearing a 5′ hexylamino function, were synthesized on a 1 μmol scale with an ABI Expedite 8909 synthesizer, using conventional β-cyanoethyl phosphoramidite chemistry. Once purified (HPLC, Macherey-Nagel Nucleodur column, 0.1 M triethylammonium acetate, pH 7.0, (acetonitrile/0.1 M triethylammonium acetate, pH 7.0: 80/20) gradient), they were conjugated to MAG3.[40] Briefly, 20 nmol of oligonucleotide were suspended in 100 μL of binding buffer (sodium bicarbonate/sodium carbonate 0.25 M, pH 8.3, sodium chloride 1 M, sodium ethylenediaminetetraacetate 1 mM) and gently stirred at room temperature. MAG3-NHS (3 mg, in 30 μL of DMF) was added in portions at room temperature over 3 h. After complete addition, the suspension was stirred for an additional hour, and the crude was directly purified by HPLC under the same conditions to afford the oligonucleotide−MAG3 conjugate in 50−90% yield. Conjugate

characterization was performed with a MALDI-ToF mass spectrometer (Reflex III, Bruker).

Human Matrix Metalloprotease-9. The human MMP-9 was purchased to Calbiochem; samples were checked for purity by SDS polyacrylamide gel electrophoresis. Batch-to-batch variation was noticed resulting in the presence of breakdown fragments likely related to self-cleavage of the protease. Only samples with low fragment content were used in our study.

Binding and Specificity Assays. The dissociation constant (K_d) of the complexes, formed by the aptamers and the hMMP-9 protein, was determined using the filter retention method. One nanomole ^{32}P 5′-end-labeled aptamer was incubated with increasing concentrations of hMMP-9 (10, 20, 40, 72, 160, 320, 500 nM) for 20 min at 23 °C in 20 μL SP buffer. Complexes were filtered and the radioactivity retained on the filter was quantified using a scintillation counter (LS 6000 IC, Beckman). K_d values were deduced from data point fitting with *Kaleidagraph 3.0* (Abelbeck software), according to the equation: $B = (B_{max}[L]_0)/([L]_0 + K_d)$, where B is the proportion of complex, B_{max} is the maximum of complex formed, and $[L]_0$ is the total concentration of unlabeled ligand.

Surface plasmon resonance (SPR) experiments were performed on a BIAcore 3000 apparatus (Biacore AB, Sweden). Two micrograms of hMMP-9 protein was injected on a carboxymethylated dextran CM5 sensorchip for immobilization, and aptamers F3B, F3C1, and F3C2 were injected at 200 nM (20 μL/min) in SP buffer. Alternatively, CM5 sensorchips were functionalized with streptavidin. 3′-End biotinylated F3B and F3Bomf were immobilized on the functionalized CM5, and hMMP-9 protein was injected at 100 nM in SP buffer. hMMP-9 was injected at different concentrations (from 5 to 160 nM) in PBS buffer. In another series of experiments, 3′-end biotinylated aptamer F3Bomf was immobilized, and hMMP-9, pro-hMMP-9, mouse pro-MMP-9, human MMP-2, or MMP-7 proteins were injected at 50 nM in PBS buffer. SPR experiments were performed at 23 °C, at 20 μL/min, and the complexes were dissociated with a pulse of a solution containing 40% formamide/3.6 M urea/30 mM EDTA.[41]

^{99m}Tc Oligonucleotides Radiolabeling. The MAG3 F3Bomf and the control sequence were labeled with ^{99m}Tc as described by Winnard et al.:[40] two fresh solutions were prepared: (i) sodium tartrate (50 mg/mL) in sterile 0.5 M sodium bicarbonate, 0.25 M ammonium acetate, 0.18 M ammonium hydroxide, pH 9.2 (The high pH of the tartrate solution was necessary so that the final pH is approximately 7.6) and (ii) a 1 mg/mL $SnCl_2{\cdot}2H_2O$ in 10 mM hydrochloric acid just prior to use. ^{99m}Tc pertechnetate solution (2−10 μL) (Elumatic III − Cis Bio International) was added to the MAG3-aptamer (10−100 μg) to provide about 3.7 MBq/μg of aptamer followed by the addition of the tartrate solution to a final concentration of 6−7 μg/μL. The stannous ion solution was added immediately thereafter (1 μg of $SnCl_2{\cdot}2H_2O$ for each 10 μg of aptamer) and left at room temperature for 15 min. The labeled aptamer was then purified by microspin column (MicroSpin G-25 columns, GE Healthcare), and the radiochemical purity was determined using thin-layer chromatography (TLC plates RP-18, Merck).

Under the above set of conditions, average labeling efficiency of 70% (N = 15, SD = 14%) was achieved. Radiochemical purity (RCP) determined by thin layer chromatography was 77% (SD = 8%). The stability of ^{99m}Tc-MAG3-aptamer over time was determined using TLC. The radiolabeled oligonucleotides RCP was about 70% at 6 h following radiolabeling, indicating good stability. Average specific activities of 2.48 MBq/μg were obtained (SD = 10%).

Tissue Samples and in Vitro Binding Assay. Tumor tissues used in these studies were obtained from the department of Pathology, University Hospital Bordeaux, France. Nine different types of well-characterized tumors: pilocytic astrocytoma grade 1, meningioma grade 1, fibrillary astrocytoma grade 2, ependymoma grade 2, anaplastic astrocytoma grade 3, medulloblastoma grade 4, primitive central nervous system lymphoma grade 4, and glioblastoma grade 4 were collected from surgical samples, including one case of normal brain tissue from a patient undergoing autopsy. Tumor grade was done according to the 2007 WHO classification of tumors of the central nervous system.[1] All tissue samples were formalin-fixed and paraffin-embedded. Representative 2.5-μm-thick tissue sections were obtained from blocks of paraffin-embedded tissue and subjected to immunohistochemistry and autoradiography analysis.

Binding studies were performed using these tissue sections incubated in the presence of either ^{99m}Tc-MAG3-F3Bomf aptamer or ^{99m}Tc-MAG3-control sequence according to the following procedure: after deparaffinization and rehydration, tissue slices were incubated with 0.037 MBq (0.00125 nmol) of ^{99m}Tc -MAG3-F3Bomf and adjacent section with ^{99m}Tc -MAG3-control for one hour in a humidified chamber at room temperature before being washed twice in PBS + 0.1% Tween and then twice in purified water. Then, sections were imaged using a Beta Imager 2000 (Biospace Mesures, Paris, France).

Immunostaining with hMMP-9 Antibodies. Immunohistochemical hMMP-9 detection was performed on serial 2.5-μm-thick sections, using a purified antimouse hMMP-9 monoclonal antibody (ab58803, Abcam). Immunohistochemical procedures were carried out with a DAKO Envision Peroxidase System (DAKO Diagnostica) according to the following protocol: paraffin-embedded sections were deparaffinized with xylene, dehydrated through a graded alcohol series, and washed with distilled water. They were then treated with 0.3% hydrogen peroxydase for 5 min to block endogenous peroxidase activity. After washing with PBS, the slides were incubated for 30 min with hMMP-9 antibody diluted 1:150 in a humidified chamber at room temperature and then washed twice in PBS. En Vision multilink was then applied as the secondary antibody for 30 min before washing and incubation with diaminobenzydine DAB substrate for 10 min, and hematoxylin counterstaining. Appropriate positive and negative controls omitting the primary antibody were included with every slide run. Immunoreactivity was evaluated in the cell cytoplasm, cytoplasmic membrane, and in the extracellular matrix.

■ RESULTS AND DISCUSSION

Characteristics and Binding Properties of hMMP-9 Aptamers. The SELEX strategy has been carried out against the recombinant human MMP-9 protein (gelatinase B), using a library of RNA candidates containing 2′-fluoropyrimidine nucleoside residues, as described in Material and Methods. The 30 nt random window is flanked by fixed regions that display partial complementarity, generating hairpin-like candidates through the formation of a weak duplex between the 5′ and 3′ parts (Figure 1A). This is expected to limit the contribution of the fixed parts to the interaction of the selected aptamer with the target and to some extent preorganize the

dx.doi.org/10.1021/bc300146c | *Bioconjugate Chem.* 2012, 23, 2192−2200

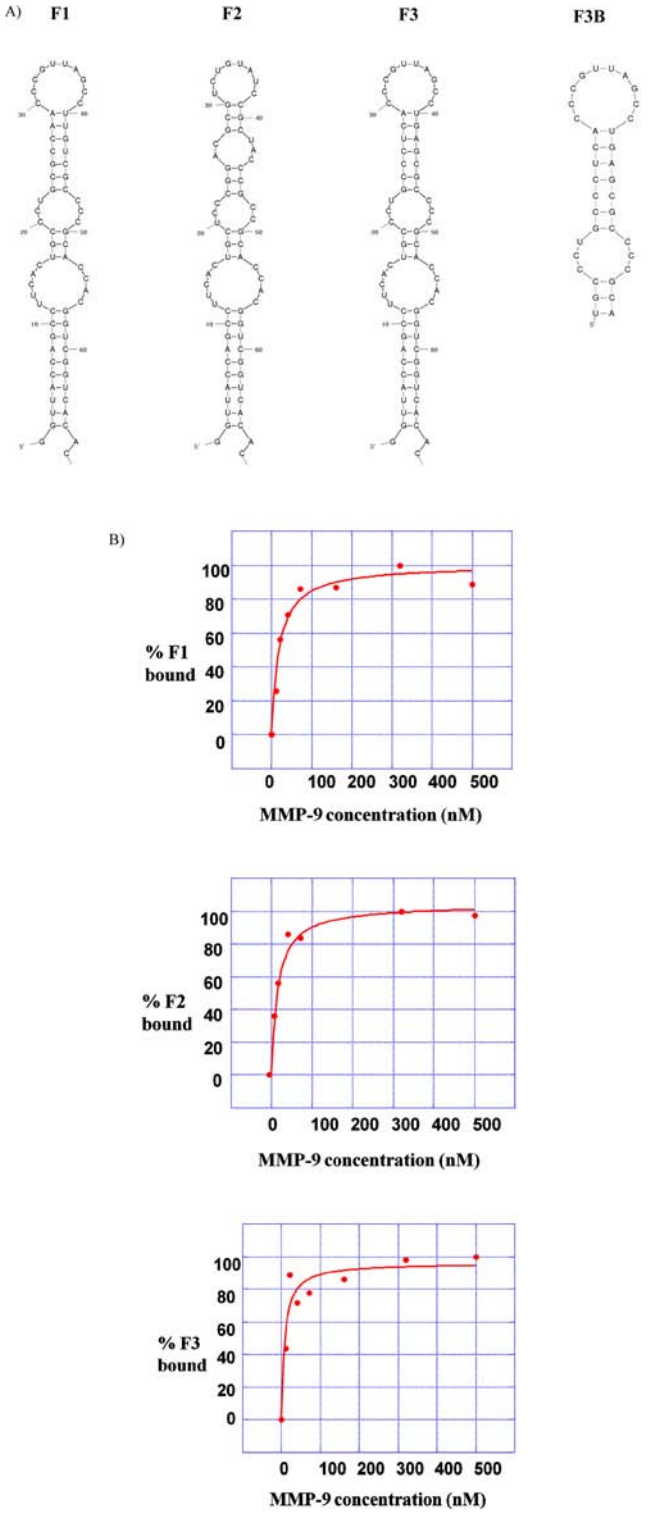

Figure 1. Predicted secondary structure and binding characteristics of hMMP-9 aptamers. (A) Secondary structure prediction of aptamers F1, F2, and F3 selected against hMMP-9 protein and of the truncated variant F3B. G-U pairs have been taken into account. Nucleotides 1−19 and 50−68 correspond to fixed flanks of the candidate sequences. (B) Radiolabeled aptamers, F1, F2, or F3 (1 nM), were incubated with increasing hMMP-9 concentration (from 10 to 500 nM) in the selection buffer. Binding constants (K_d) were deduced from filter retention assays as described in Materials and Methods.

candidates as hairpins. After 15 selection rounds, the binding properties of the selected populations improved as monitored by SPR analysis (not shown): when flowing the successive pools on a hMMP-9-grafted biochip, the resonance signal increased for rounds 9 to 14 and decreased markedly for the 15th round. Seventy-seven clones were sequenced from the 14th round of selection and compared. Three sequences named F1, F2, and F3 represented 74% of the candidates. Secondary structure prediction of the three sequences using mfold showed a very high degree of similarity; selected candidates appeared as imperfect hairpins (Figure 1A). The bottom part of F1, F2, and F3 adopts a mismatched double-stranded structure contributed by the fixed regions, the folding of which corresponds to the random region of the library shown from bottom to top: a 5 or 6 nt long pyrimidine-rich internal loop and a 6 base pair G-C-rich stem interrupted by a mismatch (F1 and F3) or a 5 nt internal loop (F2). F1 and F3 are predicted to form the same 10 nt long apical loop, whereas the F2 one is only 8 nt in length; both loops are pyrimidine-rich (Figure 1A). F1 and F3 display about 80% sequence homology in the 30 nt random region.

Binding curves of ^{32}P 5′-end-labeled F1, F2, and F3 aptamers to hMMP-9 were determined by filter retention assay revealing a similar affinity of F1, F2, or F3 for hMMP-9 (Figure 1B). Aptamer F3, with an equilibrium dissociation constant of 8.1 ± 3.4 nM, was a slightly stronger hMMP-9 binder than F2 (K_d = 15.4 ± 2.8 nM) or F1 (K_d = 18.3 ± 3.7 nM) and was chosen for further investigations.

MMPs constitute a large family of closely related enzymes. In order to assess the specificity of the aptamer F3 for hMMP-9, we monitored its binding efficiency to the human MMP-2 (hMMP-2), the matrix metalloprotease closest to hMMP-9 also called gelatinase A, and to the human MMP-7 (hMMP-7) by the filter retention procedure. Binding of F3 to hMMP-9 and pro-hMMP-9 was specific: no retention was detected by either hMMP-7 or its proform, whereas a light signal was noticed with hMMP-2 (SI Figure S1).

In order to make the synthesis and the study easier, we undertook the truncation of F3 down to the minimal size compatible with hMMP-9 binding. On the basis of the predicted structure, F3 was shortened from 68 to 36 nucleotides (variant F3B; Figure 1A), thus getting rid of most of the primer sequences except 3 residues on each side of the bottom stem. The ^{1}H NMR analysis of the resulting F3B showed a spectrum of exchangeable protons consistent with the hairpin structure shown on Figure 1A retaining a C,C mismatch in the upper part of the stem and a pyrimidine internal hexaloop in the bottom part, under the conditions of the experiment (not shown). F3B was further shortened, thus generating two variants: F3C1 (nt 3−34 of F3B, deletion of the two first base pairs of F3B; predicted abolition of the bottom double-stranded stem) and F3C2 (nt 7−30 of F3B, deletion of the first internal loop of F3B) (Figure S2). BIAcore analysis demonstrated that F3B showed the best binding efficiency for hMMP-9, whereas F3C1 was a weaker binder and F3C2 hardly yielded a SPR signal (Figure 2A, top). This suggests that the bottom internal loop of the aptamer is essential for the interaction with hMMP-9.

We then synthesized a number of mutated F3B derivatives in order to delineate the structural elements of the aptamer contributing to its binding to the target protein. Loop regions are generally crucial for the formation of aptamer−target complexes. The importance of the apical loop was first

dx.doi.org/10.1021/bc300146c | Bioconjugate Chem. 2012, 23, 2192−2200

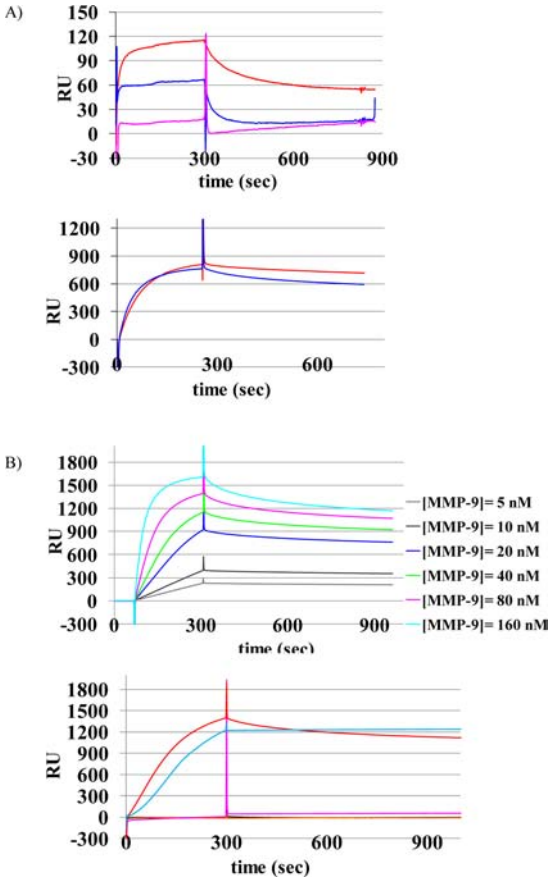

Figure 2. Surface plasmon resonance analysis of F3B/MMP complexes. (A) Top panel: hMMP-9 was immobilized on the sensorchip as described in Materials and Methods. F3B (red), F3C1 (blue), and F3C2 (pink) were injected at 200 nM in SP buffer. Bottom panel: biotinylated F3B (red), F3Bomf (blue) were immobilized (240 RU and 245 RU, respectively) on the biosensor, and hMMP-9 was injected at 100 nM in SP buffer. (B) Top panel: 3′-end biotinylated F3Bomf was immobilized on a sensorchip and hMMP-9 was injected in PBS buffer at different concentrations (from 5 to 160 nM as indicated). Bottom panel: hMMP-2 (black), hMMP-7 (orange), pro-MMP-9 (human and murine form, in blue and pink respectively), or hMMP-9 (red) (injected at 50 nM each) were assayed for interaction with aptamer F3Bomf.

investigated. In F3BΔ, the nt 14−23 of F3B were substituted by a hexaethylene glycol linker whereas the variant F3BA displayed an A_{10} loop (SI Figure S2). This resulted in a tremendously decreased (F3BA) or abolished (F3BΔ) interaction with hMMP-9 (SI Figure S3). We then modified the composition of the internal loop. This region originally composed of pyrimidine residues was replaced by six abasic sites (F3Bds) or replaced by 6 A residues (F3BP) (SI Figure S2). We also noticed a drastically decreased binding signal for either derivative (SI Figure S3). Finally, F3B stem was also modified. First, the C(9),C(28) mismatch in the upper stem was replaced either by an A,A mismatch (F3BAA), allowing the conservation of the secondary structure, or by a CG pair (F3BGC), allowing formation of a perfect double-stranded stem (SI Figure S2). Both variants bound to hMMP-9 with an efficiency similar to that of the parent F3B indicating that the C,C mismatch was not essential for the interaction with hMMP-9 (SI Figure S3). Indeed, this element was not conserved in F1 or F2 even though these aptamers did not display a perfect double-stranded upper stem either. Second, the strands of the stems of F3B were exchanged, the original 5′ strand being placed on the 3′ side and vice versa, leading to a preserved secondary structure (SI Figure S2). This did not alter the association between hMMP-9 and the derived aptamer (SI Figure S3). We conclude that apical and internal loops were the two major F3B elements ensuring the formation of the F3B/hMMP-9 complex.

Next, we optimized the F3B chemistry in the perspective of its use in biological media. In order to supply a nuclease-resistant molecular tool, the original purine ribonucleosides were substituted by 2′-*O*-methyl residues. As shown on SI Figure S4, incubation of an RNA hairpin in 10% fetal bovine serum known to contain endo- and exonuclease activities led to its total degradation after 30 min. On the contrary, F3B and F3Bomf remained mostly intact demonstrating nuclease resistance compared to the unmodified sample. However, faint high-mobility bands for F3B and F3Bomf samples indicated limited digestion after 3 and 6 h.

The resulting aptamer F3Bomf was still able to interact with hMMP-9 with a similar efficiency to the parent F3B as indicated by SPR signal (750 RU and 805 RU under the conditions of our experiment, respectively; Figure 2A, bottom). Both sensorgrams have close profiles, with a slower dissociation phase observed for the parent F3B. The binding of this F3Bomf derivative to hMMP-9 is specific: a control scrambled sequence with the same length, same base composition, and same chemistry did not lead to a detectable SPR signal (not shown). Sensorgrams for the complex F3Bomf/hMMP-9 carried out at different protein concentrations could not be properly fitted to a 1:1 model preventing the accurate determination of k_{on} and k_{off} (Figure 2B, top). However, the equilibrium constant was evaluated to be in the low nanomolar range from the variation of the amplitude of the SPR signal as a function of the MMP-9 concentration. It reached a plateau at concentrations higher than 160 nM MMP-9. The K_d was taken as the concentration leading to half saturation, i.e., about 20 nM.

This aptamer bound to pro-hMMP-9 and processed hMMP-9 with a similar efficiency but with different binding and dissociation behavior (Figure 2B, bottom) suggesting that it likely recognizes a site exposed in both active and inactive forms of the protein. In contrast, F3Bomf was able to discriminate between the human and the murine zymogen pro-MMP-9: a weak signal (49 RU) to the mouse pro-MMP-9 was detected, compared to about 1 300 RU with the human proenzyme (Figure 2B, bottom). The specificity of the parent aptamer was also maintained following modification, as F3Bomf did not bind to either hMMP-7 or hMMP-2 (Figure 2B, bottom). Surprisingly, the fully modified 2′-*O*-methylribo aptamer does not allow the formation of a complex with hMMP-9 (not shown).

The modified aptamer F3Bomf was then functionalized by conjugation at its 5′-end to *S*-acetylmercaptoacetyltriglycine (MAG3) through a hexylamino linker. This modification did not interfere with target recognition; the MAG3-F3Bomf aptamer did bind with hMMP-9, whereas preincubation of the protein with the functionalized aptamer abolished the SPR signal (SI Figure S5). Both the aptamer and the control oligonucleotide were then labeled with ^{99m}Tc as described in Materials and Methods for imaging hMMP-9 in tissues.

Human Central Nervous System Tumor Imaging. MMP-9 expression in several human tumors from central nervous system was investigated either by immunohistochemistry using specific hMMP-9 antibody or by binding assay with

^{99m}Tc-MAG3-F3Bomf anti-hMMP-9 aptamer. Immunohistochemical analysis revealed that hMMP-9 was highly expressed in glioblastomas (Figure 3A). Strong cytoplasmic reactivity was

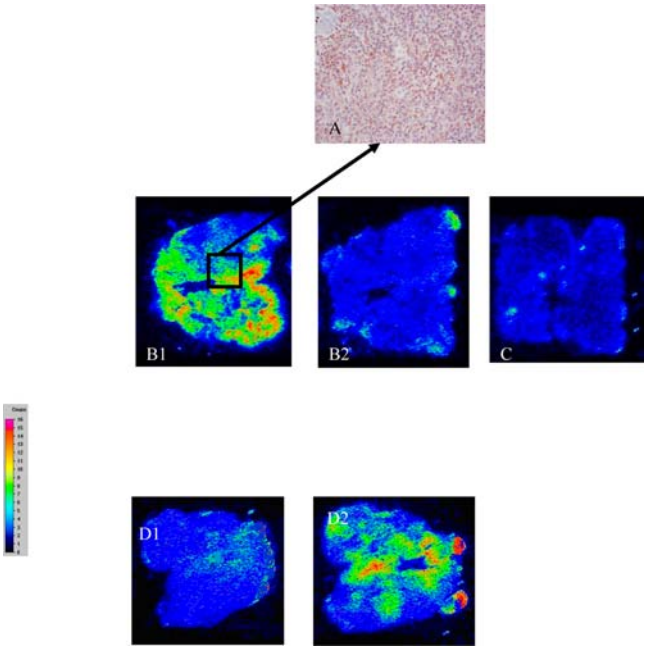

Figure 3. Labeling of human glioblastoma sections with antibody or aptamer. (A) Immunohistochemical detection of hMMP-9 using a mouse anti-MMP-9 antibody (20×). Note the specific cytoplasmic immunoreactivity in tumor cells, endothelial cells, an extra-tumoral stroma. Labeling of brain section with 1.25 pmol (0.037 MBq) of the ^{99m}Tc-MAG3-F3Bomf aptamer (B1), the ^{99m}Tc-MAG3-control sequence (B2), or ^{99m}Tc -MAG3 (C). Competition assay was carried out: incubation with ^{99m}Tc-MAG3-F3Bomf after presaturation with 1.25 pmol of either cold MAG3-F3Bomf (D1) or cold MAG3-control sequence (D2). Note that panels (B1) and (B2) on one hand and (D1) and (D2) on the other hand were prepared with the same brain section. See Materials and Methods for details.

observed for numerous tumor cells. Immunopositivity was also present in the extracellular matrix, as well as in the endothelial cells of blood vessels in the tumor environment. Of note, the antibody used for this experiment was raised against the mouse MMP-9 that does not discriminate between murine and human enzymes in contrast to the aptamer F3Bomf (Figure 2B, bottom). Therefore, the aptamer shows a higher degree of specificity than the antibody. Incubation of glioblastoma slices adjacent to the ones used for immunohistochemical analysis with the radiolabeled aptamer F3Bomf revealed a strong signal (Figure 3B1), whereas the radiolabeled control sequence induced a weaker signal (Figure 3B2). Incubation with ^{99m}Tc -MAG3 alone did not produce any detectable signal (Figure 3C). Presaturation of the slice with unlabeled MAG3-F3Bomf almost abolishes the radiolabeling by the ^{99m}Tc-aptamer (Figure 3D1), whereas presaturation with unlabeled MAG3-control sequence did not prevent the labeling with ^{99m}Tc-MAG3-F3Bomf (Figure 3D2). This indicates that, first, the aptamer is able to bind to its target in the environment of the tumor and, second, its binding to hMMP-9 is specific.

A range of other human central nervous system (CNS) tumor types also express MMP-9.[42−45] We investigated the imaging properties of the anti-hMMP-9 aptamer against pilocytic astrocytoma, meningioma, fibrillary astrocytoma, ependymoma, anaplastic astrocytoma, medulloblastoma, lymphoma, and glioblastoma. As shown in Figure 4 (left panels),

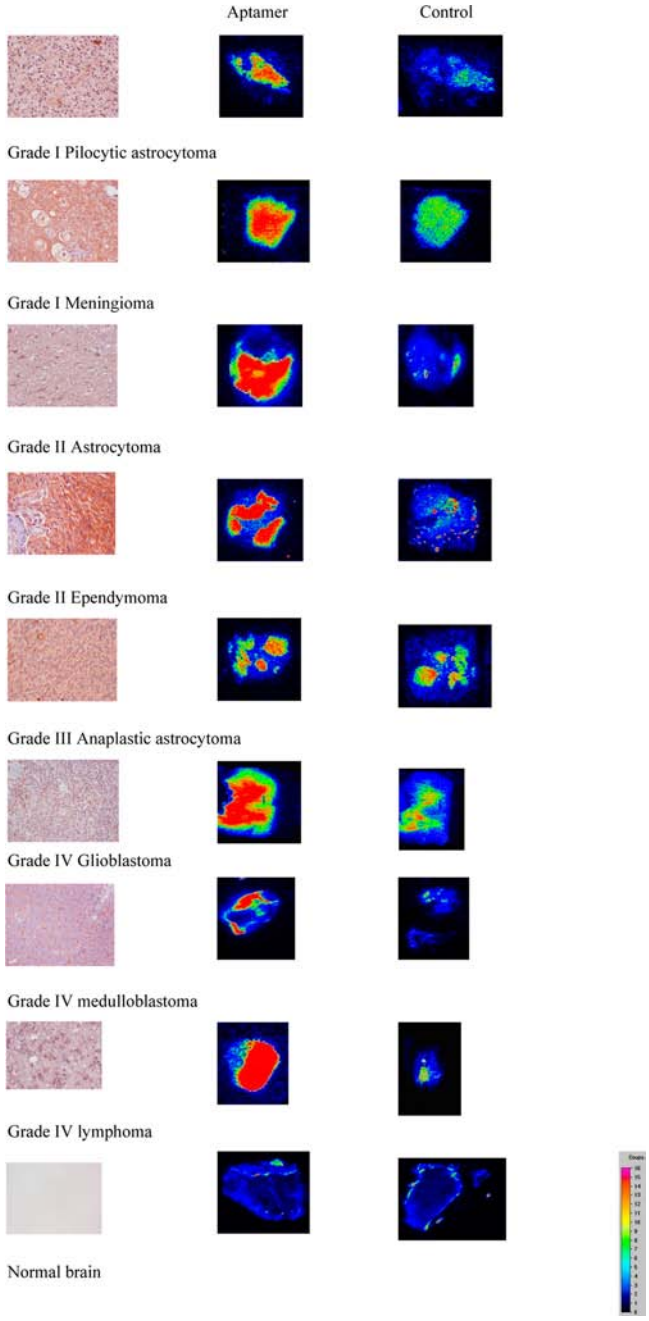

Figure 4. Labeling of human brain tumor slices. Tumor sections were incubated either with 1.25 pmol of ^{99m}Tc-MAG3-F3Bomf aptamer (central panels) or with 1.25 pmol of ^{99m}Tc-MAG3-control sequence (right panels) and compared with hMMP-9 immunoreactivity (left panels). See Materials and Methods for details.

the hMMP-9 expression, monitored by the immunohistochemical method, revealed a cytoplasmic staining dependent on the tumor grade within the group of glial infiltrative tumors. For the other primitive brain tumors explored (pilocytic astrocytoma grade 1, fibrillary astrocytoma grade 2, anaplastic astrocytoma grade 3, glioblastoma grade 4, ependymoma grade 2, meningioma grade 1, and medulloblastoma grade 4), hMMP-9 immunostaining showed a variable intensity of cytoplasmic expression. In all cases (glial and other tumor

dx.doi.org/10.1021/bc300146c | Bioconjugate Chem. 2012, 23, 2192−2200

type), immunostaining for hMMP-9 was also clearly observed within both extracellular environment and endothelial cells. For primitive central nervous system lymphoma, hMMP-9 expression was weak in cytoplasmic compartment and in extracellular matrix. Healthy brain was used as control: no immunoreactivity for hMMP-9 was detected. The same tumors were incubated with the labeled anti-hMMP-9 aptamer. Generally, ^{99m}Tc-MAG3-F3Bomf induced a strong signal on the tissues (Figure 4, central panel), whereas a much weaker signal was recorded with the control sequence (Figure 4, right panel). No signal was detected with healthy brain tissue. We were not able to quantitate the signal obtained by immunostaining. Visual analysis revealed that immunohistochemical expression of MMP-9 increased roughly in a tumor grade-dependent manner. We also generally observed an increasing binding of F3Bomf aptamer with the grade of malignancy. We estimated that binding intensities roughly correlate with the amount of MMP-9 by comparison with the immunohistochemical signal. Therefore, whatever the tumor type a good agreement was observed between antibody fixation and radiolabeled F3Bomf aptamer binding.

CONCLUSION

Aptamers are attractive in biomedicine because of their advantages over antibodies, which rely in particular on their reproducible chemical production, low immunogenicity, reversible denaturation, and small size. Aptamers show many of the requested criteria for the ideal imaging probe. They are high-affinity binding ligands and show high tissue-specific retention and rapid blood clearance for in vivo imaging.[17] Because of their easy conjugation to the appropriate label (fluorophore, radionuclide), aptamers afford a valuable alternative to antibodies for protein detection.

MMPs are relevant markers of tumor malignancy. So far, molecular imaging of MMPs has been performed in tumor-bearing mice with fluorescent peptide substrates[46] or in human carotid[47] using MMP inhibitor radiotracers[48,49] or proteolytic nanobeacons.[50] Investigation of MMP-2 and hMMP-9 expression with a ^{64}Cu radiolabeled cyclic peptide by microPET failed to demonstrate a specific uptake in gelatinase-expressing tumors,[51] whereas the same cyclic peptide ^{68}Ga-DOTA conjugate showed acceptable plasma stability and good visualization of tumor xenografts.[52] Recently, a ^{99m}Tc-monoclonal antibody was developed to target a membrane MMP for imaging atherosclerosis.[53]

In this work, we have successfully obtained and characterized aptamers displaying high affinity for hMMP-9 protein. Aptamer F3 was shortened and modified to generate MAG3-F3Bomf, an aptamer-based imaging probe. We could detect specifically hMMP-9 protein, a tumor biomarker, on different human tumor slices with ^{99m}Tc-MAG3-F3Bomf. It is the first aptamer application for hMMP-9 detection. Its high specificity will improve the signal-to-noise ratio compared to broad-spectrum MMP inhibitors, which lead to high uptake in tissues with non pathogenic MMP expression.

Our goal is to develop an aptamer-based imaging tool for specific tumor monitoring in clinical studies. Chemistry and size have been optimized, but future improvements are still needed to enhance its retention in vivo (i.e., multimers, pegylation). Aptamer injections in human tumor-bearing mice are scheduled.

ASSOCIATED CONTENT

Supporting Information

Five figures: Binding specificity of F3 aptamer; Secondary structure of F3B hMMP-9 aptamer variants; Surface Plasmon Resonance analysis of F3B hMMP-9 variants; nuclease resistance of oligonucleotide derivatives; Surface Plasmon Resonance analysis of MAG functionalized F3Bomf aptamer binding to hMMP-9. This material is available free of charge via the Internet at http://pubs.acs.org.

AUTHOR INFORMATION

Corresponding Author

*E-mail: jean-jacques.toulme@inserm.fr; Tel 335 4000 3034; Fax 335 4000 3004.

Present Address

⬢Novaptech, Pessac, France.

Notes

The authors declare no competing financial interest.

▽Co-first authors.

ACKNOWLEDGMENTS

We thank I. Lebars for ^{1}H NMR analysis of the aptamer F3B, Nathalie Pierre and Serge Moreau for oligonucleotide syntheses, and Carmelo Di Primo for SPR expertise. NMR, mass spectrometry, and SPR analysis were carried out in the IECB central facility (UMS3033/US001). This work was supported by "Régions Aquitaine et Midi Pyrénées, France".

REFERENCES

(1) Louis, D. N., Ohgaki, H., Wiestler, O. D., Cavenee, W. K., Burger, P. C., Jouvet, A., Scheithauer, B. W., and Kleihues, P. (2007) The 2007 WHO classification of tumours of the central nervous system. *Acta Neuropathol. 114*, 97−109.

(2) Laperriere, N., Zuraw, L., and Cairncross, G. (2002) Radiotherapy for newly diagnosed malignant glioma in adults: a systematic review. *Radiother. Oncol. 64*, 259−73.

(3) Heimberger, A. B., McGary, E. C., Suki, D., Ruiz, M., Wang, H., Fuller, G. N., and Bar-Eli, M. (2005) Loss of the AP-2alpha transcription factor is associated with the grade of human gliomas. *Clin. Cancer Res. 11*, 267−72.

(4) Rao, J. S. (2003) Molecular mechanisms of glioma invasiveness: the role of proteases. *Nat. Rev. Cancer 3*, 489−501.

(5) Stamenkovic, I. (2003) Extracellular matrix remodelling: the role of matrix metalloproteinases. *J. Pathol. 200*, 448−64.

(6) Binder, D. K., and Berger, M. S. (2002) Proteases and the biology of glioma invasion. *J. Neurooncol. 56*, 149−58.

(7) Auge, F., Hornebeck, W., and Laronze, J. Y. (2004) A novel strategy for designing specific gelatinase A inhibitors: potential use to control tumor progression. *Crit. Rev. Oncol. Hematol. 49*, 277−82.

(8) Bachmeier, B. E., Iancu, C. M., Jochum, M., and Nerlich, A. G. (2005) Matrix metalloproteinases in cancer: comparison of known and novel aspects of their inhibition as a therapeutic approach. *Expert Rev. Anticancer Ther. 5*, 149−63.

(9) Forget, M. A., Desrosiers, R. R., and Beliveau, R. (1999) Physiological roles of matrix metalloproteinases: implications for tumor growth and metastasis. *Can. J. Physiol. Pharmacol. 77*, 465−80.

(10) Tuerk, C., and Gold, L. (1990) Systematic evolution of ligands by exponential enrichment: RNA ligands to bacteriophage T4 DNA polymerase. *Science 249*, 505−10.

(11) Ellington, A. D., and Szostak, J. W. (1990) In vitro selection of RNA molecules that bind specific ligands. *Nature 346*, 818−22.

(12) Robertson, D. L., and Joyce, G. F. (1990) Selection in vitro of an RNA enzyme that specifically cleaves single-stranded DNA. *Nature 344*, 467−8.

(13) Mayer, G. (2009) The chemical biology of aptamers. *Angew. Chem., Int. Ed. Engl. 48*, 2672−89.
(14) Syed, M. A., and Pervaiz, S. (2010) Advances in aptamers. *Oligonucleotides 20*, 215−24.
(15) Soontornworajit, B., and Wang, Y. (2011) Nucleic acid aptamers for clinical diagnosis: cell detection and molecular imaging. *Anal. Bioanal. Chem. 399*, 1591−9.
(16) Dausse, E., Da Rocha Gomes, S., and Toulmé, J. J. (2009) Aptamers: a new class of oligonucleotides in the drug discovery pipeline? *Curr. Opin. Pharmacol. 9*, 602−7.
(17) Gomes, S. D. R., Azéma, L., Allard, M., and Toulmé, J. J. (2010) Aptamers as imaging agents. *Expert Opinion on Medical Diagnostics 4*, 511−518.
(18) Charlton, J., Sennello, J., and Smith, D. (1997) In vivo imaging of inflammation using an aptamer inhibitor of human neutrophil elastase. *Chem. Biol. 4*, 809−16.
(19) Lupold, S. E., Hicke, B. J., Lin, Y., and Coffey, D. S. (2002) Identification and characterization of nuclease-stabilized RNA molecules that bind human prostate cancer cells via the prostate-specific membrane antigen. *Cancer Res. 62*, 4029−33.
(20) Hicke, B. J., Stephens, A. W., Gould, T., Chang, Y. F., Lynott, C. K., Heil, J., Borkowski, S., Hilger, C. S., Cook, G., Warren, S., and Schmidt, P. G. (2006) Tumor targeting by an aptamer. *J. Nucl. Med. 47*, 668−78.
(21) Shangguan, D., Li, Y., Tang, Z., Cao, Z. C., Chen, H. W., Mallikaratchy, P., Sefah, K., Yang, C. J., and Tan, W. (2006) Aptamers evolved from live cells as effective molecular probes for cancer study. *Proc. Natl. Acad. Sci. U. S. A. 103*, 11838−43.
(22) Herr, J. K., Smith, J. E., Medley, C. D., Shangguan, D., and Tan, W. (2006) Aptamer-conjugated nanoparticles for selective collection and detection of cancer cells. *Anal. Chem. 78*, 2918−24.
(23) Borbas, K. E., Ferreira, C. S., Perkins, A., Bruce, J. I., and Missailidis, S. (2007) Design and synthesis of mono- and multimeric targeted radiopharmaceuticals based on novel cyclen ligands coupled to anti-MUC1 aptamers for the diagnostic imaging and targeted radiotherapy of cancer. *Bioconjugate Chem. 18*, 1205−12.
(24) Phillips, J. A., Lopez-Colon, D., Zhu, Z., Xu, Y., and Tan, W. (2008) Applications of aptamers in cancer cell biology. *Anal. Chim. Acta 621*, 101−8.
(25) Li, W., Yang, X., Wang, K., Tan, W., He, Y., Guo, Q., Tang, H., and Liu, J. (2008) Real-time imaging of protein internalization using aptamer conjugates. *Anal. Chem. 80*, 5002−8.
(26) Sefah, K., Tang, Z. W., Shangguan, D. H., Chen, H., Lopez-Colon, D., Li, Y., Parekh, P., Martin, J., Meng, L., Phillips, J. A., Kim, Y. M., and Tan, W. H. (2009) Molecular recognition of acute myeloid leukemia using aptamers. *Leukemia 23*, 235−44.
(27) Smith, J. E., Medley, C. D., Tang, Z., Shangguan, D., Lofton, C., and Tan, W. (2007) Aptamer-conjugated nanoparticles for the collection and detection of multiple cancer cells. *Anal. Chem. 79*, 3075−82.
(28) Medley, C. D., Bamrungsap, S., Tan, W., and Smith, J. E. (2011) Aptamer-conjugated nanoparticles for cancer cell detection. *Anal. Chem. 83*, 727−34.
(29) Ko, H. Y., Choi, K. J., Lee, C. H., and Kim, S. (2011) A multimodal nanoparticle-based cancer imaging probe simultaneously targeting nucleolin, integrin alphavbeta3 and tenascin-C proteins. *Biomaterials 32*, 1130−8.
(30) Zhou, J., Soontornworajit, B., and Wang, Y. (2010) A temperature-responsive antibody-like nanostructure. *Biomacromolecules 11*, 2087−93.
(31) Blank, M., Weinschenk, T., Priemer, M., and Schluesener, H. (2001) Systematic evolution of a DNA aptamer binding to rat brain tumor microvessels. selective targeting of endothelial regulatory protein pigpen. *J. Biol. Chem. 276*, 16464−8.
(32) Farokhzad, O. C., Jon, S., Khademhosseini, A., Tran, T. N., Lavan, D. A., and Langer, R. (2004) Nanoparticle-aptamer bioconjugates: a new approach for targeting prostate cancer cells. *Cancer Res. 64*, 7668−72.
(33) Shangguan, D., Meng, L., Cao, Z. C., Xiao, Z., Fang, X., Li, Y., Cardona, D., Witek, R. P., Liu, C., and Tan, W. (2008) Identification of liver cancer-specific aptamers using whole live cells. *Anal. Chem. 80*, 721−8.
(34) Li, S., Xu, H., Ding, H., Huang, Y., Cao, X., Yang, G., Li, J., Xie, Z., Meng, Y., Li, X., Zhao, Q., Shen, B., and Shao, N. (2009) Identification of an aptamer targeting hnRNP A1 by tissue slide-based SELEX. *J. Pathol. 218*, 327−36.
(35) Zhang, Z., Guo, L., Guo, A., Xu, H., Tang, J., Guo, X., and Xie, J. (2010) In vitro lectin-mediated selection and characterization of rHuEPO-alpha-binding ssDNA aptamers. *Bioorg. Med. Chem. 18*, 8016−25.
(36) Shi, H., He, X., Wang, K., Wu, X., Ye, X., Guo, Q., Tan, W., Qing, Z., Yang, X., and Zhou, B. (2011) Activatable aptamer probe for contrast-enhanced in vivo cancer imaging based on cell membrane protein-triggered conformation alteration. *Proc. Natl. Acad. Sci. U. S. A. 108*, 3900−5.
(37) Sousa, R., and Padilla, R. (1995) A mutant T7 RNA polymerase as a DNA polymerase. *Embo J. 14*, 4609−21.
(38) Bartel, D. P., and Szostak, J. W. (1994) Study of RNA-protein recognition by in vitro selection, in *RNA-Protein interactions* (Nagai, K., and Mattaj, I. W., Eds.) pp 248−268, IRL Press, Oxford.
(39) McEntee, K., Weinstock, G. M., and Lehman, I. R. (1980) recA protein-catalysed strand assimilation: stimulation by *Escherichia coli* single-stranded DNA-binding protein. *Proc. Natl. Acad. Sci. U.S.A. 77*, 857−61.
(40) Winnard, P., Jr., Chang, F., Rusckowski, M., Mardirossian, G., and Hnatowich, D. J. (1997) Preparation and use of NHS-MAG3 for technetium-99m labeling of DNA. *Nucl. Med. Biol. 24*, 425−32.
(41) Di Primo, C., Dausse, E., and Toulme, J. J. (2011) Surface plasmon resonance investigation of RNA aptamer-RNA ligand interactions. *Methods Mol. Biol. 764*, 279−300.
(42) Comincini, S., Paolillo, M., Barbieri, G., Palumbo, S., Sbalchiero, E., Azzalin, A., Russo, M. A., and Schinelli, S. (2009) Gene expression analysis of an EGFR indirectly related pathway identified PTEN and MMP9 as reliable diagnostic markers for human glial tumor specimens. *J. Biomed. Biotechnol. 2009*, 924565.
(43) Das, G., Shiras, A., Shanmuganandam, K., and Shastry, P. (2010) Rictor regulates MMP-9 activity and invasion through Raf-1-MEK-ERK signaling pathway in glioma cells. *Mol. Carcinog. 50*, 412−423.
(44) Lee, E. J., Kim, S. Y., Hyun, J. W., Min, S. W., Kim, D. H., and Kim, H. S. (2010) Glycitein inhibits glioma cell invasion through down-regulation of MMP-3 and MMP-9 gene expression. *Chem. Biol. Interact. 185*, 18−24.
(45) Veeravalli, K. K., Chetty, C., Ponnala, S., Gondi, C. S., Lakka, S. S., Fassett, D., Klopfenstein, J. D., Dinh, D. H., Gujrati, M., and Rao, J. S. (2010) MMP-9, uPAR and cathepsin B silencing downregulate integrins in human glioma xenograft cells in vitro and in vivo in nude mice. *PLoS One 5*, e11583.
(46) Bremer, C., Tung, C. H., and Weissleder, R. (2001) In vivo molecular target assessment of matrix metalloproteinase inhibition. *Nat. Med. 7*, 743−8.
(47) Wallis de Vries, B. M., Hillebrands, J. L., van Dam, G. M., Tio, R. A., de Jong, J. S., Slart, R. H., and Zeebregts, C. J. (2009) Images in cardiovascular medicine. Multispectral near-infrared fluorescence molecular imaging of matrix metalloproteinases in a human carotid plaque using a matrix-degrading metalloproteinase-sensitive activatable fluorescent probe. *Circulation 119*, e534−6.
(48) Furumoto, S., Takashima, K., Kubota, K., Ido, T., Iwata, R., and Fukuda, H. (2003) Tumor detection using 18F-labeled matrix metalloproteinase-2 inhibitor. *Nucl. Med. Biol. 30*, 119−25.
(49) Razavian, M., Zhang, J., Nie, L., Tavakoli, S., Razavian, N., Dobrucki, L. W., Sinusas, A. J., Edwards, D. S., Azure, M., and Sadeghi, M. M. (2010) Molecular imaging of matrix metalloproteinase activation to predict murine aneurysm expansion in vivo. *J. Nucl. Med. 51*, 1107−15.
(50) Scherer, R. L., VanSaun, M. N., McIntyre, J. O., and Matrisian, L. M. (2008) Optical imaging of matrix metalloproteinase-7 activity in vivo using a proteolytic nanobeacon. *Mol. Imaging 7*, 118−31.

(51) Sprague, J. E., Li, W. P., Liang, K., Achilefu, S., and Anderson, C. J. (2006) In vitro and in vivo investigation of matrix metalloproteinase expression in metastatic tumor models. *Nucl. Med. Biol. 33*, 227−37.
(52) Ujula, T., Huttunen, M., Luoto, P., Perakyla, H., Simpura, I., Wilson, I., Bergman, M., and Roivainen, A. (2010) Matrix metalloproteinase 9 targeting peptides: syntheses, 68Ga-labeling, and preliminary evaluation in a rat melanoma xenograft model. *Bioconjugate Chem. 21*, 1612−21.
(53) Kuge, Y., Takai, N., Ogawa, Y., Temma, T., Zhao, Y., Nishigori, K., Ishino, S., Kamihashi, J., Kiyono, Y., Shiomi, M., and Saji, H. (2010) Imaging with radiolabelled anti-membrane type 1 matrix metalloproteinase (MT1-MMP) antibody: potentials for characterizing atherosclerotic plaques. *Eur. J. Nucl. Med. Mol. Imaging 37*, 2093−104.

Da Rocha Gomes et al. - Supplementary materials

A ^{99m}Tc-MAG3-aptamer for imaging human tumors associated with high level of matrix metalloproteinase-9.

Supplementary informations; 5 figures

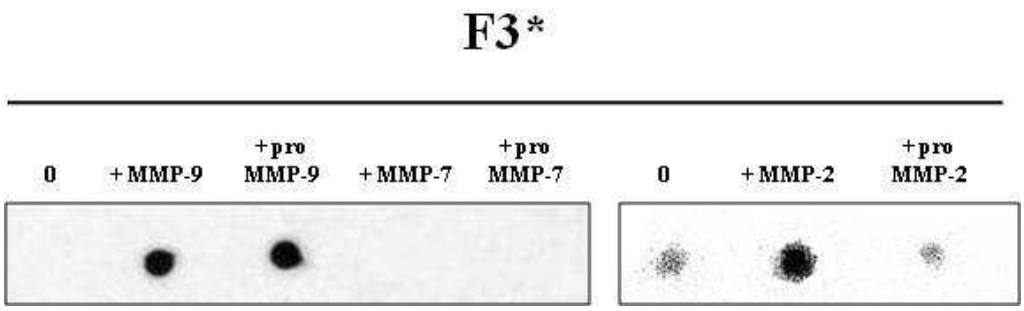

Supplementary figure 1: Binding specificity of F3 aptamer

Analysis of the binding specificity of the aptamer F3 was firstly carried out using filter retention experiment. One nanomolar of ^{32}P 5'end-labeled aptamer F3 was incubated with 50 nM of human MMP-9, pro-MMP-9, human MMP-7, pro-MMP-7, human MMP-2 or pro-MMP-2 (purchased from Calbiochem). Complexes were filtered and analysed with Instant Imager (Hewlett-Packard).

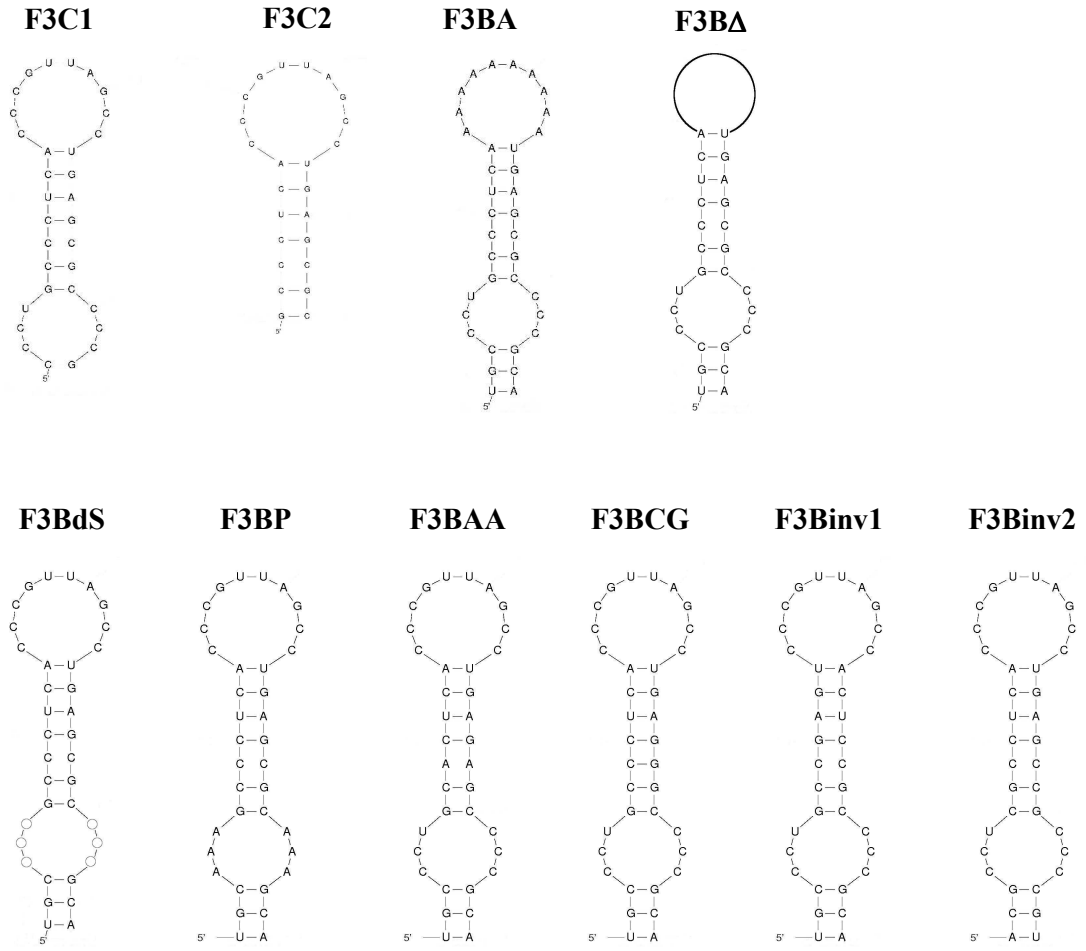

Supplementary figure 2: Secondary structure of F3B hMMP-9 aptamer variants

Predicted structures of truncated F3B variants: F3C1 (deletion of the two terminal base pairs of F3B), F3C2 (deletion of the first internal loop of F3B), F3BA (ten A apical loop), F3BΔ (apical loop substituted by a hexaethylene glycol linker), F3BdS (internal loop with six abasic sites), F3BP (internal loop with six A residues), F3BAA (C,C mismatch of F3B replaced by A,A mismatch), F3BCG (C,C mismatch of F3B replaced by a CG pair), F3Binv1 (stem strands exchanged in the upper part of the stem) and F3Binv2 (stem strands exchanged in the lower part of the stem).

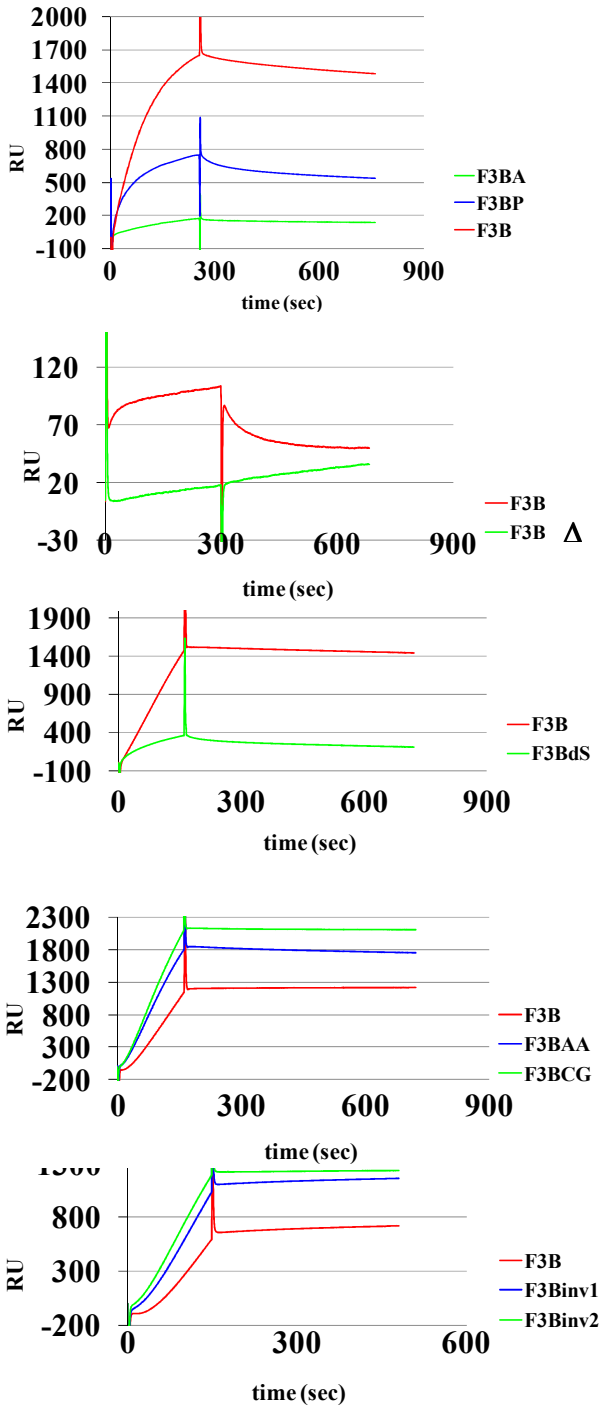

Supplementary figure 3: Surface Plasmon Resonance analysis of F3B hMMP-9 variants

3' end biotinylated F3B variants were immobilized on streptavidine functionalized-CM5 chip. hMMP-9 (100 nM) was injected alone in the selection buffer.

In the case of F3BΔ, hMMP-9 was immobilized and variant injected (500 nM) in the selection buffer.

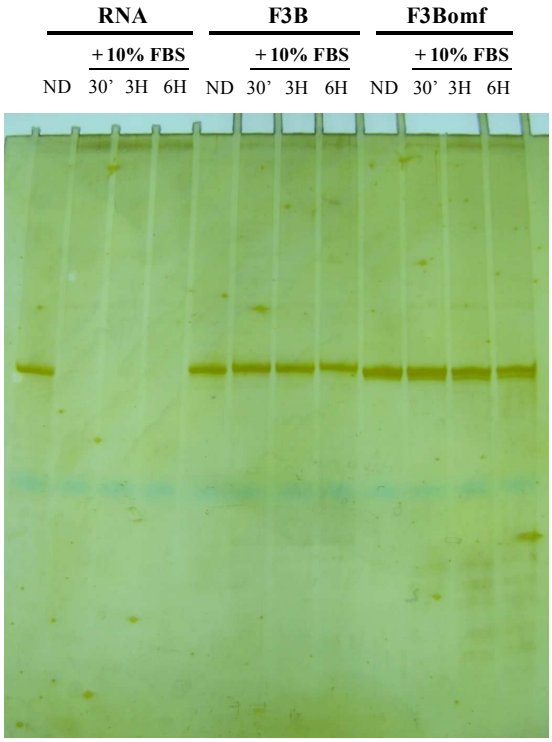

Supplementary figure 4: Nuclease resistance of oligonucleotide derivatives.

F3Bomf, F3B or 34 nt long control RNA hairpins (RNA) were incubated at 100 nM for 0 min (ND), 30 minutes, 3 hours or 6 hours in 10 % FBS (fetal bovine serum). After phenol/chloroform extraction and ethanol precipitation, samples were analyzed by electrophoresis on a 20 % polyacrylamide/ 7M urea gel.

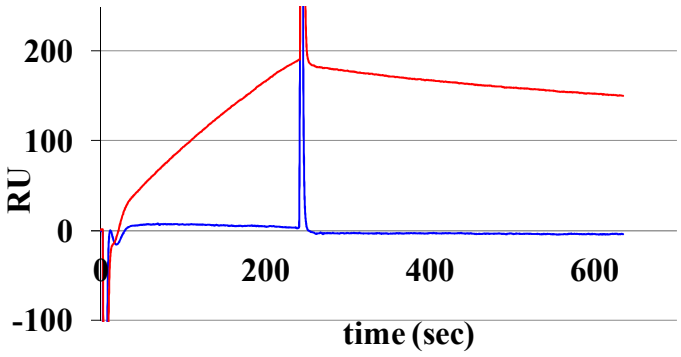

Supplementary figure 5: Surface Plasmon Resonance analysis of MAG functionalized F3Bomf aptamer binding to hMMP-9

3' end biotinylated F3Bomf was immobilized on streptavidine functionalized-CM5 chip. hMMP-9 (36 nM) was injected alone in the selection buffer (red) or following incubation with MAG3-F3Bomf (100 nM) (blue).

Bioconjugate Chemistry

Article

pubs.acs.org/bc

Hyaluronate Tethered, "Smart" Multiwalled Carbon Nanotubes for Tumor-Targeted Delivery of Doxorubicin

Satyajit R. Datir, Manasmita Das, Raman Preet Singh, and Sanyog Jain*

Centre for Pharmaceutical Nanotechnology, Department of Pharmaceutics, National Institute of Pharmaceutical Education and Research (NIPER), Sector 67, SAS Nagar (Mohali) Punjab, India 160062

Supporting Information

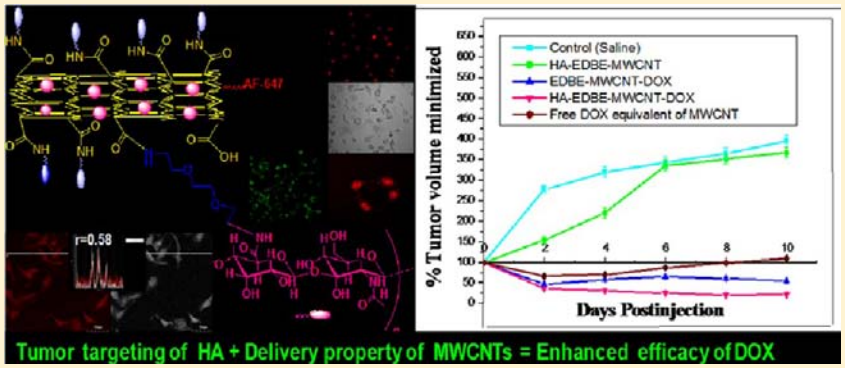

ABSTRACT: The present study reports the optimized synthesis, physicochemical characterization, and biological evaluation of a novel, multiwalled carbon nanotube-hyaluronic acid (MWCNT-HA) conjugate, complexed with an anticancer agent, Doxorubicin (DOX) via $\pi-\pi$ stacking interaction. The therapeutic conjugate was concomitantly labeled with a near-infrared fluorescent dye, Alexa-Flour-647 (AF-647), and radiotracer Technetium-99m (^{99m}Tc) to track its whereabouts both in vitro and in vivo via optical and scintigraphic imaging techniques. Covalent functionalization of MWCNTs with HA facilitated their internalization into human lung adenocarcinoma, A549 cells via hyaluronan receptors (HR) mediated endocytosis. Internalized nanotubes showed lysosomal trafficking, followed by low pH-triggered DOX release under endolysosomal conditions. Consequently, DOX-loaded HA-MWCNTs exhibited 3.2 times higher cytotoxicity and increased apoptotic activity than free DOX in equivalent concentrations. Organ distribution studies in Ehlrich ascites tumor (EAT) bearing mice model indicated that tumor specific localization of ^{99m}Tc-MWCNT-HA-DOX is significantly higher than both free drug and nontargeted MWCNTs. Pharmacodynamic studies in chemically breast-cancer-induced rats showed that the tumor-growth inhibitory effect of HA-MWCNT-DOX was 5 times higher than free DOX in equivalent concentration. DOX delivered through HA-MWCNTs was devoid of any detectable cardiotoxity, hepatotoxicity, or nephrotoxicity. All these promising attributes make HA-MWCNTs a "smart" platform for tumor-targeted delivery of anticancer agents.

Carbon nanotubes (CNTs) represent a novel class of nanomaterials, which made their appearance in the nanomedicine arena, not more than a decade ago. Ever since their emergence on the nanoplatform, their unique physicochemical properties such as high aspect ratio and surface area, high mechanical strength, ease of drug loading via $\pi-\pi$ stacking interactions, and photoacoustic effect have made them potential candidates for targeted drug delivery and imaging. A major technological barrier, which obscures the application of pristine CNTs in biomedicine, is their lack of solubility in aqueous media. Hydrophobicity of CNTs, coupled with van der Waals and strong $\pi-\pi$ interactions between the individual tubes, cause pristine CNTs to assemble as bundles, rendering them nonbiocompatible and highly toxic. Functionalization of CNTs, therefore, is crucial for their assimilation into multifarious systems for industrial as well as biomedical applications. One of the most powerful approaches for rendering CNTs soluble in aqueous medium is the covalent functionalization of their side walls and tips. Functionalized CNTs (*f*-CNTs)[1−4] can easily cross the cell membrane facilitating the internalization of various cargos inside the cells (e.g., fluorescein, plasmid DNA, proteins, etc.) that would not otherwise be taken up. In vivo biodistribution studies further confirm that well functionalized nanotubes (f-CNTs) circulate in blood with half-lives on the order of a few hours.[1,5] Recent expansion in functionalization methods has also stimulated the growth of multifunctional, drug-loaded CNTs combined with the identification of disease-specific molecular target and imaging capabilities.[4,6,7] Covalent functionalization of CNTs with tumor targeting components such as antibodies, peptides, or small molecules (viz. folic acid) promises to expand the therapeutic window for a variety of

Received: May 8, 2012
Revised: October 3, 2012
Published: October 5, 2012

 © 2012 American Chemical Society

anticancer drugs.[7,8] Although targeted delivery of anticancer agents using active-targeted CNTs has been investigated by various research groups, most of these studies are limited to the in vitro evaluation of their targeting or therapeutic efficacies. For example, Heister et al. have demonstrated that oxidized single-walled carbon nanotubes (SWCNTs) trifunctionalized with the anticancer drug Doxorubicin, a monoclonal antibody, and a fluorescent marker are efficiently taken up by cancer cells with subsequent translocation of the drug to the nucleus while the nanotubes remain in the cytoplasm.[8] Similarly, Dhar et al. have used folate as a homing device for SWCNT mediated Pt (IV) prodrug delivery.[7] Nevertheless, none of these reports have included any study to evaluate the antitumor efficacies of these functionalized CNTs in vivo. From the synthesis point of view, development of multifunctional CNTs, tethered with multiple diagnostic and therapeutic entities, is highly challenging, and even more challenging is their precise characterization and biological evaluation. The present work thus stemmed from the need to contribute some new toolboxes for the fabrication of multifunctional CNTs and subsequently evaluate their theragnostic potential in vivo.

Hyaluronic acid (HA) is a well-known, naturally occurring glycosoaminoglycan, composed of repeating disaccharide units of D-glucuronic acid and (1-β-3)-*N*-acetyl-D-glucosamine. Activated hyaluronate receptors (HR) are ubiquitously overexpressed by CD44 and receptor for hyaluronan-mediated motility (RHAMM) on tumor cells[9] that are lacking in their non-tumorigenic counterparts. The unique ability of CD44 to internalize HA reinforces its potential as a targeted drug delivery vehicle. HA generates a key signal for activating the kinase pathways and regulating angiogenesis in tumors. This unique property of HA has been previously recognized, and several preclinical studies have chemically conjugated HA with a broad spectrum of cytotoxic agents, concluding with highly effective anticancer agents in vitro.[10] The present study reports the optimized synthesis of a novel multiwalled carbon nanotube−hyaluronic acid conjugate, complexed with the anticancer drug, Doxorubicin, via $\pi-\pi$ stacking interaction. In addition to precise characterization of the conjugate, extensive in vitro and in vivo studies were undertaken to explore how conjugation of HA with MWCNTs influences the tumor-targetability and therapeutic efficacy of CNT-entrapped DOX against HR positive cancer cells. A near-infrared (NIR) fluorescent dye Alexa-Flour-647 (AF-647) and radiotracer Technetium-99m (^{99m}Tc) were further integrated with DOX-loaded HA-MWCNTs to enable real-time tracking of the localization of CNT−drug conjugates through optical and/or scintigraphic techniques. To the best of our knowledge, this is the first report in which HA-targeted MWCNTs have been successfully exploited for tumor-selective intravenous delivery of DOX, while reducing the drug-associated cardiotoxicity.

MATERIAL AND METHODS

Materials. Multiwalled carbon nanotubes (purity >95%, length 1−2 μm, and diameter 20−30 nm) were procured from Nanovatech Pvt. Ltd., USA. Sulfuric acid, nitric acid (69−72%), disodium hydrogen phosphate, sodium acetate, thionyl chloride, sodium lauryl sulfate, copper sulfate, and thiobarbituric acid were purchased from Loba Chemie Pvt. Ltd., Mumbai, India. Doxorubicin and hyaluronic acid were obtained as gift sample from Sun Pharmaceuticals, India, and Focaschem Biotech limited, China, respectively. 2,2′-(Ethylene dioxy) bis-(ethylene amine), PEG-bis-amine 3000, propidium iodide (PI), neutral red (NR), Alexa-Fluor 647, and 7,12 dimethylbenz-[α]anthracene (≥95% pure) were purchased from Sigma, USA. Annexin V staining kit, 7,12-dimethylbenz[α]anthracene (DMBA; ≥95% pure), 2,2′-(ethylene dioxy) bis(ethylene amine), poly(ethylene glycol) PEG-bis-amine M_w 3000, PEG bis(amine) M_w 6000, propidium iodide (PI), and Rhodamine 123 (Rh123) were purchased from Sigma, USA. All kits for biochemical estimations were procured from Accurex, Biomedical Ltd., Mumbai. Culture medium and serum were procured from PAA, Austria. Lung epithelial cancer cell line A549 was purchased from National Centre for Cell Sciences, Pune, India. AF-647 was purchased from Invitrogen, USA. TUNEL assay kit was purchased from Calbiochem, USA. All other chemicals and solvents were of analytical grade and procured from local suppliers unless otherwise mentioned.

Functionalization of MWCNTs. Functionalization of CNTs with hyaluronic acid (HA) and drug loading was accomplished in the following steps: (i) Surface oxidation of pristine MWCNTs; (ii) acylation of acid-oxidized carboxylated MWCNTs; (iii) amine functionalization of acylated MWCNTs via appropriate PEG spacer; (iv) HA conjugation with amine-functionalized MWCNTs; and (v) DOX loading via $\pi-\pi$ stacking interaction.

Surface Oxidation of Pristine MWCNTs. For surface oxidation, pristine MWCNTs (200 mg) with approximate length ranging 1−2 μm and diameter 20−30 nm were dispersed in a 3:1 (v/v) mixture of H_2SO_4/HNO_3 (20 mL) via ultrasonication for 5 min. Thereafter, the dispersion was refluxed at 80 °C using a hotplate cum magnetic stirrer at 900 rpm. Oxidation was continued for 3 h. After oxidation, the suspension of MWCNTs in acid was diluted up to 5 times of its volume and centrifuged at 21 000 rpm. This washing was repeated at least twice for complete removal of acid. Oxidized MWCNTs obtained were further dispersed in acetone and centrifuged, following which the supernatant was discarded and MWCNTs were air-dried for approximately 12 h to obtain fine powders of oxidized CNTs.[11] The transformation of pristine to oxidized CNTs was almost quantitative (yield ∼95% w/w).

Amine Functionalization of Oxidized MWCNTs. For amine functionalization, oxidized MWCNTs (100 mg) were dispersed in THF (10 mL) via ultrasonication for 1 min. To the resultant dispersion, $SOCl_2$ (15−20 mL) was added, and the mixture was refluxed at 80 °C for 24 h.[12] Thereafter, solvents were removed using rotavapor and the resultant acylated MWCNTs were dispersed in anhydrous THF. From thermogravimetric analysis (TGA), carboxylic density on the surface was determined to be 0.0018 mmol/mg of CNTs. This value was necessary to calculate the exact amount of PEG-3000 or EDBE that would be ideally required for complete interchange of surface carboxyl groups with 2,2′-(ethylene dioxy) bis(ethylene amine) (EDBE). On the basis of TGA results, around 3-fold molar excess of PEG-bis-amine (16.2 mg/mg of oxidized MWCNTs) or EDBE (0.810 μg/mg of oxidized MWCNTs), dissolved in anhydrous DMSO was added to a suspension of acylated MWCNTs in a 5:1 (v/v) mixture of DMSO and pyridine under ice-cold conditions. The reaction mixture was left stirring for 12 h, following which the reaction mixture was subjected to centrifugation, supernatant discarded, and the pellet of EDBE-MWCNTs/PEG 3000-MWCNTs was washed with distilled water, recentrifuged to remove the unreacted reagents, and dried by repeated washing with acetone. Surface amine density of functionalized MWCNTs was determined using the *p*-nitrobenzaldehyde, colorimetric assay (see Supporting Information,

Methods Section, for further details). The transformation of oxidized CNTs to its amine functionalized counterpart was nearly quantitative (yield ~95% w/w).

Conjugation of Hyaluronic Acid (HA) with Amine-Functionalized MWCNTs. For conjugation of HA with MWCNTs, HA (taken in a concentration equivalent to the surface amine density of MWCNTs) was dissolved in water at pH 8.0 and activated with N-hydroxy succinimide (NHS) and EDC.HCl for 6 h. To this activated HA, an aqueous suspension of EDBE-MWCNTs was added and the reaction mixture was stirred for 24 h. Subsequently, HA-EDBE-MWCNTs were separated and air-dried for 12 h (yield ~80% w/w).

Physicochemical Characterization of Synthesized Conjugate Bound to MWCNTs. *Particle Characteristics and Surface Chemistry.* Microstructure of f-MWCNTs was analyzed using scanning electron microscopy (SEM, model S30400) and transmission electron microscopy (TEM, model FEI Tecnai G2), while hydrodynamic sizes and zeta potential of the nanotubes in water were measured using the Malvern Zeta Sizer (Nano ZS, Malvern Instrument, USA). Surface chemistry of the functionalized nanotubes was studied using Fourier transform infrared (FTIR) and thermogravimetric analysis (TGA), while fine structure resolved analysis of the surface-bound ligands was performed using high-resolution magic angle spinning NMR (HRMAS-NMR) spectroscopy. FTIR spectra were recorded on Perkin-Elmer systems using KBr pellets and processed using *Spectrum* software. TGA was carried out on Mettler Toledo system (TGA/SDTA 851e) by heating CNTs at the rate of 10 °C/min. Samples for HRMAS NMR experiments were prepared by suspending 10 mg of each nanoparticle preparation in a 1:1 mixture of DMSO-d_6/D_2O (500 μL). HRMAS−NMR analysis was carried out with a 400 MHz FT-NMR spectrometer (Avance 400), equipped with a 5 mm HRMAS probe.

DOX Loading on MWCNTs. For DOX loading on MWCNTs, HA-MWCNT/DOX were mixed in the ratio of 2:1 (w/w), and the resultant mixture was incubated at four different pH values: 5.5, 7.4, 8.0, and 9.0. The CNT−drug mixture was kept in a shaker bath at 37 °C for 24 h, following which drug-loaded CNTs were separated by centrifugation and absorbance of the supernatant was measured at 480 nm. Drug loading was calculated spectrophotometrically using the following formula: % drug encapsulation efficiency = $(A_1 - A_2)/A_1 \times 100$, where A_1 = free Doxorubicin absorbance and A_2 = absorbance of supernatant after centrifugation. Percentage (%) dug loading was estimated as % drug loading = amount of drug encapsulated/weight of the pellet × 100.

pH-Dependent Release of DOX from MWCNTs. The release behavior of DOX from HA-MWCNTs was checked at two different pH conditions, viz., pH 7.4 phosphate buffered saline (15 mmol) and pH 5.5 acetate buffered saline (15 mmol), to mimic the physiological and lysosomal pH, respectively. Briefly, an aqueous dispersion of drug-loaded MWCNTs (5 mg dispersed in 2 mL water) was used to fill the dialysis membrane (MWCO 12 000 Da), poured into release medium (15 mL), and placed inside the water shaker bath for 48 h at 37 °C and 1200 rpm. Aliquots were taken at periodic intervals up to 48 h, and absorbance was recorded using UV spectroscopy at 480 nm.[13] The stability of HA-MWCNT-DOX in serum was determined by incubating the nanotubes in 100% fetal bovine serum (FBS) at 37 °C. Released DOX was removed by filtration at different time points, and absorbance was recorded using UV spectroscopy at 480 nm.

In Vitro Cellular Uptake, Cytotoxicity, and Apoptosis Studies. *Cell Culture.* Cell uptake studies were conducted in A549 lung cancer cell lines obtained from the National Centre for Cell Sciences (NCSS) Pune. All cell lines were grown in Dulbecco's modified Eagle's medium supplemented with 10% (v/v) heat inactivated fetal calf serum 2 mM glutamine, 100 units mL^{-1} penicillin 100 μg/mL streptomycin, 4 mmol L^{-1} glutamine at 37 °C in a 5% CO_2 and 95% air humidified atmosphere. Confluent cultures were harvested by trypsinization and cells counted and suitably diluted to obtain 5×10^5 cells/mL. Cell suspension (200 μL) was added in 96 well tissue culture plates and incubated overnight for cell attachment. Cell suspension (5×10^5 cells/mL; 200 μL) was added in 96 well tissue culture plates and incubated overnight for cell attachment. For all cell culture experiments, CNTs were dispersed in culture medium to obtain a stock dispersion of 1 mg/mL. The stock dispersion was bath sonicated for 5 min to aid in dispersion. This stock dispersion was serially diluted in culture medium to achieve the desired CNT concentrations.

In Vitro Cell Uptake and Colocalization Studies. For competitive inhibition studies, A549 cells were exposed to 100 μg/mL of different nanotube preparations in the absence and presence of HA (50 μg/mL).[14] After 3 h of incubation, the cells were thoroughly washed to remove the non-internalized nanotubes and confocal laser scanning microscopy (CLSM) was performed using model Olympus FV 1000. Intracellular colocalization of CNTs was examined by labeling lysosomes and mitochondria of A549 cells with neutral red (NR) and Rhodamine 123 (Rh 123), respectively, as described in our previous reports.[15] Subcellular distribution of the nanotubes was visualized through confocal microscopy.

In Vitro Cytotoxicity and Apoptosis Study. f-MWCNT-induced cytotoxicity in A549 cells was determined by MTT assay using our previously published protocol.[16]The induction of apoptosis was determined by phosphatidylserine externalization (Annexin V staining) and DNA fragmentation (TUNEL assay) after 24 h incubation using commercial kits according to manufacturer's instructions. Nuclear morphology was assessed after 24 h incubation with free DOX and CNTs. Cells were fixed in 70% ethanol and stained with 10 μg/mL PI. DNA fragmentation was determined by diphenylamine (DPA) method as described elsewhere.[17]

In Vivo Studies. *Biodistribution Studies.* Biodistribution of the ^{99m}Tc-free DOX and MWCNT−DOX was studied in an Ehlrich ascites tumor (EAT) bearing mice model. The protocol for biodistribution studies was duly approved by the Institutional Animal Ethics Committee (IAEC) of Institute of Nuclear Medicine and Allied Science (INMAS), Delhi. The tumor was implanted into the mice by injecting 0.1 mL of cell suspension of EAT cells subcutaneously in the right hind paw of the mice. The injected volume contained approximately $(1.0-1.5) \times 10^7$ cells. Tumor was allowed to grow for 10 days. The mice were divided into 3 groups of 16 animals each (total 48 mice, 4 mice each for one time interval). Each mouse received 100 μCi (100 μL) doses of the labeled formulations by tail vein injection. The mice were humanely sacrificed at 1, 4, and 24 h after the injection. The blood was collected by cardiac puncture. Subsequently, major organs/tissues were dissected/harvested, washed with Ringer's solution to remove any adherent debris, and dried using tissue paper. The organs were taken in preweighed tubes, which were then weighed again to calculate the weight of organ/tissue, and radioactivity corresponding to them was measured using a well-type γ-scintillation counter.

The results were expressed as the percentage of injected dose (ID) per gram of organ.

Tumor Growth Inhibition Studies. Female Sprague−Dawley (SD) rats of 220−230 g and 4−5 weeks old were supplied by the central animal facility (CAF), NIPER, India. For pharmacodynamics study, all animal study protocols were duly approved by the Institutional Animal Ethics Committee (IAEC) of the National Institute of Pharmaceutical Education & Research (NIPER), India. The animals were acclimatized at temperature of 25 ± 2 °C and relative humidity of 50−60% under natural light/dark cycle for one week before experiments. For tumor induction, 7,12-dimethylbenz[α]anthracene (DMBA) in soybean oil was administered orally to rats at 45 mg/kg dose at weekly interval for three consecutive weeks. Measurable mammary tumors were observed in animals after 10 weeks of last DMBA dosing, and tumor-bearing animals were separated. For pharmacodynamic assessment, animals were divided into five groups, each group containing four animals. Free DOX, DOX-deprived MWCNT-EDBE-HA, MWCNT-EDBE-DOX, and MWCNT-EDBE-HA-DOX were administered to the first four groups through a single dose of 5 mg/kg of plain DOX and MWCNTs in equivalent concentration of the free drug via intravenous injection. The last group was kept as a control, which received normal saline in a similar way. The tumor volume and body weight was measured on every alternate day post-treatment by Vernier caliper using the following equation:

$$\text{tumor volume } (V) = D \times d^2/2$$

where d is the smallest and D the longest length of the tumor.

The study was terminated after 10 days post-treatments. Blood was collected through cardiac puncture for analyzing biochemical markers of toxicity.

Toxicity Studies. In order to address the toxicity issues pertaining to free DOX and CNTs, toxicity studies were carried out in tumor-induced rats as well as in normal mice, which were treated with free DOX/functionalized MWCNTs at the dose similar to that used in efficacy studies. Toxicity studies were conducted in both rats and mice because compared to rats, mice present more sensitive models for toxicity evaluation. Cardiotoxicity of DOX-loaded f-MWCNTs was determined in breast tumor-induced Sprague−Dawley (SD) female rats. Prior to sacrifice of animals treated with free DOX and various MWCNT preparations for 10 days, blood samples were collected via cardiac puncture into heparinized capillary tubes. Plasma was separated by centrifugation at 10 000 RCF for 10 min and stored at −20 °C until analysis. Enzyme activities such as CK-MB (creatine phosphokinase) and LDH (lactate dehydrogenase) levels were analyzed in plasma, while malondialdehyde (MDA) and superoxide dismutase (SOD) were determined in heart homogenate by the commercially available kits based on the method provided by the manufacturer instructions supplied with the commercial kits. For cardiotoxicity evaluation in mice, animals were divided into 4 groups with each group containing 6 animals. Cardiotoxicity in mice was evaluated following the same protocol as described in the case of tumor-bearing rats. Hepatotoxicity and nephrotoxicity in mice was evaluated following the protocol reported in our earlier publication.[18] The detailed procedure for the determination of various biochemical markers, viz., AST, ALT, MDA, SOD, have also been detailed in the Supporting Information.

Statistical Analysis. All data unless otherwise specified are expressed as mean ± SD. Statistical analysis was performed with *Graph Pad Prism* software (v 4.03, USA) using one-way ANOVA, followed by Tukey−Kramer multiple comparison test. $P < 0.05$ was considered statistically significant.

RESULTS AND DISCUSSION

Synthesis, Optimization, and Characterization of HA-Functionalized MWCNTs. *Functionalization of MWCNTs with Hyaluronic Acid.* A schematic representation of the functionalization of MWCNTs with hyaluronic acid has been depicted in Figure 1. The conjugation of different functional molecules on MWCNTs was qualitatively analyzed using FTIR and HRMAS-NMR analysis (Figure S1, S2). The quantity of various functional molecules immobilized per unit mass of CNTs was determined using TG analysis (Figure S3, Table S1). As a preliminary step toward the multiple functionalization of MWCNTs, pristine MWCNTs having approximate length between 1 and 2 μm and diameter 20−30 nm were enriched with surface carboxyl groups via oxidation in the presence of concentrated H_2SO_4 and HNO_3 (3:1 v/v) for 3 h. The carboxyl functions on MWCNTs were interchanged with amine groups through a sequence of thionyl chloride ($SOCl_2$) induced acylation (24 h) and further reaction with around 3−5-fold molar excess of an appropriate PEG-bis amine. In order to ensure maximum interchange of surface carboxyl groups with surface-pendant amine groups, the PEGylation process was initially optimized in terms of spacer length and molecular weight. Acylated MWCNTs were reacted with a variety of PEG-bis amine ranging from the mini-PEG 2,2′-(ethylenedioxy) bis(ethylamine) [EDBE, M_w = 148.2] to PEG-bis-amine with M_w 3000 or 6000. In the case of EDBE, the majority of the surface carboxyl groups could be interchanged with amine groups as evident from the high surface amine density (0.458 μmol/mg) of EDBE-MWCNTs determined via *p*-nitrobenzaldehyde assay. On the contrary, surface amine density of MWCNTs functionalized with PEG 3000 or 6000 was even less than 0.1 μmol/mg of CNTs. Zeta potential analysis further revealed that transformation of acylated MWCNTs to EDBE-MWCNTs was accompanied with complete reversal of surface polarity from −57.5 ± 2.7 mV to +9 ± 0.6 mV. The changes in surface charge as well as amine density were perceived within one hour of addition of the reagents, whereas in the case of PEG-bis-amine 3000, even after 24 h of reaction, zeta potential of the CNT surface was completely negative (−28.6 ± 6.6 mV). The observation may be attributed to any one of the following factors: First, due to the large size of the polymer, it is quite feasible that only a fraction of the total number of COO^- groups on the surface were PEGylated. Further, it may also happen that the long PEG-Bisamine chain folds and the free amino terminal associated with the polymer binds with the unreacted COO^- groups on oxidized MWCNTs via electrostatic interaction. In addition, amine functionalization with EDBE is more economic and cost-effective as compared to its higher MW counterparts. Stoichiometric calculations revealed that 1 mg of carboxylated MWCNTs requires at least 5.4 mg of PEG-bis-amine 3000, which is approximately 20 times higher than the amount of EDBE (270 μg) required for complete interchange of all carboxyl groups on acid-oxidized MWCNTs with amine groups. Considering the distinct advantages of EDBE as compared to its higher M_w counterparts, EDBE-MWCNTs were chosen as the preferable intermediate for further

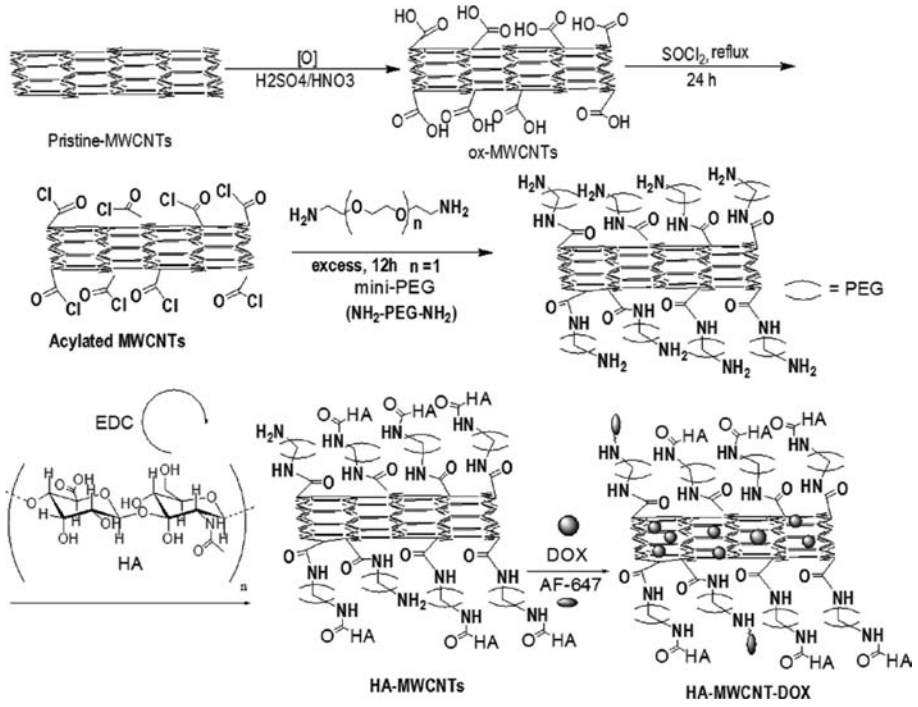

Figure 1. Schematic representation of functionalization of MWCNTs with multiple bioactives.

Table 1. Particle Characteristics of Functionalized MWCNTs[a]

f- MWCNTs	SEM features	TEM features	DLS size (nm)	PDI	zeta potential (mV)
Oxidized MWCNTs	Length 0.3−0.8 μm, Diameter 20−30 nm	Length 0.3−0.8 μm, Diameter 20−30 nm	172.8 ± 4.2	0.421 ± 0.052	−57.5 ± 2.7
EDBE-MWCNTs	Length 0.3−0.8 μm, Diameter 40−50 nm	Length 0.3−0.8 μm, Diameter 20−30 nm	225.9 ± 2.7	0.437 ± 0.034	+9 ± 0.6
HA-PEG-MWCNTs	Length 0.3−0.8 μm, Diameter 60−80 nm	Length 0.3−0.8 μm, Diameter 20−30 nm	451.3 ± 8.7	0.310 ± 0.023	−42 ± 4

[a]All values unless otherwise stated are expressed as mean ± SD (n = 6).

bioconjugation reactions. To conjugate HA with EDBE-MWCNTs, HA was activated with 1.5-fold molar excess of 1-ethyl-3-(3-dimethylaminopropyl) carbodiimide (EDC) in aqueous solution (pH ∼8) and subsequently reacted with EDBE-MWCNTs for 48 h. The bioconjugation step was accomplished with two types of HA: high M_w HA (∼120 kDA) and low M_w HA (∼5 kDA). As surface amine density of MWCNTs was determined to be around 0.458 μmol/mg, 160 μg HA/mg CNTs and 1.39 mg HA/mg CNTs were, respectively, required for the complete derivatization of the surface amine groups of CNTs with HA. Considering the relative cost of high and low M_w HA, the use of low M_w HA was found to be more effective. Moreover, high M_w HA tends to form meshwork around the CNTs and increases their effective hydrodynamic size, which negatively influence the nanotube−drug interaction and takes away from their effectiveness for intravenous delivery.

Particle characteristics of acid-oxidized carboxylated MWCNTs, EDBE-MWCNTs, and HA-EDBE-MWCNTs have been summarized in Table 1. Oxidized MWCNTs present an average hydrodynamic size and zeta potential of 173.8 ± 4.2 nm and −57.5 ± 2.7 mV, respectively. Following functionalization with EDBE, the average hydrodynamic size of CNTs increased with concomitant reversal of zeta potential, i.e., the EDBE-MWCNTs became positively charged due to the presence of free amine groups on their surface. After HA conjugation, the hydrodynamic size of the nanotubes increased to 451.3 ± 8.7 nm and zeta potential again shifted to the negative direction (−42 ± 4 mV) due to the covalent attachment of polyanionic species on the surface of CNTs. Representative SEM image of various MWCNT preparations have been presented in Figure 2. As evident from the SEM micrograph, the final conjugate (viz., HA-EDBE-MWCNT-DOX) possessed average length in the range 0.3−0.6 μm and diameter ranging from 50 to 60 nm. Consistent with SEM observation, TEM image of HA-EDBE-MWCNT-DOX reveals well-individualized structure with average diameter ranging from 0.5 ± 0.1 μm and diameter ranging from 20 to 30 nm. It should be mentioned in this regard that the diameters of HA-functionalized MWCNTs obtained from TEM are, however, smaller than the diameter obtained from SEM investigations. The result is justified because organic coatings or functionalizations adhered with solid supports like CNTs are hardly discernible by TEM. As determined by DLS studies, HA-MWCNTs present in course of the study were highly stable in aqueous medium. Their stable nature was manifested in their hydrodynamic (HD) size, polydispersity index (PDI), and zeta potential values, which remained unaffected even after six months from their date of preparation (Supporting Information, Table S2). Exposure of these functionalized nanotubes to various culture media (DMEM, RPMI, etc.) in the presence of serum revealed no significant deterioration in hydrodynamic sizes and surface charge up to 96 h of incubation (data not shown), conferring their suitability for in vitro and in vivo applications.

dx.doi.org/10.1021/bc300248t | *Bioconjugate Chem.* 2012, 23, 2201−2213

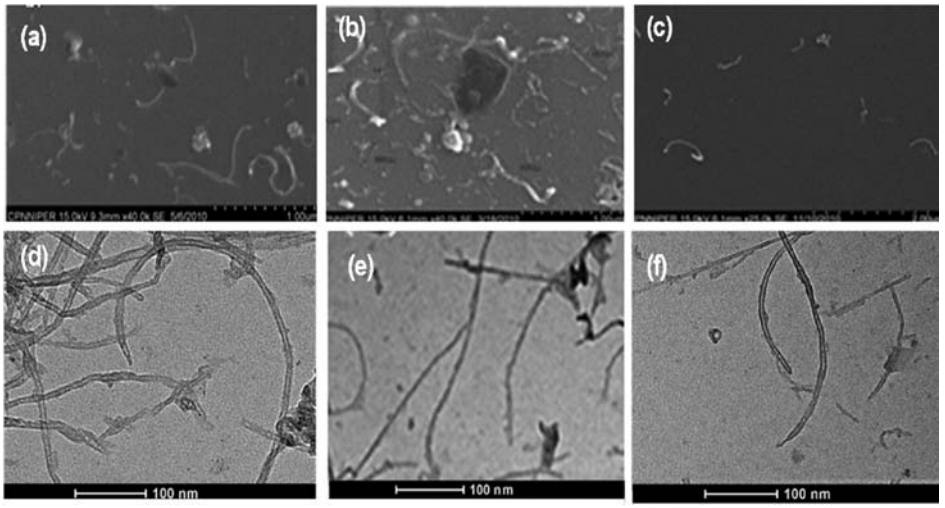

Figure 2. (a–c) Scanning electron micrographs and (d–f) transmission electron micrographs of 3 h oxidized MWCNTs, EDBE-MWCNTs, and HA-EDBE-MWCNTs, respectively.

DOX Release from CNTs. DOX was loaded to CNTs exploiting the supramolecular $\pi-\pi$ stacking interactions between drug and nanotubes (see Supporting Information, Figure S4, Table S3 for details). DOX release from HA-MWCNTs was checked at both pH 5.5 and 7.4 to mimic the tumor microenvironment and normal physiological milieu, respectively (Figure 3). At pH 7.4, only 14.26% of the entrapped drug was found to be released from the surface of MWCNTs after 32 h of exposure to the release medium. As the pH of the release medium was lowered to 5.5, around 36.50% DOX was found to be released from HA-MWCNTs just within 24 h of incubation. This particular release profile is beneficial from the standpoint of cancer targeting, since cancerous tissues have a slightly acidic pH with high enzymatic activity. This pH-dependent release behavior suggests that DOX will be released more in acidic tumor sites than in the normal tissues. Once the particles are internalized inside the cells through HR-mediated endocytosis, the decreased pH values are supposed to induce further accelerated drug release inside the acidic tumor endosomes. At this low pH, the hydrophilicity of DOX increases due to the protonation of NH_2 group native to its structure. The increased hydrophilicity aids in overcoming the $\pi-\pi$ stacking force while facilitating the release of DOX from MWCNTs. Since the present formulation was meant for intravenous administration, the release profile of DOX from nanotubes was also repeated in the presence of serum. Interestingly, only 15–17% DOX was detached from the nanotubes after 48 h of incubation (Figure 3). These results indicated that the functionalized nanotubes prepared in this study exhibited good stability in physiological solution containing various salts and proteins.

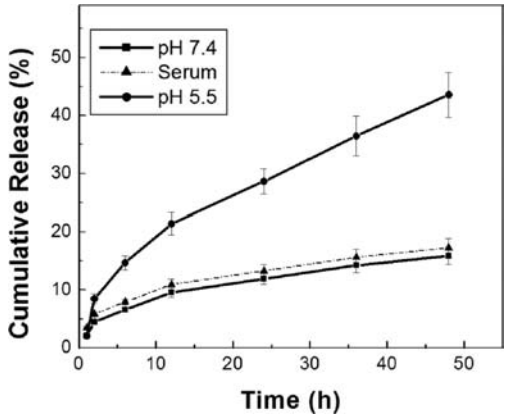

Figure 3. In vitro release profile of DOX from HA-MWCNTs at pH 7.4 (physiological pH), serum, and pH 5.5 (tumor pH).

In Vitro Cellular Uptake, Cytotoxicity, and Apoptosis Studies. *Intracellular Uptake and Colocalization Study.* Cell uptake studies were performed in human nonsmall cell lung adenocarcinoma (A549) cell lines, known to overexpress the CD44 receptors specific for HA.[19] To apprehend whether the main hyaluronate receptor (HR) is involved in the uptake of the HA-conjugated MWCNTs, A549 cells were incubated with HA-MWCNTs in the absence and presence of HA. While blockage of HR hardly altered the internalization of HA deprived, EDBE-MWCNTs amine-functionalized, the uptake of HA-functionalized CNTs was significantly suppressed (Supporting Information Figure S5). These results supported that HA-MWCNTs were internalized by A549 cells through CD44 receptor mediated endocytosis. It seems that endocytosis is not involved during translocation of EDBE into the cells, since their internalization was not affected by complete blockage of endocytic pathway either by low temperature or by sodium azide (data not shown). The results, however, are in line with the reported pathway of nanotube uptake by passive diffusion.[20] To further understand the surface-chemistry dependence of f-MWCNTs on their intracellular trafficking behavior, A549 cells were incubated with various f-MWCNTs and their colocalization with various cell organelles, viz., lysosomes, mitochondria, was studied using confocal laser scanning microscopy (CLSM). For lysosome and mitochondrial colocalization experiments, f-MWCNTs were covalently tagged with AF-647 (indicated as gray fluorescence), whereas lysosomes and mitochondria were stained with Neutral Red (NR, red fluorescence) and Rhodamine 123 (Rh123, green fluorescence), respectively. The degree of overlap between AF-647 labeled CNTs and an organelle-specific fluorescence dye was measured in terms of Pearson's correlation coefficient (r). A colocalization coefficient close to or greater than 0.5 ($r \geq 0.5$) was indicative of good colocalization. As evident from the line display of AF-647 labeled f-MWCNTs and NR stained lysosomes (Figure 4A),

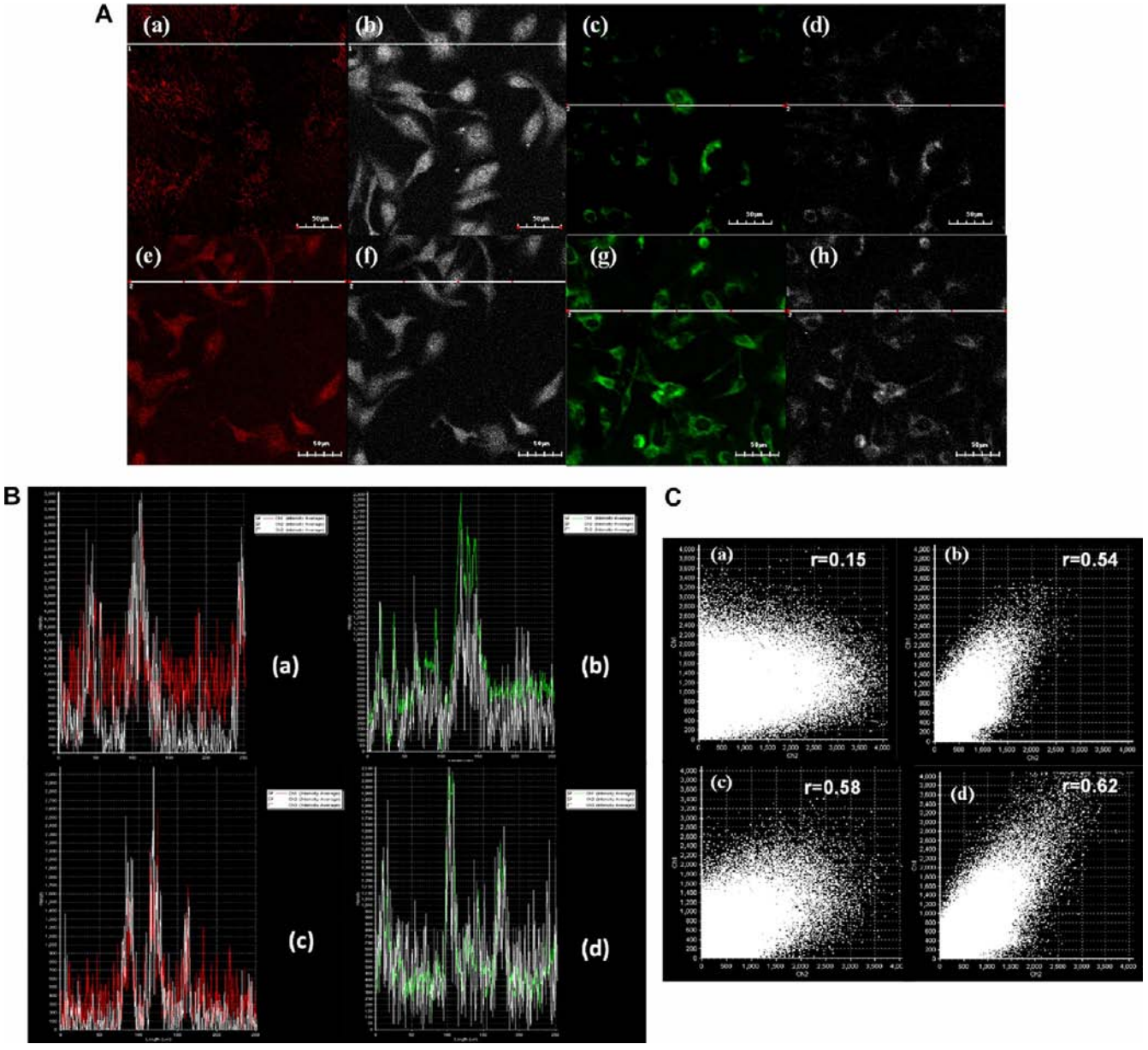

Figure 4. (A) Representative line display of A549 cells incubated with (a–d) EDBE-MWCNTs and (e–h) HA-MWCNTs. (a,e) indicates NR fluorescence; (b,d,f,h) AF-647 fluorescence and (c,g) Rh123 fluorescence. (B) Representative line plot of A549 cells incubated with (a,b) EDBE-MWCNTs and (c,d) HA-MWCNTs. (a,c) indicates line plot of AF-647 labeled CNTs and NR stained lysosomes; (b,d) line plot of AF-647 labeled CNTs and Rh123 stained mitochondria. (C) Representative scatter plot of A549 cells incubated with (a,b) EDBE-MWCNTs and (c,d) HA-MWCNTs. (a,c) indicates scatter plot of AF-647 and NR fluorescence; (b,d) scatter plot of AF-647 and Rh123 fluorescence.

following their intracellular uptake, HA-MWCNTs rapidly translocated into the lysosome, whereas their nontargeted counterparts were mainly distributed within the cellular cytoplasm. As determined from the scattered plot (Figure 4B), the Pearson's colocalization coefficients (r) of AF-647 and NR fluorescence for EDBE-MWCNTs and HA-MWCNTs were determined to be 0.2 and 0.6, respectively. These values revalidate the results of line display in which HA-MWCNTs was shown to present appreciable colocalization with cellular lysosomes. In this context, it may be noted that the colocalization determined in the entire field of view (scatter plot) cannot precisely discriminate the fluorescence associated with cell surface adhered nanotubes from those present intracellularly. To confirm the colocalization, line plot analysis (Figure 4C) was performed that measures variations in fluorescence intensity along a line. Yet again, the line plots determine variations in fluorescence intensity, just in one dimension. To revalidate the quantitative colocalization results, box-plot analyses were performed (SI Figure S6), which measure the changes in fluorescence intensity in two dimensions, that is, X and Y. Consistent with the results of scattered plot analysis, both line and box colocalization analysis established that HA conjugated MWCNTs exhibit good colocalization with the lysosomes. Binding of HA-MWCNTs to HR possibly leads to formation of endocytic vesicles,[21] which, in turn, favored their intracellular trafficking to lysosomes. This colocalization profile is beneficial from the standpoint of accelerated DOX release under lysosomal conditions. As already discussed, the acidic pH of lysosomes will aid in the protonation of NH_2 group native to the structure of DOX and trigger drug release from CNTs. We also observed some fluorescence emissions of

dx.doi.org/10.1021/bc300248t | Bioconjugate Chem. 2012, 23, 2201–2213

both EDBE-MWCNTs and HA-MWCNTs in the mitochondria. As determined from scattered plot analysis, Pearson's colocalization coefficient (r) of AF-647 and Rh123 fluorescence was approximately 0.5 in both cases. Because mitochondrial membrane is negatively charged, the mitochondrial colocalization of EDBE MWCNTs with surface-pendant amine groups is not implausible and is also consistent with the proposed transmembranal pathway of mitochondrial colocalization of PL-PEG-SWCNTs by Zhou et al. However, colocalization of negatively charged HA-MWCNTs with mitochondria is a bit paradoxical. Although the mechanism of mitochondrial localization of HA-MWCNTs is not fully understood, it is quite feasible that, following their internalization into the cells, HA-MWCNTs are translocated into lysosomes via endosomal pathway. There is a fair chance that the low pH and nonspecific proteases inside the lysosomal compartment will accelarate the hydrolysis of the amide bond between HA and EDBE so that a part of the surface amine groups is rejuvenated to interact with the negatively charged mitochondrial membrane. As suggested by some earlier reports, we cannot also disregard the possibility of electrostatic interaction between the negatively charged functional groups of the glycosaminoglycan backbone of HA and positively charged residues (viz., lys267, lys270, and arg 411) of cytochrome P450scc and adrenodoxin, some of the very well-known redox proteins involved in the electron transfer chain of the inner mitochondrial membrane.[22] However, without further studies, it is difficult to make any precise comment on the underlying mechanism that translocates HA-conjugated CNTs to mitochondria. In this regard, it may also be noted that Rh123 exhibits green emission, whereas the dye NR shows red emission. Because of the shorter wavelength of green emission, the emitted fluorescence is somewhat scattered or diffused, which might increase the apparent colocalization to some extent. Whatever the case might be, from data in hand, it is confirmed that HA-CNTs enter the cells through CD44 receptor mediated endocytosis and translocate into the lysosomes.

Cytotoxicity Study. To further check the feasibility of DOX release inside the target cells, A549 cells were cultured with free DOX as well as DOX loaded MWCNT-EDBE-HA. DOX-deprived MWCNT-EDBE-NH_2 and MWCNT-EDBE-HA were taken as a control. While DOX-deprived MWCNTs led to negligible reduction in cellular viability (EC-50 $\gg$ 100 μg/mL), both free DOX and HA-MWCNT-DOX exhibited dose-dependent reduction in cellular viability (Figure 5). At very low concentration of DOX (0.001−0.01 μg/mL), insignificant differences were noted between the cytotoxicity of free DOX and DOX-loaded CNTs. Above this concentration ($\geq$0.1 μg/mL), DOX delivered through CNTs always exerted higher cytotoxicity than the free drug in equivalent concentrations. The IC_{50} of free DOX and HA-CNT-DOX were calculated to be 2.117 and 0.8688 μg/mL, respectively. These results indicate that our formulation is approximately 2.4 times more cytotoxic than the free drug. These observations suggest that intracellular concentration of DOX delivered through MWCNTs is higher than that of free DOX. The hypothesis may be rationalized, if we consider the intracellular trafficking behavior of MWCNT-HA-DOX. As evident from the results of cell uptake and intracellular trafficking, HA-MWCNTs exhibited appreciable colocalization with the lysosomes. This selective localization possibly augmented the release of free DOX from MWCNTs. In order to confirm that CNT-encapsulated DOX is specifically released in the lysosomes, A549 cells were incubated with HA-MWCNT-DOX in the absence and presence of ammonium chloride, and cytotoxicity was determined in both cases. Notably, a marked reduction in cytotoxicity was observed when the cells were pretreated with NH_4Cl. These results suggest that addition of NH_4Cl leads to accumulation of ammonium ions in the lysosomes while increasing their pH.[23] As DOX release from nanotubes is augmented under low pH conditions, an increase in lysosomal pH condition disfavors drug release from CNTs. Overall, these observations suggest that encapsulation of DOX within HA-MWCNTs not only enhance their intracellular uptake but also traffick the therapeutic vector to the lysosomes wherein the drug detaches from the nanotube surface, diffuses out into the cytosol, and subsequently translocates to its site of action, viz., nucleus.

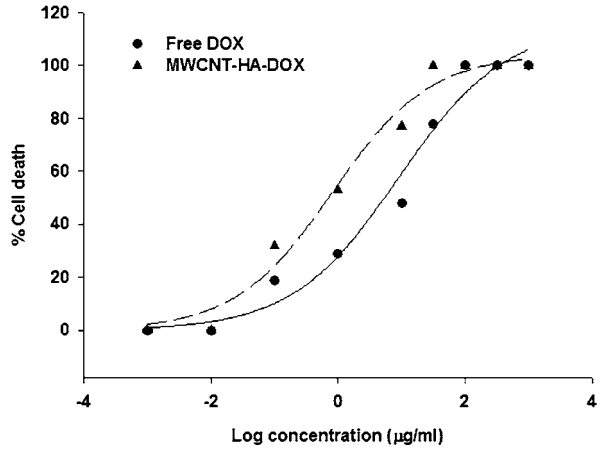

Figure 5. Dose-dependent cytotoxicity of A549 cells treated with free DOX and MWCNT-HA-DOX.

Apoptosis Study. Reduction in cellular viability is normally associated with concomitant increase in the number of apoptotic cells. In order to substantiate whether our formulation can induce cell death through the initiation of apoptosis, A549 cells were incubated in PBS with 1 μg/mL of free DOX and HA-CNTs containing equivalent amounts of free drug. The various hallmarks of apoptosis, viz., phosphatidyl serine (PS) externalization, mitochondrial depolarization, nuclear condensation, and DNA fragmentation, were studied qualitatively as well as quantitatively using Annexinn V (AV)-Cy3 apoptosis detection kit, Rh123 staining, propidium iodide (PI) staining, TUNEL, and DPA assays. While no hallmarks of apoptosis were detected with control, cells incubated with free drug as well as drug-loaded CNTs exhibited prominent features of early as well as late apoptosis including PS externalized cells, condensed and fragmented nuclei, as well as depolarized mitochondria (Figure S7). As evident from Figure.6, cells incubated with free DOX and HA-CNT-DOX presented 60 $\pm$ 5.8% and 75.1 $\pm$ 8.7% PS externalized (AV + ve) cells, and the difference was statistically insignificant. Notably, cells incubated with HA-MWCNT-DOX presented a significantly higher number of cells in late apoptosis (78 $\pm$ 7.7) when compared with the free drug (55 $\pm$ 6.8). Further cells incubated with HA-MWCNTs displayed higher percentage of fragmented nuclei and DNA, as compared to free DOX. These results suggest that DOX delivered through CNTs induced apoptosis more effectively than the free drug.

In Vivo Studies. *Biodistribution Studies after Radiolabeling of f-MWCNTs. Radiolabeling Studies.* In order to monitor the blood clearance kinetics and organ distribution behavior of our NPs in vivo, all the formulations were

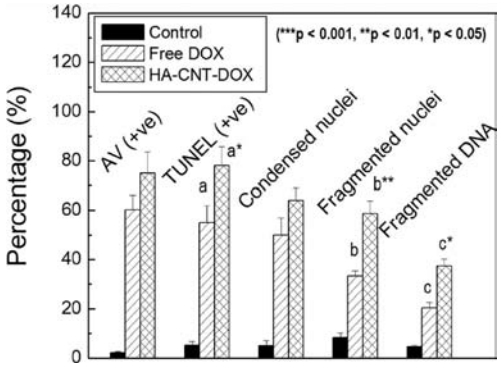

Figure 6. Evaluation of HA-MWCNT-DOX and free DOX induced apoptosis in A549 cell line: Quantitative determination of early and later apoptotic cells, condensed nuclei and fragmented nuclei/DNA using Annexin V assay, TUNEL assay, PI staining, and DPA colorimetric assay, respectively. All data are expressed as mean ± SD (***p < 0.001, **p < 0.01, *p < 0.05).

radiolabeled with ^{99m}Tc, using stannous chloride as the reducing agent. ^{99m}Tc was chosen for the present study because of its ease of availability, cost effectiveness, and low radiation dose. The half-life of Tc is only 6 h, which ensures less radiation burden when compared to other radionuclides such as I^{128} presenting a longer half-life (~60 days). HA-functionalized MWCNTs, developed in the course of the present study, were successfully labeled with Tc-99m with more than 98% labeling efficiency.[24,25] The concentration of $SnCl_2$ had a significant influence on the labeling yield. At low concentration of the stannous chloride, Tc was not properly reduced, but at higher concentration, it led to the formation of a reduced, hydrolyzed (RH) form of Tc. Therefore, to optimize the labeling procedure, the concentration of $SnCl_2$ was varied from 25 to 300 μg, keeping other parameters constant. The maximum labeling efficiency for all the formulations was obtained at 100 μg of $SnCl_2$ concentration.[25] The in vitro stability of the labeled formulations was evaluated in PBS (pH = 7.4) as well as serum. All the formulations showed excellent stability in vitro. The formulations were approximately 91−94% stable after 24 h (Table S4, Supporting Information).

Organ Distribution Studies. Biodistribution of free DOX as well as f-MWCNTs was assessed in EAT bearing mice model, a well-established animal model for CD44 receptor overexpressing tumors. We observed that the organ distribution profile of DOX-loaded CNTs insignificantly differed from those deprived of DOX (data not shown), which suggests that biodistribution of CNTs in vivo critically depends on their surface functionality and not on the encapsulated cytotoxin. In other words, biodistribution of drug-deprived f-MWCNTs may be considered equivalent to the biodistribution of their drug-loaded counterparts. The percentage injected dose of free DOX, EDBE-MWCNTs, and HA-EDBE-MWCNTs per gram (% ID/g) of tissue in different organs, at different time points, has been presented in Table 2−4. As evident from organ distribution data, not much difference could be chalked out among the distribution and accumulation of free drug, MWCNT-EDBE-DOX, and MWCNT-EDBE-HA-DOX in heart, kidney, stomach, and intestine. Notably, significant differences were observed in the distribution profile of free DOX and DOX loaded functionalized MWCNTs in the MPS organs, viz., liver, spleen, and lungs. In liver, the % ID/g for MWCNT-EDBE-DOX and MWCNT-EDBE-HA-DOX were observed to be

Table 2. In Vivo Biodistribution Profile of Free DOX

	% ID/g recovered after			
organ or tissue	0.5 h	2 h	4 h	24 h
blood	0.91 ± 0.12	0.66 ± 0.11	0.52 ± 0.13	0.15 ± 0.04
heart	0.49 ± 0.11	0.32 ± 0.08	0.23 ± 0.06	0.06 ± 0.02
lungs	5.8 ± 1.03	4.3 ± 0.97	2.1 ± 0.71	0.32 ± 0.07
liver	10.5 ± 1.52	7.04 ± 1.5	6.9 ± 1.32	2.3 ± 0.69
spleen	2.1 ± 0.48	2.13 ± 0.4	1.65 ± 0.39	0.63 ± 0.14
kidney	2.9 ± 0.8	2.01 ± 0.72	1.97 ± 0.41	0.56 ± 0.19
stomach	0.53 ± 0.12	0.48 ± 0.14	0.42 ± 0.12	0.07 ± 0.01
intestines	0.45 ± 0.13	0.31 ± 0.06	0.22 ± 0.06	0.05 ± 0.01
tumor	0.19 ± 0.04	0.39 ± 0.08	0.37 ± 0.1	0.11 ± 0.02
muscle	0.17 ± 0.03	0.15 ± 0.03	0.11 ± 0.02	0.06 ± 0.01
tumor/muscle	**1.11**	**2.6**	**2.36**	**1.83**

Table 3. In Bivo Biodistribution Profile of EDBE-MWCNTs

	% ID/g recovered after			
organ or tissue	0.5 h	2 h	4 h	24 h
blood	0.79 ± 0.03	0.65 ± 0.03	0.45 ± 0.02	0.11 ± 0.02
heart	0.29 ± 0.02	0.17 ± 0.01	0.14 ± 0.02	0.08 ± 0.01
lungs	22.65 ± 0.55	19.2 ± 0.4	15.8 ± 0.7	5.3 ± 0.4
liver	21.1 ± 1.48	16.5 ± 0.7	14.21 ± 0.03	8.15 ± 0.65
spleen	10 ± 0.2	6.91 ± 0.03	5.45 ± 0.45	4.15 ± 0.15
kidney	1.63 ± 0.13	0.94 ± 0.04	0.68 ± 0.05	0.49 ± 0.05
stomach	0.53 ± 0.03	0.49 ± 0.01	0.42 ± 0.02	0.26 ± 0.02
intestines	0.66 ± 0.05	0.52 ± 0.02	0.32 ± 0.02	0.11 ± 0.01
tumor	0.92 ± 0.06	1.09 ± 0.03	1.18 ± 0.12	0.50 ± 0.03
muscle	0.21 ± 0.02	0.15 ± 0.02	0.12 ± 0.01	0.15 ± 0.02
tumor/muscle	**4.38**	**7.26**	**9.83**	**2.33**

Table 4. In Vivo Biodistribution Profile of HA-EDBE-MWCNTs

	% ID/g recovered after			
organ or tissue	0.5 h	2 h	4 h	24 h
blood	0.62 ± 0.07	0.42 ± 0.01	0.27 ± 0.01	0.08 ± 0.01
heart	0.22 ± 0.01	0.19 ± 0.01	0.13 ± 0.02	0.03 ± 0.01
lungs	10.08 ± 0.24	7.9 ± 0.03	6.21 ± 0.02	2.12 ± 0.18
liver	17 ± 1	14.6 ± 0.7	11.3 ± 0.3	7.95 ± 0.55
spleen	7.85 ± 0.25	6.15 ± 0.35	4.95 ± 0.15	1.8 ± 0.1
kidney	1.16 ± 0.04	0.86 ± 0.06	0.68 ± 0.03	0.29 ± 0.02
stomach	0.66 ± 0.05	0.52 ± 0.03	0.41 ± 0.01	0.07 ± 0.01
intestines	0.51 ± 0.01	0.29 ± 0.02	0.16 ± 0.01	0.08 ± 0.01
tumor	1.06 ± 0.03	1.65 ± 0.15	2.5 ± 0.3	1.60 ± 0.23
muscle	0.14 ± 0.02	0.16 ± 0.01	0.18 ± 0.01	0.15 ± 0.03
tumor/muscle	**7.57**	**10.31**	**12.8**	**10.6**

21.1 ± 1.48 and 17 ± 1, respectively, after 0.5 h, while % ID/g for free DOX was calculated to be only 10.5 ± 1.52. Likewise, in spleen, the % ID/g for MWCNT-EDBE-DOX (10 ± 0.2) and MWCNT-EDBE-HA-DOX (7.85 ± 0.25) (after 0.5 h) were found to be significantly higher than free DOX (3.1 ± 0.48). Similarly, the % ID/g values in lungs after 0.5 h were detected to be 5.8 ± 1.03, 10.08 ± 0.24, and 22.65 ± 0.55 for free DOX, MWCNT-EDBE-DOX, and MWCNT-EDBE-HA-DOX, respectively. The results are justified and pretty consistent with the observations of Qu et al.[26] According to their report, both agglomerated and well-suspended MWCNTs are taken up by MPS organs. However, MWCNTs with higher degrees of agglomeration are retained in lungs and later in the liver for months, while the well-dispersed ones formed fewer aggregates

dx.doi.org/10.1021/bc300248t | *Bioconjugate Chem.* 2012, 23, 2201−2213

in lungs and liver, and seemed to be easily eliminated via excretion. In the present case, it was quite interesting to observe that % ID/g in liver, spleen, and lungs steadily decreased as a function of time. Following 24 h of administration, the % ID/g values in liver were detected to be 2.3 ± 0.69, 5.3 ± 0.4, and 3.12 ± 0.18 for free DOX, MWCNT-EDBE-DOX, and MWCNT-EDBE-HA-DOX, respectively. These data revalidate the hypothesis that functionalized MWCNTs with shorter length and high aqueous dispersibility exhibit minimum propensity to accumulate in the liver and over the course of time, eliminated via urinary excretion or biliary pathway in the feces. Organ distribution data further reveal that free DOX was gradually cleared away from the blood with time; after 24 h, the % ID/g in blood was only 0.15 ± 0.04. The results are quite justified, because DOX, being a hydrophilic drug, is rapidly eliminated from the body through urinary excretion. Careful scrutiny of the organ distribution data shows that %ID/g in kidney for free DOX at any time point is always higher than the CNT-based formulations. As in the case of free DOX, both MWCNT-EDBE, as well as its targeted counterpart, viz., MWCNT-EDBE-HA, exhibited apparent clearance from blood circulation. However, both formulations, instead of being eliminated from the body via excretory pathways, accumulated in the tumor site. In the case of free DOX, the % ID/g in tumor after 4 h was detected to be 0.38 ± 0.1% while % ID/g values in the case of MWCNT-EDBE and MWCNT-EDBE-HA were determined to be 1.18 ± 0.56 and 2.5 ± 0.3, respectively. The formulations were able to retain in these sites even after 24 h of administration. After 24 h, the tumor to muscle ratio for free DOX, MWCNT-EDBE-DOX, and MWCNT-EDBE-HA-DOX were calculated to be 1.83, 3.33, and 10.6, respectively, implying that tumor-specific accumulation of HA-targeted MWCNTs is around 5.79 and 3.18 times higher as compared to free DOX and HA nontargeted, EDBE functionalized MWCNTs.

Tumor Growth Inhibition Study. In vivo tumor growth inhibition study was carried out in DMBA induced Sprague–Dawley female rats, injected intravenously with a single dose of 5 mg/kg of plain DOX and MWCNTs in equivalent concentration of the free drug. Figure 7 presents the tumor-growth

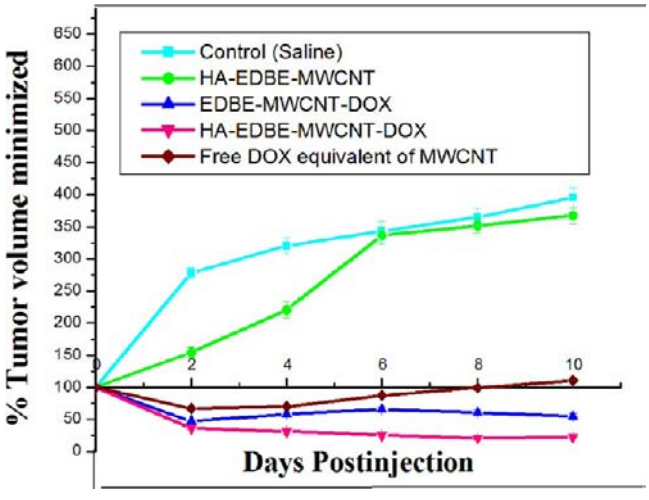

Figure 7. Tumor growth inhibition profile of SD rats intravenously administered with free DOX and various functionalized MWCNT preparations loaded with equivalent amount of the free drug.

inhibition profile of rats treated with various MWCNT preparations. A single i.v. administration of HA-PEG-MWCNT-DOX led to a significant reduction in tumor burden within 24 h of administration. The minimized tumor volume in rats after 10 days of treatment with HA-EDBE-MWCNT-DOX was approximately 18, 17, 5, and 3 times less as compared to rats exposed to saline, drug-deprived HA-EDBE-MWCNTs, free DOX, and EDBE-MWCNT-DOX, respectively. Furthermore, animals treated with free DOX at the dose level specified induced significant signs of toxicity, i.e., pronounced weight loss, that was not observed for any of the MWCNT treated groups. In fact, rats treated with free DOX appeared somewhat sluggish and congregated at the corner of the cage just after day 1 of treatment. Conversely, in the case of CNT treatment, all the animals appeared lively throughout the study, and no substantial weight loss was detected. The higher antitumor efficacy of HA-EDBE-MWCNT-DOX may be attributed to its high tumor-specific accumulation, facilitated by the following factors: (i) enhanced permeability and retention (EPR) effect, mediated by the short, hydrophilic, PEG-like chain adhered to the surface of CNTs (passive targeting); (ii) selective uptake of functionalized nanotubes via HR mediated endocytosis (active targeting); and (iii) their high intracellular penetrability. It should, however, be noted that non-HA conjugated EDBE-MWCNTs also displayed antitumor activity to an appreciable extent by virtue of EPR/stealth effect. The results of tumor-growth inhibition studies are in very good agreement with our organ-distribution data, according to which HA-conjugated MWCNTs exhibited around 5.79 and 3.18 times higher accumulation in the tumor site as compared to free drug and its nontargeted counterpart, even after 24 h of administration. Our findings are also consistent with the reports of Yadav et al. according to which antitumor efficacy of DOX loaded in PCL-PEG and PLGA-PEG core–corona nanoparticles were significantly enhanced on HA conjugation.[24,27] In the case of rats exposed to DOX deprived HA-EDBE-MWCNTs, it was quite interesting to observe that, up to 4 days post-treatment, the percentage increase in tumor volume was considerably lower as compared to the control. Following 6 days post-treatment, the increased tumor volume (%) of HA-EDBE-MWCNTs was almost comparable to that of the control group. Remarkably, at this point, no significant increase in tumor volume was observed for the MWCNT treated group, while a steady increase was still observed for the control group. The observations can be rationalized in light of a recent report by Meng et al.,[28] according to which, subcutaneous (s.c.) injection of oxidized MWCNTs could effectively enhance the immunity in mice leading to certain beneficial effects such as tumor-growth inhibition. Experimental results showed that CNT-induced significant activation of the complement system promoted production of inflammatory cytokines and stimulated subsequent phagocytosis and activation of macrophages. Collectively, all these responses are believed to increase the general activity of the host immune system and, in turn, synergized the tumor growth inhibition process.

Toxicity Studies in Rats and Mice. Drug-associated cardiotoxicity is a severe limitation of DOX therapy. Hence, it was necessary to evaluate and compare the cardiotoxicity of free DOX as well as DOX loaded f-MWCNTs. Subsequently, the various cardiotoxicity markers such as lactate dehydrogenase (LDH), cytokinin MB (CK-MB), and aspartate transaminase (AST) level in plasma and superoxide dismutase (SOD) activity in heart homogenate were determined. An increase in LDH, CK-MB, or AST level and decrease in SOD activity indicates cardiotoxicity. As evident from the

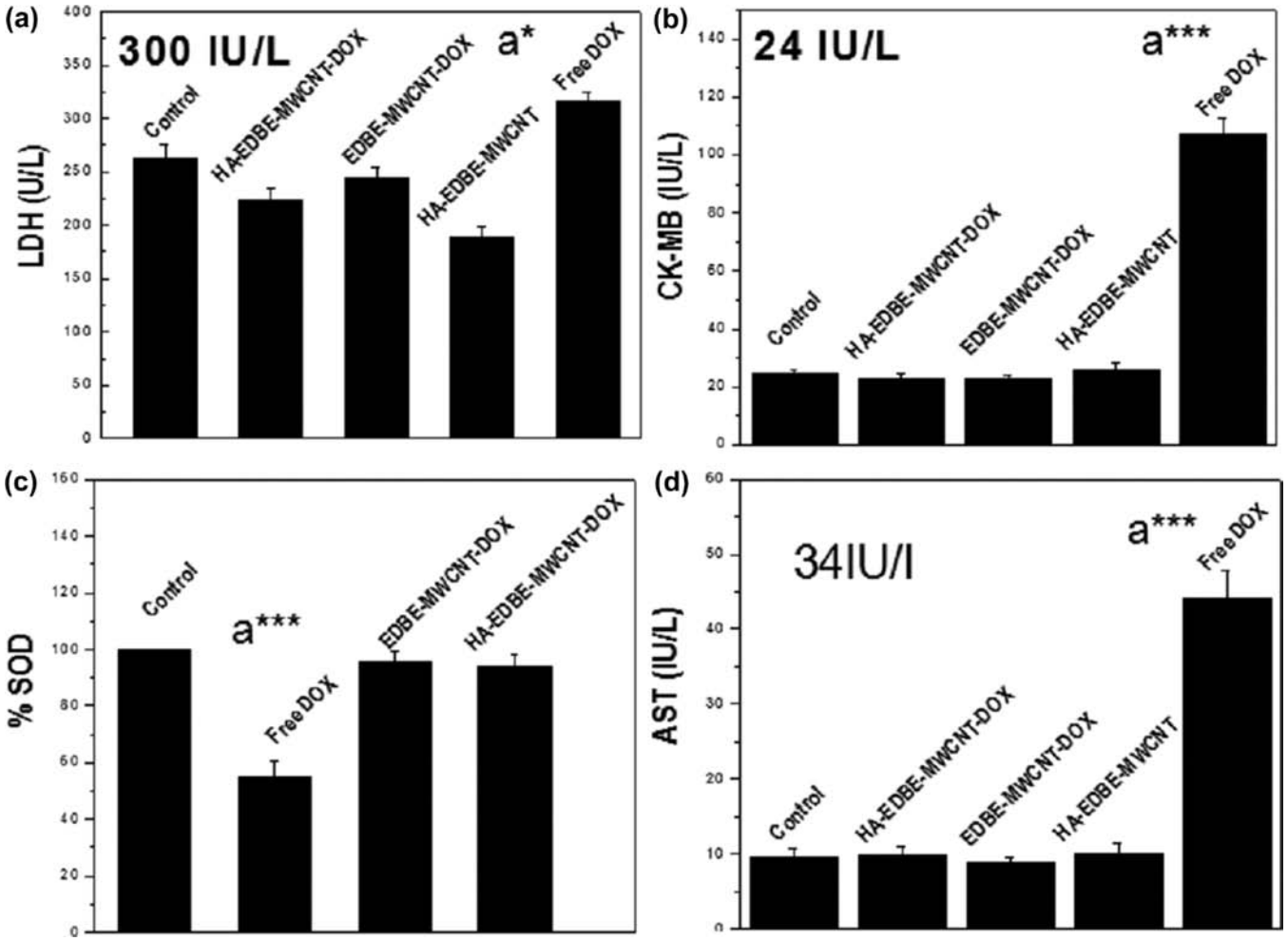

Figure 8. Evaluation of various cardiotoxicity parameters: (a) LDH; (b) CK-MB; (c) SOD; and (d) AST in tumor bearing rats treated with free DOX/DOX-loaded MWCNTs) [a* w.r.t. control (***$p < 0.001$, **$p < 0.01$, *$p < 0.05$); ULN = upper limit of normal].

various cardiotoxicity marker levels, both MWCNT-EDBE-DOX and MWCNT-EDBE-HA-DOX showed marked depreciation in cardiotoxicity as compared to free DOX. It is clear from Figure 8a,b that, after 10 days of treatment, LDH level in heart tissue and CK-MB level in the plasma were significantly increased in the animal groups treated with free DOX. Conversely, LDH and CK-MB levels of various CNT-treated groups showed insignificant differences from the control group. Concomitantly, SOD levels in the heart homogenate decreased in animals treated with free DOX, while both MWCNT-EDBE-DOX and MWCNT-EDBE-HA-DOX showed comparable SOD activity with respect to control (Figure 8c). Additionally, the AST level of free DOX treated rats was significantly elevated, indicative of myocardial infarction, whereas rats treated with functionalized CNTs showed insignificant differences from the control (Figure 8d). As in the case with rats, DOX delivered through HA-MWCNTs was devoid of any detectable cardiotoxity, hepatotoxicity, and nephrotoxicity in mice (see Supporting Information Figures S8, S9). These results overall suggest that the delivery property of MWCNTs is effectively combined with the targeting property of HA to augment the anticancer activity of DOX against hyaluronate receptor bearing tumor cells, while reducing the toxicity associated with both drug and the carrier system.

CONCLUSIONS

In conclusion, the delivery property of MWCNTs has been successfully blended with the targeting property of HA to augment the antitumor activity of DOX against HR over-expressing cancer cells while reducing the drug-associated cardiotoxicity. The therapeutic conjugate was further labeled with a near-infrared fluorescent dye, Alexa-Fluor-647 (AF-647), and radiotracer Technetium-99m to track the intracellular trafficking and biodistribution of the conjugate via optical imaging and scintigraphic techniques. Studies related to the evaluation of long-term toxicity and fate of DOX-loaded, HA-tethered MWCNTs is currently underway in our laboratory. The results may be reported in due course. Overall, the carrier system, developed in course of the present study, may expand the therapeutic transom for a broad spectrum of anticancer drugs and considered for clinical applications.

ASSOCIATED CONTENT

Supporting Information

Methods of surface oxidation of pristine MWCNTs, colorimetric assay for quantification of surface amine density, in vitro drug loading studies, radiolabeling studies, in vivo stability studies, toxicity studies, surface chemistry analysis of f-MWCNTs using FTIR and HRMAS NMR spectroscopy, quantification of functional molecules associated with

dx.doi.org/10.1021/bc300248t | Bioconjugate Chem. 2012, 23, 2201−2213

MWCNTs via TG analysis, stability of HA-MWCNTs in aqueous medium, DOX loading on HA-MWCNTs, results of competitive inhibition and apoptosis study, in vitro and in vivo stability of radiolabeled formulations and results of in vivo toxicity in mice. This material is available free of charge via the Internet at http://pubs.acs.org.

AUTHOR INFORMATION

Corresponding Author

*Tel.: +91172-2292055, Fax: +91172-2214692 E-mail addresses: sanyogjain@niper.ac.in, sanyogjain@rediffmail.com.

Notes

The authors declare no competing financial interest.

ACKNOWLEDGMENTS

The authors are thankful to Indian Council of Medical Research (ICMR) and Department of Science & Technology (DST), Government of India, New Delhi, for financial support. M.D. and R.P.S. are grateful to Department of Science and Technology (DST), GOI, New Delhi, for providing post-doctoral and senior research fellowships, respectively. Director NIPER and Director INMAS are duly acknowledged for providing the necessary infrastructure and facilities. The authors are grateful to Dr. Anil K. Mishra and his group, DCRS, INMAS for providing necessary facilities for radio-labeling and scintigraphy studies. Thanks are due to Dr. Ravi S. Amarpati, SAIF, Central Drug Research institute (CDRI, Lucknow) for assistance with HRMAS analysis. Technical assistance of Mr. Dinesh Singh Chauhan and Mr. Rahul Mahajan is also acknowledged.

REFERENCES

(1) Liu, Z., Cai, W., He, L., Nakayama, N., Chen, K., Sun, X., Chen, X., and Dai, H. (2007) In vivo biodistribution and highly efficient tumour targeting of carbon nanotubes in mice. *Nat. Nanotechnol. 2*, 47−52.

(2) Bottini, M., Cerignoli, F., Dawson, M. I., Magrini, A., Rosato, N., and Mustelin, T. (2006) Full-length single-walled carbon nanotubes decorated with streptavidin-conjugated quantum dots as multivalent intracellular fluorescent nanoprobes. *Biomacromolecules 7*, 2259−2263.

(3) Kostarelos, K., Lacerda, L., Pastorin, G., Wu, W., Wieckowski, S., Luangsivilay, J., Godefroy, S., Pantarotto, D., Briand, J. P., and Muller, S. (2007) Cellular uptake of functionalized carbon nanotubes is independent of functional group and cell type. *Nat. Nanotechnol. 2*, 108−113.

(4) Pastorin, G. (2009) Crucial functionalizations of carbon nanotubes for improved drug delivery: a valuable option? *Pharm. Res.*, 746−769.

(5) Liu, Z., Davis, C., Cai, W., He, L., Chen, X., and Dai, H. (2008) Circulation and long-term fate of functionalized, biocompatible single-walled carbon nanotubes in mice probed by Raman spectroscopy. *Proc. Natl. Acad. Sci. U.S.A. 105*, 1410.

(6) Datsyuk, V., Kalyva, M., Papagelis, K., Parthenios, J., Tasis, D., Siokou, A., Kallitsis, I., and Galiotis, C. (2008) Chemical oxidation of multiwalled carbon nanotubes. *Carbon 46*, 833−840.

(7) Dhar, S., Liu, Z., Thomale, J., Dai, H., and Lippard, S. J. (2008) Targeted single-wall carbon nanotube-mediated Pt (IV) prodrug delivery using folate as a homing device. *J. Am. Chem. Soc. 130*, 11467−11476.

(8) Heister, E., Neves, V., Tîlmaciu, C., Lipert, K., Beltrán, V. S., Coley, H. M., Silva, S. R. P., and McFadden, J. (2009) Triple functionalisation of single-walled carbon nanotubes with doxorubicin, a monoclonal antibody, and a fluorescent marker for targeted cancer therapy. *Carbon 47*, 2152−2160.

(9) Bourguignon, L. Y. W., Zhu, H., Shao, L., and Chen, Y. W. (2000) CD44 interaction with tiam1 promotes Rac1 signaling and hyaluronic acid-mediated breast tumor cell migration. *J. Biol. Chem. 275*, 1829.

(10) Luo, Y., and Prestwich, G. D. (1999) Synthesis and selective cytotoxicity of a hyaluronic acid- antitumor bioconjugate. *Bioconjugate Chem. 10*, 755−763.

(11) Osorio, A. G., Silveira, I. C. L., Bueno, V. L., and Bergmann, C. P. (2008) H2SO4/HNO3/HCl–Functionalization and its effect on dispersion of carbon nanotubes in aqueous media. *Appl. Surf. Sci. 255*, 2485−2489.

(12) Pompeo, F., and Resasco, D. E. (2002) Water solubilization of single-walled carbon nanotubes by functionalization with glucosamine. *Nano Lett. 2*, 369−373.

(13) Liu, Z., Sun, X., Nakayama-Ratchford, N., and Dai, H. (2007) Supramolecular chemistry on water-soluble carbon nanotubes for drug loading and delivery. *ACS Nano 1*, 50−56.

(14) Prestwich, G. D., Luo, Y., Kirker, K. R., Ziebell, M. R., and Shelby, J. (2002) Hyaluronan biomaterials for targeted drug delivery and wound healing. *Hyaluronan*, 277.

(15) Swarnakar, N. K., Jain, A. K., Singh, R. P., Godugu, C., Das, M., and Jain, S. (2011) Oral bioavailability, therapeutic efficacy and reactive oxygen species scavenging properties of coenzyme Q10-loaded polymeric nanoparticles. *Biomaterials 32*, 6860−6874.

(16) Jain, A. K., Swarnakar, N. K., Das, M., Godugu, C., Singh, R. P., Rao, P. R., and Jain, S. (2011) Augmented anticancer efficacy of doxorubicin loaded polymeric nanoparticles after oral administration in breast cancer induced animal model. *Mol. Pharmaceutics 8*, 1140−51.

(17) Von Knethen, A., and Brune, B. (1997) Cyclooxygenase-2: an essential regulator of NO-mediated apoptosis. *FASEB J. 11*, 887.

(18) Jain, S., Thakare, V. S., Das, M., Godugu, C., Jain, A. K., Mathur, R., Chuttani, K., and Mishra, A. K. (2011) Toxicity of multiwalled carbon nanotubes with end defects critically depends on their functionalization density. *Chem. Res. Toxicol 24*, 2028−2039.

(19) Penno, M. B., August, J. T., Baylin, S. B., Mabry, M., Linnoila, R. I., Lee, V. S., Croteau, D., Yang, X. L., and Rosada, C. (1994) Expression of CD44 in human lung tumors. *Cancer Res. 54*, 1381.

(20) Zhou, F., Xing, D., Wu, B., Wu, S., Ou, Z., and Chen, W. R. (2010) New insights of transmembranal mechanism and subcellular localization of noncovalently modified single-walled carbon nanotubes. *Nano Lett. 10*, 1677−1681.

(21) Pandey, M. S., Harris, E. N., Weigel, J. A., and Weigel, P. H. (2008) The cytoplasmic domain of the hyaluronan receptor for endocytosis (HARE) contains multiple endocytic motifs targeting coated pit-mediated internalization. *J. Biol. Chem. 283*, 21453.

(22) Strushkevich, N. V., Azeva, T. N., Lepesheva, G. I., and Usanov, S. A. (2005) Role of positively charged residues lys267, lys270, and arg411 of cytochrome p450scc (CYP11A1) in interaction with adrenodoxin. *Biochemistry (Moscow) 70*, 664−671.

(23) Christensen, K. A., Myers, J. T., and Swanson, J. A. (2002) pH-dependent regulation of lysosomal calcium in macrophages. *J. Cell Sci. 115*, 599.

(24) Yadav, A. K., Mishra, P., Jain, S., Mishra, A. K., and Agrawal, G. P. (2008) Preparation and characterization of HA-PEG-PCL intelligent core-corona nanoparticles for delivery of doxorubicin. *J. Drug Targeting 16*, 464−478.

(25) Jain, S., Mathur, R., Das, M., Swarnakar, N. K., and K., M. A. (2011) Synthesis, pharmacoscintigraphic evaluation and antitumor efficacy of methotrexate loaded, folate conjugated, stealth albumin nanoparticles. *Nanomedicine 6*, 1733−1754.

(26) Qu, G., Bai, Y., Zhang, Y., Jia, Q., Zhang, W., and Yan, B. (2009) The effect of multiwalled carbon nanotube agglomeration on their accumulation in and damage to organs in mice. *Carbon 47*, 2060−2069.

(27) Yadav, A. K., Mishra, P., Mishra, A. K., Jain, S., and Agrawal, G. P. (2007) Development and characterization of hyaluronic acid-anchored PLGA nanoparticulate carriers of doxorubicin. *Nanomedicine: Nanotechnology, Biology and Medicine 3*, 246−257.

(28) Meng, J., Duan, J., Kong, H., Li, L., Wang, C., Xie, S., Chen, S., Gu, N., Xu, H., and Yang, X. D. (2008) Carbon nanotubes conjugated to tumor lysate protein enhance the efficacy of an antitumor immunotherapy. *Small 4*, 1364−70.

Hyaluronate tethered multiwalled carbon nanotubes: A rationally designed "smart" platform for multimodal, tumor-targeted delivery of doxorubicin

Satyajit R. Datir[1], *Manasmita Das*[1], *Raman Preet Singh*[1] and *Sanyog Jain*[1,*]

Centre for Pharmaceutical Nanotechnology, Department of Pharmaceutics, National Institute of Pharmaceutical Education and Research (NIPER), Sector 67, SAS Nagar (Mohali) Punjab INDIA160062

Methods

Surface oxidation of pristine MWCNTs. For surface oxidation, pristine MWCNTs with approximate length ranging from 1-2 µm and diameter 20-30 nm were dispersed in a 3:1 (v/v) mixture of H_2SO_4:HNO_3 (20 ml) via ultrasonication for 5 minutes. Thereafter, the dispersion was refluxed at 80°C using a hot plate cum magnetic stirrer at 900 rpm. Oxidation was continued for 3 h. After oxidation, the suspension of MWCNTs in acid was diluted up to 5 times of its volume and centrifuged at 21000 rpm. This washing was repeated at least twice for complete removal of acid. Oxidized MWCNTs obtained were further dispersed in acetone and centrifuged, following which the supernatant was discarded and MWCNTs was air-dried to obtain fine powders of oxidized CNTs.

Colorimetric assay for quantification of surface amine density. MWCNTs (5mg) were paced in 1.5ml eppendorff and washed (4 times) with 1ml of coupling solution [0.8% (v/v)] glacial acetic in dry methanol. Subsequently 1ml of 4-nitrobenzaldehyde solution (7mg in 10ml of coupling solution) was added to the CNTs dispersion and the suspension was allowed to react for 3h with gentle end over end rotation. After removal of the supernatant and washing (4 times with 1ml of coupling solution), 1ml of hydrolysis solution (75 ml of H_2O, 75ml of MeOH, 0.2 ml of glacial acetic acid) was then added to the dispersion of CNTs and the tube was shaken for additional 1 hour. The supernatent was then removed from the particles by centrifugation and its absorbance was measured at 282 nm. The amount of 4-nitrobenzaldehyde in the hydrolysis solution was calculated by use of a calibration curve constructed from a range of standard solution of 4-nitrobenzaldehyde prepared separately.

In vitro drug loading studies

Optical absorbance and drug-nanotube interaction. DOX nanotube interaction was studied by recording the fluorescence quenching of DOX in presence of MWCNTs, using luminescence spectroscopy. Emission spectra of 10 µg/ml doxorubicin.HCL (DOX) solution alone and suspension

containing 10µg/ml DOX and various concentration of f-MWCNTs (1:2, 1:1 and 2:1 CNT:DOX w/w) was recorded at 480nm. The corresponding nanotube solution was taken as blank.

Radiolabeling studies. For radiolabeling of CNTs, 0.1 ml of sodium pertechnetate ($^{99m}TcO_4$-, approximately 2µCi, obtained by solvent extraction method from molybdenum) was mixed with 50 ml of $SnCl_2$ solution (defined concentration to give 25–200 mg of $SnCl_2$ in 50ml) in 10% acetic acid solution to reduce technetium. The solution pH was adjusted to 6.5–7.0 using 0.5 (M) sodium bicarbonate solution. To this mixture, 1ml of either DOX solution or nanotube suspension (1mg/ml) were added and incubated for 15 min at room temperature. This procedure could also lead to the formation of radio colloids (reduced and hydrolyzed Tc-99m, TcO_2) that were separated from the radio-labeled formulations via centrifugation, followed by repeated washing with distilled water. The purified radio-labeled formulations, thus obtained, were stored in sterile evacuated sealed vials for subsequent studies.

Labeling efficiency of the purified radio-labeled formulations was determined by ascending instant thin layer chromatography (ITLC) using silica gel (SG)-coated fibres sheets of approximately 10 cm in length (Gelman Science Inc., Ann Arbor, MI, USA). The ITLC was performed using 100% acetone as the mobile phase. A tiny drop (2–3ml) of the radio-labeled formulation was applied at a point 1 cm from one end of an ITLC-SG strip. The strip was developed in acetone and the solvent front was allowed to reach approximately 8cm from the origin. The strip was cut into two equal halves and the radioactivity in each segment was determined in a well-type g-ray counter (Gamma ray scintillation counter, Type CRS 23C; Electronics Corporation of India Ltd, Mumbai, India). The free $^{99m}TcO_4^-$ moved with the solvent (R_f = 0.9), while the radio-labeled formulation remained at the point of application. The percentage of labeling efficiency was calculated from the following formulae:

$$\% \text{ labeling efficiency} = B \times 100/ (T+B);$$

where, T and B represent the counts at the top and bottom respectively.

For determination of *in vitro* stability, 100 µl of the labeled drug/ formulations was mixed with 2.0 ml of PBS (pH 7.4) and incubated at room temperature and the change in labeling efficiency was monitored over a period of 24 h by ITLC as described before.

***In vivo* stability studies.** *In vivo* stability studies were performed in normal, healthy, female New Zealand rabbits weighing 2.5–3.5 kg. All animal experiments were carried out under the guidelines compiled by the Committee for the Purpose of Control and Supervision of Experiments on Animals, Ministry of

Culture, Government. of India and all the protocols were approved by the institutional animal ethics committee of the Institute of Nuclear Medicine and Allied Science. Rabbits were injected with approximately 500 μCi of ^{99m}Tc-labeled formulations through the dorsal ear vein. Blood was withdrawn through the dorsal vein of the other ear at different periodic intervals and spotted on the ITLC strips; the ITLC was carried out as previously described to estimate the possible separation of free 99mTc/ degradation of the complex. Assuming total blood volume as 7% of the bodyweight, persistence of activity in circulation was calculated using the following formula: *% Radioactivity (persisting in blood) = (Weight of the sample total counts injected)/ (Counts in the sample total blood volume 100)*

Toxicity studies

General Experimental Designs

For assessment of free DOX and functionalized MWCNT induced hepatotoxicity and nephrotoxicity in mice, female Swiss mice (weighing ~ 25g) were procured from Central Animal Facility, NIPER Mohali. For hepatotoxicity and nephrotoxicity evaluation, animals were divided into 3 and 6 groups respectively with each group containing 6 animals. DOX-deprived MWCNT-EDBE and HA-EDBE-MWCNT were administered into the first six groups of mice (n=6) through single dose of intravenous injection via tail vein. The seventh group was kept as control and received normal saline in similar manner. The mice were housed in plastic cages, fed with commercial diet, and given water ad libitum. The cages were placed in a conventional room, which was air-conditioned at 23°C with 55–70% humidity and 12 h light/12 h dark cycle. After the mice were exposed by intravenous injection, general conditions including appetite, activity and body weight were monitored and recorded at regular interval. At the end of 10 days, blood was collected through cardiac puncture to analyze the various biochemical parameters (AST, ALT, BUN etc.). Thereafter, animals were humanely sacrificed and the individual organs (viz. liver, spleen, kidney and lungs) in control as well as treated groups were excised and weighed to determine the organ indices. Organ index, which is a marker of general organ level toxicity, was measured by calculating the ratio of increase in organ weight due to inflammation and cellular infiltration to the reduction in total body weight. Oxidative stress markers viz. SOD and MDA were determined from the liver homogenate according to our previously reported protocol**.**

Determination of serum biochemical parameters. Serum biochemical parameters AST and ALT were analyzed using commercially available kits (ACCUREX, Biomedical Pvt. Ltd. Mumbai, India). LDH level in plasma was analyzed using commercially available kits, based on the method provided by the manufacturer instructions supplied with the commercial kits.

Lipid Peroxidation in liver: TBARS Estimation. The malondialdehyde (MDA) content, a measure of lipid peroxidation, was assayed in the form of thiobarbituric acid reacting substances (TBARS) by method reported by Okhawa et al.(*1*). Briefly, 100 µl tissue (liver/ heart) homogenate was mixed with 100 µl SDS (8.1%), 750 µl of thiobarbituric acid (0.8%) and 750 µl of 20% glacial acetic acid (pH 3.5). Excised livers from mice were homogenized in 5 volumes of ice cold PBS (pH 7.4) using polytron homogenizer. The total homogenate was used for the MDA estimation. The spectrophotometric method as reported in the literature was followed for MDA estimation. Briefly, 100 µl tissue homogenate was mixed with 100 µl SDS (8.1%), 750 µl of thiobarbituric acid (0.8%) and 750 µl of 20% glacial acetic acid (pH 3.5). Contents were mixed and incubated at 100° C for 1 h followed by cooling to room temperature and the contents were centrifuged at 10,000 rpm for 5 min to collect the supernatant. Absorbance of supernatant was measured at 532 nm. MDA standards of various concentrations were used for the standard curve. From the standard curve MDA levels were measured and expressed as nmol MDA/mg protein.

SOD activity in liver. Superoxide dismutase (SOD) represents a class of enzymes that catalyzes the dismutation of superoxide into oxygen and hydrogen peroxide. To determine reduced SOD activity in liver, fresh livers excised from various treated groups of mice were immersed in cold saline, blotted with filter paper, weighed quickly (for determination of liver indices) and then homogenized in ice-cold preparation buffer (1 mmol Tris-HCl + 0.1 mmol EDTA-2Na + 0.8% NaCl, pH = 7.4) to yield 10% (w/v) homogenate. Homogenates were centrifuged at 2000 rpm for 8 min at 4°C and the supernatants were either used immediately for the assays or stored at −80°C until used for assay. Total SOD levels in the supernatant were also determined by using spectrophotometric diagnostic kits (ACCUREX, Biomedical Pvt. Ltd. Mumbai, India) based on the method of Beauchamp and Fridovic (*2*), which were compared with a standard curve of 10 μg ml^{-1} SOD solution.

Determination of nephrotoxicity parameters. Blood urea nitrogen (BUN) level was analyzed using commercially available albumin and BUN kits purchased from ACCUREX, Biomedical Pvt. Ltd. Mumbai, India.

Supporting Figures and Tables

Surface chemistry of f-MWCNTs. Oxidized MWCNTs present a broad band at 1634.08 cm^{-1}, attributed to free carboxyl groups on the surface (**Fig. 3**). The observed blue shift may be a consequence of intra-tube hydrogen bonding between the surface carboxyl groups. Following reaction with EDBE, characteristic vibrations of amide I (-C=O stretching) and amide II (-NH bending) were visualized at 1632.78 and 1559.16 cm^{-1} respectively, the latter being ascribed to the free amine groups on the surface of EDBE-MWCNTs. Careful analysis of the spectra shows that the intensity of CH_2 vibrations at 2856 and 2925 cm^{-1} increases with EDBE and HA conjugation. In this connection, it may be noted that definitive assignment of peaks following HA conjugation was not possible because HA presents characteristic bands in the range of 1560-1620 cm^{-1} (-C=O, COO^-). These bands overlap with the amide I and amide II bands of EDBE-MWCNTs, resulting in an inherent broadness over the range of 1400-1700 cm^{-1}. Remarkably, the FTIR spectrum of free HA [Figure S1A(c)] shows a prominent absorption at 3567 cm^{-1} attributed to the –OH bond of the –COOH group. In both HA-EDBE-MWCNT, this bond shifted to 3434 cm^{-1}, which could be attributed to –NH bond

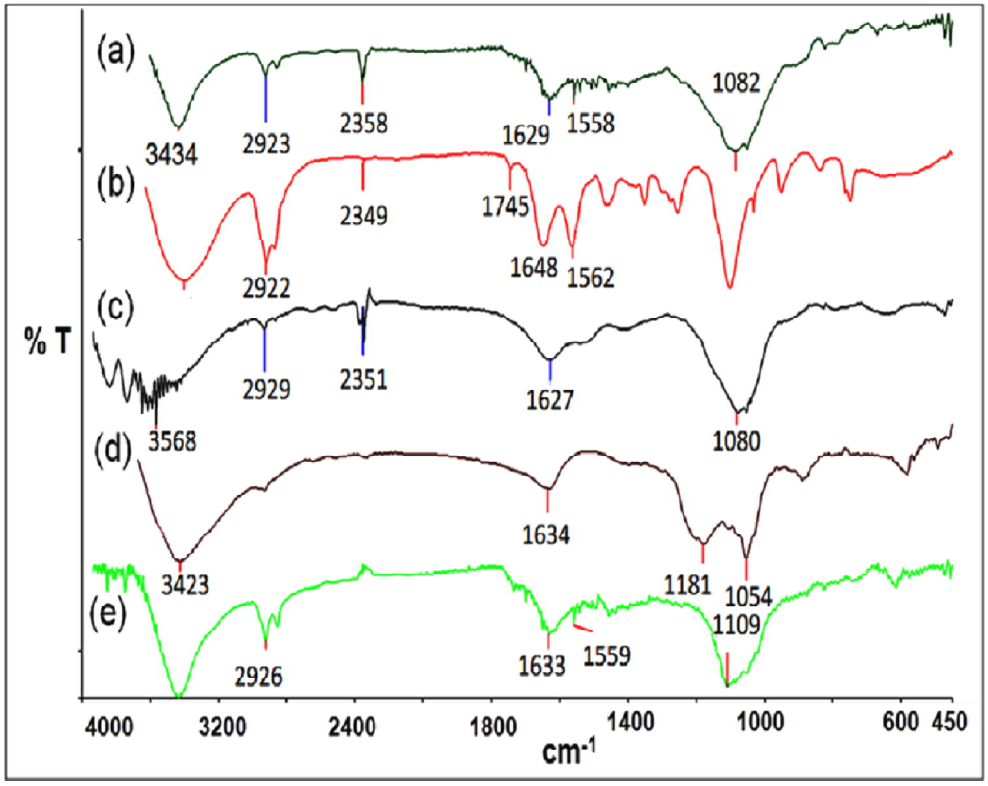

characteristics of the amide linkage between HA and EDBE.

Fig. S1 (A) FTIR spectra of **(a)** MWCNT-EDBE-HA; **(b)** HA-EDBE-NH2; **(c)** Free HA; **(d)** Oxidized MWCNT (after 3 h of acid-treatment) and **(e)** MWCNT-EDBE-NH_2

To ensure covalent bond formation between HA and EDBE, the FTIR spectra of a physical mixture of HA, EDBE and CNTs (taken in 1:1:1 molar ratio) were recorded. The spectrum was considerably different from the conjugate substantiating formation of a covalent bond between HA and EDBE-MWCNTs.

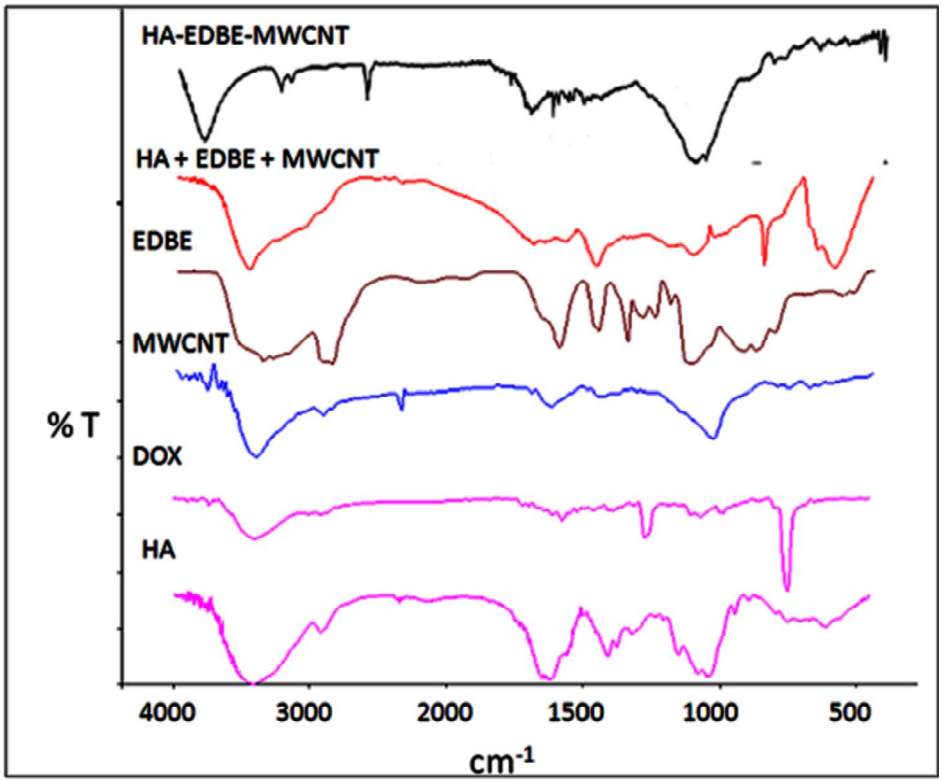

Fig. S1 (B) FTIR spectra of **(a)** HA + EDBE + MWCNT (physical mixture); **(b)** EDBE; **(c)** MWCNT; **(d)** DOX and **(e)** HA

For further detailed structure-resolved analysis of the organic layer associated with our multifunctional MWCNTs, high-resolution magic angle spinning NMR analysis (HRMAS-NMR) was performed (Fig. S2). The ^{1}H NMR spectrum of oxidized MWCNTs is almost flat and noisy excepting for the solvent peak for DMSO at δ 2.49 ppm. The ^{1}H NMR spectrum of EDBE-MWCNTs presented characteristic signals of –O-CH_2-CH_2-O and –C=O-NH-CH_2-CH_2 protons of EDBE in the range of 3.2-3.8 ppm. The chemical shifts at δ 2.1 and 1.6 ppm may be ascribed to the two chemically distinct, methylene protons of surface-pendant ethylene amine (-CH_2-CH_2-NH_2) units, adjacent to the –O- CH_2-CH_2-O- bridge of EDBE. In the NMR spectrum of HA-EDBE-MWCNTs, an apparent *N*-acetylate proton peak ($NCOCH_3$), characteristic of HA, was detected at δ 2.3 ppm. The other proton peaks that ranged between 3.5–4.0 ppm could not be distinguished because of the overlap of glucose unit peak of HA and ethylene-dioxy unit of EDBE.

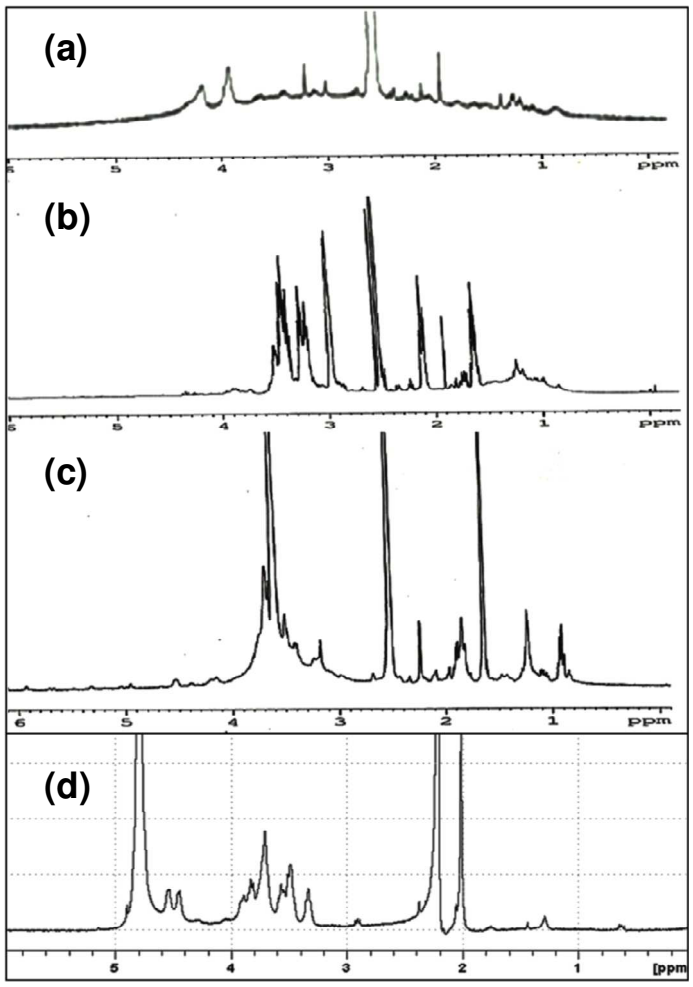

Figure S2. HRMAS-NMR spectra of oxidized MWCNTs **(a);** EDBE-MWCNTs **(b)** and HA-EDBE-MWCNTs **in** DMSO-d6 **(c)** NMR spectrum of plain HA in D_2O **(d).**

While FTIR and HRMAS-NMR analysis confirmed the successful immobilization of HA on the surface of MWCNTs, thermal analysis was used to quantify the amount of different functional molecules immobilized per unit mass of CNTs. Comparative thermogram of pristine and oxidized MWCNTs is shown in Fig. **S3A**(a, b). **Fig. S3A (c)** represents the differential thermogram where trough in the 1st derivative line shows the weight loss in the respective temperature range. Weight loss in the range 0-150°C was due to water molecule adsorbed on the surface. Weight loss in the range of 150-350°C was due to carboxylic groups generated on the surface of CNT after oxidation. Weight loss in the range 350°-450°C was due to elimination of hydroxyl functionalities attached to the ox-MWCNTs surface and above 500°C was due to disordered carbon [(3)]. Overlapped TG thermogram of pristine and oxidized MWCNTs clearly indicates that there is no weight loss in pristine MWCNTs (lower line) upto 700°C whereas in case of oxidized MWCNTs (upper line), troughs in the 1st derivative line are clear indication of weight loss. Step loss in oxidized MWCNTs of 7.97% (0.64 mg) was used to estimate the number of COOH groups generated on the surface of MWCNTs. The number of moles of $–CO_2H$ groups per unit mass of MWCNTs was calculated by dividing the weight loss of oxidized MWCNTs in between 150-350° C with the molecular weight of $–CO_2H$. The amount of $–CO_2H$ groups per unit mass of CNTs was determined to be around 0.0145 mmoles/ mg.

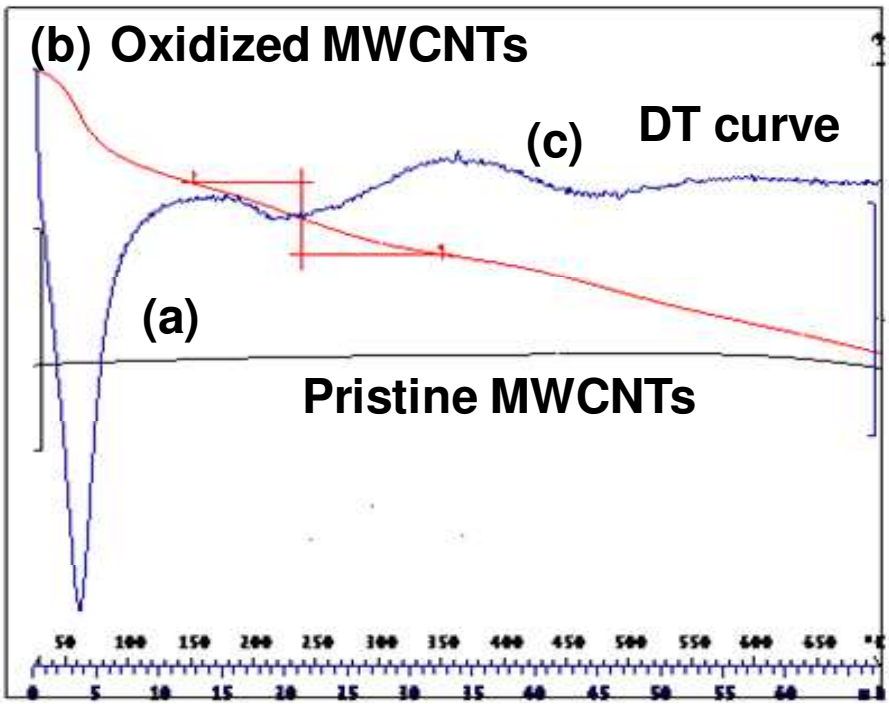

Figure S3 (A): **(a, b)** TG thermogram of pristine and oxidized MWCNTs respectively; **(c)** DT thermogram of oxidized MWCNTs. The number of moles of $–CO_2H$ groups per unit mass of MWCNTs was estimated by dividing the weight loss of oxidized MWCNTs in between 150-350° C with the molecular weight of $–CO_2H$.

To further quantify the extent of EDBE conjugation on MWCNTs, the TG thermogram of EDBE-MWCNTs was compared with ox-MWCNTs. Plain EDBE shows weight loss in the range 0-170°C (**Fig.**

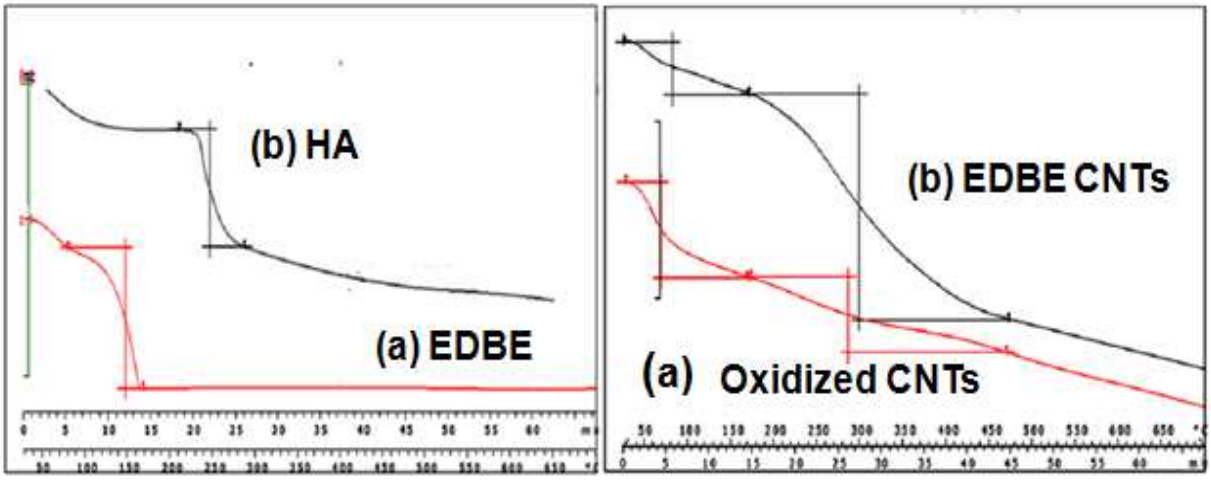

S3B) Following EDBE functionalization, MWCNTs presented only 6.2% weight loss up to 170°C which is far less compared to that of oxidized MWCNTs (13.4%). Notably, a sharp weight loss (~26.45%) was observed in the range of 170-460°C, which was almost 2.5 times higher than oxidized MWCNTs (10.5%) (**Fig. S3C**). This shift in weight loss may be due to extensive and strong covalent binding of EDBE with carboxylic groups of oxidized MWCNTs leading to increased bond strength and subsequently higher degradation temperature. Weight loss for EDBE was determined to be around (26.45%-10.5%) = 15.95% which corresponded to approximately 1.07μmol EDBE/mg of CNTs.

Fig. S3B. TG thermogram of **(a)** EDBE and **(b)** HA; **(C)** Overlapped TG thermogram of **(a)** Oxidized MWCNTs and **(b)** EDBE CNTs. TG thermogram of EDBE-MWCNTs display sharp weight loss in the range of 170-460°C. The weight loss over this range is almost 2.5 times higher than oxidized MWCNTs. The shift in weight loss is attributed to extensive and strong covalent binding of EDBE with carboxylic groups of oxidized MWCNTs, which is believed to increase the bond strength and shift the degradation temperature.

After HA conjugation, we checked the weight loss in the temperature range of 180-300°C, which is a fingerprint region for HA. In case of HA-EDBE-MWCNTs, weight loss was detected in between 180-300°C only and no shift in this particular temperature range was observed.

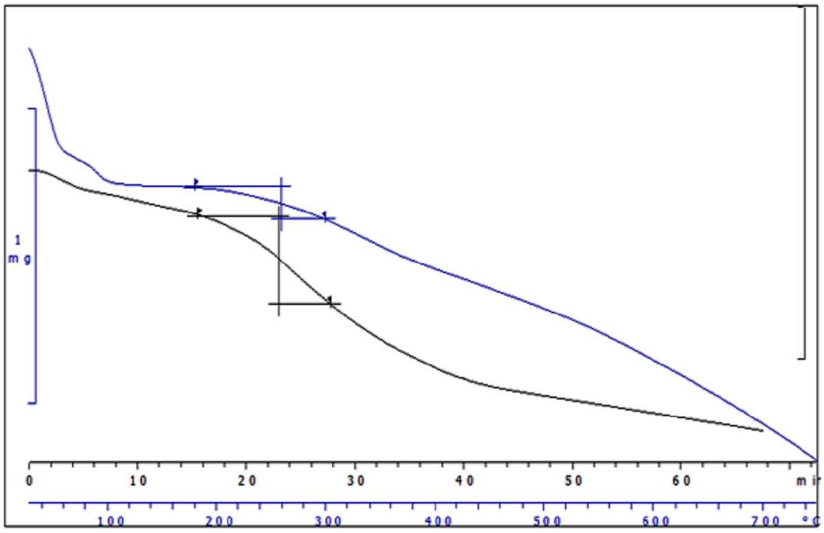

Fig. S3D. TG thermogram of HA: Weight loss in the temperature range of 180-300°C was estimated for the calculation of HA bound per unit mass of CNTs

Weight loss for MWCNT-EDBE-HA in the specified temperature region was 13.13% where as MWCNT-EDBE exhibited only 2% weight loss between 180-300°C. From these values, the weight loss due to HA was calculated as (13.13%-2%) = 11.13%, which corresponded to around 0.022 µmol HA/ mg of CNTs. **Table S1** summarizes the temperature range of thermal degradation, respective weight loss and the amount of various functional molecules immobilized per unit mass of MWCNTs.

Table S1. Quantification of various functional groups/ molecules on MWCNTs using TGA

Formulation	Functional molecule	Thermal degradation range	Weight loss (mg/mg of formulation)	Amount of functional molecule (µmole/mg)
Oxidized MWCNT	-COOH	150-350˚C	0.079	1.8
EDBE-MWCNT	-EDBE	170-470˚C	0.264	1.07
HA-EDBE-MWCNT	-HA	180-300˚C	0.252	0.022

Time (h)	1	2	3	4	6
Size (nm)	173.8±4.2	175.5±6.3	176.2±8.4	177.8±7.3	177.5±8.9
Zeta (mV)	-42±4	-42±4	-43±5	-43±5	-44±6

PDI	0.310±0.023	0.315±0.042	0.319±0.022	0.311±0.028	0.317±0.024

Table S2. Stability of HA-MWCNTs in aqueous medium[a]

DOX loading on HA-MWCNTs. MWCNTs offer very high surface area for drug loading through π-π stacking. The interaction between drug and nanotubes was studied using luminescence spectroscopy, as described in the Methods section (**Fig. S3**). Starting with 2:1 ratio (w/w) of DOX: MWCNTs, the ratio of drug: nanotube was increased up to 1:2 (w/w). The extent of quenching increased with the increasing ratio of CNT: DOX. These observations suggest that π-π stacking interactions occur between the aromatic structure of the drug and nanotube surface with maximum interaction being observed at f-MWCNT: drug ratio of 2:1 (w/w). This particular ratio was finally selected for further drug loading studies.

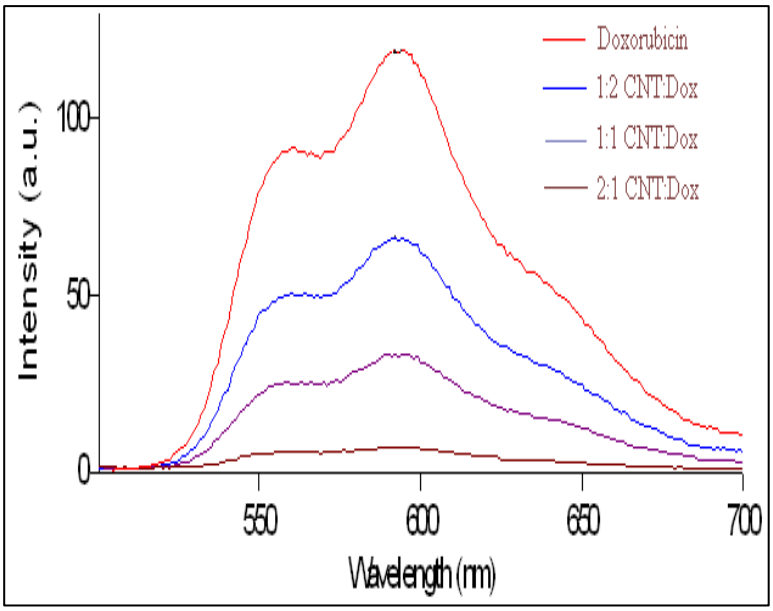

Fig. S4. DOX-nanotube interaction studied via fluorescence spectroscopy. Fluorescence of DOX is quenched on increasing the ratio of CNT: DOX

In order to ensure maximum drug loading on CNTs, the loading process was optimized with respect to various physicochemical parameters such as loading pH, spacer length between HA and MWCNTs and

molecular weight of HA [**Table S3(a-b)].** To evaluate the effect of pH on DOX loading, we selected four different pH values ranging from acidic to basic: pH 5.5, 7.4, 8 and 9. A significant improvement in entrapment efficiency from 30.525±0.625 to 98.073±1.051 and practical loading from 10.173±0.208 to 30.021±0.350 was observed on increasing the pH from 5.5 to 7.4. At pH 5, the free amine group of DOX remains highly protonated rendering the drug highly hydrophilic. On increasing the pH to 8, this amine group deprotonates so that the drug becomes relatively hydrophobic. Since CNTs are also hydrophobic, an increase in pH enhances the interaction between CNT and DOX, thereby increasing the drug loading. On further increasing the pH, a slight increase in drug loading was evident. However, considering the proclivity of DOX to degrade at alkaline pH, HA-conjugates with DOX loaded at pH 7.4 was used for subsequent *in vitro* and *in vivo* evaluation. To further check how the spacer length influences the drug loading efficiency, DOX loading studies were performed on both HA-PEG-3000-MWCNTs and HA-EDBE-MWCNTs. Notably, change of spacer had little or practically no effect on DOX loading efficiency. Having evaluated the effect of pH and spacer length on the drug loading process, we sought to examine how DOX loading on MWCNTs depended on the molecular weight of HA. For this evaluation, we selected MWCNTs functionalized with two different types of HA: HA-5kDa and HA-120 kDa. When the MW of HA was increased from 5-120 kDa, drug encapsulation efficiency reduced drastically from 98% to 78%. The reduction, however, may be attributed to large meshwork formed by HA 120 kDa around nanotubes which restricts the π-π stacking interaction between DOX and MWCNTs. DOX was found to entangle in the large HA-PEG meshwork encompassing the MWCNT core and when routine washing was applied after drug loading to remove the free drug from MWCNTs, this entangled drug leeched away from hydrophilic meshwork of HA-EDBE. Interestingly, when the molecular weight of HA was lowered to 5 kDa, drug encapsulation efficiency significantly increased up to 99% and the value was near equivalent to oxidized MWCNTs. These results clearly indicate that as a targeting agent, HA-5 kDa has no detrimental influence on the π-π stacking interaction and loading efficiency of HA-MWCNT conjugates.

Table S3 (a) Drug loading on HA-EDBE-MWCNTs using HA M_W5 kDa[a]

HA-EDBE-MWCNTs	pH used for loading			
	5.5	**7.4**	**8**	**9**
Encapsulation efficiency (%)	29.541±0.934	99.102±0.536	98.869±1.037	96.202±1.253
Practical loading (%)	9.846±0.311	33.030±0.178	32.953±0.345	32.064±0.457

TableS3 (b) Drug loading on HA-EDBE-MWCNTs using HA M_W 120 kDa[a]

HA-EDBE-MWCNTs	pH used for loading

	5.5	7.4	8	9
Encapsulation efficiency (%)	10.325±1.146	78.020±0.425	80.795±1.047	80.354±0.638
Practical loading (%)	2.441±0.382	26.004±0.141	26.923±0.349	26.781±0.212

[a]All values unless otherwise stated are expressed as mean ± SD (n=6)

Competetive inhibition studies. For competitive inhibition study, A549 cells were incubated with HA-MWCNTs in absence and presence of HA. While blockage of HR hardly altered the internalization of HA deprived, EDBE-MWCNTs amine-functionalized, the uptake of HA-functionalized CNTs was significantly suppressed.

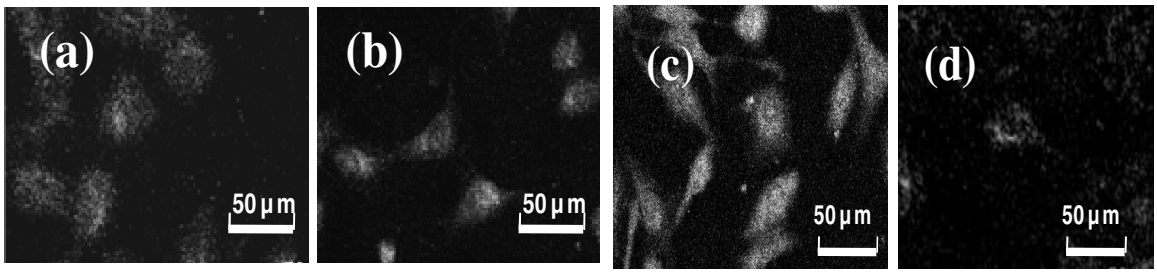

Fig. S5 (A). A549 cells incubated with **(a-b)** AF-647-EDBE-MWCNT in absence and presence of HA ; (B) AF-647-HA-EDBE-MWCNTs in absence of HA and presence of 0.1 mg/ ml HA

For quantification of cell uptake, cultured cells were exposed to 100µg/ml of different f-MWCNTs for 3h in absence and presence of HA. Thereafter, the culture medium was removed and cells were lyzed (200 µl of 0.1 % Triton X-100). The cell lysates were sonicated for 2-3 min to aid dispersion of MWCNTs. The concentration of f-MWCNTs in the cell lysates were determined by simple spectrophotometry. The optical density of CNTs was measured at 260 nm and concentrations of CNTs were determined from a standard plot.

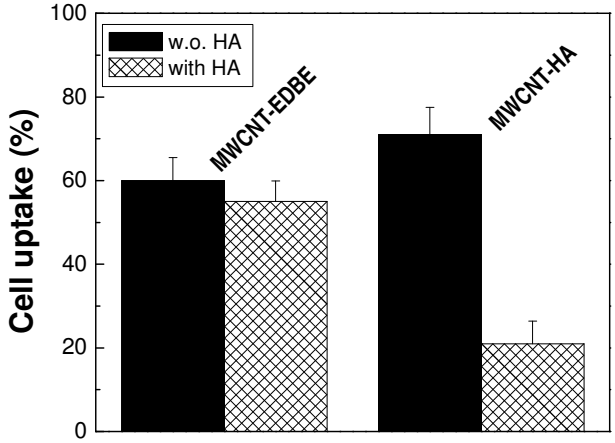

Fig. S5 (B). Uptake profile of MWCNT-EDBE and MWCNT-HA in absence and presence of HA. The uptake of HA-MWCNTs is significantly deteriorated in presence of HA suggesting the role of hyaluronate receptor in the internalization of HA-MWCNTs.

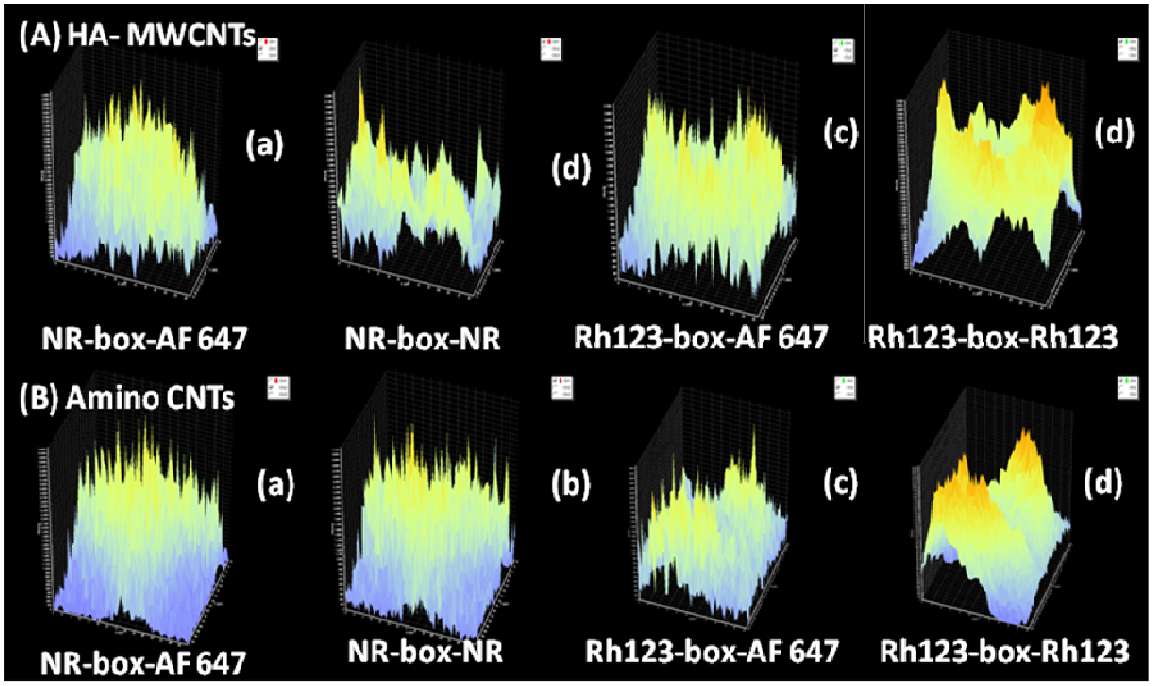

Fig. S6. Box colocalization analysis of **(A)** HA-MWCNTs and **(B)** Amino MWCNTs (EDBE-CNTs). In case of HA-MWCNTs, the AF-647 fluorescence shows good colocalization with both NR and Rh123 conferring the colocalization of HA-MWCNTs with both lysosome and mitochondria. In case of EDBE-MWCNTs, the AF-647 fluorescence shows appreciable colocalization with Rh123 but not with NR.

Apoptosis study. For evaluation of drug/ CNT induced apoptosis, A549 cells were incubated in PBS with 1µg/ml of free DOX & HA-CNTs containing equivalent amount of free drug. Representative confocal micrographs of Annexin V-Cy 3, PI and Rh 123 stained A549 cells have been furnished in **Fig. S7**. It is well known that Phosphatidylserine (PS) is present on the cytoplasmic side of the cell membrane and is externalized during apoptosis[4]. Annexin V binds to the externalized PS and labels the apoptotic cells (AV+). In **Fig. S7** [A (i) – C (i)] cells showing red fluorescence represent the Annexin V positive apoptotic cells. As evident from these images, no red fluorescence was detectable in the control cells whereas significant red fluorescence was displayed by cells incubated with free DOX as well as DOX loaded CNTs. The percentage of cells in early apoptotic cells was calculated by comparing the number of AV (+ve) with the total number of cells present in a particular field of view in the DIC image captured [**Fig. S7**, A (ii)-C (ii)].

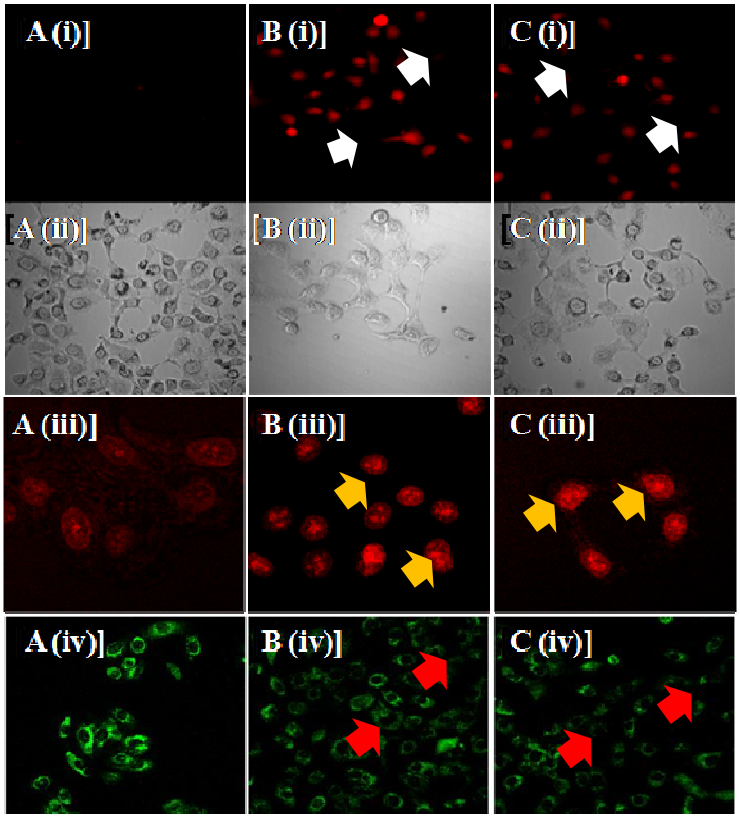

Fig. S7 Confocal Micrographs of A549 cells exposed to (A) PBS (control) (B) free DOX (1 µg/ ml) and (C) HA-EDBE-CNTs loaded with equivalent amount of free DOX for 24 h. (i), (ii) (iii) and (iv) of each incubation type represents the fluorescence images of Annexin V positive (apoptotic) cells, DIC images, fluorescence images of propidium iodide (PI) stained nuclei and Rhodamine 1,2,3 stained mitochondria respectively. The white, orange and red arrow represents AV (+ve) cells, condensed nuclei and depolarized mitochondria respectively.

It is worth mentioning that mitochondrial depolarization, nuclear condensation and fragmentation are some of the most important hallmarks of early and late apoptosis. While control cells showed no visible signs of cytotoxicity, cells incubated with free drug or drug loaded CNTs exhibited prominent features of early and late apoptosis including mitochondrial depolarization and nuclear condensation and nuclear fragmentation [**Fig. S7**, A-C (iii, iv)].

***In Vitro* and *in vivo* stability of radio-labeled formulations.** *In vitro* stability of the radiolabeled formulations were evaluated in PBS while *in vivo* stability was assessed in New Zealand rabbits, as described in the methods section. All radiolabeled formulations showed greater than 90% stability under in vitro conditions and approximately 85-87% stable under in vivo conditions.

Table S4. *In Vitro* and *in vivo* stability of radio-labeled formulations

Time (h)	Free DOX		MWCNT-EDBE-DOX		MWCNT-EDBE-HA-DOX	
	In vitro	*In vivo*	*In vitro*	*In vivo*	*In vitro*	*In vivo*
1	95.6± 0.6	91.2± 0.6	97.4± 0.6	96.7± 0.8	98.9± 0.8	97.4± 1.8
2	94.7± 0.4	87.7± 0.7	96.3± 0.5	93.8± 0.7	97.8± 0.7	94.8± 1.2
4	92.8± 0.3	86.9± 0.4	94.8± 0.5	93.2± 0.4	96.6± 0.5	93.5± 0.6
12	92.6± 0.2	86.5± 0.5	94.1± 0.6	91.1± 0.6	96.5± 0.5	92.4± 0.8
24	91.8± 0.2	83.2± 0.3	92.7± 0.2	87.1± 0.4	92.4± 0.5	88.6± 0.9

Toxicity in mice: General health conditions and organ level toxicity. As a preliminary step towards toxicity evaluation, we scrutinized the general health conditions of mice up to 15 days post-treatment. It was quite interesting to observe that mice exposed to EDBE-MWCNTs and HA-EDBE-MWCNTs appeared lively throughout the experiment without any significant alterations in vocalization, labored breathing or difficulties in movement, hunching and interactions with cage mates. Comparison of the body weight before and after treatment with the various CNT formulation revealed negligible differences between treated and control group. Organ index, which is a marker of general organ level toxicity was measured by calculating the ratio of increase in organ weight due to inflammation and cellular infiltration to the reduction in total body weight. Likewise, organ indices of EDBE-MWCNT and HA-EDBE-MWCNT treated groups showed insignificant difference from the control revalidating our hypothesis that CNTs with shorter length and well-individualized structures easily translocate across the organs while inducing minimal inflammation.

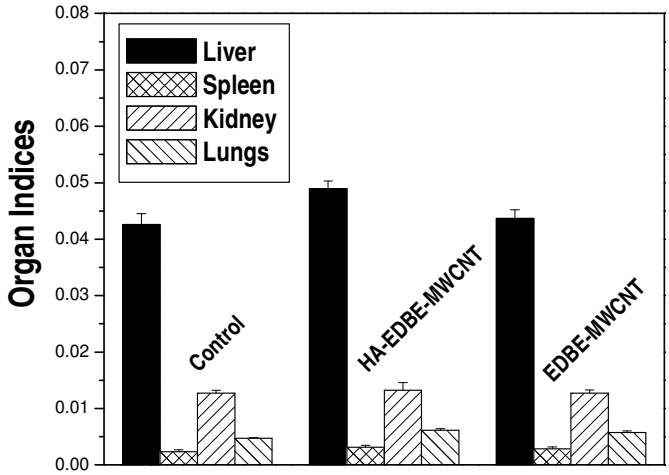

Figure S8 (A) Organ indices of mice treated with various MWCNT preparations after 15 days. Values expressed as mean ± SD (n=6)

Hepatotoxicity of f-MWCNTs in mice.

Liver is known to be the major site of accumulation and metabolism for most of the xenobiotics including carbonaceous materials and other nanomaterials. Any changes in liver enzymes are therefore, indicative of the physiological state of liver. Aspartate transaminases (AST) and alanine transaminases (ALT) are important bio-chemical enzymes reflecting hepatic injury [(5)]. Any injury or damage to liver is associated with the elevation of AST and ALT levels. **Fig. S8B (a-b)** presents the AST and ALT levels in mouse blood respectively at 15 days post-exposure. In either case, no significant change with respect to control was observed, suggesting that well-functionalized MWCNTs induced minimal hepatotoxicity in mice. Any oxidative stress damage in liver is associated with an increase in MDA level and decrease in SOD activity(*6*). **Fig. S8B(c-d)** presents the MDA levels and SOD activity in liver, following 15 days post-administration. It was quite interesting to note that MDA level of all MWCNT treated groups showed insignificant differences from the control, implying that functionalized CNTs, developed in course of the study, induce minimal oxidative stresses. In line with the results of MDA assay, no significant depreciation in SOD activity with respect to control were observed for mice treated with EDBE-MWCNTs and HA-EDBE-MWCNTs. To rationalize our observations, we tried to look into the oxidative stress model, which is often proposed to predict the toxicity of engineered nanomaterials both *in vitro* and *in vivo*. Earlier, different mechanistic pathways were proposed for CNT-induced oxidative stress. According to Sarkar et al., single walled carbon nanotubes (SWCNTs) induced oxidative stress through the activation of a specific signalling pathway in keratinocytes[(7)]. But most of the other literatures have reported that metal impurities associated with CNTs play a crucial role in the generation of ROS process [(8)]. *In vitro* studies with NR8383 and A549 cells suggested that exposure to p-MWCNTs induced cellular oxidative stress [(9)]. However, when the CNTs were acid-treated to remove metal contaminants, cellular

ROS generation is mitigated suggesting that metal contaminants play a crucial role in ROS generation. As determined from electron-dispersive X-ray (EDAX) analysis, both EDBE-MWCNT and HA-EDBE-MWCNT were highly pure containing negligible amount of metallic impurities Ni (0.041 wt %), Fe (0.015 wt %) and Zn (0.023 wt %). These data, cumulatively suggest that intensive purification and functionalization process augments the biocompatibility of CNTs in biological system.

Nephrotoxicity of f-MWCNTs in mice.

The blood urea nitrogen (BUN) levels of both EDBE-MWCNT and HA-EDBE-MWCNT treated groups after 15 days post-injection have been presented in **Fig. S8B (e)**. Interestingly, BUN levels of both the MWCNT treated groups were more or less similar to that of the control group, implying that functionalized MWCNTs, developed in course of the study, did not induce any renal toxicity in mice. According to a recent report by Lacerda et al. [10], *in vivo* transport and translocation profile of MWCNTs are critically dependant on their shape as also their degree of individualization. In course of extensive TEM and single photon emission computed tomography (SPECT) investigations [10, 11], they have observed that well-individualized SWCNTs/MWCNTs (length 0.1-0.5 µm, diameter~ 30-38 nm) not only exhibit appreciable solubility in the biological milieu but can easily translocate via their transverse dimension directly into the Bowman capsule while being excreted in the urine. In the present case, the length and diameter of our EDBE-MWCNTs or HA-EDBE-MWCNTs ranged between 0.3-0.6 µm and 50-60 nm respectively. Of note, diameter of our f-MWCNTs is smaller than the diameter of the leaky pores/ fenestrations (70-90 nm) present on the endothelial cells of glomeruli, suggesting that f-MWCNTs that are well individualized may be easily eliminated from the body via urinary excretion. As evident from the organ-distribution data, both EDBE-MWCNTs and HA-EDBE-MWCNTs presented measurable % ID/g in kidney and to some extent in the gastrointestinal organs like stomach and intestine. The values, albeit lesser than those reported by Singh et al.[11], it was quite interesting to note that the % ID/g in kidney/ gastrointestinal organs decreased systematically as a function of time. After 24 h of i.v. injection, nominal radioactivity persisted in almost all the major organs of the body. Our scintigraphy results as well as the finding of earlier workers suggests that well functionalized, well-individualized MWCNTs with average length ranging from 300-400 nm and diameter 50-60 nm effectively pass through the leaky tissue of the glomerular capillary bed via their transverse dimension and excreted through the urine, without inducing any perceptible nephrotoxicity. Alternatively, CNTs of longer dimension, which fail to clear out from the body via urinary excretion, are most likely eliminated from the body through biliary pathways in faeces[12]. Although further studies are necessary to determine the ultimate fate of our f-MWCNTs, data in hand suggests that functionalized CNTs, as a carrier, are nontoxic and safe enough to be used for clinical applications.

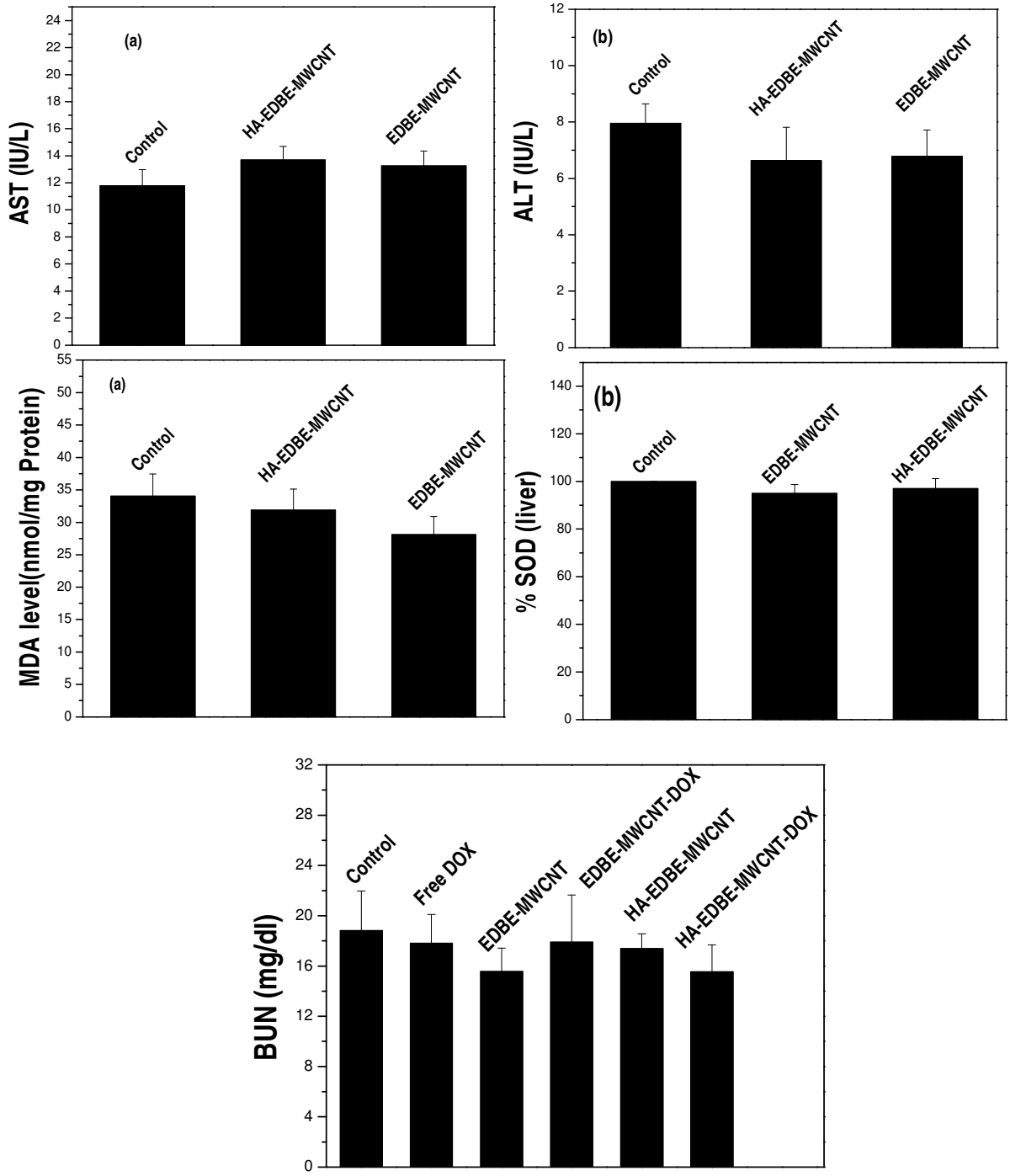

Fig. S8B (**a**) AST; (**b**) ALT; (**c**) MDA; (**d**) SOD and (**e**) BUN level of mice treated with various MWCNT preparations after 15 days. Values expressed as mean ± SD (n=6)

Cardiotoxicity of DOX-loaded MWCNTs in mice. As obvious from the various cardiotoxicity marker levels, both MWCNT-EDBE-DOX and MWCNT-EDBE-HA-DOX showed marked depreciation in cardiotoxicity as compared to free DOX. It is clear from Fig. **S9 (a-d)** that after 15 days of treatment, LDH and CK-MB level in the blood plasma were significantly increased in the animal groups treated with free DOX ($p>0.05$). Conversely, LDH and CK-MB levels of various CNT-treated groups showed insignificant differences from the control group ($p>0.05$). Concomitantly, SOD levels in the heart homogenate decreased in animals treated with free DOX while both MWCNT-EDBE-DOX and MWCNT-EDBE-HA-DOX showed comparable SOD activity with respect to control. Additionally, mice intravenously administered with free DOX exhibited a significant elevation in serum AST and slight elevation in serum ALT level while AST/ ALT levels for CNT-treated MWCNT-EDBE-DOX and MWCNT-EDBE-HA-DOX differed insignificantly from the control group [Fig. **S9(e)].** Fig. 12 (f) shows the weight of heart excised from the representative animal. As evident from the Fig., heart index was reduced significantly after intravenous administration of free DOX ($p>0.05$). Conversely, weight of heart excised from other treated groups was comparable to that of control group ($p>0.05$). It is really encouraging to find that entrapment of DOX within MWCNTs significantly mitigates the cardiotoxicity, associated with the free drug. In this connection, it should be noted that free DOX as well as DOX loaded MWCNTs were also analyzed for the various hepatotoxicity parameters, albeit no significant difference with respect to control was observed. This is quite obvious because toxicity evaluation of DOX-deprived MWCNTs has clearly established that the carrier system developed in course of the study shows negligible hepatotoxicity. Furthermore, there is no available report on the hepatotoxicity of DOX. Consistent with the behavior of DOX-deprived MWCNTs, neither HA-EDBE-MWCNT-DOX nor EDBE-MWCNT-DOX induced any nephrotoxicity in rats or mice. These data, overall, suggests that the delivery property of MWCNTs is effectively combined with the targeting property of HA to augment the anticancer activity of DOX against hyaluronate receptor bearing tumor cells, while reducing its cardiotoxicity.

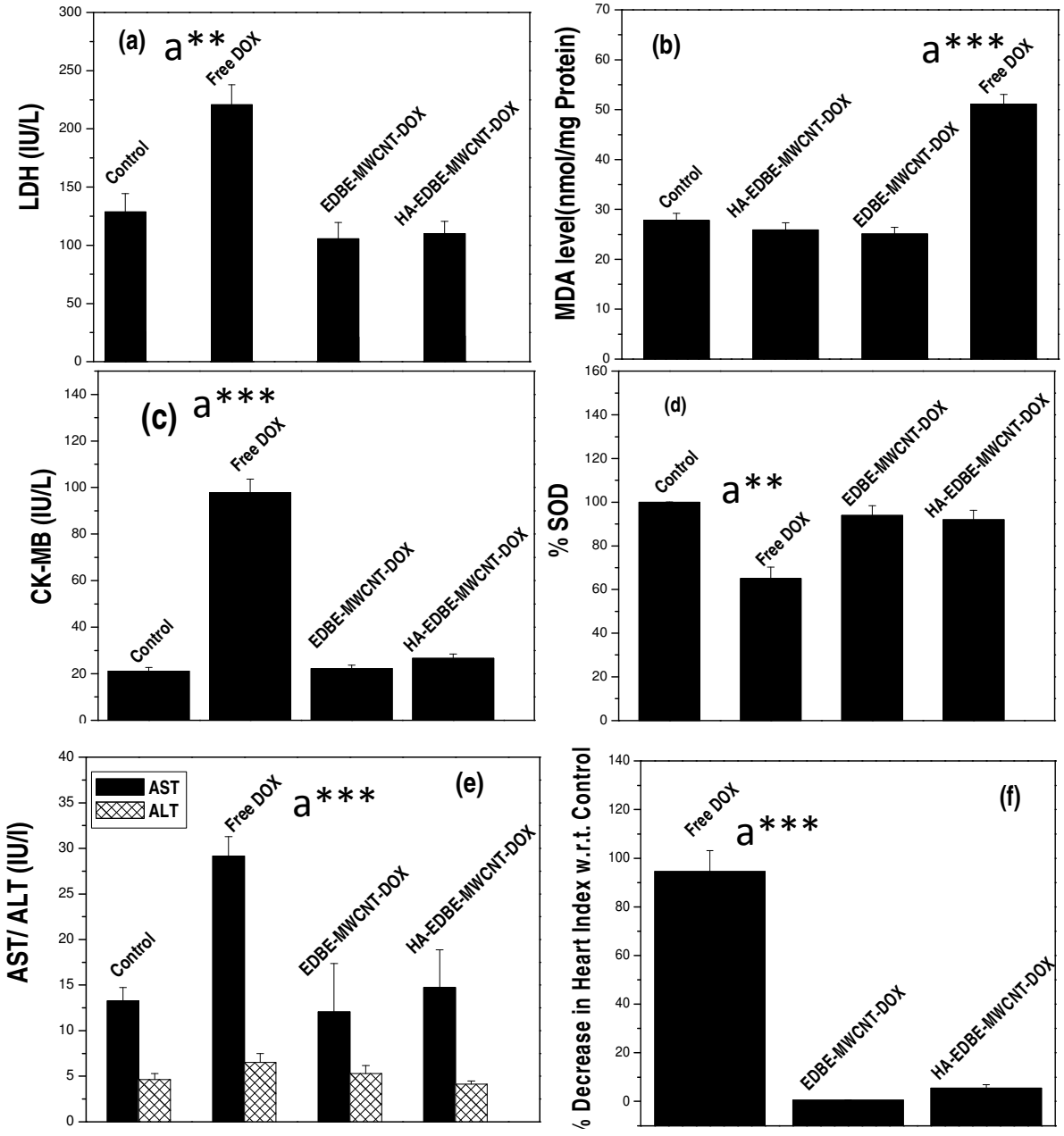

Fig. 12. Evaluation of cardiotoxicity parameters in mice treated with free DOX / DOX-loaded MWCNTs for 15 days: (a) LDH; (b) MDA; (c) CK-MB; (d) SOD; (e) AST/ALT (f) Percentage decrease in heart index with respect to control. Data expressed as mean ± SD (n=6) [a* w.r.t. control (***$p < 0.001$, **$p < 0.01$, *$p < 0.05$).

References

(1) Ohkawa, H., Ohishi, N., and Yagi, K. (1979) Assay for lipid peroxides in animal tissues by thiobarbituric acid reaction. *Analytical Biochemistry 95*, 351-358.

(2) Beauchamp, C., and Fridovich, I. (1971) Superoxide dismutase: Improved assays and an assay applicable to acrylamide gels* 1. *Analytical Biochemistry 44*, 276-287.

(3) Datsyuk, V., Kalyva, M., Papagelis, K., Parthenios, J., Tasis, D., Siokou, A., Kallitsis, I., and Galiotis, C. (2008) Chemical oxidation of multiwalled carbon nanotubes. *Carbon 46*, 833-840.

(4) Vermes, I., Haanen, C., Steffens-Nakken, H., and Reutellingsperger, C. (1995) A novel assay for apoptosis flow cytometric detection of phosphatidylserine expression on early apoptotic cells using fluorescein labelled Annexin V. *Journal of immunological methods 184*, 39-51.

(5) Murakami, S., Okubo, K., Tsuji, Y., Sakata, H., Takahashi, T., Kikuchi, M., and Hirayama, R. (2004) Changes in liver enzymes after surgery in anti-hepatitis C virus-positive patients. *World journal of surgery 28*, 671-674.

(6) Jain, S., Thakare, V. S., Das, M., Godugu, C., Jain, A. K., Mathur, R., Chuttani, K., and Mishra, A. K. (2011) Toxicity of Multiwalled Carbon Nanotubes with End Defects Critically Depends on Their Functionalization Density. *Chemical Research in Toxicology 24(11)*, 2028-2039

(7) Sarkar, S., Sharma, C., Yog, R., Periakaruppan, A., Jejelowo, O., Thomas, R., Barrera, E. V., Rice-Ficht, A. C., Wilson, B. L., and Ramesh, G. T. (2007) Analysis of stress responsive genes induced by single-walled carbon nanotubes in BJ Foreskin cells. *Journal of nanoscience and nanotechnology 7*, 584.

(8) Shvedova, A. A., Kisin, E. R., Porter, D., Schulte, P., Kagan, V. E., Fadeel, B., and Castranova, V. (2009) Mechanisms of pulmonary toxicity and medical applications of carbon nanotubes: two faces of Janus? *Pharmacology & therapeutics 121*, 192-204.

(9) Pulskamp, K., Diabaté, S., and Krug, H. F. (2007) Carbon nanotubes show no sign of acute toxicity but induce intracellular reactive oxygen species in dependence on contaminants. *Toxicology letters 168*, 58-74.

(10) Lacerda, L., Herrero, M. A., Venner, K., Bianco, A., Prato, M., and Kostarelos, K. (2008) Carbon Nanotube Shape and Individualization Critical for Renal Excretion. *Small 4*, 1130-1132.

(11) Singh, R., Pantarotto, D., Lacerda, L., Pastorin, G., Klumpp, C., Prato, M., Bianco, A., and Kostarelos, K. (2006) Tissue biodistribution and blood clearance rates of intravenously administered carbon nanotube radiotracers. *Proceedings of the National Academy of Sciences of the United States of America 103*, 3357.

(12) Dhar, S., Liu, Z., Thomale, J., Dai, H., and Lippard, S. J. (2008) Targeted single-wall carbon nanotube-mediated Pt (IV) prodrug delivery using folate as a homing device. *Journal of the American Chemical Society 130*, 11467-11476.

Bioconjugate Chemistry

Article

pubs.acs.org/bc

Site-Specific PEGylated Exendin-4 Modified with a High Molecular Weight Trimeric PEG Reduces Steric Hindrance and Increases Type 2 Antidiabetic Therapeutic Effects

Tae Hyung Kim,[†] Hai Hua Jiang,[†] Sung Mook Lim,[†] Yu Seok Youn,[†] Ki Young Choi,[‡] Seulki Lee,[‡] Xiaoyuan Chen,[‡] Youngro Byun,[§] and Kang Choon Lee*[,†]

[†]College of Pharmacy, SungKyunKwan University, 300 Chonchon-dong, Jangan-ku, Suwon City 440-746, Korea

[‡]Laboratory of Molecular Imaging and Nanomedicine, NIBIB, NIH, Bethesda, Maryland 20892, United States

[§]College of Pharmacy, Seoul National University, Seoul 151-742, Korea

ABSTRACT: The purpose of this study was to optimize an Exendin-4 (Ex4-Cys) site-specific PEGylation method with a high-molecular-weight trimeric PEG. Here, we describe the preparation of C-terminal specific PEGylated Ex4-Cys (C40-tPEG-Ex4-Cys), which was performed using cysteine and amine residue specific coupling reactions between Ex4-Cys and activated trimeric PEG. The C40-PEG-Ex4-Cys was obtained at high yields (~83%) and characterized by MALDI-TOF mass spectrometry. The receptor binding affinity of C40-PEG_{5K}-Ex4-Cys was 3.5-fold higher than that of N-terminal PEGylated Ex4-Cys (N_{ter}-PEG_{5K}-Ex4-Cys), and receptor binding by the trimeric PEG (tPEG; 23, 50 kDa) adduct was much higher than that of branched PEG (20 kDa). Furthermore, C40-$tPEG_{50K}$-Ex4-Cys was found to have greater blood circulating $t_{1/2}$ and AUC_{inf} values than native Ex4-Cys by 7.53- and 45.61-fold, respectively. Accordingly, its hypoglycemic duration was much greater at 59.2 h than that of native Ex4-Cys at 7.3 h, with a dose of 25 nM/kg. The results of this study show that C-terminal specific PEGylation using trimeric PEG is effective when applied to Ex4-Cys and suggest that C40-$tPEG_{50K}$-Ex4-Cys has considerable potential as a type 2 antidiabetic agent.

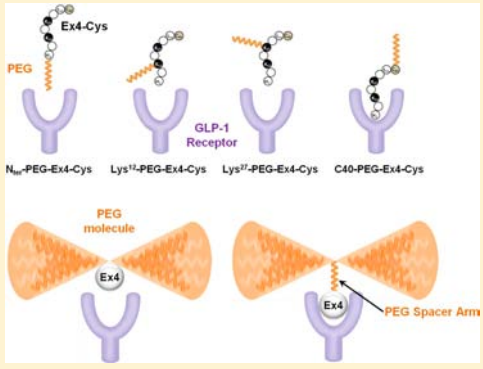

INTRODUCTION

The PEGylation of therapeutic peptides and proteins has proven to be a very useful pharmaceutical technique.[1−3] PEGylation of peptides and proteins increases molecular sizes, shields their proteolytic sites, and masks their immunogenic sites. This process can prolong in vivo pharmacokinetics, and diminish the immunogenicities of peptides and proteins, which in turn, enhances therapeutic efficacy and reduce undesirable effects versus their non-PEGylated counterparts.[4−6] Because of these benefits, PEGylation is playing an increasingly important role in the production of enhanced peptide and protein drug delivery systems.[7]

Site-specific PEGylation is an attractive approach for maximizing the therapeutic value of drugs, because this process generates only PEGylated isomers with optimized properties. In recent years, pharmaceutical technology of protein site-specific PEGylation has greatly improved with genetic engineering and various functional PEG analogues.[8] Accordingly, site-specific PEGylation has become a generally adopted procedure. The major benefit of site-specificity is its increased production yields and, therefore, significantly reduced production costs. In contrast, nonspecific PEGylation is difficult to control, and additional, often costly, separation procedures must be adopted to obtain the purified product.[9−11]

Rather than proteins, peptides can be ideal targets for site-specific PEGylation. Peptides have a short biological half-life because they have fast renal filtration and proteolytic degradation. Moreover, peptides display distinct biological activity and proteolytic stability according to the PEGylation sites because they have more specific active or metabolic sites than proteins.[3,10,11] Therefore, site-specific PEGylation must be consider for maximizing therapeutic effects of peptide.

Exendin-4 (Ex4-Cys) is viewed as a potent therapeutic peptide for type 2 diabetics, but commercial exendin-4 (Exenatide, Byetta) must be injected by diabetic patients at least twice a day because of its short in vivo lifetime. This has led to main drawbacks of less than optimal clinical compliance and poorer quality of life. Reduction of the required frequency of s.c. injections is one way that would significantly enhance compliance. It has been reported that continuous exenatide therapy reached compliance of 100%. Exendin-4 is 39 amino acids long, unlike GLP-1, which has 30 amino acids. Because of its nonmammalian (lizard) origin and unique C-terminal sequence, exendin-4 may induce immunogenic response in humans.[12−16] In the present study, we prepared C-terminal specific PEGylated Ex4-Cys using trimeric PEG (C40-tPEG-Ex4-Cys) and then explored its physicochemical and biological

Received: May 18, 2012
Revised: October 29, 2012
Published: November 1, 2012

 © 2012 American Chemical Society dx.doi.org/10.1021/bc300265n | *Bioconjugate Chem.* 2012, 23, 2214−2220

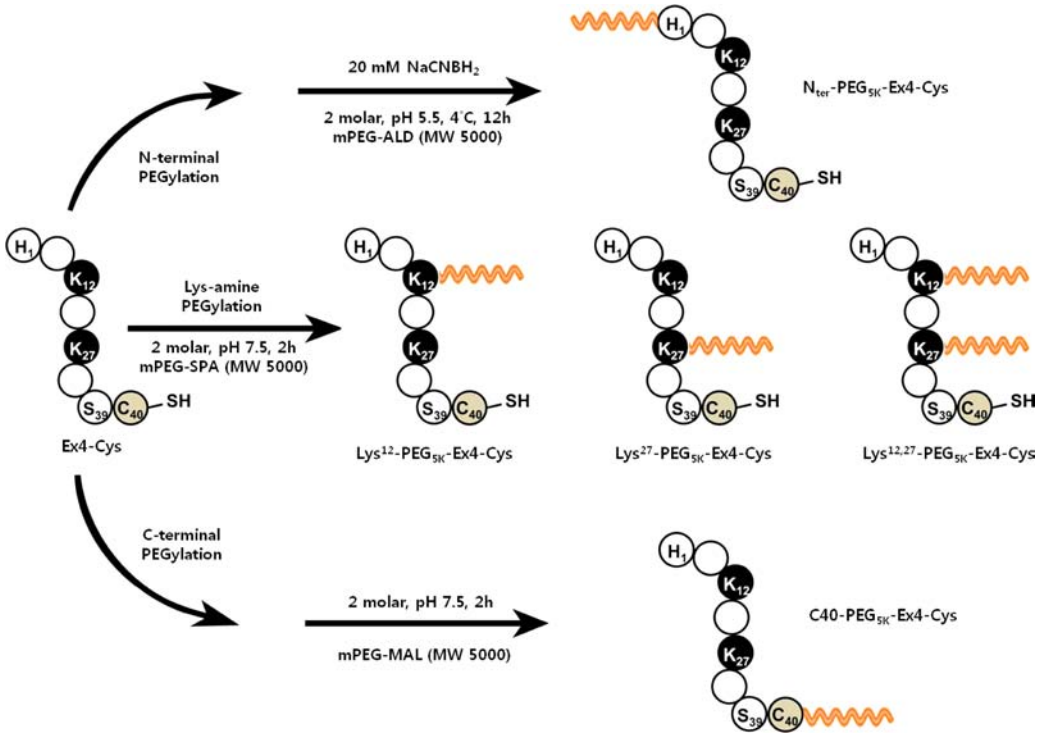

Figure 1. Site-specific PEGylation strategy for Ex4-Cys according to its target site.

characteristics. Furthermore, the pharmacokinetic and antidiabetic characteristics of C40-tPEG-Ex4-Cys were investigated and compared using a diabetic mouse model. Ex4-Cys acts as a GLP-1 receptor agonist for treatment of type 2 diabetes mellitus. We hypothesize that the site-specific PEGylation can increase the therapeutic potential of this diabetes drug.

EXPERIMENTAL PROCEDURES

Materials. Ex-4-Cys (M_w: 4290.7 Da) with the sequences HGEGTFTSDLSKQMEEEAVRLFIEWLKNGGPSS-GAPPPSC were purchased from AnyGen (Gwangju, Republic of Korea (ROK)). Monomethoxy PEG-aldehyde (mPEG-ALD, M_w: 5 kDa), Monomethoxy PEG-succinyl propionate (mPEG-SPA, M_w: 5 kDa) and Monomethoxy PEG-maleimide (mPEG-MAL, M_w: 5, 20 (branched), 23, 50 (trimer) kDa) were purchased from Nippon Oil and Fats (NOF, Tokyo, Japan). Ex4 enzyme immunoassay (EIA) kits were purchased from Phoenix Pharmaceuticals (Burlingame, CA). All other reagents, unless otherwise indicated, were purchased from Sigma Aldrich (Saint Louis, MO) and were used as received.

Experimental Animals. Type 2 diabetic C57BL/6 db/db mice (males, 6−8 weeks old) were obtained from the Korea Research Institute of Bioscience and Biotechnology (Daejon, Korea). Male Sprague−Dawley rats (200−250 g), which were used for pharmacokinetic studies, were purchased from the Hanlim Experimental Animal Laboratory (Seoul, Korea). All animals were cared for according to the guideline issued by the National Institute of Health (NIH) for the care and use of laboratory animals (NIH publication 85−23, revised 1985). Animals were housed in groups of 6−8 under a 12 h light/dark cycle (lights on at 6 a.m.), allowed food and water *ad libitum*, and acclimatized for 2 weeks. This study was approved by the Ethical Committee on Animal Experimentation at SungKyunKwan University.

Preparation of Nonspecific PEGylated Ex4-Cys. PEGylation of Ex4-Cys was achieved nonspecifically at its Lys-amine using mPEG-SPA (M_w: 5, 20, 23 kDa), as previously described.[17−20] Briefly, 100 μL of mPEG-SPA (1.6 mg/mL in dimethylsulfoxide (DMSO) containing 0.3% triethylamine (TEA)) was reacted with 100 μL of Ex4-Cys (10 mg/mL in DMSO containing 0.3% TEA) (an Ex4-Cys/mPEG-SPA molar ratio of 2) with gentle mixing at room temperature for 1 h. The reaction was then stopped by adding 100 μL of stop solution (deionized water (DW) containing 1% trifluoroacetic acid (TFA)). PEG-Ex4-Cys analogues were purified from reaction mixtures by preparative RP-HPLC using a Capcell-pak RP-18 column (250 × 4.6 mm, 5 μm, Shiseido, Japan) at ambient temperature and a constant flow-rate of 1.0 mL/min under UV monitoring at 215 nm. The mobile phase consisted of 0.1% TFA in DW (eluent A) and acetonitrile (AN) containing 0.1% TFA (eluent B), and these were applied as linear gradients from 34% B to 48% B over 27 min. HPLC fractions corresponding to observed peaks were collected and flushed with nitrogen. The products obtained were characterized by MALDI-TOF mass spectroscopy, and stored at −70 °C until required for further experiments. At predetermined times, production yields were expressed as a percentage of the HPLC peak area of PEG-Ex4-Cys produced versus the HPLC peak area of initial Ex4-Cys.

Preparation of N_{ter}-PEG-Ex4-Cys. N-terminus amine specific PEGylation was performed using a PEG-aldehyde derivative known to attach specifically to the α-amines of peptides, as previously described.[17−20] The mPEG-ALD (2.4 mg; M_w: 5 kDa) was added to 1 mL of Ex4-Cys (2 mg/mL) in a 50 mM acetate buffer solution (pH 5.5) containing 20 mM sodium cyanoborohydride ($NaCNBH_3$) (an Ex4-Cys/mPEG-ALD molar ratio of 2). The reaction was allowed to continue at 4 °C for 2 h, and was then quenched by adjusting the pH to ~2.2 with 1% TFA/DW. HPLC purification and yield calculations were performed as described above.

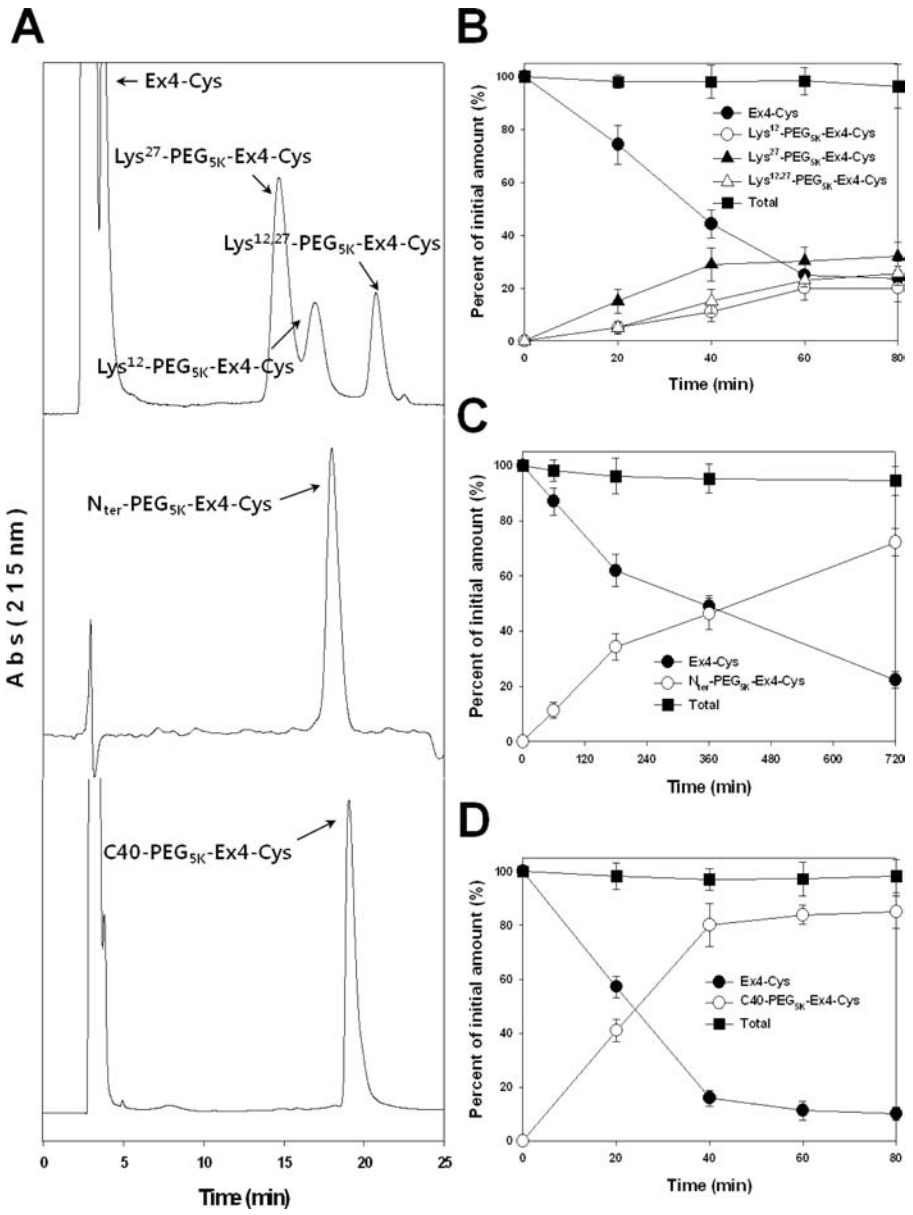

Figure 2. (A) Purification of PEG-Ex4-Cys analogues. RP-HPLC chromatogram of Lys-amine PEGylated Ex4-Cys mixture, N-terminal specific PEGylated Ex4-Cys mixture, C-terminal specific PEGylated Ex4-Cys mixture. Stoichiometric reaction profiles of (B) Lys-amine PEGylation, (C) N-terminal specific PEGylation, (D) C-terminal specific PEGylation.

Preparation of C40-PEG-Ex4-Cys. PEGylation of Ex4-Cys was achieved specifically using mPEG-MAL (M_w: 5, 20, 23, 50 kDa). Briefly, 100 μL of mPEG-MAL (1.6 mg/mL in DMSO containing 0.3% TEA) was reacted with 100 μL of Ex4-Cys (10 mg/mL in DMSO containing 0.3% TEA) (an Ex4-Cys/mPEG-MAL molar ratio of 2) with gentle mixing at room temperature for 1 h. The reaction was then stopped by adding 100 μL of stop solution (DW containing 1% TFA). HPLC purification and yield calculations were also performed as described above.

Characterization of PEG-Ex4-Cys Analogues. PEG-Ex4-Cys analogues were identified using a MALDI-TOF MS (Voyager-RP Biospectrometry Workstation, PerSeptive Biosystems, Cambridge, MA) before and after lysyl endoproteinase Lys-C digestion, as described previously.[17−20] For MS analysis, each sample was crystallized using an α-cyano-4-hydroxycinnamic acid matrix, and molecular masses were determined.

In Vitro Biological Activity Testing. The biological activities of PEG-Ex4-Cys analogues were determined using competitive receptor-binding assays in the steady state using RIN-m5F cells (ATCC, Manassas, VA).[17−20] Briefly, RIN-m5F cells were seeded in 12 well plates at 3×10^5 cells per well, grown for 48 h, washed twice with binding buffer (120 mM NaCl, 1.2 mM $MgSO_4$, 13 mM sodium acetate, 5 mM KCl, 1.2 g/L Tris, 2 g/L bovine serum albumin, and 1.8 g/L glucose, pH 7.6), cotreated with the unlabeled PEG-Ex4-Cys analogues (final concentrations: 0.001−1000 nM) containing 30 pM of ^{125}I-exendin-4 (9−39, PerkinElmer, Boston, MA), incubated for 2 h at room temperature, and washed three times with chilled PBS containing 1 mg/mL of bovine serum albumin. Cells were then lysed with cell lysis buffer (0.5 N NaOH containing 1% SDS) for 15 min, and ^{125}I radioactivity levels were measured using a γ counter (GMI, Inc., Ramsey, MN).

dx.doi.org/10.1021/bc300265n | *Bioconjugate Chem.* 2012, 23, 2214−2220

Table 1. Structural Characterization of Ex4-Cys and PEG-Ex4-Cys Analogues by MALDI-TOF Mass Spectrometry (before and after Lys-C Digestion)

	total mass		Lys-C digested fragments		
samples	calculated mass	observed mass	fragments	calculated mass	observed mass
Ex4-Cys	4290.7	4297.4	His^{1}-Lys^{12}	1278.3	1285.3
			Gln^{13}-Lys^{27}	1921.7	1934.8
			Asn ^{28}-Cys^{40}	1090.7	1102.5
Lys^{12}-PEG_{5K}-Ex4-Cys	9739.8	9747.9	His^{1}-(Lys^{12}-PEG_{5K})-Lys^{27}	8649.1	8667.8
			Asn^{28}-Cys^{40}	1090.7	1098.6
Lys^{27}-PEG_{5K}-Ex4-Cys	9739.8	9791.7	Gln^{13}-(Lys^{27}-PEG_{5K})-Cys^{40}	8461.5	8492.1
			His^{1}-Lys^{12}	1278.3	1292.3
$Lys^{12,27}$-PEG_{5K}-Ex4-Cys	15188.9	15241.5	His^{1}-(Lys^{12}-PEG_{5K})-(Lys^{27}-PEG_{5K})-Cys^{40}	15188.9	15241.5
N_{ter}-PEG_{5K}-Ex4-Cys	9739.8	9801.2	(His^{1}-PEG_{5K})-Lys^{12}	6727.4	6791.2
			Gln^{13}-Lys^{27}	1921.7	1983.7
			Asn^{28}-Cys^{40}	1090.7	1123.1
C40-PEG_{5K}-Ex4-Cys	9741.6	9798.9	His^{1}-Lys^{12}	1278.3	1302.4
			Gln^{13}-Lys^{27}	1921.7	1969.6
			Asn^{28}-(Cys^{40}-PEG_{5K})	6539.8	6590.1

Hypoglycemic Efficacy Tests in Nonfasted db/db Mice. The hypoglycemic efficacies of PEG-Ex4-Cys analogues were evaluated using a modification of a previously described method[17−20] in male db/db mice (6−7 weeks old). Under nonfasting conditions with free access to food and water, animals were administered a single s.c. injection of saline, Ex4-Cys, or of the PEG-Ex4-Cys analogues (25 nM/kg body wt). Blood glucose levels were monitored using the procedure mentioned above. In addition, a drop of blood was drawn from a tail vein of each animal at different times (0, 0.5, 1, 2, 3, 4, 6, 8, 12, 24, 36, 48, 60, 72, 96, 120 h), and blood glucose levels were determined using a one-touch blood glucose meter (ACCU-CHEK Sensor, Roche Diagnostics Corp., USA). Hypoglycemic durations to a blood glucose level of <8.35 nmol/L (150 mg/dL) were checked.

Pharmacokinetic Tests. The pharmacokinetic profiles of subcutaneously administered Ex4-Cys, C40-tPEG$_{23K}$-Ex4-Cys and C40-tPEG$_{50K}$-Ex4-Cys were assessed as previously described.[21,22] Briefly, a jugular vein was cannulated in male Sprague−Dawley rats the day before the experiment. On the day of the experiment, Ex4-Cys, C40-tPEG$_{23K}$-Ex4-Cys, or C40-tPEG$_{50K}$-Ex4-Cys (25 nM/kg, s.c.) was administered, and blood samples were drawn at predetermined times and placed in ice-cold polyethylene tubes containing anticoagulant (heparin solution, 1/100 volume of blood). Plasma samples were obtained by centrifugation and stored at −70 °C until required for assay. Plasma concentrations of Ex4-Cys, C40-tPEG$_{23K}$-Ex4-Cys, or C40-tPEG$_{50K}$-Ex4-Cys were determined using commercial Ex4 EIA kits.

Data Analysis. Data are presented as means ± SDs. Statistical significances were determined by one-way ANOVA, and P values of <0.05 were considered statistically significant. Pharmacokinetic parameters were calculated by two-compartmental analysis (WinNolin, Scientific Consulting, Inc., Cary, NC).

RESULTS

Preparation and Characterization of the PEG-Ex4-Cys Analogues. PEG-Ex4-Cys analogues were synthesized as described above (Lys^{12}, Lys^{27}, $Lys^{12,27}$, N_{ter}, and C40-PEG_{5K}-Ex4-Cys), and finally, we obtained five different products containing control molecules (Figures 1, 2A). The apparent molecular weights of the five analogues were determined by MALDI-TOF MS. As shown in Table 1, experimental mass-to-charge (m/z) ratios closely matched calculated values. Positional isomers (Lys^{12}, Lys^{27}, $Lys^{12,27}$, N_{ter}, C40-PEG_{5K}-Ex4-Cys) were also confirmed by MALDI-TOF MS after Lys-C digestion. Furthermore, production yield was found to be greatest for C-terminal specific PEGylation (~83%) (Figure 2B−D).

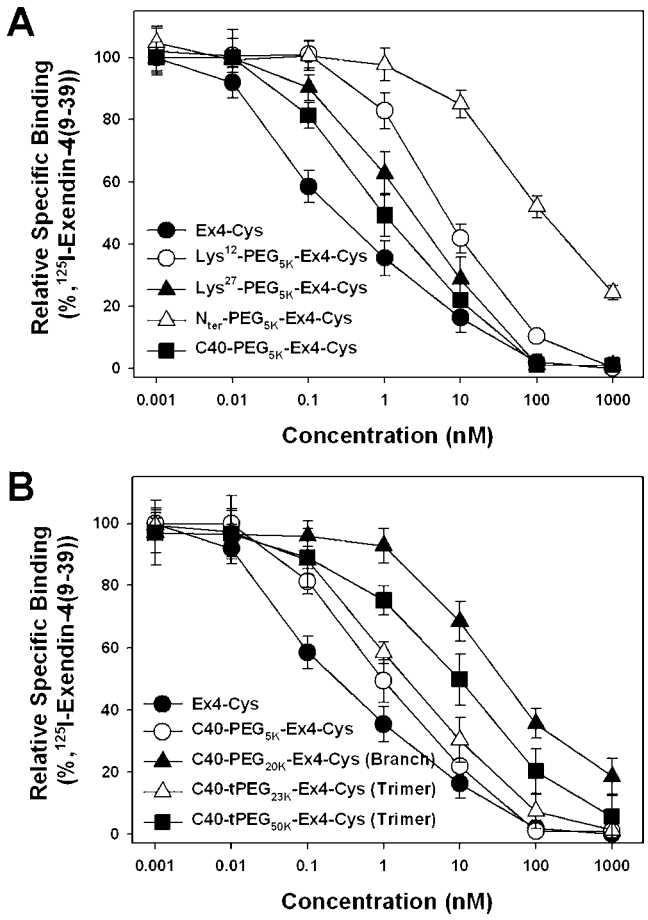

Figure 3. In vitro biological activity of PEG-Ex4-Cys analogues in RIN-m5F cells. (A) In positional isomer cases, receptor-binding affinities of PEG-Ex4-Cys analogues. (B) In PEG structure cases, receptor-binding affinities of PEG-Ex4-Cys analogues. Data represent the means ± SDs of five results.

In Vitro Biological Activity Testing. The receptor-binding affinities of PEG-Ex4-Cys analogues were examined in RIN-m5F cells, which express high levels of GLP-1 receptor

dx.doi.org/10.1021/bc300265n | Bioconjugate Chem. 2012, 23, 2214−2220

(GLP-1R). In positional isomer cases, C40-PEG$_{5K}$-Ex4-Cys was found to have 132.8-fold higher affinity for GLP-1R (IC_{50} = 1.04 ± 0.23 nM) than N_{ter}-PEG$_{5K}$-Ex4-Cys (IC_{50} = 138.09 ± 12.52 nM) and similar to Lys^{27}-PEG$_{5K}$-Ex4-Cys, as shown in Figure 3A. In PEG structure cases, C40-tPEG$_{23K}$-Ex4-Cys (containing a PEG trimer) was found to have 16.8-fold greater affinity for GLP-1R (IC_{50} = 2.29 ± 0.57 nM) than C40-PEG$_{20K}$-Ex4-Cys (containing branched PEG; IC_{50} = 38.36 ± 2.81 nM), as shown in Figure 3B.

Hypoglycemic Duration Tests in Nonfasted db/db Mice. The hypoglycemic effects of the C40-PEG-Ex4-Cys analogues were examined at 25 nM/kg s.c. in db/db mice. Hypoglycemic durations of all analogues were much greater than Ex4-Cys, and times required to rebound to a glucose level of 8.35 mmol/L were much longer than the ~7.3 h taken in Ex4-Cys treated mice (Figure 4A). In terms of PEG structures, hypoglycemic durations of C40-tPEG$_{23K}$-Ex4-Cys (trimeric PEG) mice were much greater than those of C40-PEG$_{20K}$-Ex4-Cys (branched PEG), and the time required to rebound to a glucose level of 8.35 mmol/L was ~42.2 h in C40-tPEG$_{23K}$-Ex4-Cys mice as compared with ~12.1 h in C40-PEG$_{20K}$-Ex4-Cys (branched PEG structure) treated mice (Figure 4A). In particular, the $t_{\sim 8.35\ mmol/L}$ value was 59.2 h for C40-tPEG$_{50K}$-Ex4-Cys, which meant that a single C40-tPEG$_{50K}$-Ex4-Cys administration stabilized blood glucose levels for nearly 4−5 days in db/db mice.

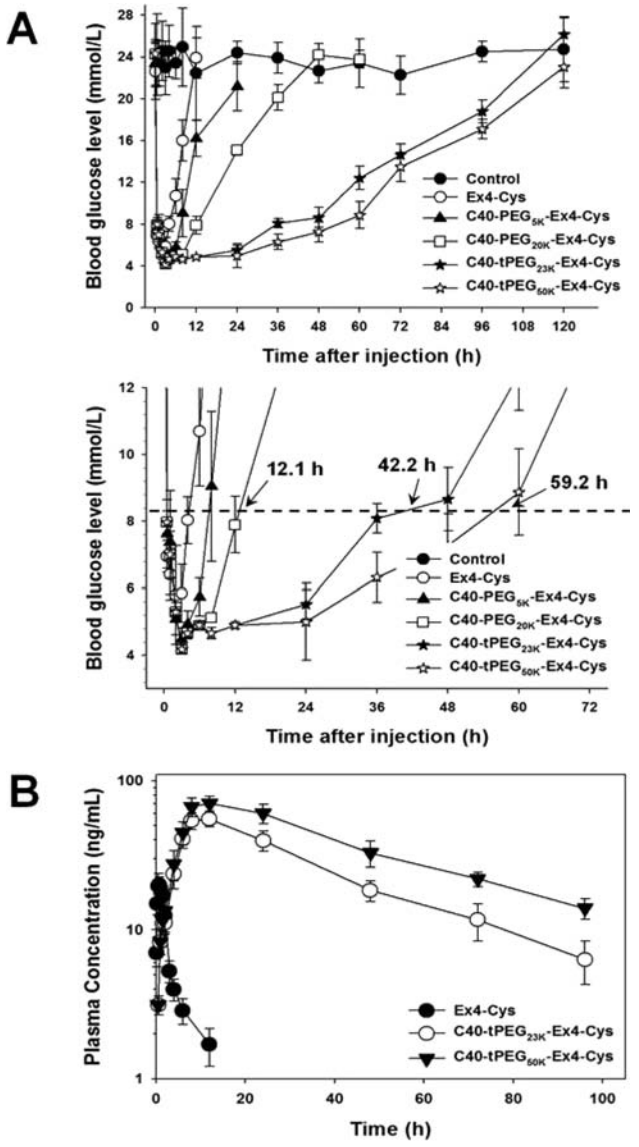

Figure 4. (A) Hypoglycemic efficacies of PEG-Ex4-Cys analogues in nonfasted db/db mice (upper), the focused profile of A (0−75 h, 3−12 mmol/L) (below). Times depict hypoglycemic duration rebound to 8.35 mmol/L. Data represent five mice and are presented as means ± SDs. (B) Pharmacokinetic profiles of Ex4-Cys and C40-tPEG$_{50K}$-Ex4-Cys in SD rats administered 25 nM/kg, s.c. Data represent four rats and are presented as mean ± SDs.

In Vivo Pharmacokinetic Study. C40-PEG-Ex4-Cys with high-molecular-weight trimeric PEG, C40-tPEG$_{23K}$-Ex4-Cys, and C40-tPEG$_{50K}$-Ex4-Cys showed much improved pharmacokinetic profiles. The blood concentration vs time curves were plotted for C40-tPEG$_{50K}$-Ex4-Cys. As shown in Table 2 and Figure 4B, subcutaneously administered Ex4-Cys was rapidly removed from the circulation with a $t_{1/2}$ of 6.8 ± 1.6 h, whereas the $t_{1/2}$ of C40-tPEG$_{50K}$-Ex4-Cys was 51.2 ± 12.8 h, resulting in a 7.53-fold greater time than that of native Ex4-Cys. Furthermore, its AUC_{inf} value (4098.6 ± 672.2 ng/mL*h) was 46.31 times greater than that of native Ex4-Cys (88.5 ± 12.3 ng/mL*h).

Table 2. Pharmacokinetic Parameters of Ex4-Cys, C40-PEG$_{23K}$-Ex4-Cys, and C40-PEG$_{50K}$-Ex4-Cys after s.c. Administration to SD Rats[a]

parameter	Ex4-Cys	C40-PEG$_{23K}$-Ex4-Cys	C40-PEG$_{50K}$-Ex4-Cys
C_{max}[b] (ng/mL)	21.7 ± 4.2	63.3 ± 11.2	72.5 ± 7.9
T_{max}[c] (h)	0.8 ± 0.1	12.8 ± 4.5	13.5 ± 2.7
$t_{1/2}$[d] (h)	6.8 ± 1.6	39.6 ± 8.4	51.2 ± 12.8
AUC_{inf}[e] (ng·h/mL)	88.5 ± 12.3	2882.3 ± 440.8	4098.6 ± 672.2

[a]Data are means ± S.D. (n = 4). [b]C_{max}: maximum concentration after administration. [c]T_{max}: required time to reach C_{max}. [d]$t_{1/2}$: elimination half-life. [e]AUC_{inf}: area under the curve from zero to infinity.

DISCUSSION

Site-specific PEGylation is considered an effective way of avoiding the pharmacologic heterogeneity and inefficiency of nonspecific PEGylation.[23−25] This technique enables the production of chemically well-defined PEGylated species with greatest bioactivity. Furthermore, if the overall process is robust, site-specific PEGylation can greatly increase production yields. So, we undertook to develop a high-yield version of C40-PEG-Ex4-Cys with superior bioactivity.

For successful clinical application, the PEG size and structure must first be optimized. PEGs with slightly different physicochemical properties can have markedly different effects on the pharmaceutical properties of PEG-protein hybrids.[1−3] In this study, we used PEG with trimer structures (tPEG$_{23K}$, tPEG$_{50K}$) in an effort to improve pharmacokinetic and receptor binding properties, and characterized the C40-PEG-Ex4-Cys analogues prepared.

We prepared and characterized PEG-Ex4-Cys analogues using different site-specific PEGylation reactions and determined yields and identities by preparative HPLC and MALDI-TOF-MS (Figure 2A, Table 1). Consistent with our previous findings,[17−20] conjugation preferentially occurs at Lys^{27} rather than Lys^{12}. Furthermore, Lys^{12}-PEG-Ex4-Cys has substantially shorter HPLC retention times than Lys^{27}-PEG-Ex4-Cys, presumably due to minimal deterioration of the α-helix structure of the 9−30 amino acid domain of Ex4-Cys (Figure 2A).

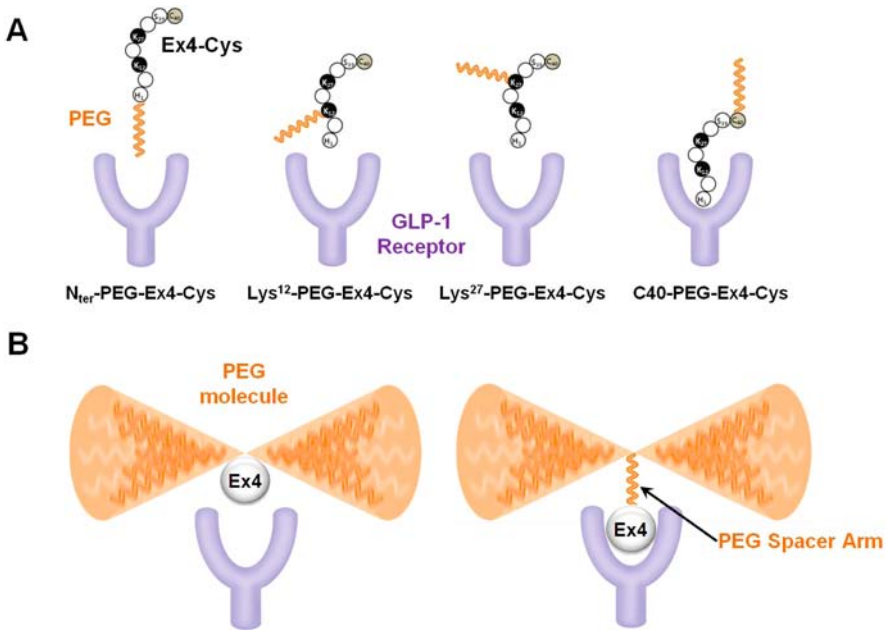

Figure 5. (A) In positional isomer cases, scheme of PEG-Ex4-Cys analogues for GLP-1 receptor binding. (B) In PEG structure cases, scheme of PEG-Ex4-Cys analogues for GLP-1 receptor binding.

Additionally, our results (Figure 2B–D) showed that C40-PEG-Ex4-Cys was prepared at highest yields.

C40-PEG-Ex4-Cys was found to have higher receptor binding affinity than Lys^{12}, Lys^{27}, or N_{ter}-PEG-Ex4-Cys. As shown in Figure 5A, the C-terminus of PEG is considerably removed from the receptor binding site. In terms of PEG structure, Figure 5B shows that the trimeric structure inhibits receptor binding less than the branched PEG, which probably explains why C40-tPEG$_{23K}$-Ex4-Cys has higher receptor binding affinity than C40-PEG$_{20K}$-Ex4-Cys. Ex4-Cys is apparently more resistant to enzymatic degradation than GLP-1. It is hardly degraded by DPP-IV and a poor substrate for other enzymes. Furthermore, glomerular filtration of Ex4-Cys is not faster than GLP-1.[16] For these reasons, PEGylated Ex4-Cys modified with a high-molecular-weight PEG (50 kDa) preserved its in vitro biological activity and in vivo hypoglycemic durations. However, to maximize Ex4-Cys therapeutic effects, we performed C-terminal specific PEGylation with trimeric PEG (23, 50 kDa). C-terminal PEGylation provides an alternative to the serious activity reduction caused by N-terminal acylation, which prevents the N-terminal domain participating in GLP-1 receptor activation.[14,15] Therefore, trimeric PEG is a significantly better option for GLP-1 receptor binding than branched PEG.

In vivo biological activities were evaluated in db/db mice. The hypoglycemic durations of C40-PEG-Ex4-Cys analogues in db/db mice were much greater than that of Ex4-Cys regardless of the dose administered (Figure 4A). Blood glucose levels of <8.35 mmol/L (150 mg/dL) were regarded as normal, and euglycemic durations under this value are considered a practical indication of the potentials of antidiabetic drugs. C40-tPEG$_{50K}$-Ex4-Cys sustained normal glycemia 8.22 times longer than Ex4-Cys. In addition, drug clearance in humans is known to be much slower than in rodents, and thus, the antidiabetic duration of C40-tPEG$_{50K}$-Ex4-Cys may be substantially greater in humans than the 1 week observed in db/db mice.

On the basis of pharmacodynamic data, C40-tPEG$_{23K}$-Ex4-Cys and C40-tPEG$_{50K}$-Ex4-Cys are also expected to have improved pharmacokinetics over Ex4-Cys. The pharmacokinetic profiles of C40-tPEG$_{50K}$-Ex4-Cys were markedly better than that of Ex4-Cys as their AUCs were 45.61-fold higher and their circulating $t_{1/2}$ values were 7.53-fold higher than that of Ex4-Cys (Table 2 and Figure 4B). These improved pharmacokinetics and pharmacodynamics were caused by high-molecular-weight trimeric PEG. It should also be mentioned that Ex4-Cys is a foreign material to mice, because of its reptile origins, and thus, Ex4-Cys could induce immunological side effects. However, PEGylation diminishes the potential for immunogenicity, presumably because PEG protects C40-tPEG$_{50K}$-Ex4-Cys from mouse antibodies.

In summary, we prepared C-terminal specific PEGylated Ex4-Cys, which was performed using Ex4-Cys and activated trimeric PEG (C40-tPEG-Ex4-Cys). C-terminal of Ex4-Cys is an optimal site for GLP-1 receptor binding. High-molecular-weight trimeric PEG (tPEG$_{23K,\ 50K}$) shows reduced steric hindrance and increasing type 2 antidiabetic therapeutic effects of Ex4-Cys. Importantly, the longevity of C40-tPEG$_{50K}$-Ex4-Cys in vivo, investigated by pharmacokinetics and pharmacodynamics, suggests that it has therapeutic potential as an effective long-acting GLP-1 receptor agonist for the treatment of type 2 diabetes mellitus.

■ AUTHOR INFORMATION

Corresponding Author

*Tel.: +82-31-290-7704. Fax: +82-31-290-7724. E-mail: kclee@skku.edu.

Notes

The authors declare no competing financial interest.

■ ACKNOWLEDGMENTS

This work was supported in part by the Converging Research Center Program through the National Research Foundation of Korea (NRF) funded by the Ministry of Education, Science, and Technology (2011-K000796).

REFERENCES

(1) Katre, N. V. (1993) The conjugation of proteins with polyethylene glycol and other polymers: Altering properties of proteins to enhance their therapeutic potential. *Adv. Drug Delivery Rev. 10*, 91−114.

(2) Veronese, F. M., Monfardini, C., Caliceti, P., Schiavon, O., Scrawen, D., and Beer, D. (1996) Improvement of pharmacokinetic, immunological and stability properties of asparaginase by conjugation to linear and branched monomethoxy poly(ethylene glycol). *J. Controlled Release 40*, 199−209.

(3) Kang, J. S., Deluca, P. P., and Lee, K. C. (2009) Emerging PEGylated drugs. *Expert Opin. Emerg. Drugs 14*, 363−380.

(4) Bailon, P., Palleroni, A., Schaffer, C. A., Spence, C. L., Fung, W. J., Porter, J. E., Ehrlich, G. K., Pan, W., Xu, Z. X., Modi, M. W., Farid, A., Berthold, W., and Graves, M. (2001) Rational design of a potent, long-lasting form of interferon: a 40 kDa branched polyethylene glycol-conjugated interferon alpha-2a for the treatment of hepatitis C. *Bioconjugate Chem. 12*, 195−202.

(5) Parkinson, C., Scarlett, J. A., and Trainer, P. J. (2003) Pegvisomant in the treatment of acromegaly. *Adv. Drug Delivery Rev. 55*, 1303−1314.

(6) Edwards, C. K., 3rd, Martin, S. W., Seely, J., Kinstler, O., Buckel, S., Bendele, A. M., Ellen Cosenza, M., Feige, U., and Kohno, T. (2003) Design of PEGylated soluble tumor necrosis factor receptor type I (PEG sTNF-RI) for chronic inflammatory diseases. *Adv. Drug Delivery Rev. 55*, 1315−1336.

(7) Whelan, J. (2005) Beyond PEGylation. *Drug Discovery Today 10*, 301.

(8) Youn, Y. S., Na, D. H., Yoo, S. D., Song, S. C., and Lee, K .C. (2005) Carbohydrate-specifically polyethylene glycol-modified ricin A-chain with improved therapeutic potential. *Int. J. Biochem. Cell Biol. 37*, 1525−1533.

(9) Deiters, A., Cropp, T. A., Summerer, D., Mukherji, M., and Schultz, P. G. (2004) Site-specific PEGylation of proteins containing unnatural amino acids. *Bioorg. Med. Chem. Lett. 14*, 5743−5745.

(10) Youn, Y. S., and Lee, K. C. (2007) Site-specific PEGylation for high-yield preparation of Lys(21)-amine PEGylated growth hormone-releasing factor (GRF) (1−29) using a GRF(1−29) derivative FMOC-protected at Tyr(1) and Lys(12). *Bioconjugate Chem 18*, 500−506.

(11) Youn, Y. S., Na, D. H., and Lee, K. C. (2007) High-yield production of biologically active mono-PEGylated salmon calcitonin by site-specific PEGylation. *J. Controlled Release 117*, 371−379.

(12) Kolterman, O. G., Buse, J. B., Fineman, M. S., Gaines, E., Heintz, S., Bicsak, T. A., Taylor, K., Kim, D., Aisporna, M., Wang, Y., and Baron, A. D. (2003) Synthetic exendin-4 (exenatide) significantly reduces postprandial and fasting plasma glucose in subjects with type 2 diabetes. *J. Clin. Endocrinol. Metab. 88*, 3082−3089.

(13) Szayna, M., Doyle, M. E., Betkey, J. A., Holloway, H. W., Spencer, R. G., Greig, N. H., and Egan, J. M. (2000) Exendin-4 decelerates food intake, weight gain, and fat deposition in Zucker rats. *Endocrinology 141*, 1936−1941.

(14) Nielsen, L. L., Young, A. A., and Parkes, D. G. (2004) Pharmacology of exenatide (synthetic exendin-4): a potential therapeutic for improved glycemic control of type 2 diabetes. *Regul. Pept. 117*, 77−88.

(15) Drucker, D. J., and Nauck, M. A. (2006) The incretin system: glucagon-like peptide-1 receptor agonists and dipeptidyl peptidase-4 inhibitors in type 2 diabetes. *Lancet 368*, 1696−1705.

(16) Simonsen, L., Holst, J. J., and Deacon, C. F. (2006) Exendin-4, but not glucagon-like peptide-1, is cleared exclusively by glomerular filtration in anaesthetised pigs. *Diabetologia 49*, 706−712.

(17) Jin, C. H., Chae, S. Y., Son, S., Kim, T. H., Um, K. A., Youn, Y. S., Lee, S., and Lee, K. C. (2009) A new orally available glucagon-like peptide-1 receptor agonist, biotinylated exendin-4, displays improved hypoglycemic effects in db/db mice. *J. Controlled Release 133*, 172−177.

(18) Chae, S. Y., Jin, C. H., Shin, J. H., Son, S., Kim, T. H., Lee, S., Youn, Y. S., Byun, Y., Lee, M. S., and Lee, K. C. (2010) Biochemical, pharmaceutical and therapeutic properties of long-acting lithocholic acid derivatized exendin-4 analogs. *J. Controlled Release 142*, 206−213.

(19) Son, S., Chae, S. Y., Kim, C. W., Choi, Y. G., Jung, S. Y., Lee, S., and Lee, K. C. (2009) Preparation and structural, biochemical, and pharmaceutical characterizations of bile acid-modified long-acting exendin-4 derivatives. *J. Med. Chem. 52*, 6889−6896.

(20) Kim, T. H., Jiang, H. H., Lee, S., Youn, Y. S., Park, C. W., Byun, Y., Chen, X., and Lee, K. C. (2011) Mono-PEGylated dimeric exendin-4 as high receptor binding and long-acting conjugates for type 2 anti-diabetes therapeutics. *Bioconjugate Chem. 22*, 625−632.

(21) Kim, T. H., Youn, Y. S., Jiang, H. H., Lee, S., Chen, X., and Lee, K. C. (2011) PEGylated TNF-related apoptosis-inducing ligand (TRAIL) analogues: pharmacokinetics and antitumor effects. *Bioconjugate Chem. 22*, 1631−1637.

(22) Chae, S. Y., Kim, T. H., Park, K., Jin, C. H., Son, S., Lee, S., Youn, Y. S., Kim, K., Jo, D. G., Kwon, I. C., Chen, X., and Lee, K. C. (2010) Improved antitumor activity and tumor targeting of NH(2)-terminal-specific PEGylated tumor necrosis factor-related apoptosis-inducing ligand. *Mol. Cancer Ther. 9*, 1719−1729.

(23) Yamamoto, Y., Tsutsumi, Y., Yoshioka, Y., Nishibata, T., Kobayashi, K., Okamoto, T., Mukai, Y., Shimizu, T., Nakagawa, S., Nagata, S., and Mayumi, T. (2003) Site-specific PEGylation of a lysine-deficient TNF-alpha with full bioactivity. *Nat. Biotechnol. 21*, 546−552.

(24) Moreadith, R. W., and Collen, D. (2003) Clinical development of PEGylated recombinant staphylokinase (PEG-Sak) for bolus thrombolytic treatment of patients with acute myocardial infarction. *Adv. Drug Delivery Rev. 55*, 1337−1345.

(25) Rosendahl, M. S., Doherty, D. H., Smith, D. J., Carlson, S. J., Chlipala, E. A., and Cox, G. N. (2005) A long-acting, highly potent interferon alpha-2 conjugate created using site-specific PEGylation. *Bioconjugate Chem. 16*, 200−207.

Bioconjugate Chemistry

Article

pubs.acs.org/bc

Bioluminescent Capsules for Live-Cell Imaging

Sung Bae Kim,*[,†] Yuzuru Ito,[‡] and Masaki Torimura[†]

[†]Research Institute for Environmental Management Technology, National Institute of Advanced Industrial Science and Technology (AIST), Onogawa 16-1, Tsukuba, Ibaraki 305-8569, Japan

[‡]Research Center for Stem Cell Engineering, National Institute of Advanced Industrial Science and Technology (AIST), Higashi 1-1-1, Tsukuba, Ibaraki 305-8562, Japan

Supporting Information

ABSTRACT: A bioluminescent capsule was designed for illuminating cell signaling and protein localization. The capsule consists of four components, namely, a secretion peptide (SP), a luciferase body, a cargo protein (or peptide), and a membrane-localization signal (MLS). Any functional proteins sandwiched between the luciferase body and MLS may be cartable to the plasma membrane (PM), where the capsule waits for outer signals and quickly releases the embedded luciferase in response to the signals. With this strategy of locating the capsule in the PM, the bioluminescence intensity was greatly prolonged and strengthened. A staurosporine (STS)-activated apoptosis signaling was efficiently imaged with the capsule carrying a DEVD peptide. Other functional proteins, such as fluorescent proteins and luciferases, were efficiently transported to the membrane by the capsule. A 60-nm-red-shifted bioluminescence was observed with a capsule fused with other luciferases or fluorescent proteins in living cells. This study gives a new insight regarding how to illuminate cellular signals with bioluminescence in living mammalian cells.

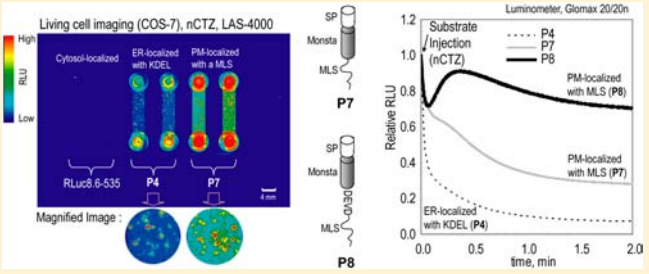

INTRODUCTION

Bioluminescence is an emerging optical readout to compensate drawbacks of fluorescence, such as poor signal-to-background ratios and the requirement of an outer light source.[1,2] However, bioluminescence also comprises intrinsic demerits, such as poor optical intensity and requirement of substrate, which severely hamper the use in living cells and organisms.[3]

To address the poor optical properties of bioluminescence, new variants of marine and beetle luciferases have been developed.[4,5] We have also created a series of superluminescent variants of marine luciferases with prolonged bioluminescence.[6] These engineered luciferases have greatly improved the optical intensities and sensorial efficiency of bioassays, such as two-hybrid assays, protein-fragment complementation assays (PCA),[7] single-chain probes,[8] and metastasis imaging of tumors in living mice.[6]

On the other hand, substrate-derived issues of luciferases in bioassays are still a major drawback, especially when being used in live cells. The drawbacks include (i) membrane permeability of the substrates and (ii) biased diffusion of the substrate into the compartments of mammalian cells. In particular, organelle-sequestered luciferases should immediately consume nearby coelenterazine (CTZ) and molecular oxygen (O_2), and may fall into substrate anoxia in living mammalian cells and tissues. This is a common problem of marine and beetle luciferases localized in cellular compartments of live cells, because sufficient amounts of the substrates and O_2 should rapidly pass through the plasma membrane (PM) and endomembranes to reach the luciferases in the organelles. Under the deficiency of substrate and O_2, the optical intensities should be dominated simply by the rates of the substrate and O_2 supply.

Santos et al. previously represented a display of a *Gaussia* luciferase (GLuc) fusion on the PM of T cells for mouse imaging,[9] where GLuc was inserted between the leader peptide (1−18 AA) and transmembrane domain (137−212 AA) of CD8. Suzuki et al. also reported a GLuc fusion linked with the signal peptide sequence (1−46 AA) of dopamine-β-hydroxylase (DBH), which was displayed on the PM surface.[10] However, these molecular designs are monotonous and focused on the outer membrane display of a luciferase. Furthermore, these methods do not guide on how to determine intracellular signal transductions in living cells.

To address the above-mentioned drawbacks of conventional approaches, we constructed a bioluminescent capsule located in the PM of mammalian cells, where the capsule waits for the outer signals and signal-dependently provokes the embedded luciferase release. The capsule consists of a secretion peptide (SP), a luciferase body, a cargo protein (or peptide), and a membrane-localization signal (MLS). Any cargo proteins with specific functionalities may be cartable by the capsule to the endoplasmic reticulum (ER) and PM. An apoptosis signaling pathway was examined with the capsule carrying caspase-substrate peptides comprising Asp-Glu-Val-Asp (DEVD) or Ile-Glu-Thr-Asp (IETD) motifs as an example of cellular molecular

Received: June 19, 2012
Revised: September 4, 2012
Published: October 31, 2012

ACS Publications © 2012 American Chemical Society

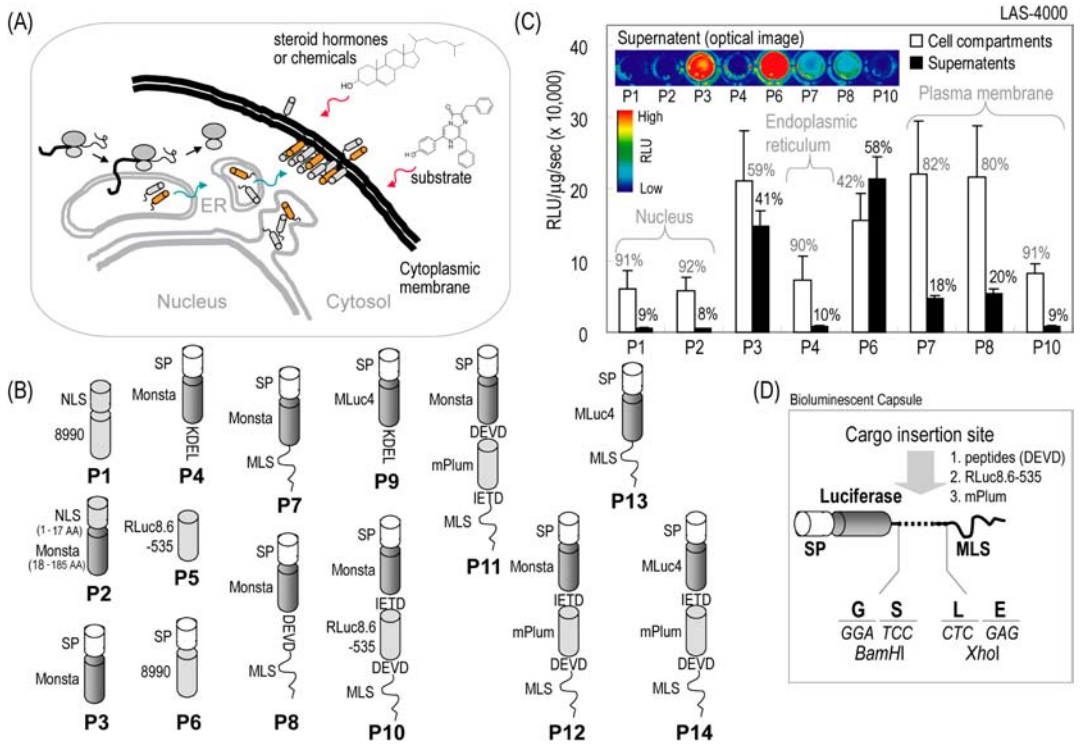

Figure 1. Bioluminescent capsules localized in the plasma membrane. (A) Localization of luciferases in the cellular compartments of living cells. (B) Schematic cartoon of fusion luciferases used in the present study. The fusion luciferases were named **P1**−**P14**, according to the designed structures. (C) Relative optical intensities of the cell lysates and the supernatants (culture medium) (n = 5). Inset shows an optical image of the supernatants. (D) Basic formation of bioluminescent capsules for live-cell imaging. Any cargo proteins may be inserted into the capsule for the membrane localization. Abbreviations: NLS, nuclear localization signal; SP, secretion peptide; MLS, membrane localization signal.

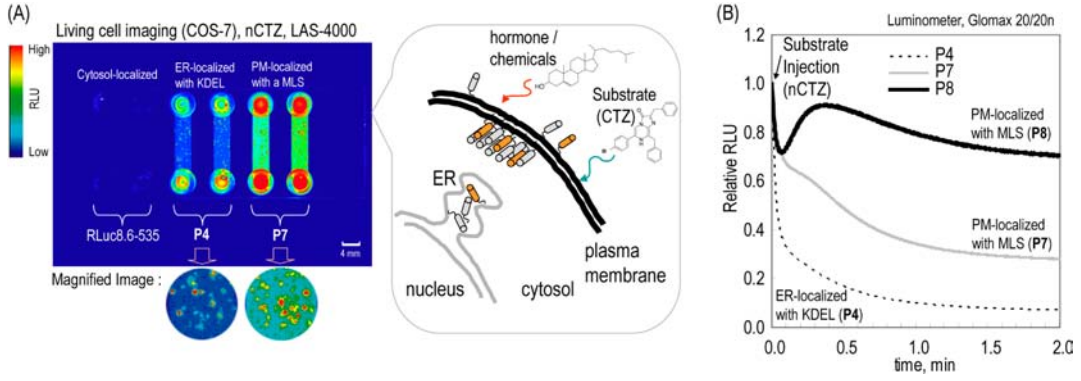

Figure 2. Bioluminescent capsules for live-cell imaging. (A) Relative optical intensities of luciferases localized in the cytosol (RLuc8.6−535; **P5**), endoplasmic reticulum (ER; **P4**), and plasma membrane (PM; **P7**) of live COS-7 cells on a microslide (2.5 × 7.5 cm, ibidi) (n = 2). Upon interaction of luciferases with the substrate on the PM, bioluminescence is efficiently developed. (B) Time course of luciferase reactions in the ER (**P4**) and PM (**P7** and **P8**) of live COS-7 cells using a luminometer (GloMax 20/20n, Promega) (n = 2). Abbreviations: nCTZ, native coelenterazine; RLuc8.6, Renilla luciferase 8.6; MLS, membrane localization signal; KDEL, an ER-localization signal consisting of amino acids, K, D, E, and L.

dynamics. Not only the peptides, but also fluorescent proteins and luciferases were found to be portable by the capsule. We have discussed in detail the enhanced optical properties and advantages of the capsules in mammalian cells.

■ EXPERIMENTAL PROCEDURES

Reagents and Instrumentation. The substrates, native coelenterazine (nCTZ) and Viviren, were purchased from Promega. A bioluminescence assay kit (cat. E2820) was purchased from Promega and used (Figures 1 and 3B, and Supporting Figure 3A). A Hanks' balanced salt solution (HBSS) buffer was obtained from Wako Pure Chemical and used for cell imaging (Figures 2, 3A, 4, and 5, and Supporting Figures 2A and 4). Microslides (2.5 × 7.5 cm, μ-slide VI$^{0.4}$) were purchased from ibidi (Germany). pcDNA3.1(+) and TransIT-LT1 were obtained from Invitrogen and Mirus, respectively. Both staurosporine (STS) and carbobenzoxy-valyl-alanyl-aspartyl-[o-methyl]-fluoromethylketone (Z-VAD-FMK) were purchased from Enzo Life Science.

Bioluminescence was quantified with a luminometer (GloMax 20/20n; Promega) or a microplate reader (SH-9000, Corona electric). The spectra for bioluminescent capsules

dx.doi.org/10.1021/bc300323x | Bioconjugate Chem. 2012, 23, 2221−2228

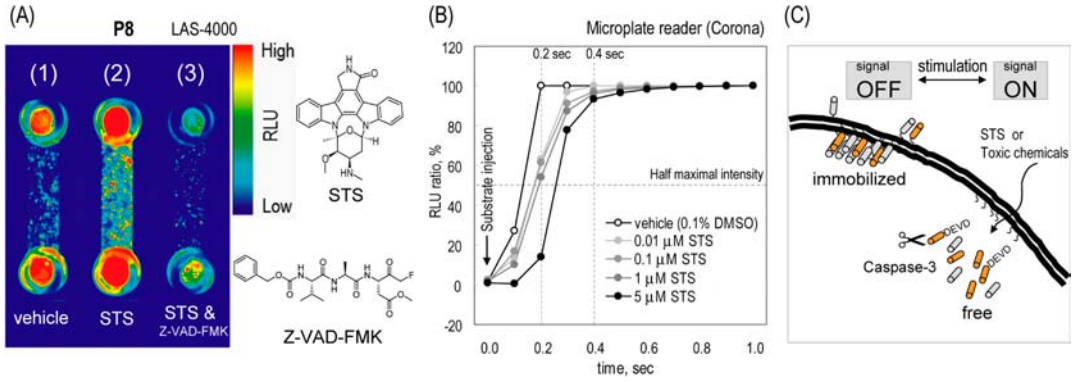

Figure 3. Bioluminescent imaging of apoptosis signaling with **P8** in live COS-7 cells. (A) Optical images of apoptosis signaling in live COS-7 cells in the presence or absence of 1 μM STS. (B) Short-time optical dynamics of live COS-7 cells carrying **P8** within 1 s after stimulation with varying concentrations of staurosporine (STS). The vehicle-stimulated bioluminescent capsule exhibited the most rapid elevation of the intensity after injection of nCTZ. The elevation of luminescence intensities was recorded every 0.1 s using a microplate reader (Corona), (n = 2). (C) Schematic diagram of apoptosis signaling at the plasma membrane before and after a chemical stimulation. Toxic chemicals activate caspase-3 that cleaves a specific sequence, DEVD. Abbreviations: STS, an apoptosis inducer named staurosporine; Z-VAD-FMK, an apoptosis inhibitor; DEVD, a peptide cleaved by active caspase-3 during apoptosis; DMSO, dimethyl sulfoxide.

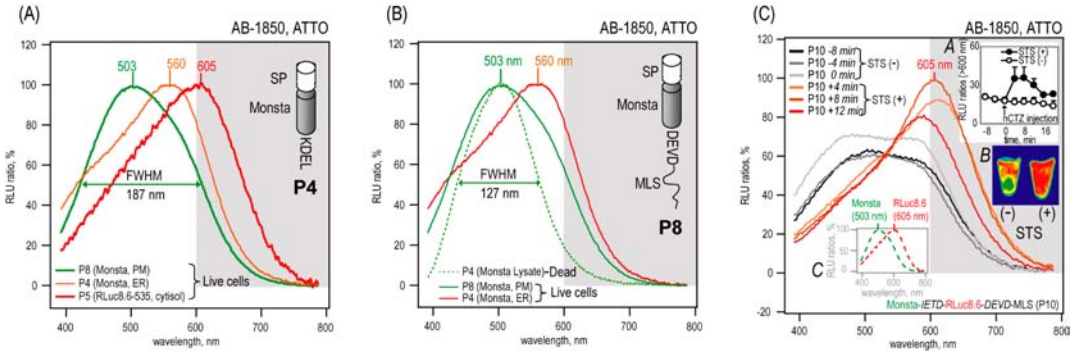

Figure 4. Normalized spectra of bioluminescent capsules in organelles of live COS-7 cells. The gray boxes highlight red and near-infrared region in the spectra. (A) Variation of bioluminescent spectra of the capsules localized in different compartments of live COS-7 cells (n = 2). (B) Variation of bioluminescent spectra of Monsta in **P4** and **P8** (n = 2). The λ_{max} of Monsta varies according to the localization and the host cell state—alive or dead (lysate). (C) Time course of bioluminescent spectra of **P10** from live COS-7 cells before and after the stimulation with 1 μM staurosporine (STS). Inset *A* shows the percent of emitted photons that are greater than 600 nm (red and near-infrared region) in the presence or absence of stimulation with 1 μM STS (n = 2). Inset *B* exhibits a bioluminescence image of COS-7 cells carrying **P10**, captured using LAS-4000 (FujiFilm) equipped with a 600-nm-long-pass filter. Inset *C* shows the spectra of individual Monsta and RLuc8.6−535. Abbreviations: fwhm, full width at half maximal intensity; PM, plasma membrane; ER, endoplasmic reticulum; IETD, a peptide cleaved by caspase-8; STS, an apoptosis inducer named staurosporine.

were determined with a high-sensitivity charge-coupled-device (CCD) spectrophotometer for accurate calculation of the light-collection efficiency (AB-1850, ATTO).[11] The bioluminescence images shown in Figures 1C, 2A, and 3A were taken with an image analyzer (LAS-4000 mini, FujiFilm).

Construction of Plasmids. As a template for polymerase chain reaction (PCR), cDNAs encoding the following luciferases were obtained from the corresponding providers: *Renilla* luciferase 8.6−535 (RLuc8.6−535) was kindly provided by Prof. Gambhir (Stanford University); cDNAs encoding 8990, *Metridia pacifica* luciferase 4 (MpLuc4), *Metridia longa* luciferase 4 (MLuc4), and Monsta were custom-synthesized.[6,12] cDNA encoding mPlum was purchased from Clontech.

The cDNAs encoding 8990, RLuc8.6−535, and mPlum were generated by PCR using corresponding primers to introduce unique restriction sites, *Hind*III, *Bam*HI, and *Xho*I, according to the design of DNA constructs shown in Supporting Figure 1. Both the ends of cDNAs encoding 8990, Monsta, RLuc8.6−535, and mPlum were extended by PCR to introduce specific nucleotides encoding DEVD, nuclear localization signal (NLS), MLS, and IETD as shown in Supporting Figure 1. The cDNA fragments were ligated to make a series of chimera constructs, and subcloned into a mammalian expression vector, *p*cDNA 3.1(+) vector (Invitrogen).

The generated plasmids were named *p*P1, *p*P2, *p*P3, and so forth according to the serial numbers, as shown in Figure 1. The plasmid encoding RLuc8.6−535 was named *p*RLuc8.6−535. The corresponding fusion proteins after expression were named **P1**, **P2**, **P3**, and so forth. The sequences of the plasmids were confirmed by a custom order to a sequencing service of Operon (Tokyo, Japan).

Relative Optical Intensities of the Cell Compartments and the Culture Media. Intracellular retention ratios of the capsules were examined according to the localization signals (Figure 1C). COS-7 cells raised in 96-well plates were transiently transfected with an aliquot (0.1 μg/μL/well) of *p*P1, *p*P2, *p*P3, *p*P4, *p*P6, *p*P7, *p*P8, or *p*P10 using a lipofection reagent, TransIT-LT1 (Mirus). The cells were incubated for 16 h and 10 μL of the supernatants (culture media) were stocked in a new 96-well plate, named Plate 1. The remaining culture media were decanted from the original plate. The cells on the original plate were then lysed in a lysis buffer (E291A,

dx.doi.org/10.1021/bc300323x | *Bioconjugate Chem.* 2012, 23, 2221−2228

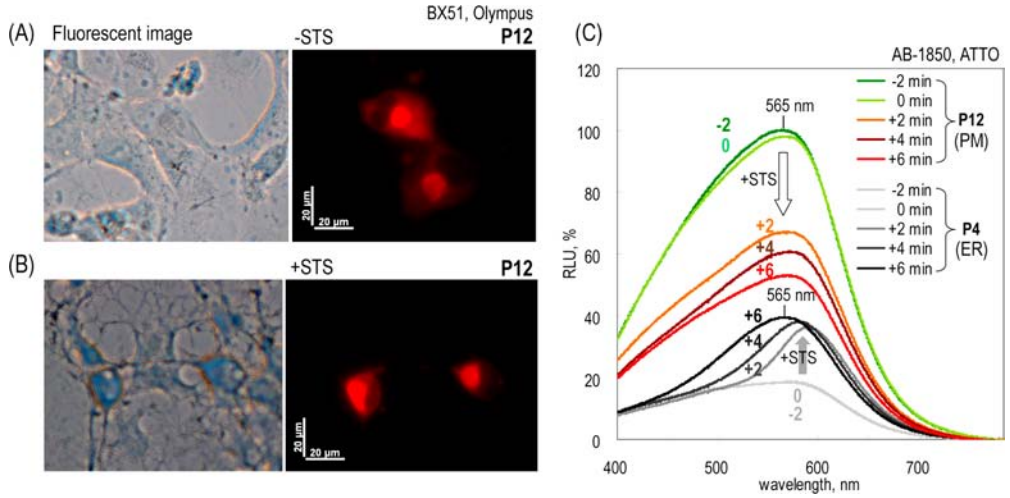

Figure 5. Subcellular localization of **P12** in COS-7 cells. (A) Fluorescent image of intracellular localization of **P12** without staurosporine (STS) stimulation. (B) Fluorescent image of intracellular localization of **P12** after stimulation with 10 μM STS. (C) Time course of bioluminescent spectra for **P4** and **P12** from live COS-7 cells before and after the stimulation with 1 μM STS (n = 2). The digits, from −2 to +6, indicate specific times in minutes before and after the STS stimulation. The spectra were taken for an integration time of 30 s and an interval of 2 min. Abbreviations: STS, an apoptosis inducer named staurosporine.

Promega) for 20 min and 10 μL of the lysates were transferred into a separate microplate, named Plate 2.

The optical intensities from each well of Plates 1 and 2 were determined with the image analyzer (LAS-4000, FujiFilm) after simultaneous injection of 40 μL of nCTZ dissolved in an assay buffer (E290B, Promega) using an 8-channel pipet. The optical image was recorded for 2 s and quantitatively analyzed with a specific software (*Multi Gauge v 3.1*, FujiFilm).

The amounts of total proteins in 10 μL of the lysates and supernatants were determined for normalization using a Bradford reagent (Bio-Rad). The brief procedure for the normalization of bioluminescence is as follows: The luminescence intensities in relative luminescence unit (RLU; arbitrary unit) were divided by integration time (s) and protein amounts (μg), i.e., RLU/μg/s.

An assay, similar to the one presented in Figure 1C, determining an intracellular retention of luciferases in the capsules, was also conducted with a microplate reader (Supporting Figure 2A).

Relative Optical Intensity and Stability of Luciferases in Live COS-7 Cells. An optical image of live COS-7 cells on a microplate (μ-slide VI$^{0.4}$, ibidi) was taken with an image analyzer, LAS-4000 (Figure 2A). COS-7 cells raised in the microslide were transiently transfected with an aliquot of *p*RLuc8.6−535 (two channels in the left), *p*P4 (two channels in the middle), or *p*P7 (two channels in the right), and incubated for 20 h. The culture media in the slide were replaced with an nCTZ-dissolved HBSS buffer. The optical image of the slide was finally obtained after 30 s of integration time with LAS-4000 (FujiFilm). The optical intensities from the microslide were compared using an image analyzing software (*Multi Guage v 3.1*, FujiFilm).

The optical stability of **P4**, **P7**, and **P8** was also examined using a luminometer (GloMax 20/20*n*, Promega) (Figure 2B). COS-7 cells raised in 35 mm glass-bottom plates (Iwaki) were transiently transfected with an aliquot of *p*P4, *p*P7, or *p*P8, and incubated for 16 h. The culture media in the plates were replaced with an HBSS buffer and placed in the luminometer. The time course of the optical intensities was recorded after programmed automatic injection of nCTZ. The optical intensities were normalized to the maximal intensity at time zero.

Imaging Apoptosis Signaling in Live COS-7 Cells. Apoptosis-driven elevation of bioluminescence intensity was determined with a microslide (μ-slide VI$^{0.4}$, ibidi) raising COS-7 cells (Figure 3A). The COS-7 cells raised in the microslide were transiently transfected with *p*P8, and incubated for 16 h. The culture media in the plates were replaced with a 50-mM-KI-added HBSS buffer carrying (i) vehicle (0.1% DMSO), (ii) 0.01 μM STS, or (iii) 1 μM STS plus 50 μM Z-VAD-FMK. Two hours after stimulation, the HBSS buffers in the microplates were then replaced with a fresh HBSS buffer carrying nCTZ for imaging. The optical image was determined with the image analyzer (LAS-4000, FujiFilm), with 4 s integration. The result was confirmed using COS-7 cells carrying **P8** and Viviren (Supporting Figure 3A).

Optical dynamics of COS-7 cells carrying **P8** was estimated 30 min after stimulation with varying concentrations of STS (Figure 3B). The COS-7 cells raised in a 96-well plate were transiently transfected with *p*P8 and incubated for 16 h in a CO_2 incubator (Sanyo). The culture media were replaced with fresh media carrying vehicle (0.1% DMSO), 0.01 μM STS, 0.1 μM STS, 1 μM STS, or 5 μM STS. The plate was additionally incubated for 20 min in the CO_2 incubator and transferred into a microplate reader (SH-9000, Corona) equipped with an automatic injector after culture media removal. The elevation of optical intensities was monitored every 0.1 s after programmed injection of nCTZ dissolved in an assay buffer (E290B, Promega). The optical dynamics was normalized to the saturated maximal intensity.

On the basis of the above-mentioned understanding, toxicity of several steroids and chemicals was evaluated using COS-7 cells carrying **P8** (Supporting Figure 3B). The COS-7 cells raised in a 96-well plate were transiently transfected with *p*P8 and incubated in a CO_2 incubator for 16 h. The COS-7 cells in one part of the plate were stimulated with varying concentrations of STS for 20 min, while those in the remaining part were stimulated with 10^{-5} M of steroids or chemicals for 20 min. The optical intensities of the plate were then estimated after automatic injection of nCTZ to the wells of the plate.

dx.doi.org/10.1021/bc300323x | *Bioconjugate Chem.* 2012, 23, 2221−2228

Spectra for Bioluminescent Capsules in Organelles of Live COS-7 Cells. Characteristic spectra for luciferases and bioluminescent capsules were determined and compared (Figure 4). The COS-7 cells raised in 35 mm glass-bottom plates were transiently transfected with *p*Monsta, *p*P4, *p*P8, *p*P9, or *p*P10 using a lipofection reagent, TransIT-LT1 (Mirus), and incubated for 20 h.

For the experiments illustrated in Figure 4A,B, the culture media in the plates were replaced with an nCTZ-dissolved HBSS buffer. The bioluminescence spectra were determined with a high-sensitivity CCD spectrophotometer (AB-1850, ATTO) at 0 and 10 min after medium replacement. Integration time was 1 min. The spectra were normalized to the maximal intensity.

Meanwhile, for the experiment presented in Figure 4C, the culture media in the plates were first replaced with an nCTZ-dissolved HBSS buffer. Variation of the bioluminescence spectra before and after addition of 1 μM STS (final concentration) was monitored every 4 min using the CCD spectrophotometer (AB-1850, ATTO) with 1 min integration time. The spectra were normalized to the maximal intensity.

Locating Fluorescent Proteins in the PM. A red fluorescent protein, mPlum, was inserted into the capsule and carried to the PM (Figure 5).

The COS-7 cells raised in 3.5 cm glass-bottom dishes (Iwaki) were transiently transfected with *p*P12, and incubated for 16 h in a CO_2 incubator (Figure 5A and 5B). The cells on the dishes were then stimulated with vehicle (0.1% DMSO) or 5 μM STS for 20 min. The culture media on the dishes were replaced with HBSS buffer. The cells were then placed in a fluorescent microscope (BX51, Olympus) equipped with a band-pass filter at an excitation of 510−560 nm and with a long-pass filter at an emission of over 590 nm. The optical images were taken in an automatic exposure mode and managed using controlling software (*AxioVision v 4.6*). A similar study was also conducted with COS-7 cells carrying **P11** (Supporting Figure 4).

The COS-7 cells raised in 3.5 cm glass-bottom dishes (Iwaki) were transiently transfected with *p*P4 or *p*P12, and incubated for 16 h in a CO_2 incubator (Figure 5C). The culture media on the plates were replaced with an nCTZ-dissolved HBSS buffer. Bioluminescence spectra of each plate were determined every 4 min using the CCD spectrophotometer (AB-1850, ATTO) with 1 min integration time. The spectra were normalized to the maximal intensity.

RESULTS

MLS Efficiently Suppresses Secretion of Copepod Luciferases. The bioluminescent capsules were grouped into four and their intracellular retention efficiency was compared (Figure 1); i.e., (i) luciferases carrying only SP as a control (**P3**, **P6**), (ii) luciferases additionally fused with NLS (**P1**, **P2**), (iii) luciferases fused with an ER-localization signal (KDEL) (**P4**), and (iv) luciferases fused with MLS (**P7**, **P8**, **P10**). In the absence of any intracellular retention signals, a large portion of **P3** and **P6** is efficiently secreted into the extracellular matrix, whereas in the presence of a localization signal, the majority of the other luciferases carrying NLS (ca. 90%), KDEL (ca. 90%), or MLS (ca. 80%) is retained in the intracellular compartments. The comparison among **P7**, **P8**, and **P10** revealed that (i) a cargo protein (peptide) can be inserted between Monsta and MLS, and (ii) a larger cargo protein contributes to greater retention of the host capsule in the intracellular compartments; e.g., retention ratios of **P7** and **P10** were found to be 82% and 91%, respectively.

The above-mentioned study demonstrates that any cargo proteins or peptides may be inserted between Monsta and MLS, and carried to the PM for protein display and imaging.

MLS Enhances the Optical Intensities and Stability of the Host Luciferases. The relative optical intensities of RLuc8.6−535, **P4**, and **P7** were compared with a microslide raising live COS-7 cells (Figure 2). In the microslide, the COS-7 cells carrying **P4** (located in the ER) and **P7** (located in the PM) exhibited 35 and 70 times stronger bioluminescence intensities, respectively, than those carrying RLuc8.6−535 (cytosol) (Supporting Figure 2A). Furthermore, the kinetic study shown in Figure 2B indicates that the COS-7 cells carrying **P7** and **P8** (PM) emit bioluminescence with an excellent optical stability, when compared with those carrying **P4** (ER). It is interesting to compare the optical stability of **P7** and **P8**. The only difference between **P8** from **P7** is the peptide spacer, DEVD, inserted between Monsta and MLS. This insertion of the peptide surprisingly elevated the optical stability of **P8**. The poor optical stability of **P7** may be caused by a steric hindrance.

The above-mentioned results demonstrate that (i) locating fusion luciferases in the PM improves the optical properties in living mammalian cells, (ii) locating fusion luciferases in the PM is advantageous with regard to point of access of the substrate and O_2, and (iii) a cargo peptide, DEVD, in **P8** may act as a spacer and, thus, exert flexibility to the host luciferase.

P8 Efficiently Illuminates STS-Induced Apoptosis Signaling of Live COS-7 Cells. Activation of caspase-3 during apoptosis signaling was visualized with live COS-7 cells carrying **P8** (Figure 3A). The optical intensity from COS-7 cells carrying **P8** was two times enhanced by stimulation with 0.01 μM STS for 2 h (Lane 2), whereas the intensity was invariable by co-stimulation with 1 μM STS and 50 μM Z-VAD-FMK (Lane 3). This result demonstrates that (i) STS-stimulated caspase-3 cleaved the specific peptide, DEVD, in the membrane-immobilized **P8**, enhancing the optical intensities of the cells, and (ii) the enhanced optical intensity in Lane 2 indicates activation of caspase-3 during apoptosis, considering the efficient inhibition effect of Z-VAD-FMK. A corresponding result was obtained with the same COS-7 cells carrying **P8**, exhibiting STS-dependent elevation of the optical intensities (Supporting Figure 3A). Furthermore, the toxicity of steroids and chemicals was examined with the above-mentioned COS-7 cells carrying **P8** (Supporting Figure 3B). We found that 10^{-5} M of DHT, cortisol, and mifepristone weakly elevate the optical intensities, indicating their biotoxicity to COS-7 cells.

The optical dynamics of COS-7 cells carrying **P8** was estimated after stimulation of the cells with varying concentrations of STS (Figure 3B). The elevation speed of the optical intensities was found to depend on the concentration of STS. At 0.2 s after substrate injection, the optical intensity from vehicle-stimulated COS-7 cells was already saturated, whereas that from COS-7 cells stimulated with 5 μM STS reached merely 15% of the maximal intensity at the same time point (closed circle). This result is considered as indirect evidence of cleavage of **P8** by caspase-3, because most of the **P8** should be localized at the PM in the absence of STS, which is immediately accessed by the substrate and O_2. On the other hand, **P8** was freed by cleavage of caspase-3 and localized all over the cytosol. In this case, the substrate took time to access **P8**. This on−off mechanism is illustrated in Figure 3C.

dx.doi.org/10.1021/bc300323x | *Bioconjugate Chem.* 2012, 23, 2221−2228

Monsta Varies Its Colors in an Organelle-Dependent Manner in Living Cells. The bioluminescence spectra of COS-7 cells carrying **P4**, **P5**, and **P8** were determined using a high-sensitivity CCD spectrophotometer (AB-1850, ATTO) (Figure 4A). Monsta immobilized at the PM (**P8**) exhibited maximal intensity (λ_{max}) at 503 nm (green), whereas Monsta localized in the ER (**P4**) showed λ_{max} at 560 nm (orange). Furthermore, the λ_{max} of RLuc8.6−535 located in the cytosol (i.e., **P9**) was 605 nm (red) in live COS-7 cells.

We further compared the λ_{max} of **P4** and **P8** in live and lysed (dead) COS-7 cells (Figure 4B). The λ_{max} of live COS-7 cells carrying **P4** was 503 nm, which was found to be equivalent to that of lysed COS-7 cells carrying **P4**. The obtained λ_{max} of **P4** is exactly the same as the previously reported value.[6] Notable difference in the spectra of the live and lysed COS-7 cells was only found in the full width at half-maximal intensity (fwhm). FWHMs of the spectra from live and lysed COS-7 cells were 188 and 127 nm, respectively.

P10 Transiently Enhances Red Color upon Apoptosis Signaling by STS. The variance in the spectra of live COS-7 cells carrying **P10** was monitored before and after stimulation with STS (Figure 4C). In the absence of STS stimulation, the spectra of live COS-7 cells were almost invariant, whereas they showed dynamically enhanced intensity in the red region after addition of 1 μM STS (final concentration). The percent of emitted photons greater than 600 nm was transiently elevated up to ca. 40% (Figure 4C, inset).

mPlum in P11 and p12 is Transported to the PM via the ER. Subcellular localization of the bioluminescent capsules carrying a cargo protein, mPlum (**P12**), was examined in the COS-7 cells (Figure 5A). In the absence of STS, the overall cell image appeared smear. The nucleus was relatively transparent, indicating absence of **P12**, whereas the ER region showed acute bioluminescence intensity, exhibiting that a considerable amount of **P12** is located in the ER.

Comparison between the fluorescent and transmission images (Figure 5A) demonstrated that the capsules, **P12**, are mainly localized in the ER and PM at the basal condition (absence of STS). The smear fluorescent image was observed and superimposed with the area of the host cells. The capsules in the presence of STS were found to be fragmented by caspase-3 and -8, and released from the PM (Figure 5B). The characteristic smear of the fluorescent images was notably faded with the addition of l μM STS. A corresponding feature was observed with the COS-7 cells carrying **P11** (Supporting Figure 4).

Kinetic variance of the spectra of **P4** and **P12** was monitored before and after the addition of 1 μM STS (Figure 5C). The strong bioluminescence intensities by **P12** quickly decayed with the addition of 1 μM STS. In contrast, the optical intensities by **P4** were elevated with the addition of the same concentration of STS.

■ DISCUSSION

The PM defines the cell boundaries and acts as a key interface that senses external signals, allowing the cells to change its behavior in response to environmental cues.[13] It is considered that the PM has particularly distinct privileges over other cellular compartments as a localization target of luciferases and bioluminescent probes upon molecular imaging; e.g., (i) the luciferases and probes on the PM immediately respond even to poor membrane-permeable signals, and (ii) the luciferases and probes on the PM can easily contact numerous substrates and O_2. It is a critical advantage because, under deficiency of the substrate and O_2, bioluminescence intensities are predominantly influenced by the supply. The sufficient supply of the substrate and O_2 is the reason for the excellent optical intensity and stability (Figure 2).

As a bioluminescent leader, copepod luciferases are advantageous over other luciferases with respect to the smallest molecular weight (20−24 kDa) and busting optical intensity. However, in contrast to the merits, copepod luciferases comprise multiple disulfide bonds that exert poor folding efficiency in the cytosol; thus, the ER is preferred for the folding. This secretion nature has been suppressed using an ER-localization peptide, e.g., KDEL.[14] In the present study, a bioluminescent capsule was designed (i) to carry any cargo protein to the PM via the ER and (ii) to quickly sense outer apoptosis stimulators. The present approach is characteristic with respect to dynamic variation of locations of the capsule: i.e., (i) it started folding in the cytosol, (ii) was translocated to the ER for maximal folding efficiency, and (iii) anchored on the PM awaiting outer signals, where the substrate and O_2 could favorably access the capsules (signal off), and (iv) finally returned to the cytosol through an outer stimulator (luciferase release; signal on). Apoptosis signaling was quantitatively illuminated with the capsules in live cells. This strategy addressed the common defects of luciferase-based bioassays, such as (i) biased diffusion of the substrate and O_2 in the organelles, (ii) poor folding efficiency of copepod luciferases in the cytosol, and (iii) poor sensitivity to less membrane-permeable ligands. The present study has demonstrated that any functional proteins, such as RLuc8.6−535 and mPlum, may be portable to the PM by the capsule.

STS-stimulated apoptosis signaling in COS-7 cells is considered to undergo the following process: (i) the protein kinase inhibitor, STS, first activates both caspase-2 and -9, which are apoptosis initiators mediated by ER and mitochondria, respectively.[15] (ii) Activation of these initiator caspases results in the activation of caspase-3, cleaving the specific sequence, DEVD, in the bioluminescent capsule. STS-induced apoptosis provokes the embedded luciferase (Monsta) release by active caspase-3. Interestingly, the released Monsta in free state exhibited ca. two times stronger optical intensity than membrane-immobilized Monsta in live COS-7 cells (Figure 3A). Furthermore, the optical intensity of the released Monsta in free state exhibited relatively slower elevation than that of immobilized Monsta (Figure 3C). The above-mentioned results can be interpreted as follows: (i) nCTZ and O_2 could easily access the membrane-immobilized Monsta rather than the released Monsta in free state, which is dispersed far from the PM, delaying the substrate access. (ii) The above-mentioned results suggest that the optical intensity and elevation rates of bioluminescence can be utilized as an optical readout of apoptosis signaling in living mammalian cells.

It is interesting to reason the color variance of Monsta in live COS-7 cells (Figure 4). Figure 4A shows that λ_{max} of **P4** in the ER of living cells surprisingly exhibits ca. 60 nm stock shift toward the red region, when compared with those of **P8** and **P4** in the PM and lysates of live cells, respectively.

This is a confusing result, because λ_{max} values of GLuc and its variants were found to be ca. 470−503 nm,[6,14,16] with all of the previous spectra determined with cell lysates (dead), instead of live cells. One of the persuasive reasons of the considerable stock shift may be the pH variance according to the organelles: It was previously reported that the pH of the endosomes of live

cells and a lysis buffer of Promega (i.e., dead cells) are about 5.8−6.3 and 5.5, respectively (more acidic), whereas the pH of the cytosol of live cells is around 7.0 (more basic).[17] This report suggests that the λ_{max} of the spectrum of Monsta was influenced by pH. Interestingly, the same pH dependency of λ_{max} was previously reported with firefly luciferase,[18] where the spectra gradually red-shifted with increasing acidity. This feature is consistent with the present results (Figure 4A,B).

Another interesting feature of the spectra was observed with the kinetics study on **P10** (Figure 4C). In the absence of STS, the shapes of the spectra of **P10** were almost invariant, whereas the addition of STS quickly enhanced the optical intensities at near 605 nm in the spectra. This feature may be interpreted as follows: (i) the optical intensities of RLuc8.6−535 fused in **P10** may have been initially suppressed, and (ii) the optical intensities may have been increased by free RLuc8.6−535 released from **P10** by active caspases. The dramatic intensity variance between free RLuc8.6−535 and fused RLuc8.6−535 was also reported by Kim et al. [19]

An interesting result was obtained with the comparison between **P4** and **P12** (Figure 5): The optical intensities of **P4** were immediately increased by 1 μM STS, whereas those of **P12** were quickly decreased by the same stimulation. This result can be interpreted as follows: Considering that **P4** is located in the ER, the intensity elevation by STS may have been caused by improved accessibility of the substrate to the ER or leakage of free Monsta from the ER to the PM during the apoptosis process. We also speculate that, in the case of **P12** located at the PM, digestion of the IETD and DEVD peptides by caspases might have caused cancellation of a synergistic energy transfer between Monsta and mPlum.

According to the results presented in Figures 4C and 5C, the capsules at the PM quickly respond to stimulation with 1 μM STS and vary its spectra merely within 2 min. These kinetic data were reviewed with precedent references as follows: A previous study, using a backscattering spectrum of mammalian cells, reported that a duration of 10 min is sufficient to activate proteases after STS addition.[20] Another study on measurement of caspase activities was conducted with a FRET probe. This study demonstrated that a few minutes after STS stimulation are sufficient to digest a major amount of a DEVD peptide inside the FRET probe.[21] These studies show that the present time scale on STS-induced apoptosis corresponds to the previous consensus.

In conclusion, the PM is an interface of material transfers and antenna of outer signals. With the present strategy of locating a bioluminescent capsule at the PM, intracellular molecular events can be efficiently explored with an environment of numerous substrates and O_2. This feature acts advantageously on the enhanced optical intensity and stability of the capsules in living mammalian cells. The live cells with **P7** were found to exhibit 70 times stronger optical intensities than those with RLuc8.6−535. Any cargo proteins may be portable to the PM with the capsule. Bioluminescent capsules carrying a DEVD peptide, RLuc8.6−535, or mPlum were observed to exhibit a dramatic signal-dependent conversion of the spectra in the presence of STS. The present approach addresses common drawbacks of reporter luciferases and luciferase-framed molecular probes, such drawbacks as deficient supply and biased diffusion of the substrate and O_2 in the organelles, and provides a new insight into design of molecular probes and investigation of the molecular nature of each intracellular compartment of living mammalian cells.

■ ASSOCIATED CONTENT

Supporting Information

Supplemental experimental data providing further information on (i) the schematic representations of domain structures of bioluminescent capsules, (ii) normalized optical intensities of the cell lysates and supernatants of COS-7 cells carrying **P4**, **P7**, and **P8**, (iii) relative optical intensities of **P4** and **P7** to **P5** (RLuc8.6−535) in a microslide, (iv) optical image of apoptosis signaling on a microslide 20 min after addition of varying concentrations of staurosporine (STS), (v) subcellular localization of **P11** in COS-7 cells, (vi) a table comparing characteristics of the constructed probes in the present study. This material is available free of charge via the Internet at http://pubs.acs.org.

■ AUTHOR INFORMATION

Corresponding Author

*E-mail: kimu-sb@aist.go.jp.

Notes

The authors declare no competing financial interest.

■ ACKNOWLEDGMENTS

This work was supported by a Grant-in-Aid for Young Scientists (B) from Japan Society for the Promotion of Science (JSPS) [Grant number: 23750096], and by a Grant-in-Aid for an A-Step program from Japan Science and Technology Agency (JST) [Grant number: AS232Z02075F].

■ REFERENCES

(1) Villalobos, V., Naik, S., and Piwnica-Worms, D. (2007) Current state of imaging protein-protein interactions in vivo with genetically encoded reporters. *Ann. Rev. Biomed. Eng. 9*, 321−349.

(2) Piston, D. W., and Kremers, G. J. (2007) Fluorescent protein FRET: the good, the bad and the ugly. *Trends Biochem. Sci. 32*, 407−414.

(3) Kim, S. B., Tao, H., and Umezawa, Y. (2009) Wiley-VCH, Darmstadt.

(4) Loening, A. M., Dragulescu-Andrasi, A., and Gambhir, S. S. (2010) A red-shifted Renilla luciferase for transient reporter-gene expression. *Nat. Methods 7*, 5−6.

(5) Li, X. Y., Nakajima, Y., Niwa, K., Viviani, V. R., and Ohmiya, Y. (2010) Enhanced red-emitting railroad worm luciferase for bioassays and bioimaging. *Protein Sci. 19*, 26−33.

(6) Kim, S. B., Suzuki, H., Sato, M., and Tao, H. (2011) Superluminescent variants of marine luciferases for bioassays. *Anal. Chem. 83*, 8732−8740.

(7) Kim, S. B., Sato, M., and Tao, H. (2009) Split Gaussia Luciferase-based bioluminescence template for tracing protein dynamics in living cells. *Anal. Chem. 81*, 67−74.

(8) Kim, S. B., Takenaka, Y., and Torimura, M. (2011) A bioluminescent probe for salivary cortisol. *Bioconjugate Chem. 22*, 1835−1841.

(9) Santos, E. B., Yeh, R., Lee, J., Nikhamin, Y., Punzalan, B., Punzalan, B., La Perle, K., Larson, S. M., Sadelain, M., and Brentjens, R. J. (2009) Sensitive in vivo imaging of T cells using a membrane-bound Gaussia princeps luciferase. *Nat. Med. 15*, 338−344.

(10) Suzuki, T., Usuda, S., Ichinose, H., and Inouye, S. (2007) Real-time bioluminescence imaging of a protein secretory pathway in living mammalian cells using Gaussia luciferase. *FEBS Lett. 581*, 4551−4556.

(11) Ando, Y., Niwa, K., Yamada, N., Irie, T., Enomoto, T., Kubota, H., Ohmiya, Y., and Akiyama, H. (2007) Development of a quantitative bio/chemiluminescence spectrometer determining quantum yields: Re-examination of the aqueous luminol chemiluminescence standard. *Photochem. Photobiol. 83*, 1205−1210.

(12) Kim, S. B., and Ozawa, T. (2010) Creating bioluminescent indicators to visualise biological events in living cells and animals. *Supramol. Chem. 22*, 440−449.
(13) Alberts, B. (1994) *Molecular biology of the cell*, 3rd ed., Garland Pub., New York.
(14) Tannous, B. A., Kim, D. E., Fernandez, J. L., Weissleder, R., and Breakefield, X. O. (2005) Codon-optimized Gaussia luciferase cDNA for mammalian gene expression in culture and in vivo. *Mol. Ther. 11*, 435−443.
(15) Caballero-Benitez, A., and Moran, J. (2003) Caspase activation pathways induced by staurosporine and low potassium: Role of caspase-2. *J. Neurosci. Res. 71*, 383−396.
(16) Rathnayaka, T., Tawa, M., Sohya, S., Yohda, M., and Kuroda, Y. (2010) Biophysical characterization of highly active recombinant Gaussia luciferase expressed in Escherichia coli. *Biochem. Biophys. Acta 1804*, 1902−1907.
(17) Schindler, M., Grabski, S., Hoff, E., and Simon, S. M. (1996) Defective pH regulation of acidic compartments in human breast cancer cells (MCF-7) is normalized in adriamycin-resistant cells (MCF-7adr). *Biochemistry 35*, 2811−2817.
(18) Viviani, V. R., Arnoldi, F. G. C., Neto, A. J. S., Oehlmeyer, T. L., Bechara, E. J. H., and Ohmiya, Y. (2008) The structural origin and biological function of pH-sensitivity in firefly luciferases. *Photochem. Photobiol. Sci. 7*, 159−169.
(19) Kim, S. B., Sato, M., and Tao, H. (2009) Molecular tension-indexed bioluminescent probe for determining protein-protein interactions. *Bioconjugate Chem. 20*, 2324−2330.
(20) Mulvey, C. S., Sherwood, C. A., and Bigio, I. J. (2009) Wavelength-dependent backscattering measurements for quantitative real-time monitoring of apoptosis in living cells. *J. Biomed. Opt. 14*.
(21) O'Connor, C. L., Anguissola, S., Huber, H. J., Dussmann, H., Prehn, J. H. M., and Rehm, M. (2008) Intracellular signaling dynamics during apoptosis execution in the presence or absence of X-linked-inhibitor-of-apoptosis-protein. *Biochim. Biophys. Acta 1783*, 1903−1913.

Suppl. Figure 1. Kim et al.

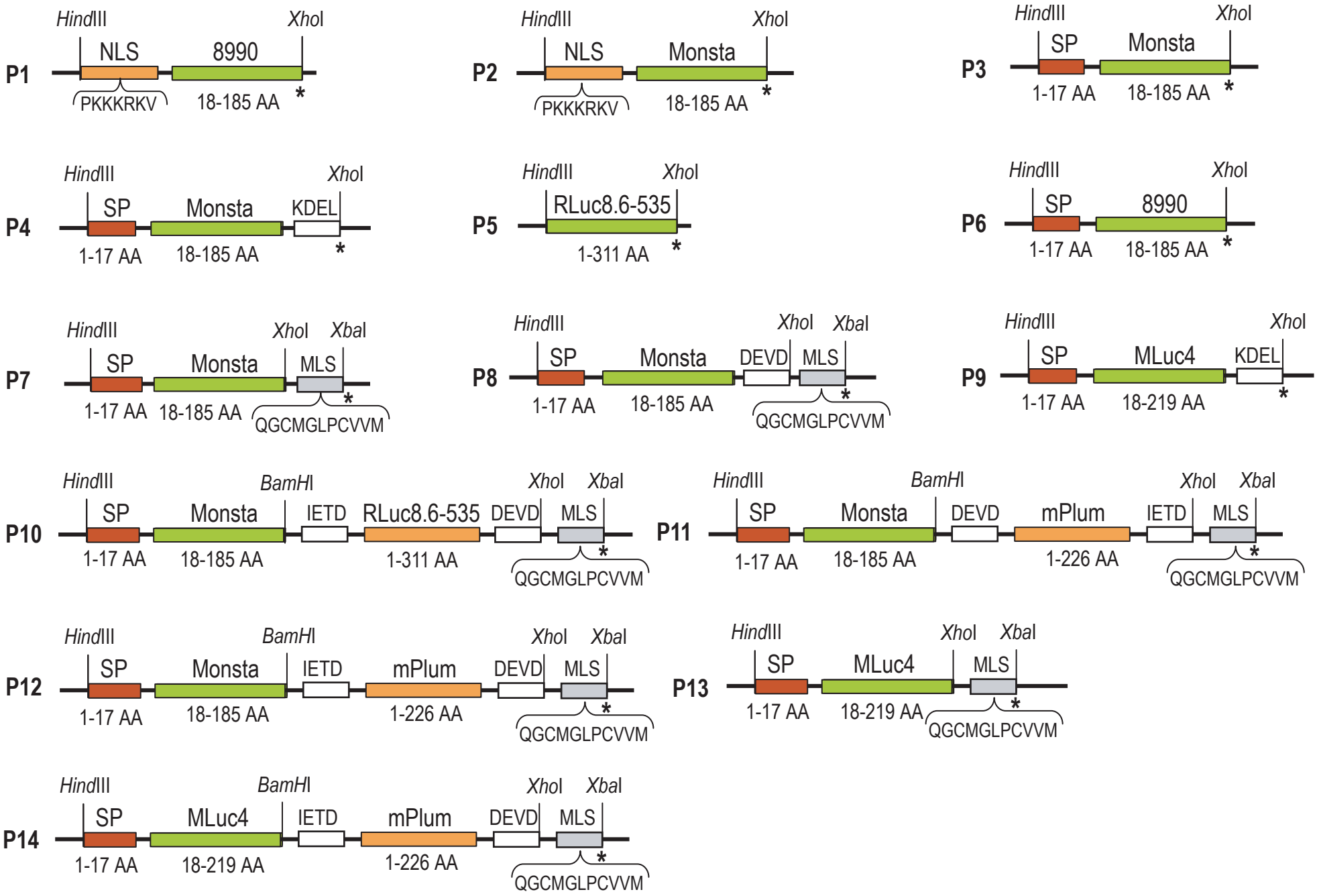

Supp. Figure 2. Kim et al.

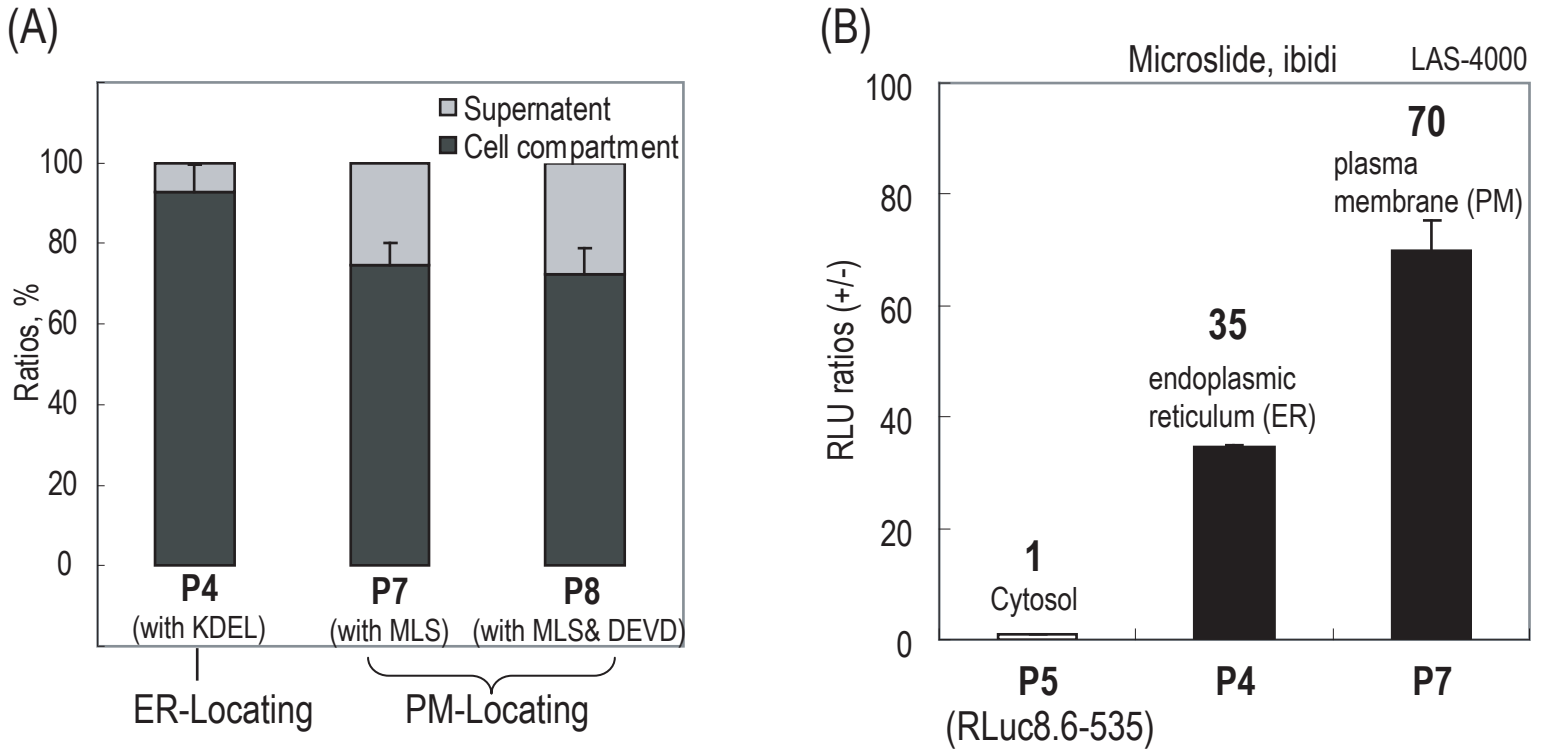

Suppl. Figure 3 Kim et al.

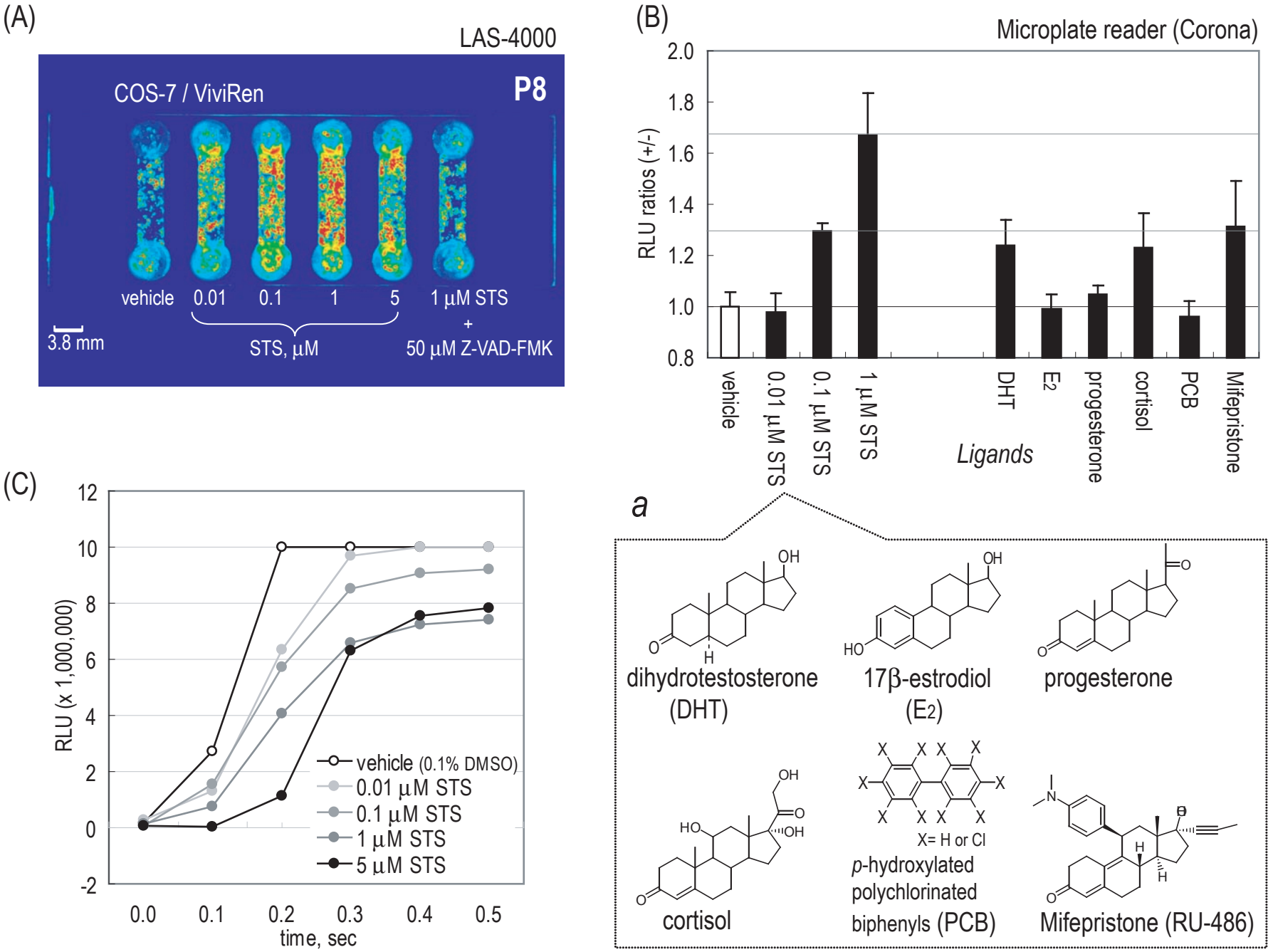

Suppl. Figure 4. Kim et al.

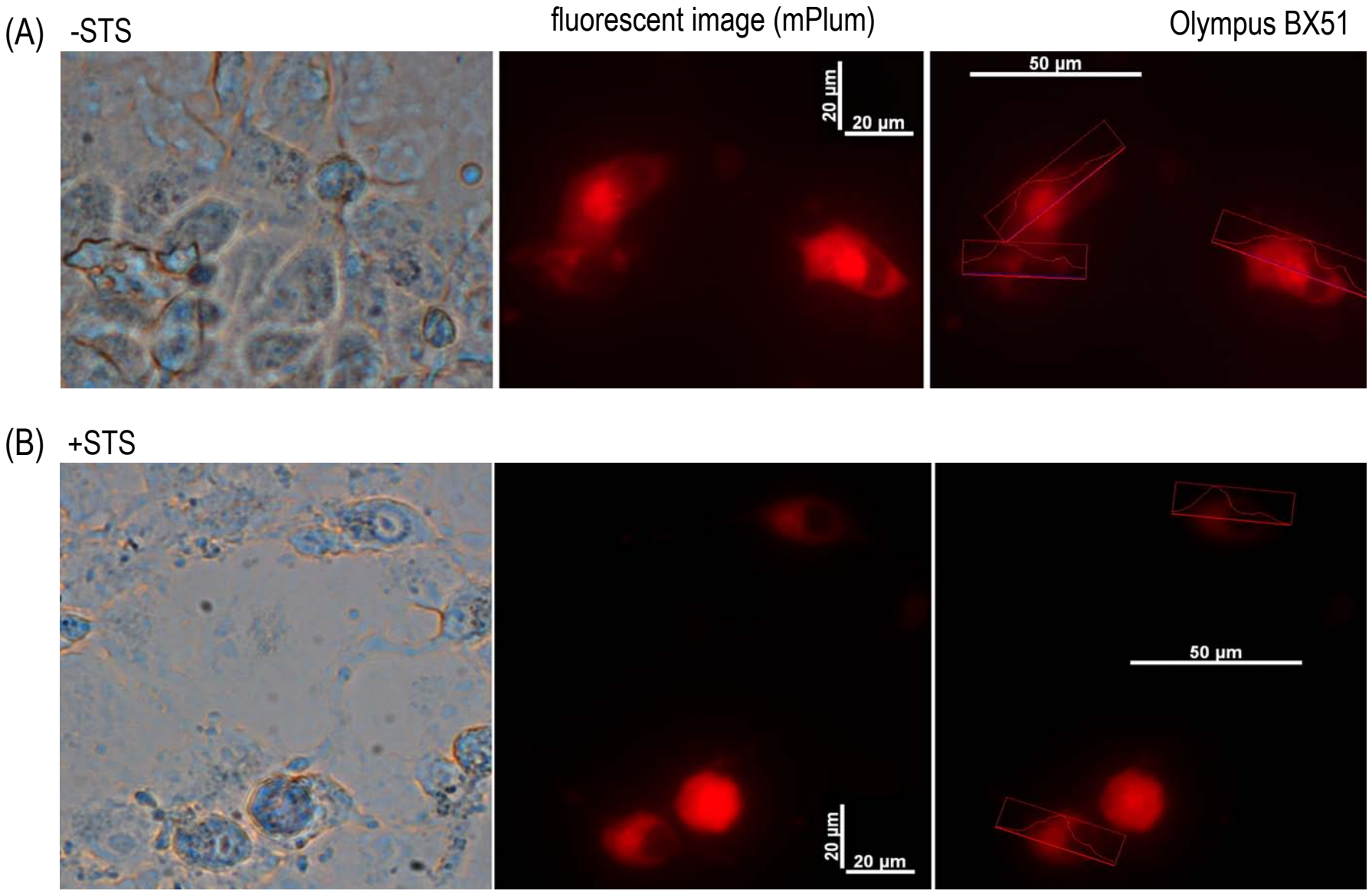

Suppl. Table 1. Characteristics of constructed probes, **P1**-**P14**. Major localization organelles of each probe is listed. The ER and the PM means the endoplasmic reticulum and the plasma membrane, respectively.

Probe name	Intracellular localization	Optical signal	Capase sensitivity (caspase name)	Secretion ability
P1	The nucleus	bioluminescence	No	No
P2	The nucleus	bioluminescence	No	No
P3	The ER	bioluminescence	No	Yes
P4	Located in the ER	bioluminescence	No	No
P5	The cytosol and the nucleus	bioluminescence	No	No
P6	Secreted via the ER	bioluminescence	No	Yes
P7	The PM	bioluminescence	No	No
P8	The PM	bioluminescence	Yes (capase-3)	No
P9	The ER	bioluminescence	No	No
P10	The PM	Two colors of bioluminescence	Yes (capase-3 and caspase-8)	No
P11	The PM	Bioluminescence and fluorescence	Yes (capase-3 and caspase-8)	No
P12	The PM	Bioluminescence and fluorescence	Yes (capase-3 and caspase-8)	No
P13	The PM	bioluminescence	No	No
P14	The PM	Bioluminescence and fluorescence	Yes (capase-3 and caspase-8)	No

Bioconjugate Chemistry

Article

pubs.acs.org/bc

Synthesis and Evaluation of Diastereoisomers of 1,4,7-Triazacyclononane-1,4,7-tris-(glutaric acid) (NOTGA) for Multimeric Radiopharmaceuticals of Gallium

Francisco L. Guerra Gomez,[†] Tomoya Uehara,[†] Takemi Rokugawa,[†] Yusuke Higaki,[†,‡] Hiroyuki Suzuki,[†] Hirofumi Hanaoka,[†] Hiromichi Akizawa,[§] and Yasushi Arano*[,†]

[†]Graduate School of Pharmaceutical Sciences, Chiba University, Chiba, Japan, 260-8675

[‡]School of Health Sciences, College of Medical, Pharmaceutical and Health Sciences, Kanazawa University, Ishikawa, Japan, 920-0942

[§]Health Science University of Hokkaido, 1757 Kanazawa, Tobetsu-cho, Ishikari-gun, Hokkaido, Japan 061-0293

Supporting Information

ABSTRACT: In the conventional synthesis of 1,4,7-tris-(glutaric acid)-1,4,7-triazacyclononane (NOTGA), four isomeric species are usually generated by the alkylation of 1,4,7-triazacyclononane with α-bromoglutaric acid diester. To estimate their biological efficacies as well as their stability and radiochemistry, the *RRR/SSS* and *RRS/SSR* NOTGA-^{t}Bu prochelators were isolated and the corresponding cyclic RGDfK (RGD) conjugates with triethylene glycol linkages were prepared. The *RRR/SSS* and *RRS/SSR* diastereomers were obtained in 69% and 17% yields, respectively. In the complexation reaction with $^{67}GaCl_3$, both diastereomers provided >98% radiochemical yields at pH 5 within 10 min when the reaction was conducted at room temperature. However, the *RRR/SSS* diastereomer exhibited more pH-sensitive radiochemical yields between pH 3.5 to 4.5. Despite their diasteromeric nature, both ^{67}Ga-labeled RGD-NOTGA remained stable during the apo-transferrin challenge, exhibiting similar affinity for integrin $\alpha_v\beta_3$ and biodistribution with predominant renal excretion. Similar tumor uptake was also observed in mice bearing U87MG tumor xenograft, which resulted in impressively high contrast SPECT/CT images. These findings indicate that the RGD-NOTGA conjugates of both diastereomers presented here possess equivalent biological efficacies and their combined usage would be feasible. It is worth noting that specific properties of a given biomolecule, cell expression levels of the corresponding target molecule, and presence or absence of a pharmacokinetic modifier would affect the structural differences between diastereomers on the ligand−receptor interactions and pharmacokinetics. Thus, the preparation of corresponding conjugates and evaluation of their chemical and biological performances still remains important for applying NOTGA to other biomolecules of interest using the diastereomerically pure NOTGA-^{t}Bu prochelator.

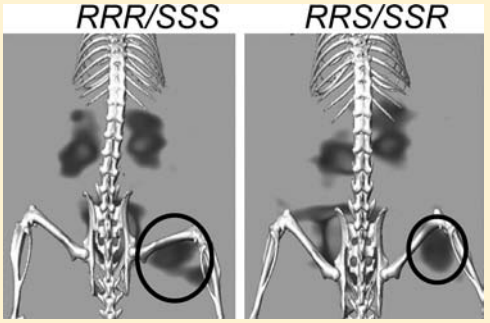

INTRODUCTION

Gallium radioisotopes are of great interest for molecular imaging. Gallium-68 (^{68}Ga) is a PET radioisotope available from long-lived ^{68}Ge/^{68}Ga generator systems allowing potentially cost-effective production of ^{68}Ga radiotracers far away from a cyclotron facility. Its physical half-life of 67.7 min is attractive for labeling low-molecular-weight probes with rapid pharmacokinetics.[1] Meanwhile, ^{67}Ga is a γ-emitter ($T_{1/2}$ = 3.3 d) currently used in the diagnosis of infection and inflammatory processes as well as tumor imaging by SPECT.[2,3]

For preparing $^{67/68}$Ga-based radiotracers, a macrocyclic chelator 1,4,7-triazacyclononane-*N*,*N*′,*N*″-triacetic acid (NOTA) is preferably used due to the formation of a hexadentate gallium complex of high thermodynamic (Log K = 30.98)[4] and kinetic stabilities arising from the good fit of the relatively small gallium cation in the cyclic cavity.[1] Moreover, this chelator has been efficiently radiolabeled with ^{68}Ga, even at room temperature.[5−7] Since the conjugation of targeting molecules to the carboxylic acids of NOTA compromises its coordination ability with Ga, several NOTA-based bifunctional chelating agents (BCA) with dissimilar functional groups in a pendant arm or on ethylene bridge have been developed.[6,8−10] Triazacyclononane (TACN) has been selected as the core of the scaffold containing phosphinic acid (triazacyclononane phosphinic acids; TRAP)[11,12] or glutaric acid (nonane triglutaric acid; NOTGA)[13,14] for multiattachment of biomolecules to the three pendant arms as a way to apply to the multimeric concept (Figure 1).

Recently, Singh et al.[14] exemplarily demonstrated that the binding affinity and tumor accumulation of a trivalent cyclic RGD peptide conjugated-NOTGA (^{68}Ga-**3**) increased with respect to its bivalent and monovalent counterparts. Similarly, Notni et al. reported that the targeting ability of the trivalent ^{68}Ga-TRAP(RGD)$_3$ was superior to that of the monovalent ^{18}F-Galacto-RGD.[12] However, one aspect to consider when

Received: June 26, 2012
Revised: October 7, 2012
Published: October 8, 2012

 © 2012 American Chemical Society dx.doi.org/10.1021/bc300340g | *Bioconjugate Chem.* 2012, 23, 2229−2238

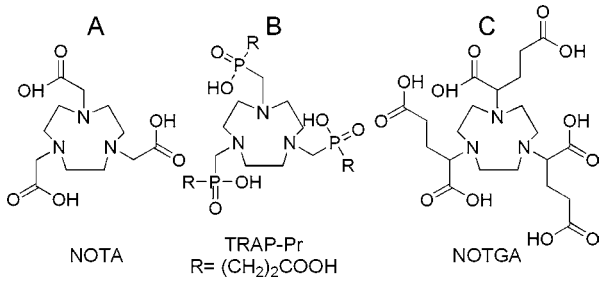

Figure 1. Structures of (A) NOTA and the NOTA-based BCAs, (B) TRAP, and (C) NOTGA. TRAP contains phosphinic acids, whereas NOTGA contains glutaric acids.

preparing NOTGA- and TRAP-based radiopharmaceuticals is the presence of chiral centers in their pendant arms leading to *RRR*, *SSS*, *RRS*, and *SSR* stereoisomers. In NOTGA, these stereoisomers are formed as a result of the alkylation of TACN with racemic (*R*/*S*) α-bromoglutaric acid diester (Figure 2),

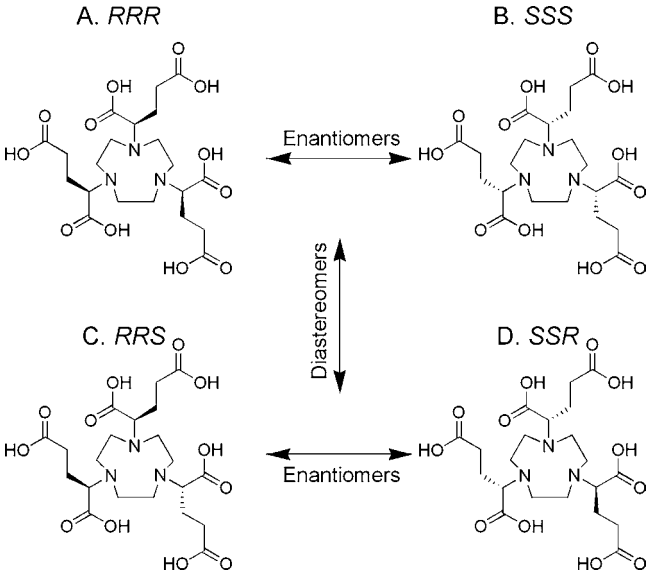

Figure 2. Structures of the isomeric forms of NOTGA. The *RRR* and *SSS*, as well as *RRS* and *SSR*, constitute enantiomers; while the pairs *RRR*/*SSS* and *RRS*/*SSR* are diastereomers.

which was also observed in the alkylation of tetraazacyclododecane,[15,16] where the *RRRR* isomer of gadolinium complex exhibited faster water exchange rate than the other isomers.[16] In TRAP ligands, the phosphorpous atoms become chiral upon coordination with the metal ion and four *RRR*, *SSS*, *RRS*, and *SSR* isomers are formed depending on the substituent.[11,17] A mixture of diastereomers, with differences in spatial orientation of the chelating unit or targeting molecules and physicochemical properties, might influence the biodistribution of the molecular probe.[18,19] In cases where radiopharmaceuticals can form distinct isomeric species, it is important to evaluate the individual product separately to ensure that they both possess good biological efficacy,[18] as well as stability and radiochemistry.

In TRAP-based radiolabeled probes, separation of a potential diastereomer can only be conducted after radiolabeling reaction. On the other hand, the isolation of diastereomers in NOTGA is feasible after alkylation of TACN, and diastereomerically pure conjugates can be obtained. In NOTGA-based radiolabeled probes, therefore, a diastereomerically pure $^{67/68}$Ga-labeled compound can be obtained without postlabeling purification by selecting a diastereomer of preferable chemical and biological performance. In the present study, pure diastereomers of NOTGA using RGDfK as the targeting molecule, were synthesized, and compared their performance in terms of radiochemical yields with $^{67}GaCl_3$, kinetic stability, affinity for integrin $\alpha_v\beta_3$, and biological behavior of each complex in normal and nude mice bearing U87MG tumor xenografts.

EXPERIMENTAL SECTION

General. All commercially obtained chemicals were of analytical grade and used without further purification. 9-Fluorophenylmethoxycarbonyl (Fmoc)-protected amino acids and H-Gly-2-Cl-Trt Resin were purchased from Watanabe Chemical Industries, Ltd. (Hiroshima, Japan). $^{67}GaCl_3$ was supplied by FUJIFILM RI Pharma Co., Ltd. (Tokyo, Japan). 1,4,7-Triazacyclononane (TACN) was purchased from Sigma Aldrich Chem. Co. (Milwaukee, WI, USA). Apo-transferrin (apo-Tf) Iron free was purchased from Nacalai Tesque Inc. (Kyoto, Japan). Reversed-phase HPLC was performed with a Cosmosil $5C_{18}$-AR-300 column (4.6 mm i.d. × 150 mm, Nacalai Tesque Inc.) at 1 mL/min with a gradient mobile phase starting from 90% A (0.1% aqueous trifluoroacetic acid (TFA) and 10% B (acetonitrile with 0.1% TFA) to 70% A and 30% B at 30 min. The eluent was monitored online with an UV−vis single-beam spectroscopy detector (L-7405, Hitachi Co. Ltd., Tokyo) coupled to a NaI(Tl) radioactivity detector (Gibi star, Raytest, Strubenhardt, Germany). TLC analyses was performed with silica plates (Silica gel 60 F_{254}, Merck Ltd., Tokyo) developed with MeOH/0.1 M $AcONH_4$ (1:1). Radioactivity was measured using a MiniGita Star Gamma TLC Scanner (Raytest) and an autowell γ counter (ARC-380M, Aloka, Tokyo). Mass spectrometry was carried out using an Agilent 6130 Series Quadrupole LC/MS electrospray system (Agilent Technologies, Tokyo) or MALDI TOF MS Kratos Axima CFR Plus (Shimadzu Corporation, Kyoto). ^1H, ^{13}C NMR spectra were recorded on a JEOL JNM-ECP-400 (400 MHz) spectrometer (JEOL Ltd., Tokyo).

(2-{2-[2-(9*H*-Fluoren-9-ylmethoxycarbonylamino)-ethoxy]-ethoxy}-ethoxy)-acetic acid (1) (Fmoc-TEG). 11-Amino-3,6,9-trioxaundecanoic acid (0.79 g, 3.79 mmol) and K_2CO_3 (1.04 g, 7.50 mmol) were dissolved in 5.8 mL of water and stirred at room temperature for 15 min after which *N*-(9-fluorenylmethoxycarbonyl) succinimide (1.28 g, 3.79 mmol) was added and the mixture was stirred for 24 h, while the progress of the reaction was monitored by TLC ($CHCl_3$/MeOH/AcOH, 5:1:0.06). The salt was filtered and the filtrate was washed with 3 × 3 mL of Et_2O, acidified to pH 1 using 3 N HCl, and the desired compound extracted with 5 × 5 mL of CH_2Cl_2. After removing the solvent in vacuo, the residue was purified with open column chromatography using silica gel and subsequent elution with $CHCl_3$/MeOH/AcOH (40:1:0.1) to afford Fmoc-TEG (1.19 g, 73%). ESI-MS, *m*/*z*: 430 $[M+H]^+$: Found 430.

Synthesis of Fmoc-TEG-c(-Arg(Pbf)-Gly-Asp(OtBu)-DPhe-Lys-) (2). Fmoc-TEG (0.16 g, 0.36 mmol), c(-Arg(Pbf)-Gly-Asp(O^{t}Bu)-DPhe-Lys-) (0.3 g, 0.33 mmol)[20] and 1-hydroxybenzotriazole monohydrate (HOBt, 0.049 g, 0.36 mmol) were dissolved in 13 mL of dimethylformamide (DMF) and cooled to −3 °C. Subsequently, 1-ethyl-3-(3-dimethylaminopropyl)-carbodiimide·hydrochloride (EDC, 0.21 g, 1.08 mmol) in 12 mL of DMF was added dropwise during 1 h under N_2 pressure. The reaction mixture was further stirred for 1 h and reacted overnight at room temperature. The solvent was removed in vacuo, and then, the residue dissolved in 100 mL of CH_2Cl_2, washed with 5% citric

dx.doi.org/10.1021/bc300340g | *Bioconjugate Chem.* 2012, 23, 2229−2238

acid (2 × 40 mL). The organic layer collected and dried over $MgSO_4$. After removing the solvent in vacuo, the residue was purified with open column chromatography using silica gel and subsequent elution with $CHCl_3$/MeOH (20:1) to obtained compound **2** as a white solid (0.22 g, 51%). ESI-MS, *m/z*: 1345 $[M+Na]^+$: Found 1345.

Synthesis of TEG-c(-Arg(Pbf)-Gly-Asp(OtBu)-DPhe-Lys-) (3). Fmoc-TEG-c(-Arg(Pbf)-Gly-Asp(OtBu)-DPhe-Lys-) (0.47 g, 0.35 mmol) was dissolved in 23 mL of 10% piperidine DMF solution and stirred for 2 h. After concentrating the solvent, Et_2O was added to the solution. The white precipitate was filtrated, washed alternatively with Et_2O and *n*-hexane, dried in vacuum overnight to obtain compound **3** as a yellow solid (0.30 g, 76%). ESI-MS, *m/z*: 1101 $[M+H]^+$: Found 1101.

1,4,7-Tris-(1-*tert*-butoxycarbonyl-3-benzyloxycarbony-propyl)-1,4,7-triazacyclononane (4) (NOTGA-^{t}Bu$_3$-Bz$_3$). (*R/S*) α-Bromoglutaric acid 1-*tert*-butyl ester 5-benzyl ester (1.3 g, 3.64 mmol)[21] was dissolved in 3.5 mL of acetonitrile and added dropwise to a solution of 1,4,7-triazacyclononane (0.142 g, 1.10 mmol) in 3.3 mL acetonitrile with K_2CO_3 (0.913 g, 6.62 mmol) during 2 h at 0 °C under N_2. The mixture was stirred at room temperature for 24 h. The reaction mixture was filtrated and the solvent was evaporated in vacuo. The residue was dissolved in dichloromethane (15 mL) and washed with 5% of $NaHCO_3$ (3 × 10 mL), and the organic layer was dried over $MgSO_4$. After removing the solvent in vacuo, the residue was purified with open column chromatography using silica gel and subsequent elution with chloroform/acetone (50:1) to afford compound **4** as a yellowish oil. *RRR/SSS* (0.637 g, 69%): ^{1}H NMR (400 MHz, $CDCl_3$), δ (ppm): 7.28−7.34 (m, 15H, Ph); 5.10 (s, 6 H, CH_2−Ph); 3.09−3.13 (t, 3H, N−CH); 2.68, 2.95 (d, *J* = 0.031, 12H, N-CH_2-CH_2-N); 2.53−2.42 (m, 6H, CH_2−COOBz); 1.82−2.03 (m-m, 6H, N-CH-CH_2); 1.43 (s, 27H, $C(CH_3)_3$). ^{13}C NMR (100 MHz, $CDCl_3$), δ (ppm): 173.37 (COOBzl); 172.59 (COO-tBu); 128.44, 128.48, 128.81, 136.34 (Ph); 81.11 (C-Me3); 67.58 (C-Ph); 66.46 (N-C); 54.55 (N-C-C-N); 31.59 (C-COO-Bzl); 28.58 (tBu); 25.58 (C-COO-Bzl). *RRS/SSR* (0.165 g, 17%): ^{1}H NMR (400 MHz, $CDCl_3$), δ (ppm): 7.26−7.34 (m, 15H, Ph); 5.09, 5.10 (d, 6 H, CH_2−Ph); 3.09−3.13 (m, 3H, N−CH); 2.58, 2.93 (d, *J* = 0.031, 4H, N-CH_2-CH_2-N), 2.70−2.84 (m, 8H, N-CH_2-CH_2-N); 2.44−2.51 (m, 6H, CH_2-COOBz); 1.82−2.02 (m-m, 6H, N-CH-CH_2); 1.43, 1.44 (d, 27H, $C(CH_3)_3$). ^{13}C NMR (100 MHz, $CDCl_3$), δ (ppm): 173.02, 173.13 (d, COOBzl); 172.30, 172.42 (d, COO-tBu); 128.10, 128.14, 128.46, 135.99 (Ph); 80.77, 80.79 (C-Me_3); 66.93 (C-Ph); 66.10, 66.27 (N−C); 54.29, 53.85, 53.54 (N−C−C−N); 31.02, 31.18 (C−COO−Bzl); 28.24 (tBu); 25.17, 25.33 (C−COO−Bzl). ESI-MS, *m/z*: 958 $[M+H]^+$, Found 958.

1,4,7-(α-Bromoglutaric Acid 1-*tert*-Butyl Ester 5-Benzyl Ester)-1,4,7-triazacyclononane (5, 6) (NOTGA-^{t}Bu$_3$). The *RRR/SSS* (0.57 g, 0.59 mmol) and *RRS/SSR* (0.15 g, 0.16 mmol) fractions were dissolved in methanol/water (5:1) and then 10% Pd/C (381 and 103 mg, respectively) was added portionwise. The mixtures were stirred for 12 h under H_2 atmosphere, then filtered over Celite, and evaporated to dryness to obtain compounds **5** and **6** as white solids. The products were used without further purification. *RRR/SSS* (408 mg, 96.4%). ^{1}H NMR (400 MHz, CD_3OD), δ(ppm): 3.69−3.70 (br, 3H, N−CH); 2.99−3.13 (br, 12H, N−CH_2−CH_2−N); 2.52−2.64 (br, 6H, CH_2−COOH); 2.06−2.19 (br, 6H, N−CH−CH_2); 1.51 (s, 27H, $C(CH_3)_3$). *RRS/SSR* (104 mg, 95%). ^{1}H NMR (400 MHz, CD_3OD), δ(ppm): 3.62−3.72 (br, 3H, N−CH); 2.87−3.22 (br, 12H, N−CH_2−CH_2−N); 2.44−2.81 (br, 6H, CH_2−COOH); 2.1.9−2.15 (br, 6H, N−CH−CH_2); 1.51 (s, 27H, $C(CH_3)_3$). ESI-MS, *m/z*: 688 $[M+H]^+$, Found 688.

NOTGA-(TEG-RGD)$_3$ (7). NOTGA-^{t}Bu$_3$ (*RRR/SSS*, 8.52 mg, 12.4 μmol; *RRS/SSR*, 10 mg, 14.5 μmol) was dissolved in dry CH_2Cl_2 (0.5 mL) and 0.3 equiv of 4-dimethylaminopyridine (DMAP), 3.5 equiv of TEG-c(-Arg(Pbf)-Gly-Asp(OtBu)-DPhe-Lys-), 3.6 equiv of 1-ethyl-3-(3-dimethylaminopropyl) carbodiimide·hydrochloride (EDC) dissolved in 0.5 mL of CH_2Cl_2 were added dropwise on an ice bath. After stirring at room temperature for 12 h under N_2, the solvent was evaporated in vacuo. The residue was dissolved in CH_2Cl_2 (10 mL), washed with 5% $NaHCO_3$ (3 × 7 mL), and dried over $MgSO_4$. After removing the solvent, the residue was taken up by a small amount of $CHCl_3$. The precipitate formed upon addition of excess of Et_2O was filtered and dried in vacuum overnight to obtain a yellow solid (*RRR/SSS*, 33.3 mg, 68.2%; *RRS/SSR*, 38.7 mg, 67.6%). ESI-MS, *m/z*: 1313 $[M+H]^{2+}$, Found 1313. After treatment with TFA/triethylsilane/H_2O (90:5:5) at room temperature for 3 h, the solvent was evaporated in vacuo and the precipitate formed upon addition of excess of Et_2O (*RRR/SSS*, 17.8 mg, 64.6%; *RRS/SSR*, 16 mg, 57.1%). ESI-MS, *m/z*: 1422 $[M+2H]^{2+}$, Found 1422.

Ga-NOTGA-(TEG-RGD)$_3$. NOTGA-(TEG-RGD)$_3$ (*RRR/SSS*, 0.8 mg, 0.28 μmol; *RRS/SSR*, 3 mg, 1.05 μmol) was dissolved in 500 μL of water, and 0.1 M $Ga(NO_3)_3$ solution (4.4 and 14.3 μL, respectively) was added. After 10 min heating at 70 °C, the pH was adjusted from 1.9 to 3.5 using 1 M sodium acetate and heated for another 30 min. The complex was purified by preparative HPLC and lyophilized to obtain Ga-NOTGA-(TEG-RGD)$_3$ (*RRR/SSS*, 0.7 mg, 85%; *RRS/SSR*, 2.67 mg, 87%). ESI-MS, *m/z*: 1455 $[M+2H]^{2+}$, Found 1455.

^{67}Ga-Radiolabeling. The complexation of ^{67}Ga by both diastereomeric pairs of ligands was studied regarding the reaction pH and time at r.t. $^{67}GaCl_3$ (10 μL, 1.5 MBq) in 0.05 M HCl was mixed with 10 μL of 0.5 M sodium acetate buffer pH 4−5.5. The mixtures were added to Eppendorf tubes containing 0.4 nmol of ligand in 20 μL of 0.25 M acetate buffer pH 3−5.5 to give final solutions of 0.25 M A.B, pH 3.5−5.5, and 10 μM of ligand concentration. The mixtures were incubated at 25 °C for 5, 10, and 15 min, and radiochemical yields were determined by Radio-TLC.

In Vitro Stability. ^{67}Ga-labeled complexes (*RRR/SSS, RRS/SSR*) were purified by RP-HPLC to remove unlabeled ligands. The radioactive peak was collected and the solvent was removed in vacuo. The residue was reconstituted in apo-transferrin (apo-Tf) solution (50 μM, 0.1 M carbonate buffer, pH 7.4) and incubated at 37 °C. Samples were withdrawn at 1, 3, and 6 h and analyzed by Radio-TLC (*n* = 3).

Binding Affinity to Integrin $\alpha_v\beta_3$. To evaluate the binding affinity of Ga-labeled compounds to integrin $\alpha_v\beta_3$, surface plasmon resonance (SPR) technology-based ProteOn XPR36 protein interaction array system (Biorad Laboratories Japan, Yokohama, Japan) was used. The SPR experiment was performed according to the manufacturer's instruction. In brief, human purified integrin $\alpha_v\beta_3$ (20 μg/mL, Chemicon International, Temecula, CA, USA) dissolved in 10 mM acetate buffer (pH 4.0) was immobilized on a ProteOn GLH sensor chip (Biorad Laboratories Japan) by standard amine coupling method. The Ga-NOTGA-(TEG-RGD)$_3$ complexes (*RRR/SSS, RRS/SSR*) at 10, 5, 2.5, and 1.25 μM concentrations and *c*(RGDfk) at 200, 100, 50, 25, and 12.5 μM as a positive control

in 10 mM Tris-HCl buffer (50 mM NaCl, 1 mM $MgCl_2$, 1 mM $MnCl_2$, pH 7.4) were injected simultaneously into the six horizontal channels of the chip. Kinetic analysis was performed by globally fitting curves describing a simple 1:1 biomolecular model to the set of five sensorgrams.

Cell Line. Human glioblastoma U87MG cells were grown in a 75 cm^2 tissue culture flask with canted neck (Becton, Dickinson and Company, Tokyo) in Dulbecco's Modified Eagle Medium (Sigma-Aldrich Japan K.K., Tokyo) supplemented with 10% fetal calf serum (FCS, Nippon Biosupply Center, Tokyo) and GIBCO BRL 1% penicillin−streptomycin (5000 unit-5000 μg/mL, Invitrogen, Life Technologies Japan Ltd., Tokyo), at 37 °C in a humidified atmosphere containing 5% CO_2.

Biodistribution Studies. Animal studies were conducted in accordance with institutional guidelines approved by the Chiba University Animal Care Committee. Male 6-week-old ddY mice[22] (Japan SLC, Inc., Shizuoka, Japan) were injected via tail vein with either *RRR/SSS* or *RRS/SSR* diastereomers of ^{67}Ga-NOTGA-(TEG-RGD)$_3$ (100 μL, 11.1 KBq, 10 μM ligand concentration). The animal were sacrificed and dissected at 30 min, 1 h, 3 h, and 6 h after administration. Tissues of interest were removed, weighed, and the radioactivity counts determined with an autowell gamma counter. The urine and feces were collected for 6 h and the radioactivity was also measured. Values were expressed as mean ± SD for a group of 3−5 animals.

BALBc nu/nu male mice (Japan SLC, Inc., Shizuoka, Japan) of 6 weeks old, weighing 18−20 g, were xenografted by subcutaneous (s.c.) injection of U87MG human glioblastoma cells (5×10^6 cells/80 μL of culture medium) into their right hind legs. The mice were subjected to biodistribution studies as well as SPECT/CT imaging studies when the tumor volume reached 100−300 mm^3.

Biodistribution studies were also conducted in male BALBc nu/nu mice bearing U87MG xenografts 30 min after administration of each radiotracer (n = 4). The integrin $\alpha_v\beta_3$ specificity was estimated by coinjection of either *RRR/SSS* or *RRS/SSR* diastereomers of ^{67}Ga-NOTGA-(TEG-RGD)$_3$ (100 μL, 11.1 KBq, 10 μM ligand concentration) and c(RGDyV) peptide (3 mg/kg mouse body weight) into mice bearing U87MG tumors. The animals were sacrificed and dissected at 2 h after administration (n = 4).

Small Animal SPECT/CT Imaging Studies. SPECT/CT images were taken 30 min after administration of either *RRR/SSS* or *RRS/SSR* diastereomers of [^{67}Ga]-NOTGA-(TEG-RGD)$_3$ (100 μL, 4.5 MBq, 10 μM ligand concentration) to male BALBc nu/nu mice bearing U87MG xenografts from the tail vein (n = 3). The mice were anaesthetized with 1−2% (v/v) isoflurane (DS Pharma Animal Health, Osaka, Japan) and positioned on the animal bed where anesthesia was continuously delivered via a nose cone system. SPECT imaging and X-ray CT imaging were performed by use of small animal SPECT/CT system (FX-3200, Gamma Medica Inc., CA) equipped with a five pinhole (0.5 mm) collimator. Data acquisition was performed for 64 min at 60 s per projection with stepwise rotation of 64 projections over 360°.

Statistical Analysis. Quantitative data were expressed as means ± SD. Means were compared using unpaired two-tailed Student's t test. P values <0.05 were considered statistically significant.

RESULTS

Synthesis. TACN was alkylated with (R/S) α-bromoglutaric acid 1-*tert*-butyl ester 5-benzyl ester[10,21,23] in acetonitrile and potassium carbonate at room temperature to obtain the fully protected NOTGA-^{t}Bu$_3$-Bz$_3$ **4** (Scheme 1). Purification was carried out using silica-gel column chromatography and a mixture of chloroform and acetone as the mobile phase. Two fractions (a major fraction of 69% and the following of 17%) were verified to be the target compound by mass spectrometry. Structure assignment was possible by ^{1}H NMR and ^{13}C NMR, which provides deeper insights into their structural differences (Supporting Information). Focusing on the chiral carbon resonance (label b in Figure 1S), a singlet was observed in the 69% fraction Figure 1S A) indicating equivalent carbons, and a doublet in the 17% fraction indicating the presence of two chemically nonequivalent carbons (Figure 1SB). The 69% fraction was assigned to the *RRR/SSS* diastereomeric pair and the 17% to the *RRS/SSR*.

In order to evaluate the differences of both diastereomeric pairs, each fraction was treated separately. After debenzylation by palladium-catalyzed hydrogenolysis, the diastereomeric orthogonally protected NOTGA-^{t}Bu$_3$ prochelator were obtained in quantitative yields.

The peptide substituent was prepared using an Fmoc chemistry to introduce the TEG spacer in the lysine side chain of c(RGDfK) in 50% yield. The prochelators of NOTGA-^{t}Bu$_3$ were then conjugated to the partially protected TEG-c(-Arg(Pbf)-Gly-Asp(OtBu)-DPhe-Lys-) by in situ activation using the standard EDC-based coupling method followed by complete removal of all protecting groups to obtain the desired ligands at moderate yields after HPLC purification (>95% purity).

Radiochemistry. The *RRR/SSS* and *RRS/SSR* pairs of NOTGA-(TEG-RGD)$_3$ were radiolabeled with ^{67}Ga and the resulting complexes were analyzed by HPLC (Figure 3). In both cases, a single peak was observed and the retention time of the *RRR/SSS* was 24.5 min, slightly longer than that of *RRS/SSR* (24.3 min). In both cases, their retention times were identical to those of the corresponding nonradioactive gallium complexes verified by mass spectrometry.

Formation kinetics as a function of pH is presented in Figure 4. In both cases, radiochemical yields were low under acidic conditions (pH 3.5) and quantitative at more basic pH 5 where the time variation of the radiochemical yield was essentially the same for both pairs (Figure 4B) and complete radiolabeling with more than 98% yield was attained after 10 min of reaction. Interestingly, while *RRR/SSS* was preferentially labeled at pH 5, the *RRS/SSR* was pH-independent from pH 4 to 5.5 (Figure 4A). Under the present condition, the specific activity of the ^{67}Ga-labeled compounds was 4500 Mq/μmol.

In Vitro Stability. The kinetic stability of [^{67}Ga]-NOTGA-(TEG-RGD)$_3$ diastereomeric pairs purified by HPLC in order to remove the excess ligand was estimated in an apo-transferrin challenge (Table 1). After 6 h of incubation at 37 °C, more than 98% of the radioactivity was still bound to the NOTGA tripeptide conjugates of both pairs.

Binding Affinity. The binding kinetics of the two diasteromeric gallium complexes of NOTGA-(TEG-RGD)$_3$ to $\alpha_v\beta_3$ integrin was estimated with the SPR technology using a monovalent c(RGDfK) as a reference (Table 2). Both diastereomeric trivalent complexes exhibited higher association and lower dissociation rates than that of a monovalent c(RGDfK) with the rate constants similar each other. As a result, both trivalent complexes showed 10-fold higher dissociation constant values (K_D) than that of monovalent c(RGDfK).

In Vivo Experiments. The results of the biodistribution studies of [^{67}Ga]-NOTGA-(TEG-RGD)$_3$ in normal mice at

Scheme 1. Synthesis of NOTGA-(TEG-RGD)$_3$[a]

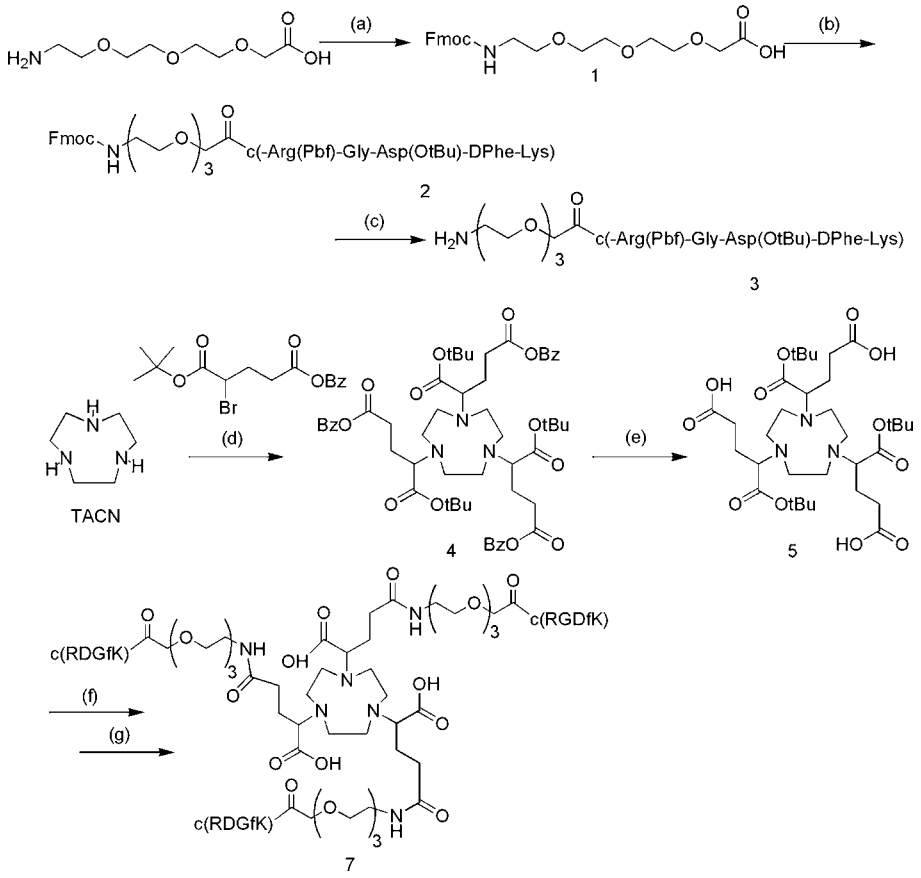

[a](a) Fmoc-O-Su, K_2CO_3, H_2O; (b) c(-Arg(Pbf)-Gly-Asp(O^{t}Bu)-DPhe-Lys-), WSCI/HCl, HOBt, DMF; (c) 10% piperidine/DMF; (d) 1,4,7-triazacyclononane, K_2CO_3, MeCN; (e) 10%Pd/C MeOH,H_2O; (f) H_2N-TEG-c(R(Pbf)GD(O^{t}Bu)fK), WSCI·HCl, DIMAP, CH_2Cl_2; (g) TFA/Water/Et_3Si.

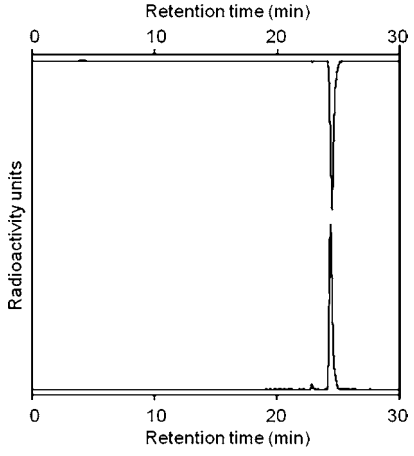

Figure 3. HPLC radiochromatograms of ^{67}Ga-NOTGA-(TEG-RGD)$_3$. The *RRR/SSS* diastereomer (top) was eluted at 24.5 min, slightly longer than that of the *RRS/SSR* counterpart (bottom, 24.3 min).

30 min, 1 h, 3 h, and 6 h after administration are shown in Table 3 (*RRR/SSS*) and Table 4 (*RRS/SSR*). No significant differences were observed in the uptake of both diastereomers in almost all organs and tissues. These profiles were characterized by rapid blood clearance with low accumulation in the liver, and the majority of the radioactivity was localized in the kidneys. Both radioligands were excreted in the urine with a small amount in feces. Although in absolute terms the uptake in

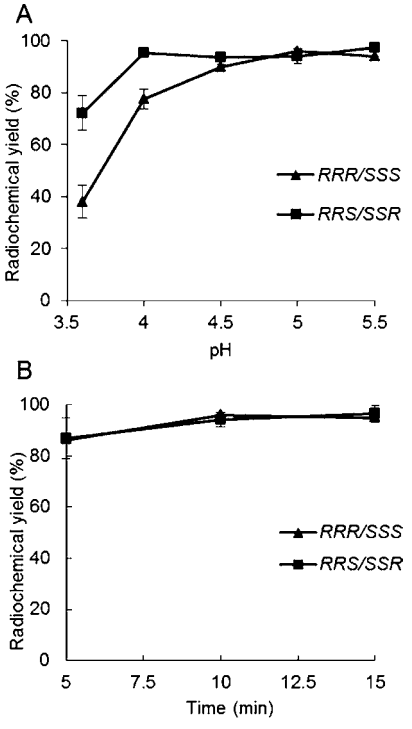

Figure 4. Radiochemical yields of each diastereomer of ^{67}Ga-NOTGA-(TEG-RGD)$_3$ (*RRR/SSS*, squares; and *RRS/SSR*, triangles) (A) at different pH values for 10 min and (B) different reaction times at pH 5.0.

dx.doi.org/10.1021/bc300340g | *Bioconjugate Chem.* 2012, 23, 2229−2238

Table 1. Stability of ^{67}Ga-NOTGA-(TEG-RGD)$_3$ Diastereomers against Apo-Transferrin[a]

time (h)	percent of intact radiolabeled complex	
	RRR/SSS	*RRS/SSR*
1	98.6 ± 0.2	98.9 ± 0.4
3	98.9 ± 0.3	98.3 ± 0.9
6	98.0 ± 0.4	98.4 ± 0.2

[a]Results are expressed as mean ± SD of three experiments.

the intestines was very low, a slight tendency of the *RRR/SSS* to be excreted through the intestinal tract can be noted. Its intestine accumulation was significantly higher at 1, 3, and 6 h p.i. Likewise, relatively higher radioactivity in feces and lower radioactivity in urine for the *RRR/SSS* were observed.

Figure 5 shows the biodistribution studies of [^{67}Ga]-NOTGA-(TEG-RGD)$_3$ (*RRR/SSS* and *RRS/SSS*) at 30 min postinjection to nude mice bearing U87MG xenografts. The biodistribution profiles of both diastereomeric pairs were characterized by rapid blood clearance and high tumor uptake with comparatively low accumulation in nontarget organs and renal excretion pathway. In agreement with the studies in normal mice, the uptakes of the diastereomeric pairs in organs of interest were comparable. Tumor uptakes were 4.40 ± 0.38 and 4.77 ± 0.76%ID/g ($p < 0.05$) for *RRR/SSS* and *RRS/SSR*, respectively. Tumor to organ ratios (Figure 5B) were high for blood and muscle, moderate for the liver, and much lower for the kidney. A combination of slightly higher tumor and lower blood uptakes led to a statistically significantly higher tumor to blood ratio for the *RRS/SSR* pair. When the radiolabeled probes were coinjected with a high amount of RGDyV, tumor accumulation was significantly decreased ($p < 0.05$) to 0.82 ± 0.17 and 0.68 ± 0.2%ID/g at 2 h p.i. (*RRR/SSS* and *RRS/SSR*, respectively), demonstrating integrin $\alpha_v\beta_3$ targeting specificity (Figure 6).

SPECT/CT imaging studies were performed for both *RRR/SSS* and *RRS/SSS* diastereomers of [^{67}Ga]-NOTGA-(TEG-RGD)$_3$

Table 2. Kinetic Binding Constants of ^{67}Ga-NOTGA-(TEG-RGD)$_3$ (*RRR/SSS* and *RRS/SSR*), c(RGDfK) to Integrin $\alpha_v\beta_3$ Determined Using the SPR Technology

analyte	K_a (1/Ms)	K_d (1/s)	K_D (M)
RRR/SSS	$1.13 \times 10^5 \pm 6.8 \times 10^3$	$8.03 \times 10^{-3} \pm 1.7 \times 10^{-4}$	$7.13 \times 10^{-8} \pm 4.5 \times 10^{-9}$
RRS/SSR	$0.94 \times 10^5 \pm 5.3 \times 10^3$	$8.12 \times 10^{-3} \pm 1.6 \times 10^{-4}$	$8.64 \times 10^{-8} \pm 4.9 \times 10^{-9}$
c(RGDfK)	$2.57 \times 10^4 \pm 6.1 \times 10^3$	$1.38 \times 10^{-2} \pm 6.2 \times 10^{-4}$	$5.37 \times 10^{-7} \pm 2.7 \times 10^{-7}$

Table 3. Biodistribution of *RRR/SSS* Diastereomer of ^{67}Ga-NOTGA-(TEG-RGD)$_3$ in Normal Mice[a]

	RRR/SSS			
organ	30 min	1 h	3 h	6 h
blood	0.61 ± 0.13	0.16 ± 0.02	0.07 ± 0.02	0.09 ± 0.02
liver	1.27 ± 0.22	1.32 ± 0.15	1.49 ± 0.32	1.50 ± 0.30
spleen	2.09 ± 0.35	1.26 ± 0.12	1.32 ± 0.21	1.77 ± 0.56
kidneys	5.82 ± 1.22	5.04 ± 1.15	3.48 ± 0.54	3.00 ± 0.43
pancreas	1.06 ± 0.19	0.72 ± 0.09	0.65 ± 0.10	0.66 ± 0.13
heart	1.00 ± 0.07	0.69 ± 0.05	0.65 ± 0.09	0.73 ± 0.11*
lung	2.52 ± 0.33	1.41 ± 0.11	1.08 ± 0.37	1.25 ± 0.47
muscle	0.84 ± 0.14	0.55 ± 0.12	0.51 ± 0.07	0.52 ± 0.04
stomach[c]	0.63 ± 0.06	0.74 ± 0.16	0.56 ± 0.13	0.47 ± 0.14
intestines[b,c]	2.98 ± 0.54	3.67 ± 0.27**	5.23 ± 0.80*	4.44 ± 0.26**
urine[c]				63.22 ± 6.83
feces[c]				4.25 ± 1.30

[a]Data expressed as %ID/g ± SD ($n = 5$). [b](* $p < 0.05$, ** $p < 0.01$). [c]Expressed as %ID.

Table 4. Biodistribution of *RRS/SSR* Diastereomer of ^{67}Ga-NOTGA-(TEG-RGD)$_3$ in normal mice[a]

	RRS/SSR			
organ	30 min	1 h	3 h	6 h
blood	0.58 ± 0.18	0.19 ± 0.02	0.09 ± 0.03	0.08 ± 0.02
liver	1.22 ± 0.12	1.19 ± 0.07	1.56 ± 0.38	1.33 ± 0.19
spleen	1.42 ± 0.59	1.20 ± 0.17	1.40 ± 0.06	1.57 ± 1.17
kidneys	5.38 ± 0.89	4.74 ± 0.87	3.58 ± 0.39	3.04 ± 0.28
pancreas	0.85 ± 0.07	0.69 ± 0.03	0.71 ± 0.09	0.58 ± 0.11
heart	0.93 ± 0.16	0.73 ± 0.08	0.73 ± 0.09	0.55 ± 0.05*
lung	1.94 ± 0.53	1.36 ± 0.16	1.33 ± 0.35	1.00 ± 0.04
muscle	1.22 ± 0.91	0.55 ± 0.04	0.55 ± 0.06	0.62 ± 0.17
stomach[c]	0.59 ± 0.06	0.63 ± 0.11	0.61 ± 0.11	0.40 ± 0.02
intestines[b,c]	2.59 ± 0.35	3.00 ± 0.27**	4.10 ± 0.62*	2.90 ± 0.38**
urine[c]				71.52 ± 2.64
feces[c]				2.24 ± 0.89

[a]Data expressed as %ID/g ± SD ($n = 5$). [b](* $p < 0.05$, ** $p < 0.01$). [c]Expressed as %ID.

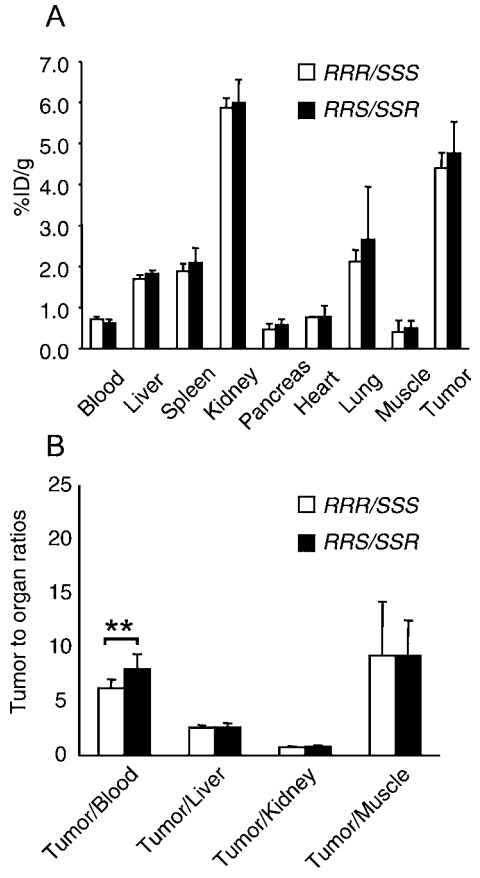

Figure 5. (A) Biodistribution of ^{67}Ga-NOTGA-(TEG-RGD)$_3$ in tumor-bearing male nude mice at 30 min after intravenous injection of 11.1 KBq of *RRR/SSS* (white) or *RRS/SSR* (black). (B) The tumor to organ ratios of the ^{67}Ga labeled conjugates. Data expressed as %ID/g ± SD (n = 4, ** p < 0.01).

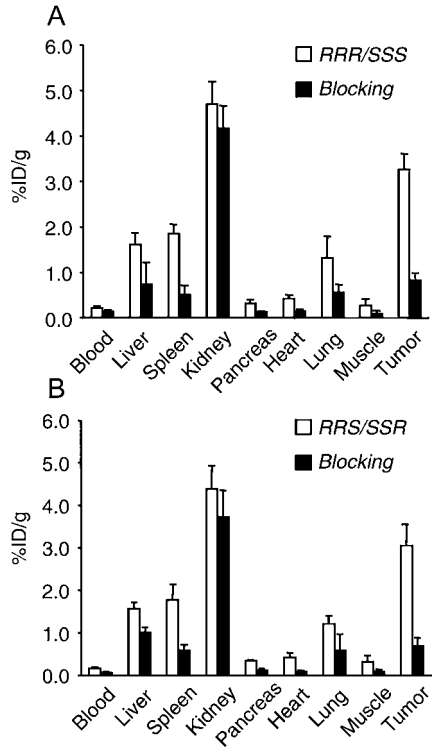

Figure 6. Biodistribution data in tumor-bearing male nude mice at 2 h after administration of ^{67}Ga-NOTGA-(TEG-RGD)$_3$ with (black) and without (white) the presence of an excess of RGDyV. (A) *RRR/SSS*; (B) *RRS/SSR*. Data expressed as %ID/g ± SD (n = 4).

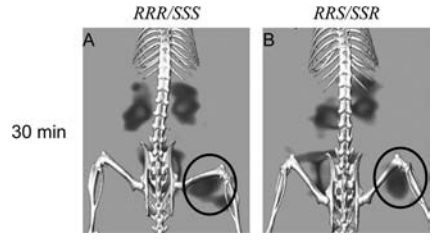

Figure 7. SPECT/CT images of U87MG tumor-bearing male nude mice after 30 min of i.v. injection of 4.5 MBq of each diastereomer of [^{67}Ga]-NOTGA-(TEG-RGD)$_3$. (A) *RRR/SSS* and (B) *RRS/SSR*. Images were shown at the same signal intensity scale.

using nude mice bearing U87MG xenografts (Figure 7). Tumors were clearly visualized as early as 30 min after administration. Radioactivity was concentrated in the kidneys and bladder. Impressively, nonspecific accumulation in liver or bowel was not observed, resulting in high-contrast images.

DISCUSSION

The cyclic RGD peptides have been widely study as a targeting molecule due to its high affinity for integrin $\alpha_v\beta_3$ overexpressed during tumor angiogenesis.[24] It has also been well recognized that in vitro binding affinity and in vivo tumor targeting ability of multimeric RGD peptides are enhanced due to the multivalent effect and the enriched local RGD concentration.[24−28] Moreover, it has been demonstrated that the spacer units of appropriate length and hydrophilicity between a radiometal chelate and each RGD motif increase avidity of the radiotracers and simultaneously may act as pharmacokinetic modifiers to improve pharmacokinetics of the radiotracer.[24,29,30]

The preparation of NOTA-based radiopharmaceuticals was conducted according to the procedure reported previously.[13,14] In brief, the synthesis of the orthogonally protected prochelator NOTGA-^{t}Bu$_3$, followed by conjugation of the bioactive molecules to each carboxylic acid of the pendant arm and final deprotection. Since racemic (*R*/*S*) α-bromoglutaric acid 1-*tert*-butyl ester 5-benzyl ester was used in the alkylation of TACN, intermediate **4** exists in different isomeric forms,[15,16] *RRR*, *SSS*, *RRS*, and *SSR* (Figure 2). The *RRR* and *SSS* isomers constitute enantiomers, as supported by similar MS and ^{13}C NMR spectra. Further isolation was not possible by the conventional methods. In ^{13}C NMR, since the three chiral carbons in *RRR/SSS* are equivalent, this pair was assigned to the 69% fraction with a single resonance. Similarly, two different carbons (*R*, *S*) are present in *RRS/SSR* and were associated with the doublet observed in the 17% fraction, as also observed in the tetraazacyclodecane analogue.[16]

It should be mentioned that, besides the isomerism in NOTGA ligands coming from the chiral carbon in the pendant arms, NOTA-based complexes are chiral depending on the orientation of the pendant arms around the metal center (Λ: clockwise or Δ: anticlockwise) and the relative puckering of the ethylenediamine subunit chelate rings ($\delta\delta\delta$ or $\lambda\lambda\lambda$ conformers)[31,32] in the case of gallium, only the enantiomeric $\Delta(\lambda\lambda\lambda)/\Lambda(\delta\delta\delta)$ combination was observed.[31] Therefore, each *RRR/SSS* and *RRS/SSR* of Ga-NOTGA diastereomeric pair may further exist as the enantiomeric combinations $\Delta(\lambda\lambda\lambda)$-*RRR*/$\Lambda(\delta\delta\delta)$-*SSS* or $\Delta(\lambda\lambda\lambda)$-*SSS*/$\Lambda(\delta\delta\delta)$-*RRR*, as well as $\Delta(\lambda\lambda\lambda)$-*RRS*/$\Lambda(\delta\delta\delta)$-*SSR*

dx.doi.org/10.1021/bc300340g | *Bioconjugate Chem.* 2012, 23, 2229−2238

or Δ(λλλ)-*SSR*/Λ(δδδ)-*RRS*. Nevertheless, both diastereomeric ligands provided gallium complexes of high inertness, indicating good retention of the metal inside the complex cavity.

^{67}Ga radiolabeling was performed at room temperature as previously reported for NOTA and its derivatives.[5−7] The reaction condition allowed assessing the differences in the complexation ability of the diastereomeric ligands that otherwise would be suppressed by heating. Lower radiochemical yields under acidic conditions were also found by Singh et al.[14] when labeling NOTGA and its disubstituted parent, in comparison to the monosubstituted and the *p*-SCN-Bn-NOTA RGD conjugates, possibly due to steric hindrance caused by the three substituents. On the other hand, pH 5 was found optimal for labeling NODAGA-RGD with ^{68}Ga,[33] and a study of the Ga-NOTA formation in acetate solutions found faster reaction rates at higher pH.[34] Intriguingly, the *RRS*/*SSR* was almost pH-independent from pH 4 to 5.5. A hypothesis to account for this observation would be related to the formation mechanism of the Ga-NOTA complex and the structural differences between the diastereomers. It has been reported that complexation of NOTA and other polyazamycrocycles containing pendant arms proceed in two steps. The first step comprises a fast formation of a monoprotonated intermediate species in which the metal ion is outside of the macrocyclic cage and coordinated to the three peripheric carboxylate oxygen atoms. The ring nitrogen atoms remain unbound and the proton would be attached to one of them. In the second step, deprotonation takes place followed by migration of the metal to inside the cavity where it also becomes coordinated to the nitrogen atoms.[35] Due to electrostatic repulsion between the nitrogen's proton and the metal, removal of the proton is considered to be the rate-determining step.[34,36,37] It has been proposed that this is an OH-catalyzed deprotonation,[34−37] explaining the faster complexation at higher pH. It has also been proposed that the migration of the proton from the NH^+ group to a carboxylate facilitates the accessibility with respect to OH^- ions.[37] In either case, the *RRS*/*SSR* conformation might facilitate access of the OH^- ions to the nitrogen-bound proton or the proton migration to the carboxylate, making the complexation less pH-dependent.

To further estimate the differences between the two diastereomers, the binding affinity of the two gallium complexes of NOTGA-(TEG-RGD)$_3$ to $\alpha_v\beta_3$ integrin were estimated by SPR assay and found that the structural differences in the NOTGA diastereomers presented here do not affect the interaction with the targets (Table 2). The binding to $\alpha_v\beta_3$ integrin is strongly dependent on the molecular design of multimeric RGD probes. There are two factors underneath the enhanced target affinity: multivalency and enhanced local RGD concentration. Although the local concentration factor is innate in all multimeric probes, an appropriate distance between each of two sets of cyclic RGD motifs is required to achieve multivalency.[24,38,39] In this design, the triethylene glycol spacer was inserted to provide a distance between the three carboxylates in NOTGA and the lysine side chains of the RGD motifs of 37 bonds. According to the previous study,[38] the distance between the two cyclic RGD motifs of [^{67}Ga]-NOTGA-(TEG-RGD)$_3$ would be suitable for simultaneous $\alpha_v\beta_3$ integrin binding. In addition, Syngh et al. reported that a trimeric RGD linked to NOTGA showed enhanced tumor uptake and retention compared with monomeric RGD counterpart, due to the multivalent effect partially.[14] From these findings, a combination of multivalency and enhanced local RGD concentration might be attributable to higher targeting capabilities of [^{67}Ga]-NOTGA-(TEG-RGD)$_3$, reflected in a binding affinity 10-folder higher than that of the monovalent cRGDfK. Thus, both diastereomers might act as trivalent compounds and the spatial arrangement of the RGD motifs in each complex would be equivalent with respect to binding affinity to $\alpha_v\beta_3$ integrin.

No significant differences were also observed in the biodistribution of the ^{67}Ga labeled diastereomers (Tables 3 and 4, Figure 5). Both exhibited rapid blood clearance and renal excretion in normal and nude mice bearing U87MG tumors. The high renal uptake was consistent with previous studies of other multimeric RGD peptides.[14,26,40−42] It was reported that endothelial cells of the glomeruli vessels in the kidneys express integrin $\alpha_v\beta_3$,[43] which could partially explain the observation. The presence of three guanidine groups in the trivalent RGD conjugate would increase positive charge, which may have facilitated reabsorption in proximal renal tubular cells.[26,27,43,44] While both diastereomers exhibited similar biodistribution, the elution order of the diastereomers from HPLC (Figure 3; *RRS*/*SSR* followed by *RRR*/*SSS*) suggests that a small difference in the lipophilicity between the two may be responsible for the slight tendency of the *RRR*/*SSS* to be excreted through the intestinal tract, though the excretion route is minimal. The similar affinity for integrin $\alpha_v\beta_3$ along with similar pharmacokinetics of the diastereomers resulted in similar tumor accumulation of the two compounds (Figure 5), yielding SPECT/CT images of high contrast as shown in Figure 7.

The longer-lived ^{67}Ga was used throughout the study. The outcomes of this study would also be applicable to the synthesis of ^{68}Ga labeled NOTA-(TEG-RGD)$_3$. Moreover, given the efforts in processing generator eluates to reduce metal impurities[5,45−47] and the sensitivity of PET imaging techniques, superior images of in vivo integrin $\alpha_v\beta_3$ expression can be obtained.

CONCLUSIONS

The findings in this study show that the RGD conjugates of both diastereomers presented here possess equivalent biological efficacy, and the combined usage of the diastereomic mixture would be feasible as far as the present compounds are concerned. It is worth noting that the specific properties of a given biomolecule, cell expression levels of the corresponding target molecule, and presence or absence of pharmacokinetic modifier might affect the structural differences between diastereomers on the ligand−receptor interactions and biodistribution. Since the synthesis of diastereomerically pure NOTGA-^{t}Bu prochelators has been established, the preparation of corresponding conjugates and evaluation of their chemical and biological performances still remains important for applying NOTGA to other biomolecules of interest.

ASSOCIATED CONTENT

Supporting Information

^{1}H and ^{13}C NMR and LC-MS spectra of the diastereomeric pairs of NOTGA-^{t}Bu$_3$-Bz$_3$. This material is available free of charge via the Internet at http://pubs.acs.org.

AUTHOR INFORMATION

Corresponding Author

*Tel: +81-43-256-1782. Fax: +81-43-226-2897. E-mail: arano@chiba-u.jp.

Notes

The authors declare no competing financial interest.

■ ACKNOWLEDGMENTS

This work was partially supported by Special Funds for Education and Research (Development of SPECT Probes for Pharmaceutical Innovation) from the Ministry of Education, Culture, Sports, Science and Technology, Japan. We would also like to thank FUJIFILM RI Pharma Co., Ltd. for providing [^{67}Ga]Cl_3.

■ REFERENCES

(1) Fani, M., André, J. P., and Maecke, H. R. (2008) ^{68}Ga-PET: a powerful generator-based alternative to cyclotron-based PET radiopharmaceuticals. *Contr. Media Mol. Imaging 3*, 67−77.

(2) Green, M. A., and Welch, M. J. (1989) Gallium radiopharmaceutical chemistry. *Int. J. Radiat. Appl. Instrum. Part B 16*, 435−443 445−448.

(3) Weiner, R. E. (1996) The mechanism of ^{67}Ga localization in malignant disease. *Nucl. Med. Biol. 23*, 745−751.

(4) Clarke, E. T., and Martell, A. E. (1991) Stabilities of the Fe(III), Ga(III) and In(III) chelates of N,N′,N″-triazacyclononanetriacetic acid. *Inorg. Chim. Acta 181*, 273−280.

(5) Ferreira, C. L., Lamsa, E., Woods, M., Duan, Y., Fernando, P., Bensimon, C., Kordos, M., Guenther, K., Jurek, P., and Kiefer, G. E. (2010) Evaluation of bifunctional chelates for the development of gallium-based radiopharmaceuticals. *Bioconjugate Chem. 21*, 531−536.

(6) Jae, M. J., Mee, K. H., Young, S. C., Lee, Y. S., Young, J. K., Gi, J. C., Dong, S. L., Chung, J. K., and Myung, C. L. (2008) Preparation of a promising angiogenesis PET imaging agent: ^{68}Ga-labeled c-(RGDyK)-isothiocyanatobenzyl-1,4,7-triazacyclononane-1, 4,7-triacetic acid and feasibility studies in mice. *J. Nucl. Med. 49*, 830−836.

(7) Velikyan, I., Maecke, H., and Langstrom, B. (2008) Convenient preparation of ^{68}Ga-based PET-radiopharmaceuticals at room temperature. *Bioconjugate Chem. 19*, 569−573.

(8) André, J. P., Maecke, H. R., Zehnder, M., Macko, L., and Akyel, K. G. (1998) 1,4,7-Triazacyclononane-1-succinic acid-4,7-diacetic acid (NODASA): A new bifunctional chelator for radio gallium-labelling of biomolecules. *Chem. Commun.*, 1301−1302.

(9) Riss, P. J., Kroll, C., Nagel, V., and Rösch, F. (2008) NODAPA-OH and NODAPA-(NCS)n: Synthesis, ^{68}Ga-radiolabelling and in vitro characterisation of novel versatile bifunctional chelators for molecular imaging. *Bioorg. Med. Chem. Lett. 18*, 5364−5367.

(10) Eisenwiener, K. P., Prata, M. I. M., Buschmann, I., Zhang, H. W., Santos, A. C., Wenger, S., Reubi, J. C., and Mäcke, H. R. (2002) NODAGATOC, a new chelator-coupled somatostatin analogue labeled with [$^{67/68}$Ga] and [^{111}In] for SPECT, PET, and targeted therapeutic applications of somatostatin receptor (hsst2) expressing tumors. *Bioconjugate Chem. 13*, 530−541.

(11) Notni, J., Hermann, P., Havlíčková, J., Kotek, J., Kubíček, V., Plutnar, J., Loktionova, N., Riss, P. J., Rösch, F., and Lukeš, I. (2010) A triazacyclononane-based bifunctional phosphinate ligand for the preparation of multimeric ^{68}GA tracers for positron emission tomography. *Chem.—Eur. J. 16*, 7174−7185.

(12) Notni, J., Šimeček, J., Hermann, P., and Wester, H. J. (2011) TRAP, a powerful and versatile framework for gallium-68 radiopharmaceuticals. *Chem.—Eur. J. 17*, 14718−14722.

(13) Uehara, T., Guerra Gomez, F. L., Rokugawa, T., and Arano, Y. (2011) A new triazacyclononane-based ligand for trivalent ^{68}Ga tracers of high stability for positron emission tomography. *J. Nucl. Med. 52*, 1473.

(14) Singh, A. N., Liu, W., Hao, G., Kumar, A., Gupta, A.O. Z O. K., Hsieh, J.-T., and Sun, X. (2011) Multivalent bifunctional chelator scaffolds for gallium-68 based positron emission tomography imaging probe design: signal amplification via multivalency. *Bioconjugate Chem. 22*, 1650−1662.

(15) Abiraj, K., Jaccard, H., Kretzschmar, M., Helm, L., and Maecke, H. R. (2008) Novel DOTA-based prochelator for divalent peptide vectorization: Synthesis of dimeric bombesin analogues for multimodality tumor imaging and therapy. *Chem. Commun.*, 3248−3250.

(16) Woods, M., Aime, S., Botta, M., Howard, J. A. K., Moloney, J. M., Navet, M., Parker, D., Port, M., and Rousseaux, O. (2000) Correlation of water exchange rate with isomeric composition in diastereoisomeric gadolinium complexes of tetra(carboxyethyl)dota and related macrocyclic ligands. *J. Am. Chem. Soc. 122*, 9781−9792.

(17) Šimeček, J., Schulz, M., Notni, J., Plutnar, J., Kubíček, V., Havlíčková, J., and Hermann, P. (2012) Complexation of metal ions with TRAP (1,4,7-triazacyclononane phosphinic acid) ligands and 1,4,7-triazacyclononane-1,4,7-triacetic acid: Phosphinate-containing ligands as unique chelators for trivalent gallium. *Inorg. Chem. 51*, 577−590.

(18) Cantorias, M. V., Howell, R. C., Todaro, L., Cyr, J. E., Berndorff, D., Rogers, R. D., and Francesconi, L. C. (2007) MO tripeptide diastereomers (M = $^{99/99m}$Tc, Re): models to identify the structure of ^{99m}Tc peptide targeted radiopharmaceuticals. *Inorg. Chem. 46*, 7326−7340.

(19) Cyr, J. E., Pearson, D. A., Nelson, C. A., Lyons, B. A., Zheng, Y., Bartis, J., He, J., Cantorias, M. V., Howell, R. C., and Francesconi, L. C. (2007) Isolation, characterization, and biological evaluation of syn and anti diastereomers of [^{99m}Tc]technetium depreotide: a somatostatin receptor binding tumor imaging agent. *J. Med. Chem. 50*, 4295−4303.

(20) Haubner, R., Wester, H. J., Reuning, U., Senekowitsch-Schmidtke, R., Diefenbach, B., Kessler, H., Stöcklin, G., and Schwaiger, M. (1999) Radiolabeled $\alpha v\beta 3$ integrin antagonists: A new class of tracers for tumor targeting. *J. Nucl. Med. 40*, 1061−1071.

(21) Eisenwiener, K. P., Powell, P., and Mäcke, H. R. (2000) A convenient synthesis of novel bifunctional prochelators for coupling to bioactive peptides for radiometal labelling. *Bioorg. Med. Chem. Lett. 10*, 2133−2135.

(22) Imai, S., Morimoto, J., Tsubura, Y., Esaki, K., Michalides, R., Holmes, R. S., von Deimling, O., and Hilgers, J. (1986) Genetic marker patterns and endogenous mammary tumor virus genes in inbred mouse strains of Japan. *Exp. Anim. 35*, 263−273.

(23) Pierrard, J. C., Rimbault, J., Aplincourt, M., Le Greneur, S., and Port, M. (2008) New synthesis of a high molecular weight ligand derived from dota; thermodynamic stability of the MRI contrast agent formed with gadolinium. *Contr. Media Mol. Imaging 3*, 243−252.

(24) Liu, S. (2009) Radiolabeled cyclic RGD peptides as integrin $\alpha v\beta 3$-targeted radiotracers: Maximizing binding affinity via bivalency. *Bioconjugate Chem. 20*, 2199−2213.

(25) Chen, X., Tohme, M., Park, R., Hou, Y., Bading, J. R., and Conti, P. S. (2004) Micro-PET imaging of $\alpha v\beta 3$-integrin expression with^{18}F-labeled dimeric RGD peptide. *Mol. Imaging 3*, 96−104.

(26) Dijkgraaf, I., Yim, C.-B., Franssen, G., Schuit, R., Luurtsema, G., Liu, S., Oyen, W., and Boerman, O. (2011) PET imaging of $\alpha v\beta 3$ integrin expression in tumours with ^{68}Ga-labelled mono-, di- and tetrameric RGD peptides. *Eur. J. Nucl. Med. Mol. Imaging 38*, 128−137.

(27) Li, Z. B., Chen, K., and Chen, X. (2008) ^{68}Ga-labeled multimeric RGD peptides for microPET imaging of integrin $\alpha v\beta 3$ expression. *Eur. J. Nucl. Med. Mol. Imaging 35*, 1100−1108.

(28) Liu, S. (2006) Radiolabeled multimeric cyclic RGD peptides as integrin $\alpha v\beta 3$ targeted radiotracers for tumor imaging. *Mol. Pharmaceutics 3*, 472−487.

(29) Jia, B., Liu, Z., Shi, J., Yu, Z., Yang, Z., Zhao, H., He, Z., Liu, S., and Wang, F. (2008) Linker effects on biological properties of ^{111}In-labeled DTPA conjugates of a cyclic RGDfK dimer. *Bioconjugate Chem. 19*, 201−210.

(30) Chen, X., Park, R., Shahinian, A. H., Bading, J. R., and Conti, P. S. (2004) Pharmacokinetics and tumor retention of ^{125}I-labeled RGD peptide are improved by PEGylation. *Nucl. Med. Biol. 31*, 11−19.

(31) Moore, D. A., Fanwick, P. E., and Welch, M. J. (1990) A novel hexachelating amino-thiol ligand and its complex with gallium(III). *Inorg. Chem. 29*, 672−676.

(32) Bandoli, G., Dolmella, A., Tisato, F., Porchia, M., and Refosco, F. (2009) Mononuclear six-coordinated Ga(III) complexes: A comprehensive survey. *Coord. Chem. Rev. 253*, 56−77.

(33) Knetsch, P. A., Petrik, M., Griessinger, C. M., Rangger, C., Fani, M., Kesenheimer, C., Von Guggenberg, E., Pichler, B. J., Virgolini, I., Decristoforo, C., and Haubner, R. (2011) NODAGA-RGD for

imaging $\alpha v\beta 3$ integrin expression. *Eur. J. Nucl. Med. Mol. Imaging 38*, 1303−1312.
(34) Morfin, J. F., and Tóth, E. (2011) Kinetics of Ga(NOTA) formation from weak Ga-citrate complexes. *Inorg. Chem. 50*, 10371−10378.
(35) Brucher, E., and Sherry, A. D. (1990) Kinetics of formation and dissociation of the 1,4,7-triazacyclononnonane-N,N′,N″-triacetate complexes of cerium(III), gadolinium(III), and erbium(III) ions. *Inorganic Chem. 29*, 1555−1559.
(36) Chang, C. A., Liu, Y. L., Chen, C. Y., and Chou, X. M. (2001) Ligand preorganization in metal ion complexation: Molecular mechanics/dynamics, kinetics, and laser-excited luminescence studies of trivalent lanthanide complex formation with macrocyclic ligands TETA and DOTA. *Inorg. Chem. 40*, 3448−3455.
(37) Moreau, J., Guillon, E., Pierrard, J. C., Rimbault, J., Port, M., and Aplincourt, M. (2004) Complexing mechanism of the lanthanide cations Eu^{3+}, Gd^{3+}, and Tb^{3+} with 1,4,7,10-tetrakis (carboxymethyl)-1,4,7, 10-tetraazacyclododecane (dota) - characterization of three successive complexing phases: Study of the thermodynamic and structural properties of the complexes by potentiometry, luminescence spectroscopy, and EXAFS. *Chem.—Eur. J. 10*, 5218−5232.
(38) Wang, L., Shi, J., Kim, Y.-S., Zhai, S., Jia, B., Zhao, H., Liu, Z., Wang, F., Chen, X., and Liu, S. (2008) Improving tumor-targeting capability and pharmacokinetics of ^{99m}Tc-labeled cyclic RGD dimers with PEG4 linkers. *Mol. Pharmaceutics 6*, 231−245.
(39) Liu, Z., Niu, G., Shi, J., Liu, S., Wang, F., and Chen, X. (2009) ^{68}Ga-labeled cyclic RGD dimers with Gly3 and PEG4 linkers: Promising agents for tumor integrin α v$\beta 3$ PET imaging. *Eur. J. Nucl. Med. Mol. Imaging 36*, 947−957.
(40) Li, Z. B., Cai, W., Cao, Q., Chen, K., Wu, Z., He, L., and Chen, X. (2007) ^{64}Cu-labeled tetrameric and octameric RGD peptides for small-animal PET of tumor $\alpha v\beta 3$ integrin expression. *J. Nucl. Med. 48*, 1162−1171.
(41) Garanger, E., Boturyn, D., Coll, J.-L., Favrot, M.-C., and Dumy, P. (2006) Multivalent RGD synthetic peptides as potent $\alpha v\beta 3$ integrin ligands. *Org. Biomol. Chem. 4*, 1958−1965.
(42) Wu, Y., Zhang, X., Xiong, Z., Cheng, Z., Fisher, D. R., Liu, S., Gambhir, S. S., and Chen, X. (2005) microPET imaging of glioma integrin $\alpha v\beta 3$ expression using ^{64}Cu-labeled tetrameric RGD peptide. *J. Nucl. Med. 46*, 1707−1718.
(43) Wu, Z., Li, Z.-B., Chen, K., Cai, W., He, L., Chin, F. T., Li, F., and Chen, X. (2007) microPET of tumor integrin $\alpha v\beta 3$ expression using ^{18}F-labeled PEGylated tetrameric RGD peptide (^{18}F-FPRGD4). *J. Nucl. Med. 48*, 1536−1544.
(44) Akizawa, H., Uehara, T., and Arano, Y. (2008) Renal uptake and metabolism of radiopharmaceuticals derived from peptides and proteins. *Adv. Drug Delivery Rev. 60*, 1319−1328.
(45) Breeman, W. A. P., De Jong, M., De Blois, E., Bernard, B. F., Konijnenberg, M., and Krenning, E. P. (2005) Radiolabelling DOTA-peptides with ^{68}Ga. *Eur. J. Nucl. Med. Mol. Imaging 32*, 478−485.
(46) Loktionova, N. S., Belozub, A. N., Filosofov, D. V., Zhernosekov, K. P., Wagner, T., Türler, A., and Rösch, F. (2011) Improved column-based radiochemical processing of the generator produced ^{68}Ga. *Appl. Radiat. Isot. 69*, 942−946.
(47) Tolmachev, V., and Stone-Elander, S. (2010) Radiolabelled proteins for positron emission tomography: Pros and cons of labelling methods. *Biochim. Biophys. Acta 1800*, 487−510.

Synthesis and evaluation of diastereoisomers of 1,4,7-triazacyclononane-1,4,7-tris-(glutaric acid) (NOTGA) for multimeric radiopharmaceuticals of gallium.

Supporting Information

Francisco L. Guerra Gomez[†], Tomoya Uehara[†], Takemi Rokugawa[†], Yusuke Higaki[†,‡], Hiroyuki Suzuki[†], Hirofumi Hanaoka[†], Hiromichi Akizawa[£], and Yasushi Arano*[†]

Affiliations and addresses of the authors:

[†]Graduate School of Pharmaceutical Sciences, Chiba University, Chiba, Japan, 260-8675

[‡]School of Health Sciences, College of Medical, Pharmaceutical and Health Sciences, Kanazawa University, Ishikawa, Japan, 920-0942

[£]Health Science University of Hokkaido, 1757 Kanazawa, Tobetsu-cho, Ishikari-gun, Hokkaido, Japan 061-0293

For correspondence or reprint contact to: Yasushi Arano Ph.D. Department of Molecular Imaging and Radiotherapy, Graduate School of Pharmaceutical Sciences, Chiba University, 1-8-1 Inohana, Chuo-ku, Chiba, 260-8675 Japan. Tel: +81-43-226-2896, Fax: +81-43-226-2897; E-mail: arano@p.chiba-u.ac.jp

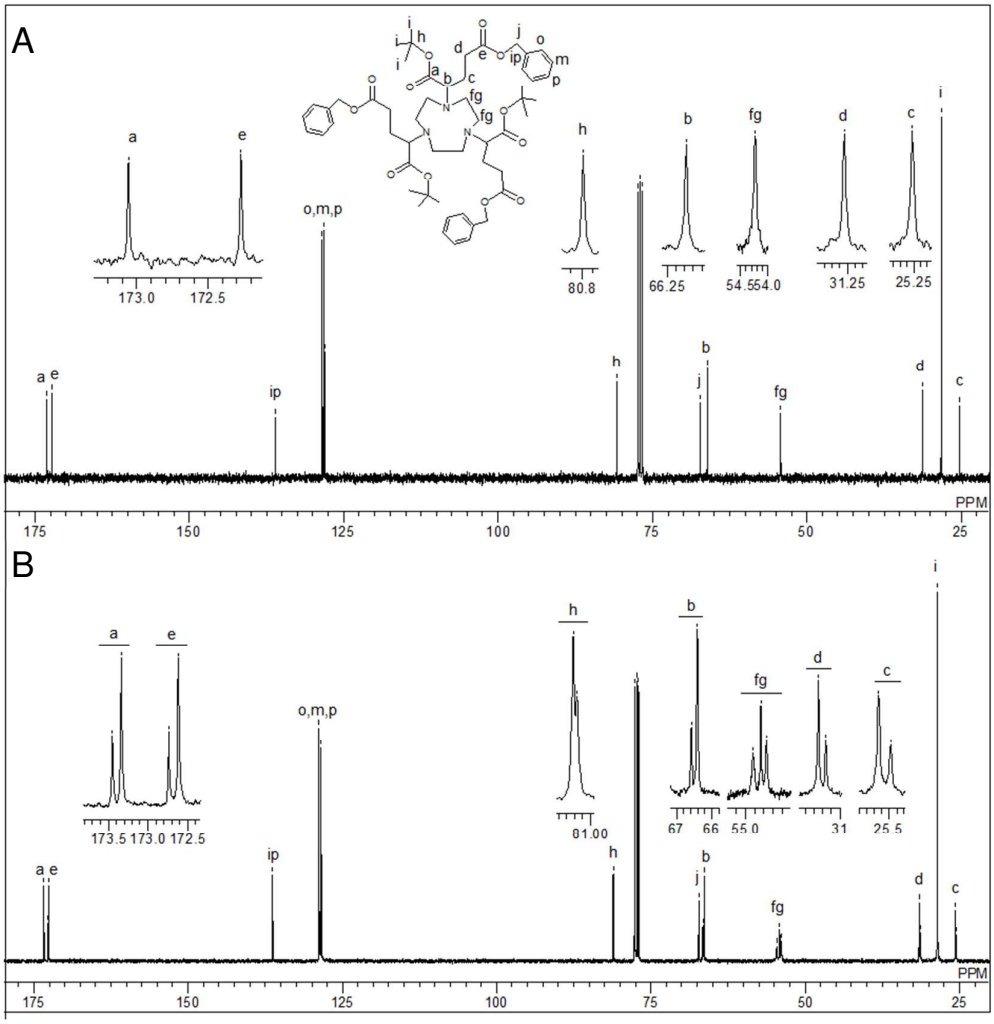

Figure S1. ^{13}C NMR (100MHz, $CDCl_3$, 25 °C) spectra of NOTGA-$^{t}Bu_3$-Bz_3 products obtained from alkylation of TACN with (R/S)-α-bromoglutaric acid 1-tert-butyl ester 5-benzyl ester, followed by column chromatography. The major (A: 69 %) fraction is corresponding to *RRR*/*SSS* enantiomers while the minor (B; 17 %) fraction to *RRS*/*SSR* diastereomers. See inserted structural formula for assignments.

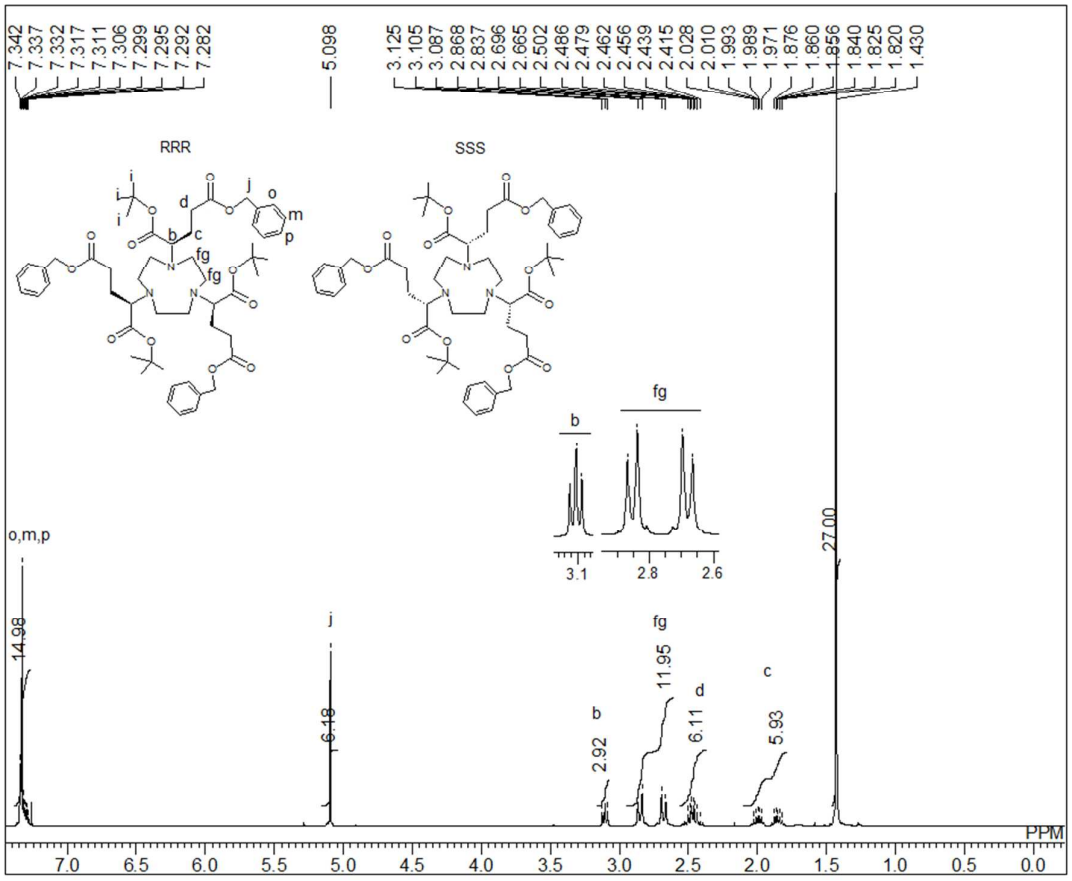

Figure S2. ^{1}H NMR (400 MHz, $CDCl_3$, 25 °C) spectra of NOTGA-$^{t}Bu_3$-Bz_3 from the alkylation of TACN with (R/S)-α-bromoglutaric acid 1-tert-butyl ester 5-benzyl ester. Column chromatography isolated. 69% fraction corresponding to *RRR*/*SSS* enantiomers. See inserted structural formulas for assignments

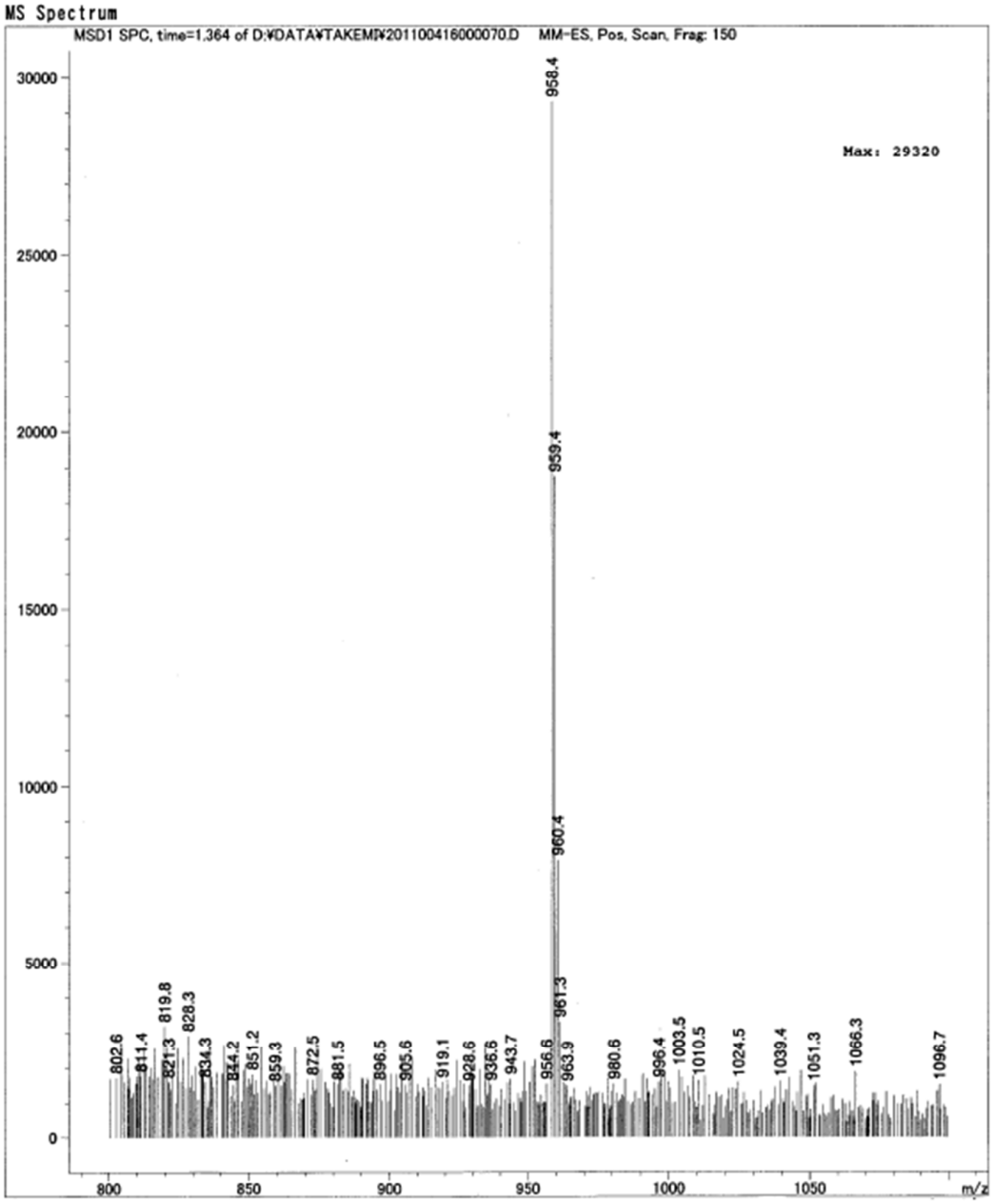

Figure S3. MS spectra of NOTGA-^{t}Bu$_3$-Bz$_3$ from the alkylation of TACN with (R/S)-α-bromoglutaric acid 1-tert-butyl ester 5-benzyl ester. Column chromatography isolated. 69% fraction corresponding to *RRR*/*SSS* enantiomers. LC-MS (ESI-positive), m/z: 958.5 $[M+H]^+$, Found 958.5

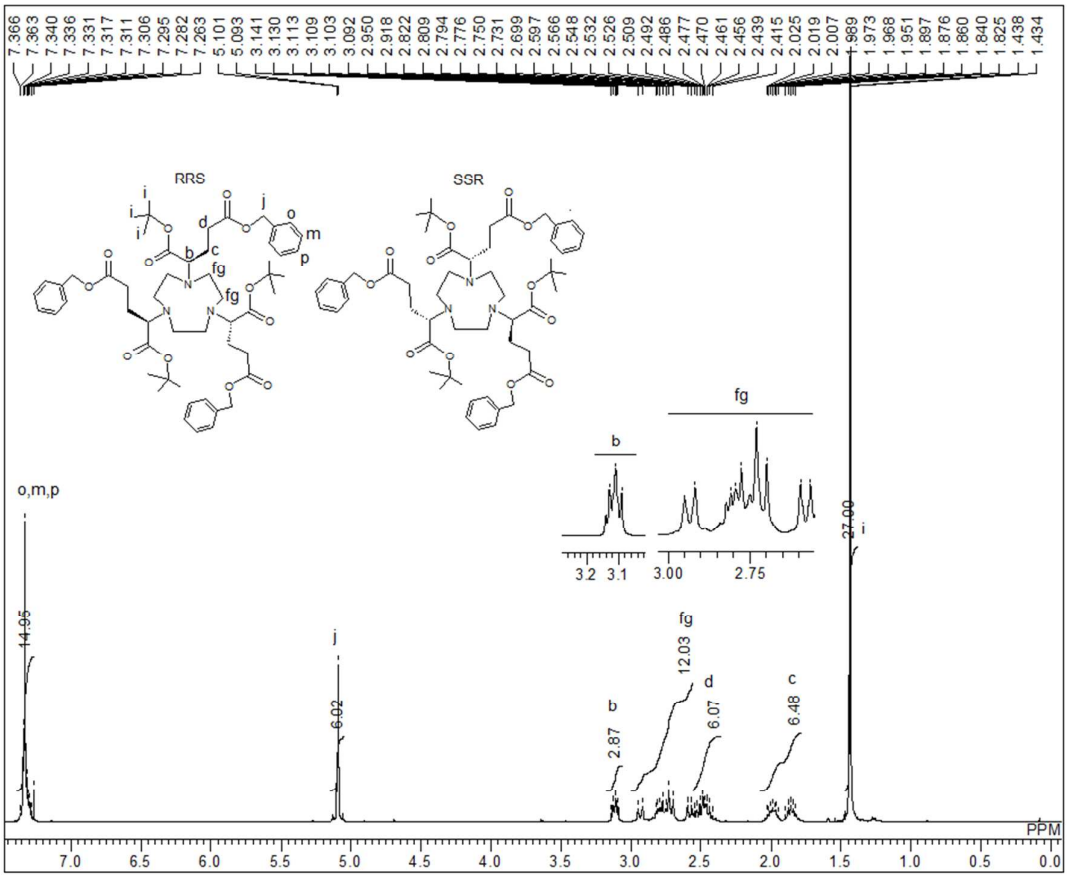

Figure S4. ^{1}H NMR (400MHz, $CDCl_3$, 25 °C) spectra of NOTGA-$^{t}Bu_3$-Bz_3 from the alkylation of TACN with (R/S)-α-bromoglutaric acid 1-tert-butyl ester 5-benzyl ester. Column chromatography isolated. 17% fraction corresponding to the *RRS*/*SSR* diastereomers. See inserted structural formulas for assignments

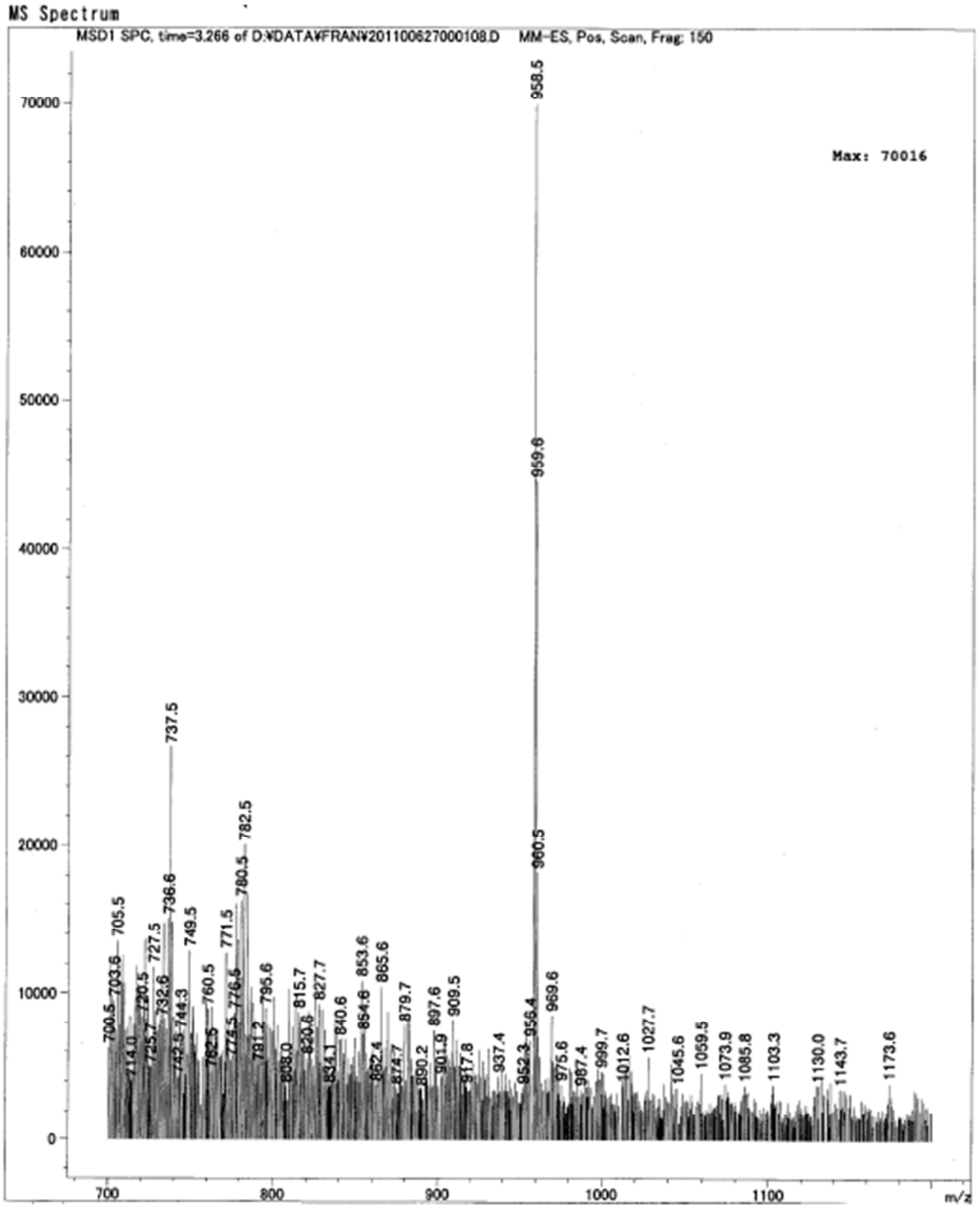

Figure S5. MS spectra of NOTGA-^{t}Bu$_3$-Bz$_3$ from the alkylation of TACN with (R/S)-α-bromoglutaric acid 1-tert-butyl ester 5-benzyl ester. Column chromatography isolated. 17% fraction corresponding to the *RRS*/*SSR* diastereomers. LC-MS (ESI-positive), m/z: 958.5 $[M+H]^+$, Found 958.5

Bioconjugate Chemistry

Article

pubs.acs.org/bc

^{68}Ga Small Peptide Imaging: Comparison of NOTA and PCTA

Cara L. Ferreira,*[,†] Donald T. T. Yapp,*[,‡] Derek Mandel,[†] Rajanvir K. Gill,[‡] Eszter Boros,[§,∥] May Q. Wong,[‡] Paul Jurek,[⊥] and Garry E. Kiefer[⊥]

[†]Nordion, 4004 Wesbrook Mall, Vancouver, British Columbia, Canada, V6T 2A3

[‡]Department of Experimental Therapeutics, BC Cancer Agency, Vancouver, British Columbia, Canada

[§]TRIUMF, Vancouver, British Columbia, Canada

[∥]Chemistry Department, University of British Columbia, Vancouver, British Columbia, Canada

[⊥]Macrocyclics, Dallas, Texas, United States

ABSTRACT: In this study, a bifunctional version of the chelate PCTA was compared to the analogous NOTA derivative for peptide conjugation, ^{68}Ga radiolabeling, and small peptide imaging. Both *p*-SCN-Bn-PCTA and *p*-SCN-Bn-NOTA were conjugated to cyclo-RGDyK. The resulting conjugates, PCTA-RGD and NOTA-RGD, retained their affinity for the peptide target, the $\alpha_v\beta_3$ receptor. Both PCTA-RGD and NOTA-RGD could be radiolabeled with ^{68}Ga in >95% radiochemical yield (RCY) at room temperature within 5 min. For PCTA-RGD, higher effective specific activities, up to 55 MBq/nmol, could be achieved in 95% RCY with gentle heating at 40 °C. The ^{68}Ga-radiolabeled conjugates were >90% stable in serum and in the presence of excess apo-transferrin over 4 h; ^{68}Ga-PCTA-RGD did have slightly lower stability than ^{68}Ga-NOTA-RGD, 93 ± 2% compared to 98 ± 1%, at the 4 h time point. Finally, the tumor and nontarget organ uptake and clearance of ^{68}Ga-radiolabeled PCTA-RGD and NOTA-RGD was compared in mice bearing HT-29 colorectal tumor xenografts. Activity cleared quickly from the blood and muscle tissue with >90% and >70% of the initial activity cleared within the first 40 min, respectively. The majority of activity was observed in the kidney, liver, and tumor tissue. The observed tumor uptake was specific with up to 75% of the tumor uptake blocked when the mice were preinjected with 160 nmol (100 μg) of unlabeled peptide. Uptake observed in the blocked tumors was not significantly different than the background activity observed in muscle tissue. The only significant difference between the two ^{68}Ga-radiolabeled bioconjugates in vivo was the kidney uptake. ^{68}Ga-radiolabeled PCTA-RGD had significantly lower ($p < 0.05$) kidney uptake (1.1 ± 0.5%) at 2 h postinjection compared to ^{68}Ga-radiolabeled NOTA-RGD (2.7 ± 1.3%). Overall, ^{68}Ga-radiolabeled PCTA-RGD and NOTA-RGD performed similarly, but the lower kidney uptake for ^{68}Ga-radiolabeled PCTA-RGD may be advantageous in some imaging applications.

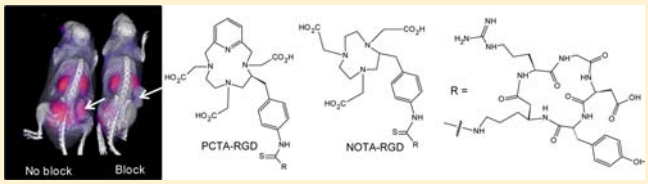

INTRODUCTION

The high-resolution nuclear imaging technique positron emission tomography (PET) has been growing in clinical use over the past decade. Complementary interest in the generator-produced positron-emitting radionuclide ^{68}Ga has also been on the rise in recent years. ^{68}Ga can be acquired from a parent/daughter ^{68}Ge/^{68}Ga generator, much like ^{99m}Tc, the mainstay for single photon emission computed tomography (SPECT) imaging, is acquired from a ^{99}Mo/^{99m}Tc generator. In contrast, the majority of positron-emitting nuclides used clinically are cyclotron-produced. For example, ^{18}F, a widely used PET nuclide, has a short 110 min half-life and requires local production of the isotope within hours of use. The availability of an appropriate generator-produced radionuclide such as ^{68}Ga could further facilitate the growth of PET centers in areas that are remote from cyclotron facilities.[1]

^{68}Ga has a short half-life of only 68 min, which makes it ideal for imaging small molecules and peptides that clear quickly from the background tissue. The short half-life of the isotope necessitates fast radiolabeling chemistry, preferably delivering >95% radiochemical yield in high specific activity to obviate time-consuming purification processes, in order to minimize significant loss of the imaging agent to decay. The ability to obtain the final radiolabeled compound in high effective specific activity (activity per total moles of both labeled and unlabeled compound) is particularly important for low/medium density receptors where the excess unlabeled compound will compete for binding sites effectively reducing target uptake.[2] The ability to radiolabel efficiently at room temperature in buffered aqueous solutions would be ideal because small peptides and molecules can be sensitive to harsh conditions, such as high temperature and low pH. Stability, especially kinetic stability of the radiolabeled agent in the presence of ubiquitous in vivo proteins with an affinity for Ga, such as the iron-transport protein transferrin, is important over a period of several hours. High thermodynamic and long-term stabilities are less relevant, again due to short half-life and early imaging time frame of ^{68}Ga-based PET agents.

Received: June 28, 2012
Revised: September 25, 2012
Published: October 5, 2012

ACS Publications © 2012 American Chemical Society

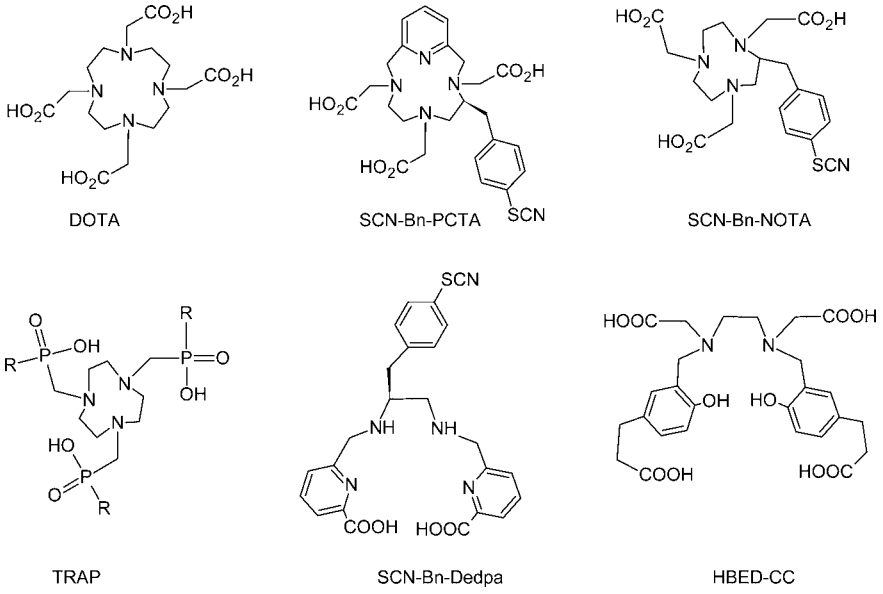

Figure 1. Structures of bifunctional chelates applicable to Ga radioisotopes.

Bifunctional chelates (BFCs; Figure 1) are used to facilitate the ^{68}Ga radiolabeling of biologically relevant targeting vectors, such as small molecules and peptides. 1,4,7,10-Tetraazacyclododecane-1,4,7,10-tetraacetic acid (DOTA), a chelate utilized for coordination of a myriad of d- and f-block metals, was one of the first chelates used for ^{68}Ga radiolabeling. Somatostatin-targeted conjugates of DOTA, such as DOTATOC, DOTANOC, and DOTATATE, radiolabeled with ^{68}Ga are now prepared in clinics throughout the world for imaging of neuroendocrine tumors. However, radiolabeling DOTA with ^{68}Ga requires high temperatures to obtain high radiochemical yields in a reasonable reaction time.[3,4] Moreover, DOTA and some DOTA-containing conjugates have also been shown to release ^{68}Ga via transchelation by proteins due to the similar size and charge of Ga^{3+} and Fe^{3+};[5] iron sequestering and iron transporting proteins are most culpable.[6] With the increasing interest in ^{68}Ga, there has been a rising amount of research on novel BFCs for ^{68}Ga. The smaller macrocyclic core of 1,4,7-triazacyclononane-1,4,7-triacetic acid (NOTA) has been shown to be more efficiently radiolabeled at lower temperatures with ^{68}Ga and to yield a radiolabeled agent with superior in vivo stability.[7] ^{68}Ga is predisposed to form six-coordinate complexes, so while DOTA, which has eight potential coordinating groups, has a "spare" carboxylate available for conjugation, NOTA, which only has six coordinating groups, compromises stability if a carboxylate is used for conjugation. Derivatives of the NOTA chelator such as NOTA-Bn-SCN, NODAGA, and TRAP allow for facile conjugation of biological targeting vectors without compromising one of the six coordinating groups.[8−11] The TRAP chelator has also been reported to achieve exceptionally high specific activities, over 700 MBq/nmol with radiochemical yields >95%.[11] The acyclic chelates Dedpa and HBED have been reported to be radiolabeled at room temperature with ^{68}Ga with even higher efficiency, producing higher radiochemical yields in shorter reaction times using lower concentrations of BFC compared to NOTA.[12,13] Despite the predicted lower stability of acyclic chelates over macrocyclic chelates, attributed to the increased rigidity and smaller loss of entropy upon coordination of the latter, both Dedpa and HBED have been reported to be stable to the loss of ^{68}Ga in the presence of serum proteins.

Previously, we reported the evaluation of two novel backbone-functionalized chelates, *p*-NO_2-Bn-PCTA and *p*-NO_2-Bn-Oxo-DO3A, for use with ^{68}Ga.[14] The chelates were directly compared to analogous derivatives of DOTA and NOTA with respect to radiochemistry, in vitro stability, and biodistribution properties. PCTA was found to have superior radiolabeling efficiency compared to DOTA. PCTA required shorter reaction times and lower reaction temperatures to obtain the same radiochemical yields and effective specific activities as DOTA when all other reaction conditions were identical. As well, when challenged with human apo-transferrin, DOTA was shown to lose ^{68}Ga to the protein, in contrast PCTA and NOTA were shown to be impervious to transchelation by the protein. We concluded that PCTA may be a useful BFC for the development of ^{68}Ga-based radiopharmaceuticals.

In this study, we investigated the utility of *p*-SCN-Bn-PCTA for ^{68}Ga radiolabeling and imaging of small peptides, specifically cyclo-RGDyK. Small peptides containing the RGD motif have been widely investigated for PET imaging of angiogenesis, a hallmark of cancer and potential indicator of metastatic potential. ^{68}Ga radiolabeling and imaging using RGD containing peptides has been reported with a multitude of chelates,[8,15] and the radiolabeling and imaging properties have been shown to be dependent on the choice of chelate. Thus, we chose to utilize conjugates of cyclo-RGDyK to scrutinize the ^{68}Ga small peptide labeling and imaging properties of PCTA in direct comparison with NOTA.

EXPERIMENTAL SECTION

Materials. All solvents and reagents were used as received unless otherwise noted. The BFCs, *p*-SCN-Bn-NOTA, and *p*-SCN-Bn-PCTA were acquired from Macrocyclics Inc. (Dallas, TX). ^{125}I-Echistatin was purchased from PerkinElmer (Boston, MA). ^{67}Ga was obtained as a dilute HCl solution (Nordion, Vancouver, Canada). ^{68}Ga was obtained from a generator consisting of ^{68}Ge on a titanium dioxide sorbent and eluted with 1 or 5 mL of 0.1 N HCl. Cyclo-(RGDyK) was purchased

dx.doi.org/10.1021/bc300348d | *Bioconjugate Chem.* 2012, 23, 2239−2246

from Peptides International (Louisville, KY). Water was deionized using a Milli-Q biocel A-10 water purification system.

Conjugation Chemistry. The bioconjugates were prepared by combining cyclo-(RGDyK) and a slight excess (1.1 equiv) of each of the BFCs in pH 9, 50 mM HEPES buffer. The solutions were left at room temperature overnight. The resulting conjugates were purified by HPLC with a Waters XBridge BEH130 4.6 × 150 mm analytical column using a gradient of 5% water/95% ethanol to 100% ethanol over 30 min at 1 mL/min. The bioconjugates were characterized by mass spectroscopy and HPLC. Mass spectroscopy was done using positive-ion mode electrospray ionization with a Micromass Q-TOF Ultima API Time-of-Flight mass spectrometer by Mr. Andras Szeitz (University of British Columbia, Department of Pharmaceutical Sciences). A calibrated VWR symphony pH meter was used to adjust the pH of all buffer solutions.

Radiochemistry. Initial radiolabeling and stability studies were conducted using the longer-lived gallium radioisotope ^{67}Ga. The radioisotope (37−185 MBq) was added to the conjugate (1−100 nmol) dissolved in 1 mL of 10 mM sodium acetate buffer pH 4.5 and then incubated at room temperature or in a heated water bath or in a Biotage Initiator 2.5 microwave reactor for a predetermined amount of time ranging 5−30 min. ^{68}Ga radiolabeling was accomplished similarly. The radioisotope (37−740 MBq) was added to the conjugate (1−50 nmol) dissolved in 1 mL of 200 mM sodium acetate buffer pH 4.5. Alternatively, sodium acetate (10.2 mg) was added to the conjugate (1−50 nmol) in a minimal amount of water followed by 1 mL of the generator eluent containing the radioisotope (185−740 MBq) yielding a reaction solution with a pH of ∼4.5. The radiolabeling reactions were then incubated at room temperature or heated in a water bath or in a Biotage Initiator 2.5 microwave reactor for a predetermined period of time.

The radiochemical yield and purity were determined by HPLC analysis using a Waters Alliance HT 2795 separation module equipped with a Raytest Gabi star NaI detector and a Waters 996 photodiode array (PDA) detector. The HPLC method used a Waters XBridge BEH130 RPC18 4.6 × 150 mm analytical column eluting with a binary solvent system; solvent A = acetonitrile, solvent B = 0.05% trifluoroacetic acid in water, gradient elution 5% A/95% B to 100% A over 30 min at 1 mL/min. The guard column was monitored after each run to confirm no colloids or impurities remained on the column.

In Vitro Stability. The stability of the radiolabeled conjugates was examined by challenging each radiolabeled conjugate with human apo-transferrin. Each bioconjugate was first radiolabeled with ^{67}Ga in >95% radiochemical purity. Aliquots of the radiolabeled conjugates containing ∼37 MBq of radioisotope were added to a 3 mg/mL solution of apo-transferrin in 10 mM $NaHCO_3$ buffer at pH 6.9. The challenge samples were incubated in a hot water bath at 37 °C for different periods of time and then analyzed using the HPLC method described above or using size-exclusion PD-10 columns (GE) eluting with PBS (pH 7.2).

Cell Lines. U87MG human glioblastoma cells were maintained in DMEM supplemented with 2 mM L-glutamine (Invitrogen, Vancouver, BC) and 10% fetal bovine serum (FBS) (Invitrogen, United States) under 95% air and 5% CO_2 at 37 °C. Prior to use, the cells were washed twice with PBS, detached from the surface of the tissue culture flask by treatment with 0.25% Trypsin/EDTA (Sigma), and then resuspended (1 × 10^6 cells/mL) in binding buffer (20 mM Tris, pH 7.4, 150 mM NaCl, 2 mM $CaCl_2$, 1 mM $MgCl_2$, 1 mM $MnCl_2$, 0.1% bovine serum albumin).

HT-29 human colon adenocarcinoma cell lines were obtained from the ATCC (Manassas, VA, USA) and were certified Mycoplasma negative. Cells were cultured in McCoy's 5A (StemCell Technologies; Vancouver, CA), supplemented with 1% L-glutamine, 1% penicillin/streptomycin, and 10% FBS. Plated flasks were kept in a humidified incubator (5% CO_2, 37 °C) and passaged at ∼80−90% confluence. Tissue culture flasks, tubes, and plates (BD Falcon) were obtained from BD Sciences (Bedford, MA). Prior to use, cells were detached from the surface of the tissue culture flask by treatment with 0.25% Trypsin/EDTA (Sigma).

In Vitro Studies. The method for determining the binding affinity of each of the bioconjugates has been reported previously.[8,16] Briefly, filter plates (Multiscreen DV plates, 96 well, 0.65 μm pore size, Millipore, Ireland B.V.) were seeded with $\alpha_v\beta_3$ positive U87MG glioblastoma cells, 10^5 cells per well, and incubated with ^{125}I-Echistatin (20 000 cpm) along with increasing concentrations (0 to 2 mM) of one of the bioconjugates. After incubating for two hours, unbound ^{125}I-Echistatin was removed with several washes, the filters were collected and the activity measured (γ counter, Cobra-II Auto Gamma, Canberra Packard Canada) to determine the amount of bound ^{125}I-Echistatin.

In Vivo Studies. Animal studies were conducted with the full approval of the University of British Columbia's Animal Care Committee, operating under the auspices of the Canadian Animal Care Committee. HT29 tumors were grown subcutaneously on Rag2M (disrupted recombination activating gene) mice as reported previously;[17] briefly, 5 × 10^6 cells (50 uL) were injected subcutaneously on the lower back of Rag2M mice. Once the tumors reached ∼100−150 mm^3, the mice were anesthetized with isoflurane (5% induction, 3% maintenance) and injected intravenously with the ^{68}Ga radiolabeled cyclo-(RGDyK) conjugates of NOTA or PCTA (∼7−11 MBq, 18.5 GBq/μmol). Groups (n = 4−5) of mice were injected with one of the three radiolabeled bioconjugates and were imaged for 110 min postinjection, framed as 5 × 2 min, 6 × 5 min, 5 × 10 min, and 2 × 15 min. Imaging was carried out in the Siemens Inveon multimodality CT-PET small animal scanner.[18] Images were reconstructed in 3D using OSEM-MAP3D algorithms supplied by Siemens following CT-based attenuation scans to correct for the animal's body mass.

3D regions of interest (ROIs) were placed on the heart (to approximate the activity present in the blood), kidney, liver, muscle (lower leg), and tumor in reconstructed images of the imaged mice. Only ROIs greater than 75 mm^3 were used in the analysis to minimize partial volume effects. The activity present in each ROI was determined in Bq/mL based on a calibration scan done with a phantom of known activity to determine camera efficiency and sensitivity.

Two hours after injection, mice were euthanized. The blood, liver, kidney, muscle, and tumor tissue were harvested, weighed, and placed in a scintillation counter to determine the activity present per gram of tissue.

Statistical Analysis. Data from the animal studies for each of the radiolabeled conjugates, both the blocked and non-blocked groups, were compared using ANOVA analysis for comparing means. P-values ≤0.05 were considered statistically significant. The %ID/g calculated from the biodistribution at 2 h and determined from the ROI analysis at 110 min were compared using a Pearson correlation coefficient.

RESULTS

Bioconjugate Preparation and Characterization. Both of the BFCs were conjugated to cyclo-(RGDyK) by coupling the lysine amine of the peptide with the isothiocyanate functionality of the BFC, as reported previously.[8] Characterization information for the bioconjugates (Figure 2) can be found in Table 1. The identity of the conjugates was confirmed by mass spectroscopy, in which peaks of both the singly charged parent and the dication were observed. The purity of the bioconjugates was determined by HPLC and was >90% in all cases. Finally, the affinity of the bioconjugates for the $\alpha_v\beta_3$ integrin receptors was examined by competitive binding assay with ^{125}I-echistatin, a known high-affinity ligand for $\alpha_v\beta_3$. Both of the bioconjugates produced concentration-dependent inhibition of ^{125}I-echistatin and the determined IC_{50} values for PCTA-RGD (1.8 ± 0.6 μM) and NOTA-RGD (1.0 ± 0.3 μM) were not statistically different from one another.

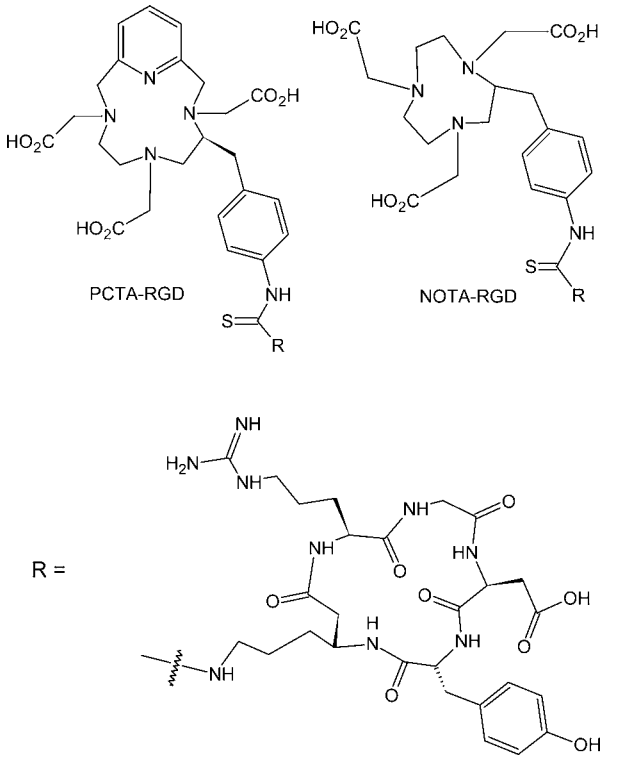

Figure 2. Bioconjugate structures.

Table 1. Characterization of the Bioconjugates (MS, HPLC, binding affinity)

	mass spectroscopy			
bioconjugate	calculated	observed	HPLC[a] retention time	IC_{50} μmol/L
PCTA-RGD	1147.2	1147.0 $[M^+]$, 574.7 $[M+2]^{2+}$	12.8 min	1.8 ± 0.6
NOTA-RGD	1070.2	1070.0 $[M^+]$, 535.7 $[M+2]^{2+}$	13.4 min	1.0 ± 0.3

[a]Waters XBridge BEH130 RPC18 4.6 × 150 mm analytical column gradient elution 5% A/95% B to 100% A over 30 min at 1 mL/min; solvent A = acetonitrile, solvent B = 0.05% trifluoroacetic acid in water.

Radiochemistry. The radiochemistry was initially evaluated using the longer-lived radioisotope ^{67}Ga. Once the optimized reaction parameters were determined using ^{67}Ga, the same parameters were used with ^{68}Ga. Previously, it was determined that the optimal pH conditions for efficient Ga radiolabeling of these BFCs is between pH 4 and pH 5, although PCTA and NOTA were less sensitive to changes in pH than DOTA.[14] So, all reactions were done by adding the radioisotope to the bioconjugate dissolved in a pH 4.5 sodium acetate solution at a concentration with an appropriate buffering capacity. Comparison of the reaction conditions and radiochemical yields are given in Table 2. Similar labeling efficiency was observed for both Ga radioisotopes. NOTA-RGD was labeled most efficiently, achieving >95% RCY in 5 min. PCTA-RGD could also achieve >95% RCY in 5 min, but required slightly elevated temperatures.

The majority of ^{68}Ga-radiolabeled RGD conjugates, including the NOTA-RGD conjugate used in this study, have been previously reported with an effective specific activity of ~18 MBq/nmol achievable with optimized reaction conditions.[3,8,9,15,19,20] In this study, higher effective specific activities, up to 55 MBq/nmol, were achievable for both the NOTA-RGD and the PCTA-RGD systems radiolabeling at room temperature.

Stability. To estimate the potential in vivo stability of each of the bioconjugates, challenge experiments were undertaken where each of the radiolabeled bioconjugates was incubated with apo-transferrin. The amount of the Ga-radiolabeled bioconjugate that remained intact and not associated with the protein at various time points was measured with size exclusion chromatography. There was no difference in the measured stability of the two complexes within the first 2 h of incubation. By the 4 h time point, Ga-radiolabeled PCTA-RGD and NOTA-RGD had only lost 7 ± 2% and 2 ± 1% to transferrin, respectively, which was significantly different (p = 0.03).

In Vivo Studies. The in vivo properties of both of the ^{68}Ga-radiolabeled RGD conjugates were compared in a human colorectal tumor model (HT-29), that has been shown to have a high vascular density and high levels of $\alpha_v\beta_3$ expression

Table 2. Optimized Reaction Conditions (Temperature and Time), Product HPLC Retention Times, and Radiochemical Yields (%RCY) for ^{67}Ga and ^{68}Ga Labeling of PCTA and NOTA Conjugates of cyclo-RGDyK

bioconjugate	temp.	reaction time	% RCY with ^{67}Ga	% RCY with ^{68}Ga	specific activity MBq/nmol
PCTA-RGD	Ambient	30 min	95.9 ± 0.8	96.2 ± 0.5	55 ± 1
PCTA-RGD	Ambient	5 min	94.9 ± 0.8	95.2 ± 0.8	17.5 ± 0.4
PCTA-RGD	40 °C	5 min	95.8 ± 0.5	97.1 ± 0.4	55 ± 0.4
NOTA-RGD	Ambient	5 min	99 ± 1	99 ± 1	18 ± 2
NOTA-RGD	Ambient	5 min	99.8 ± 0.5	98.9 ± 0.3	17.5 ± 0.4

[a]Waters XBridge BEH130 RPC18 4.6 × 150 mm analytical column gradient elution 5% A/95% B to 100% A over 30 min at 1 mL/min; solvent A = acetonitrile, solvent B = 0.05% trifluoroacetic acid in water.

dx.doi.org/10.1021/bc300348d | Bioconjugate Chem. 2012, 23, 2239−2246

attributed to tumor neovasculature.[21] Mice were inoculated with HT-29 human colon cancer cells, and the tumors were allowed to grow to ~150−200 mm^3. Immunohistochemical staining of the cells and excised tumors confirmed the absence of $\alpha_v\beta_3$ expression on the HT-29 cells, but the presence of $\alpha_v\beta_3$ expression on the activated endothelial cells present in tumor.

Groups of 3−5 mice with HT-29 xenografts were injected with one of the ^{68}Ga BFC-RGD conjugates and imaged over 110 min. At 120 min postinjection, the animals were sacrificed and the %ID/g present in select tissues was determined. Results from the imaging and biodistribution studies are summarized in Table 3 and Figures 3 and 4. The imaging results at 112 min and the biodistribution results at 120 min were highly correlated; Pearson correlation coefficients of 0.97 and 0.90 were determined for Ga-PCTA-RGD and Ga-NOTA-RGD, respectively. Time activity curves in Figure 3 show that both of the radiolabeled bioconjugates cleared from nontarget tissues. Higher uptake was observed in the kidney and liver, but cleared with time. Uptake in the tumor cleared slower than in other tissues, resulting in increasing tumor-to-background ratios over the course of the imaging experiment. Tumor uptake was significantly lower ($p < 0.05$), reduced by approximately 67−75%, when $\alpha_v\beta_3$ receptor sites were blocked with excess (160 nmol) of cyclo-RGDyK peptide.

Table 3. %ID/g and Tumor to Tissue Ratios for Selected Organs 2 h Post-Injection (7−11 MBq) in Rag2M Mice with Subcutaneous HT29 Tumors

organ	Ga-NOTA-RGD %ID/g	Ga-NOTA-RGD blocked[a] %ID/g	Ga-PCTA-RGD %ID/g	Ga-PCTA-RGD blocked[a] %ID/g
blood	0.23 ± 0.07	0.5 ± 0.1	0.29 ± 0.09	0.5 ± 0.1
tumor	1.5 ± 1.1	0.5 ± 0.2	1.3 ± 0.7	0.3 ± 0.2
kidney	2.7 ± 1.3*	5.3 ± 1.5	1.1 ± 0.5*	8.3 ± 3.1
liver	1.1 ± 0.5	1.5 ± 0.6	0.8 ± 0.5	0.9 ± 0.5
muscle	0.11 ± 0.09	0.5 ± 0.2	0.15 ± 0.10	0.4 ± 0.2
		ratios		
tumor to blood	6.1 ± 2.2		4.1 ± 1.1	
tumor to kidneys	0.7 ± 0.4*		1.5 ± 0.4*	
tumor to liver	1.9 ± 0.7		1.7 ± 0.8	
tumor to muscle	9.9 ± 5.4		11 ± 7.5	

[a]Blocked injected with 160 nmol (100 μg) of cyclo-(RGDyK). *Statistically different $p < 0.05$.

Statistical analysis was done to determine if any of the differences between the radiolabeled bioconjugates observed in the biodistribution study were significant based on a 95% confidence level. The only tissue that showed a statistically different uptake was the kidneys. The %ID/g at 2 h in the kidneys for Ga-PCTA-RGD was 1.1 ± 0.5% which was significantly ($p < 0.05$) lower compared to Ga-NOTA-RGD at 2.7 ± 1.3%. Tumor-to-background ratios were not found to be significantly different for the two bioconjugates, with the exception of the tumor-to-kidney ratio, which was double at 1.5 ± 0.5% for Ga-PCTA-RGD compared to 0.7 ± 0.4% for Ga-NOTA-RGD. Interestingly, $\alpha_v\beta_3$ blocked animals that were administered excess cyclo-RGDyK, showed much higher kidney uptake after 2 h, but this is likely attributable to slower renal filtration rates for animals under isoflurane anesthesia combined with the larger amount of peptide injected.

DISCUSSION

Radiochemistry. It has been widely reported that DOTA conjugated peptides require higher temperatures and sometimes longer reaction times to obtain high (>95%) radiochemical yields at reasonable effective specific activities.[3,9,19] Although this limitation has not stopped ^{68}Ga-based agents such as ^{68}Ga-DOTATOC from moving into the clinic, more efficient Ga radiochemistry would better facilitate the translation of ^{68}Ga-based radiopharmaceuticals into the clinic. Room temperature radiolabeling in an aqueous buffer appropriate for injection would be ideal, as it would be applicable to most biological targeting vectors, including temperature sensitive peptides. It would also facilitate the preparation of simple kit formulations analogous to the ^{99m}Tc-based radiopharmaceutical kits that are widely used in hospital radiopharmacy settings today.

The RGD bioconjugate of PCTA was shown to have favorable radiolabeling efficiency. In comparison to Ga radiolabeling of reported RGD bioconjugates of DOTA, which require high temperatures and longer reaction times,[3,9,19] PCTA-RGD could be radiolabeled at room temperature in 30 min or in shorter reaction times and/or higher effective SA at 40 °C. Previous studies using NOTA-RGD or other RGD conjugates of bifunctional NOTA derivatives have reported elevated temperatures and longer reaction times for radiolabeling.[8,15] More recent studies have reported high radiochemical yields with short reaction times and room temperature conditions,[9,10,20] in agreement with our results for optimized NOTA-RGD ^{68}Ga radiolabeling. Both PCTA-RGD and NOTA-RGD are applicable to room temperature kit type radiolabeling in high RCY at acceptable SA and both were found to be stable under physiological conditions.

In Vivo Studies. The objective of the studies was to compare the in vivo properties of the Ga-radiolabeled RGD conjugates prepared from either *p*-SCN-Bn-PCTA or *p*-SCN-Bn-NOTA. Both systems were effective at specifically imaging $\alpha_v\beta_3$ in HT-29 tumors, which is expressed primarily on the neovasculature in this tumor model. Overall, Ga-radiolabeled PCTA-RGD and NOTA-RGD were similar in their tissue uptake and clearance patterns in tumor bearing mice, with the exception of minor differences in kidney uptake and clearance. Previously, comparative biodistribution studies of Ga-radiolabeled analogous nonconjugated bifunctional chelates *p*-NO_2-Bn-PCTA and *p*-NO_2-Bn-NOTA in healthy mice showed substantially higher kidney uptake for Ga-radiolabeled *p*-NO_2-Bn-NOTA. The same trend was observed in this study with Ga-radiolabeled NOTA-RGD having significantly higher kidney uptake than the Ga-radiolabeled PCTA-RGD. The lower kidney uptake and the higher tumor to kidney ratio for Ga-radiolabeled PCTA-RGD may be advantageous, especially for delineating tumors in the abdominal area.

Numerous other publications have investigated different chelates for peptide imaging with ^{68}Ga, several using the RGD motif containing peptides. Previous reports of the mouse biodistribution in nontarget organs for Ga-radiolabeled NOTA-RGD were consistent with the results reported here.[15,20] Our results and previously published results with Ga-radiolabeled NOTA-RGD are also consistent with the biodistribution measurements of Ga-radiolabeled NODAGA-RGD, another system containing the NOTA chelate.[9,10] In contrast, other

dx.doi.org/10.1021/bc300348d | Bioconjugate Chem. 2012, 23, 2239−2246

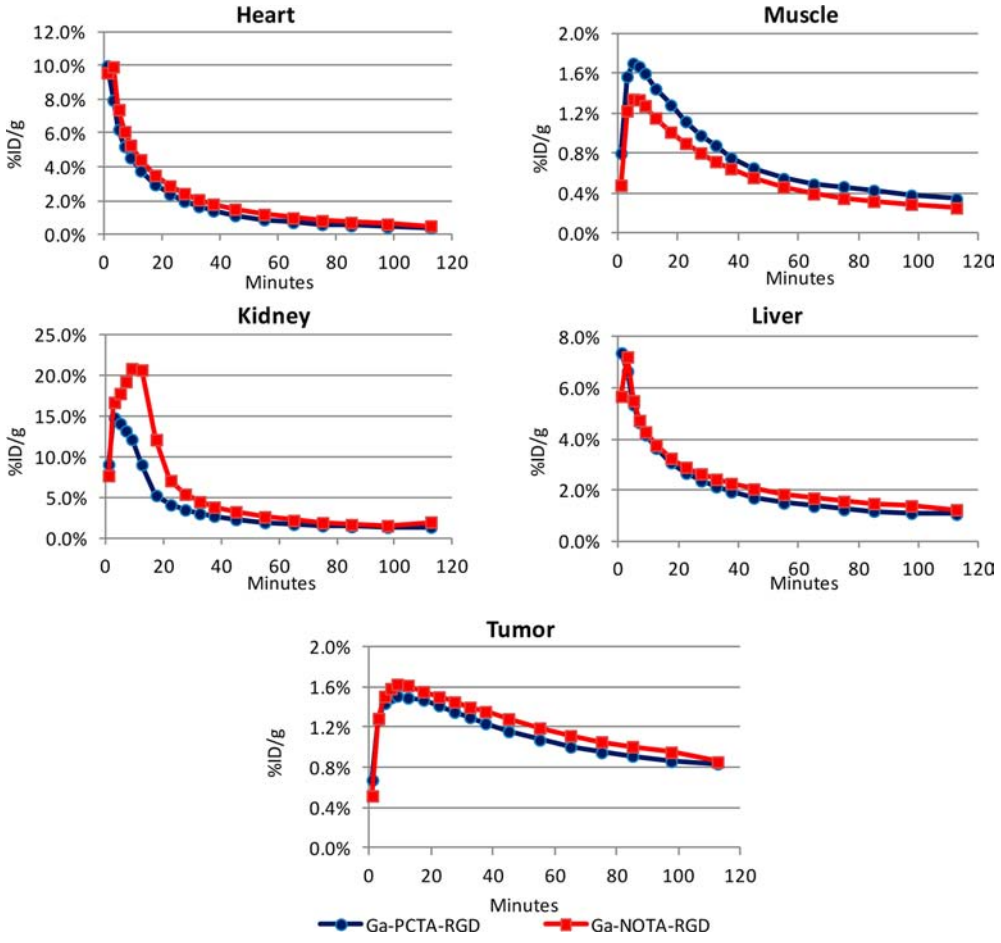

Figure 3. Time activity (%ID/g) curves from regions of interest analysis of PET images over 112 min for ^{68}Ga-radiolabeled PCTA-RGD and NOTA-RGD (n = 4−5). Note the different %ID/g axis ranges.

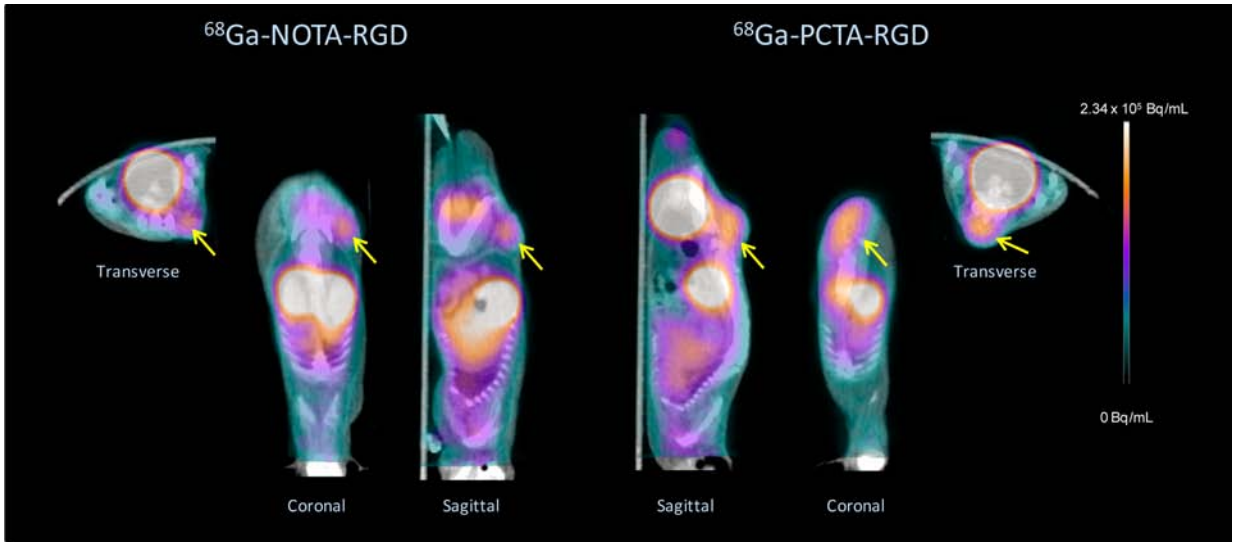

Figure 4. Images of HT-29 xenograft Rag2M Mice anesthetized with isoflurane 120 min after injection with ^{68}Ga-radiolabeled NOTA-RGD and ^{68}Ga-radiolabeled PCTA-RGD. From left to right: transverse, coronal, and sagittal views for each radiolabeled bioconjugate, respectively. Yellow arrows indicate the location of the tumors.

chelate systems that have been used to radiolabel RGD peptides with ^{68}Ga, including RGD conjugates of DOTA,[3,9,10] SarAr,[22] and dedpa,[23] have been reported to have higher background uptake than reported for NOTA or NODAGA and compared to what is reported here for PCTA.

CONCLUSION

The bifunctional chelate *p*-SCN-Bn-PCTA was compared to the analogous NOTA BFC for small peptide imaging. Both *p*-SCN-Bn-PCTA and *p*-SCN-Bn-NOTA were conjugated to

dx.doi.org/10.1021/bc300348d | *Bioconjugate Chem.* 2012, 23, 2239−2246

cyclo-RGDyK for targeting the $\alpha_v\beta_3$ integrin. The resulting conjugates, PCTA-RGD and NOTA-RGD, allowed for facile room temperature radiolabeling generating the ^{68}Ga-radiolabeled products in high RCY and effective specific activity. The radiolabeling conditions are amenable to simple kit-type radiopharmaceutical preparation, optimal for translation to a radiopharmacy setting. Although lower stability was observed after 4 h in the presence of apo-transferrin for ^{68}Ga-PCTA-RGD compared to ^{68}Ga-NOTA-RGD, no difference in stability was observed during the 2 h window that was optimal for imaging. With the exception of kidney uptake, the in vivo uptake and clearance of ^{68}Ga-radiolabeled PCTA-RGD and NOTA-RGD were not statistically different; both demonstrated specific uptake in tumors and cleared quickly from background tissue such as blood and muscle. ^{68}Ga-radiolabeled PCTA-RGD did have slightly lower average kidney uptake and consequentially somewhat better tumor to kidney ratio than ^{68}Ga-radiolabeled NOTA-RGD, which may be useful for imaging applications in the vicinity of the kidneys. The efficient radiochemistry, kinetic stability, and positive in vivo properties of the bifunctional chelate *p*-SCN-PCTA make it a valuable addition to the BFCs available for radiopharmaceutical development with ^{68}Ga. The potential of *p*-SCN-PCTA could be further improved by modifying the conjugation strategy, as has been investigated with the NOTA chelate.[9,10]

AUTHOR INFORMATION

Corresponding Author

*E-mail cara.ferreira@nordion.com, Tel +1 604 228 8952, Fax +1 604 228 5990 (C.F.); E-mail dyapp@bccrc.ca, Tel +1 604 675 8023, Fax +1 604 675 8183 (D.Y.).

Notes

The authors declare the following competing financial interest(s): Cara Ferreira is currently employed by Nordion. Paul Jurek and Garry Kiefer are currently employed by Macrocyclics. No other authors have any competing interests to disclose.

ACKNOWLEDGMENTS

The authors wish to thank the Natural Sciences and Engineering Research Council (NSERC) for an industrial undergraduate research award for Derek Mandel.

REFERENCES

(1) Fani, M., Andre, J. P., and Maecke, H. (2008) ^{68}Ga-PET: a powerful generator-based alternative to cyclotron-based PET radiopharmaceuticals. *Contr. Media Mol. Imaging 3*, 53−62.

(2) Velikyan, I., Beyer, G. J., Bergstrom-Pettermann, E., Johansen, P., Bergstrom, M., and Langstrom, B. (2008) The importance of high specific radioactivity in the performance of ^{68}Ga-labeled peptide. *Nucl. Med. Biol. 35*, 529−536.

(3) Decristoforo, C., Gonzalez, I. H., Carlsen, J., Rupprich, M., Huisman, M., Virgolini, I., Wester, H.-J., and Haubner, R. (2008) ^{68}Ga- and ^{111}In-labelled DOTA-RGD peptides for imaging $\alpha_v\beta_3$ integrin expression. *Eur. J. Nucl. Med. Mol. Imaging 35*, 1507−1515.

(4) Velikyan, I., Beyer, G. J., and Langstrom, B. (2004) Microwave-supported preparation of ^{68}Ga bioconjugates with high sepcific radioactivity. *Bioconjugate Chem. 15*, 554−560.

(5) Shannon, R. D. (1976) Revised effective radii and systematic studies of interatomic distances in halide and chalcogenides. *Acta Crystallogr. A32*, 751−767.

(6) Vallabhajosula, J. F., Harwig, J. K., Siemsen, N., and Wolf, W. (1980) Radiogallium localization in tumors: blood binding and the role of transferrin. *J. Nucl. Med. 225*, 4629−4633.

(7) Velikyan, I., Maecke, H., and Langstrom, B. (2008) Convenient preparation of Ga-68 based PET-radiopharmaceuticals at room temperature. *Bioconjugate Chem. 19*, 569−573.

(8) Jeong, J. M., Hong, M. K., Chang, Y. S., Lee, Y.-S., Kim, Y.-J., Cheon, G. J., Lee, D. S., Chung, J.-K., and Lee, M. C. (2008) Preparation of a Promising Angiogenesis PET Imaging Agent: ^{68}Ga-Labeled c(RGDyK)-Isothiocyanatobenzyl- 1,4,7-triazacyclononane-1,4,7-Triacetic Acid and Feasibility Studies in Mice. *J. Nucl. Med. 49*, 830−836.

(9) Dumont, R. A., Deininger, F., Haubner, R., Maecke, H., Weber, W. A., and Fani, M. (2011) Novel ^{64}Cu- and ^{68}Ga-labeled RGD conjugates show improved PET imaging of $\alpha_v\beta_3$ integrin expression and facile radiosynthesis. *J. Nucl. Med. 52*, 1276−1284.

(10) Knetsch, P. A., Petrik, M., Griessinger, C. M., Rangger, C., Fani, M., Kesenhemer, C., von Guggenberg, E., Pichler, B. J., Virgolini, I., Decristoforo, C., and Haubner, R. (2011) [68Ga]NODAGA-RGD for imaging $\alpha v\beta 3$ integrin expression. *Eur. J. Nucl. Med. Mol. Imaging 38*, 1303−1312.

(11) Notni, J., Simecek, J., Hermann, P., and Wester, H.-J. (2011) TRAP, a powerful and verstaile framework for Gallium-68 radiopharmaceuticals. *Chem.—Eur. J. 17*, 14718−14722.

(12) Eder, M., Krivoshein, A. V., Backer, M., Backer, J. M., Haberkorn, U., and Eisenhut, M. (2010) ScVEGF-PEG-HBED-CC and scVEGF-PET-NOTA conjugates: comparison of easy-to-label recombinant proteins for [^{68}Ga]PET imaging of VEGF receptors in angiogenic vasculature. *Nucl. Med. Biol. 37*, 405−412.

(13) Boros, E., Ferreira, C. L., Cawthray, J. F., Price, E. W., Patrick, B. O., Wester, D. W., Adam, M. J., and Orvig, C. (2010) Acyclic chelate with ideal properties of ^{68}Ga PET imaging agent elaboration. *J. Am. Chem. Soc. 132*, 15726−15733.

(14) Ferreira, C. L., Lamsa, E., Woods, M., Duan, Y., Fernando, P., Bensimon, C., Kordos, M., Guenther, K., Jurek, P., and Kiefer, G. E. (2010) Evaluation of bifunctional chelates for development of gallium based radiopharmaceuticals. *Bioconjugate Chem. 21*, 531−536.

(15) Li, Z.-B., Chen, K., and Chen, X. (2008) ^{68}Ga-labled multimeric RGD peptides for microPET imaging of integrin $\alpha_v\beta_3$ expression. *Eur. J. Nucl. Med. Mol. Imaging 35*, 1100−1108.

(16) Shi, J., Kim, Y.-S., Zhai, S., Liu, Z., Chen, X., and Liu, S. (2009) Improving tumor uptake and pharmcokinetics of ^{64}Cu-labeled cyclic RGD peptide dimers with Gly_3 and PEG_4 linkers. *Bioconjugate Chem. 20*, 750−759.

(17) Baker, J. H. E., Lam, J., Kyle, A. H., Sy, J. T., Oliver, T., Co, S., Dragowska, W. H., Ramsay, E., Anatha, M., Ruth, T., Adam, M., Yung, A., Kozloxski, P., Minchinton, A. I., Ng, S. S. W., Bally, M. B., and Yapp, D. T. T. (2008) Irinophore CTM, a novel nano-formulation of irinotecan, alters tumor vascular function and enhances the distribution 5-FU and doxorubicin. *Clin. Cancer Res. 14*, 7260−7271.

(18) Wieholt, C., Hsiao, I., Lin, K., Chung, Y., Chen, C., and Yen, T. (2008) Performance evaluation of small animal PET system using NEMA standards. *J. Nucl. Med. 49*, 119P.

(19) Haukkala, J., Laitinen, I., Luoto, P., Iveson, P., Wilson, I., Karlsen, H., Cuthbertson, A., Laine, J., Leppänen, P., Ylä-Herttula, S., Knuuti, J., and Roivainen, A. (2009) ^{68}Ga-DOTA-RGD peptide: biodistribution and binding into atherosclerotic plaques in mice. *Eur. J. Nucl. Med. Mol. Imaging 36*, 2058−2067.

(20) Singh, A. N., Liu, W., Hao, G., Kumar, A., Gupta, A., Oz, O. K., Hsieh, J.-T., and Sun, X. (2011) Multivalent bifunctional chelator scaffolds for Gallium-68 based positron emission tomography imaging probe design: signal amplication via multivalency. *Bioconjugate Chem. 22*, 1650−1662.

(21) Zhou, Y., Kim, Y.-S., Chakraborty, S., Shi, J., Gao, H., and Liu, S. (2011) ^{99m}Tc-Labeled cyclic RGD peptides for noninvasive monitoring of tumor integrin $\alpha_v\beta_3$ expression. *Mol. Imaging 10*, 386−397.

(22) Ma, M. T., Neels, O. C., Denoyer, D., Roselt, P., Karas, J. A., Scanlon, D. B., White, J. M., Hicks, R. J., and Donnelly, P. S. (2011) Gallium-68 complex of a macrobicyclic cage amine chelator tethered to two integrin-targeting peptides for diagnostic tumor imaging. *Bioconjugate Chem. 22*, 2093−2103.

(23) Boros, E., Ferreira, C. L., Yapp, D. T., Gill, R. K., Price, E. W., Adam, M. J., and Orvig, C. (2012) RGD conjugates of the H_2dedpa scaffold: synthesis, labeling and imaging with ^{68}Ga. *Nucl. Med. Biol. 39*, 785−794.

Bioconjugate Chemistry

Article

pubs.acs.org/bc

Hyaluronic Acid Immobilized Polyacrylamide Nanoparticle Sensors for CD44 Receptor Targeting and pH Measurement in Cells

Honghao Sun,[†,‡] Rikke V. Benjaminsen,[‡,§] Kristoffer Almdal,[‡] and Thomas L. Andresen*[,‡,§]

[†]Department of Pharmacy, College of Bioengineering, Hubei University of Technology, Wuhan 430068, China

[‡]Department for Micro- and Nanotechnology, DTU Nanotech, [§]Center for Nanomedicine and Theranostics, Technical University of Denmark, 2800 Lyngby, Denmark

ABSTRACT: Our ability to design receptor-targeted nanocarriers aimed at drug release after endocytosis is limited by the current knowledge of intracellular nanoparticle (NP) trafficking. It is not clear if NP size, surface chemistry, and/or targeting of cell surface receptors changes the intracellular fate of NPs; i.e., will all NPs enter acidic compartments and eventually end up in lysosomes or are there escape mechanisms or receptor-specific signaling that can be induced to change the cellular processing of an internalized NP? To give new insight into the intracellular trafficking of NPs that target the CD44 receptor, which is overexpressed on the surface of a broad variety of cancer cells, we have synthesized an NP pH sensor system that targets CD44. We used a polyacrylamide nanoparticle matrix bearing hyaluronic acid (HA) on the surface as a CD44 targeting ligand. The HA-coated NPs were prepared by radical polymerization followed by post functionalization with sensor fluorophores and physically absorbed or chemically conjugated HA. Cell uptake studies showed significant uptake of HA-coated nanosensors in HeLa cells and no uptake under the same conditions without the HA targeting ligand. The pH distribution profile in cells was measured for nanosensors with HA, cationic, and noncharged NP surface coatings giving a clear indication of the intracellular pH environment that the different NPs experience after internalization. The pH profile of cationic nanosensors in comparison to HA conjugated nanosensors indicates that the intracellular trafficking is aimed at lysosomes regardless of whether CD44 receptor-specific or unspecific uptake is induced.

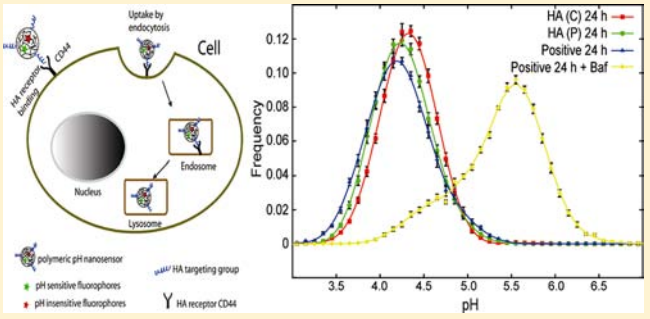

INTRODUCTION

Advanced nanoparticle systems with complex chemical coatings and surface conjugated ligands that target specific cell surface receptors on diseased cells are continuously being reported.[1,2] However, our basic understanding of nanoparticle internalization and intracellular trafficking mechanisms is insufficient, and we have limited knowledge of the cellular environment a nanoparticle experiences after internalization.[3] This could be one reason many advanced drug delivery systems aimed at cellular internalization through receptor targeting often show disappointing in vivo efficacy. Many advanced drug delivery systems are designed to be pH-sensitive by providing structural changes in the nanoparticle leading to drug release in response to decrease in pH after endocytosis and during intracellular trafficking to lysosomes.[4−7] However, the pH profile and kinetics that these systems experience after cellular internalization is not known for the individual drug carriers, and in principle, we are flying blind. Examples of receptor binding ligands that have been attached to nanoparticle-based drug delivery systems for inducing cell internalization include folate, hyaluronic acid, peptides, and antibodies, which all target receptors that are overexpressed on the surface of cells that are associated with disease.[8−15]

One possibility for enhancing our understanding of intracellular nanoparticle trafficking is to develop nanoparticle sensors (nanosensors) for live cell fluorescence microscopy measurements that can report the metabolite profiles and pH that a nanoparticle experiences after cellular internalization.[16−19] Until recently, the reported pH nanosensors were far from optimal for live cell imaging due to one major limitation, the dynamic measurement range of the reported nanosensors was too narrow for conducting reliable measurements in living cells. The reason for this limitation was that only one sensor fluorophore was used in sensor designs, which gave a measurement range of the fluorophore $pK_a \pm 1$ pH units, as a rule of thumb; however, we recently showed that the actual reliable measurement range is much less.[17] Thus, previously reported nanosensors could not be used to measure the pH of the physiological environment of endocytotic pathways in cells, where the pH is expected to be between pH 4 and pH 7.[17]

We have previously reported that it is possible to expand the reliable measurement range of nanosensors by combining two or more sensor fluorophores into a nanosensor giving reliable

Received: June 29, 2012
Revised: October 13, 2012
Published: November 1, 2012

ACS Publications © 2012 American Chemical Society

dx.doi.org/10.1021/bc300349n | *Bioconjugate Chem.* 2012, 23, 2247−2255

measurements in live cells in a broad pH range, >3.5 pH units.[17,20,21] This new development in the field makes it possible to explore cellular trafficking events of nanoparticles with different surface coatings using nanosensors. By attaching specific targeting ligands to the surface of the nanoparticle sensors, we can monitor internalization and pH profile kinetics during intracellular transport and provide new insight into nanoparticle targeting and trafficking, which is of particular relevance to the drug delivery field.

In this report, we synthesize and evaluate nanosensor systems that target CD44 (Cluster Determinant 44) receptors on the surface of cancer cells with hyaluronic acid as the targeting ligand and compare it with nonreceptor targeting nanosensors with neutral and cationic surface chemistries. We utilize triple-fluorophore-labeled polyacrylamide pH nanosensors, which are functionalized with two pH-sensitive and one pH-insensitive fluorophores. The pH determination in cells is hereby based on fluorescence intensity ratio measurements (fluoresensce intensity from pH sensitive/pH insensitive fluorophores).[22] HA is an anionic naturally occurring polysaccharide (copolymer of *N*-acetyl D-glucosamine and D-glucuronic acid), and a major component in the extracellular matrix that contributes significantly to cell proliferation and migration.[14,23] HA appears to exert its biological effects through binding interactions with three types of cell surface receptors: CD44, RHAMM (receptor for HA-mediated motility), and ICAM-1 (Intercellular Adhesion Molecule-1).[23] CD44 has been reported to be overexpressed in several cancer types (prostate, ovarian, breast) and is known to be strongly associated with cancerous angiogenesis and tumor progression. Furthermore, HA possesses excellent biocompatibility and biodegradability and has found growing interest as surface coating of nanoparticle drug delivery systems for targeting of CD44 overexpressing cancer cells.[10,14,23,24] To elucidate the trafficking of HA-coated nanoparticles and the intracellular pH profile that such particles experience, here we investigate nanosensors that target CD44 (Figure 1). It has been reported that kinetics and the mechanism of nanoparticle uptake are critically dependent on the surface chemistry and charge of nanoparticles,[25] and in this study, we are comparing a number of different nanoparticle surface chemistries as part of nanosensor designs. Thus, the study aims to contribute to our current understanding of nanoparticle trafficking where quantitative pH measurements in live cells provide new information about the cellular environment the nanoparticles experience upon cellular internalization.

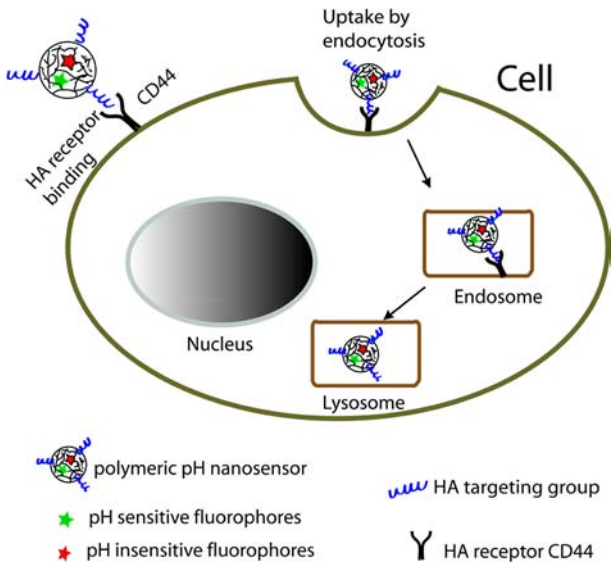

Figure 1. Illustration of the nanosensor cellular internalization.

EXPERIMENTAL PRECEDURES

Materials. *N*-(3-Aminopropyl) methacrylamide hydrochloride (APAC) was purchased from Polyscience, and sodium hyaluronate with different molecular weights (6.4, 12, 26, 66, 1000 kDa) from Lifecore Biomedical. Oregon green isothiocyanate (OG) and Rhodamine Red-X succinimidyl ester 5-isomer (RhX) from Invitrogen. *N,N*-Methylenebis-(acrylamide), acrylamide, *N,N,N′,N′*-tetrathylmethylenediamine (TEMED), ammonium persulfate (APS), Triton X-100, 1-hexanol, *N*-succinimidyl-*N*-methylcarbamate, *N*-hydroxysuccinimidyl (NHS), 1-ethyl-3-(3-dimethylaminopropyl)-carbodiimide hydrochloride (EDC), rhodamine B isothiocyanate (RhB), fluorescein isothiocyanate (FS), dimethyl sulfoxide (DMSO), and cyclohexane were purchased from Sigma-Aldrich. Cellulose ester dialysis membranes (MWCO 300 kDa and 1000 kDa) were received from Spectrum Laboratories Inc.

UV Spectrophotometry. UV spectra were recorded using a Shimadzu UV−visible spectrophotometer (phasmaspec UV-1700). The analysis was performed using Shimadzu UV Probe software.

Zeta Potential Measurements. The electrodes were conditioned before measurement with KCl aqueous solution (0.5 M) for 200 cycles. Zeta potential was measured with a ZetaPALS zeta potential analyzer (Brookhaven Instruments Corporation) at room temperature. The samples were diluted with Milli-Q water to a final concentration 0.25 mg/mL. Each data point is the average of 7 measurements.

Dynamic Light Scatting Measurements. 1.6 mL of pH nanosensors (0.25 mg/mL) in Milli-Q water was subjected to ultrasonic treatment and filtered through a 0.45 μM needle filter before measurement. The hydrodynamic diameter of the NP was measured with a ZetaPALS, zeta potential analyzer (Brookhaven Instruments Corporation) at room temperature with a fixed scattering angle of 90°. Each data point is an average of 3 measurements.

Fluorescence Spectra. The fluorescence spectra were measured on a refurbished SLS8000 (Olis Instruments). The samples were irradiated at 488 nm (FS and OG) and 543 nm (RhB and RhX) in a quartz cuvette at room temperature. The dwell time was 0.2 s, and each sample point was scanned twice. Each sample was prepared by adding 5 μL pH nanosensor (40 mg/mL) to 1 mL buffer.

Preparation of Amine-Containing NPs. The polymeric NPs were prepared by radical polymerization in a reverse microemulsion, which included a water phase with monomers and an oil phase with surfactant. Typically, 2.27 g of acrylamide, 0.566 g of methylbisacrylamide, and 0.0567 g of (3-propylamine) methylacrylamine hydrochloride were dissolved in 6.8 mL of Milli-Q water. A 8.8 mL aliquot of this monomer solution was added dropwise to 308 mL of oil phase (62.5 g TX-100 and 153.27 g 1-hexanol are diluted to 1000 mL with cyclohexane). After stirring for 10 min, the reverse microemulsion was formed, and then, the reaction mixture was degassed using freeze−vacuum−thaw method for at least four cycles and stirred under argon atmosphere. Thirty microliters of 30% (w/w) ammonium persulfate solution and 15 μL of

TEMED were added to initiate the polymerization. The reaction was stirred at room temperature for 3 h, and the reaction mixture was monitored by ^{1}H NMR to ensure the completion of the polymerization. The NPs were precipitated in ethanol, and then filtered in an Amicon ultrafiltration cell (Millipore Corp., Bedford, MA). Then, NPs were dispersed in Milli-Q water with ultrasonic treatment and dialyzed against Milli-Q water and kept at 5 °C.

Preparation of NP-OG-FS-RhB. The primary amino groups in the NPs were used to conjugate the sensor dyes. To deprotonate the primary amine, 300 μL of $NaHCO_3$/Na_2CO_3 buffer (0.2 M, pH 9.2) was added to 5 mL of NP aqueous solution (50 mg/mL), followed by adding 83 μL fluorescein isothiocyanate (1 mg/mL in DMSO), 99 μL oregon green isothiocyanate (1 mg/mL in DMSO), and 175 μL rhodamine B isothiocyanate (1 mg/mL in DMSO) to the NP solution. The reaction mixture was stirred for 4 h and was dialyzed against Milli-Q water for 4 days using cellulose dialysis tubing (MW cutoff 300 kDa) to remove any free fluorophores and DMSO. The conjugation yields of the fluorophores were determined by fluorescence spectroscopy after dialysis. The concentrations of unbound fluorophores were measured by fluorescence intensity in the dialysate, which was compared to the intensity from the total amount of fluorophores added. It was determined that the reaction yields of the conjugation of all fluorophores were >92%. As fluorescein and oregon green have overlapping fluorescence spectra, it was verified that the coupling efficiency of fluorescein isothiocyanate and oregon green isothiocyanate were the same by carrying out individual coupling of the fluorophores to nanoparticles. The samples were covered by aluminum foil to prevent photobleaching during the processes.

Preparation of NP-OG-FS-RhB-HA(P) by Physical Adsorbtion. HA with five different molecular weights (6.4, 12, 26, 66, 1000 kDa) was used for the physical adsoption of HA to the NP-OG-FS-RhB surface. Two milligrams of HA was added to 1 mL NP-OG-FS-RhB solution (40 mg/mL) and stirred for 12 h, followed by dialysis against water for 4 days (4× water change) using cellulose dialysis tubing (MW cutoff 300 kDa or 1000 kDa) to remove free HA.[24]

Preparation of NP-OG-FS-RhB-HA(C) by Chemical Conjugation. Two milligrams of HA (66 kDa) was added to 1 mL NP-OG-FS-RhB (40 mg/mL) and stirred for 2 h, followed by adding aqueous solution of EDC and NHS. Three different NHS/EDC concentrations (1 mg/mL NHS and 3 mg/mL EDC; 0.06 mg/mL NHS and 0.18 mg/mL EDC; 0.02 mg/mL NHS and 0.06 mg/mL EDC) were used. The mixture was stirred for 12 h followed by dialyzing against water for 4 days (4 times water change) using cellulose dialysis tubing (MW cutoff 300 kDa) to remove free HA, EDC, and NHS.[27]

Preparation of NP-OG-FS-RhB-capped. To 1 mL of NP-OG-FS-RhB aqueous solution (40 mg/mL) was added 100 μL of PBS buffer (pH 8.5) followed by addition of 20 mg of *N*-succinimidyl-*N*-methylcarbamate (NMC). The mixture was stirred for 1.5 h, after which it was dialyzed against water for 24 h using cellulose dialysis tubing (MW cutoff 300 kDa) to remove unreacted NMC and byproduct.

Preparation of NP-OG-FS-RhX. The synthesis and purification were carried out as described for NP-OG-FS-RhB, however, using Rhodamine Red-X succinimidyl ester 5-isomer instead of rhodamine B isothiocyanate.

Preparation of NP-OG-FS-RhX-HA(P) by Physical Adsoption, Prepration of NP-OG-FS-RhX-HA(C) by Chemical Conjugation, And Preparation of NP-OG-FS-RhX-Capped. All were prepared as described above.

Cellular Measurements. HeLa cells and MCF-7 cells were maintained in DMEM and RPMI 1640 medium, respectively, supplemented with 10% fetal bovine serum (Sigma-Aldrich) and 100 UI/mL penicilin and streptomycin (Lonza). Cell cultures were incubated in a 5% CO_2 humidified incubator at 37 °C. Cells were seeded on 9 mm cover glass slides in 24 well plates at a density of 2×10^4 HeLa cells per well the day before treatment or 3×10^4 MCF-7 cells two days before treatment. Cells were in total incubated with 10 μg/mL nanoparticles for 2, 4, or 24 h at 37 °C, depending on the measurement point. The cells were washed three times with ice-cold phosphate buffered saline (PBS) supplemented with heparin (20 units/mL), once with PBS, and kept in growth medium without phenol red and bicarbonate, but supplemented with 30 mM HEPES for control of pH without CO_2 incubation for observation by confocal microscopy. For the reference pH measurements, HeLa cells with internalized positive nanosensors were treated with 200 nM bafilomycin A1 for 45 min just prior to image acquisition. Images were captured by a Leica TCS SP5 confocal microscope with a 63× water-immersed objective (Leica Microsystems, Germany).

Image Acquisition and Analysis for pH Measurements. Images of nanosensor-containing cells was collected by sequential line scanning, with excitation at 488 and 561 nm, and emission at 493−560 nm and 566−700 nm, respectively, obtained by tunable high-reflectance mirrors. Along with the fluorescence images, a differential interference contrast (DIC) image or bright field image was obtained. In vitro calibration curves were generated from fluorescence images of 8 mg/mL nanosensor in 60 mM buffers (20 mM phosphate/20 mM citric acid/20 mM malice acid/100 mM NaCl) from pH 2.8 to 8.2. The microscope was focused in a plane within the solution, and images were taken with the same settings as the images of cells. The image analysis was performed as reported previously.[17] Briefly, custom-made software was utilized for background subtraction and image processing after which ratio intensities of green and red were converted to pH via the calibration curve for each pixel and presented in pH histograms.

RESULTS

The nanosensor polymer matrix was based on polyacrylamide nanoparticles, which were prepared by reverse microemulsion polymerization using the monomers acrylamide (AC), bismethylacrylamide (BisAC), and APAC (Figure 2). The APAC provides primary amines that can be used to functionalize the nanoparticles with targeting groups and fluorophores.[17,18] Two sensor systems for ratiometric measurements were synthesized and investigated: (1) using two pH-sensitive fluorophores: FS with a pK_a of ∼6.4 and OG with a pK_a of ∼4.8 and RhB as reference fluorophore with no/low pH sensitivity; (2) using FS and OG as pH-sensitive fluorophores but with RhX as the pH-insensitive reference fluorophore. A combination of two pH-sensitive fluorophores is used to expand the measurement range of the sensor as we previously described,[17,18] and is highly important for conducting reliable cellular measurements in the endosome−lysosome pathway. The structures of fluorophores used are shown in Figure 2. The NPs were conjugated with isothiocyanate-functionalized derivatives of the pH-sensitive fluorophores OG and FS and the pH-insensitive fluorophore RhB, which in reaction with amines on the NPs gives a stable thiourea conjugation of the

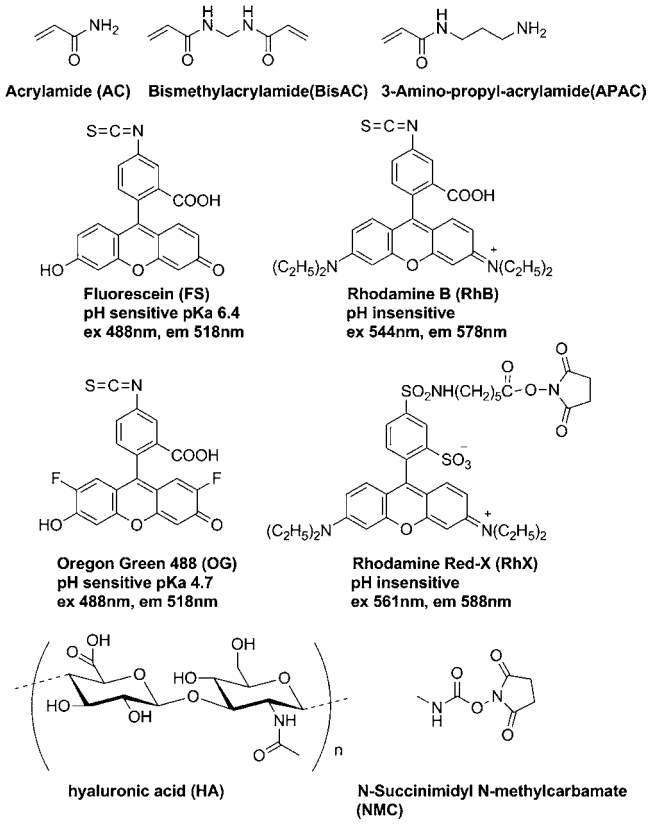

Figure 2. Chemical structure of the monomers used for hydrogel synthesis, fluorophores, HA, and the capping agent NMC used to remove the excess free amines in the pH nanosensors after functionalization and thereby control the surface charge.

The NP sensors were hereafter surface-modified as illustrated in Scheme 1. The nanosensors NP-OG-FS-RhB and NP-OG-FS-RhX were coated by HA using either physical adsorption (P) or chemical conjugation (C). The physical adsorption is achieved through electrostatic interaction of negatively charged HA and the positively charged nanosensors. Chemical conjugation of the HA was carried out using EDC and NHS forming stable amide bonds. First, HA in 5 different sizes (molecular weight of 6.4, 12, 26, 66, 1000 kDa) was physically adsorbed to NP-OG-FS-RhB to give NP-OG-FS-RhB-HA(P). NP-OG-FS-RhB had a zeta potential of +18 mV, which changed to −4.1, −2.4, and −4.2 mV after coating with 6.4, 12 and, 26 kDa HA by physical adsorption (Figure 3). The change

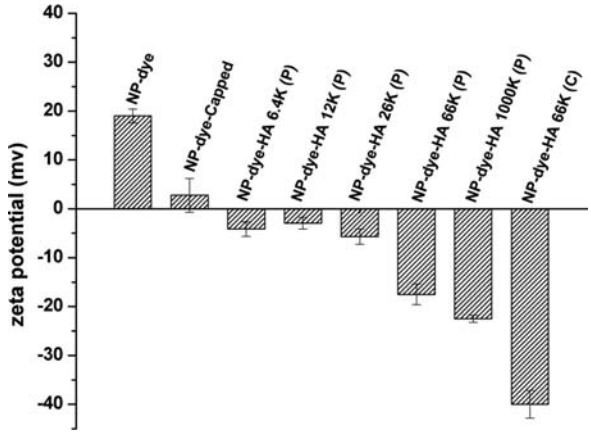

Figure 3. Zeta potential of surface-modified nanosensors before (NP-dye) and after HA physical adsorption, with amine capping using NMC, and after HA chemical conjugation. The sensor dyes were OG, FS, and RhB.

fluorophores. A succinimidyl derivative of RhX was used to conjugate RhX to the NPs resulting in amide bond formation.

in zeta potential after HA coating showed that HA was successfully adsorbed to the NPs. The coated NP-OG-FS-RhB-

Scheme 1. Synthetic Procedure of NP-OG-FS-RhB(or RhX)-HA (P) and NP-OG-FS-RhB(or RhX-HA(C)[a]

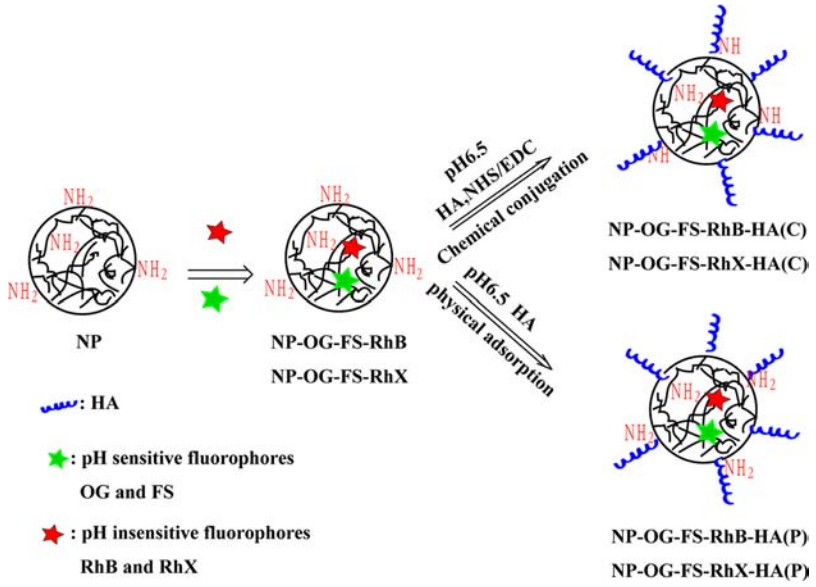

[a]FS and OG were used as pH-sensitive fluorophores, RhB or RhX as references. For the physical adsorption, the HA was coated on the particles surface via electrostatic interaction. For the chemical conjugation, the HA was coated on the particles surface by using NHS and EDC. The coating processes were carried out at pH 6.5.

dx.doi.org/10.1021/bc300349n | Bioconjugate Chem. 2012, 23, 2247−2255

HA(P) was subjected to dialysis for 7 days against water, which did not change the zeta potentials significantly, showing that the physical coating is relatively stable in a simple environment (water) where there are no competitive binding events, even though the electrostatic interaction is relatively small for the shorter polymers. When higher-molecular-weight HA of 66 kDa or 1000 kDa was employed, a significantly lower zeta potential of −18 mV and −22 mV, respectively, was obtained. Thus, the surface charge of NP-OG-FS-RhB-HA(P) is HA molecular-weight-dependent.

The HA coating did not result in any significant size change of the particles for the small HAs of 6.4, 12, and 26 kDa, while 66 kDa and 1000 kDa HA resulted in a particle size increase from 65 nm before coating to 79 nm, and 121 nm, respectively, after coating. The larger size after coating of the longer HA can potentially be an effect of HA stretching from the NP surface. The dramatic size increase (121 nm) using HA 1000 kDa is supposed to arise from two possibilities which contribute either alone or together. One is that the HA (1000 kDa) chain is partially coated on particles and partially stretched out from the particle surface. The other possibility is that the long HA (1000 kDa) chain may associate with more than one nanoparticle and cause a low degree of aggregation.

On the basis of the knowledge obtained from the physical coating of polyacrylamide NP, HA 66 kDa was chosen for the study of chemical conjugation with NP-OG-FS-RhB. This choice was based on the fact that physical adsorption of HA 66 kDa to the nanosensor increased its size by 13 to 79 nm, which was considered to be within the desired nanosensor size range 50−100 nm that is typically effectively internalized by cells. The adsorption also resulted in a relatively low zeta potential of −18 mV, indicating a substantial degree of coating of the HA polymer. HA was chemically conjugated to NP-OG-FS-RhB with a water solution of EDC in combination with NHS to give NP-OG-FS-RhB-HA66K(C), where the HA was conjugated to the NPs through amide bonds. The sizes of the resulting coated particles are shown in Figure 4. Three different NHS/EDC concentrations (1 mg/mL NHS and 3 mg/mL EDC; 0.06 mg/mL NHS and 0.18 mg/mL EDC; 0.02 mg/mL NHS and 0.06 mg/mL EDC) were used to investigate the effect of NHS/EDC concentrations on the HA coating. The lowest NHS/EDC concentration (0.02 mg/mL NHS/0.06 mg/mL EDC) resulted in a zeta potential and dynamic diameter of NP-OG-FS-RhB-HA66K(C) of −18 mV and 75 nm, respectively, which was very similar to that of NP-OG-FS-RhB-HA66K(P). When a higher NHS/EDC concentration (0.06 mg/mL NHS/0.18 mg/mL EDC) was used, the zeta potential of the resulting particles NP-OG-FS-RhB-HA66K(C) was −40 mV, and the size 92 nm; thus, in this case a clear change was observed as a result of the coupling reagent. Increasing the NHS/EDC concentration further (to 1 mg/mL NHS and 3 mg/mL EDC) did not substantially change the zeta potential and size (−44 mV, and 96 nm, respectively) any further, although a small change could be seen. The fact that the HA chemically coated NPs results in larger size and zeta-potential compared to physical adorption (when sufficient coupling reagent is used) indicates that the chemical conjugation leads to a more dense HA coating on the NP surface. This may drive HA to stretch out from the surface and thereby give a larger diameter measured by DLS.

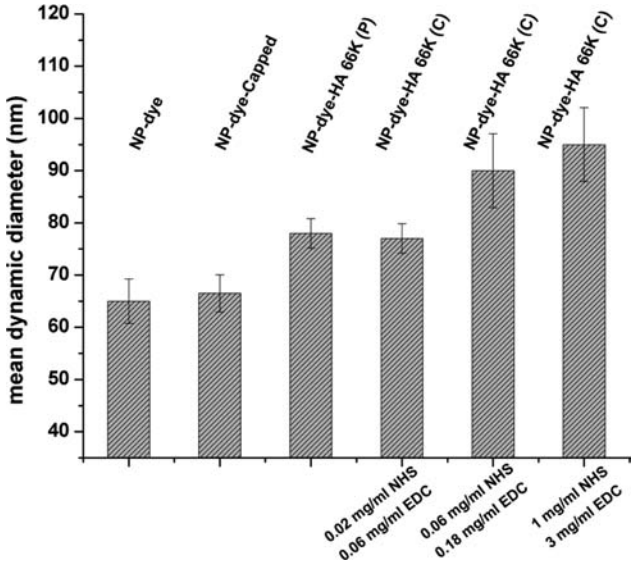

Figure 4. Hydrodynamic diameter of NP-OG-FS-RhB, NP-OG-FS-RhB-HA66K(P), and HA covalently coated sensor NP-OG-FS-RhB-HA66K (C) using chemical conjugation with three different concentrations of coupling reagent (NHS/EDC). The hydrodynamic diameter of NP was measured by dynamic light scatting.

Förster resonance energy transfer (FRET) may occur between OG/FS and RhB and a high fluorophore concentration in the nanoparticle sensor may furthermore result in self-quenching. We have in previous work focused our attention on the pH-sensitive fluorophores;[17,18] however, the pH-insensitive fluorophore also affects sensor properties. Parallel to investigating RhB-based pH nanosensors, we therefore investigated RhX as an alternative reference fluorophore. RhX has a higher $\lambda_{\text{max excitation}}$ ~571 nm than RhB $\lambda_{\text{max excitation}}$ ~ 543 nm, which potentially lowers possible FRET effects. The short linker in RhX (Figure 1) has furthermore been found to lower fluorophore quenching in some cases. Figure 5 shows the fluorescence spectra of RhB and RhX based pH sensors at different pH values. It shows that the fluorescence intensity of OG and FS increases with pH values, whereas the fluorescence intensities of RhB and RhX are relatively constant in the investigated pH interval. Even though the HA coating of the nanoparticles changed their charge from positive to negative, no changes in the pH measurement range and apparent fluorophore pK_a values were observed (Figure 6). This is consistent with our previously published results showing that incorporation of negative charge components in the particle does not seem to alter the pK_a of pH nanosensors for this polyacrylamide system.[20]

When RhB was used as reference fluorophore, both sensors NP-OG-FS-RhB-HA66K(P) and NP-OG-FA-RhB-HA66K(C) have the same measurement pH range from pH 3.9 to pH 7.3 (Figure 6), but the substitution of RhB with RhX giving the new sensors NP-OG-FS-RhX-HA66K(P) and NP-OG-FA-RhX-HA66K(C) resulted in a measurement range from pH 4.0 to pH 7.6. The reason for this small shift in measurement range and expansion of RhX-sensors compared to RhB-sensors is not clear. It is likely that a small decrease in FRET transfer between OG/FS and RhX relatively to RhB may be contributing to this effect. In addition, the short linker in RhX may also change the fluorophore local environment slightly relative to the RhB that is attached directly through an isothiocynate-based conjugation to the nanoparticle amines.

The nanosensors NP-OG-FS-RhB and NP-OG-FS-RhX have a positive surface potential due to the presence of primary amines on the nanoparticle surface, which are used to physically

dx.doi.org/10.1021/bc300349n | Bioconjugate Chem. 2012, 23, 2247−2255

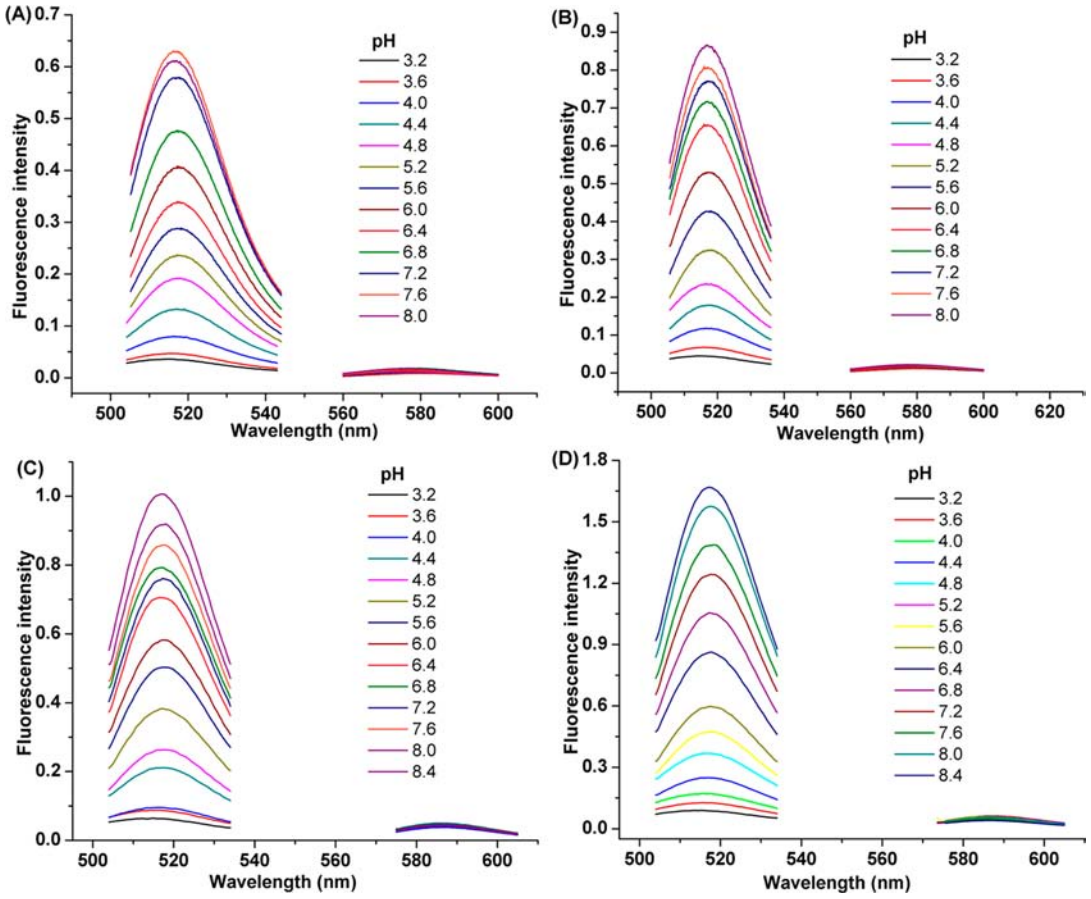

Figure 5. Fluorescence spectra of pH nanosensors at different pH values: (A) NP-OG-FS-RhB-HA(P), (B) NP-OG-FS-RhB-HA(C), (C) NP-OG-FS-RhX-HA(P), and (D) NP-OG-FS-RhX-HA(C). OG and FS were excited at 488 nm; RhB and RhX were excited at 543 and 561 nm, respectively.

adsorb or chemically conjugate the HA to the nanoparticle. Positively charged particles are internalized to a large extent by cells in vitro due to electrostatic attraction to the negatively charged cell membrane. Therefore, to have reference nanoparticle sensors that are expected to have weak interactions with cells, the amine groups of NP-OG-FS-RhB and NP-OG-FS-RhX were capped by NMC (Figure 1) resulting in NP-OG-FS-RhB-capped NP-OG-FS-RhX-capped with a zeta potential close to zero (Table 1).

To investigate the cellular uptake by the HA receptor CD44 overexperessed on some tumor cells, HeLa cells and MCF-7 cells were selected as a CD44-positive and negative cell line, respectively. Cell uptake experiments of NP-OG-FS-RhB, NP-OG-FS-RhB-capped, NP-OG-FS-RhB-HA(P), and NP-OG-FS-RhB-HA(C) are shown in Figure 7a. The results show that both NP-OG-FS-RhB-HA66K(P) and NP-OG-FS-RhB-HA66K(C) was taken up by the CD44-positive HeLa cells, whereas the NP-OG-FS-RhB-capped nanosensor did not show cellular uptake. Furthermore, only a few MCF-7 cells internalized the HA nanosensors, and again, no uptake of the capped nanosensor was observed. Similar results were obtained with the RhX-based nanosensors. The results highlight the important role of CD44 in the uptake processes. As a "positive" control, both cell lines were exposed to positively charged nanosensors bearing primary amines (NP-OG-FS-RhB), and significant cellular uptake of this nanoparticle was observed in both cell lines. Next, pH measurements were performed in CD44-positive HeLa cells with sensors having HA physically adsorbed and chemically conjugated. These sensors were furthermore compared with positively charged sensors that are expected to have a different internalization mechanism (Figure 7b). No difference in the pH profile was observed for the HA-coated nanosensors compared with positively charged nanosensors. As a reference measurement, the V-ATPase inhibitor bafilomycin A1 was added to HeLa cells with internalized positive nanosensors, and a significant increase in pH was measured as expected. Lastly, we investigated if there is any noticeable difference in the kinetic pH profile that a positively charged nanoparticle experiences after cellular internalization in comparison to a HA-coated nanoparticle that is internalized by the CD44 receptor. Figure 7c shows that no significant difference was found and that the internalization and intracellular trafficking is relatively fast for all the tested nanoparticle sensors, as they reach the lysosomes within 2 h.

■ DISCUSSION

We have successfully synthesized HA-coated polyacrylamide pH nanosensors, which were triple fluorophore labeled to ensure reliable measurements of pH in the endosome–lysosome pathway, as pH-sensitive fluorophores OG and FS were used to expand the pH measurement range and two pH-insensitive fluorophores were investigated (RhB and RhX). The sensors using RhB or RhX as reference fluorophores have the capability of measuring pH changes from pH 3.9 to 7.3 and pH 4.0 to 7.6, respectively. We investigated several HA polymer sizes and both physical adsorption and chemical conjugation of HA. The HA coatings of nanosensors that were employed proved to be stable in aqueous solution. The density of

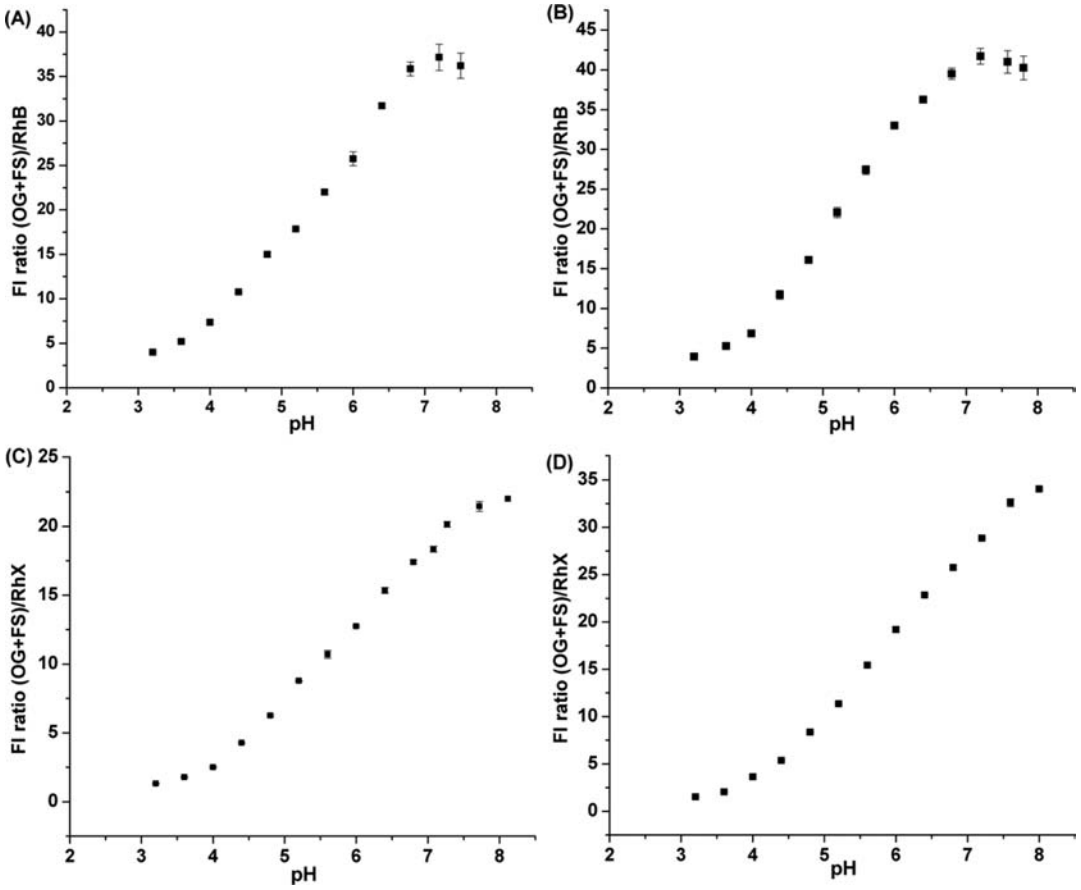

Figure 6. Fluorescence intensity ratio (OG+FS)/RhB vs pH of nanosensors: (A) NP-OG-FS-RhB-HA(P), (B) NP-OG-FS-RhB-HA(C), (C) NP-OG-FS-RhX-HA(P), and (D) NP-OG-FS-RhX-HA(C). OG and FS were excited at 488 nm; RhB and RhX were excited at 543 and 561 nm, respectively.

Table 1. Structure, Size, and Zeta Potential of the pH Nanosensors Used for Cellular Experiments[a]

	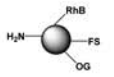		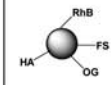	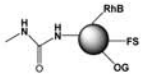	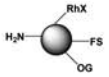	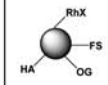		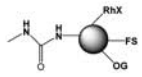
Name	NP-OG-FS-RhB	NP-OG-FS-RhB-HA(P)	NP-OG-FS-RhB-HA(C)	NP-OG-FS-RhB-Capped	NP-OG-FS-RhX	NP-OG-FS-RhX-HA(P)	NP-OG-FS-RhX-HA(C)	NP-OG-FS-RhX-Capped
ξ (mV)	18.0±1.4	-17.8±1.4	-44.0±1.3	6.1±0.5	16.8±1.3	-20.1±1.6	-42.0±3.3	0.3±0.03
Size (nm)	67±22	79±28	92±24	67±22	71±25	71±32	109±41	71±25

[a]All the particles containing HA are with 66 kDa HA.

chemically conjugated HA on the nanoparticle surface was higher than for physically adsorbed HA. Both HA-coated sensors NP-OG-FS-RhB-HA(P) and NP-OG-FS-RhB-HA(C) specifically bind to CD44 receptors on HeLa cells after which they are internalized through enodcytosis. MCF-7 cells that have limited CD44 receptor expression do not internalize HA-functionalized sensors. The pH measurement of HA nanosensors showed the same pH profile and similar transport kinetics through the endosomes and lysosomes as measured by the encountered pH profile in the cells. This indicates that there could be a similar endocytosis pattern for HA-coated nanoparticles that are internalized by receptor-mediated endocytosis (CD44) and positively charged nanoparticles that are considered to be internalized by a nonspecific mechanism or through multiple internalization pathways. One hyptothesis is therefore that nanoparticles above a certain size may dictate transport to lysosomes irrespective of the surface chemistry and targeting ligands responsible for initial cellular interactions. In this regard, a recent report has argued that there are differences in the internalization mechanism of HA-coated and positively

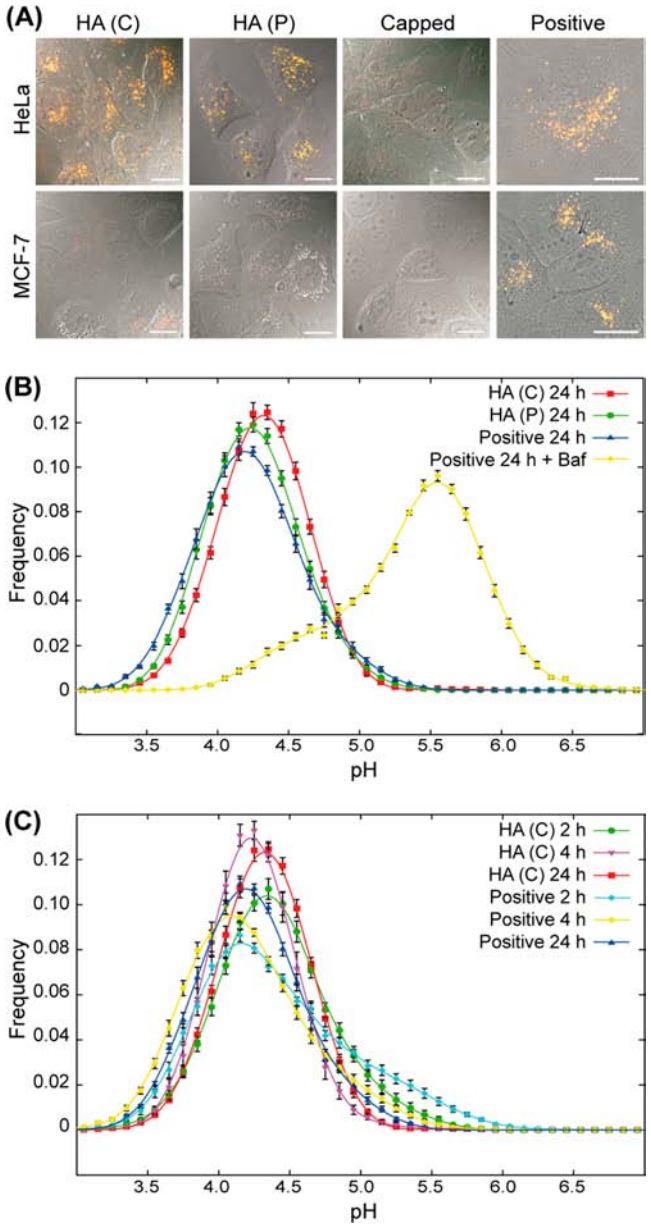

Figure 7. (A) Uptake of HA-conjugated nanosensors by CD44-positive HeLa cells and CD44-negative MCF-7 cells. Cells were treated with 10 μg/mL of the indicated nanosensors for 20 h. Images show overlay of red and green fluorescence with a DIC image for cells exposed to NP-OG-FS-RhB-HA66K(C) (HA(C)), NP-OG-FS-RhB-HA66K(P) (HA(P)), the positively charged NP-OG-FS-RhB (positive), and the capped nanosensors NP-OG-FS-RhB-capped (capped). Scale bars, 15 μm. (B,C) Histograms of pH measured in HeLa cells with the indicated nanosensors at indicated time points. Mean ± SEM (n = 7–10). Less than 0.2% of measurements fall outside the pH range 3–7.

charged particles;[26] however, the trafficking after cellular internalization was not documented. Thus, more studies are warranted to further clarify nanoparticle transport inside cells. Our abilities to design nanosensors are just starting to make it possible for us to conduct measurements that elucidate nanoparticle cellular trafficking, and we envisage that, e.g., pH nanosensors will become important tools in the development of new nanomedicines where pH-sensitive drug delivery systems have been heavily investigated in recent years.

AUTHOR INFORMATION

Corresponding Author

*Phone: +45 45258168, Fax: +45 45887762, E-mail: Thomas.andresen@nanotech.dtu.dk.

Notes

The authors declare no competing financial interest.

ACKNOWLEDGMENTS

The authors thank Kræftens Bekæmpelse and the Danish Research Council for Technology and Production (Grant 274-07-0172) for financial support. The authors declare no competing financial interests.

REFERENCES

(1) Andresen, T. L., Thompson, D. H., and Kaasgaard, T. (2010) Enzyme-triggered nanomedicine: Drug release strategies in cancer therapy. *Mol. Membr. Biol. 27*, 353–363.

(2) Rajendran, L., Knölker, H. J., and Simons, K. (2009) Subcellular targeting strategies for drug design and delivery. *Nat. Rev. 9*, 29–42.

(3) Kaasgaard, K., and Andresen, T. L. (2010) Liposomal cancer therapy: Exploiting tumor characteristics. *Exp. Opin. Drug Delivery 7*, 225–243.

(4) Andresen, T. L., Jensen, S. S., and Jørgensen, K. (2005) Advanced strategies in liposomal cancer therapy: Problems and prospects of active and tumor specific drug release. *Prog. Lipid Res. 44*, 68–97.

(5) Lee, E. S., Gao, Z. G., and Bae, Y. H. (2008) Recent progress in tumor pH targeting nanotechnology. *J. Controlled Release 132*, 164–170.

(6) Bertin, P. A., Smith, D. D., and Nguyen, S. T. (2005) High-density doxorubicin-conjugated polymeric nanoparticles via ring-opening metathesis polymerization. *Chem. Commun. 30*, 3793–3795.

(7) Griset, A. P., Walpole, J., Liu, R., Gaffey, A., Colson, Y. L., and Grinstaff, M. W. (2009) Expansile nanoparticles: synthesis, characterization, and in vivo efficacy of an acid-responsive polymeric drug delivery system. *J. Am. Chem. Soc. 131*, 2469–2471.

(8) Sabharanjak, S, and Mayor, S. (2004) Folate receptor endocytosis and trafficking. *Adv. Drug Delivery Rev. 56*, 1099–1109.

(9) Leamon, C. P., and Low, P. S. (1991) Delivery of macromolecules into living cells: a method that exploits folate receptor endocytosis. *Proc. Natl. Acad. Sci. U.S.A. 88*, 5572–5576.

(10) Lee, H., Lee, K., and Park, T. G. (2008) Hyaluronic acid-paclitaxel conjugate micelles: synthesis, characterization, and antitumor activity. *Bioconjugate Chem. 19*, 1319–1325.

(11) Fuchs, S. M., and Raines, R. T. (2004) Pathway for polyarginine entry into mammalian cells. *Biochemistry 43*, 2438–2444.

(12) Petersen, A. L., Binderup, T., Jølck, R. I., Rasmussen, P., Henriksen, J. R., Pfeifer, A. K., Kjær, A., and Andresen, T. L. (2012) Positron emission tomography evaluation of somatostatin receptor targeted (64)Cu-TATE-liposomes in a human neuroendocrine carcinoma mouse model. *J. Controlled Release 160*, 254–263.

(13) Chen, X. Y., Plasencia, C., Hou, Y. P., and Neamati, N. (2005) Synthesis and biological evaluation of dimeric RGD peptide-paclitaxel conjugate as a model for integrin-targeted drug delivery. *J. Med. Chem. 48*, 1098–1106.

(14) Bachar, G., Cohen, K., Hod, R., Feinmesser, R., Mizrachi, A., Shpitzer, T., Katz, O., and Peer, D. (2011) Hyaluronan-grafted particle clusters loaded with Mitomycin C as selective nanovectors for primary head and neck cancers. *Biomaterials 32*, 4840–4848.

(15) ElBayoumi, T. A., and Torchilin, V. P. (2009) Tumor-targeted nanomedicines: enhanced antitumor efficacy in vivo of doxorubicin-loaded, long-circulating liposomes modified with cancer-specific monoclonal antibody. *Clin. Cancer Res. 15*, 1973–1980.

(16) Kreft, O., Javier, A. M., Sukhorukov, G. B., and Parak, W. G. (2007) Polymer microcapsules as mobile local pH-sensors. *J. Mater. Chem. 17*, 4471–4476.

(17) Benjaminsen, R. V., Sun, H. H., Henriksen, J. R., Christensen, N. M., Almdal, K., and Andresen, T. L. (2011) Evaluating nanoparticle

sensor design for intracellular pH measurements. *ACS Nano 5*, 5864−5873.
(18) Sun, H. H., Almdal, K., and Andresen, T. L. (2011) Expanding the dynamic measurement range for polymeric nanoparticle pH sensors. *Chem. Commun. 47*, 5268−5270.
(19) Sun, H. H, Scharff-Poulsen, A. M., Gu, H., and Almdal, K. (2006) Synthesis and characterization of ratiometric pH sensing nanoparticles with covalently attached fluorescent dyes. *Chem. Mater. 18*, 3381−3384.
(20) Sun, H. H., Andresen, T. L., Benjaminsen, R. V., and Almdal, K. (2009) Polymeric nanosensors for measuring the full dynamic pH range of endosomes and lysosomes in mammalian cells. *J. Biomed. Nanotechnol. 5*, 1−7.
(21) Kumar, E. K. P., Almdal, K., and Andresen, T. L. (2012) Synthesis and characterization of ratiometric nanosensors for pH quantification: A mixed micelle approach. *Chem. Commun. 48*, 4776−4778.
(22) Buck, S. M., Xu, H., Brasuel, M, Philbert, M. A., and Kopelman, R. (2004) Nanoscale probes encapsulated by biologically localized embedding (PEBBLEs) for ion sensing and imaging in live cells. *Talanta 63*, 41−59.
(23) Cerroni, B., Chiessi, E., Margheritelli, S., Oddo, L., and Paradossi, G. (2011) Polymer shelled microparticles for a targeted doxorubicin delivery in cancer therapy. *Biomacromolecules 12*, 593−601.
(24) Barbault, F. S., Grefa, R., Russoa, P., Guechotb, J., and Bochota, A. (2002) Design of poly-ε-caprolactone nanospheres coated with bioadhesive hyaluronic acid for ocular delivery. *J. Controlled Release 83*, 365−375.
(25) Lunov, O., Syrovets, T., Loos, C., Beil, J., Delacher, M., Tron, K., Nienhaus, G. U., Musyanovych, A., Mailänder, V., Landfester, K., and Simmet, T. (2011) Differential uptake of functionalized polystyrene nanoparticles by human macrophages and a monocytic cell line. *ACS Nano 5*, 1657−1669.
(26) Hsu, S.-H., Ho, T.-T., and Tseng, T.-C. (2012) Nanoparticle uptake and gene transfer efficiency for MSCs on chitosan and chitosan-hyaluronan substrates. *Biomaterials 33*, 3639−3650.
(27) Richert, L., Boulmedais, F., Lavalle, P., Mutterer, J., Ferreux, E., Decher, Gero., Schaaf, P., Voegel, J. C., and Picart, C. (2004) Improvement of stability and cell adhesion properties of polyelectrolyte multilayer films by chemical cross-linking. *Biomacromolecules 5*, 284−294.

Bioconjugate Chemistry

Article

pubs.acs.org/bc

Development of a Simple Method for Protein Conjugation by Copper-Free Click Reaction and Its Application to Antibody-Free Western Blot Analysis

Sohye Jang,[†] Kalme Sachin,[‡] Hui-jeong Lee,[†] Dong Wook Kim,*[,‡] and Hyun Soo Lee*[,†]

[†]Department of Chemistry, Sogang University, Mapo-gu, Seoul 121-742, Republic of Korea

[‡]Department of Nuclear Medicine, Cyclotron Research Center, Research Institute of Clinical Medicine, Chonbuk National University Medical School, Jeonju, Jeonbuk 561-712, Republic of Korea

Supporting Information

ABSTRACT: There are currently many methods available for labeling proteins in order to study their structure and function. However, the utility of these methods is hampered by low efficiency, slow reaction rates, nonbiocompatible reaction conditions, large-sized labeling groups, and the requirement of specific side chains such as cysteine or lysine. In this study, a simple and efficient method for protein labeling was developed, in which an azide-containing amino acid was introduced into a protein and conjugated to a labeling reagent by strain-promoted azide−alkyne cycloaddition (SPAAC). This method allowed us to label proteins by simply mixing a protein and a labeling reagent in physiological conditions with a labeling yield of approximately 80% in 120 min. In addition, the specificity of SPAAC made it possible to analyze the expression level of a protein quantitatively by simple mixing and SDS-PAGE analysis with no need for antibodies or multistep incubations. Because the genetic incorporation of the azide-containing amino acid can be generally applied to any protein and the SPAAC reaction is highly specific, this method should prove useful for labeling and analyzing proteins.

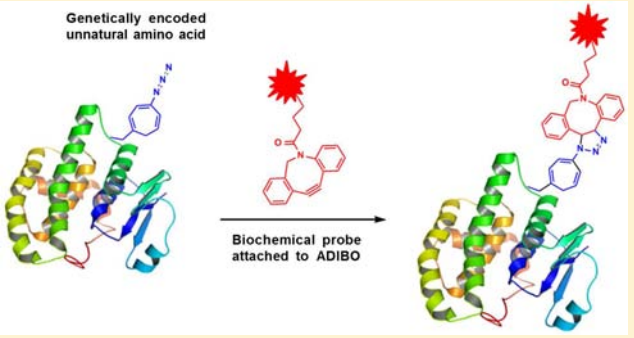

INTRODUCTION

A number of chemical tools have been developed labeling proteins with biochemical probes in order to study protein structure and function. One such method is the chemical modification of proteins in which a biochemical probe is covalently attached to cysteines or lysines by alkylation or amide bond formation reactions.[1,2] Although chemical modification is useful and has been applied to many different proteins and probes, it is dependent on the reactivity of specific amino acid side chains, and therefore, the intrinsic selectivity and the overall efficiency of this approach is limited. Alternative methods include labeling proteins with peptide/protein tags such as fluorescent proteins,[3] SNAP-tag,[4] HaloTag,[5] and tetracysteine.[6] Although these tagging methods are particularly useful for in vivo applications, most of these tags can perturb the structure and function of proteins because of their large size. Moreover, the restriction of tag locations to proteins' N- or C-terminals also limits their application.

In order to overcome these limitations, unnatural amino acids with bio-orthogonal reactivity have been incorporated into proteins by using a recently developed genetic incorporation method.[7−9] The major advantage of this method is that it allows for site-specific conjugation of proteins with a biochemical probe. In addition, the method is technically simple and applicable to any protein. The bio-orthogonal functional groups incorporated into proteins by the genetic method include ketones,[10] azides,[11,12] alkynes,[13] alkenes,[14] aryl halides,[15] and aryl boronates.[16] Although site-specific incorporation of these functional groups into proteins is quite useful, the method's applicability is limited by harsh reaction conditions and the slow reaction rate of conjugation reactions. Imine formation by ketones and alkoxyamines requires acidic conditions (pH 4−5),[17] and the click reaction involving azides and alkynes requires biologically incompatible copper(I) catalysts.[18] Recently, copper-free click reactions with cyclooctyne,[19] cyanobenzothiazole condensation with 1,2-aminothiol,[20] and tetrazine-based cycloaddition to norbornene-containing proteins[21] have introduced significant improvements, but continue to have limitations such as low conjugation yields, slow reaction rates, the necessity of an extra step and challenges in the synthesis of labeling compounds. There is, therefore, a need for improved methods for efficiently labeling proteins by simply mixing the protein of interest with a labeling reagent under physiologically friendly conditions. Here, we

Received: July 4, 2012
Revised: September 24, 2012
Published: October 5, 2012

 © 2012 American Chemical Society

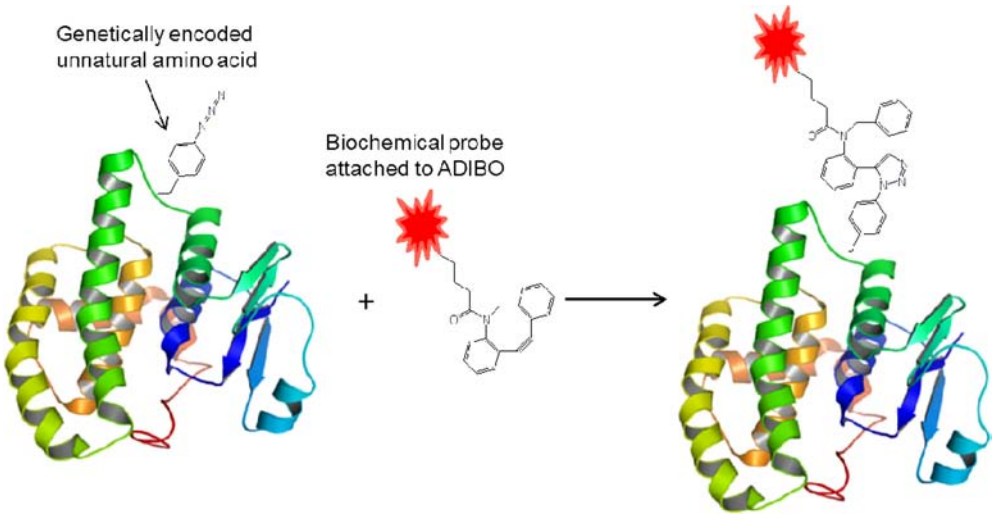

Figure 1. Protein conjugation with a genetically encoded azide-containing protein. An azide-containing amino acid is genetically incorporated into a protein and the azido group reacts with a conjugation reagent containing dibenzocyclooctyne.

have developed a simple and efficient method of introducing a biochemical probe into proteins by strain-promoted azide-akyne cycloaddition (SPAAC) with a genetically encoded azide-containing amino acid.

EXPERIMENTAL PROCEDURES

General. All chemicals and DNA oligomers were obtained from commercial sources and used without further purification. Fluorescence images for SDS-PAGE analysis were obtained using the Typhoon 9210 variable mode imager.

Synthesis of Cy5.5-Linked Aza-dibenzocyclooctyne (Cy5.5-ADIBO). Diisopropylethylamine (0.45 mg, 3.6 μmol) was added to a mix of aza-dibenzocyclooctynyl amine derivative[22,23] (ADIBO-NH_2, 4.0 mg, 13.8 μmol) and Cy5.5 NHS-ester (2.0 mg, 1.8 μmol) in anhydrous DMF (300 μL), and the reaction mixture was stirred at room temperature for 1 h. The crude product was purified by RP-HPLC (C_{18} silica gel, 10 μm, 10 × 250 mm; 10 mM aqueous NH_4HCO_3/acetonitrile = 70:30 (v/v); 254 nm; 2 mL/min) to obtain Cy5.5-ADIBO (2.0 mg, 93%). The Cy5.5-ADIBO product was confirmed by MALDI-TOF-MS: m/z 1211.08 for [M-3Na] ($C_{62}H_{59}N_4O_{14}S_4$ calculated molecular weight [MW] 1211.29). Retention time = 16.4 min.

Expression and Purification of the Mutant GST Containing AZF. A wild-type GST gene was amplified from a commercial vector containing the gene and inserted between the NcoI and *Kpn*I sites of pBAD/Myc-His (Invitrogen) to generate pBAD-GST. Site-directed mutagenesis was used to introduce an amber mutation (F47TAG) into the GST gene. The plasmid containing the amber mutation (pBAD-GST-F47TAG) was cotransformed with pEvol-AZF[24] into *E. coli* DH10B. Cells were amplified in lysogeny broth (LB) supplemented with ampicillin (100 μg/mL) and chloramphenicol (35 μg/mL). Starter culture (2.5 mL) was used to inoculate 100 mL LB supplemented with ampicillin (100 μg/mL), chloramphenicol (35 μg/mL), and 1 mM AZF at 37 °C; and the expression was induced at OD 0.8 (550 nm) by adding L-arabinose (0.2%, final concentration). Cells were grown at 37 °C overnight, harvested by centrifugation, and frozen at −80 °C. Glutathione resin purification was performed according to the manufacturer's protocol (Clontech Laboratories, Inc.). Protein concentrations were calculated by measuring absorbance at 280 nm and by using calculated extinction coefficients (4.3×10^4 cm^{-1} M^{-1}) (http://www.biomol.net/en/tools/proteinextinction.htm).

Conjugation Reactions with Purified GST. The conjugation reaction was performed in 10 mM phosphate buffer (pH 7.0) containing 100 mM NaCl by adding the GST mutant (GST-F47AZF) (20 μM, final concentration) and Cy5.5-ADIBO (200 μM, final concentration) at room temperature. The reaction was quenched by adding excess AZF and the mixture was directly analyzed by SDS-PAGE. Fluorescence images were taken using the Typhoon 9210 variable mode imager and the gel was stained with Coomassie Brilliant Blue R-250.

Conjugation Reactions with Crude Cell Extract. Cells from GST-F47AZF-expressing bacterial cell cultures (50 mL) were harvested by centrifugation and frozen at −80 °C. The frozen cell pellets were thawed on ice, resuspended in 10 mM phosphate buffer (pH 7.0, 5 mL) containing 100 mM NaCl, and sonicated. Alternatively, the thawed cells were resuspended in BugBuster (Novagen) containing 10 mM phosphate buffer (pH 7.0), 100 mM NaCl, and benzonase (125 U/ml) (cat. No. 70746−3, Novagen) and incubated for 30 min at room temperature. Removal of cell debris by centrifugation (12 000 rpm) afforded crude cell extracts. The conjugation reaction was performed by adding Cy5.5-ADIBO (200 μM, final concentration) to the cell extract (10 μL) and incubating the reaction mixture for 1 h at 37 °C. The reaction was quenched by adding excess AZF and the mixture was directly analyzed by SDS-PAGE.

Conjugation Reactions for Analysis of Protein Expression Levels (Antibody-Free Western Blot Analysis). Cells were grown using the method described above, with different concentrations of L-arabinose. For lysate preparation, conjugation reactions, and SDS-PAGE analysis, the same methods described in the previous section were used.

RESULTS AND DISCUSSION

Strain-Promoted Azide−Alkyne Cycloaddition (SPAAC). It has been well-known that SPAAC with dibenzocyclooctyne derivatives is ideal for bioconjugation since it requires no additional reagent and has a high rate constant (0.1−1.0 M^{-1} s^{-1}).[25−28] Because of these advantages,

dx.doi.org/10.1021/bc300364z | *Bioconjugate Chem.* 2012, 23, 2256−2261

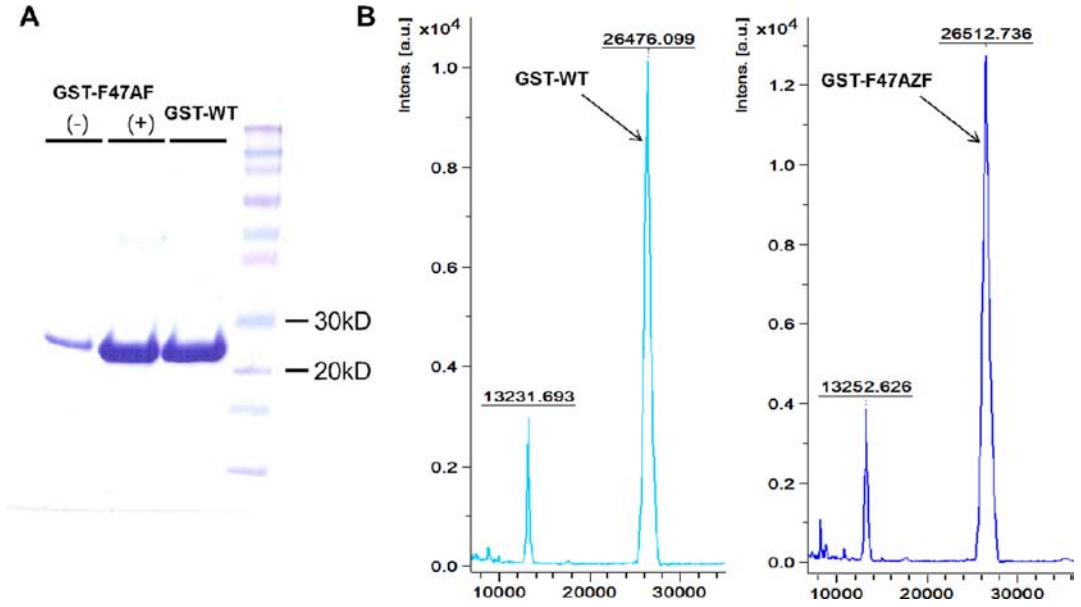

Figure 2. Expression of GST with an amber codon at position 47 (F47) in the presence of the corresponding evolved tRNA/aaRS pair. (A) SDS-PAGE analysis of the mutant GST (GST-F47AZF) and GST-WT; (B) MALDI-TOF mass analysis: expected mass difference between GST-WT (left) and GST-F47AZF (right) = 41 Da; observed mass difference = 37 Da.

SPAAC has been employed for various processes, including labeling proteins and cell surfaces.[29−36] However, in order to apply this method to protein conjugation, the counterpart, azide, must first be introduced into a protein of interest. The incorporation of the azide group into a protein can be achieved by genetic incorporation,[11,12] and it was, therefore, proposed that the application of SPAAC to genetically incorporated azide-containing amino acids would make it possible to label proteins efficiently (Figure 1).

Incorporation of AZF into GST. To introduce the azide group into proteins, *p*-azidophenylalanine (AZF) was chosen as an azide-containing amino acid and glutathione *S*-transferase (GST) as a target protein. Based on the X-ray crystal structure of GST, a solvent-exposed residue, F47, was chosen to be replaced by AZF. To incorporate the amino acid, an amber codon (TAG) was substituted for F47 by site-directed mutagenesis. The GST mutant containing AZF (GST-F47AZF) was expressed in the presence of the corresponding evolved tRNA/amino-acyl tRNA synthetase (aaRS) pair[24] and 1 mM AZF in *E. coli* strain DH10B grown in LB. Mutant and wild-type (WT) proteins were purified by glutathione affinity purification, and the yields of GST-F47AZF and GST-WT were 10−15 mg/L and 15−20 mg/L, respectively. SDS-PAGE analysis showed that a small amount of full-length protein was produced in the absence of AZF (Figure 2A) because of background incorporation. However, MALDI-TOF mass spectrometry (MS) analysis of the purified protein expressed in the presence of AZF confirmed the incorporation of AZF (Figure 2B) with no detectable incorporation of natural amino acids.

GST Conjugation by SPAAC. Next, conjugation of GST-F47AZF with a Cy5.5-linked aza-dibenzocyclooctyne derivative (Cy5.5-ADIBO) was carried out. Cy5.5-ADIBO was prepared from ADIBO-NH_2 (Scheme 1). The amide bond formation reaction with ADIBO-NH_2 and Cy5.5 *N*-hydroxysuccinimide ester (Cy5.5 NHS ester) was carried out in DMF at room temperature for 1 h, and reverse-phase HPLC purification afforded the bioorthogonal azide acceptor in 93% yield. The

Scheme 1. Preparation of Cy5.5-ADIBO as a Bioorthogonal Azide Acceptor

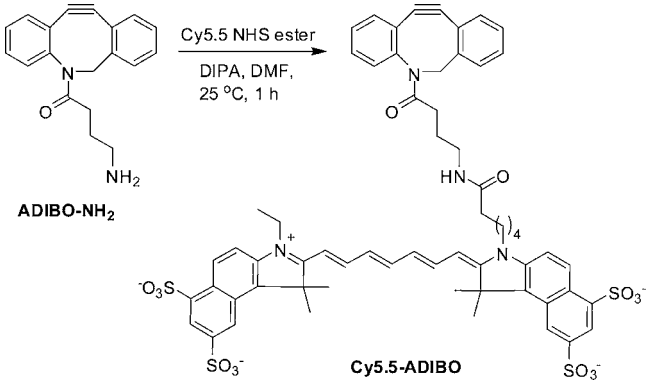

conjugation reaction was performed by adding Cy5.5-ADIBO to the mixture containing the mutant GST in 10 mM phosphate buffer (pH 7.0) and 100 mM NaCl at room temperature. The conjugation reaction was analyzed by SDS-PAGE at different reaction times (Figure 3A,B). Fluorescence images from SDS-PAGE analysis showed that Cy5.5-ADIBO was efficiently conjugated to the mutant GST. The same conjugation reaction with GST-WT showed no fluorescence in SDS-PAGE analysis, meaning that the fluorescence observed in the conjugation reaction with the GST mutant was a result of the specific conjugation of Cy5.5-ADIBO with the azido group incorporated into the target protein (Figure 3A,B). The conjugation reaction was also evaluated by MALDI-TOF MS analysis (Figure 3C). The MS analysis showed that specific conjugation occurred and that approximately 80% of the mutant GST was conjugated. These results show that the AZF-containing protein can be site-specifically conjugated within 120 min by simply mixing the mutant protein with the dibenzocyclooctyne derivative. Compared to the published method (50% labeling yield in 12 h) using cyclooctyne,[19] the reaction time is 6-fold shorter and the labeling yield is 1.6-fold

dx.doi.org/10.1021/bc300364z | *Bioconjugate Chem.* 2012, 23, 2256−2261

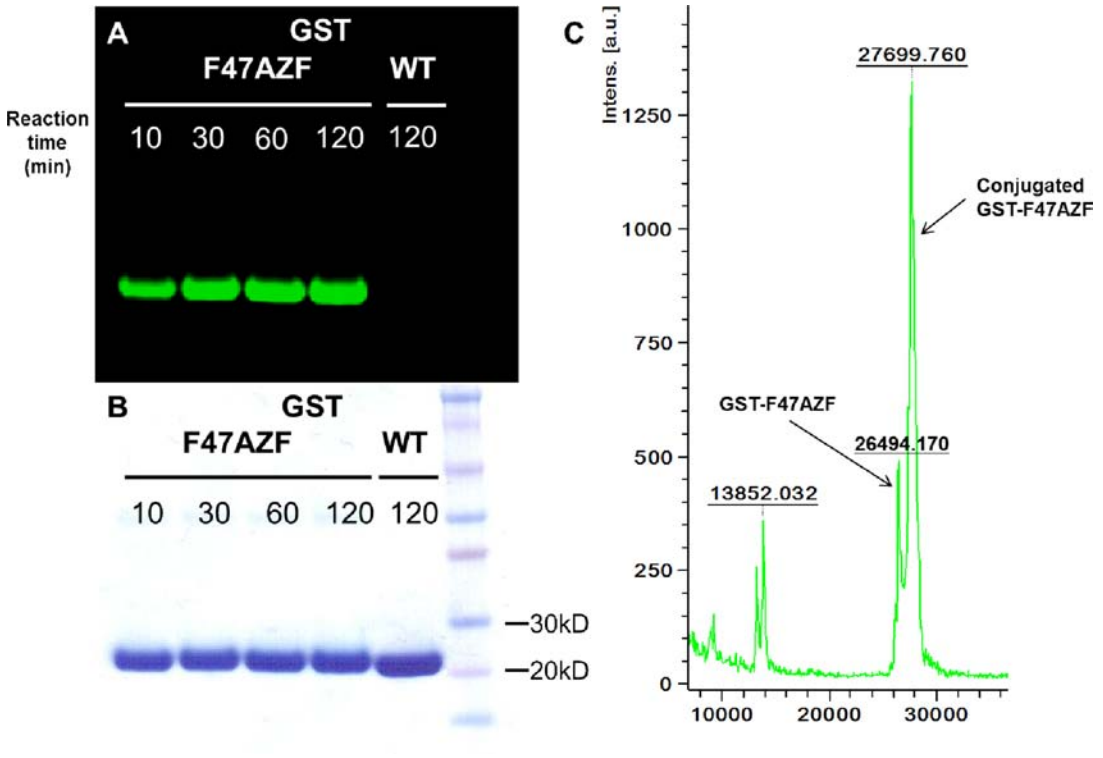

Figure 3. Labeling of GST-F47AZF with Cy5.5-ADIBO. Reaction mixtures were analyzed by SDS-PAGE at different reaction times. Reaction condition: 20 μM GST, 200 μM Cy5.5-ADIBO in 10 mM phosphate buffer (pH 7.0) containing 100 mM NaCl, 10 μL total volume, room temperature. The same reaction was performed with GST-WT and analyzed at 120 min as a control. (A) Fluorescence gel image; (B) Coomassie-stained gel image; (C) MALDI-TOF mass analysis of GST-F47AZF reacted for 120 min: expected mass difference between GST-F47AZF and the conjugated protein = 1190 Da, observed mass difference = 1206 Da.

higher. Although other methods[17,20] can result in slightly better yield, they require harsh reaction conditions or extra steps before labeling as discussed above.

Application to Antibody-Free Western Blot Analysis. The utility of this method was further demonstrated by applying the method to antibody-free Western blot analysis. Western blotting is a powerful analytical technique used to detect a specific protein. While the method provides high specificity and sensitivity, it requires an antibody specific to the protein of interest, and multiple incubation and wash steps for analysis. Therefore, a simple and antibody-free method for protein analysis combining high specificity and sensitivity would be of enormous potential and wide-ranging application. It was proposed that the SPAAC of dibenzocyclooctyne derivatives to genetically encoded AZF could be used for protein analysis, with acceptable specificity and sensitivity.

GST Conjugation with Crude Cell Lysates. To test the specificity of the SPAAC, the same conjugation reaction for purified GST-F47AZF was performed with cell lysate prepared from GST-F47AZF-expressing cells. Cy5.5-ADIBO was added to the cell lysate, and the mixture was incubated for 1 h at 37 °C, followed by SDS-PAGE analysis. The result shows that clear conjugation of the target protein occurs in the lysates from GST-F47AZF-expressing cells, while no conjugation is observed in the lysates from GST-F47AZF-expressing cells grown in the absence of AZF or in those from GST-WT-expressing cells (Figure 4). In addition, minimal background fluorescence was observed from nonspecific conjugation reactions, meaning that the SPAAC is specific to the target protein containing AZF.

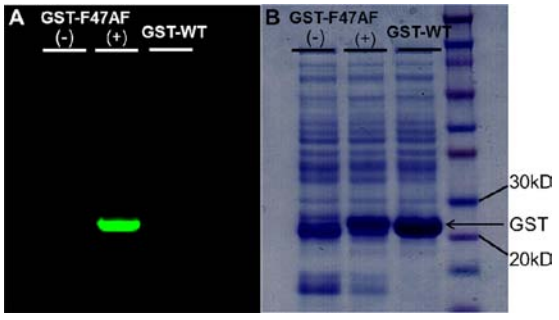

Figure 4. Labeling of GST-F47AZF in crude cell lysate with Cy5.5-ADIBO. Crude cell lysates were prepared from cells expressing GST-WT and GST-F47AZF in the presence (+) and absence (−) of 1 mM AZF. Reaction condition: 10 μL cell lysate, 200 μM Cy5.5-ADIBO in 10 mM phosphate buffer (pH 7.0) containing 100 mM NaCl, 15 μL total volume, 37 °C, 60 min. (A) Fluorescence gel image; (B) Coomassie-stained gel image.

Sensitivity and Utility of the Method. Next, the sensitivity of this method was tested. The product of the reaction between GST-F47AZF and Cy5.5-ADIBO was analyzed by serial dilution. Figure 5 shows that as little as 8–20 ng of labeled protein can be detected. To verify if this method can be used to analyze protein expression levels, GST-F47AZF expression was carried out with different concentrations of L-arabinose. Cell lysates were treated with Cy5.5-ADIBO and analyzed by SDS-PAGE. The results showed clear differences in the expression levels, corresponding to the expression levels expected based on the L-arabinose concentrations provided (Figure 6). Upon comparison, fluorescence

dx.doi.org/10.1021/bc300364z | Bioconjugate Chem. 2012, 23, 2256–2261

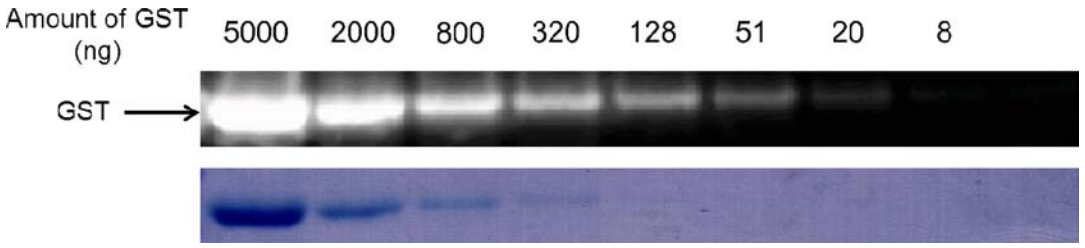

Figure 5. Comparison of gel imaging by fluorescence scanning (top) and Coumassie-staining (bottom) for the GST-Cy5.5-ADIBO conjugate. As little as 8−20 ng of the conjugated protein can be detected by fluorescence scanning.

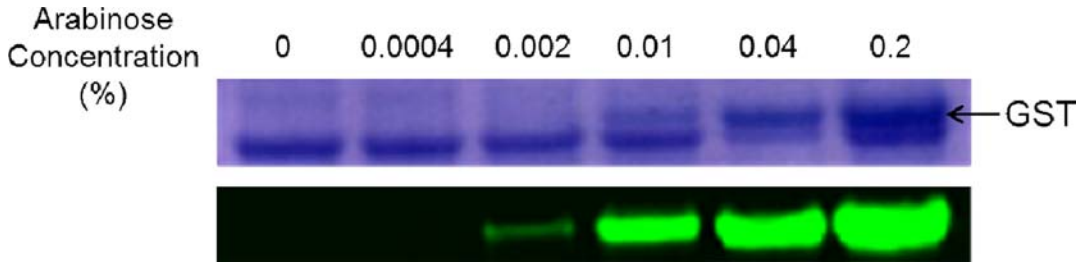

Figure 6. Analysis of protein expression levels by labeling the target protein with Cy5.5-ADIBO. GST-F47AZF is expressed in different concentrations of L-arabinose, the cell lysates were treated with the labeling reagent, and the mixtures were directly analyzed by SDS-PAGE. Top, Coumassie-stained gel image; bottom, fluorescence gel image.

and Coomassie-stained images showed the same patterns of expression. Although this method is not as sensitive as antibody-based Western blotting (which typically detects as little as 0.1 ng when a chemiluminescent substrate is used), it is still much more sensitive than Coomassie staining and appears to have excellent specificity. The most important advantage of this method is that a target protein can be analyzed by simple mixing and SDS-PAGE.

In conclusion, a simple and efficient method for protein labeling was developed in which an azide-containing amino acid was introduced into GST and conjugated with Cy5.5 by SPAAC. This method allows us to label proteins by simply mixing a target protein and a labeling reagent, with a labeling yield of 80% in just 120 min. In addition, the specificity of SPAAC made it possible to analyze the expression levels of a protein quantitatively by simple mixing and SDS-PAGE analysis with no need for antibodies and multistep incubations and washings. Because the genetic incorporation of the azide-containing amino acid can be generally applied to any protein and SPAAC reactions are highly specific, this method should prove very useful for labeling and analyzing proteins.

■ ASSOCIATED CONTENT

Supporting Information

MALDI-TOF-MS spectrum of Cy5.5-ADIBO. This material is available free of charge via the Internet at http://pubs.acs.org.

■ AUTHOR INFORMATION

Corresponding Author

*E-mail: kimdw@chonbuk.ac.kr (D.W. K.); hslee76@sogang.ac.kr (H. S. L.).

Notes

The authors declare no competing financial interest.

■ ACKNOWLEDGMENTS

We would like to thank P. G. Schultz for providing us plasmids. This research was supported by Basic Science Research Program through the National Research Foundation of Korea (NRF) funded by the Ministry of Education, Science and Technology (2012-0003521), the Converging Research Center Program through the Ministry of Education, Science and Technology (2011K000705), the Sogang University Research Grant No. 201010048.01 and 201214006.01, and the Nuclear Research & Development Program of the National Research Foundation of Korea (NRF) grant funded by the Korean government (MEST) (grant code: 2012-0004884) .

■ REFERENCES

(1) Chalker, J. M., Bernardes, G. J., Lin, Y. A., and Davis, B. G. (2009) Chemical modification of proteins at cysteine: opportunities in chemistry and biology. *Chem. Asian J. 4*, 630−640.

(2) Carrico, I. S. (2008) Chemoselective modification of proteins: hitting the target. *Chem. Soc. Rev. 37*, 1423−1431.

(3) Tsien, R. Y. (1998) The green fluorescent protein. *Annu. Rev. Biochem. 67*, 509−544.

(4) Keppler, A., Gendreizig, S., Gronemeyer, T., Pick, H., Vogel, H., and Johnsson, K. (2003) A general method for the covalent labeling of fusion proteins with small molecules in vivo. *Nat. Biotechnol. 21*, 86−89.

(5) Los, G. V., Encell, L. P., McDougall, M. G., Hartzell, D. D., Karassina, N., Zimprich, C., Wood, M. G., Learish, R., Ohane, R. F., Urh, M., Simpson, D., Mendez, J., Zimmerman, K., Otto, P., Vidugiris, G., Zhu, J., Darzins, A., Klaubert, D. H., Bulleit, R. F., and Wood, K. V. (2008) HaloTag: a novel protein labeling technology for cell imaging and protein analysis. *ACS Chem. Biol. 3*, 373−382.

(6) Griffin, B. A., Adams, S. R., and Tsien, R. Y. (1998) Specific covalent labeling of recombinant protein molecules inside live cells. *Science 281*, 269−272.

(7) Wang, L., and Schultz, P. G. (2005) Expanding the genetic code. *Angew. Chem., Int. Ed. 44*, 34−66.

(8) Wu, X., and Schultz, P. G. (2009) Synthesis at the interface of chemistry and biology. *J. Am. Chem. Soc. 131*, 12497−12515.

(9) Liu, C. C., and Schultz, P. G. (2010) Adding new chemistries to the genetic code. *Annu. Rev. Biochem. 79*, 413−444.

(10) Wang, L., Zhang, Z., Brock, A., and Schultz, P. G. (2003) Addition of the keto functional group to the genetic code of Escherichia coli. *Proc. Natl. Acad. Sci. U.S.A. 100*, 56−61.

(11) Chin, J. W., Santoro, S. W., Martin, A. B., King, D. S., Wang, L., and Schultz, P. G. (2002) Addition of *p*-azido-L-phenylalanine to the genetic code of Escherichia coli. *J. Am. Chem. Soc. 124*, 9026−9027.
(12) Nguyen, D. P., Lusic, H., Neumann, H., Kapadnis, P. B., Deiters, A., and Chin, J. W. (2009) Genetic encoding and labeling of aliphatic azides and alkynes in recombinant proteins via a pyrrolysyl-tRNA synthetase/$tRNA_{CUA}$ pair and click chemistry. *J. Am. Chem. Soc. 131*, 8720−8721.
(13) Deiters, A., and Schultz, P. G. (2005) In vivo incorporation of an alkyne into proteins in Escherichia coli. *Bioorg. Med. Chem. Lett. 15*, 1521−1524.
(14) Zhang, Z., Wang, L., Brock, A., and Schultz, P. G. (2002) The selective incorporation of alkenes into proteins in Escherichia coli. *Angew. Chem., Int. Ed. 41*, 2840−2842.
(15) Spicer, C. D., Triemer, T., and Davis, B. G. (2012) Palladium-mediated cell-surface labeling. *J. Am. Chem. Soc. 134*, 800−803.
(16) Brustad, E., Bushey, M. L., Lee, J. W., Groff, D., Liu, W., and Schultz, P. G. (2008) *Angew. Chem., Int. Ed. 47*, 8220−8223.
(17) Brustad, E. M., Lemke, E. A., Schultz, P. G., and Deniz, A. A. (2008) A general and efficient method for the site-specific dual-labeling of proteins for single molecule fluorescence resonance energy transfer. *J. Am. Chem. Soc. 130*, 17664−17665.
(18) Kolb, H. C., Finn, M. G., and Sharpless, K. B. (2001) Click chemistry: diverse chemical function from a few good reactions. *Angew. Chem., Int. Ed. 40*, 2004−2021.
(19) Plass, T., Milles, S., Koehler, C., Schultz, C., and Lemke, E. A. (2011) Genetically encoded copper-free click chemistry. *Angew. Chem., Int. Ed. 50*, 3878−3881.
(20) Nguyen, D. P., Elliott, T., Holt, M., Muir, T. W., and Chin, J. W. (2011) Genetically encoded 1,2-aminothiols facilitate rapid and site-specific protein labeling via a bio-orthogonal cyanobenzothiazole condensation. *J. Am. Chem. Soc. 133*, 11418−11421.
(21) Lang, K., Davis, L., Torres-Kolbus, J., Chou, C., Deiters, A., and Chin, J. W. (2012) Genetically encoded norbornene directs site-specific cellular protein labelling via a rapid bioorthogonal reaction. *Nat. Chem. 4*, 298−304.
(22) Cheng, Z., Elias, D. R., Kamat, N. P., Johnston, E. D., Poloukhtine, A., Popik, V., Hammer, D. A., and Tsourkas, A. (2011) Improved tumor targeting of polymer-based nanovesicles using polymer-lipid blends. *Bioconjugate Chem. 22*, 2021−2029.
(23) Sachin, K., Jadhav, V. H., Kim, E. M., Kim, H. L., Lee, S. B., Jeong, H. J., Lim, S. T., Sohn, M. H., and Kim, D. W. (2012) F-18 labeling protocol of peptides based on chemically orthogonal strain-promoted cycloaddition under physiologically friendly reaction conditions. *Bioconjugate Chem. 23*, 1680−1686.
(24) Young, T. S., Ahmad, I., Yin, J. A., and Schultz, P. G. (2010) An enhanced system for unnatural amino acid mutagenesis in E. coli. *J. Mol. Biol. 395*, 361−374.
(25) Jewett, J. C., Sletten, E. M., and Bertozzi, C. R. (2010) Rapid Cu-free click chemistry with readily synthesized biarylazacyclooctynones. *J. Am. Chem. Soc. 132*, 3688−3690.
(26) Sletten, E. M., and Bertozzi, C. R. (2011) From mechanism to mouse: a tale of two bioorthogonal reactions. *Acc. Chem. Res. 44*, 666−676.
(27) Debets, M. F., van Berkel, S. S., Schoffelen, S., J., Rutjes, F. P. J. T., van Hest, J. C. M., and van Delft, F. L. (2010) Aza-dibenzocyclooctynes for fast and efficient enzyme PEGylation via copper-free (3 + 2) cycloaddition. *Chem. Commun. 46*, 97−99.
(28) Debets, M. F., van Berkel, S. S., Dommerholt, J., Dirks, A. J., Rutjes, F. P. J. T., and van Delft, F. L. (2011) Bioconjugation with strained alkenes and alkynes. *Acc. Chem. Res. 44*, 805−815.
(29) Kuzmin, A., Poloukhtine, A., Wolfert, M. A., and Popik, V. V. (2011) Surface functionalization using catalyst-free azide-alkyne cycloaddition. *Bioconjugate Chem. 21*, 2076−2085.
(30) Mbua, N. E., Guo, J., Wolfert, M. A., Steet, R., and Boons, G.-J. Strain-promoted alkyne−azide cycloadditions (SPAAC) reveal new features of glycoconjugate biosynthesis. *ChemBioChem 12*, 1912−1921.
(31) Friscourt, F., Ledin, P. A., Mbua, N. E., Flanagan-Steet, H. R., Wolfert, M. A., Steet, R., and Boons, G.-J. (2012) Polar dibenzocyclooctynes for selective labeling of extracellular glycoconjugates of living cells. *J. Am. Chem. Soc. 134*, 5381−5389.
(32) Yao, J. Z., Uttamapinant, C., Poloukhtine, A., Baskin, J. M., Codelli, J. A., Sletten, E. M., Bertozzi, C. R., Popik, V. V., and Ting, A. Y. (2012) Fluorophore targeting to cellular proteins via enzyme-mediated azide ligation and strain-promoted cycloaddition. *J. Am. Chem. Soc. 134*, 3720−3728.
(33) Hao, Z., Hong, S., Chen, X., and Chen, P. R. (2011) Introducing bioorthogonal functionalities into proteins in living cells. *Acc. Chem. Res. 44*, 742−751.
(34) Khatwani, S. L., Kang, J. S., Mullen, D. G., Hast, M. A., Beese, L. S., Distefano, M. D., and Taton, T. A. (2012) Covalent protein−oligonucleotide conjugates by copper-free click reaction. *Bioorg. Med. Chem. 20*, 4532−4539.
(35) Reddington, S. C., Tippmann, E. M., and Jones, D. D. (2012) Residue choice defines efficiency and influence of bioorthogonal protein modification via genetically encoded strain promoted Click chemistry. *Chem. Commun. 48*, 8419−8421.
(36) Nessen, M. A., Kramer, G., Back, J. W., Baskin, J. M., Smeenk, L. E. J., de Koning, L. J., van Maarseveen, J. H., de Jong, L., Bertozzi, C. R., Hiemstra, H., and de Koster, C. G. (2009) Selective enrichment of azide-containing peptides from complex. *J. Proteome Res. 8*, 3702−3711.

Supporting Information

Development of a simple method for protein conjugation by copper-free click reaction and its application to antibody-free western blot analysis

Sohye Jang[†], Kalme Sachin[‡], Hui-jeong Lee[†], Dong Wook Kim*[‡], Hyun Soo Lee*[†]

[†] *Department of Chemistry, Sogang University, Mapo-gu, Seoul 121-742, Republic of Korea*

[‡] *Department of Nuclear Medicine, Chonbuk National University Medical School, Jeonju, Jeonbuk 561-712, Republic of Korea*

MALDI-TOF-MS Spectrum of Cy5.5-ADIBO.

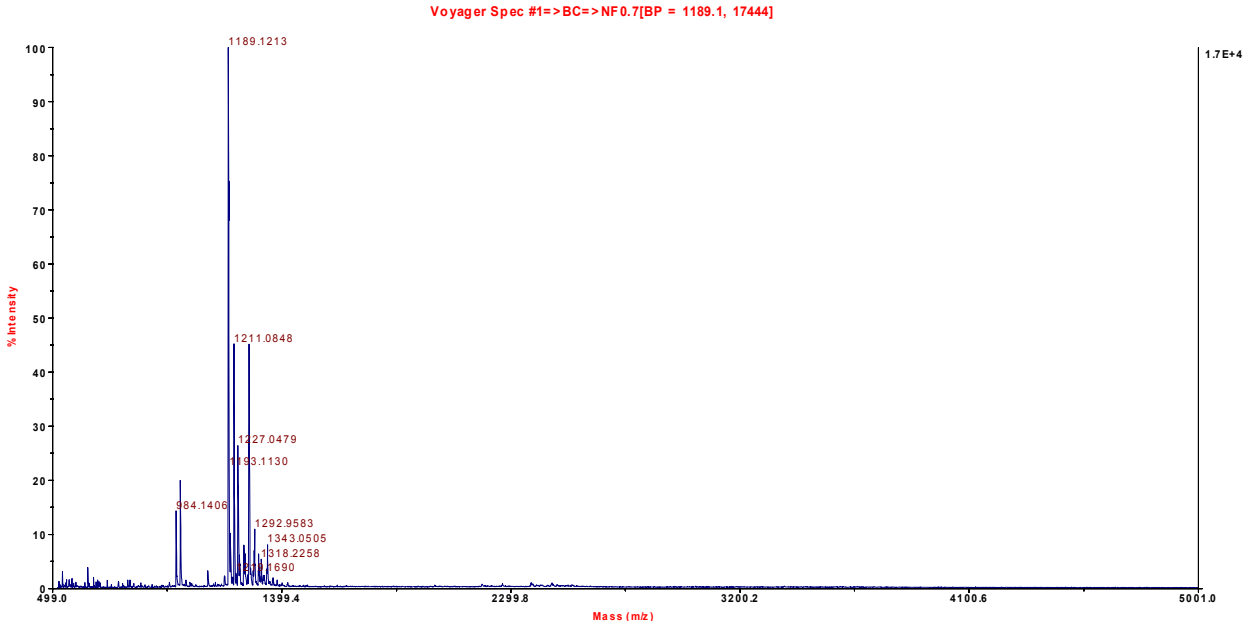

Bioconjugate Chemistry

Article

pubs.acs.org/bc

Comparative Binding of Disulfide-Bridged PEG-Fabs

Hanieh Khalili,[†,‡] Antony Godwin,[‡] Ji-won Choi,[‡] Rebecca Lever,[†] and Steve Brocchini*[,†,‡]

[†]UCL School of Pharmacy, University College London, 29-39 Brunswick Square, London WC1N 1AX, United Kingdom

[‡]PolyTherics Ltd, The London Bioscience Innovation Centre, 2 Royal College Street, London NW1 0NH, United Kingdom

Supporting Information

ABSTRACT: Protein PEGylation is the most clinically validated method to improve the efficacy of protein-based medicines. Antibody fragments such as Fabs display rapid clearance from blood circulation and therefore are good candidates for PEGylation. We have developed PEG-*bis*-sulfone reagents **1** that can selectively alkylate both sulfurs derived from a native disulfide. Using PEG-*bis*-sulfone reagents **1**, conjugation of PEG specifically targets the disulfide distal to the binding region of the Fab (Scheme 2). PEG-*bis*-sulfone reagents **1** (10−40 kDa) were used to generate the corresponding PEG-*mono*-sulfones **2** that underwent essentially quantitative conjugation to give the PEG-Fab product **4**. Four Fabs were PEGylated: Fab_{beva}, Fab'_{beva}, Fab_{rani}, and Fab_{trast}. Proteolytic digestion of bevacizumab with papain gave Fab_{beva}, while digestion of bevacizumab with IdeS gave $F(ab')_{2\text{-}beva}$, which after reaction with DTT and PEG-*mono*-sulfone **2** gave PEG_2-Fab'_{beva}. Ranibizumab, which is a clinically used Fab, was directly PEGylated to give PEG-Fab_{rani}. Trastuzumab was proteolytically digested with papain, and its corresponding Fab was PEGylated to give PEG-Fab_{trast}. Purification of the PEGylated Fabs was accomplished by a single ion exchange chromatography step to give pure PEG-Fab products as determined by silver-stained SDS-PAGE. No loss of PEG was detected post conjugation. A comparative binding study by SPR using Biacore with low ligand immobilization density was conducted using (i) $VEGF_{165}$ for the bevacizumab and ranibizumab derived products or (ii) HER2 for the trastuzumab derived products. $VEGF_{165}$ is a dimeric ligand with two binding sites for bevacizumab. HER2 has one domain for the binding of trastuzumab. Binding studies with PEG-Fab_{beva} indicated that the apparent affinity was 2-fold less compared to the unPEGylated Fab_{beva}. Binding properties of the PEG-Fab_{beva} products appeared to be independent of PEG molecular weight. Site-specific conjugation of two PEG molecules gave $PEG_{2\times20}$-Fab'_{beva}, whose apparent binding affinity was similar to that observed for PEG-Fab_{beva} derivatives. The k_d values were similar to those of the unPEGylated Fab_{beva}; hence, once bound, PEG-Fab_{beva} remained bound to the same degree as Fab_{beva}. Biacore analysis indicated that both Fab_{rani} and PEG_{20}-Fab_{rani} did not dissociate from the immobilized VEGF at 25 °C, but ELISA using immobilized VEGF showed 2-fold less apparent binding affinity for PEG_{20}-Fab_{rani} compared to the unPEGylated Fab_{rani}. Additionally, the apparent binding affinities for trastuzumab and Fab_{trast} were comparable by both Biacore and ELISA. Biacore results suggested that trastuzumab had a slower association rate compared to Fab_{trast}; however, both molecules displayed the same apparent binding affinity. This could have been due to enhanced rebinding effects of trastuzumab, as it is a bivalent molecule. Analogous to PEG-Fab_{beva} products, PEG_{20}-Fab_{trast} displayed 2-fold lower binding compared to Fab_{trast} when evaluated by ELISA. The variations in the apparent affinity for the PEGylated Fab variants were all related to the differences in the association rates (k_a) rather than the dissociation rates (k_d). We have shown that (i) Fabs are well-matched for site-specific PEGylation with our *bis*-alkylation PEG reagents, (ii) PEGylated Fabs display only a 2-fold reduction in apparent affinity without any change in the dissociation rate, and (iii) the apparent binding rates and affinities remain constant as the PEG molecular weight is varied.

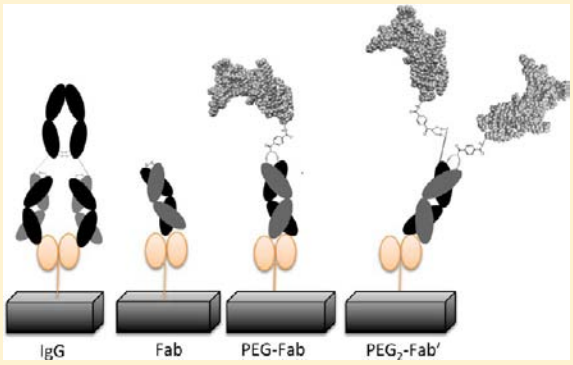

INTRODUCTION

Monoclonal antibodies comprise an important class of protein-based medicines. There are at least 25 antibody-based medicines approved for human therapy and more than 240 antibodies that are being evaluated clinically.[1] There are also a small number of antibody fragments (e.g., Fabs) that are clinically used.[2] Several classes of engineered antibody fragments (e.g., scFv, diabodies, etc.)[2−4] and other binding molecules (i.e., scaffolds)[5−7] are also in development. To capitalize on the potential of these many antibody fragments and engineered proteins in development, there is a constant need to address limitations associated with the rapid clearance of these proteins from the blood circulation.

Often, a proportion of patients suffer from side effects related to immune derived responses to most protein-based medicines that are currently in use.[8−11] Rapid clearance results in the need for more frequent dosing, which increases both the incidence of side effects and the chances for immunogenicity. Efficacy can be

Received: July 6, 2012
Revised: September 20, 2012
Published: September 21, 2012

 © 2012 American Chemical Society

Scheme 1. Elimination of 1 equiv of Sulfinic Acid Anion 3 from PEG-*bis*-sulfone 1 Gives the PEG-*mono*-sulfone 2, which then Undergoes Conjugation by *bis*-Alkylation with a Fab after Previously Being Treated with DTT

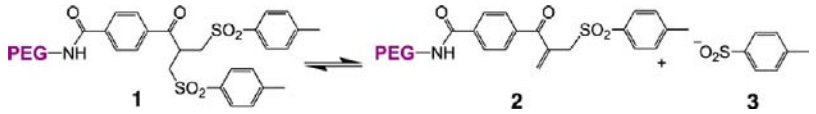

Scheme 2. Mechanism Envisaged for the Conjugation of PEG-*mono*-Sulfone 2 by *bis*-Alkylation with a Fab to Give PEG-Fab 4

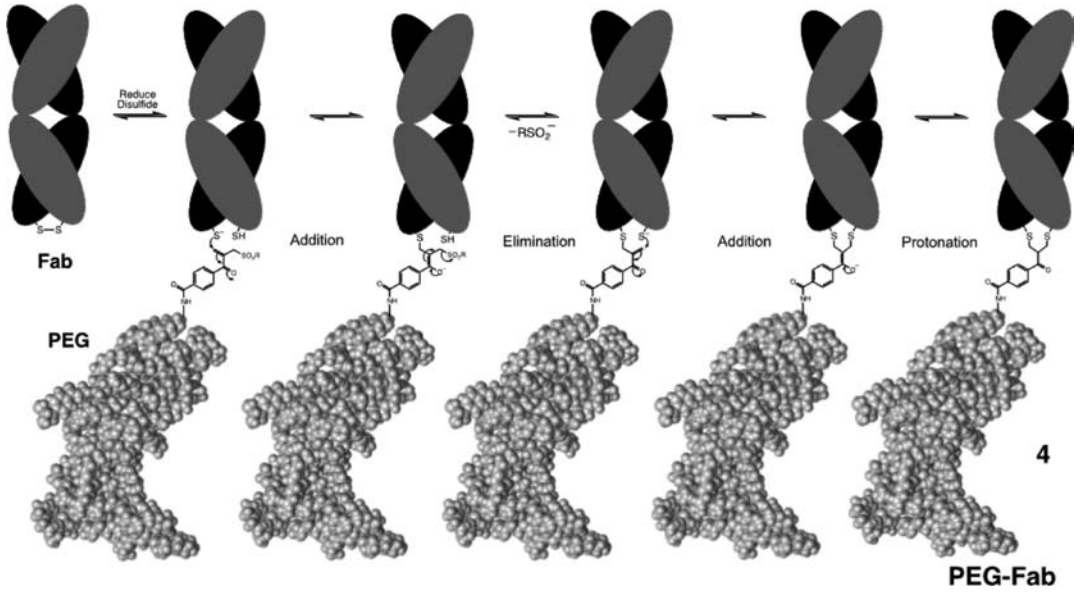

further compromised by dose-dumping and the inability to maintain a therapeutic concentration during the time between doses. The pharmacokinetics of therapeutic proteins is a fundamental property that must be optimized during development to help ensure maximal efficacy and safety profiles.

The covalent conjugation of poly(ethylene glycol) (PEG) to proteins (PEGylation) is a general approach to extend the half-life. There are at least 11 PEGylated medicines from a range of different protein classes that have been approved for clinical use.[12−22] PEGylated medicines have been shown to be clinically safe and PEGylation is considered to be generally safe as a development paradigm for new medicines.[23] PEGylation has also been used to reduce immunogenicity, especially for nonhuman-derived enzymes such as uricase and asparaginase.

To develop improved PEGylated proteins, there is a need to utilize scalable, efficient conjugation technologies that are site-specific. The majority of clinically used PEGylated medicines are heterogeneous mixtures that have been produced by nonspecific and inefficient PEG conjugation reactions to different nucleophilic sites on the protein. Since heterogeneous PEGylated mixtures display different biological properties for each isomer,[20,24,25] there continues to be a need to achieve site-specific conjugation of PEG.[26−30]

To address the problem of structural heterogeneity, recently approved PEGylated products (peginesatide and certolizumab pegol) have adopted site-specific approaches. Peginesatide is a peptide that is PEGylated during solid-phase synthesis.[30,31] This approach is not possible for recombinantly derived proteins. Certolizumab pegol is a recombinant Fab that is PEGylated at the free cysteine introduced for conjugation using a PEG-maleimide reagent.[32,33] While thiol conjugation is more efficient compared to amine conjugation, the addition of an unpaired cysteine can result in disulfide scrambling and protein aggregation. Recent evidence also indicates that maleimide derived reagents are labile to hydrolysis[34] and can undergo exchange reactions *in vivo*.[35] Therefore, site-specific PEGylation strategies and reagents that address low conjugation efficiency and PEG conjugate stability continue to be needed.

To exploit the efficiency of thiol conjugation and the fact that many therapeutically relevant proteins already have thiol groups as paired cysteines in disulfides, we have developed PEGylation reagents that are capable of undergoing conjugation by *bis*-alkylation.[36,37] The PEG-*bis*-sulfone **1** can undergo elimination of an equivalent of the sulfinic anion leaving group **3** to generate the PEG-*mono*-sulfone **2** (Scheme 1), which then undergoes conjugation. PEGylation using PEG-*mono*-sulfone **2** is particularly appropriate for Fabs because there is an easily reducible disulfide that is distal to the antigen binding region (Scheme 2), and which can undergo facile reaction with reagent **2** to give the PEG-Fab **4**. Conjugation occurs by the formation of a three-carbon bridge linking the two cysteine sulfurs with PEG attached through the middle carbon of the bridge. PEGylation of a Fab using the *mono*-sulfone reagent **2** essentially replaces the heavy chain below the Fab with PEG. It would be expected that conjugation of PEG at this site would have minimal impact on the binding properties of the Fab.

Since conjugation with PEG-*mono*-sulfone **2** can be very efficient and site-specific, we wished to use this reagent to correlate the binding properties of PEGylated Fabs using different molecular weight PEGs to prepare a small family of PEG-Fabs for comparative analysis. Earlier work had suggested that the *in vitro* biological activity for some proteins could remain broadly independent of PEG molecular weight when conjugation was conducted at the same site.[36,37] This is an important observation, as pharmacokinetic properties can in principle be varied without changing biological activity. As far

dx.doi.org/10.1021/bc300372r | *Bioconjugate Chem.* 2012, 23, 2262−2277

Scheme 3. Preparation of PEG-Fab 4 and PEG_2-Fab′ 5 Starting from a Parent IgG

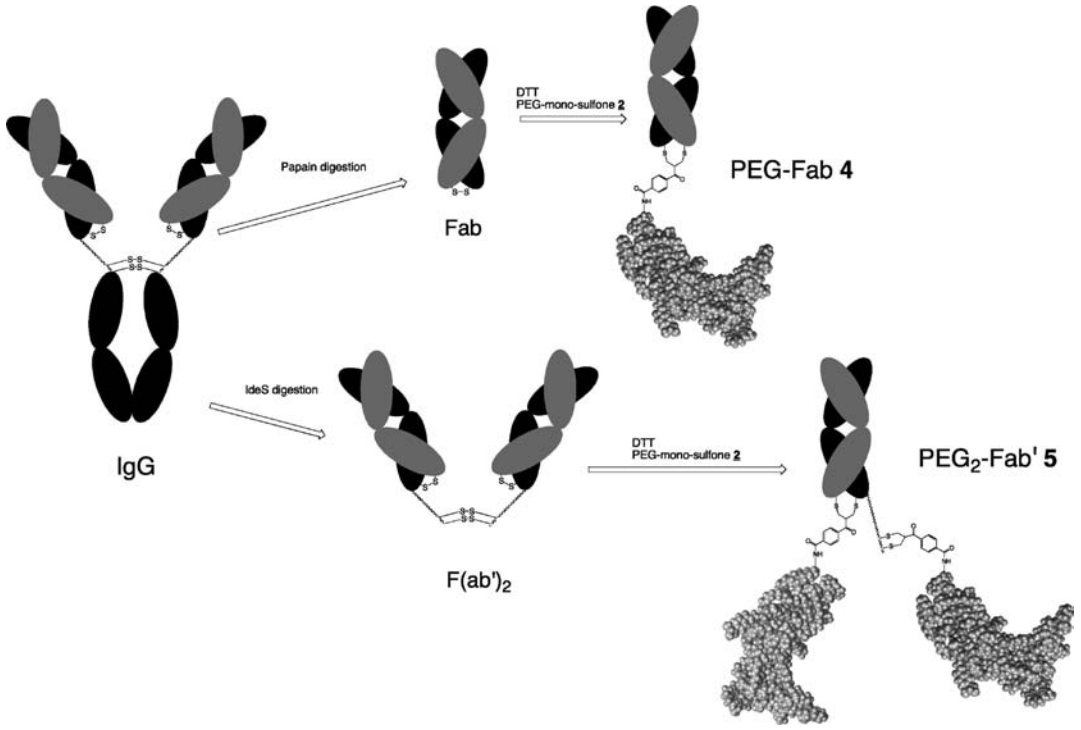

as we can discern, this is one of the few ways to separate pharmacokinetic variation from biological activity. Making these into independent parameters has the potential to aid development of protein-based medicines. Since the natural placement of the easily reducible disulfide in a Fab is maximally distal from the binding region, we hypothesized that any loss of binding due to PEG steric shielding effects would be minimal.

We elected to obtain Fabs for PEGylation by the proteolytic digestion of a parent IgG antibody (Scheme 3). This provided a means to compare binding differences between the non-PEGylated IgG and the PEG-Fab products. Proteolytic digestion with papain yields Fab and digestion with IdeS enzyme provides $F(ab')_2$. Subsequent treatment with dithiothrietol (DTT) and PEG-*mono*-sulfone **2** generates PEG-Fab **4** and PEG_2-Fab′ **5**, respectively (Scheme 3). Treatment of $F(ab')_2$ with DTT yields 2 equiv of Fab′, which has two pairs of free cysteines that are available for *bis*-alkylation with PEG-*mono*-sulfone **2**. In this way, we could compare the binding of the parent IgG and its Fab with PEG-Fab **4** and PEG_2-Fab′ **5** products. Since our PEGylation is site-specific for free thiols that are liberated after disulfide reduction, we also PEGylated the parent antibody in our comparative study.

Two clinically used monoclonal antibodies were evaluated, bevacizumab and trastuzumab. Of these two antibodies, the Fab from bevacizumab (Fab_{beva}) was studied in more detail than was the Fab from trastuzumab (Fab_{trast}). Bevacizumab binds to VEGF.[38−40] Ranibizumab is a therapeutic Fab (called here, Fab_{rani}) that also binds to VEGF and was also PEGylated for comparison with the PEGylated Fab_{beva} products.

Binding studies were conducted by surface plasmon resonance (SPR) using Biacore as a means to examine the association and dissociation properties of the PEGylated proteins.[41−43] Steric shielding effects of PEG are thought to influence association ("on rate") more than dissociation ("off rate")[41,42] to immobilized ligand. We therefore wished to determine the correlations of the kinetic rate constants for association (k_a) and dissociation (k_d) with the different PEGylated Fabs. Our effort was focused on using a low density of ligand immobilization to avoid mass transfer effects.[44] Comparative ELISA experiments were also conducted to determine if the binding trends were the same as were determined by SPR.

Trastuzumab binds to HER2[45,46] and was PEGylated because HER2 has one epitope for binding, while the $VEGF_{165}$ ligand that was used has two binding sites. We wanted to examine the effects of PEG steric effects on the association and dissociation rates for these two ligand binding situations. There is some speculation that PEG steric shielding of a bound protein may influence the binding of additional molecules of the PEGylated protein,[41,47] and so our binding studies were designed to try to observe binding phenomena related to the target alone. It was hoped that with very low immobilization density there would be minimal influence from any PEG-Fab that was bound to neighboring ligand.

EXPERIMENTAL SECTION

Materials. Bevacizumab (Avastin, 25 mg/mL, Genentech) and trastuzumab (Herceptin, 150 mg, Genentech) were purchased from a pharmacy for research purposes. Ranibizumab (Lucentis, 10 mg/mL, Genentech) was obtained from the pooled remains of vials that had been used clinically. Immobilized papain slurry gel, NAP protein-A spin columns, elution immunoPure IgG buffers (0.1 M glycine, pH 2.8), neutralization buffer (1.0 M Tris buffer, pH 8.5), and binding buffer (1.0 M Tris buffer containing EDTA, pH 8.0) were purchased from Thermo Fisher (Pierce). IdeS enzyme (FabRICATOR for 5.0 mg IgG) was purchased from Genovis (Sweden). Phosphate buffered saline (PBS) containing NaCl (0.16 M), KCl (0.003 M), Na_2HPO_4 (0.008 M), and KH_2PO_4 (0.001 M) was prepared with tablets purchased from Oxoid.

dx.doi.org/10.1021/bc300372r | Bioconjugate Chem. 2012, 23, 2262−2277

Novex Bis-tris 4−12% gels, Sharp blue standard protein markers, NuPAGE MOPS running buffer, NuPAGE LDS sample buffer, and SilverXpress silver staining kit were purchased from Invitrogen. InstantBlue was purchased from Expedeon Ltd. Perchloric acid (0.1 M) and barium chloride (5.0%) solutions for barium iodide staining were prepared in the lab. PD-10 columns, cation exchange columns (HiTrap SP HP 1.0 mL), and a Superdex 200 prep grade size exclusion column (34.0 μm particle size) along with Biacore consumables including immobilization reagents and buffers, *N*-hydroxysuccinimide (NHS), 1-ethyl-3-(3-dimethylaminopropyl)-carbodiimide (EDC), ethanolamine-HCl (1.0 M, pH 8.5), glycine buffer (10 mM, pH range of 1.5 to 2.5), HBS-EP buffer, and sensor chips, were all purchased from GE Healthcare. Antihuman IgG (Fab specific)-peroxidase, 3,3′,5,5′-tetramethylbenzidine (TMB), and human vascular endothelial growth factor ($VEGF_{165,}$ 10 μg) were purchased from Sigma-Aldrich. Recombinant human ErbB2/HER2 (100 μg) was purchased from Sino Biological Inc. Both size exclusion chromatography (SEC) and ion-exchange chromatography (IEC) were conducted using a system comprising a UV detector (Jasco UV-1570) and HPLC pump (Jasco PU-980 Intelligent). *Azur* software was used to process chromatographic data. A dual-beam UV spectrophotometer (Hitachi, U-2800A) and Biacore X-100 (GE Healthcare) were used.

Methods. *Antibody Digestion.* Digestion buffer (20 mM sodium phosphate, pH 7.4, 2 mM EDTA, 20 mM cysteine-HCl) was prepared immediately prior to use. Immobilized 50% papain slurry (1.0 mL) was equilibrated with the digestion buffer. To obtain Fab_{beva}, bevacizumab (12.5 mg/mL, 1.0 mL) was then added to the slurry and the digestion solution was incubated at 37 °C for 5.5 h while being gently shaken at a speed of 250 × rpm. After the incubation period, the solution was separated from the immobilized papain by centrifugation (4000 × *g* for 4 min). For maximum recovery, the immobilized papain was washed once with the binding buffer (2.0 mL, Tris buffer with EDTA, pH 8.0). The digestion mixture was then eluted over a protein A column (pre-equilibrated with Tris buffer, pH 8.0) to remove Fc. The collected fractions were evaluated by SDS-PAGE, and the protein concentration was determined by UV spectrometry. Digestions starting with 12.5 mg of bevacizumab typically gave after purification 5.2−6.4 mg (~70% yield) of Fab_{beva}.

To obtain $F(ab')_2$, bevacizumab (5.0 mg/mL, 1.0 mL) was digested using IdeS enzyme[48−50] (FabRICATORE, 75 μL) at 37 °C for 30 min. SEC was used to purify $F(ab')_2$ from the enzyme and the digested Fc peptide fragments (Superdex 200 prep grade). The mobile phase was PBS, pH 7.3, at a flow rate of 1.0 mL/min. The injection volume was 0.96 mL and the run time was 100 min. A yield of 86% was obtained for the purified $F(ab')_2$.

To obtain Fab_{trast}, a solution of trastuzumab (6.5 mg/mL) was prepared by dilution of 0.5 mL of trastuzumab (12.9 mg/mL) with 0.5 mL of digestion buffer. Trastuzumab was then incubated with pre-equilibrated papain at 37 °C for 20 h while being gently shaken at a speed of 250 × rpm. The crude Fab was then purified from the digestion mixture by SEC using a mobile phase of PBS, pH 7.3, at a flow rate of 1.0 mL/min.[51] The Fab_{trast} was obtained at a yield of 26%.

Concentration Determination. An absorbance of 1.40 at 280 nm was used for a concentration of 1.0 mg/mL Fab.[48−52] This value was tested with a solution of Fab_{rani} (1.0 mg/mL) that was prepared from the pharmaceutical formulation (10 mg/mL) used in the clinic. Fab_{rani} displayed an absorbance of 1.40 at 280 nm. The bicinchoninic acid (BCA) assay[15] was also used to determine protein concentration and was found to show good correlation with UV measurement at 280 nm using Fab_{beva} (0.093 mg/mL vs 0.092 mg/mL, respectively). UV spectroscopy at 280 nm was generally used to determine the concentrations of unPEGylated proteins. Due to the contribution of the PEG linker at 280 nm, BCA was generally used to determine the concentration of the protein after it had been PEGylated.

Preparation of mono-PEG-Fabs and $PEG_{2\times20}$-Fab'_{beva}. PEGylation reaction buffer (20 mM sodium phosphate, pH 7.4, 10 mM EDTA) was prepared. A solution of Fab (1.0 mg/mL, 1.0 mL of PBS, pH 7.3) was first treated with DTT (1.0 mg) and then incubated at ambient temperature without shaking for 30 min. DTT was then removed using a PD-10 column during buffer exchange into the PEGylation reaction buffer. The PEG-*mono*-sulfone **2** (2.0 equiv; 10, 20, 30, or 40 kDa) in water (e.g., 0.26 mL from 20 kDa PEG 3.0 mg/mL) was then added to the Fab solution, which was allowed to incubate for 3 h without shaking. PEGylation of $F(ab')_{2\text{-beva}}$ and bevacizumab was accomplished in the same way using PEG-*mono*-sulfone **2** (4.0 equiv). The PEG-Fabs and PEG_2-Fab'_{beva} were then purified by IEC with an SP HP column (1.0 mL, flow rate of 1.0 mL/min). Mono-PEG-bevacizumab was purified by SEC and then by IEC. For SEC purification, a mobile phase of PBS, pH 7.3, at a flow rate of 1.0 mL/min was used with a run time of 100 min.

Analysis of Binding by Biacore. Human recombinant $VEGF_{165}$ (38 kDa) was immobilized on a CM5 (208 RU) and a CM3 (57 RU) chip. The immobilization levels were selected for binding and kinetic assays, respectively. An extracellular domain of recombinant human HER2 (110 kDa M_w) was immobilized on a CM3 chip (51 RU) for kinetic analysis. The immobilization was performed using standard carbodiimide mediated coupling (NHS/EDC, 50/50) followed by exposure to ethanolamine (pH 8.5) to quench the activated surface carboxylates after exposure to the ligand (i.e., VEGF or HER2). Samples were prepared in HBS-EP running buffer (10 mM HEPES, pH 7.4, 150 mm NaCl, 3.0 mM EDTA, 0.005% surfactant P20). All kinetic measurements were conducted at 25 °C at a flow rate of 30 μL/min with an association time of 180 s and dissociation time of 1200 s. Chip regeneration was accomplished by exposure to 10.0 mM glycine−HCl (pH 2.0) for 1200 s. Double-referencing was performed to account for bulk effects caused by changes in the buffer composition or nonspecific binding.[52] Data were evaluated with *BIAevaluation* software (v 2.1), and the best fit (lowest χ^2) was obtained using a 1:1 binding model. The sensorgram was fitted globally over the association and dissociation phases. Equilibrium dissociation constants (affinity) were calculated from the rate constants ($K_D = k_{off}/k_{on}$).

Analysis of Binding by ELISA. The ELISA plate was coated with human recombinant $VEGF_{165}$ (0.1 μg/mL) to evaluate the molecules derived from bevacizumab and ranibizumab. The ELISA plate was coated with HER2 (0.25 μg/mL) to analyze molecules derived from trastuzumab. Briefly, the ligand (VEGF or HER2) was coated overnight at 4 °C on a 96-well plate. The ligand solution was then removed, and then, without washing 300 μL of the blocking buffer (PBS, 1% BSA, 0.05% Tween-20) was added to each well and incubated at ambient temperature for 2 h. The wells were then washed with 300 μL of PBS-T buffer (PBS, 0.05% Tween-20). Samples were prepared in PBS

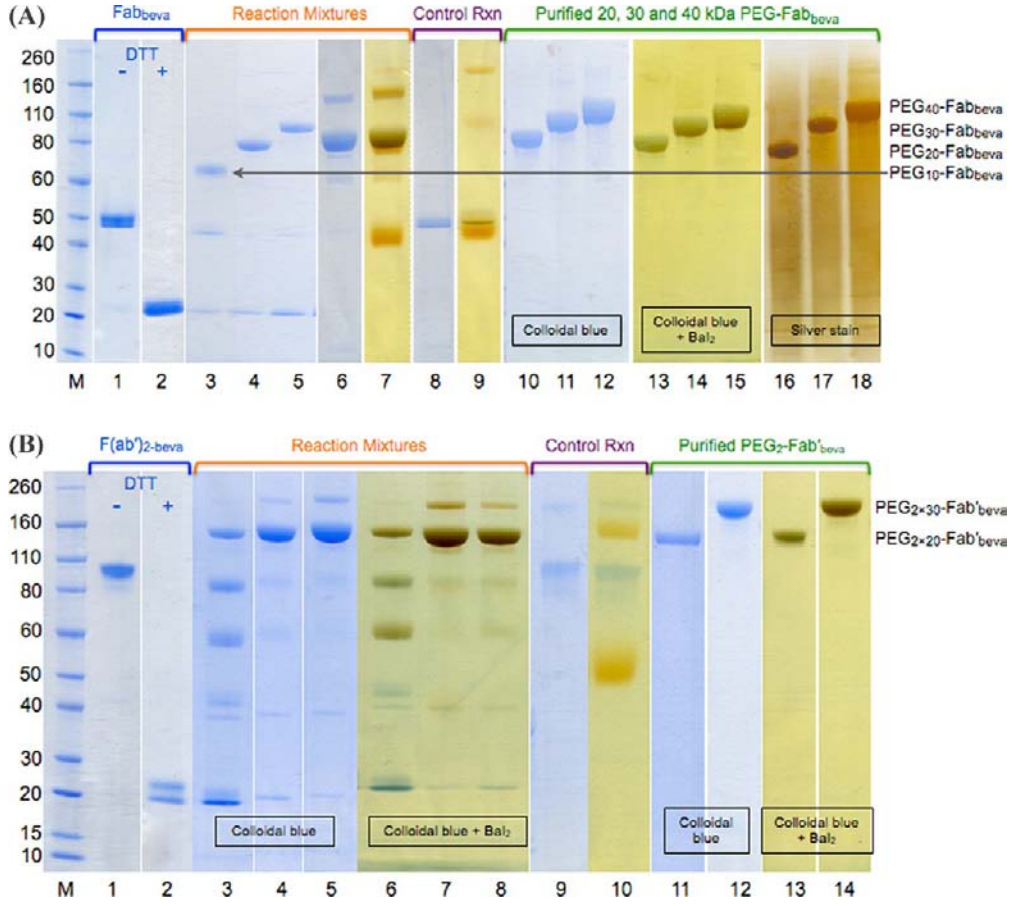

Figure 1. Representative SDS-PAGE gels of the PEGylation reactions and purified products obtained with PEG-*mono*-sulfone **2**. For all of the gels, Lane M: protein standards (colloidal blue). (A) PEGylation of the Fab derived from the proteolytic digestion of bevacizumab with papain. Lane 1: Fab_{beva} obtained after digestion. Lane 2: Fab_{beva} after DTT treatment. Lanes 3–5: reaction mixtures for the PEGylation after DTT treatment of Fab_{beva} with 1 equiv of PEG-*mono*-sulfone **2** (10, 20, and 30 kDa PEG). Lanes 6–7: reaction mixture for the PEGylation of Fab_{beva} (2 equiv 20 kDa PEG) (colloidal blue + BaI_2, lane 7). Lanes 8–9: control reaction of PEG-*mono*-sulfone **2** (2 equiv, 20 kDa PEG) and Fab_{beva} without prior DTT treatment (colloidal blue + BaI_2, lane 9). Lanes 10–18: purified PEG-Fab_{beva} (20, 30, and 40 kDa PEG) detected with colloidal blue (lanes 10–12), colloidal blue + BaI_2 (lanes 13–15) and silver stain (lanes 16–18). (B) Preparation of the $PEG_{2\times30}$-Fab'_{beva} and $PEG_{2\times20}$-Fab'_{beva}. Lane 1: $F(ab')_2$ obtained after proteolytic digestion of bevacizumab with IdeS enzyme. Lane 2: $F(ab')_2$ after DTT treatment. Lanes 3, 6: reaction mixture for the PEGylation of $F(ab')_2$ after DTT treatment with PEG-*mono*-sulfone **2** (1 equiv, 20 kDa PEG) (colloidal blue + BaI_2, lane 6). Lanes 4, 7: reaction mixture for the PEGylation of $F(ab')_2$ after DTT treatment with PEG-*mono*-sulfone **2** (3 equiv, 20 kDa PEG) (colloidal blue + BaI_2, lane 7). Lanes 5, 8: reaction mixture for the PEGylation of $F(ab')_2$ after DTT treatment with PEG-*mono*-sulfone **2** (4 equiv, 20 kDa PEG) (colloidal blue + BaI_2, lane 8). Lanes 9–10: control reaction of PEG-*mono*-sulfone **2** (4 equiv, 20 kDa PEG) with $F(ab')_2$ without prior DTT treatment (colloidal blue + BaI_2, lane 10). Lanes 11, 13: purified $PEG_{2\times20}$-Fab'_{beva} (colloidal blue + BaI_2, lane 13). Lanes 12, 14: purified $PEG_{2\times30}$-Fab'_{beva} (colloidal blue + BaI_2, lane 14). Lanes 15, 16: treatment of purified $PEG_{2\times20}$-Fab'_{beva} with excess DTT and heat (80 °C) for 10 min (colloidal blue + BaI_2, lane 16).

at a range of concentrations, and were added (100 μL) to each well. The plate was then incubated for 2 h at ambient temperature. The protein solutions were then removed, and the wells washed three times with PBS-T buffer. To detect the samples, 100 μL of antihuman IgG (Fab specific)-peroxidase (1:5000 dilution) was added into each well and incubated for 1 h at ambient temperature. The solutions were then removed and the plate was washed with PBS-T three times. TMB (100 μL/well) was then added. After approximately 5 min, when the blue color was sufficiently visible, 50 μL of 1.0 M HCl solution was added to each well to stop the enzymatic reaction as indicated by the solution turning yellow. The absorbance was read using a microplate reader at 450 nm within 30 min.

RESULTS AND DISCUSSION

PEGylation. *Preparation of PEG-Fab_{beva}.* Proteolytic digestion of an IgG antibody to obtain Fab is often conducted with papain, which is a thiol-protease. In principle, 2 mol of Fab and 1 mol of Fc can be generated from 1 mol of IgG.[53−55] Following routine procedures, Fab_{beva} was obtained from bevacizumab using immobilized papain in the presence of cysteine-HCl, which is required for papain activation. Fab_{beva} was purified from the Fc fragment and other small fragments after eluting over a protein A column (Figure S1 A, lanes 3–7). Cysteine that was present in the digestion buffer coeluted with Fab_{beva}. These fractions were pooled and the cysteine was removed by elution over a PD-10 column.

From 12.5 mg of bevacizumab, about 70% of Fab_{beva} was generally isolated. Analysis by SDS-PAGE suggested that the heavy and light chains of the Fab_{beva} remained associated and that the interchain disulfide was oxidized after purification (Figure S1 B). Both bevacizumab and the purified Fab_{beva} were then analyzed by MALDI-TOF mass spectroscopy (Figures S4 A,B) and Fab_{beva} displayed a molecular weight of 48 kDa. Size exclusion chromatography (SEC) using PBS, pH 7.4, indicated that bevacizumab and Fab_{beva} had a retention time of 72 and 90

dx.doi.org/10.1021/bc300372r | *Bioconjugate Chem.* 2012, 23, 2262−2277

min, respectively (Figure S1 C,D). A model Fab (Chromopure human Fab) and ranibizumab (Fab_{rani}) were evaluated by SEC as controls and both Fabs eluted at 90 min (Figure S1 E,F).

Prior to PEGylation, an Ellman's assay was conducted with Fab_{beva} to determine if there were any free thiols on the protein. Cysteine hydrochloride monohydrate was used as a calibration standard (Figure S2). No free thiol was observed with the purified Fab_{beva} or bevacizumab after incubation with Ellman's reagent (Table S1).

Fab_{beva} was first treated with excess dithiothreitol (DTT), followed by elution over a PD-10 column to remove the DTT to avoid competitive reactions with the PEG-*mono*-sulfone **2**. It is well-known that the Fab structure can be maintained after reduction of the interchain disulfide,[56−58] but when an aliquot of the mixture of Fab_{beva} and DTT is subjected to SDS-PAGE analysis, the heavy and light chains of the Fab_{beva} dissociate due to the presence of SDS (Figure 1A, lane 2). The method to use a PD-10 column to remove DTT was the same as the method that was used to remove the cysteine during the purification of the Fab after papain digestion. To avoid reoxidation of the disulfide, it was necessary to exclude metal ions (e.g., Cu) by using EDTA in the buffer and to exclude oxygen from the solution. Ellman's assay after DTT treatment and elution over PD-10 column indicated that a single disulfide had been reduced (Table S1). Since a Fab typically has four buried intrachain disulfides in addition to the accessible hinge disulfide, it was necessary to determine if the reduction conditions that were used resulted only in the reduction of one disulfide.

There are a wide range of reagents and techniques that can be used to reduce protein disulfide bonds.[57,59−61] While we have used DTT in the experiments described here and for other proteins,[37,56] other reducing reagents have also been found to work for different proteins when using PEG reagents **2**. These include reagents such as 2-mercaptoethylamine (2-MA), 2-mercaptoethanol (2-ME), 2-mercaptoethylamine-HCl (2-MEA), and *tris*(2-carboxyethyl) phosphine (TCEP). Using TCEP, we are able to add stoichiometric amounts of this reagent to the protein[56] to avoid the need for a separate step to remove excess TCEP using a PD-10 column as TCEP can react with the PEG reagent. Addition of a slight excess of PEG-*mono*-sulfone **2** can then achieve good yields of the PEGylated product. The use of TCEP also allows reduction of a disulfide in acidic conditions. Since the Ellman's assay indicated that the disulfide of Fab_{beva} remained reduced when using DTT and that only one disulfide was reduced in these conditions, we elected to use this reducing agent.

A solution of the PEG-*mono*-sulfone reagent **2** at different molecular weights (10, 20, 30, and 40 kDa) was then added to the reduced-Fab_{beva} (up to 1.0 mg) after elution over the PD-10 column. One equivalent of the PEG reagent **2** gave nearly quantitative conversion to the PEGylated Fab (Figure 1A, lanes 3−5). When 2.0 equiv of the PEG-*mono*-sulfone **2** (Figure 1A, lanes 6−7) was used, complete conversion was observed with the appearance of only a small amount of a di-PEG-Fab_{beva} species (Figure 1A, lanes 6−7).

Control reactions with PEG-*mono*-sulfone **2** were conducted with Fab_{beva} under the same conditions but without prior treatment of the Fab with DTT (Figure 1A, lanes 8−9). No PEGylation was observed. The only protein species observed was the unPEGylated Fab_{beva}. The conditions such as buffer and pH, incubation time, concentration of the Fab, and the PEG reagent were exactly the same as the conditions used when Fab_{beva} had been treated with DTT. These control reactions indicated that the amine groups (e.g., lysine) of the Fab_{beva} do not undergo reaction with the PEG-*mono*-sulfone reagent **2** in the reaction conditions (pH 7.4) that we used for conjugation.

The PEG-Fab_{beva} conjugates were purified by a single elution using ion exchange chromatography (IEC) (Figure S3). PEG-Fab_{beva} and Fab_{beva} bound to the column, while unconjugated PEG species, which are uncharged, eluted during the loading step. Due to shielding effects of PEG, the di- and mono-PEGylated conjugates eluted first followed by the unPEGylated Fab. In SDS-PAGE analysis, fractions containing highly pure PEG_{20}-Fab_{beva} were identified (Figure S3 B). These fractions were pooled, concentrated (Vivaspin column; 4 min, 4000 × *g*) to a 1.0 mL solution, and then buffer exchanged to PBS, pH 7.4 (Nap-10 column), for long-term storage at 4 °C. The purity of these PEG-Fab_{beva} products was confirmed by using silver staining (Figure 1A, lanes 16−18), which is ∼100-fold more sensitive than colloidal blue staining.[62] No unPEGylated protein was observed, which was important to ensure that binding studies would not be distorted by the presence of native Fab_{beva}.

PEG_{20}-Fab_{beva} was selected for MALDI-TOF mass spectrometry (Figure S4 C). The result indicated that the mass of the conjugate was 68 kDa, which was expected for PEG_{20}-Fab_{beva} (48 kDa Fab_{beva} + 20 kDa PEG = 68 kDa). Using 1.0 mg of starting Fab_{beva}, the typical isolated yields for PEG_{20}-Fab_{beva} were in the range of 60−66% (n = 10). Similar yields were obtained for PEG_{30}-Fab_{beva} and PEG_{40}-Fab_{beva} (n = 3).

Preparation of PEG_2-Fab′$_{beva}$. The di-PEGylated Fab′$_{beva}$ products were obtained by first digesting bevacizumab to give $F(ab')_2$, which we label as $F(ab')_{2\text{-beva}}$. Initial efforts to obtain $F(ab')_{2\text{-beva}}$ focused on digesting bevacizumab with immobilized pepsin; however, only a low yield (<10%) of purified $F(ab')_{2\text{-beva}}$ could be obtained. IdeS enzyme[48−50] was then found to give the desired $F(ab')_{2\text{-beva}}$ in the range of 80−90% yield (n = 5) starting from 5.0 mg of bevacizumab. Ellman's assay indicated that there were no free cysteines present in the purified $F(ab')_{2\text{-beva}}$ (Table S1).

It is thought that there are two disulfides in the hinge region of bevacizumab.[63,64] Hence, when $F(ab')_{2\text{-beva}}$ is treated with excess DTT and then incubated with PEG-*mono*-sulfone **2** it was expected to give PEG_2-Fab′$_{beva}$ (**5**) (Scheme 3). SDS-PAGE analysis after DTT treatment of $F(ab')_{2\text{-beva}}$ showed the presence of two proteins of approximately 25 and 30 kDa, presumably light and heavy chains, respectively, which had dissociated in the presence of SDS (Figure 1B, lane 2). Due to the differences in digestion between papain and IdeS, the heavy chain for $F(ab')_{2\text{-beva}}$ comprised an extra length of peptide extending into the hinge region. As comparison, DTT reduction of papain-digested bevacizumab generates a single band for Fab_{beva} (Figure 1A, lane 2), indicating the absence of the excess hinge sequence in the heavy chain of the Fab′.

After removal of DTT with a PD-10 column, the PEG-*mono*-sulfone **2** (20 kDa) was added. Exploratory conjugations were conducted using 1, 3, and 4 equiv of the PEG reagent **2** (Figure 1B, lanes 3−5). A single PEGylated product was formed in what appeared to be almost quantitative conversion and which migrated by SDS-PAGE to about 140 kDa (Figure 1B, lanes 4−5) when 3 and 4 equiv of PEG-*mono*-sulfone **2** was used. A control reaction was conducted without prior treatment of the $F(ab')_{2\text{-beva}}$ with DTT. The $F(ab')_{2\text{-beva}}$ was incubated in the presence of PEG-*mono*-sulfone **2** (4.0 equiv) in the same conjugation conditions (i.e., buffer, pH, concentration, temper-

ature, and incubation time). Again, no conjugation was observed (Figure 1B, lanes 9 and 10) unless the protein was first treated with DTT.

The band for the conjugated product at about 140 kDa (e.g., Figure 1B, lane 4) is consistent with 2 PEG molecules being conjugated to a Fab'_{beva}. Since a 20 kDa PEG reagent was used, then 2 × 20 kDa PEG gives a total PEG contribution of 40 kDa, which by SDS-PAGE would be expected to contribute 80 kDa in terms of migration on the gel. The Fab'_{beva} contributes about 55 kDa. The $PEG_{2\times20}$-Fab'_{beva} conjugate would have an apparent molecular weight on a SDS-PAGE gel of about 135 kDa, which is consistent with what was observed (Figure 1B).

Disulfide bridging PEGylation yields stable conjugates[56,65] that do not undergo exchange reactions with other thiols in solution, although this is one of the limitations of PEG maleimide reagents that is difficult to avoid.[34,35] A sample of $PEG_{2\times20}$-Fab'_{beva} and excess DTT was heated (80 °C) for 10 min. No change in the SDS-PAGE gel (Figure 1B, lanes 15 and 16) was observed, indicating that the conjugate had to be $PEG_{2\times20}$-Fab'_{beva} rather than a conjugate such as PEG_{20}-$F(ab')_{2\text{-}beva}$. A conjugate such as PEG_{20}-$F(ab')_{2\text{-}beva}$ with one PEG conjugated to an intact $F(ab')_{2\text{-}beva}$ would have been expected to have at least 2 disulfides that would have been reduced in these conditions to generate a range of protein bands on the gel.

The purified $PEG_{2\times20}$-Fab'_{beva} conjugate (Figure 1B, lanes 11 and 13) was obtained by a single elution over an ion exchange column (SP HP) in the same way as was done to purify PEG-Fab_{beva}. Using the 30 kDa PEG-*mono*-sulfone **2**, the $PEG_{2\times30}$-Fab'_{beva} product was also prepared (Figure 1B, lanes 12 and 14). Both di-PEG-Fab′ derivatives were isolated as purified products with a yield of 30−35% (n = 4).

Stability of PEGylated Bevacizumab Fragments. Prior to conducting any binding studies, we examined the stability of the purified PEGylated products. While we had established purity of the conjugates, it was important to determine if dePEGylation was facile. As already described for $PEG_{2\times20}$-Fab'_{beva}, no dePEGylation was observed when a sample of this conjugate was exposed to excess DTT at 80 °C for 10 min (Figure 1B, lanes 15 and 16).

Fab molecules tend to aggregate when not formulated.[66,67] PEG conjugation can help to decrease the propensity for protein aggregation.[43] Since our PEGylated products were stored without any additive in PBS, pH 7.4, at 4 °C, a three-month stability study was conducted with Fab_{beva} and the PEG-Fab_{beva} conjugates. SDS-PAGE analysis of PEG-Fab_{beva} (20, 30, and 40 kDa PEG) was conducted at the start (T0) and after 3 months (T3) (Figure S5, lanes 1−9). Samples of PEG_{30}-Fab_{beva} and PEG_{40}-Fab_{beva} were also analyzed by SDS-PAGE (Figure S5, lanes 10−13) after 24 months (T24) storage in PBS at 4 °C. No de-PEGylation was observed in the PEG-Fab solutions up to T24.

Dynamic light scattering (DLS) was also used to analyze Fab_{beva} and PEG_{20}-Fab_{beva} after storage over a three-month period (T0 to T3). Considerable aggregation of Fab_{beva} was observed at the three-month time point (T3) (Table S2). An average particle size of approximately 9.0 nm was measured for Fab_{beva} at T0, while an average particle size of about 14.2 nm was observed at T3 (Table S2) with aggregation observed at T3. The PEG_{20}-Fab_{beva} showed one peak in DLS analysis at T0 and T3 with an average particle size of 21.0 nm indicating that the PEG_{20}-Fab_{beva} was less prone to aggregation and remained essentially the same over the 3-month period. DLS analysis also showed that the PEG-Fab_{beva} solution at T3 was homogeneous with no trace of dePEGylation (data not shown).

Preparation of PEG-Fab_{trast} and PEG-Fab_{rani}. Two other Fabs were PEGylated using PEG-*mono*-sulfone **2** (20 kDa). Fab_{rani} is a clinically approved Fab that binds to VEGF, which was used directly for conjugation. Fab_{trast} was obtained from the papain digestion of trastuzumab followed by SEC purification. The digestion of trastuzumab required different purification conditions than were used for the bevacizumab digestion. In contrast to Fab_{beva}, Fab_{trast} also binds to protein A along with the Fc from trastuzumab.[51] SEC was therefore used to purify Fab_{trast} rather than using a protein A column.

PEGylation for both Fab_{rani} and Fab_{trast} was conducted in the same way as was done for Fab_{beva}. The Fab were first treated with excess DTT (Figure 2A, lanes 2 and 8), and then, the DTT was removed using a PD-10 column. PEG-*mono*-sulfone **2** (20 kDa, 2.0 equiv) was then added to the Fab solution, and after 3 h incubation, a full conversion into the PEGylated Fab was achieved (Figure 2A, lanes 3−4). As with PEG conjugates of Fab_{beva}, highly pure product was achieved by a single elution using ion exchange chromatography (Figure 2A, lanes 5−6 and 9−10). A yield of approximately 65% was obtained for both PEG_{20}-Fab_{rani} (n = 7) and PEG20-Fab_{trast} (n = 5) after purification.

PEGylation of Bevacizumab. Preliminary experiments were conducted to PEGylate bevacizumab. Scouting experiments with TCEP (1−24 equiv) suggested that the accessible disulfide from one of the Fabs, rather than both of the hinge disulfides, were more susceptible to reduction due to the presence of the light chain when treatment with TCEP was conducted at low stoichiometry and low conversion (Figure S6, lanes 1−10).[68] However, it is possible to be misled by such experiments because of the possibility for incomplete dissociation of the heavy chains in the conditions used for SDS-PAGE.

All the accessible disulfides appeared to be reduced (Figure 2B, lane 2) when using excess DTT, suggesting that, if the hinge disulfides were reduced, then heavy chain dissociation would have occurred in the conditions used. After removal of DTT (PD-10 column), the PEG-*mono*-sulfone **2** (1−4 equiv) was added and a good conversion to the PEGylated bevacizumab (Figure 2B, lane 3) was observed using 4 equiv of reagent **2**. The light chain that was present after DTT treatment at 25 kDa (Figure 2B, lane 2) broadly disappeared after addition of the PEG-*mono*-sulfone **2** (Figure 2B, lane 3) indicating that the conjugation site for PEG was likely to be at the Fab with the conditions that were used. What appeared to be mostly the mono-PEGylated bevacizumab was isolated by SEC (Figure S7A) followed by IEC (Figure S7B−C; Figure 2B, lanes 4−6). Most important for binding studies, silver staining indicated that no non-PEGylated bevacizumab was present after purification (Figure 2B, lane 6). No PEGylation was observed when bevacizumab was incubated with 4 equiv PEG **2** without prior treatment with DTT (Figure 2B, lane 7).

Binding Studies. *SPR Study Design.* Surface plasmon resonance (SPR) was used to determine the apparent binding affinities and kinetic rate constants of the unPEGylated starting materials and several of the purified PEG−Fab conjugates (Table 1, Figure 3). Since Fab_{beva}, $F(ab')_{2\text{-}beva}$, and Fab_{trast} were obtained by proteolytic digestion of the corresponding full-length antibody, it was necessary to determine if any of the binding properties for these Fabs had been retained. To examine the correlations with changes in PEG size, mono-PEG-Fab_{beva} conjugates with 20, 30, and 40 kDa PEG (Figure 3,

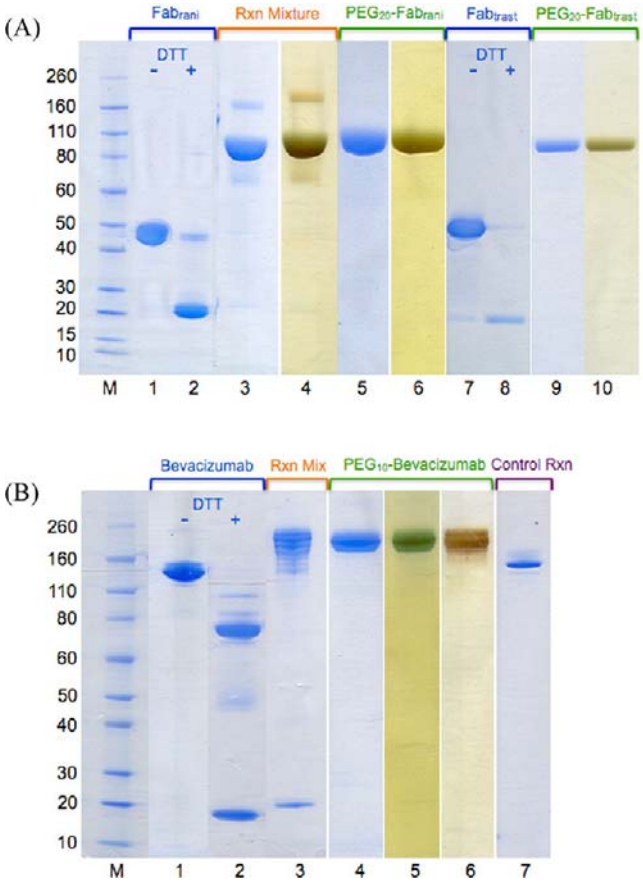

Figure 2. (A) PEGylation of ranibizumab (Fab_{rani}) and Fab_{trast} derived from the proteolytic digestion of trastuzumab with papain. For all of the gels, Lane M: protein standards (colloidal blue). Lane 1: Fab_{rani}. Lane 2: Fab_{rani} treated with DTT. Lanes 3–4: reaction mixture for the PEGylation after DTT treatment of Fab_{rani} with 2 equiv of PEG *mono*-sulfone **2** (20 kDa PEG) colloidal blue (lane 3) and colloidal blue + BaI_2 (lane 4). Lanes 5–6: purified PEG_{20}-Fab_{rani} colloidal blue (lane 5) and colloidal blue + BaI_2 (lane 6). Lane 7: Fab_{trast} obtained after digestion. Lane 8: Fab_{trast} after DTT treatment. Lanes 9–10: Purified PEG_{20}-Fab_{trast}, colloidal blue (lane 9) and colloidal blue + BaI_2 (lane 10). (B) PEGylation of bevacizumab with PEG-*mono*-sulfone **2** (10 kDa PEG). Lane 1: bevacizumab. Lane 2: bevacizumab treated with DTT. Lane 3: reaction mixture for the PEGylation of bevacizumab after treatment with DTT with PEG-*mono*-sulfone **2** (4 equiv, 10 kDa PEG). Lanes 4–6: purified PEG_{10}-bevacizumab detected with colloidal blue (lane 4), colloidal blue + BaI_2 (lane 5) and silver staining (lane 6). Lane 7: control reaction of PEG-*mono*-sulfone **2** (4 equiv, 10 kDa PEG) and bevacizumab without prior DTT treatment. PEG tends to migrate at about twice its molecular weight in SDS-PAGE, so as an example, PEG_{20}-Fab_{beva} (lane 10) appears at the 90 kDa protein marker band ((2 × 20)kDa + 50 kDa = 90 kDa).

lanes 4–6) and $PEG_{2\times20}$-Fab'_{beva} (Figure 3, lane 7) were studied. Both ranibizumab and PEG_{20}-Fab_{rani} were evaluated (Figure 3, lanes 8–9) to compare with the PEGylated Fab_{beva} products.

The SPR binding studies with bevacizumab and ranibizumab were conducted using $VEGF_{165}$ that was immobilized onto either a CM3 or CM5 sensor chip. HER2 was similarly immobilized to evaluate trastuzumab, Fab_{trast} and PEG_{20}-Fab_{trast} (Table 1, Figure 3 lanes 10–11).

Both Fab_{beva} and $F(ab')_{2\text{-}beva}$ were evaluated using a series of concentrations (0.18–2.88 μM for Fab_{beva} and 0.07–1.25 μM for $F(ab')_{2\text{-}beva}$). The binding sensorgrams (Figure 4A,B)

Table 1. Summary of the Purified Constructs Used in the Biacore Study[a]

antibody	PEG-antibody	Fab	PEG-Fab
Bevacizumab	PEG_{10}-bevacizumab	Fab_{beva}	PEG_{20}-Fab_{beva}
			PEG_{30}-Fab_{beva}
			PEG_{40}-Fab_{beva}
			$PEG_{2\times20}$-Fab'_{beva}
	Ranibizumab (Fab_{rani})		PEG_{20}-Fab_{rani}
Trastuzumab		Fab_{trast}	PEG_{20}-Fab_{trast}

[a]The concentration ranges used were: 0.04–0.60 μM for bevacizumab, PEG_{10}-bevacizumab, and trastuzumab; and 0.07–2.00 μM for Fab_{beva}, Fab_{trast}, Fab_{rani} and their PEGylated derivatives. A minimum of two independent kinetic assays was performed for each construct.

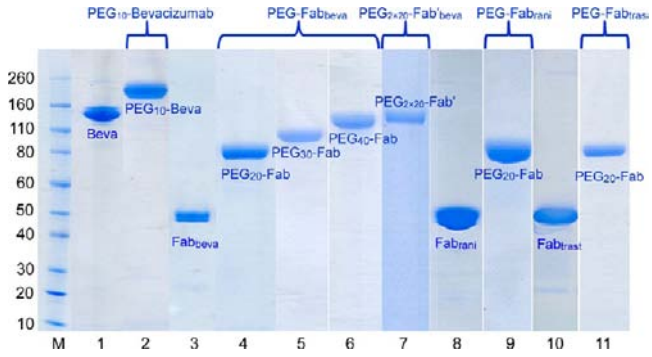

Figure 3. SDS-PAGE gel of the purified constructs listed in Table 1 that were evaluated by Biacore, Novex Bis-Tris 4–12% gel stained with colloidal blue (Lanes M-11). Lane 1: Bevacizumab. Lane 2: Purified PEG_{10}-bevacizumab. Lane 3: Fab_{beva}. Lanes 4–6: Purified 20, 30, and 40 kDa PEG-Fab_{beva}. Lane 7: Purified $PEG_{2\times20}$-Fab'_{beva}. Lane 8: Fab_{rani}. Lane 9: Purified PEG_{20}-Fab_{rani}. Lane 10: Fab_{trast}. Lane 11: Purified PEG_{20}-Fab_{trast}.

indicated that concentration-dependent binding was maintained to VEGF (CM5 chip, 208 RU or response units) for both Fab_{beva} and $F(ab')_{2\text{-}beva}$.

To determine the apparent binding affinity (K_D) and the association (k_a) and dissociation rate constants (k_d), CM3 sensor chips were prepared with lower immobilized levels of the $VEGF_{165}$ ligand (57–61 RU) to minimize mass transfer and rebinding effects.[69,70] One mass transfer limitation is the situation where the binding rate of the analyte (i.e., sample) is faster than the rate that the analyte can be delivered to the immobilized ligand surface. In such a situation, the association (k_a) and dissociation (k_d) rate constants cannot be accurately measured. It is also possible, in principle, that analyte cross-linking may occur at a relatively high immobilization density or concentration on the chip surface. If a high amount, or density, of a ligand is immobilized on the chip, a bivalent analyte such as bevacizumab can in principle bind to two different VEGF molecules (illustrated in Figure S8 A), making it difficult to estimate a kinetic fitting model. A low level of immobilized ligand would be expected to minimize such cross-linking (Figure S8 B).

Experiments for each PEG product were conducted with two different sensor chips that were evaluated on different days. Examples of the kinetic fitting curves and residual plots are given in Figure S9. The kinetic rate constants and affinities were calculated using a 1:1 binding model (Table 2) using the fitting parameters listed in Table S3. The association rate constant (k_a) is analogous to the "on rate" (k_{on}).[70,71] Likewise, the

dx.doi.org/10.1021/bc300372r | *Bioconjugate Chem.* 2012, 23, 2262–2277

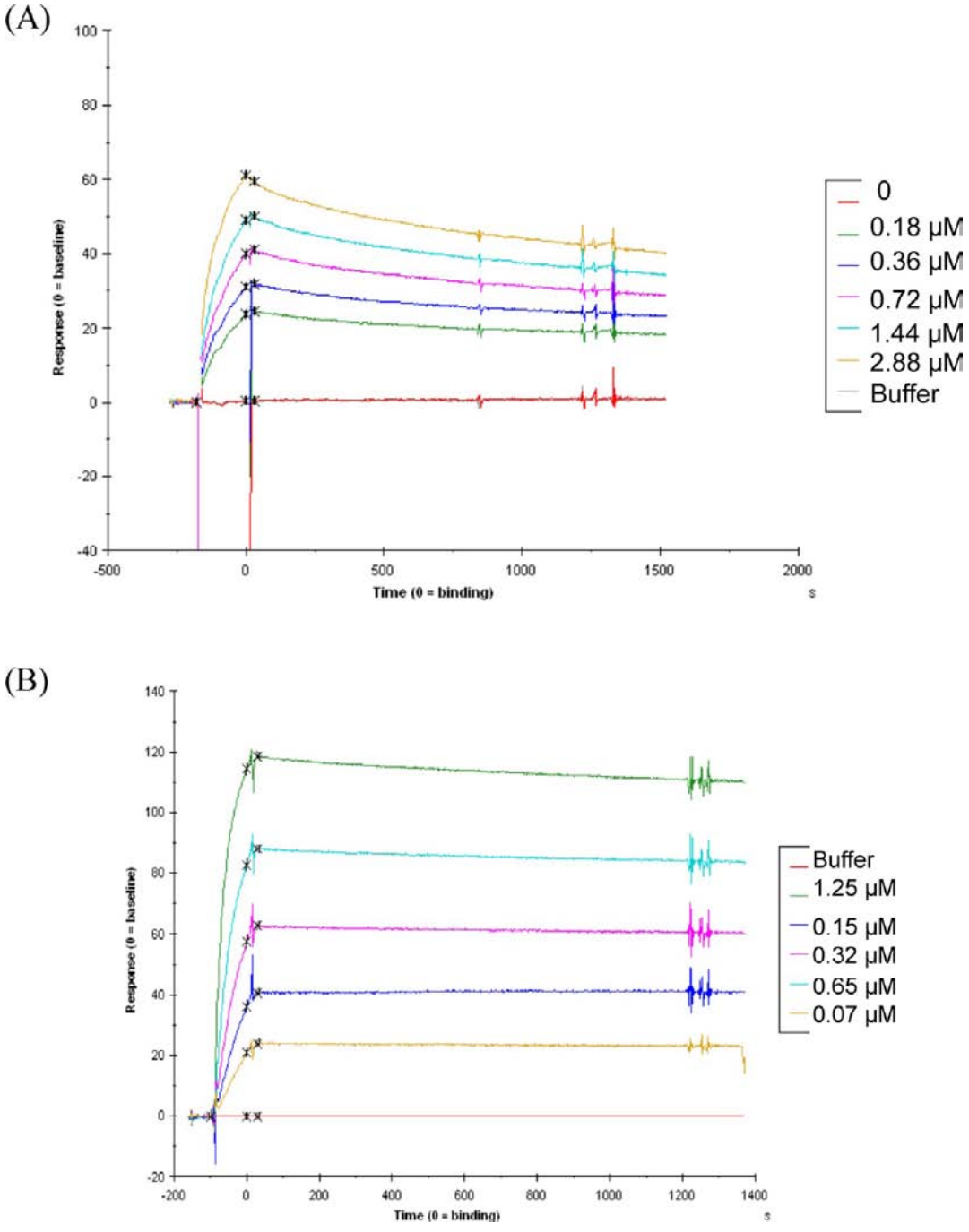

Figure 4. A CM5 chip with immobilized VEGF (208 RU) was used to obtain the binding sensorgrams of (A) Fab_{beva} and (B) $F(ab')_{2\text{-}beva}$.

dissociation rate constant (k_d) is analogous to the "off rate" (k_{off}).

Binding of unPEGylated Molecules to Immobilized VEGF. An apparent K_D of 1.33 nM (25 °C) was determined for bevacizumab (Table 2) and is comparable to a K_D for bevacizumab that had been obtained in another study at 37 °C (2.2 nM).[72] It is important to note that binding constants change with temperature[73] and some variation is often seen between different studies.

Fab_{beva} displayed an apparent K_D of 6.66 nM (25 °C) (Table 2). A related Fab (Fab-12) that binds to VEGF was reported to display an apparent K_D of 8.5 nM (37 °C) using a 1:1 binding model.[72] It is thought that Fab-12 has the same binding region or CDR as bevacizumab. Fab_{beva} displays a lower apparent binding affinity compared to bevacizumab because Fab_{beva} displays slower association and faster dissociation rate constants (Table 2). These differences between association and dissociation rate constants of Fab_{beva} and bevacizumab were similar to what was reported for Fab-12 and bevacizumab[72,74] (Table S4).

Since immobilized VEGF is a dimeric ligand with two binding sites, bevacizumab would be expected to display a better apparent affinity than the monomeric Fab_{beva} due to the cooperativity (or avidity) of the two Fabs that are present in intact bevacizumab.[74,75] Indeed, the association constant for Fab_{beva} (2.01×10^4 M^{-1} s^{-1}) was less than that of bevacizumab (6.12×10^4 M^{-1} s^{-1}). Also, Fab_{beva} showed a greater propensity to dissociate (k_d = 13.40×10^{-5} s^{-1}) from the immobilized

dx.doi.org/10.1021/bc300372r | Bioconjugate Chem. 2012, 23, 2262−2277

Table 2. Average Kinetic Rate Constants and Apparent Affinities of Fab_{beva}, Fab_{rani}, and Their PEGylated Conjugates in Biacore Using CM3 Chips with Immobilized VEGF (57 or 61 RU)[a]

sample	k_a ($\times 10^4$) M^{-1} s^{-1}	k_d ($\times 10^{-5}$) s^{-1}	K_D (k_d/k_a) nM
Bevacizumab	6.12	8.16	1.33
$F(ab')_{2\text{-beva}}$	5.49	6.39	1.16
Fab_{beva}	2.01	13.40	6.66
PEG_{20}-Fab_{beva}	0.96	12.10	12.00
PEG_{30}-Fab_{beva}	0.88	9.67	10.98
PEG_{40}-Fab_{beva}	1.01	11.90	10.79
$PEG_{2\times20}$-Fab'_{beva}	1.13	10.92	9.59
Fab_{rani}	3.65	NA	NA
PEG_{20}-Fab_{rani}	1.74	NA	NA
PEG_{10}-bevacizumab	1.51	8.20	5.49

[a]A minimum of two independent kinetic assays were performed on each construct except for PEG_{40}-Fab_{beva}, PEG_{10}-bevacizumab, and $PEG_{2\times20}$-Fab'_{beva}. NA: Not available as no dissociation was measured at 25 °C.

VEGF than bevacizumab (8.16×10^{-5} s^{-1}) (Table 2). These observed differences in k_a, k_d, and K_D between Fab_{beva} and bevacizumab confirm the enhanced binding effects that can be caused by the bivalency of bevacizumab. The cooperative nature of two Fab_{beva} binding moieties in the same molecule was further corroborated, as there was little difference in the apparent affinity and kinetic values for $F(ab')_{2\text{-beva}}$ and bevacizumab (Table 2). These observations also confirmed that the two fragments, Fab_{beva} and $F(ab')_{2\text{-beva}}$, which had been obtained by the proteolytic digestion of bevacizumab, had maintained their binding properties.

To illustrate the relative dissociation profiles of the unPEGylated molecules, the sensorgrams of bevacizumab, Fab_{beva} and $F(ab')_{2\text{-beva}}$ were overlaid (Figure 5A). Dissociation rate is an important parameter, as it indicates the tendency for a bound pair of molecules to remain bound together. Bevacizumab, Fab_{beva}, and $F(ab')_{2\text{-beva}}$ displayed equivalent RU at the end of the binding phase at different concentrations (0.3 μM, 2.0 μM, and 1.7 μM, respectively). These sensorgrams were then superimposed across the dissociation time (1400 s) and normalized by adjustment of the baseline to zero with a dissociation phase equal to 100 RU. The result showed that the rate of dissociation for bevacizumab and $F(ab')_{2\text{-beva}}$ were similar, but less than that of Fab_{beva}.

The observed association rate constant (k_a) for Fab_{rani} was less than for bevacizumab (Table 2), but greater than what was observed for Fab_{beva}. This is consistent with the report that the CDR for Fab_{rani} has a higher apparent affinity for VEGF than that for bevacizumab.[76] We calculated the k_a for Fab_{rani} to be 3.65×10^4 M^{-1} s^{-1} (25 °C), which is similar to the k_a values reported in the literature, such as 5.6×10^4 M^{-1} s^{-1} (25 °C) using a 1:1 binding model[77] (Table S4). As others have found,[84] it was not possible to calculate the dissociation constant, k_d, and consequently K_D, by SPR for Fab_{rani}, since dissociation was too slow at 25 °C.

A similar result was observed when the apparent binding affinity of a Fab-12 mutant that was evaluated using Biacore at 25 °C.[84] Amino acids in the CDR region of Fab-12 were substituted to improve the binding affinity of Fab-12 to $VEGF_{165}$ and the affinity values of these different mutants were compared. The dissociation rate constant of one of the highest-affinity mutants (Y0317) was very slow and could not be determined in the SPR experiments that had been conducted at 25 °C (Table S4). However, it was possible to calculate the k_d of Y0317 when the kinetic assay temperature in the Biacore was increased to 37 °C. Y0317 later became known as ranibizumab;[76] however, it is not clear from the literature what further structural differences may have been made.

Binding of PEG-Fab_{beva} and PEG-Fab_{rani} to Immobilized VEGF. Three purified PEG-Fab_{beva} products derived from PEG molecular weights of 20, 30, and 40 kDa were evaluated (Table 2). Compared to the unPEGylated Fab_{beva}, the PEGylated products associated more slowly with the immobilized VEGF by about a factor of 2. All three PEGylated products displayed nearly equivalent k_a values (Table 2). All PEGylated Fab_{beva} products displayed similar k_d values, which were about the same as the unPEGylated Fab_{beva} (Table 2, Figure 5B). This suggests that, while PEGylation slows the association of the PEGylated Fab to the immobilized VEGF, once bound, the PEG-Fab_{beva} behaves like its unPEGylated precursor protein. The invariance of the dissociation rate to site-specific PEGylation compared to the unPEGylated precursor protein has been observed previously with single chain fragments engineered with a free cysteine and PEGylated with maleimide reagents.[41,42,78,79]

The slower rate of association for the three PEG-Fab_{beva} products compared to the unPEGylated Fab_{beva} may be due to a combination of effects related to the steric mass and shielding of the conjugated PEG molecule. Considering how the Biacore experiment is conducted, PEG-Fab_{beva} would be expected to diffuse from the bulk solution to the sensor surface less readily due to its increased molecular mass. However, such diffusion effects for PEGylated proteins appears to play a lesser role in an SPR experiment.[41] Another plausible explanation is that, once a PEGylated protein is bound to an immobilized ligand, the bound PEG molecule can block the association of neighboring, incoming PEGylated molecules.[41] This certainly could be the case for ligands immobilized at densities that allow such steric effects to influence association rates.

Association rate (k_a) rather than dissociation rate (k_d) appears to most influence the differences in the apparent affinities (K_D) between Fab_{beva} and its PEGylated products. We observed a 1.5- to 2-fold reduction in K_D values for the PEG-Fab_{beva} compared to Fab_{beva} (Table 2). This is due to an approximate 2-fold reduction in k_a values for the PEG-Fab_{beva} products. Other related SPR studies also describe reduced apparent affinities (up to 10-fold) due to reduced association rates.[42,78] When the PEGylated protein is immobilized to the sensor chip, there is often no reduction in the association rate. Hence, it is important that the PEGylated protein of interest is in the mobile phase when evaluated by Biacore.

Similarly, PEG_{20}-Fab_{rani} also displayed an approximately 2-fold reduction in the association rate compared to Fab_{rani}, although their k_d values could not be measured due to their tight binding to immobilized VEGF (Table 2). Furthermore, the conjugation of two PEG molecules to Fab'_{beva} ($PEG_{2\times20}$-Fab'_{beva}) did not change the k_a or the k_d values compared to the mono-PEGylated Fab_{beva} constructs (Table 2). Together, these results demonstrate using two anti-VEGF Fabs that site-specific PEGylation using the PEG-*mono*-sulfone **2** results in a similar reduction in the association rate for the PEGylated products regardless of size and number of PEG molecules that are conjugated, and that the dissociation rate remains unchanged compared to that of the native Fab.

These observations are consistent with the previous reports that activity is broadly independent of PEG molecular weight

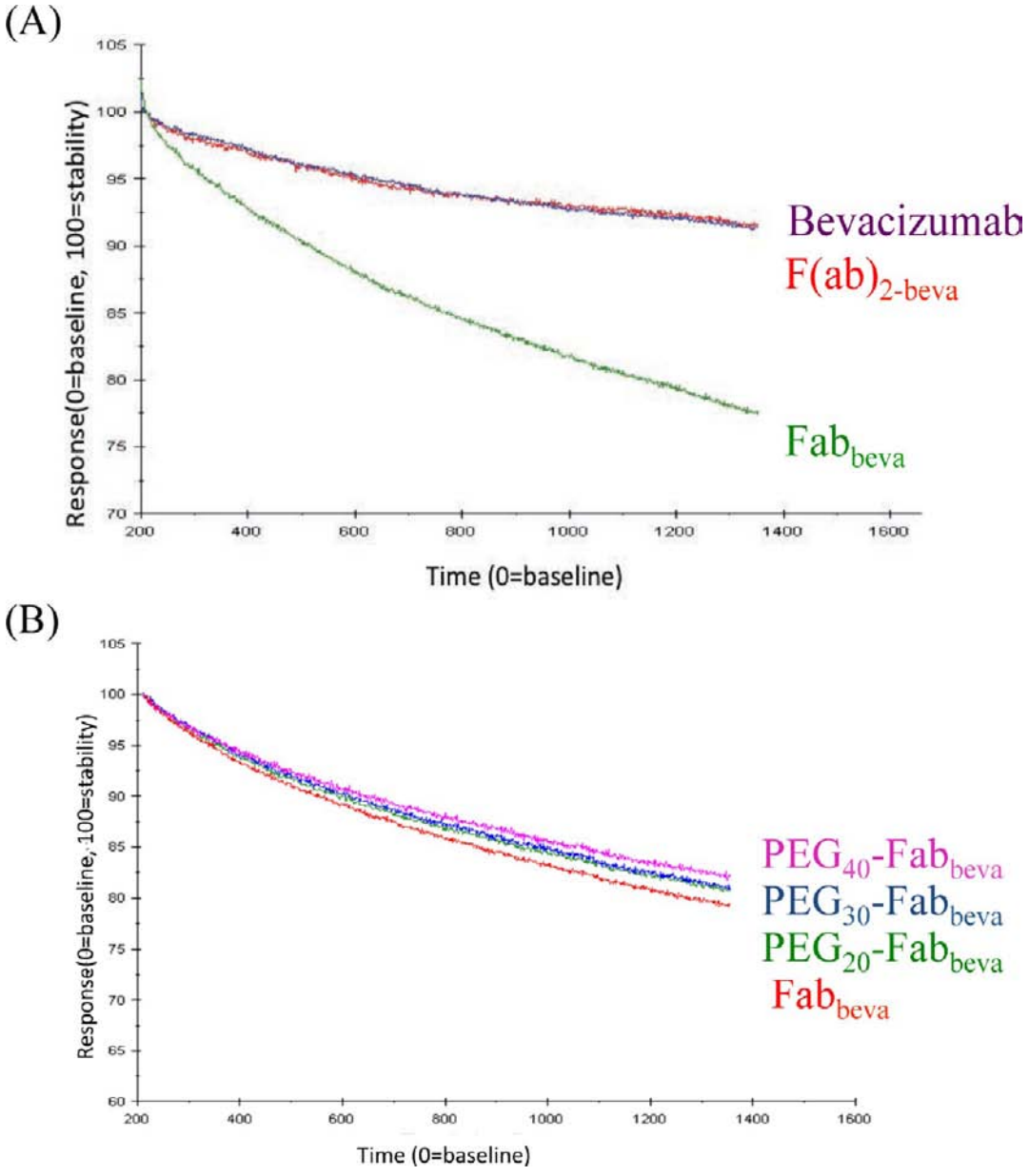

Figure 5. Dissociation rate profile of (A) bevacizumab, $F(ab')_{2\text{-beva}}$ and $Fab_{beva,}$ and (B) Fab_{beva}, 20, 30, and 40 kDa PEG-Fab_{beva}.

when the PEG is conjugated site-specifically.[36] Presumably, this is due to the site-specific nature of the PEGylation that was used and by the fact, that in the Fabs described here, the PEG molecules were as far from the binding region of the Fab as possible. Some effects of PEG steric shielding probably have a threshold molecular weight. Once this threshold molecular weight is achieved, then some effects or properties may not significantly change with further increases in PEG molecular weight if the PEG is conjugated to the same site on the molecule. The concept of the invariance of some polymer properties with further increases in polymer molecular weight after a threshold molecular weight has been achieved is well-known in polymer science. This property has the potential to aid in the development of new protein-based medicines, because pharmacokinetics, biodistribution, and formulation properties can be optimized without varying binding properties.

Binding of PEG_{20}-Fab_{beva} and PEG_{20}-Fab_{rani} as Determined by ELISA. A direct enzyme-linked immunosorbent assay (ELISA) was utilized as a means to determine if the binding trends that were observed by SPR between the unPEGylated and PEGylated variants of Fab_{beva} and Fab_{rani} would again be observed. ELISA is appropriate for evaluating strongly interacting molecules,[80,81] so we reasoned that it would be possible to measure the apparent relative affinities of Fab_{rani} and PEG_{20}-Fab_{rani}. While the affinity values obtained by ELISA were expected to differ compared to SPR,[82] the purpose was to determine if the relative trends in binding between the Fab and the PEG-Fab products were similar to what was observed by Biacore.

We first confirmed that the trends in apparent affinity observed for bevacizumab, $F(ab')_{2\text{-beva}}$, and Fab_{beva} by ELISA were the same as observed in the Biacore study (Figure 6A, Table 3). When the saturation binding curves for PEG_{20}-Fab_{beva} was compared against Fab_{beva}, a 2-fold lower binding affinity was again observed for the PEGylated Fab (Figure 6B, Table 3). Similar results were obtained for PEG_{20}-Fab_{rani} (Figure 6C,

dx.doi.org/10.1021/bc300372r | *Bioconjugate Chem.* 2012, 23, 2262−2277

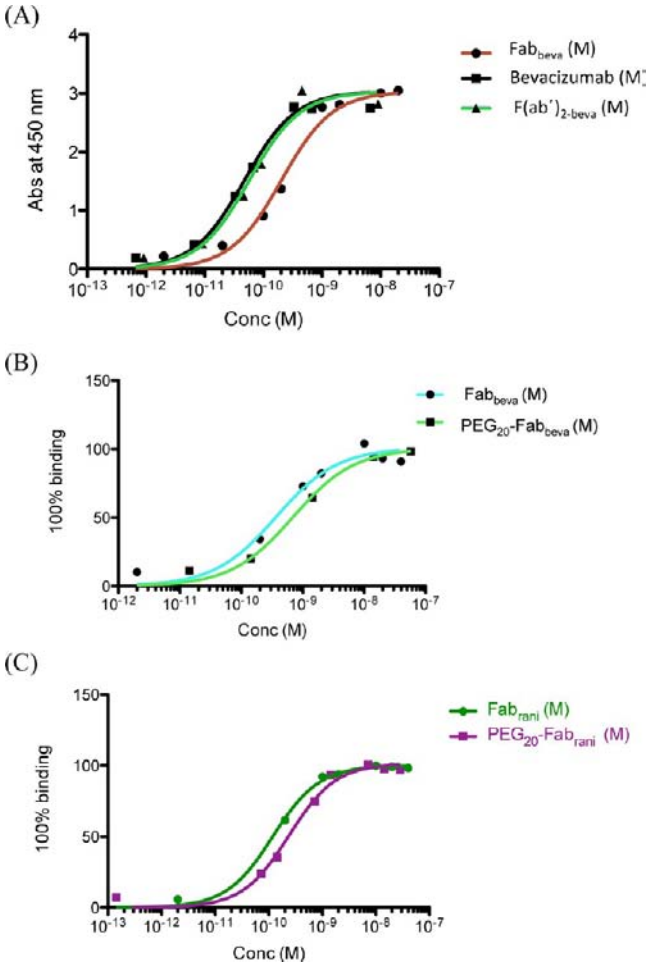

Figure 6. Superimposed ELISA binding curves of (A) bevacizumab, F(ab′)$_{2\text{-beva}}$ and Fab$_{beva}$, (B) Fab$_{beva}$ and PEG$_{20}$-Fab$_{beva}$, and (C) Fab$_{rani}$ and PEG$_{20}$-Fab$_{rani}$.

Table 3. Average Apparent Binding Affinity Values of Fabs and PEG−Fabs in ELISA[a]

sample	K_D (nM)
Bevacizumab	0.08
F(ab′)$_2$	0.07
Fab$_{beva}$	0.32
PEG$_{20}$-Fab$_{beva}$	0.61
Fab$_{rani}$	0.11
PEG$_{20}$-Fab$_{rani}$	0.22

[a]The concentration ranges were 4×10^{-12} to 2×10^{-8} M for the unPEGylated Fabs; 2×10^{-12} to 2×10^{-8} M for the PEGylated Fabs and 6×10^{-13} to 6×10^{-9} M for bevacizumab and F(ab′)$_{2\text{-beva}}$. The apparent binding affinities were obtained from two measurements and two independent ELISA assays.

Table 3). These results suggest that, although the apparent affinity constants were different, the trend obtained by ELISA was the same as by Biacore.

Considering the Dissociation Rate and the Contribution of Bivalency. Similar to what has been described elsewhere,[76] we observed by ELISA that the apparent affinity of Fab$_{rani}$ to VEGF was similar to that of bevacizumab and about 3-fold better than Fab$_{beva}$ (Figure S10, Table 3). There are therapeutic applications where a monovalent protein such as a Fab is needed rather than a bivalent IgG.[73,83,84] On the basis of our results comparing the apparent affinities of Fab$_{rani}$ to bevacizumab, only a modest 3- to 4-fold improvement in affinity is needed for a monovalent Fab to achieve the affinity of a bivalent IgG.

In the Biacore analysis, the dissociation rate of bevacizumab and its digested fragments was shown to be unaffected by PEGylation (Table 2). This is an important and desired property for PEGylated proteins. Low dissociation rates have the potential to extend residency time of a molecular species in a target tissue through sequestration or retention, while unbound molecules clear from circulation and other parts of the body.[85] This could become a strategy in the development of PEGylated molecules to optimize dosing schedules and efficacy.

Binding of PEG-Fab$_{trast}$ to Immobilized HER2. It is thought that trastuzumab binds to a single domain on HER2. Compared to VEGF$_{165}$, which is a homodimer, HER2 is a monomer. When HER2 is immobilized at a low density, then cross-linking with trastuzumab is not expected to occur. Using a low immobilization level of HER2 on a CM3 chip (51 RU), similar apparent affinities of 0.11 and 0.13 nM at 25 °C were calculated for trastuzumab and Fab$_{trast}$, respectively (Table 4). The

Table 4. Average Kinetic Rate Constants and Apparent Affinities of Trastuzumab, Fab$_{trast}$, and PEG$_{20}$-Fab$_{trast}$ as Determined by Biacore Using Immobilized HER2 (CM3 chip, 51 RU)[a]

sample	k_a ($\times 10^4$) M^{-1} s^{-1}	k_d ($\times 10^{-5}$) s^{-1}	K_D (k_d/k_a) nM
Trastuzumab	38.0	4.20	0.11
Fab$_{trast}$	102.0	11.50	0.13
PEG$_{20}$-Fab$_{trast}$	26.0	13.10	0.49

[a]Two independent kinetic assays were performed on trastuzumab and Fab$_{trast}$ and one assay was performed on PEG$_{20}$-Fab$_{trast}$.

association rate for trastuzumab was comparable to what has been previously observed using immobilized HER2 in the range 50−150 RU.[86] ELISA results also indicated that the relative binding affinity for trastuzumab and Fab$_{trast}$ were similar (Table 5, Figure 7), although again, the apparent K_D values from the

Table 5. Average Binding Affinity Values for Trastuzumab, the Fab$_{trast}$ and PEG$_{20}$-Fab$_{trast}$ in ELISA[a]

sample	K_D (nM)
Trastuzumab	0.06
Fab$_{trast}$	0.05
PEG$_{20}$-Fab$_{trast}$	0.09

[a]The concentration ranges used were 4×10^{-12} to 2×10^{-8} M for Fab$_{trast}$; 2×10^{-12} to 2×10^{-8} M for PEG$_{20}$-Fab$_{trast}$; and 6×10^{-13} to 6×10^{-9} M for trastuzumab. One ELISA assay was performed for trastuzumab, Fab$_{trast}$ and PEG$_{20}$-Fab$_{trast}$.

Biacore and ELISA analyses were different. Interestingly, Biacore measurements markedly differed for a monovalent Affibody compared to the bivalent form of the Affibody when the HER2 immobilization density was much higher (~2200 RU)[87] than was used previously[86] or in our study.

In the Biacore analysis (Table 4), the k_a and k_d values were substantially different between trastuzumab and Fab$_{trast}$. While the k_a value could be influenced by mass transfer and diffusion processes that are inherent in this experiment, the dissociation of Fab$_{trast}$ was about 3-fold faster than that observed for trastuzumab. This is consistent with dissociation being

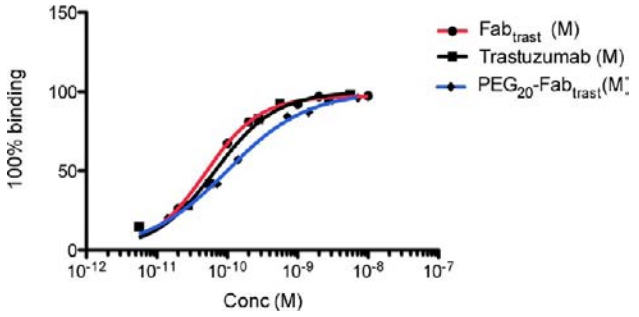

Figure 7. Superimposed ELISA binding saturation curves of trastuzumab, Fab_{trast} and PEG_{20}-Fab_{trast}.

influenced by the valency of the binding molecule to a monovalent target. When a bivalent molecule such as an IgG dissociates from a monovalent target, there is a greater chance of reassociation compared to a monovalent Fab. While the orientation of an immobilized ligand[88] may influence binding, higher functional affinity would be expected with an immobilized bivalent ligand (VEGF) than with a monovalent ligand (HER2).[44,89−92]

The apparent affinity of PEG_{20}-Fab_{trast} was about 4- to 5-fold less than observed for trastuzumab and unPEGylated Fab_{trast} (Table 4). A similar 5-fold decrease was observed for an anti-$p185^{HER2}$ scFv that had been site-specifically PEGylated on an inserted cysteine thiol far from the binding site.[41] As with the other PEGylated Fabs described in this study, the dissociation rate of PEG_{20}-Fab_{trast} was similar to that of the unPEGylated Fab_{trast}.

CONCLUSIONS

Fabs undergo near-quantitative PEGylation with PEG-*bis*-sulfone reagents **1** (10−40 kDa). PEG is essentially conjugated at the same site in the Fab as the heavy chain when the Fab is part of an IgG (Scheme 3). No PEGylation was observed unless the Fab was first incubated with DTT. Purification of the corresponding PEG-Fab was accomplished by a single elution over an ion exchange column to give a pure PEGylated product as determined by silver stained SDS-PAGE. The PEGylated products all appeared to be stable without evidence of de-PEGylation.

Fabs used in this study were selected so that binding properties could be compared to the corresponding Fab when part of an IgG framework. The two ligands selected were $VEGF_{165}$, which is a dimeric ligand with two binding sites, and the other ligand was HER2 with one domain for binding. In the SPR experiments using Biacore, we examined the comparative binding of a small family of PEG-Fab constructs derived from bevacizumab, ranibizumab, and trastuzumab under low ligand immobilization densities. The combination of the PEGylated products from these antibodies and the two ligands allowed us to examine some aspects of mono- and bivalency.

In the SPR studies using Biacore, the apparent K_D value for PEG-Fab_{beva} was 2-fold less compared to the unPEGylated Fab_{beva}. Binding properties of the PEG-Fab_{beva} products appear to be independent of PEG molecular weight. A similar result was achieved for $PEG_{2\times20}$-Fab'_{beva} that has two PEG chains at a similar location to PEG-Fab_{beva} (Scheme 3). The lower K_D values for the PEGylated Fab_{beva} and Fab'_{beva} were due to the changes in k_a. The different PEG molecular weight versions of PEG-Fab_{beva} appear to remain bound to the immobilized VEGF to about the same degree as Fab_{beva}.

As with ranibizumab (Fab_{rani}), it was not possible to obtain the K_D value of PEG_{20}-Fab_{rani} by Biacore, since once bound, both of these molecules did not dissociate from the immobilized VEGF at 25 °C. However, in the ELISA, PEG_{20}-Fab_{rani} showed a 2-fold lower apparent K_D value compared to the unPEGylated Fab_{rani}.

The apparent K_D values for trastuzumab and Fab_{trast} were similar when analyzed in Biacore and ELISA. Interestingly, trastuzumab had a slower k_a compared to Fab_{trast}, but both molecules displayed the same K_D value due to the slower k_d of trastuzumab. This could be due to a localized rebinding effect of the bivalent trastuzumab to immobilized HER2. Analogous to PEGylated Fab_{beva}, PEG_{20}-Fab_{trast} also displayed an almost 2-fold lower apparent affinity compared to Fab_{trast} when evaluated by ELISA. Biacore results showed that, while the k_d values were again similar between unPEGylated and PEGylated Fab, there was a substantial difference in the k_a values in this experiment. This resulted in PEG_{20}-Fab_{trast} displaying a 4-fold lower apparent affinity compared to the unPEGylated Fab_{trast}. The variations in the apparent affinity of the PEGylated products were all broadly related to the differences in the association rates (k_a).

ASSOCIATED CONTENT

Supporting Information

Additional data include (i) SDS-PAGE gel, IEC, and representative SECs for the proteolytic digestion of bevacizumab to obtain Fab_{beva}; (ii) representative IEC and SDS-PAGE gel of the collected fractions of PEG_{20}-Fab_{beva}; (iii) representative MALDI-TOF spectra of bevacizumab, Fab_{beva}, and PEG_{20}-Fab_{beva}; (iv) representative SDS-PAGE gels from the stability studies PEG-Fab_{beva} conjugates; (v) SDS-PAGE gel showing the partial reduction of bevacizumab and the SEC of PEG_{10}-bevacizumab; (vi) illustration of the difference between high and low immobilization density of VEGF for SPR studies; (vii) representative fitting curves and residual plots of bevacizumab, Fab_{beva}, $F(ab')_{2\text{-}beva}$, PEG_{20}-Fab_{beva}, and PEG_{20}-Fab_{trast}; (viii) representative ELISA binding saturation curves for bevacizumab, Fab_{rani} and Fab_{beva}; (ix) representative data and calculation to determine the amount of free thiol using the Ellman's assay; (x) DLS data for Fab_{beva} and PEG_{20}-Fab_{beva} after storage for 3 months; (xi) the SPR kinetic constants and parameters of bevacizumab, ranibizumab, trastuzumab, and their PEGylated derivatives; and (xii) comparative SPR derived binding data from the literature of bevacizumab, ranibizumab and Fab-12. This material is available free of charge via the Internet at http://pubs.acs.org.

AUTHOR INFORMATION

Corresponding Author

*E-mail: steve.brocchini@ucl.ac.uk.

Notes

The authors declare the following competing financial interest(s): S.B. is a full-time academic employee of the UCL School of Pharmacy, University College London. As a co-founder of PolyTheris Ltd he has equity in the company, but receives no financial compensation. He is a non-paid director and acts as a non-paid CSO. A.G. and J.C. are full-time employees of PolyTherics.

■ ACKNOWLEDGMENTS

H.K. gratefully acknowledges funding from the Overseas Research Student Fund and PolyTherics Ltd. S.B. is grateful for funding from NIHR Moorfields Biomedical Research Centre and the UK Engineering & Physical Sciences Research Council (EPSRC) for the EPSRC Centre for Innovative Manufacturing in Emergent Macromolecular Therapies. Financial support from the consortium of industrial and governmental users is also acknowledged. We are also grateful to Mr. Farzad Khayrzad of PolyTherics Ltd. for the synthesis and provision of the PEGylation reagents.

■ REFERENCES

(1) Elbakri, A., Nelson, P. N., and Abu Odeh, R. O. (2010) The state of antibody therapy. *Hum. Immunol. 71* (12), 1243−1250.
(2) Holliger, P., and Hudson, P. J. (2005) Engineered antibody fragments and the rise of single domains. *Nat. Biotechnol. 23* (9), 1126−1136.
(3) Nelson, A. L., and Reichert, J. M. (2009) Development trends for therapeutic antibody fragments. *Nat. Biotechnol. 27* (4), 1−7.
(4) Fischer, N., and Leger, O. (2007) Bispecific antibodies: Molecules that enable novel therapeutic strategies. *Pathobiology 74* (1), 3−14.
(5) Gebauer, M., and Skerra, A. (2009) Engineered protein scaffolds as next-generation antibody therapeutics. *Curr. Opin. Chem. Biol. 13* (3), 245−255.
(6) Boersma, Y. L., and Plückthun, A. (2011) Darpins and other repeat protein scaffolds: Advances in engineering and applications. *Curr. Opin. Biotechnol. 22* (6), 849−857.
(7) Lipovsek, D. (2011) Adnectins: Engineered target-binding protein therapeutics. *Protein Eng. 24* (1−2), 3−9.
(8) Schellekens, H. (2002) Immunogenicity of therapeutic proteins: Clinical implications and future prospects. *Clin. Ther. 24* (11), 1720−1740.
(9) Farrell, R. A., Marta, M., Gaeguta, A. J., Souslova, V., Giovannoni, G., and Creeke, P. I. (2012) Development of resistance to biologic therapies with reference to ifn-. *Rheumatology 51* (4), 590−599.
(10) Giezen, T., Mantel-Teeuwisse, A., Straus, S., Schellekens, H., Leufkens, H., and Egberts, A. (2008) Safety-related regulatory actions for biologicals approved in the united states and the european union. *J. Am. Med. Assoc. 300* (16), 1887−1896.
(11) Singh, S. K. (2011) Impact of product-related factors on immunogenicity of biotherapeutics. *J. Pharm. Sci. 100* (2), 354−387.
(12) Bailon, P., and Won, C. (2009) Peg-modified biopharmaceuticals. *Expert Opin. Drug Delivery 6* (1), 1−16.
(13) Hamidi, M., Rafiei, P., and Azadi, A. (2008) Designing pegylated therapeutic molecules: Advantages in admet properties. *Expert Opin. Drug Discovery 3* (11), 1293−1307.
(14) Jevsevar, S., Kunstelj, M., and Porekar, V. G. (2010) Pegylation of therapeutic proteins. *Biotechnol. J. 5* (1), 113−128.
(15) Smith, P., Krohn, R., Hermanson, G., Mallia, A., Gartner, F., Provenzano, M., Fujimoto, E., Goeke, N., Olson, B., and Klenk, D. (1985) Measurement of protein using bicinchoninic acid. *Anal. Biochem. 150*, 76−85.
(16) Payne, R. W., Murphy, B. M., and Manning, M. C. (2010) Product development issues for pegylated proteins. *Pharm. Dev. Technol.*, 1−18.
(17) Pisal, D. S., Kosloski, M. P., and Balu-Iyer, S. V. (2010) Delivery of therapeutic proteins. *J. Pharm. Sci. 99* (6), 2557−2575.
(18) Veronese, F. (2001) Peptide and protein pegylation a review of problems and solutions. *Biomaterials 22* (5), 405−417.
(19) Veronese, F. M. (2009) *Pegylated protein drugs: Basic science and clinical applications. Milestones in drug therapy* (Parnham, M. J., and Bruinvels, J., Eds.) Birkhauser, Basel.
(20) Harris, J. M., and Chess, R. B. (2003) Effect of pegylation on pharmaceuticals. *Nat. Rev. Drug Dis. 2* (3), 214−221.
(21) Kochendoerfer, G. G. (2005) Site-specific polymer modification of therapeutic proteins. *Curr. Opin. Chem. Biol. 9*, 555−560.
(22) Pasut, G., Guiotto, A., and Veronese, F. M. (2004) Protein, peptide and non-peptide drug pegylation for therapeutic application. *Expert Opin. Ther. Pat. 14* (5), 1−36.
(23) Webster, R., Didier, E., Harris, P., Siegel, N., Stadler, J., Tilbury, L., and Smith, D. (2007) Pegylated proteins:Evaluation of their safety in the absence of definitive metabolism studies. *Drug Metab. Dispos. 35* (1), 9−16.
(24) Zalipsky, S. (1995) Chemistry of poly(ethylene glycol) conjugates with biologically active molecules. *Adv. Drug Delivery Rev. 16*, 157−182.
(25) Roberts, M. J., Bentley, M. D., and Harris, J. M. (2002) Chemistry for peptide and protein pegylation. *Adv. Drug Delivery Rev. 54*, 459−476.
(26) Rosendahl, M. S., Doherty, D. H., Smith, S. J., Carlson, S. J., Chlipala, E. A., and Cox, G. N. (2005) A long-acting, highly potent interferon a-2 conjugate created using site-specific pegylation. *Bioconjugate Chem. 16*, 200−207.
(27) Doherty, D. H., Rosendahl, M. S., Smith, D. J., Hughes, J. M., Chlipala, E. A., and Cox, G. N. (2005) Site-specific pegylation of engineered cysteine analogues of recombinant human granulocyte-macrophage colony-stimulating factor. *Bioconjugate Chem. 16* (5), 1291−1298.
(28) Mei, B., Pan, C., Jiang, H., Tjandra, H., Strauss, J., Chen, Y., Liu, T., Zhang, X., Severs, J., Newgren, J., Chen, J., Gu, J. M., Subramanyam, B., Fournel, M. A., Pierce, G. F., and Murphy, J. E. (2010) Rational design of a fully active, long-acting pegylated factor viii for hemophilia a treatment. *Blood 116* (2), 270−279.
(29) Yang, K., Basu, A., Wang, M., Chintala, R., Hsieh, M., Liu, S., Hua, J., Zhang, Z., Zhou, J., Li, M., Phyu, H., Petti, G., Mendez, M., Janjua, H., Peng, P., Longley, C., Borowski, V., Mehlig, M., and Filpula, D. (2003) Tailoring structure-function and pharmacokinetic properties of single-chain Fv proteins by site-specific pegylation. *Protein Eng. 16* (10), 761−770.
(30) Mooler, I., Thomas, A., Geyer, H., Schanzer, W., and Thevis, M. (2011) Synthesis, characterisation, and mass spectrometric detection of a pegylated epo-mimetic peptide for sports drug testing purpose. *Rapid Commun. Mass Spectrom. 25*, 2115−2123.
(31) Locatelli, F., and Vecchio, L. D. (2009) Hematide for the treatment of chronic kidney disease-related anemia. *Expert Rev. Hematol. 2* (4), 377−383.
(32) Nelson, A. L. (2010) Antibody fragments; hope and hype. *MABS 2* (1), 77−83.
(33) Tracey, D., Klereskog, L., Sasso, E. H., Salfeld, J. G., and Tak, P. P. (2008) Tumor necrosis factor antagonist mechanisms of action: A comprehensive review. *Pharmacol. Therapeut. 117*, 244−279.
(34) Alley, S. C., Benjamin, D. R., Jeffrey, S. C., Okeley, N. M., Meyer, D. L., Sanderson, R. J., and Senter, P. D. (2008) Contribution of linker stability to the activities of anticancer immunoconjugates. *Bioconjugate Chem. 19*, 759−765.
(35) Shen, B. Q., Xu, K., Liu, L., Raab, H., Bhakta, S., Kenrick, M., Parsons-Reponte1, K. L., Tien, J., Yu, S., Mai, E., Li, D., Tibbitts, J., Baudys, J., Saad, O. M., Scales, S. J., Mcdonald, P. J., Hass, P. E., Eigenbrot, C., Nguyen, T., Solis, W. A., Fuji, R. N., Flagella, K. M., Patel1, D., Spencer, S. D., Khawli, L. A., Ebens, A., Wong, W. L., Vandlen, R., Kaur1, S., Sliwkowski1, S. X., Scheller, R. H., Polakis, P., and Junutula1, J. R. (2012) Conjugation site modulates the in vivo stability and therapeutic activity of antibody-drug conjugates. *Nat. Biotechnol.*, 1−7.
(36) Shaunak, S., Godwin, A., Choi, J. W., Balan, S., Pedone, E., Vijayarangam, D., Heidelberger, S., Teo, I., Zloh, M., and Brocchini, S. (2006) Site-specific pegylation of native disulfide bonds in therapeutic proteins. *Nat. Chem. Biol.*, 312−313.
(37) Balan, S., Choi, J. W., Godwin, A., Teo, I., Laborde, C. M., Heidelberger, S., Zloh, M., Shaunak, S., and Brocchini, S. (2007) Site-specific pegylation of protein disulfide bonds using a three-carbon bridge. *Bioconjugate Chem. 18* (1), 61−76.

(38) Bakri, S. J., Snyder, M. R., Reid, J. M., Pulido, J. S., and Singh, R. J. (2007) Pharmacokinetics of intravitreal bevacizumab (avastin). *Ophthalmology 114* (5), 855−859.
(39) Ferrara, N., Hillan, K. J., Gerber, H. P., and Novotny, W. (2004) Discovery and development of bevacizumab, an anti-VEGF antibody for treating cancer. *Nat. Rev. Drug Discovery 3* (5), 391−400.
(40) Shih, T., and Lindley, C. (2006) Bevacizumab: An angiogenesis inhibitor for the treatment of solid malignancies. *Clin. Ther. 28* (11), 1779−1802.
(41) Kubetzko, S., Sarkar, C. A., and Plückthun, A. (2005) Protein pegylation decreases observed target association rates via a dual blocking mechanism. *Mol. Pharmacol. 68* (5), 1439−1454.
(42) Mabry, R., Rani, M., Geiger, R., Hubbard, G. B., Carrion, R., Brasky, K., Patterson, J. L., Georgiou, G., and Iverson, B. L. (2005) Passive protection against anthrax by using a high-affinity antitoxin antibody fragment lacking an Fc region. *Infect. Immun. 73* (12), 8362−8368.
(43) Chapman, A. P. (2002) PEGylated antibodies and antibody fragments for improved therapy: A review. *Adv. Drug Delivery Rev. 54*, 531−545.
(44) Gestwicki, J. E., Cairo, C. W., Mann, D. A., Owen, R. M., and Kiessling, L. L. (2002) Selective immobilization of multivalent ligands for surface plasmon resonance and fluorescence microscopy. *Anal. Biochem. 305* (2), 149−155.
(45) Colombo, M., Corsi, F., Foschi, D., Mazzantini, E., Mazzucchelli, S., Morasso, C., Occhipinti, E., Polito, L., Prosperi, D., Ronchi, S., and Verderio, P. (2010) HER2 targeting as a two-sided strategy for breast cancer diagnosis and treatment: Outlook and recent implications in nanomedical approaches. *Pharmacol. Res. 62* (2), 150−165.
(46) Cho, H. S., Mason, K., Ramyar, K. X., Stanley, A. M., Gabelli, S. B., Denney, D. W., Jr, and Leahy, D. J. (2003) Structure of the extracellular region of HER2 alone and in complex with the herceptin Fab. *Nature 421* (6924), 753−756.
(47) Kubetzko, S., Balic, E., Waibel, R., Wittke, U. Z., and Pluckthun, A. (2006) Pegylation and multimeriztion of the anti-p185 HER2 single chain fv fragment 4d5. *J. Biol. Chem. 281*, 35186−35201.
(48) Johansson, B. P., Shannon, O., and Björck, L. (2008) Ides: A bacterial proteolytic enzyme with therapeutic potential. *PLoS ONE 3* (2), e1692.
(49) Vincents, B., Von Pawel-Rammingen, U., BjöRck, L., and Abrahamson, M. (2004) Enzymatic characterization of the streptococcal endopeptidase, IdeS, reveals that it is a cysteine protease with strict specificity for IgG cleavage due to exosite binding. *Biochemistry 43*, 15540−15549.
(50) Akesson, P., Moritz, L., Truedsson, M., Christensson, B., and Pawel-Rammingen, U. V. (2006) Ides, a highly specific immunoglobulin g (IgG)-cleaving enzyme from streptococcus pyogenes, is inhibited by specific IgG antibodies generated during infection. *Infect. Immun. 74* (1), 497−503.
(51) Scollard, D. A., Chan, C., Holloway, C. M. B., and Reilly, R. M. (2011) A kit to prepare 111in-dtpa-trastuzumab (herceptin) Fab fragments injection under gmp conditions for imaging or radioimmunoguided surgery of her2-positive breast cancer. *Nucl. Med. Biol. 38* (1), 129−136.
(52) Myszka, D. G. (1999) Improving biosensor analysis. *J. Mol. Recognit. 12*, 279−284.
(53) Cresswell, C., Newcombe, A. P., Davies, S., Macpherson, I., Nelson, P., Apos, K. O., and Donovan, F. R. (2005) Optimal conditions for the papain digestion of polyclonal ovine IgG for the production of biotherapeutic Fab fragments. *Biotechnol. Appl. Biochem. 42* (2), 163.
(54) Rousseaux, J., Rousseaux-Prevost, R., and Bazin, H. (1983) Optimal conditions for the preparation of Fab and $F(ab)_2$ fragments from monoclonal IgG of different rat IgG subclasses. *J. lmmunol. Methods 64* (1−2), 141−146.
(55) Mitchel, R. E., Chaiken, I. M., and Smith, E. L. (1970) The complete amino acid sequence of papain. *J. Biol. Chem. 245* (14), 3485−3492.
(56) Brocchini, S., Godwin, A., Balan, S., Choi, J. W., Zloh, M., and Shaunak, S. (2008) Disulfide bridge based pegylation of proteins. *Adv. Drug Delivery Rev.*, 3−12.
(57) Humphreys, D. P., Heywood, S. P., Henry, A., Ait-Lhadj, L., Antoniw, P., Palframan, R., Greenslade, K. J., Carrington, B., Reeks, D. G., Bowering, L. C., West, S., and Brand, H. A. (2007) Alternative antibody Fabs; fragment pegylation strategies: Combination of strong reducing agents, disruption of the interchain disulphide bond and disulphide engineering. *Protein Eng. Des. Sel. 20* (5), 227−234.
(58) Humphreys, D. P., Vetterlein, O. M., Chapman, A. P., King, D. J., Antoniw, P., Suitters, A. J., Reeks, D. G., Parton, T. a. H., King, L. M., Smith, B. J., L.Ang, V., and Stephens, P. E. (1998) $F(ab)_2$ molecules made from escherichia coli produced Fab' with hinge sequences conferring increased serum survival in an animal model. *J. Immunol. Methods 217*, 1−10.
(59) Begg, G. E., and Speicher, D. W. (1999) Mass spectrometry detection and reduction of disulfide adducts between reducing agents and recombinant proteins with highly reactive cysteines. *J. Biomol. Technol. 10*, 17−20.
(60) Brocchini, S., Balan, S., Godwin, A., Choi, J. W., Zloh, M., and Shaunaik, S. (2006) Pegylation of native disulfide bonds in proteins. *Nat. Protoc. 1* (5), 2241−2252.
(61) Netto, L. E. S., and Stadtman, E. R. (1996) The iron-catalyzed oxidation of dithiothreitol is a biphasic process: Hydrogen peroxide is involved in the initiation of a free radical chain of reactions. *Arch. Biochem. Biophys. 330* (1), 233−242.
(62) Bjellqvist, B., Pasquali, C., Ravier, F., Sanchez, J., and Hochstrasser, D. (1993) A nonlinear wide-range immobilised ph gradient for two-dimensional electrophoresis and its definition in a relvent pH scale. *Electrophoresis 14*, 1357−1365.
(63) Liu, H., Chumsae, C., Gaza-Bulseco, G., Hurkmans, K., and Radziejewski, C. H. (2010) Ranking the susceptibility of disulfide bonds in human IgG1 antibodies by reduction, differential alkylation, and lc-ms analysis. *Anal. Chem.*, 1−8.
(64) Liu, X. Y., Pop, L. M., and Vitetta, E. S. (2008) Engineering therapeutic monoclonal antibodies. *Immunol. Rev. 222*, 9−27.
(65) Cong, Y., Pawlisz, E., Bryant, P., Balan, S., Laurine, E., Tommasi, R., Singh, R., Dubey, S., Peciak, K., Bird, M., Sivasankar, A., Swierkosz, J., Muroni, M., Heidelberger, S., Farys, M., Khayrzad, F., Edwards, J., Badescu, G., Hodgson, I., Heise, C., Somavarapu, S., Liddell, J., Powell, K., Zloh, M., Choi, J.-W., Godwin, A., and Brocchini, S. (2012) Site-specific pegylation at histidine tags. *Bioconjugate Chem. 23* (2), 248−263.
(66) Knappik, A., and Brundiers, R. (2009) Recombinant antibody expression and purification, in *The protein protocol handbook* (Walker, J. M., Ed.) Springer, Berlin.
(67) Chennamsetty, N., Voynov, V., Kayser, V., Helk, B., and Trout, B. L. (2010) Prediction of aggregation prone regions of therapeutic proteins. *J. Phys. Chem. 114*, 6614−6624.
(68) Sun, M. M. C., Beam, K. S., Cerveny, C. G., Hamblett, K. J., Blackmore, R. S., Torgov, M. Y., Handley, F. G. M., Ihle, N. C., Senter, P. D., and Alley, S. C. (2005) Reduction−alkylation strategies for the modification of specific monoclonal antibody disulfides. *Bioconjugate Chem. 16* (5), 1282−1290.
(69) Karlsson, R., Hakan Roos, R., Fagerstam, L., and Persson, B. (1994) Kinetic and concentration analysis using bia technology. *Methods 6*, 99−110.
(70) Myszka, D. G. (1997) Kinetic analysis of macro molecular interactions using surface plasmon resonance biosensors. *Curr. Opin. Biotechnol. 8*, 50−57.
(71) Harding, S. E., and Chowdhry, B. Z., Eds. (2001) Surface plasmon resonance. In *Protein-ligand interaction: Hydrodynamics and calorimetry*, Oxford University Press, Oxford.
(72) Liang, W., Wu, X., Peale, F. V., Lee, C. V., Meng, Y. G., Gutierrez, J., Fu, L., Malik, A. K., Gerber, H. P., Ferrara, N., and Fuh, G. (2006) Cross-species vascular endothelial growth factor (VEGF)-blocking antibodies completely inhibit the frowth of human tumor xenografts and measure the contribution of stormal VEGF. *J. Biol. Chem. 281* (2), 951−961.

(73) Patel, R., and Andrien, B. A. (2010) Kinetic analysis of a monoclonal therapeutic antibody and its single-chain homolog by surface plasmon resonance. *Anal. Biochem. 396* (1), 59−68.
(74) Chen, Y., Weismann, C., Fun, G., Li, B., Christinger, H. W., Mckay, P., M. De Vos, A., and Lowman, H. B. (1999) Selection and analysis of an optimized anti-VEGF antibody: Crystal structure of an affinity-matured Fab in complex with antigen. *J. Mol. Biol. 293*, 865−881.
(75) Fuh, G., Wei-Ching, P. W., Mark, L., Chingwei, U., Moffat, V. L., and Wiesmann, C. (2006) Structure-function studies of two synthetic anti-vascular endothelial growth factor Fabs and comparison with the Avastin Fab. *J. Biol. Chem. 281* (10), 6625−6631.
(76) Meyer, C. H., and Holz, F. G. (2011) Preclinical aspects of anti-VEGF agents for the treatment of wet amd: Ranibizumab and bevacizumab. *Eye 25* (6), 661−672.
(77) Lowe, J., Araujo, J., Yang, J., Reich, M., Oldendorp, A., Shiu, V., Quarmby, V., Lowman, H., Lien, S., Gaudreault, J., and Maia, M. (2007) Ranibizumab inhibits multiple forms of biologically active vascular endothelial growth factor in vitro and in vivo. *Exp. Eye Res. 85* (4), 425−430.
(78) Chen, C., Constantinou, A., and Deonarain, M. (2011) Modulating antibody pharmacokinetics using hydrophilic polymers. *Exp. Opin. Drug Delivery 8* (9), 1221−1236.
(79) Chapman, A. P., Antoniw, P., Spitali, M., West, S., Stephens, S., and King, D. J. (1999) Therapeutic antibody fragments with prolonged in-vivo half-lives. *Nat. Biotechnol. 17*, 780−783.
(80) Bobrovnik, S. A. (2003) Determination of antibody affinity by ELISA. Theory. *J. Biochem. Biophys. Methods 57* (3), 213−236.
(81) Regenmortel, M. H. V., and Azimzadeh, A. (2000) Determination of antibody affinity. *J. Immunoassay 211* (21), 211−234.
(82) Heinrich, L., Tissot, N., Hartmann, D. J., and Cohen, R. (2010) Comparison of the results obtained by ELISA and surface plasmon resonance for the determination of antibody affinity. *J. Immunol. Methods 352* (1−2), 13−22.
(83) Baer, M., Sawa, T., Flynn, P., Luehrsen, K., Martinez, D., Wiener-Kronish, J. P., Yarranton, G., and Bebbington, C. (2009) An engineered human antibody Fab fragment specific for pseudomonas aeruginosa pcrv antigen has potent antibacterial activity. *Infect. Immun. 77* (3), 1083−1090.
(84) Pacchiana, G., Chiriaco, C., Stella, M. C., Petronzelli, F., De Santis, R., Galluzzo, M., Carminati, P., Comoglio, P. M., Michieli, P., and Vigna, E. (2010) Monovalency unleashes the full therapeutic potential of the dn-30 anti-met antibody. *J. Biol. Chem. 285* (46), 36149−36157.
(85) Vauquelin, G., and Charlton, S. J. (2010) Long-lasting target binding and rebinding as mechanisms to prolong in vivo drug action. *Br. J. Pharmacol. 161* (3), 488−508.
(86) Bostrom, J., Haber, L., Koenig, P., Kelley, R. F., and Fuh, G. (2011) High affinity antigen recognition of the dual specific variants of herceptin is entropy-driven in spite of structural plasticity. *PLoS ONE 6* (4), e17887.
(87) Steffen, A.-C., Wikman, M., Tolmachev, V., Adams, G. P., Nilsson, F. Y., Ståhl, S., and Carlsson, J. (2005) In vitro characterization of a bivalent anti-her-2 affibody with potential for radionuclide-based diagnostics. *Cancer Biother. Radiopharm. 20* (3), 239−248.
(88) Godula, K., Umbel, M. L., Rabuka, D., Botyanszki, Z., Bertozzi, C. R., and Parthasarathy, R. (2009) Control of the molecular orientation of membrane-anchored biomimetic glycopolymers. *J. Am. Chem. Soc. 131* (29), 10263−10268.
(89) Howorka, S., Nam, J., Bayley, H., and Kahne, D. (2004) Stochastic detection of monovalent and bivalent protein−ligand interactions. *Angew. Chem., Int. Ed. 43* (7), 842−846.
(90) Kiessling, L. L., Gestwicki, J. E., and Strong, L. E. (2006) Synthetic multivalent ligands as probes of signal transduction. *Angew. Chem., Int. Ed. 45* (15), 2348−2368.
(91) Gestwicki, J. E., Cairo, C. W., Strong, L. E., Oetjen, K. A., and Kiessling, L. L. (2002) Influencing receptor−ligand binding mechanisms with multivalent ligand architecture. *J. Am. Chem. Soc. 124* (50), 14922−14933.
(92) Belardi, B., O'donoghue, G. P., Smith, A. W., Groves, J. T., and Bertozzi, C. R. (2012) Investigating cell surface galectin-mediated cross-linking on glycoengineered cells. *J. Am. Chem. Soc. 134* (23), 9549−9552.

Supporting Information

Figure S1

(A)

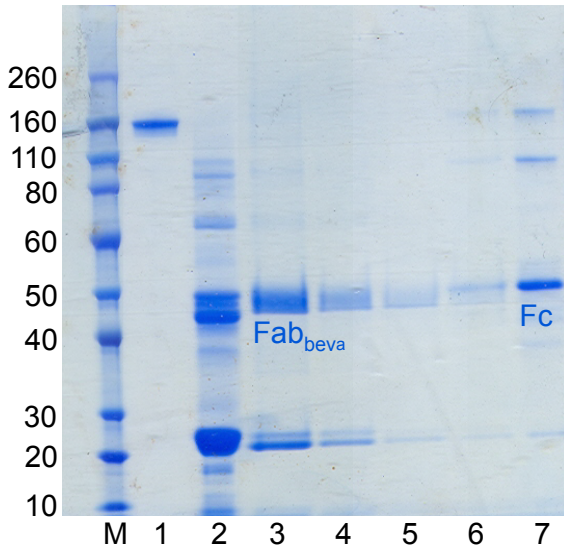

Figure S1 (A) Digestion of bevacizumab using immobilised papain and protein A column for Fab$_{beva}$ purification. *Lane 1*; bevacizumab, *Lane 2*; digestion mixture after 5.5 h digestion, *Lanes 3-6*; Fab$_{beva}$ fractions after protein A column using binding buffer (pH 8.0), *Lane 7*; undigested protein and Fc fragment isolated from protein A column using elution buffer (pH 2.8).

(B)

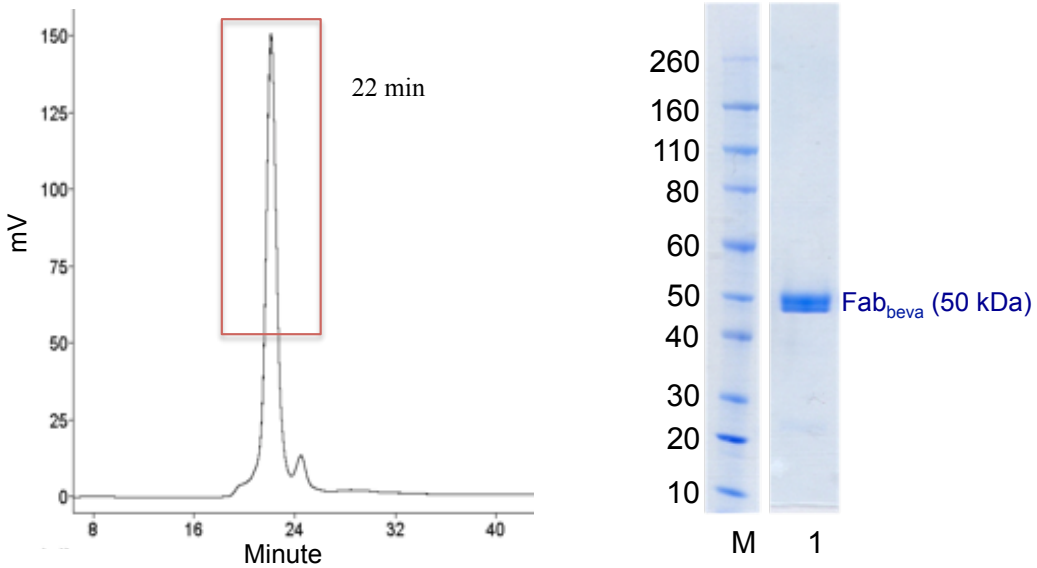

Figure S1 (B) SP HP ion exchange chromatography (IEC) of the Fab$_{beva}$ after protein A column and SDS-PAGE gel of IEC fraction, *Lane 1;* IEC fraction at 22 min corresponded to the Fab$_{beva}$.

(C)

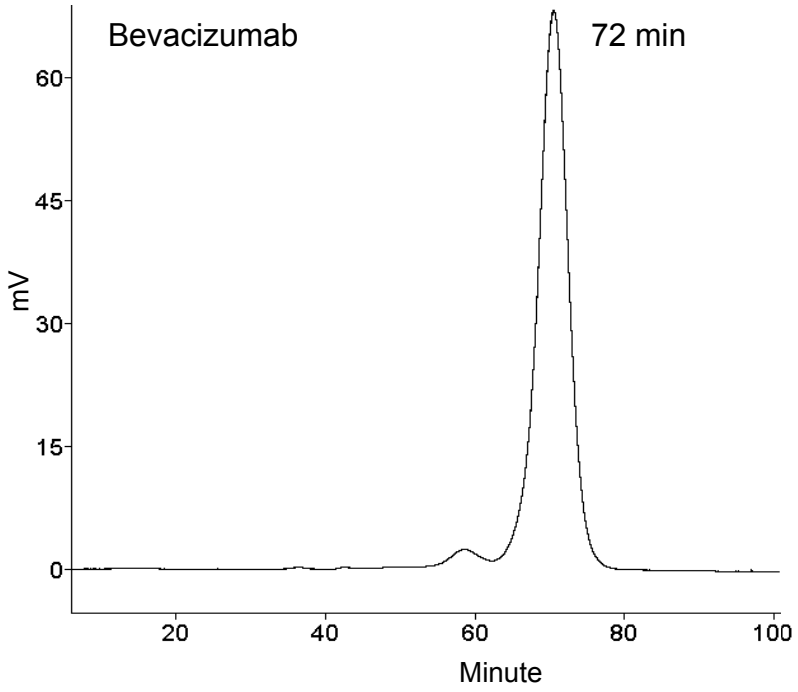

(D)

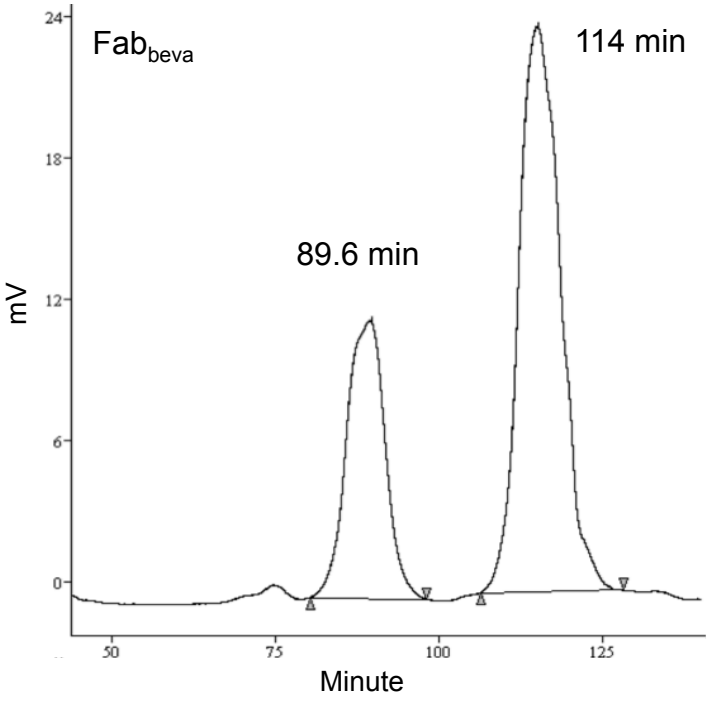

Figure S1 (C-D) SEC chromatograms: (**C**) bevacizumab and **(D)** Fab$_{beva}$. The peak at 114 min corresponds to the salt in the injected sample in the SEC mobile phase.

(E)

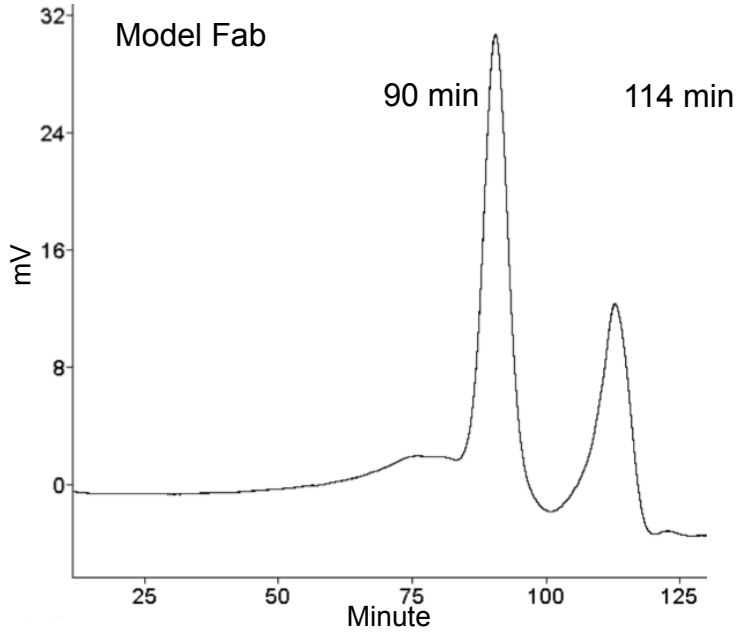

(F)

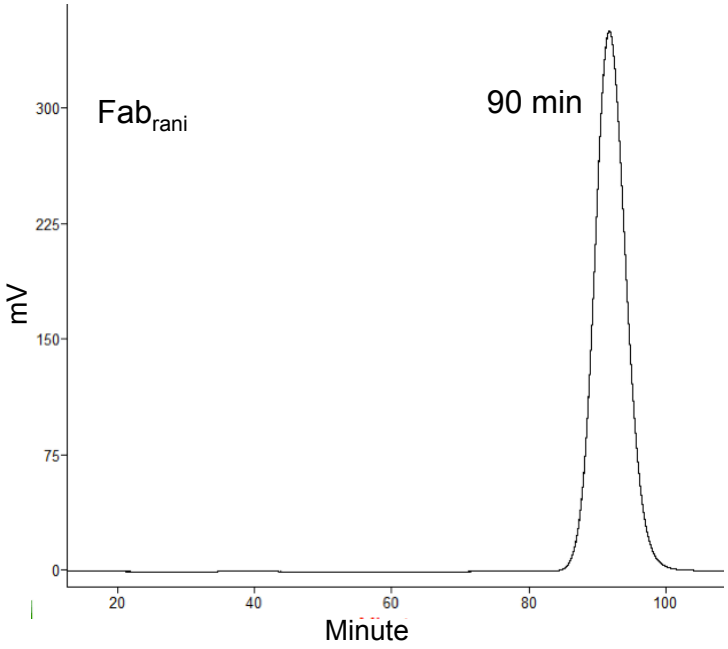

Figure S1 (E-F). SEC chromatograms: **(E)** a model Fab (ChromoPure human Fab) and **(F)** Fab$_{rani}$. The peak at 114 min corresponds to the salt in the injected sample in the SEC mobile phase.

Figure S2

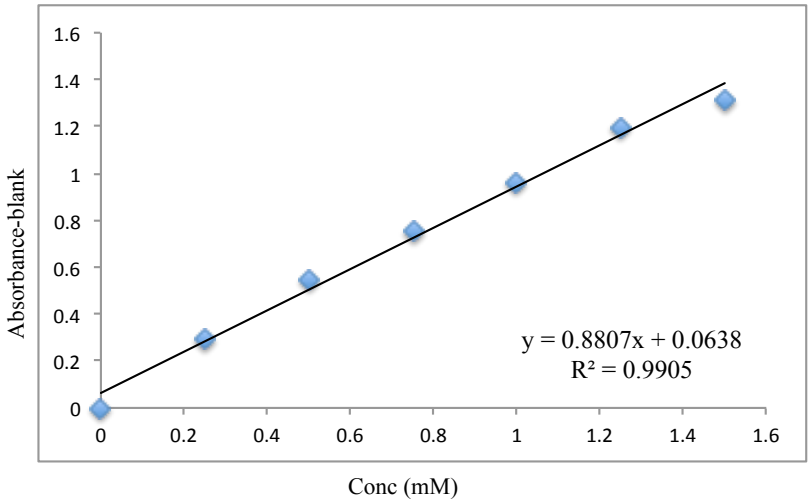

Figure S2. Calibration curve (412 nm) derived from cysteine for the Ellmans assay.

Figure S3

(A)

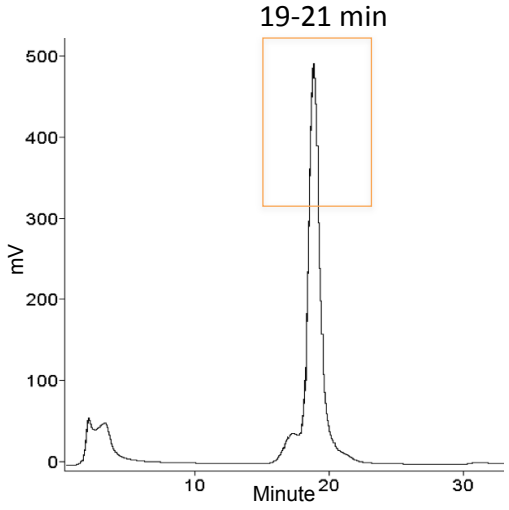

(B)

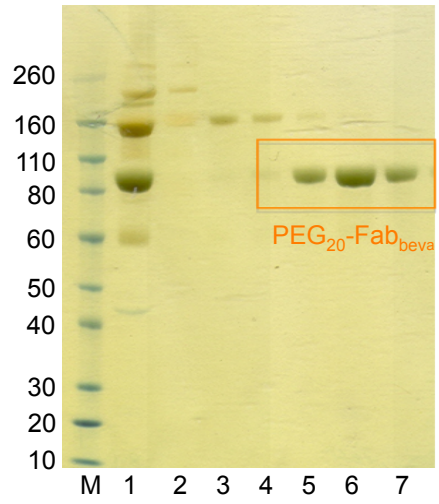

Figure S3. (A) SP HP IEC chromatogram for the purification of PEG_{20}-Fab_{beva} which was prepared using PEG-*mono*-sulfone **2** (2.0 eq.; 20 kDa) and **(B)** SDS-PAGE gel of the IEC fractions of PEG_{20}-Fab_{beva}; Novex Bis-Tris 4-12% gel stained with colloidal blue and barium iodide (Lanes M-7). *Lane M;* protein standards, *Lane 1;* PEGylation reaction mixture before IEC, *Lane 2;* IEC fraction at 5 min (PEG species), *Lanes 3, 4;* IEC fractions at 17 and 18 min (trace PEG_2-Fab_{beva}), *Lanes 5-7;* IEC fractions at 19-21 min (PEG-Fab_{beva}).

Figure S4

(A)

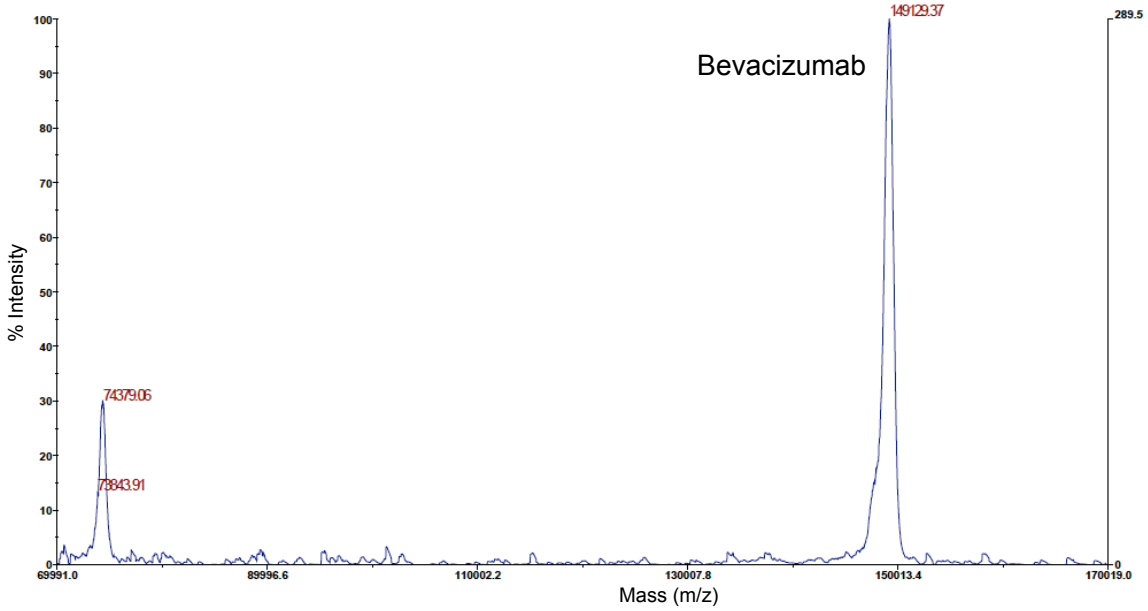

(B)

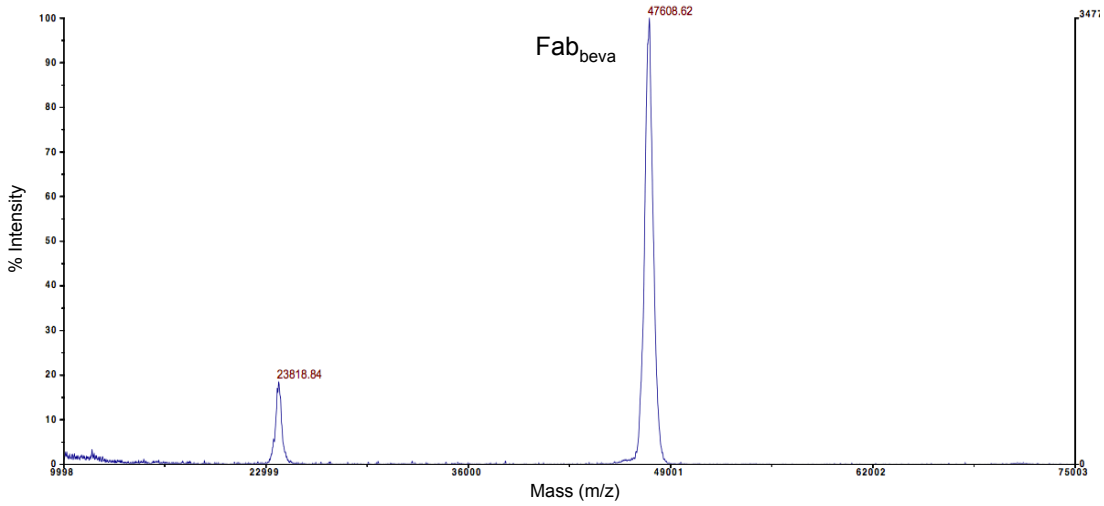

Figure S4 (A-B). MALDI-TOF mass spectra of **(A)** bevacizumab (~150 kDa) and **(B)** Fab$_{beva}$ (~48 kDa).

(C)

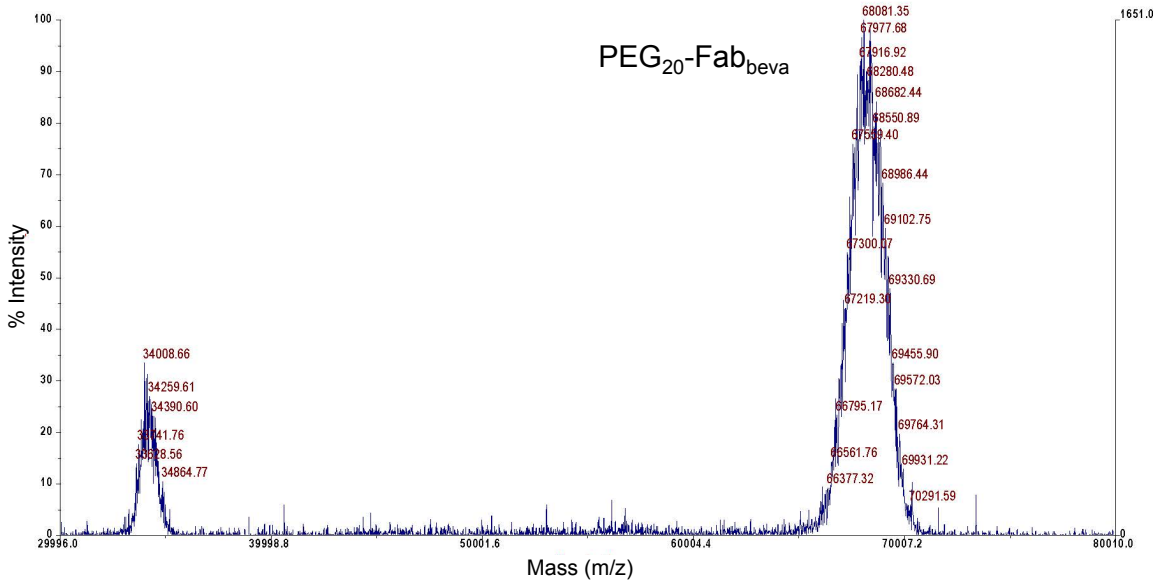

Figure S4 (C). MALDI-TOF mass spectra of PEG_{20}-Fab_{beva} (~68 kDa).

Figure S5

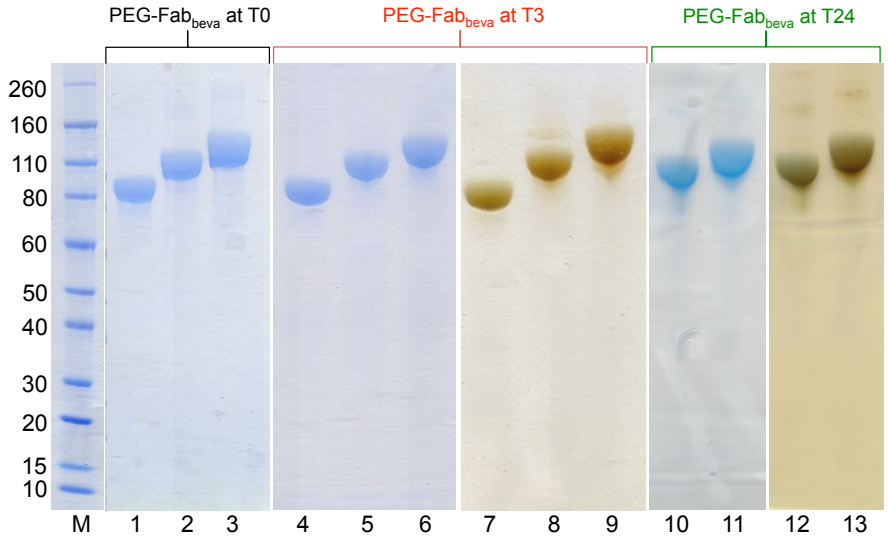

Figure S5. SDS-PAGE gel displaying representative samples from a stability study of PEG-Fab$_{beva}$ at T0, T3 and T24 stored in PBS at 4 °C. SDS-PAGE gels were stained with colloidal blue (lanes 1-6 and 10-11), colloidal blue/BaI_2 (lanes 7-9 and lane 12-13). *Lane M;* protein standards (colloidal blue). *Lanes 1-3;* purified PEG-Fab$_{beva}$ (20, 30 and 40 kDa PEG) samples at T0 at 4 °C, *Lanes 4-9;* purified PEG-Fab$_{beva}$ (20, 30 and 40 kDa PEG) samples at T3 at 4 °C, *Lanes 10-13;* purified PEG-Fab$_{beva}$ (30 and 40 kDa PEG) samples at T24 at 4 °C.

Figure S6

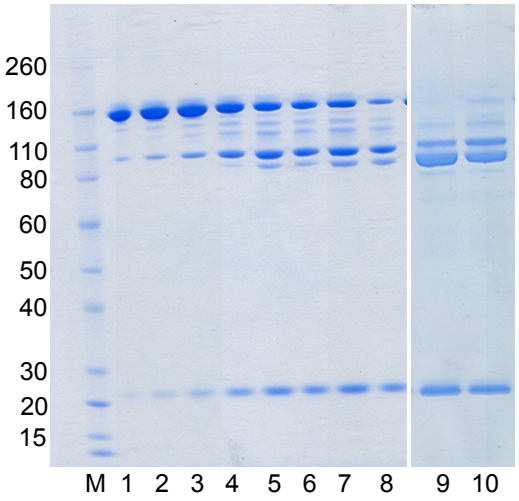

Figure S6. Reduction studies of bevacizumab with TCEP (1-24 eq.). Novex Bis-Tris 4-12%, 15 well (lanes M-8) and 10 well (lanes 9-10) stained with colloidal blue. *Lane M;* protein standards. Reduction of bevacizumab with: *Lane 1*; 1.0 eq. TCEP, *Lane 2*; 1.5 eq. TCEP, *Lane 3*; 2.0 eq. TCEP, *Lane 4*; 3.0 eq. TCEP, *Lane 5*; 4.0 eq. TCEP, *Lane 6*; 4.5 eq. TCEP, *Lane 7*; 5.0 eq. TCEP, *Lane 8*; 6.0 eq. TCEP, *Lane 9*; 12 eq. TCEP, *Lane 10*; 24.0 eq. TCEP.

Figure S7

(A)

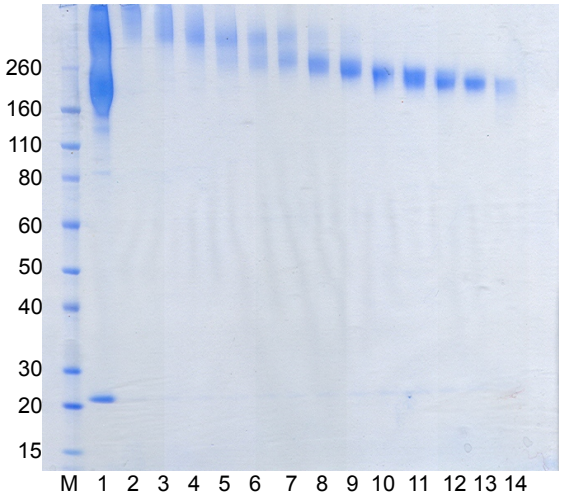

(B)

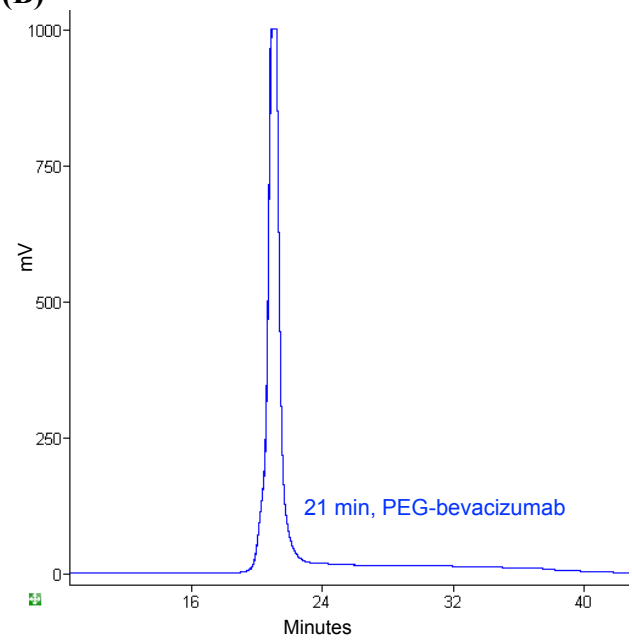

(C)

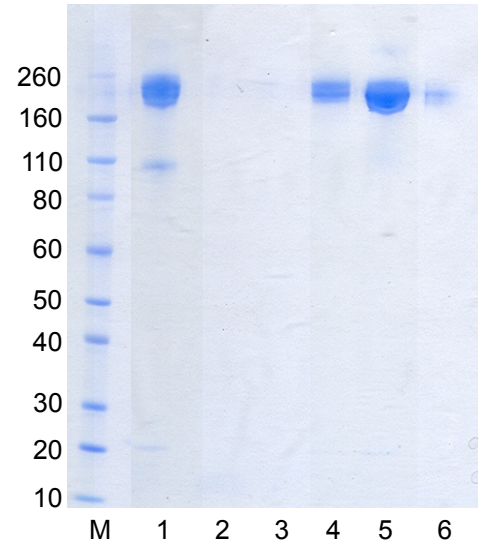

Figure S7. (A) SEC fractions of the PEGylation of bevacizumab. Novex Bis-Tris 4-12% gel stained with colloidal blue, *Lane M;* Protein standards, *Lane 1;* PEGylation reaction mixture (4 eq., 10 kDa PEG reagent **2**), *Lane 2*; fraction at 48 min, *Lane 3;* fraction at 49 min, *Lane 4;* fraction at 50 min, *Lane 5;* fraction at 51 min, *Lane 6;* fraction at 52 min, *Lane 7;* fraction at 53 min, *Lane 8;* fraction at 54 min, *Lane 9;* fraction at 55 min, *Lane 10;* fraction at 57 min, *Lane 11;* fraction at 58 min, *Lane 12*; fraction at 60 min, *Lane 13;* fraction at 61 min, *Lane 14;* fraction at 65 min. **(B)** SP HP IEC purification and **(C)** fractions of PEGylated bevacizumab *Lane 1;* pooled SEC fractions of PEGylated bevacizumab before IEC, *Lane 2;* IEC fraction at 18.5 min, *Lane 3;* IEC fraction at 19 min, *Lane 4;* IEC fraction at 20 min, *Lane 5;* IEC fraction at 21 min, *Lane 6;* IEC fraction at 21.5 min.

Figure S8

(A)

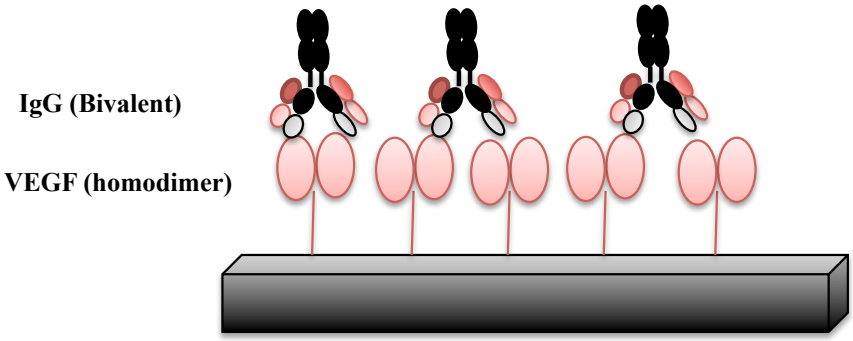

(B)

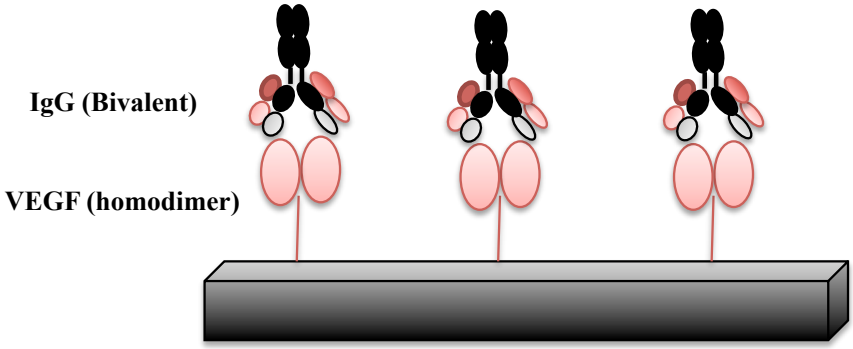

Figure S8. The binding of an IgG antibody to an immobilised bivalent ligand at **(A)** high and **(B)** low ligand immobilisation densities. Low density immobilisation would be expected to cause less cross-linking when exposed to a bivalent binding molecule such as an antibody.

Figure S9

(A)

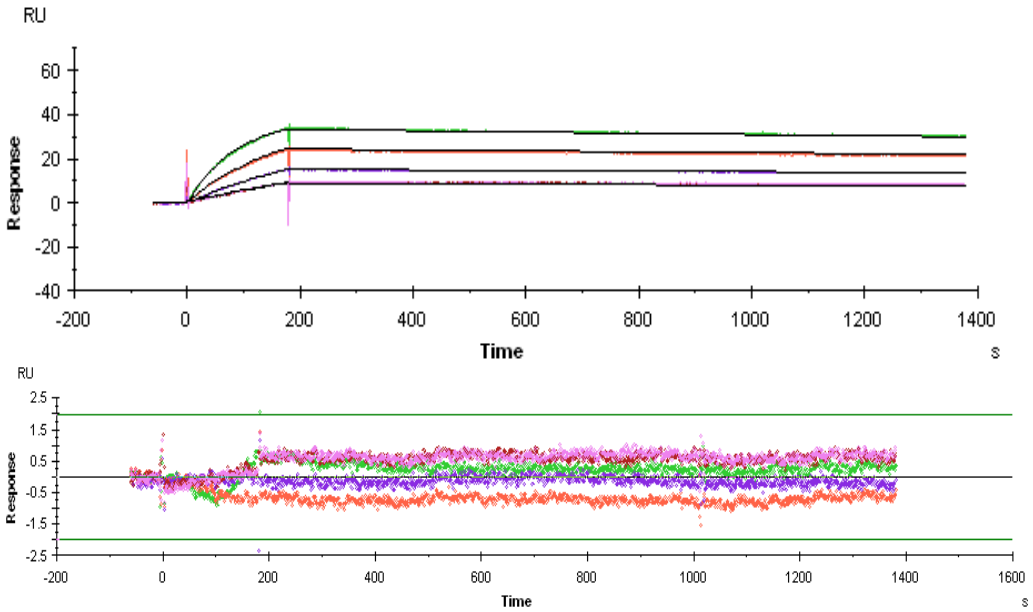

(B)

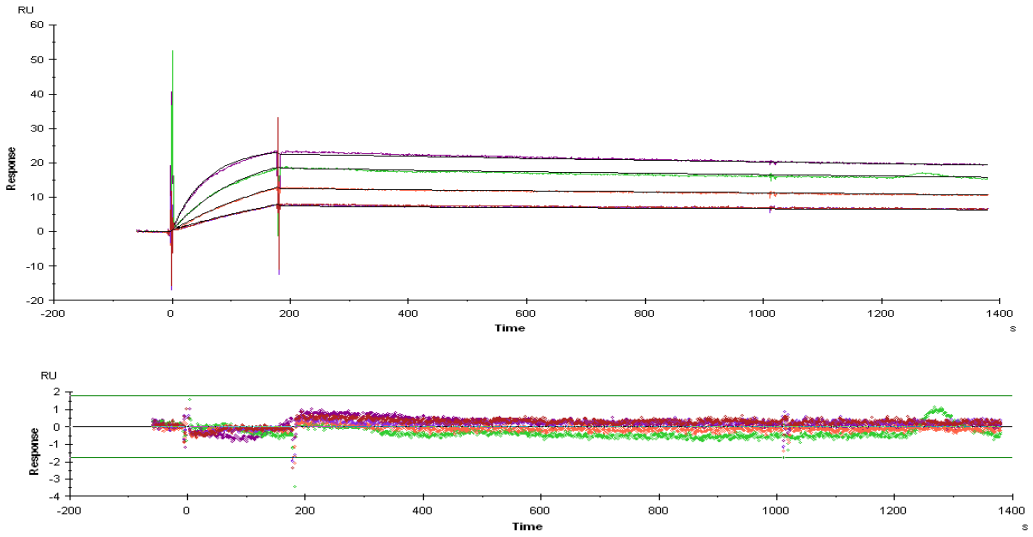

Figure S9 (A-B). The fitting curves and residual plots of the constructs derived from bevacizumab using a 1:1 fitting model of **(A)** bevacizumab and **(B)** Fab_{beva}.

(C)

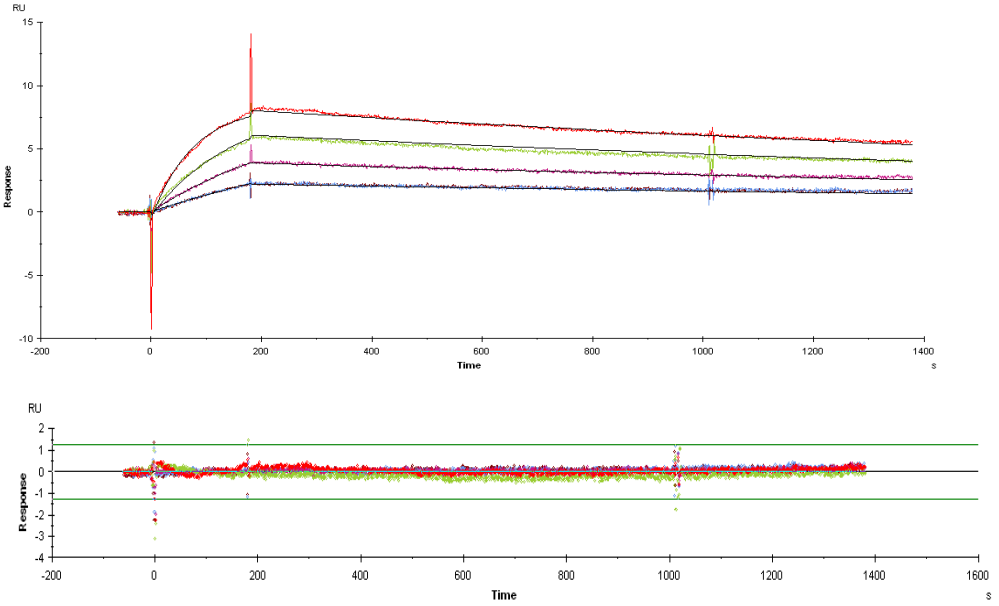

(D)

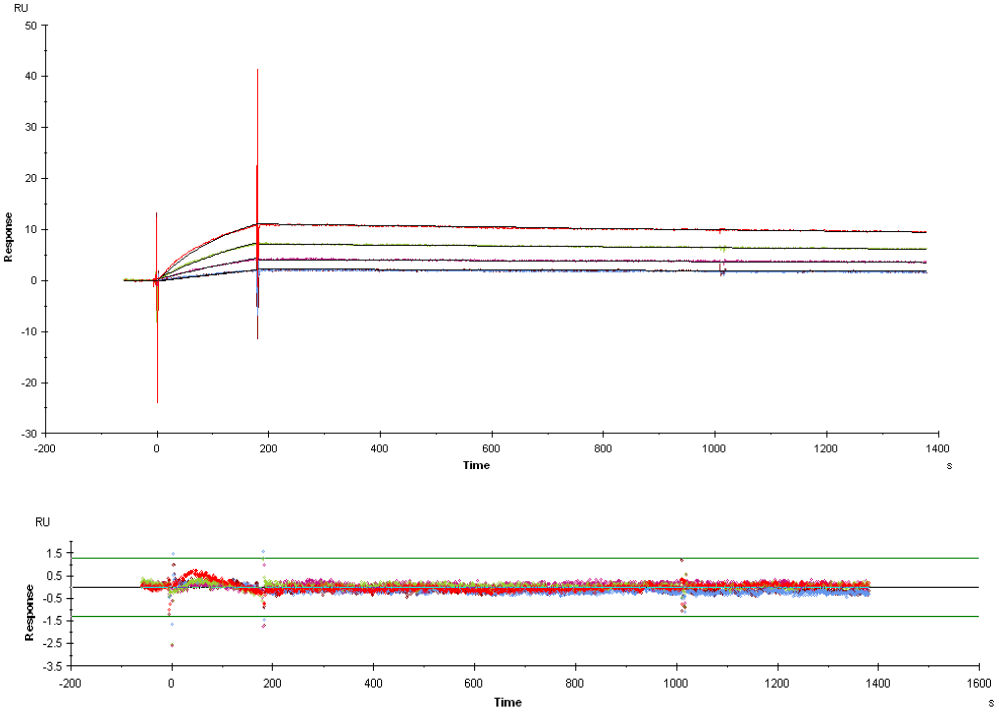

Figure S9 (C-D). The fitting curves and residual plots of the constructs derived from bevacizumab using a 1:1 fitting model of **(C)** $F(ab')_{2\text{-beva}}$ and **(D)** $PEG_{20}\text{-}Fab_{beva}$.

(E)

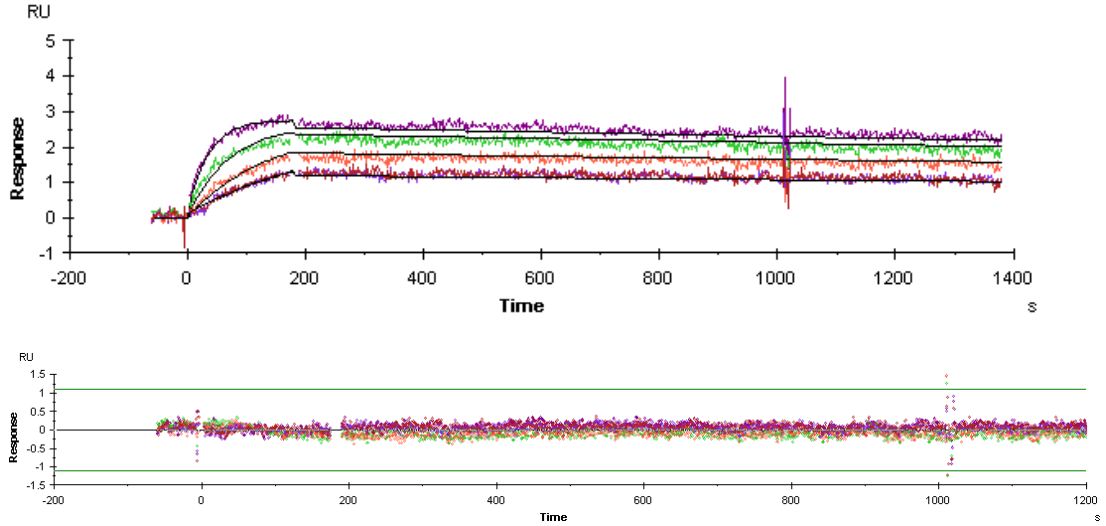

Figure S9 (E). The fitting curves and residual plots of the constructs derived from trastuzumab using a 1:1 fitting model of **(E)** PEG_{20}-Fab_{trast}.

Figure S10

(A)

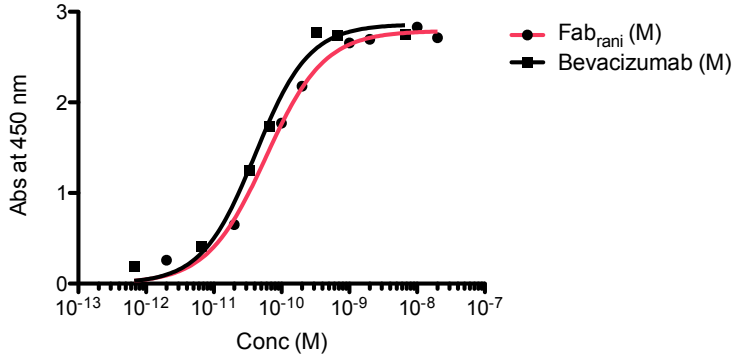

(B)

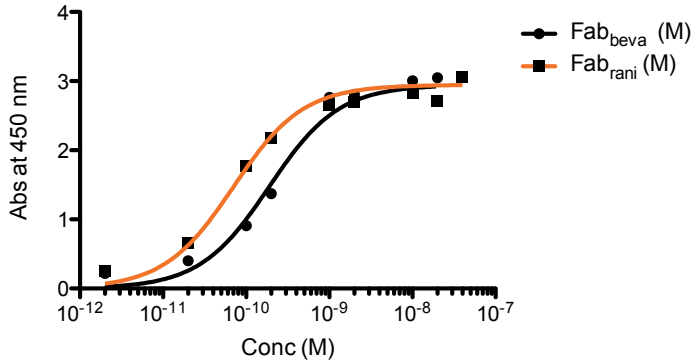

Figure S10. Supperimposed ELISA binding saturation curves of **(A)** Fab$_{rani}$ and bevacizumab (concentration range; 4×10^{-12} to 2×10^{-8} M) and **(B)** Fab$_{beva}$ and Fab$_{rani}$ (concentration range; 4×10^{-12} to 2×10^{-8} M). Each graph is derived from two measurements with four independent ELISA assays being performed for bevacizumab and Fab$_{beva}$, and three independent ELISA assays for Fab$_{rani}$.

Supplementary Tables.

Table S1

(A) *Ellman's assay-absorbance at 412 nm*

Samples	Absorbance
Cysteine 0.0 mM (blank)	0.005
Cysteine 0.25 mM	0.300
Cysteine 0.5 mM	0.550
Cysteine 0.75 mM	0.760
Cysteine 1.0 mM	0.970
Cysteine 1.25 mM	1.200
Cysteine 1.5 mM	1.320
Bevacizumab	0.004
Purified Fab_{beva}	0.005
$F(ab')_{2\text{-}beva}$	0.004
Reduced Fab_{beva}	0.026

(B) *Calculation of the number of free thiols in reduced Fab_{beva}:*
$\varepsilon = 14150\ M^{-1}cm^{-1}$ $A = \varepsilon . b . c$
(1) (0.026-0.005) = 14150 x 1 x c
c (mole/lit) = 1.48×10^{-6} M concentration of the solution in the cuvette
(2) 1.48×10^{-6} M × 2.8 mL (dilution factor, 2.5 mL reaction buffer + 0.25 mL sample + 0.05 mL DTNB) x 1 L/1000 mL = 4.15×10^{-9} number of sulfhydryl moles in the 0.25 mL solution.
(3) 4.15×10^{-9} mole/0.25 mL × 1000 mL = 1.66×10^{-5} M concentration of sulfhydryl in 0.25 mL solution.
(4) To calculate the number of free thiols, the concentration of sulfhydryl was divided by the concentration of the protein $1.66 \times 10^{-5} / 0.9 \times 10^{-5} = 1.85$ number of free thiols.

Table S1. (A) Absorbance at 412 nm using Ellman's reagent for solutions of cysteine standards, bevacizumab, Fab_{beva}, $F(ab')_2$ and reduced Fab_{beva}. **(B)** Representative calculation for the number of free thiols in reduced Fab_{beva}.

Table S2

Sample	Z-average size (d. Nm)	PdI
Fab_{beva} at T0	9.02 ± 0.07	0.21± 0.005
Fab_{beva} at T3	14.18 ± 0.09	0.52 ± 0.010
PEG_{20}-Fab_{beva} at T0	21.02	0.35
PEG_{20}-Fab_{beva} at T3	23.20	0.33

Table S2. DLS analysis of Fab_{beva} and PEG_{20}-Fab_{beva} at T0 and T3. The DLS analysis was performed three times for Fab_{beva} at T0 and T3 and two times for PEG_{20}-Fab_{beva} at T0 and T3.

Table S3

Sample	k_a ($M^{-1}s^{-1}$)	SE (ka)	k_d (s^{-1})	SE (kd)	K_D nM	Rmax	SE (Rmax)	Chi^2	tc
Bevacizumab	6.93×10^{4}	2.70×10^{2}	9.04×10^{-5}	2.02×10^{-6}	1.30	38.3	0.092	0.21	1.04×10^{19}
F(ab´)$_2$	5.19×10^{4}	1.9×10^{2}	9.19×10^{-5}	2.70×10^{-6}	1.77	28.5	0.06	0.40	1.03×10^{22}
Fab_{beva}	2.98×10^{4}	67	1.34×10^{-4}	1.26×10^{-6}	4.2	19.1	0.024	0.16	2.5×10^{13}
PEG_{20}-Fab_{beva}	1.0×10^{4}	55	1.35×10^{-4}	2.10×10^{-6}	13.0	17.57	0.058	0.03	9.1×10^{17}
PEG_{30}-Fab_{beva}	8.12×10^{3}	17	1.0×10^{-4}	1.10×10^{-6}	12.30	17.8	0.024	0.03	2.3×10^{13}
PEG_{40}-Fab_{beva}	1.10×10^{4}	34	1.19×10^{-4}	1.0×10^{-6}	10.79	11.88	0.026	0.02	2.08×10^{15}
$PEG_{2\times20}$-Fab´$_{beva}$	1.13×10^{4}	26	1.92×10^{-4}	1.20×10^{-6}	9.50	8.8	0.031	0.02	4.8×10^{16}
PEG_{10}-bevacizumab	1.51×10^{4}	73	8.20×10^{-5}	2.70×10^{-7}	5.49	16.6	0.051	0.13	2.08×10^{14}
Fab_{rani}	3.65×10^{4}	49	$\leq 10^{-6}$	ND	ND	23.96	ND	0.19	2.30×10^{16}
PEG_{20}-Fab_{rani}	1.74×10^{4}	46	$\leq 10^{-6}$	ND	ND	20.39	ND	0.23	8.17×10^{19}
Trastuzumab	0.34×10^{6}	1.30×10^{3}	0.42×10^{-4}	1.70×10^{-6}	0.10	6.4	0.008	0.03	1.2×10^{10}
Fab_{trast}	1.01×10^{6}	2.1×10^{4}	1.15×10^{-4}	2.10×10^{-6}	0.13	2.67	0.003	0.02	6.8×10^{19}
PEG_{20}-Fab_{trast}	0.26×10^{6}	1.10×10^{3}	1.30×10^{-4}	2.90×10^{-6}	0.49	2.59	0.006	0.02	2.4×10^{19}

Table S3. Kinetic constants and parameters of bevacizumab, ranibizumab, trastuzumab and their PEGylated derivatives that were evaluated in this study.

Table S4

Sample	k_a ($M^{-1}s^{-1}$)	k_d (s^{-1})	K_D nM	Temp.	Reference
Bevacizumab	9.2×10^{4}	2.0×10^{-4}	2.2	37 °C	1
Fab-12	7.5×10^{4}	6.4×10^{-4}	8.5	37 °C	1
Y0317 (Ranibizumab)	8.1×10^{4}	0.02×10^{-4}	0.02	37 °C	1
Fab-12	3.5×10^{4}	3.5×10^{-4}	1.8	25 °C	2
Ranibizumab	5.6×10^{4}	ND	ND	25 °C	3
Y0317 (Ranibizumab)	3.6×10^{4}	ND	ND	25 °C	4
Y0317 (Ranibizumab)	5.3×10^{4}	0.074×10^{-4}	0.14	37 °C	4
Fab-12	5.5×10^{4}	11×10^{-4}	20	37 °C	4

Table S4. Comparative SPR binding data from the literature.

References

(1) Liang, W., Wu, X., Peale, F., Lee, C., Meng, G., Gutierrez, J., Fu, L., Malik, A., Gerber H., Ferrara, N., and Fuh, G. (2006) Cross-species vascular endothelial growth factor (VEGF)-blocking antibodies completely inhibit the growth of human tumor xenografts and measure the contribution of stromal VEGF. *J. Biol. Chem. 281(2)*, 951-961.

(2) Presta, L.G., Chen, H., O'Connor, S.J., Chisholm, V., Meng, G., Krummen, L., Winkler, M., and Ferrara, N., (1997) Humanization of an anti-vascular endothelial growth factor monoclonal antibody for the therapy of solid tumors and other disorders. *Cancer Res. 57*, 4593-4599.

(3) Lowe, J., Araujo, J., Yang, J., Reich, M., Oldendorp, A., Shiu, V., Quarmby, V., Lowman, H., Lien, S., Gaudreault, J., and Maia, M. (2007) Ranibizumab inhibits multiple forms of biologically active vascular endothelial growth factor *in vitro* and *in vivo*. *Exp. Eye Res. 85(4)*, 425-430.

(4) Chen, Y., Weismann, C., Fun, G., Li, B., Christinger, H.W., Mckay, P., de Vos, A., and Lowman, H.B. (1999) Selection and analysis of an optimized anti-VEGF antibody: Crystal structure of an affinity-matured Fab in complex with antigen., *J. Mol. Biol. 293(4)*, 865-881.

Bioconjugate Chemistry

Article

pubs.acs.org/bc

Functionalization of Microstructured Open-Porous Bioceramic Scaffolds with Human Fetal Bone Cells

Franziska Krauss Juillerat,[†,⊥] Françoise Borcard,[‡,⊥] Davide Staedler,[‡] Corinne Scaletta,[§] Lee Ann Applegate,[§] Horacio Comas,[‡] Ludwig J. Gauckler,[†] Sandrine Gerber-Lemaire,[‡] Lucienne Juillerat-Jeanneret,*[,∥] and Urs T. Gonzenbach*[,†]

[†]Nonmetallic Inorganic Materials, ETHZ, CH-8093 Zurich, Switzerland

[‡]Institute of Chemical Sciences and Engineering, EPFL, CH-1015, Lausanne, Switzerland

[§]Department of Musculoskeletal Medicine, Cellular Therapy Unit, University Hospital, CH-1011 Lausanne, Switzerland

[∥]Institute of Pathology, CHUV-UNIL, CH-1011 Lausanne, Switzerland

Supporting Information

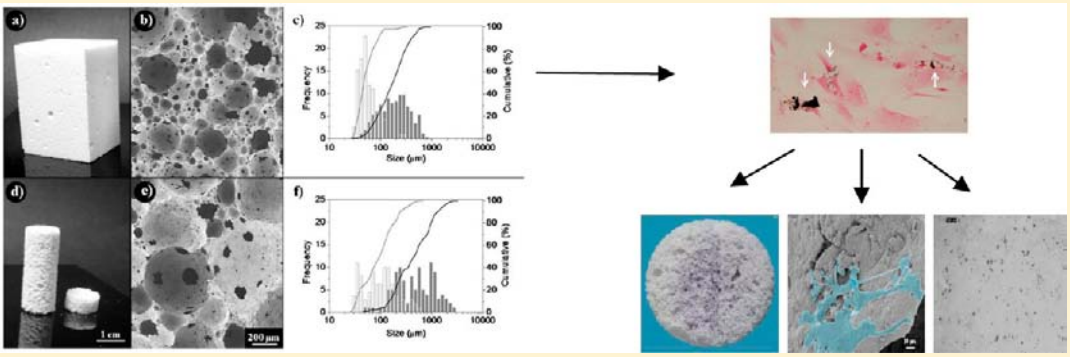

ABSTRACT: Bone substitute materials allowing trans-scaffold migration and in-scaffold survival of human bone-derived cells are mandatory for development of cell-engineered permanent implants to repair bone defects. In this study, we evaluated the influence on human bone-derived cells of the material composition and microstructure of foam scaffolds of calcium aluminate. The scaffolds were prepared using a direct foaming method allowing wide-range tailoring of the microstructure for pore size and pore openings. Human fetal osteoblasts (osteo-progenitors) attached to the scaffolds, migrated across the entire bioceramic depending on the scaffold pore size, colonized, and survived in the porous material for at least 6 weeks. The long-term biocompatibility of the scaffold material for human bone-derived cells was evidenced by *in-scaffold* determination of cell metabolic activity using a modified MTT assay, a repeated WST-1 assay, and scanning electron microscopy. Finally, we demonstrated that the osteo-progenitors can be covalently bound to the scaffolds using biocompatible click chemistry, thus enhancing the rapid adhesion of the cells to the scaffolds. Therefore, the different microstructures of the foams influenced the migratory potential of the cells, but not cell viability. Scaffolds allow covalent biocompatible chemical binding of the cells to the materials, either localized or widespread integration of the scaffolds for cell-engineered implants.

INTRODUCTION

The demand of materials for the repair and substitution of damaged tissues, including bone tissue, is increasing. Presently, the standard treatment for bone defects is autologous iliac crest bone grafting. However, this procedure requires a second surgery with its increased risk of infections and possible morbidity at the donor site. These disadvantages show a need for the development of synthetic bone graft materials presently used in only about 15% of the cases.[1] Therefore, the development of scaffolds able to integrate into bone tissue and support bone regeneration across defects that are too large to heal naturally or which cannot heal spontaneously[2] is mandatory for the success of reconstructive strategies for the treatment of critical-sized bone defects.[3,4]

To achieve these requirements, two possibilities could be envisioned. The bone substitute is biodegradable and transitory and will be replaced by tissue from the organ, an approach that has mainly been developed until now. However, for large bone defects, such as those seen in major bone loss, this strategy is not always possible. Permanent implants are necessary, which can be prepared in shapes similar to that of the bone to be replaced and integrated in the tissue of implantation. These permanent implants must also allow the growth of bone cells in

Received: July 25, 2012
Revised: October 11, 2012
Published: November 1, 2012

ACS Publications © 2012 American Chemical Society

dx.doi.org/10.1021/bc300407x | *Bioconjugate Chem.* 2012, 23, 2278−2290

the implant in order to provide cell-engineered implant materials prior to implantation.

The understanding of bone tissue structure allows for rational material design, capable of mimicking the tissue structure and specific biochemistry of bone. Bone is a highly organized tissue that assembles from nano- to macroscales to produce complex structural interconnected porous networks. Therefore, development of permanent bone substitute materials, containing trans-scaffold channels which allow migration and in-scaffold survival of human bone-derived cells, is mandatory for ultimately developing a functional bone tissue to repair large bone defects. Such materials will also need to ultimately support the formation of differentiated bone cell structures inside the permanent implant. To obtain a physical support for permanent artificial bone tissue, synthetic and porous scaffolds must therefore be produced from inert biocompatible materials, such as alumina or titanium.[5−7]

To develop permanent implants which have been engineered with human bone cells prior to implantation for the repair of human bone defects, histocompatibility problems of the cells associated with the implant must also be considered. Human fetal cells have an interesting potential for therapeutic use for tissue engineering and regeneration, including bone tissue engineering. These cells show a rapid growth rate and an ability to differentiate in vitro into mature cells, and also display histocompatibility properties,[8,9] eliminating the need for antigraft rejection medication of the patients. However, presently, the developments for artificial bone implants performed with human fetal cells have used materials that were designed to be biodegradable.[10−12]

In the present study, our goals were to develop calcium aluminate scaffolds suitable for permanent bone replacement. These scaffolds must display open-porous channel microstructures allowing the engraftment and migration through the ceramics of human histocompatible bone-derived cells. These calcium aluminate scaffolds were produced according to a modified direct foaming method[13−19] which allows the production of macroporous scaffolds that are tailored in pore size, microstructure, and shape. This method is based upon using partially hydrophobized particles to stabilize the air−liquid interface in wet foams. For calcium aluminate foams, we have previously shown that propyl gallate is a suitable short-chain amphiphile to import hydrophobicity and activate the surface of the particles.[13,14,18,19] We have previously reported in detail the development of porous calcium aluminate foams and their microstructural mechanical and compressive strength properties,[18] showing their potential interest in bone engineering. In the present study, we particularly aimed to determine the optimal pore sizes to allow survival and migration of human bone-derived cells across the scaffolds. Therefore, we investigated the interaction of calcium aluminate scaffolds of varying composition and pore size first with human osteosarcoma cells to select the bioceramic composition displaying optimal pore sizes and pore opening sizes, then with primary human fetal osteoblasts (osteo-progenitors) as models for histocompatible human bone-derived cells. We also determined if the adhesion of the human osteo-progenitors to these scaffolds was improved by their chemical functionalization using a biocompatible click-chemistry covalent approach.

EXPERIMENTAL PROCEDURES

Preparation and Characterization of the Scaffolds. *Preparation of the Scaffold Materials.* The particles used to prepare the suspensions were a high-purity α-Al_2O_3 powder (HPA-0.5w/MgO, Ceralox, Tucson, AZ) with an average particle size of 200 nm. The short-chain amphiphile selected to in situ modify the alumina particles was propyl gallate (Fluka AG, Buchs, Switzerland). Further chemicals used in the present study were hydrochloric acid, sodium hydroxide (both Titrisol, Merck, Germany), and deionized water (18.2 MΩ/cm). To consolidate the wet scaffolds, the calcium aluminate cement "CA-270" (Almatis GmbH, Ludwigshafen/Rhein, Germany) and the setting accelerator lithium carbonate (Fluka AG, Buchs, Switzerland) were used.

Alumina suspensions were prepared by stepwise addition of alumina powder to an aqueous solution containing 27 mM NaOH and 22 mM propyl gallate. The suspension solids loading was initially fixed to 50 vol %. Homogenization and deagglomeration of the suspensions were carried out on a ball mill for 18 h using polyethylene milling bottles (1 L) and alumina balls (10 mm in diameter, weight ratio balls to suspension ∼2:1). After ball milling, three different suspensions were prepared as follows: the propyl gallate content was adjusted to 2, 1.2, or 1 wt % to the amount of alumina particles by dissolving it in a NaOH aqueous solution displaying a pH higher than 10. These solutions were then added dropwise to the ball-milled suspensions under stirring to avoid local particle agglomeration. Finally, the pH was set to 9.9 and the solids loadings were adjusted to the respective volume fractions (12.7, 32.9, or 10.8 vol %) by adding water to the suspensions. Immediately before the foaming step, the desired amount of cement powder (33.7, 4.3, or 26.3 vol %) and the setting accelerator lithium carbonate (5 wt % to the amount of cement) were added to the suspensions and dispersed under stirring.

Foaming of the cement containing suspensions was carried out using a household food processor (Kenwood, Major Classic) at maximum power level (800 W) for 3 min. The wet foams were then poured into cylindrical molds, 10 cm in diameter and 5 cm high, and left to set at ambient temperature overnight in a moist atmosphere to prevent drying. After setting and drying, the specimens were sintered in an electrical furnace (HT 40/16, Nabertherm, Germany) at 1575 °C for 2 h. The heating rate was controlled to 1 °C/min and the cooling rate was controlled to 3 °C/min. The sintered samples were then drilled into cylinders 10 mm in diameter and 2 mm high, ultrasonicated in ethanol and acetone, and dried at 110 °C.

Characterization of the Scaffold Microstructure. The porosity was determined by weighing a defined volume of a scaffold sample, and calculating the air content using the following formula: air content (vol %) = $(1 - \rho_{measured}/\rho_{dense}) \times 100\%$, where ρ = density in g/cm^3. To define the diameters of the pores and pore openings, scanning electron microscopy (SEM) (LEO 1530, Zeiss Oberkochen in SE2 mode and at low magnifications) micrographs were analyzed using the software *Linear Intercept* (TU Darmstadt, Germany), defining 250 intersections on 5 representative images.

We have previously shown that the compressive strength of samples with 76 vol % porosity (similar to the samples used in this study) reached about 900 kPa.[18]

Chemistry. Commercial reagents (Fluka, Aldrich, VWR, Switzerland) were used without further purification. Anhydrous solvents were obtained by filtration (PureSolv MD Series, Innovative Technology). TLCs for reaction monitoring were performed on Merck silica gel 60 F254 plates, and spots were revealed with UV light and reaction with $KMnO_4$ or

ninhydrine. IR spectra were recorded on a Perkin-Elmer-1420 spectrometer. ^{1}H NMR spectra were recorded on a Bruker-ARX-400 spectrometer (400 MHz) using MeOD as solvent and calibrated using the solvent's residual signal at 3.31 ppm as an internal reference. ^{13}C NMR spectra were recorded on a Bruker-ARX-400 spectrometer (100.6 MHz) using MeOD as solvent and calibrated using the solvent's residual signal at 49.0 ppm as an internal reference. Chemical shifts are expressed in parts per million (ppm) and coupling constants (J) in hertz. Mass spectra were obtained on a Nermag R-10−10C spectrometer with chemical ionization (NH_3) and mode m/z (amu) [% relative base peak (100%)]. Semipreparative HPLC was performed on a Waters Autopurification ZQ System equipped a 2767 Sample Manager, a 2525 Binary Gradient Module, and a 2996 Photodiode Array Detector, coupled to Waters Micromass ZQ analyzer. The HPLC purifications were performed on XTerra Prep RP C18 (19 × 150) columns, using reverse-phase conditions (2−100% acetonitrile with 0.1% TFA over 20 min).

*Chemical Syntheses. 5-[(6-Aminohexyl)carbamoyl]-benzene-1,2,3-triyl triacetate (**3**).* 3,4,5-Triacetoxy benzoic acid (**1**) was obtained by treatment of gallic acid with acetic anhydride in the presence of pyridine, in 81% yield. A few drops of DMF were added to **1** (1 g, 3.4 mmol, 1 equiv) in dry DCM (6 mL). The solution was cooled to 0 °C and oxalyl chloride (0.31 mL, 3.7 mmol, 1.5 equiv) was added dropwise. After 15 min, the reaction mixture was allowed to reach room temperature and was stirred for 1 h. The reaction mixture was concentrated under reduced pressure and the residue was resuspended in dry DCM (4.5 mL). A solution containing N-Boc-1,6-hexadiamine (0.72 g, 3.4 mmol, 1 equiv) and (*i*-Pr)$_2$NEt (1.73 mL, 10.1 mmol, 3 equiv) in DCM (4.5 mL) was added dropwise at 0 °C. After 15 min, the reaction mixture was allowed to reach room temperature and was stirred for 1 h. The reaction mixture was concentrated under reduced pressure and purified by flash column chromatography (AcOEt/petroleum ether 1:1). The resulting product was dissolved in 4 M HCl in dioxane and stirred for 1 h at room temperature. HCl was coevaporated three times with diethyl ether to afford a white paste (mass: 400 mg, yield: 30% for 2 steps). IR (film): 3265, 2935, 2860, 2225,1770, 1635, 1585, 1550, 1490, 1435, 1370, 1315, 1180, 1120, 1050, 1010, 975, 890, 870, 820, 760, 730, 700 590 cm^{-1}.^{1}H NMR (400 MHz, MeOD): δ = 7.64 (s, 1H, C**H**), 3.39 (t, 2H, C**H$_2$**), 2.92 (t, 1H, C**H$_2$**), 2.30 (s, 9H, (C**H$_3$**)$_3$), 1.66 (m, 4H, (C**H$_2$**)$_2$), 1.44 (m, 4H, (C**H$_2$**)$_2$). ^{13}C NMR (101 MHz, MeOD): δ = 169.50 (**Cq**), 168.35 (**Cq**), 133.72 (C(aromatic)), 121.00 (C(aromatic)), 40.81 (**CH$_2$**), 40.63 (**CH$_2$**), 30.11 (**CH$_2$**), 28.44 (**CH$_2$**), 27.32 (**CH$_2$**), 26.96 (**CH$_2$**), 20.38 (**CH$_3$**), 19.96 (**CH$_2$**). MS (ESI): HRMS (ESI) m/z calcd for $C_{19}H_{26}N_2O_7$+H, 395.1818; found 395.1823.

*11,12-Didehydro-5,6-dihydrodibenzo[a,e][8]annulen-5-yl(6-{[(3,4,5-trihydroxy phenyl)carbonyl]amino}hexyl) carbamate (**5**).* 5-[(6-Aminohexyl)carbamoyl]benzene-1,2,3-triyl triacetate **3** (75 mg, 0.2 mmol, 1 equiv) was dissolved in DMF (18 mL) and carbonic acid, 5,6-dihydro-11,12-didehydrodibenzo[*a*,*e*]cycloocten-5-yl ester, 4-nitrophenyl ester 4,[20,21] (80 mg, 0.2 mmol, 1 equiv) followed by triethylamine (0.08 mL, 0.6 mmol, 3 equiv) were added. The reaction mixture was stirred overnight at room temperature. DMF was removed under reduced pressure and the product was purified by flash column chromatography (AcOEt/petroleum ether 1:1 then 2:1) (mass: 150 mg, yield: 46%). The resulting product (33 mg, 0.05 mmol, 1 equiv) was dissolved in THF at 0 °C and a 1 M solution of LiOH (0.15 mL, 0.15 mmol, 3 equiv) was added. The reaction was monitored by MS until total conversion of the starting material. The product was purified by HPLC ((XTerra Prep RP C18, (25 × 150 mm Waters)) to give compound **5** (mass: 10 mg, yield: 38%). IR (film): 3275, 2935, 1695, 2595, 1515, 1450, 1330, 1200, 1135, 1035, 865, 755, 720, 645, 585 cm^{-1}. ^{1}H NMR (400 MHz, MeOD): δ = 7.38 (d, 1H, aromatic, C**H**), 7.37−7.29 (m, 7H, aromatics, (C**H**)$_7$), 6.82 (s, 2H, (C**H**)$_2$), 5.42 (m, 1H, C(1′)**H**), 3.22 (dd, 1H, ^2J = 15.0, ^3J = 2.0 Hz (C**H$_2$**)), 3.11 (t, 2H, ^2J = 2.0 Hz (C**H$_2$**)), 2.82 (dd, 1H, ^2J = 15.0, ^3J = 3.8 Hz (C**H$_2$**)), 1.60−1.29 (m, 10H, (C**H$_2$**)$_5$). ^{13}C NMR (100 MHz, MeOD): δ = 169.12 (**Cq**), 156.64 (**Cq**), 152.34 (**Cq**), 151.03 (**Cq**), 136.52 (**Cq**), 129.57 (C-(aromatic)), 127.92 (C(aromatic)), 127.81 (C(aromatic)), 126.89 (C(aromatic)), 126.84 (C(aromatic)), 125.74 (C-(aromatic)), 125.48 (C(aromatic)), 124.99 (C(aromatic)), 123.47 (C(aromatic)), 112.39 (**Cq**), 109.57 (**Cq**), 76.40 (**CH**), 45.74 (**CH$_2$**), 40.28 (**CH$_2$**), 39.36 (**CH$_2$**), 29.40 (**CH$_2$**), 29.10 (**CH$_2$**), 26.25 (**CH$_2$**), 26.06 (**CH$_2$**). MS (ESI): HRMS (ESI) m/z calcd for $C_{30}H_{30}N_2O_6$+H, 515.2182; found 515.2180. $[\alpha]_D^{25}$ = 0.1 (c = 0.004, CH_2Cl_2).

Chemical Coating of the Scaffold Discs. Disks (d = 2.5 cm, h = 0.5 cm) of aluminum oxide scaffolds were incubated in an aqueous solution of compound **5** at increasing concentrations (0, 5, and 10 μM) for 24 h at room temperature in the dark under slight stirring. The disks were washed three times with water and dried under vacuum for 24 h.

Cell Assays. *Cell Cultures and Treatments.* Human SaOs and U$_2$Os osteosarcoma cells were obtained from the American Tissue Culture Collection (ATCC, Manassas, VA, USA). Human adult skin fibroblasts were derived from human skin biopsy and were kindly provided by M. Benathan, CHUV, Lausanne, Switzerland. Human fetal osteoblasts (osteoprogenitors) were derived by the explant technique from the femoral bone of a 12-week-old fetus according to a protocol accepted by the Lausanne Hospital and University Ethics Committee and with the mother's oral and written approval (protocol no. 51/01, 2008). These cells were used at passage 6. Cells were routinely grown in DMEM medium containing 4.5 g/L glucose, 10% fetal calf serum (FCS), and antibiotics (all from Gibco, Basel, Switzerland). On the day of the experiments, cells were detached for the flasks using trypsin-EDTA (Gibco), washed once in complete culture medium, and suspended in complete culture medium. Then, 50−75 μL (~500 × 10^3 cells/scaffold) of the cell suspension were slowly added on the top center of the scaffold discs (1 cm diameter) inserted into a well of a 24-well culture plate (Costar, Corning Inc., NY, USA) until the red cell suspension was completely absorbed by the scaffolds. Then, 2 × 100 μL of complete culture medium was added. After 6 h, 200 μL of complete culture medium was added on the bottom of the culture well. Estimation of cell behavior in the scaffolds was determined at different times post seeding (see below).

Evaluation of Cell Repartition in the Scaffold Compartments. The quantification of cell repartition in the 3 compartments of the culture system, i.e., the scaffold, the bottom of the cell culture well under the scaffold, and the cells and/or fragments from dead cells in the culture medium, was performed by adapting a previously published radioactive-labeling procedure for cell−cell adhesion[22] to the scaffold system. Briefly, cell DNA was stably prelabeled for 24−144 h (depending on the rate of cell proliferation) by tritiated thymidine (0.5 μCi/mL [^{3}H]-thymidine, Amersham Pharmacia,

Dübendorf, Switzerland), then added to the scaffolds as described above. At the end of the incubation of cells in the scaffolds, 25 μL of the culture medium of the cell−scaffolds was removed and dissolved in 0.5 mL 1% SDS in 0.1 M NaOH. To quantify cell-associated radioactivity repartition in the foam system, cell−scaffolds were removed from their wells, washed twice in 0.9% NaCl, and then immersed for 2 h in 0.5 mL SDS-NaOH. The cell layers at the bottom of the wells were treated in the same manner. Five milliliters of scintillation cocktail (Optiphase Hisafe 3, Perkin-Elmer, Shelton, CT, USA) was added to all samples and radioactivity was quantified in a beta-counter (WinSpectra, Wallac, Germany). Means ± standard deviation (sd) were calculated.

Evaluation of Cell Survival and Metabolic Activity in Scaffolds Using the MTT Assay. To quantify metabolically active cells in the scaffolds, the MTT reduction assay for in-scaffold end-point determinations was used. Briefly, scaffolds loaded with cells were exposed to 0.25 mg/mL (final concentration) MTT ((3,4,5-dimethylthiazol-yl)-2,5-diphenyl tetrazolium, Sigma, Buchs, Switzerland) added to complete culture medium for 1 h (osteosarcoma cells) or 4 h (human osteo-progenitors), and the blue−violet precipitated formazan in the scaffolds was fixed in 4% buffered paraformaldehyde and photographed. Alternatively, MTT reduction was quantified according to a modification of a previously described procedure.[23] Following exposure to MTT for 2 h, the scaffolds were washed twice in PBS and immersed in 0.1 N HCl in isopropanol to dissolve the blue precipitated formazan, and the extracts were quantified in a multiwell-plate reader (iEMS, Labsystems) at 540 nm.

Evaluation of Cell Proliferation in the Scaffolds Using Alamar Blue. To quantify osteosarcoma cell proliferation in the scaffolds, the Alamar Blue reduction test was used. This assay allows repeated determination of cell metabolic activity in the same sample, providing a cell proliferation time course. One day after seeding, the scaffolds containing the cells were transferred to a new well containing 0.5 mL of fresh complete culture medium, then 40 μL Alamar Blue (Serotec, Düsseldorf, Germany) was added and the fluorescence was measured in 100 μL aliquots removed at 0 and 45 min after the addition of the Alamar Blue in a multiwell-plate fluorescence reader (Cytofluor, PerSeptive BioSystems) at $\lambda_{ex}/\lambda_{em}$ = 530 nm/580 nm. Then, the cell-scaffolds were transferred in fresh complete culture medium to continue the incubation for another day, and the process was repeated at day 2 and at day 3. Experiments were repeated at least twice.

Evaluation of Long-Term Survival and Proliferation of Osteo-Progenitors in the Scaffolds Using the WST-1 Assay. For long-term cultures (6 weeks) of osteo-progenitors, a repeated WST-1 (2-(4-iodophenyl)-3-(4-nitrophenyl)-5-(2,4-disulphophenyl)-2*H*-tetrazolium, Roche Diagnostics, Rotkreuz, Switzerland) assay was performed at two week intervals. In a 24-well plate, fetal osteoblasts were seeded on S3 scaffolds (~500 × 10^3 cells/scaffold) and left to adhere and grow in complete culture medium as above. The culture medium of all cell−scaffolds was changed once a week to fresh complete medium. At two week intervals, the culture medium of 2−3 scaffolds was removed, 500 μL of fresh complete medium containing 50 μL WST-1 added, and the scaffolds returned to the cell culture incubator. After 5, 30, 60, and 120 min, 100 μL aliquots of WST-1-culture medium were removed and added to a well of a sterile 96-well plate. Optical density of the supernatants was measured at 450 nm in a multiwell-plate reader (iEMS Reader MF), and the medium was returned to their respective wells and culture continued until the next time point. At the end of the measurements, the metabolic activity of cells in the scaffolds was controlled using an in-scaffold MTT test.

Scanning Electron Microscopy (SEM) of Cells Inside the Scaffolds. Cells were seeded onto the scaffolds as described above and incubated for 24 h to 6 weeks in complete culture medium. Scaffolds containing the cells were then washed twice in PBS and fixed in 2 mL of 4% buffered paraformaldehyde. The scaffold disks were broken in half and their cross section analyzed by means of SEM (LEO 1530, Zeiss Oberkochen). To visualize the cells, mixed mode detection (combining the SE2 and Inlens signal) was used at an acceleration voltage of 3 kV.

Osteogenic Cell Differentiation. Human U_2Os cells, SaOs cells, or osteo-progenitors were grown in differentiating medium (adapted from ref 24), consisting of complete culture medium supplemented with dexamethasone (10 nM final concentration, Sigma-Aldrich), 2-phosphate-ascorbic acid (0.15 mM final concentration, Sigma-Aldrich), and β-glycerophosphate (0.25 mM or 2.5 mM, final concentration, Sigma-Aldrich) for 7 or 14 days. Medium was changed once a week to complete differentiating medium, and then the cell layer was washed and extracted either in RIPA buffer for Western blotting experiments or in 15 mM Tris pH 8.8/0.1% Triton X-100 (Fluka, Sigma-Aldrich) for 10 min at 4 °C for alkaline phosphatase activity determination. Protein content of the extracts was quantified using the BCA kit (BCA Protein Assay Kit, Pierce, Rockford, USA) and bovine serum albumin (BSA) as standard.

To determine alkaline phosphatase activity (adapted from ref 25), 10−200 μL aliquots of cell extracts adjusted to 200 μL with 15 mM Tris pH 8.8 were added in wells of a 96-well plate, then 10 μL of *para*-nitrophenyl phosphate (pNp, stock solution 1 mg/mL H_2O, Sigma-Aldrich) was added, and the increase in absorbance at 405 nm was recorded for 30 min at 37 °C in a multiwell plate reader (iEMS, Labsystems). Enzymatic activity was expressed as units of enzymatic activity [1 U = 1 μmol pNp hydrolyzed/min, using ε = 1.8 × 10^4 M^{-1} cm^{-1} for *p*-nitrophenol]. U/mg proteins were calculated and the enzymatic activities of differentiated cells were compared to the enzymatic activities of undifferentiated cells.

For determination of collagen type I by Western blotting, cells were grown in 9-cm-diameter Petri dishes, then the cell layers were washed with cold PBS and lysed in 200 μL of lysis buffer (150 mM NaCl, 2 mM EDTA, 0.5% Triton X-100, 50 mM Tris-HCl, 2 mM vanadate, 50 mM NaF, pH 7.2) and 10 μL of proteinase inhibitor cocktail (Sigma-Aldrich), scraped with a cell scraper, extracted by 4 cycles of freeze/thawing, and centrifuged at 10 000 rpm at 4 °C for 10 min. Protein content in the supernatants was quantified using the BCA reagent and an extract volume corresponding to 30 μg protein was heated for 5 min at 95 °C in the absence of a reducing agent, submitted to SDS-PAGE and transferred onto a nitrocellulose membrane (Whatman, Dassel, Germany). The membranes were blocked with 5% fat-free milk in PBS, washed in 0.05% Tween-20 (Sigma-Aldrich) in PBS and incubated overnight at 4 °C with a polyclonal antihuman collagen type I proα2 chain antibody (Abcam, Cambridge, UK; anti-Col1A2, ab96723; diluted 1:2500 in 1% fat-free milk and 0.05% Tween-20 in PBS), then exposed for 60 min to peroxidase-conjugated anti-rabbit antibody (Promega, diluted 1:5000) and visualized using chemiluminescence (ECL, GE Healthcare, Amersham, UK). To

control for loading, the membranes were stripped by successive incubation in 0.1 M glycine pH 2.3, 1 M NaCl in PBS and 0.05% Tween-20 in PBS, blocked for 1 h with 5% fat-free milk in PBS, and exposed to a monoclonal antihuman α-tubulin antibody (Abcam, diluted 1:10000) for 1 h, then to a peroxidase-conjugated antimouse antibody (Sigma-Aldrich, diluted 1:5000) at rt and treated as above. For the purpose of comparison, human adult skin fibroblasts[26] were treated under the same conditions.

Click-Reaction on the Biomaterial. L-Azidohomoalanine (AHA) was purchased from Invitrogen, and BSA from Sigma-Aldrich, Buchs, Switzerland. Nine centimeter Petri dishes (Costar) were coated with 1000 μg/mL Rat Tail collagen I (Invitrogen) according to the supplier's protocol, and human osteo-progenitors were then grown in the dishes for 24 h until the cells are 80−90% confluent. The cells were washed with PBS and incubated in methionine-free DMEM culture medium (Gibco) for 60 min to deplete methionine reserves. Then, the cells were incubated overnight in the presence of AHA (50 μM final concentration) in fresh complete methionine-free culture medium. The culture medium was removed and the cell layers were washed twice with PBS. Collagen coating was degraded by adding 0.1 mg/mL collagenase (Sigma-Aldrich) in PBS at 37 °C for 45 min. The osteo-progenitors were then counted. Three milliliter aliquots of the cell suspension (10^5 cells/mL) were added on unfunctionalized scaffolds or scaffolds functionalized with compound **5** in a 6-well plate (Costar) and incubated for 1 h at rt under slight agitation. The disks were washed once with PBS, fixed in cold methanol (−20 °C) for 5 min, and incubated in 5% BSA for 1 h at rt. Cells were stained for 5 min at rt with a solution containing 0.05% crystal violet (Sigma-Aldrich) and 1.5% glacial acetic acid in water. Cells were imaged by stereomicroscopy (MZ16 FA Leica/DFC 480 Leica, 0.63× and 1.6×, zoom 72×), three pictures for each treatment were taken, and the cell number was evaluated using *Image J* software.

RESULTS

Preparation and Characterization of the Scaffolds. We have previously designed techniques to prepare porous ceramics via a direct foaming method.[13,17] The adaption of this foaming method allowed the production of macroporous scaffolds which are tailored not only in pore size, but also in pore interconnectivity.[18,19] In the present study, we were able to implement this direct foaming method to produce scaffolds from calcium aluminate and then evaluated them as potential permanent bone graft materials. To obtain porous scaffolds with different microstructures, ceramic foams with varying pore sizes and porosities were produced from slightly varying compositions (Table 1). The sintered specimens could easily be machined into different shapes (Figure 1a), and the SEM micrographs showed an open porosity, resulting in a network of interconnected pores (Figure 1b−d). Size distributions of the scaffold pores and pore-openings were determined (Figure 2). As shown in Table 1 and Figure 2, scaffolds S1 and S2 are equal in average pore diameter (170 μm) and display pore openings (or windows) of similar sizes (50 and 60 μm in diameter, respectively). The microstructure of scaffold S3 has a two to three times larger average pore size of 460 μm and pore openings of 95 μm. The porosity (or air content) of the different scaffolds is the same for scaffolds S1 and S2 (76 vol %) and is higher for scaffold S3 (86 vol %). Thus, by varying the suspension composition, foam scaffolds with different microstructures and porosities were obtained.

Table 1. Physicochemical Characteristics of the Different Scaffolds

scaffold no	average pore size [μm]	average pore opening [μm]	porosity [vol %]	Al_2O_3 [wt %]	CA-270 [wt %]	ratio cement to alumina
S1	170	50	76	12.7	33.7	2.7
S2	170	60	76	32.9	4.3	0.1
S3	460	95	86	10.8	26.3	2.4

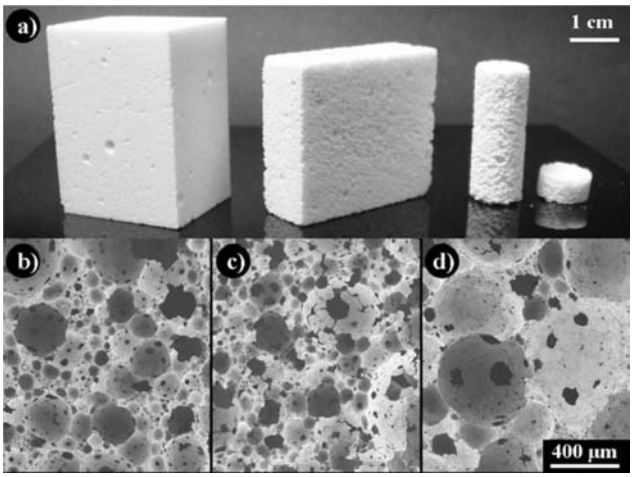

Figure 1. Macroscopic and microscopic aspect of the scaffolds. Upper panel: (a) macrophotographs of the three different scaffold materials (from left to right: scaffold S1, scaffold S2, and two pictures of scaffold S3). Lower panels: SEM micrographs of (b) scaffold S1; (c) scaffold S2; (d) scaffold S3.

Interaction of Human Osteosarcoma Cells with Scaffolds. U_2Os and SaOs human osteosarcoma cells are widely used as cell models for human bone-derived cells and are more readily available than primary human bone cells. Thus, in order to select the scaffolds with optimal characteristics allowing human bone cells to adhere, survive, and migrate, these cells were used as initial screening tools. To evaluate the biocompatibility of the scaffold materials, the metabolic activity of human U_2O_S osteosarcoma cells 1 to 3 days after seeding in the 3 scaffolds was determined using the Alamar Blue assay, which allowed repeated evaluation of the same samples (Figure 3). Cells were seeded in the scaffolds by placing complete cell culture medium containing phenol red and cells onto the top of the scaffolds. After the absorption of the cell culture medium in the scaffolds, the red cell culture medium slightly drained from below the three scaffolds, indicating that the microstructures of the scaffolds allow the flow through of cell culture medium. Under an inverted optical microscope after 1 day culture, few cells were seen adhered on the bottom of the culture wells under scaffolds S1 and S2, while more cells were found on the bottom of the wells under scaffold S3. Thus, the initial trans-scaffold migration of the cells, as expected, was mainly determined by the pore size and the size of the interpore openings of the scaffolds. The cells which migrated outside the 3 scaffolds were well-spread and attached to the well plate bottoms and were metabolically active as demonstrated using a MTT test (not shown), suggesting that the cell viability was not

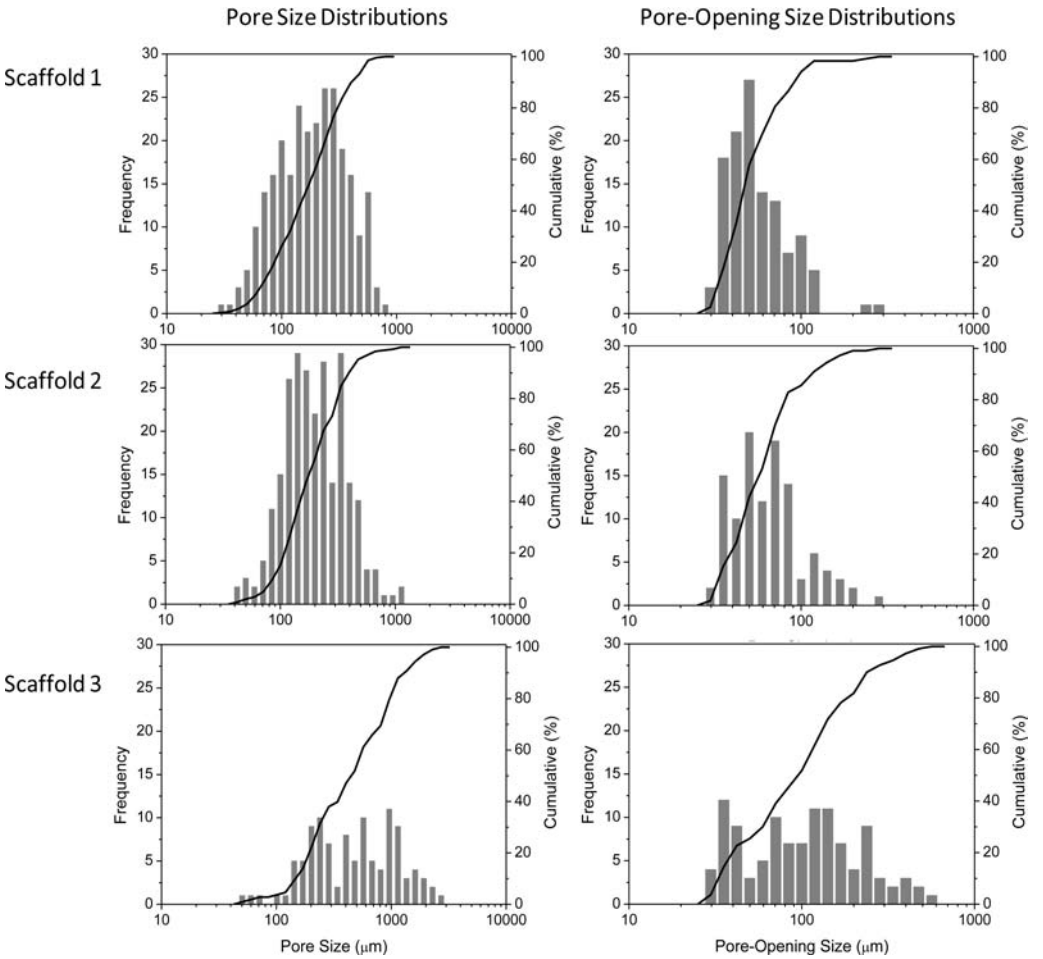

Figure 2. Size distribution of the pores and pore openings for the 3 different scaffolds. To define the diameters of the pores and pore-openings, SEM micrographs at low magnifications were analyzed (gray bars) using the software *Linear Intercept*, then the cumulative values were calculated (solid lines).

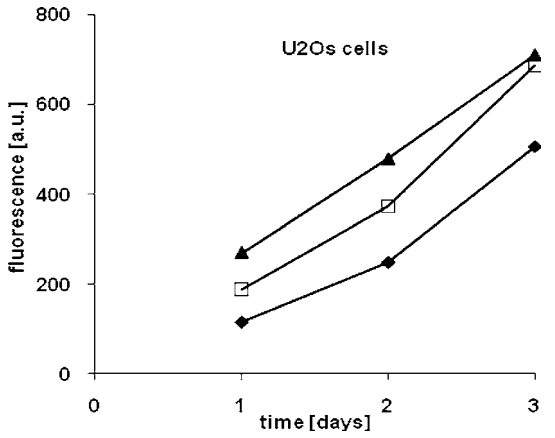

Figure 3. Determination of the proliferation of human U_2Os osteosarcoma cells 1 to 3 days after seeding in the scaffolds. To evaluate for cell proliferation in the scaffolds, U_2Os cells were seeded onto one of each of the three scaffolds (S1, S2, S3) and culture was performed for 24 h. AlamarBlue was added to the cell–scaffolds, and fluorescence measured after 45 min. Then, fresh medium was added and culture continued, and the process was repeated after 48 and 72 h of cell culture in the scaffolds, allowing the same cell–scaffold system to be sequentially analyzed on day 1, day 2, and day 3. ♦ scaffold S1; □ scaffold S2; ▲ scaffold S3.

affected by the scaffold material during initial cell migration across the scaffolds.

In order to determine the repartition of cells and cell components in the 3 compartments of the scaffold culture system, i.e., the cells in the scaffolds, the cells on the bottom of the cell culture wells under the scaffold, and the culture medium bathing the scaffolds, the DNA of U_2Os and SaOs human osteosarcoma cells was stably prelabeled with radioactive [^{3}H]-thymidine and the radioactivity was quantified in the different partitions of the cell–scaffold systems (Supporting Information, Table S1). For all cell–scaffolds, the amount of radioactivity measured in the scaffolds was always much higher than in the well plate bottoms or in the culture media, for all time periods and both cell lines, strongly suggesting that most cells were retained inside the scaffolds. Thus, calcium aluminate bioceramic scaffolds are good substrates for long-term adhesion and survival of human bone-derived cells.

Human SaOs and U_2Os osteosarcoma cells grown for either 1 day or 4 days in the three different scaffolds were examined using SEM (Figure 4A). The micrographs showed that the cells adhered to and spread onto the ceramic surface of all three scaffolds, indicating a good acceptance of the scaffold material by the living cells. To determine if the cells were able to migrate across the whole scaffold, U_2Os cells were seeded on the top of scaffold S3 (Figure 4B, arrow) and grown for 4 days in the scaffolds, then after fixation in buffered paraformaldehyde, the

dx.doi.org/10.1021/bc300407x | *Bioconjugate Chem.* 2012, 23, 2278–2290

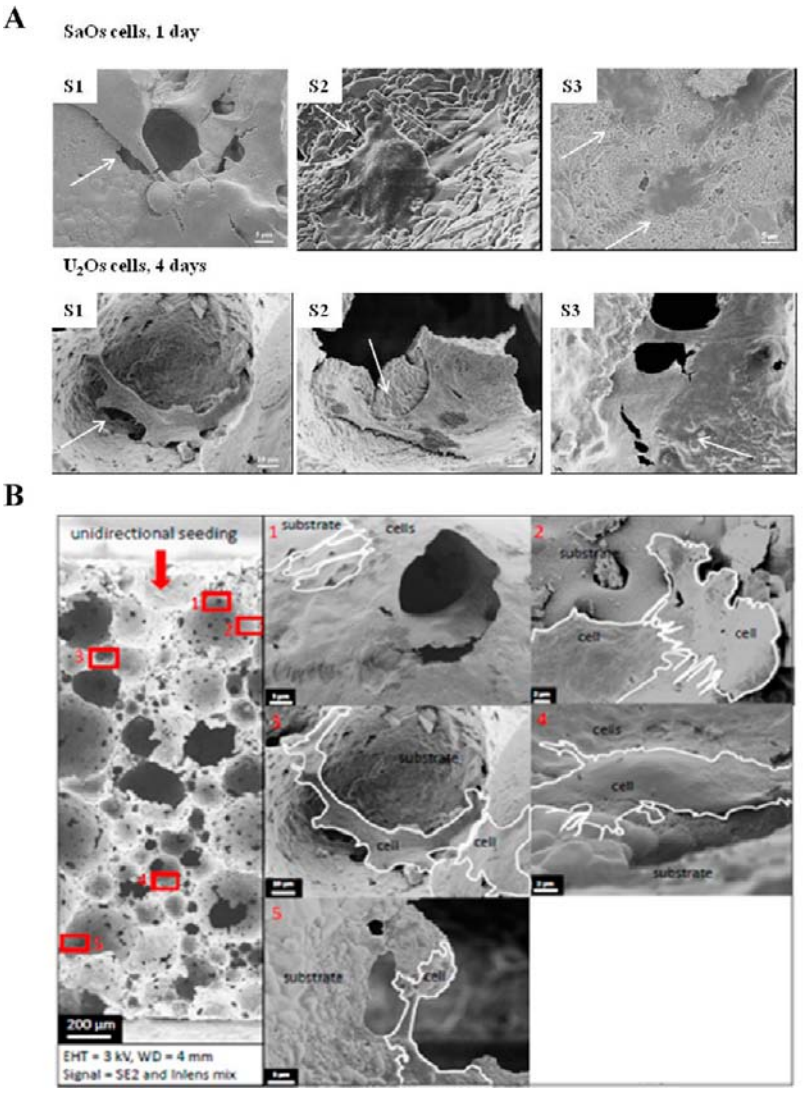

Figure 4. SEM micrographs of human osteosarcoma cells inside the scaffolds. (A) Human SaOs (upper panels) and U_2Os (lower panels) osteosarcoma cells were grown in scaffold S1 (S1), scaffold S2 (S2), or scaffold S3 (S3) for, respectively, 1 day or 4 days. After fixation in paraformaldehyde, the scaffolds were split and SEM pictures of the cells inside the scaffolds taken, showing that the cells adhered and spread onto the ceramic materials. White arrows indicate the cells. (B) Human U_2Os osteosarcoma cells were unidirectionally (red arrow) seeded on top of the scaffold and grown for 4 days in scaffold S3. Then, the scaffold was fixed in paraformaldehyde, split in the middle, and the fracture section scanned by SEM. Isolated cells (labeled 1−5) are shown at higher magnification in panels 1−5. For improved viewing, the cell shapes are surrounded by a white line.

scaffold was broken in the middle and the whole fracture section examined by SEM (Figure 4B, left panel), showing cells located at different levels of the scaffold from the initial seeding point at the top of the scaffold. The cells were examined at higher magnification (Figure 4B, panels 1 to 5) showing well-spread cells on their substrate at all levels of localization in the scaffolds. Thus, the SEM images and the proliferation experiments strongly suggested biocompatibility of the different scaffold materials and ability of living cells to migrate across the scaffolds. In particular, scaffold S3 presented with optimal properties for cell migration, and was selected for further evaluation using human primary osteo-progenitors.

Interaction of Human Osteo-Progenitors with Scaffold S3. Human primary osteo-progenitors derived from the femoral bone of a 12-week-old fetus[27,28] were first compared to human osteosarcoma cells for their expression of differentiation markers of bone cells, either under standard culture conditions or in differentiating cell culture medium. Three markers of the human osteoblast cell lineage were analyzed: the expression of the proα2 chain of type I collagen (Figure 5A), alkaline phosphatase activity (Figure 5B), and the cell ability to deposit calcium (Figure 5C). Collagen type I is found in most connective tissues, and defects of this protein have been involved in disorders of the bone, such as osteogenesis imperfecta. Human skin fibroblasts were used as positive controls of the expression of collagen type I. Human osteo-progenitors and skin fibroblasts expressed collagen type I, but not the two human osteosarcoma cell lines. This expression could not be induced when the osteosarcoma cells were grown in differentiating medium for 7 to 14 days, and no further increase in collagen I expression by osteo-progenitors grown in differentiating medium for up to 14 days was observed (results not shown). Alkaline phosphatase activity was increased over basal activity level by a factor 2 in the two human osteosarcoma cells and by a factor 20 in the osteo-progenitors by culturing them for up to 14 days in differentiating medium. It must be

dx.doi.org/10.1021/bc300407x | *Bioconjugate Chem.* 2012, 23, 2278−2290

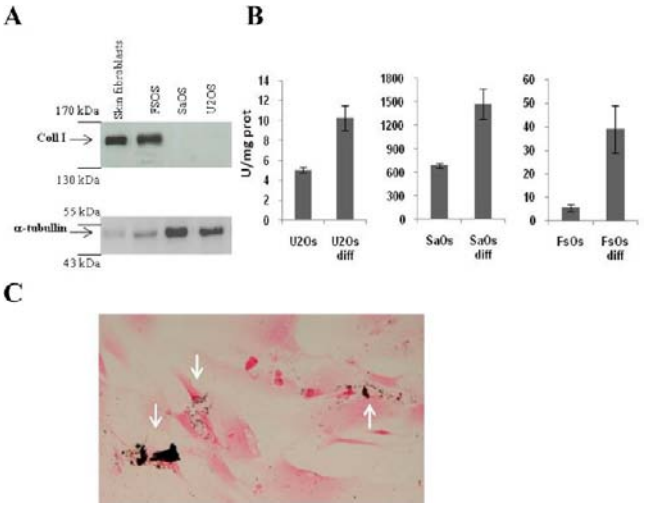

Figure 5. Expression of collagen I, alkaline phosphatase activity, and calcium deposits by human bone-derived cells. (A) Human cells (skin fibroblasts, osteo-progenitors (FsOS) and osteosarcoma cells (SaOs, U_2Os)) were grown to confluence in Petri dishes and extracted. Cell extracts were submitted to Western blotting experiments using an antihuman collagen I antibody, and loading was controlled using an antihuman α-tubulin antibody. When the cells were grown in differentiating medium for 7 to 14 days, no induction of collagen I expression by U_2Os and SaOs cells and no further enhancement of collagen I expression by FsOs cells by differentiation medium was observed (not shown). (B) Alkaline phosphatase activity (U/mg protein) was determined in human osteo-progenitors (FsOs), along with osteosarcoma cells (SaOs, U2Os) grown either in standard or in differentiating culture medium (diff) for 10 days. Means of triplicate wells ± sd were calculated. Experiments were repeated three times with similar information. No further enhancement of alkaline phosphatase activity by FsOs cells by differentiation medium was observed for longer culture in differentiation medium (not shown). (C) Kossa staining of calcium deposits (black staining, arrows) in terminally differentiated, nonproliferating human osteo-progenitors. Cell cytoplasm is stained light pink and cell nuclei dark pink.

emphasized that the basal alkaline phosphatase activity of SaOs cells is much higher than that of the two other cells, U_2Os cells or osteo-progenitors. Human osteo-progenitors were able to deposit calcium. Therefore, these human bone-derived histocompatible fetal cells represent human bone-derived cells able to differentiate into bone cells, and are relevant models to evaluate the interaction of human primary bone-derived cells with the newly prepared scaffolds S3.

The radioactivity of human osteo-progenitors stably prelabeled with radioactive [^{3}H]-thymidine was quantified in the cells in the scaffold S3, in the cells on the bottom of the cell culture wells under the scaffold, and in the culture medium bathing the scaffolds 2 days and 6 days after seeding (Figure 6A). As for human osteosarcoma cells, the amount of radioactivity measured in the scaffolds was much higher than in the two other compartments of the system, but some cells could be detected on the bottom of the culture wells, under the scaffold. Six days after seeding in scaffold S3, osteo-progenitors were examined using SEM (Figure 6B). The micrographs showed that the cells adhered to and spread onto the ceramic surface of the scaffolds, able to make cell bridges across the pores in the image which we selected as an example. Therefore, the long-term proliferation of human osteo-progenitors in the scaffolds was evaluated using a WST-1 assay demonstrating that the cells proliferated in the scaffolds for up to 6 weeks (Figure 6C). The proliferative properties of human osteo-progenitors were maintained for cells seeded in scaffold S3 in differentiating medium and were comparable to the proliferation of cells grown in the same medium on cell culture plastic (results not shown). To confirm the long-term in-scaffold viability and metabolic activity of osteo-progenitors after culture inside the scaffolds, the human osteo-progenitors were grown for 6 weeks in scaffold S3 or scaffold S1 for the purpose of comparison. Then, a modified in-scaffold MTT assay (which is based upon the reduction of the soluble yellow MTT molecules to a violet formazan precipitate by the respiratory chain of living cell mitochondria) was developed. The cell-associated violet precipitate proved cell metabolic activity and viability inside the scaffold S3 for a long period of time (Figure 6D). The violet cell staining on both the top and bottom sides of scaffold S3 suggested that viable cells still colonized the whole scaffold after 6 weeks, whereas for scaffold S1, only the top side where the cells were initially seeded, but not the bottom side of the scaffolds, was stained. Thus, a large-porosity microstructure facilitates primary human osteo-progenitor migration across the scaffolds and allows their survival in the scaffolds for at least 6 weeks.

In order to further determine the repartition of primary human osteo-progenitors in the scaffolds S3 6 weeks after seeding, the scaffolds were fixed in buffered paraformaldehyde, broken in the middle, and the whole fracture section examined by SEM. Low magnification (Figure 7a) was used to visualize cells located at different levels of the scaffold (highlighted by white circles and numbers) from the initial seeding at the top of the scaffold. Cells were examined at higher magnification (Figure 7b, panels 1 to 9), showing good distribution and viable cells at all levels of localization in the scaffolds.

Therefore, the porous calcium aluminate ceramic scaffolds that we developed, in particular, scaffold S3, displayed the requested characteristics that we initially defined: allowing human bone cell trans-scaffold migration and in-scaffold survival and proliferation. However, we observed that the addition of human bone-derived cells, either osteosarcoma cells or osteo-progenitors, on the top side of scaffolds S3 resulted in the rapid appearance of a few cells on the bottom side of the scaffolds, suggesting that the adhesion of the cells to the bioceramics was not rapid enough to ensure the optimal cellularization of these scaffolds with bone cells and should be improved

Click-Functionalization of the Scaffolds and Adhesion of Human Osteo-Progenitors. We have previously shown that alumina-based scaffolds can be chemically functionalized with gallate-based ligands.[29] In particular, the pyrogallol moiety allows efficient complex formation with the aluminum present in the inorganic matrix, thus ensuring stable functionalization of the scaffold surface. We have also previously shown that human osteo-progenitors can be chemically functionalized using biocompatible click chemistry.[30] Thus, in order to enhance the adhesion of the osteo-progenitors to the scaffold, we combined these two approaches by designing and synthesizing (Scheme 1) compound **5**, a heterobifunctional ligand bearing a gallate functionality and an activated alkyne. The alumina scaffolds were functionalized with compound **5**, and then the azido-modified human osteo-progenitors (10^6 cells per scaffold) were added to scaffolds that were either unfunctionalized or had been prefunctionalized with compound **5** (5 or 10 μM). After the washing and fixation steps, the cells were stained with crystal violet (Figure 8A). Cell adhesion to the scaffolds

dx.doi.org/10.1021/bc300407x | Bioconjugate Chem. 2012, 23, 2278−2290

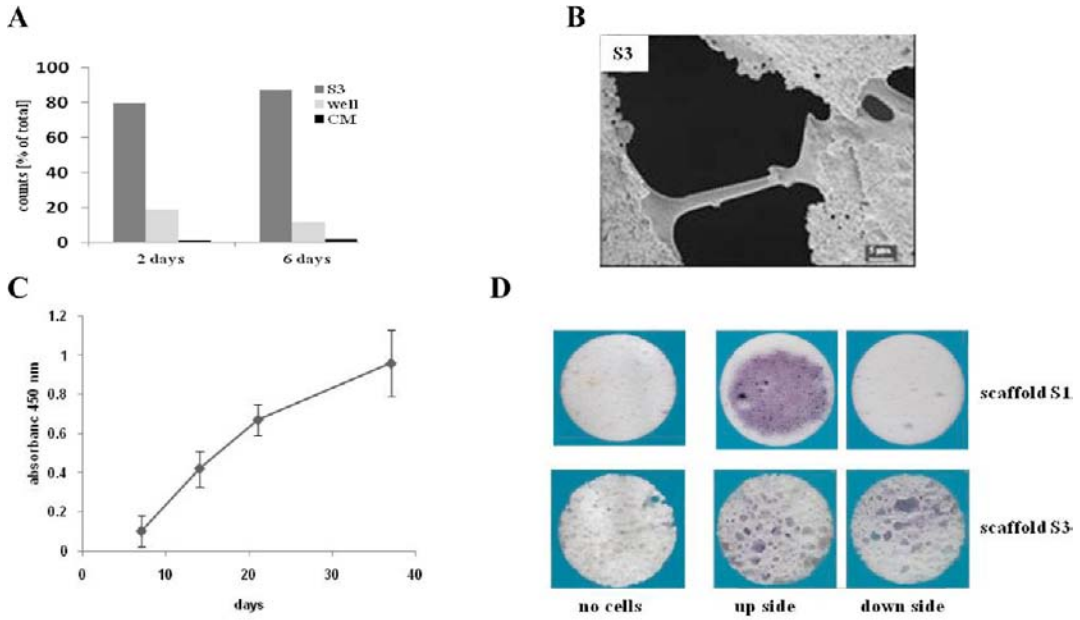

Figure 6. Human osteo-progenitors grown in scaffold S3 are retained, proliferate, and are metabolically active in the scaffolds for at least 6 weeks (A) Human osteo-progenitors were prelabeled with [^{3}H]-thymidine, then grown in the scaffolds for 2 or 6 days. Radioactivity was quantified in extracts of the cells in the scaffolds (dark gray), associated to the cells at the bottom of the wells (light gray) and in the soluble culture media (black). The experiments were repeated twice, with comparable information. (B) Human osteo-progenitors were grown in scaffolds S3 for 6 days. After fixation in paraformaldehyde, the scaffolds were split and SEM pictures of the cells inside the scaffolds taken, showing that the cells adhered and moved into the ceramic materials, spanning across the pores in the selected SEM picture. (C) Human osteo-progenitors were seeded on scaffold S3 and grown in culture medium. After 7, 14, 21, and 38 days of osteo-progenitor culture in the scaffolds, WST-1 was added to the culture medium bathing the scaffolds (2−3 scaffolds per time-point) and absorbance kinetically measured for 30 min. Metabolically active cells reduce WST1 to a soluble red compound whose absorbance is directly proportional to the number of living cells. Differences in absorbance between 30 and 0 min were determined, and means ± sd calculated. (D) Human osteo-progenitors were seeded on the top of scaffolds S3 and grown for 6 weeks in the scaffolds. MTT was added to the culture medium bathing the scaffolds for 3 h, the scaffolds were washed and fixed in paraformaldehyde, and the upper and lower sides of the scaffolds were photographed. Metabolically active cells reduce MTT to a violet precipitate. Scaffolds without cells but exposed to MTT do not color violet. In scaffold S3, cells can be found on both sides of the scaffolds. Experiments performed with scaffolds S1 in the same conditions for comparison demonstrate the presence of cells only on the upward side of these scaffolds.

was imaged with a stereomicroscope and the number of adhered cells was quantified by *Image J* software (Figure 8B). Quantification of the adhered cells showed that the functionalization of the scaffolds with compound **5** increased the number of adhered cells, with a very strong dependency (r = 1.00, 10 μM vs 5 μM) on the amount of compound **5** used for the functionalization of the scaffolds. The observed increase in the number of adhered cells was statistically significant ($p <$ 000.1) and correlated with the concentration of compound **5** used for the functionalization of the scaffold.

DISCUSSION

Major challenges in the development of permanent bone substitutes are biocompatibility and ability of the implant to allow the migration of bone and bone-associated cells across the whole structure. Such characteristics would ultimately facilitate development of adequate bone-mimicking tissue and improve integration of the implant in the patient tissue. Many previous studies have addressed the development of biodegradable materials for small bone defects, whereas studies of three-dimensional scaffolds able to support the survival of bone-derived cells for permanent replacement of bone defects are rare. These permanent scaffolds should be able to reproduce the structure of the bone matrix and be modeled into shapes and characteristics similar to those of the bone tissue to be replaced, while maintaining their structural stability. The ability of such scaffolds to form a porous interconnected network spanning the entire structure is also necessary in order for relevant cells to develop into a functional bone tissue. Ceramics-based materials fulfill many such requirements and are osteoconductive and biocompatible. However, few ceramics with controlled pores spanning the scaffold structures allowing migration and adhesion of cells across the whole structure have been described to date.

Most described methods used to produce porous scaffolds include organic materials and their subsequent elimination from the structure during the sintering process. Previous work by others has shown that titanium-based metal implants of the second generation can be made more porous to allow bone growth through the implant.[31,32] Titanium-based foams are made by impregnating polyurethane forms with titanium powder, hardening of the structure, and washing away the polyurethane, resulting in a material with lower stiffness than solid titanium and that is less brittle than ceramic materials. The materials performed well as permanent implants for disk replacement in animal models.[33−35] Ceramics derived from calcium phosphate mimics the mineral structure of bone, and bone cells were shown to recognize and bind to such ceramics.[36,37] Calcium phosphate-based ceramics have been previously shown to display bone integration properties,[38,39] and calcium aluminate further increases osteointegration.[40,41] Alumina ceramics, including porous alumina, support the attachment, growth, and differentiation of bone cells, the material grain microstructure being important for cell behavior,

dx.doi.org/10.1021/bc300407x | *Bioconjugate Chem.* 2012, 23, 2278−2290

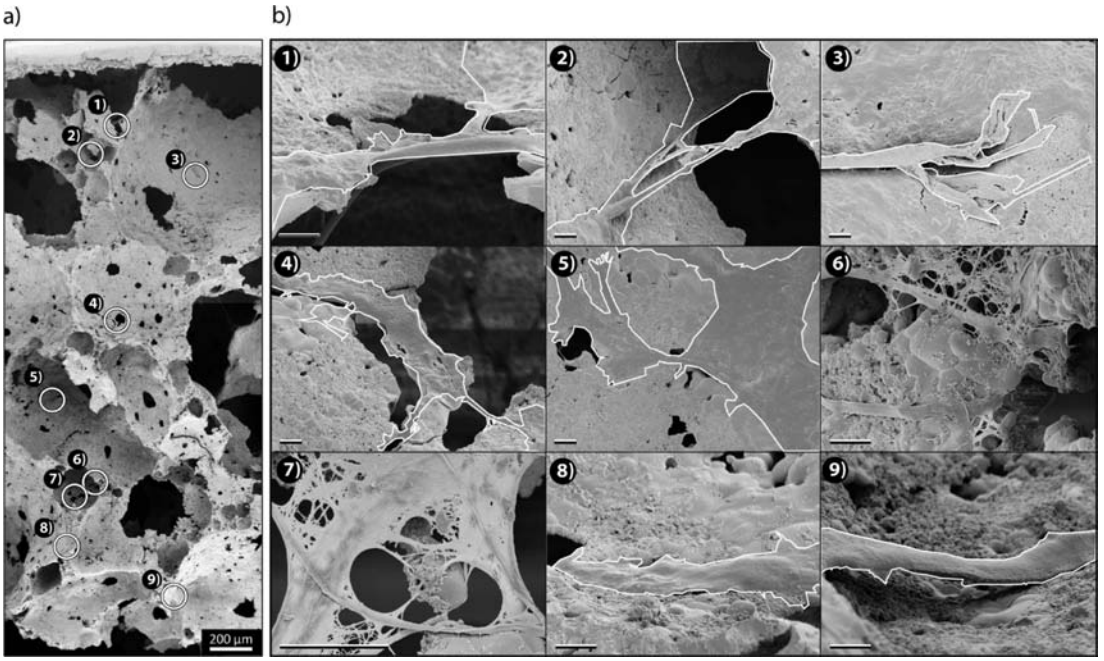

Figure 7. SEM micrographs of human osteo-progenitors inside the scaffolds. Human osteo-progenitors were grown for 6 weeks in scaffold S3. After fixation in paraformaldehyde, the scaffold was split in the middle and the fracture section was scanned by SEM and SEM pictures of the cells inside the scaffolds taken, showing that the cells adhered and spread onto the ceramic materials at all levels of the materials. (a) Cross section of a S3 scaffold, unidirectionally seeded (seeding direction from top to bottom) with osteo-progenitors and cultured in the scaffolds for 6 weeks; bar = 200 μm. (b) Closeups of the cells indicated by a number (1 to 9) in (a). For improved viewing, the cells in the scaffolds were outlined with white lines except in panels b6 and b7 where most of the area is covered by cells; bars = 5 μm.

Scheme 1Synthesis of Compound 5 for the Click-Reaction of Human Fetal Osteoblasts on Scaffolds[a]

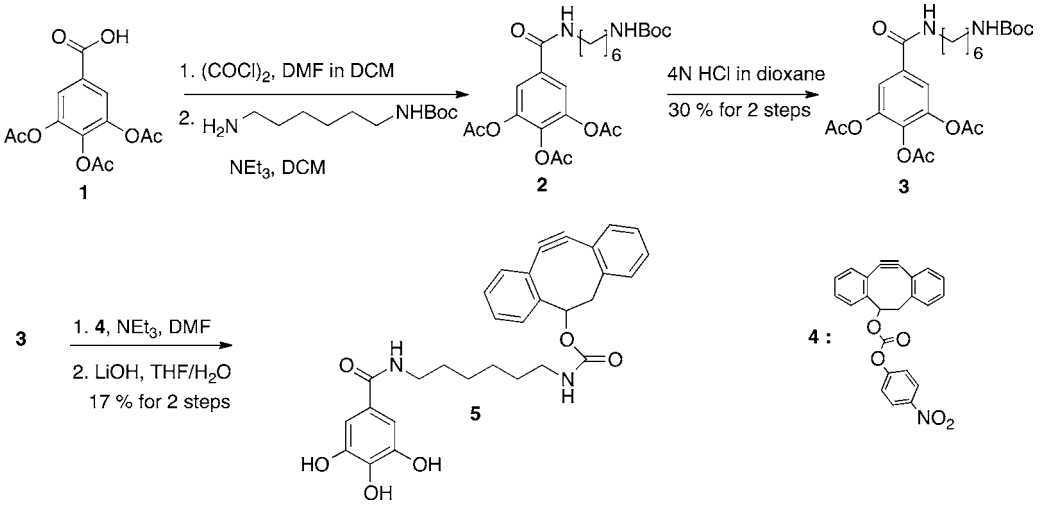

[a]3,4,5-Triacetoxy benzoic acid acid **1** was first converted into the corresponding acyl chloride by reaction with oxalylchloride in presence of DMF and then coupled to N-Boc-1,6-hexanediamine to afford intermediate **2**. After deprotection of the amine under acidic conditions, compound **3** reacted with 6-dihydro-11,12-didehydro-dibenzo[*a*,*e*]cycloocten-5-yl ester, 4-nitrophenyl ester **4**[20,21] in the presence of triethylamine. Finally, deprotection of the three hydroxyl groups under basic conditions provided the desired compound **5**, which was further used for the functionalization of the biomaterial and the click reaction with human osteo-progenitors.

including for a human bone-derived cell line.[5−7] The surface reactivity of bioactive glass ceramics and the sintering process were shown to affect interaction with human osteoblasts, and ultimately their bone integration potential.[42]

In order to develop a permanent bone replacement, which could display an open porous microstructure allowing the establishment of a continuous cellular network of bone-derived cells, we developed a different methodology based on calcium aluminate scaffolds produced from a recently modified direct foaming method.[13−19,43] In order to meet the needs and challenges of the open-pore microstructures required, the so-called *limited coalescence* phenomenon was exploited, where bubbles start to disproportion and coalesce instantly after foaming, until a new equilibrium is reached.[12−17] Then, upon bubble growth, the foam lamellae start to thin, layer by layer, until the bubble eventually ruptures. This second phenomenon,

dx.doi.org/10.1021/bc300407x | *Bioconjugate Chem.* 2012, 23, 2278−2290

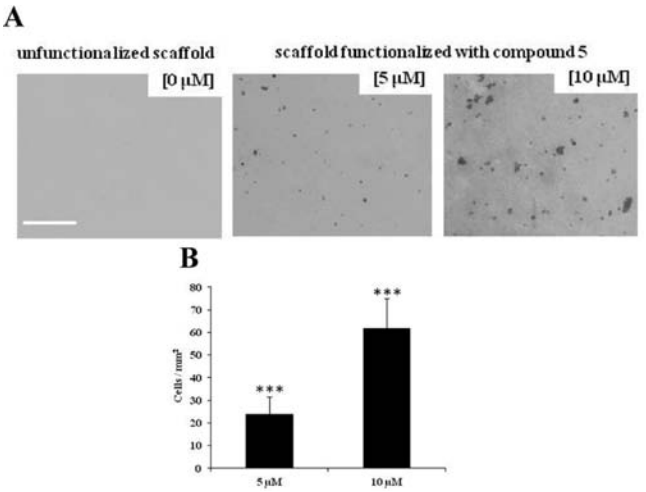

Figure 8. Enhancement of rapid adhesion of human osteo-progenitors by click-functionalization of the scaffolds. (A) Disks of scaffolds functionalized with 0, 5, or 10 μM of compound **5** were incubated with osteo-progenitors for 1 h, and then the cells were stained and photographed. (B) The quantification of the number of adhered osteo-progenitors was performed by analysis of stereomicroscopy pictures. Results are mean ± sd of triplicates of three independent experiments. The numbers of cells adhering to the bioceramics disks were compared among unfunctionalized scaffolds (0 μM) and scaffolds functionalized with compound **5** (5 μM or 10 μM) using a Student's *t*-test: *** $p < 0.001$. The correlation coefficient was calculated between the number of adhered cells on scaffolds functionalized with 5 μM and 10 μM of compound **5**: $r = 1.00$.

which is called *partial coalescence*, can occur during the limited coalescence step, especially if the interparticle forces are attractive. The *freezing* of this transitory state of partial coalescence will then lead to an open-porous microstructure. For the present study, foams made from alumina particles were combined with a calcium aluminate cement reaction.[18,19] Upon setting and sintering, open-porous scaffolds with different microstructures, which can be machined into the desired shapes, were produced, characterized, and engineered with human bone-derived cells. In the present feasibility study, we investigated three scaffolds with various pores and pore openings for biocompatibility, and the adhesion behavior, the in-scaffold viability, and the metabolic activity of human bone-derived cells. For these experiments, we evaluated first human osteosarcoma cells to select the scaffolds with optimal porosities, then primary human osteo-progenitors[27,28] as potential histocompatible cells[9] for cell-engineering the scaffolds prior to their implantation into patients. These studies demonstrated the biocompatibility of the three scaffolds for human bone-derived cells regardless of their fine chemical and physical characteristics. Importantly, these experiments also demonstrated that the scaffold porosities determined the potential of cells to migrate across the entire scaffolds and form functional cellular networks across the entire structure. Therefore, these experiments allowed us to define a minimal pore opening limit, which was around 100 μm, in order to allow cell passage and whole structure colonization. Following this passage, cells were still alive after long-term culture, and cells inside the scaffolds demonstrated a steady potential for proliferation without any sign of cytotoxicity. The SEM observations showing cells throughout the entire scaffold proved that open channels span the entire scaffold structures and the material will allow human cell migration and proliferation. SEM also confirmed that the cells adhered to and spread well on the ceramic surface, again indicating a good acceptance and biocompatibility of the scaffold materials by living human primary fetal cells. These results provided a proof-of-concept of the potential interest of these new ceramic scaffolds as permanent implants for bone tissue engineering.

However, the adhesion of human bone-derived cells onto the large pore scaffolds was not rapid enough to ensure optimal cellularization of these scaffolds. Combining our previous observations that alumina-based scaffolds can be chemically functionalized with gallate-based ligands, including ligands bearing peptides,[29,44] and that human osteo-progenitors can be chemically functionalized using biocompatible click chemistry,[30] we showed herein that the number of human osteo-progenitors adhering to the scaffolds can be enhanced by their covalent binding to the scaffolds using a heterobifunctional ligand and biocompatible click-chemistry. Therefore, large-pore alumina-based scaffolds and primary human fetal cells derived from fetal bones are an interesting potential source of bone precursor cells to prepare permanently cellularized bone implants for tissue engineering, using chemical functionalization of the scaffolds. This proven biocompatibility of the developed scaffolds by such cells is encouraging for further development toward bone tissue engineering.

■ ASSOCIATED CONTENT

Ⓢ Supporting Information

Repartition of thymidine-labeled osteosarcoma cells in the three compartments of the cell-scaffold systems. Detailed chemical syntheses: Synthesis and characterization of compound 5-[(6-aminohexyl)carbamoyl]benzene-1,2,3-triyl triacetate (**3**); synthesis and characterization of 11,12-didehydro-5,6-dihydrodibenzo[*a*,*e*][8]annulen-5-yl(6-{[(3,4,5-trihydroxyphenyl) carbonyl] amino}hexyl) carbamate (**5**). This material is available free of charge via the Internet at http://pubs.acs.org.

■ AUTHOR INFORMATION

Corresponding Author

*Dr. Urs T. Gonzenbach, e-mail: urs.gonzenbach@mat.ethz.ch. Dr. Lucienne Juillerat, e-mail: lucienne.juillerat@chuv.ch.

Author Contributions

⊥These two authors participated equally to this work.

Author Contributions

F.K.J. designed, prepared, characterized the scaffolds, and participated in the cell experiments and the writing of the manuscript; F.B. designed, performed the covalent functionalization of the scaffolds, and participated in the cell experiments; C.S. and L.A.A. prepared the human osteo-progenitors; H.C. and S.G.L. participated in the chemical characterization of the scaffolds; D.S. participated in the click-chemistry cell experiments; L.J.G. participated in the design of the scaffolds; L.J.J. designed and participated in the cell experiments and prepared the manuscript; U.T.G. designed and characterized the scaffolds and participated in the writing of the manuscript.

Notes

The authors declare no competing financial interest.

■ ACKNOWLEDGMENTS

We thank Mr. P. Elser and Mrs. C. Chappuis-Bernasconi for excellent technical assistance. This work was supported by the Swiss National Research Foundation (grants No CR23I2-

124753/1 and CR2313-124753), the Sandoz Family Foundation, and the Foundation S.A.N.T.E.

■ ABBREVIATIONS

AHA, L-azidohomoalanine; BSA, bovine serum albumin; DAPI, 4′,6-diamidino-2-phenylindole; DMEM, Dulbecco modified Eagle medium; FCS, fetal calf serum; PBS, phosphate buffered saline; pNp, *para*-nitrophenyl-phosphate; MTT, 3,4,5-dimethylthiazol-yl)-2,5-diphenyl tetrazolium; SDS, sodium dodecylsulfate; SEM, scanning electron microscopy; WST-1, 2-(4-iodophenyl)-3-(4-nitrophenyl)-5-(2,4-disulphophenyl)-2*H*-tetrazolium.

■ REFERENCES

(1) Bohner, M. (2010) Resorbable biomaterials as bone graft substitutes. *Mater. Today 13* (1−2), 24−30.
(2) Cortet, B. (2011) Bone repair in osteoporotic bone: postmenopausal and cortisone-induced osteoporosis. *Osteoporosis Int. 22*, 2007−2010.
(3) Triplett, R. G., and Schow, S. R. (1996) Autologous bone grafts and endosseous implants: Complementary techniques. *J. Oral Maxillofac. Surg. 54*, 486−494.
(4) Griffith, L. G., and Naughton, G. (2002) Tissue engineering–current challenges and expanding opportunities. *Science 295*, 1009−1014.
(5) Ryan, G., Pandit, A., and Apatsidis, D. P. (2006) Fabrication methods of porous metals for use in orthopaedic applications. *Biomaterials 27*, 2651−2670.
(6) Heinl, P., Muller, L., Korner, C., Singer, R. F., and Muller, F. A. (2008) Cellular Ti-6Al-4V structures with interconnected macro porosity for bone implants fabricated by selective electron beam melting. *Acta Biomater. 4*, 1536−1544.
(7) Chanda, A., Singha Roy, R., Xue, W., Bose, S., and A. Bandyopadhyay, A. (2009) Bone cell-materials interaction on alumina ceramics with different grain sizes. *Mater. Sci. Eng. 29C*, 1201−1206.
(8) Hohlfeld, J., de Buys Roessingh, A. D., Hirt-Burri, N., Chaubert, P., Gerber, S., Scaletta, C., Hohlfeld, P., and Applegate, L. A. (2005) Tissue engineered fetal skin constructs for paediatric burns. *Lancet 366*, 840−842.
(9) Montjovent, M. O., Bocelli-Tyndall, C., Scaletta, C., Scherberich, A., Mark, S., Martin, I., Applegate, L. A., and Pioletti, D. P. (2009) In vitro characterization of immune-related properties of human fetal bone cells for potential tissue engineering applications. *Tissue Eng. 15A*, 1523−1532.
(10) Montjovent, M. O., Mathieu, L., Hinz, B., Applegate, L. A., Bourban, P. E., Zambelli, P. Y., Månson, J. A., and Pioletti, D. P. (2005) Biocompatibility of bioresorbable poly(L-lactic acid) composite scaffolds obtained by supercritical gas foaming with human fetal bone cells. *Tissue Eng. 11*, 1640−1649.
(11) Montjovent, M. O., Mark, S., Mathieu, L., Scaletta, C., Scherberich, A., Delabarde, C., Zambelli, P. Y., Bourban, P. E., Applegate, L. A., and Pioletti, D. P. (2008) Human fetal bone cells associated with ceramic reinforced PLA scaffolds for tissue engineering. *Bone 42*, 554−564.
(12) Ergun, A., Yu, X., Valdevit, A., Ritter, A., and Kalyon, D. M. (2011) In vitro analysis and mechanical properties of twin screw extruded single-layered and coextruded multilayered poly(caprolactone) scaffolds seeded with human fetal osteoblasts for bone tissue engineering. *J. Biomed. Mater. Res. 99A*, 354−366.
(13) Gonzenbach, U. T., Studart, A. R., Tervoort, E., and Gauckler, L. J. (2006) Ultrastable particle-stabilized foams. *Angew. Chem., Int. Ed. 45*, 3526−3530.
(14) Gonzenbach, U. T., Studart, A. R., Tervoort, E., and Gauckler, L. J. (2006) Stabilization of foams with inorganic colloidal particles. *Langmuir 22*, 10983−10988.
(15) Gonzenbach, U. T., Studart, A. R., Steinlin, D., Tervoort, E., and Gauckler, L. J. (2007) Processing of particle-stabilized wet foams into porous ceramics. *J. Am. Ceram. Soc. 90*, 3407−3414.
(16) Gonzenbach, U. T., Studart, A. R., Tervoort, E., and Gauckler, L. J. (2007) Tailoring the microstructure of particle-stabilized wet foams. *Langmuir 23*, 1025−1032.
(17) Gonzenbach, U. T., Studart, A. R., Tervoort, E., and Gauckler, L. J. (2007) Macroporous ceramics from particle-stabilized wet foams. *J. Am. Ceram. Soc. 90*, 6−22.
(18) Krauss Juillerat, F., Gonzenbach, U. T., Studart, A. R., and Gauckler, L J. (2010) Self-setting particle stabilized foams with hierarchical pore structures. *Mater. Lett. 64*, 1468−1470.
(19) Krauss Juillerat, F., Gonzenbach, U. T., Elser, P., Studart, A. R., and Gauckler, L J. (2011) Microstructural control of self-setting particle-stabilized ceramic foams. *J. Am. Ceram. Soc. 94*, 184−190.
(20) Ning, X., Guo, J., Wolfert, M. A., and Boons, G. J. (2008) Visualizing metabolically labeled glycoconjugates of living cells by copper-free and fast huisgen cycloadditions. *Angew. Chem., Int. Ed. 47*, 2253−2255.
(21) Mbua, N. E., Guo, J., Wolfert, M. A., Steet, R., and Boons, G. J. (2011) Strain-promoted alkyne-azide cycloadditions (SPAAC) reveal new features of glycoconjugate biosynthesis. *ChemBioChem 12*, 1912−1921.
(22) Lohm, S., Peduto-Eberl, L., Lagadec, P., Renggli-Zulliger, N., Dudler, J., Jeannin, J. F., and L. Juillerat-Jeanneret, L. (2005) Evaluation of the interaction between TGF beta and nitric oxide in the mechanisms of progression of colon carcinoma. *Clin. Exp. Metastasis 22*, 341−349.
(23) Berger, Y., Greppi, A., Siri, O., Neier, R., and Juillerat-Jeanneret, L. (2000) Ethylene glycol and amino acid derivatives of 5-aminolevulinic acid as new photosensitizing precursors of protoporphyrin IX in cells. *J. Med. Chem. 43*, 4738−4746.
(24) Sottile, V., Halleux, F., Bassilana, F., Keller, H., and Seuwen, K. (2002) Stem cell characteristics of human reabecular bone-derived cells. *Bone 5*, 699−704.
(25) Nifuji, A., Ideno, H., Ohyama, Y., Takanabe, R., Araki, R., Abe, M., Noda, M., and H. Shibuya, H. (2010) Nemo-like kinase (NLK) expression in osteoblastic cells and suppression of osteoblastic differentiation. *Exp. Cell Res. 316*, 1127−1136.
(26) Fiaux, H., Popowycz, F., Favre, S., Schütz, C., Vogel, P., Gerber-Lemaire, S., and Juillerat-Jeanneret, L. (2005) Functionalized pyrrolidines inhibit α-mannosidase activity and growth of human glioblastoma and melanoma cells. *J. Med. Chem. 48*, 4237−4246.
(27) Quintin, A., Hirt-Burri, N., Scaletta, C., Schizas, C., Pioletti, D. P., and Applegate, L. A. (2007) Consistency and safety of cell banks for research and clinical use: preliminary analysis of fetal skin banks. *Cell Transplant. 16*, 675−684.
(28) Quintin, A., Schizas, C., Scaletta, C., Jaccoud, S., Chapuis-Bernasconi, C., Gerber, S., Osterheld, M. C., Juillerat, L., Applegate, L. A., and Pioletti, D. P. (2009) Isolation and in vitro chondrogenic potential of human foetal spine cells. *J. Cell. Mol. Med. 13*, 2559−2569.
(29) Comas, H., Laporte, V., Borcard, F., Miéville, P., Krauss Juillerat, F., Caporini, M. A., Gonzenbach, U. T, Juillerat-Jeanneret, L., and Gerber-Lemaire, S. (2012) Surface functionalisation of alumina ceramic foams with organic ligands. *ACS Appl. Mater. Interfaces 4*, 573−576.
(30) Borcard, F., Chapuis-Bernasconi, C., Comas Blanco, H., Dumont, A. L., Scaletta, C., Applegate, L. A., Krauss Juillerat, F., Gonzenbach, U. T., Gerber-Lemaire, S., and Juillerat-Jeanneret, L. (2011) Covalent cell surface functionalization of human fetal osteoblasts for tissue engineering. *Bioconjugate Chem. 22*, 1422−1432.
(31) Imwinkelried, T. (2007) Mechanical properties of open-pore titanium foam. *J. Biomed. Mater. Res. 81A*, 964−970.
(32) Singh, R., Lee, P. D., Lindley, T. C., Kohlhauser, C., Hellmich, C., Bram, M., Imwinkelried, T., and Dashwood, R. J. (2010) Characterization of the deformation behavior of intermediate porosity interconnected Ti foams using micro-computed tomography and direct finite element modeling. *Acta Biomater. 6*, 2342−2351.

(33) Wazen, R. M., Lefebvre, L. P., Baril, E., and Nanci, A. (2010) Initial evaluation of bone ingrowth into a novel porous titanium coating. *J. Biomed. Mater. Res. 94B*, 64−71.
(34) Willie, B. M., Yang, X., Kelly, N. H., Merkow, J., Gagne, S., Ware, R., Wright, T. M., and Bostrom, M. P. (2010) Osseointegration into a novel titanium foam implant in the distal femur of a rabbit. *J. Biomed. Mater. Res. 92B*, 479−488.
(35) Willie, B. M., Yang, X., Kelly, N. H., Han, J., Nair, T., Wright, T. M., van der Meulen, M. C., and Bostrom, M. P. (2010) Cancellous bone osseointegration is enhanced by in vivo loading. *Tissue Eng. 16C*, 1399−1406.
(36) Trojani, C., Boukhechba, F., Scimeca, J. C., Vandenbos, F., Michiels, J. F., Daculsi, G., Boileau, P., Weiss, P., Carle, G. F., and Rochet, N. (2006) Ectopic bone formation using an injectable biphasic calcium phosphate/Si-HPMC hydrogel composite loaded with undifferentiated bone marrow stromal cells. *Biomaterials 27*, 3256−3264.
(37) Klenke, F. M., Liu, Y. L., Yuan, H. P., Hunziker, E. B., Siebenrock, K. A., and Hofstetter, W. (2008) Impact of pore size on the vascularization and osseointegration of ceramic bone substitutes in vivo. *J. Biomed. Mater. Res. 85A*, 777−786.
(38) Ducheyne, P., and Qiu, Q. (1999) Bioactive ceramics: the effect of surface reactivity on bone formation and bone cell function. *Biomaterials 20*, 2287−2303.
(39) Meijer, G. J., de Bruijn, J. D., Koole, R., and van Bitterswijk, C. A. (2007) Cell-based bone tissue engineering. *PloS Med. 4*, e9.
(40) Axen, N., Engqvist, H., Lööf, J., Thomsen, P., and Hermansson, L. (2004) In vivo hydrating calcium aluminate coatings for anchoring of metal implants in bone. *Key Eng. Mater. 254−256*, 265−268.
(41) Axen, N., Persson, T., Björklund, K., Engqvist, H., and L. Hermansson, L. (2005) An injectable bone void filler cement based on Ca-aluminate. *Key Eng. Mater. 284−286*, 831−834.
(42) Gough, J. E., Clupper, D. C., and Hench, L. L. (2004) Osteoblast responses to tape-cast and sintered bioactive glass ceramics. *J. Biomed. Mater. Res. 69A*, 621−628.
(43) Wong, J. C. H., Tervoort, E., Busato, S., Gonzenbach, U. T., Studart, A. R., Ermanni, P., and Gauckler, L. J. (2009) Designing macroporous polymers from particle-stabilized foams. *J. Mater. Chem. 19*, 5129−5133.
(44) Borcard, F., Staedler, D., Comas, H., Krauss Juillerat, F., Sturzenegger, P. N., Heuberger, R., Gonzenbach, U. T., Juillerat-Jeanneret, L., and Gerber-Lemaire, S. (2012) Chemical functionalization of bio-ceramics to enhance endothelial cells adhesion for tissue engineering. *J. Med. Chem. 55*, 7988−7997.

Supporting information

Functionalization of microstructured open-porous bio-ceramic scaffolds with human fetal bone cells

Franziska Krauss Juillerat, Françoise Borcard, Davide Staedler, Corinne Scaletta, Lee Ann Applegate, Horacio Comas, Ludwig J. Gauckler, Sandrine Gerber-Lemaire, Lucienne Juillerat-Jeanneret, Urs T. Gonzenbach

Content:

Table S1: *Radioactivity repartition of thymidine-labeled osteosarcoma cells in the three compartments of the cell-scaffold systems: in the scaffolds, on the bottom of the wells and in the culture medium.*

Chemical systheses*: Synthesis and characterization of compounds* ***3*** *and* ***5***

Table S1: *Radioactivity repartition of thymidine-labeled osteosarcoma cells in the three compartments of the cell-scaffold systems: in the scaffolds, on the bottom of the wells and in the culture medium.*

Human U_2O_S and SaO_S osteosarcoma cells were prelabeled with [^{3}H]-thymidine, then grown in the scaffolds for 24, 48 or 72 h. Radioactivity was quantified for the different scaffolds and cells used in the 3 compartments of the culture systems: associated to the cells in the scaffolds (foam), associated to the cells at the bottom of the wells (well) and in the soluble culture media (CM). The experiments were repeated twice, with comparable information.

Cells	***U_2Os***			***SaOs***		
	foam	*well*	*CM*	*foam*	*well*	*CM*
time[h]						
scaffold 1						
24h	98.1	1.4	0.5	97.2	1.6	1.2
48h	93.4	4.6	2.0	95.4	3.3	1.3
72h	98.1	1.2	0.7	91.7	7.2	1.1
scaffold 2						
24h	99.4	0.4	0.2	98.5	0.7	0.8
48h	98.4	0.8	0.8	96.5	1.5	2.0
72h	98.5	1.2	0.3	97.4	0.6	2.0
scaffold 3						
24h	94.0	5.6	0.4	88.4	10.8	0.8
48h	95.0	4.1	0.9	94.4	3.7	1.9
72h	93.2	4.4	2.4	88.6	6.9	4.5

*Synthesis and characterization of compound **3:***

5-[(6-aminohexyl)carbamoyl]benzene-1,2,3-triyl triacetate (3)

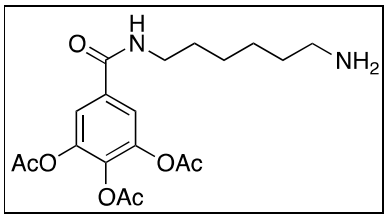

Few drops of DMF were added to acetoxygallic acid (1 g, 3.4 mmol, 1 equiv) in dry DCM (6 mL). The solution was cooled to 0 °C and oxalyl chloride (0.31 mL, 3.7 mmol, 1.5 equiv) was added dropwise. After 15 min the reaction mixture was allowed to reach room temperature and was stirred for 1 h. The reaction mixture was concentrated under reduced pressure and the residue was resuspended in dry DCM (4.5 mL). A solution containing N-Boc-1,6-hexadiamine (0.72 g, 3.4 mmol, 1 equiv) and $(i\text{-Pr})_2$NEt (1.73 mL, 10.1 mmol, 3 equiv) in DCM (4.5 mL) was added dropwise at 0°C. After 15 min the reaction mixture was allowed to reach room temperature and was stirred for 1 h. The reaction mixture was concentrated under reduced pressure and purified by flash column chromatography (AcOEt/petroleum ether 1:1). The resulting product was dissolved in 4 M HCl in dioxane and stirred for 1 h at room temperature. HCl was coevaporated three times with diethyl ether to afford a white paste (mass: 400 mg, yield: 30 % for 2 steps). IR (film): 3265, 2935, 2860, 2225,1770, 1635, 1585, 1550, 1490, 1435, 1370, 1315, 1180, 1120, 1050, 1010, 975, 890, 870, 820, 760, 730, 700 590 cm^{-1}.^{1}H NMR (400 MHz, MeOD): δ=7.64 (s, 1H, C**H**), 3.39 (t, 2H, C$\mathbf{H_2}$), 2.92 (t, 1H, C$\mathbf{H_2}$), 2.30 (s, 9H, (C$\mathbf{H_3}$)$_3$), 1.66 (m, 4H, (C$\mathbf{H_2}$)$_2$), 1.44 (m, 4H, (C$\mathbf{H_2}$)$_2$).^{13}C NMR (101 MHz, MeOD): δ=169.50 (**Cq**), 168.35 (**Cq**), 133.72 (C(aromatic)), 121.00 (C(aromatic)), 40.81 (**C**H_2), 40.63 (**C**H_2), 30.11 (**C**H_2), 28.44 (**C**H_2), 27.32 (**C**H_2), 26.96 (**C**H_2), 20.38 (**C**H_3), 19.96 (**C**H_2). MS (ESI): HRMS (ESI): (*m*/*z*): calcd for $C_{19}H_{26}N_2O_7$+H: 395.1818, found: 395.1823.

^{1}H-NMR spectrum of compound **3**

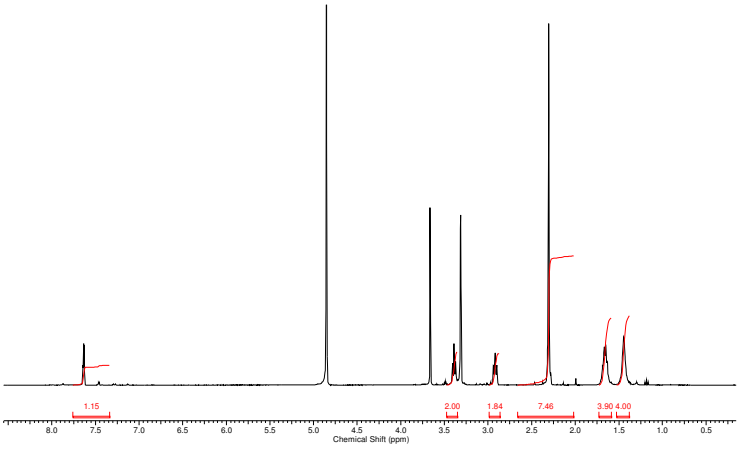

^{13}C-NMR spectrum of compound **3**

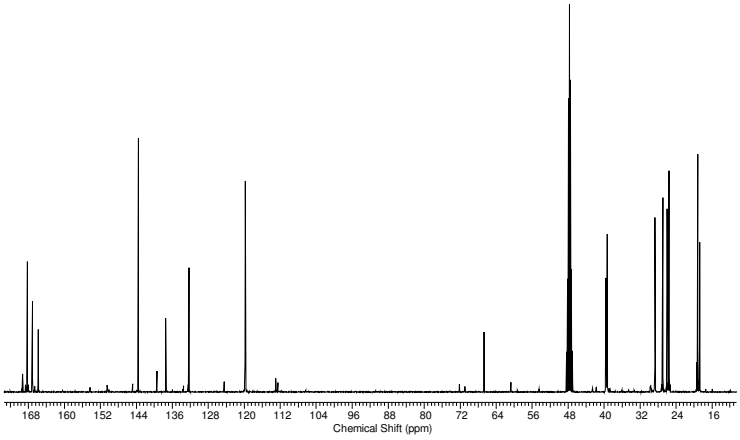

*Synthesis and characterization of compound **5:***

11,12-didehydro-5,6-dihydrodibenzo[a,e][8]annulen-5-yl(6-{[(3,4,5-trihydroxy phenyl)carbonyl]amino}hexyl) carbamate (5)

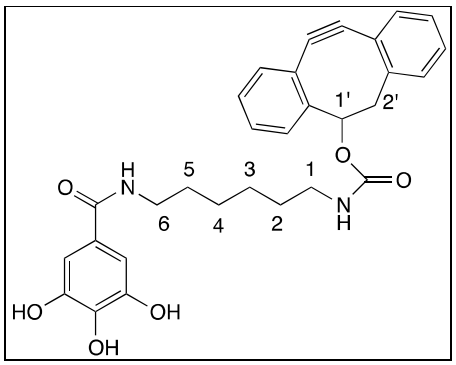

5-[(6-aminohexyl)carbamoyl]benzene-1,2,3-triyl triacetate **3** (75 mg, 0.2 mmol, 1 equiv) was dissolved in DMF (18 mL) and carbonic acid, 5,6-dihydro-11,12-didehydro-dibenzo[*a*, *e*]cycloocten-5-yl ester, 4-nitrophenyl ester **4**[1] (80 mg, 0.2 mmol, 1 equiv) followed by triethylamine (0.08 mL, 0.6 mmol, 3 equiv) were added. The reaction mixture was stirred overnight at room temperature. DMF was removed under reduced pressure and the product was purified by flash column chromatography (AcOEt/petroleum ether 1:1 then 2:1) (mass: 150 mg, yield: 46 %). The resulting product (33 mg, 0.05 mmol, 1 equiv) was dissolved in THF at 0 °C and a 1 M solution of LiOH (0.15 mL, 0.15 mmol, 3 equiv) was added. The reaction was monitored by MS until total conversion of the starting material. The product was purified by HPLC ((XTerra Prep RP C18, (25x150 mm Waters)) to give compound **5** (mass: 10 mg, yield: 38 %). IR (film): 3275, 2935, 1695, 2595, 1515, 1450, 1330, 1200, 1135, 1035, 865, 755, 720, 645, 585 cm-^{1}.^{1}H NMR (400 MHz, MeOD): δ=7.38 (d, 1H, aromatic, C**H**), 7.37-7.29 (m, 7H, aromatics, (C**H**)$_7$), 6.82 (s, 2H, (C**H**)$_2$), 5.42 (m, 1H, C(1')**H**), 3.22 (dd, 1H, ^{2}J= 15.0 ^{3}J= 2.0 Hz (C**H**$_2$)), 3.11 (t, 2H, ^{2}J= 2.0 Hz (C**H$_2$**)), 2.82 (dd, 1H, ^{2}J= 15.0 ^{3}J= 3.8 Hz (C**H**$_2$)), 1.60-1.29 (m, 10H, (C**H$_2$**)$_5$).^{13}C NMR (100 MHz, MeOD): δ=169.12 (**Cq**), 156.64 (**Cq**), 152.34 (**Cq**), 151.03 (**Cq**), 136.52 (**Cq**), 129.57 (C(aromatic)), 127.92 (C(aromatic)), 127.81 (C(aromatic)), 126.89 (C(aromatic)), 126.84 (C(aromatic)), 125.74 (C(aromatic)), 125.48 (C(aromatic)), 124.99 (C(aromatic)), 123.47 (C(aromatic)), 112.39 (**Cq**), 109.57 (**Cq**), 76.40 (**C**H), 45.74 (**C**H$_2$), 40.28 (**C**H$_2$), 39.36 (**C**H$_2$), 29.40 (**C**H$_2$), 29.10 (**C**H$_2$), 26.25 (**C**H$_2$), 26.06 (**C**H$_2$).MS (ESI): HRMS (ESI): (*m*/*z*): calcd for $C_{30}H_{30}N_2O_6$+H: 515.2182, found: 515.2180. $[\alpha]_D^{25}$ = 0.1 (*c*=0.004, CH_2Cl_2).

^{1}H-NMR spectrum of compound **5**:

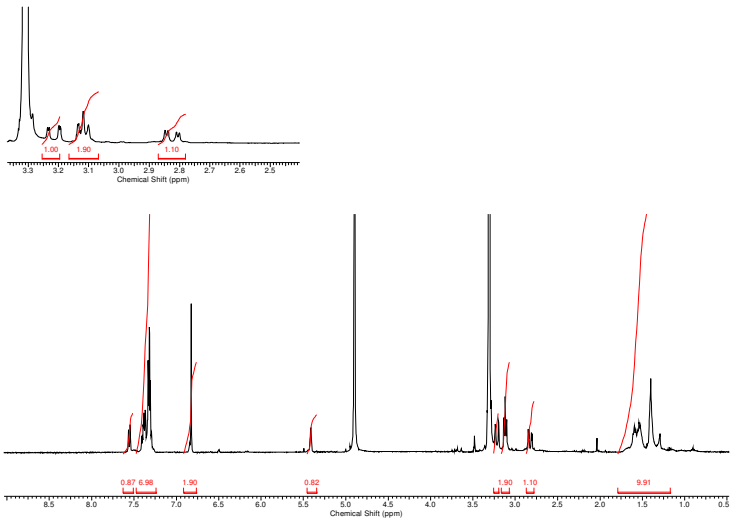

^{13}C-NMR spectrum of compound **5**:

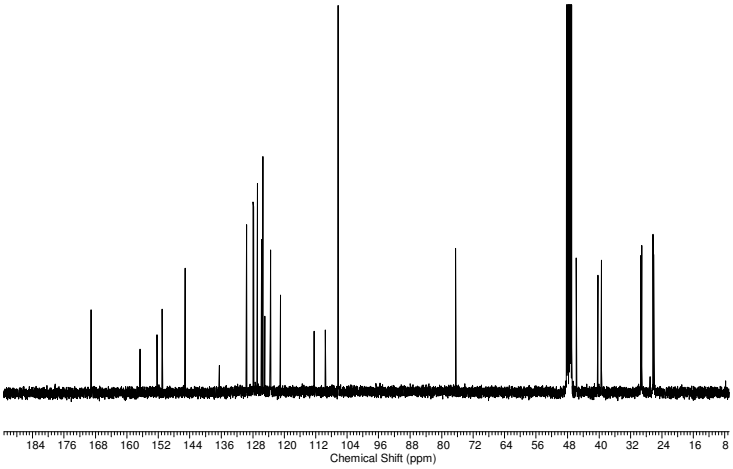

Reference:

1. Mbua, N. E., Guo, J., Wolfert, M. A., Steet, R., and Boons, G.-J.(2011) Strain-promoted alkyne-azide cycloadditions (SPAAC) reveal new features of glycoconjugate biosynthesis. *ChembioChem*, *12*, 1912-1921.

Bioconjugate Chemistry

Article

pubs.acs.org/bc

Gadolinium MRI Contrast Agents Based on Triazine Dendrimers: Relaxivity and In Vivo Pharmacokinetics

Jongdoo Lim,[†] Baris Turkbey,[‡] Marcelino Bernardo,[§] L. Henry Bryant, Jr.,[∥] Matteo Garzoni,[⊥] Giovanni M. Pavan,[⊥] Takahito Nakajima,[‡] Peter L. Choyke,[‡] Eric E. Simanek,[†] and Hisataka Kobayashi*[,‡]

[†]Department of Chemistry, Texas Christian University, Fort Worth, Texas 76129, United States

[‡]Molecular Imaging Program, Center for Cancer Research, National Cancer Institute, National Institutes of Health, Bethesda, Maryland 20892, United States

[§]SAIC-Frederick, Inc., NCI-Frederick, National Cancer Institute, National Institutes of Health, Frederick, Maryland 21702, United States

[∥]Laboratory of Diagnostic Radiology Research, Radiology & Imaging Sciences, Warren Magnuson Clinical Center, National Institutes of Health, Bethesda, Maryland 20892, United States

[⊥]Department of Innovative Technologies, University of Applied Science of Southern Switzerland, Galleria 2, Manno 6928, Switzerland

Supporting Information

ABSTRACT: Four gadolinium (Gd)-based macromolecular contrast agents, **G3-(Gd-DOTA)$_{24}$**, **G5-(Gd-DOTA)$_{96}$**, **G3-(Gd-DTPA)$_{24}$**, and **G5-(Gd-DTPA)$_{96}$**, were prepared that varied in the size of dendrimer (generation three and five), the type of chelate group (DTPA or DOTA), and the theoretical number of metalated chelates (24 and 96). Synthesis relied on a dichlorotriazine derivatized with a DOTA or DTPA ligand that was incorporated into the dendrimer and ultimately metalated with Gd ions. Paramagnetic characteristics and in vivo pharmacokinetics of all four contrast agents were investigated. The DOTA-containing agents, **G3-(Gd-DOTA)$_{24}$** and **G5-(Gd-DOTA)$_{96}$**, demonstrated exceptionally high $r1$ relaxivity values at off-peak magnetic fields. Additionally, **G5-(Gd-DOTA)$_{96}$** showed increased $r1$ relaxivity in serum compared to that in PBS, which was consistent with in vivo images. While **G3-(Gd-DOTA)$_{24}$** and **G3-(Gd-DTPA)$_{24}$** were rapidly excreted into the urine, **G5-(Gd-DOTA)$_{96}$** and **G5-(Gd-DTPA)$_{96}$** did not clear as quickly through the kidneys. Molecular simulation of the DOTA-containing dendrimers suggests that a majority of the metalated ligands are accessible to water. These triazine dendrimer-based MRI contrast agents exhibit several promising features such as high in vivo $r1$ relaxivity, desirable pharmacokinetics, and well-defined structure.

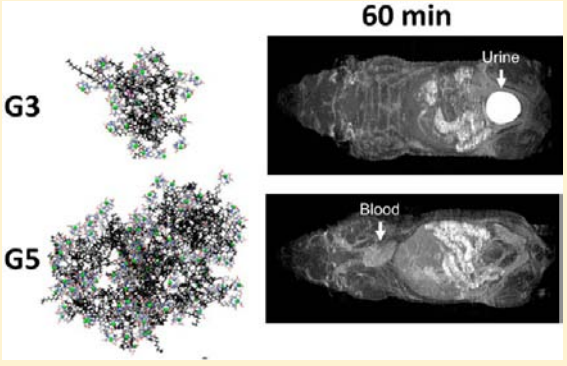

INTRODUCTION

Numerous nanomaterials—inorganic, organic, and hybrid—with unique chemical and physical characteristics are being explored for biological applications. Among them, synthetic dendritic macromolecules are versatile and promising for biological and medical applications because of their flexible, reproducible syntheses and biocompatible characteristics.[1] When used as macromolecular MRI contrast agents, several advantages over low-molecular-weight gadolinium chelates emerge including enhanced $r1$ relaxivity[2,3] because of efficient water exchange, unique pharmacokinetics that can be adapted to target the blood pool,[4,5] liver,[6,7] kidney,[8,9] and lymphatic flows,[10,11] the ability to be a drug carrier, and flexibility for labeling due to their inherent multivalency.[12,13] The improved relaxivity and prolonged pharmokinetics help minimize the injected dose of gadolinium ions, thus reducing the risk of nephrogenic systemic fibrosis (NSF),[14−16] a recent concern in the design of gadolinium-based contrast agents.[17]

Monodispersity, a feature of lower-generation dendrimers, is a desirable characteristic of macromolecular contrast agents, because it facilitates characterization and confidence in composition, which lead to materials with batch-to-batch consistency vis a vis in vivo behavior. On increasing generation, however, the dispersity of most dendrimers increases. For instance, more than 10% of commercial PAMAM dendrimers larger than generation 4 appear to be defective, containing missing branches, molecular loops, and dimers[18,19] leading to inconsistent product quality that can be a potential regulatory concern when pursuing clinical application of dendrimers.

Received: August 21, 2012
Revised: September 28, 2012
Published: October 4, 2012

 © 2012 American Chemical Society dx.doi.org/10.1021/bc300461r | *Bioconjugate Chem.* 2012, 23, 2291−2299

Chart 1. Representation of the Two Triazine Dendrimers (left) and the Metalated Chelates that Appear on Each Peripheral Piperazine

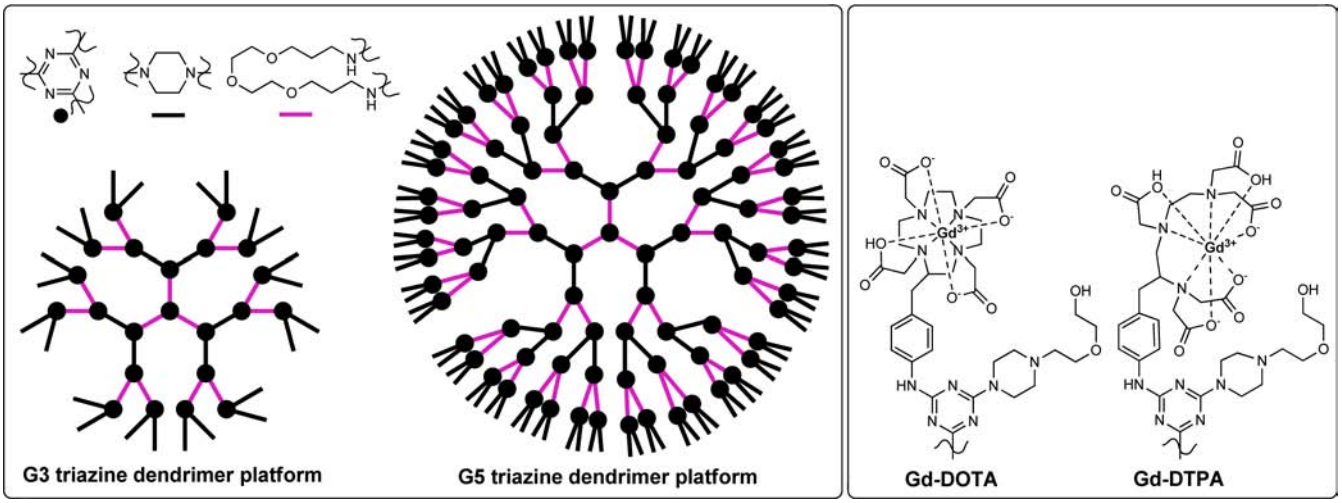

Scheme 1. Synthesis of the Triazine Dendrimers (1—4) Containing DOTA or DTPA Ligands (G3 and G5 Dendrimer Platforms Depicted as Black Dot Spheres)

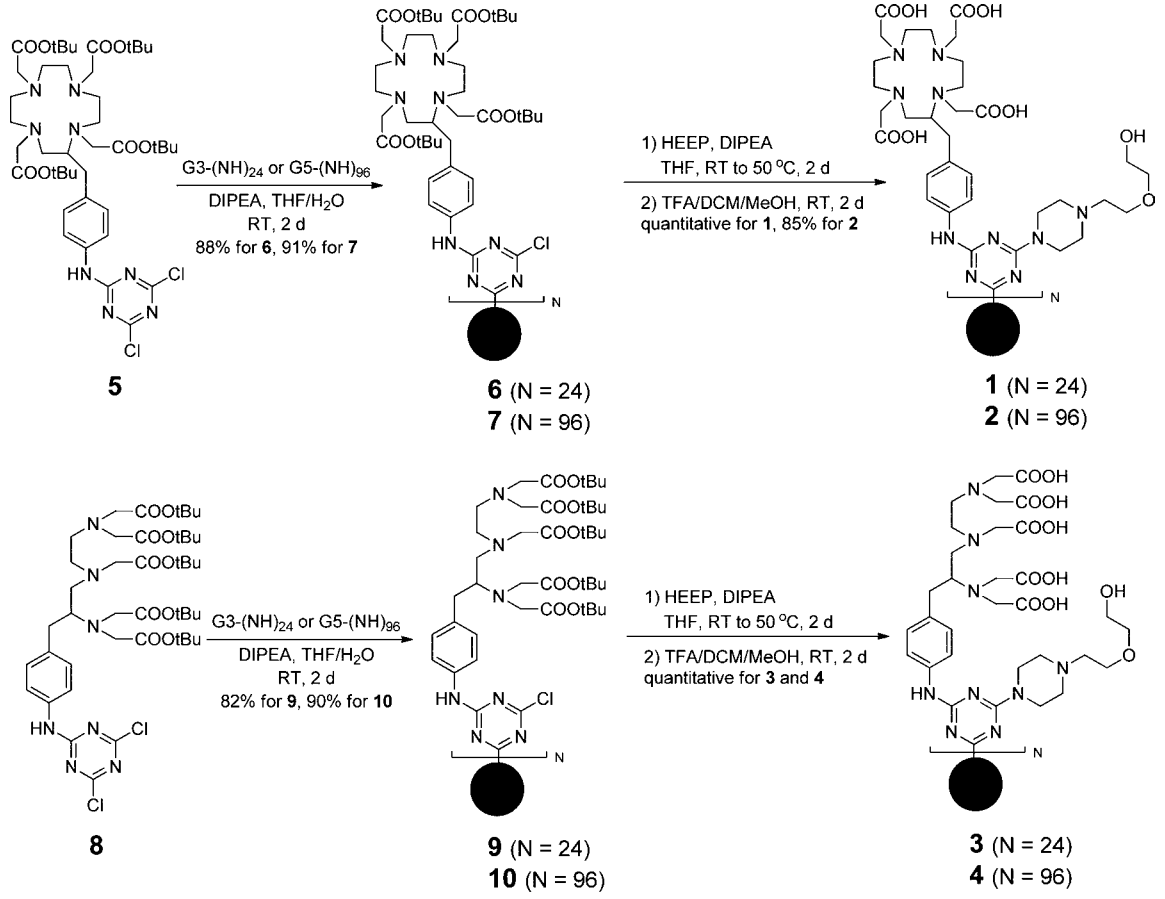

These defects may be critical because in vivo pharmacokinetics of dendrimers can be influenced by the nature of the chemical core, interior, and surface of the dendrimer although this is still poorly understood. Even with the same surface modifications and similar sizes, dendrimers with different interiors such as PAMAM and PPI showed distinct in vivo pharmacokinetics.[8] Moreover, the number of generations and nature of the conjugated chelates used to bind gadolinium are also critical factors that alter relaxivity and pharmacokinetics.[20,21]

Triazine dendrimers can be reproducibly synthesized with well-defined structure.[22−28] Their syntheses are straightforward. They are amenable to multiple characterization methods. They are stable. These characteristics offer distinct advantages over other classes of dendrimers, creating opportunities for drugs or diagnostic agents with more predictable and tunable

dx.doi.org/10.1021/bc300461r | Bioconjugate Chem. 2012, 23, 2291−2299

pharmacokinetic profiles. Here, we describe a family of Gd-based MRI contrast agents that utilize monodisperse triazine dendrimers of two different generations[24] to yield generations 3 and 5 targets upon conjugation with the DOTA or DTPA-containing ligands (Chart 1).

MATERIALS AND METHODS

Synthesis. The macromolecular Gd^{3+} chelates were synthesized using the triazine dendrimers of generations 3 and 5 prepared as previously reported.[24] To incorporate either DOTA or DTPA groups, a conjugation strategy using a functionalized monomer was adopted (Scheme 1). That is, the *t*-butyl ester-protected ligands were incorporated into the dichlorotriazine **5** or **8** in 88% yield. Reactions with the dendrimer platforms afforded the four poly(monochlorotriazine) dendrimers, **6**, **7**, **9**, and **10**, respectively. The surface group HEEP, 1-[2-(2-hydroxyethoxy)ethyl]-piperazine, was chosen due to high reactivity of the cyclic secondary amine toward monochlorotriazines and the hydrophilic auxiliary groups. Following an acidic deprotection, the desired macromolecular ligands, **1**, **2**, **3**, and **4**, were obtained. From the G3 and G5 dendritic platforms, these agents were synthesized in four steps in 70−80% overall yield.

Preparation of Gd(III) Complexes. The dendrimers (**1**−**4**) were dissolved in deionized water. $Gd(OAc)_3$ (24 equiv for **1** and **3**, 96 equiv for **2** and **4**) was added to the solution at room temperature. The pH of the solution was adjusted to 5.5−6 by adding dilute NaOH (aq). Xylenol orange solution was used to monitor the presence of free gadolinium ions. The reaction solution was stirred at 50 °C for 2 days. In order to remove nonspecifically bound Gd^{3+} ions, the solution was stirred with 3 mM of EDTA at room temperature for 2 h. The resulting solution was purified by diafiltration using Amicon stirred ultrafiltration cell equipment (PLCC membrane, MWCO 5 kDa for **1** and **3**, 10 kDa for **2** and **4**) in deionized water over 3 days. No free Gd^{3+} ions were observed from the purified solution with xylenol orange test. Each solution was lyophilized to provide the dendrimer-Gd complexes, **G3-(Gd-DOTA)$_{24}$** (from **1**), **G5-(Gd-DOTA)$_{96}$** (from **2**), **G3-(Gd-DTPA)$_{24}$** (from **3**), and **G5-(Gd-DTPA)$_{96}$** (from **4**), respectively.

Computational Procedure. The protocol used for the creation and the parametrization of the **G3-(Gd-DOTA)$_{24}$** and **G5-(Gd-DOTA)$_{96}$** dendrimers has been previously used by us for the simulation of other dendritic molecules.[29] The dendritic scaffolds were constructed as composed by different residues: a central (CEN) unit, the flexible (FLX) units composing the branches, the rigid triazine residues (RIG), and the surface units, namely, the DOTA (DOT) groups and the protective terminal units (END). The entire modeling work was carried out using the *AMBER 11* suite of programs.[30] The DOTA groups were parametrized as previously reported.[31] The force field parameters for the other nonstandard residues composing the dendrimers were assigned consistently with the "general AMBER force field (GAFF)" (*gaff.dat*).[32] The partial charges for these residues were obtained using the AM1-BCC[33,34] calculation method within the *antechamber*[35] module of *AmberTools 1.4* (*AMBER 11*). The models for **G3-(Gd-DOTA)$_{24}$** and **G5-(Gd-DOTA)$_{96}$** were immersed in a periodic box containing TIP3P water molecules[36] extending 14 Å from the solute atoms. A suitable number of ions were added in solution using the standard *addIons* utility of the *leap* module (*AMBER 11*) to guarantee the system neutrality and the ionic concentration of 150 mM [NaCl]. Water molecules were eventually replaced with ions when superposition occurred. The *parm99* all-atom force field[37] was used to parametrize the standard residues in the system. The two solvated dendrimers were initially minimized. The first two steps of molecular dynamics simulations (MD) followed, lasting 50 ps in NVT and NPT conditions, respectively, to reach the simulation temperature of 300 K and to equilibrate the solution density inside the periodic box. The systems were then equilibrated for 100 ns (ns) in NPT periodic boundary condition at 300 K and 1 atm, using a time step of 2 fs, the Langevin thermostat, and a 10 Å cutoff. During this time, both dendrimers reached the equilibrium with good stability. The SHAKE algorithm was used during the simulations on the bonds involving hydrogen atoms,[38,39] and the particle mesh Ewald[40] (PME) approach was adopted to treat the long-range electrostatic effects. The equilibrated phase of the MD trajectories was further processed with the *ptraj* module of *AMBER 11* to the extract structural data (i.e., the radius of gyration, R_g, and the radial distribution functions, RDF).

Paramagnetic Characteristics. Relaxivity was measured by a custom-designed variable-field *T*1-*T*2 analyzer (Southwest Research Institute, San Antonio, TX) and a 3T MR system (Signa LX, GE Healthcare, Waukesha, WI, USA). For the variable field analyzer, the field strength was varied from 0.035 to 1.5 T (1.5−63 MHz) and the sample temperature was set at 23 °C. Solutions of **G3-(Gd-DOTA)$_{24}$**, **G5-(Gd-DOTA)$_{96}$**, **G3-(Gd-DTPA)$_{24}$**, **G5-(Gd-DTPA)$_{96}$**, **Gd-DOTA** (Prohance), and **Gd-DTPA** (Magnevist, Berlex, Princeton, NJ) (1 mMGd, PBS, pH 7.4) were prepared, and *T*1 was measured using a saturation recovery pulse sequence with 32 incremental recovery times. *T*2 was measured using a Carr-Purcel-Meiboom-Gill pulse sequence of 500 echoes and an interecho time of 2 ms. To investigate the temperature dependency, additional measurements were performed at 0.8 T field strength.

Relaxivity was measured at 23 °C using a 3.0 T clinical scanner (Signa Excite, GE Healthcare, Waukesha, WI, USA) equipped with a rectangular single loop receiver coil (84 × 126 × 6 mm^3). Phantom solutions in 1× PBS consisting of 0, 0.1, 0.25, 0.5, 0.75, and 1 mM in Gd(III) together with Gd-DTPA as reference controls were prepared. A series of single-slice 2D inversion recovery (IR) fast-spin echo images of all solutions were obtained at an echo time (TE) of about 7.54 ms using different inversion recovery times (TI) of 50, 100, 350, 750, 1250, 2500, and 5000 ms. The *r*1 values for each dilution were determined by fitting ROI intensity values from variable IR images using *Igor Pro* (http://www.wavemetrics.com). *r*2 values were measured from ROI values from *T*2 maps, which were calculated from the multiecho images in *ImageJ* (http://rsb.info.nih.gov/ij) using the MRI analysis plug-in (http://rsb.info.nih.gov/ij/plugins/mri-analysis.html). The molar relaxivities, *r*1 and *r*2, were obtained from the slope of 1/*T*1 or 1/*T*2 vs [Gd(III)] plots determined from region of interest measurements.

Contrast-Enhanced Dynamic 3D-Micro MRI of Mice. All dynamic micro-MRI images were obtained at 3 T with a 1 in. round receive-only modified Alderman-Grant resonators. Mice were chemically restrained with 2% isoflurane (Abbott Laboratories, NJ) in O_2 delivered using a Summit Anesthesia Solutions vaporizer (Bend, OR) at a flow rate of 0.8 L/min. Respiration rate was maintained at 25−30 respirations per min and monitored using a Biopac System MP150 (Biopac Inc.,

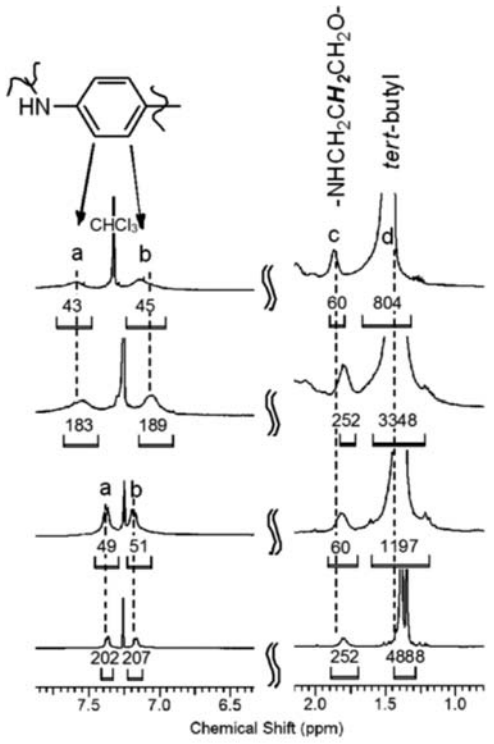

		^{1}H NMR theo. # of H	^{1}H NMR exp. # of H	MW (kDa) theo.	MW (kDa) exp.[a]
6	a	48	43	27.8	27.5
	b	48	45		
	c	60	60		
	d	864	804		
7	a	192	183	113.0	N.A.[b]
	b	192	189		
	c	252	252		
	d	3456	3348		
9	a	48	49	28.9	29.3
	b	48	51		
	c	60	60		
	d	1080	1197		
10	a	192	202	117.3	117.3
	b	192	207		
	c	252	252		
	d	4320	4888		

[a] Determined by MALDI-TOF MS
[b] Unable to be ionized by MALDI

Figure 1. ^{1}H NMR spectra and molecular weights of the dendrimers, **6**, **7**, **9**, and **10**, containing DOTA or DTPA ligands.

Table 1. Chemical Summary of the Macromolecular Ligands (1—4) and the Corresponding Gd^{3+} Complexes

	MW (kDa)		ligands			metalation	
compound	theo.	exp.[a]	name	theo. #	exp. #[a]	name	Gd^{3+} #[b]
1	25.8	25.5	DOTA	24	23.6	**G3-(Gd-DOTA)$_{24}$**	23.7
2	104.6	105.7	DOTA	96	97.5	**G5-(Gd-DOTA)$_{96}$**	95.8
3	25.5	24.8	DTPA	24	23.1	**G3-(Gd-DTPA)$_{24}$**	23.5
4	103.6	104.7	DTPA	96	97.5	**G5-(Gd-DTPA)$_{96}$**	95.6

[a]Determined by MALDI-TOF MS. [b]Determined by titration assay.

Chart 2. Equilibrated Configurations of G3-(Gd-DOTA)$_{24}$ (a) and G5-(Gd-DOTA)$_{96}$ (b)[a]

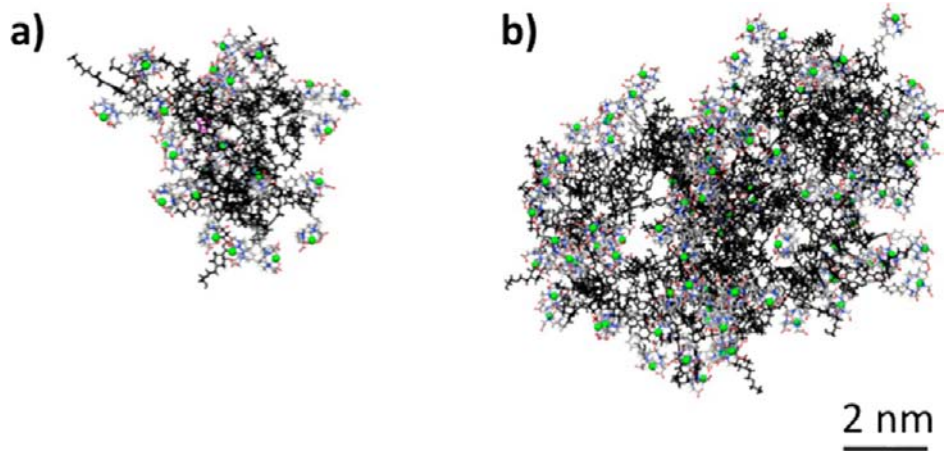

[a]The dendritic scaffold is colored in black, DOTA chelates are colored by atoms (C: grey, N: blue, O: red, and H: white) and Gd atoms are colored in green. The center of the dendrimer is colored in pink. Explicit water molecules and Cl^- and Na^+ atoms are not shown for clarity.

Goleta, CA). The temperature of the mouse was maintained at 32 ± 1 °C using a Polyscience model 210 heating recirculator with 3 M Fluorinert Electronic Liquid FC-77 with body temperature monitored using FOT-M fiberoptic sensors (Fiso Technologies Inc., San Jose, CA) and a UMI-8 multichannel instrument (Fiso Technologies Inc.). A tail vein cannula

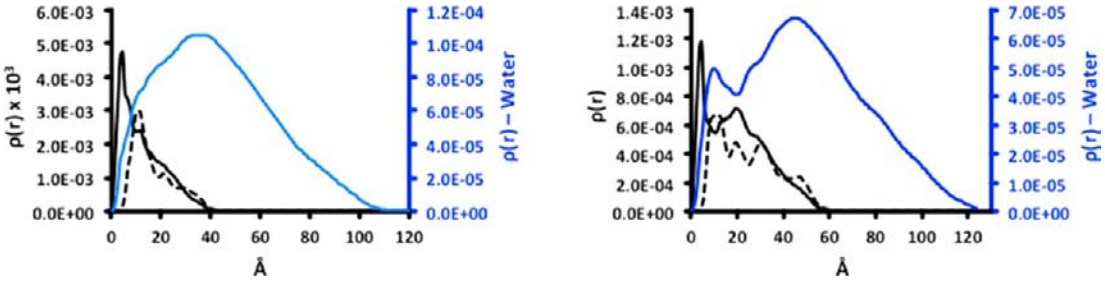

Figure 2. Radial distribution functions of dendrimer (black solid line) and metalated chelates (black dotted line) and water molecules (blue line) of **G3-(Gd-DOTA)$_{24}$** (left) and **G5-(Gd-DOTA)$_{96}$** (right).

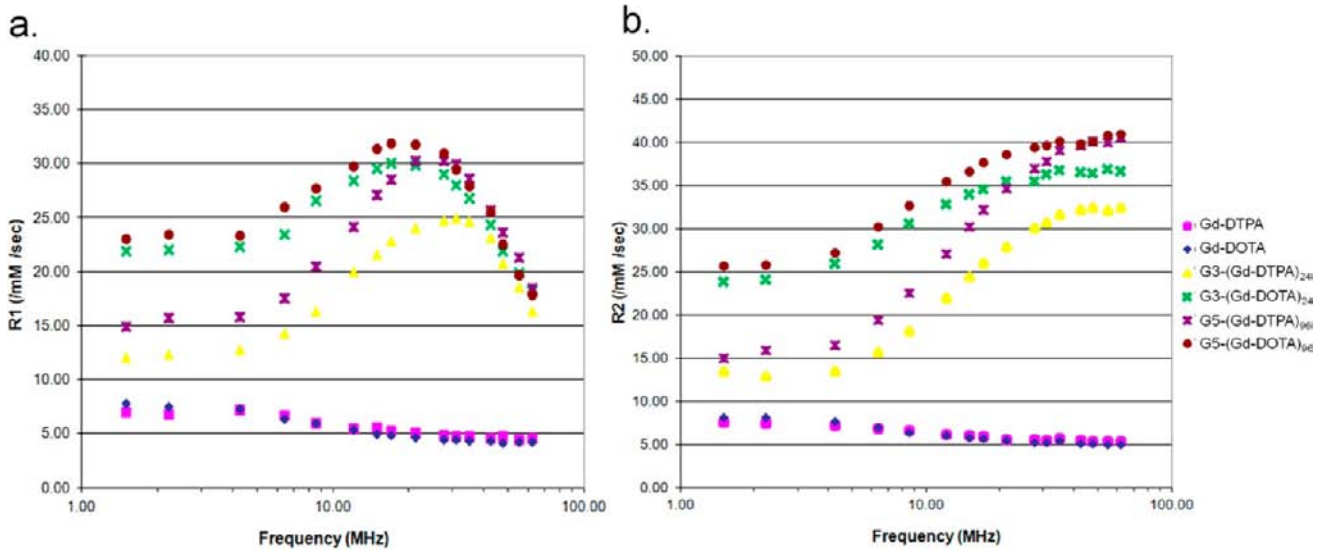

Figure 3. *r*1 (a) and *r*2 (b) relaxivity profiles of triazine dendrimer-based conjugates compared with low-molecular-weight Gd-chelates (Gd-DTPA and Gd-DOTA) below 63 MHz magnetic field at 23 °C.

consisting of a 30-gauge needle attached to Tygon tubing (0.01 in i.d.) was then established. Prior to injection of the contrast agent, a *T*1 map was obtained by using a 3D-fast spoiled gradient echo image (3D-fSPGR) sequence at two different flip angles (repetition time/echo time 10.888/3.86 ms; flip angles 8° and 24°; bandwidth 31.25 kHz; matrix size 512 × 128 × 40; voxel resolution 156 × 156 × 600 μm^3; slice thickness 0.6 mm; two averages; scan time ~2 min). One hundred microliter (100 μL) of the **G3-(Gd-DOTA)$_{24}$**, **G5-(Gd-DOTA)$_{96}$**, **G3-(Gd-DTPA)$_{24}$**, **G5-(Gd-DTPA)$_{96}$**, or **PAMAM-G4-Gd-DTPA** was injected (0.03 mmolGd/kg) from the tail vein. The region of interest was placed on the liver, the cortex and medulla of the kidney, the muscle at the femoral region, and the jugular vein, and the time−intensity curves were made. In addition, the slice data were processed into 3D images with the maximum intensity protection (MIP) method.

RESULTS AND DISCUSSION

Characterization of Compounds. Characterization of compounds rests on NMR spectroscopy and mass spectrometry. After conjugation reaction of the dendrimer platform with the dichlorotriazine monomer containing ligands, the resulting poly(monochlorotriazines), **6**, **7**, **9**, and **10**, were characterized by ^{1}H NMR and MALDI-TOF MS. While the peaks derived from ^{1}H NMR spectroscopy are somewhat broad in Figure 1, integration yields an estimate of the number of chelate groups. That is, signals from the chelate groups (a, b, and d) can be compared to those from the dendrimer platform (c). The integrated intensity of signal c was used as a standard for the comparison as the dendrimer platforms. We assume from the reasonable match that the reaction to install chelate on the dendrimer proceeded exceedingly well given the small deviations between theoretical expectations and experimental observations. Analyzing the extent of reaction is more difficult with MALDI-TOF MS (Figure 1), but the results are consistent. Table 1 represents the chemical summary of the macromolecular ligands (**1**−**4**). All the compounds contain around 24 (for G3) or 96 (for G5) ligands, the maximum number that can be theoretically attached. After metalation with Gd^{3+}, these materials comprise approximately 13 wt % of gadolinium as determined by a titration assay: A known amount of dendrimer stock solution was titrated with a 10 mM of $Gd(OAc)_3$ (aq) at pH 5.5−6 until the solution tested positive for free gadolinium ions using xylenol orange solution. The

Table 2. Relaxivities of Gd Contrast Agents at 128 MHz

	*r*1 (/mM/s)		*r*2 (/mM/s)	
chelates	in PBS	in serum	in PBS	in serum
G3-(Gd-DOTA)$_{24}$	7.5	11.4	33	44
G5-(Gd-DOTA)$_{96}$	9.6	24	48	70
G3-(Gd-DTPA)$_{24}$	6.7	11	31	40
G5-(Gd-DTPA)$_{96}$	7.4	13	42	51
PAMAM-G4-Gd-DTPA	12	15	33	41
Gd-DTPA	4.8	N.A.	5.3	N.A.

dx.doi.org/10.1021/bc300461r | *Bioconjugate Chem.* 2012, 23, 2291−2299

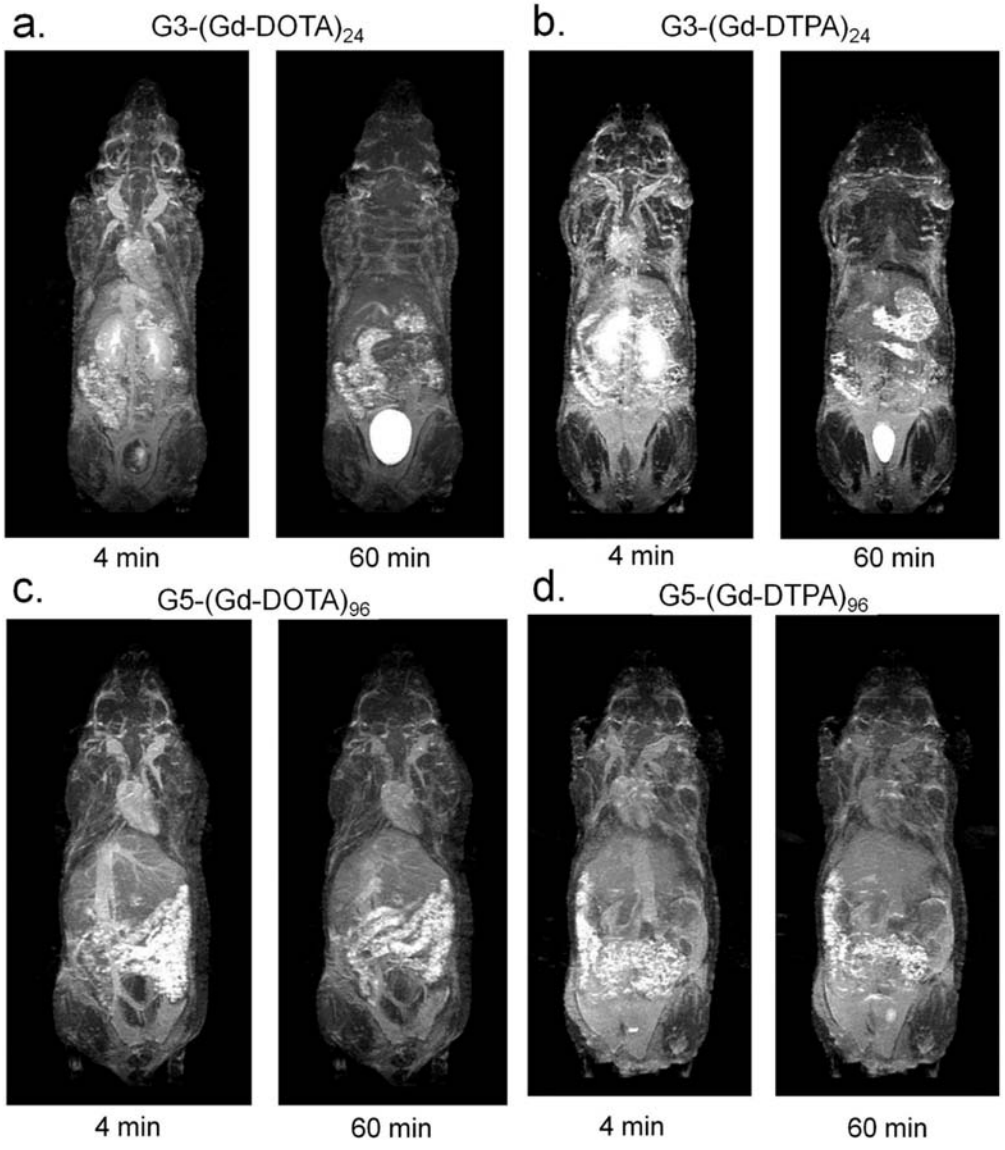

Figure 4. Early (4 min) and late (60 min) whole body MIP MR images of mice injected with 0.03 mmol/kg of **G3-(Gd-DOTA)$_{24}$** (a), **G3-(Gd-DTPA)$_{24}$** (b), **G5-(Gd-DOTA)$_{96}$** (c), and **G5-(Gd-DTPA)$_{96}$** (d) are shown. Entire dynamic MR images, which were taken every 2 min, are shown as SI videos 1−4. (1: **G3-(Gd-DOTA)$_{24}$**; 2: **G3-(Gd-DTPA)$_{24}$**; 3: **G5-(Gd-DOTA)$_{96}$**; 4: **G5-(Gd-DTPA)$_{96}$**). Both G3 agents show enhanced kidneys (arrows) as well as blood pool in images 4 min after injection; however, the urine in the bladder is only shown 60 min after injection. In contrast, both G5 agents show blood pool up to 60 min after injection with minimal enhancement in the kidney and the bladder.

solution was stirred at 50 °C for 2 days and then titrated with a 1 mM EDTA (aq) until no free Gd^{3+} was observed from xylenol orange test. By this method, the molar ratio of Gd^{3+} per dendrimer was determined, which was consistent with the theoretical number of ligands of each dendrimer (Table 1).

Computational Modeling. Computational models with explicit solvent and ions have provided a unique insight into the structure of triazine dendrimers. The simulations shown in Chart 2 are obtained from 100 ns of molecular dynamics (MD) simulations at 300 K and 1 atm of pressure. Both the equilibrated structures of DOTA chelates **G3-(Gd-DOTA)$_{24}$** and **G5-(Gd-DOTA)$_{96}$** are presented. From these computational models, we can calculate a number of interesting parameters. At the equilibrium, **G3-(Gd-DOTA)$_{24}$** and **G5-(Gd-DOTA)$_{96}$** showed a radius of gyration (R_g) of 22.6 ± 0.2 Å and 35.1 ± 0.3 Å, respectively.

These computations provide insights into interactions between these macromolecular chelates and water, as well as the accessibility of the chelate to solvent as shown by radial distribution functions (RDFs). An RDF represents the density and the distribution of atoms in space with respect to the center of a given system of reference (the center of mass of the dendrimer). The RDFs shown in Figure 2 show the dendrimer platform (black continuous line), the DOTA chelates complexed with Gd ions (black dotted line), and water molecules (blue profile) with respect to the center. This plot gives indications about the presence of solute or solvent atoms in a certain zone of the system (spatial density). Since these curves are calculated at each step of the simulation, and they are reported in the plots as averaged over the equilibrated phases of the dynamic trajectories, they give information also on the dynamics of the system. These plots provide an indication on the time period in which a certain atom is present in a certain area in the space (dynamic density). In RDF plots, high and narrow peaks in a small area of these graphs mean not only high density of atoms in a certain zone, but also high localization and

dx.doi.org/10.1021/bc300461r | *Bioconjugate Chem.* 2012, 23, 2291−2299

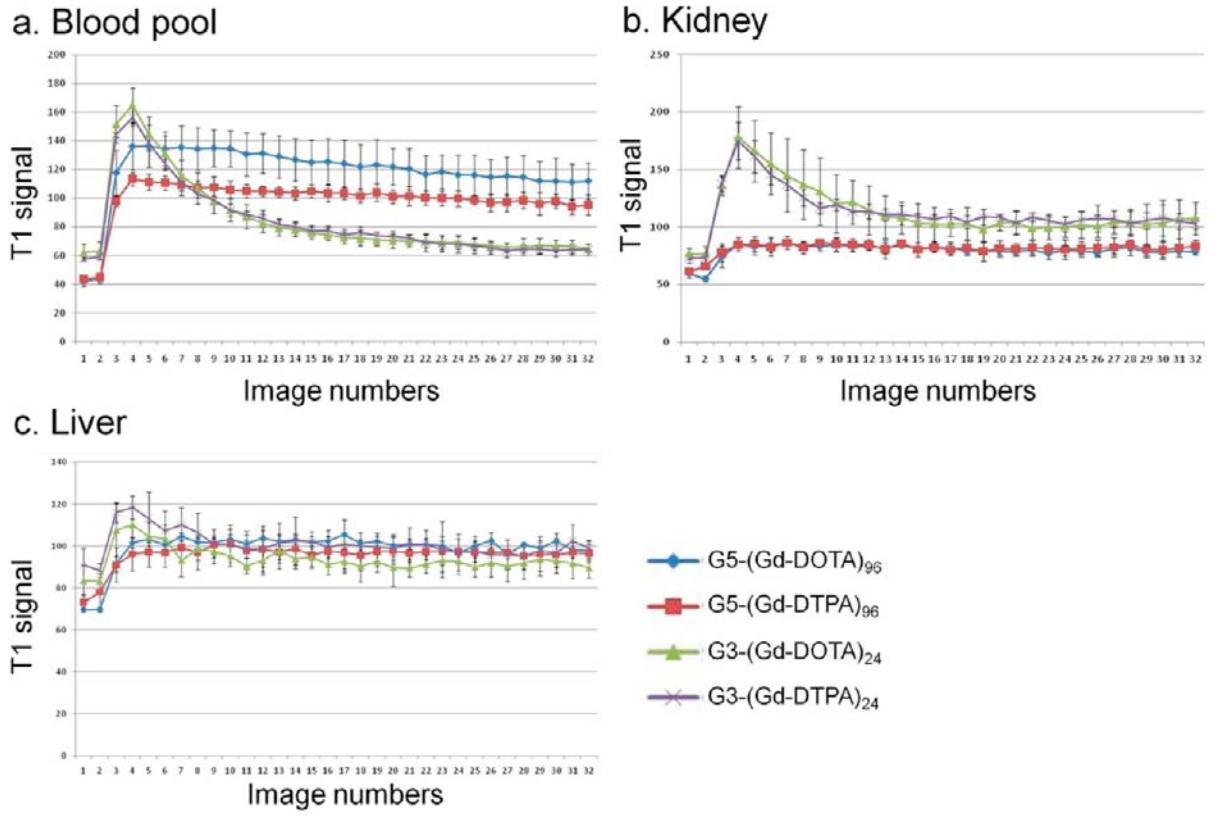

Figure 5. Serial dynamic *T*1 signals of the blood pool (a), the kidney (b), and the liver (c) are plotted. *T*1 signals are consistent with the dynamic image shown in Figure 4and SI videos. Image 1 is precontrast and image 2 is obtained after contrast agent administration. Images were obtained every 2 min after injection (images 2−32).

low mobility of these atoms whether dendrimer, DOTA, or water. Conversely, broad and low intensity peaks indicate low density and high mobility.

RDF plots show reduced surface DOTA backfolding most likely due to the large size of the DOTA indicators. From these data, we infer that the metalated ligands are accessible to water, with more groups available on **G5-(Gd-DOTA)$_{96}$** than **G3-(Gd-DOTA)$_{24}$**. The larger dendrimer presents a higher surface density of Gd-DOTA groups than smaller dendrimer (the second peak at 20 Å). Thus, the 96 Gd-DOTA groups of the generation 5 dendrimer may induce a higher surface density through structural crowding. This crowding is consistent with a decrease of water in that zone. In addition, some of these DOTA groups appear backfolded toward the dendrimer's core as indicated by peaks between ca. 15 and 25 Å from the dendrimer's center. **G3-(Gd-DOTA)$_{24}$** shows a more uniform structure and a more flexible surface. After the first high-intensity peak, the decrease in RDF is continuous and uniform.

Computation suggests that both dendrimers allow for consistent water penetration—even with waters found in close proximity to the cores. Whether these waters can exchange with bulk solvent is less certain, as peaks could also be generated by trapped molecules close to the dendrimer's center.

Relaxivity. Relaxivity profiles of triazine dendrimers conjugated with Gd-DOTA were different from those conjugated with DTPA-Gd or similar dendrimer agents that use PAMAM as a core instead of triazines. Both **G5-(Gd-DOTA)$_{96}$** and **G3-(Gd-DOTA)$_{24}$** showed higher *r*1 and *r*2 relaxivity compared with **G5-(Gd-DTPA)$_{96}$** and **G3-(Gd-DTPA)$_{24}$**, especially at lower magnetic field than 30 MHz (Figure 3), where all dendrimer-based macromolecular MRI contrast agents showed the peak *r*1 relaxivity. The *r*1 relaxivity of all agents decreased at high magnetic field such as 128 MHz (3-T) and 300 MHz (7-T). Furthermore, triazine dendrimer-based agents, especially when conjugated with Gd-DOTA, showed higher *r*1 relaxivity in serum than in PBS (Table 2), which can be advantageous in vivo imaging.

A striking finding of this study is the differences in relaxivity profiles between triazine dendrimers and PAMAM dendrimers based on the chelate used. DOTA conjugated to G3 and G5 triazine dendrimers showed much higher *r*1 and *r*2 relaxivity at low magnetic field (12 MHz or lower) and higher *r*1 relaxivity at high magnetic field (128 MHz) than comparable PAMAM dendrimers even in the PBS buffer. The peak *r*1 relaxivity values of both dendrimers of the same generation were similar at 30 MHz. This increased relaxivity may be caused by the chelate conformation, which allows either fast or slow water exchange. DOTA is known to form a variety of conformations, when conjugated to different moieties via a side chain.[31,32] Therefore, benzyl-DOTA conjugated with triazine dendrimer can exchange water rapidly leading to high *r*1 relaxivity at off peak magnetic fields.[33]

Another advantage of triazine G5 agents is that *r*1 increased dramatically in serum vs PBS. Although the *r*1 values of both triazine G5s and PAMAM-G4 in PBS were around 10/mM/s, the *r*1 of triazine G5s in serum increased more than 2-fold up to above 20/mM/s at 128 MHz, a finding that did not occur with PAMAM-based MRI-CAs. In particular, triazine G5-DOTA demonstrated an *r*1 of 24/mM/s, which is 85% higher than triazine G5-DTPA (13/mM/s). This high relaxivity is likely

related to loose serum protein binding, which further slows the molecular tumbling rate.

In Vivo Dynamic Imaging Studies. In vivo pharmacokinetics using dynamic MRI was different for G3-based and G5-based agents. **G3-(Gd-DTPA)$_{24}$** and **G3-(Gd-DOTA)$_{24}$** quickly cleared from the kidneys. Dynamic MRI showed a quick decrease in blood signal and a temporally rapid increase of signal in the kidneys, followed by a gradual signal increase in the bladder (Figure 4a,b, SI Videos 1 and 2, and Figure 5a,b). In contrast, **G5-(Gd-DTPA)$_{96}$** and **G5-(Gd-DOTA)$_{96}$** did not show clearance through the kidney, but demonstrated a steady signal in the blood and the kidneys, and no or minimal signal increase in the bladder (Figure 4c,d, SI Videos 3 and 4, and Figure 5a,b). In addition, **G5-(Gd-DOTA)$_{96}$** showed higher signal than **G5-(Gd-DTPA)$_{96}$** in vivo, which is consistent with its high serum relaxivity (Figure 4c,d) that has never been seen, when PAMAM dendrimer was employed as a platform (SI Figure 22). No significant difference of *T*1 signals in the liver was observed among the macromolecular chelates regardless of the generation and the ligand (Figure 5c).

CONCLUSIONS

Gd-based macromolecular contrast agents were synthesized using a well-characterized G3 or G5 triazine platform. NMR spectroscopy and mass spectrometry confirmed that both G3 and G5 contrast agents conjugated with either DTPA or DOTA contained approximately 24 and 96 chelates, respectively, which represents the theoretical limit which is also unusual for such conjugations with other dendrimers. Both G3 dendrimers, as expected, showed a shorter half-life in blood and more rapid renal excretion than G5 dendrimers. Although triazine G5 agents are smaller than PAMAM G4 agents, they show reduced their renal excretion.[23] The *r*1 relaxivity of dendrimers chelated with DOTA was higher than that of dendrimers chelated with DTPA. **G5-(Gd-DOTA)$_{96}$** had a markedly higher relaxivity in serum than in PBS. Thus, this agent had a 4−5-fold improvement in relaxivity compared to low-molecular-weight Gd-DOTA or Gd-DTPA. The pharmacokinetics of dendrimer chelated with either DTPA or DOTA was similar. Taken together, the DOTA version of the triazine dendrimer has advantages in relaxivity in comparison to DTPA chelates at widely accessible MRI frequencies/field strengths (64−128 MHz; 1.5−3 T) especially in vivo, and has the added advantage of higher association constants for gadolinium, making it more attractive for clinical translation. Such aspirations benefit from the ease of characterization associated with these materials.

ASSOCIATED CONTENT

Supporting Information

Details of synthesis and spectral data. This material is available free of charge via the Internet at http://pubs.acs.org.

AUTHOR INFORMATION

Corresponding Author

*Phone: 301-451-4220. Fax: 301-402-3191. E-mail: kobayash@mail.nih.gov.

Notes

The authors declare no competing financial interest.

ACKNOWLEDGMENTS

This research was supported by the Intramural Research Program of the National Institutes of Health, National Cancer Institute, Center for Cancer Research and the National Institutes of Health (GM 65460 to EES) and the Robert A. Welch Foundation (EES, A-0008).

REFERENCES

(1) Menjoge, A. R., Kannan, R. M., and Tomalia, D. A. (2010) Dendrimer-based drug and imaging conjugates: design considerations for nanomedical applications. *Drug Discovery Today 15*, 171−185.

(2) Bryant, L. H., Jr., Brechbiel, M. W., Wu, C., Bulte, J. W., Herynek, V., and Frank, J. A. (1999) Synthesis and relaxometry of high-generation (G = 5, 7, 9, and 10) PAMAM dendrimer-DOTA-gadolinium chelates. *J. Magn. Reson. Imaging 9*, 348−352.

(3) Ogawa, M., Regino, C. A., Marcelino, B., Williams, M., Kosaka, N., Bryant, L. H., Jr., Choyke, P. L., and Kobayashi, H. (2010) New nanosized biocompatible MR contrast agents based on lysine-dendrigraft macromolecules. *Bioconjugate Chem. 21*, 955−960.

(4) Kobayashi, H., Sato, N., Hiraga, A., Saga, T., Nakamoto, Y., Ueda, H., Konishi, J., Togashi, K., and Brechbiel, M. W. (2001) 3D-micro-MR angiography of mice using macromolecular MR contrast agents with polyamidoamine dendrimer core with references to their pharmacokinetic properties. *Magn. Reson. Med. 45*, 454−460.

(5) Kobayashi, H., Sato, N., Kawamoto, S., Saga, T., Hiraga, A., Ishimori, T., Konishi, J., Togashi, K., and Brechbiel, M. W. (2001) 3D MR angiography of intratumoral vasculature using a novel macromolecular MR contrast agent. *Magn. Reson. Med. 46*, 579−585.

(6) Kobayashi, H., Kawamoto, S., Saga, T., Sato, N., Hiraga, A., Ishimori, T., Akita, Y., Mamede, M. H., Konishi, J., Togashi, K., and Brechbiel, M. W. (2001) Novel liver macromolecular MR contrast agent with a polypropylenimine diaminobutyl dendrimer core: comparison to the vascular MR contrast agent with the polyamidoamine dendrimer core. *Magn. Reson. Med. 46*, 795−802.

(7) Kobayashi, H., Saga, T., Kawamoto, S., Sato, N., Hiraga, A., Ishimori, T., Konishi, J., Togashi, K., and Brechbiel, M. W. (2001) Dynamic micro-magnetic resonance imaging of liver micrometastasis in mice with a novel liver macromolecular magnetic resonance contrast agent DAB-Am64-(1B4M-Gd)(64). *Cancer Res. 61*, 4966−4970.

(8) Kobayashi, H., Kawamoto, S., Jo, S., Bryant, L. H., Jr., Brechbiel, M. W., and Star, R. A. (2003) Macromolecular MRI contrast agents with small dendrimers: pharmacokinetic differences between sizes and cores. *Bioconjugate Chem. 14*, 388−394.

(9) Kobayashi, H., Kawamoto, S., Jo, S., Sato, N., Saga, T., Hiraga, A., Konishi, J., Hu, S., Togashi, K., Brechbiel, M. W., and Star, R. A. (2002) Renal tubular damage detected by dynamic micro-MRI with a dendrimer-based MR contrast agent. *Kidney Int. 61*, 1980−1985.

(10) Kobayashi, H., Kawamoto, S., Sakai, Y., Choyke, P. L., Star, R. A., Brechbiel, M. W., Sato, N., Tagaya, Y., Morris, J. C., and Waldmann, T. A. (2004) Lymphatic drainage imaging of breast cancer in mice by micro-magnetic resonance lymphangiography using a nano-size paramagnetic contrast agent. *J. Natl. Cancer Inst. 96*, 703−708.

(11) Kobayashi, H., Kawamoto, S., Star, R. A., Waldmann, T. A., Tagaya, Y., and Brechbiel, M. W. (2003) Micro-magnetic resonance lymphangiography in mice using a novel dendrimer-based magnetic resonance imaging contrast agent. *Cancer Res. 63*, 271−276.

(12) Kobayashi, H., Koyama, Y., Barrett, T., Hama, Y., Regino, C. A., Shin, I. S., Jang, B. S., Le, N., Paik, C. H., Choyke, P. L., and Urano, Y. (2007) Multimodal nanoprobes for radionuclide and five-color near-infrared optical lymphatic imaging. *ACS Nano 1*, 258−264.

(13) Kobayashi, H., Longmire, M. R., Ogawa, M., and Choyke, P. L. (2011) Rational chemical design of the next generation of molecular imaging probes based on physics and biology: mixing modalities, colors and signals. *Chem. Soc. Rev. 40*, 4626−4648.

(14) Haemel, A. K., Sadowski, E. A., Shafer, M. M., and Djamali, A. (2011) Update on nephrogenic systemic fibrosis: are we making progress? *Int. J. Dermatol. 50*, 659−666.

(15) Hellman, R. N. (2011) Gadolinium-induced nephrogenic systemic fibrosis. *Semin. Nephrol. 31*, 310−316.

(16) Zou, Z., Zhang, H. L., Roditi, G. H., Leiner, T., Kucharczyk, W., and Prince, M. R. (2011) Nephrogenic systemic fibrosis: review of 370 biopsy-confirmed cases. *JACC Cardiovasc. Imaging 4*, 1206−1216.
(17) Longmire, M. R., Ogawa, M., Choyke, P. L., and Kobayashi, H. (2011) Biologically optimized nanosized molecules and particles: more than just size. *Bioconjugate Chem. 22*, 993−1000.
(18) Sedlakova, P., Svobodova, J., Miksik, I., and Tomas, H. (2006) Separation of poly(amidoamine) (PAMAM) dendrimer generations by dynamic coating capillary electrophoresis. *J. Chromatogr., B 841*, 135−139.
(19) Shi, X., Majoros, I. J., and Baker, J. R., Jr. (2005) Capillary electrophoresis of poly(amidoamine) dendrimers: from simple derivatives to complex multifunctional medical nanodevices. *Mol. Pharmaceutics 2*, 278−294.
(20) Kobayashi, H., and Brechbiel, M. W. (2004) Dendrimer-based nanosized MRI contrast agents. *Curr. Pharm. Biotechnol. 5*, 539−549.
(21) Kobayashi, H., and Brechbiel, M. W. (2005) Nano-sized MRI contrast agents with dendrimer cores. *Adv. Drug Delivery Rev. 57*, 2271−2286.
(22) Chen, H. T., Neerman, M. F., Parrish, A. R., and Simanek, E. E. (2004) Cytotoxicity, hemolysis, and acute in vivo toxicity of dendrimers based on melamine, candidate vehicles for drug delivery. *J. Am. Chem. Soc. 126*, 10044−10048.
(23) Lim, J., Guo, Y., Rostollan, C. L., Stanfield, J., Hsieh, J. T., Sun, X., and Simanek, E. E. (2008) The role of the size and number of polyethylene glycol chains in the biodistribution and tumor localization of triazine dendrimers. *Mol. Pharmaceutics 5*, 540−547.
(24) Lim, J., Mintzer, M. A., Perez, L. M., and Simanek, E. E. (2010) Synthesis of odd generation triazine dendrimers using a divergent, macromonomer approach. *Org. Lett. 12*, 1148−1151.
(25) Lim, J., Pavan, G. M., Annunziata, O., and Simanek, E. E. (2012) Experimental and computational evidence for an inversion in guest capacity in high-generation triazine dendrimer hosts. *J. Am. Chem. Soc. 134*, 1942−1945.
(26) Lim, J., and Simanek, E. E. (2012) Triazine dendrimers as drug delivery systems: From synthesis to therapy. *Adv. Drug Delivery Rev. 64*, 826−835.
(27) Neerman, M. F., Zhang, W., Parrish, A. R., and Simanek, E. E. (2004) In vitro and in vivo evaluation of a melamine dendrimer as a vehicle for drug delivery. *Int. J. Pharm. 281*, 129−132.
(28) Simanek, E. E., Abdou, H., Lalwani, S., Lim, J., Mintzer, M. A., Venditto, V. J., and Vittur, B. (2010) The 8 year thicket of triazine dendrimers: strategies, targets and applications. *Proc. R. Soc. London, Ser. A 466*, 1445−1468.
(29) Garzoni, M., Cheval, N., Fahmi, A., Danani, A., and Pavan, G. M. (2012) Ion-selective controlled assembly of dendrimer-based functional nanofibers and their ionic-competitive disassemby. *J. Am. Chem. Soc. 134*, 3349−3357.
(30) Case, D. A., Darden, T. A., Cheatham, T. E., III, Simmerling, C. L., Wang, J., Duke, R. E., Luo, R., Walker, R. C., Zhang, W., Merz, K. M., Robertson, B.., Wang, B., Hayik, S., Roitberg, A., Seabra, G., Kolossvary, I., Wong, K. F., Paesani, F., Vanicek, J., Liu, J., Wu, X., Brozell, S., Steinbrecher, T., Gohlke, H., Cai, Q., Ye, X., Wang, J., Hsieh, M.-J., Cui, G., Roe, D. R., Mathews, D. H., Seetin, M. G., Sangui, C., Babin, V., Luchko, T., Gusarov, S., Kovalenko, A., and Kollman, P. A. *AMBER 11*; University of California, San Francisco, 2010.
(31) Dimelow, R. J., Burton, N. A., and Hillier, I. H. (2007) The dynamics of water exchange in gadolinium DOTA complexes studied by transition path sampling and potential of mean force methods. *Phys. Chem. Chem. Phys. 9*, 1318−1323.
(32) Wang, J., Wolf, R. M., Caldwell, J. W., Kollman, P. A., and Case, D. A. (2004) Development and testing of a general amber force field. *J. Comput. Chem. 25*, 1157−1174.
(33) Jakalian, A., Bush, B. L., Jack, D. B., and Bayly, C. I. (2000) Fast, efficient generation of high-quality atomic Charges. AM1-BCC model: I. Method. *J. Comput. Chem. 21*, 132−146.
(34) Jakalian, A., Jack, D. B., and Bayly, C. I. (2002) Fast, efficient generation of high-quality atomic charges. AM1-BCC model: II. Parameterization and validation. *J. Comput. Chem. 25*, 1623−1641.
(35) Wang, J., Wang, W., Kollman, P. A., and Case, D. A. (2006) Automatic atom type and bond type perception in molecular mechanical calculations. *J. Mol. Graphics Model. 25*, 247−260.
(36) Jorgensen, W. L., Chandrasekhar, J., Madura, J. D., Impey, R. W., and Klein, M. L. (1983) Comparison of simple potential functions for simulating liquid water. *J. Chem. Phys. 79*, 926−35.
(37) Cornell, W. D., Cieplak, P., Bayly, C. I., Gould, I. R., Merz, K. M., Ferguson, D. M., Spellmeyer, D. C., Fox, T., Caldwell, J. W., and Kollman, P. A. (1995) A 2nd generation force-field for the simulation of proteins, nucleic-acids and organic-molecules. *J. Am. Chem. Soc. 117*, 5179−5197.
(38) Ryckaert, J.-P., Ciccotti, G., and Berendsen, H. J. C. (1977) Numerical-integration of cartesian equations of motion of a system with constraints - molecular-dynamics of n-alkanes. *J. Comput. Phys. 23*, 327.
(39) Krautler, V., van Gunsteren, W. F., and Hanenberger, P. H. (2001) A fast SHAKE: Algorithm to solve distance constraint equations for small molecules in molecular dynamics simulations. *J. Comput. Chem. 5*, 501.
(40) Darden, T., York, D., and Pedersen, L. (1993) Particle mesh Ewald - an n.log(n) method for Ewald sums in large systems. *J. Chem. Phys. 98*, 10089−10092.

Gadolinium MRI Contrast Agents Based on Triazine Dendrimers: Relaxivity and In Vivo Pharmacokinetics

Jongdoo Lim,[†] *Baris Turkbey,*[‡] *Marcelino Bernardo,*[§] *L. Henry Bryant Jr.,*[#] Matteo Garzoni,[¶] *Giovanni M. Pavan,*[¶] *Peter L. Choyke,*[‡] *Eric E. Simanek,*[†] *and Hisataka Kobayashi*[‡,*]

[†]Department of Chemistry, Texas Christian University, Fort Worth, TX 76129

[‡]Molecular Imaging Program, Center for Cancer Research, National Cancer Institute, National Institutes of Health, Bethesda, Maryland 20892

[§]SAIC-Frederick, Inc., NCI-Frederick,, National Cancer Institute, National Institutes of Health, Frederick, Maryland 21702

[#]Laboratory of Diagnostic Radiology Research, Radiology &Imaging Sciences,, Warren Magnuson Clinical Center, National Institutes of Health, Bethesda, Maryland 20892

[¶]Department of Innovative Technologies, University of Applied Science of Southern Switzerland, Galleria 2 Manno, SZ

Table of Contents

page

General Procedures S2

Synthetic Procedures S2

Spectra..... .S7

General procedures

G3 and G5 dendrimers were prepared using methods previously described.[s1] p-NH_2-Bn-DOTA-tetra(t-Bu ester) and p-NH_2-Bn-DTPA-penta(t-Bu ester) were purchased from Macrocyclics. All other chemicals were purchased from Aldrich and Acros. All solvents were ACS grade and used without further purification. Diafiltration purification was performed with Amicon stirred ultrafiltration cell equipment (Model 8050, PLCC membrane, Millipore Corp.) at 35 psi of N_2. NMR spectra were recorded on a Varian Mercury 300 MHz or Inova 500 MHz spectrometer in $CDCl_3$, or $CDCl_3$:MeOH-d_4 (10:1). All mass spectral analyses were carried out by the Laboratory for Biological Mass Spectrometry at Texas A&M.

Synthetic Procedures

Compound 1. A solution of **6** (40 mg, 1.44 μmol), 1-[2-(2-hydroxyethoxy)ethyl]piperazine (60 mg, 0.344 mmol), and DIPEA (0.2 mL, 1.14 mmol) in THF (15 mL) was stirred for 24 h at room temperature. After the temperature was raised to 50 ^oC, the reaction solution was stirred for an additional 24 h and evaporated under vacuum. The residue was dissolved with dichloromethane, washed with brine, dried over $MgSO_4$, filtered, and evaporated under vacuum. The resulting product was dissolved in a solution of trifluoroacetic acid (4 mL), dichloromethane (1 mL), and methanol (1 mL). The solution was stirred for 48 h at room temperature and evaporated under vacuum. The crude product was dissolved in dichloromethane and methanol and precipitated by adding hexanes. The precipitation was repeated twice more to afford **1** (37 mg, quantitative) as a white solid. MS (MALDI-TOF) calcd for $C_{1152}H_{1794}N_{396}O_{285}$ 25735.81, found 25500 $(M+H)^+$.

Compound 2. A solution of **7** (0.19 g, 1.68 μmol), 1-[2-(2-hydroxyethoxy)ethyl]piperazine (0.80 g, 4.59 mmol), and DIPEA (0.2 mL, 1.14 mmol) in THF (10 mL) was stirred for 24 h at room temperature. After the temperature was raised to 50 ^oC, the reaction solution was stirred for an additional 24 h and evaporated under

[s1] Lim, J.; Mintzer, M. A.; Perez, L. M.; Simanek, E. E. Synthesis of odd generation triazine dendrimers using a divergent, macromonomer approach. *Org. Lett.* **2010**, *12*, 1148-1151.

vacuum. The residue was dissolved with dichloromethane, washed with brine, dried over $MgSO_4$, filtered, and evaporated under vacuum. The resulting product was dissolved in a solution of trifluoroacetic acid (6 mL), dichloromethane (1.5 mL), and methanol (1.5 mL). The solution was stirred for 48 h at room temperature and evaporated under vacuum. The crude product was dissolved in dichloromethane and methanol and precipitated by adding hexanes. The precipitation was repeated twice more to afford **2** (150 mg, 85%) as a white solid. MS (MALDI-TOF) calcd for $C_{4680}H_{7290}N_{1620}O_{1149}$ 104570.18, found 105700 $(M+H)^+$.

Compound 3. A solution of **9** (66 mg, 2.28 μmol), 1-[2-(2-hydroxyethoxy)ethyl]piperazine (0.10 g, 0.574 mmol), and DIPEA (0.2 mL, 1.14 mmol) in THF (15 mL) was stirred for 24 h at room temperature. After the temperature was raised to 50 ^oC, the reaction solution was stirred for an additional 24 h and evaporated under vacuum. The residue was dissolved with dichloromethane, washed with brine, dried over $MgSO_4$, filtered, and evaporated under vacuum. The resulting product was dissolved in a solution of trifluoroacetic acid (4 mL), dichloromethane (1 mL), and methanol (1 mL). The solution was stirred for 48 h at room temperature and evaporated under vacuum. The crude product was dissolved in dichloromethane and methanol and precipitated by adding hexanes. The precipitation was repeated twice more to afford **1** (58 mg, quantitative) as a white solid. MS (MALDI-TOF) calcd for $C_{1104}H_{1674}N_{372}O_{333}$ 25470.55, found 24800 $(M+H)^+$.

Compound 4. A solution of **10** (193 mg, 1.65 μmol), 1-[2-(2-hydroxyethoxy)ethyl]piperazine (0.80 g, 4.59 mmol), and DIPEA (0.2 mL, 1.14 mmol) in THF (10 mL) was stirred for 24 h at room temperature. After the temperature was raised to 50 ^oC, the reaction solution was stirred for an additional 24 h and evaporated under vacuum. The residue was dissolved with dichloromethane, washed with brine, dried over $MgSO_4$, filtered, and evaporated under vacuum. The resulting product was dissolved in a solution of trifluoroacetic acid (8 mL), dichloromethane (2 mL), and methanol (2 mL). The solution was stirred for 48 h at room temperature and evaporated under vacuum. The crude product was dissolved in dichloromethane and methanol and precipitated by adding

hexanes. The precipitation was repeated twice more to afford **4** (170 mg, quantitative) as a light yellow solid. MS (MALDI-TOF) calcd for $C_{4488}H_{6810}N_{1524}O_{1341}$ 103509.15, found 104700 $(M+H)^+$.

Compound 5. Cyanuric chloride (51 mg, 0.277 mmol) was added to an ice-bath cooled solution of p-NH_2-Bn-DOTA-tetra(t-Bu ester) (0.20 g, 0.272 mmol) and DIPEA (0.20 mL, 1.14 mmol) in THF (20 mL). The solution was stirred for 2 h at 0 ^oC and then concentrated under vacuum. The residue was dissolved in dichloromethane, washed with brine, dried over $MgSO_4$, filtered, and evaporated under vacuum. The crude product was purified by silica gel chromatography (DCM:MeOH = 8:1) to give **5** (0.21 g, 88%) as a white solid. ^1H NMR (300 MHz, $CDCl_3$) δ 7.64 (d, J = 8.1 Hz, 2H), 6.93 (t, J = 9.2 Hz, 2H), 3.35-1.75 (m, 25H), 1.34 (m, 36H); ^{13}C NMR (75 MHz, $CDCl_3$) δ 172.9, 172.8, 172.7, 172.6 (two lines), 172.5, 170.0, 169.3, 168.7, 167.2, 163.6, 135.5, 135.4, 135.2, 134.8, 128.8, 128.7, 122.2, 122.0, 82.2, 82.1 (two lines), 82.0, 81.9, 81.8, 60.8, 56.3, 55.9, 55.5, 55.3, 52.6, 52.4, 52.3, 52.0, 50.6, 48.6, 48.5, 48.0, 47.8, 42.5, 31.6, 31.0, 27.7; MS (MALDI-TOF) calcd for $C_{42}H_{66}Cl_2N_8O_8$ 880.4381, found 903.4241 $(M+Na)^+$.

Compound 6. A solution of **G3** (40 mg, 5.31 μmol) in THF (1 mL) and H_2O (0.3 mL) was slowly added to a solution of **5** (0.16 g, 0.181 mmol) and DIPEA (0.1 mL, 0.57 mmol) in THF (2 mL) at 0 ^oC. The solution was stirred for 48 h at room temperature and evaporated under vacuum. The residue was dissolved with dichloromethane, washed with brine, dried over $MgSO_4$, filtered, and evaporated under vacuum. The crude product was purified by precipitation from ethyl acetate to give **6** (0.13 g, 88%) as a white solid. ^1H NMR (500 MHz, $CDCl_3$) δ 7.52 (br, 48H), 7.08 (br, 48H), 3.81-1.80 (m, 1140H), 1.42 (m, 864H); ^{13}C NMR (75 MHz, $CDCl_3$) δ 173.2, 173.0, 172.9, 172.8, 168.9, 167.1, 166.3, 165.2, 164.6, 163.8, 136.7, 134.2, 129.3, 120.7, 82.4, 82.2 (two lines), 82.1, 82.0, 70.6, 70.3, 69.4, 61.4, 55.8, 52.7, 50.9, 48.1, 43.0, 38.3, 31.7, 31.1, 29.7, 28.0; MS (MALDI-TOF) calcd for $C_{1344}H_{2154}Cl_{24}N_{348}O_{237}$ 27801.97, found 27459.14 $(M+H)^+$.

Compound 7. A solution of **G5** (60 mg, 1.89 μmol) in THF (2 mL) and H_2O (0.5 mL) was slowly added to a solution of **5** (0.28 g, 0.317 mmol) and DIPEA (0.2 mL, 1.14 mmol) in THF (3 mL) at 0 ^oC. The solution was stirred for 48 h at room temperature and evaporated under vacuum. The residue was dissolved with dichloromethane, washed with brine, dried over $MgSO_4$, filtered, and evaporated under vacuum. The crude product was purified by precipitation with hexanes from ethyl acetate to give **7** (0.195 g, 91%) as a white solid. ^1H NMR (300 MHz, $CDCl_3$) δ 7.55 (d, J = 7.2 Hz, 192H), 7.07 (br, 192H), 3.81-1.81 (m, 4668H), 1.42 (m, 3456H); ^{13}C NMR (75 MHz, $CDCl_3$/MeOH-d_4) δ 172.9, 172.7 (two lines), 172.6, 172.5, 172.4, 168.6, 167.1, 166.0, 164.9, 164.7, 164.2, 136.5, 133.5, 128.9, 120.6, 82.2, 82.1, 82.0, 81.9, 70.3, 69.9, 69.0, 61.0, 55.3, 52.2, 50.6, 48.5, 43.3, 42.3, 37.7, 31.4, 30.9, 29.3, 27.6; MS (MALDI-TOF) calcd for $C_{5448}H_{8730}Cl_{96}N_{1428}O_{957}$ 112834.85, not found.

Compound 8. Cyanuric chloride (48 mg, 0.260 mmol) was added to an ice-bath cooled solution of p-NH_2-Bn-DTPA-penta(t-Bu ester) (0.20 g, 0.257 mmol) and DIPEA (0.20 mL, 1.14 mmol) in THF (20 mL). The solution was stirred for 2 h at 0 ^oC and then concentrated under vacuum. The residue was dissolved in dichloromethane, washed with brine, dried over $MgSO_4$, filtered, and evaporated under vacuum. The crude product was purified by silica gel chromatography (EtOAc:Hex = 2:3) to give **8** (0.21 g, 88%) as a sticky clear oil. ^1H NMR (300 MHz, $CDCl_3$) δ 7.41 (d, J = 8.4 Hz, 2H), 7.25 (d, J = 8.4 Hz, 2H), 3.43-3.38 (m, 10 H), 3.15-2.50 (m, 9H), 1.40 (m, 45H); ^{13}C NMR (75 MHz, $CDCl_3$) δ 171.4, 171.2, 170.8, 170.0, 164.0, 138.4, 133.7, 130.1, 121.4, 80.9, 80.7, 63.0, 56.2, 56.0, 55.9, 53.5, 53.0, 52.4, 36.7, 28.2 (two lines); MS (MALDI-TOF) calcd for $C_{44}H_{69}Cl_2N_7O_{10}$ 925.4483, found 926.5064 $(M+H)^+$.

Compound 9. A solution of **G3** (25 mg, 3.32 μmol) in THF (1 mL) and H_2O (0.3 mL) was slowly added to a solution of **8** (0.10 g, 0.108 mmol) and DIPEA (0.1 mL, 0.57 mmol) in THF (2 mL) at 0 ^oC. The solution was stirred for 48 h at room temperature and evaporated under vacuum. The residue was dissolved with dichloromethane, washed with brine, dried over $MgSO_4$, filtered, and evaporated under vacuum. The crude product was purified by silica gel chromatography (from EtOAc:Hex = 2:1 to EtOAc:MeOH:H_2O =

7:2:1) to give **9** (79 mg, 82%) as a white solid. ^{1}H NMR (300 MHz, $CDCl_3$) δ 7.39 (d, J = 8.1 Hz, 48H), 7.19 (d, J = 7.8 Hz, 48H), 3.80-2.40 (m, 936H), 1.82 (br, 60H), 1.39 (m, 1080H); ^{13}C NMR (75 MHz, $CDCl_3$) δ 171.4, 171.2, 170.7, 169.1, 166.3, 165.3, 164.6, 163.7, 136.3, 135.6, 129.8, 120.2, 80.8, 80.6, 70.7, 70.3, 69.1, 63.0, 56.0, 55.8, 53.6, 53.0, 52.5, 43.6, 42.8, 38.2, 36.7, 29.7, 28.2; MS (MALDI-TOF) calcd for $C_{1392}H_{2226}Cl_{24}N_{324}O_{285}$ 28882.22, found 29324.78 $(M+H)^+$.

Compound 10. A solution of **G5** (60 mg, 1.89 μmol) in THF (2 mL) and H_2O (0.5 mL) was slowly added to a solution of **8** (0.30 g, 0.324 mmol) and DIPEA (0.2 mL, 1.14 mmol) in THF (3 mL) at 0 ^{o}C. The solution was stirred for 48 h at room temperature and evaporated under vacuum. The residue was dissolved with dichloromethane, washed with brine, dried over $MgSO_4$, filtered, and evaporated under vacuum. The crude product was purified by precipitation with hexanes from ethyl acetate to give **10** (0.20 g, 90%) as a white solid. ^{1}H NMR (500 MHz, $CDCl_3$) δ 7.37 (d, J = 7.5 Hz, 192H), 7.17 (d, J = 7.5 Hz, 192H), 3.81-2.45 (m, 3840H), 1.80 (br m, 252H), 1.39 (m, 4320H); ^{13}C NMR (125 MHz, $CDCl_3$) δ 171.4, 171.2, 170.7, 169.1, 166.3, 165.3, 164.6, 163.6, 136.2, 135.6, 129.7, 120.2, 80.8, 80.5, 70.6, 70.2, 69.3, 62.9, 56.0, 55.7, 53.5, 52.9, 52.4, 43.6, 42.9, 42.7, 38.2, 36.6, 29.6, 28.3, 28.2, 28.1, 28.0 (two lines); MS (MALDI-TOF) calcd for $C_{5640}H_{9018}Cl_{96}N_{1332}O_{1149}$ 117155.83, found 117277.83 $(M+H)^+$.

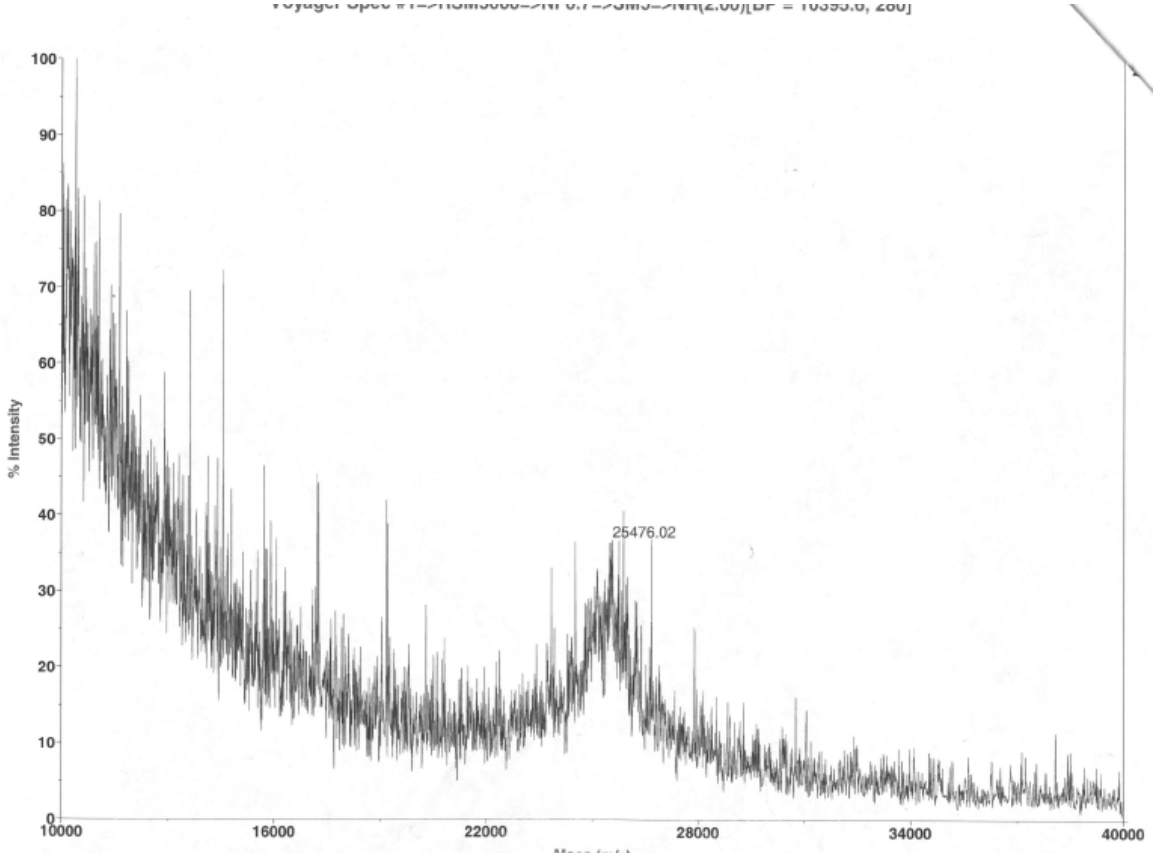

Figure S1. MALDI-TOF mass spectrum of compound **1.**

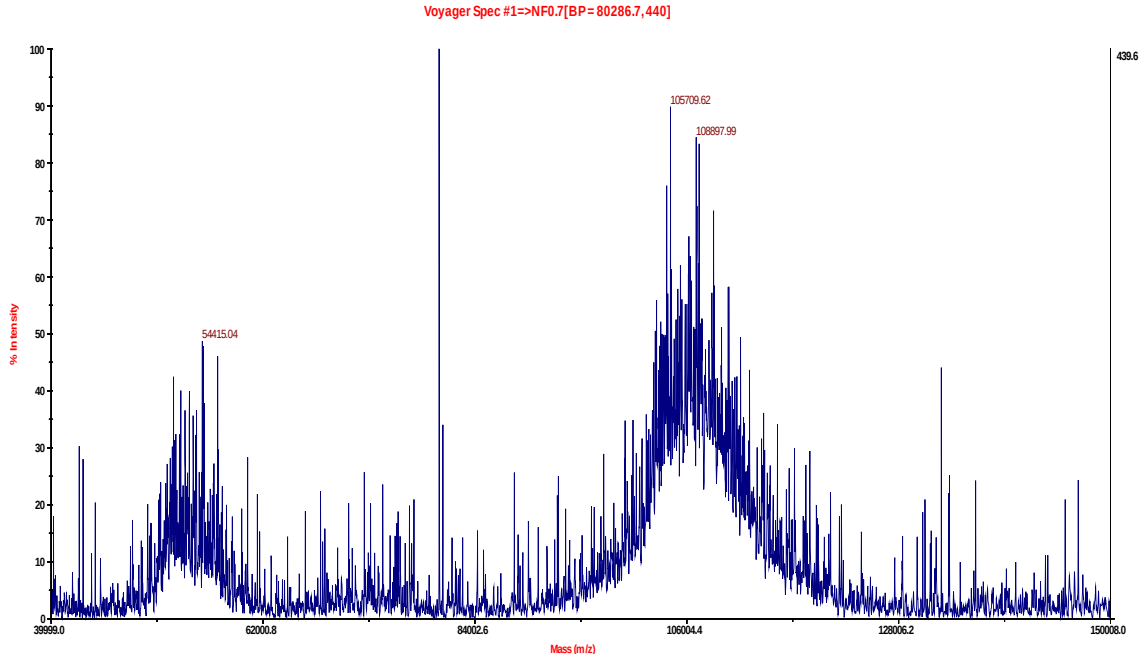

Figure S2. MALDI-TOF mass spectrum of compound **2.**

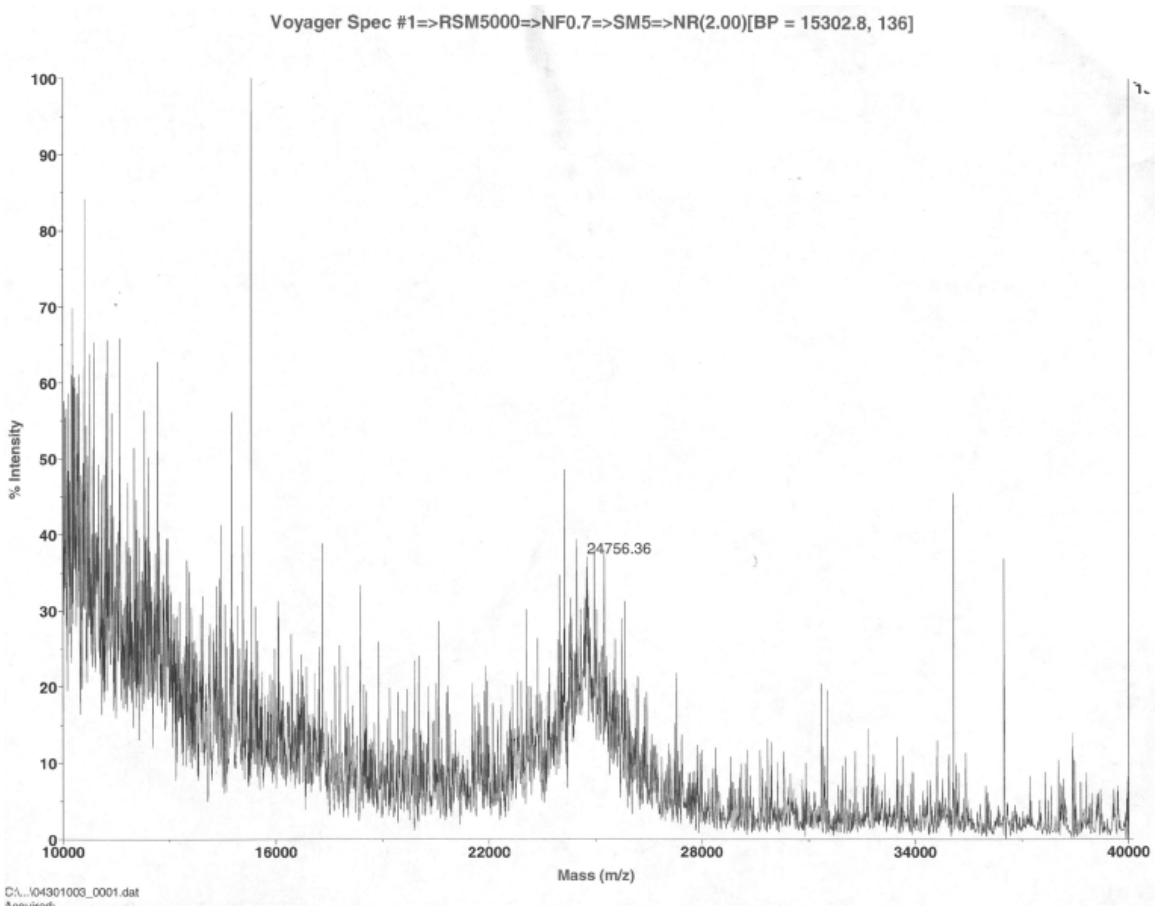

Figure S3. MALDI-TOF mass spectrum of compound **3.**

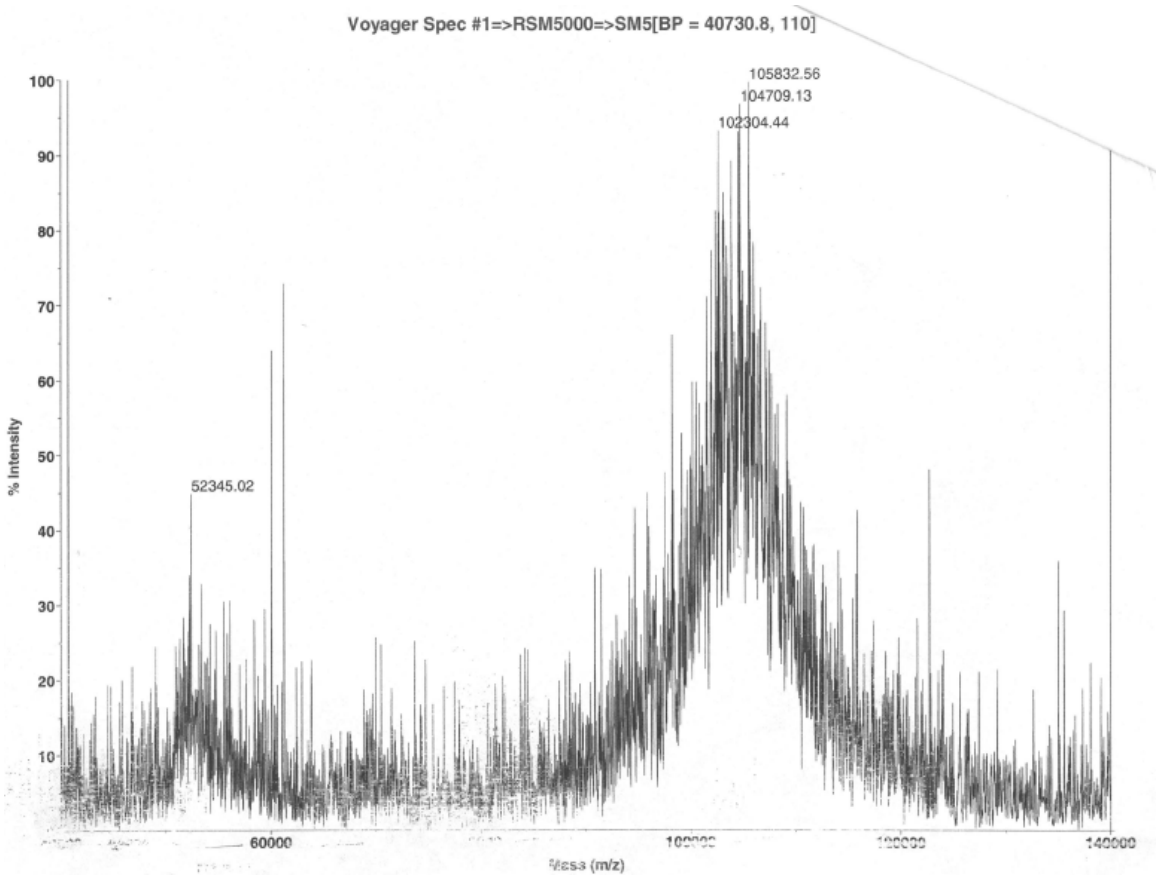

Figure S4. MALDI-TOF mass spectrum of compound **4.**

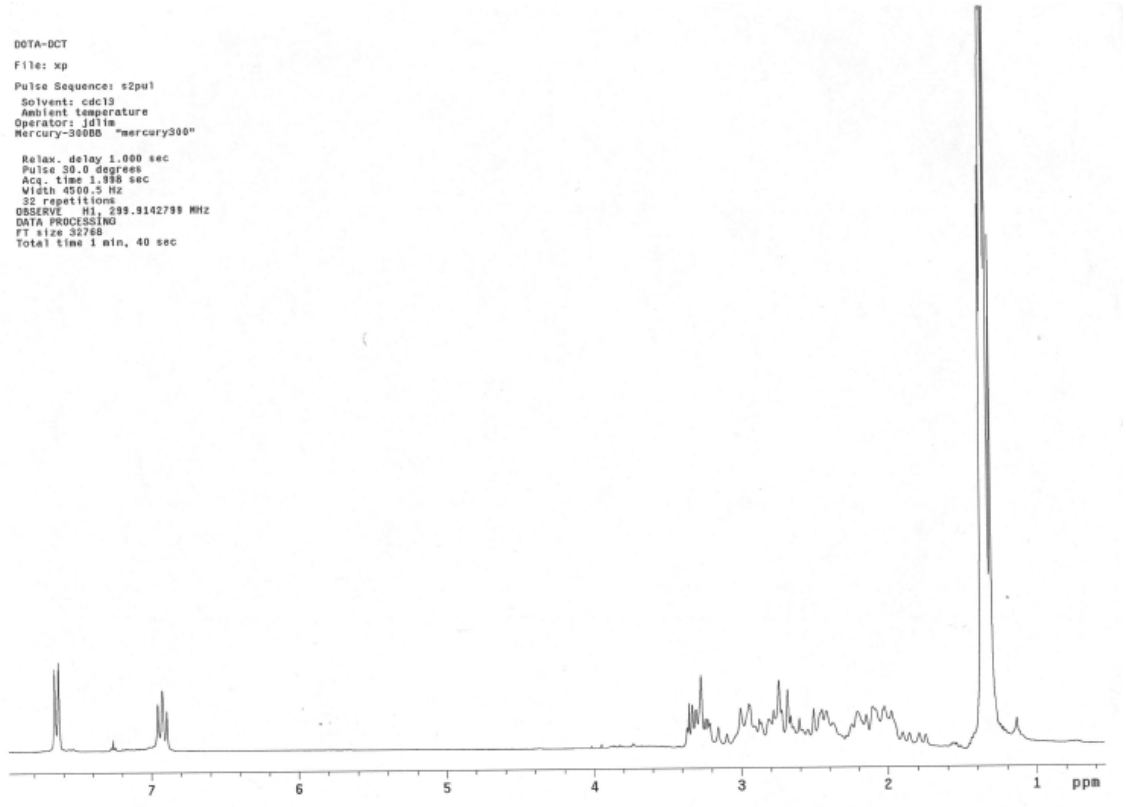

Figure S5. ^{1}H NMR spectrum of compound **5** (300 MHz, $CDCl_3$).

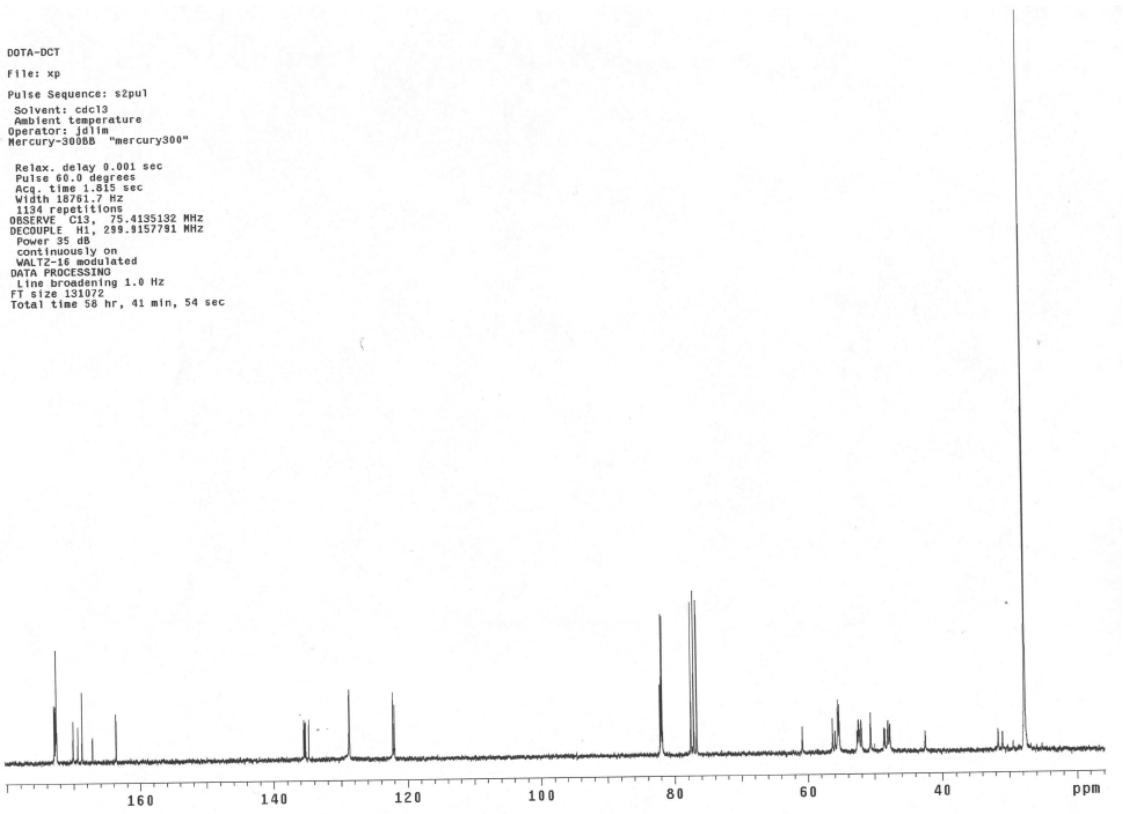

Figure S6. ^{13}C NMR spectrum of compound **5** (75 MHz, $CDCl_3$).

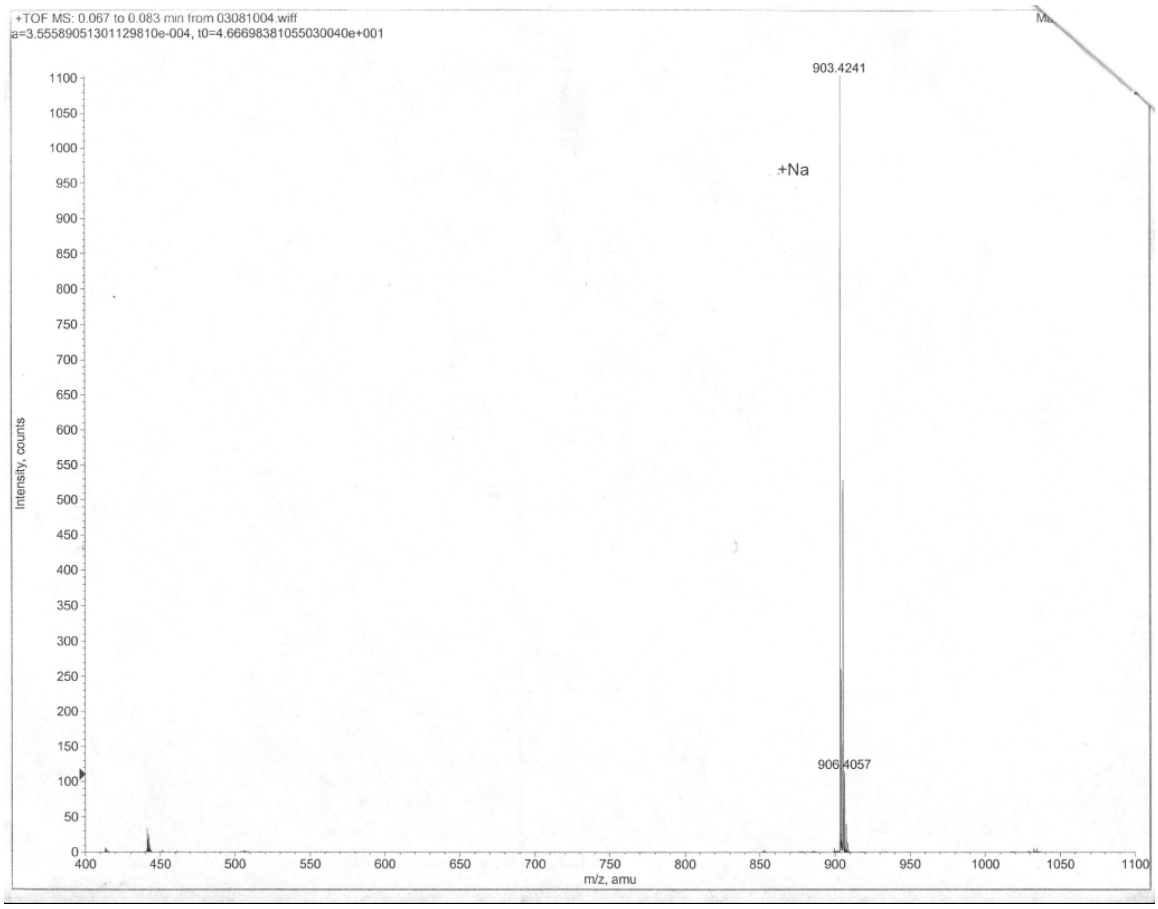

Figure S7. ESI-TOF mass spectrum of compound **5.**

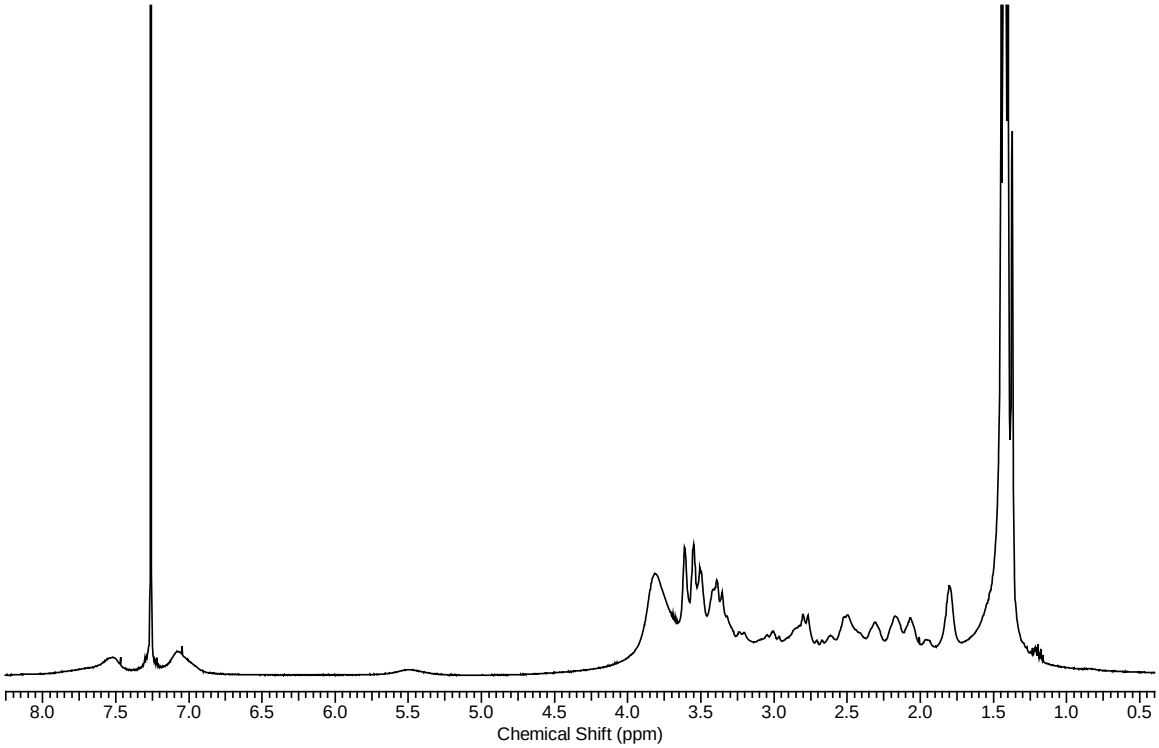

Figure S8. ^{1}H NMR spectrum of compound **6** (500 MHz, $CDCl_3$).

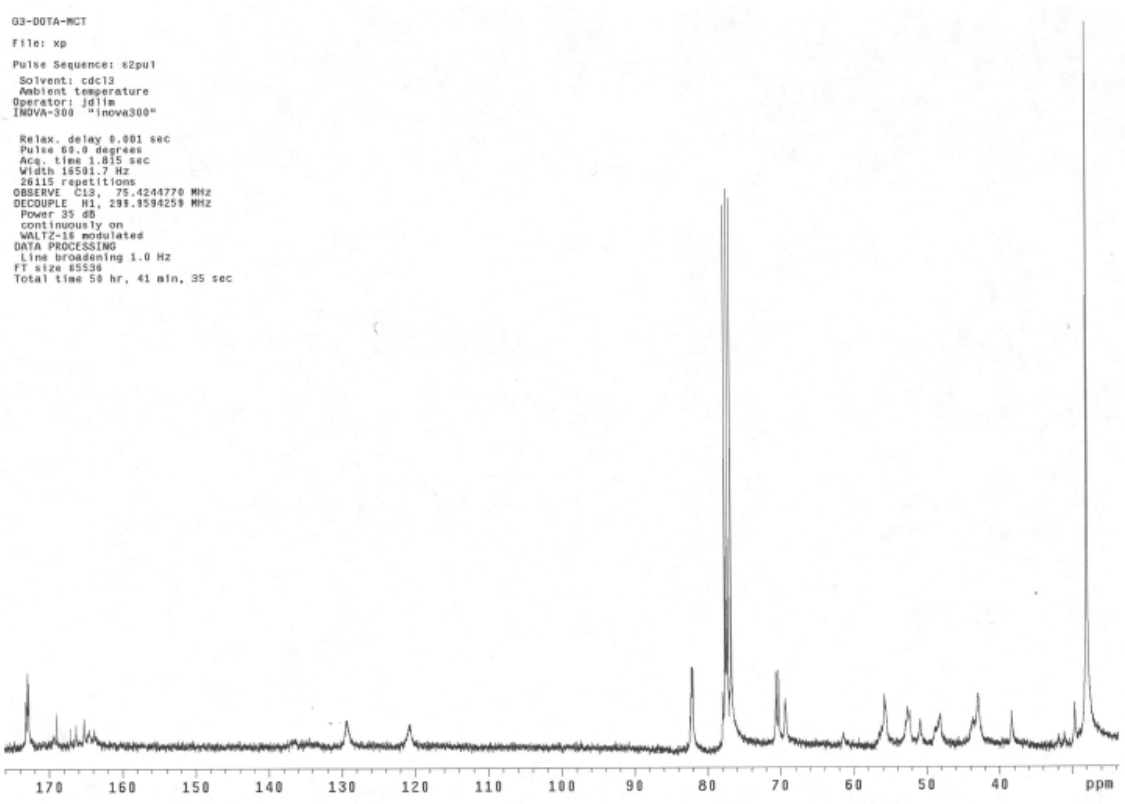

Figure S9. ^{13}C NMR spectrum of compound **6** (75 MHz, $CDCl_3$).

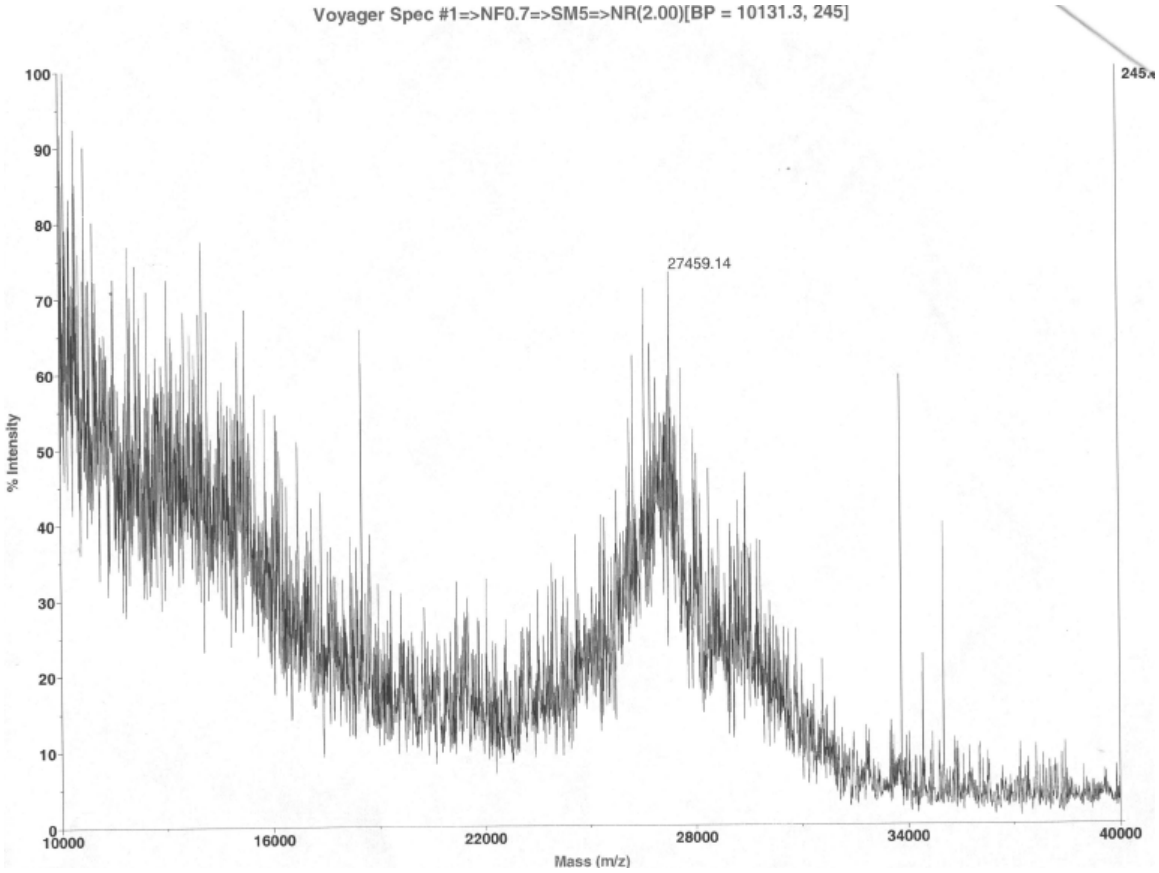

Figure S10. MALDI-TOF mass spectrum of compound **6.**

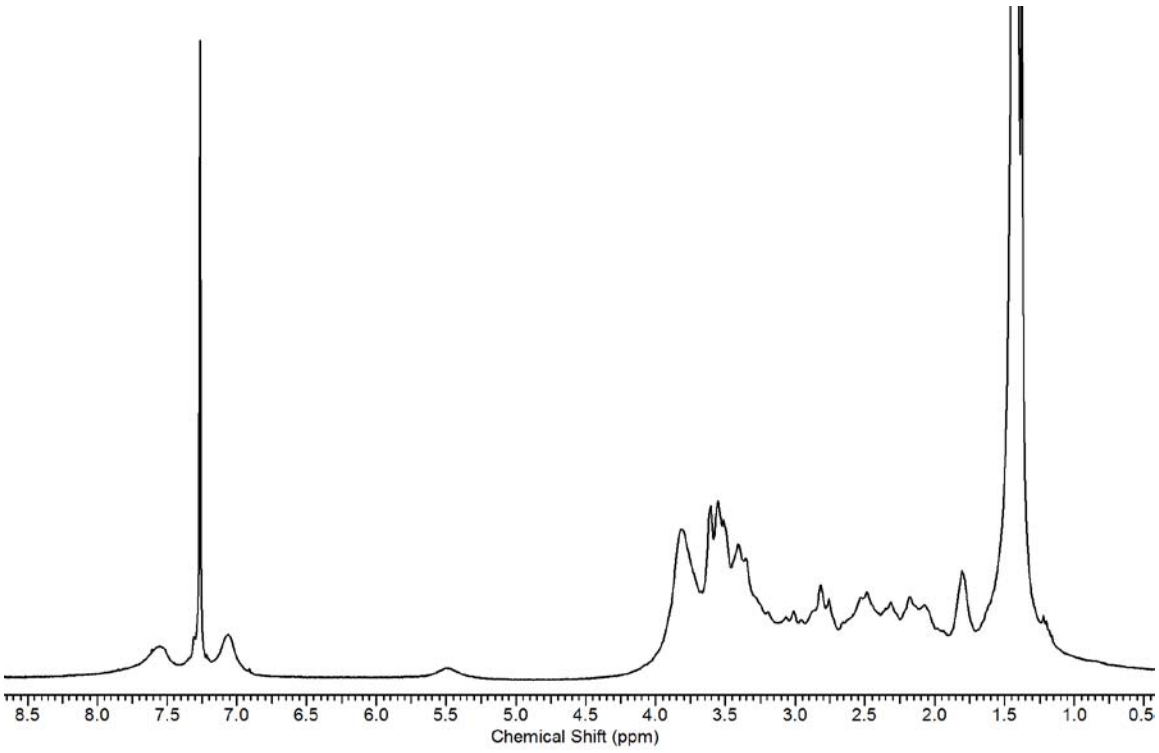

Figure S11. ^{1}H NMR spectrum of compound **7** (300 MHz, $CDCl_3$).

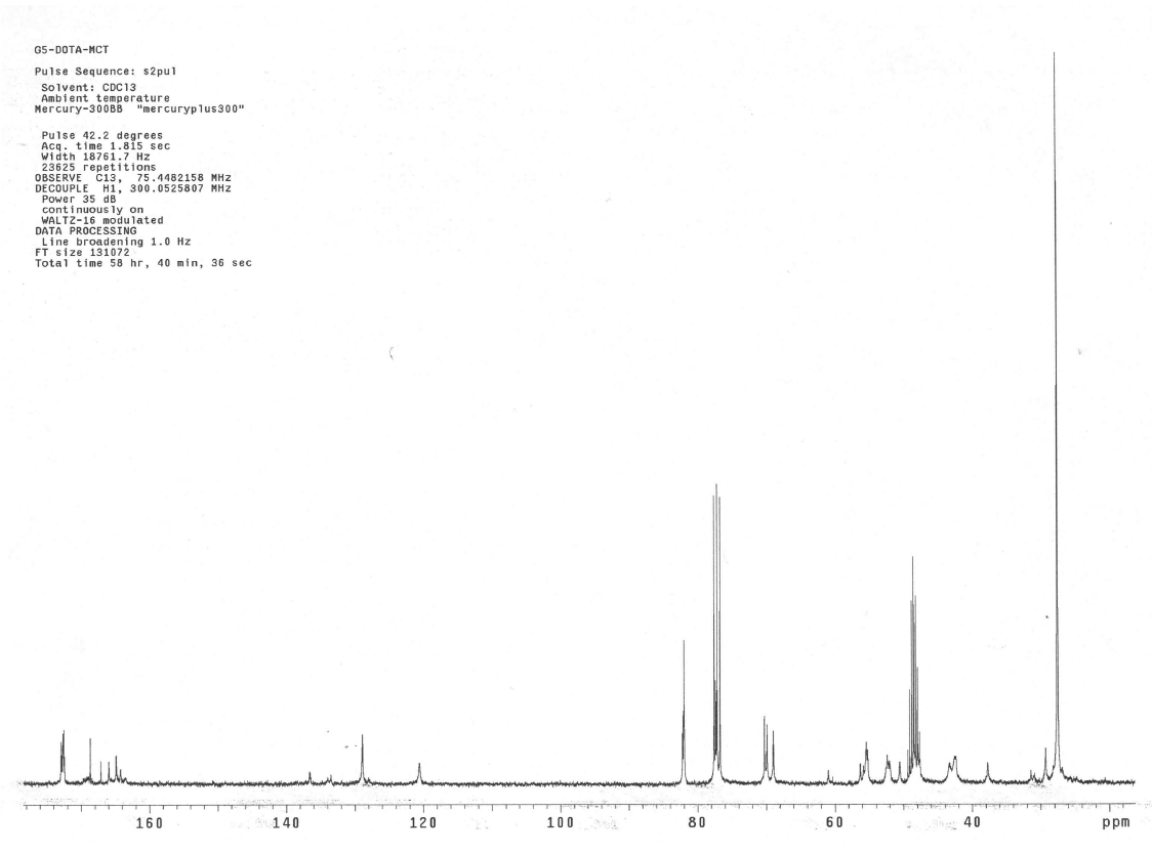

Figure S12. ^{13}C NMR spectrum of compound **7** (75 MHz, $CDCl_3$/MeOH-d_4).

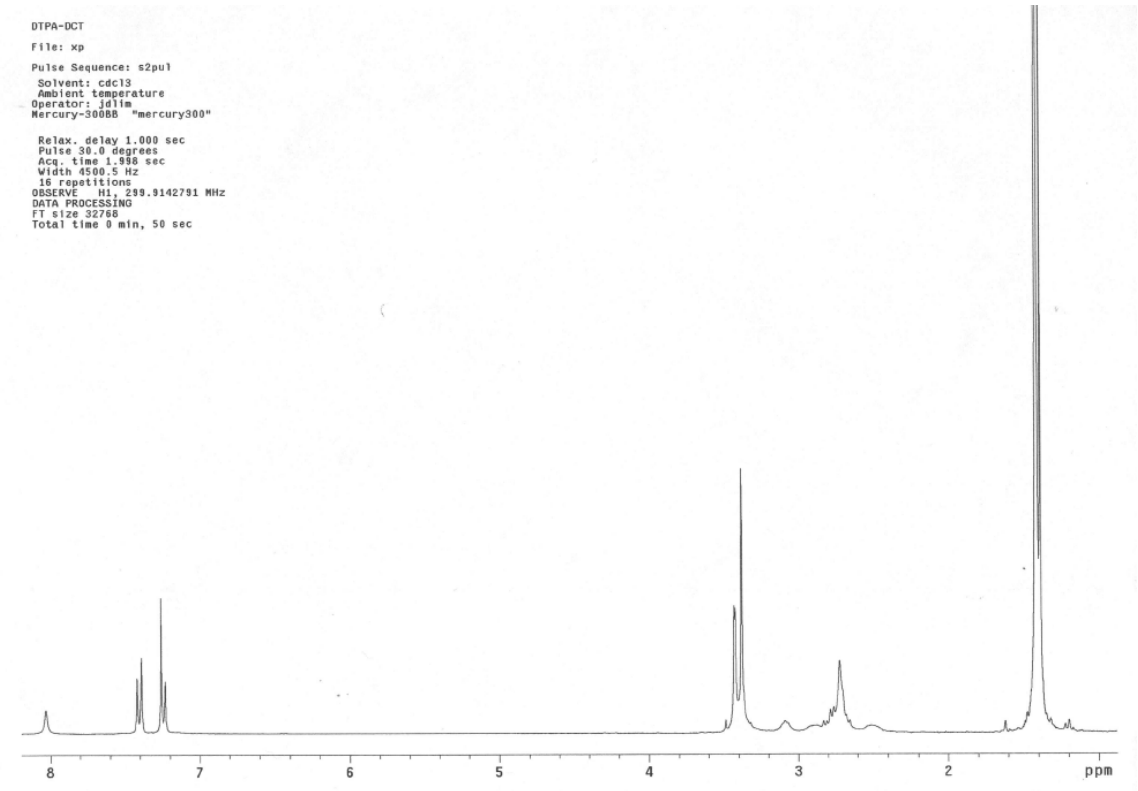

Figure S13. ^{1}H NMR spectrum of compound **8** (300 MHz, $CDCl_3$).

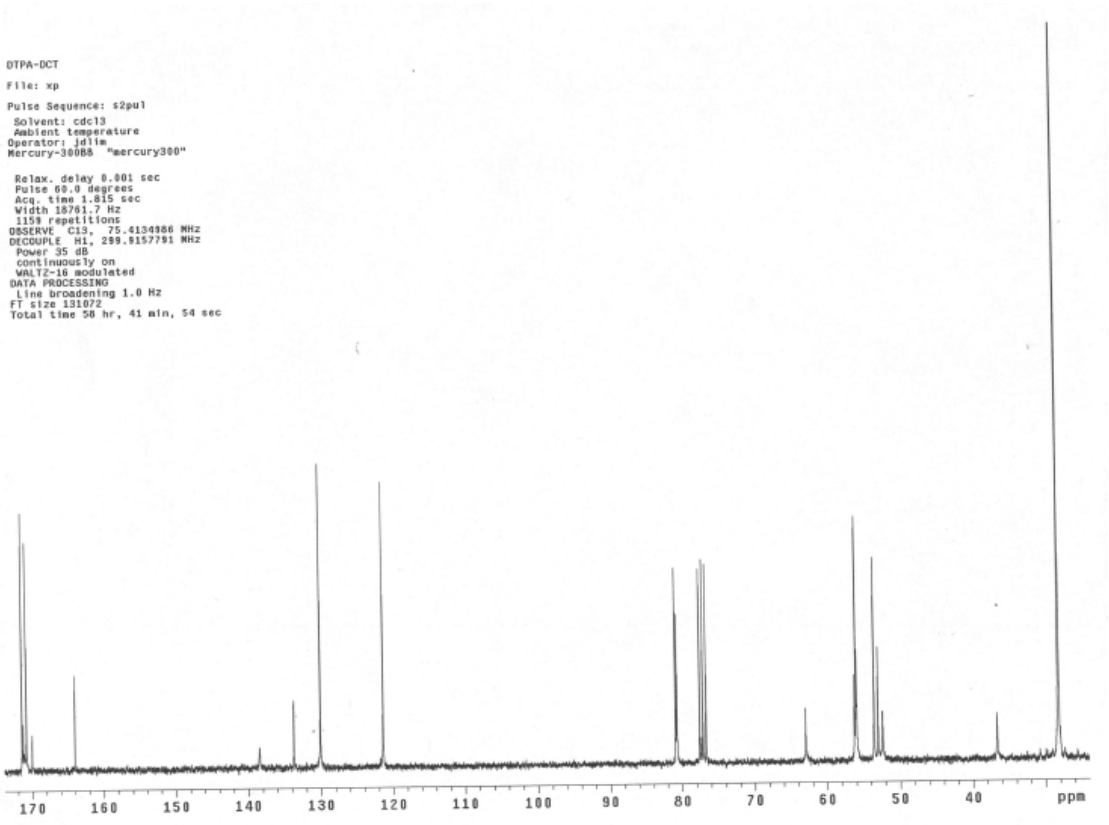

Figure S14. ^{13}C NMR spectrum of compound **8** (75 MHz, $CDCl_3$).

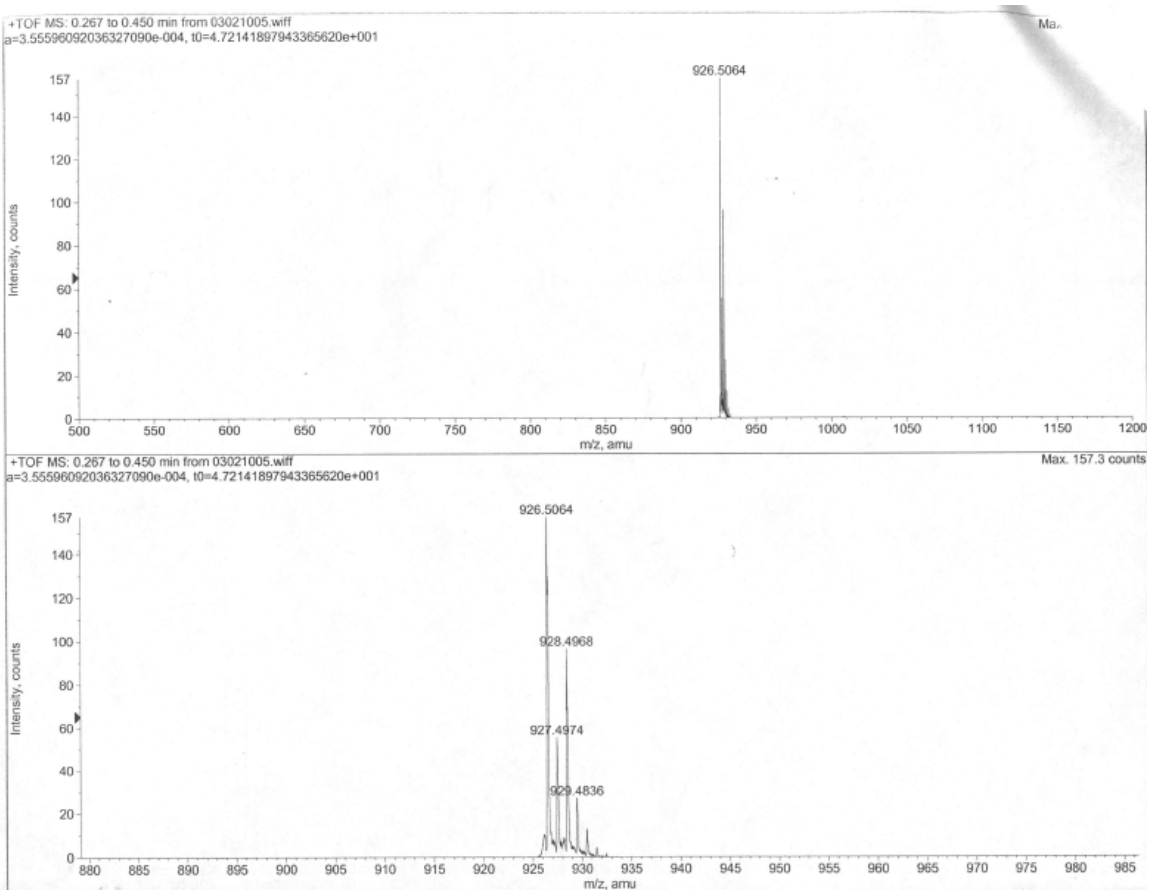

Figure S15. ESI-TOF mass spectrum of compound **8.**

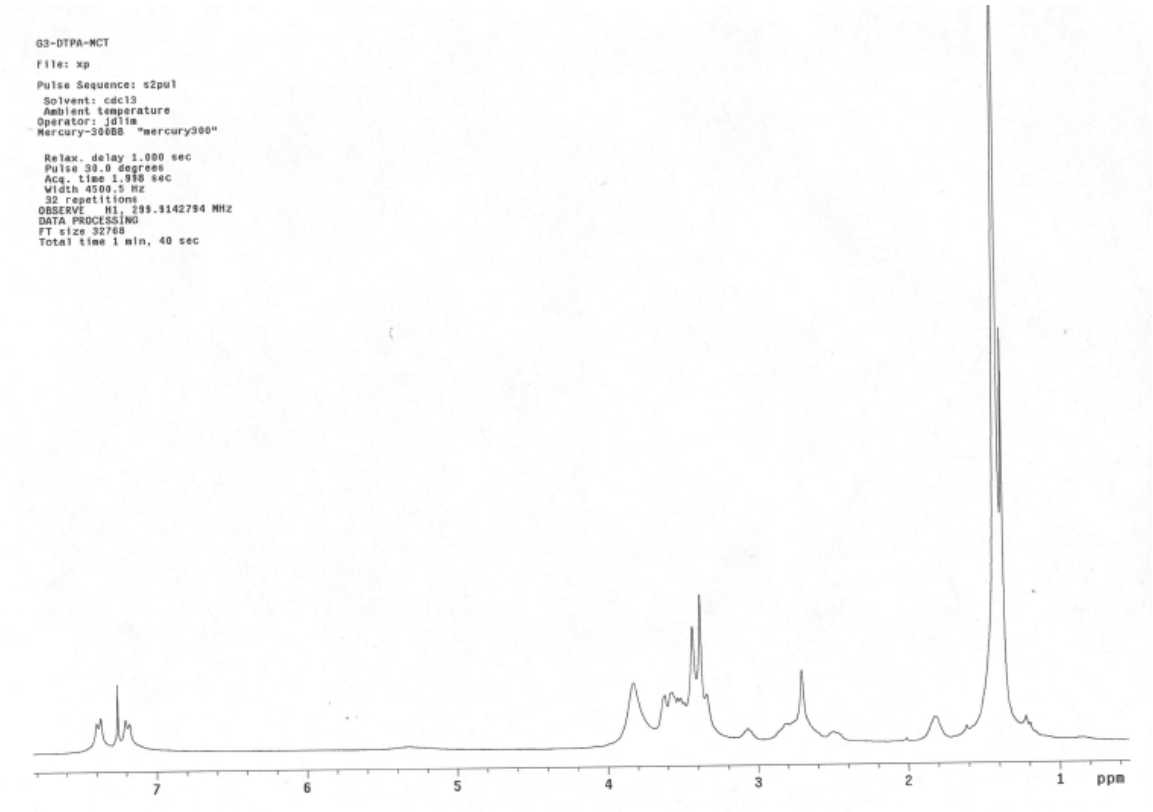

Figure S16. ^{1}H NMR spectrum of compound **9** (300 MHz, $CDCl_3$**).**

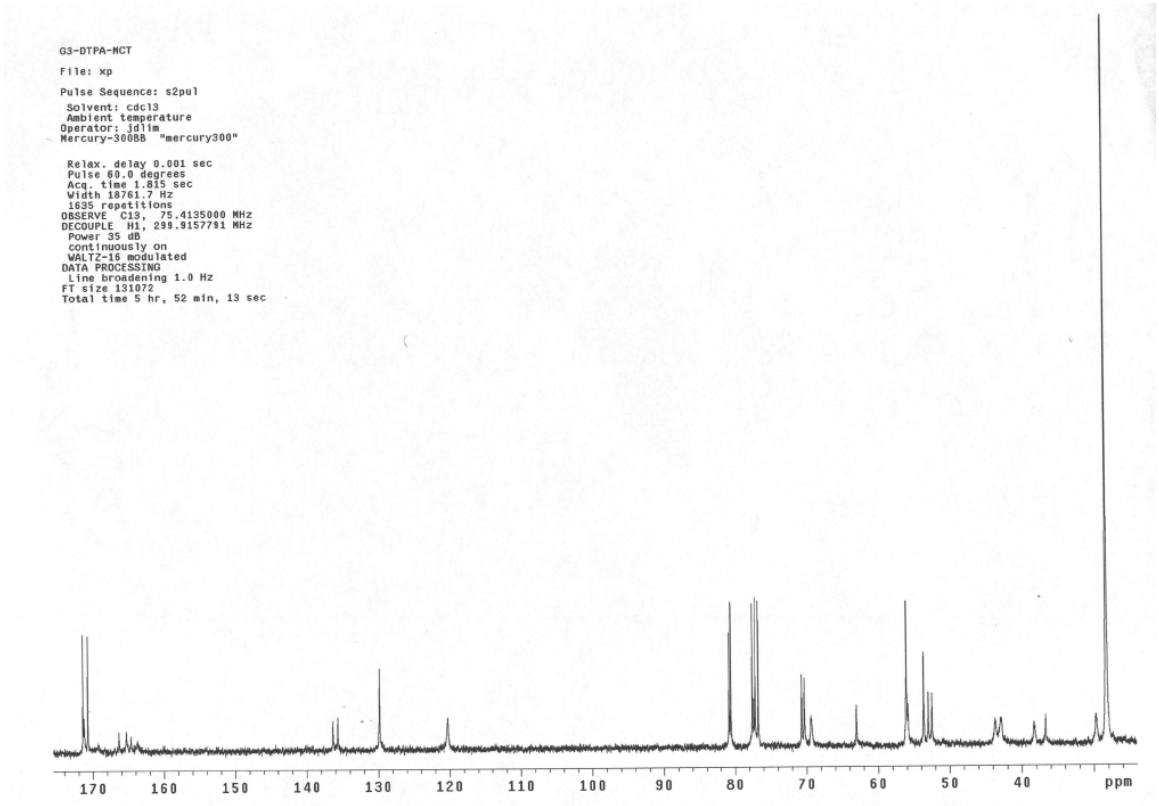

Figure S17. ^{13}C NMR spectrum of compound **9** (75 MHz, $CDCl_3$**).**

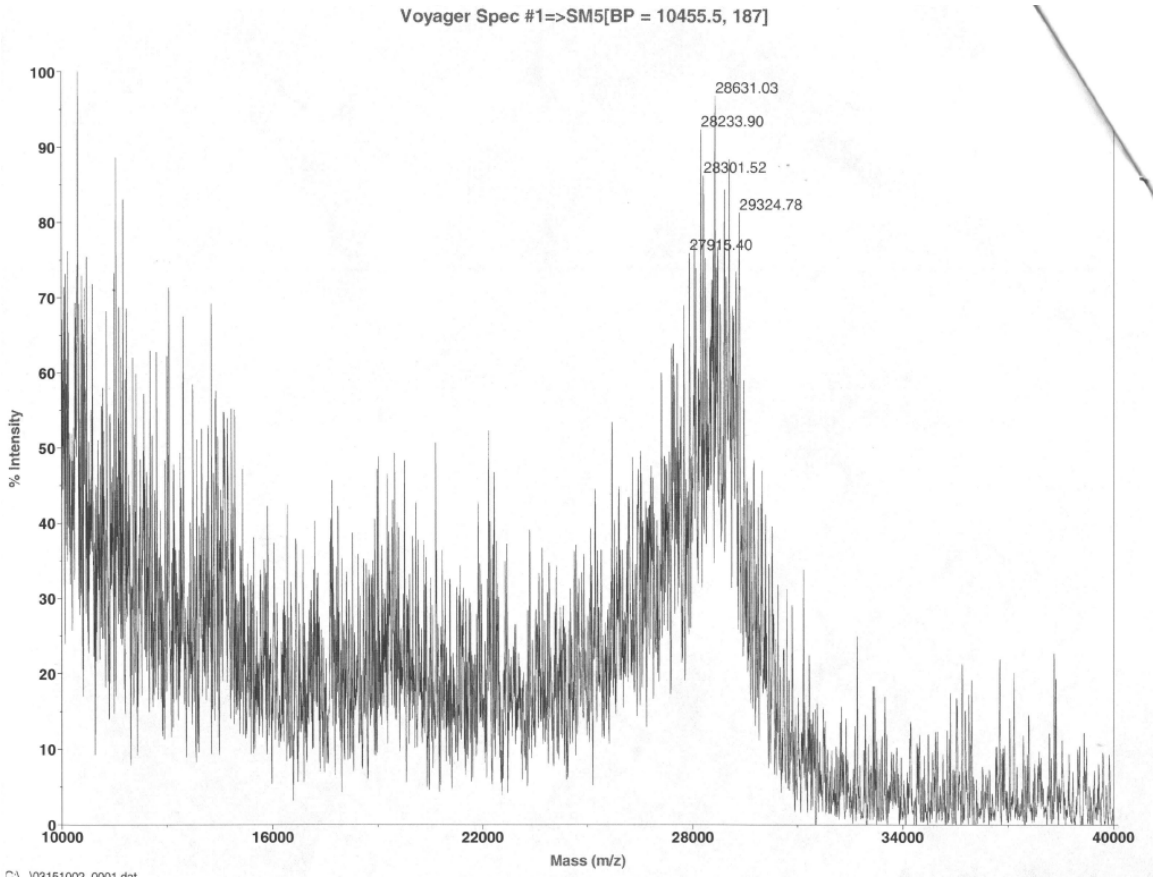

Figure S18. MALDI-TOF mass spectrum of compound **9.**

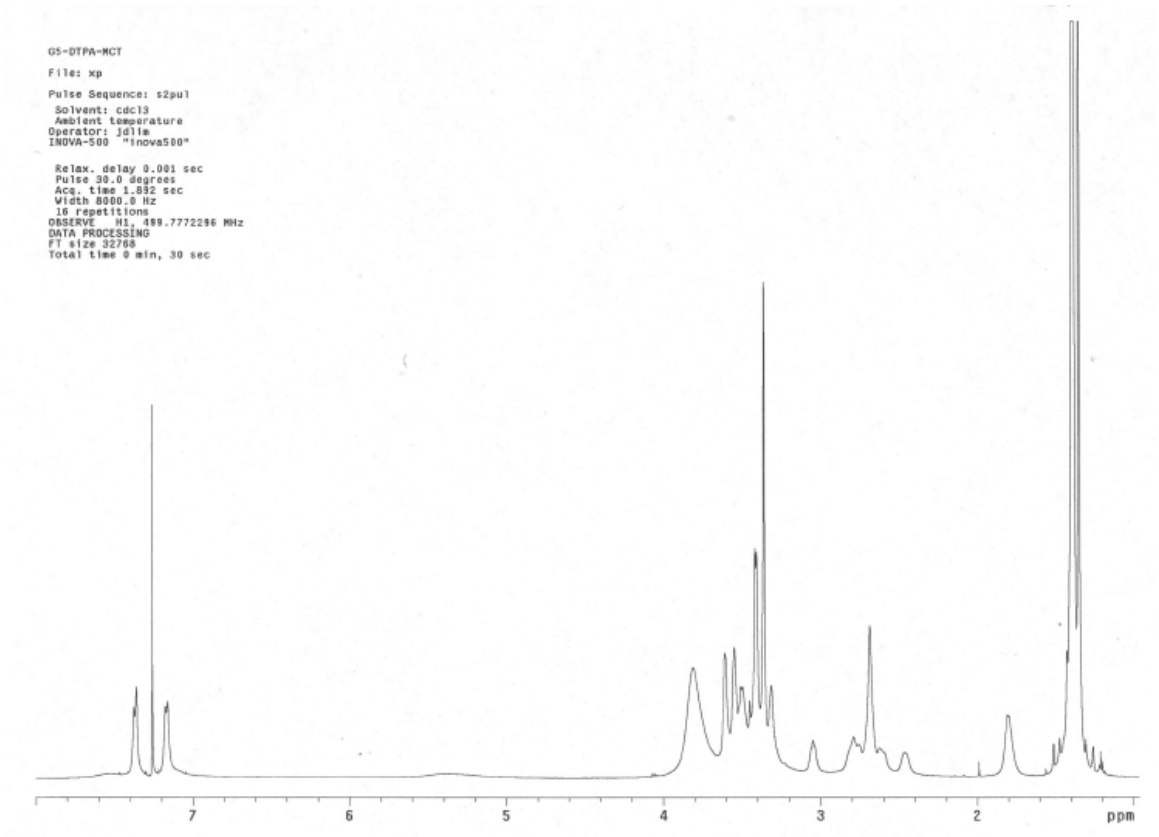

Figure S19. ^{1}H NMR spectrum of compound **10** (500 MHz, $CDCl_3$**).**

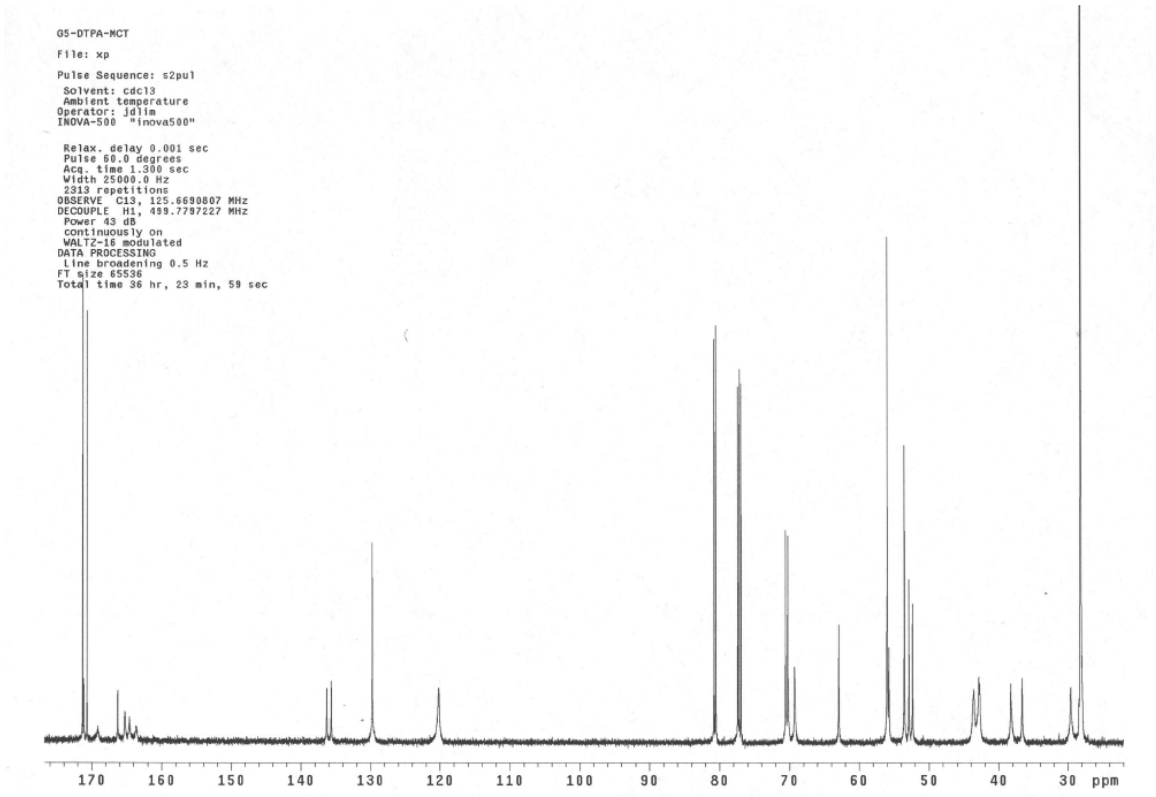

Figure S20. ^{13}C NMR spectrum of compound **10** (125 MHz, $CDCl_3$**).**

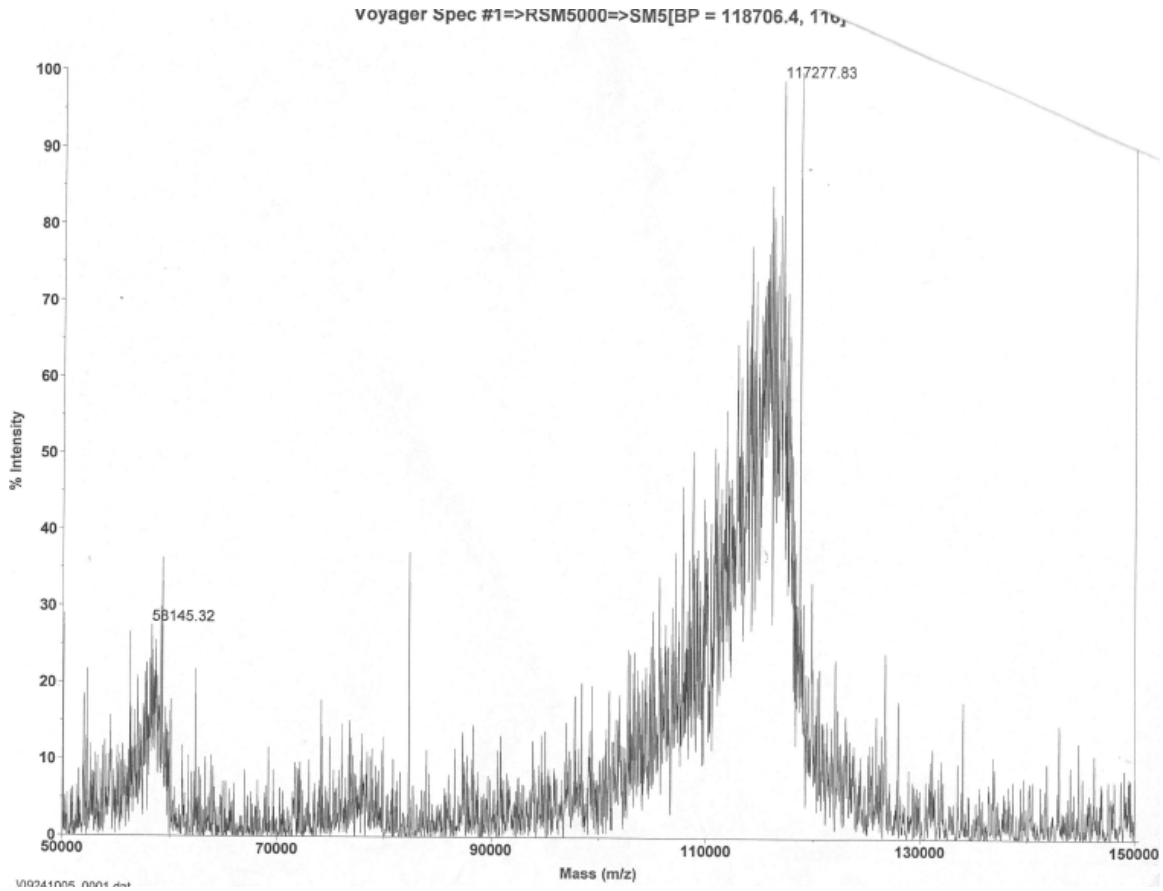

Figure S21. MALDI-TOF mass spectrum of compound **10**.

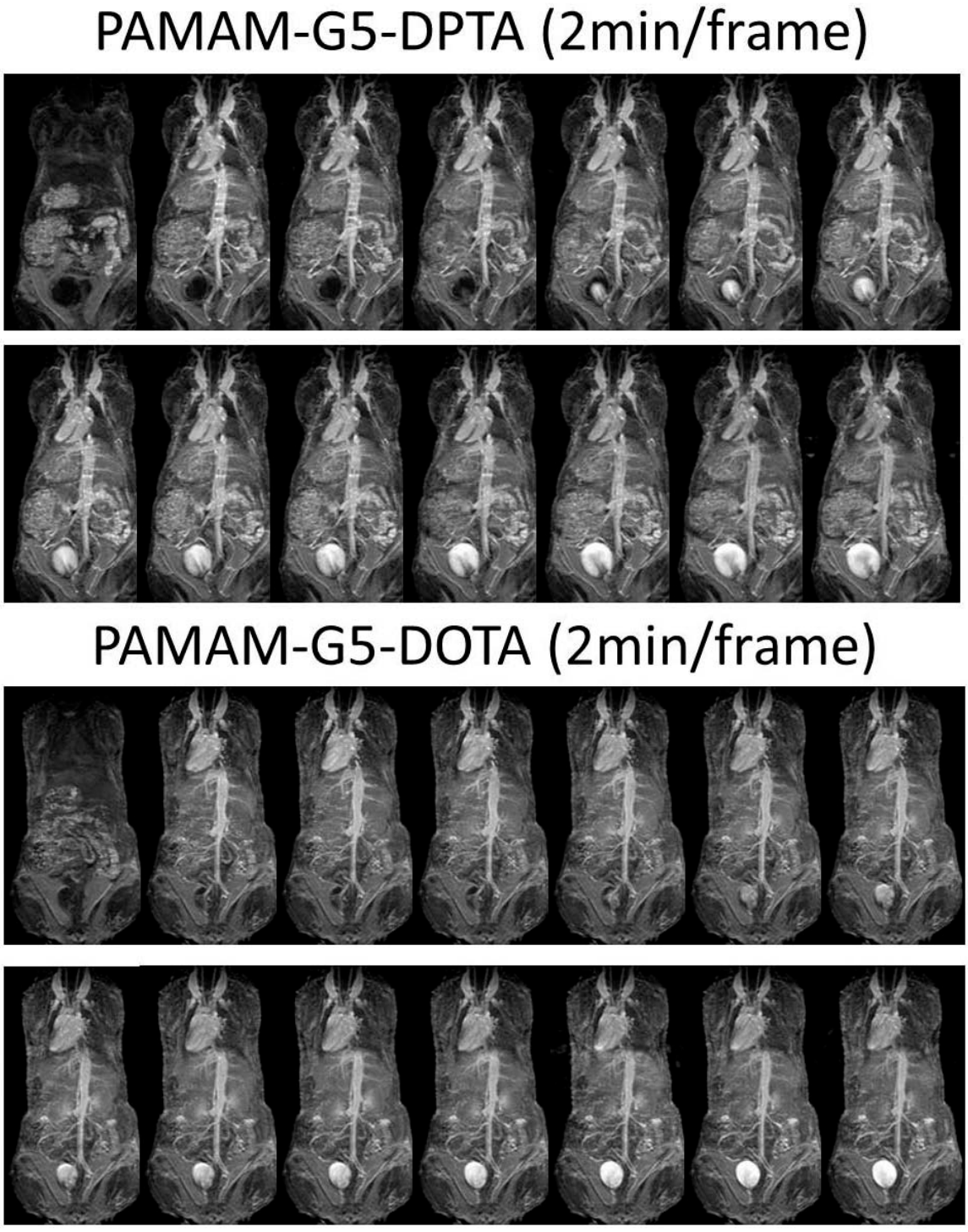

Figure S22. Dynamic MRI of mice using 0.03mmolGd/kg of PAMAM-G5-DPTA and PAMAM-G5-DOTA. No clear difference on relaxivity is shown between DPTA and DOTA conjugates.

Bioconjugate Chemistry

Article

pubs.acs.org/bc

Novel, Cysteine-Modified Chelation Strategy for the Incorporation of $[M^{I}(CO)_3]^+$ (M = Re, ^{99m}Tc) in an α-MSH Peptide

Han Jiang,[†,‡,#] Benjamin B. Kasten,[§,#] Hongguang Liu,[‡] Shibo Qi,[‡] Yang Liu,[†,‡] Mei Tian,[†] Charles L. Barnes,[∥] Hong Zhang,*[,†] Zhen Cheng,*[,‡] and Paul D. Benny*[,§]

[†]Department of Nuclear Medicine, Second Affiliated Hospital of Zhejiang University School of Medicine, Institute of Nuclear Medicine and Molecular Imaging of Zhejiang University, Center of Excellence in Medical Molecular Imaging of Zhejiang State, Hangzhou, 310009, China

[‡]Molecular Imaging Program at Stanford (MIPS), Department of Radiology, Bio-X Program and Canary Center at Stanford for Cancer Early Detection, Stanford University, Stanford, California 94305, United States

[§]Department of Chemistry, Washington State University, Pullman, Washington 99164, United States

[∥]Department of Chemistry, University of Missouri, Columbia, Missouri 65211-7600, United States

Supporting Information

ABSTRACT: Engineering peptide-based targeting agents with residues for site-specific and stable complexation of radionuclides is a highly desirable strategy for producing diagnostic and therapeutic agents for cancer and other diseases. In this report, a model N−S−N_{Py} ligand (**3**) and a cysteine-derived α-melanocyte stimulating hormone (α-MSH) peptide (**6**) were used as novel demonstrations of a widely applicable chelation strategy for incorporation of the $[M^{I}(CO)_3]^+$ (M = Re, ^{99m}Tc) core into peptide-based molecules for radiopharmaceutical applications. The structural details of the core ligand−metal complexes as model systems were demonstrated by full chemical characterization of *fac*-$[Re^{I}(CO)_3(N,S,N_{Py}\text{-}\mathbf{3})]^+$ (**4**) and comparative high-performance liquid chromatography (HPLC) analysis between **4** and $[^{99m}Tc^{I}(CO)_3(N,S,N_{Py}\text{-}\mathbf{3})]^+$ (**4a**). The α-MSH analogue bearing the N−S−N_{Py} chelate on a modified cysteine residue (**6**) was generated and complexed with $[M^{I}(CO)_3]^+$ to confirm the chelation strategy's utility when applied in a peptide-based targeting agent. Characterization of the $Re^{I}(CO)_3$-**6** peptide conjugate (**7**) confirmed the efficient incorporation of the metal center, and the $^{99m}Tc^{I}(CO)_3$-**6** analogue (**7a**) was explored as a potential single photon emission computed tomography (SPECT) compound for imaging the melanocortin 1 receptor (MC1R) in melanoma. Peptide **7a** showed excellent radiolabeling yields and in vitro stability during amino acid challenge and serum stability assays. In vitro B16F10 melanoma cell uptake of **7a** reached a modest value of 2.3 ± 0.08% of applied activity at 2 h at 37 °C, while this uptake was significantly reduced by coincubation with a nonlabeled α-MSH analogue, NAPamide (3.2 μM) ($P < 0.05$). In vivo SPECT/X-ray computed tomography (SPECT/CT) imaging and biodistribution of **7a** were evaluated in a B16F10 melanoma xenografted mouse model. SPECT/CT imaging clearly visualized the tumor at 1 h post injection (p.i.) with high tumor-to-background contrast. Blocking studies with coinjected NAPamide (10 mg per kg of mouse body weight) confirmed the in vivo specificity of **7a** for MC1R-positive tumors. Biodistribution results with **7a** yielded a moderate tumor uptake of 1.20 ± 0.09 percentage of the injected radioactive dose per gram of tissue (% ID/g) at 1 h p.i. Relatively high uptake of **7a** was also seen in the kidneys and liver at 1 h p.i. (6.55 ± 0.36% ID/g and 4.44 ± 0.17% ID/g, respectively), although reduced kidney uptake was seen at 4 h p.i. (3.20 ± 0.48% ID/g). These results demonstrate the utility of the novel $[M^{I}(CO)_3]^+$ chelation strategy when applied in a targeting peptide.

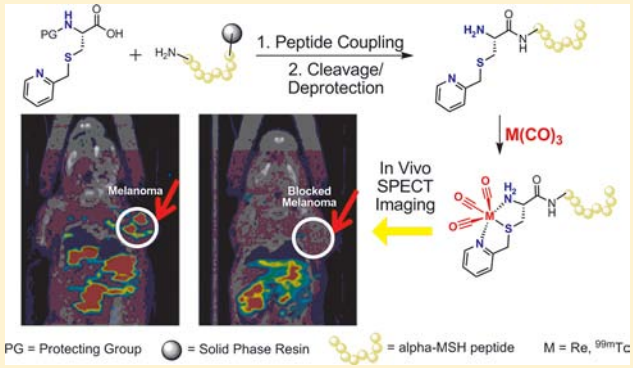

INTRODUCTION

A wide variety of radionuclides exist for generating diagnostic radiopharmaceutical agents. Among these, ^{99m}Tc is often the preferred radiometal for single photon emission computed tomography (SPECT) imaging applications due to its favorable low-energy γ-emission (140 keV), 6.02 h half-life, and wide availability from commercial ^{99}Mo-^{99m}Tc generators at low cost. The $[^{99m}Tc^{I}(CO)_3(OH_2)_3]^+$ core is a particularly attractive choice for radiolabeling biomolecules due to its low molecular volume, straightforward aqueous preparation from nontoxic reagents, and facile coordination to a variety of both hard and soft donor atoms.[1−3]

Received: September 11, 2012
Revised: October 29, 2012
Published: October 31, 2012

 © 2012 American Chemical Society

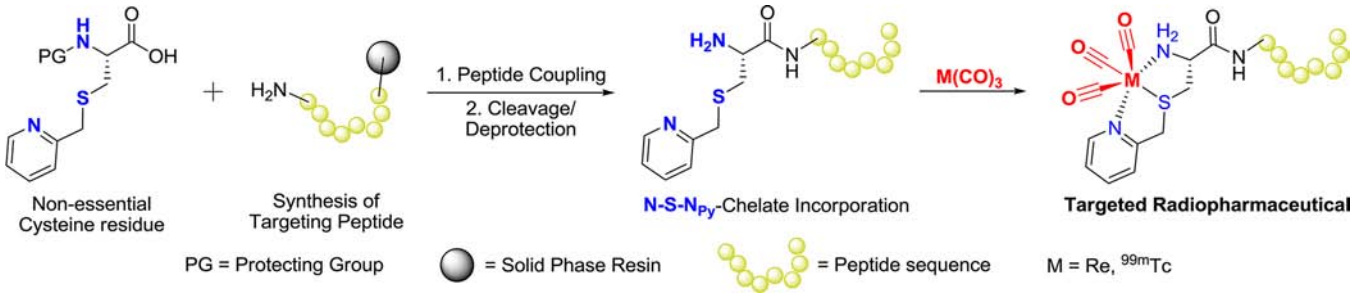

Figure 1. General strategy for introducing a cysteine-based N−S−N_{Py} chelate system for the $[M^{I}(CO)_3]^+$ core to generate peptide-based targeted radiopharmaceuticals.

For targeted molecular imaging applications, the radiometal must form kinetically and thermodynamically stable complexes with the targeting molecule at residues which are not essential for interacting with the biological target. A bifunctional chelator is often used for site-specific and stable complexation of the $[^{99m}Tc^{I}(CO)_3]^+$ center in peptide-based targeting agents. Traditionally, a separately optimized chelate system is covalently attached through an extension or linker to the *N*- or *C*-terminus or to an inner amino acid residue of the peptide.[4−6] Modified amino acids containing the desired chelate (e.g., single amino acid chelate)[7,8] or containing orthogonal chemical moieties (e.g., azides, alkynes) for chelate generation or attachment[9−11] can be introduced at specific locations within a peptide sequence during solid-phase production strategies. Such site-specific chelate incorporation is more difficult in larger, recombinantly produced proteins (e.g., antibodies, antibody fragments, affibodies) as multiple solvent-exposed residues with similar chemical reactivity are usually available on these molecules.

Another desirable method for $[^{99m}Tc^{I}(CO)_3]^+$ chelate formation is to engineer the targeting molecule with specific residues which can selectively coordinate the radiometal directly. Such a strategy offers the advantage of not requiring additional synthetic steps or modifications for chelate incorporation after the initial production and purification of the peptide sequence. Furthermore, it can be applied to ligands produced by either solid-phase or recombinant methods. This approach has been demonstrated in peptides bearing the hexahistidine-tag (H_6-tag)[12−23] or a variant sequence containing alternating histidine and glutamic acid residues [$(HE)_3$-tag].[24] Both sequences have been shown to successfully complex the $[^{99m}Tc^{I}(CO)_3]^+$ core during radiolabeling. Unfortunately, animal biodistribution studies with these radiolabeled peptides have yielded relatively high nonspecific uptake of the radiotracer in some normal organs, such as the liver and intestines, suggesting possible transchelation of the metal in vivo.[13,14,17,20,24] Furthermore, the exact coordination modes around the metal center in these chelation strategies remain undefined. Additional chelate engineering strategies with well-defined and stable coordination spheres and which are applicable to both recombinant and synthetic peptide production strategies would be of great value for generating clinically relevant, $^{99m}Tc^{I}(CO)_3$-based radiopharmaceutical agents.

In this report, we demonstrate a widely applicable method to introduce a site-specific chelate group for the $[M^{I}(CO)_3]^+$ core (M = Re, ^{99m}Tc) into peptide-based molecules for radiopharmaceutical applications in vitro and in vivo. Our strategy is to introduce a nonessential cysteine residue containing an *S*-alkylated 2-(methyl)pyridine moiety at the *N*-terminus of a targeting peptide (Figure 1). As discussed below, this chelate structure can be incorporated during solid-phase production of the peptide. Therefore, we envision that this method can be applied to a large number of targeting peptides, since these molecules are commonly produced by solid-phase techniques. Such a strategy is expected to minimally affect the nature of the free peptide compared to alternative chelating methods while generating an efficient N−S−N_{Py} chelate group for the $[M^{I}(CO)_3]^+$ core consisting of the derivatized cysteine's α-amine, thioether, and pyridal nitrogen.[3,25−27] We chose to incorporate our ligand design into a melanoma-targeting peptide as the first demonstration of our chelation strategy for complexing $[M^{I}(CO)_3]^+$ in peptide-based radiopharmaceutical agents.

Malignant melanoma is a serious public health problem due to its increasing incidence and high mortality rate.[28] The latter factor results mainly from limitations in the early detection and treatment of melanoma metastases.[29−31] Identification of melanoma cell signaling pathways and biomarkers in recent years has allowed the development of molecular imaging agents such as radiolabeled antibodies[32] and antibody fragments[33] for diagnosing melanoma metastases at earlier stages.[34] Unfortunately, many of these agents have met with limited success due to their antigenicity,[35] reduced rates of tumor penetration,[36] and slow circulation.[37] α-Melanocyte stimulating hormone (α-MSH) peptide analogues, which target the melanocortin 1 receptor (MC1R) on melanoma cells, are an emerging class of molecular agents with promise for imaging and treating metastatic melanoma.

Melanocortin receptors, including MC1R and its variants, fall within the membrane bound, G-protein-coupled receptor (GPCR) family. Of these receptors, MC1R is the most prominent member in regulating normal melanocyte function.[38] The overexpression of MC1R (~400 to 22 000 receptors/cell) observed in both murine and human melanoma compared to normal melanocytes presents this receptor as an attractive biomarker for primary and metastatic melanoma in both clinical settings and animal models.[30,39−42] Due to their favorable pharmacokinetics and high affinity for MC1R, low-molecular-weight α-MSH peptides are nearly ideal compounds for targeting melanoma and its metastases.[43]

Several general strategies have been employed to incorporate PET (e.g., ^{18}F,[44] ^{64}Cu[42]) and SPECT (e.g., ^{99m}Tc,[30] ^{111}In,[45] and ^{188}Re[46]) imaging radionuclides into α-MSH peptides for targeting MC1R in melanoma models. In one approach, ligands or bifunctional chelators for metal complexation are appended to the termini or side chains of α-MSH peptides with linear[42,44,47−53] or cyclic (via lactam rings[54−56] or disulfide

dx.doi.org/10.1021/bc300509k | *Bioconjugate Chem.* 2012, 23, 2300−2312

Scheme 1. Ligand 3 Synthesis and Coordination Reactions[a]C

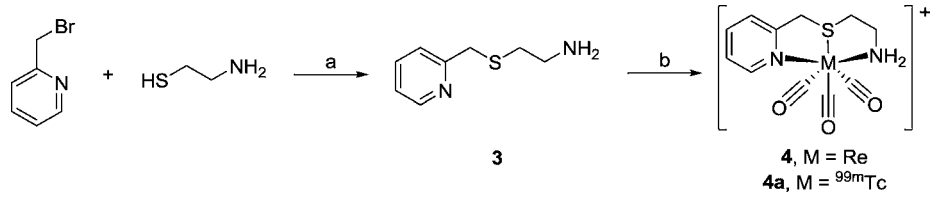

[a](a) aq. $NaHCO_3$; (b) aq. *fac*-$[M^I(CO)_3(OH_2)_3]^+$, 70−75 °C.

Chart 1. Structures and Abbreviated Designations of Cysteine-Based Molecules and Peptides

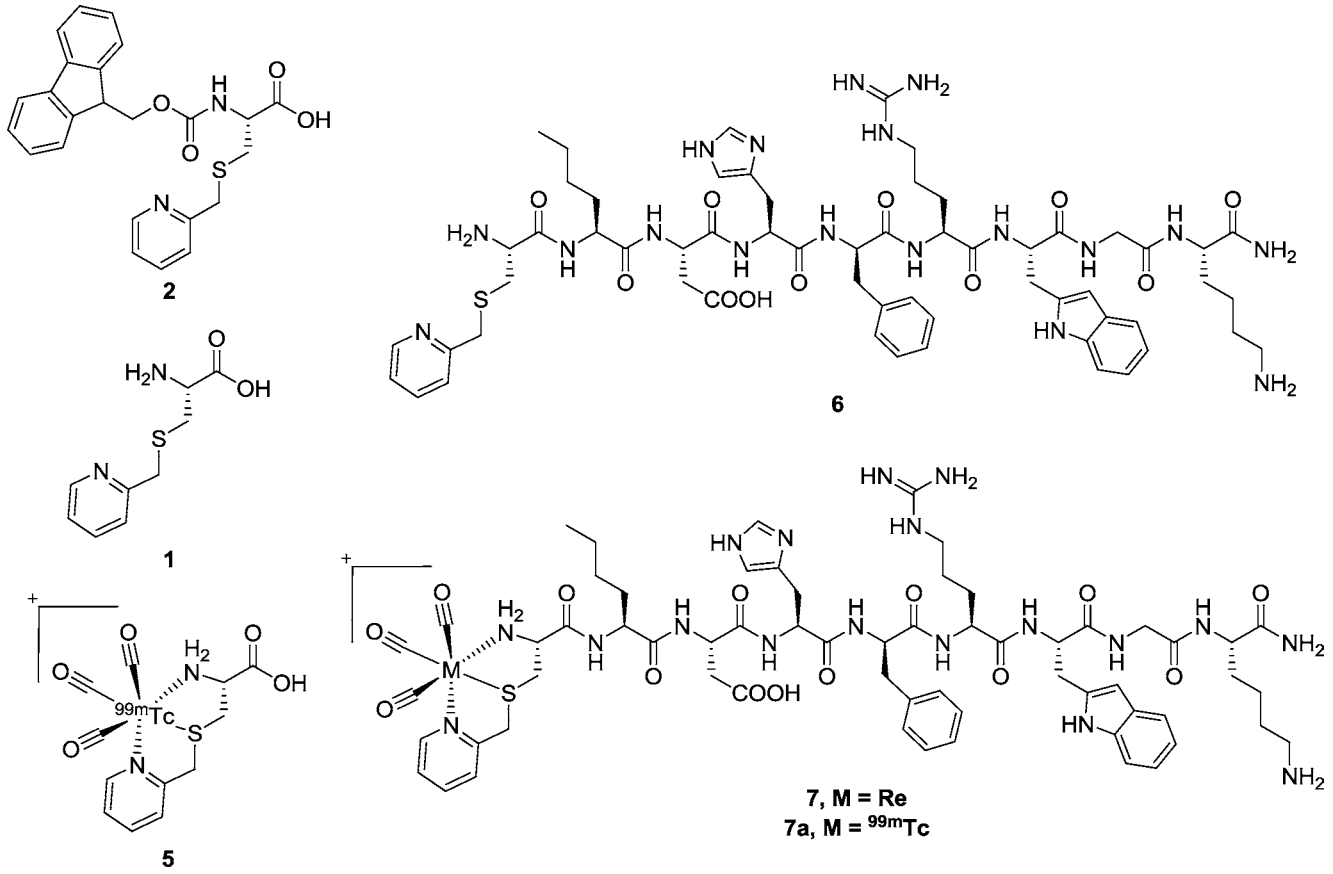

bridges[57,58]) conformations.[59,60] A second strategy takes advantage of coordination bonds between the metal and the peptide to convert a linear peptide into a metal cyclized version.[30,58,61,62] The majority of these α-MSH complexes contain the M^V oxo core, which generally improves the overall system's resistance to chemical and proteolytic degradation.[60,61,63] Many of the metal cyclized peptides contain nonradioactive rhenium for structural purposes only and are functionalized with ligands for incorporating alternative radionuclides similar to the other cyclic and linear α-MSH analogues.[58,62−65] The cyclized α-MSH peptides typically show higher in vivo potencies than linear analogues, although the in vitro MC1R affinities of both peptide conformations generally fall within the low to subnanomolar IC_{50} range.[59,60] Of the various radiolabeled α-MSH peptides, the metal-cyclized analogues usually demonstrate the most favorable in vivo stabilities and tumor uptake values with high kidney clearance.[58,60,62,64]

To address affinity and to minimize the additional mass and potential negative impacts of bifunctional chelate attachment, we report a novel strategy to incorporate the $[M^I(CO)_3]^+$ core into a peptide framework by modification of a terminal cysteine residue to generate a potent tridentate chelate. Initial studies presented here demonstrated the feasibility of the $N-S-N_{Py}$ ligand system with the $[M^I(CO)_3]^+$ core through structural, complexation efficiency and metal-chelate stability studies. A linear α-MSH analogue [Ac-Nle-Asp-His-D-Phe-Arg-Trp-Gly-Lys-NH_2 (NAPamide)] with excellent MC1R targeting ability and pharmacokinetic properties[42,44,49] was selected to implement this chelate strategy. The cysteine-modified NAPamide analogue bearing the $N-S-N_{Py}$ chelate system was successfully synthesized and complexed with the $[M^I(CO)_3]^+$ core. The ^{99m}Tc-radiolabeled peptide was evaluated both in vitro to determine its stability and uptake in B16F10 melanoma cells and in vivo to assess its biodistribution in B16F10 mouse xenograft models.

EXPERIMENTAL PROCEDURES

All reagents and solvents were of reagent grade or higher from commercial suppliers (Aldrich, Fluka, Acros, Fisher) and used

as received unless noted otherwise. *fac*-[$Re^{I}(CO)_3(OH_2)_3$]-(SO_3CF_3) and *S*-(pyridin-2-ylmethyl)-L-cysteine (ligand **1**) were prepared as previously described.[25,26] ^{99m}Tc-pertechnetate ([$^{99m}TcO_4$]$^-$) was purchased from Cardinal Health in Spokane, WA, or obtained from Stanford Nuclear Medicine Clinic. ^{125}I-(Tyr^2)-[Nle^4,D-Phe^7]-α-MSH [^{125}I-(Tyr^2)-NDP] was purchased from Perkin-Elmer (Waltham, MA). Elemental analysis was performed by Quantitative Technologies, Inc. (NJ). Nuclear magnetic resonance (NMR) spectra were recorded at 293 K on a Varian Mercury Vx 300 spectrometer using 5 mm NMR tubes. ^{1}H and ^{13}C NMR spectra peak positions were referenced using residual solvent signals or trimethylsilane as an internal standard. Spectra were processed using Varian *VNWR 6.1* software. Mass spectra were obtained on a Thermo-Finnigan LCQ Advantage instrument for electrospray ionization mass spectrometry (ESI-MS) or a Perseptive Voyager-DE RP Biospectrometry instrument (Framingham, MA) for matrix assisted laser desorption/ionization time-of-flight mass spectrometry (MALDI-TOF-MS). Infrared (IR) spectra were recorded on a Thermo Nicolett 6700 FTIR with an ATR cell and analyzed with *OMNIC 7.1a* software. UV/vis spectra were recorded on a Varian Cary 50 Bio spectrophotometer and analyzed with Cary *WinUV 3.00* software. Solutions of the compounds were prepared in UV/vis quality methanol and measured in quartz cuvettes. Analytical separation and identification of small molecules (**1**, **2**, **3**, **4**, **4a**, **5**; Scheme 1 and Chart 1) and the $Re^{I}(CO)_3$-conjugated peptide (**7**; Chart 1) by reversed-phase high-performance liquid chromatography (RP-HPLC) were conducted using a Varian Pursuit XRs column (C18, 5 μm, 4.6 × 250 mm) with a Phenomenex security guard cartridge (C18, 4.0 × 3.0 mm). A Perkin-Elmer Series 200 analytical chromatography system and a Hitachi D-7000 series analytical chromatography system (L-7100 pump, L-7400 UV detector) were used for the above compounds. Unless noted otherwise, elutions performed on these systems used a gradient profile as previously described (Gradient 1)[26] with 0.1% TFA in water (solvent A) and MeOH (solvent B). Chromatograms were plotted using *OriginPro 8.5.1* (OriginLab Corporation, MA). Preparatory HPLC separations and purifications used an Agilent Zorbax column (SB-C18, 7 μm, 21.2 × 250 mm) on a Hitachi D-7000 series semipreparative chromatography system (L-7150 pump, L-7400 UV detector). Chromatographic purification and analysis of the nonlabeled peptide (**6**; Chart 1) was performed on a Dionex Ultimate 300 HPLC system (Dionex Corp.) using both semipreparative (Vydac; 218TP510-C18, 5 μm, 10 × 250 mm) and analytic (Vydac; 214TP54-C18, 5 μm, 4.6 × 250 mm) peptide RP-HPLC columns. The mobile phase gradients used 0.1% TFA in water and 0.1% TFA in acetonitrile (MeCN). Radio-HPLC purification and analysis with the radiolabeled peptide (**7a**; Chart 1) was conducted with the semipreparative RP-HPLC Vydac peptide column on a Dionex 680 chromatography system with a UVD 170U absorbance detector and model 105S single-channel radiation detector (Carroll & Ramsey Associates, Berkley, CA). The recorded data were processed with use of *Chromeleon v 6.50* software (Sunnyvale, CA). Phosphate buffered saline (PBS, 0.01 M, pH 7.4) was obtained from Gibco/Invitrogen (Carlsbad, CA). The B16F10 murine melanoma cell line was obtained from American Type Culture Collection (Manassas, VA). Female C57BL/6 mice were purchased from Charles River Laboratory (Wilmington, MA).

Small Molecule Synthesis and Radiolabeling. *S-(Pyridin-2-ylmethyl)-Fmoc-L-cysteine, **2**.* This compound was prepared using procedures shown previously for *N*-terminal Fmoc-protection of amino acids.[66] A solution of Fmoc-Cl (0.3 g, 0.974 mmol) in 7 mL of dioxane was added dropwise over 2 h to an ice-cooled, stirred solution of **1** (0.464 g, 1.16 mmol) in 15 mL of 10% Na_2CO_3. The solution was then warmed to room temperature and stirred for an additional 2 h. Water (130 mL) was added to quench the reaction, and the solution was extracted with diethyl ether (3 × 15 mL). The aqueous layer was cooled in an ice-bath and the pH was adjusted to 4−5 with 6 M HCl. The resulting white precipitate was collected by extraction with ethyl acetate (5 × 50 mL). The combined organic layers were concentrated to ∼70 mL by rotary evaporation and washed with water (3 × 25 mL), then brine (1 × 15 mL), and dried with Na_2SO_4. The solvent was removed by rotary evaporation, and residual solvent was removed by several rounds of adding diethyl ether followed by rotary evaporation. The resulting solid was dried under vacuum to yield 0.37 g of **2** (82%). Anal. Calcd for $C_{24}H_{24}N_2O_5S$: C, 63.70; H, 5.35; N, 6.19. Found: C, 63.70; H, 5.14; N, 6.08. ^{1}H NMR [δ(ppm), $CDCl_3$]: 8.61 (d, $C_{Py}H$, 1 H), 7.82 (dd, $C_{Py}H$, 1 H), 7.71 (m, $C_{Ar}H$, 2 H), 7.60 (dd, $C_{Ar}H$, 2 H), 7.43 (d, $C_{Py}H$, 1 H), 7.38−7.23 (m, $C_{Ar}H$, 5 H), 6.37 (d, N*H*, 1 H), 4.62 (m, N−C*H*, 1 H), 4.38 (m, O−CH_2, 2 H), 4.20 (t, C*H*, 1 H), 4.08 (d, J = 13.8 Hz, Py-CH_{2a}-S, 1 H), 3.91 (d, J = 14.1 Hz, Py-CH_{2b}-S, 1 H), 3.09 (dd, S−CH_2, 2H). ^{13}C NMR [δ(ppm), $CDCl_3$]: 173.4 (*C*OO), 157.3 (*C*O), 156.1 (C_{Ar}), 147.0 (C_{Ar}H), 144.0 (C_{Ar}H), 141.3 (C_{Ar}H), 139.3 (C_{Ar}H), 127.7 (2 C_{Ar}H), 127.2 (2 C_{Ar}H), 125.3 (2 C_{Ar}H), 124.7 (C_{Ar}H), 123.1 (C_{Ar}H), 120.0 (2 C_{Ar}H), 67.0 (CH_2, Fmoc), 54.7 (*C*H), 47.3 (*C*H, Fmoc), 37.0 (CH_2), 35.0 (CH_2). MS (-ESI): 433.0; calcd for [M-H]$^-$: 433.1.

*2-((Pyridin-2-ylmethyl)thio)ethanamine, **3**.* Ligand **3** has previously been synthesized and characterized.[67,68] However, an alternative synthetic strategy using aqueous conditions which are amenable for selective *S*-alkylation of peptide-based molecules was used for the current report. Cysteamine hydrochloride (0.085 g, 0.75 mmol) and 2-(bromomethyl)-pyridine hydrobromide (0.189 g, 0.75 mmol) were dissolved in 5 mL of water. The solution was brought to pH 7−8 with 1 M $NaHCO_3$ and stirred at room temperature overnight. The reaction mixture was concentrated by rotary evaporation, acidified with 0.1% aqueous TFA, and purified by preparatory HPLC using the following gradient system (Gradient 2) with a flow rate of 10 mL/min: 0−5 min 100% A; step to 90% A/10% B and hold from 5 to 15 min; 15−21.5 min linear gradient to 75% A/25% B; 21.5−25 min linear gradient to 100% B; 25−28 min 100% B; linear gradient to 100% A by 30 min. Fractions with the product were pooled, solvent was removed by rotary evaporation, and the residue was dried under vacuum to yield 0.161 g of **3** (54%). ^{1}H NMR [δ(ppm), CD_3CN]: 8.65 (d, 1 H), 8.19 (dd, 1 H), 7.74 (d, 1 H), 7.65 (dd, 1 H), 6.89 (broad s, 3 H), 4.08 (s, 2 H), 3.22 (t, 2 H), 2.91 (t, 2 H). ^{13}C NMR [δ(ppm), CD_3CN]: 156.0, 145.2, 144.5, 127.4, 125.8, 39.5, 33.5, 29.4. MS (+ESI): 169.0; calcd for [M+H]$^+$: 169.1. The spectral data were consistent with those reported previously for **3**.[67,68]

*fac-[$Re^{I}(CO)_3$(N,S,N_{Py}-**3**)]($C_2F_3O_2$), **4**.* Ligand **3** (0.030 g, 0.076 mmol) was dissolved in 1.3 mL of water, 0.1 M *fac*-[$Re^{I}(CO)_3(OH_2)_3$](SO_3CF_3) (0.677 mL, 0.068 mmol) was added, and the solution's pH was brought to 3−4 with 0.1 M HCl. The solution was stirred and heated with a condenser at 75 °C for 26 h, while the pH was kept at 3−5 with the addition of 0.1 M HCl or 0.1 M $NaHCO_3$ as needed. The solution was

purified by preparatory HPLC using the following gradient system (Gradient 3) with a flow rate of 12 mL/min: 0−3 min 100% A; step to 75% A/25% B and hold from 3 to 9 min; 9−25 min linear gradient to 100% B; 25−32 min 100% B; linear gradient to 100% A by 33 min. Fractions with the product were pooled, solvent was removed by rotary evaporation, and the residue was dried under vacuum to yield 0.024 g of **4** (64%). X-ray quality crystals were obtained by slow diffusion of benzene into an MeCN solution of **4**. X-ray crystallography experimental procedures, crystal data, and structure refinement parameters can be found in the Supporting Information. Anal. Calcd for $C_{13}H_{12}F_3N_2O_5ReS$: C, 28.31; H, 2.19; N, 5.08. Found: C, 29.16; H, 2.44; N, 5.15. ^{1}H NMR [δ(ppm), CD_3CN]: 8.98 (d, $C_{Py}H$, 1 H), 8.05 (dd, $C_{Py}H$, 1 H), 7.73 (d, $C_{Py}H$, 1 H), 7.47 (dd, $C_{Py}H$, 1 H), 4.83 (d, J = 17.7 Hz, Py-CH_{2a}-S, 1 H), 4.58 (broad s, NH, 1 H), 4.48 (d, J = 17.7 Hz, Py-CH_{2b}-S, 1 H), 4.02 (broad s, NH, 1 H), 2.96 (m, CH, 1 H), 2.85 (m, CH, 1 H), 2.65 (m, CH, 1 H), 2.25 (m, CH, 1 H). ^{13}C NMR [δ(ppm), CD_3CN]: 184.9 (COO, TFA), 161.0 (C_{Py}), 156.0 (C_{Py}H), 142.7 (CF_3, TFA), 141.1 (C_{Py}H), 126.3 (C_{Py}H), 125.3 (C_{Py}H), 45.4 (CH_2), 44.2 (CH_2), 36.5 (CH_2). MS (+ESI): 439.2; calcd for $[M]^+$: 439.0. IR (solid, cm^{-1}): 2030, 1921, 1668, 1199, 1125. UV/vis ε_{max} (251 nm): 9400 M^{-1} cm^{-1}.

*[^{99m}Tc^{I}(CO)$_3$(N,S,N$_{Py}$-**3**)]$^+$, **4a**.* The $[^{99m}Tc^{I}(CO)_3(OH_2)_3]^+$ solution was prepared from an Isolink kit (Tyco, Inc.) by injecting $^{99m}TcO_4^-$ solution into the vial and heating at 95 °C for 25 min, cooling the vial on ice for 15 min after acidifying to pH 3−4 with 1 M HCl, and neutralizing to pH 7 with 1 M NaOH. Solutions of **3** in water (1×10^{-3} to 1×10^{-5} M) were added to the appropriate buffer (10 mM sodium phosphate pH 6.0 or pH 7.4; 10 mM sodium acetate pH 4.5) in a sealable labeling vial. The vial was sealed and degassed with nitrogen for 7−10 min and $[^{99m}Tc^{I}(CO)_3(OH_2)_3]^+$ solution was added to bring the final ligand concentration to values of 1×10^{-4} to 1×10^{-6} M (SI Table S1) in final volumes of 200−300 μL. The vials were heated at 70 °C for 30 min, cooled on ice, and analyzed or purified by radio-HPLC on the Perkin-Elmer Series 200 chromatography system described above equipped with a Perkin-Elmer Radiomatic 610TR detector.

Amino Acid Challenge Assays with ^{99m}Tc^{I}(CO)$_3$-Ligand Complexes. Complex **5** (Chart 1), described previously as $[^{99m}Tc^{I}(N,S,N_{Py}\text{-}\mathbf{1})(CO)_3]^+$,[26] was produced by reacting **1** at 1×10^{-4} M (final concentration) with $[^{99m}Tc^{I}(CO)_3(OH_2)_3]^+$ at pH 7.4 using analogous conditions as for generating **4a** above. Solutions of HPLC-purified **4a** or **5** (100 μL) were mixed with solutions containing L-cysteine or L-histidine at 2 mM in 10 mM sodium phosphate buffer pH 7.4 (200 μL) and incubated at 37 °C. Aliquots were periodically monitored by radio-HPLC up to 4 h to determine complex resistance to transchelation in the presence of the competing amino acids.

NAPamide Analogue Synthesis, Complexation Reactions, and Biological Evaluations. *(S-(Pyridin-2-ylmethyl)-Cys)-Nle-Asp-His-D-Phe-Arg-Trp-Gly-Lys-NH$_2$, **6**.* The NAPamide derivative was synthesized on an automated peptide synthesizer (CS Bio, CS 336X). Briefly, Rink Amide LS resin (200 mg, 40 μmol, Advanced ChemTech, 0.2 mmol/g loading) was swollen in *N*,*N*-dimethylformamide (DMF) for 30 min. With the exception of **2** (synthesized above), Fmoc-protected amino acids were purchased from Novabiochem/EMD Chemicals Inc. Fmoc groups were removed with 20% piperidine in DMF. The aliquots of amino acids (0.20 mmol) were activated in a solution containing 0.20 mmol of *N*-hydroxybenzotriazole hydrate and 0.5 M diisopropylcarbodiimide in DMF. Peptide deprotection and cleavage were carried out by 3 h incubation in a mixture of TFA/thioanisole/ethanedithiol/water (92.5:2.5:2.5:2.5). The mixture was filtered, and the peptide in solution was precipitated with anhydrous diethyl ether. The resulting peptide was washed four times with ice-cold anhydrous diethyl ether, dried, and dissolved in water. The peptide was purified by RP-HPLC on a C-4 column. Fractions were collected and lyophilized to yield the target product, **6**, in 55% yield. The purified peptide was analyzed by RP-HPLC (C-18) using the following gradient system (Gradient 4) with solvent A and 0.1% TFA in MeCN (solvent C): 0−3 min 95% A/5% C, 3−33 min linear gradient to 35% A/65% C, 33−36 min linear gradient to 5% A/95% C, 36−39 hold at 5% A/95% C, 39−42 min linear gradient to 95% A/5% C, equilibrate in 95% A/5% C. MS (MALDI-TOF): 1251.4; calcd for $[M+H]^+$: 1251.6.

*fac-[Re^{I}(CO)$_3$(N,S,N$_{Py}$-**6**)]$^+$, **7**.* To a solution of **6** (750 μg) in 185 μL of PBS (adjusted to pH 6.0 with 1 M HCl) was added 1 mol equiv of 0.1 M *fac*-$[Re^{I}(CO)_3(OH_2)_3](SO_3CF_3)$ (5.7 μL). The mixture was initially mixed by vortex (10 s) and was then heated at 60 °C for 6 h with periodic mixing by vortex. The solution was purified by analytical RP-HPLC using the following gradient system (Gradient 5) with a flow rate of 1 mL/min: 0−3 min 100% A; step to 75% A/25% B and hold 3−12 min; 12−28.5 min linear gradient to 100% B; 28.5−33.5 min 100% B; step to 100% A at 33.6 min, and equilibrate in 100% A. The fraction with the desired product was bubbled with nitrogen to evaporate MeOH. The solution was frozen and lyophilized to yield 600 μg of **7** (74%). MS (+ESI): 761.6, 1521.2/1519.4; calcd for $[M+2H]^{2+}$: 761.8, calcd for $[M]^+$: 1521.6/1519.6.

*[^{99m}Tc^{I}(CO)$_3$(N,S,N$_{Py}$-**6**)]$^+$, **7a**.* A solution of **6** (50 μg) in water was added to PBS (adjusted to pH 6.0 with 1 M HCl) in a sealable labeling vial. $[^{99m}Tc^{I}(CO)_3(OH_2)_3]^+$ solution (3.4 mCi) was added to bring the final volume to 200−300 μL. The vial was heated at 70 °C for 30 min, cooled in an ice bath, and analyzed by radio-HPLC on the Dionex 680 chromatography system described above. Purification used the following gradient system (Gradient 6): 0−2 min 72% A/28% C, 2−32 min linear gradient to 67% A/33% C, 32−35 min linear gradient to 15% A/85% C, 35−38 min linear gradient to 72% A/28% C, 38−42 min hold at 72% A/28% C. Subsequent analysis of **7a** used the following gradient system (Gradient 7): 0−3 min 95% A/5% C, 3−33 min linear gradient to 5% A/95% C, 33−36 hold at 5% A/95% C, 36−39 min linear gradient to 95% A/5% C, 39−42 min hold at 95% A/5% C.

In Vitro Stability Analysis. *Serum Stability Assay.* **7a** (100 μCi) in 50 μL of PBS was added to 500 μL of mouse serum (Sigma). After incubation at 37 °C for 4 h, the solution was filtered through a NanoSep device (10 K; Pall Corp.). The filtrate was then injected into the radio-HPLC column under conditions identical to those used for analyzing the purified radiolabeled peptide (Gradient 7). The fractions eluted from HPLC were collected into plastic tubes every 30 s. The radioactivity of each tube was measured by a γ-counter (Perkin-Elmer model 1470), and the radio-HPLC chromatogram was plotted using *Origin* v 6.0 (MicroCal).

Amino Acid Challenge Assays. ^{99m}Tc radiolabeled NAPamide analogue was subject to transchelation in the presence of histidine and cysteine (1 mM) as an assay of label stability. Solutions of HPLC-purified **7a** (400 μL) were added to solutions containing L-cysteine or L-histidine at 1 mM in 10

mM sodium phosphate buffer pH 7.4 (600 μL). The solutions were stirred and incubated at 37 °C for 4 h. Aliquots were periodically monitored by radio-HPLC (Gradient 7) to determine complex stability.

Cell Culture and Animal Model. B16F10 murine melanoma cells were cultured in Dulbecco's modified Eagle's high-glucose medium (GIBCO, Carlsbad, CA) and supplemented with 10% fetal bovine serum (FBS) and 1% penicillin−streptomycin in a humidified incubator containing 5% CO_2 at 37 °C. A 70−80% confluent monolayer was detached with 0.25% trypsin−ethylenediaminetetraacetic acid (EDTA) and dissociated into a single-cell suspension for further cell culture and assays. All animal studies were carried out in compliance with federal and local institutional rules for the conduct of animal experimentation. Approximately 1×10^6 cultured B16F10 cells were suspended in 100 μL of PBS and subcutaneously implanted in the right shoulders of C57BL/6 mice. Tumors were grown to a size of 0.5−1 cm in diameter (1−2 weeks) prior to imaging and biodistribution studies.

In Vitro B16F10 Cell Assays. *IC_{50} Cell Binding Assay.* The receptor binding affinity of **7** for MC1R in B16F10 cells was performed as previously described.[69] Briefly, 5×10^5 cells were resuspended in Dulbecco's Modified Eagle's Medium containing 25 mM *N*-(2-hydroxyethyl)piperazine-*N*′-(2-ethanesulfonic acid), 0.2% bovine serum albumin, and 0.3 mM 1,10-phenanthroline. The cells were then incubated at 37 °C for 90 min with **7** (peptide concentration varying from 10^{-11}−10^{-5} M) and approximately 20 000 counts per min (cpm) of ^{125}I-(Tyr^2)-NDP. Cells were washed three times with PBS and the radioactivity of the cells was measured. The experiment was performed in triplicate. Data were analyzed using Graphpad *Prism 5.0* (Northampton, MA), and the IC_{50} value (the concentration of competitor required to inhibit 50% of the radioligand binding) of the peptide was calculated.

Cell Uptake Assay. Cell uptake studies of **7a** B16F10 cells were performed as previously described.[42] Briefly, 3×10^5 cells were seeded in 12-well tissue culture plates and allowed to attach overnight. After a wash with PBS, the cells were incubated with **7a** (1 μCi per well, in culture medium) with or without NAPamide (3.2 μM/well) at 37 or 4 °C for 0.5, 1, and 2 h. The cells were then washed 3 times with PBS and lysed in 1 mL of 1.0 M NaOH and 0.1% sodium dodecyl sulfate. Radioactivity was measured by a γ-counter (Perkin-Elmer model 1470). Cell uptake was expressed as the percentage of added radioactivity. Experiments were performed twice with triplicate wells.

Small-Animal SPECT/CT Imaging. Small animal SPECT/X-ray computed tomography (SPECT/CT) imaging was performed on a combined SPECT/CT scanner for small animals (X-SPECT; Gamma Medica). Mice bearing B16F10 xenografts were injected via the tail vein with approximately 200 μCi of **7a** with or without 10 mg of NAPamide per kg of mouse body weight. At 1 h post injection (p.i.), mice were anesthetized with 2% isoflurane and placed in the prone position near the center of the field of view (FOV) of the scanner. For micro-CT image acquisition, 512 images (170 μm slice thickness) were acquired in 5 min at 0.4 mA and 80 kVp. SPECT was performed using a 1 mm multipinhole collimator (single head, 360° rotation, 64 projections, 30 s/projection, and a 5 cm FOV). CT images were reconstructed by using a cone-beam filtered backprojection algorithm into a $512 \times 512 \times 512$ matrix with a voxel size of 170 μm. The SPECT images were reconstructed using a two-dimensional ordered-subsets expectation maximization (OSEM) algorithm with 8 subsets and 10 iterations into a $64 \times 64 \times 60$ matrix size with a voxel size of 1.5 mm. All data were imported into Amira (Mercury Computing Systems, Chelmsford) for processing and visualization.

Biodistribution Studies. For biodistribution studies, nude mice bearing B16F10 xenografts (n = 4 per group) were injected via the tail vein with approximately 200 μCi of **7a** and were euthanized at 1 and 4 h p.i. Tumor and normal tissues of interest were removed and weighed, and their radioactivity was measured in a γ-counter. Radioactivity uptake was expressed as a percentage of the injected radioactive dose per gram of tissue (% ID/g).

Statistical Methods. Statistical analysis was performed using the Student's t test for unpaired data. A 95% confidence level was chosen to determine the significance between groups, with $P < 0.05$ being designated as significantly different.

RESULTS AND DISCUSSION

Model Ligand Synthesis, Rhenium Complexation, and Characterization. Although several N−S−N_{Py} chelate structures incorporating the $[M^I(CO)_3]^+$ core have been shown in the literature,[26,70,71] full structural characterization of the underivatized 2-*S*-(pyridin-2-ylmethyl)ethanamine-$M^I(CO)_3$ complexes is shown here for the first time. The synthetic route for producing these compounds is outlined in Scheme 1. Ligand **3** was generated by mild alkylation of 2-(bromomethyl)-pyridine with cysteamine at room temperature in a pH 7−8 bicarbonate solution. Following preparatory HPLC purification of the reaction, ligand **3** was isolated in a moderate yield (54%) with spectral properties corresponding to those reported previously for this known compound.[67] An aqueous solution of **3** was subsequently heated with *fac*-$[Re^I(CO)_3(OH_2)_3]$-(SO_3CF_3) at 75 °C while keeping the pH moderately acidic (pH 3−5). The reaction was monitored by analytical HPLC and after 26 h showed a single major peak at 18.5 min, indicating completion of the reaction. The reaction solution was cooled to room temperature and allowed to sit undisturbed for several days, during which crystals spontaneously formed. Although they were not suitable for X-ray analysis, NMR characterization showed these crystals to be the desired complex, **4**. The singlet for the methylene hydrogens (S−CH_2−Py) in ligand **3** yielded characteristic H_a-H_b splitting (J = 17.7) and downfield shifts (from 4.08 ppm to 4.83 and 4.48 ppm) upon coordination to the $[Re^I(CO)_3]^+$ center.[26] Similarly, the other hydrogen atoms along the ligand backbone (S−CH_2−CH_2−NH_2) became diastereotopic in **4** compared to **3** with unique NMR resonances and intense splitting patterns for each atom. The complex splitting patterns could be explained by the presence of overlapping or interconverting diastereomeric structures in solution. Diastereomeric products are expected upon complexation to the metal center due to the prochiral thioether of the free ligand,[25,26] and such sulfur−rhenium bonds have been shown to readily undergo pyramidal inversion to yield interconverting isomers at room temperature.[72,73] Preparatory HPLC was used to purify the crude crystals and reaction solution, yielding **4** with TFA as the counterion. NMR characterization of this purified product matched that of the crystals isolated from the crude reaction mixture. IR analysis showed two strong bands at 2030 and 1921 cm^{-1}, indicating tridentate ligand coordination to yield a *fac*-$[Re^I(CO)_3]^+$ complex.

dx.doi.org/10.1021/bc300509k | Bioconjugate Chem. 2012, 23, 2300−2312

X-ray quality crystals of the purified product were obtained by slow diffusion of benzene into a MeCN solution containing **4**. The structure revealed the tridentate coordination of N–S–N_{Py} to *fac*-$[Re^{I}(CO)_3]^+$ (Figure 2, Table 1). The facial

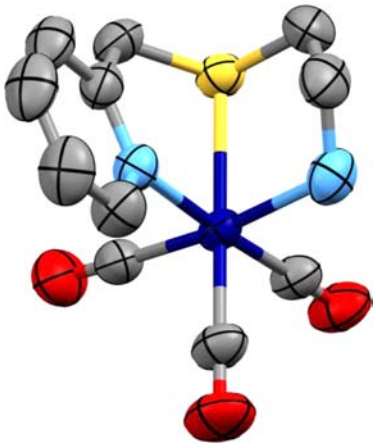

Figure 2. Crystal structure of **4** with thermal ellipsoids shown at the 30% probability level. Hydrogen atoms and counterion (TFA) omitted for clarity. Atoms are colored as follows: C, gray; N, light blue; O, red; Re, dark blue; S, yellow.

Table 1. Selected Bond Distances (Å) and Angles (°) for Compound 4

bond distances [å]		bond angles [deg]	
Re–NH_2	2.218(4)	N_{Py}–Re–NH_2	83.34(14)
Re–N_{Py}	2.206(4)	NH_2–Re–S	80.01(11)
Re–S	2.4488(11)	N_{Py}–Re–S	79.83(10)
Re–CO	1.922(5)	CO–Re–CO	87.3(2)
	1.923(5)		87.8(2)
	1.926(5)		90.2(2)
S–CH_2(N_{Py})	1.806(5)	CH_2–S–CH_2	104.3(3)
S–CH_2(CH_2)	1.810(5)	Re–NH_2–CH_2	114.6(3)

orientated ligand formed two strained five-membered coordination rings on the metal center. The rhenium–nitrogen bond lengths (Re–NH_2, 2.218(4) Å; Re–N_{Py}, 2.206(4) Å) and rhenium–sulfur bond length (2.4488(11) Å) were similar to those observed for several analogous N–S–N_{Py} cysteine-based ligand complexes of *fac*-$[Re^{I}(CO)_3]^+$ (Re-NH_2, 2.219–2.227 Å; Re–N_{Py}, 2.205–2.218 Å; Re–S, 2.447–2.453 Å).[26] However, the rhenium–sulfur bond in **4** was slightly shorter than observed in other ligands with thioether donors coordinated to *fac*-$[Re^{I}(CO)_3]^+$ (2.455–2.504 Å).[25,72] Similarly, the bond angles of the ligand relative to the metal observed in **4** (N_{Py}–Re–NH_2, 83.34(14)°; NH_2–Re–S, 80.01(11)°; N_{Py}–Re–S 79.83(10)°) were equally constricted as other five-membered coordination rings found with thioether pyridine ligands with *fac*-$[Re^{I}(CO)_3]^+$ (N_{Py}–Re–NH_2, 82.0–85.26°; NH_2–Re–S, 79.97–81.29°; N_{Py}–Re–S, 79.23–80.52°).[26,71] However, the N_{Py}–Re–S angle in **4** was more restricted than the corresponding six-membered ring (88.93°) in a comparable *fac*-$[Re^{I}(CO)_3]^+$ complex with *S*-(2-(2′-pyridyl)ethyl)-cysteamine.[71] The Re-CO bond angles of 87.3–90.2° in **4** were comparable to those of other distorted octahedral complexes (86.5–90.3°)[25,26,71] and confirmed the facial coordination of the ligand.

Model Ligand Radiolabeling and Stability Assessment. Following structural analysis of the metal–chelate complex with rhenium, the corresponding radioactive complex was generated. Ligand **3** was complexed with $[^{99m}Tc^{I}(CO)_3(OH_2)_3]^+$ at 70 °C for 30 min at various ligand concentrations (10^{-4} to 10^{-6} M) and reaction pH values (4.5, 6.0, 7.4) to investigate chelation efficiency. All conditions explored led to a single new peak after analysis by radio-HPLC with a retention time of 18.6 min. The identity of this species was confirmed as the desired complex **4a**, as its retention time closely matched that of **4** (18.5 min) under similar HPLC conditions (Figure 3). Excellent yields were obtained for **4a** at

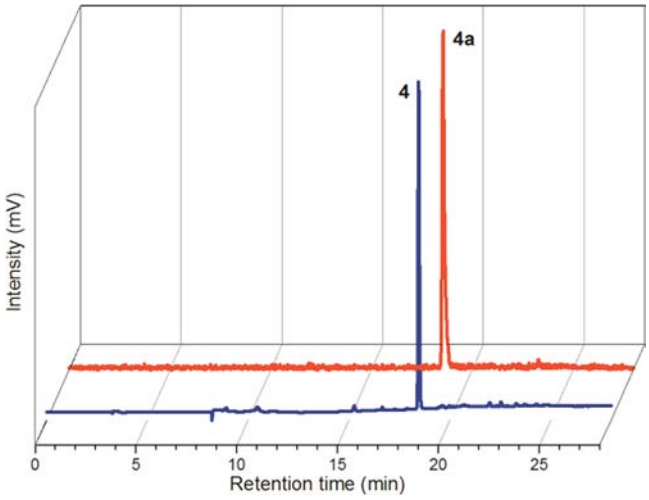

Figure 3. Normalized and offset HPLC chromatograms for purified solutions of **4** (UV absorbance, 254 nm; lower blue trace) at 18.5 min and **4a** (radiodetector, counts per minute (cpm); higher red trace) at 18.6 min.

all pH values explored at 10^{-4} M ligand concentrations, although yields declined slightly at 10^{-5} M ligand concentration and substantially below this (Table S1). Reaction pH was found to affect labeling yields at these lower concentrations, giving higher yields at lower pH values. Although this result was anticipated based on previous results seen with ligand **3** during ^{99m}Tc radiolabeling,[70] the corresponding cysteine derived complex, **5**, (Chart 1) showed the opposite trend between pH and labeling yields.[26] This could be due to ionic attractions between the cationic $[^{99m}Tc^{I}(CO)_3(OH_2)_3]^+$ species and the anionic carboxylate in ligand **1** (Chart 1) which would become more pronounced at higher pH values. Such ionic interactions would not occur with **3**, since this ligand lacks a carboxyl group.

While **4a** was previously seen to be stable when challenged with cysteine or glutathione for 1 h,[70] the stability of **5** under challenge conditions has not yet been shown. For this report, challenge experiments were performed with **4a** and **5** using a large excess of histidine or cysteine, which are high affinity, biologically relevant competitive ligands for the $[^{99m}Tc^{I}(CO)_3]^+$ core.[74] Purified, carrier-free **4a** and **5** showed no disassociation or trans-chelation in the presence of the competing ligands under biologically relevant temperature and pH values (37 °C, pH 7.4) up to 4 h as determined by radio-HPLC analysis (SI Table S2). The encouraging radiolabeling yields and stabilities seen in these studies confirmed the N–S–N_{Py} donor system to be a favorable tridentate chelate group for $[M^{I}(CO)_3]^+$ centers.

dx.doi.org/10.1021/bc300509k | *Bioconjugate Chem.* 2012, 23, 2300–2312

This prompted us to incorporate this moiety within a targeting peptide for radiopharmaceutical applications.

NAPamide Analogue Synthesis, Rhenium Complexation, and Characterization. α-MSH analogues are favorable peptides for targeted radiopharmaceutical applications as they can accommodate a variety of amino acid residues or linkers for radionuclide integration while maintaining high affinity for MC1R and rapid clearance from normal tissues in vivo.[44,54,64] While a variety of α-MSH peptides have incorporated rhenium and technetium as $M^{V}O$ cores by either chelate attachment or peptide cyclization methods,[30,59,62−65,69,75,76] examples of these peptides with the $[M^{I}(CO)_3]^+$ core have been much more limited.[50,53,54] We hypothesized that introducing the N−S−N_{Py} chelate group via attachment of an *S*-functionalized cysteine at the *N*-terminus of a high-affinity NAPamide analogue would allow efficient complexation of the $[M^{I}(CO)_3]^+$ core for generating a novel radiolabeled peptide for melanoma detection. Such an analogue would be the first demonstration of a biomolecule bearing the N−S−N_{Py} chelate for $[M^{I}(CO)_3]^+$ incorporation.

To attach the chelate structure within the peptide under standard solid-phase synthesis conditions, the amino group of ligand **1** was protected with Fmoc following procedures used previously with other amino acids.[66] Both ^{1}H and ^{13}C NMR analysis of the resulting compound **2** (Chart 1) confirmed the attachment of the Fmoc group due to the anticipated increased number of resonances in the aromatic regions of the spectra. Mass spectral and elemental analysis also confirmed this compound's identity. Compound **2** was subsequently incorporated at the *N*-terminus of the NAPamide sequence during standard Fmoc solid-phase peptide production. The resulting peptide, **6** (Chart 1), was isolated in moderate overall yield (55%) following purification. MALDI-TOF-MS analysis confirmed the successful production of the peptide as the mass obtained (1251.4 *m*/*z*) matched the anticipated mass for **6**. RP-HPLC analysis (Gradient 4) of **6** yielded a single peak with a retention time of 15.6 min in greater than 98% purity (SI Figure S1), indicating it was ready for use in subsequent reactions.

The $[Re^{I}(CO)_3]^+$ conjugate of peptide **6**, peptide **7**, was produced to characterize the incorporation of the $[M^{I}(CO)_3]^+$ core into the chelate bearing NAPamide. Heating **6** at pH 6.0 for 6 h at 60 °C with 1 equiv of *fac*-$[Re^{I}(CO)_3(OH_2)_3]$-(SO_3CF_3) led to efficient conversion to **7**. Periodic RP-HPLC analysis of the reaction mixture using an aqueous/MeOH gradient (Gradient 1) showed the disappearance of the starting peptide (17.1 min) and the appearance of a single new peak with a later retention time (18.1 min) as would be expected for complexation of the $[Re^{I}(CO)_3]^+$ core to the peptide (SI Figure S2). Following RP-HPLC purification of the reaction mixture and lyophilization of the product peak, **7** was isolated in good yield (>70%) and its identity confirmed by ESI-MS. The base peak observed during MS analysis (761.6 *m*/*z*) correlated with the expected mass of the doubly protonated peptide-$Re^{I}(CO)_3$ conjugate ($[M+2H]^{2+}$). The spectrum also showed a prominent set of ions for the parent peak, $[M]^+$, with *m*/*z* values of 1521.2 and 1519.4, representing the characteristic isotopic ratio for naturally abundant ^{187}Re and ^{185}Re. These results confirmed the complexation of a single $[Re^{I}(CO)_3]^+$ center to the peptide as anticipated for **7** and encouraged us to pursue radiolabeling studies with ^{99m}Tc.

NAPamide Analogue Radiolabeling and In Vitro Stability. To generate a novel peptide labeled with a SPECT isotope for imaging melanoma, the NAPamide analogue, **6**, was complexed with $[^{99m}Tc^{I}(CO)_3(OH_2)_3]^+$ at pH 6.0 and heated at 70 °C for 30 min. Initial analysis and purification of the reaction mixture by RP-HPLC using an aqueous/MeCN gradient (Gradient 6) showed a single major peak with a retention time of 14.1 min, assigned as **7a** (Chart 1). Complex **7a** was obtained in decay-corrected yields above 71% with high specific activities (1010−1900 mCi/μmol), demonstrating the excellent radiolabeling efficiency of the peptide. **7a** was then analyzed by radio-HPLC using the same conditions as for analyzing **7** above (Gradient 1). Its retention time of 18.5 min correlated closely to the 18.2 min retention time observed with purified **7** (Figure 4), indicating similar $[M^{I}(CO)_3]^+$ complexation between the two analogues and confirming the identity of **7a**. Subsequent radio-HPLC analysis of **7a** using an alternative aqueous/MeCN gradient (Gradient 7) showed a single peak with a retention time of 18.7 min (SI Figure S3A). This alternative gradient was used for further analysis of **7a** in the studies below.

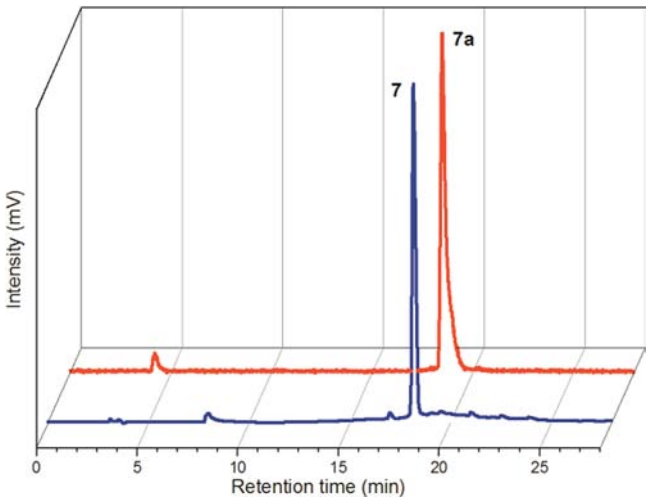

Figure 4. Normalized and offset HPLC chromatograms for purified solutions of **7** (UV absorbance, 254 nm; lower blue trace) at 18.2 min and **7a** (radiodetector, cpm; higher red trace) at 18.5 min.

High stability of radiolabeled complexes toward competitive ligands is essential for developing biologically relevant imaging compounds. The in vitro stability of **7a** was assessed for a 4 h period at 37 °C in mouse serum or in histidine or cysteine solutions at pH 7.4. More than 90% of the radiolabeled complex remained unaltered after 4 h incubation in mouse serum (SI Figure S3B). Similar to the results seen with **4a** and **5**, the radiolabeled peptide remained stable after 4 h incubation with excess histidine or cysteine (SI Figures S3C and S3D, respectively). These results showed the inertness of **7a** toward transchelation or degradation and warranted its further exploration for targeting MC1R in vitro and in vivo.

In Vitro Cell Analyses of the $M^{I}(CO)_3$-NAPamide Complexes. The MC1R binding affinity of **7** in B16F10 cells was determined by a competitive binding study with ^{125}I-(Tyr^2)-NDP as a radioligand and yielded an IC_{50} value of 2.0 ± 0.9 nM. The low nanomolar affinity of the rhenium-conjugated peptide indicated that incorporation of the cysteine-based ligand system and subsequent $[M^{I}(CO)_3]^+$ complexation of the functionalized peptide did not hinder the peptide's ability to bind to MC1R. This encouraging result suggested the

$M^{I}(CO)_3$-NAPamide complex to potentially be a useful in vitro MC1R targeting peptide and prompted further cell uptake and MC1R specificity studies with **7a** in B16F10 cells. Levels of cell uptake of **7a** observed after 0.5, 1, and 2 h incubation at 37 or 4 °C are shown in Figure 5. **7a** exhibited moderate accumulation

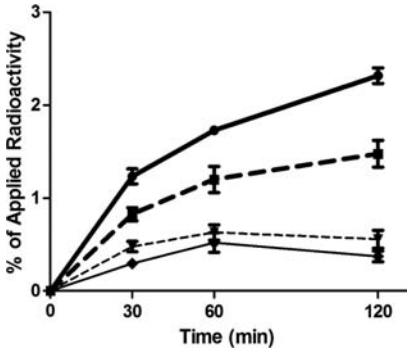

Figure 5. In vitro B16F10 cell uptake assay. B16F10 cells were incubated with 1 μCi of **7a** for 0.5, 1, and 2 h at 37 and 4 °C, with or without NAPamide as a blocking agent. Data represent the mean percentage of total radioactivity added. The experiment was performed in triplicate, and the error bars represent standard deviation. **7a** only at 37 °C (thick line), **7a** with unlabeled NAPamide at 37 °C (thick dotted line), **7a** only at 4 °C (thin line), **7a** with unlabeled NAPamide at 4 °C (thin dotted line).

in B16F10 cells at 37 °C, reaching 1.2 ± 0.08%, 1.7 ± 0.01%, and 2.3 ± 0.08% of applied activity at 0.5, 1, and 2 h, respectively. This uptake was significantly reduced at 4 °C, reaching only 0.3 ± 0.05%, 0.5 ± 0.08%, and 0.4 ± 0.09% of applied activity at 0.5, 1, and 2 h, respectively. To further confirm whether the binding of **7a** with B16F10 cells was specific for MC1R, the cells were incubated with solutions containing both **7a** and excess amounts of unlabeled NAPamide for 0.5, 1, and 2 h at 37 °C. As shown in Figure 5, radiolabel uptake at 2 h decreased from 2.3 ± 0.08% to 1.4 ± 0.1% ($P < 0.05$) under these conditions. Thus, the unlabeled NAPamide reduced the binding of **7a** to B16F10 cells to a statistically significant degree, indicating that the uptake of the radiolabeled peptide was mediated by the MC1R. At 4 °C, however, there were no significant differences in B16F10 cell uptake of **7a** when administered alone or when coincubated with unlabeled NAPamide. This suggests that the pathway of receptor-mediated ligand binding and internalization is no longer active at 4 °C and only nonspecific uptake and internalization occurs at this temperature.

In Vivo Imaging and Biodistribution Studies with the Radiolabeled NAPamide Ananlogue. In vivo studies were then performed in a mouse model of melanoma to determine the imaging potential and biodistribution of the radiolabeled peptide. SPECT/CT images of a B16F10 tumor-bearing mouse at 1 h p.i. of **7a** are shown in Figure 6. The tumor was clearly visible at 1 h p.i., and high tumor-to-background contrast was achieved. The radiolabeled peptide showed low accumulation in most normal organs, resulting in high tumor imaging quality. Relatively high accumulation of radioactivity was observed in the kidneys and liver. Co-injection of excess NAPamide as a blocking agent considerably reduced tumor uptake, confirming the in vivo tumor-targeting specificity of **7a**.

The in vivo biodistribution of **7a** was examined in B16F10 tumor-bearing mice at 1 and 4 h p.i. Biodistribution studies confirmed that **7a** had modest uptake in tumors and low

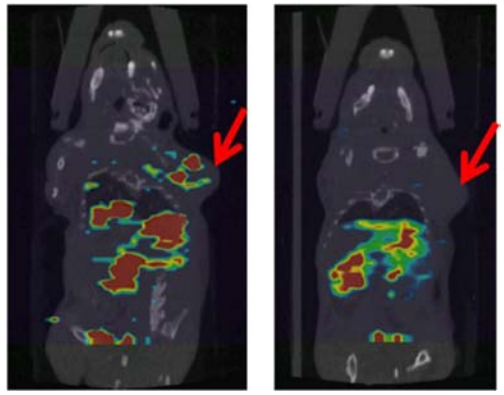

Figure 6. SPECT/CT imaging of **7a** in C57BL/6 mice bearing B16F10 tumor xenografts (n = 4 per group). Coronal SPECT/CT image of B16F10 tumor-bearing mice at 1 h post injection of approximately 200 μCi of **7a** alone (left image) or of **7a** coinjected with 10 mg NAPamide per kg of mouse body weight (right image) at 1 h after injection. Arrows indicate the location of tumors.

accumulation in most normal organs (Figure 7) and were consistent with the results observed during SPECT imaging. Tumor uptake of **7a** was 1.20 ± 0.09% ID/g at 1 h p.i. and decreased slightly to 0.84 ± 0.10% ID/g at 4 h p.i., although this decrease was not statistically significant ($P > 0.2$). The accumulation of **7a** within muscle, blood, and most other normal tissues, however, was remarkably lower at 4 h compared to 1 h. High tumor-to-normal tissue ratios were observed 4 h after injection, including a tumor-to-blood ratio of 2.02 ± 0.58 and a tumor-to-muscle ratio of 14.09 ± 0.58 (Figure 7B). This finding demonstrated that there was good retention of the radiolabeled peptide in tumors compared to the other organs.

Some nonspecific accumulation in normal organs was found during in vivo analysis. Relatively high uptake of **7a** was found in the kidneys, reaching 6.55 ± 0.36% ID/g at 1 h p.i. This initially high renal accumulation was expected since the clearance of low-molecular-weight compounds, such as small peptides, from the body is mainly through the kidneys. The uptake of **7a** within the kidneys reduced to 3.20 ± 0.48% ID/g at 4 h p.i., demonstrating the relatively rapid clearance of **7a** from these organs. The liver uptake of **7a** remained relatively high at both time points (4.44 ± 0.17% ID/g and 4.11 ± 0.07% ID/g at 1 and 4 h after injection, respectively). The undesirable increased liver retention observed may be attributed to the changes in lipophilicity associated with the $[^{99m}Tc^{I}(CO)_3]^{+}$ core or the pyridal group leading to hepatobiliary rather than renal clearance of the peptide from circulation. This general trend with $^{99m}Tc^{I}(CO)_3$-appended systems has been observed with other peptides incorporating chelators with dipyridal groups.[8]

The overall in vivo performance of **7a**, which employed the labeling strategy of incorporating the chelate and radiometal into the peptide backbone, indicated this complex had similar properties to other linear MSH analogues with the NAP-amide sequence using alternative radiolabeling strategies. In a chelate appended strategy, DOTA-conjugated peptides labeled with ^{111}In[49,51] and ^{67}Ga[48] showed fairly low uptake in most normal tissues compared to the melanoma tumors at 4 h p.i., while a ^{64}Cu[42] DOTA-conjugated analogue yielded greater nonspecific retention in normal tissues compared to **7a**. While these DOTA-functionalized conjugates showed greater overall uptake in melanoma tumors at 4 h p.i. (>2% ID/g) compared to **7a**,

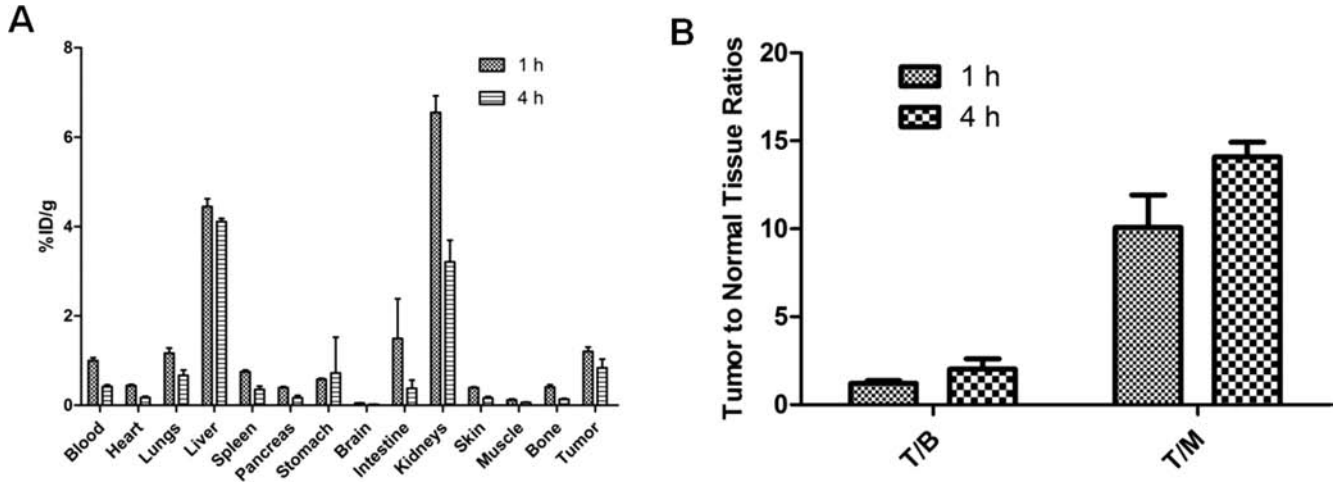

Figure 7. Biodistribution (A) and tumor-to-normal tissue ratios (B) of **7a** in B16F10 tumor-bearing C57BL/6 mice 1 and 4 h after injection of approximately 200 μCi of **7a**. Data are expressed as % ID/g ± SD (n = 4 per group).

they also had greater kidney retention (>3.9% ID/g) than did **7a**. A nonmetal analogue, an ^{18}F-fluorobenzoate α-MSH peptide,[44] had similar melanoma uptake at 1 h p.i. (1.19% ID/g) and lower melanoma uptake at 4 h p.i. (0.52% ID/g) compared to **7a**. Comparable linear α-MSH peptide analogues for targeting MC1R in melanoma applications have employed a ligand appended pyrazolyl-diamine (pz) chelate for $[M^I(CO)_3]^+$ incorporation.[50,53,54] While **7a** demonstrated lower uptake in B16F10 tumor xenografts in mice at 1 h p.i. (1.20 ± 0.09% ID/g) compared to these other $^{99m}Tc^I(CO)_3$-labeled peptides (>1.9% ID/g), **7a** also had lower nontumor accumulation in major excretory organs (liver, kidneys, intestines). The liver showed the highest retention of radioactivity (4.11 ± 0.07% ID/g) at 4 h p.i. for **7a** in contrast with the intestines[50,54] or kidneys[53] for the pz-$^{99m}Tc^I(CO)_3$ analogues. These variations in biodistribution patterns are likely due to variations in peptide sequences, inherent chelate properties, and locations of chelate incorporation employed for radiolabeling; these factors have been shown to impact the in vivo performance of radiolabeled peptides.[8,77]

Overall, the in vivo performance of **7a** falls within the spectrum of ranges observed for similar metal and nonmetal based radiolabeling strategies with linear α-MSH peptides, although its tumor uptake was lower and its liver retention was higher than for several ^{99m}Tc-cyclized α-MSH peptides.[30,58,62] **7a** yielded modest tumor uptake 4 h p.i. with reasonable clearance from other organs (e.g., lungs, pancreas, intestines, spleen) correlated with melanoma metastases.[78] Additional optimization is needed to reduce the nonspecific accumulation of **7a** in the liver and gastrointestinal tract, which are also common sites of melanoma metastases.[78] Although the clearance pathway of **7a** may have been undesirably affected by the lipophilicity of the $[^{99m}Tc^I(CO)_3]^+$ core, the advantages associated with the $[^{99m}Tc^I(CO)_3]^+$ core such as small molecular size, stability, and reproducible formation may outweigh lipophilicity shortcomings in alternative peptide applications with the labeling strategy employed here. These initial studies demonstrate the feasibility of the N−S−N_{Py} chelate strategy for functionalization of the N-terminus of peptides. This chelate system can also be readily extended to peptide side chains with free amines, small molecules, or peptidomimetic molecules for incorporation of $[M^I(CO)_3]^+$ centers in radiopharmaceutical applications.

CONCLUSIONS

In summary, this study presents the first application of the novel, cysteine-derived, N−S−N_{Py} chelate strategy for $[M^I(CO)_3]^+$ complexation within an α-MSH peptide to generate a targeted imaging radiopharmaceutical. The model ligand systems in this study demonstrated the core ligand−metal interactions and the stability of the radiolabeled complex in vitro. The NAPamide analogue, **7a**, was prepared as a model peptide system and evaluated for MC1R binding properties, tumor uptake, and tissue distribution in B16F10 melanoma. The radiolabeled peptide showed high stability and MC1R binding specificity in vitro. Biodistribution and small animal SPECT/CT imaging studies with **7a** yielded promising in vivo properties such as rapid tumor targeting, tumor retention, and generally good tumor-to-normal tissue ratios. These favorable results demonstrate the utility of the novel chelation strategy when applied in a targeting peptide and suggest its extension to other biomolecules. We expect this strategy to be applicable to a broad range of peptide-based radiopharmaceutical agents due to its ease in incorporation via solid-phase synthesis and its efficiency for coordinating the widely used $[M^I(CO)_3]^+$ core.

ASSOCIATED CONTENT

Supporting Information

Radiolabeling yields for **4a**. Stability of **4a** and **5** during in vitro amino acid challenge assays. HPLC chromatogram of purified **6**. Normalized and offset HPLC chromatograms of **6** and **7**. In vitro stability of **7a**. X-ray crystallography experimental procedures and tables with crystal data, structure refinement, bond lengths, and bond angles for **4** (CCDC deposition number: 877545). This material is available free of charge via the Internet at http://pubs.acs.org.

AUTHOR INFORMATION

Corresponding Author

*Hong Zhang: E-mail hzhang21@gmail.com; Phone/Fax 0086-571-87767188. Zhen Cheng: E-mail zcheng@stanford.edu; Phone (650) 723-7866; Fax (650) 736-7925. Paul Benny: E-mail bennyp@wsu.edu; Phone (509) 335-3858; Fax (509) 335-8867.

Author Contributions

#These authors contributed equally to this work.

Notes

The authors declare no competing financial interest.

■ ACKNOWLEDGMENTS

The authors wish to thank Mary Dyszlewski of Covidien, Inc., for the Isolink kits. This research was funded in part by the NIH Biotechnology Training Program at Washington State University (T32 GM008336), the National Cancer Institute (NCI) *In Vivo* Cellular Molecular Imaging Center (ICMIC) grant P50 CA114747 and Melanoma Research Alliance (ZC), the Zhejiang Provincial Natural Science Foundation of China (Z2110230), the Health Bureau of Zhejiang Province (2010ZA075, 2011ZDA013), the National Science Foundation of China (NSFC) (No. 81101023, 81170306, 81173468), the Ministry of Science and Technology of China (2011CB504400) and the National Science Technology Support Program (2012BAI13B06, 2012BAI13B06).

■ ABBREVIATIONS

CT, X-ray computed tomography; cpm, counts per minute; DMF, *N*,*N*-dimethylformamide; ESI-MS, electrospray ionization mass spectrometry; Fmoc, 9-Fluorenylmethoxycarbonyl; FOV, field of view; HPLC, high-performance liquid chromatography; ^{125}I-(Tyr^2)-NDP, ^{125}I-(Tyr^2)-[Nle^4,D-Phe^7]-α-MSH; % ID/g, percent injected dose per gram of tissue; IR, infrared; MALDI-TOF-MS, matrix assisted laser desorption/ionization time-of-flight mass spectrometry; MC1R, melanocortin 1 receptor; MeCN, acetonitrile; MeOH, methanol; α-MSH, alpha-melanocyte stimulating hormone; NAPamide, Ac-Nle-Asp-His-D-Phe-Arg-Trp-Gly-Lys-NH_2; NMR, nuclear magnetic resonance; p.i., post injection; pz, pyrazolyl-diamine tridentate chelate group; RP-HPLC, reversed-phase HPLC; SPECT, single photon emission computed tomography; TFA, trifluoroacetic acid.

■ REFERENCES

(1) Alberto, R., Schibli, R., Egli, A., Schubiger, A. P., Abram, U., and Kaden, T. A. (1998) A novel organometallic aqua complex of technetium for the labeling of biomolecules: synthesis of $[^{99m}Tc(OH_2)_3(CO)_3]^+$ from $[^{99m}TcO_4]^-$ in aqueous solution and its reaction with a bifunctional ligand. *J. Am. Chem. Soc. 120*, 7987−7988.

(2) Rattat, D., Eraets, K., Cleynhens, B., Knight, H., Fonge, H., and Verbruggen, A. (2004) Comparison of tridentate ligands in competition experiments for their ability to form a $[^{99m}Tc(CO)_3]$ complex. *Tetrahedron Lett. 45*, 2531−2534.

(3) Lazarova, N., Babich, J., Valliant, J., Schaffer, P., James, S., and Zubieta, J. (2005) Thiol- and thioether-based bifunctional chelates for the $\{M(CO)_3\}^+$ Core (M = Tc, Re). *Inorg. Chem. 44*, 6763−6770.

(4) Alberto, R., Kyong Pak, J., van Staveren, D., Mundwiler, S., and Benny, P. (2004) Mono-, bi-, or tridentate ligands? The labeling of peptides with 99mTc-carbonyls. *Pept. Sci. 76*, 324−333.

(5) Banerjee, S. R., Babich, J. W., and Zubieta, J. (2005) Site directed maleimide bifunctional chelators for the $M(CO)_3^+$ core (M = ^{99m}Tc, Re). *Chem. Commun.*, 1784−1786.

(6) Chakraborty, S., and Liu, S. (2010) ^{99m}Tc and ^{111}In-labeling of small biomolecules: Bifunctional chelators and related coordination chemistry. *Curr. Top. Med. Chem. (Sharjah, United Arab Emirates) 10*, 1113−1134.

(7) Stephenson, K. A., Zubieta, J., Banerjee, S. R., Levadala, M. K., Taggart, L., Ryan, L., McFarlane, N., Boreham, D. R., Maresca, K. P., Babich, J. W., and Valliant, J. F. (2003) A new strategy for the preparation of peptide-targeted radiopharmaceuticals based on an fmoc-lysine-derived single amino acid chelate (SAAC). Automated solid-phase synthesis, NMR characterization, and in vitro screening of fMLF(SAAC)G and fMLF[$(SAAC\text{-}Re(CO)_3)^+$]G. *Bioconjugate Chem. 15*, 128−136.

(8) Maresca, K. P., Marquis, J. C., Hillier, S. M., Lu, G., Femia, F. J., Zimmerman, C. N., Eckelman, W. C., Joyal, J. L., and Babich, J. W. (2010) Novel polar single amino acid chelates for technetium-99m tricarbonyl-based radiopharmaceuticals with enhanced renal clearance: application to octreotide. *Bioconjugate Chem. 21*, 1032−1042.

(9) Mindt, T. L., Struthers, H., Brans, L., Anguelov, T., Schweinsberg, C., Maes, V., Tourwé, D., and Schibli, R. (2006) "Click to chelate": synthesis and installation of metal chelates into biomolecules in a single step. *J. Am. Chem. Soc. 128*, 15096−15097.

(10) Mindt, T. L., Schweinsberg, C., Brans, L., Hagenbach, A., Abram, U., Tourwé, D., Garcia-Garayoa, E., and Schibli, R. (2009) A click approach to structurally diverse conjugates containing a central di-1,2,3-triazole metal chelate. *ChemMedChem 4*, 529−539.

(11) Ferro-Flores, G., Rivero, I. A., Santos-Cuevas, C. L., Sarmiento, J. I., Arteaga de Murphy, C., Ocampo-García, B. E., García-Becerra, R., and Ordaz-Rosado, D. (2010) Click chemistry for $[^{99m}Tc(CO)_3]$ labeling of Lys^3-bombesin. *Appl. Radiat. Isot. 68*, 2274−2278.

(12) Waibel, R., Alberto, R., Willuda, J., Finnern, R., Schibli, R., Stichelberger, A., Egli, A., Abram, U., Mach, J.-P., Plückthun, A., and Schubiger, P. A. (1999) Stable one-step technetium-99m labeling of His-tagged recombinant proteins with a novel Tc(I)-carbonyl complex. *Nat. Biotechnol. 17*, 897−901.

(13) Francis, R. J., Mather, S. J., Chester, K., Sharma, S. K., Bhatia, J., Pedley, R. B., Waibel, R., Green, A. J., and Begent, R. H. J. (2004) Radiolabelling of glycosylated MFE-23::CPG2 fusion protein (MFECP1) with ^{99m}Tc for quantitation of tumour antibody-enzyme localisation in antibody-directed enzyme pro-drug therapy (ADEPT). *Eur. J. Nucl. Med. Mol. Imaging 31*, 1090−1096.

(14) Orlova, A., Nilsson, F. Y., Wikman, M., Widström, C., Ståhl, S., Carlsson, J., and Tolmachev, V. (2006) Comparative in vivo evaluation of technetium and iodine labels on an anti-HER2 affibody for single-photon imaging of HER2 expression in tumors. *J. Nucl. Med. 47*, 512−519.

(15) Iyer, A. K., Lan, X., Zhu, X., Su, Y., Feng, J., Zhang, X., Gao, D., Seo, Y., VanBrocklin, H. F., Broaddus, V. C., Liu, B., and He, J. (2011) Novel human single chain antibody fragments that are rapidly internalizing effectively target epithelioid and sarcomatoid mesotheliomas. *Cancer Res. 71*, 2428−2432.

(16) He, J., Wang, Y., Feng, J., Zhu, X., Lan, X., Iyer, A. K., Zhang, N., Seo, Y., VanBrocklin, H. F., and Liu, B. (2010) Targeting prostate cancer cells in vivo using a rapidly internalizing novel human single-chain antibody fragment. *J. Nucl. Med. 51*, 427−432.

(17) Ahlgren, S., Wållberg, H., Tran, T. A., Widström, C., Hjertman, M., Abrahmsén, L., Berndorff, D., Dinkelborg, L. M., Cyr, J. E., Feldwisch, J., Orlova, A., and Tolmachev, V. (2009) Targeting of HER2-expressing tumors with a site-specifically ^{99m}Tc-labeled recombinant affibody molecule, $Z_{HER2:2395}$, with C-terminally engineered cysteine. *J. Nucl. Med. 50*, 781−789.

(18) Berndorff, D., Borkowski, S., Moosmayer, D., Viti, F., Müller-Tiemann, B., Sieger, S., Friebe, M., Hilger, C. S., Zardi, L., Neri, D., and Dinkelborg, L. M. (2006) Imaging of tumor angiogenesis using ^{99m}Tc-labeled human recombinant anti-ED-B fibronectin antibody fragments. *J. Nucl. Med. 47*, 1707−1716.

(19) Gainkam, L. O. T., Huang, L., Caveliers, V., Keyaerts, M., Hernot, S., Vaneycken, I., Vanhove, C., Revets, H., De Baetselier, P., and Lahoutte, T. (2008) Comparison of the biodistribution and tumor targeting of two ^{99m}Tc-labeled anti-EGFR nanobodies in mice, using pinhole SPECT/Micro-CT. *J. Nucl. Med. 49*, 788−795.

(20) Cortez-Retamozo, V., Lahoutte, T., Caveliers, V., Gainkam, L. O. T., Hernot, S., Packeu, A., De Vos, F., Vanhove, C., Muyldermans, S., De Baetselier, P., and Revets, H. (2008) ^{99m}Tc-labeled nanobodies: a new type of targeted probes for imaging antigen expression. *Curr. Radiopharm. 1*, 37−41.

(21) Wang, X., Zhang, M., Yang, Z., Lin, B., and Zhang, Q. (2002) Pre-clinical study on tumor vasoactive intestinal peptide receptor scintigraphy. *Zhonghua Zhongliu Zazhi 24*, 331−334.

(22) Zahnd, C., Kawe, M., Stumpp, M. T., de Pasquale, C., Tamaskovic, R., Nagy-Davidescu, G., Dreier, B., Schibli, R., Binz, H. K., Waibel, R., and Plückthun, A. (2010) Efficient tumor targeting with high-affinity designed ankyrin repeat proteins: effects of affinity and molecular size. *Cancer Res. 70*, 1595−1605.

(23) Tavaré, R., De Rosales, R. T. M., Blower, P. J., and Mullen, G. E. D. (2009) Efficient site-specific radiolabeling of a modified C2A domain of Synaptotagmin I with $[^{99m}Tc(CO)_3]^+$: a new radiopharmaceutical for imaging cell death. *Bioconjugate Chem. 20*, 2071−2081.

(24) Tolmachev, V., Hofström, C., Malmberg, J., Ahlgren, S., Hosseinimehr, S. J., Sandström, M., Abrahmsén, L., Orlova, A., and Gräslund, T. (2010) HEHEHE-tagged affibody molecule may be purified by IMAC, is conveniently labeled with $[^{99m}Tc(CO)_3]^+$, and shows improved biodistribution with reduced hepatic radioactivity accumulation. *Bioconjugate Chem. 21*, 2013−2022.

(25) He, H., Lipowska, M., Xu, X., Taylor, A. T., Carlone, M., and Marzilli, L. G. (2005) $Re(CO)_3$ complexes synthesized via an improved preparation of aqueous *fac*-$[Re(CO)_3(H_2O)_3]^+$ as an aid in assessing ^{99m}Tc imaging agents. Structural characterization and solution behavior of complexes with thioether-bearing amino acids as tridentate ligands. *Inorg. Chem. 44*, 5437−5446.

(26) He, H., Morley, J. E., Twamley, B., Groeneman, R. H., Bučar, D.-K., MacGillivray, L. R., and Benny, P. D. (2009) Investigation of the coordination interactions of S-(pyridin-2-ylmethyl)-L-cysteine ligands with $M(CO)_3^+$ (M = Re, ^{99m}Tc). *Inorg. Chem. 48*, 10625−10634.

(27) van Staveren, D. R., Benny, P. D., Waibel, R., Kurz, P., Pak, J.-K., and Alberto, R. (2005) S-Functionalized cysteine: powerful ligands for the labelling of bioactive molecules with triaquatricarbonyltechnetium-99m(1+) ($[^{99m}Tc(OH_2)_3(CO)_3]^+$). *Helv. Chim. Acta 88*, 447−460.

(28) Jemal, A., Siegel, R., Ward, E., Hao, Y., Xu, J., Murray, T., and Thun, M. J. (2008) Cancer statistics, 2008. *CA: A Cancer Journal for Clinicians 58*, 71−96.

(29) Anderson, C. M.; Buzaid, A. C.; Legha, S. S. (1995) Systemic treatments for advanced cutaneous melanoma. *Oncology (Williston Park) 9*, 1149−1158, discussion 1163−1164, 1167−1168.

(30) Chen, J., Cheng, Z., Hoffman, T. J., Jurisson, S. S., and Quinn, T. P. (2000) Melanoma-targeting properties of ^{99m}Technetium-labeled cyclic α-melanocyte-stimulating hormone peptide analogues. *Cancer Res. 60*, 5649−5658.

(31) Marghoob, A. A., Slade, J., Salopek, T. G., Kopf, A. W., Bart, R. S., and Rigel, D. S. (1995) Basal cell and squamous cell carcinomas are important risk factors for cutaneous malignant melanoma. Screening implications. *Cancer 75*, 707−714.

(32) Larson, S. M., Brown, J. P., Wright, P. W., Carrasquillo, J. A., Hellstrom, I., and Hellstrom, K. E. (1983) Imaging of melanoma with I-131-labeled monoclonal-antibodies. *J. Nucl. Med. 24*, 123−129.

(33) Wahl, R. L., Swanson, N. A., Johnson, J. W., Natale, R., Petry, N. A., Mallette, S., Kasina, S., Reno, J., Sullivan, K., and Abrams, P. (1992) Clinical experience with Tc-99m labeled (N2S2) anti-melanoma antibody fragments and single photon emission computed tomography. *Am. J. Physiol. Imaging. 7*, 48−58.

(34) Ren, G., Pan, Y., and Cheng, Z. (2010) Molecular probes for malignant melanoma imaging. *Curr. Pharm. Biotechnol. 11*, 590−602.

(35) Frontiera, M., Murray, J. L., Lamki, L., Thomas, J., Satterlee, W., Schmelter, R., Rosenblum, M. G., Khazaeli, M. B., Unger, M. W., Robinson, W. A., et al. (1989) Sequential use of indium-111 labeled monoclonal antibodies 96.5 and ZME-018 does not increase detection sensitivity for metastatic melanoma. *Clin. Nucl. Med. 14*, 357−366.

(36) Ong, G. L., and Mattes, M. J. (1989) Penetration and binding of antibodies in experimental human solid tumors grown in mice. *Cancer Res. 49*, 4264−4273.

(37) Halpern, S. E., and Bartholomew, R. (1995) Pharmacokinetics of an indium-labeled IgG monoclonal antibody over a prolonged period. *Eur. J. Nucl. Med. 22*, 1323−1325.

(38) Mountjoy, K. G., Robbins, L. S., Mortrud, M. T., and Cone, R. D. (1992) The cloning of a family of genes that encode the melanocortin receptors. *Science 257*, 1248−1251.

(39) Siegrist, W., Solca, F., Stutz, S., Giuffrè, L., Carrel, S., Girard, J., and Eberle, A. N. (1989) Characterization of receptors for α-melanocyte-stimulating hormone on human melanoma cells. *Cancer Res. 49*, 6352−6358.

(40) Salazar-Onfray, F., Lopez, M., Lundqvist, A., Aguirre, A., Escobar, A., Serrano, A., Korenblit, C., Petersson, M., Chhajlani, V., Larsson, O., and Kiessling, R. (2002) Tissue distribution and differential expression of melanocortin 1 receptor, a malignant melanoma marker. *Br. J. Cancer 87*, 414−422.

(41) Lopez, M. N., Pereda, C., Ramirez, M., Mendoza-Naranjo, A., Serrano, A., Ferreira, A., Poblete, R., Kalergis, A. M., Kiessling, R., and Salazar-Onfray, F. (2007) Melanocortin 1 receptor is expressed by uveal malignant melanoma and can be considered a new target for diagnosis and immunotherapy. *Invest. Ophthalmol. Vis. Sci. 48*, 1219−1227.

(42) Cheng, Z., Xiong, Z., Subbarayan, M., Chen, X., and Gambhir, S. S. (2007) ^{64}Cu-labeled alpha-melanocyte-stimulating hormone analog for microPET imaging of melanocortin 1 receptor expression. *Bioconjugate Chem. 18*, 765−772.

(43) Schaffer, J. V., and Bolognia, J. L. (2001) The melanocortin-1 receptor: red hair and beyond. *Arch. Dermatol. 137*, 1477−1485.

(44) Cheng, Z., Zhang, L., Graves, E., Xiong, Z., Dandekar, M., Chen, X., and Gambhir, S. S. (2007) Small-animal PET of Melanocortin 1 receptor expression using a ^{18}F-labeled α-melanocyte-stimulating hormone analog. *J. Nucl. Med. 48*, 987−994.

(45) Eberle, A. N., and Froidevaux, S. (2003) Radiolabeled alpha-melanocyte-stimulating hormone analogs for receptor-mediated targeting of melanoma: From tritium to indium. *J. Mol. Recognit. 16*, 248−254.

(46) Miao, Y., Whitener, D., Feng, W., Owen, N. K., Chen, J., and Quinn, T. P. (2003) Evaluation of the human melanoma targeting properties of radiolabeled α-melanocyte stimulating hormone peptide analogues. *Bioconjugate Chem. 14*, 1177−1184.

(47) Giblin, M. F., Jurisson, S. S., and Quinn, T. P. (1997) Synthesis and characterization of rhenium-complexed α-melanotropin analogs. *Bioconjugate Chem. 8*, 347−353.

(48) Froidevaux, S., Calame-Christe, M., Schuhmacher, J., Tanner, H., Saffrich, R., Henze, M., and Eberle, A. N. (2004) A gallium-labeled DOTA-α-melanocyte-stimulating hormone analog for PET imaging of melanoma metastases. *J. Nucl. Med. 45*, 116−123.

(49) Froidevaux, S., Calame-Christe, M., Tanner, H., and Eberle, A. N. (2005) Melanoma targeting with DOTA-α-melanocyte-stimulating hormone analogs: structural parameters affecting tumor uptake and kidney uptake. *J. Nucl. Med. 46*, 887−895.

(50) Raposinho, P. D., Correia, J. D. G., Alves, S., Botelho, M. F., Santos, A. C., and Santos, I. (2008) A $^{99m}Tc(CO)_3$-labeled pyrazolyl-α-melanocyte-stimulating hormone analog conjugate for melanoma targeting. *Nucl. Med. Biol. 35*, 91−99.

(51) Bapst, J.-P., Calame, M., Tanner, H., and Eberle, A. N. (2009) Glycosylated DOTA−α-melanocyte-stimulating hormone analogues for melanoma targeting: influence of the site of glycosylation on in vivo biodistribution. *Bioconjugate Chem. 20*, 984−993.

(52) Baumhover, N. J., Martin, M. E., Parameswarappa, S. G., Kloepping, K. C., O'Dorisio, M. S., Pigge, F. C., and Schultz, M. K. (2011) Improved synthesis and biological evaluation of chelator-modified α-MSH analogs prepared by copper-free click chemistry. *Bioorg. Med. Chem. Lett. 21*, 5757−5761.

(53) Morais, M., Raposinho, P. D., Oliveira, M. C., Correia, J. D. G., and Santos, I. (2012) Evaluation of novel $^{99m}Tc(I)$-labeled homobivalent α-melanocyte-stimulating hormone analogs for melanocortin-1 receptor targeting. *J. Biol. Inorg. Chem. 17*, 491−505.

(54) Raposinho, P., Xavier, C., Correia, J., Falcão, S., Gomes, P., and Santos, I. (2008) Melanoma targeting with α-melanocyte stimulating hormone analogs labeled with *fac*-$[^{99m}Tc(CO)_3]^+$: effect of cyclization on tumor-seeking properties. *J. Biol. Inorg. Chem. 13*, 449−459.

(55) Miao, Y., Gallazzi, F., Guo, H., and Quinn, T. P. (2008) ^{111}In-labeled lactam bridge-cyclized α-melanocyte stimulating hormone peptide analogues for melanoma imaging. *Bioconjugate Chem. 19*, 539−547.

(56) Guo, H., Yang, J., Shenoy, N., and Miao, Y. (2009) Gallium-67-labeled lactam bridge-cyclized α-melanocyte stimulating hormone peptide for primary and metastatic melanoma imaging. *Bioconjugate Chem. 20*, 2356−2363.
(57) Chen, J., Cheng, Z., Owen, N. K., Hoffman, T. J., Miao, Y., Jurisson, S. S., and Quinn, T. P. (2001) Evaluation of an ^{111}In-DOTA-rhenium cyclized α-MSH analog: a novel cyclic-peptide analog with improved tumor-targeting properties. *J. Nucl. Med. 42*, 1847−1855.
(58) Chen, J., Cheng, Z., Miao, Y., Jurisson, S. S., and Quinn, T. P. (2002) α−melanocyte-stimulating hormone peptide analogs labeled with technetium-99m and indium-111 for malignant melanoma targeting. *Cancer 94*, 1196−1201.
(59) Raposinho, P. D., Correia, J. D. G., Oliveira, M. C., and Santos, I. (2010) Melanocortin-1 receptor-targeting with radiolabeled cyclic α-melanocyte-stimulating hormone analogs for melanoma imaging. *Pept. Sci. 94*, 820−829.
(60) Quinn, T. P., Zhang, X., and Miao, Y. (2010) Targeted melanoma imaging and therapy with radiolabeled alpha-melanocyte stimulating hormone peptide analogues. *G. Ital. Dermatol. Venereol. 145*, 245−258.
(61) Giblin, M. F., Wang, N., Hoffman, T. J., Jurisson, S. S., and Quinn, T. P. (1998) Design and characterization of α-melanotropin peptide analogs cyclized through rhenium and technetium metal coordination. *Proc. Natl. Acad. Sci. U. S. A. 95*, 12814−12818.
(62) Miao, Y., Benwell, K., and Quinn, T. P. (2007) ^{99m}Tc- and ^{111}In-labeled α-melanocyte-stimulating hormone peptides as imaging probes for primary and pulmonary metastatic melanoma detection. *J. Nucl. Med. 48*, 73−80.
(63) Cheng, Z., Chen, J., Quinn, T. P., and Jurisson, S. S. (2004) Radioiodination of rhenium cyclized α-melanocyte-stimulating hormone resulting in enhanced radioactivity localization and retention in melanoma. *Cancer Res. 64*, 1411−1418.
(64) Cheng, Z., Chen, J., Miao, Y., Owen, N. K., Quinn, T. P., and Jurisson, S. S. (2002) Modification of the structure of a metallopeptide: synthesis and biological evaluation of ^{111}In-labeled DOTA-conjugated rhenium-cyclized α-MSH analogues. *J. Med. Chem. 45*, 3048−3056.
(65) Ren, G., Liu, Z., Miao, Z., Liu, H., Subbarayan, M., Chin, F. T., Zhang, L., Gambhir, S. S., and Cheng, Z. (2009) PET of malignant melanoma using ^{18}F-labeled metallopeptides. *J. Nucl. Med. 50*, 1865−1872.
(66) Carpino, L. A., and Han, G. Y. (1972) The 9-Fluorenylmethoxycarbonyl amino-protecting group. *J. Org. Chem. 37*, 3404−3409.
(67) El-Badry, O. M., Knaus, E. E., and McNeill, J. H. (1985) Pyridine and reduced pyridine analogues as histamine H_2-receptor antagonists. *Eur. J. Med. Chem. 20*, 403−407.
(68) Mountford, S. J., Campi, E. M., Robinson, A. J., and Hearn, M. T. W. (2011) Synthesis of N-heterocyclic ligands for use in affinity and mixed mode chromatography. *Tetrahedron 67*, 471−485.
(69) Ren, G., Liu, S., Liu, H., Miao, Z., and Cheng, Z. (2010) Radiofluorinated rhenium cyclized α-MSH analogues for PET imaging of melanocortin receptor 1. *Bioconjugate Chem. 21*, 2355−2360.
(70) Zhang, X.-b.; Zhu, L.; Zhao, X.-y.; Liu, B.-l. (2004) Research of novel bifunctional chelating agents for the Tc-tricarbonyl precursor $[^{99}Tc^{m}(CO)_3(H_2O)_3]^+$. *He Huaxue Yu Fangshe Huaxue 26*, 11−17, 22.
(71) Karagiorgou, O., Patsis, G., Pelecanou, M., Raptopoulou, C. P., Terzis, A., Siatra-Papastaikoudi, T., Alberto, R., Pirmettis, I., and Papadopoulos, M. (2005) (S)-(2-(2′-Pyridyl)ethyl)cysteamine and (S)-(2-(2′-Pyridyl)ethyl)-D,L-homocysteine as Ligands for the "*fac*-$[M(CO)_3]^{+}$" (M = Re, ^{99m}Tc) Core. *Inorg. Chem. 44*, 4118−4120.
(72) Moura, C., Gano, L., Santos, I. C., Santos, I., and Paulo, A. (2011) $^{99m}Tc^{I}/Re^{I}$ tricarbonyl complexes with tridentate cysteamine based ligands: synthesis, characterization and in vitro/in vivo evaluation. *Eur. J. Inorg. Chem. 2011*, 5405−5413.
(73) Moura, C., Gano, L., Mendes, F., Raposinho, P. D., Abrantes, A. M., Botelho, M. F., Santos, I., and Paulo, A. (2012) ^{99m}Tc(I)/Re(I) tricarbonyl complexes for *in vivo* targeting of melanotic melanoma: Synthesis and biological evaluation. *Eur. J. Med. Chem. 50*, 350−360.
(74) Egli, A., Alberto, R., Tannahill, L., Schibli, R., Abram, U., Schaffland, A., Waibel, R., Tourwe, D., Jeannin, L., Iterbeke, K., and Schubiger, P. A. (1999) Organometallic ^{99m}Tc-aquaion labels peptide to an unprecedented high specific activity. *J. Nucl. Med. 40*, 1913−1917.
(75) Yang, J., Guo, H., and Miao, Y. (2010) Technetium-99m-labeled Arg-Gly-Asp-conjugated alpha-melanocyte stimulating hormone hybrid peptides for human melanoma imaging. *Nucl. Med. Biol. 37*, 873−883.
(76) Yang, J., Lu, J., and Miao, Y. (2012) Structural modification on the lys linker enhanced tumor to kidney uptake ratios of ^{99m}Tc-labeled RGD-conjugated α-MSH hybrid peptides. *Mol. Pharmaceutics 9*, 1418−1424.
(77) Maresca, K. P., Hillier, S. M., Femia, F. J., Zimmerman, C. N., Levadala, M. K., Banerjee, S. R., Hicks, J., Sundararajan, C., Valliant, J., Zubieta, J., Eckelman, W. C., Joyal, J. L., and Babich, J. W. (2009) Comprehensive radiolabeling, stability, and tissue distribution studies of technetium-99m single amino acid chelates (SAAC). *Bioconjugate Chem. 20*, 1625−1633.
(78) King, D. M. (2006) Imaging of metastatic melanoma. *Cancer Imaging 6*, 204−208.

Supporting Information

A novel, cysteine-modified chelation strategy for the incorporation of $[M^{I}(CO)_3]^+$ (M = Re, ^{99m}Tc) in an α-MSH peptide

Han Jiang[†,‡,□], Benjamin B. Kasten[§,□], Hongguang Liu[‡], Shibo Qi[‡], Yang Liu[†,‡], Mei Tian[†], Charles L. Barnes[∞], Hong Zhang[†*], Zhen Cheng[‡*], Paul D. Benny[§*]

[†]Department of Nuclear Medicine, Second Affiliated Hospital of Zhejiang University School of Medicine, Institute of Nuclear Medicine and Molecular Imaging of Zhejiang University, Center of Excellence in Medical Molecular Imaging of Zhejiang State, Hangzhou, 310009, China

[‡]Molecular Imaging Program at Stanford (MIPS), Department of Radiology, Bio-X Program and Canary Center at Stanford for Cancer Early Detection, Stanford University, Stanford, CA 94305, USA

[§]Department of Chemistry, Washington State University, Pullman WA 99164, USA

[∞]Department of Chemistry, University of Missouri, Columbia MO 65211-7600, USA

[□]These authors contributed equally to this work

[*]Corresponding Authors:

Hong Zhang
hzhang21@gmail.com
Phone/Fax: 0086-571-87767188

Zhen Cheng
zcheng@stanford.edu
Phone: (650) 723-7866
Fax: (650) 736-7925

Paul Benny
bennyp@wsu.edu
Phone: (509) 335-3858
Fax: (509) 335-8867

Contents: Radiolabeling yields for **4a**. Stability of **4a** and **5** during *in vitro* amino acid challenge assays. HPLC chromatogram of purified **6**. Normalized and offset HPLC chromatograms of **6** and **7**. *In vitro* stability of **7a**. X-ray crystallography experimental procedures and tables with crystal data, structure refinement, bond lengths, and bond angles for **4**.

Buffer pH	Ligand concentration (M)		
	10^{-4}	10^{-5}	10^{-6}
4.5	>99	93	46
6.0	>99	85	27
7.4	>99	82	19

Table S1. Radiolabeling yields (%) for **4a** following reactions at 70 °C for 30 min.

	4a		**5**	
Time	*Histidine*	*Cysteine*	*Histidine*	*Cysteine*
1 h	>99%	>99%	>99%	>99%
2 h	>99%	>99%	>99%	>99%
3 h	>99%	>99%	>99%	>99%
4 h	>99%	>99%	>99%	>99%

Table S2. Stability of **4a** and **5** during *in vitro* amino acid challenge assays. The values represent the radioactive counts corresponding to the original complexes compared to the total radioactivity in the chromatogram after incubating HPLC-purified **4a** or **5** (100 μL) with L-cysteine or L-histidine at 2 mM in 10 mM sodium phosphate buffer pH 7.4 (200 μL) at 37 °C.

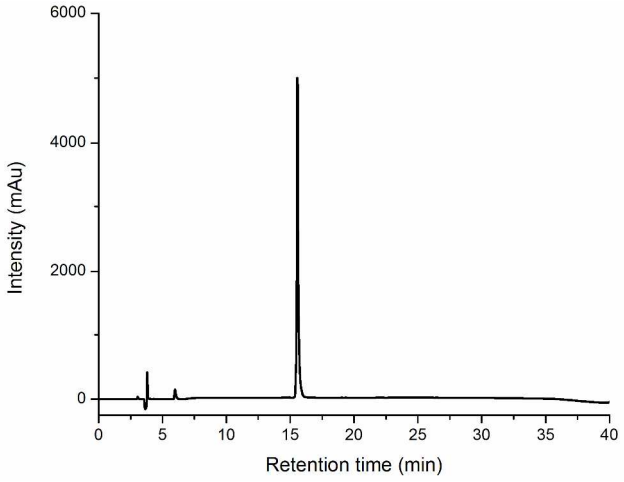

Figure S1. HPLC chromatogram of purified **6** (UV absorbance, 214 nm) at 15.6 min.

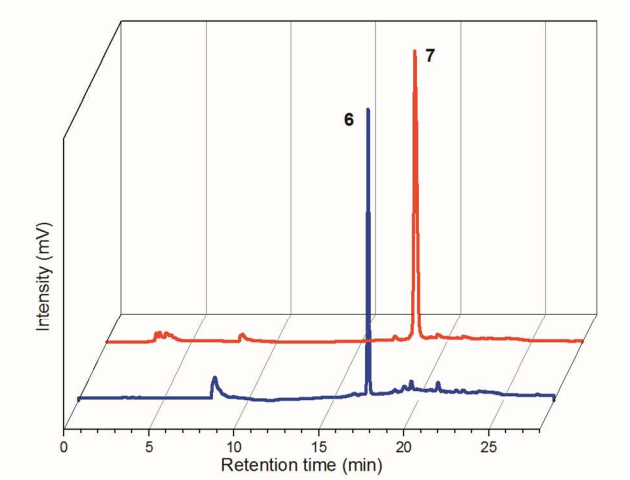

Figure S2. Normalized and offset HPLC chromatograms of **6** (lower blue trace) at 17.1 min and **7** (higher red trace) at 18.1 min (UV absorbance, 254 nm).

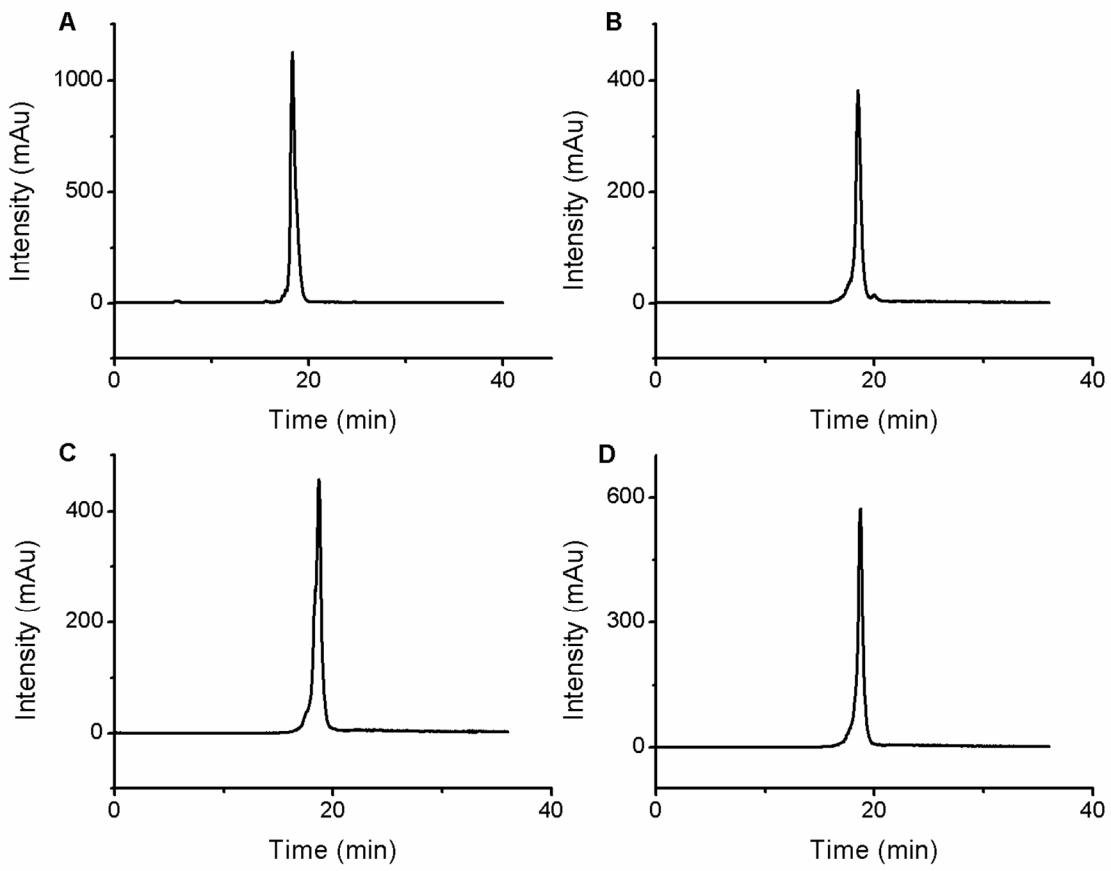

Figure S3. *In vitro* stability of **7a**. Chromatograms show **7a** after purification (A) and after incubation in mouse serum (B), cysteine (C) and histidine (D) solutions at 37 °C for 4 h. Complex stability was analyzed by radio-HPLC and γ-counting.

X-ray crystallography experimental procedure for 4. Intensity data were obtained on a Bruker APEX II CCD Area Detector system using the ω scan technique with Mo Kα radiation from a graphite monochromator. The data was collected at room temperature because the sample underwent a partial phase transition when cooled to -100 °C. Intensities were corrected for Lorentz and polarization effects. Equivalent reflections were merged, and absorption corrections were made using the multi-scan method. Space group, lattice parameters and other relevant information are given in the supplementary material. The structures were solved by direct methods followed by full-matrix least-squares refinement, using the SHELX package[1] with the aid of the program X-Seed.[2] All non-hydrogen atoms were refined with anisotropic thermal parameters. The hydrogen atoms were placed at calculated positions and included in the refinement using a riding model, with fixed isotropic *U*. The final difference maps contained no features of chemical significance.

Table S3. Crystal data and structure refinement for **4**.

Identification code	**4**
Empirical formula	$C_{13}H_{12}F_3N_2O_5ReS$
Formula weight	551.51
Temperature	296(2) K
Wavelength	0.71073 Å
Crystal system	monoclinic
Space group	*P* 21/*c*
Unit cell dimensions	a = 8.4168(9) Å α = 90°
	b = 18.993(2) Å β = 110.1880(10)°
	c = 11.4760(12) Å γ = 90°
Volume	1721.9(3) Å^3
Z	4
Calculated density	2.127 g/cm^3
Absorption coefficient	7.235 mm^{-1}
F(000)	1048
Crystal size	0.30 x 0.15 x 0.15 mm
θ range for data collection	2.14° to 27.53°
Limiting indices	$-10 \le h \le 10$, $-24 \le k \le 24$, $-14 \le l \le 14$

Reflections collected/unique	19936/3932 [R(int) = 0.0234]
Completeness to θ = 27.53°	99.5 %
Absorption correction	semi-empirical from equivalents
Max. and min. transmission	0.41 and 0.28
Refinement method	full-matrix least-squares on F^2
Data/restraints/parameters	3932/0/226
Goodness-of-fit on F^2	1.045
Final R indices [I > 2σ(I)]	$R1$ = 0.0255, w$R2$ = 0.0615
R indices (all data)	$R1$ = 0.0311, w$R2$ = 0.0639
Largest diff. peak and hole	1.182 and -0.857 e. Å^{-3}

Table S4. Bond lengths [Å] and angles [°] for **4**.

Re(1)-C(10)	1.922(5)
Re(1)-C(9)	1.923(5)
Re(1)-C(11)	1.926(5)
Re(1)-N(1)	2.206(4)
Re(1)-N(2)	2.218(4)
Re(1)-S(1)	2.4488(11)
S(1)-C(1)	1.806(5)
S(1)-C(7)	1.810(5)
F(1)-C(13)	1.246(8)
O(1)-C(9)	1.146(6)
N(1)-C(2)	1.357(6)
N(1)-C(6)	1.359(6)
C(1)-C(2)	1.497(7)
C(1)-H(1A)	0.9700
C(1)-H(1B)	0.9700
F(2)-C(13)	1.351(9)
O(2)-C(10)	1.144(6)
N(2)-C(8)	1.478(6)
N(2)-H(2A)	0.9000
N(2)-H(2B)	0.9000
C(2)-C(3)	1.376(7)
F(3)-C(13)	1.224(7)
O(3)-C(11)	1.140(5)
C(3)-C(4)	1.382(8)
C(3)-H(3)	0.9300

O(4)-C(12)	1.234(7)
C(4)-C(5)	1.380(9)
C(4)-H(4)	0.9300
O(5)-C(12)	1.185(6)
C(5)-C(6)	1.370(7)
C(5)-H(5)	0.9300
C(6)-H(6)	0.9300
C(7)-C(8)	1.513(8)
C(7)-H(7A)	0.9700
C(7)-H(7B)	0.9700
C(8)-H(8A)	0.9700
C(8)-H(8B)	0.9700
C(12)-C(13)	1.501(8)
C(10)-Re(1)-C(9)	87.3(2)
C(10)-Re(1)-C(11)	87.8(2)
C(9)-Re(1)-C(11)	90.2(2)
C(10)-Re(1)-N(1)	176.62(16)
C(9)-Re(1)-N(1)	95.68(17)
C(11)-Re(1)-N(1)	93.70(16)
C(10)-Re(1)-N(2)	94.86(18)
C(9)-Re(1)-N(2)	96.3(2)
C(11)-Re(1)-N(2)	173.14(17)
N(1)-Re(1)-N(2)	83.34(14)
C(10)-Re(1)-S(1)	97.06(13)
C(9)-Re(1)-S(1)	174.44(15)
C(11)-Re(1)-S(1)	93.40(13)
N(1)-Re(1)-S(1)	79.83(10)
N(2)-Re(1)-S(1)	80.01(11)
C(1)-S(1)-C(7)	104.3(3)
C(1)-S(1)-Re(1)	97.05(16)
C(7)-S(1)-Re(1)	100.91(18)
C(2)-N(1)-C(6)	117.6(4)
C(2)-N(1)-Re(1)	120.2(3)
C(6)-N(1)-Re(1)	122.2(3)
C(2)-C(1)-S(1)	114.6(3)
C(2)-C(1)-H(1A)	108.6
S(1)-C(1)-H(1A)	108.6
C(2)-C(1)-H(1B)	108.6
S(1)-C(1)-H(1B)	108.6
H(1A)-C(1)-H(1B)	107.6
C(8)-N(2)-Re(1)	114.6(3)
C(8)-N(2)-H(2A)	108.6
Re(1)-N(2)-H(2A)	108.6
C(8)-N(2)-H(2B)	108.6
Re(1)-N(2)-H(2B)	108.6
H(2A)-N(2)-H(2B)	107.6
N(1)-C(2)-C(3)	122.0(5)
N(1)-C(2)-C(1)	117.7(4)
C(3)-C(2)-C(1)	120.3(5)
C(2)-C(3)-C(4)	119.6(5)
C(2)-C(3)-H(3)	120.2
C(4)-C(3)-H(3)	120.2
C(5)-C(4)-C(3)	118.9(5)

C(5)-C(4)-H(4)	120.6
C(3)-C(4)-H(4)	120.6
C(6)-C(5)-C(4)	119.1(5)
C(6)-C(5)-H(5)	120.4
C(4)-C(5)-H(5)	120.4
N(1)-C(6)-C(5)	122.8(5)
N(1)-C(6)-H(6)	118.6
C(5)-C(6)-H(6)	118.6
C(8)-C(7)-S(1)	113.3(4)
C(8)-C(7)-H(7A)	108.9
S(1)-C(7)-H(7A)	108.9
C(8)-C(7)-H(7B)	108.9
S(1)-C(7)-H(7B)	108.9
H(7A)-C(7)-H(7B)	107.7
N(2)-C(8)-C(7)	109.4(4)
N(2)-C(8)-H(8A)	109.8
C(7)-C(8)-H(8A)	109.8
N(2)-C(8)-H(8B)	109.8
C(7)-C(8)-H(8B)	109.8
H(8A)-C(8)-H(8B)	108.2
O(1)-C(9)-Re(1)	178.7(5)
O(2)-C(10)-Re(1)	178.0(4)
O(3)-C(11)-Re(1)	177.5(4)
O(5)-C(12)-O(4)	128.7(6)
O(5)-C(12)-C(13)	119.2(6)
O(4)-C(12)-C(13)	112.1(6)
F(3)-C(13)-F(1)	105.6(8)
F(3)-C(13)-F(2)	99.2(7)
F(1)-C(13)-F(2)	105.7(7)
F(3)-C(13)-C(12)	120.3(6)
F(1)-C(13)-C(12)	115.8(6)
F(2)-C(13)-C(12)	108.2(6)

References

1. Sheldrick, G. M. (2008) A short history of SHELX. *Acta Cryst*. A64, 112-122.
2. Barbour, L. J. (2001) X-Seed - A software tool for supramolecular crystallography. *J. Supramol. Chem. 1,* 189-191.

Bioconjugate Chemistry

Article

pubs.acs.org/bc

Functionalized Low-Density Lipoprotein Nanoparticles for in Vivo Enhancement of Atherosclerosis on Magnetic Resonance Images

Andrew N. Lowell,[†] Hui Qiao,[§] Ting Liu,[§] Takashi Ishikawa,[‡] Hualei Zhang,[§] Sean Oriana,[#] Miao Wang,[∥,⊥] Emanuela Ricciotti,[∥,⊥] Garret A. FitzGerald,[∥,⊥] Rong Zhou,*[,⊥,§] and Yoko Yamakoshi*[,§,#]

[†]Department of Chemistry, and [§]Molecular Imaging Laboratories, Department of Radiology, University of Pennsylvania, 231 South 34th Street, Philadelphia, Pennsylvania 19104-6323, United States

[‡]Paul-Scherrer Institute, CH-5232, Villigen, Switzerland

[∥]Department of Pharmacology and [⊥]Institute for Translational Medicine and Therapeutics (ITMAT), University of Pennsylvania, 3400 Civic Center Boulevard, Philadelphia, Pennsylvania 19104-6160, United States

[#]Laboratorium für Organische Chemie, ETH-Zürich, Wolfgang-Pauli-Strasse 10, CH-8093 Zürich, Switzerland

Supporting Information

ABSTRACT: To allow visualization of macrophage-rich and miniature-sized atheromas by magnetic resonance (MR) imaging, we have converted low-density lipoprotein (LDL) into MR-active nanoparticles via the intercalation of a 1,4,7,10-tetraazacyclodecane-1,4,7-triacetic acid (DO3A) derivative and the subsequent coordination reaction with Gd^{3+}. After careful removal of nonchelated Gd^{3+}, an MR-active LDL (Gd^{3+}-LDL) with a remarkably high payload of Gd^{3+} (in excess of 200 Gd^{3+} atoms per particle) and a high relaxivity (r_1 = 20.1 s^{-1} mM^{-1} per Gd^{3+} or 4040 s^{-1} mM^{-1} per LDL) was obtained. Dynamic light-scattering photon correlation spectroscopy (DLS) and cryo transmission electron microscope (cryoTEM) images showed that Gd^{3+}-LDL particles did not aggregate and remained of a similar size (25−30 nm) to native LDL. Intravenous injection of Gd^{3+}-LDL into an atherosclerotic mouse model (*ApoE*$^{-/-}$) resulted in an extremely high enhancement of the atheroma-bearing aortic walls at 48 h after injection. Free Gd^{3+} dissociation from Gd^{3+}-LDL was not detected over the imaging time window (96 h). Because autologous LDL can be isolated, modified, and returned to the same patient, our results suggest that MR-active LDL can potentially be used as a noninfectious and nonimmunogenic imaging probe for the enhancement of atheroplaques presumably via the uptake into macrophages inside the plaque.

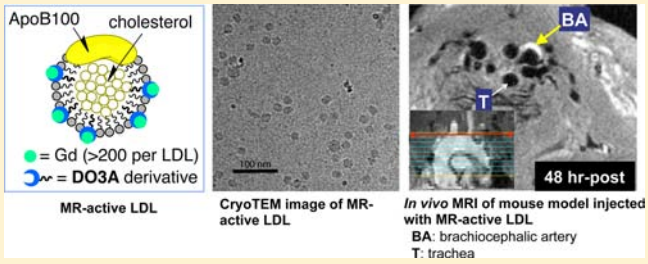

INTRODUCTION

The blockage of coronary and carotid arteries due to the growth or rupture of atherosclerotic plaques (atheromas) often leads to lethal syndromes such as heart attack and stroke, which are the leading causes of death worldwide. Magnetic resonance imaging (MRI), owing to its high soft tissue contrast and high spatial resolution, is well suited for visualizing atheroplaques harbored in the aortic wall in a noninvasive manner. While MR imaging of atheromas enriched with macrophages or other inflammatory effector cells has been attempted using contrast agents (CAs) with various nanoparticle scaffolds such as polymeric materials,[1−4] micelles or liposomes,[5−8] and high-density lipoprotein (HDL),[6,9−19] the potential of modifying naturally occurring low-density lipoprotein (LDL) nanoparticles for MR imaging of atheromas has not been assessed so far. The critical role of LDL in the formation and progression of atherosclerosis has been well established by epidemiological studies, which revealed a high correlation between the plasma LDL level and the chance of the patient to develop atherosclerosis or to die from coronary heart disease. In addition, the idea of infusing the patient's own LDL labeled with an MR-active probe, converting it into a nonimmunogenic targeting vehicle to visualize inflammatory atheroplaques, is a powerful example of personalized medicine.

The present study describes the resolution of a number of challenges that allowed us to realize a strong and discrete enhancement of submillimeter-size mouse atheromas on MR images. Most importantly, a high payload of MR contrast molecules (Gd^{3+}-chelate) per LDL particle was achieved. Toxic unbound Gd^{3+} were successfully eliminated to provide a good safety profile for these nanoparticles, and the modified LDL remained stable during the imaging time window (at least 96 h) without detectable dissociation of Gd^{3+} and maintained a size distribution similar to that of native LDL.

EXPERIMENTAL PROCEDURES

Synthesis of a DO3A Derivative for Intercalation into LDL.[20] DO3A−oleic acid conjugate **A** (1,4,7,10-tetraazacyclodecane-1,4,7-triacetic acid-oleic acid, DO3A-OA) was synthe-

Received: October 12, 2012
Published: October 18, 2012

 © 2012 American Chemical Society

sized as shown in Scheme 1 by the conjugation of oleic acid to *t*-butyl protected DO3A (**2**) via a diamine. Purification of the

Scheme 1. Synthesis of DO3A-OA (A)

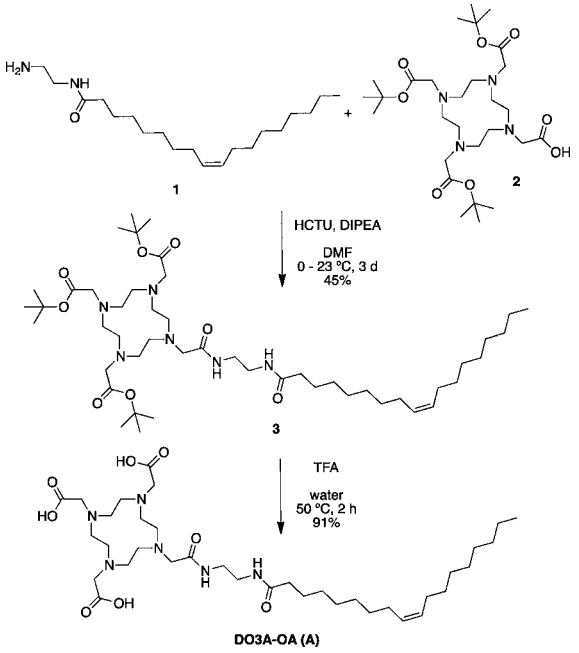

products and intermediates was carried out by HPLC (JASCO PU-2080 pump and UV-2077 plus UV−vis detector, JASCO Co., Tokyo, Japan) with a reversed-phase semipreparatory column (YMC R-ODS-10A 250 × 20 mm, YMC Co., Ltd., Kyoto, Japan). As **A** was not visible by UV−vis detection, all the fractions were collected from the semipreparative HPLC and analyzed by both an analytical HPLC (YMC R-ODS-10A 250 × 4.6 mm) equipped with a Nano Quantity Analyte Detector (NQAD, Quant Technology, Blaine, MN, USA) and ESI-MS (Waters SQD and Acuity UPLC, Waters Co., Milford, MA, USA). After purification, the purity of **A** was checked again by HPLC with a reversed-phase analytical column (YMC R-ODS-10A, 250 × 4.6 mm) and then was fully characterized by ^{1}H and ^{13}C NMR (Bruker Advance AVII-500 NMR spectrometer, Bruker, Billerica, MA, USA), HR-MS (Waters LCT Premier XE LC/MS system), and FT-IR (JASCO FT/IR-4100).

LDL. Human LDL (density 1.024−1.050 g/mL) was isolated from the fresh plasma of healthy normolipidemic donors by sequential density gradient ultracentrifugation in the laboratory of Dr. Lund-Katz at the Children's Hospital of Philadelphia[21] and was filtered (0.22 μm Millex GVdurapore PVDF membrane filter, Millipore, Billerica, MA, USA) and dialyzed (Spectra/Por4 dialysis tubing with a flat width of 25 mm and a MWCO of 12−14 kD, Spectrum Laboratories, Inc., Rancho Dominguez, CA, USA) against phosphate buffered saline, Ca^{2+} and Mg^{2+} free, (PBS(−)) at 4 °C for 20 h before use. The amount of LDL was estimated from its protein content as calculated by the Lowry assay (Peterson's modification, Sigma-Aldrich, St. Louis, MO, USA)[22,23] based on the assumption that only one copy of apoB-100 protein (MW 534 kD) presents per LDL nanoparticle.[24]

General Preparation of Gd^{3+}-LDL.[25] Compound **A** was dissolved in a minimal amount of DMSO (∼0.1 mL). Dialyzed LDL was added to this solution in a molar ratio of approximately 1:600 (LDL:**A**). The mixture was agitated at 37 °C for 4 h on a circular shaker (120 rpm), filtered (0.22 μm Millex), and dialyzed (Spectra/Por4) against PBS(−) at 4 °C for 16 h to remove unbound **A** (*STEP 1* in Figure 2). Gd^{3+} citrate solution (2.1 mM) was added to the LDL sample in a molar ratio of approximately 1400:1 Gd^{3+} to LDL and the mixture was agitated (120 rpm) at 37 °C for 4 h (*STEP 2* in Figure 2). Freshly prepared tropolone solution in PBS(−) (10 mM) was added in excess to the Gd^{3+}-treated LDL sample (*STEP 3* in Figure 2, 15 mol equiv of tropolone was used for each equivalent of Gd^{3+} used during *STEP 2*),[26,27] and the resulting mixture was agitated (4 °C, 120 rpm, 4 h). The precipitated Gd^{3+}-tropolone complex was removed by filtration (0.22 μm), and the filtrate was subsequently dialyzed against PBS(−) (4 °C, 120 rpm, 18 h).

DLS. The particle size of intact LDL or modified LDL was analyzed by dynamic light-scattering photon correlation spectroscopy (DLS, Zetasizer 3000HS, Malvern Instruments, Malvern, UK) on a spectrometer equipped with a 10 mW He−Ne laser operating at a fixed wavelength of 633 nm and a detector angle of 90°. The data, in the form of autocorrelation functions, were analyzed assuming that the particles were spherical and undergoing Brownian motion.

ICP-MS. The ICP-MS analysis of the Gd^{3+} content of functionalized LDL (ng of Gd^{3+} per mg of LDL sample) was carried out at the Pennsylvania Animal Diagnostic Laboratory System in New Bolton Center (Kennett Square, PA, USA).

CryoTEM.[28] An aliquot (3.5 μL) of the LDL or modified LDL specimen was mounted on holey carbon grids (Quantifoil Micro Tools GmbH, Jena, Germany) and frozen using a Vitrobot apparatus (FEI Co., Eindhoven, Netherlands). The grids were examined at liquid nitrogen temperature using a cryo-holder (626, Gatan, Inc., Pleasanton, CA, USA) and a Tecnai G2 F20 microscope (FEI Co.) equipped with a field emission gun and an energy filter (Tridem, Gatan, Inc.) operated at an accelerating voltage of 200 kV. The data were recorded by a 2k × 2k CCD camera (US1000, Gatan, Inc.) with an underfocus of 4−7 μm. Each image was recorded with a dose of ∼10 e^{-}/Å^{2}.

Relaxivity. The proton longitudinal relaxation rates ($1/T_1$) were measured on an mq60 minispec NMR Analyzer (Bruker, Inc., The Woodlands, TX, USA) at 60 MHz. The T_1 measurements were carried out in PBS(−) with an inversion−recovery pulse sequence using 10 to 20 inversion delay values. The r_1 relaxivity was calculated from the slope of a plot of $1/T_1$ versus Gd^{3+} concentration.

Animal Models. *ApoE*$^{-/-}$ mice and their wild-type controls (C57BL/6j) were purchased from Jackson Laboratory (Bar Harbor, ME, USA). The *ApoE*$^{-/-}$mice were fed a high fat diet (0.2% cholesterol, 21% saturated fat; formula TD 88137, Harlan Laboratories, Indianapolis, IN, USA) for 4−5 months to expedite the development of atheromas, while the C57BL/6j mice were on normal chow.

In Vivo MR Imaging. All the procedures were carried out in accordance with the in vivo animal protocols approved by the Institutional Animal Care and Use Committee at the University of Pennsylvania. Prior to the injection, the Gd^{3+}-LDL sample was concentrated in filter tubes (Amcon Ultra-4) by centrifugation (3000 rpm at 4 °C) to a suitable volume (≤0.5 mL) for tail vein injection into a mouse. No aggregation was detected after the centrifugation. Animals were positioned prone in a quadrature volume ^{1}H coil (i.d. = 3.5 cm, length = 8 cm), which was interfaced to a 9.4 T horizontal bore MR

spectrometer (DirectDrive, Varian, Palo Alto, CA). During imaging, the animal was sedated with 0.8−1% of isoflurane, and its vital signs (including ECG, respiration, and core temperature) were monitored. The rectal temperature was maintained at 36 °C by directing warm air into the magnet bore. "White Blood" (WB) images, where the blood signal in the aorta lumen is not suppressed, were acquired using a multislice gradient echo sequence (TR = 1 heart beat, about 120 ms, TE = 2.4 ms), while "Black Blood" (BB) images, where the blood signal is suppressed, were obtained using a multislice fast spin echo sequence (TR = 1000 ms, TE =10.4 ms, echo train length =1). For both WB and BB images, field of view (FOV) = 26 × 26 mm^2, matrix size = 256 × 192, and slice thickness = 0.5 mm. The percent of normalized signal enhancement, %NSE,[29,30] was measured for enhanced versus unenhanced artery walls on MR images.

RESULTS AND DISCUSSION

Synthesis of DO3A-OA (A) and Modification of LDL. To achieve a high payload of Gd^{3+}, we implemented a method where DO3A-OA (**A** in Scheme 1) was first intercalated into the lipid monolayer of LDL and then subjected to a coordination reaction with Gd^{3+}. This approach allowed higher yields in the initial intercalation step by taking advantage of the higher water-solubility of **A** as opposed to prechelated Gd**A**, which is poorly soluble, to provide LDL nanoparticles with a remarkably high Gd^{3+} payload. The synthesis of **A** is described in the Methods section and is shown in Scheme 1.[31] The DO3A moiety was chosen as the ligand due to its higher affinity for Gd^{3+} compared to other common Gd^{3+}-ligands such as diethylenetriaminepentaacetic acid (DTPA, Figure 1) while providing the same level of contrast enhancement.[32,33]

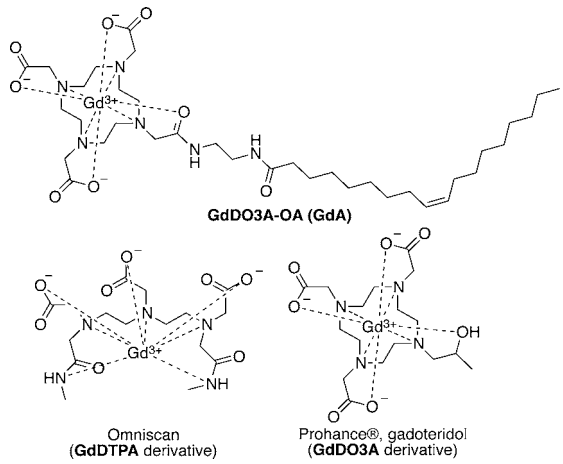

Figure 1. Structures of **GdDO3A-OA** (**GdA**) designed for LDL modification in this study and MRI contrast agents (Omniscan and Prohance) approved by the FDA for routine clinical use.

The general scheme for infusing LDL nanoparticles with Gd^{3+} and the optimizations used to achieve a high loading are shown in Table 1. After the intercalation of **A** into LDL (*STEP 1*), the Gd^{3+} coordination was carried out by exposing the LDL-**A** particles to Gd^{3+} citrate (*STEP 2*).

Because a substantial amount of the potentially toxic Gd^{3+} was expected to bind nonspecifically on the surface of LDL without chelating to the DO3A moiety, its efficient removal was investigated in detail (*STEP 3* of Table 1). For the removal of such nonspecifically bound Gd^{3+}, a tropolone precipitation protocol was used (scheme in a footnote of Table 1). Tropolone is known to strongly coordinate Gd^{3+} resulting in an insoluble precipitate that can be removed by filtration.[27,34] As a control, intact LDL without **A** was subjected to the same Gd^{3+} chelation conditions with Gd^{3+} citrate as were used for LDL-**A** (*STEP 2*) and subsequently treated with tropolone (*STEP 3*). Initial reaction conditions with a short incubation interval (1 h) and a diluted condition in *STEP 2* did not remove the nonspecifically bound Gd^{3+} from the surface of LDL efficiently (68 atoms of Gd^{3+} per LDL were still remaining, Table 1 run 1). By extending the reaction time (4 h) and reducing the reaction volume (1.5 mL), efficient removal could be achieved (only 2 atoms of Gd^{3+} per LDL remained, Table 1 run 3). Application of these optimized conditions to LDL-**A** resulted in a significantly higher Gd^{3+} loading (20 atoms per LDL, Table 1 run 4) showing that Gd^{3+} specifically bound to the DO3A moiety was retained by the LDL.

Further efforts to increase the payload of Gd^{3+} per LDL were carried out by increasing equivalents of **A** and Gd^{3+} citrate in *STEPs 1* and *2*, respectively, and provided a significantly higher loading rate (210 Gd^{3+} per LDL, Table 1 run 5). A control reaction with intact LDL confirmed that the tropolone treatment remained effective at these higher Gd^{3+} condition (2 Gd^{3+} per LDL, run 6). This high payload of Gd^{3+} per LDL is a 40-fold increase compared to our preliminary study where one-step modification of LDL with premade Gd**A** led to only 5 Gd^{3+} per LDL due to the lower solubility of Gd**A**.[29]

Characterization of Gd^{3+}-LDL by DLS, CryoTEM, and Relaxivity Measurements. Because the aggregation of particles affects their availability to target tissues, LDL particle morphology before and after modification was carefully examined. Dynamic light-scattering photon correlation spectroscopy (DLS) and single particle observation using a cryo transmission electron microscope (cryoTEM) were used to analyze the particle diameter distribution. DLS showed that, when compared to intact LDL (mean 25 nm, width 13 nm, Figure 2c), Gd^{3+}-LDL remained in the similar size (mean 28 nm, width 16 nm, Figure 2a) and did not significantly aggregate through the modification. This result was consistent with cryoTEM images of Gd^{3+}-LDL and intact LDL (Figure 2b,d) and suggested that Gd^{3+}-LDL could be used for tail vein injection in mice without causing adverse effects.

The proton longitudinal relaxation rate ($1/T_1$) of Gd^{3+}-LDL nanoparticle was measured at 60 MHz (Table 2). The r_1 relaxivity of Gd^{3+}-LDL (200 Gd^{3+} per particle) was 20.2 s^{-1} mM^{-1} per Gd^{3+} (4040 s^{-1} mM^{-1} per particle), which is much higher than small molecule contrast agent Prohance (3.77 s^{-1} mM^{-1} per Gd^{3+} at 60 MHz[35]). Gd^{3+}-LDL with lower loadings (40 Gd^{3+} per particle) gave a relaxivity per Gd^{3+} of 12.1 s^{-1} mM^{-1}. The higher relaxivity of Gd^{3+}-LDL with 200 Gd^{3+} per particle could result from a slower tumbling rate of the labeled LDL.

Stability of Gd^{3+}-LDL Particles. The stability of the LDL nanoparticles was analyzed by observing changes in particle morphology and the dissociation of free Gd^{3+} by DLS and ICP-MS measurements, respectively. The Gd^{3+}-LDL nanoparticles were kept at 4 or −20 °C in PBS(−) for a variable time period and then analyzed by DLS. The particle size remained regular for approximately 6 days at 4 °C. After 10−18 days of storage at 4 °C, however, the particle size gradually increased from the intact size of 20−30 nm to >40 nm (mean) with the appearance of a small, broad distribution around 150−200

dx.doi.org/10.1021/bc300561e | *Bioconjugate Chem.* 2012, 23, 2313−2319

Table 1. Reaction Conditions for the Preparation of MR-Active LDL Nanoparticles by the Intercalation of A (*STEP 1*), Chelation with Gd^{3+} (*STEP 2*), and Removal of Uncoordinated Gd^{3+} with Tropolone (*STEP3*)

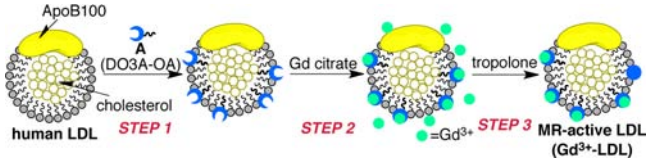

	STEP 1		*STEP 2*	*STEP 3*[b]			
				reaction conditions with tropolone			
run	initial amount of LDL [mmol][a]	mol. ratio of **A** [eq. to LDL]	mol. ratio of Gd^{3+} [eq. to LDL]	time [h]	rection volume [mL]	Gd^{3+} atoms per LDL particle[c]	DLS mean (SE) [nm]
1	2.25×10^{-6}	0	156	1	4.5	68	31.3 (25.5)
2	2.12×10^{-6}	0	189	4	5.0	20	24.9 (13.2)
3	2.12×10^{-6}	0	189	4	1.5	2	20.9 (17.5)
4	2.12×10^{-6}	123	189	4	1.5	20	28.0 (15.8)
5	7.42×10^{-5}	665	1401	4	60	210	26.3 (16.3)
6	1.48×10^{-6}	0	1401	4	1.2	2	23.8 (12.2)

[a]Estimated by Lowry test. [b]The 15 mol equivalents of tropolone were added to each Gd^{3+} used in *STEP2*. Reaction was carried out at 4 °C. Reaction scheme of Gd^{3+} and tropolone:

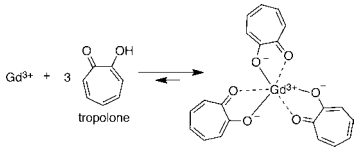

[c]Obtained by ICP-MS analysis.

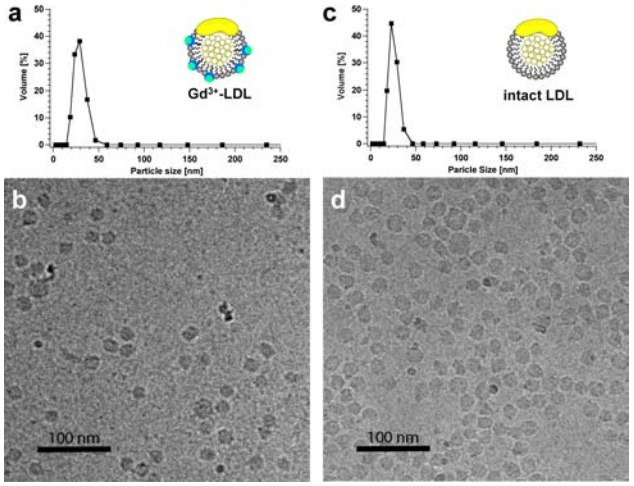

Figure 2. DLS and cryoTEM images of Gd^{3+}-LDL (a and b) and intact LDL (c and d) nanoparticles. Both data sets indicate that both the modified and intact LDL nanoparticles exist as dispersed single particles in buffer (the small dark spots in cryoTEM images are ice crystals generated during sample preparation).

nm to indicate that aggregation was starting (Figure S3 in the SI). The frozen samples, however, did not show significant aggregation after 34 days stored at −20 °C (Figure S3f in the SI).

A Gd^{3+} leaching experiment was carried out over the same time window (96 h) within which the MR imaging was performed by dialyzing an aliquot of Gd^{3+}-LDL against PBS(−) at 4 °C. Quantification by ICP-MS of the amount of Gd^{3+} in the sample inside the dialysis tube showed no significant change over 96 h (Table S5 in the SI). The Gd^{3+} level of the sample outside the dialysis tube at 96 h was below ICP-MS detection limit, also indicating that no Gd^{3+} dissociated from the particles over the 96 h period.

Table 2. Comparison of the Relaxivity of Gd^{3+}-LDL and Gadoteridol[a]

contrast agents	r_1 relaxivity per Gd^{3+} [mM^{-1} s^{-1}]	r_1 relaxivity per particle [mM^{-1} s^{-1}]
Gd^{3+}-LDL (40:1)	12.1	484
Gd^{3+}-LDL (200:1)	20.2	4040
Gadoteridol (Prohance)	3.8	–

[a]Relaxivity measurements were carried out at 60 MHz and at room temperature. The numbers 40:1 and 200:1 indicate the molar ratios of Gd^{3+} to LDL, which were calculated from the results of ICP-MS analysis and the Lowry assay, respectively.

In Vivo MRI of Atheroma in Mice Receiving Gd^{3+}-LDL. In order to assess the utility of Gd^{3+}-LDL for the enhancement of atheromas, in vivo studies were carried out in a murine atherosclerosis model and its control. *ApoE*$^{-/-}$ mice and their wild-type controls (C57BL/6j) weighing 20−42 g were injected with Gd^{3+}-LDL at Gd^{3+} doses of 0.019−0.055 mmol/kg via the tail vein. A serial in vivo MRI was performed on *ApoE*$^{-/-}$ and C57BL/6j mice pre- and 24−96 h post-Gd^{3+}-LDL injection. Because the animals were allowed to recover from anesthesia during the interval of the pre- and postinjection imaging sessions, we relied on the unique anatomy of the thoracic arteries for the comparison of pre- and postinjection images. Specifically, the thoracic aorta, including the aortic arch and its three branches, was visualized on coronal scout images as shown in the inset of Figure 3a−c. The orientation of these vessels was matched on the pre- and postinjection images to ensure that the identical plaque region was compared. On the basis of the scout images, multiple axial images were acquired in

dx.doi.org/10.1021/bc300561e | *Bioconjugate Chem.* 2012, 23, 2313−2319

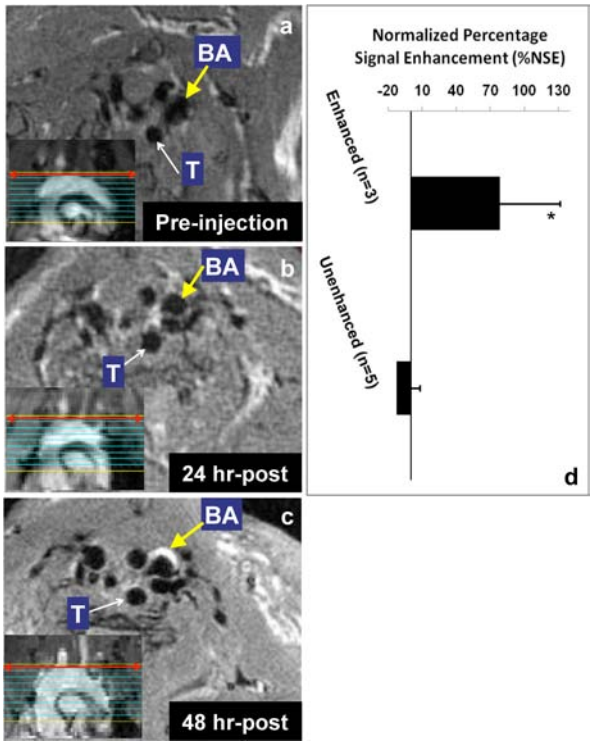

Figure 3. (a–c) In vivo MR images of an atheroma in the artery of an $ApoE^{-/-}$ mouse taken preinjection (a) and 24 h (b) and 48 h after injection (c) of Gd^{3+}-LDL (T = trachea, BA = brachiocephalic artery). The inset images in a–c are scout images in the coronal view where the thoracic aorta and its three branches are clearly shown; the branch on the left is the BA. The red line in the scout images indicates the position of the axial image shown in the same panel. (d) Signal enhancement estimated from MR images by the formula below using the chest muscle as a reference (p = 0.01 comparing enhanced versus unenhanced arteries by the Student's t-test). %NSE =100% × $((I_{wallpost}/I_{musclepost})/(I_{wallpre}/I_{musclepre}) - 1)$. $I_{wallpre}$ and $I_{wallpost}$ are signal intensity from the artery wall pre- and 48 h postinjection, respectively. $I_{musclepre}$ and $I_{musclepost}$ are defined similarly.

"white blood" (WB) or "black blood" (BB) fashion. BB images, in which the blood signals were suppressed, can better visualize the artery wall. As shown in Figure 3a–c, a remarkably intense enhancement of the wall of the brachiocephalic artery (BA) was detected at 48 h postinjection, whereas images obtained at 24 h show little enhancement compared to the preinjection image (the entire data sets of preinjection, 24 h and 48 h postinjectin for the mouse shown in Figure 3 are provided in Figure S6 in the SI). Despite the limited volume of Gd^{3+}-LDL that can be administrated intravenously to a mouse (≤0.5 mL), the strong enhancement of miniature-sized murine atheromas was observed suggesting that the payload of Gd^{3+} and selective LDL accumulation into atheroma were sufficient for the enhancement. The normalized signal enhancement (%NSE is defined in the caption of Figure 3) suggests an excellent contrast between the enhanced and unenhanced artery walls on MR images of $ApoE^{-/-}$ mice. No significant enhancement was found on images obtained from control (C57BL/6j) mice (data not shown).

CONCLUSION

While LDL has been utilized as a cancer-targeting vehicle for the efficient delivery of anticancer drugs[36−38] and imaging probes[27,34,39−48] based on the overexpression of LDL receptors on many malignant cancers, the utility of this natural nanoparticle has not been reported for MR imaging of atheroplaques, especially those that are prone to rupture due to a high content of inflammatory cells such as macrophages. The MR-active LDL reported here carries a high payload of Gd^{3+} (>200 Gd^{3+} atoms per particle). The high relaxivity of the nanoparticle led to discrete enhancement of an aortic wall bearing atheroplaques on MR images. The efficient loading of Gd^{3+} has the following important consequences: (1) the dose of LDL that needs to be administered into animals (or patients) can be reduced while providing sufficient MRI enhancement; (2) highly efficient enhancement, which is necessary for visualizing lesions inside of the aorta wall, can be attained as demonstrated in the images of a minuscule murine atheroma. The LDL nanoparticles circulating in the blood of hyperlipidemia patients directly participates in the growth of atheroplaques because they are absorbed by macrophages residing in the plaque. Therefore, macrophages could be the specific cellular component of the atheroplaque that absorbs the Gd^{3+}-LDL nanoparticles, but further validation is needed. While the long-term safety of Gd^{3+}-LDL still needs to be demonstrated, we have shown that the particles did not aggregate and remained in the 20–30 nm size range. Importantly, leaching of toxic free Gd^{3+} from the particles was not detectable by ICP-MS. We conclude that human LDL can be converted into nontoxic, nonimmunogenic, and highly MR-active nanoparticles for the selective detection of atherosclerotic plaques by high-resolution MRI. This work lays the foundation for exploring a personalized medicine strategy by directing a patient's own LDL to the inflammatory effector cells in vulnerable atheroplaques.

ASSOCIATED CONTENT

Supporting Information

Details of the synthesis of probe **A**, particle preparation, and in vivo experiments. This material is available free of charge via the Internet at http://pubs.acs.org.

AUTHOR INFORMATION

Corresponding Author

*E-mail: yamakoshi@org.chem.ethz.ch; zhou@rad.upenn.edu.

Notes

The authors declare no competing financial interest.

ACKNOWLEDGMENTS

The authors thank Prof. Dr. Daniel Rader and Prof. Dr. Sissel Lund-Katz for their insightful discussions on modifying human LDL for imaging atherosclerosis, Dr. Hoon Choi and Prof. Dr. I-Wei Chen for their help with the dynamic light scattering measurements, Prof. Dr. Andrew Tsourkas for his assistance with the relaxation time measurements, and Prof. Dr. Jerry Glickson and Dr. Hui Li for their helpful discussions at the University of Pennsylvania. This study was supported in part by a Scientist Development Awards from the American Heart Association (No. 0930140N (Y.Y.)), the PRESTO program of the Japan Science and Technology Agency (Y.Y.), in part by Grant Number UL1RR024134 from the National Center for Research Resources of NIH, and in part by the Institute for Translational Medicine and Therapeutics (ITMAT) Transdisciplinary Program in Translational Medicine and Therapeutics of the University of Pennsylvania (R.Z.). The use of electron microscopy in EMEZ (EM Center) in ETH Zürich

and MRI in SAIF (Small Animal Imaging Facility) at the University of Pennsylvania are also acknowledged.

REFERENCES

(1) Aime, S., Botta, M., Geninatti Crich, S., Giovenzana, G., Palmisano, G., and Sisti, M. (1999) Novel paramagnetic macromolecular complexes derived from the linkage of a macrocyclic Gd(III) complex to polyamino acids through a squaric acid moiety. *Bioconjugate Chem. 10*, 192−199.

(2) Park, K., Hong, H. Y., Moon, H. J., Lee, B. H., Kim, I. S., Kwon, I. C., and Rhee, K. (2008) A new atherosclerotic lesion probe based on hydrophobically modified chitosan nanoparticles functionalized by the atherosclerotic plaque targeted peptides. *J. Controlled Release 128*, 217−223.

(3) Nahrendorf, M., Keliher, E., Marinelli, B., Waterman, P., Feruglio, P. F., Fexon, L., Pivovarov, M., Swirski, F. K., Pittet, M. J., Vinegoni, C., and Weissleder, R. (2010) Hybrid PET-optical imaging using targeted probes. *Proc. Natl. Acad. Sci. U. S. A. 107*, 7910−7915.

(4) Chan, J. M., Zhang, L., Tong, R., Ghosh, D., Gao, W., Liao, G., Yuet, K. P., Gray, D., Rhee, J. W., Cheng, J., Golomb, G., Libby, P., Langer, R., and Farokhzad, O. C. (2010) Spatiotemporal controlled delivery of nanoparticles to injured vasculature. *Proc. Natl. Acad. Sci. U. S. A. 107*, 2213−2218.

(5) Peters, D., Kastantin, M., Kotamraju, V. R., Karmali, P. P., Gujraty, K., Tirrell, M., and Ruoslahti, E. (2009) Targeting atherosclerosis by using modular, multifunctional micelles. *Proc. Natl. Acad. Sci. U. S. A. 106*, 9815−9819.

(6) Beilvert, A., Cormode, D. P., Chaubet, F., Briley-Saebo, K. C., Mani, V., Mulder, W. J., Vucic, E., Toussaint, J. F., Letourneur, D., and Fayad, Z. A. (2009) Tyrosine polyethylene glycol (PEG)-micelle magnetic resonance contrast agent for the detection of lipid rich areas in atherosclerotic plaque. *Magn. Reson. Med. 62*, 1195−1201.

(7) Srinivasan, R., Marchant, R. E., and Gupta, A. S. (2010) In vitro and in vivo platelet targeting by cyclic RGD-modified liposomes. *J. Biomed. Mater. Res. A 93*, 1004−1015.

(8) van Tilborg, G. A., Vucic, E., Strijkers, G. J., Cormode, D. P., Mani, V., Skajaa, T., Reutelingsperger, C. P., Fayad, Z. A., Mulder, W. J., and Nicolay, K. (2010) Annexin A5-functionalized bimodal nanoparticles for MRI and fluorescence imaging of atherosclerotic plaques. *Bioconjugate Chem. 21*, 1794−1803.

(9) Briley-Saebo, K. C., Mulder, W. J., Mani, V., Hyafil, F., Amirbekian, V., Aguinaldo, J. G., Fisher, E. A., and Fayad, Z. A. (2007) Magnetic resonance imaging of vulnerable atherosclerotic plaques: current imaging strategies and molecular imaging probes. *J. Magn. Reson. Imaging 26*, 460−479.

(10) Sanz, J., and Fayad, Z. A. (2008) Imaging of atherosclerotic cardiovascular disease. *Nature 451*, 953−957.

(11) Douma, K., Prinzen, L., Slaaf, D. W., Reutelingsperger, C. P., Biessen, E. A., Hackeng, T. M., Post, M. J., and van Zandvoort, M. A. (2009) Nanoparticles for optical molecular imaging of atherosclerosis. *Small 5*, 544−557.

(12) Buxton, D. B. (2009) Current status of nanotechnology approaches for cardiovascular disease: a personal perspective. *Wiley Interdiscip. Rev. Nanomed. Nanobiotechnol. 1*, 149−155.

(13) Frias, J. C., Williams, K. J., Fisher, E. A., and Fayad, Z. A. (2004) Recombinant HDL-like nanoparticles: a specific contrast agent for MRI of atherosclerotic plaques. *J. Am. Chem. Soc. 126*, 16316−16317.

(14) Cormode, D. P., Briley-Saebo, K. C., Mulder, W. J., Aguinaldo, J. G., Barazza, A., Ma, Y., Fisher, E. A., and Fayad, Z. A. (2008) An ApoA-I mimetic peptide high-density-lipoprotein-based MRI contrast agent for atherosclerotic plaque composition detection. *Small 4*, 1437−1444.

(15) Chen, W., Vucic, E., Leupold, E., Mulder, W. J., Cormode, D. P., Briley-Saebo, K. C., Barazza, A., Fisher, E. A., Dathe, M., and Fayad, Z. A. (2008) Incorporation of an apoE-derived lipopeptide in high-density lipoprotein MRI contrast agents for enhanced imaging of macrophages in atherosclerosis. *Contrast Media Mol. Imaging 3*, 233−242.

(16) Cormode, D. P., Chandrasekar, R., Delshad, A., Briley-Saebo, K. C., Calcagno, C., Barazza, A., Mulder, W. J., Fisher, E. A., and Fayad, Z. A. (2009) Comparison of synthetic high density lipoprotein (HDL) contrast agents for MR imaging of atherosclerosis. *Bioconjugate Chem. 20*, 937−943.

(17) Skajaa, T., Zhao, Y., van den Heuvel, D. J., Gerritsen, H. C., Cormode, D. P., Koole, R., van Schooneveld, M. M., Post, J. A., Fisher, E. A., Fayad, Z. A., de Mello Donega, C., Meijerink, A., and Mulder, W. J. (2010) Quantum dot and Cy5.5 labeled nanoparticles to investigate lipoprotein biointeractions via Forster resonance energy transfer. *Nano Lett. 10*, 5131−5138.

(18) Thaxton, C. S., Daniel, W. L., Giljohann, D. A., Thomas, A. D., and Mirkin, C. A. (2009) Templated spherical high density lipoprotein nanoparticles. *J. Am. Chem. Soc. 131*, 1384−1385.

(19) Mackiewicz, M. R., Hodges, H. L., and Reed, S. M. (2010) C-reactive protein induced rearrangement of phosphatidylcholine on nanoparticle mimics of lipoprotein particles. *J. Phys. Chem. B 114*, 5556−5562.

(20) The detail of the synthesis and spectroscopic data are provided in the SI.

(21) Lund-Katz, S., Laplaud, P. M., Phillips, M. C., and Chapman, M. J. (1998) Apolipoprotein B-100 conformation and particle surface charge in human LDL subspecies: implication for LDL receptor interaction. *Biochemistry 37*, 12867−12874.

(22) Lowry, O. H., Rosebrough, N. J., Farr, A. L., and Randall, R. J. (1951) Protein measurement with the Folin phenol reagent. *J. Biol. Chem. 193*, 265−275.

(23) Peterson, G. L. (1977) A simplification of the protein assay method of Lowry et al. which is more generally applicable. *Anal. Biochem. 83*, 346−356.

(24) Protein content values were 1.9−3.8 mg/mL.

(25) Details are described in the SI.

(26) Tropolone concentration for removal of Gd3+ from the nanoparticle solution was optimized as shown in Table S3 of SI.

(27) Jasanada, F., Urizzi, P., Souchard, J. P., Le Gaillard, F., Favre, G., and Nepveu, F. (1996) Indium-111 labeling of low density lipoproteins with the DTPA-bis(stearylamide): evaluation as a potential radiopharmaceutical for tumor localization. *Bioconjugate Chem. 7*, 72−81.

(28) Ishikawa, T., Sakakibara, H., and Oiwa, K. (2007) The architecture of outer dynein arms in situ. *J. Mol. Biol. 368*, 1249−1258.

(29) Yamakoshi, Y., Qiao, H., Lowell, A. N., Woods, M., Paulose, B., Nakao, Y., Zhang, H. L., Liu, T., Lund-Katz, S., and Zhou, R. (2011) LDL-based nanoparticles for contrast enhanced MRI of atheroplaques in mouse models. *Chem. Commun. 47*, 8835−8837.

(30) van Bochove, G. S., Paulis, L. E. M., Segers, D., Mulder, W. J. M., Krams, R., Nicolay, K., and Strijkers, G. J. (2011) Contrast enhancement by differently sized paramagnetic MRI contrast agents in mice with two phenotypes of atherosclerotic plaque. *Contrast Media Mol. Imaging 6*, 35−45.

(31) The detailed synthetic procedure is described in SI.

(32) Magerstadt, M., Gansow, O. A., Brechbiel, M. W., Colcher, D., Baltzer, L., Knop, R. H., Girton, M. E., and Naegele, M. (1986) Gd(DOTA): an alternative to Gd(DTPA) as a T1,2 relaxation agent for NMR imaging or spectroscopy. *Magn. Reson. Med. 3*, 808−812.

(33) Nwe, K., Bernardo, M., Regino, C. A., Williams, M., and Brechbiel, M. W. (2010) Comparison of MRI properties between derivatized DTPA and DOTA gadolinium-dendrimer conjugates. *Bioorg. Med. Chem. 18*, 5925−5931.

(34) Corbin, I. R., Li, H., Chen, J., Lund-Katz, S., Zhou, R., Glickson, J. D., and Zheng, G. (2006) Low-density lipoprotein nanoparticles as magnetic resonance imaging contrast agents. *Neoplasia 8*, 488−498.

(35) Mastarone, D. J., Harrison, V. S., Eckermann, A. L., Parigi, G., Luchinat, C., and Meade, T. J. (2011) A modular system for the synthesis of multiplexed magnetic resonance probes. *J. Am. Chem. Soc. 133*, 5329−5337.

(36) Firestone, R. A. (1994) Low-density-lipoprotein as a vehicle for targeting antitumor compounds to cancer-cells. *Bioconjugate Chem. 5*, 105−113.

(37) Zheng, G., Li, H., Yang, K., Blessington, D., Licha, K., Lund-Katz, S., Chance, B., and Glickson, J. D. (2002) Tricarbocyanine cholesteryl laurates labeled LDL: new near infrared fluorescent probes (NIRFs) for monitoring tumors and gene therapy of familial hypercholesterolemia. *Bioorg. Med. Chem. Lett. 12*, 1485−1488.
(38) Nikanjam, M., Gibbs, A. R., Hunt, C. A., Budinger, T. F., and Forte, T. M. (2007) Synthetic nano-LDL with paclitaxel oleate as a targeted drug delivery vehicle for glioblastoma multiforme. *J. Controlled Release 124*, 163−171.
(39) Zheng, G., Li, H., Zhang, M., Lund-Katz, S., Chance, B., and Glickson, J. D. (2002) Low-density lipoprotein reconstituted by pyropheophorbide cholesteryl oleate as target-specific photosensitizer. *Bioconjugate Chem. 13*, 392−396.
(40) Li, H., Zhang, Z., Blessington, D., Nelson, D. S., Zhou, R., Lund-Katz, S., Chance, B., Glickson, J. D., and Zheng, G. (2004) Carbocyanine labeled LDL for optical imaging of tumors. *Acad. Radiol. 11*, 669−677.
(41) Zheng, G., Chen, J., Li, H., and Glickson, J. D. (2005) Rerouting lipoprotein nanoparticles to selected alternate receptors for the targeted delivery of cancer diagnostic and therapeutic agents. *Proc. Natl. Acad. Sci. U. S. A. 102*, 17757−17762.
(42) Li, H., Marotta, D. E., Kim, S., Busch, T. M., Wileyto, E. P., and Zheng, G. (2005) High payload delivery of optical imaging and photodynamic therapy agents to tumors using phthalocyanine-reconstituted low-density lipoprotein nanoparticles. *J. Biomed. Opt. 10*, 41203.
(43) Wu, S. P., Lee, I., Ghoroghchian, P. P., Frail, P. R., Zheng, G., Glickson, J. D., and Therien, M. J. (2005) Near-infrared optical imaging of B16 melanoma cells via low-density lipoprotein-mediated uptake and delivery of high emission dipole strength tris-[(porphinato)zinc(II)] fluorophores. *Bioconjugate Chem. 16*, 542−550.
(44) Chen, J., Corbin, I. R., Li, H., Cao, W., Glickson, J. D., and Zheng, G. (2007) Ligand conjugated low-density lipoprotein nanoparticles for enhanced optical cancer imaging in vivo. *J. Am. Chem. Soc. 129*, 5798−5799.
(45) Corbin, I. R., and Zheng, G. (2007) Mimicking nature's nanocarrier: synthetic low-density lipoprotein-like nanoparticles for cancer-drug delivery. *Nanomedicine (Lond.) 2*, 375−380.
(46) Li, H., Gray, B. D., Corbin, I., Lebherz, C., Choi, H., Lund-Katz, S., Wilson, J. M., Glickson, J. D., and Zhou, R. (2004) MR and fluorescent imaging of low-density lipoprotein receptors. *Acad. Radiol. 11*, 1251−1259.
(47) Crich, S. G., Lanzardo, S., Alberti, D., Belfiore, S., Ciampa, A., Giovenzana, G. B., Lovazzano, C., Pagliarin, R., and Aime, S. (2007) Magnetic resonance imaging detection of tumor cells by targeting low-density lipoprotein receptors with Gd-loaded low-density lipoprotein particles. *Neoplasia 9*, 1046−1056.
(48) Geninatti-Crich, S., Alberti, D., Szabo, I., Deagostino, A., Toppino, A., Barge, A., Ballarini, F., Bortolussi, S., Bruschi, P., Protti, N., Stella, S., Altieri, S., Venturello, P., and Aime, S. (2011) MRI-guided neutron capture therapy by use of a dual gadolinium/boron agent targeted at tumour cells through upregulated low-density lipoprotein transporters. *Chem.—Eur. J. 17*, 8479−8486.

Functionalized Low-Density Lipoprotein Nanoparticles for *in vivo* Enhancement of Atherosclerosis on Magnetic Resonance Images

Supporting information

Andrew N. Lowell,[†] Hui Qiao,[§] Ting Liu,[§] Takashi Ishikawa,[∞] Hualei Zhang,[§] Sean Oriana,[#] Miao Wang,[Ω‡] Emanuela Ricciotti,[Ω,‡] Garret A. FitzGerald,[Ω‡] Rong Zhou,[‡§] and Yoko Yamakoshi*[§#]*

[†]Department of Chemistry, University of Pennsylvania, 231 South 34th Street, Philadelphia PA19104-6323 USA, [§]Molecular Imaging Laboratories, Department of Radiology, University of Pennsylvania, 231 South 34th Street, Philadelphia PA19104-6323 USA, [∞] Paul-Scherer Institute, CH5232, Villigen Switzerland, [Ω]Department of Pharmacology, University of Pennsylvania, [‡]Institute for Translational Medicine and Therapeutics (ITMAT), University of Pennsylvania, 421 Curie Boulevard, Philadelphia PA19104-6160 USA, [#]Laboratorium für Organische Chemie, ETH-Zürich, Wolfgang-Pauli-Strasse 10, CH8093 Zürich, Switzerland
zhou@rad.upenn.edu, yamakoshi@org.chem.ethz.ch

1. Synthesis and purification of DO3A-OA

Scheme S1. Synthesis of DO3A-OA (**A**).

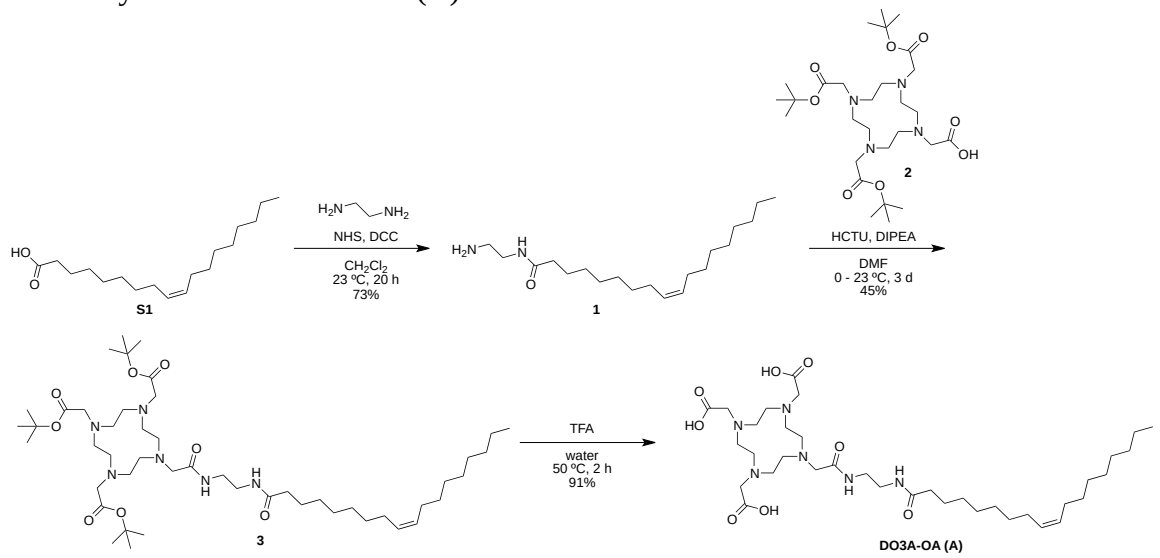

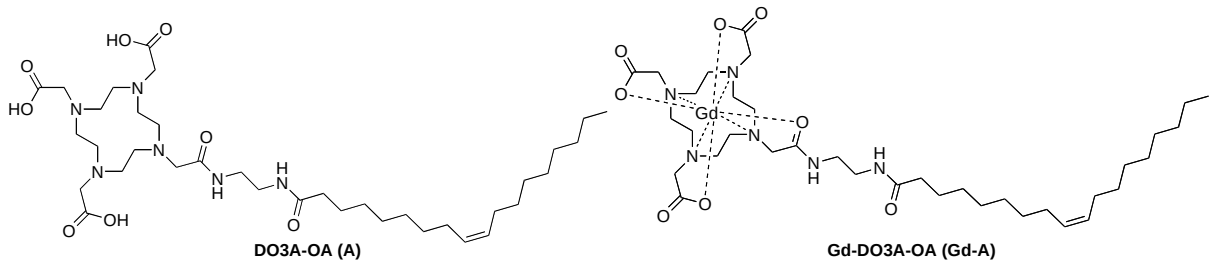

Figure S1. Structures of DO3A-OA (**A**) and GdDO3A-OA (**GdA**).

Octadec-9-enoic acid (2-amino-ethyl)-amide (1). To a stirring solution of oleic acid (1.00 g, 3.54 mmol) and *N*-hydroxysuccinimide (0.415 g, 3.61 mmol) in CH_2Cl_2 (50 mL) was added DCC (0.743 g, 3.60 mmol) in CH_2Cl_2 (10 mL) dropwise. After stirring for 3 h, the mixture was filtered to remove the solid urea and the filtrate was added dropwise to a stirring solution of ethylenediamine (5.00 mL, 74.8 mmol) dissolved in CH_2Cl_2 (50 mL). The resulting mixture was stirred for 20 h. The mixture was filtered to remove the white precipitate and concentrated to a colorless oil containing some white solid. This residue was diluted with acetonitrile (30 mL) and heated to boiling. The mixture was cooled overnight in a freezer. The resulting white solid was further diluted with cold acetonitrile (50 mL) and filtered. After rinsing with cold acetonitrile (50 mL), the filter cake was dried yielding **1** (0.839 g, 73%) as a white powder: mp 107-112 °C; ^{1}H NMR (500 MHz, $CDCl_3$) δ 6.07 (br s, 1H), 5.27-5.31 (m, 2H), 3.18-3.22 (m, 2H), 2.73-2.75 (m, 2H), 2.17 (br s, 2H), 2.08-2.11 (m, 2H), 1.95-1.98 (m, 4H), 1.53-1.55 (m, 2H), 1.23-1.26 (m, 20H), 0.82-0.85 (m, 3H); ^{13}C NMR (125 MHz, $CDCl_3$) δ 173.5, 130.3, 130.1, 42.0, 41.7, 37.0, 34.3, 32.3, 30.16, 30.13, 29.9, 29.70, 29.68, 29.6, 27.6, 26.1, 26.0, 25.4, 23.1, 14.3; HRMS (ESI) calcd for $C_{20}H_{41}N_2O$ (MH^+) 325.3219, found 325.3224.

{4,7-Bis-carboxymethyl-10-[(2-octadec-9-enoylamino-ethylcarbamoyl)-methyl]-1,4,7,10-tetraaza-cyclododec-1-yl}-acetic acid (DO3A-OA) (A). Compounds **2** (0.255 g, 0.445 mmol) and **1** (0.145 g, 0.447 mmol) were dissolved in DMF (25 mL) by heating. The mixture was cooled in an ice bath under N_2 and DIPEA (0.48 mL, 2.76 mmol) was added followed by HCTU (0.624 g, 1.51 mmol) in one portion. The mixture was allowed to warm to rt stirring eventually for 3 d. The mixture was diluted with CH_2Cl_2 (500 mL) and extracted with saturated $NaHCO_3$ (5 x 400 mL), water (400 mL), and brine (400 mL). The organic layer was dried with Na_2SO_4 and concentrated to a red oil with white solid. This residue was dissolved in methanol and loaded onto the column as a liquid through a Biotage C-18 loading disk and run on a 12 g C-18 column (75-100% MeOH/H_2O for 10 min, 100% MeOH for 30 min, 10 mL/min). The fractions were analyzed by LC/MS. The material eluted from 12 to 38 minutes. The product containing fractions were combined, concentrated, and lyophilized yielding **3** (0.176 g,

45%) as a waxy white solid. Compound **3** (0.0274 g, 0.0312 mmol) was dissolved in water (1.5 mL) and TFA (4.5 mL). The mixture was heated (oil bath, 50 °C) for 2 h. The mixture was concentrated to a yellow oil. The residue was dissolved in methanol and purified on a Biotage 12 g C-18 column (75-100% MeOH/H_2O for 15 min, 100% MeOH for 10 min, 10 mL/min). The fractions were analyzed by LC/MS. The product containing fractions (14-21 min) were combined, concentrated, and lyophilized to give **A** (0.0203 g, 91%) as fluffy white wax. ^{1}H NMR (500 MHz, CD_3OD) δ 5.33-5.35 (m, 2H), 3.73 (br s, 4H), 3.57 (br s, 2H) 3.34-3.42 (m, 8H), 3.38 (br s, 2H) 3.33-3.35 (m, 4H) 3.01-3.06 (m, 8H), 2.23-2.61 (m, 2H) 2.01-2.04 (m, 4H), 1.58-1.60 (m, 2H), 1.30-1.32 (m, 20H), 0.89-0.91 (m, 3H); ^{13}C NMR (125 MHz, CD_3OD) δ 176.9, 175.4, 172.6, 170.0, 131.0 (2C), 57.9, 57.6, 55.0, 52.8, 52.0, 50.4, 50.1, 40.3, 39.8, 37.4, 33.2, 31.04, 31.00, 30.8, 30.62, 30.61, 30.57, 30.50, 30.46, 28.33, 28.28, 27.1, 23.9, 14.6. Spectra are shown in below.

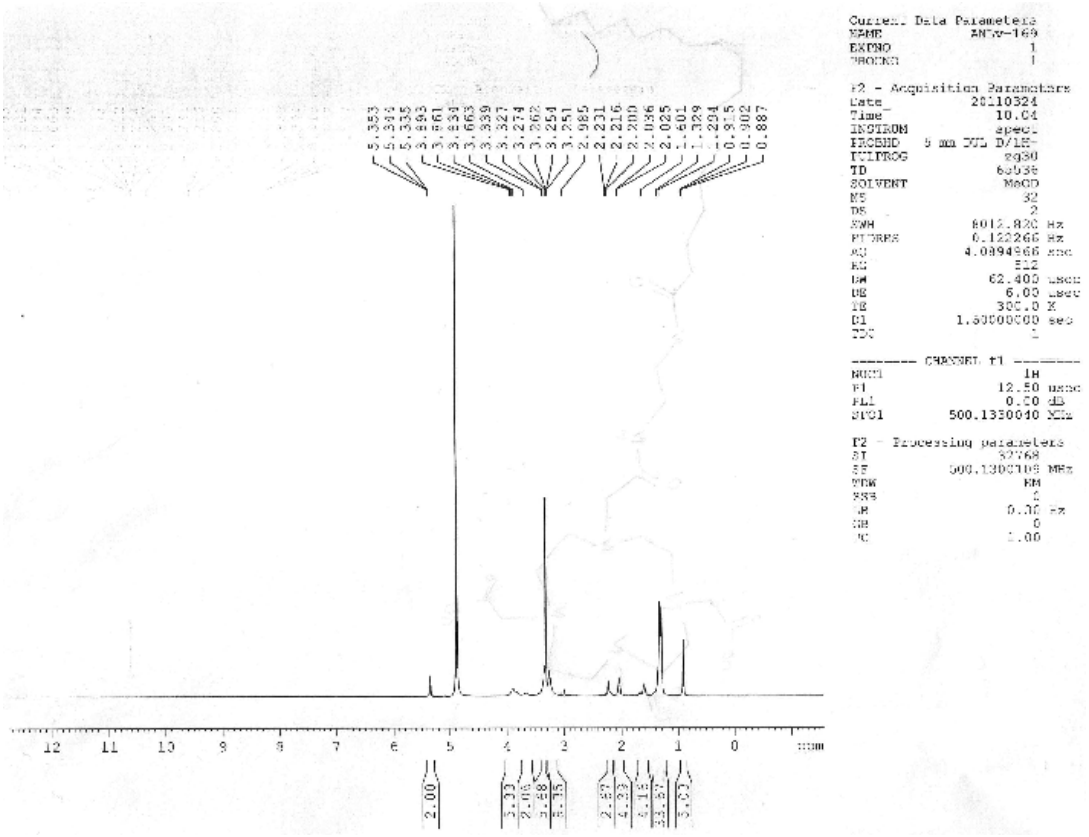

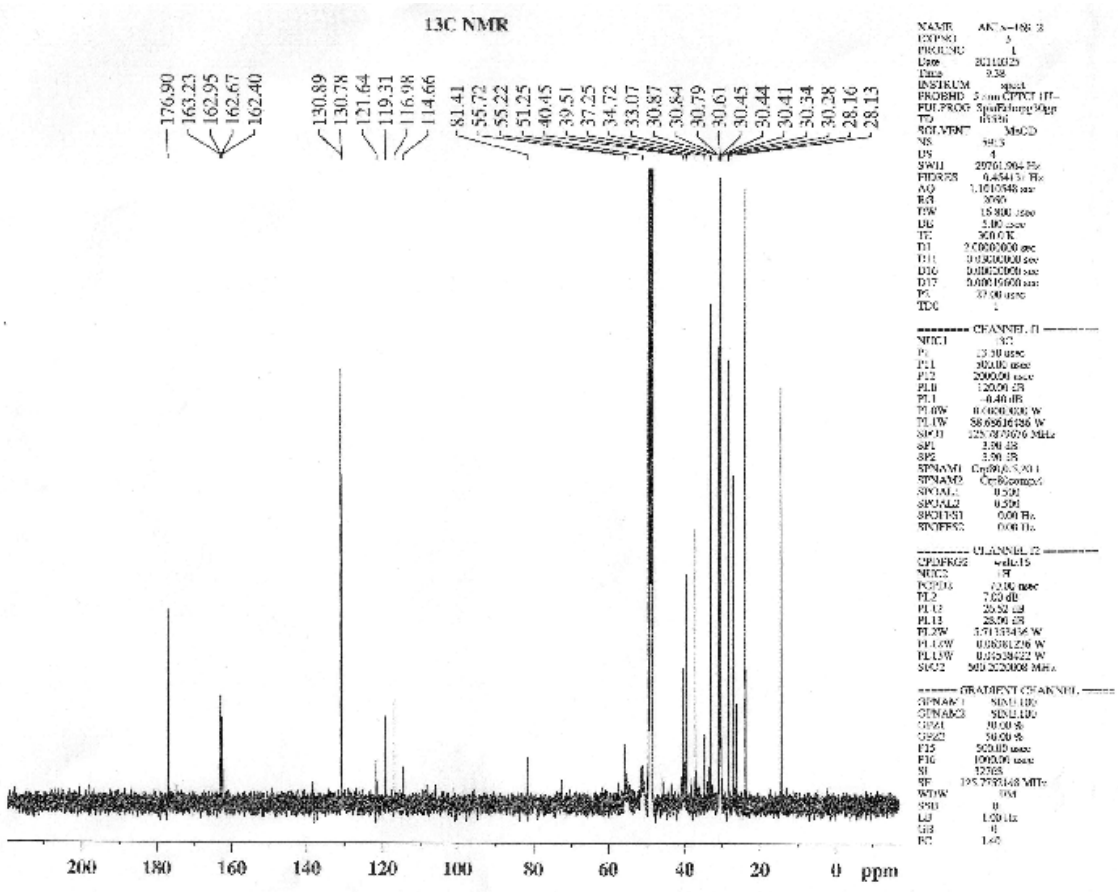
13C NMR
176.90
163.23
162.95
162.67
162.40
130.89
130.78
121.64
119.31
116.98
114.66
81.41
55.72
55.22
51.25
40.45
39.51
37.25
34.72
33.07
30.87
30.84
30.79
30.61
30.45
30.44
30.41
30.34
30.28
28.16
28.13
200
180
160
140
120
100
80
60
40
20
0
ppm

2. Preparation of MR-active LDL nanoparticles (Gd^{3+}-LDL)

An optimized Gd^{3+}-LDL preparation is described below. The protein content of the fresh LDL varied between batches.

2.1. Intercalation of DO3A into LDL

A dialysis tube was activated (microwaved 2 min in DI water (100 mL)) before use. The LDL sample (10 mL) was filtered through 0.22 micrometer Millex GV durapore PVDF Membrane filter units and dialyzed against 500 mL of PBS(–) (phosphate buffered saline, Ca^{2+} and Mg^{2+} free) (4 °C, 120 rpm) for 18 h. The dialyzed sample (11 mL) was taken from the dialysis tube and placed into a 50 mL centrifuge tube. The protein content was quantified by Lowry method to provide the value of 3.96 mg protein/mL (7.42×10^{-6} mmol/mL).

DO3A-OA (**A**, 35 mg) was dissolved in DMSO (0.2 mL) or a basic buffer and diluted with PBS (0.2 mL) before the addition of dialyzed LDL (10 mL, 3.96 mg/mL). The mixture was agitated (120 rpm) at 37 °C for 4 h and the solution was subsequently filtered (0.22 micrometer Millex GV durapore PVDF Membrane filter units) and dialyzed against PBS (500 mL) for 18 h (4 °C, 120 rpm). The resulting solution was transferred to a vial.

2.2. Chelating reaction of Gd^{3+} to DO3A-LDL

A bulk Gd^{3+}citrate solution was prepared by dissolving $GdCl_3 \cdot 6H_2O$ (0.502 g) in concentrated HCl (120 mL) and combining this solution with sodium citrate (2.45 g) in water (480 mL). The resulting solution was acidified to pH 7.4 using aqueous NaOH and aqueous HCl to give a final volume of 650 mL and a concentration of 0.00208 mmol/mL of Gd^{3+}.

To the DO3A-LDL (10 mL, 7.42×10^{-5} mmol protein), Gd^{3+}-citrate solution (50 mL, 0.104 mmol) was added and the mixture was agitated (120 rpm) at 37 °C for 4 h. Freshly prepared tropolone solution (156 mL, 10 mM) was added and the mixture was agitated for 4 h (4 °C, 120 rpm). The solution was subsequently filtered (0.2 micrometer PES 250 mL Nalgene filter unit) and dialyzed against PBS (1 L) for 16 h (4 °C, 120 rpm). The resulting mixture was filtered to provide a sample of 224 mL. A portion (4 mL) of the resulting solution was reserved for analysis and half of the remaining mixture (110 mL) was frozen for future use. The remaining 110 mL was filtered (0.2 micrometer PES 150 mL Nalgene filter unit), transferred to centrifuge tubes (Amican Ultra, Ultracel – 3K, Regenerated Cellulose 3,000 MWCO), and concentrated by centrifugation (Coulter Beckman Allegra X-15R centrifuge, SX4750 rotor, 3,000 rpm, 4 °C) to give approximately 0.3 mL of Gd^{3+}-LDL sample. This sample was transferred to an Ependorf tube via micropipette and used to inject two mice.

2.3. Preparation and characterization of LDL nanoparticles

Table S1. The effect of temperature and reaction time on the Gd^{3+} loading to **Gd^{3+}-LDL** through intercalation (*step 1)* and chelation reaction (*step 2*)

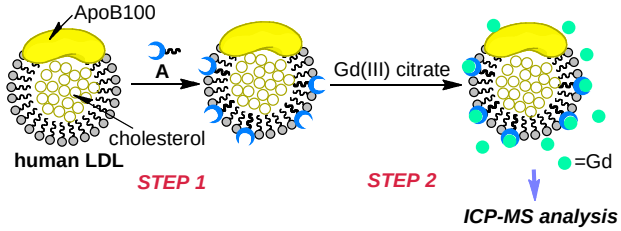

Run	*Step 1** Temp. (ºC)	*Step 2*** Temp. (ºC)	*Step 2*** Time (h)	Total Gd^{3+} binding on DO3A-LDL****
1	23	23	2	20
2	23	37	1	25
3	23	37	2	31
4	37	23	2	17
5	37	37	1	35
6	37	37	2	31

* The initial loading ratio of **A** to LDL was 116:1.
** The molecular ratio of Gd^{3+}-citrate was 178 eq. to LDL.
*** The value is per LDL particle. Gd^{3+} contents were calculated from the ICP-MS results and include both specifically and non-specifically bound Gd^{3+} on DO3A-LDL.

Table S2. The effect of tropolone concentration on the removal of free or non-specifically bound Gd^{3+}. The amount of tropolone was held constant at a ratio of 1:15 Gd:tropolone.

Run	Conc. of tropolone [mM]	Gd^{3+} amount			DLS mean (width) [nm]
		Gd^{3+} content	Conc. of protein [mM]	Number of Gd^{3+} atoms per LDL	
1	10	4.67 ppm	9.47×10^{-4}	31	31.6 (15)
2	20	1.92 ppm	4.69×10^{-4}	26	28.1 (21.3)
3	40	1.83 ppm	4.40×10^{-4}	26	30.9 (17.7)

* Determined by ICP-MS results and Lowry assay.

Table S3. The effect of increasing the amount of Gd^{3+} relative to **DO3A-OA**

Run	Initial molar ratio of LDL to DO3A-OA	Initial molar ratio of LDL to Gd^{3+}	Ratio of Gd^{3+} to DO3AOA subjected	Tropolone*	Gd^{3+} per LDL particle**	DLS mean (width) [nm]
1	1:830	1:857	1.0	+	40	33.2 (15.3)
2	1:830	1:1714	2.1	+	200	26.1 (17.5)
3	1:830	1:3428	4.1	+	168	22.2 (13.0)
4	1:665	1:1401	2.1	+	211	26.3 (16.3)
5	1:0	1:1401	–	+	2	23.8 (12.2)
6	1:0	1:2802	–	+	4	36.3 (14.7)
7	1:0	1:1401	–	–	242	aggregation

* 15 molar equivalents of tropolone were added for each equivalent of Gd^{3+}.

** The Gd^{3+} content was obtained by ICP-MS analysis and protein content by the Lowry test.

Table S4. Characterization of LDL nanoparticles by dynamic light scattering *

Particle type	DLS mean (SE) [nm]
Intact LDL (dialyzed)	24.7 (12.7)
DO3A-LDL	23.6 (12.3)
GdDO3A-LDL	25.4 (5.2): 97%, 104 (22.1): 3%
GdDO3A-LDL (dialyzed)	27.4 (13.8)
GdDO3A-LDL + tropolone	36.4 (14.6): 98%, 144.2 (57.9): 2%
GdDO3A-LDL + tropolone (filtered and dialyzed)	28.0 (15.8)

*Particle size distributions were compared by the relative volume size for each type of particle.

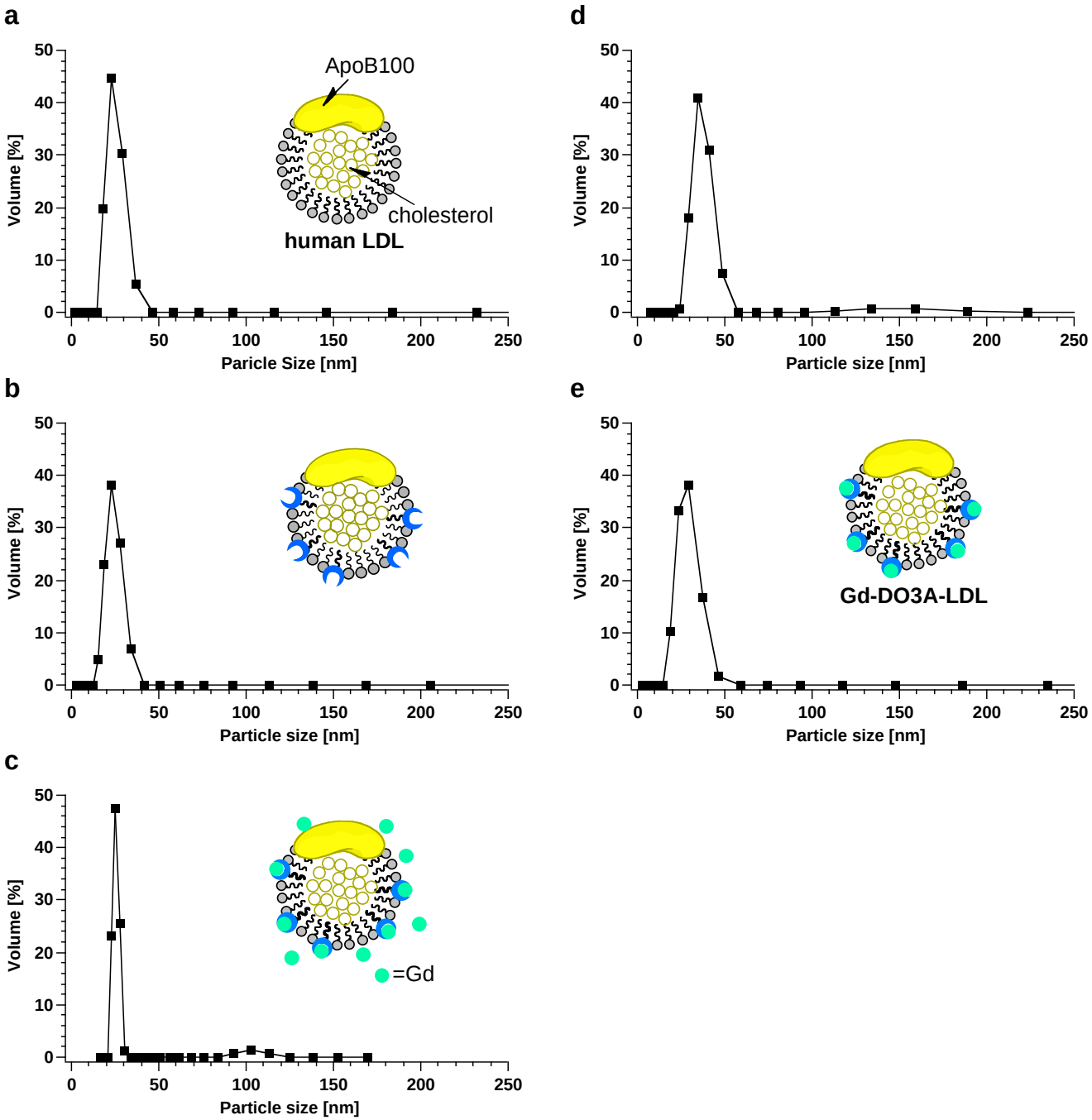

Figure S2. Distribution of particle size estimated by dynamic light scattering measurements by volume. (a) Intact LDL (mean 24.7 nm, width 12.7 nm), (b) LDL after addition of **A** (**DO3A-LDL**) (mean 23.6 nm, width 12.3 nm), (c) LDL with **A** after the reaction with Gd-citrate (**Gd^{3+}-LDL** with free Gd^{3+}) (peak 1: 97%, mean 25.4 nm, width 5.2 nm; peak 2: 3%, mean 104 nm, width 22.1 nm), (d) **Gd^{3+}-LDL** after reaction with toropolone (peak 1: 98%, mean 36.4 nm, width 14.6 nm; peak 2: 2%, mean 144.2 nm, width: 57.9 nm), (e) **Gd^{3+}-LDL** with tropolone after filtration and dialysis (mean 28.0 nm, width 15.8 nm).

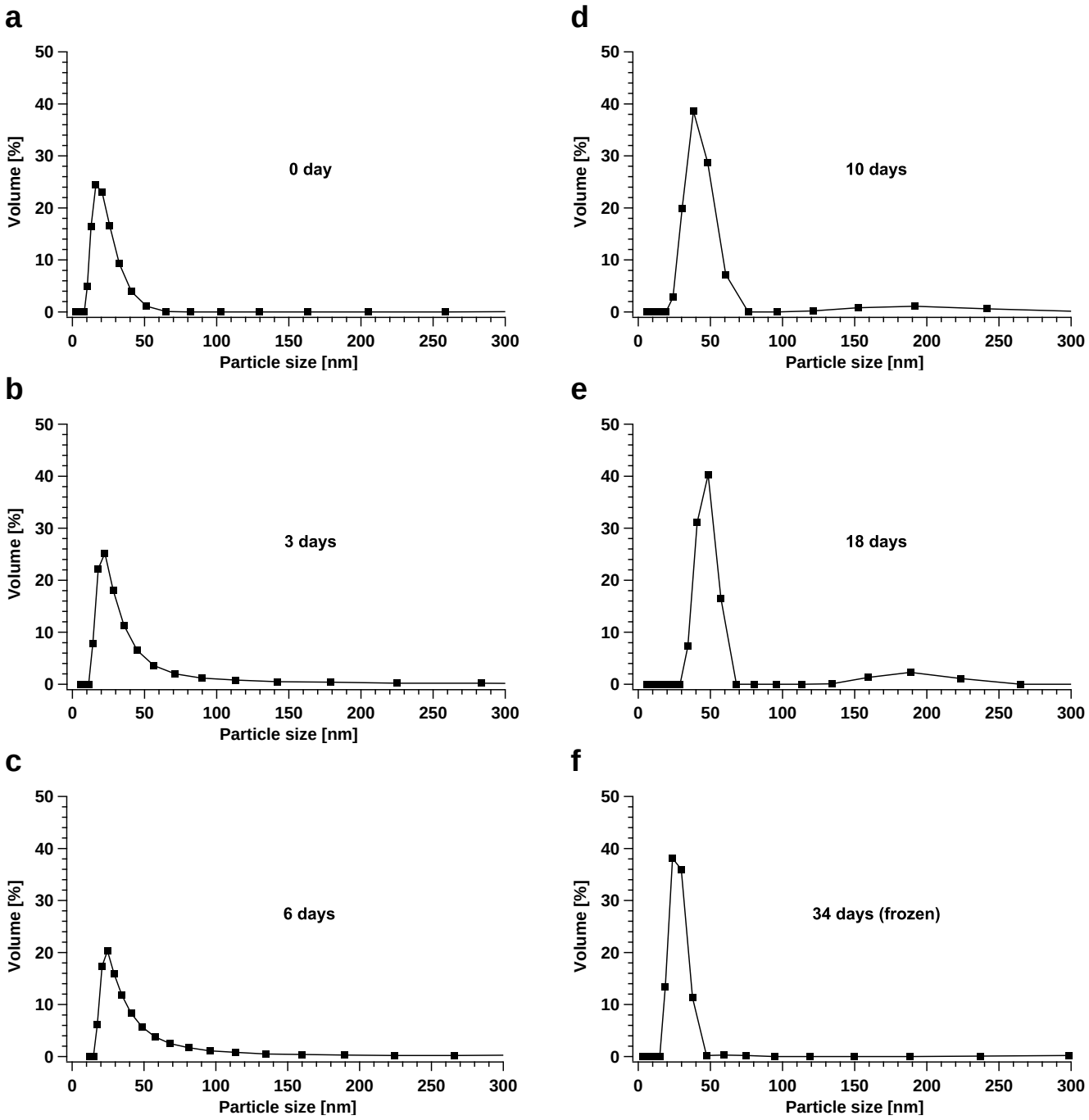

Figure S3. Change in particle size distribution during the storage of **Gd^{3+}-LDL** estimated by DLS measurements. (a) Freshly prepared sample, 20.9 (17.9) 100%; (b) stored at 4 ºC for 3 days, 31.2 (18.9) 100%; (c) for 6 days, 35.9 (18.8) 97%, 414.3 (174.9) 3%; (d) for 10 days, 40.8 (23.5) 97%, 193 (113.4) 3%; (e) for 18 days, 46.4 (18.1) 95%, 188.6 (65.4) 5%; (f) stored at -20 ºC for 34 days, 26.9 (15.2) 100%.

Table S5. Leaching studies on Gd^{3+}-LDL sample by dialysis against PBS(–) (4 °C, 120 rpm)*

Incubation time [h]	0	1	2	4	8	24	48	96
Gd^{3+} amount of the sample inside of dialysis bag [ppm]	5.54	5.62	5.57	5.56	5.58	5.42	5.14	4.92
Loading rate** (Gd^{3+} per LDL)	63	64	63	63	63	61	58	66

***** The leaching test was carried out by checking the decrease of Gd^{3+} amount in the sample inside of the dialysis tube measured by ICP-MS. For time points 0-48 the 0 h protein content was used; for 96 h the protein content was individually analyzed. The Gd^{3+} content of the PBS(–) outside of the dialysis bag after 96 h was below detection limit by ICP-MS analysis.
** Estimated from the protein amount by Lowry assay and Gd^{3+} amount by ICP-MS.

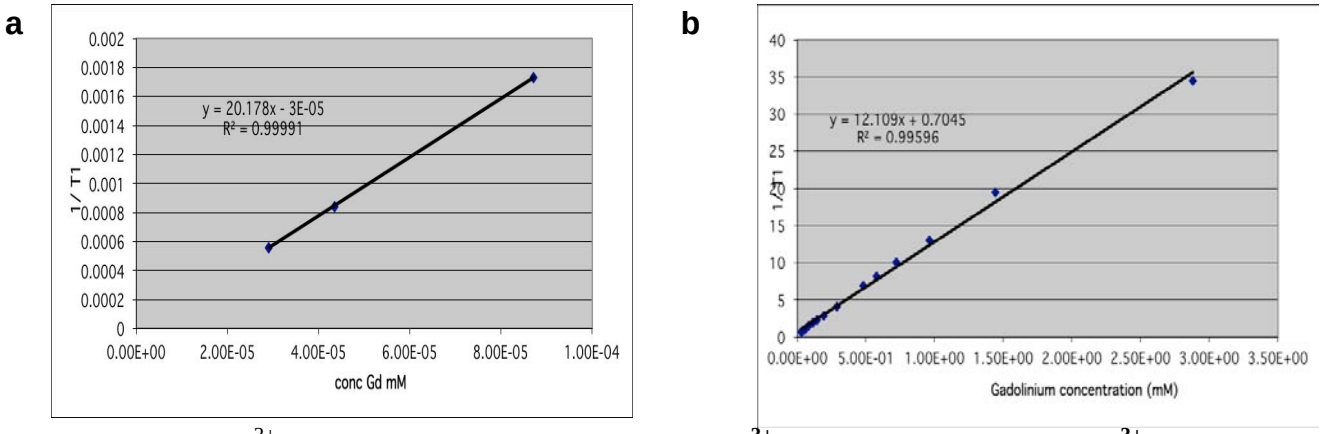

Figure S4. The Gd^{3+} concentration versus $1/T_1$ of the **Gd^{3+}-LDLs** to calculate R_1. **Gd^{3+}-LDLs** with loading rate of Gd^{3+}-LDL (200:1) (a) and with Gd^{3+}-LDL (40:1) (b) were used. The slope of the line fitted to the data was calculated as 20.1 or 12.1 $s^{-1}mM^{-1}$ (R_1) for each particle.

3. *In vivo* MRI with *ApoE*$^{-/-}$ mouse model of atherosclerosis

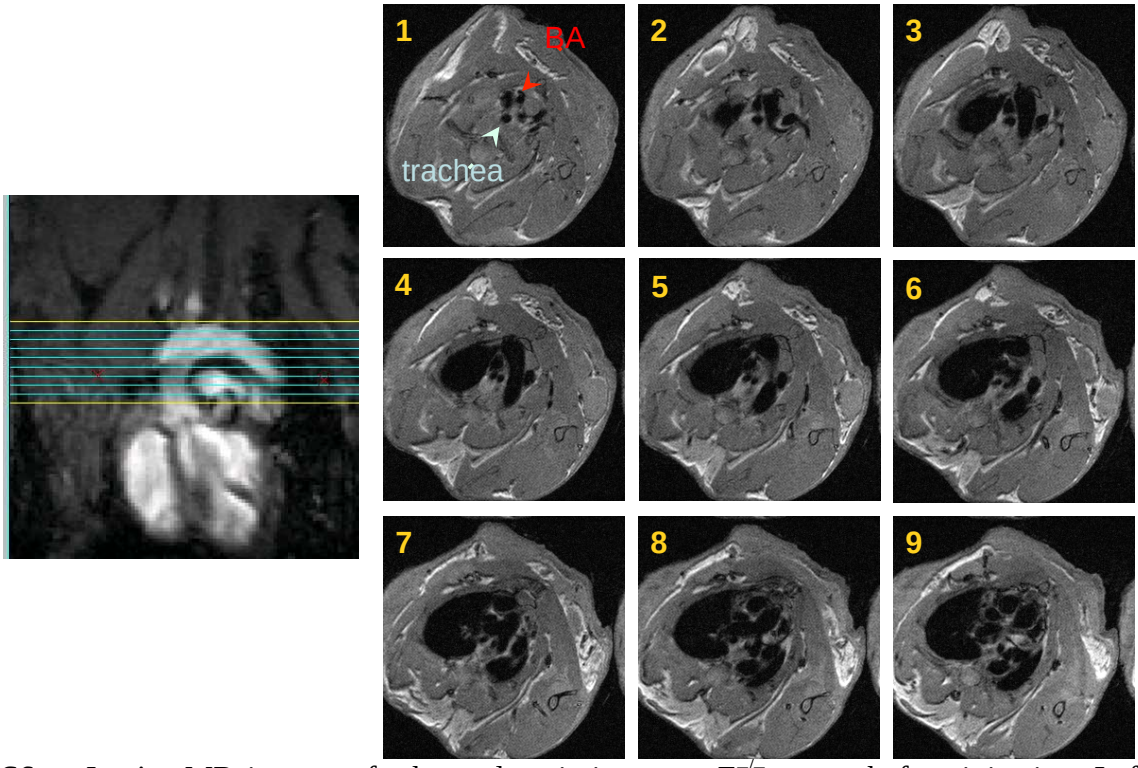

Figure S6a. *In vivo* MR images of atherosclerosis in an apoE$^{-/-}$ mouse before injection. Left panel: Scout image showing the aortic arch with image planes corresponding to images (#1-9) on right panels. BA: branchiocephalic artery.

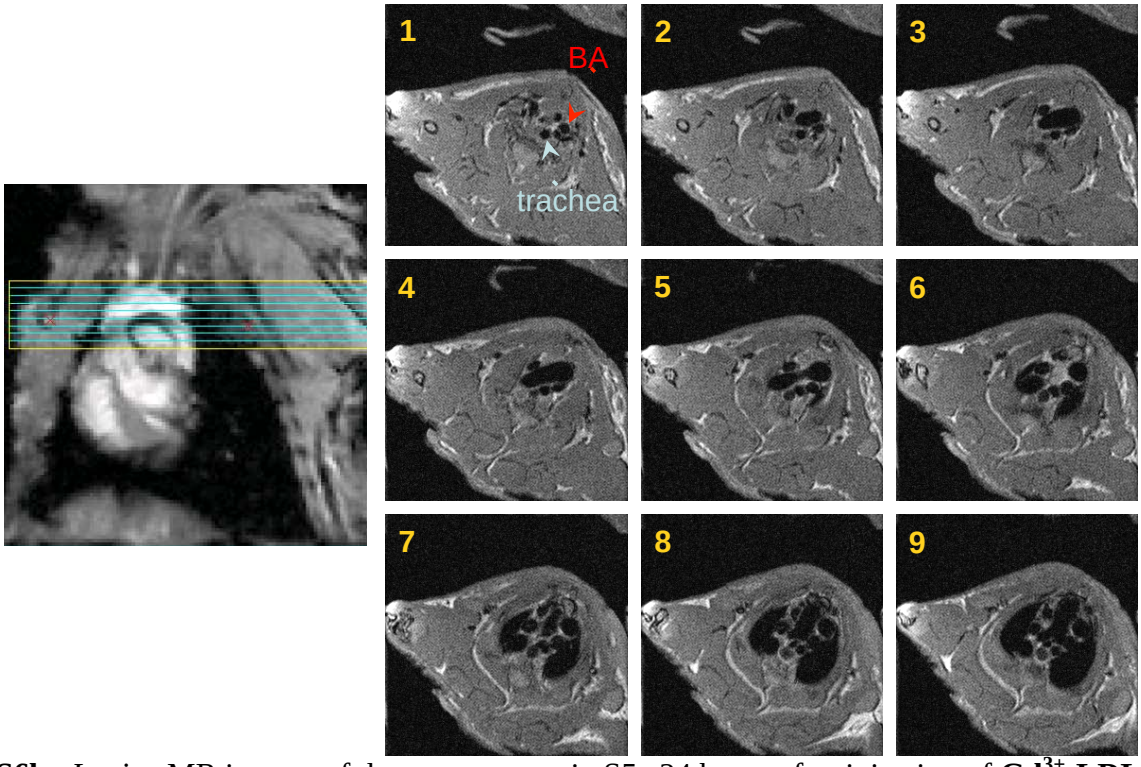

Figure S6b. *In vivo* MR images of the same mouse in S5a 24 hours after injection of **Gd^{3+}-LDL**.

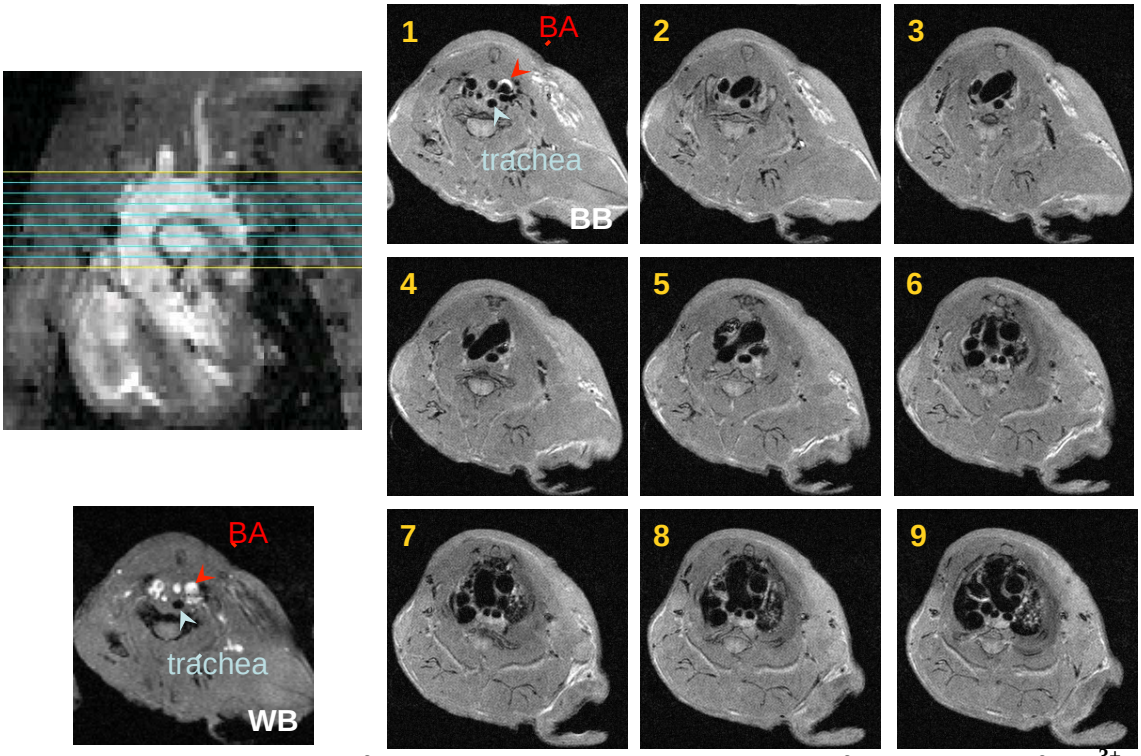

Figure S6c. *In vivo* MR images of the same mouse in S5a 48 hours after injection of **Gd^{3+}-LDL.** A white blood image (left bottom), in which the blood signals were bright, was used to distinct trachea from blood vessels.

Bioconjugate Chemistry

Communication

pubs.acs.org/bc

Formylbenzene Diazonium Hexafluorophosphate Reagent for Tyrosine-Selective Modification of Proteins and the Introduction of a Bioorthogonal Aldehyde

Julia Gavrilyuk,[†] Hitoshi Ban,[†] Masanobu Nagano, Wataru Hakamata, and Carlos F. Barbas, III*

Departments of Chemistry and Molecular Biology, The Skaggs Institute for Chemical Biology, The Scripps Research Institute, 10550 North Torrey Pines Rd., La Jolla, California 92037, United States

Supporting Information

ABSTRACT: 4-Formylbenzene diazonium hexafluorophosphate (FBDP) is a novel bench-stable crystalline diazonium salt that reacts selectively with tyrosine to install a bioorthogonal aldehyde functionality. Model studies with *N*-acyl-tyrosine methylamide allowed us to identify conditions optimal for tyrosine ligation reactions with small peptides and proteins. FBDP-based conjugation was used for the facile introduction of small molecule tags, poly(ethylene glycol) chains (PEGylation), and functional small molecules onto model proteins and to label the surface of living cells.

INTRODUCTION

Diazonium reagents have been used for selective modification of tyrosine[1−3] but are often not extensively applied to the modification of proteins and/or antibodies due to several limitations. For a precise site-specific modification of a protein, complete control over reagent stability, reactivity, and stoichiometry is required. Instability of the currently reported diazonium reagents makes it difficult to control the stoichiometry of the reaction, and a high excess of the reagent is often required. Diazonium reagents are generally prepared from anilines in situ under strongly acidic conditions,[4] whereas the diazo coupling reaction with protein optimally proceeds under mildly basic conditions. The significant pH adjustment required is not necessarily possible with pH-sensitive proteins. Perhaps the greatest barrier to the widespread use of diazonium labeling reagents is the prerequisite of in situ preparation just prior to use.[1,2,5,6] This requirement limits their utility and access to a select group of practitioners. We herein present a practical protein modification method for the introduction of a bioorthogonal aldehyde group[7−11] based on the development of a novel bench-stable diazonium reagent.

A bifunctional diazonium reagent was designed to satisfy two key requirements: (1) improved reagent stability while maintaining high reactivity in aqueous buffer and (2) ability to introduce a bioorthogonal functionality into the protein. The 4-formyl benzenediazonium with hexafluorophosphate (PF_6^-) or tetrafluoroborate (BF_4^-) counterions were chosen as suitable candidates (Scheme 1). Hexafluorophosphate[12] and tetrafluoroborate[13−16] were chosen as stabilizing counterions, and the aldehyde provides an excellent functional handle for the formation of oxime or hydrazone bonds.[7,17,18] The formyl group is essential for the stability of diazonium ion, as it prevents cation formation at C4 and release of nitrogen gas; furthermore, it activates the N−N triple bond as an electrophile. The importance of the electron withdrawing substituents on the phenyl ring of diazonium reagent has been emphasized in several previous studies. Unlike many diazonium reagents, these reagents avoid the use of the potentially immunogenic NO_2-substituted benzene.[5,19−21]

Scheme 1

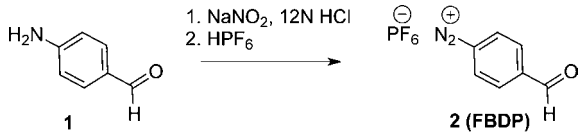

Metal-free and mild tyrosine modification reactions[1,3,22−26] are an attractive alternative to the commonly used lysine and cysteine modification protocols. The high abundance of lysine in a typical protein or antibody significantly complicates control of the stoichiometry and specificity of bioconjugation reactions. Cysteines, although less abundant, require reductive pretreatment before bioconjugation. In addition, modification of cysteine may alter the stability and function of an antibody or other protein wherein disulfide linkages are key to stability.[27−29] Tyrosines are less common than lysine and do not form stabilizing linkages like cysteine. Introduction of the aldehyde functionality through tyrosine conjugation has an additional advantage: targeting modules containing hydrazine form stable but exchangeable hydrazone linkages with aldehyde that can later undergo site-specific exchange into the oxime linkage with a different targeting molecule, drug, or dye.[30,31]

Received: July 25, 2012
Revised: October 24, 2012
Published: November 26, 2012

 © 2012 American Chemical Society dx.doi.org/10.1021/bc300410p | *Bioconjugate Chem.* 2012, 23, 2321−2328

MATERIALS AND METHODS

General. ^{1}H NMR and ^{13}C NMR spectra were recorded on Bruker DRX-600 (600 MHz), Varian Inova-400 (400 MHz), or Varian MER-300 (300 MHz) spectrometers in the stated solvents using tetramethylsilane as an internal standard. Chemical shifts were reported in parts per million (ppm) on the δ scale from an internal standard (NMR descriptions: s, singlet; d, doublet; t, triplet; q, quartet; h, heptet; m, multiplet; br, broad). Coupling constants, J, are reported in hertz. Mass spectroscopy was performed by the Scripps Research Institute Mass Spectrometer Center. Analytical thin-layer chromatography and flash column chromatography were performed on Merck Kieselgel 60 F254 silica gel plates and Silica Gel ZEOprep 60 ECO 40−63 Micron, respectively. Visualization was accomplished with anisaldehyde or $KMnO_4$. Unless otherwise noted, all the materials were obtained from commercial suppliers, and were used without further purification. All solvents were commercially available grade.

4-Formyl Benzene Diazonium Hexafluorophosphate (2). To a suspension of 4-aminobenzaldehyde polymer (5.00 g, 41.3 mmol) in 12 N HCl (85 mL) was added the solution of $NaNO_2$ (3.42 g, 49.5 mmol) in water (67 mL) at −10 °C. The resulting solution was stirred at −10 °C. After 1.5 h, 60% HPF_6 in water (10.3 mL, 70.2 mmol) was added at −10 °C and stirred for 30 min. Then, the reaction mixture was stirred at room temperature for 30 min. The resulting solids were collected by filtration and washed with water and AcOEt to give **2** (FBDP) (4.77 g, 42%) as an off-white solid. ^{1}H NMR (300 MHz, DMSO-d_6): δ 10.2 (s, 1H), 8.85 (d, J = 5.2 Hz, 2H), 8.39 (d, J = 5.0 Hz, 2H). ^{13}C NMR (75 MHz, acetone-d_6): δ 190.32, 143.69, 133.39, 131.02, 119.41. ^{31}P NMR (162 MHz, acetone-d_6): δ −143.89 (h, J_{P-F} = 707 MHz), ^{19}F NMR (376 MHz, acetone-d_6): δ −72.57 (d, J_{P-F} = 707 MHz). HRMS: calcd for $C_7H_5N_2O^+$ (M^+) 133.0402, found 133.0401.

(*S*,*E*)-2-Acetamido-3-(3-((4-formylphenyl)diazenyl)-4-hydroxyphenyl)-*N*-methylpropanamide (5). To a solution of *N*-acyl tyrosine methylamide **4** (20 mg, 0.0846 mmol) in 100 mM pH 7.0 NaH_2PO_4/Na_2HPO_4 buffer (2.83 mL)/DMSO (1.41 mL) was added the diazonium reagent **2** (25.9 mg, 0.0931 mmol) at room temperature. The resulting solution was stirred at room temperature for 45 min. After the reaction, water (2.82 mL) was added. The generated solid was filtered then washed with water and AcOEt to give **5** (31.0 mg, 99%) as a yellow solid. ^{1}H NMR (300 MHz, DMSO-d_6): δ 10.9 (s, 1H), 10.1 (s, 1H), 8.16 (d, J = 8.6 Hz, 2H), 8.11 (d, J = 8.7 Hz, 2H), 7.93 (q, J = 4.7 Hz, 1H), 7.63 (d, J = 2.1 Hz, 1H), 7.32 (dd, J = 8.5, 2.2 Hz, 1H), 7.00 (d, J = 8.5 Hz, 1H), 4.45−4.37 (m, 1H), 2.94 (dd, J = 13.3, 5.0 Hz, 1H), 2.70 (dd, J = 13.5, 9.5 Hz, 1H), 2.56 (d, J = 4.6, 3H), 1.77 (s, 3H). ^{13}C NMR (150 MHz, DMSO-d_6): δ 192.59, 171.36, 168.93, 154.82, 154.14, 138.40, 137.05, 135.61, 130.65, 129.53, 123.08, 121.33, 117.94, 54.03, 36.82, 25.40, 22.40. HRMS: calcd for $C_{19}H_{21}N_4O_4$ (MH^+) 369.1557, found 369.1556.

(*S*)-2-Acetamido-3-(3-((*E*)-(4-((*E*)-(ethoxyimino)-methyl)phenyl)diazenyl)-4-hydroxyphenyl)-*N*-methyl-propanamide methylpropanamide (6). To a suspension of compound **3** (15 mg, 0.041 mmol) in 100 mM pH 7.0 NaH_2PO_4/Na_2HPO_4 buffer (0.531 mL)/DMSO (1.54 mL) was added ethoxyamine hydrochloride **4** (4.37 mg, 0.045 mmol) at room temperature. The resulting suspension was stirred at room temperature for 2 h. After the reaction, water (4.00 mL) was added. The generated solid was filtered, then washed with water and AcOEt to give **5** (17.2 mg, quant.) as a yellow solid.^{1}H NMR (300 MHz, DMSO-d_6) (*E*:*Z* isomer ratio = 9: 1): δ 10.9 (s, 1H), 8.33 (s, H), 8.13 (d, J = 8.5 Hz, 1H), 8.01 (d, J = 8.6 Hz, 2H), 7.93 (q, J = 4.5 Hz, 1H), 7.82 (d, J = 8.4 Hz, 2H), 7.62 (d, J = 2.0 Hz, 1H), 7.28 (dd, J = 8.4, 2.2 Hz, 1H), 6.97 (d, J = 8.4 Hz, 1H), 4.44−4.37 (m, 1H), 4.21 (q, J = 7.0 Hz, 2H), 2.94 (dd, J = 13.7, 5.1 Hz, 1H), 2.69 (dd, J = 13.6, 9.6 Hz, 1H), 2.56 (d, J = 4.6, 3H), 1.77 (s, 3H), 1.28 (t, J = 7.0 Hz, 3H). ^{13}C NMR (150 MHz, DMSO-d_6): δ 171.39, 168.93, 153.30, 151.92, 147.74, 138.05, 134.38, 129.48, 127.71, 122.96, 122.57, 117.72, 69.30, 54.07, 36.84, 25.40, 22.40, 14.41. HRMS: calcd for $C_{21}H_{26}N_5O_4$ (MH^+) 412.1979, found 412.1980.

General Procedure for Amino Acid Selectivity Study. N-Acyl methyl amides of amino acid were obtained as previously described.[3] Equimolar solution of six amino acids *N*-acyl methyl amides (Tyr, His, Cys, Ser, Lys, Trp) was prepared in 0.1 M Na_2HPO_4 buffer (pH 7, 7.4, 8). Final concentration of each amino acid was 100 μM (1 equiv). One milliliter of the amino acid mixture solution was transferred into LCMS sample vial and 5 μL of FBDP solution in acetonitrile (20 mM solution, 1 equiv) was added. Reaction mixture was vortexed gently and allowed to react at room temperature. Each reaction was performed independently at least 3 times. Aliquot of reaction mixture (5 μL) was analyzed by LCMS after 30 min of reaction time using Agilent LC/MSD SL mass spectrometer with Zorbax 300SP-C8, 5 μm, 4.6 × 50 mm column (Agilent). HPLC parameters were as follows: flow rate 0.5 mL/min, 5% mobile phase B over 2 min followed by a gradient of 5% to 95% B from 2 to 8 min, post time 4 min. Mobile phase A was 0.1% formic acid (v/v) in HPLC-grade H_2O, and mobile phase B was 0.1% formic acid (v/v) in acetonitrile (v/v). API-ESMS data was collected for 115−1000 m/z positive and negative polarity. Data were analyzed using Agilent analysis software. MS TIC positive polarity trace was used to evaluate reaction selectivity. For clarity and quantification purposes, traces corresponding to expected product ions were extracted from the MS TIC spectra (refer to Supporting Information Figures S1−S6). Area under the peak was used to calculate content of each product (refer to Supporting Information Tables S3, S4, S5).

Tocinoic Acid Modification Procedure. To 1 mL of 100 μM solution of tocinoic acid (Sigma-Aldrich) in 0.1 M Na_2HPO_4 buffer pH 7 or pH 8 was added 10 μL of 20 mM solution of FBDP in acetonitrile. The reaction was vortexed gently and allowed to react at room temperature. Aliquot of reaction mixture (5 μL) was analyzed by LCMS after 30 min of reaction time using Agilent LC/MSD SL mass spectrometer with Zorbax 300SP-C8, 5 μm, 4.6 × 50 mm column (Agilent). HPLC parameters were as follows: flow rate 0.5 mL/min, 5% mobile phase B over 2 min followed by a gradient of 5% to 95% B from 2 to 8 min, post time 4 min. Mobile phase A was 0.1% formic acid (v/v) in HPLC-grade H_2O, and mobile phase B was 0.1% formic acid (v/v) in acetonitrile (v/v). API-ESMS data were collected for 115−1000 m/z positive and negative polarity. Data was analyzed using Agilent analysis software. MS TIC positive polarity trace was used to evaluate reaction selectivity. For clarity and quantification purposes, traces corresponding to starting material and expected product ions were extracted from the MS TIC spectra (refer to Supporting Information Figure S7). Area under the peak was used to calculate content of remaining starting material and product (refer to Supporting Information Table S6). No *N*-terminal modification product has been found in the reaction mixture. LCMS: calcd for $C_{37}H_{49}N_{10}O_{11}S_2$ (MH^+) 873.2, found 873.2.

BSA Modification. Method A (Stepwise). To the 0.5 mL Eppendorf tube containing 99 μL of BSA solution (30 μM solution in 0.1 M phosphate buffer pH 2−10) was added 1 μL of reagent solution (10 mM solution in CH_3CN), and reaction mixture was vortexed briefly. Reaction was kept at room temperature for 30 min and the conversion was followed by visual observation (Figure S9) and UV−vis measurement at 340 nm that corresponds to the absorbance of diazene functionality (data not shown). The reaction products were purified using Zeba Spin desalting column (7000 Da MWC, Pierce) and the buffer was exchanged to PBS pH 5. In the 1.5 mL Eppendorf tube, 99 mL of 30 μM solution of BSA−aldehyde in 0.1 M PBS pH 5 was treated with biotin hydrazide (1 μL of 100 mM solution in DMSO), overnight 4 °C, followed by removal of the excess of small molecule by Zeba Spin desalting column. The reaction products were tested in streptavidin ELISA (Figure S11) and characterized by MALDI-TOF (Figure S13).

Method B (One Step Diazo-Coupling). In the 0.5 mL Eppendorf tube were combined biotin hydrazide (10 μL of 100 mM solution in CH_3CN; 1 equiv), trifluoroacetic acid (10 μL of 200 mM solution in CH_3CN; 2 equiv), and FBDP (10 μL of 100 mM solution in CH_3CN; 1 equiv). The reaction mixture was mixed and allowed to react for 1 h. An aliquot of the reagent was diluted and analyzed by LCMS (Figure S10) confirming formation of the hydrazide. To the 0.5 mL Eppendorf tube containing 99 μL of BSA solution (30 μM solution in 0.1 M phosphate buffer pH 2−10) was added 1 μL or reagent solution (10 mM solution in CH_3CN), and reaction mixture was vortexed briefly. Reaction was kept at room temperature for 30 min, and reaction products were purified using Zeba Spin desalting column (7000 Da MWC, Pierce). The reaction products were tested in streptavidin ELISA (Figure S12) and characterized by MALDI-TOF and ESI-MS.

Streptavidin ELISA. Costar 96-well ELISA plate (Corning, Acton, MA) was coated with 100 ng of protein in 100 μL of PBS pH 7.4 and incubated overnight at 4 °C. The plate was washed with PBS containing 0.01% Tween-20 (100 μL × 3). After blocking with 100 μL of 3% BSA/PBS, 0.01% Tween-20 for 1 h at 37 °C, and washing (100 μL of PBS containing 0.01% Tween-20 × 5), 100 μL of streptavidin-HRP (Zymed, 1:3000 dilution in PBS) was added to each well and the plate was incubated for 1 h at 37 °C. The plate was thoroughly washed with PBS/0.01% Tween (100 μL × 5). Upon addition of the ABTS developing solution and incubation at room temperature for 10 min, the absorbance was read at 405 nm. All measurements were done in triplicate and an average normalized result was graphed.

Chymotrypsinogen A Modification and Activity Assay. Chymotrypsinogen was modified with 3.3 equiv of FBDP at pH 8.0 following the BSA modification procedure described above. Activity assay was performed essentially as described by Francis et al.[1] In brief, a 114 μL aliquot of reaction mixture for the modification of chymotrypsinogen (1.0 mg/mL, 38 μM total protein content) was treated with 2.6 μL of a solution of sequencing grade modified trypsin (Promega, 20 μg reconstituted with 200 μL of 50 mM acid). The activation of the zymogen was allowed to proceed for 10 min at room temperature before being purified and performing buffer exchange into 0.1 M Tris buffer (pH 7.6) using Zeba Spin desalting column (Pierce). 40 μL aliquots of the activated protease were then added to 160 μL of 0.5 mM chymotrypsin substrate I, colorimetric (Suc-GGF-pNA, Calbiochem 230912) in 50 mM $CaCl_2$, 20 mM Tris buffer, pH 7.6 (light green triangles). An analogous procedure was followed for reagent-modified chymotrypsinogen A samples (light purple squares). In a negative control experiment, the enzyme was not activated with trypsin before addition of the tripeptide substrate (red squares), or the substrate was monitored with addition of only Tris buffer (blue diamonds). The progress of the reaction was monitored by UV−vis spectrophotometry at 379 nm every 30 s for 10 min (Figure S14). Each measurement was done in duplicate and the average value was plotted.

FBDP Modification of Trastuzumab Antibody. To 200 μL of trastuzumab solution in 0.1 M phosphate buffer pH 8 (1.5 mg/mL) was added FBDP solution in CH_3CN (2 μL of 20 μM solution). Reaction mixture was vortexed gently and allowed to react for 30 min. Reaction mixture turned yellow. The reaction was run through the Zeba spin desalting column (7K MWCO, Pierce) to remove excess FBDP and exchange into phosphate buffer pH 6.0. Then, 4 μL of 20 μM solution of biotin−oxyamine (Cayman Chemical, cat. no 10009350) was added, and reaction was vortexed and allowed to react at 4 °C for 18 h. Excess unconjugated biotin was removed using Zeba desalting column. Obtained conjugate was characterized by MALDI-TOF (Figure S23) and ELISA assays (Figure S22).

ErbB2 ELISA. ErbB2 binding ELISA was performed as described.[2] In brief, Costar 96-well ELISA plates (Corning, Acton, MA) were coated with 25 ng of antigen (human ErbB2 or BSA) in 25 μL of PBS pH 7.4 and incubated overnight at 4 °C. The plate was washed with PBS containing 0.01% Tween-20 (100 μL × 3). After blocking with 100 μL of 3% BSA/PBS, 0.01% Tween-20 for 1 h at 37 °C, and washing (100 μL of PBS containing 0.01% Tween-20 × 5), 100 ng/50 μL/well of trastuzumab, trastuzumab−CHO (trastuzumab modified only with FBDP, but not ligated with biotin-oxyamine) or trastuzumab−biotin (trastuzumab modified with FBDP followed by oxime ligation with biotin-oxyamine) construct or rituximab (negative control) solution was added, and the plates were incubated for 1 h at 37 °C. The plate was thoroughly washed with PBS/0.01% Tween (100 μL × 5) followed by addition of 100 μL/well of secondary antibody solution (donkey anti-human HRP, diluted 1:1000). The plate was incubated for 1 h at 37 °C and washed with PBS/0.01% Tween (100 μL × 5). Upon addition of the ABTS developing solution and incubation at room temperature for 20 min, the absorbance was read at 405 nm. All measurements were done in triplicatem and an average normalized result was graphed.

Streptavidin ELISA. In brief, Costar 96-well ELISA plates (Corning, Acton, MA) were coated with 200 ng of antigen (streptavidin or BSA) in 100 μL of PBS pH 7.4 and incubated overnight at 4 °C. The plate was washed with PBS containing 0.01% Tween-20 (100 μL × 3). After blocking with 100 μL of 3% BSA/PBS, 0.01% Tween-20 for 1 h at 37 °C and washing (100 μL of PBS containing 0.01% Tween-20 × 5), 100 ng/100 μL/well of trastuzumab, trastuzumab−CHO (trastuzumab modified only with FBDP, but not ligated with biotin−oxyamine) or trastuzumab−biotin (trastuzumab modified with FBDP followed by oxime ligation with biotin−oxyamine) construct, rituximab (negative control), biotinylated goat anti-rabbit antibody (positive control; Vector, cat. no F1207) solution was added and the plates were incubated for 1 h at 37 °C. The plate was thoroughly washed with PBS/0.01% Tween (100 μL × 5) followed by addition of 100 μL/well of appropriate secondary antibody solution (AP goat anti-human IgG $F(ab)_2$ from Pierce, diluted 1:3000; or AP rabbit antigoat

dx.doi.org/10.1021/bc300410p | *Bioconjugate Chem.* 2012, 23, 2321−2328

IgG from Pierce, diluted 1:3000). The plate was incubated for 1 h at 37 °C and washed with PBS/0.01% Tween (100 μL × 5). Upon addition of the AP developing solution and incubation at room temperature for 20 min, the absorbance was read at 405 nm. All measurements were done in triplicate, and an average normalized result was graphed.

Cell Surface Labeling with FBDP. HeLa cells were harvested and washed twice with PBS pH 8.0. Washed cells were resuspended in PBS pH 8.0 to a final concentration of 5 × 10^6 cells/mL, and 50 μL aliquots were transferred to the V-bottom non-TC-treated plate followed by addition of FBDP (50 μL aliquots in PBS pH 8.0, 0.01% acetonitrile; final concentrations of FBDP were 100 μM, 10 μM, and 1 μM). Cells were incubated with the reagent for 15 min at 37 °C. Cells were washed with PBS pH 6.0 (3 × 150 μL/well) followed by addition of 100 μL/well of 1 mM biotin−hydrazide (Sigma-Aldrich) in PBS pH 6.0 and incubation at room temperature for 30 min. Cells were washed with FACS buffer (3 × 150 μL/well; PBS pH 7.4, 1% BSA, 0.01% NaN_3). Streptavidin−FITC (Jackson Laboratories) solution in FACS buffer was added to the cells (100 μL/well; 1:100 dilution) followed by incubation for 30 min at room temperature. The cells were washed with FACS buffer (5 × 150 μL/well) followed by propidium iodide staining for 15 min at room temperature (1 μg/mL; 100 μL/well). Cells were washed and transferred to the filter-top FACS tubes. Cells were analyzed on LSRII flow cytometer; 30 000 events were collected. Data were analyzed using *FlowJo 8.7.1* and Microsoft *Excel*. All samples were tested in triplicate. Representative graphs from two independent experiments are shown (Figure S24).

RESULTS AND DISCUSSION

4-Formyl benzene diazonium hexafluorophosphate (FBDP, **2**) and 4-formyl benzene diazonium tetrafluoroborate (FBDB) were prepared, and reagent stability and reactivity were investigated. FBDP was synthesized on a gram scale from commercially available 4-aminobenzaldehyde polymer (Scheme 1). The aniline was treated with $NaNO_2$ in concentrated HCl, followed by Cl^- exchange to PF_6^- by treatment with 60% HPF_6 aqueous solution. The product precipitated from aqueous solution upon anion exchange making isolation straightforward. The FBDB reagent was prepared according to a previously reported procedure.[32,33]

The reactivity profile of 4-formyl diazonium salts has not been extensively studied; only two reports were found in the literature and these concerned reactivity with phenol.[34,35] Therefore, a model reaction of the diazonium reagents with *N*-acyl tyrosine methylamide **4** was studied first. The reaction was performed in 67% sodium phosphate buffer/DMSO at room temperature. Buffer pH was varied from pH 5.0 to 8.0 (Scheme 2). The substrate concentration was 20 mM, and only a small excess of the FBDP reagent was used (1.1 equiv). FBDP reacted slowly with the model substrate at pH 5.0 and 6.0 providing the desired product **5** in 9% and 33% yields, respectively, after 12 h. In contrast, the reaction of FBDP at neutral pH and at mildly basic pH (pH 8.0) gave coupling product in excellent isolated yields of 96% and 99%, respectively. FBDP was stable and maintained excellent reactivity after more than 3 months of storage at 4 °C under air and/or after 1 week at room temperature under air. The isolated yields of the reaction at pH 8 performed with reagent stored at 4 °C and room temperature were 91% and 93%, respectively. In contrast, FBDB had good reactivity but much

Scheme 2

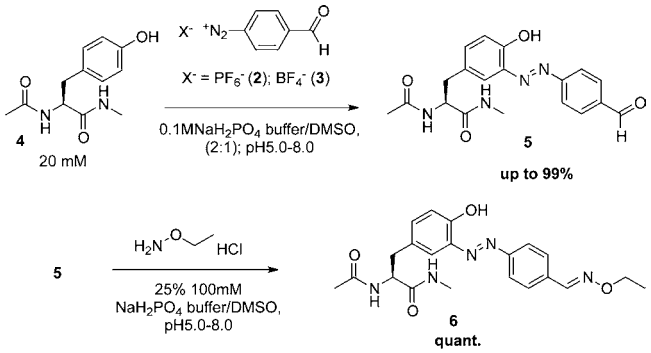

lower stability compared to FBDP. The isolated yield of the model reaction with freshly prepared FBDB was 84% under optimal pH conditions but only 21% after storing the reagent at room temperature for 1 week under air. Therefore, FBDP was chosen for further studies.

We then studied formation of the oxime bond as a bioorthogonal linkage based on the introduction of the aldehyde handle. The reaction between the aldehyde and hydroxylamine hydrochloride (1.1 equiv) was performed in 25% 0.1 M Na_2PO_4 buffer/DMSO at room temperature (Scheme 2). As expected, the reaction proceeded smoothly and gave quantitative yield of **6** at pHs ranging from 5.0 to 8.0. Considering that a one-pot, three-component reaction would be more convenient for protein modification, we evaluated the reaction of 4 with FBDP (1.1 equiv) for 1 h in 67% 0.1 M Na_2PO_4 buffer/DMSO at room temperature. Hydroxylamine hydrochloride (1.1 equiv) was added into the reaction mixture, and the reaction was stirred for 2 h. The one-pot reaction gave **6** in 93% isolated yield. Hydrazines could be used rather than hydroxylamine, but the reaction time had to be extended. Reactions with methylhydrazine, acylhydrazine, and benzohydrazide gave 92%, 85%, and 87% isolated yields, respectively. The alternative protocol involving premixing of the aldehyde and hydrazine or of the hydroxylamine components followed by diazonium coupling was also studied (see Supporting Information). After reaction between FBDP and hydroxylamine hydrochloride in the presence of AcOH in DMSO for 2 h, the resultant solution was added to **4** in 0.138 M Na_2PO_4 buffer (pH 8.0). This protocol provided 47% isolated yield of **6**.

Our observations suggested that use of FBDP in the pH range of 7 to 8 would be optimal for protein bioconjugation. Therefore, we conducted a selectivity study[25] with *N*-acyl methylamides of the amino acids potentially reactive with FBDP under the conditions closely resembling the intended protein modification reaction (Scheme 3). An equimolar mixture of *N*-acyl methylamides of tyrosine, histidine, tryptophan, lysine, serine, and cysteine (100 μM concentration of each amino acid) in 0.1 M Na_2PO_4 buffer at pHs of 7.0, 7.4, and 8.0 were treated with 1 equiv of FBDP solution in acetonitrile (final content of acetonitrile in reaction mixture <1%), and the reaction progress was monitored by LCMS. Preferential diazo coupling to tyrosine was observed after 30 min at room temperature with average 95.3% conversion to diazene product **5** at pH 8.0, 89.1% conversion at pH 7.4, and 87.2% conversion at pH 7.0. The other amino acids were less reactive with histidine (1% at pH 8.0, 5.5% at pH 7.4, 7% at pH 7.0) more reactive than tryptophan (2% at pH 8.0, 3.2% at pH 7.4, 3.4% at pH 7.0) with unoxidized cysteine being the least

dx.doi.org/10.1021/bc300410p | *Bioconjugate Chem.* 2012, 23, 2321−2328

Scheme 3

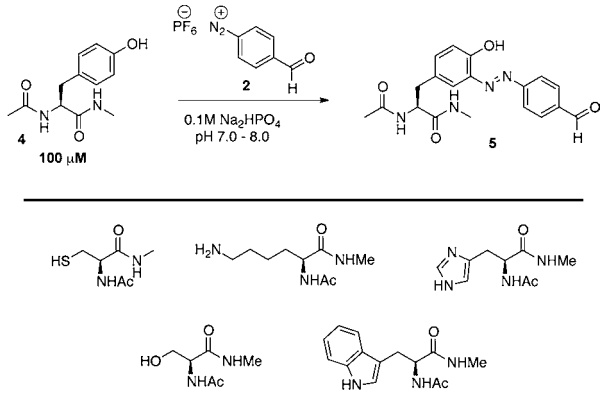

reactive (1.7% at pH 8.0, 2.2% at pH 7.4, 2.2% at pH 7.0) (see Supporting Information). No reaction was observed with the lysine and serine amides. Thus, high tyrosine selective labeling is achieved at the modestly basic pH of 8. To further study selectivity, we examined the labeling efficiency and specificity using a more complex peptide. Reaction with a 100 μM solution of a the cyclic peptide tocinoic acid **7** proceeded cleanly with 2 equiv of FBDP in 30 min to give only the tyrosine-modified adduct **8** in 88.5% and 91.4% conversions at pHs of 7.4 and 8.0, respectively (Scheme 4). No modification at the *N*-terminal amine was observed. On the basis of these results, we expected that the FBDP reagent would preferentially modify surface-exposed tyrosine residues on proteins.

We then tested the FBDP reagent in reactions with model proteins including bovine serum albumin (BSA), human serum albumin (HSA), and chymotrypsinogen A. These proteins contain 21, 19, and 4 tyrosines, respectively. The one-pot vs stepwise introduction of the biotin tag to BSA was studied with 30 μM BSA in 0.1 M Na_2PO_4 (pH 2.0−10) using 3.3 equiv of FBDP reagent (Figure 1). In the stepwise reaction, BSA was treated with FBDP reagent for 30 min at room temperature, excess reagent was removed by gel filtration, and the protein exchanged into pH 6.0 buffer. Aldehyde-containing protein was then treated with excess biotin-hydrazide for 18 h at 4 °C and excess biotin was removed by gel filtration. In the one-pot reaction, biotin−hydrazide was premixed with FBDP solution in acetonitrile in the presence of 2 equiv of TFA for 1 h (hydrazide formation was confirmed by LCMS). Subsequently, 3.3 equiv of the obtained reagent were added to the 30 μM BSA solution in 0.1 M Na_2PO_4 (pH 2.0−10). The reaction was allowed to proceed for 30 min at room temperature, and then excess reagent was removed by gel filtration. Formation of diazene adduct was observed visually (upon reaction, the

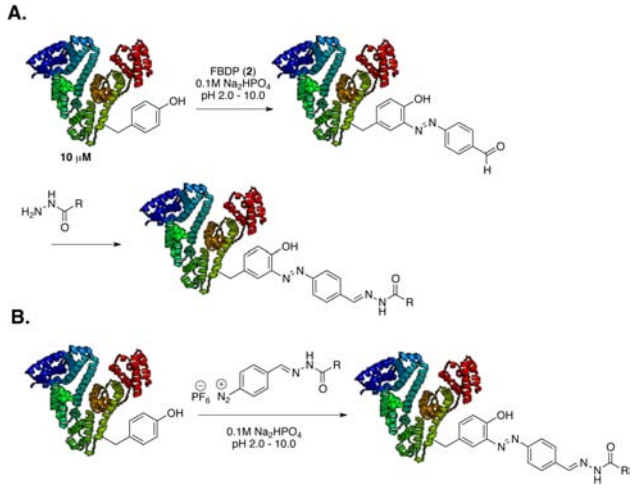

Figure 1. Diazonium-based biotinylation of proteins.

solution turns yellow) and by UV−vis spectroscopy (characteristic absorption at 340 nm). Biotin conjugation was confirmed by MALDI-TOF, ESI-MS, and a biotin−streptavidin ELISA assay (Figure 2). The stepwise protocol resulted in better

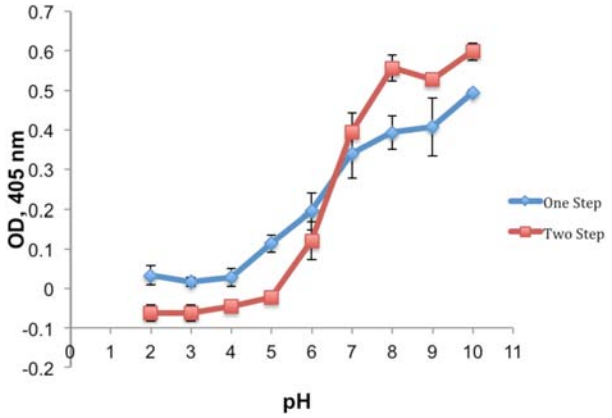

Figure 2. Diazonium-based biotinylation efficiency as a function of pH.

conjugation efficiency than did the one-pot reaction. Only monoconjugated product was observed by ESI-MS (see Supporting Information). This labeling strategy is versatile since a stock of aldehyde-containing protein can be prepared and used for conjugation with a variety of oxyamine and/or hydrazine tags.

Scheme 4

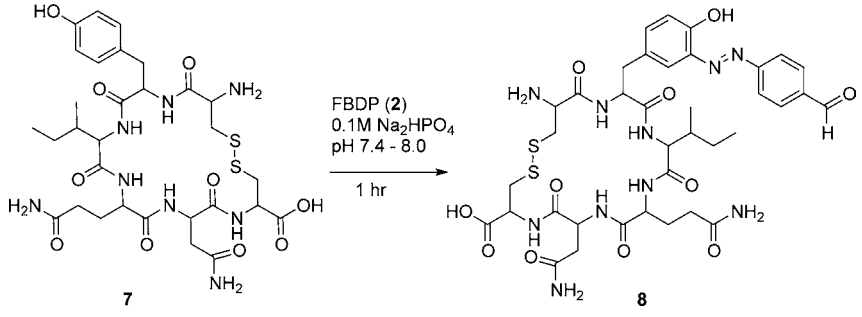

dx.doi.org/10.1021/bc300410p | *Bioconjugate Chem.* 2012, 23, 2321−2328

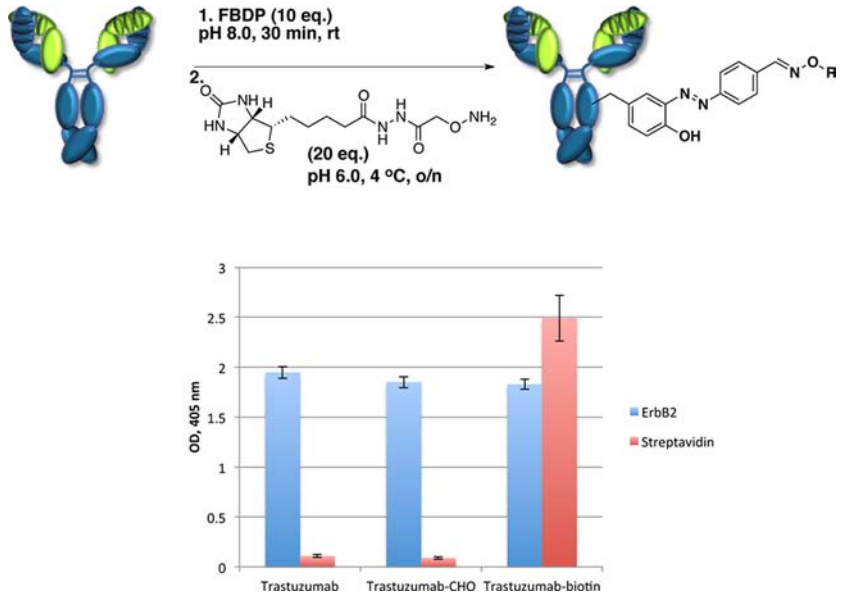

Figure 3. ELISA evaluation of the FBDP modified trastuzumab and binding to ErbB2 and streptavidin.

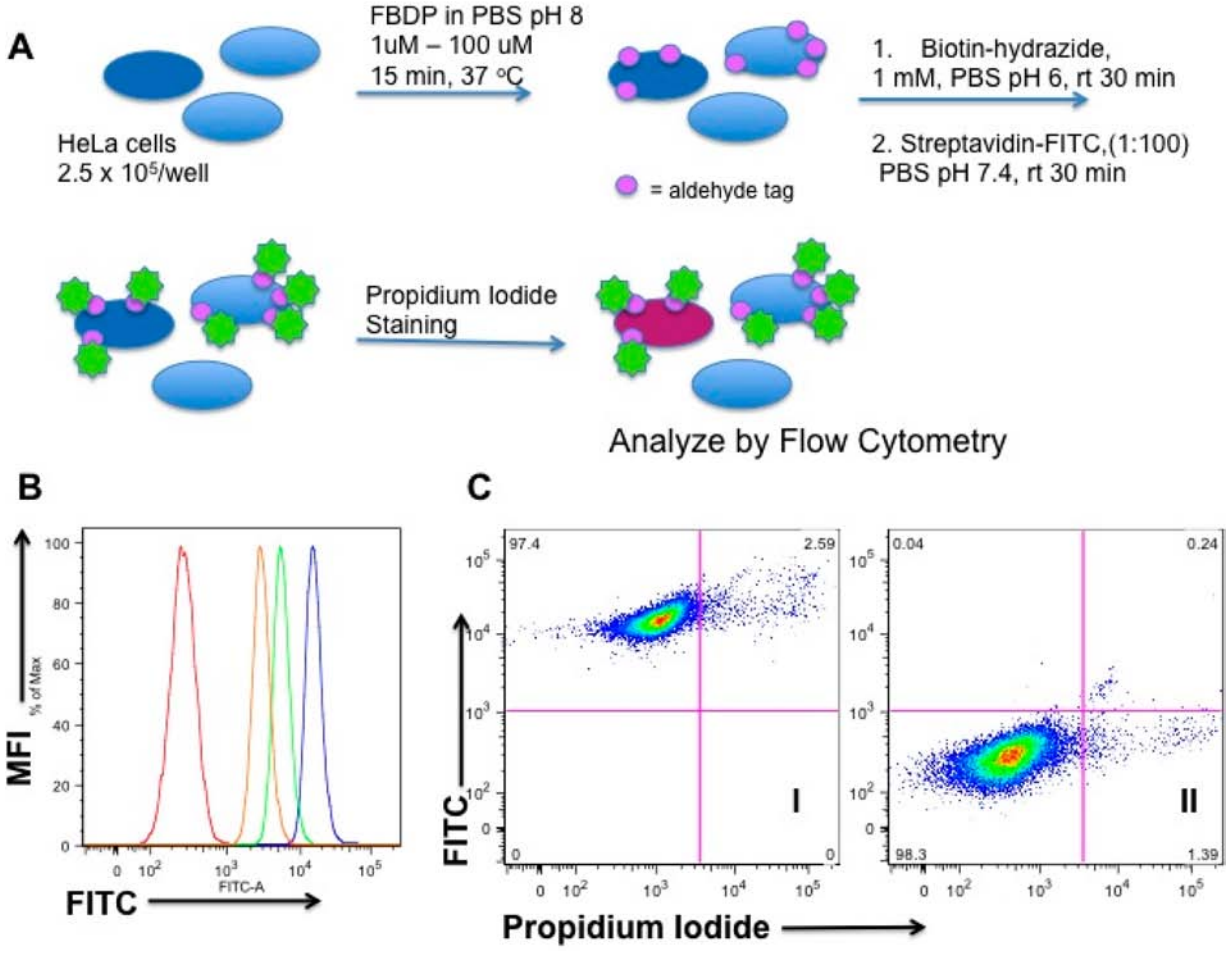

Figure 4. HeLa cells labeling with FBDP. (a) Schematic representation of the labeling procedure; (b) FITC histogram overlay of unlabeled cells (red), cells treated with 100 uM FBDP (blue) or 10 uM FBDP (green) or 1 uM FBDP (orange); (c) Representative dot plots of cells labeled with 100 uM FBDP (I) and unlabeled cells (II).

We next evaluated FBDP modification of chymotrypsinogen A using the stepwise protocol; modification proceeded smoothly at pH 8.0 with 3.3 equiv of FBDP and did not affect activity of the enzyme (see Supporting Information). We then used the reaction with HSA to evaluate the influence of conditions including pH (7.0, 7.4, 7.6, 7.8, 8.0, 8.4), reaction

dx.doi.org/10.1021/bc300410p | *Bioconjugate Chem.* 2012, 23, 2321−2328

time (30 min, 1 h, 2 h, 3 h, 4 h), temperature (4 °C, 25 °C, 37 °C), reagent excess (1−100 equiv), and protein concentration (2.5−20 mg/mL). Factors that influenced the reaction the most were reaction temperature (reaction slowed at 4 °C and yielded only ∼0.7 modifications/protein in 30 min) and amount of excess reagent used (over 20 equiv of reagent provided >2 modifications/protein in 30 min at pH 8.0). A pH range of 7.4−8.0 was optimal and provided an average of ∼1 modification/protein. At pH 8.0, an extended reaction time (>1 h) resulted in incorporation of ∼1.5 modifications/protein. Protein concentration had no effect on reaction outcome and provided ∼1 modification/protein for all tested protein concentrations. Optimal reaction conditions are therefore 10 equiv of FBDP at pH 8.0 for 30 min at room temperature (see Supporting Information for further details of these experiments). Since the introduction of poly(ethylene glycol) chains (PEGylation) is widely used to modify the pharmacokinetic properties of proteins, we studied the potential of this approach in protein PEGylation.[36,37] This was achieved by simply reacting FBDP-modified HSA with 5K linear poly(ethylene glycol)−hydrazide (PEG-hydrazide) at pH 5.0 for 18 h; exclusively mono-PEGylated product was formed, however in low conversion in this unoptimized study (see Supporting Information). Although the reaction was incomplete after 18 h, separation of homogeneous product from starting material was straightforward and starting material could be recycled. For comparison, reaction with 10 equiv of 5k PEG-NHS for the same amount of time resulted in a mixture of mono-, bis-, tri-, and tetra-PEGylated products and starting material.

Our protein modification results are in accord with studies published by other research groups and provide further support to the observation that diazonium salts react preferentially with surface-exposed tyrosine residues. Therefore, some degree of control over the reaction selectivity can be expected with this approach.

Since antibodies constitute perhaps the most important class of proteins in bioconjugation chemistry, we studied the potential of FBDP labeling of the antibody trastuzumab.[38] Antibody was modified using the optimized two-step protocol with 10 equiv of FBDP (pH 8.0, 30 min, rt) and 20 equiv of biotin−oxyamine (pH 6.0, 4 °C, o/n). Chemically modified trastuzumab was found to incorporate an average of 1.8 biotin tags per antibody molecule according to MALDI-TOF characterization. ESI-MS characterization revealed adducts containing one, two, and three modifications per antibody molecule. Chemical modification did not affect ErbB2 recognition of trastuzumab, and the biotin tag was readily detected through binding to streptavidin (Figure 3).

Considering that diazocoupling reaction with FBDP takes place rapidly and under relatively mild conditions, we have tested its potential for cell surface labeling of live cells. Freshly harvested HeLa cells were treated with FBDP for 15 min at 37 °C followed by conjugation of the aldehyde tag to the biotin hydrazide and detection of biotin with streptavidin-FITC. Toxicity of the FBDP modification procedure was monitored by staining cells with propidium iodide. This study demonstrated that human cells were efficiently labeled in a concentration-dependent fashion using 1−100 μM FBDP (Figure 4) and that, even at the highest reagent concentration used, we did not observe any significant toxicity(see Supporting Information for full details).

In summary, we have synthesized a novel and unusually stable 4-formyl benzenediazonium hexafluorophosphate salt that can be used for tyrosine-selective modification of peptides and proteins to introduce bioorthogonal aldehyde tags suitable for classical oxime and hydrazide ligations. The hexafluorophosphate counterion was essential for stability of the diazonium salt and allows preparation of the reagent as a crystalline solid on a multigram scale. This convenient new reagent should facilitate the preparation of a wide variety of peptide and protein conjugates and may be utilized for cell surface labeling. Through an agreement with Sigma-Aldrich, FBDP is now commercially available (product number: L-511382).

■ ASSOCIATED CONTENT

Supporting Information

Detailed syntheses and analytical data of molecules, coupling protocols, selectivity studies, protein and cell labeling studies, and assay details are provided. This material is available free of charge via the Internet at http://pubs.acs.org.

■ AUTHOR INFORMATION

Corresponding Author

*E-mail: carlos@scripps.edu. Phone: (858) 784-9098. Fax: (858) 784-2583.

Author Contributions

†These authors contributed equally to this study.

Notes

The authors declare the following competing financial interest(s): A patent concerning the use of this reagent has been applied for.

■ ACKNOWLEDGMENTS

This study was supported by U.S. National Institutes of Health grant AI 095038 and The Skaggs Institute for Chemical Biology.

■ ABBREVIATIONS

FBDP, 4-formyl benzene diazonium hexafluorophosphate; FBDB, 4-formyl benzene diazonium tetrafluoroborate; BSA, bovine serum albumin; HSA, human serum albumin.

■ REFERENCES

(1) Hooker, J. M., Kovacs, E. W., and Francis, M. B. (2004) Interior surface modification of bacteriophage MS2. *J. Am. Chem. Soc. 126*, 3718−9.

(2) Schlick, T. L., Ding, Z., Kovacs, E. W., and Francis, M. B. (2005) Dual-surface modification of the tobacco mosaic virus. *J. Am. Chem. Soc. 127*, 3718−23.

(3) Jones, M. W., Mantovani, G., Blindauer, C. A., Ryan, S. M., Wang, X., Brayden, D. J., and Haddleton, D. M. (2012) Direct peptide bioconjugation/PEGylation at tyrosine with linear and branched polymeric diazonium salts. *J. Am. Chem. Soc. 134*, 7406−13.

(4) Roglans, A., Pla-Quintana, A., and Moreno-Manas, M. (2006) Diazonium salts as substrates in palladium-catalyzed cross-coupling reactions. *Chem. Rev. 106*, 4622−43.

(5) Hooker, J. M., Datta, A., Botta, M., Raymond, K. N., and Francis, M. B. (2007) Magnetic resonance contrast agents from viral capsid shells: a comparison of exterior and interior cargo strategies. *Nano Lett. 7*, 2207−10.

(6) Le Callonnec, F., Fouquet, E., and Felpin, F. X. (2011) Unprecedented substoichiometric use of hazardous aryl diazonium salts in the Heck-Matsuda reaction via a double catalytic cycle. *Org. Lett. 13*, 2646−9.

(7) Sletten, E. M., and Bertozzi, C. R. (2009) Bioorthogonal chemistry: fishing for selectivity in a sea of functionality. *Angew. Chem., Int. Ed. Engl. 48*, 6974−98.
(8) Hudak, J. E., Yu, H. H., and Bertozzi, C. R. (2011) Protein glycoengineering enabled by the versatile synthesis of aminooxy glycans and the genetically encoded aldehyde tag. *J. Am. Chem. Soc. 133*, 16127−35.
(9) Iyer, G., Pinaud, F., Xu, J., Ebenstein, Y., Li, J., Chang, J., Dahan, M., and Weiss, S. (2011) Aromatic aldehyde and hydrazine activated peptide coated quantum dots for easy bioconjugation and live cell imaging. *Bioconjugate Chem. 22*, 1006−11.
(10) Hudak, J. E., Barfield, R. M., de Hart, G. W., Grob, P., Nogales, E., Bertozzi, C. R., and Rabuka, D. (2012) Synthesis of heterobifunctional protein fusions using copper-free click chemistry and the aldehyde tag. *Angew. Chem., Int. Ed. Engl. 51*, 4161−5.
(11) Key, J. A., Li, C., and Cairo, C. W. (2012) Detection of cellular sialic acid content using nitrobenzoxadiazole carbonyl-reactive chromophores. *Bioconjugate Chem. 23*, 363−71.
(12) Han, S.-Y., and Kim, Y.-A. (2004) Recent development of peptide coupling reagents in organic synthesis. *Tetrahedron 60*, 2447−2467.
(13) Cygler, M., Przybylska, M., and Elofson, R. M. . (1982) The crystal structure of benzenediazonium tetrafluoroborate, C6H5N2+•BF4−. *Can. J. Chem. 60*, 2852−2855.
(14) Ebrahimi, N., and Zarchi, M. A. K. (2011) Iodination of stable aromatic diazonium salt using crosslinked poly (4-vinylpyridine)-supported iodide. *J. Appl. Polym. Sci. 124*, 2807−2813.
(15) Mahouche-Chergui, S., Gam-Derouich, S., Mangeney, C., and Chehimi, M. M. (2011) Aryl diazonium salts: a new class of coupling agents for bonding polymers, biomacromolecules and nanoparticles to surfaces. *Chem. Soc. Rev. 40*, 4143−66.
(16) Hari, D. P., Schroll, P., and Konig, B. (2012) Metal-free, visible-light-mediated direct C-H arylation of heteroarenes with aryl diazonium salts. *J. Am. Chem. Soc. 134*, 2958−61.
(17) Dirksen, A., Hackeng, T. M., and Dawson, P. E. (2006) Nucleophilic catalysis of oxime ligation. *Angew. Chem., Int. Ed. Engl. 45*, 7581−4.
(18) Dirksen, A., and Dawson, P. E. (2008) Rapid oxime and hydrazone ligations with aromatic aldehydes for biomolecular labeling. *Bioconjugate Chem. 19*, 2543−8.
(19) Kovacs, E. W., Hooker, J. M., Romanini, D. W., Holder, P. G., Berry, K. E., and Francis, M. B. (2007) Dual-surface-modified bacteriophage MS2 as an ideal scaffold for a viral capsid-based drug delivery system. *Bioconjugate Chem. 18*, 1140−7.
(20) Datta, A., Hooker, J. M., Botta, M., Francis, M. B., Aime, S., and Raymond, K. N. (2008) High relaxivity gadolinium hydroxypyridonate-viral capsid conjugates: nanosized MRI contrast agents. *J. Am. Chem. Soc. 130*, 2546−52.
(21) Hooker, J. M., O'Neil, J. P., Romanini, D. W., Taylor, S. E., and Francis, M. B. (2008) Genome-free viral capsids as carriers for positron emission tomography radiolabels. *Molecular Imaging and Biology 10*, 182−91.
(22) Joshi, N. S., Whitaker, L. R., and Francis, M. B. (2004) A three-component Mannich-type reaction for selective tyrosine bioconjugation. *J. Am. Chem. Soc. 126*, 15942−3.
(23) McFarland, J. M., Joshi, N. S., and Francis, M. B. (2008) Characterization of a three-component coupling reaction on proteins by isotopic labeling and nuclear magnetic resonance spectroscopy. *J. Am. Chem. Soc. 130*, 7639−44.
(24) Guo, H. M., Minakawa, M., Ueno, L., and Tanaka, F. (2009) Synthesis and evaluation of a cyclic imine derivative conjugated to a fluorescent molecule for labeling of proteins. *Bioorg. Med. Chem. Lett. 19*, 1210−3.
(25) Ban, H., Gavrilyuk, J., and Barbas, C. F., 3rd (2010) Tyrosine bioconjugation through aqueous ene-type reactions: a click-like reaction for tyrosine. *J. Am. Chem. Soc. 132*, 1523−5.
(26) Lorenzi, M., Puppo, C., Lebrun, R., Lignon, S., Roubaud, V., Martinho, M., Mileo, E., Tordo, P., Marque, S. R., Gontero, B., Guigliarelli, B., and Belle, V. (2011) Tyrosine-targeted spin labeling and EPR spectroscopy: an alternative strategy for studying structural transitions in proteins. *Angew. Chem., Int. Ed. Engl. 50*, 9108−11.
(27) McAuley, A., Jacob, J., Kolvenbach, C. G., Westland, K., Lee, H. J., Brych, S. R., Rehder, D., Kleemann, G. R., Brems, D. N., and Matsumura, M. (2008) Contributions of a disulfide bond to the structure, stability, and dimerization of human IgG1 antibody CH3 domain. *Protein Sci. 17*, 95−106.
(28) Traxlmayr, M. W., Wozniak-Knopp, G., Antes, B., Stadlmayr, G., Ruker, F., and Obinger, C. (2011) Integrin binding human antibody constant domains–probing the C-terminal structural loops for grafting the RGD motif. *J. Biotechnol. 155*, 193−202.
(29) Almagro, J. C., Raghunathan, G., Beil, E., Janecki, D. J., Chen, Q., Dinh, T., LaCombe, A., Connor, J., Ware, M., Kim, P. H., Swanson, R. V., and Fransson, J. (2012) Characterization of a high-affinity human antibody with a disulfide bridge in the third complementarity-determining region of the heavy chain. *J. Mol. Recognit. 25*, 125−35.
(30) Takaoka, Y., Tsutsumi, H., Kasagi, N., Nakata, E., and Hamachi, I. (2006) One-pot and sequential organic chemistry on an enzyme surface to tether a fluorescent probe at the proximity of the active site with restoring enzyme activity. *J. Am. Chem. Soc. 128*, 3273−80.
(31) Wakabayashi, H., Miyagawa, M., Koshi, Y., Takaoka, Y., Tsukiji, S., and Hamachi, I. (2008) Affinity-labeling-based introduction of a reactive handle for natural protein modification. *Chem.—Asian J. 3*, 1134−9.
(32) Lai, L.-L., Ho, C.-H., Lin, Y.-J., Wang, E., Liu, Y.-H., Wang, Y., Lin, Y.-C., and Cheng, K.-L. (2002) Synthesis and study of an N,N-disubstituted 4-[(4-aminophenyl)diazenyl]benzaldehyde. *Helv. Chim. Acta 85*, 108−114.
(33) Haque, A. M., and Kim, K. (2011) Aldehyde-functionalized benzenediazonium cation for multiprobe immobilization on microelectrode array surfaces. *Langmuir 27*, 882−6.
(34) Lan, Y.-X., Qiu, Y.-G., Lin, W.-S., Yan, S., Na, G., and Biao, G. (2004) Synthesis of 2- (4-formylphenylazo)-7-(4-antipyrylazo)-1,8-dihydroxynaphthalene-3,6-disulphonic acid. *Journal of Shenyang Institute of Chemical Technology 3*, 165−168.
(35) Kuvshinova, S., Zavyalov, A., Burmistrov, V., Aleksandriiskii, V., and Koifman, O. (2006) Mesogenic 4-alkoxy-2-hydroxy-4-formylazobenzenes. *Russ. J. Org. Chem. 42*, 393−395.
(36) Veronese, F. M., and Mero, A. (2008) The impact of PEGylation on biological therapies. *BioDrugs 22*, 315−29.
(37) Bailon, P., and Won, C. Y. (2009) PEG-modified biopharmaceuticals. *Expert Opin. Drug Delivery 6*, 1−16.
(38) Goldenberg, M. M. (1999) Trastuzumab, a recombinant DNA-derived humanized monoclonal antibody, a novel agent for the treatment of metastatic breast cancer. *Clin. Therapeutics 21*, 309−18.

Formylbenzene diazonium hexafluorophosphate reagent for tyrosine-selective modification of proteins and the introduction of a bioorthogonal aldehyde

Julia Gavrilyuk, Hitoshi Ban, Masanobu Nagano, Wataru Hakamata, and Carlos F. Barbas, III*

Departments of Chemistry and Molecular Biology, The Skaggs Institute for Chemical Biology, The Scripps Research Institute, 10550 N. Torrey Pines Rd., La Jolla, CA 92037.

Supporting Information

Table of Contents

1. General Experimental 2
2. Synthesis of diazonium reagent 2
3. General procedure for the diazonium coupling reaction 3
6. NMR spectra of compounds 8
7. Amino Acid Selectivity Study 14
8. Tocinoic adic modification with FBDP 19
9. BSA modification with FBDP 20
10. Chymotrypsinogen A modification and activity assay 25
11. FBDP-based PEGylation of Human Serum Albumin 27
12. Optimization study for FBDP modification of HSA 28
13. FBDP modification of antibody trastuzumab 33
14. Cell Surface Labeling with FBDP 37
15. References 39

1. General Experimental

^{1}H NMR and ^{13}C NMR spectra were recorded on Bruker DRX-600 (600 MHz), Varian Inova-400 (400 MHz), or Varian MER-300 (300 MHz) spectrometers in the stated solvents using tetramethylsilane as an internal standard. Chemical shifts were reported in parts per million (ppm) on the δ scale from an internal standard (NMR descriptions: s, singlet; d, doublet; t, triplet; q, quartet; h, heptet; m, multiplet; br, broad). Coupling constants, *J*, are reported in Hertz.

Mass spectroscopy was performed by the Scripps Research Institute Mass Spectrometer Center. Analytical thin-layer chromatography and flash column chromatography were performed on Merck Kieselgel 60 F254 silica gel plates and Silica Gel ZEOprep 60 ECO 40-63 Micron, respectively. Visualization was accomplished with anisaldehyde or KMnO4.

Unless otherwise noted, all the materials were obtained from commercial suppliers, and were used without further purification. All solvents were commercially available grade.

2. Synthesis of diazonium reagent

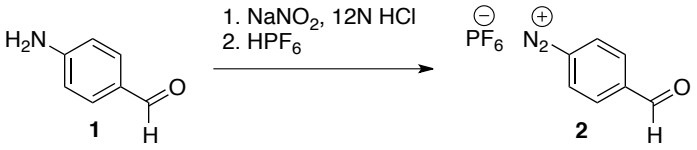

4-Formyl benzene diazonium hexafluorophosphate (2). To a suspension of 4-aminobenzaldehyde polymer (5.00 g, 41.3 mmol) in 12N HCl (85 mL) was added the solution of $NaNO_2$ (3.42 g, 49.5 mmol) in water (67 mL) at -10 ^{0}C. The resulting solution was stirred at -10 ^{0}C. After 1.5 h, 60% HPF_6 in water (10.3 mL, 70.2 mmol) was added at -10 ^{0}C and stirred for 30 min. Then the reaction mixture was stirred at room temperature for 30 min. The resulting solids were collected by filtration, and washed with water and AcOEt to give **2 (FBDP)** (4.77 g, 42%) as an off-white solid.

^{1}H NMR (300 MHz, DMSO-d6): δ 10.2 (s, 1H), 8.85 (d, *J* = 5.2 Hz, 2H), 8.39 (d, *J* = 5.0 Hz, 2H). ^{13}C NMR (75 MHz, acetone-d6): δ 190.32, 143.69, 133.39, 131.02, 119.41. ^{31}P NMR (162 MHz, acetone-d6): δ -143.89 (h, J_{P-F} = 707 MHz), ^{19}F NMR (376 MHz, acetone-d6): δ -72.57 (d, J_{P-F} = 707 MHz).HRMS: calcd for $C_7H_5N_2O^+$ (M^+) 133.0402, found 133.0401.

3. General procedure for the diazonium coupling reaction

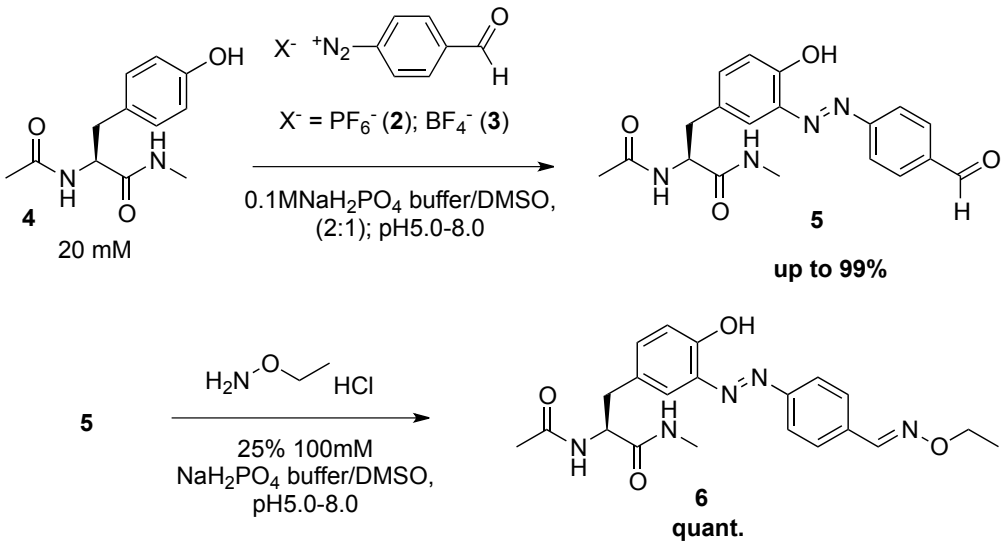

(*S*,*E*)-2-acetamido-3-(3-((4-formylphenyl)diazenyl)-4-hydroxyphenyl)-*N*-methylpropanamide (5). To a solution of *N*-acyl tyrosine methylamide **4** (20 mg, 0.0846 mmol) in 100 mM pH 7.0 NaH_2PO_4/Na_2HPO_4 buffer (2.83 mL) - DMSO (1.41 mL) was added the diazonium reagent **2** (25.9 mg, 0.0931 mmol) at room temperature. The resulting solution was stirred at room temperature for 45 min. After the reaction, water (2.82 mL) was added. The generated solid was filtered then washed with water and AcOEt to give **5** (31.0 mg, 99%) as a yellow solid.

^{1}H NMR (300 MHz, DMSO-d6): δ 10.9 (s, 1H), 10.1 (s, 1H), 8.16 (d, *J* = 8.6 Hz, 2H), 8.11 (d, *J* = 8.7 Hz, 2H), 7.93 (q, *J* = 4.7 Hz, 1H), 7.63 (d, *J* = 2.1 Hz, 1H), 7.32 (dd, *J* = 8.5, 2.2 Hz, 1H), 7.00 (d, *J* = 8.5 Hz, 1H), 4.45-4.37 (m, 1H), 2.94 (dd, *J* = 13.3, 5.0 Hz, 1H), 2.70 (dd, *J* = 13.5, 9.5 Hz, 1H), 2.56 (d, *J* = 4.6, 3H), 1.77 (s, 3H). ^{13}C NMR (150 MHz, DMSO-d6): δ 192.59, 171.36, 168.93, 154.82, 154.14, 138.40, 137.05, 135.61, 130.65, 129.53, 123.08, 121.33, 117.94, 54.03, 36.82, 25.40, 22.40.

HRMS: calcd for $C_{19}H_{21}N_4O_4$ (MH^+) 369.1557, found 369.1556.

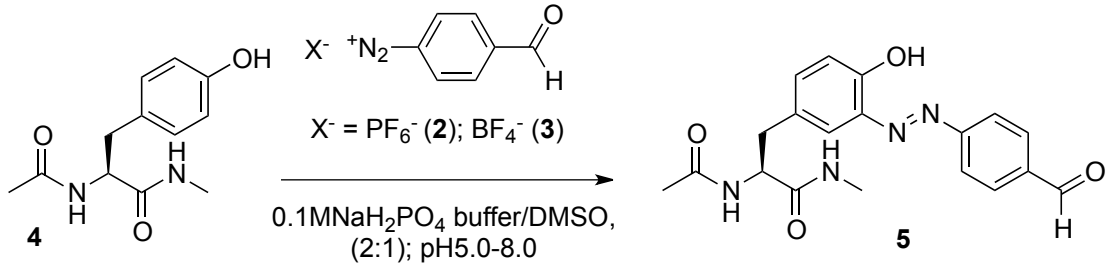

Table S1

Entry	Buffer	X^-	time	Isolated yield (%)
1	67 % 100 mM NaH_2PO_4-Na_2HPO_4, pH5-DMSO	PF_6^-	12 h	9
2	67 % 100 mM NaH_2PO_4-Na_2HPO_4, pH6-DMSO	PF_6^-	12 h	33
3	67 % 100 mM NaH_2PO_4-Na_2HPO_4, pH7-DMSO	PF_6^-	45 min	99
4a	67 % 100 mM NaH_2PO_4-Na_2HPO_4, pH7-DMSO	PF_6^-	45 min	93
5b	67 % 100 mM NaH_2PO_4-Na_2HPO_4, pH7-DMSO	PF_6^-	45 min	91
6	67 % 100 mM NaH_2PO_4-Na_2HPO_4, pH8-DMSO	PF_6^-	5 min	96
7	67 % 100 mM NaH_2PO_4-Na_2HPO_4, pH7-DMSO	BF_4^- c	45 min	84
8b	67 % 100 mM NaH_2PO_4-Na_2HPO_4, pH7-DMSO	BF_4^- c	45 min	63

a. the reagent was used after stocking at 4 ^oC for 3 months under air. b. the reagent was used after stocking at room temperature for a week under air. c. *Helv. Chim. Acta* **2002**, *85*, 108-114.

4. General procedure for oxime formation

(*S*)-2-acetamido-3-(3-((*E*)-(4-((*E*)-(ethoxyimino)methyl)phenyl)diazenyl)-4-hydroxyphenyl)-*N*-methylpropanamide (6). To a suspension of compound **3** (15 mg, 0.041 mmol) in 100 mM pH 7.0 NaH_2PO_4/Na_2HPO_4 buffer (0.531 mL) - DMSO (1.54 mL) was added ethoxyamine hydrochloride **4** (4.37 mg, 0.045 mmol) at room temperature. The resulting suspension was stirred at room temperature for 2 h. After the reaction, water (4.00 mL) was added. The generated solid was filtered then washed with water and AcOEt to give **5** (17.2 mg, quant.) as a yellow solid.

^1H NMR (300 MHz, DMSO-d6) (E:Z isomer ratio = 9 : 1): δ 10.9 (s, 1H), 8.33 (s, H), 8.13 (d, *J* = 8.5 Hz, 1H), 8.01 (d, *J* = 8.6 Hz, 2H), 7.93 (q, *J* = 4.5 Hz, 1H), 7.82 (d, *J* = 8.4 Hz, 2H), 7.62 (d, *J* = 2.0 Hz, 1H), 7.28 (dd, *J* = 8.4, 2.2 Hz, 1H), 6.97 (d, *J* = 8.4 Hz, 1H), 4.44-4.37 (m, 1H), 4.21 (q, *J* = 7.0 Hz, 2H), 2.94 (dd, *J* = 13.7, 5.1 Hz, 1H), 2.69 (dd, *J* = 13.6, 9.6 Hz, 1H), 2.56 (d, *J* = 4.6, 3H), 1.77 (s, 3H), 1.28 (t, *J* = 7.0 Hz, 3H). ^{13}C NMR (150 MHz, DMSO-d6): δ 171.39, 168.93, 153.30, 151.92, 147.74, 138.05, 134.38, 129.48, 127.71, 122.96, 122.57, 117.72, 69.30, 54.07, 36.84, 25.40, 22.40, 14.41. HRMS: calcd for $C_{21}H_{26}N_5O_4$ (MH^+) 412.1979, found 412.1980.

Table S2

Entry	Buffer	time	Isolated yield

			(%)
1	25 % 100 mM NaH_2PO_4-Na_2HPO_4, pH5-DMSO	30 min	Quant. [a]
2	25 % 100 mM NaH_2PO_4-Na_2HPO_4, pH6- DMSO	1 h	Quant.
3	25 % 100 mM NaH_2PO_4-Na_2HPO_4, pH7- DMSO	2 h	Quant.
4	25 % 100 mM NaH_2PO_4-Na_2HPO_4, pH8- DMSO	2 h	Quant.

a. quantitative yield.

5. General procedure for the three component reaction

Method 1

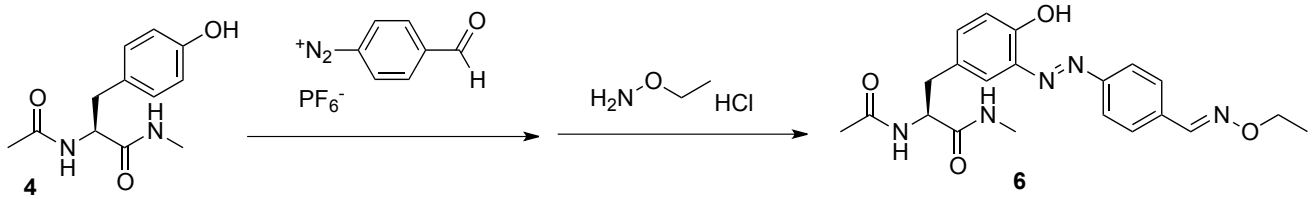

Compound (6). To a solution of *N*-acyl tyrosine methylamide **4** (20 mg, 0.0846 mmol) in 100 mM pH 7.0 NaH_2PO_4/Na_2HPO_4 buffer (2.83 mL) - DMSO (1.41 mL) was added the diazonium reagent **2** (25.9 mg, 0.0931 mmol) at room temperature. The resulting solution was stirred at room temperature for 1 h. After adding DMSO (1.41 mL), ethoxyamine hydrochloride (8.25 mg, 0.0846 mmol) was added at room temperature. The resulting suspension was stirred at room temperature for 2 h. The generated solid was filtered then washed with water and AcOEt to give **6** (32.5 mg, 93%) as a yellow solid.

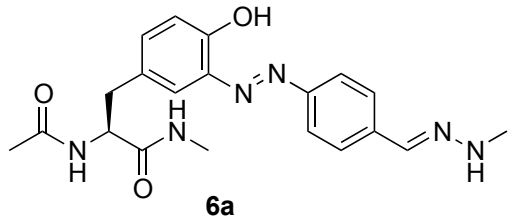

Compound (6a). The compound **6a** was prepared from methylhydrazine (4.50 μL, 0.0846 mmol), and was obtained as a brown solid (30.7 mg, 92%). The mixed suspension was stirred at room temperature for 12 h.

^{1}H NMR (300 MHz, DMSO-d6): δ 11.1 (s, 1H), 8.13 (d, *J* = 8.4 Hz, 1H), 7.92-7.91 (m, 3H), 7.82 (q, *J* = 4.4 Hz, 1H), 7.68 (d, *J* = 8.4 Hz, 1H), 7.62 (m, 1H), 7.46 (s, 1H), 7.26-7.23 (m, 1H), 6.94 (d, *J* = 8.4 Hz, 1H), 4.45-4.37 (m, 1H), 2.94 (dd, *J* = 14.3, 5.4 Hz, 1H), 2.87 (d, *J* = 4.1 Hz, 3H), 2.72 (dd, *J* =

13.5, 9.4 Hz, 1H), 2.57 (d, *J* = 4.4, 3H), 1.77 (s, 3H). ^{13}C NMR (150 MHz, DMSO-d6): δ 171.43, 168.94, 152.62, 149.66, 140.13, 137.83, 133.99, 129.42, 129.13, 125.37, 123.73, 122.93, 117.51, 54.09, 36.85, 33.13, 25.40, 22.40. HRMS: calcd for $C_{20}H_{25}N_6O_3$ (MH^+) 397.1983, found 397.1982.

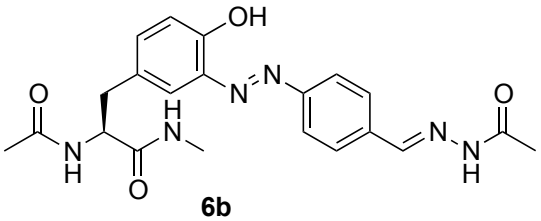

6b

Compound (6b). To a solution of *N*-acyl tyrosine methylamide **4** (9.69 mg, 0.041 mmol) in 100 mM pH 7.0 NaH_2PO_4/Na_2HPO_4 buffer (1.37 mL) - DMSO (0.686 mL) was added the diazonium reagent **2** (12.5 mg, 0.045 mmol) at room temperature. The resulting solution was stirred at room temperature for 1 h. After adding DMSO (2.05 mL), acetyl hydrazine (3.33 mg, 0.045 mmol) was added at room temperature. The resulting suspension was stirred at room temperature for 12 h. AcOEt and brine were added. The organic layer was separated and the aqueous layer was extracted once with AcOEt. The combined organic layer was concentrated *in vacuo*. The residue was washed with water and AcOEt to give **7** (14.8 mg, 85%) as a brown solid.

^{1}H NMR (300 MHz, DMSO-d6) (E:Z isomer ratio = 5 : 2): δ 11.4 (s, 1H), 11.0 (br, 1H), 8.14(d, *J* = 8.5 Hz, 1H), 8.07 (s, 1H), 8.02 (d, *J* = 8.5 Hz, 2H), 7.93 (q, *J* = 4.7 Hz, 1H), 7.86 (d, *J* = 8.5 Hz, 2H), 7.62 (d, *J* = 2.1 Hz, 1H), 7.28 (dd, *J* = 8.5, 2.1 Hz, 1H), 6.97 (d, *J* = 8.5 Hz, 1H), 4.44-4.37 (m, 1H), 2.94 (dd, *J* = 13.7, 4.7 Hz, 1H), 2.71 (dd, *J* = 13.2, 9.1 Hz, 1H), 2.56 (d, *J* = 4.5 Hz, 3H), 2.24 (s, 1H), 1.77 (s, 3H). ^{13}C NMR (150 MHz, DMSO-d6): δ 172.04, 171.42, 168.95, 153.26, 151.78, 141.42, 138.08, 136.63, 134.74, 129.49, 127.54, 122.99, 122.67, 117.71, 54.10, 36.85, 25.42, 22.41, 20.19. HRMS: calcd for $C_{21}H_{25}N_6O_4$ (MH^+) 425.1932, found 425.1925.

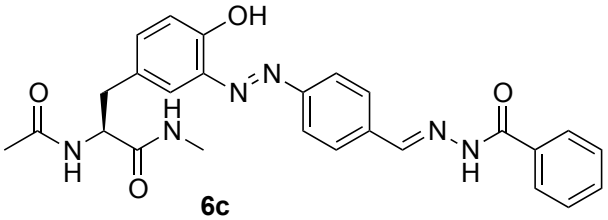

6c

Compound (6c). The compound **6c** was prepared from benzohydrazide (6.13 mg, 0.045 mmol), and was obtained as a brown solid (17.4 mg, 87%).

^{1}H NMR (300 MHz, DMSO-d6): δ 12.1 (br, 1H), 11.0 (br, 1H), 8.85 (br, 1H), 8.15(d, *J* = 8.4 Hz, 1H), 8.07 (d, *J* = 8.5 Hz, 2H), 7.96-7.93 (m, 5H), 7.64-7.52 (m, 4H), 7.31-7.28 (m, 1H), 6.98 (d, *J* = 8.4 Hz, 1H), 4.45-4.38 (m, 1H), 2.95 (dd, *J* = 13.7, 4.7 Hz, 1H), 2.72 (dd, *J* = 13.2, 9.9 Hz, 1H), 2.57 (d, *J* =

4.5 Hz, 3H), (s, 3H). ^{13}C NMR (150 MHz, DMSO-d6): δ 171.44, 168.97, 163.15, 153.35, 152.09, 146.59, 138.14, 136.69, 134.81, 133.19, 131.82, 129.51, 128.44, 128.03, 127.63, 123.06, 122.68, 117.75, 54.12, 36.86, 25.43, 22.43. HRMS: calcd for $C_{26}H_{27}N_6O_4$ (MH^+) 487.2088, found 487.2086.

Method 2

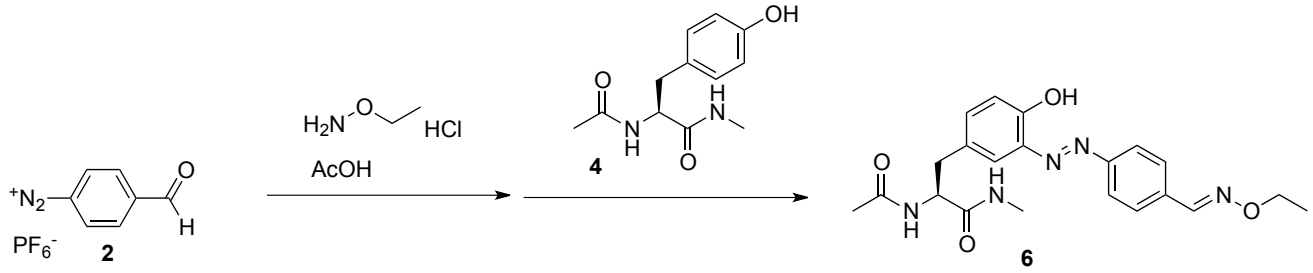

Compound (6). To a solution of diazonium salt 2 (25.9 mg, 0.0931 mmol) in DMSO (1.41 mL) were added the ethoxyamine hydrochloride (9.95 mg, 0.102 mmol) and AcOH (5.32 µL, 0.0931 mmol) at room temperature. The resulting solution was stirred at room temperature for 2 h, and was added to the solution of *N*-acyl tyrosine methylamide **4** (20.0 mg, 0.0847 mmol) in 138 mM pH 8.0 NaH_2PO_4/Na_2HPO_4 buffer (4.25 mL) - DMSO (0.686 mL). After the reaction, water (4.00 mL) was added. The generated solid was filtered and then washed with water and AcOEt to give **6** (15.8 mg, 45%) as a yellow solid.

6. NMR spectra of compounds

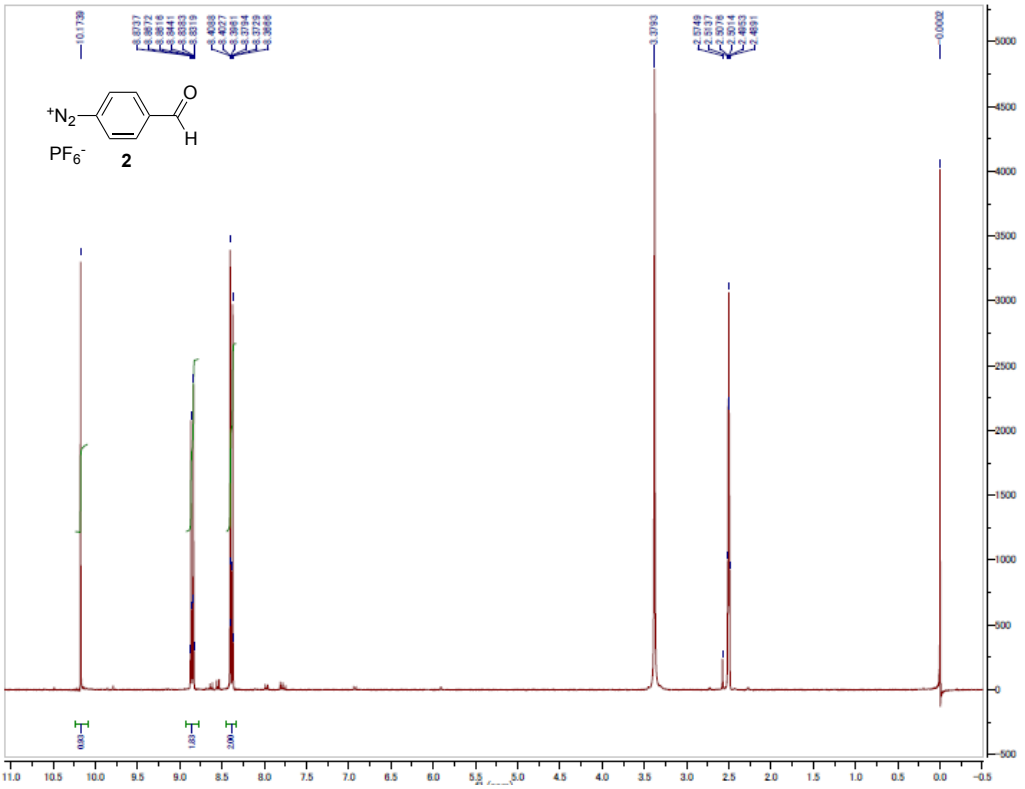

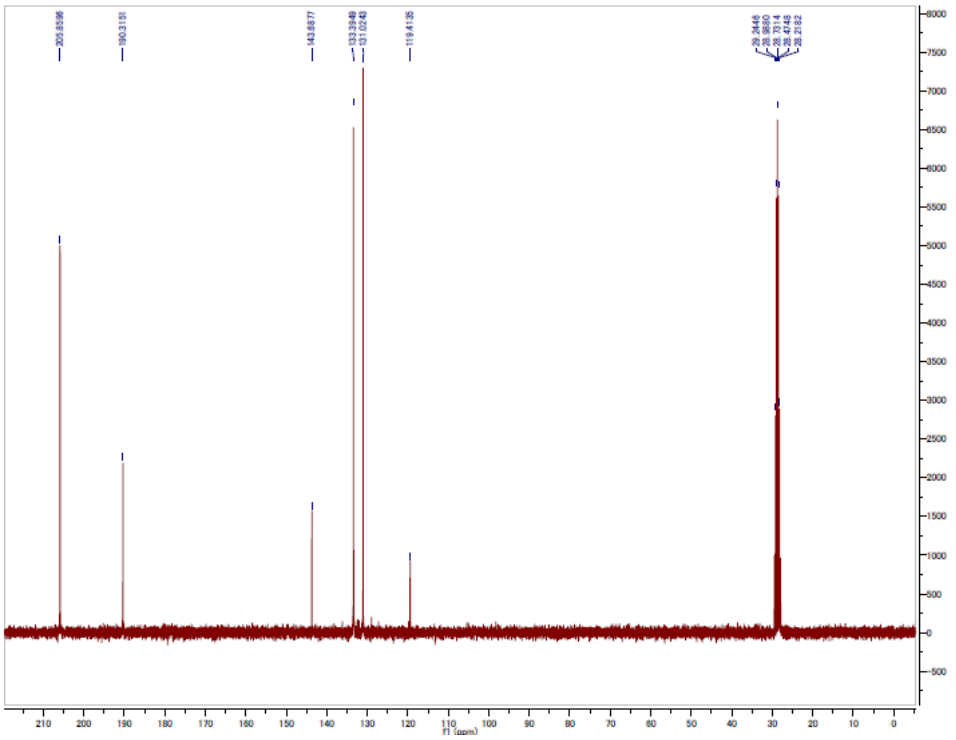

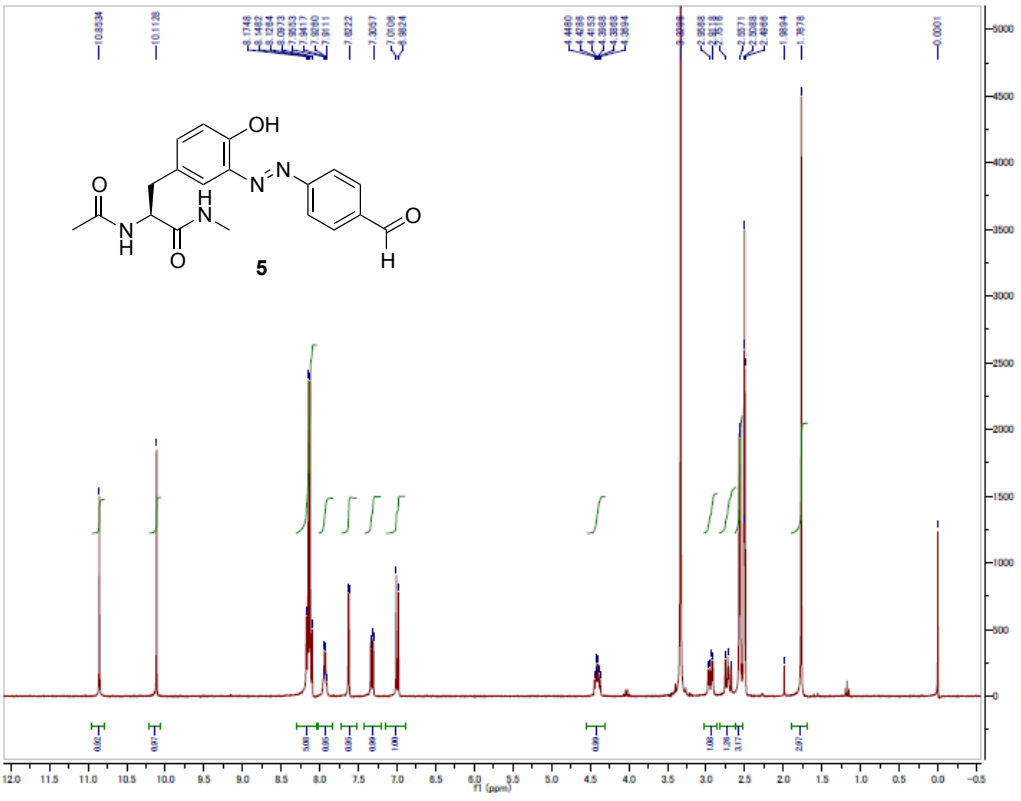
OH
N
N
O
N
H
O
N
H
O
H
5

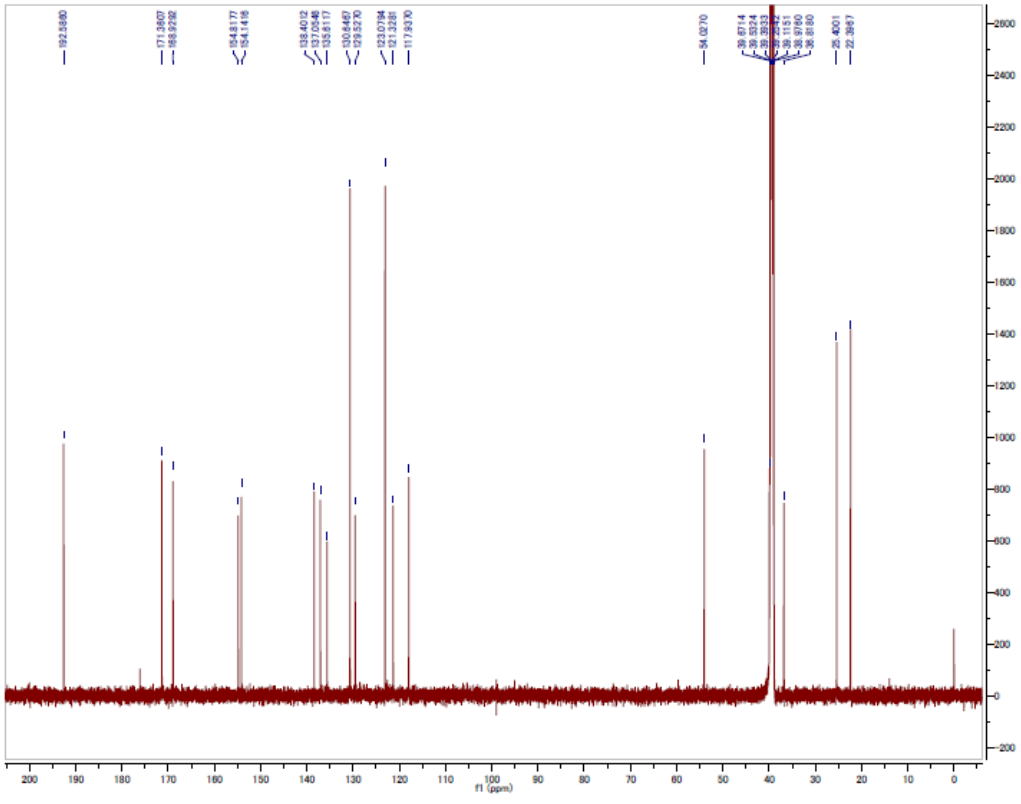

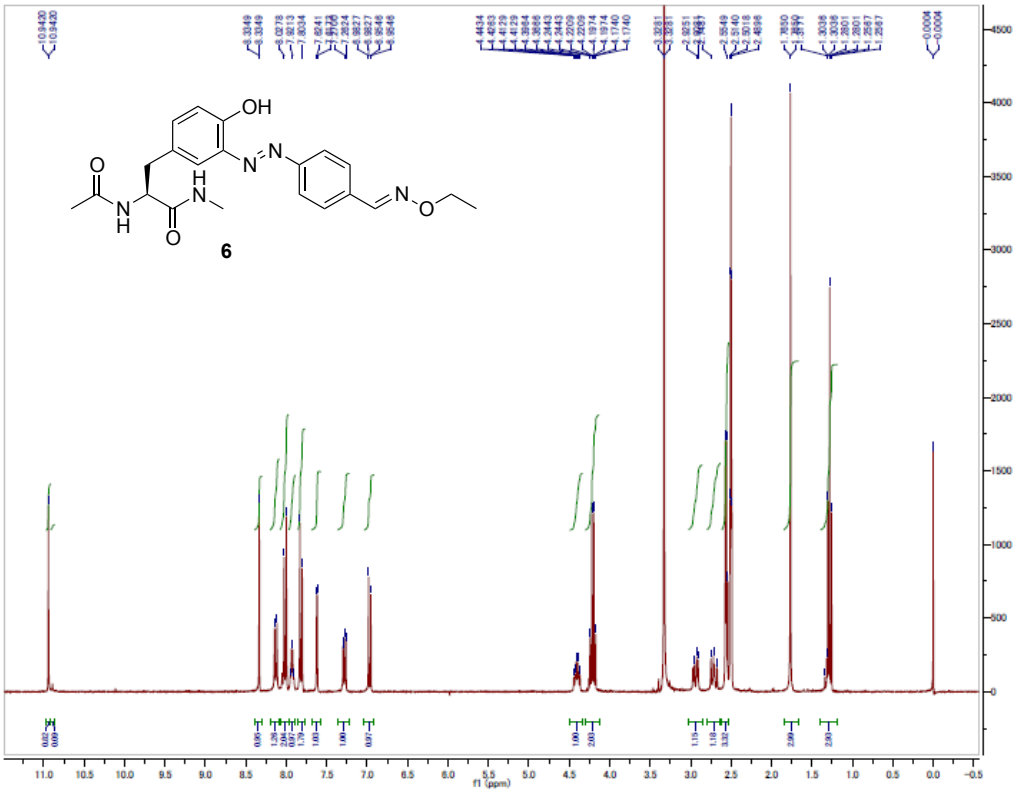
OH
N
N
O
N
H
N
O
O
6

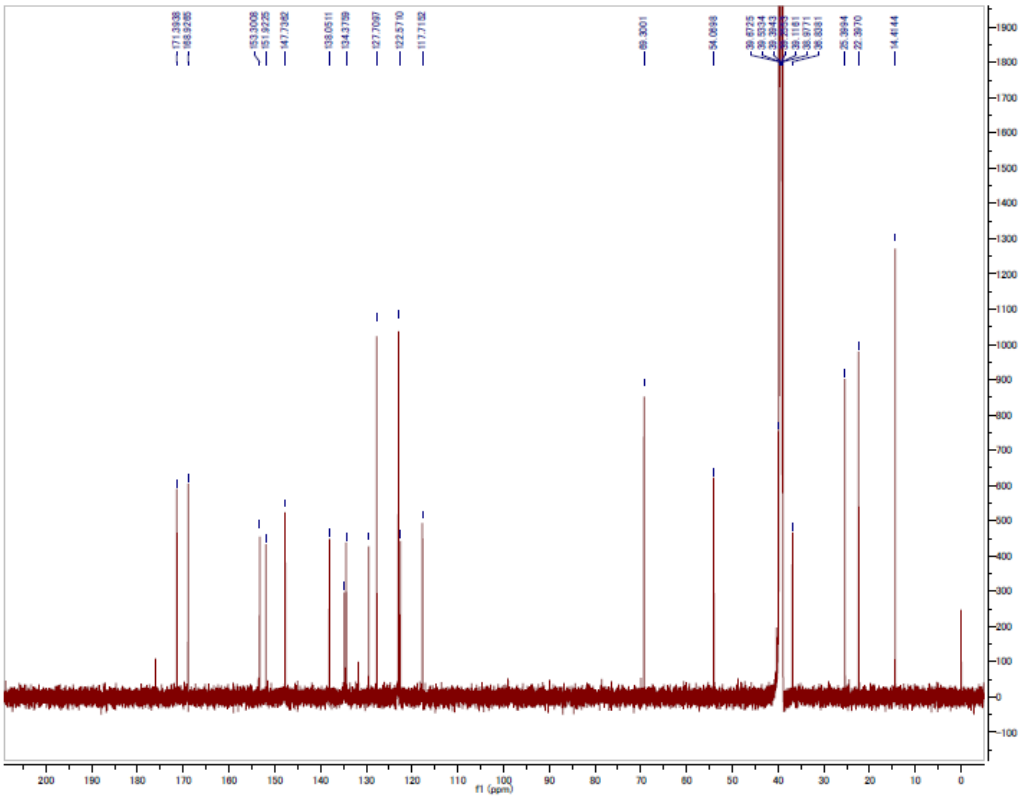

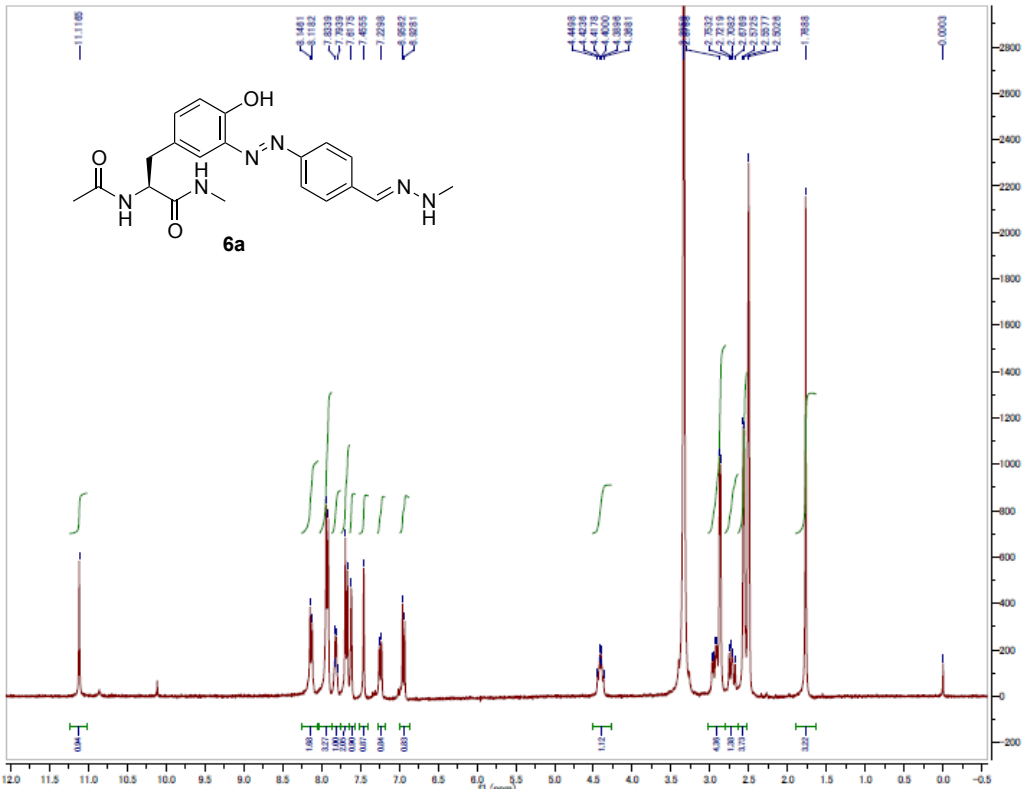
OH
O
N
H
N
N
N
H
N
O
6a

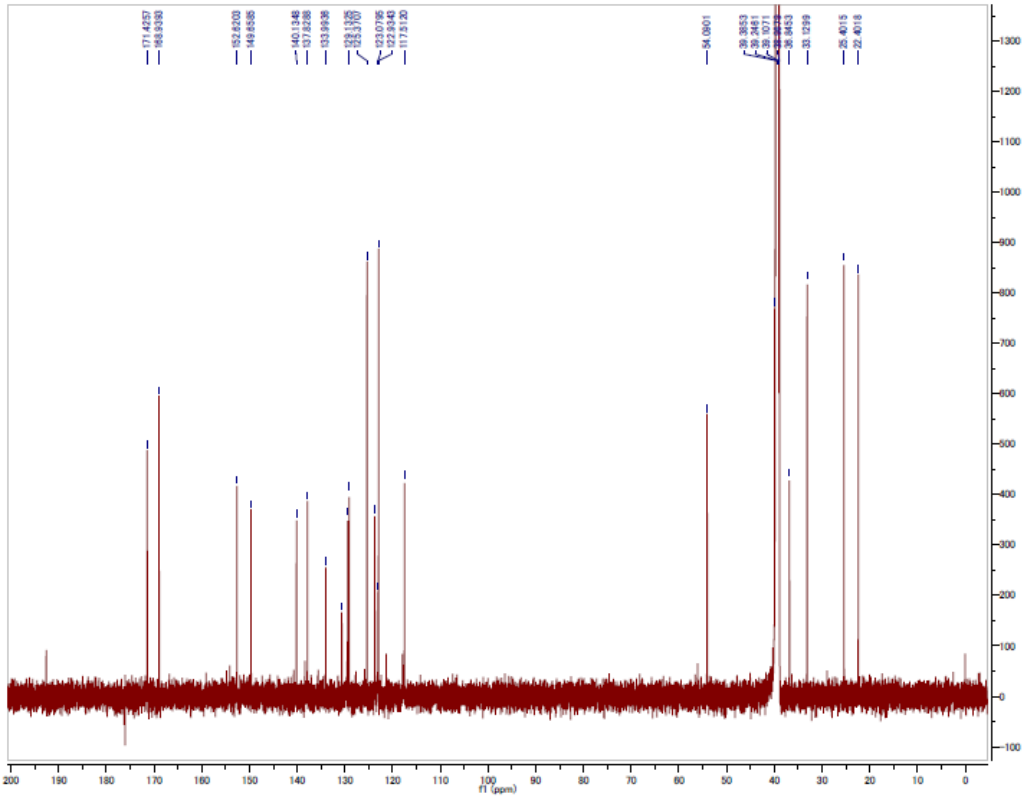

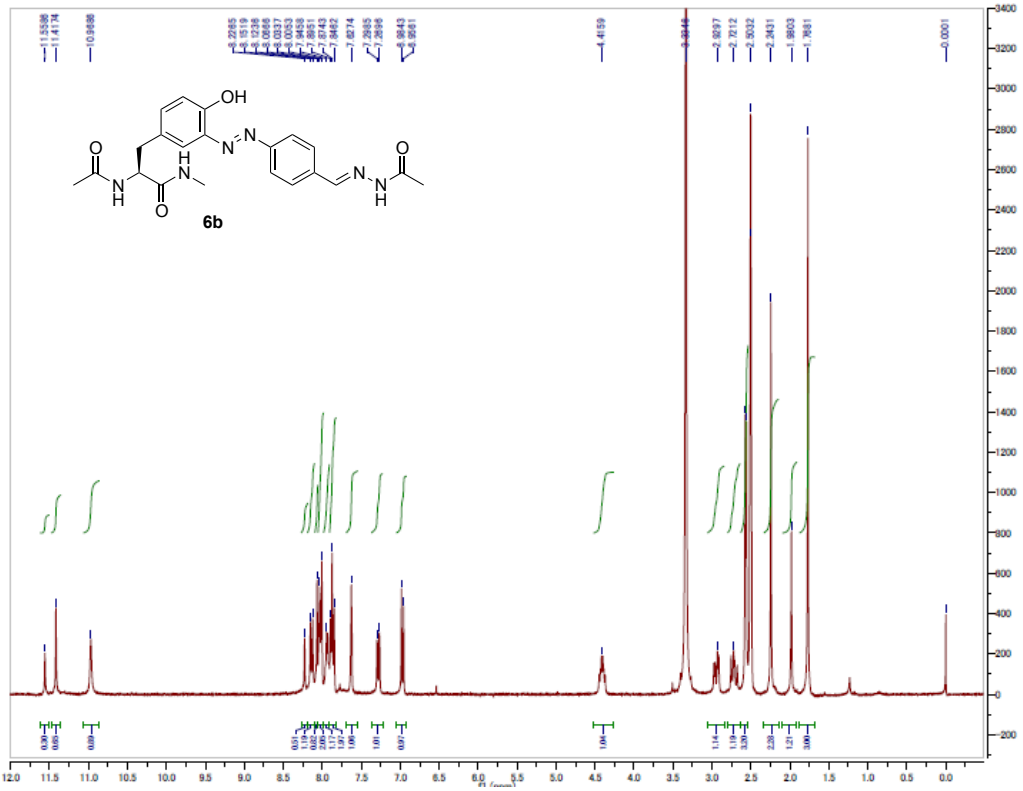
OH
O
N
H
N
O
N
N
H
N
O
6b

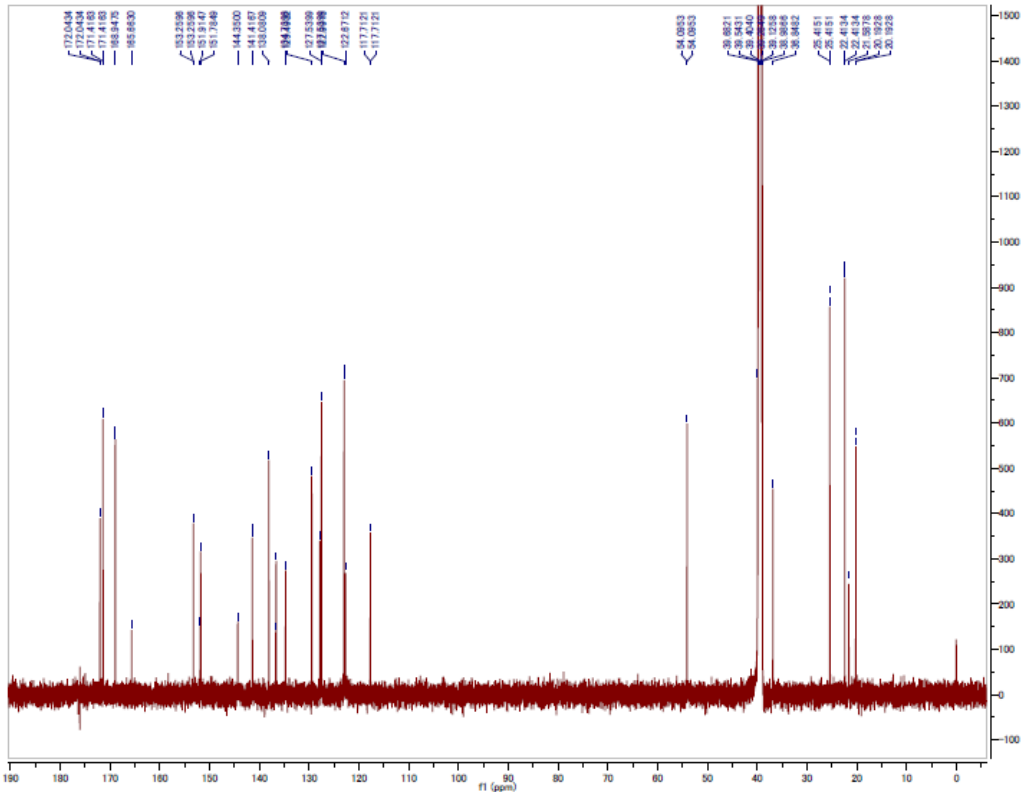

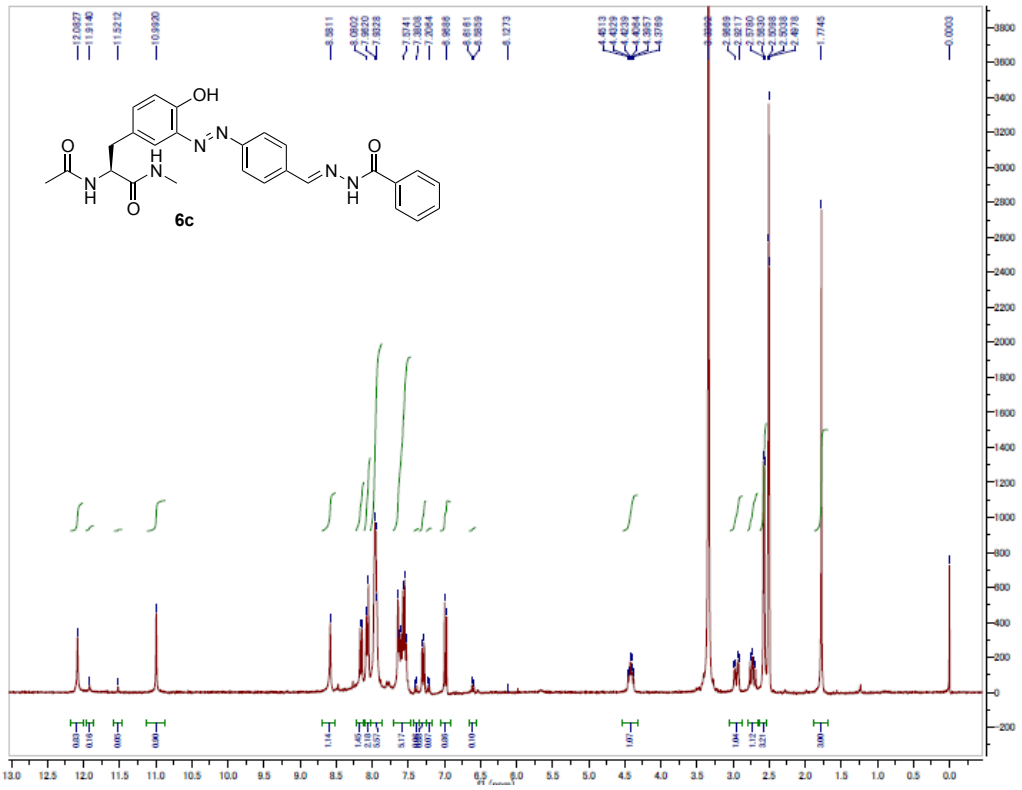
OH
N
N
H
N
O
N
N
H
O
O
N
H
O
6c

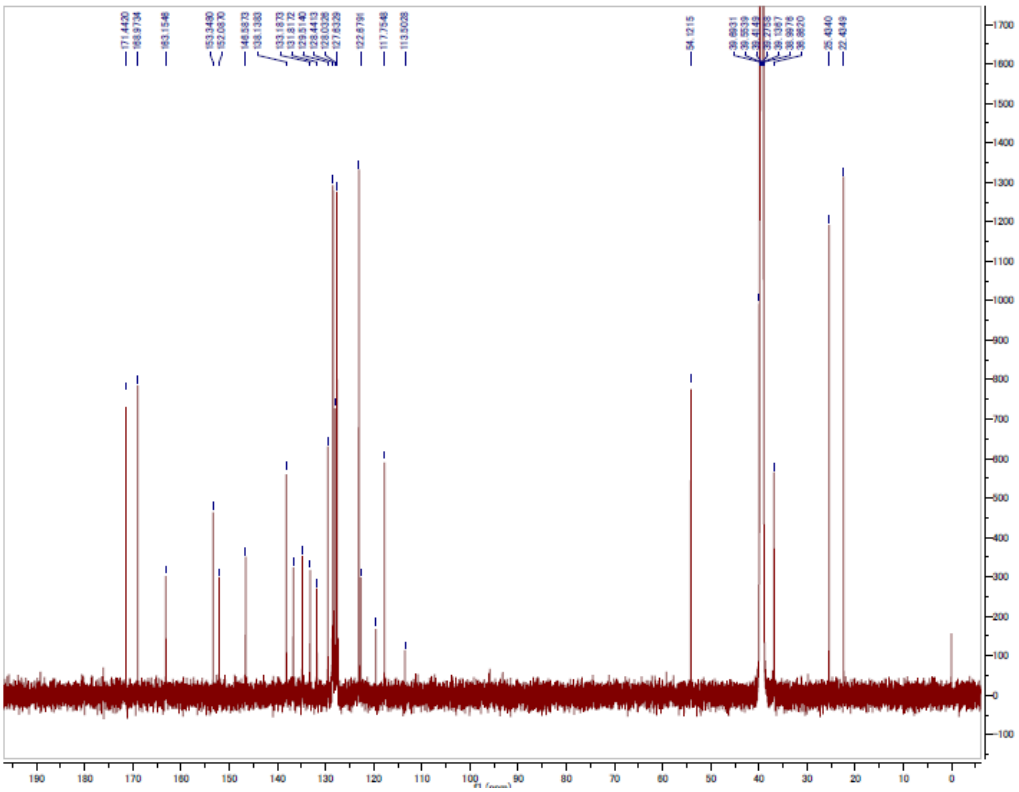

7. Amino Acid Selectivity Study

General procedure.

N-acyl methyl amides of amino acid were obtained as previously described.[3] Equimolar solution of six amino acids *N*-acyl methyl amides (Tyr, His, Cys, Ser, Lys, Trp) was prepared in 0.1M Na_2HPO_4 buffer (pH 7, 7.4, 8). Final concentration of each amino acid was 100 μM (1 eq). 1 mL of the amino acid mixture solution was transferred into LCMS sample vial and 5 μL of FBDP solution in acetonitrile (20 mM solution, 1 eq) was added. Reaction mixture was vortexed gently and allowed to react at room temperature. Each reaction was performed independently at least 3 times. Aliquot of reaction mixture (5 μL) was analyzed by LCMS after 30 min of reaction time using Agilent LC/MSD SL mass spectrometer with Zorbax 300SP-C8, 5 μm, 4.6x50 mm column (Agilent). HPLC parameters were as follows: flow rate 0.5 ml/min, 5% mobile phase B over 2 min followed by a gradient to 5 to 95% B from 2 to 8 min, post time 4 min. Mobile phase A was 0.1% formic acid (v/v) in HPLC-grade H_2O, and mobile phase B was 0.1% formic acid (v/v) in acetonitrile (v/v). API-ESMS data was collected for 115-1000 m/z positive and negative polarity. Data was analyzed using Agilent analysis software. MS TIC positive polarity trace was used to evaluate reaction selectivity. For clarity and quantification purposes traces corresponding to expected product ions were extracted from the MS TIC spectra (Figures S1-S6). Area under the peak was used to calculate content of each product (Tables S3, S4, S5).

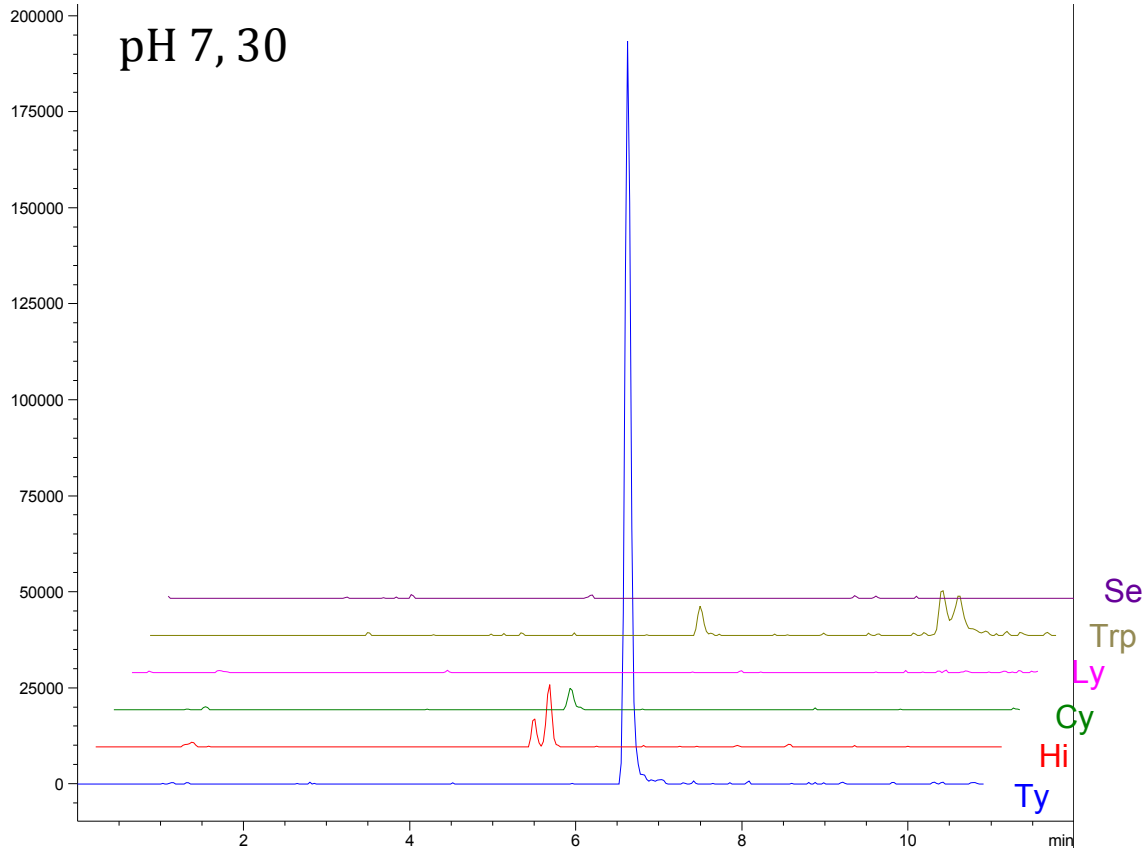

Figure S1. Example of 3D overlay of the extracted product ion traces for amino acids in the reaction mixture at pH 7.

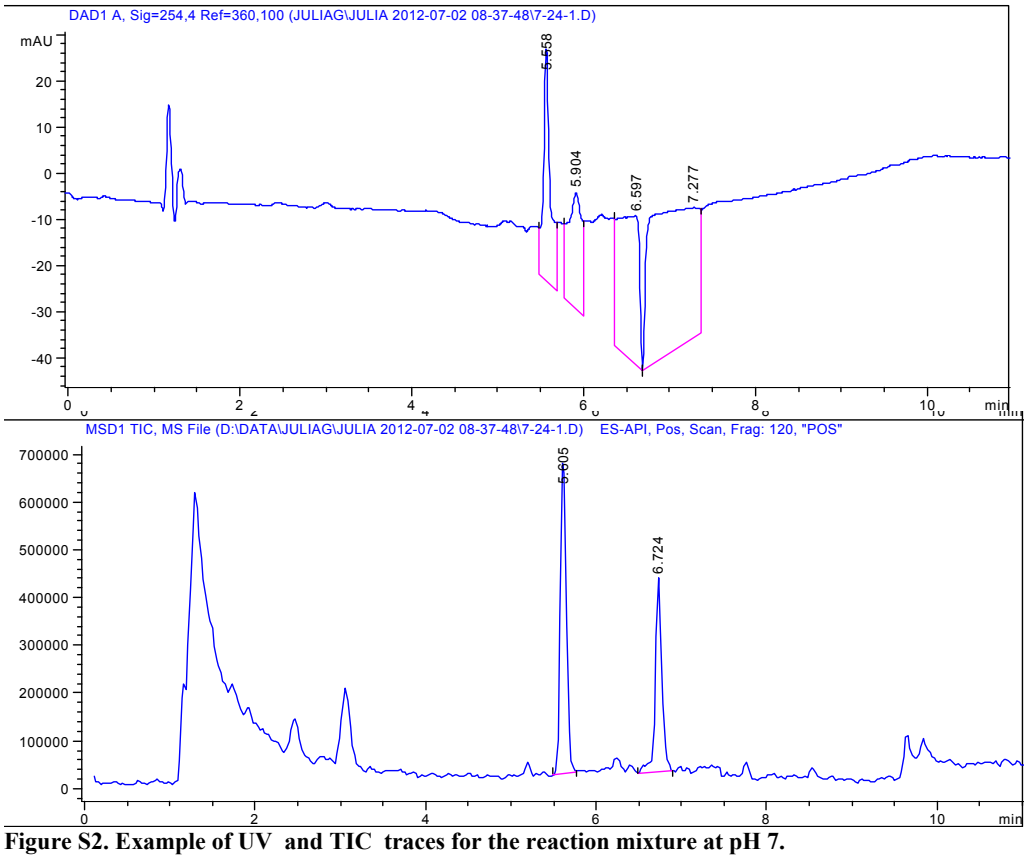

Figure S2. Example of UV and TIC traces for the reaction mixture at pH 7.

Table S3. Summary of the amino acid modification in the equimolar mixture at pH 7.

pH 7	% conversion				
Amino Acid Adduct	**1**	**2**	**3**	**Average**	**STD**
Tyr	89.2	84.7	87.7	87.2	2.305
His	7.1	11.0	2.8	7.0	4.091
Cys	2.0	1.9	2.7	2.2	0.429
Lys	0.0	0.0	0.0	0.0	0
Trp	1.0	2.4	6.8	3.4	3.021
Ser	0.6	0.0	0.0	0.2	0.361

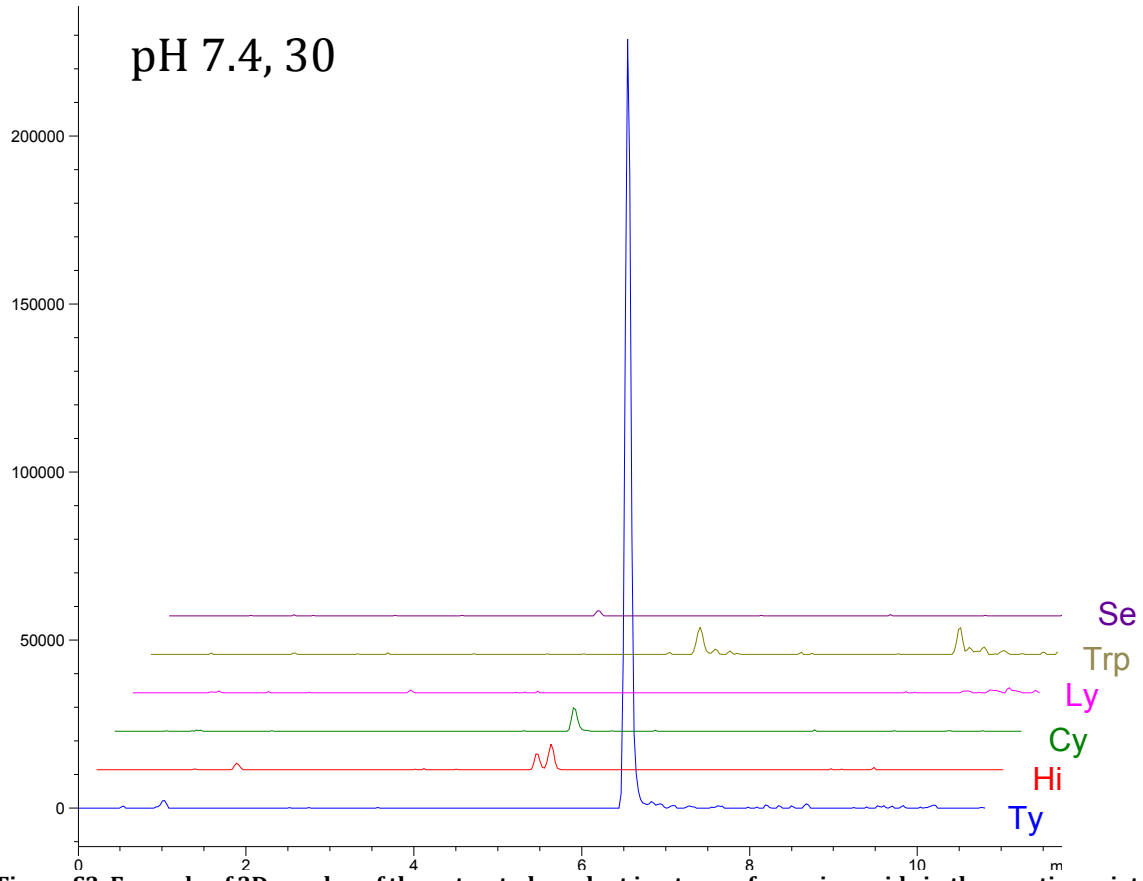

Figure S3. Example of 3D overlay of the extracted product ion traces for amino acids in the reaction mixture at pH 7.4.

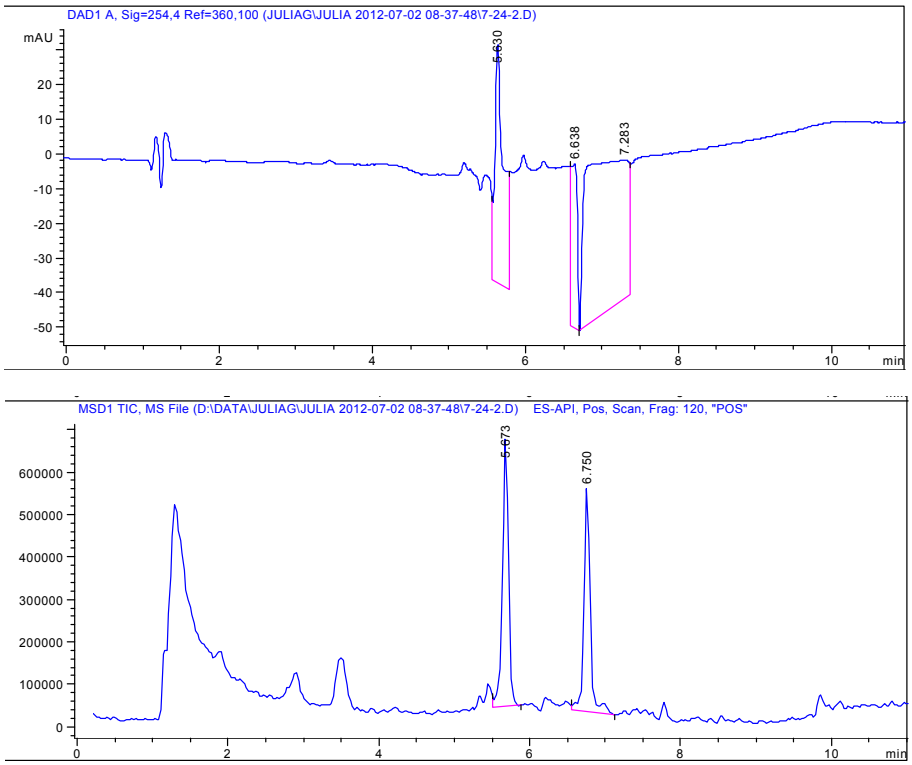

Figure S4. Example of UV and TIC traces for the reaction mixture at pH 7.4.

Table S4. Summary of the amino acid modification in the equimolar mixture at pH 7.4.

pH 7.4	% conversion				
Amino Acid Adduct	**1**	**2**	**3**	**Average**	**STD**
Tyr	92.8	90.4	84.0	89.1	4.537
His	0.6	5.3	10.6	5.5	5.005
Cys	2.6	1.7	2.4	2.2	0.463
Lys	0.0	0.0	0.0	0.0	0
Trp	4.0	2.7	3.0	3.2	0.697
Ser	0.0	0.0	0.0	0.0	0

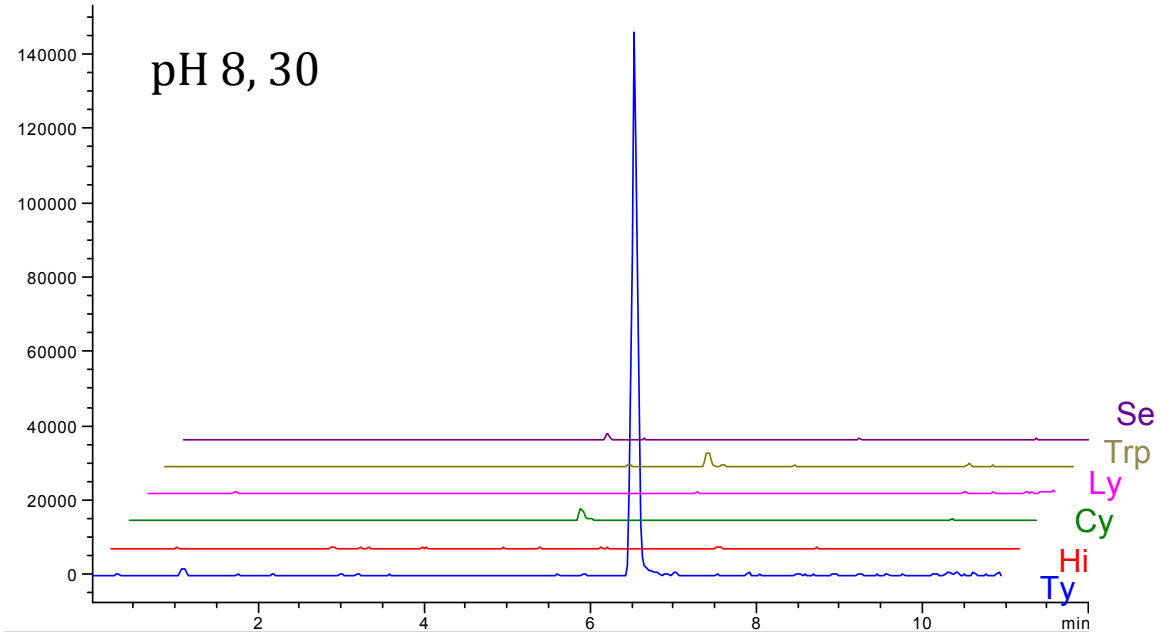

Figure S5. Example of 3D overlay of diazocoupling products MS traces for reaction at pH 8.

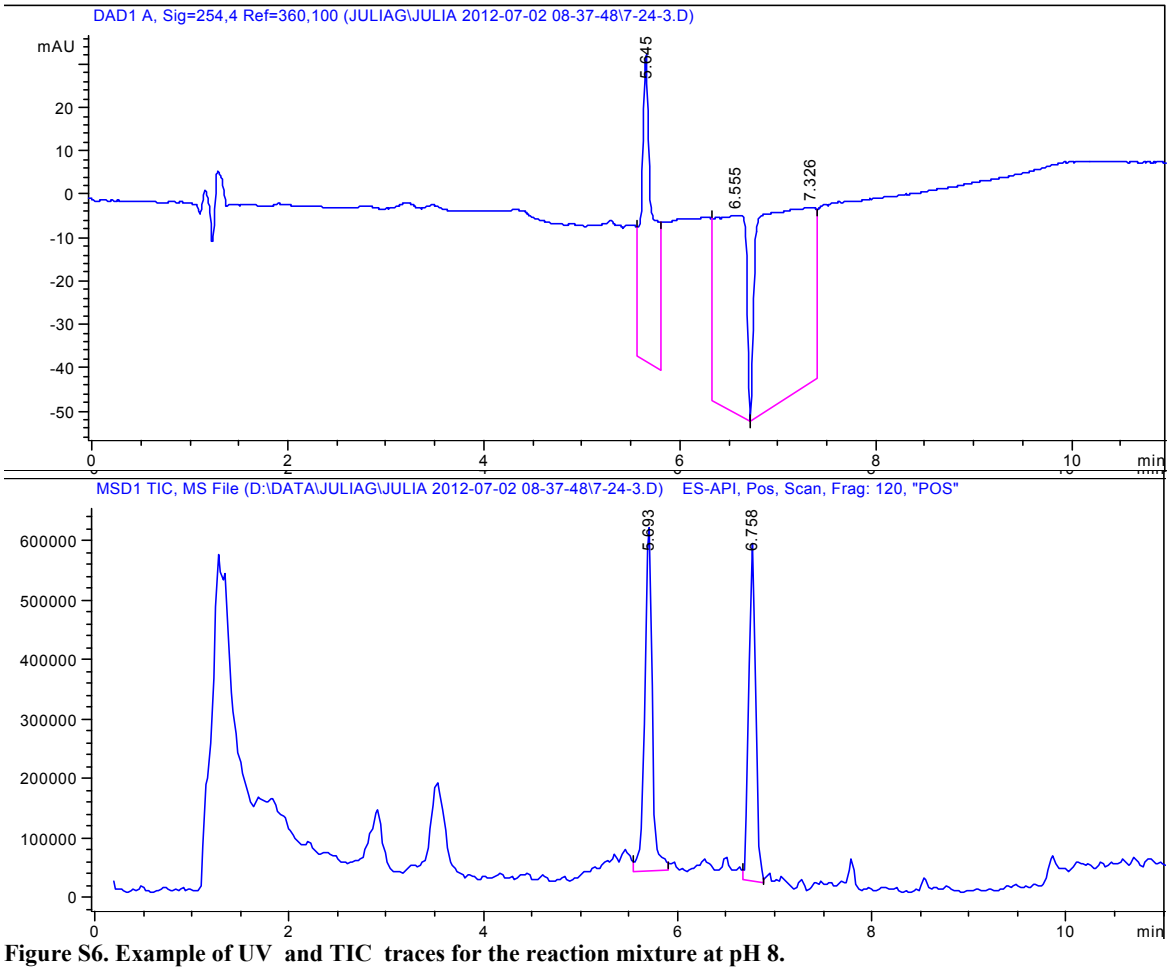

Figure S6. Example of UV and TIC traces for the reaction mixture at pH 8.

Table S5. Summary of the amino acid modification in the equimolar mixture at pH 8.

pH 8	% Conversion				
Amino Acid Adduct	**1**	**2**	**3**	**Average**	**STD**
Tyr	97.0	94.8	94.0	95.3	1.559
His	0.0	1.2	1.7	1.0	0.874
Cys	2.1	2.0	1.2	1.8	0.454
Lys	0.0	0.0	0.0	0.0	0
Trp	0.9	2.0	3.1	2.0	1.076
Ser	0.0	0.0	0.0	0.0	0

8. Tocinoic adic modification with FBDP

To the 1 ml of 100 μM solution of tocinoic acid (Sigma-Aldrich) in 0.1 M Na_2HPO_4 buffer pH 7 or pH 8 was added 10 μL of 20 mM solution of FBDP in acetonitrile. Reaction was vortexed gently and allowed to react at room temperature. Aliquot of reaction mixture (5 μL) was analyzed by LCMS after 30 min of reaction time using Agilent LC/MSD SL mass spectrometer with Zorbax 300SP-C8, 5 μm, 4.6x50 mm column (Agilent). HPLC parameters were as follows: flow rate 0.5 ml/min, 5% mobile phase B over 2 min followed by a gradient to 5 to 95% B from 2 to 8 min, post time 4 min. Mobile phase A was 0.1% formic acid (v/v) in HPLC-grade H_2O, and mobile phase B was 0.1% formic acid (v/v) in acetonitrile (v/v). API-ESMS data was collected for 115-1000 m/z positive and negative polarity. Data was analyzed using Agilent analysis software. MS TIC positive polarity trace was used to evaluate reaction selectivity. For clarity and quantification purposes traces corresponding to starting material and expected product ions were extracted from the MS TIC spectra (Figure S7). Area under the peak was used to calculate content of remaining starting material and product (Table S6). No *N*-terminal modification product has been found in the reaction mixture.

Table S6. Tocinoic acid modification summary.

pH	Tocinoic acid	Expected [MH+]	Found [MH+]	Peak area	%
7	Starting material	741.2	741.2	4304.12646	11.5
	Product	873.2	873.2	3.32795e4	88.5
8	Starting material	741.2	741.2	8853.909	8.6
	Product	873.2	873.2	9.4148e4	91.4

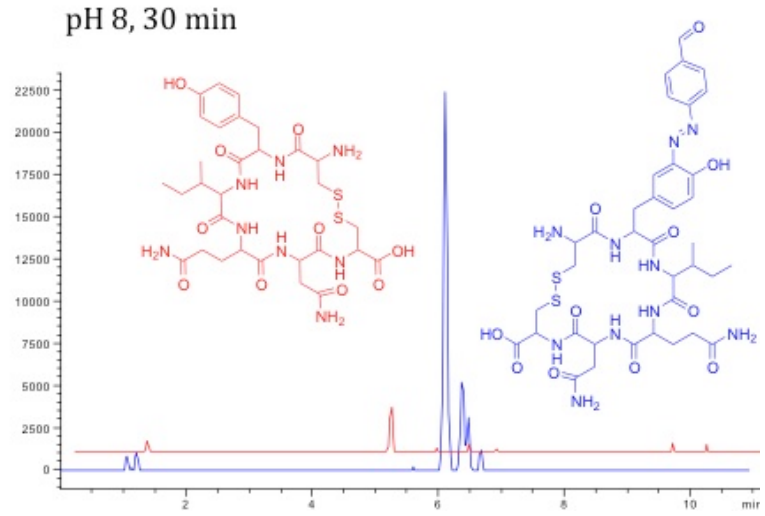

Figure S7. Example of the 3D overlay of extracted starting material and product ions, reaction at pH 8.

9. BSA modification with FBDP

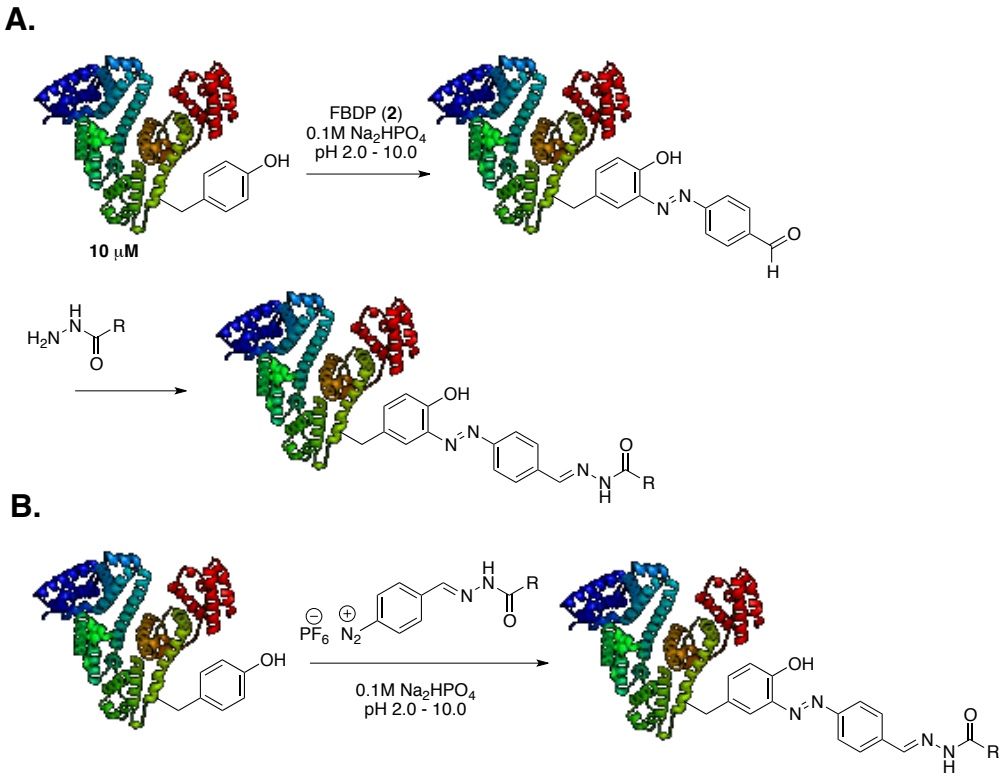

Figure S8. Schematic representation of the BSA modification methods.

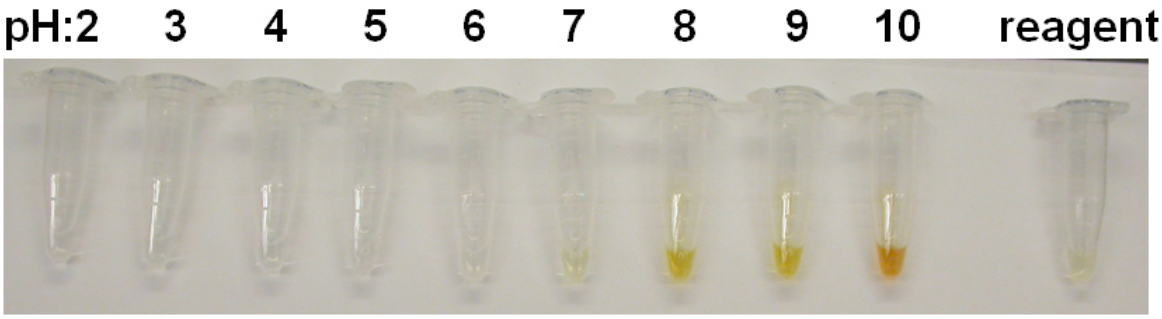

Figure S9. Visual follow up of the reaction of 100μM FBDP reagent 2 with 30 μM solution of BSA at pH 2-10.

General modification procedure.

Method A (Figure S8).

To the 0.5 ml Eppendorf tube containing 99 μL of BSA solution (30 μM solution in 0.1M phosphate buffer pH 2-10) was added 1 μL or reagent solution (10 mM solution in CH_3CN) and reaction mixture was vortexed briefly. Reaction was kept at room temperature for 30 minutes and the conversion was followed by visual observation (Figure S9) and UV-vis measurement at 340 nm that corresponds to the absorbance of diazene functionality (data not shown). The reaction products were purified using Zeba Spin desalting column (7,000Da MWC, Pierce) and the buffer was exchanged to PBS pH 5. In the 1.5 mL Eppendorf tube 99 mL of 30 μM solution of BSA-aldehyde in 0.1 M PBS pH 5 was treated with biotin hydrazide (1 μL of 100 mM solution in DMSO), over night 4 ^{o}C, followed by removal of the excess of small molecule by Zeba Spin Desaltin column. The reaction products were tested in streptavidin ELISA (Figure S11) and characterized by MALDI-TOF (Figure S13).

Method B (Figure S8).

In the 0.5 ml Eppendorf tube were combined biotin hydrazide (10 μL of 100 mM solution in CH_3CN; 1 eq), trifluoroacetic acid (10 μL of 200 mM solution in CH_3CN; 2 eq) and FBDP (10 μL of 100 mM solution in CH_3CN; 1 eq). The reaction mixture was mixed and allowed to react for 1 hr. Aliquot of the reagent was diluted and analyzed by LCMS (Figure S10) confirming formation of the hydrazide.

To the 0.5 ml Eppendorf tube containing 99 μL of BSA solution (30 μM solution in 0.1M phosphate buffer pH 2-10) was added 1 μL or reagent solution (10 mM solution in CH_3CN) and reaction mixture was vortexed briefly. Reaction was kept at room temperature for 30 minutes and reaction products were purified using Zeba Spin desalting column (7,000Da MWC, Pierce). The reaction products were tested in streptavidin ELISA (Figure S12) and characterized by MALDI-TOF.

Streptavidin ELISA.

Costar 96-well ELISA plate (Corning, Acton, MA) was coated with 100 ng of protein in 100 μL of PBS pH 7.4 and incubated overnight at 4 ^{o}C. The plate was washed with PBS containing 0.01% tween-20 (100 μL x 3). After blocking with 100 μL of 3% BSA/PBS, 0.01% tween-20 for 1 h at 37 ^{o}C and washing (100 μL of PBS containing 0.01% tween-20 x 5), 100 μL of streptavidin-HRP (Zymed, 1:3000 dilution in PBS) was added to each well and the plate was incubated for 1 hr at 37 ^{o}C. The plate was thoroughly washed with PBS/0.01% tween (100 μL x 5). Upon addition of the ABTS developing solution and incubation at room temperature for 10 min the absorbance was read at 405 nm. All measurements were done in triplicate and an average normalized result was graphed.

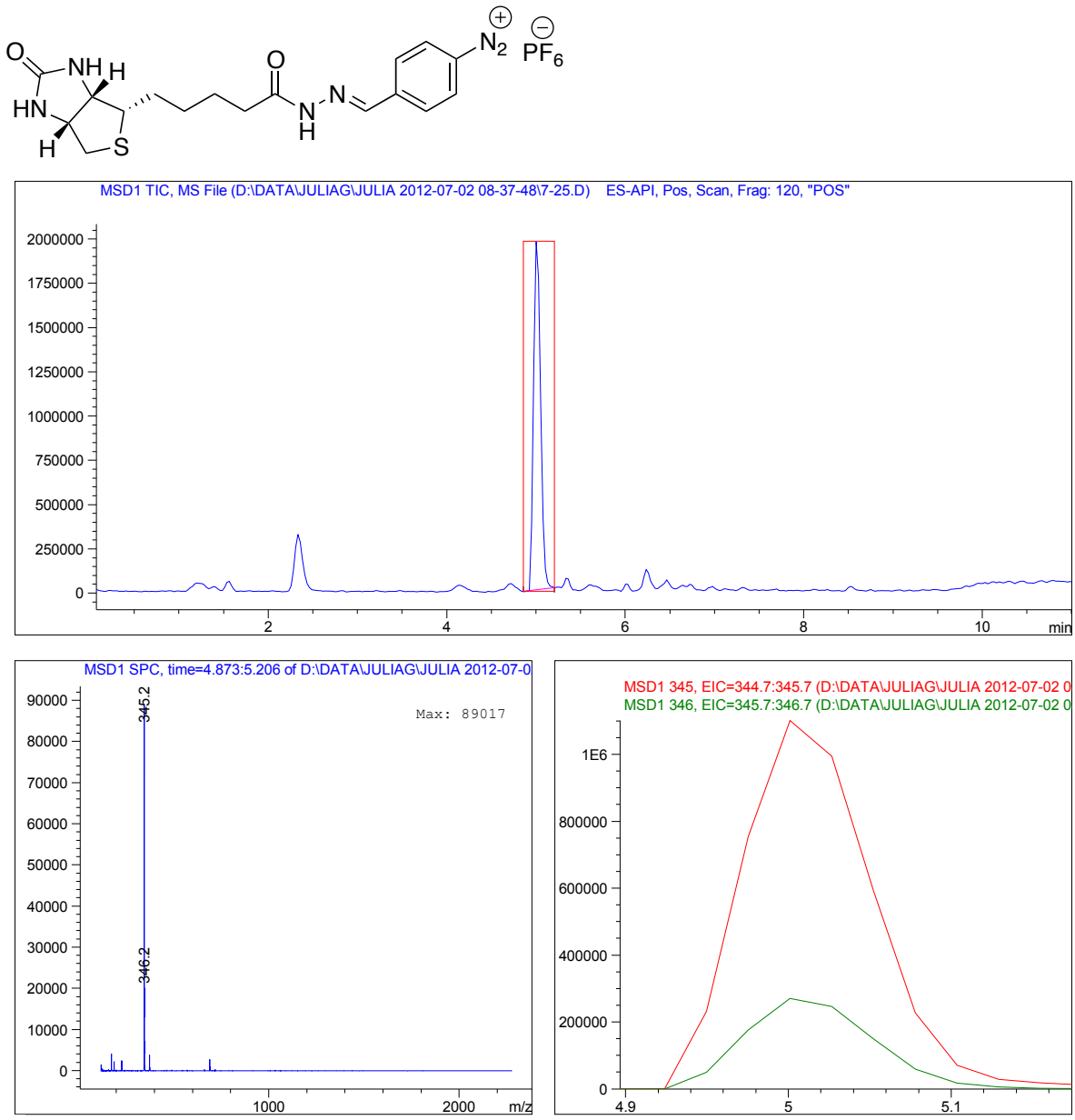


```
Peak #1 at  5.008 min ( 4.862 to  5.209 min)
-> The analysis found only one component, indicating a pure peak. <-

Component 1:  Peak at Scan 193.3. Top ions are  345 346 344
```

Figure S10. **LCMS analysis of the *in situ* formed biotin-hydrazine-diazonium. Found [M+]=345.2 corresponds to –N_2 adduct formed under MS ionization conditions**

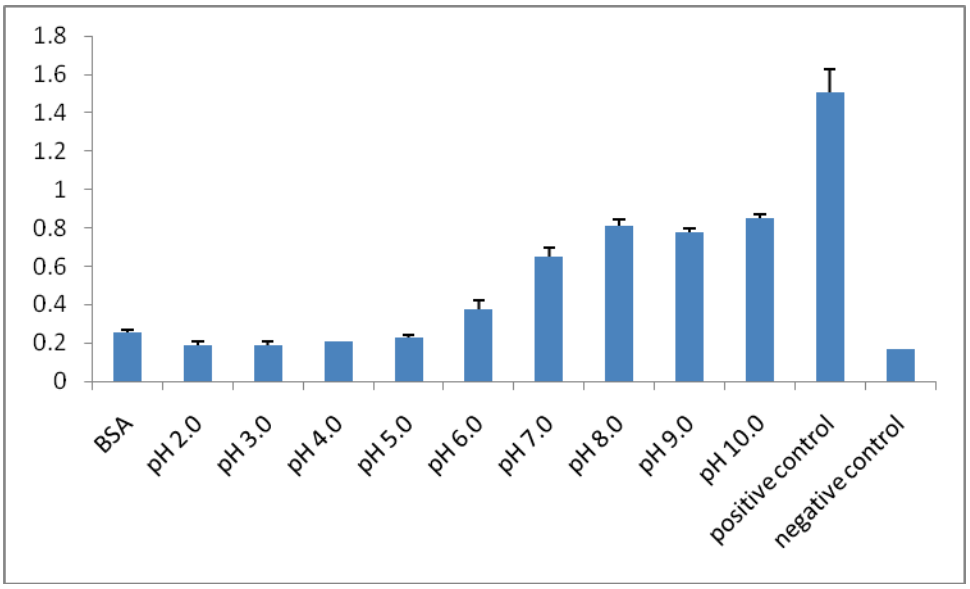

Figure S11. Streptavidin ELISA for the products of Method A. Biotinylated human IgG was used as positive control. Negative control reaction: 99 mL of 30 mM solution of BSA in 0.1 m PBS pH 6 was treated with biotin hydrazide(1 mL of 100 mM solution in DMSO), over night 4 ^{o}C, followed by removal of the excess of small molecule by Zeba Spin Desalting column.

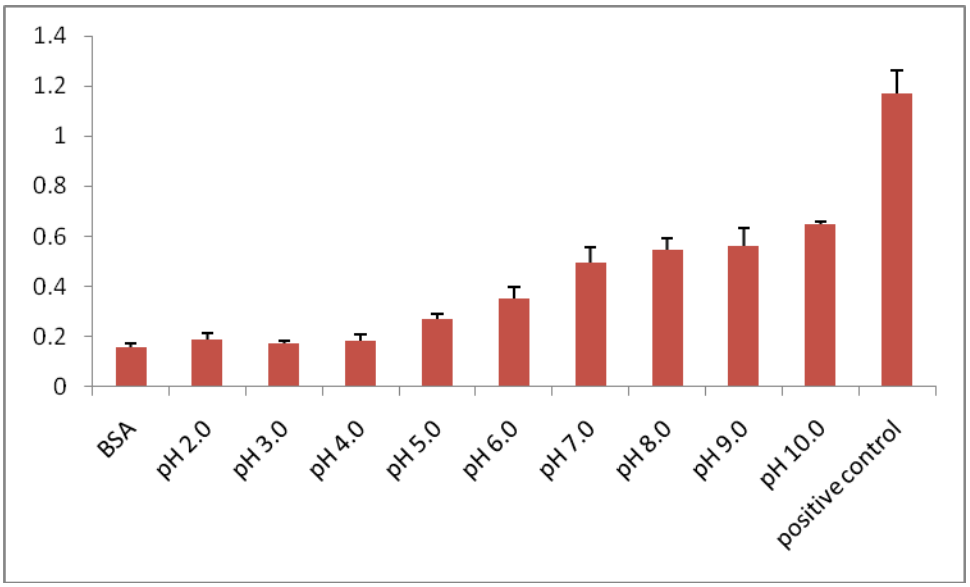

Figure S11. Streptavidin binding ELISA results for the products of Method B. Biotinylated human IgG was used as a positive control.

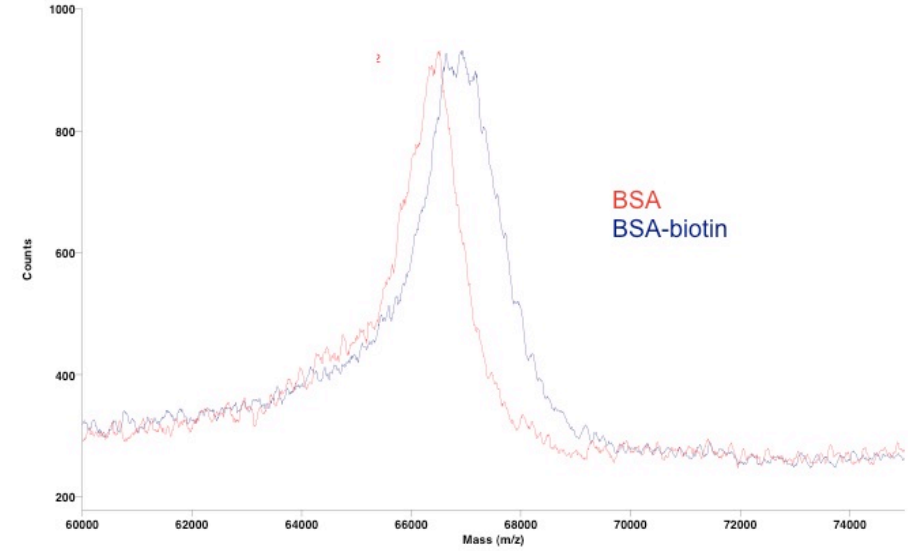

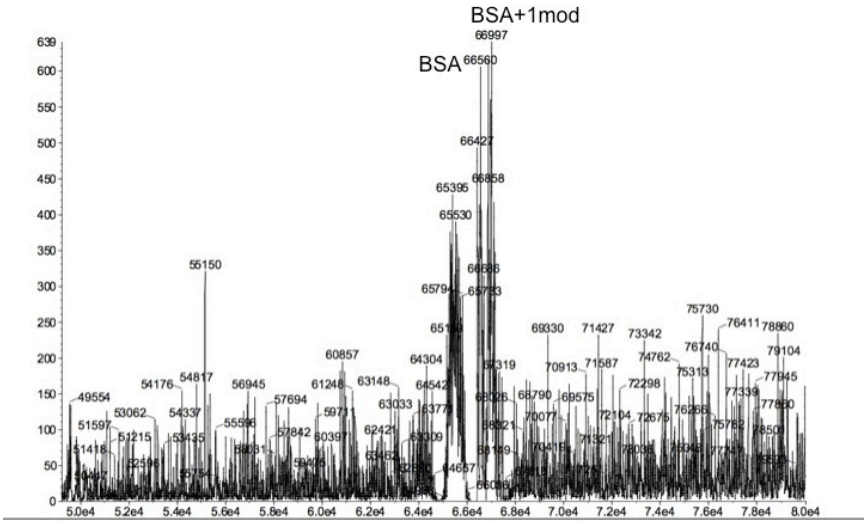

Figure S12. (A)Example of MALDI-TOF characterization of FBDP-based biotin modification of BSA. (BSA, red, MWav= 66417; BSA-biotin, blue, MWav=66892). (B) ESI-MS characterization of biotin modified BSA (MW of modification 446Da).

10. Chymotrypsinogen A modification and activity assay

Chymotrypsinogen was modified with 3.3 equivalents of FBDP at pH 8.0 following BSA modification procedure described above. Activity assay was performed essentially as described by Francis et al.[1] In brief, an 114 µL aliquot of a reaction mixture for the modification of chymotrypsinogen (1.0 mg/mL, 38 µM total protein content) was treated with 2.6 µL of a solution of sequencing grade modified trypsin (Promega, 20 µg reconstituted with 200 µL of 50 mM acid). The

activation of the zymogen was allowed to proceed for 10 minutes at room temperature before being purified and performing buffer exchange into 0.1 M Tris buffer (pH 7.6) using Zeba spin desalting column (Pierce). 40 µL aliquots of the activated protease were then added to 160 µL of 0.5 mM chymotrypsin substrate I, colorimetric (Suc- GGF-pNA, Calbiochem 230912) in 50 mM CaCl2, 20 mM Tris buffer, pH 7.6 (light green triangles). An analogous procedure was followed for reagent modified chymotrypsinogen A samples (light purple squares). In a negative control experiment, the enzyme was not activated with trypsin before addition of the tripeptide substrate (red squares), or the substrate was monitored with addition of only Tris buffer (blue diamonds). The progress of the reaction was monitored by UV-Vis spectrophotometry at 379 nm every 30 sec for 10 min (Figure S14). Each measurement was done in duplicate and the average value was plotted.

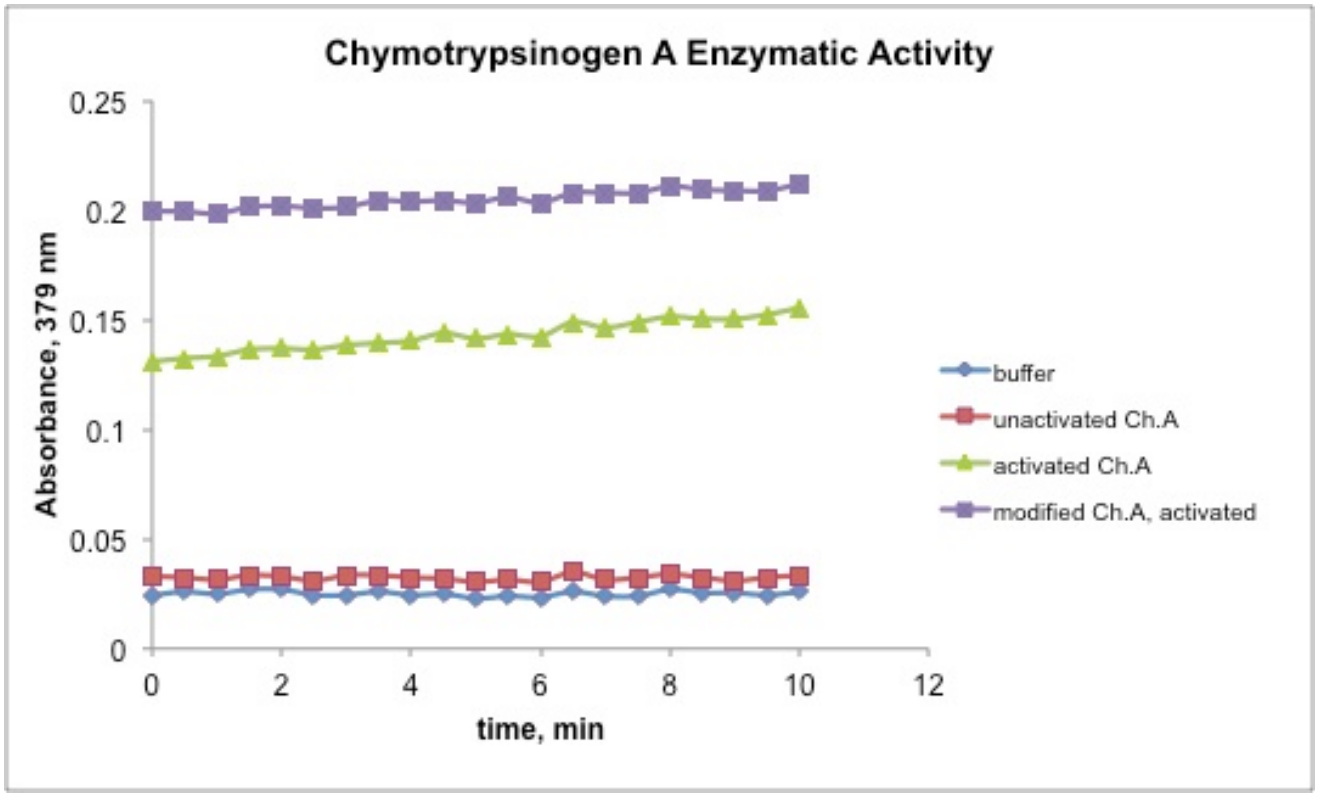

Figure S13. Chymotrypsinogen A activity assay.

11. FBDP-based PEGylation of Human Serum Albumin

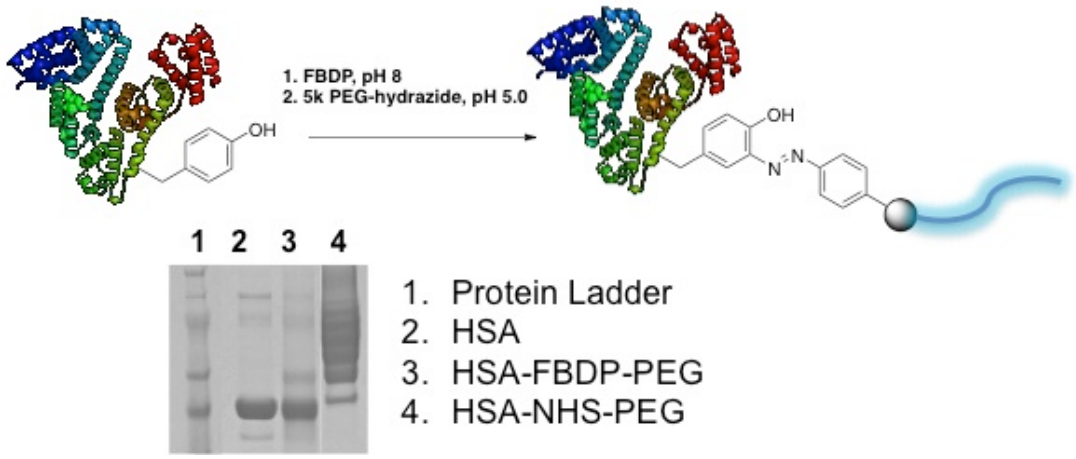

Figure S14. PEGylation of Human Serum Albumin.

5K linear PEG-hydrazide was prepared from commercially available 5k linear PEG-NHS (NOF corporation) by reacting it with 10 equivalents of anhydrous hydrazine in MeOH for 24 h, rt, followed by capping of any unreacted activated ester groups with excess methylamine. Resulting PEG-hydrazide was precipitated out with cold diethyl ether and washed extensively with ice-cold ether to provide desired hydrazide polymer as fine white powder. Hydrazide formation was confirmed by MALDI-TOF characterization (data not shown, MW_{av} (PEG-hydrazide)=5312, MW_{av} (PEG-NHS)=5533).

To the 100 μL of human serum albumin solution (2.5 mg/ml in 0.1M phosphate buffer pH 8.0, 1 eq) was added 1 μL of FBDP (37.5 μM in acetonitrile, 10 eq). Reaction mixture was vortexed gently and left at room temperature for 30 min. Reaction mixture turned yellow. Excess FBDP was removed using Zeba Spin desalting column (7K MWCO, Pierce) and the buffer was exchanged to 0.1M phosphate buffer pH 5. To the solution of HSA-aldehyde was added 5k PEG-hydrazide (1 μL of 37.5 μM solution in DMF, 10 eq). Reaction mixture was vortexed gently and allowed to react for 18h at rt. For a comparison, reaction of HSA (100 μL, 2.5 mg/ml, PBS pH 7.4) with 5k PEG-NHS (NOF corporation; 1 μL of 37.5 μM solution in DMF, 10 eq)) was set in parallel. Crude reaction products were characterized by SDS-PAGE gel electrophoresis using 4-13% Bis-Tris gel (Invitrogen)(Figure S15).

12. Optimization study for FBDP modification of HSA

Reaction procedure to determine pH effect.

Each reaction performed in duplicate. To the100 μL of HSA solution (2.5 mg/ml) in 0.1M phosphate buffer (pH 7; 7.4; 7.6; 7.8; 8; 8.4) was added 1 μL of FBDP solution in acetonitrile (37.7 μM). Reaction mixture was vortexed gently and allowed to react for 30 min at rt followed by removal of excess FBDP using Zeba Spin desalting column. Protein concentration was measured by two independent methods (Bradford assay and absorption at 280nm (Nanodrop, ThermoFisher Scientific), correction factor for diazene adduct = 0.436). Diazene content was estimated based on the absorption at 340 nm and by streptavidin ELISA of HSA-biotin conjugate derived from HSA-aldehyde reaction with biotin-oxyamine (20 eq). The values in all assays were found to correlate well and number of modifications/protein derived from measurement of absorption at 280nm and 340nm were used thereafter. HSA-biotin conjugate was also characterized by MALDI-TOF and LSMS-ESI (Figure S17)

Number of modifications/HSA was plotted as a function of pH (Figure 16).

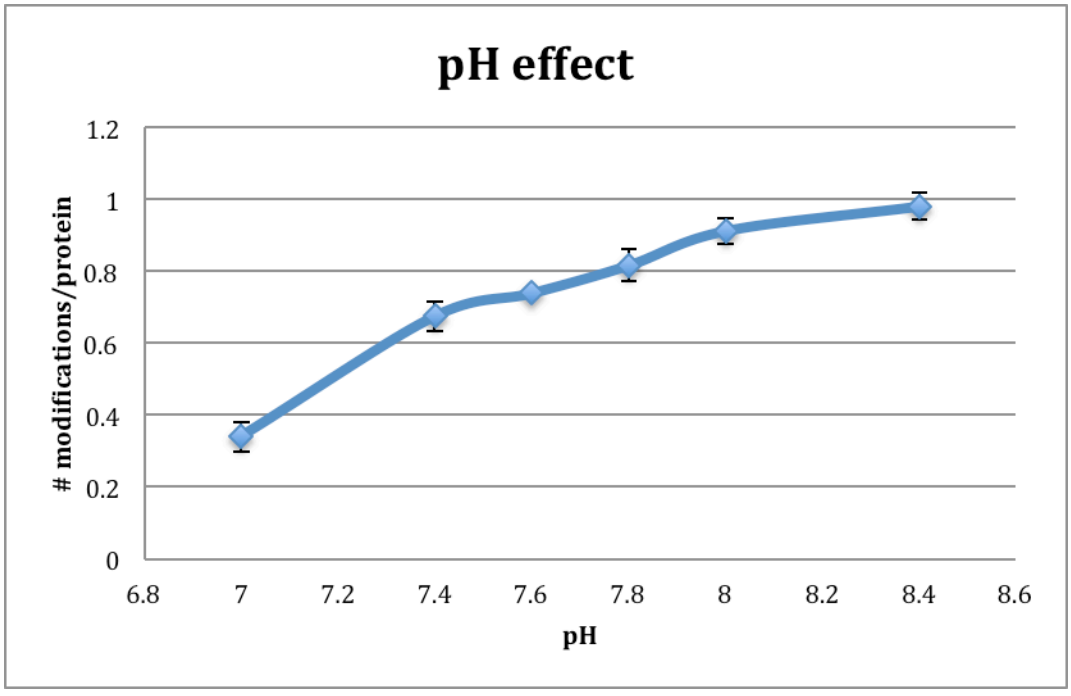

Figure S15.

A.

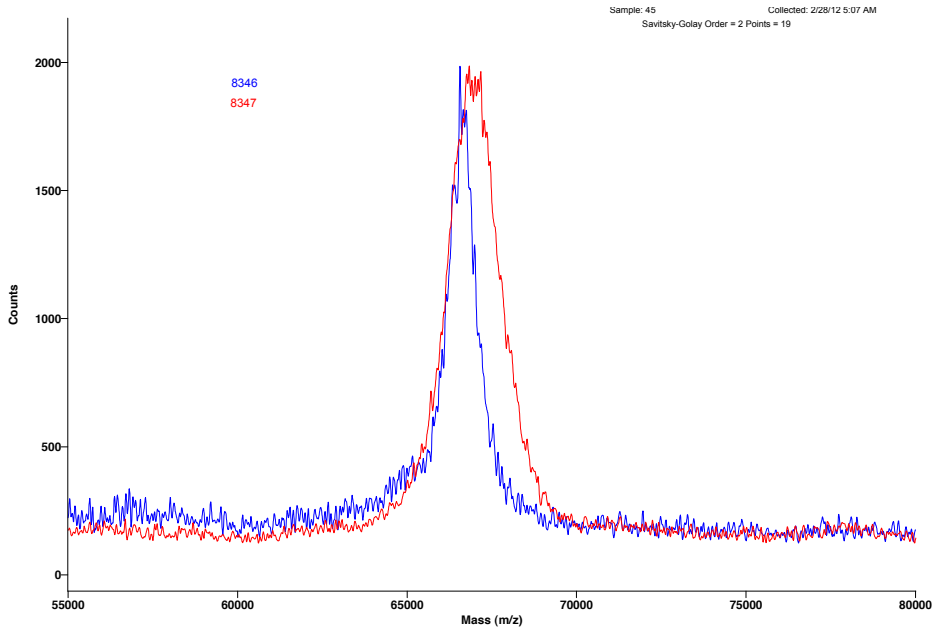

B.

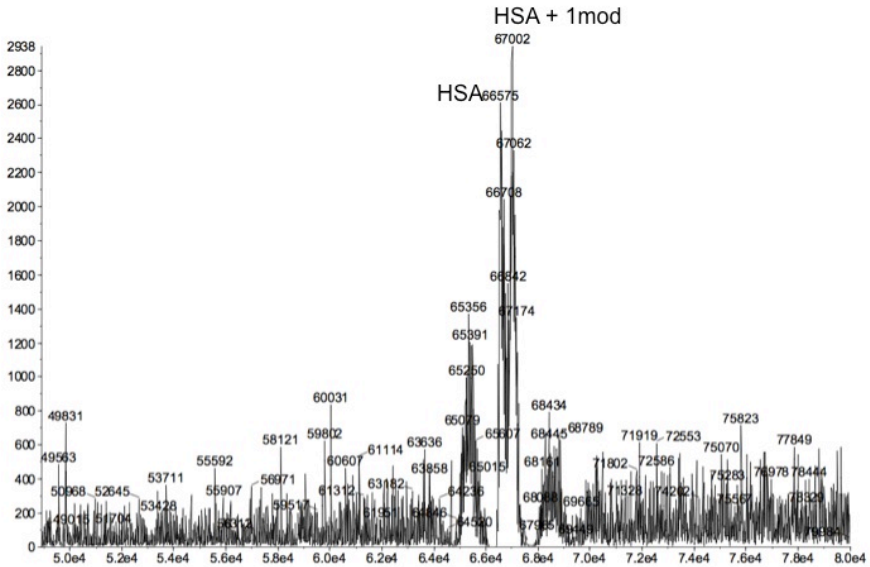

Figure S16. (A) Overlay of MALDI-TOF spectra of HSA (blue, MW_{av}=66525) and HSA-biotin (red, MW_{av}=66931). (B) ESI-MS characterization of HSA-FBDP-biotin conjugate (MW of modification 446 Da)

Reaction procedure to determine time effect.

Each reaction performed in duplicate. To the100 μL of HSA solution (2.5 mg/ml) in 0.1M phosphate buffer (pH 8) was added 1 μL of FBDP solution in acetonitrile (37.7 μM). Reaction mixture was vortexed gently and allowed to react for set amount of time (0.5hr, 1hr, 2hr, 3hr, 4hr) at rt followed by removal of excess FBDP using Zeba Spin desalting column. Protein concentration was measured by two independent methods (Bradford assay and absorption at 280nm (Nanodrop, ThermoFisher Scientific), correction factor for diazene adduct = 0.436). Diazene content was estimated based on the absorption at 340 nm and by streptavidin ELISA of HSA-biotin conjugate derived from HSA-aldehyde reaction with biotin-oxyamine (20 eq).

Number of modifications/HSA was plotted as a function of time (Figure S18).

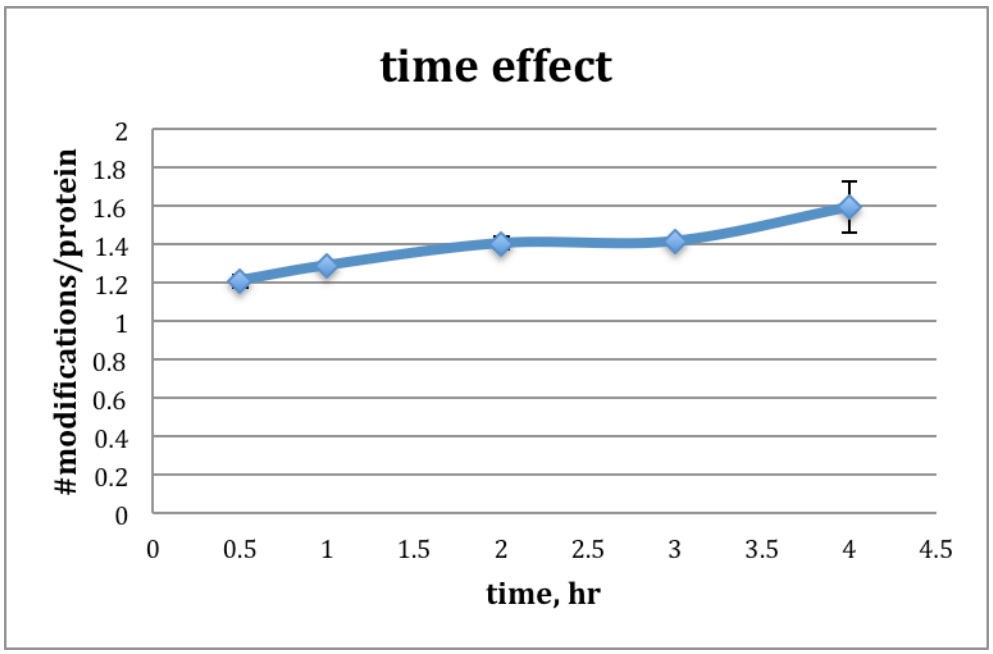

Figure S17

Reaction procedure to determine temperature effect.

Each reaction performed in duplicate. To the100 μL of HSA solution (2.5 mg/ml, 1 eq) in 0.1M phosphate buffer (pH 8) was added 1 μL of FBDP solution in acetonitrile (37.7 μM, 10 eq). Reaction mixture was vortexed gently and allowed to react for 30 min at either 4 ^{o}C or rt or 37 ^{o}C followed by removal of excess FBDP using Zeba Spin desalting column. Protein concentration was measured by two independent methods (Bradford assay and absorption at 280nm (Nanodrop, ThermoFisher Scientific), correction factor for diazene adduct = 0.436). Diazene content was estimated based on the absorption at 340 nm and by streptavidin ELISA of HSA-biotin conjugate derived from HSA-aldehyde reaction with biotin-oxyamine (20 eq).

Number of modifications/HSA was plotted as a function of temperature (Figure S19).

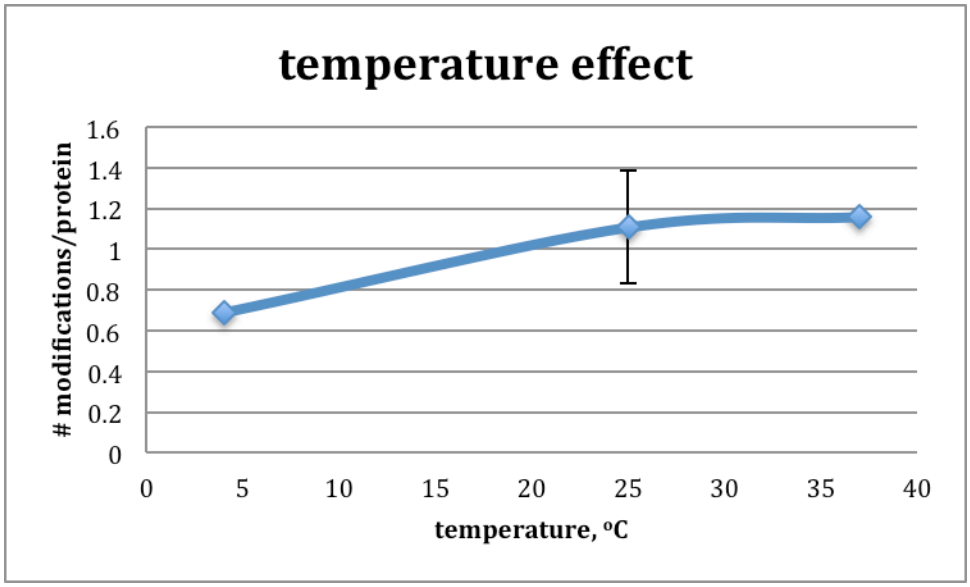

Figure S18

Reaction procedure to determine effect of the excess of reagent.

Each reaction performed in duplicate. To the100 μL of HSA solution (2.5 mg/ml, 1 eq) in 0.1M phosphate buffer (pH 8) was added 1 μL of FBDP solution in acetonitrile at concentrations that would result in the following excess of the reaget: 1 eq, 5 eq, 10 eq, 20 eq, 50 eq. Reaction mixture was vortexed gently and allowed to react for 30 min at rt followed by removal of excess FBDP using Zeba Spin desalting column. Protein concentration was measured by two independent methods (Bradford assay and absorption at 280nm (Nanodrop, ThermoFisher Scientific), correction factor for diazene adduct = 0.436). Diazene content was estimated based on the absorption at 340 nm and by streptavidin ELISA of HSA-biotin conjugate derived from HSA-aldehyde reaction with biotin-oxyamine (20 eq).

Number of modifications/HSA was plotted as a function of reagent excess (Figure S20).

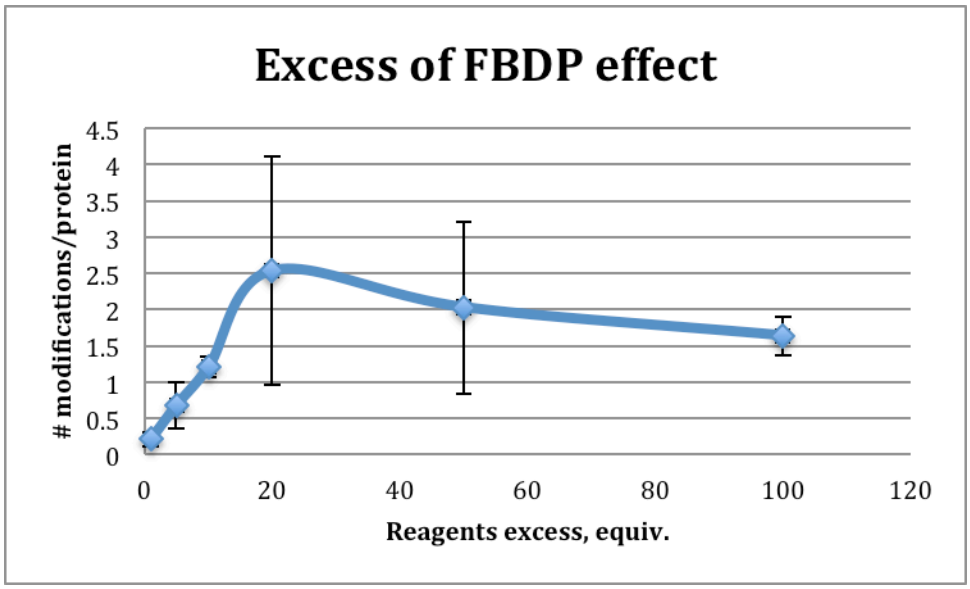

Figure S19

Reaction procedure to determine effect of HSA concentration.

Each reaction performed in duplicate. To the100 μL of HSA solution at the following concentrations: 2.5 mg/ml, 5 mg/ml, 10 mg/ml, 20 mg/ml in 0.1M phosphate buffer (pH 8) was added 1 μL of FBDP solution in acetonitrile at concentrations that would result in the 10 fold excess of the reaget. Reaction mixture was vortexed gently and allowed to react for 30 min at rt followed by removal of excess FBDP using Zeba Spin desalting column. Protein concentration was measured by two independent methods (Bradford assay and absorption at 280nm (Nanodrop, ThermoFisher Scientific), correction factor for diazene adduct = 0.436). Diazene content was estimated based on the absorption at 340 nm and by streptavidin ELISA of HSA-biotin conjugate derived from HSA-aldehyde reaction with biotin-oxyamine (20 eq).

Number of modifications/HSA was plotted as a function of protein concentration (Figure S21).

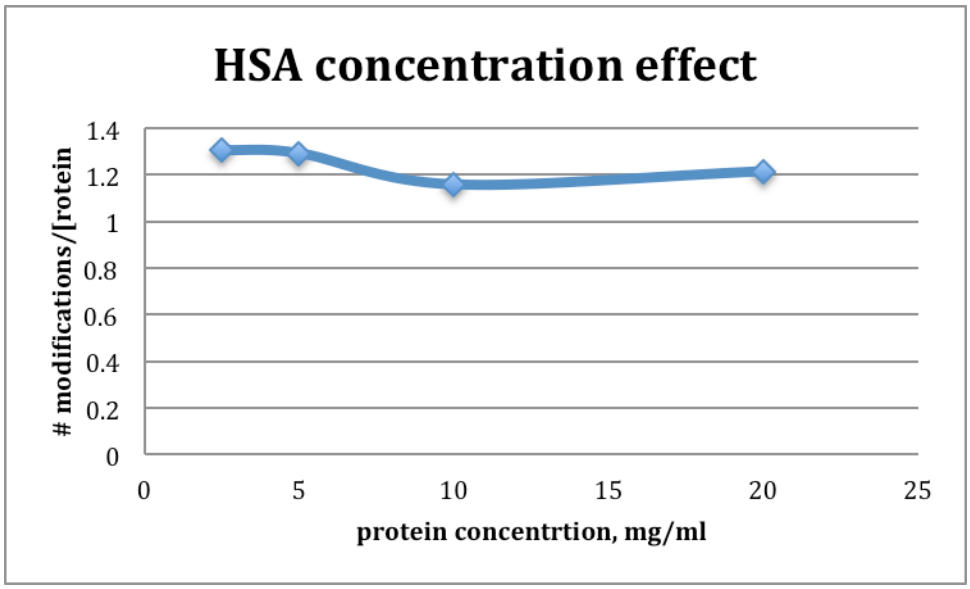

Figure S20

13. FBDP modification of antibody trastuzumab

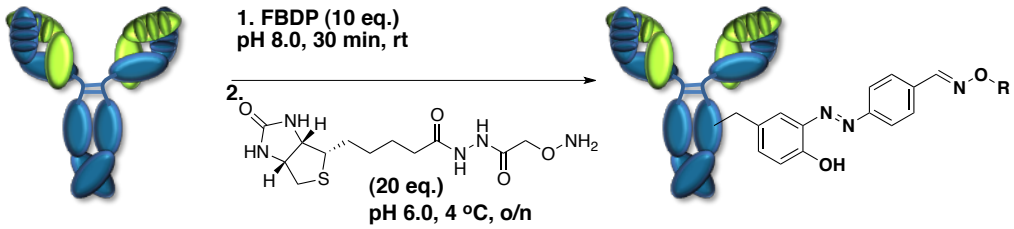

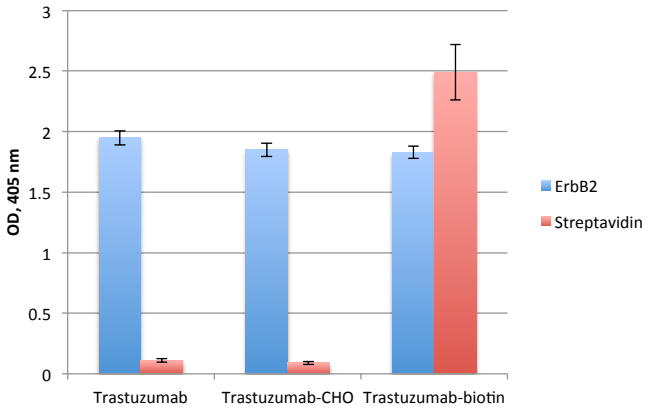

Figure S21.

Modification procedure.

To the 200 μL of trastuzumab solution in 0.1M phosphate buffer pH 8 (1.5 mg/ml) was added FBDP solution in CH_3CN (2 μL of 20 μM solution). Reaction mixture was vortexed gently and allowed to react for 30 min. Reaction mixture turned yellow. The reaction was run through the Zeba spin desalting column (7K MWCO, Pierce) to remove excess FBDP and exchange into phosphate buffer pH 6.0. Then, 4 μL of 20 μM solution of biotin-oxyamine (Cayman Chemical, Cat.# 10009350) was added, reaction was vortexed and allowed to react at 4 ^{o}C for 18h. Excess of unconjugated biotin was removed using Zeba desalting column. Obtained conjugate was characterized by MALDI-TOF (Figure S22) and ELISA assays (Figure S21).

ErbB2 ELISA.

ErbB2 binding ELISA was performed as described.[2] In brief; Costar 96-well ELISA plates (Corning, Acton, MA) were coated with 25 ng of antigen (human ErbB2 or BSA) in 25 μL of PBS pH 7.4 and incubated overnight at 4 ^{o}C. The plate was washed with PBS containing 0.01% tween-20 (100 μL x 3). After blocking with 100 μL of 3% BSA/PBS, 0.01% tween-20 for 1 h at 37 $_{o}$C and washing (100 μL of PBS containing 0.01% tween-20 x 5), 100ng/50 μL /well of trastuzumab, trastuzumab-CHO (trastuzumab modified only with FBDP, but not ligated with biotin-oxyamine) or trastuzumab-biotin(trastuzumab modified with FBDP followed by oxime ligation with biotin-oxyamine) construct or rituximab (negative control) solution was added and the plates were incubated for 1 hr at 37 ^{o}C. The plate was thoroughly washed with PBS/0.01% tween (100 μL x 5) followed by addition of 100 μL /well of secondary antibody solution (donkey anti-Human HRP, diluted 1:1000). The plate was incubated for 1h at 37 ^{o}C and washed with PBS/0.01% tween (100 μL x 5). Upon addition of the ABTS developing solution and incubation at room temperature for 20 min the absorbance was read at 405 nm. All measurements were done in triplicate and an average normalized result was graphed.

Streptavidin ELISA.

Streptavidin ELISA was performed as previously described. In brief, Costar 96-well ELISA plates (Corning, Acton, MA) were coated with 200 ng of antigen (streptavidin or BSA) in 100 μL of PBS pH 7.4 and incubated overnight at 4 ^{o}C. The plate was washed with PBS containing 0.01% tween-20 (100 μL x 3). After blocking with 100 μL of 3% BSA/PBS, 0.01% tween-20 for 1 h at 37 ^{o}C and washing (100 μL of PBS containing 0.01% tween-20 x 5), 100ng/100 μL /well of trastuzumab, trastuzumab-CHO (trastuzumab modified only with FBDP, but not ligated with biotin-oxyamine) or trastuzumab-biotin (trastuzumab modified with FBDP followed by oxime ligation with biotin-oxyamine) construct, rituximab (negative control), biotinylated goat anti-rabbit antibody (positive

control; Vector, Cat. # F1207) solution was added and the plates were incubated for 1 hr at 37 ^{o}C. The plate was thoroughly washed with PBS/0.01% tween (100 µL x 5) followed by addition of 100 µL /well of appropriate secondary antibody solution (AP goat anti-Human IgG F(ab)$_2$ from Pierce, diluted 1:3000; or AP rabbit anti-goat IgG from Pierce, diluted 1:3000). The plate was incubated for 1h at 37 ^{o}C and washed with PBS/0.01% tween (100 µL x 5). Upon addition of the AP developing solution and incubation at room temperature for 20 min the absorbance was read at 405 nm. All measurements were done in triplicate and an average normalized result was graphed.

(A)

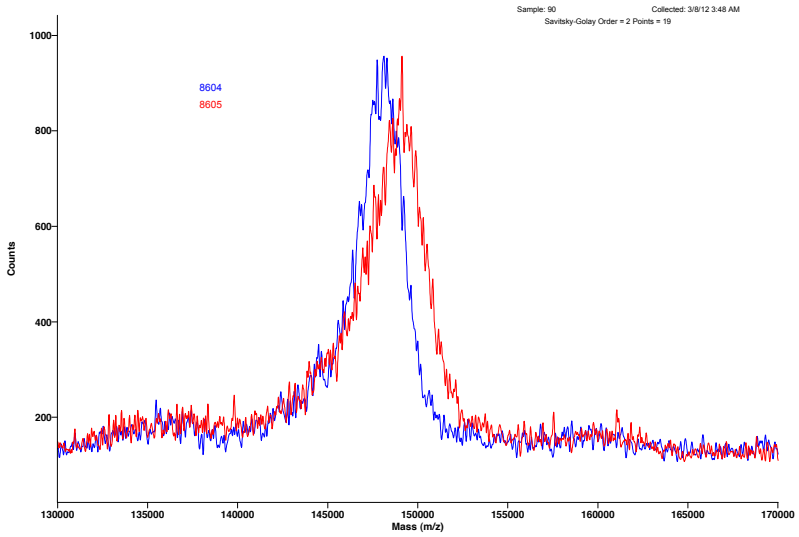

(B)

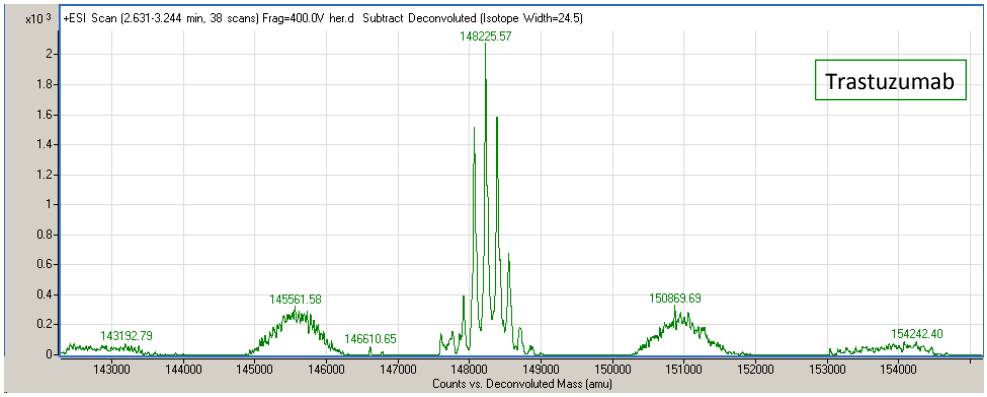

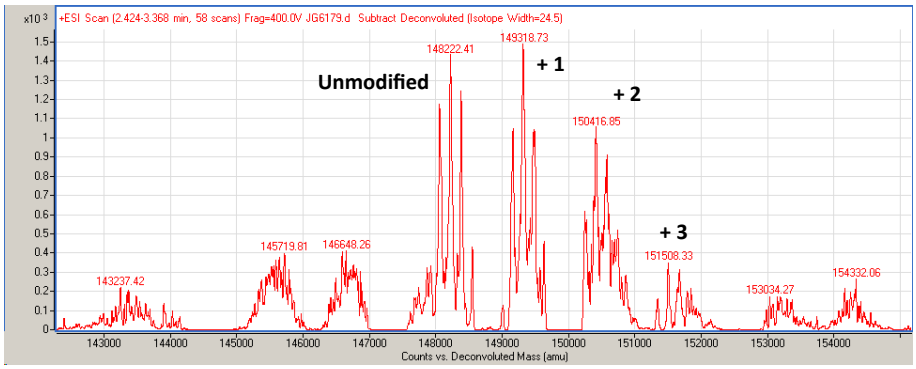

Figure S22. (A) Overlay of MALDI-TOF spectra for trastuzumab (blue, MWav=148302) and trastuzumab-biotin (red, MW_{av}=149053); MWmodification =446Da (B) Deconvoluted ESI spectra of trastuzumab (green) and trastuzumab conjugate (red); MWmodification = 1096Da.

14. Cell Surface Labeling with FBDP

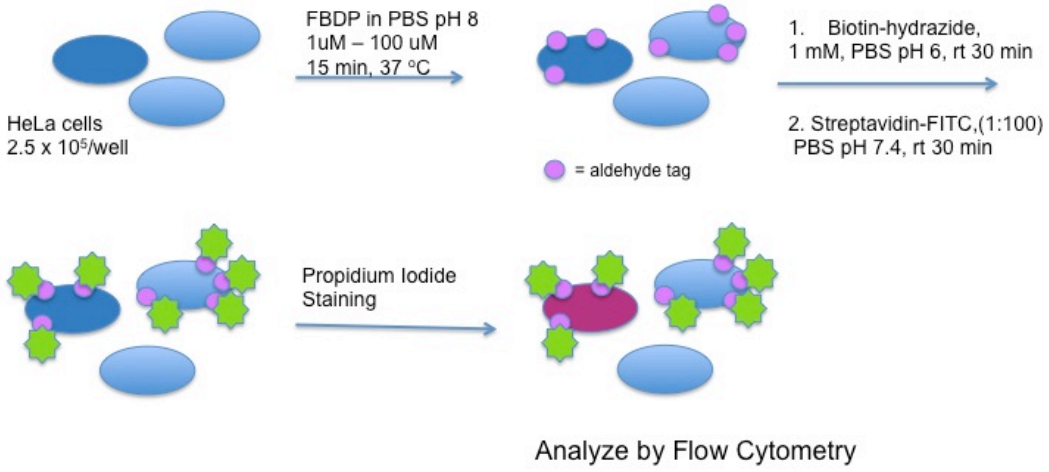

HeLa cells were harvested and washed twice with PBS pH 8.0. Washed cells were resuspended in PBS pH 8.0 to a final concentration of $5x10^6$ cells/ml and 50 μL aliquots were transferred to the V-bottom non-TC treated plate followed by addition of FBDP (50 μL aliquots in PBS pH 8.0, 0.01% acetonitrile; final concentrations of FBDP were 100 μM, 10 μM and 1 μM). Cells were incubated with the reagent for 15 min at 37 °C. Cells were washed with PBS pH 6.0 (3 x 150 μL/well) followed by addition of 100 μL/well of 1 mM biotin-hydrazide (Sigma-Aldrich) in PBS pH 6.0 and incubation at room temperature for 30 min. Cells were washed with FACS buffer (3 x 150 μL/well; PBS pH 7.4, 1% BSA, 0.01% NaN_3). Streptavidin-FITC (Jackson Laboratories) solution in FACS buffer was added to the cells (100 μL/well; 1:100 dilution) followed by incubation for 30 min at room temperature. The cells were washed with FACS buffer (5 x 150 μL/well) followed by Propidium Iodide staining for 15 min at room temperature (1 μg/ml; 100 μL/well). Cells were washed and transferred to the filter-top FACS tubes. Cells were analyzed on LSRII flow cytometer, 30000 events were collected. Data was analyzed usingFlowJo 8.7.1 and Microsoft Excel. All samples were tested in triplicate. Representative graphs from two independent experiments are shown (Figure S23).

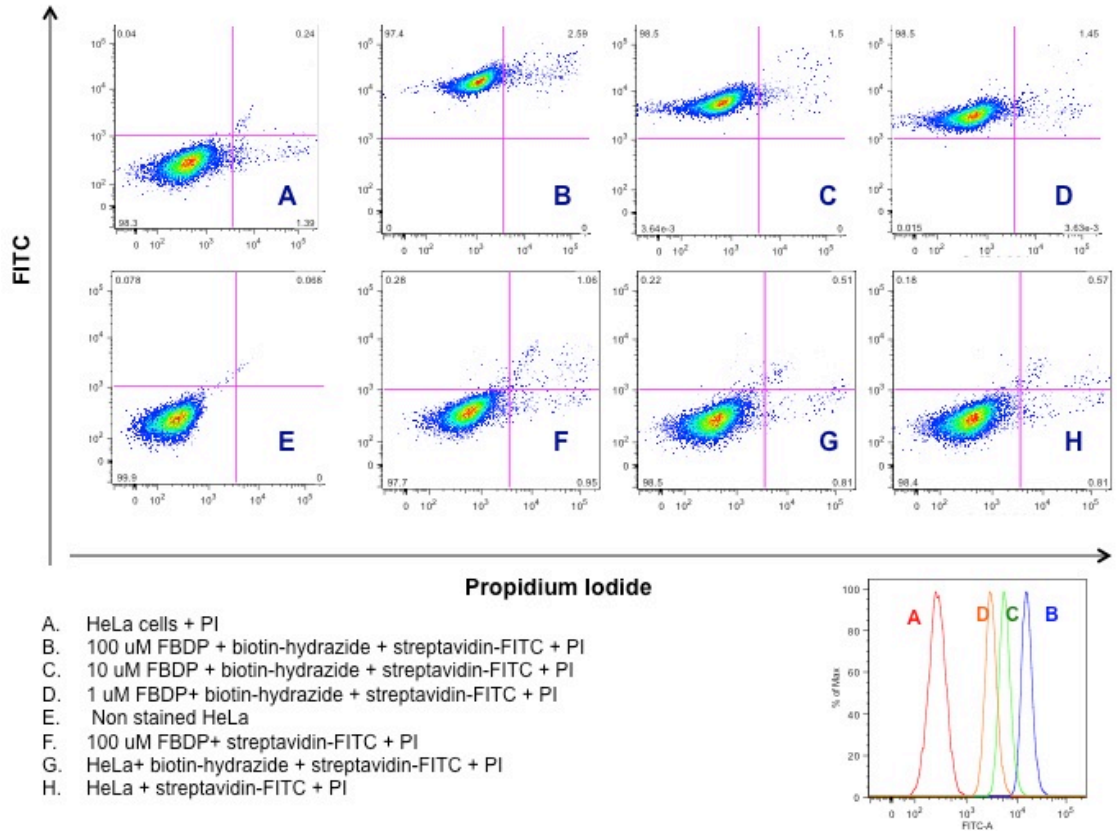

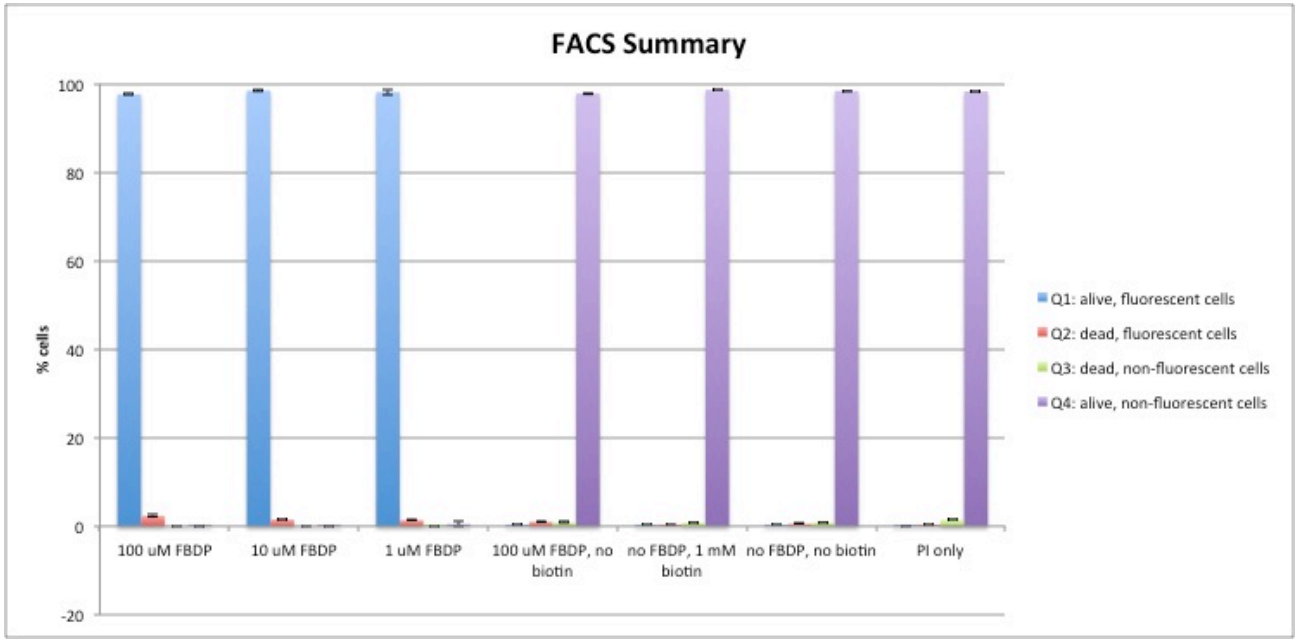

Figure S23. Summary of the HeLa cells surface labeling with FBDP.

15. References

1. Antos, J. M.; Francis, M. B. *J*. *Am*. *Chem*. *Soc*. 2004, *126*, 10256-7.

2. (a) Corte, M.D.; Rodil, J.A,; Vázquez, J.; García, L.; Rodríguez ,J. C.; Bongera, M.; Fernández, J. C.; González, L. O.; Lamelas, M. L.; Allende, M.; García-Muñiz, J.L.; Feyo, A.; Vizoso, F. J. *J Cancer Res Clin Oncol*. 2005, *131*,701-14. (b) Liu X, He Z, Zhou M, Yang F, Lv H, Yu Y, Chen Z. *Protein Expr Purif*. 2007, *53*, 247-54.

3. Ban, H.; Gavrilyuk, J.; Barbas, C.F. *J*. *Am*. *Chem*. *Soc*. 2010, *13*2, 1523-1525.

Bioconjugate Chemistry

Communication

pubs.acs.org/bc

Rapid Catalyst-Free Hydrazone Ligation: Protein-Pyridoxal Phosphoramides

Xiaojian Wang and James W. Canary*

Department of Chemistry, New York University, New York, New York 10003, United States

Supporting Information

ABSTRACT: Pyridoxal-5′-phosphate (PLP) represents an active form of Vitamin B_6 that shows relatively fast imine formation with hydrazines under physiological conditions without the need of a catalyst. A convenient phosphate/amine conjugation protocol was developed to covalently link PLP to proteins, affording proteins capable of hydrazone formation with bioorthogonal hydrazinyl functional groups. Thus, the lectin Concanavalin A (Con A) was labeled with PLP. Pretreatment with fluorescein hydrazide gave dye-labeled Con A that labeled cell surfaces efficiently. Alternatively, pretargeting was achieved by labeling cells with Con A-PLP, then treatment in vitro with Alexa Fluor 488 hydrazide.

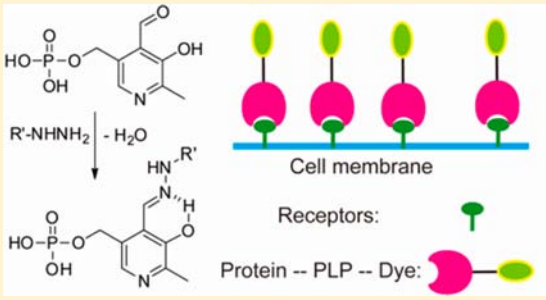

The bioorthogonal chemical reporter strategy has become an important method for labeling biomolecules such as nucleic acids, lipids, proteins, and carbohydrates.[1−4] Prominent among a variety of click reactions is the copper-catalyzed azide−alkyne cycloaddition, limited to in vitro application because the Cu(I) catalyst is toxic to both bacterial and mammalian cells,[5] and the strain-promoted azide−alkyne cycloaddition, which is suitable for live-cell and in vivo applications, with moderate reaction rates.[5−9] The reactions between highly reactive tetrazine and *trans*-cyclooctene show good reaction rates, but require special procedures for reagent preparation,[2,10,11] and care in handling and storage.[12−14]

Imine ligations have found significant utility in labeling biomolecules.[15−17] As one recent example, Francis and colleagues creatively generate keto-amides at the N-terminus of peptides and proteins for conjugation.[18−22] Aldehydes are more reactive than ketones, and aryl carbonyls are more reactive than aliphatic ones, but in general, imine ligations are slow at physiological pH.[23−25] Dawson's group reported significantly accelerated hydrazone and oxime formation with aniline catalysis.[26,27] However, the required high aniline concentration cannot always be accommodated in living systems due to its acknowledged bioincompatibility and for which less toxic substitutes introduce lower catalytic efficiency.[28−30] Herein, we report the use of the enzyme cofactor pyridoxal-5′-phosphate (PLP, an active form of Vitamin B_6) as the source of aldehyde in hydrazone formation. This cofactor is involved in many enzymatic reactions requiring transamination to occur at physiological pH.[31] Both the hydroxyl and the phosphate groups of PLP enhance the rate of Schiff base formation,[32−35] and so it would be expected to react more efficiently in bioconjugation reactions than other previously studied aldehydes and ketones.

Hydrazine compounds react with PLP over a large pH range.[36] We compared the relative reactivity of 2-hydrazinopyridine (HP) with PLP vs 4-formyl benzoic acid (FBA, both HP and FBA are widely used in labeling biomolecules) in phosphate buffered saline (PBS, pH 7.4).[37−39] The reactions were monitored by the characteristic absorbance of the formed hydrazones (Figure 1). The data fit the rate equation for a reversible second-order reaction.[40] For the reaction between PLP and HP, the rate constant for formation of the hydrazone (k_1) was determined to be 10.5 ± 0.1 M^{-1} s^{-1}, the equilibrium constant (K_{eq}) was (1.2 ± 0.1) × 10^5 M^{-1}, and the rate constant of hydrolysis of the hydrazone ($k_{-1} = k_1/K_{eq}$) was calculated to be (9.0 ± 0.8) × 10^{-5} s^{-1}. The formation of PLP-HP hydrazone in aqueous solution was also observed by ^{1}HNMR; PLP and HP in D_2O with pD adjusted to about 7.5 with NaOD gave a diminished aldehyde hydrogen peak at 10.3 ppm and a new hydrazone hydrogen peak at 8.2 ppm (Figure S2, Supporting Information). The effect of aniline catalysis was examined with 100 mM aniline present, where the k_1 was greatly enhanced to 506 ± 7 M^{-1} s^{-1}.

The efficiency of the reaction of HP and PLP was measured and compared to the reactions of HP and FBA with or without aniline catalysis. For FBA/HP without aniline, the k_1 was 0.144 ± 0.003 M^{-1} s^{-1} and K_{eq} was (2.4 ± 0.1) × 10^3 M^{-1}. For FBA/HP with 100 mM aniline, the k_1 was 18.4 ± 0.5 M^{-1} s^{-1} and K_{eq} was (1.3 ± 0.1) × 10^5 M^{-1}. The PLP/HP system showed much faster reaction rate than uncatalyzed FBA/HP and formed a much more stable Schiff base product. The reaction between glyoxylic acid and HP was also examined and the k_1 was 2.56 ± 0.09 M^{-1} s^{-1} and K_{eq} was (2.5 ± 0.3) × 10^4 M^{-1} (Figure S1, Supporting Information). To the best of our knowledge, the PLP/HP is the fastest reported Schiff-base formation reaction. The uncatalyzed PLP/HP system exhibited a comparable k_1

Received: August 4, 2012
Revised: October 19, 2012
Published: November 27, 2012

ACS Publications © 2012 American Chemical Society

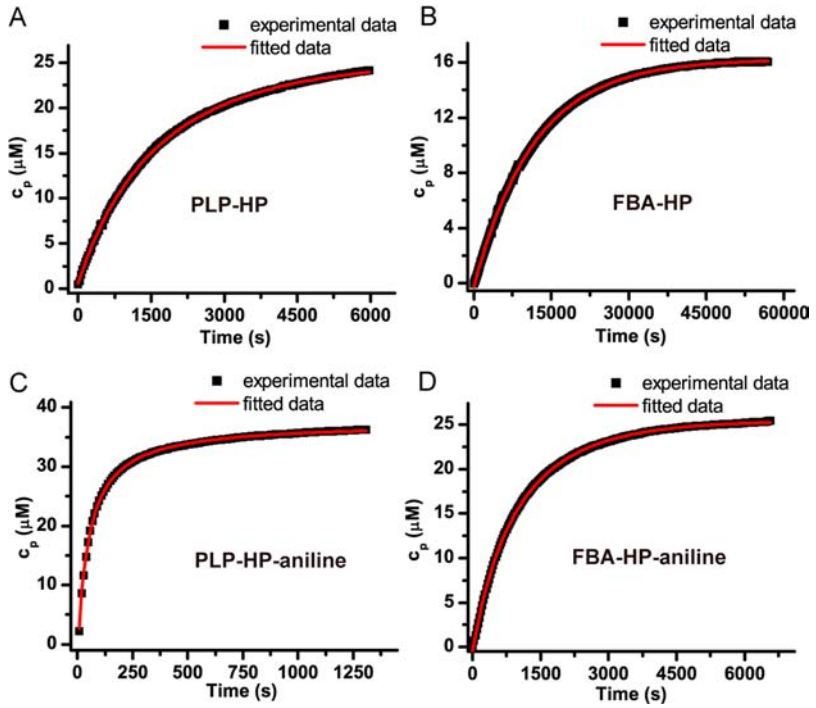

Figure 1. Formation of hydrazone over time. (A) 40 μM PLP and 40 μM HP, (B) 100 μM FBA and 100 μM HP, (C) 40 μM PLP, 40 μM HP, and 100 mM aniline, (D) 40 μM FBA, 40 μM HP, and 100 mM aniline. The black dots were experimental data which were collected every 30 s (except for PLP-HP-aniline system, where data was collected every 10 s), and the red solid line was the data fitted to the rate equation.

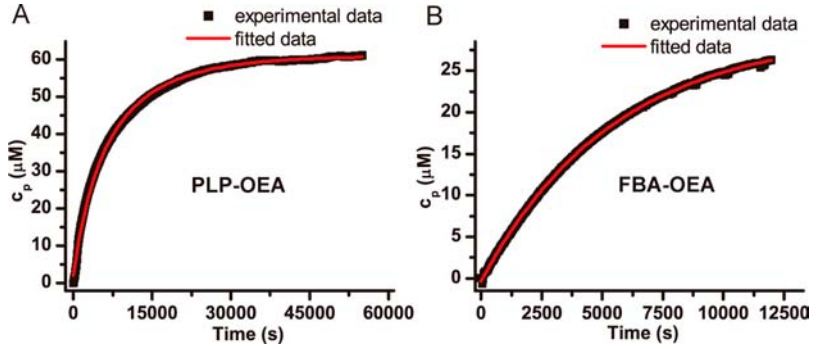

Figure 2. Formation of oxime over time. (A) 80 μM PLP and 80 μM OEA, (B) 30 μM FBA, 2 mM OEA. The black dots were experimental data which were collected every 30 s, and the red solid line was the data fitted to the rate equation.

Scheme 1. PLP Modification of Protein and Subsequent Hydrazone Formation

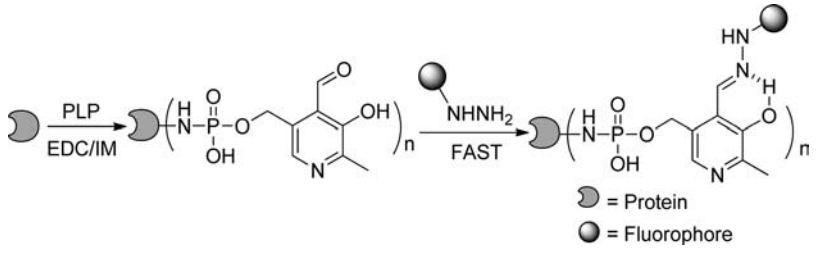

and K_{eq} to the more toxic aniline-catalyzed FBA/HP reaction, and it is about 10 times faster than the reported fastest Cu-free azide−alkyne cycloaddition (k_1 = 0.96 M^{-1} s^{-1}).[6]

Oxime formation from PLP and *O*-ethoxyamine (OEA) was slower and gave product of surprisingly similar stability (k_1 = 1.64 ± 0.03 M^{-1} s^{-1} and K_{eq} = (1.2 ± 0.1) × 10^5 M^{-1}, Figure 2).[41] However, the reaction was much faster than FBA/OEA, which gave k_1 = 0.085 ± 0.05 M^{-1} s^{-1}; the latter control reaction did not reach equilibrium even after two days with 400 μM reactants.

An activated ester strategy (Scheme 1) provided conjugation to Concanavalin A (Con A).[42] PLP was activated with 1-ethyl-3-[3-dimethylaminopropyl] carbodiimide hydrochloride (EDC) and reacted with imidazole (IM) at pH 5. The reactive ester was then basified to pH 8.5 and mixed with Con A solution (in phosphate buffer, pH 8.5) to react with primary

dx.doi.org/10.1021/bc300430k | *Bioconjugate Chem.* 2012, 23, 2329−2334

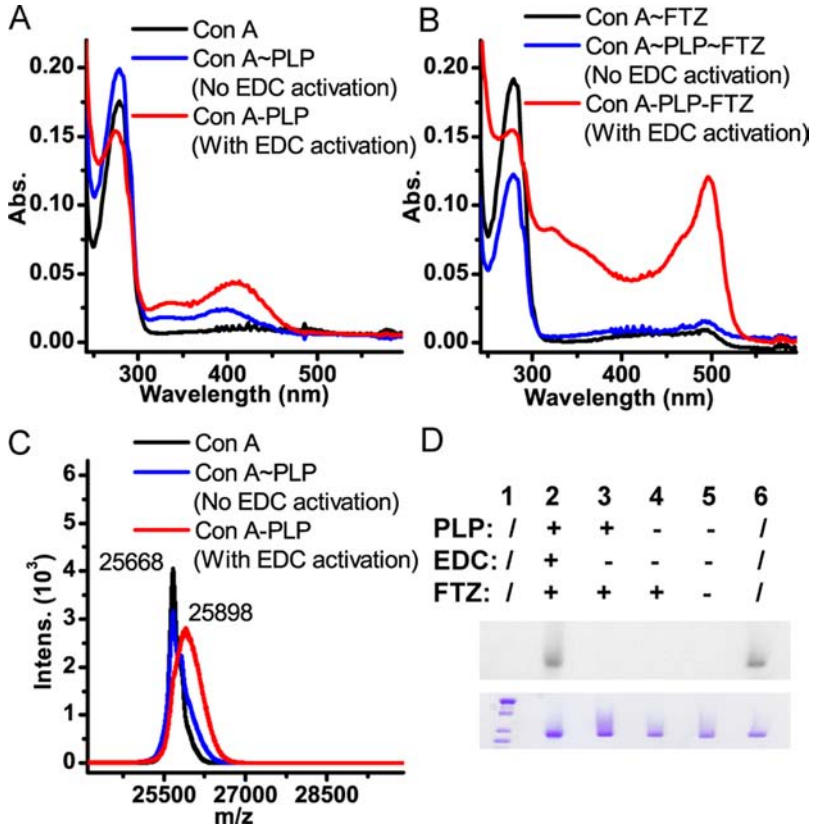

Figure 3. Characterization of Con A conjugates. (A) UV−vis absorption spectra of Con A (1.29 μM, black), Con A~PLP (1.57 μM, blue), and Con A-PLP (1.10 μM, red); (B) UV−vis absorption spectra of Con A~FTZ (1.46 μM, black), Con A~PLP~FTZ (0.90 μM, blue), and Con A-PLP-FTZ (0.90 μM, red); (C) MALDI-TOF MS spectrum of Con A (black), Con A~PLP (blue), and Con A-PLP (red); (D) SDS-PAGE visualized under UV light (top) and after Coomassie blue stain (bottom). Well: protein ladder (each line: 50 kDa, 40 kDa, 30 kDa, and 25 kDa, from top to bottom), Con A-PLP-FTZ, Con A~PLP~FTZ, Con A~FTZ, Con A, and Con A-FITC from 1 to 6.

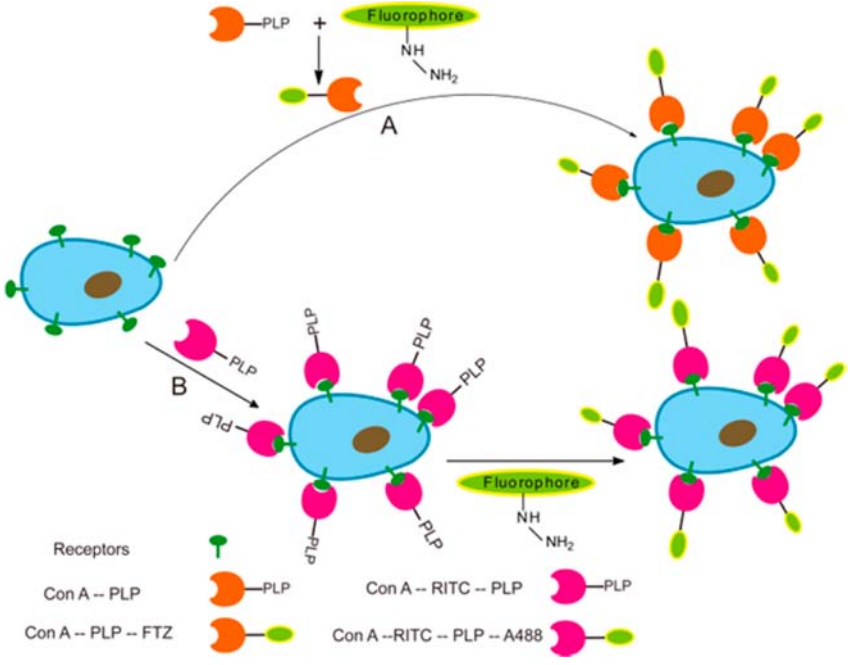

Figure 4. Imaging strategies: (A) Preconjugate method, Con A-PLP-FTZ was preformed in solution and purified before adding to the cells; (B) In vitro labeling method, cells were first treated with Con A-PLP and then with AF488 hydrazide.

amines on the protein (2 h at room temperature) and form stable protein−PLP phosphoramide conjugate (Con A-PLP). The formation of the conjugate was confirmed by UV−vis spectroscopy, where the PLP characteristic absorbance around

dx.doi.org/10.1021/bc300430k | *Bioconjugate Chem.* 2012, 23, 2329−2334

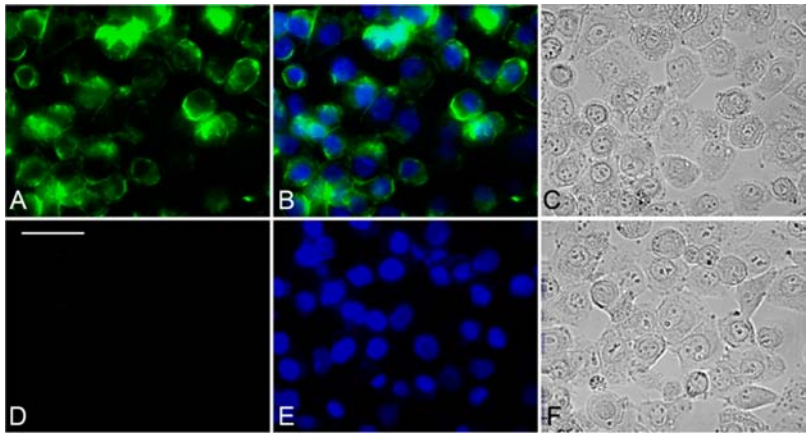

Figure 5. Preconjugate strategy: Fluorescence microscopy of PANC-1 cells. (A) Fluorescein channel of cells labeled with Con A-PLP-FTZ; (B) Merged DAPI and green channels for cells labeled with Con A-PLP-FTZ; (C) Bright field image of Con A-PLP-FTZ labeled cells; (D) Fluorescein channel for cells treated Con A∼FTZ. Scale bar: 50 μm. (E) Merged DAPI and green channels for cells treated with Con A∼FTZ; (F) Bright field image of Con A∼FTZ labeled cells.

400 nm was observed (Figure 3A), and MALDI-TOF MS, where the mass of mono-PLP modified Con A monomer was observed (Figure 3C). The availability of conjugated PLP for the hydrazone formation was confirmed with the coupling in solution of Con A-PLP and a hydrazine containing dye, fluorescein-5-thiosemicarbazide (FTZ). The resulting Con A-PLP-FTZ conjugate showed an average of 0.5 FTZ per Con A monomer by UV−vis spectroscopy (Figure 3B).

To the best of our knowledge, PLP has not previously been conjugated to proteins in this fashion. Control experiments confirmed conjugation via PLP phosphoramide and Schiff base formation. Imine formation between the aldehyde of PLP and protein amines is a competing reaction, but imine linked PLP washes away during the filtration because of the weak equilibrium (K_{eq} = 250 M^{-1} for PLP and *n*-hexylamine)[43] and cannot lead to protein−dye conjugate. Keto-amide formation is unlikely, as PLP-mediated deamination prefers acidic conditions (pH 6.5), heating (37 °C or higher), and long reaction time (24 h or longer) to achieve a good yield.[18,19] Influences of PLP-aldehyde/amine and keto-amide ligation were excluded by repeating the conjugation sequence in the absence of the EDC. Treatment of Con A with PLP and imidazole yielded a sample (Con A∼PLP, "∼" denotes the variant preparation) showing some PLP Schiff base formation to free amines based on UV−vis spectra (Figure 3A). However, after treating Con A∼PLP with FTZ (Con A∼PLP∼FTZ), <10% of the characteristic absorbance of fluorescein was observed, while the characteristic peak of PLP diminished (Figure 3B). The Con A-PLP-FTZ conjugate was further tested with sodium dodecyl sulfate polyacrylamide gel electrophoresis (SDS-PAGE). As shown in Figure 3D, only Con A-PLP-FTZ (column 2) showed fluorescence under UV light, while Con A∼PLP∼FTZ (column 3) or Con A∼FTZ (column 4) gave no obvious signal. Con A was also modified with fluorescein isothiocyanate (FITC, Figure 3D, column 6) to confirm the Con A-PLP-FTZ band in SDS-PAGE under UV light. The survival of the Con A-PLP-FTZ conjugate in SDS-PAGE where the running buffer contained concentrated glycine (0.192 M) further proved that the hydrazone formed with PLP was very stable, and suitable for bioorthogonal labeling.

To demonstrate the utility of the reaction of PLP with hydrazine for live-cell labeling, we chose to label the mannose expressed on human PANC-1 cells with Con A.[44] Two strategies were employed in cell studies as shown in Figure 4, where route A represents a preconjugate method and route B represents an in vitro labeling method.

For the preconjugate method (Figure 4A), Con A-PLP was first reacted with FTZ in solution to form the Con A-PLP-FTZ conjugate, and purified by size exclusion to separate the excess free FTZ. Cells were incubated with Con A-PLP-FTZ (1 μM) in complete culture medium (DMEM) for 30 min at 37 °C, washed with PBS and fixed with cold methanol. Fixed cells were then stained with 4′,6-diamidino-2-phenylindole (DAPI), washed, and imaged immediately (Figure 5). As expected, strong fluorescence was observed when cells were treated with Con A-PLP-FTZ (Figure 5A). In a control experiment, Con A was treated with FTZ in the same manner as Con A-PLP, and the resulting Con A∼FTZ was used to treat cells. No fluorescence was observed (Figure 5D). This confirmed the successful labeling of FTZ to PLP modified Con A and that it was suitable to be used in live-cell labeling.

For in vitro labeling (Figure 4B), Con A was modified with both PLP and rhodamine B isothiocyanate (RITC). The RITC dye was conjugated to Con A in addition to PLP to track the location of the protein and to determine the specificity of sequential Alexa Fluor 488 hydrazide (AF488 hydrazide) labeling. PANC-1 cells were first incubated with Con A-RITC-PLP (1 μM) for 30 min in DMEM at 37 °C. The cells were then washed, incubated at 37 °C with AF488 hydrazide (20 μM) for 1 h in DMEM, washed again, and fixed with cold methanol. Fixed cells were then stained with DAPI, washed, and imaged immediately (Figure 6). Direct labeling of the Con A with RITC was monitored in the red channel (Figure 6B, red). Covalently bound AF488 hydrazide was visualized clearly in the green channel (Figure 6C, green). Overlay of the red and green channels revealed good colocalization of the red and green signals. Control experiments in which we treated cells with either unlabeled Con A followed by AF488 hydrazide or directly with AF488 hydrazide resulted in no green fluorescence (Figure S3, Supporting Information). The efficiency of route B is not as good as route A, mainly because of the limited concentration of dye used to minimize the nonspecific binding, and part of the bound Con A-PLP was washed away during multiple washing steps. Cells treated with Con A and then 100 mM aniline as required for aniline catalysis almost completely

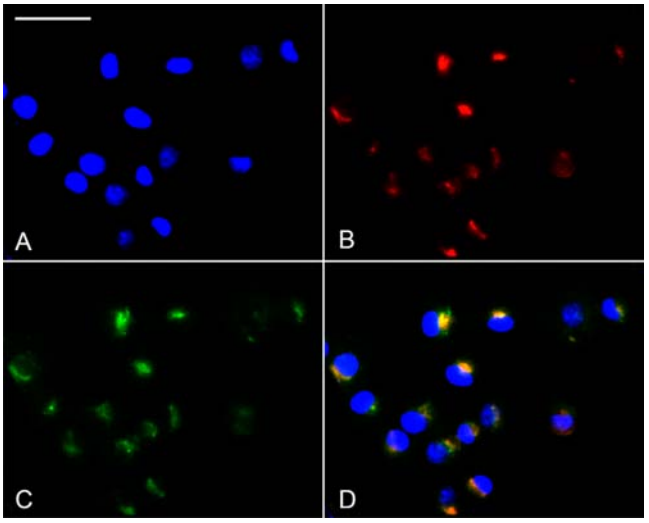

Figure 6. Labeling in vitro. Fluorescence microscopy of Con A-RITC-PLP labeled PANC-1 cells after AF488 conjugation. (A) DAPI channel. Scale bar: 50 μm. (B) Red channel: Con A were also labeled with RITC directly and imaged in the rhodamine channel. (C) Fluorescein channel showing the location of bound AF488 hydrazide probe. (D) Merged DAPI, red, and green channels.

disappeared after the 1 h incubation (Figure S4, Supporting Information).

Besides Con A, two other proteins were labeled in a similar manner. Human transferrin (hTf) was modified to yield hTf-PLP conjugate that behaved similarly to the Con A conjugate (Figure S5, Supporting Information). The hTf-PLP was used to react with AF488 hydrazide in solution and resulting hTf-PLP-AF488 hydrazide conjugate was tested in live cell labeling with PANC-1 cells, targeting the overexpressed transferrin receptor.[45,46] As expected, cells were labeled by the conjugate (Figure S6, Supporting Information). A monoclonal antibody, cetuximab, was also modified and characterized, behaving similarly as well (Figure S7, Supporting Information). Cell labeling experiments utilized the EKVX cell line, which overexpresses epidermal growth factor receptor (EGFR).[47,48] The expected green fluorescence was observed when cells were treated with the cetuximab-PLP-AF488 hydrazide conjugate (Figure S8, Supporting Information).

These data show that PLP can easily be attached to a protein and is a useful aldehyde for hydrazine conjugation. Through a simple two-step aqueous reaction with inexpensive and commercially available reagents, PLP can be conjugated onto protein through a phosphoramide bond, leaving the aldehyde group on PLP free for hydrazone formation. Both preconjugation and in vitro assembly strategies ultimately deliver a sensitive (μM) technique for the covalent labeling of live cells on the basis of hydrazone formation of a hydrazine to pyridoxal-5′-phosphate. Three different proteins were labeled with PLP and worked successfully in live cell labeling, suggesting that other targeting proteins with abundant surface amine groups, like avidin or other antibodies, could be modified by PLP using similar protocols. Given its ready availability, simple reaction with proteins, excellent reaction rate under physiological conditions, successful conjugation with hydrazines in complete culture medium, and obvious biocompatibility, this bioorthogonal conjugation strategy should find wide application. The ″plug and play″ nature of the method requires a single preparation of labeled protein that can be readily labeled with various dyes, other imaging modalities, or therapeutics as desired.

■ ASSOCIATED CONTENT

Ⓢ Supporting Information

Experimental details and control experiment. This material is available free of charge via the Internet at http://pubs.acs.org.

■ AUTHOR INFORMATION

Corresponding Author

*E-mail: canary@nyu.edu.

Notes

The authors declare no competing financial interest.

■ ACKNOWLEDGMENTS

We thank the National Science Foundation (CHE 0848234, CHE 0958457, CMMI-0957834), the NYU Cancer Institute, and the Office of Naval Research (N000014-09-1-118) for support of our research. We thank Leonard Liebes and Lara Mahal for helpful discussions.

■ ABBREVIATIONS

AF 488 hydrazide, Alexa Fluor 488 hydrazide; Con A, Concanavalin A; DAPI, 4′,6-diamidino-2-phenylindole; DMEM, complete culture medium; EDC, 1-ethyl-3-[3-dimethylaminopropyl] carbodiimide hydrochloride; EGFR, epidermal growth factor receptor; FBA, 4-formyl benzoic acid; FITC, fluorescein isothiocyanate; FTZ, fluorescein-5-thiosemicarbazide; HP, 2-hydrazinopyridine; hTf, human transferrin; IM, imidazole; OEA, *O*-ethoxyamine; PLP, pyridoxal-5′-phosphate; RITC, rhodamine B isothiocyanate; SDS-PAGE, sodium dodecyl sulfate polyacrylamide gel electrophoresis

■ REFERENCES

(1) Poloukhtine, A. A., Mbua, N. E., Wolfert, M. A., Boons, G.-J., and Popik, V. V. (2009) Selective labeling of living cells by a photo-triggered click reaction. *J. Am. Chem. Soc. 131*, 15769−15776.

(2) Becer, C. R., Hoogenboom, R., and Schubert, U. S. (2009) Click chemistry beyond metal-catalyzed cycloaddition. *Angew. Chem., Int. Ed. 48*, 4900−4908.

(3) Laughlin, S. T., and Bertozzi, C. R. (2009) Imaging the glycome. *Proc. Natl. Acad. Sci. U. S. A. 106*, 12−17.

(4) Kolb, H. C., Finn, M. G., and Sharpless, K. B. (2001) Click chemistry: Diverse chemical function from a few good reactions. *Angew. Chem., Int. Ed. 40*, 2004−2021.

(5) Agard, N. J., Prescher, J. A., and Bertozzi, C. R. (2004) A strain-promoted [3 + 2] azide-alkyne cycloaddition for covalent modification of biomolecules in living systems. *J. Am. Chem. Soc. 126*, 15046−15047.

(6) Jewett, J. C., Sletten, E. M., and Bertozzi, C. R. (2010) Rapid Cu-free click chemistry with readily synthesized biarylazacyclooctynones. *J. Am. Chem. Soc. 132*, 3688−3690.

(7) Laughlin, S. T., Baskin, J. M., Amacher, S. L., and Bertozzi, C. R. (2008) In vivo imaging of membrane-associated glycans in developing zebrafish. *Science 320*, 664−667.

(8) Baskin, J. M., Prescher, J. A., Laughlin, S. T., Agard, N. J., Chang, P. V., Miller, I. A., Lo, A., Codelli, J. A., and Bertozzi, C. R. (2007) Copper-free click chemistry for dynamic in vivo imaging. *Proc. Natl. Acad. Sci. U. S. A. 104*, 16793−16797.

(9) Jao, C. Y., Roth, M., Welti, R., and Salic, A. (2009) Metabolic labeling and direct imaging of choline phospholipids in vivo. *Proc. Natl. Acad. Sci. U.S.A. 106*, 15332−15337.

(10) Blackman, M. L., Royzen, M., and Fox, J. M. (2008) Tetrazine ligation: fast bioconjugation based on inverse-electron-demand Diels-Alder reactivity. *J. Am. Chem. Soc. 130*, 13518−13519.
(11) Devaraj, N. K., Upadhyay, R., Hatin, J. B., Hilderbrand, S. A., and Weissleder, R. (2009) Fast and sensitive pretargeted labeling of cancer cells through a tetrazine/trans-cyclooctene cycloaddition. *Angew. Chem., Int. Ed. 48*, 7013−7016.
(12) Brown, W. H., Foote, C. S., Iverson, B. L., and Anslyn, E. V. (2010) *Organic Chemistry: Enhanced*, Cengage Learning, Kentucky.
(13) Oxley, J. C., Smith, J. L., and Zhang, J. (2000) Decomposition pathways of some 3,6-substituted s-tetrazines. *J. Phys. Chem. A 104*, 6764−6777.
(14) Oxley, J. C., Smith, J. L., and Chen, H. (2002) Thermal decomposition of high-nitrogen energetic compounds—dihydrazido-S-tetrazine salts. *Thermochim. Acta 384*, 91−99.
(15) Chen, I., Howarth, M., Lin, W. Y., and Ting, A. Y. (2005) Site-specific labeling of cell surface proteins with biophysical probes using biotin ligase. *Nat. Methods 2*, 99−104.
(16) Carrico, I. S., Carlson, B. L., and Bertozzi, C. R. (2007) Introducing genetically encoded aldehydes into proteins. *Nat. Chem. Biol. 3*, 321−322.
(17) King, T. P., Zhao, S. W., and Lam, T. (1986) Preparation of protein conjugates via intermolecular hydrazone linkage. *Biochemistry 25*, 5774−5779.
(18) Gilmore, J. M., Scheck, R. A., Esser-Kahn, A. P., Joshi, N. S., and Francis, M. B. (2006) N-Terminal protein modification through a biomimetic transamination reaction. *Angew. Chem. 118*, 5433−5437.
(19) Dedeo, M. T., Duderstadt, K. E., Berger, J. M., and Francis, M. B. (2009) Nanoscale protein assemblies from a circular permutant of the tobacco mosaic virus. *Nano Lett. 10*, 181−186.
(20) Witus, L. S., Moore, T., Thuronyi, B. W., Esser-Kahn, A. P., Scheck, R. A., Iavarone, A. T., and Francis, M. B. (2010) Identification of highly reactive sequences for PLP-mediated bioconjugation using a combinatorial peptide library. *J. Am. Chem. Soc. 132*, 16812−16817.
(21) Witus, L. S., and Francis, M. B. (2011) Using synthetically modified proteins to make new materials. *Acc. Chem. Res. 44*, 774−783.
(22) Gao, W., Liu, W., Mackay, J. A., Zalutsky, M. R., Toone, E. J., and Chilkoti, A. (2009) In situ growth of a stoichiometric PEG-like conjugate at a protein's N-terminus with significantly improved pharmacokinetics. *Proc. Natl. Acad. Sci. U.S.A. 106*, 15231−15236.
(23) Hermanson, G. T. (2008) *Bioconjugate techniques*, Academic Press, New York.
(24) Jencks, W. P. (1959) Studies on the mechanism of oxime and semicarbazone formation1. *J. Am. Chem. Soc. 81*, 475−481.
(25) Haas, J. W., and Kadunce, R. E. (1962) Rates of reaction of nitrogen bases with sugars. I. Studies of aldose oxime, semicarbazone and hydrazone formation. *J. Am. Chem. Soc. 84*, 4910−4913.
(26) Dirksen, A., and Dawson, P. E. (2008) Rapid oxime and hydrazone ligations with aromatic aldehydes for biomolecular labeling. *Bioconjugate Chem. 19*, 2543−2548.
(27) Zeng, Y., Ramya, T. N. C., Dirksen, A., Dawson, P. E., and Paulson, J. C. (2009) High-efficiency labeling of sialylated glycoproteins on living cells. *Nat. Methods 6*, 207−209.
(28) Sihtmae, M., Mortimer, M., Kahru, A., and Blinova, I. (2010) Toxicity of five anilines to crustaceans, protozoa and bacteria. *J. Serb. Chem. Soc. 75*, 1291−1302.
(29) Anon. (2001) Aniline. *Inhalation Toxicol. 13*, 7−42.
(30) Blanden, A. R., Mukherjee, K., Dilek, O., Loew, M., and Bane, S. L. (2011) 4-Aminophenylalanine as a biocompatible nucleophilic catalyst for hydrazone ligations at low temperature and neutral pH. *Bioconjugate Chem. 22*, 1954−1961.
(31) Hayashi, H. (1995) Pyridoxal enzymes: mechanistic diversity and uniformity. *J. Biochem. 118*, 463−473.
(32) Vázquez, M. A., Muñoz, F., Donoso, J., and García Blanco, F. (1992) Stability of Schiff bases of amino acids and pyridoxal-5′-phosphate. *Amino Acids 3*, 81−94.
(33) Cordes, E. H., and Jencks, W. P. (1962) Semicarbazone formation from pyridoxal, pyridoxal phosphate, and their schiff bases. *Biochemistry 1*, 773−778.
(34) Salvà, A., Donoso, J., Frau, J., and Muñoz, F. (2002) Theoretical studies on Schiff base formation of vitamin b6 analogues. *THEOCHEM 577*, 229−238.
(35) Wiegand, R. G. (1956) The formation of pyridoxal and pyridoxal 5-phosphate hydrazones1. *J. Am. Chem. Soc. 78*, 5307−5309.
(36) Echevarría, G. R., Basagoitia, A., Santos, J. G., and García Blanco, F. (2000) Determination of the rates of formation and hydrolysis of the Schiff bases formed by pyridoxal 5′-phosphate and hydrazinic compounds. *J. Mol. Catal. A: Chem. 160*, 209−215.
(37) Fredriksson, S., Dixon, W., Ji, H., Koong, A. C., Mindrinos, M., and Davis, R. W. (2007) Multiplexed protein detection by proximity ligation for cancer biomarker validation. *Nat. Meth. 4*, 327−329.
(38) Egli, S., Nussbaumer, M. G., Balasubramanian, V., Chami, M., Bruns, N., Palivan, C., and Meier, W. (2011) Biocompatible functionalization of polymersome surfaces: a new approach to surface immobilization and cell targeting using polymersomes. *J. Am. Chem. Soc. 133*, 4476−4483.
(39) Bailey, R. C., Kwong, G. A., Radu, C. G., Witte, O. N., and Heath, J. R. (2007) DNA-encoded antibody libraries: A unified platform for multiplexed cell sorting and detection of genes and proteins. *J. Am. Chem. Soc. 129*, 1959−1967.
(40) Dirksen, A., Dirksen, S., Hackeng, T. M., and Dawson, P. E. (2006) Nucleophilic catalysis of hydrazone formation and transimination: implications for dynamic covalent chemistry. *J. Am. Chem. Soc. 128*, 15602−15603.
(41) Kalia, J., and Raines, R. T. (2008) Hydrolytic stability of hydrazones and oximes. *Angew. Chem., Int. Ed. 47*, 7523−7526.
(42) Chollet, A., and Kawashima, E. H. (1985) Biotin-labeled synthetic oligodeoxyribonucleotides - chemical synthesis and uses as hybridization probes. *Nucleic Acids Res. 13*, 1529−1541.
(43) del Vado, M. A. G., Donoso, J., Muñoz, F., Echevarria, G. R., and Blanco, F. G. (1987) Kinetic and thermodynamic parameters for Schiff's base formation between pyridoxal 5′-phosphate and n-hexylamine. *J. Chem. Soc., Perkin Trans. 2*, 445−448.
(44) Lis, H., and Sharon, N. (1998) Lectins: Carbohydrate-specific proteins that mediate cellular recognition. *Chem. Rev. 98*, 637−674.
(45) Ferris, D. P., Lu, J., Gothard, C., Yanes, R., Thomas, C. R., Olsen, J.-C., Stoddart, J. F., Tamanoi, F., and Zink, J. I. (2011) Synthesis of biomolecule-modified mesoporous silica nanoparticles for targeted hydrophobic drug delivery to cancer cells. *Small 7*, 1816−1826.
(46) Yang, P.-H., Sun, X., Chiu, J.-F., Sun, H., and He, Q.-Y. (2005) Transferrin-mediated gold nanoparticle cellular uptake. *Bioconjugate Chem. 16*, 494−496.
(47) Zhang, Y. W., Staal, B., Su, Y., Swiatek, P., Zhao, P., Cao, B., Resau, J., Sigler, R., Bronson, R., and Vande Woude, G. F. (2006) Evidence that MIG-6 is a tumor-suppressor gene. *Oncogene 26*, 269−276.
(48) Mantha, A. J., Hanson, J. E. L., Goss, G., Lagarde, A. E., Lorimer, I. A., and Dimitroulakos, J. (2005) Targeting the mevalonate pathway inhibits the function of the epidermal growth factor receptor. *Clin. Cancer. Res. 11*, 2398−2407.

Supporting Information

Rapid Catalyst-Free Hydrazone Ligation:

Protein-Pyridoxal Phosphoramides

Xiaojian Wang and James W. Canary*

Department of Chemistry, New York University, New York, NY

10003

Experimental Details.

General Experimental. Pyridoxal-5'-phosphate monohydrate (PLP), imidazole (IM), 1-ethyl-3-(3-dimethylaminopropyl) carbodiimide hydrochloride (EDC), 2-hydrazinopyridine (HP), fluorescein isothiocyanate (FITC), trifluoroacetic acid (TFA), α- cyano-4-hydroxycinnamic (CHCA), tris(hydroxymethyl)aminomethane (Tris), glycine, 2X protein gel loading dye, sodium dodecyl sulfate (SDS) and coomassie blue were purchased from Acros Organics (Geel, Belgium). Rhodamine B isothiocyanate (RITC), Concanavalin A (Con A), human Transferrin (partially iron-saturated, hTf), glyoxylic acid monohydrate (GA) were purchased from Sigma Aldrich (St. Louis, MO). Cetuximab was kindly provided by Dr. Leonard Liebes (New York University, Department of Medicine and NYU Cancer Institute). Phosphate buffered saline (10 mM pH 7.4, PBS 7.4), Dulbecco's phosphate-buffered saline with calcium and magnesium (10 mM pH 7.4, DPBS), Dulbecco's modified eagle's medium (DMEM), RPMI-1640 medium (RPMI), fetal bovine serum (FBS), and Trypsin-EDTA solution were purchased from Mediatech (Herndon, VA). Protein ladder was purchased from Fisher Scientific Inc. (Pittsburgh, PA). Penicillin-Streptomycin 100X Solution was purchased from Thermo Scientific (Waltham, MA). Deuterium oxide (D_2O) and 50% sodium deuteroxide D_2O solution (50% NaOD) were purchased from Cambridge Isotope Laboratories, Inc. (Andover, MA). Fluorescein-5-thiosemicarbazide (FTZ), 4',6-diamidino-2-phenylindole (DAPI) and Alexa Fluor 488 hydrazide (AF488 hydrazide) were purchased from Invitrogen (Carlsbad, CA). All aqueous solutions were prepared using distilled, deionized water (DI water) (Barnstead Mega-Pure MP-3A, Thermo Scientific, Waltham, MA). YM-10 spin filters were purchased from Millipore (Danver, MA). NAP-5 columns were purchased from GE healthcare (Little Chalfont, UK). UV-VIS spectra were acquired on an Agilent 8453 UV-VIS spectrometer.

MALDI-TOF MS was obtained from Bruker UltrafleXtreme Maldi-TOF TOF Mass Spectrometer. ^{1}HNMR was obtained from Bruker AV-400 High Performance Digital NMR Spectrometer (400 MHz). ESI-MS was obtained from Agilent 1100 Series Capillary LCMSD Trap XCT Spectrometer. Cell images were obtained on Leica inverted DMIRE2 fluorescence microscope.

Preparation of Protein-PLP conjugate. Pyridoxal-5'-phosphate (26.5 mg), 6.8 mg of IM and 19.2 mg of EDC were dissolved in 1 mL of DI water to obtain a 0.1 M PLP, 0.1 M IM, and 0.1 M EDC solution. This solution was then adjusted with 1 M HCl to pH 5-5.5. After stirring for 2 h at room temperature (RT), 2 M KOH was added to bring the solution pH between 7.4 and 7.6. The formation of PLP-IM ester was confirmed with ESI-MS, *m*/*e* calculated ($M+H^+$): 298.05, found: 297.9; *m*/*e* calculated ($M-H^+$): 296.04, found: 296.1. The resulting PLP-IM ester solution was used in the following steps without further purification.

Protein of interest (5 mg) was dissolved in 0.5 mL of PBS 7.4, resulting in a 10 mg/mL solution. The quantity 0.5 mL of PLP-IM ester solution was added. After stirring at RT for 2 h (for solution studies and cell studies) or overnight (for MALDI-TOF MS studies), the resulting solution was washed with PBS 7.4 in YM-10 filters. The resulting Protein-PLP solution was stored in PBS 7.4 at 4 °C. The yield of Protein-PLP is about 90%.

Preparation of Con A-RITC-PLP conjugate. Concanavalin A (5 mg) was dissolved in 0.5 mL PBS 7.4 and 25 μL 10 mg/mL RITC in DMF was added. The pH of the solution was adjusted to 8.5 with 1 M KOH aqueous solution. After stirring at RT for 2 h, the solution was passed through a NAP-5 column to get rid of the excess RITC. The quantity 0.5 mL yielded Con A-RITC solution was added to 0.5 mL PLP-IM ester

solution prepared as previously described. After stirring at RT for 2 h, the resulting solution was washed with PBS 7.4 in YM-10 filters. The resulting Con A-RITC-PLP solution was stored in PBS 7.4 at 4 °C. The overall yield is about 90%.

Preparation of Protein~PLP. Pyridoxal-5'-phosphate (26.5 mg) and 6.8 mg of IM were dissolved in 1 mL of DI water to obtain a 0.1 M PLP and 0.1 M IM solution. This solution was then adjusted with 1 M HCl to pH 5-5.5. After stirring for 2 h at room temperature (RT), 2 M KOH was added to bring the solution pH between 7.4 and 7.6.

Protein (5 mg) was dissolved in 0.5 mL of PBS 7.4, resulting in a 10 mg/mL solution. The quantity 0.5 mL of PLP~IM mixture was added. After stirring at RT for 2 h (for solution studies and cell studies) or overnight (for MALDI-TOF MS study), the resulting solution was washed with PBS 7.4 in YM-10 filters. The resulting Protein~PLP solution was stored in PBS 7.4 at 4 °C.

Preparation of protein-FTZ conjugate. The quantity 10 μL 10 mg/mL FTZ in DMF was added to 200 μL 10 mg/mL protein solution. After stirring at RT for 2 h, the solution was passed through a NAP-5 column to get rid of the excess FTZ. The resulting protein-FTZ conjugate was examined by UV-VIS spectroscopy. The concentration of either protein or FTZ was quantitated by the absorption at 280 nm and 490 nm respectively. The yield of the conjugate is about 90%.

Preparation of protein-AF488 hydrazide conjugate. The quantity 50 μL 2mM AF488 hydrazide in PBS 7.4 was added to 50 μL 10 mg/mL protein solution. After stirring at RT for 2 h, the solution was passed through a NAP-5 column to get rid of the excess AF488 hydrazide. The resulting protein-AF488 hydrazide conjugate was examined by UV-VIS spectroscopy. The concentration of either protein or AF488 hydrazide was quantitated by the absorption at 280 nm and 490 nm respectively. The

yield of the conjugate is about 90%.

MALDI-TOF MS Study. The quantity 1 μL 10 μM protein solution was mixed with 10 μL matrix solution, which was saturated CHCA in 69.9% water, 30% acetonitrile, 0.1% TFA (V/V/V), and then loaded onto the MALDI-TOF target. After the solution dried in air, the MALDI-TOF MS spectrum was obtained.

Kinetic Study. Solvent (PBS 7.4) was first ultrasonicated 15 min to degas. To a UV-VIS cuvette, 3 mL of reactants in degased PBS 7.4 were added. The concentration of the reactants were as follows: for PLP/HP, both were 40 μM, for PLP/HP/aniline, PLP and HP were 40 μM and aniline was 100 mM, for FBA/HP/aniline, FBA and HP were 40 μM and aniline was 100 mM, for FBA/HP both were 100 μM, for GA/HP both were 100 μM, for PLP/OEA both were 80 μM, and for FBA/DEA FBA was 30 μM and OEA was 2 mM (Caution: HP is not stable in solution, and thus needs to be prepared fresh). For FBA/OEA, because the reaction is too slow, OEA was used in large excess, and *pseudo*-first order reaction rate, k_{obs}, was obtained. The reaction was monitored by UV-VIS spectrometer at proper wavelengths, 355 nm for PLP/HP, 350 nm for FBA/HP, 308 nm for GA/HP, 337 nm for PLP/OEA and 275 nm for FBA/OEA. Data collected was then fitted to the rate equation (1) for a reversible second-order reaction, except for FBA/OEA which was fitted to the rate equation (2) for a first-order reaction:

$$c_p = c_0 - \frac{a_+(c_0-a_-)-a_-(c_0-a_+)e^{-k_1(a_+-a_-)t}}{(c_0-a_-)-(c_0-a_+)e^{-k_1(a_+-a_-)t}} \quad (1)$$ [s1]

$$c_p = c_0(1-e^{-k_{obs}t}) \quad (2)$$

In which

$$a_+ = \frac{-k_{-1}+\sqrt{k_{-1}^2+4k_1k_{-1}x_0}}{2k_1}, a_- = \frac{-k_{-1}-\sqrt{k_{-1}^2+4k_1k_{-1}x_0}}{2k_1}$$

$$k_{-1} = \frac{k_1}{K_{eq}}\ , k_{obs} = k_1 c_{OEA}$$

and c_p is the concentration of the product (hydrazone or oxime), c_0 is the initial concentration of the aldehyde, c_{OEA} is the concentration of OEA, t is the reaction time, k_1 is rate constant of hydrazone (oxime) formation, k_{-1} is rate constant of hydrazone (oxime) hydrolysis, and K_{eq} is the equilibrium constant. The results of k_1, k_{-1}, and K_{eq} were reported as an average of three independent experiments.

Characterization of PLP-HP. The stock solution of 10 mg/mL PLP and 10 mg/mL HP was prepared fresh with D_2O and 50% NaOD. To an NMR tube, 530 μL stock PLP solution and 218 μL stock HP solution were added. The pD of this solution was adjusted with 30% NaOD to around 7.5 and the HNMR spectrum was then obtained. The ESI-MS was also obtained, *m*/*e* calculated ($M+H^+$): 339.09, found: 339.0; *m*/*e* calculated ($M-H^+$): 337.07, found: 337.1.

Sodium Dodecyl Sulfate Polyacrylamide Gel Electrophoresis (SDS-PAGE). Protein samples were first diluted with the running buffer, which was 25 mM Tris, 0.192 M glycine, and 0.1% (w/w) SDS, pH 8.3, to a final concentration of 1 mg/mL. This protein solution was further diluted with 2X protein gel loading dye with a 1:1 ratio. To each well in the gel, 8 μL of sample was loaded. The gel was run at 200 V for 35 min at RT. Then gel was washed with DI water, and imaged in KODAK Gel Logic 200 Imaging System for fluorescent signal. The gel was then stained in 0.2 g/L coomassie blue solution (water: methanol: acetic acid = 5:5:2, v/v/v). After gently shaking for 1 h at RT, the gel was transferred into the destain solution (water: methanol: acetic acid = 6:3:1, v/v/v). The destain solution was changed every half hour till the background was clear on the gel. The gel was then scanned in Canon CanoScan LiDE

100 flatbed scanner and images were acquired.

Cell lines and cell culture. The PANC-1 cell line was kindly provided by Dr. Leonard Liebes and the EKVX cell line was kindly provided by Dr. Lara Mahal (New York University, Department of Chemistry). Cells were grown in 6 cm polystyrene plates to about 80% confluence in medium (DMEM for panc-1 and RPMI for EKVX) containing 10% FBS, 100 units/mL penicillin and 100 μg/mL streptomycin at 37 °C in a humidified atmosphere containing 5% CO_2. The cells were trypsinized and subsequently suspended in 8 mL of medium (10% FBS). After mixing, this cell suspension was further diluted 1:10 in medium (10% FBS) and the cells were plated on a 48-well plate. The cells were then incubated and allowed to grow to about 80% confluence, which was then used for the imaging study.

Cell Study with Con A conjugate and PANC-1 cell. For the preconjugated study, Con A-PLP-FTZ or Con A~FTZ solution was diluted with PBS 7.4 to 20 μM and 10 μL of this diluted solution was added to 48-well plate which contained 190 μL of DMEM (10% FBS) in each well. The cells were incubated for 30 min at 37 °C, then washed with PBS 7.4 four times to remove the free Con A conjugates. After fixing the cells with cold methanol (-18 ˚C), they were stained with 200 μL of 300 nM DAPI for 10 min at RT and washed with PBS 7.4 twice prior to imaging.

For *in vitro* assembly study, 10 μL of PBS 7.4, or 10 μL of 20μM Con A, or 20 μM Con A-PLP was added to each well containing 190 μL DMEM (10% FBS). After incubating for 30 min at 37 ˚C and washing twice with PBS 7.4, 190 μL of DMEM (10% FBS) and 10 μL of 0.4 mM AF488 hydrazide PBS 7.4 solution were added. After incubating for 1 h at 37 ˚C, the cells were washed with PBS 7.4 three times. Cold methanol was used to fix the cells. After a PBS 7.4 wash, the fixed cells were stained

with DAPI. The cells were then washed twice with PBS 7.4 and imaged on the fluorescence microscope (Figure S3). The expected green signal was observed for Con A-PLP treated cells, with slightly nonspecific binding of AF488 hydrazide in Con A treated cells.

For biocompatibility study, 10 μL of 20μM Con A was added to each well containing 190 μL DMEM (10% FBS). After incubating for 30 min at 37 ˚C and washing twice with PBS 7.4, 200μL DMEM (10% FBS) with or without 100 mM aniline were added. After incubating for 1 h at 37 ˚C, the cells were washed with PBS 7.4 three times. Cold methanol was used to fix the cells. The cells were then washed twice with PBS 7.4 and imaged on the microscope (Figure S4).

Cell Study with hTf conjugate and PANC-1 cell. For the preconjugated study, hTf-PLP-AF488 hydrazide or hTf~AF488 hydrazide solution was diluted with PBS 7.4 to 50 μM and 20 μL of this diluted solution was added to 48-well plate which contained 180 μL of DPBS in each well. The cells were incubated for 30 min at 37 °C, then washed with PBS 7.4 four times to remove the free hTf conjugates. To each well 200 μL DPBS was added and images were acquired immediately after with live cells.

Cell Study with cetuximab conjugate and EKVX cell. For the preconjugated study, cetuximab-PLP-AF488 hydrazide or cetuximab ~AF488 hydrazide solution was diluted with PBS 7.4 to 20 μM and 20 μL of this diluted solution was added to 48-well plate which contained 180 μL of DPBS in each well. The cells were incubated for 30 min at 37 °C, then washed with PBS 7.4 four times to remove the free cetuximab conjugates. To each well 200 μL DPBS was added and images were acquired immediately after with live cells.

All pictures were processed with ImageJ and treated identically.

Table S1. Structures and abbreviations of the chemicals

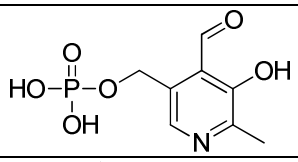	pyridoxal-5'-phosphate (PLP)
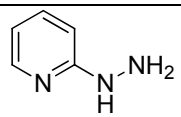	2-hydrazinopyridine (HP)
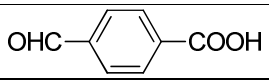	4-formyl benzoic acid (FBA)
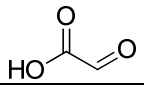	glyoxylic acid (GA)
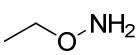	O-ethoxyamine (OEA)
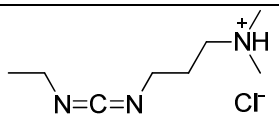	1-ethyl-3-[3-dimethylaminopropyl] carbodiimide hydrochloride (EDC)
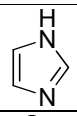	imidazole (IM)
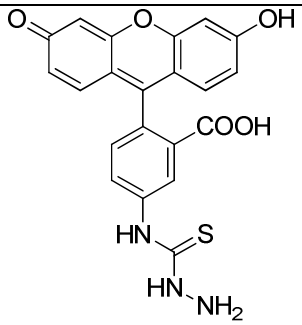	fluorescein-5-thiosemicarbazide (FTZ)
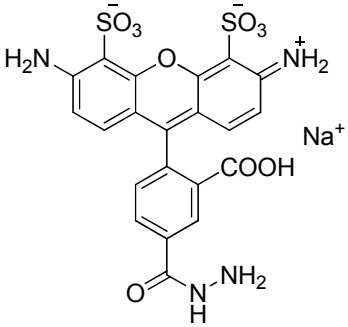	Alexa Fluor 488 hydrazide (AF488 hydrazide)
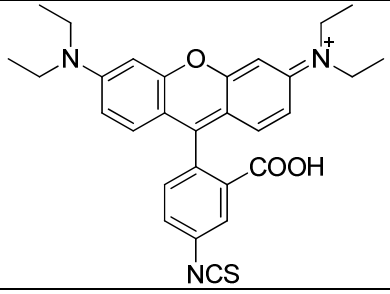	rhodamine B isothiocyanate (RITC)

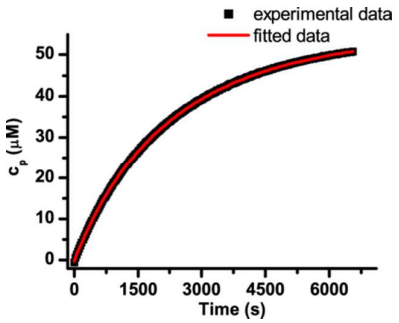

Figure S1. Formation of hydrazone by 100 μM GA and 100 μM HP over time. The black dots were experimental data which were collected every 30 s and the red solid line was the data fitted to the rate equation.

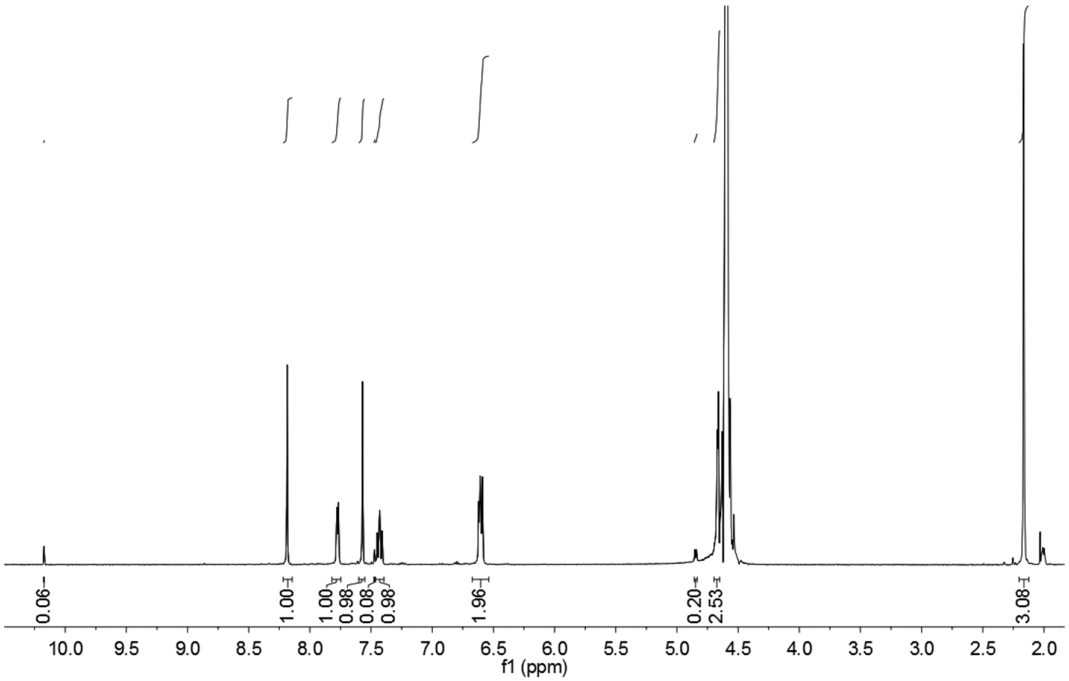

Figure S2. [1]HNMR spectrum of PLP-HP formed in the NMR tube.

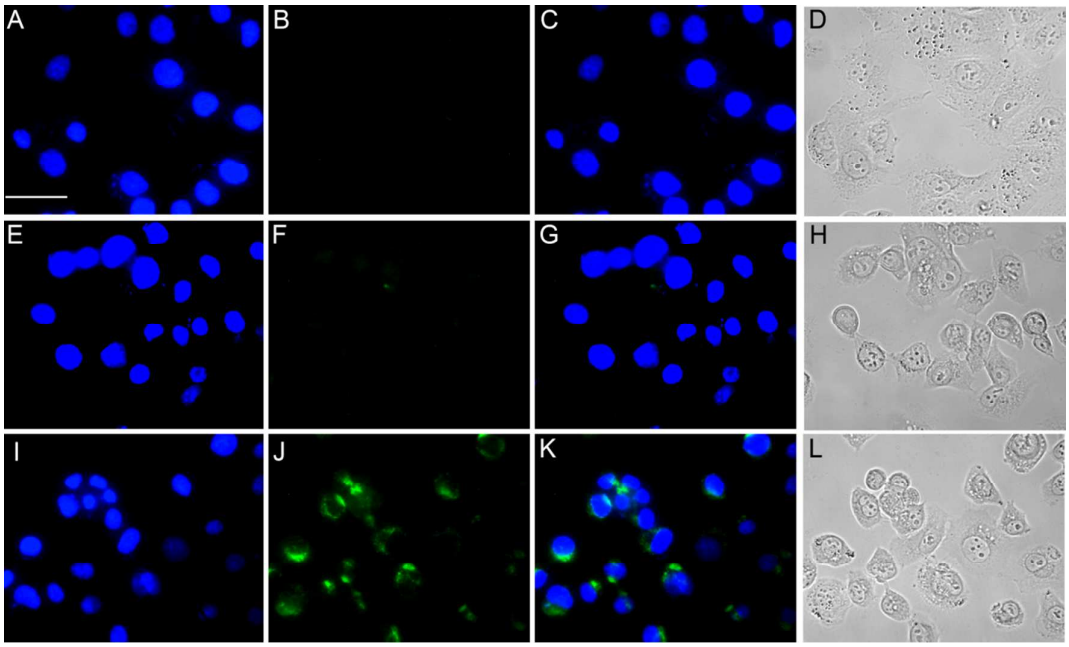

Figure S3. Fluorescent microscopy of PANC-1 cells. (A), (B), (C), (D) cells were first treated with PBS and then AF488 hydrazide. (E), (F), (G), (H) cells were first treated with Con A and then AF488 hydrazide. (I), (J), (K), (L) cells were first treated with Con A-PLP and then AF488 hydrazide. (A), (E), (I): DAPI channel. (B), (F), (J): Fluorescein channel. (C), (G), (K): Merging of DAPI and green channels. (D), (H), (L): bright field images. Scale bar: 50 μm.

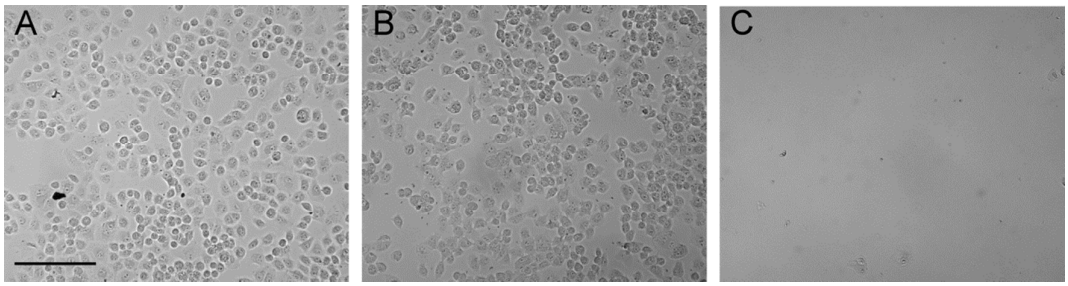

Figure S4. Bight field microscopy of PANC-1 cells. (A) cells without any treatment; (B) cells were first treated with Con A and then incubated in DMEM; (C) cells were first treated with Con A and then incubated in DMEM with 100 mM aniline. Scale bar: 200 μm.

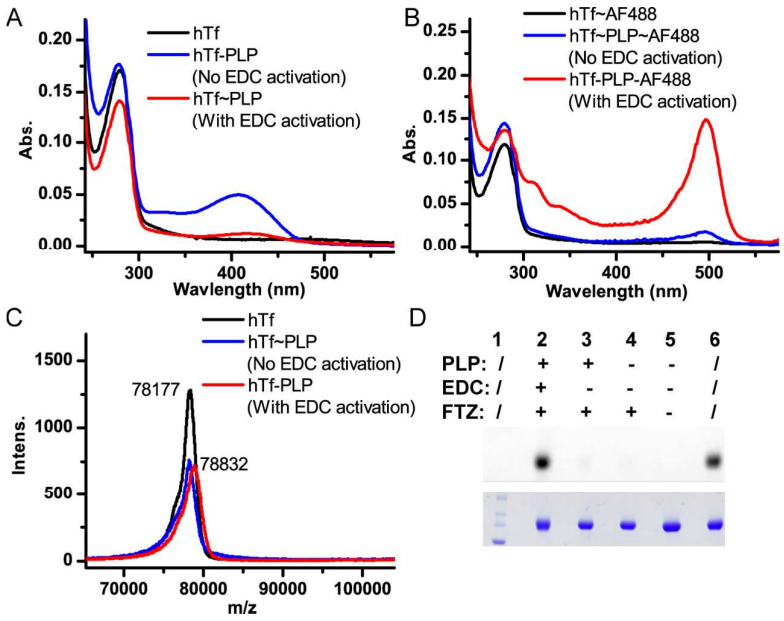

Figure S5. Characterization of hTf conjugates. (A) UV-Vis absorption spectra of hTf (2.26 μM, black), hTf~PLP (1.94 μM, blue), and hTf-PLP (2.21 μM, red); (B) UV-Vis absorption spectra of hTf~AF488 hydrazide (1.20 μM, black), hTf~PLP~AF488 hydrazide (1.83 μM, blue), and hTf-PLP-AF488 hydrazide (1.63 μM, red); (C) MALDI-TOF MS spectrum of hTf (black), hTf~PLP (blue), and hTf-PLP (red). (D) SDS-PAGE visualized under UV light (top) and after Coomassie blue stain (bottom). Well: protein ladder (each line: 85 kDa, 70 kDa, 60 kDa, and 50 kDa, from top to bottom), hTf-PLP-FTZ, hTf~PLP~FTZ, hTf~FTZ, hTf, and hTf-FITC from 1 to 6.

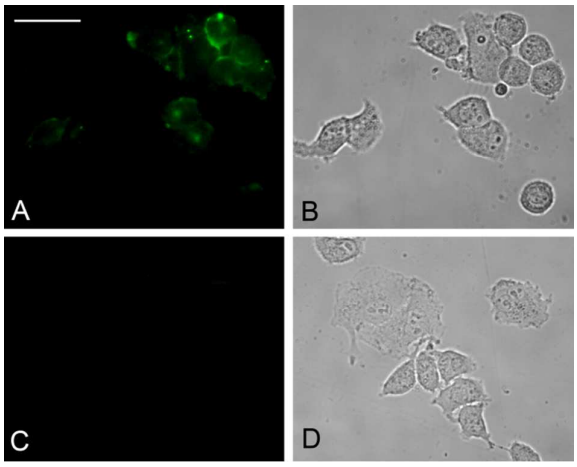

Figure S6. Preconjugate strategy: Fluorescence microscopy of PANC-1 cells. (A) Fluorescein channel of cells labeled with hTf-PLP-AF488 hydrazide, Scale bar: 50 μm; (B) Bright field image of hTf-PLP-AF488 hydrazide labeled cells; (C) Fluorescein channel of cells treated hTf~AF488 hydrazide; (D) Bright field image of hTf~AF488 hydrazide labeled cells.

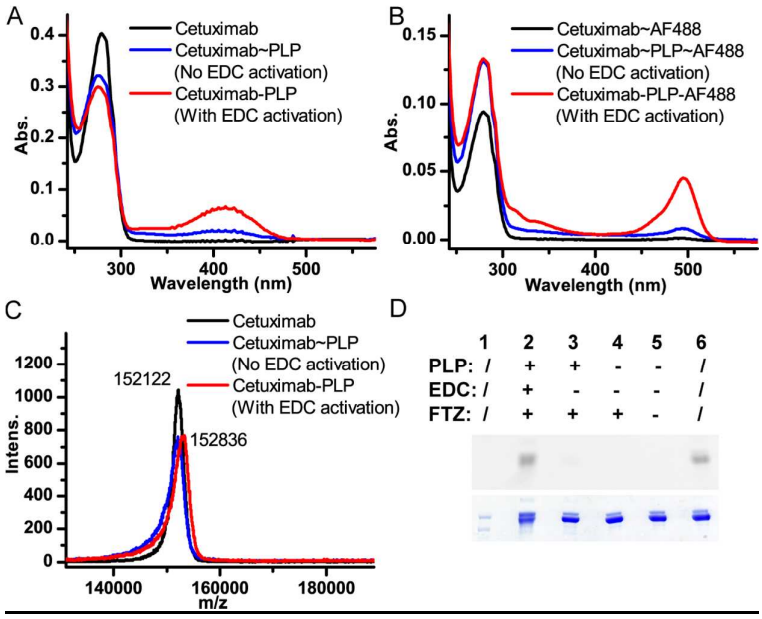

Figure S7. Characterization of cetuximab conjugates. (A) UV-Vis absorption spectra of cetuximab (1.87 μM, black), cetuximab~PLP (1.51 μM, blue), and cetuximab-PLP (1.37 μM, red); (B) UV-Vis absorption spectra of cetuximab~AF488 hydrazide (0.52 μM, black), cetuximab~PLP~AF488 hydrazide (0.65 μM, blue), and cetuximab-PLP-AF488 hydrazide (0.63 μM, red). (C) MALDI-TOF MS spectrum of cetuximab (black), cetuximab~PLP (blue), and cetuximab-PLP (red). (D) SDS-PAGE visualized under UV light (top) and after Coomassie blue stain (bottom). Well: protein ladder (each line: 200 kDa, 150 kDa, from top to bottom), cetuximab -PLP-FTZ, cetuximab ~PLP~FTZ, cetuximab ~FTZ, cetuximab, and cetuximab -FITC from 1 to 6.

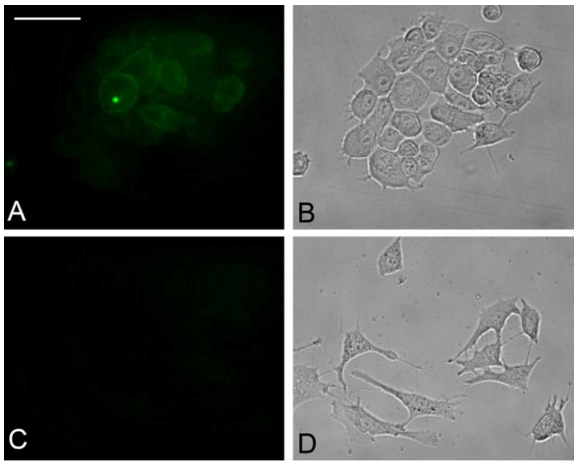

Figure S8. Preconjugate strategy: Fluorescence microscopy of EKVX cells. (A) Fluorescein channel of cells labeled with Cetuximab-PLP-AF488 hydrazide, Scale bar: 50 μm; (B) Bright field image of Cetuximab-PLP-AF488 hydrazide labeled cells; (C) Fluorescein channel of cells treated Cetuximab~AF488 hydrazide; (D) Bright field image of Cetuximab~AF488 hydrazide labeled cells.

Supporting references:

(S1) Dirksen, A.; Dirksen, S.; Hackeng, T. M.; Dawson, P. E. *J. Am. Chem. Soc.* **2006**, *128*, 15602-15603.

Bioconjugate Chemistry

Article

pubs.acs.org/bc

Layer-by-Layer Assembled Polypeptide Capsules for Platinum-Based Pro-Drug Delivery

Dongfang Zhou,[†] Haihua Xiao,[†] Fanbo Meng,*[,‡] Shaoyang Zhou,[§] Jinshan Guo,[†] Xiaoyuan Li,[†] Xiabin Jing,[†] and Yubin Huang*[,†]

[†]State Key Laboratory of Polymer Physics and Chemistry, Changchun Institute of Applied Chemistry, Chinese Academy of Sciences, Graduate School of Chinese Academy of Sciences, Renmin Str. 5625, Changchun 130022, P. R. China

[‡]The Cardiology Department of China-Japan Union Hospital of Jilin University, No. 126 Xiantai Str., Changchun 130033, P. R. China

[§]Northeast Normal University, Changchun 130024, P. R. China

Supporting Information

ABSTRACT: Platinum(IV), a pro-drug of platinum(II), was conjugated to poly(L-lysine) (PLL), and then assembled with poly(glutamic acid) (PGA) through a layer-by-layer (LbL) approach on colloidal silica templates. After removal of the templates, biodegradable PGA/PLL-Pt(IV) multilayer capsules (diameter = 0.5 μm) with 10 μg of platinum incorporated into each bilayer were obtained. Under acidic and/or reductive conditions, the amount and rate of platinum released from the capsules were increased, which are desirable traits for platinum-based anticancer drug delivery systems. Furthermore, in vitro evaluation showed that the PGA/PLL-Pt(IV) multilayer microcapsules displayed higher cytotoxicity (IC_{50Pt} = 3.5 μg/mL) against colon cancer cells CT-26 than that of free cisplatin (IC_{50Pt} = 8.6 μg/mL). This enhanced cytotoxicity was attributed to the effective internalization of the capsules by the cancer cells, which was observed by confocal laser scanning microscopy (CLSM) imaging.

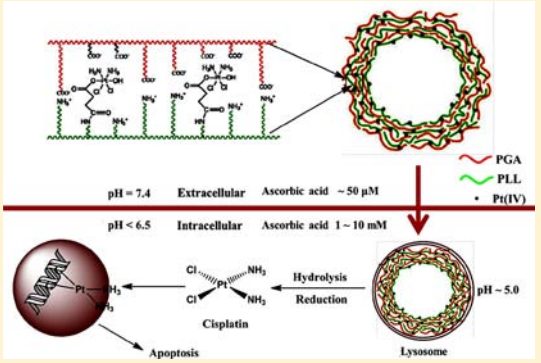

INTRODUCTION

The ability of platinum(II) to inhibit the growth of cancer cells by interfering with transcription and other DNA-mediated cellular functions has been elucidated over the past 30 years.[1] Platinum(II) is a widely used antitumor agent against a variety of solid tumors, such as testicular, breast, ovarian, bladder, lung, head, and neck cancer.[2,3] However, a number of side effects, such as nephrotoxicity, cumulative neurotoxicity, and ototoxicity, can occur which greatly limit its clinical applications.[4] In order to develop more reliable platinum anticancer agents, much attention has been paid to Pt (IV) complexes. Pt (IV) complexes with octahedral structure are known to have less toxicity compared to their Pt (II) counterparts,[5−8] but need to be reduced to the bioactive Pt (II) form by biological reductive agents, such as glutathione, ascorbic acid, and cysteine.[9,10] Therefore, Pt (IV) complexes can be considered to be pro-drugs of Pt (II) complexes. If such Pt (IV) complexes could retain their +4 valence state in the circulatory system but are then reduced to +2 valence state when they enter cancer cells, high antitumor efficacy without severe side effects could be attained. From this point of view, it is of great significance to increase cellular uptake and to protect Pt (IV) from immature reduction before they enter cancer cells.

Several types of inorganic nanoparticles have been applied to Pt (IV) pro-drug delivery.[11−14] However, detailed biocompatibility studies have shown that inorganic nanoparticles can cause severe systemic toxicity at high concentrations in vivo.[15,16] Polymeric nanocarriers, such as polymer particles, polymer micelles, polymer−drug conjugates, and polymer capsules are seen as promising alternative materials for drug delivery.[17,18] Polymeric nanocarriers usually enter the cancer cells with considerable efficiency and preferentially enter the cancerous tissue via the enhanced permeability and retention (EPR) effect.[19−21] Some efforts have been made to deliver Pt (IV) pro-drugs through polymer particles and polymer−drug conjugates.[22−25] Among the various polymeric nanocarriers, layer-by-layer (LbL) assembled polymer capsules are particularly attractive for drug delivery,[26] as the capsules can be loaded with biologically active cargos, degraded via various mechanisms, engineered with low-fouling properties, and have the potential for targeting.[27−31] However, the effective delivery and controlled release of chemotherapeutics using capsules remains a challenge, mainly due to leakage of small cytotoxic cargos from the inherently semipermeable LbL carrier systems.[32,33] Recent methods toward the controlled delivery of small cytotoxic cargos via LbL assembled polymer capsules include multiple compartments, mesoporous templates, and polymer−drug conjugates.[34−36] Due to limited solubility and

Received: March 21, 2012
Revised: November 4, 2012
Published: November 26, 2012

 © 2012 American Chemical Society

Scheme 1. Preparation of Platinum Complex 2 and PLL-Pt(IV) Conjugate

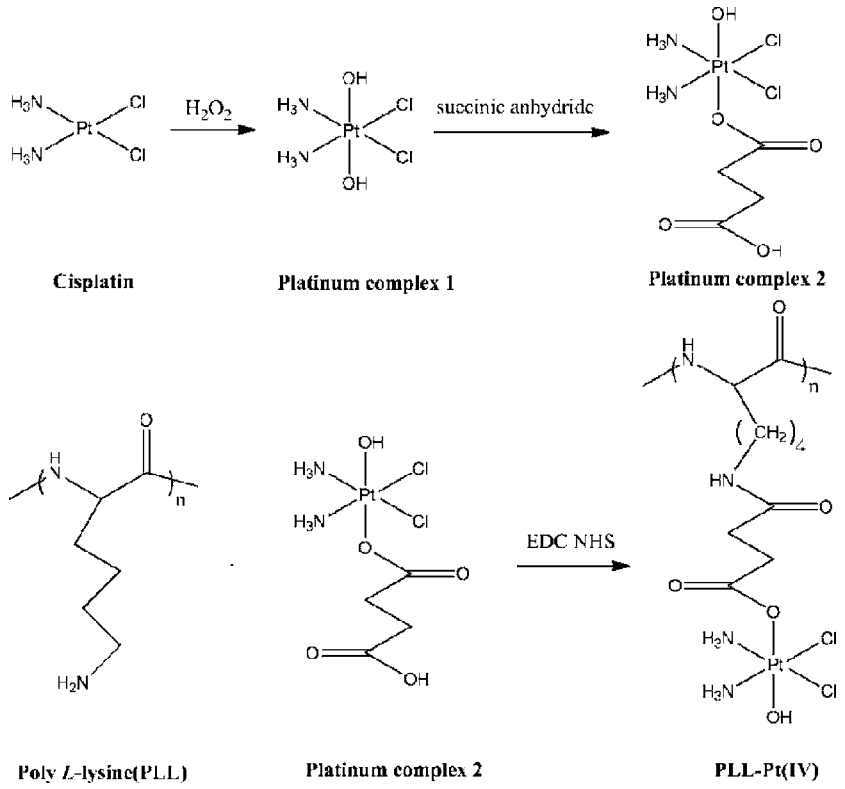

the absence of functional groups, it can be difficult to encapsulate platinum(II) into polymer capsules at high loadings and to effect controlled release.[37]

In this work, we used LbL polypeptide capsules as a carrier for platinum drug delivery. As a pro-drug of cisplatin(II), a Pt (IV) complex with a carboxyl group was synthesized and conjugated to the side chains of poly(L-lysine) (PLL), resulting in a polypeptide−drug conjugate, PLL-Pt(IV). PLL-Pt(IV) was then assembled with poly(glutamic acid) (PGA) through an LbL technique on a colloidal support into biodegradable, controllably drug-loaded, and environmentally responsive polypeptide capsules. Platinum release from the capsules was found to be greatly enhanced under low pH and reductive conditions. These platinum-loaded LbL capsules exhibited effective internalization by CT-26 colon cancer cells and showed higher cytotoxicity than that of free cisplatin, indicating that the platinum-loaded polypeptide microcapsules could be an option for platinum delivery in vivo and have potential applications in targeted intracellular cancer therapy.

EXPERIMENTAL PROCEDURES

Materials. Hydrogen peroxide (H_2O_2), hydrofluoric acid (HF), ammonium fluoride (NH_4F), *N*-hydroxysuccinimide (NHS), 1-ethyl-(3-dimethylaminopropyl) carbodiimide hydrochloride (EDC.HCl), *N,N′*-dicyclohexyl carbodiimide (DCC), Rhodamine B, and succinic anhydride were purchased from Sigma-Aldrich and used as received. Cisplatin (purity 99%) was bought from Shandong Boyuan Chemical Company, China. Silica microspheres (0.5 and 1.5 μm) were purchased from Wuhan Sphere Scientific Corporation. Poly(L-lysine) (PLL, M_w 7000−9000 g/mol) and poly(glutamic acid) (PGA, M_w 8000−10 000 g/mol) were synthesized according to the reported method.[38] Water used in all experiments was prepared in a Millipore purification system and had a resistivity higher than 18 MΩ cm. All other chemicals were purchased from Sigma-Aldrich and used as received.

Methods. ζ-Potentials were measured on a Zetasizer 2000 (Malvern) instrument. Film thicknesses were determined using spectroscopic ellipsometer (Horiba Jobin Yvon). Typical measurements were carried out between 400 and 800 nm with a 2 nm increment. Layer thicknesses were extracted with the integrated software by fitting the experimental data with a classical wavelength dispersion model. For scanning electron microscopy (SEM) and transmission electron microscopy (TEM) measurements, 1 μL of a concentrated capsule solution was placed on a clean silicon wafer slide (or TEM grid) and allowed to dry. SEM samples were sputter-coated with gold and analyzed with a Philips XL 30 microscope at voltages of 10 kV. TEM images were obtained from a JEOL JEM-1011 electron microscope. Confocal laser scanning microscopy (CLSM) images were taken with an Olympus confocal system. Inductively coupled plasma optical emission spectrometry (ICP-OES, iCAP 6300, Thermoscientific, USA) was used to determine the platinum contents in samples. Energy-dispersive X-ray (EDX) analysis was carried out using NORAN Instruments Voyager. ^{1}H NMR spectra were measured by a Unity-300 MHz NMR spectrometer (Bruker) at room temperature. Fourier transform infrared (FT-IR) spectra were recorded on a Bruker Vertex 70 spectrometer. Mass spectroscopy (ESI-MS) measurements were performed on a Quattro Premier XE system (Waters) equipped with an electrospray interface (ESI).

Synthesis of Pt (IV) Complex 2. Pt (IV) complex 2 (Scheme 1) was synthesized as described previously.[25] Briefly, succinic anhydride (100 mg, 1 mmol) was added to a DMSO solution (10 mL) of Pt (IV) complex 1 (c,c,t-[Pt-

dx.doi.org/10.1021/bc300144e | Bioconjugate Chem. 2012, 23, 2335−2343

$(NH_3)_2Cl_2(OH)_2]$) (334 mg, 1 mmol), and the reaction mixture was stirred at 40 °C for 12 h. The solution was lyophilized, and acetone (10 mL) was added to precipitate a light yellow solid. The solid was washed three times with diethyl ether, and then dried to obtain platinum(IV) complex 2 with a yield of 62%. ESI-MS (negative mode): Calc. = 434, Found 433; ^{1}H NMR (DMSO-d_6): 6.00 (br, 6H), 2.45−2.25 (m, 4H). Anal. Calc. for $C_4H_{12}Cl_2N_2O_5Pt$ (434.13): C, 11.07; H, 2.79; N, 6.45; Found: C, 10.95; H, 2.63; N, 6.52 (Figures S1−S3 in Supporting Information).

Preparation of PLL-Pt(IV) Conjugate (PLL-Pt(IV)). Pt (IV) complex 2 was conjugated to PLL via amidation in aqueous solution. Briefly, EDC.HCl (47 mg) and NHS (27 mg) were dissolved in deionized water with stirring. Pt (IV) complex 2 (37 mg) was then added into the above aqueous solution. After the mixture became clear, PLL (50 mg) in water (50 mL) was added, and the reaction mixture was stirred at room temperature for 24 h. Finally, the solution was dialyzed against water for another 24 h and lyophilized to obtain PLL-Pt(IV) conjugate (PLL-Pt(IV)).

Preparation of PLL-RhB and PLL-FITC Conjugates (PLL-RhB and PLL-FITC). Rhodamine B (6 mg), DCC (7 mg) and NHS (4 mg) were dissolved in 2 mL of DMSO. After 30 min, the solution was added into a DMSO solution (10 mL) of PLL (40 mg). The reaction was kept for 24 h at room temperature and the solution then dialyzed for 3 days against water to remove unreacted Rhodamine B. The RhB-labeled PLL conjugate (PLL-RhB) was finally obtained after lyophilization.

FITC (2 mg) was added to a water (50 mL) solution of PLL (50 mg) and the reaction mixture was kept stirring at room temperature for 12 h. The solution was then dialyzed against water for another 24 h and lyophilized to obtain the FITC-labeled PLL conjugate (PLL-FITC).

Multilayer Assembly on Planar Supports. Silicon wafer slides (10 × 10 mm^2) were treated with a mixture containing 2 mL of ethanol, 400 μL of 3-aminopropyltriethoxysilane (APTS), and 100 μL of 28% ammonia solution for 2 h to create positively charged surface. The slides were then rinsed thrice with ethanol, then water, and dried under a stream of nitrogen. The obtained wafer slides were sequentially immersed into PGA and PLL solutions (1 mg/mL) at pH 7.0. A period of 15 min was allowed for the deposition of each layer. Finally, the slides were rinsed with water at pH 7.0 three times and dried with nitrogen.

Multilayer Assembly on Colloidal Templates. Approximately 5 mg of silica spheres (0.5 or 1.5 μm) were treated with a mixture containing 1 mL of ethanol, 200 μL of APTS, and 60 μL of 28% ammonia solution for 3 h to create positively charged surface. The modified silica spheres were added to the PGA solution (1 mg/mL, pH was adjusted to 7.0 with 0.01 M of NaOH) with constant shaking for 15 min. After that, the particles were isolated by centrifugation (600 *g* for 3 min) and washed with 1 mL of water (pH = 7.0). The particles were redispersed, centrifuged, and washed three times. The PLL layer was then adsorbed to the particles using the same procedure above. The same cycle was repeated until three PGA/PLL bilayers were deposited (named $(PGA/PLL)_3$). For the assembly of drug-loaded or fluorescent-labeled capsules, PLL solution was substituted with PLL-Pt(IV), PLL-RhB, or PLL-FITC conjugate solution (1 mg/mL, pH = 7.0) to obtain $(PGA/PLL\text{-}Pt(IV))_3$, $(PGA/PLL\text{-}RhB)_3$, or $(PGA/PLL\text{-}FITC)_3$ microcapsules.

The hollow $(PGA/PLL)_3$, $(PGA/PLL\text{-}Pt(IV))_3$, $(PGA/PLL\text{-}RhB)_3$, and $(PGA/PLL\text{-}FITC)_3$ microcapsules were obtained by dissolving the silica sphere templates in HF/NH_4F solution (pH = 5.0) for 1 min, followed by three centrifugation (1000 *g* for 15 min)/water washing cycles.

Drug Release from $(PGA/PLL\text{-}Pt(IV))_3$ Capsules. A solution of 1.5 mL $(PGA/PLL\text{-}Pt(IV))_3$ capsules (0.5 μm) in a dialysis bag (molecular weight cutoff = 3.5 kDa) was immersed into 15 mL of PBS (0.1 mol/L, pH = 7.4 or 5.0). The dialysis was conducted at 37 °C in a shaking culture incubator. 0.5 mL of sample solution was withdrawn from the outer PBS medium at specified time intervals and measured for Pt concentration by ICP-OES. After sampling, an equal volume of fresh PBS was immediately added to keep the total volume of the outer phase constant. The platinum released from the capsules was expressed as the cumulative amount (percentage) of platinum outside the dialysis bag relative to the total amount of platinum in the capsules.

The same drug release procedure was also performed in the presence of sodium ascorbate (5.0 mM or 0.1 mM) in the dialysis bag.

MTT Assay. The cytotoxicity of cisplatin, Pt (IV) complex 2, $(PGA/PLL)_3$ capsules, and $(PGA/PLL\text{-}Pt(IV))_3$ capsules (0.5 μm) was assessed using a 3-[4,5-dimethylthiazol-2-yl]-2,5-diphenyltetrazolium bromide (MTT) assay. Colon cancer cell line CT-26 cells were grown in Roswell Park Memorial Institute (RPMI) 1640 medium with 10% fetal bovine serum, 0.03% L-glutamine, and 1% penicillin/streptomycin at 37 °C under 5% CO_2. The cells were split into 96-well plates (1×10^4 cells per well), and after 12 h incubation, cells were exposed to the solutions of cisplatin, Pt (IV) complex 2, $(PGA/PLL)_3$ capsules, and $(PGA/PLL\text{-}Pt(IV))_3$ capsules at six different concentrations. After further incubation for 24 h (37 °C, 5% CO_2), 20 μL of MTT in PBS (5 mg/mL) was added to each well and the plates were incubated for another 4 h at 37 °C, followed by removal of the culture medium containing MTT. 150 μL of DMSO was added to each well to dissolve the formed formazan crystals. The plates were then shaken for 10 min, and the absorbance of formazan was measured at 492 nm by a microplate reader.

Cell Internalization. Colon cancer cell line CT-26 cells were grown in Roswell Park Memorial Institute (RPMI) 1640 medium with 10% fetal bovine serum, 0.03% L-glutamine, and 1% penicillin/streptomycin at 37 °C under 5% CO_2. The cells were seeded in 6-well plates (1×10^5 cells per well) and allowed to adhere overnight. Cells were then incubated with LysoTracker Red (1 μg/mL) in RPMI 1640 medium at 37 °C for 1 h, then incubated with $(PGA/PLL\text{-}FITC)_3$ capsules (0.5 μm) for 12 h. After three washes with PBS, 4% paraformaldehyde was added for another 30 min at 37 °C. Finally, nuclei were counterstained with the blue dye 4′,6-diamidino-2-phenylindole (DAPI) (1 μg/mL) for 15 min at room temperature. Cellular uptake was observed with an Olympus FV1000 confocal laser scanning microscope (CLSM) imaging system (Japan).

RESULTS AND DISCUSSION

Synthesis of PLL-Pt(IV) Conjugate. It is difficult to encapsulate cisplatin(II) in polymer capsules or other polymeric nanocarriers due to the limited solubility and the absence of any functional groups.[37] To solve this problem, a soluble cisplatin pro-drug Pt (IV) complex 2 with a carboxyl group was synthesized. Then, the pro-drug was covalently

conjugated to a biodegradable and biocompatible polypeptide PLL to form the PLL-Pt(IV) conjugate. Controllable Pt content loading was realized by adjusting the grafting ratio of platinum complex 2 to PLL (Scheme 1). In the experiments described in this paper, the grafting ratio of Pt (IV) complex 2 to PLL was fixed at 10%, and the Pt content as measured by ICP-OES was 10.9% (w/w).

PGA/PLL-Pt(IV) Multilayer Film Assembly on Planar Supports. Direct structural analysis of the assembled multilayers on silica microspheres was hindered by a lack of appropriate analytical apparatus. As an alternative, alternating layers of PGA/PLL were sequentially deposited on silicon wafer slides, featuring a positively charged surface, using an LbL technique. In situ spectroscopic ellipsometry experiments were carried out to study the thickness variation as a function of the deposited layers of PGA/PLL multilayer films at pH 7.0 on these planar supports. As shown in Figure 1, the PLL/PGA

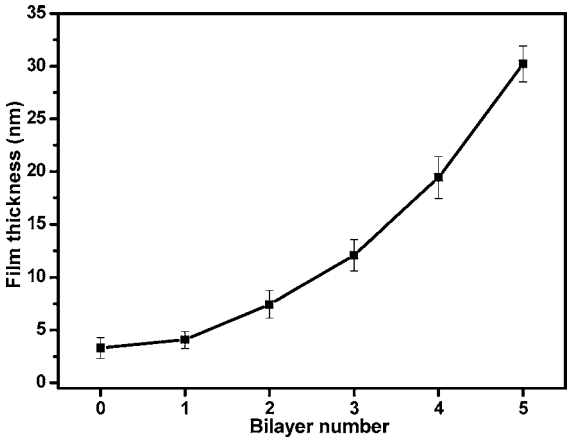

Figure 1. Film thickness of the PGA/PLL multilayer assembled on planar supports.

multilayer films exhibited a nonlinear growth tendency, which was quite different from the linear growth behavior of normal polyelectrolyte films.[39] This discrepancy could be explained by the fact that the growth of such multilayer films is entropy-driven and is an endothermic complexation process as evidenced by previous reports.[40−43]

PGA/PLL-Pt(IV) Multilayer Film Assembly on Colloidal Templates. Similar assembly behavior could be assumed with the microsphere system. Using the same conditions as those employed for planar supports, PGA/PLL bilayers were also deposited onto colloidal silica microspheres. Since PLL is positively charged (PI = 9) and PGA is negatively charged (PI = 3.5) at pH 7.0, the stepwise growth of the multilayer on the surface of silica spheres could be easily monitored by checking the ζ-potential change of the spheres after each deposition step (Figure 2). The original ζ-potential of the APTS-treated silica spheres was about +65 mV. During the polymer deposition procedure, the surface charge of the silica spheres alternated between −75 mV and +40 mV, as the PGA and PLL layers were successively deposited. This result indicated that after adsorption the charge on the surface of each layer was overcompensated, facilitating the adsorption of the next oppositely charged polypeptide, forming the multilayer film on the silica spheres.

The successful preparation and characterization of the PGA/PLL coated microspheres made a good foundation for the

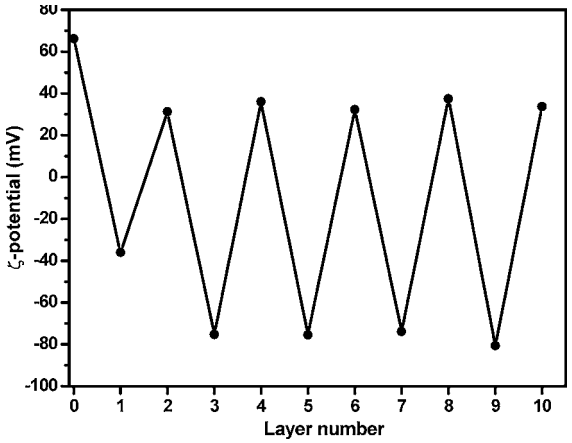

Figure 2. Variation in the ζ-potential for the deposition of PGA/PLL-Pt(IV) multilayer films on silica particles.

introduction of the PLL-Pt(IV) polymer−drug conjugate. This was achieved by simply replacing PLL with PLL-Pt(IV) using the same LbL assembly technique with PGA on silica templates. The assembly of the PGA/PLL-Pt(IV) multilayer on colloidal templates was observed by TEM and SEM (Figure 3). All the microspheres had a uniform morphology and did not show any obvious change in size after film coating. Compared with uncoated silica microspheres (Figure 3a), the polypeptide-treated microspheres (Figure 3b) showed a higher electron density on the shell, indicating successful surface coating. After removal of the silica templates, $(PGA/PLL\text{-}Pt(IV))_3$ capsules were obtained and the size of capsules could be easily adjusted by changing the size of the starting templates. In this work, $(PGA/PLL\text{-}Pt(IV))_3$ capsules with diameters of 0.5 and 1.5 μm were prepared. The larger-sized capsules were for the convenience of investigations on structure and composition. The typical collapsed structure (with folds and creases) of a range of polyelectrolyte capsules[44−46] was also examined (Figure 3c,d,f). The close contact between the capsules was due to the drying process required for TEM and SEM analyses. No shrinkage or breakage of the hollow capsules indicated that the $(PGA/PLL\text{-}Pt(IV))_3$ coating was stable under the dissolution conditions of the silica core.

In order to further confirm the structure of $(PGA/PLL\text{-}Pt(IV))_3$, RhB-labeled PLL (PLL-RhB) was used in the LbL multilayer assembly for confocal laser scanning microscopy (CLSM) imaging. The red fluorescence in the CLSM image confirmed the hollow vesicle-like structure of the $(PGA/PLL\text{-}RhB)_3$ capsules (Figure 3e). The capsule size of approximately 1.5 μm suggested that the resultant hollow capsules exhibited the same shape and size as the original silica microsphere templates.

Energy-dispersive X-ray (EDX) was used to analyze the chemical constitution of the capsules. As shown in Figure 4, the existence of a Pt peak clearly demonstrated the successful incorporation of Pt (IV) onto the silica microspheres. Si signal disappearance after template removal verified the complete dissolution of the silica cores. The Pt peak remained after dissolution of the Si core, confirming that the conjugation between Pt (IV) and PLL was stable under the silica dissolution conditions.

The amount of Pt in the LbL multilayer assembly system was determined using ICP-OES measurements (Figure 5). After deposition of a PGA/PLL-Pt(IV) bilayer, the Pt concentration

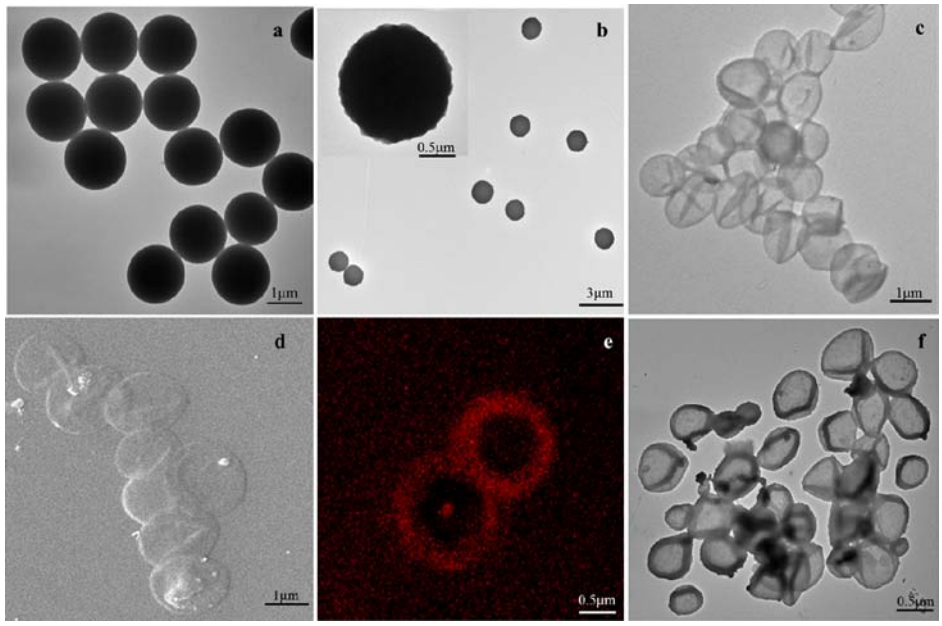

Figure 3. Images of the particles and capsules. TEM images of silica particles before (a) and after (b) coating with $(PGA/PLL\text{-}Pt(IV))_3$ films; TEM (c), SEM (d), and CLSM (e) of 1.5 μm $(PGA/PLL\text{-}Pt(IV))_3$ capsules and TEM (f) of 0.5 μm $(PGA/PLL\text{-}Pt(IV))_3$ capsules.

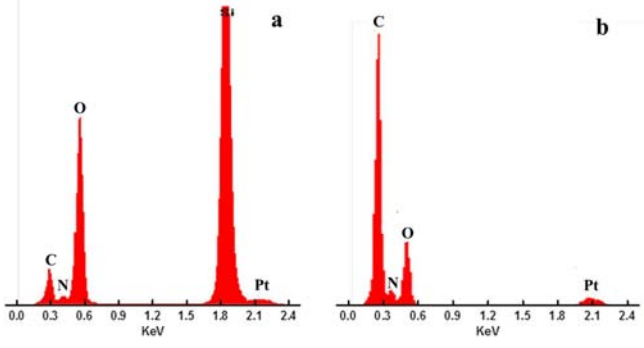

Figure 4. EDX analysis of the particles and capsules. (a) Silica particles coated with $(PGA/PLL\text{-}Pt(IV))_3$ films. (b) $(PGA/PLL\text{-}Pt(IV))_3$ capsules after silica template removal.

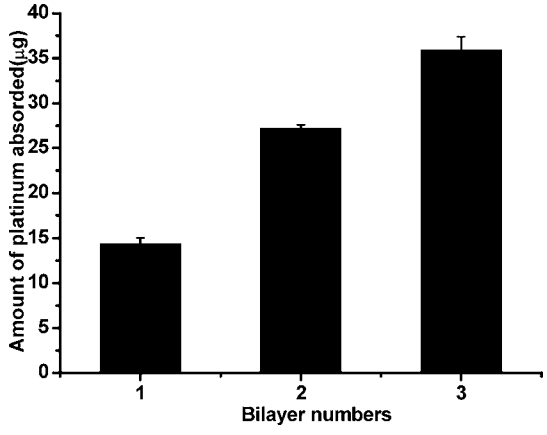

Figure 5. Amount of platinum incorporated per bilayer in the PGA/PLL-Pt(IV) multilayer capsules.

in the supernatant was measured. Compared to the total amount of Pt applied for assembly, the amount of Pt adsorbed onto the silica microspheres (0.5 μm) could be calculated. The amount of Pt incorporated in each bilayer on silica microspheres followed an approximately linear trend (~10 μg per bilayer), which implied that the amount of incorporated drug could be precisely controlled.

It was assumed that the varied size of $(PGA/PLL\text{-}Pt(IV))_3$ capsules would not lead to any property changes; but for practical applications, capsules with smaller diameter (such as 0.5 μm) would be more suitable for drug delivery via blood circulation and aid cell internalization. In these regards, only the $(PGA/PLL\text{-}Pt(IV))_3$ capsules with diameter of 0.5 μm were used in the following biorelated experiments.

Drug Release from $(PGA/PLL\text{-}Pt(IV))_3$ Capsules. Drug release experiments from the $(PGA/PLL\text{-}Pt(IV))_3$ capsules were performed with variable pH and different concentrations of reductive agent (sodium ascorbate). Again, ICP-OES was used to determine the amount of released Pt. The weight ratio of cumulative released Pt to the total Pt payload in the $(PGA/PLL\text{-}Pt(IV))_3$ capsules was calculated as a function of release time. Figure 6a shows the release kinetics for the $(PGA/PLL\text{-}Pt(IV))_3$ capsules at pH 5.0 and pH 7.4, respectively. Overall, the rate of Pt release was much greater from the capsules at pH 5.0 than at pH 7.4. Almost 40% of the Pt was rapidly released during the initial 10 h at pH 5.0 and Pt continued to be released to >60% in 120 h at pH 5.0. In contrast, less than 25% Pt release was detected after 120 h at pH 7.4. The reason for faster platinum release rate from the $(PGA/PLL\text{-}Pt(IV))_3$ capsules under acidic conditions was thought to be the increased hydrolysis of the amide or ester bonds between the Pt(IV) pro-drug and PLL. Acidic degradation of the polypeptide layers could also have contributed to some extent to this rapid release behavior. This character ensured long-term circulation of $(PGA/PLL\text{-}Pt(IV))_3$ capsules without significant Pt loss before reaching the tumor site, followed by increased Pt release in the acidic environment of the cancer cells.

As described above, only when the Pt (IV) species are reduced to Pt (II) species like cisplatin(II) can they display antitumor activity. The reduction of Pt (IV) pro-drug is more likely to take place inside cells which possess a reductive environment, such as the presence of glutathione or other

dx.doi.org/10.1021/bc300144e | Bioconjugate Chem. 2012, 23, 2335−2343

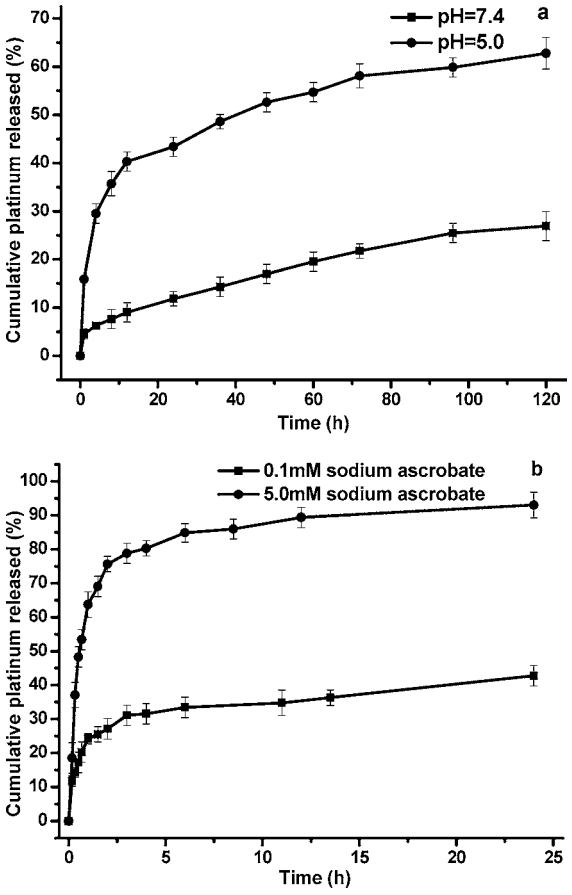

Figure 6. Platinum release profiles of $(PGA/PLL\text{-}Pt(IV))_3$ capsules. (a) In PBS at pH = 7.4 and pH = 5.0; (b) in the presence of 0.1 and 5.0 mM of sodium ascorbate.

reductive agents. Therefore, the $(PGA/PLL\text{-}Pt(IV))_3$ capsules could be considered a pro-drug of cisplatin(II). Under reductive conditions, Pt (IV) complexes in the $(PGA/PLL\text{-}Pt(IV))_3$ capsules could be reduced to the active Pt (II) species and released from the carrying capsules (Scheme 2). In order to mimic the reductive environment in blood plasma and within cells, release experiments from the $(PGA/PLL\text{-}Pt(IV))_3$ capsules were carried out in the presence of sodium ascorbate. As shown in Figure 6b, a higher concentration of reductive agent induced much faster Pt release. About 75% of the total Pt amount was released from the capsules within 2 h in the presence of 5 mM of sodium ascorbate, (corresponding to the same concentration as GSH within tumor cells[47]). This was nearly three times faster than with 0.1 mM of sodium ascorbate (the ascorbic acid concentration in blood plasma[48]). This suggested that Pt (II) could be selectively released from $(PGA/PLL\text{-}Pt(IV))_3$ capsules under reductive conditions in vivo, providing a potentially excellent intracellular targeting delivery system for platinum drugs.

When 5 mM of sodium ascorbate was applied, enhanced Pt release at pH 7 compared to that at pH 5 (in the absence of sodium ascorbate) was observed. This suggested that the $(PGA/PLL\text{-}Pt(IV))_3$ capsules were more sensitive to a reductive environment than to pH, which could be attributed to the difference in rate between reduction and hydrolysis. These results indicate that platinum drug could be well-protected by the $(PGA/PLL\text{-}Pt(IV))_3$ capsules during blood circulation, but exhibit burst release after internalization into cancer cells.

In Vitro Cytotoxicity. Next, the cytotoxicity of $(PGA/PLL\text{-}Pt(IV))_3$ capsules, together with cisplatin, Pt (IV) complex 2, and $(PGA/PLL)_3$ capsules, was examined against colon cancer cells CT-26 using the MTT assay after incubation for 24 h at 37 °C (Figure 7). Nearly 90% cell viability was observed for the $(PGA/PLL)_3$ capsules, even at high concentrations, indicating that the $(PGA/PLL)_3$ capsule was a safe drug delivery system. As expected, cisplatin exhibited a higher cytotoxicity (IC_{50Pt} = 8.6 μg/mL) than Pt (IV) complex 2 (IC_{50Pt} > 10 μg/mL), since Pt (IV) needs to be reduced to Pt (II) to become bioactive. Surprisingly, the $(PGA/PLL\text{-}Pt(IV))_3$ capsules exhibited a somewhat higher cytotoxicity (IC_{50Pt} = 3.5 μg/mL) than cisplatin. It is proposed that this enhanced cytotoxicity was due to effective higher intracellular accumulation of Pt caused by a high degree of internalization of the $(PGA/PLL\text{-}Pt(IV))_3$ capsules. In contrast to free cisplatin, which is known to

Scheme 2. Schematic Illustration of the Structure of $(PGA/PLL\text{-}Pt(IV))_3$ Microcapsules and Intracellular Release of Cisplatin(II)

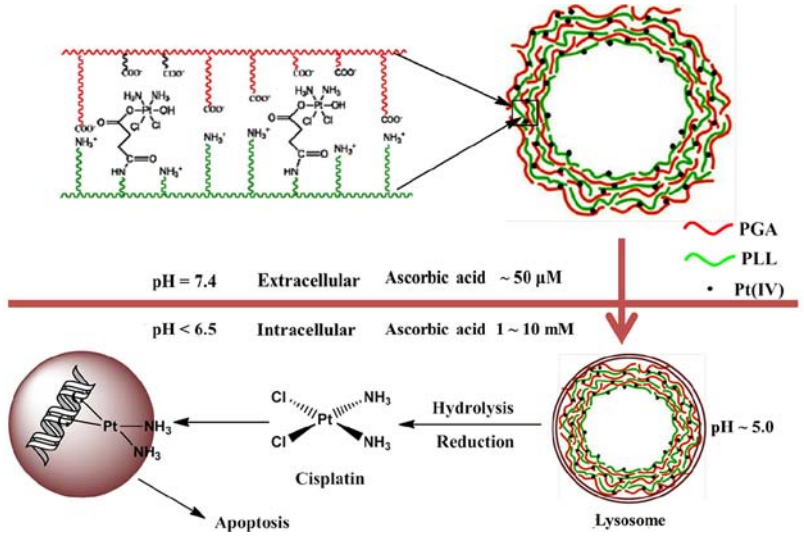

dx.doi.org/10.1021/bc300144e | Bioconjugate Chem. 2012, 23, 2335−2343

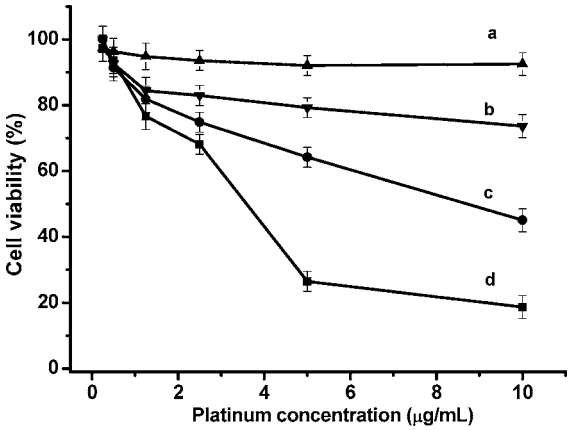

Figure 7. Cytotoxicity of different drug systems after 24 h incubation against CT-26 cells at 37 °C, 5% CO_2. (a) $(PGA/PLL)_3$ capsules, (b) Pt (IV) complex 2, (c) cisplatin, and (d) $(PGA/PLL\text{-}Pt(IV))_3$ capsules.

enter cells by passive diffusion, the $(PGA/PLL\text{-}Pt(IV))_3$ capsules were internalized with high efficacy (supported by the cellular internalization experiments in the next section). It is possible that reduction of the capsules in the cell plasma and hydrolysis in late endosomes or lysosomes could bring about a higher concentration of bioactive Pt (II) species inside the cancer cells, affording a higher cell-killing capacity than the pure drug (cisplatin).

Cell Internalization. Previous reports have demonstrated that submicrometer-sized drug-loaded LbL polymer capsules can be internalized by several different cell types (e.g., dendritic cells, monocytes, and colorectal cancer cells) via macropinocytosis or phagocytosis and display increased cytotoxicity than the corresponding low-molecular-weight drugs alone.[49−51] To correlate the observed cytotoxicity with cellular uptake and release of platinum, the internalization and intracellular distribution of the $(PGA/PLL\text{-}FITC)_3$ capsules was observed by CLSM after 12 h incubation with CT-26 cells (Figure 8). $(PGA/PLL\text{-}FITC)_3$ capsules here served as the fluorescent probe (green fluorescence) in the place of $(PGA/PLL\text{-}Pt(IV))_3$ capsules. To visualize the endocytic compartments, lysosomes were labeled with LysoTracker Red (red fluorescence). The CLSM images clearly revealed the internalization of $(PGA/PLL\text{-}FITC)_3$ capsules, with obvious green fluorescence visible in the cells after 12 h incubation. The majority of the internalized $(PGA/PLL\text{-}FITC)_3$ capsules were confirmed to be localized in the lysosomal compartments; colocalization of the red and green fluorescence was observed. These results implied that cell internalization and fusion with lysosomes were feasible with the drug-loaded $(PGA/PLL))_3$ capsules with a diameter of 0.5 μm. Compared with free cisplatin(II), a greater amount of Pt complex could be transported into the cancer cells in the form of capsules, achieving a higher intracellular concentration of Pt. The active Pt (II) could then be released under the acidic environment of the lysosomes and the reductive environment of the cytoplasm, which might be the reason for the increased efficiency of tumor cell kill of the $(PGA/PLL\text{-}Pt(IV))_3$ capsules.

CONCLUSIONS

This paper provided the first detailed investigation of layer-by-layer assembled polymer capsules for platinum-based pro-drug delivery. $(PGA/PLL\text{-}Pt(IV))_3$ microcapsules, with 10 μg of platinum incorporated into each bilayer, were obtained through

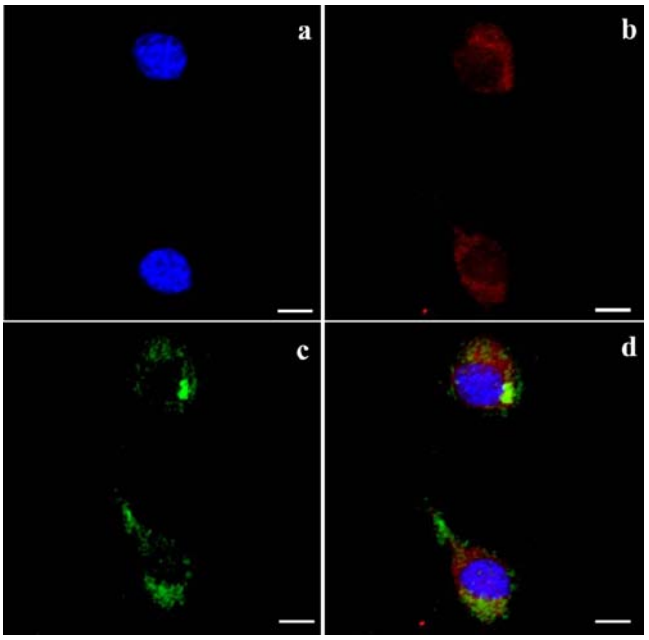

Figure 8. CLSM images of CT-26 cells with internalized $(PGA/PLL\text{-}FITC)_3$ capsules (0.5 μm) for 12 h at 37 °C, 5% CO_2. (a) Nuclear DNA was stained blue with DAPI. (b) Late endosomes and lysosomes were stained with LysoTracker Red. (c) Green fluorescence corresponds to $(PGA/PLL\text{-}FITC)_3$. (d) Overlaid image. All scale bars = 10 μm.

LbL assembly of PGA and a PLL-Pt(IV) conjugate on colloidal silica templates. The $(PGA/PLL\text{-}Pt(IV))_3$ microcapsules showed enhanced Pt release under low pH and reductive conditions. In vitro evaluation showed that these $(PGA/PLL\text{-}Pt(IV))_3$ microcapsules had higher cytotoxicity against CT-26 tumor cells than free cisplatin, likely due to the enhanced cell internalization of Pt in the form of capsules. These biodegradable polypeptide capsules could also provide an excellent vehicle for delivery of other pro-drugs or insoluble anticancer drugs. In an attempt to further improve the therapeutic efficacy, future studies will be focused toward surface functionalization of the drug-loaded LbL capsules with targeting ligands for the promotion of enhanced cell uptake and specificity. In vivo evaluation of the platinum-loaded polymer capsules described herein is also underway.

ASSOCIATED CONTENT

Supporting Information

IR, ^{1}H NMR, and ESI mass spectra of Pt (IV) complex 2. This material is available free of charge via the Internet at http://pubs.acs.org.

AUTHOR INFORMATION

Corresponding Author

*F.M.: Tel & Fax +86-13159757035; E-mail mengfb@jlu.edu.cn. Y.H.: Tel & Fax +86-431-85262769; E-mail ybhuang@ciac.jl.cn.

Notes

The authors declare no competing financial interest.

ACKNOWLEDGMENTS

The authors would like to thank the financial support from National Natural Science Foundation of China (No. 51021003

and 21174143), the Ministry of Science and Technology of China (973 Project, No. 2009CB930102), "100 Talents Program" of the Chinese Academy of Sciences (No. KGCX2-YW-802), and Jilin Provincial Science and Technology Department (No. 20100588). The authors would also like to thank Dr. Gavin T. Noble for proofreading and help with the final edit.

REFERENCES

(1) Wang, D., and Lippard, S. J. (2005) Cellular processing of platinum anticancer drugs. *Nat. Rev. Drug Discovery 4*, 307−320.
(2) Rosengerg, B., VanCamp, L., Trosko, J. E., and Mansour, V. H. (1969) Platinum compounds: A new class of potent antitumour agents. *Nature 222*, 385−386.
(3) Galanski, M., Jakupec, M. A., and Keppler, B. K. (2005) Update of the preclinical situation of anticancer platinum complexes: Novel design strategies and innovative analytical approaches. *Curr. Med. Chem. 12*, 2075−2094.
(4) Pinzani, V., Bressolle, F., Haug, I. J., Galtier, M., Blayac, J. P., and Balmhs, P. (1994) Cisplatin-induced renal toxicity and toxicity-modulating strategies: a review. *Cancer Chem. Pharm. 35*, 1−9.
(5) Schilder, R. J., LaCreta, F. P., Perez, R. P., Johnson, S. W., Brennan, J. M., Rogatko, A., Nash, S., McAleer, C., Hamilton, T. C., Roby, D., Young, R. C., Ozols, R. F., and O'Dwyer, P. J. (1994) Phase-1 and pharmacokinetic study of ormaplatin (tetraplatin, NSC-363812) administered on a day-1 and day-8 schedule. *Cancer Res. 54*, 709−717.
(6) Gurney, H., Crowther, D., Anderson, H., Murphy, D., Prendiville, J., Ranson, M., Mayor, P., Swindell, R., Buckley, C. H., and Tindall, V. R. (1990) 5 year follow-up and dose delivery analysis of cisplatin, iproplatin or carboplatin in combination with cyclophosphamide in advanced ovarian-carcinoma. *Ann. Oncol. 1*, 427−433.
(7) Trask, C., Silverstone, A., Ash, C. M., Earl, H., Irwin, C., Bakker, A., Tobias, J. S., and Souhami, R. L. (1991) A randomized trial of carboplatin versus iproplatin in untreated advanced ovarian-cancer. *J. Clin. Oncol. 9*, 1131−1137.
(8) Kelland, L. R., Abel, G., McKeage, M. J., Jones, M., Goddard, P. M., Valenti, M., Murrer, B. A., and Harrap, K. R. (1993) Preclinical antitumor evaluation of bis-acetato-ammine-dichloro- cyclohexylamine platinum(IV) - an orally active platinum drug. *Cancer Res. 3*, 2581−2586.
(9) Shi, T., Berglund, J., and Elding, L. I. (1996) Kinetics and mechanism for reduction of *trans*-dichlorotetracyanoplatinate(IV) by thioglycolic acid, L-cysteine, DL-penicillamine, and glutathione in aqueous solution. *Inorg. Chem. 35*, 3498−3503.
(10) Choi, S., Filotto, C., Bisanzo, M., Delaney, S., Lagasee, D., Whitworth, J. L., Jusko, A., Li, C., Wood, N. A., Willingham, J., Schwenker, A., and Spaulding, K. (1998) Reduction and anticancer activity of platinum(IV) complexes. *Inorg. Chem. 37*, 2500−2504.
(11) Feazell, R. P., Nakayama-Ratchford, N., Dai, H., and Lippard, S. J. (2007) Soluble single-walled carbon nanotubes as longboat delivery systems for platinum(IV) anticancer drug design. *J. Am. Chem. Soc. 129*, 8438−8439.
(12) Della Rocca, J., Huxford, R. C., Comstock-Duggan, E., and Lin, W. (2011) Polysilsesquioxane nanoparticles for targeted platin-based cancer chemotherapy by triggered release. *Angew. Chem., Int. Ed. 50*, 10330−10334.
(13) Xu, C., Wang, B., and Sun, S. (2009) Dumbbell-like Au-Fe3O4 nanoparticles for target-specific platin delivery. *J. Am. Chem. Soc. 131*, 4216−4217.
(14) Dhar, S., Daniel, W. L., Giljohann, D. A., Mirkin, C. A., and Lippard, S. J. (2009) Polyvalent oligonucleotide gold nanoparticle conjugates as delivery vehicles for platinum(IV) warheads. *J. Am. Chem. Soc. 131*, 14652−14653.
(15) Lewinski, N., Colvin, V., and Drezek, R. (2008) Cytotoxicity of nanoparticles. *Small 4*, 26−49.
(16) Fadeel, B., and Garcia-Bennett, A. E. (2010) Better safe than sorry: understanding the toxicological properties of inorganic nanoparticles manufactured for biomedical applications. *Adv. Drug Delivery Rev. 62*, 362−374.
(17) Duncan, R. (2003) The dawning era of polymer therapeutics. *Nat. Rev. Drug Discovery 2*, 347−360.
(18) Kiick, K. L. (2007) Polymer Therapeutics. *Science 317*, 1182−1183.
(19) Maeda, H., Sawa, T., and Konno, T. (2001) Mechanism of tumor-targeted delivery of macromolecular drugs, including the EPR effect in solid tumor and clinical overview of the prototype polymeric drug SMANCS. *J. Controlled Release 74*, 47−61.
(20) Maeda, H. (2001) The enhanced permeability and retention (EPR) effect in tumor vasculature: the key role of tumor-selective macromolecular drug targeting. *Adv. Enzym. Regul. 41*, 189−207.
(21) Maeda, H., Bharate, G. Y., and Daruwalla, J. (2009) Polymeric drugs for efficient tumor targeted drug delivery based on EPR-effect. *Eur. J. Pharm. Biopharm. 71*, 409−419.
(22) Aryal, S., Hu, C., and Zhang, L. (2010) Polymer-cisplatin conjugate nanoparticles for acid-responsive drug delivery. *ACS Nano 4*, 251−258.
(23) Duong, H. T., Huynh, V. T., Souza, P., and Stenzel, M. H. (2010) Core-cross-linked micelles synthesized by clicking bifunctional Pt(IV) anticancer drugs to isocyanates. *Biomacromolecules 11*, 2290−2299.
(24) Dhar, S., Gu, F. X., Langer, R., Farokhzad, O. C., and Lippard, S. J. (2008) Targeted delivery of cisplatin to prostate cancer cells by aptamer functionalized Pt(IV) prodrug-PLGA-PEG nanoparticles. *Proc. Natl. Acad. Sci. 105*, 17356−17361.
(25) Xiao, H., Qi, R., Liu, S., Hu, X., Duan, T., Zheng, Y., Huang, Y., and Jing, X. (2011) Biodegradable polymer-cisplatin(IV) conjugate as a pro-drug of cisplatin(II). *Biomaterials 32*, 7732−7739.
(26) Tang, Z., Wang, Y., Podsiadlo, P., and Kotov, N. A. (2006) Biomedical applications of layer-by-layer assembly: from biomimetics to tissue engineering. *Adv. Mater. 18*, 3203−3224.
(27) Jewell, C. M., and Lynn, D. M. (2008) Multilayered polyelectrolyte assemblies as platforms for the delivery of DNA and other nucleic acid-based therapeutics. *Adv. Drug Delivery Rev. 60*, 979−999.
(28) Zelikin, A. N., Li, Q., and Caruso, F. (2008) Disulfide-stabilized poly(methacrylic acid) capsules: formation, cross-linking, and degradation behavior. *Chem. Mater. 20*, 2655−2661.
(29) Itoh, Y., Matsusaki, M., Kida, T., and Akashi, M. (2006) Enzyme-responsive release of encapsulated proteins from biodegradable hollow capsules. *Biomacromolecules 7*, 2715−2718.
(30) Yap, H. P., Johnston, A. P. R., Such, G. K., Yan, Y., and Caruso, F. (2009) Click-engineered, bioresponsive, drug-loaded PEG spheres. *Adv. Mater. 21*, 4348−4352.
(31) Cortez, C., Tomaskovic-Crook, E., Johnston, A. P. R., Radt, B., Cody, S. H., Scott, A. M., Nice, E. C., Heath, J. K., and Caruso, F. (2006) Targeting and uptake of multilayered particles to colorectal cancer cells. *Adv. Mater. 18*, 1998−2003.
(32) Sukhorukov, G. B., Brumen, M., Donath, E., and Mohwald, H. (1999) Hollow polyelectrolyte shells: exclusion of polymers and donnan equilibrium. *J. Phys. Chem. B 103*, 6434−6440.
(33) Schneider, A., Vodouhe, C., Richert, L., Francius, G., Le Guen, E., Schaaf, P., Voegel, J. C., Frisch, B., and Picart, C. (2007) Multifunctional polyelectrolyte multilayer films: combining mechanical resistance, biodegradability, and bioactivity. *Biomacromolecules 8*, 139−145.
(34) Wang, Y., Yan, Y., Cui, J., Hosta-Rigau, L., Heath, J. K., Nice, E. C., and Caruso, F. (2010) Encapsulation of water-insoluble drugs in polymer capsules prepared using mesoporous silica templates for intracellular drug delivery. *Adv. Mater. 22*, 4293−4297.
(35) Hosta-Rigau, L., Städler, B., Yan, Y., Nice, E. C., Heath, J. K., Albericio, F., and Caruso, F. (2010) Capsosomes with multilayered subcompartments: assembly and loading with hydrophobic cargo. *Adv. Funct. Mater. 20*, 59−66.
(36) Ochs, C. J., Such, G. K., Yan, Y., Koeverden, M. P., and Caruso, F. (2010) Biodegradable click capsules with engineered drug-loaded multilayers. *ACS Nano 4*, 1653−1663.

(37) Haxton, K. J., and Burt, H. M. (2009) Polymeric drug delivery of platinum-based anticancer agents. *J. Pharm. Sci. 98*, 2299−2316.
(38) Guo, J., Huang, Y., Jing, X., and Chen, X. (2009) Synthesis and characterization of functional poly(γ-benzyl-l-glutamate) (PBLG) as a hydrophobic precursor. *Polymer 50*, 2847−2855.
(39) Bieker, P., and Schönhoff., M. (2010) Linear and exponential growth regimes of multilayers of weak polyelectrolytes in dependence on pH. *Macromolecules 43*, 5052−5059.
(40) Yu, A., Gentle, I. R., and Lu, G. Q. (2009) Biocompatible polypeptide microcapsules via templating mesoporous silica spheres. *J. Colloid Interface Sci. 333*, 341−345.
(41) Lavalle, P., Gergely, C., Cuisinier, F. J. G., Decher, G., Schaaf, P., Voegel, J. C., and Picart, C. (2002) Comparison of the structure of polyelectrolyte multilayer films exhibiting a linear and an exponential growth regime: An in situ atomic force microscopy study. *Macromolecules 35*, 4458−4465.
(42) Halthur, T. J., and Elofsson, U. M. (2004) Multilayers of charged polypeptides as studied by in situ ellipsometry and quartz crystal microbalance with dissipation. *Langmuir 20*, 1739−1745.
(43) Laugel, N., Betscha, C., Winterhalter, M., Voegel, J. C., Schaaf, P., and Ball, V. (2006) Relationship between the growth regime of polyelectrolyte multilayers and the polyanion. *J. Phys. Chem. B 110*, 19443−19449.
(44) Such, G. K., Tjipto, E., Postma, A., Johnston, A. P., and Caruso, F. (2007) Ultrathin, responsive polymer click capsules. *Nano Lett. 7*, 1706−1710.
(45) Ochs, C. J., Such, G. K., Stadler, B., and Caruso, F. (2008) Low-fouling, biofunctionalized, and biodegradable click capsules. *Biomacromolecules 9*, 3389−3396.
(46) Connal, L. A., Kinnane, C. R., Zelikin, A. N., and Caruso, F. (2009) Stabilization and functionalization of polymer multilayers and capsules via thiol−ene click chemistry. *Chem. Mater. 21*, 576−578.
(47) Hassan, S. S. M., and Rechnitz, G. A. (1982) Determination of glutathione and glutathione reductase with a silver sulfide membrane electrode. *Anal. Chem. 54*, 1972−1976.
(48) Dexter, C., Nicholas, W., Ailsa, W., Sheila, B., Robert, L., Nicholas, D., and Kay-Tee, K. (2005) Plasma ascorbic acid concentrations and fat distribution in 19068 British men and women in the European prospective investigation into cancer and nutrition norfolk cohort study. *Am. J. Clin. Nutr. 82*, 1203−1209.
(49) Sexton, A., Whitney, P. G., Chong, S.-F., Zelikin, A. N., Johnston, A. P. R., De Rose, R., Brooks, A. G., Caruso, F., and Kent, S. J. (2009) A protective vaccine delivery system for *in vivo* T cell stimulation using nanoengineered polymer hydrogel capsules. *ACS Nano 3*, 3391−3400.
(50) De Koker, S., De Geest, B. G., Cuvelier, C., Ferdinande, L., Deckers, W., Hennink, W. E., De Smedt, S. C., and Mertens, N. (2007) In vivo cellular uptake, degradation, and biocompatibility of polyelectrolyte microcapsules. *Adv. Funct. Mater. 17*, 3754−3763.
(51) Yan, Y., Johnston, A. P. R., Dodds, S. J., Kamphuis, M. M. J., Ferguson, C., Parton, R. G., Nice, E. C., Heath, J. K., and Caruso, F. (2010) Uptake and intracellular fate of disulfide-bonded polymer hydrogel capsules for doxorubicin delivery to colorectal cancer cells. *ACS Nano 4*, 2928−2936.

Supporting Information

Layer-by-Layer Assembled Polypeptide Capsules for Platinum Delivery

Dongfang Zhou,[a] Haihua Xiao,[a] Fanbo Meng**,[b], Shaoyang Zhou,[c] Jinshan Guo,[a] Xiaoyuan Li,[a] Xiabin Jing,[a] and Yubin Huang*,[a]

[a] State Key Laboratory of Polymer Physics and Chemistry, Changchun Institute of Applied Chemistry, Chinese Academy of Sciences, Graduate School of Chinese Academy of Sciences, Renmin Str. 5625, Changchun 130022, P. R. China

[b] The Cardiology Department of China-Japan Union Hospital of Jilin University, No. 126 Xiantai Str., Changchun 130033, P. R. China

[c] Northeast Normal University, Changchun 130024, P. R. China

*****Correspondence to: Yubin Huang, State Key Laboratory of Polymer Physics and Chemistry, Changchun Institute of Applied Chemistry, Chinese Academy of Sciences, Changchun 130022, People's Republic of China. Tel & Fax: +86-431-85262769; E-mail: ybhuang@ciac.jl.cn

******Co-correspondence to: Fanbo Meng, The Cardiology Department of China-Japan Union Hospital of Jilin University, No. 126 Xiantai Str., Changchun 130033, P. R. China. Tel & Fax: +86-13159757035; E-mail: mengfb@jlu.edu.cn

Figure S1. IR spectrum of cisplatin (a), Pt(IV) complex 1 (b) and Pt(IV) complex 2(c).

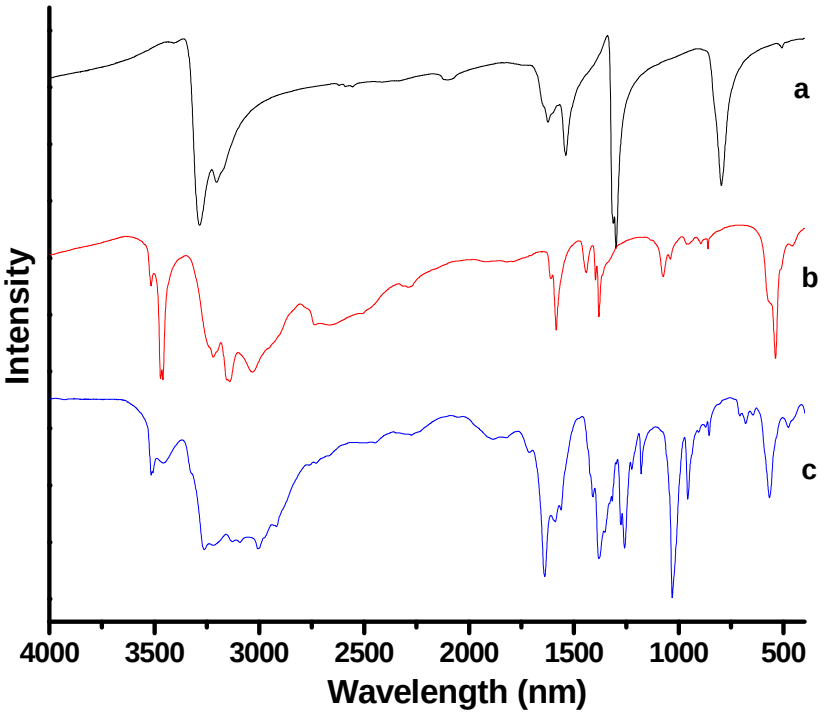

Figure S2. ^{1}H-NMR spectrum of Pt(IV) complex 2.

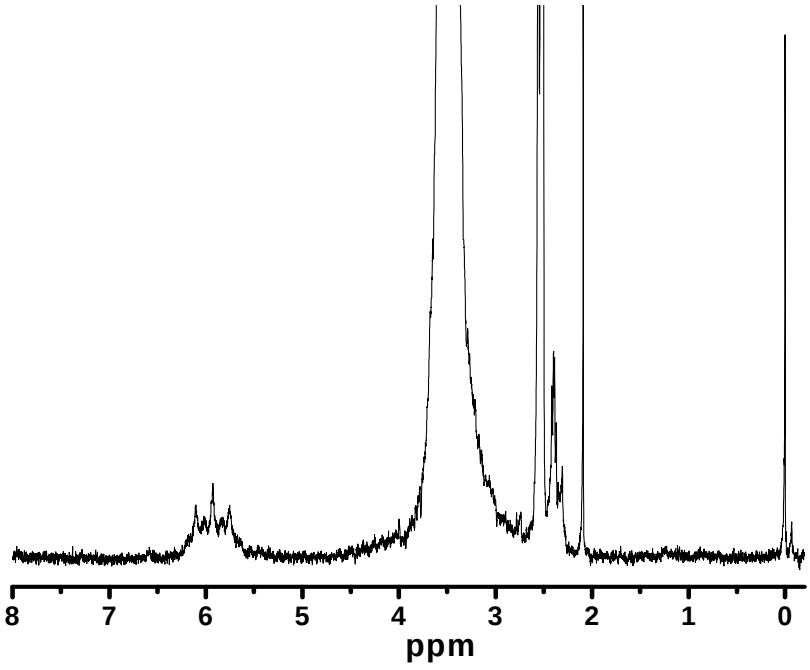

Figure S3. ESI-MS spectrum of Pt(IV) complex 2.

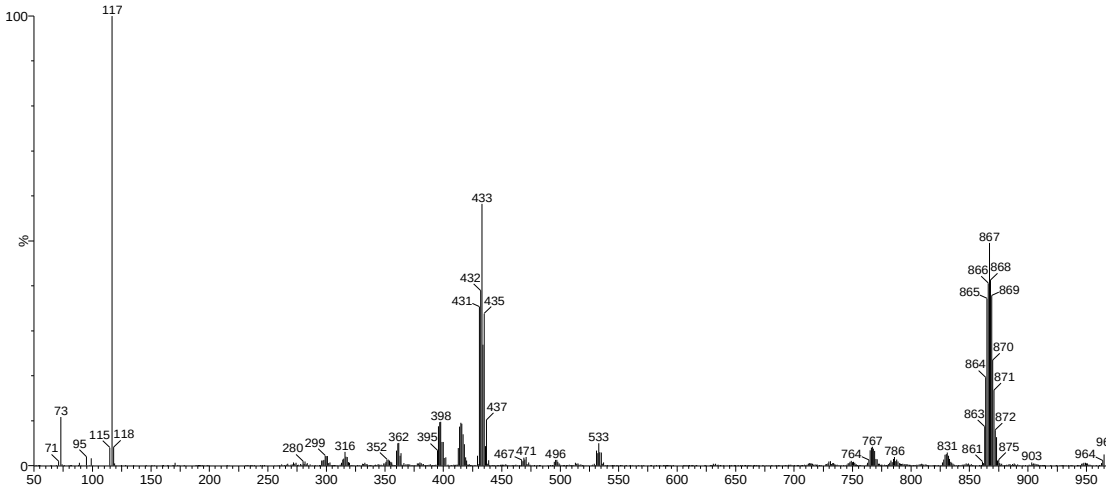

Bioconjugate Chemistry

Article

pubs.acs.org/bc

Glutathionylation Induced Structural Changes in Oxy Human Hemoglobin Analyzed by Backbone Amide Hydrogen/Deuterium Exchange and MALDI-Mass Spectrometry

Gopa Mitra,[#] Monita Muralidharan,[#] Sreekala Narayanan, Jennifer Pinto, Krishnamachari Srinivasan, and Amit Kumar Mandal*

Clinical Proteomics Unit, Division of Molecular Medicine, St. John's Research Institute, St. John's National Academy of Health Sciences, 100 ft Road, Koramangala, Bangalore -560034, India

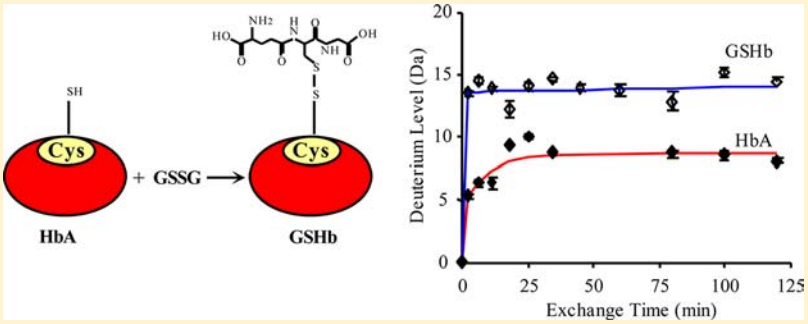

ABSTRACT: Glutathionyl hemoglobin, a post-translationally modified form of hemoglobin, has been reported to serve as a marker of oxidative stress in several clinical conditions. This modification causes perturbations in the hemoglobin functionality by increasing oxygen affinity and reducing cooperativity. Moreover, glutathionylation of sickle hemoglobin was reported to lead to a significant reduction in the propensity of sickling of erythrocytes. The root cause of the above functional abnormality is not known in detail, as the crystal structure of the molecule is yet to be discovered. In this study, we investigated the effects of glutathionylation on quaternary structure of hemoglobin using hydrogen/deuterium exchange (H/DX) based mass spectrometry. H/DX kinetics of nine peptides from α and β globin chains of hemoglobin were analyzed to understand the conformational change in deoxy to oxy transition of normal hemoglobin and structural perturbations associated with glutathionylation of oxy hemoglobin. Significant structural changes brought about by the glutathionylation of oxy hemoglobin were observed in the following regions of globin chains: β86−102, β1−14, α34−46, β32−41, β130−146, β115−129, β73−81. Isotope exchange kinetics monitored through mass spectrometry is a useful technique to understand structural perturbation on post-translational modification of proteins in solution phase.

INTRODUCTION

The redox status of erythrocytes is defined by the ratio of reduced (GSH) to oxidized (GSSG) glutathione (γ-L-glutamyl-L-cysteinyl-glycine), which is the most abundant thiol present as antioxidant in erythrocyte. In the event of cellular defense against reactive oxygen species (ROS), the GSH/GSSG ratio decreases and free thiols of cytosolic proteins are maintained in its reduced form. As a result of oxidative insult, the accumulation of GSSG within the cell may lead to post-translational modification of proteins such as S-glutathionylation via thiol/disulfide exchange mechanism.[1] Several studies have reported glutathionyl hemoglobin (GSHb) as a possible biomarker of oxidative stress in various medical conditions such as hyperlipidemia,[2] diabetes mellitus,[2] Friedreich's ataxia,[3] atherosclerosis,[4] and chronic renal failure.[5] Oxidative stress level can be better assessed from the analysis of glutathionylated proteins (GSSPs) compared to the measurement of GSH and/or GSSG, as GSSPs are more stable than GSSG and less susceptible to enzymatic reduction by glutathione reductase.[6,7]

Hemoglobin (HbA) is a widely studied allosteric protein consisting of α and β globin chains in duplicate. Oxidative imbalance in erythrocytes causes glutathionylation of hemoglobin at βCys93 residue, which is the most accessible free thiol on the molecular surface.[5] The above nonenzymatic post-translational modification of hemoglobin was elevated on incubation of erythrocytes with *tert*-butylhydroperoxide.[8] Compared to HbA, GSHb was found to have 6-fold tighter oxygen binding capacity.[9] The Hill coefficient at half saturation (n_{50}) is 1.5 for GSHb compared to 2.9 in HbA.[9] The function of hemoglobin is mainly driven by the conformational transition between its deoxy and oxy forms. Therefore, it is likely that the reported functional abnormality in GSHb was induced by the structural perturbation associated with glutathionylation of hemoglobin in its deoxy and/or oxy states.

Received: May 30, 2012
Revised: September 25, 2012
Published: November 16, 2012

ACS Publications © 2012 American Chemical Society

dx.doi.org/10.1021/bc300291u | *Bioconjugate Chem.* 2012, 23, 2344−2353

Using NMR spectroscopy, it was shown that the tertiary structural changes in the oxy state of GSHb resulted in the movement of βVal67 residue toward the heme center and movement of helix F and FG corner in the β chain away from the heme center. The salt bridge between βAsp94 and βHis146 is destabilized.[9] Quaternary structural changes included destabilization of the hydrogen bond between βAsp99-αTyr42, βHis146-αLys40, and βHis97-αPro44 at the αβ interface.[9] However, the crystal structure of the oxy state of GSHb has not been discovered to date.

In our previous communication, we described the structural changes linked to glutathionylation of the deoxy state of HbA.[10] In this study, we report glutathionylation-associated structural perturbation in the oxy state of HbA using hydrogen/deuterium exchange (H/DX) based mass spectrometry.

EXPERIMENTAL PROCEDURES

Materials. Pepsin crystalline, deuterium oxide (99.9%), 2,2′-dithiodipyridine (2-PDS), Sephadex G-50, reduced glutathione (GSH), and sinapinic acid were purchased from Sigma (St. Louis, MO). Synthesis-grade trifluoroacetic acid (TFA) was obtained from Merck, Germany. Poly(ethylene glycol) (PEG) mix, the external calibrant for mass spectrometer, was purchased from Waters, Milford, MA. α-Cyano-4-hydroxycinnamic acid, MALDI matrix, was obtained from Fluka, Germany. All other chemicals used were of analytical grade.

Isolation and Chemical Modification of Hemoglobin. Blood was collected from healthy volunteers with their prior consent. Isolation of hemoglobin was done from whole blood according to the procedure described previously.[10] Glutathionyl hemoglobin was synthesized in vitro following protocol described earlier.[10] GSHb with the abundance of more than 85% was used for structural characterization.

Preparation of Oxyhemoglobin. Hemoglobin was maintained at 300 μM in 50 mM ammonium bicarbonate buffer (pH 7.4). Pure oxygen gas was continuously bubbled through the solution at a rate of 40 mL/min for an hour to make it completely saturated with oxygen. The solution was then diluted 15-fold with buffered D_2O to start the isotope exchange kinetics with oxygen being continuously bubbled throughout the exchange experiment. The resulting solution was used for isotope exchange kinetics experiments. A similar procedure was followed for oxygenation of glutathionyl hemoglobin.

Hydrogen−Deuterium Exchange Experiment. Hydrogen/deuterium exchange experiments were done according to the protocol described previously.[10] In brief, the exchange reaction was initiated in hemoglobin by the addition of 15-fold excess of 50 mM ammonium bicarbonate/D_2O buffer (pD 7.4) at 25 °C. At different time intervals, 10 μL of reaction mixture was added to 90 μL of ice-cold aqueous 0.1% TFA (pH 2.5) solution to stop the H/DX kinetics and 2 μL of aqueous pepsin solution was added immediately to the aforementioned acidified protein solution maintaining enzyme/substrate ratio 1:10 mol/mol, and digestion was continued for 5 min at 0 °C. 1 μL of digested sample was mixed with 1 μL of matrix solution (5 mg/mL) and 0.5 μL of the above mixture was spotted on the MALDI plate. The spot was dried rapidly using moderate vacuum in a desiccator and spectra were acquired immediately. Both 100% and 0% control experiments were done as reported previously.[10] The issue of back-exchange of backbone amide hydrogens has been taken care of by quenching the H/DX reaction at 0 °C and pH 2.5, as discussed in our previous communication.[10]

Mass Spectrometry. All MS analyses were performed on a Waters Synapt HDMS mass spectrometer equipped with a MALDI source in the positive ion V mode, using 200 Hz solid state laser (λ = 355 nm). The mass spectrometer was calibrated using an external calibrant, PEG mix.

Data Analysis. The experimental mass spectra were baseline-corrected and the isotope averaged centroid mass of each molecular ion (M_t) at a given time t was measured using the software *HX Express* version Beta (http://www.hxms.com/HXExpress). The number of deuterium incorporated into a peptide $D(t)$ was calculated[11]

$$D(t) = \frac{(M_t - M_0)}{(M_\infty - M_0)} \times N \quad (1)$$

where M_0 and M_∞ are the observed masses at zero time control experiment and for a fully deuterated molecule, respectively,[10] and N is the total number of backbone amide hydrogens in the peptide.

The peptide backbone amide hydrogens can be categorized into fast (A), intermediate (B), and slow exchanging (C) groups and $D(t)$ can be represented as follows:[12]

$$D = N - Ae^{-k_1 t} - Be^{-k_2 t} - Ce^{-k_3 t} \quad (2)$$

where k_1, k_2, and k_3 are the average rate constants for fast, intermediate, and slow exchanging amide hydrogens, respectively. The exchange rate constants and the population of amide hydrogens in different groups were varied to minimize the sum of squared residuals (SSR). The SSR for each data set was calculated using the following equation:

$$\mathrm{SSR} = \sum_i [(y_{i\,\mathrm{obs}} - y_{i\,\mathrm{calc}})/y_{i\,\mathrm{obs}}]^2 \quad (3)$$

$y_{i\,\mathrm{obs}}$ and $y_{i\,\mathrm{calc}}$ were calculated from eq 1 and eq 2, respectively.[13]

RESULTS AND DISCUSSION

Glutathionylation, an oxidative stress induced post-translational modification of hemoglobin in erythrocytes, is an important event at the molecular as well as at the cellular level. It leads to modification in molecular functionality of hemoglobin through a change in the oxygen binding equilibrium.[9] At the cellular level, glutathionylation of sickle hemoglobin leads to a significant reduction in the propensity of sickling of erythrocytes.[14] The functional abnormality is most likely a result of glutathione-induced perturbation in the tertiary and quaternary structure of hemoglobin. To explore the probable perturbation in hemoglobin structure, particularly in its oxy state, we have used hydrogen/deuterium exchange based mass spectrometry (H/DX-MS). H/DX-MS has emerged as a powerful technique to investigate solution-phase conformational dynamics of proteins. Depending on the local environment, inductive and charge effect of the neighboring groups, different polar hydrogen exchanges with deuterium from the surrounding solvents at different rates. Except for peptide amide backbone hydrogens, which exchange on a convenient and measurable time scale, all other solvent-accessible polar hydrogens in protein molecule exchange very rapidly. Mass spectrometric analysis of proteolytic peptides obtained from deuterated protein provides information that eventually helps in understanding the conformational dynamics of the region of

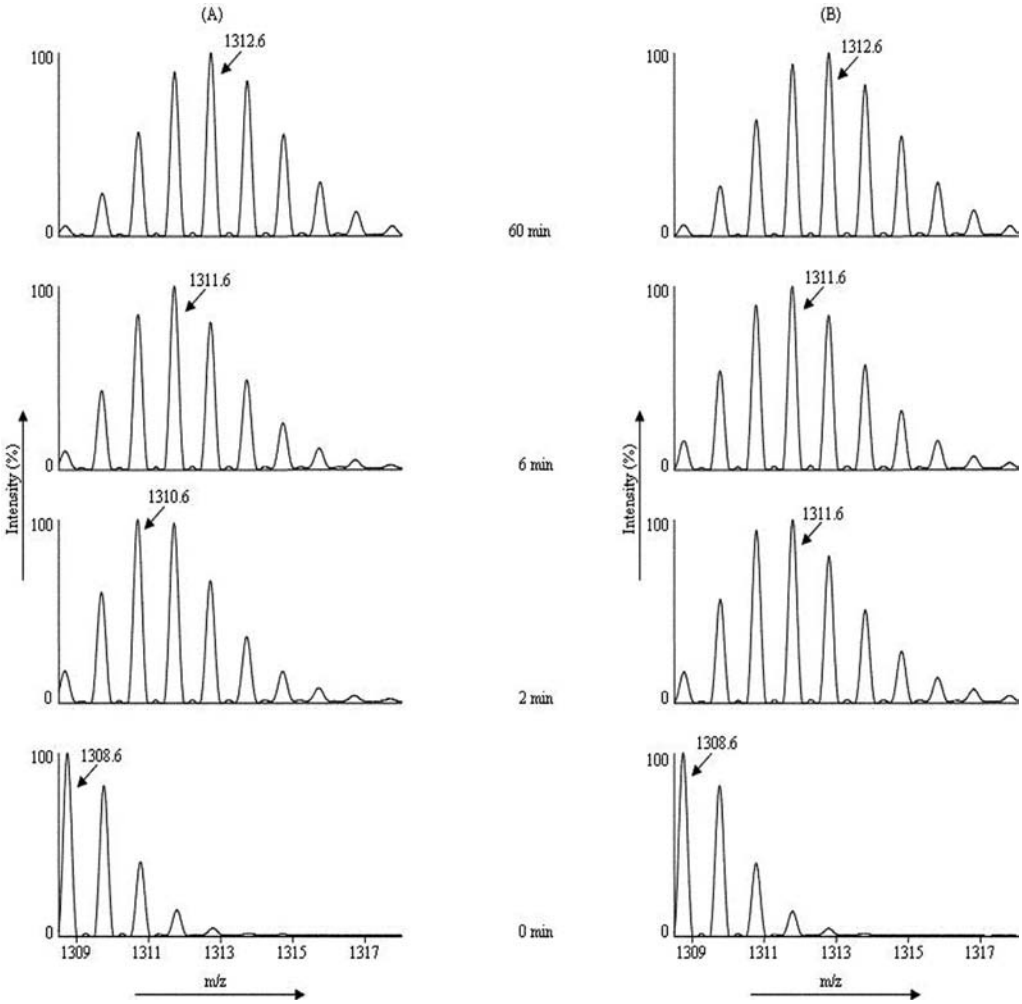

Figure 1. MALDI mass spectra for the peptide with m/z 1308.6 obtained on hydrogen/deuterium exchange kinetics. Panels A and B represent the isotope exchange kinetics for the peptide fragment in HbA and GSHb, respectively.

origin of experimental peptide in the intact protein molecule. The novelty of the H/DX-MS approach is linked to its high precision in measurement, requirement of picomoles of protein, and short time duration for the analysis of the entire molecule.

In the hemoglobin molecule, the cysteine residue in the α globin subunit is completely inaccessible. Between the two cysteine residues in the β globin subunit of HbA, βCys93 is the preferred site for glutathione binding.[5] All H/DX-MS experiments were carried out using glutathionyl hemoglobin synthesized in vitro where the molecular abundance was greater than 85%. Figure 1 represents deuterium exchange kinetics of peptic peptide with m/z 1308.6 obtained from both HbA and GSHb molecules in their oxy state. On replacement of one hydrogen atom by deuterium, the mass increases by one unit, and as more hydrogens are replaced by deuterium with time, the envelope corresponding to the peptide molecular ion shows mass shift progressively toward higher mass. While panel A represents the envelope for the peptide in HbA, panel B represents the same in GSHb.

The peptide backbone amide hydrogens were assigned into three groups, fast (A), intermediate (B), and slow (C) exchanging in each individual peptide fragment, and the corresponding average rate constants for exchange kinetics were k_1, k_2, and k_3, respectively. The number of differentially grouped peptide amide hydrogens and rate constants for all nine peptic peptides are listed in Table 1. The parameters have been provided for both oxy HbA and oxy GSHb as well as for the previously reported deoxy HbA.

The analysis of tandem mass spectra followed by sequence assignment confirmed that the peptic peptide of HbA with m/z 1921.9 was a β globin fragment consisting of residues 86−102 (ATLSELHCDKLHVDPEN). The same fragment in GSHb digest appeared at 2226.1 m/z, showing a shift in mass consistent with the presence of glutathione moiety attached to βCys93 through disulfide linkage. The number of exchangeable peptide amide hydrogens was 15 and 17 for fragments 1921.9 m/z and 2226.1 m/z, respectively. Glutathione moiety contributed two additional amide hydrogens in 2226.1 m/z. Figure 2A represents the best fit curve obtained from deuterium incorporation kinetics data for peptide 1921.9 m/z in the oxy state of HbA (HbA_{oxy}) (trace 1) and 2226.1 m/z in glutathionyl HbA_{oxy} ($GSHb_{oxy}$) (trace 2) fitted to eq 3. A close review of our data obtained in the present study for HbA_{oxy} and that reported previously for deoxy HbA (HbA_{deoxy}) showed that, upon transition from deoxy to oxy state of normal hemoglobin, the rate constants increased significantly for the fast and intermediate exchanging group of amide hydrogens (Table 1). The population of the fast exchanging amide hydrogen increased from 8.20% to 29.73%, which was compensated by a decrease in the population of the intermediate and the slow

dx.doi.org/10.1021/bc300291u | *Bioconjugate Chem.* 2012, 23, 2344−2353

Table 1. Kinetic Parameters for Isotope Exchange of Different Peptic Peptides[a]

peptide mass (m/z)	residues	molecule	N	k_1(min^{-1})	k_2(min^{-1})	k_3(min^{-1})	A (%)	B (%)	C (%)
1921.9[b]	β86−102 ATLSELHCDKLHVDPEN	HbA_{deoxy}	15	1.5419	0.0893	1.60×10^{-05}	8.20	41.93	49.87
		HbA_{oxy}	15	7.8536	0.1000	1.25×10^{-05}	29.73	28.80	41.47
		$GSHb_{oxy}$	17	2.7340	1.6988	1.18×10^{-03}	69.94	10.24	19.82
1868.9	β130−146 YQKVVAGVANALAHKYH	HbA_{deoxy}	16	0.0427	0.0018	2.00×10^{-03}	55.31	34.00	10.75
		HbA_{oxy}	16	0.0220	0.0058	6.27×10^{-04}	43.75	43.75	12.50
		$GSHb_{oxy}$	16	0.1491	0.0088	3.89×10^{-03}	48.31	13.75	37.94
1494.8	β1−14 VHLTPEEKSAVTAL	HbA_{deoxy}	12	0.6677	0.0552	1.00×10^{-04}	48.83	35.33	15.92
		HbA_{oxy}	12	6.8633	0.1526	3.20×10^{-04}	48.37	37.97	13.66
		$GSHb_{oxy}$	12	1.4629	1.4220	3.75×10^{-03}	84.42	8.42	7.17
1585.8	α34−46 LSFPTTKTYFPHF	HbA_{deoxy}	10	0.1553	0.0456	2.00×10^{-05}	11.10	28.70	60.20
		HbA_{oxy}	10	7.9650	0.0933	2.38×10^{-04}	1.40	40.03	58.58
		$GSHb_{oxy}$	10	4.9998	0.1581	5.99×10^{-07}	19.54	10.36	70.10
1308.6	β32−41 LVVYPWTQRF	HbA_{deoxy}	8	0.0240	0.0080	1.40×10^{-05}	37.38	25.13	37.50
		HbA_{oxy}	8	0.0802	0.0045	2.27×10^{-03}	39.07	28.97	31.96
		$GSHb_{oxy}$	8	1.0647	0.0527	3.30×10^{-03}	26.25	24.75	49.00
1635.8	β115−129 AHHFGKEFTPPVQAA	HbA_{deoxy}	12	0.0199	0.0013	4.15×10^{-06}	35.42	11.92	52.67
		HbA_{oxy}	12	0.0924	0.0002	6.58×10^{-05}	28.79	25.77	45.44
		$GSHb_{oxy}$	12	0.9887	0.3933	4.05×10^{-04}	31.71	26.46	41.83
2910.4	α1−29 VLSPADKTNVKAAW GKVGAHAGEYGAEAL	HbA_{deoxy}	27	1.3112	0.0495	1.90×10^{-03}	34.96	53.81	11.19
		HbA_{oxy}	27	9.3418	0.1239	2.74×10^{-03}	49.68	41.19	9.13
		$GSHb_{oxy}$	27	2.8777	0.7210	5.28×10^{-02}	58.00	23.89	18.11
1798.9	β15−31 WGKVNVDEVGGEALGRL	HbA_{deoxy}	16	0.7153	0.0723	1.00×10^{-04}	24.80	39.40	35.80
		HbA_{oxy}	16	7.6332	0.1191	3.66×10^{-03}	30.80	28.30	40.90
		$GSHb_{oxy}$	16	1.6751	0.0111	4.97×10^{-03}	68.50	6.50	25.00
967.5	β73−81 DGLAHLDNL	HbA_{deoxy}	8	0.2964	0.0011	2.00×10^{-04}	32.00	15.25	52.75
		HbA_{oxy}	8	7.6826	0.0378	3.88×10^{-04}	4.80	32.30	62.90
		$GSHb_{oxy}$	8	7.9639	0.0169	5.67×10^{-04}	18.75	47.25	34.00

[a]Total numbers of exchangeable amide hydrogens for each peptide are given by N, while A, B, and C represent the number of fast, intermediate, and slow exchangeable hydrogens, respectively. The corresponding rate constants are given by k_1, k_2, and k_3, respectively. [b]For the peptide 1921.9, after glutathionylation, the number of exchangeable hydrogens is 17, taking into account two hydrogens from glutathione moiety.

exchanging hydrogens (Table 1). This suggests that the peptide 1921.9 became more solvent-exposed upon oxygenation. Perutz MF reported that the salt bridge between the carboxyl group of βAsp94 and the imidazole group of βHis146 in HbA_{deoxy} is broken on oxygenation.[15] This in turn might have resulted in loosening of the region, leading to more solvent exposure and hence an increase in the isotope exchange rate. In the deoxy state, the side chain of βTyr145 is hydrogen-bonded to the carboxyl group of βVal98, while in the liganded state, the bond is present only for a short period.[16] Oxygen binding results in a decrease in the distance between proximal histidine (βHis92) and porphyrin ring, which triggers a series of changes in the tertiary structure in the molecule. The side chains of βLeu88, βLeu91, and βHis92 undergo slight conformational changes to stay in contact with the heme unit.[16] Upon oxygenation, βCys93 shifts its orientation from solvent-exposed state to the pocket between helix F and H.[16] αβ inter-subunit interactions play an important role in the cooperativity of hemoglobin, and significant structural change takes place during deoxy to oxy transition in this region of the molecule.[17] The residue βAsp99 forms inter-subunit hydrogen bonds with αTyr42 in the αβ interface, which stabilizes the deoxy state (T).[18] The residue βAsn102 stabilizes the oxy state (R) by forming a hydrogen bond with αAsp94.[19] Shih et al. reported that, on deoxy to oxy transition, the polarity of the βGlu101 residue, which is positioned between βAsp99 and βAsn102, influences the switchover of the two neighboring interchain hydrogen bonds on its either side. This switchover in hydrogen bond plays an important role in the allosterism of hemoglobin.[20] Therefore, the movement of the aforementioned residues on transition from deoxy to oxy state might have increased the solvent accessibility of the peptide 1921.9, thus resulting in an increase in the isotope exchange rates. The fitted parameters for H/DX kinetics of the peptide 2226.1 m/z showed that, upon glutathionylation of HbA_{oxy}, there was an increase in the fast exchanging hydrogen population from 29.73% to 69.94% (Table 1). This increase in the fast exchanging population was compensated by a decrease in the intermediate and slow exchanging amide hydrogens. In $GSHb_{oxy}$, the rate constants for the fast exchanging hydrogens decreased by 3-fold while that of the intermediate and slow exchanging hydrogens increased by 17-fold and 99-fold, respectively (Table 1). Hence, on glutathionylation, there is an overall increase in the conformational flexibility in this part of the molecule. On the basis of NMR data, Craescu et al. showed that the characteristic intra-subunit salt bridge βAsp94-βHis146 and inter-subunit hydrogen bond at the αβ interface, βAsp99-αTyr42 in HbA_{deoxy}, were perturbed significantly on glutathionylation.[9] It was reported that, in Hb Creteil, a hemoglobin variant with high oxygen affinity, βCys93 is located in the pocket between the FG corner and F and H helices.[21] By comparing the NMR spectra of Hb Creteil and $GSHb_{oxy}$, Craescu et al. reported that, for both the molecules, the conformational perturbation of the β globin chain near the oxy heme pocket was similar.[9] According to the experimental data and our previously reported H/DX kinetics data of $GSHb_{deoxy}$, we observed that the increases in the fast

dx.doi.org/10.1021/bc300291u | Bioconjugate Chem. 2012, 23, 2344−2353

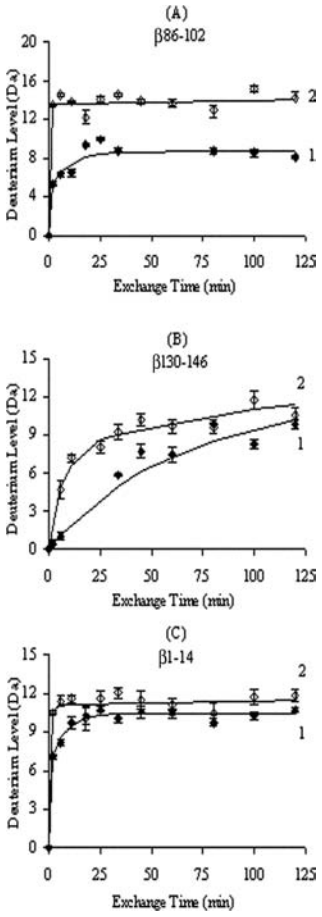

Figure 2. Representation of hydrogen/deuterium exchange kinetics of peptic peptides. The *Y*-axis is labeled with number of deuterium incorporated and *X*-axis with the corresponding exchange time. Trace 1 in each panel (filled diamond) represents the best fit curve of the exchange kinetics for the corresponding peptide obtained from native hemoglobin, and trace 2 in each panel (hollow diamond) represents the same for the peptide obtained from glutathionyl hemoglobin. Panel A represents peptide fragment 1921.9 m/z (β86−102). Panel B represents peptide fragment 1868.9 m/z (β130−146). Panel C represents peptide fragment 1494.8 m/z (β1−14).

exchanging population on $GSHb_{deoxy}$ to $GSHb_{oxy}$ transition and on Hb_{deoxy} to Hb_{oxy} transition were 22.88% and 21.53%, respectively.[10] The oxygenation of deoxy glutathionyl hemoglobin resulted in an increase in the fast exchange rate by 1.35-fold, while oxygenation of deoxy normal hemoglobin led to an increase in the same by 5.1-fold.[10] Therefore, in the case of fast exchange kinetics in the above two transitions, the population increase was very similar but the increase in the rate was much larger for normal hemoglobin compared to glutathionyl hemoglobin. Thus, covalent binding of glutathione might introduce conformational constraints in the molecule causing βCys93 to adopt oxy-like conformation, which might be the probable cause of the higher oxygen affinity of glutathionyl hemoglobin.

Sequence assignment of the peptide fragment with m/z 1868.9 confirmed that it is the C-terminal β chain fragment spanning residues 130−146 (YQKVVAGVANALAHKYH) with 16 exchangeable amide hydrogens. Figure 2B represents the best fit curve of H/DX kinetics data of the peptide 1868.9 for both HbA_{oxy} (trace 1) and $GSHb_{oxy}$ (trace 2) molecules. The fitted parameters of HbA_{oxy} and $GSHb_{oxy}$ molecules along with the previously reported data for HbA_{deoxy} are shown in Table 1. The kinetics data showed that, on oxygenation of HbA_{deoxy}, the rate constant and the population of fast-exchanging hydrogens decreased by 1.94-fold and 11.56%, respectively. For intermediate exchanging hydrogens, the rate constant increased by 3.22-fold with an increase in population by 9.75%. The change in population and rate constants for all three groups of hydrogens indicated that oxygenation of hemoglobin might result in a decrease in the solvent exposure and rigidity in the conformation of this region of molecule. It was reported that a new set of salt bridges involving βAsn139-βArg104, βLys132-βGlu7, and a hydrogen bond involving βHis146-βLys144 are formed in the oxy state of hemoglobin.[22] The penultimate Tyr145 and C-terminal His146 of β globin chain are part of this peptide. In HbA_{deoxy}, the C-terminal residue is anchored by two salt bridges. The α-carboxyl group of βHis146 is linked to ε-amino group of αLys40 and its imidazole to βAsp94.[15] Tyr145 residue is also firmly anchored inside the pocket between helices F and H through van der Waals force and by hydrogen bonds between its hydroxyl group and carbonyl group of Val98.[15] On oxygen binding to hemoglobin, the helix F moves toward the center of the molecule, narrowing the pocket occupied by Tyr145 and ultimately expelling it. The expelled Tyr145 pulls His146 along with it and breaks its salt bridges.[15] Perutz had proposed a central role for the salt bridge involving C-terminal residues of hemoglobin in its cooperativity.[15] Disruption in these contacts causes the shift of R-T equilibrium toward the R state, thus resulting in an increased oxygen affinity and loss of allosteric function. βHis146 was reported to contribute 40% to the alkaline Bohr effect of hemoglobin.[23] Louie et al. reported that several allosterically sensitive hydrogens which are present at the β C-terminus account for about 70% of allosterically significant structural changes.[24] Therefore, a change in the aforementioned interactions might have imparted rigidity to the oxy conformer resulting in solvent shielding. The fitted parameters of H/DX kinetics showed that, on glutathionylation of HbA_{oxy}, there was more than a 6-fold increase in the rates for both the fast and the slow exchanging hydrogens with 1.5-fold increase in the rate for the intermediate one. The fast and slow exchanging population increased by 4.56% and 25.44%, respectively, whereas the intermediate group decreased by 30%. The observed data indicated that glutathionylation of HbA_{oxy} led to an increase in flexibility in the conformation for this peptide. Compared to our earlier report of a dramatic increase in the population of the fast exchanging amide hydrogens on glutathionylation of deoxy hemoglobin, the magnitude of the increase in the fast exchanging population on glutathionylation of oxy hemoglobin was modest. On the basis of NMR data, Craescu et al. showed that the salt bridge between βHis146 and βAsp94 was absent in $GSHb_{deoxy}$. The displacement of βHis146 on glutathionylation might lead to breakage of βHis146-αLys40 salt bridge.[9] A significant increase in the fast exchange kinetics in $GSHb_{deoxy}$ was indicative of removal of the above-mentioned structural constraints. The existence of additional salt bridges and hydrogen bonds specific to oxy state might be the reason for relatively lower flexibility in the conformation of $GSHb_{oxy}$ compared to $GSHb_{deoxy}$.

The peptic peptide with m/z 1494.8 is an N-terminal fragment of the β globin chain (β1−14) (VHLTPEEKSAVTAL) consisting of 12 exchangeable amide hydrogens. Figure 2C illustrates the best fit curve of H/DX kinetics for both HbA_{oxy} (trace 1) and $GSHb_{oxy}$ (trace 2) molecules. Oxygen-

ation of HbA_{deoxy} resulted in an increase in rates by 10.28-fold, 2.76-fold, and 3.20-fold for the fast, intermediate, and slow exchanging amide hydrogens, respectively (Table 1). The population of all exchange groups remained almost unaltered. Hence, oxygenation might increase the solvent accessibility of this peptide. The residues βVal1 and βHis2 contribute amino groups to the binding site of 2,3-diphosphoglycerate (DPG) and is defined as an allosteric effector of hemoglobin.[25] DPG binds between two β chains. Its presence reduces oxygen affinity, which ultimately facilitates unloading of oxygen in tissues.[26,27] Hence, DPG stabilizes the deoxy state of hemoglobin. In the oxy state of hemoglobin, the salt bridges between DPG and β subunits are ruptured resulting in the liberation of DPG.[15] Therefore, on deoxy to oxy transition, the solvent accessibility of this region in β globin chain of HbA_{oxy} might increase, as observed in our experiment. On glutathionylation of HbA_{oxy}, the population of the fast exchanging hydrogens increased by 36.05%, whereas the intermediate and the slow exchanging hydrogens decreased by 29.55% and 6.49%, respectively (Table 1). On glutathionylation, the rate constants for the intermediate and slow exchanging hydrogens increased by 9.32- and 11.72-fold, respectively, whereas that of fast exchanging hydrogens decreased by 4.2-fold. Therefore, glutathionylation of HbA_{oxy} might cause an overall increase in the conformational flexibility of the residues in peptide 1494.8 with a shift in the population of amide hydrogens from intermediate to fast exchanging groups resulting in a decrease in the average rate of the latter. Glutathionylation had been reported to increase the oxygen affinity of hemoglobin by 6-fold.[9] A comparison of kinetic data of GSHb in its deoxy and oxy states clearly depicts that there is a higher degree of conformational freedom in the oxy state of the molecule. Similar comparison between deoxy and oxy states of HbA showed that all rate constants increased for the oxy state, but the number of exchangeable amide hydrogens remained unaltered. In the case of GSHb, the number of fast exchanging hydrogens increased significantly upon oxygenation. Hence, oxygenation of $GSHb_{deoxy}$ was accompanied by a relatively larger increase in conformational freedom in the region of peptide 1494.8 compared to that in the HbA_{deoxy} molecule. Therefore, the $GSHb_{deoxy}$ to $GSHb_{oxy}$ transition is entropically more favored compared to HbA_{deoxy} to HbA_{oxy} transition. This might be the probable reason behind the higher degree of oxygen affinity of GSHb.

The tandem mass spectra for the proteolytic fragment ion 1585.8 m/z showed that it is a part of the α globin chain of hemoglobin consisting of residues 34 to 46 (LSFPTTKTYFPHF) with ten exchangeable backbone amide hydrogens. Figure 3A shows the fitted curve of H/DX kinetics data of the peptide 1585.8 in HbA_{oxy} (trace 1) and $GSHb_{oxy}$ (trace 2) molecules. Upon oxygenation of HbA_{deoxy}, the population for the fast exchanging hydrogens decreased from 11.10% to 1.40% and that of the intermediate exchanging hydrogens increased from 28.70% to 40.03% with a very small decrease in the population for slowest exchanging hydrogens (Table 1). The above change in population is indicative of a reduction in the conformational flexibility of the residues in this region of the molecule on HbA_{deoxy} to HbA_{oxy} transition. As the reported rate constants represent an average of all amide hydrogen exchange rates in a particular group, a shift in the population from fast to intermediate exchanging groups might have resulted in an effective increase in the average value of corresponding rate constants in both groups. The constituent

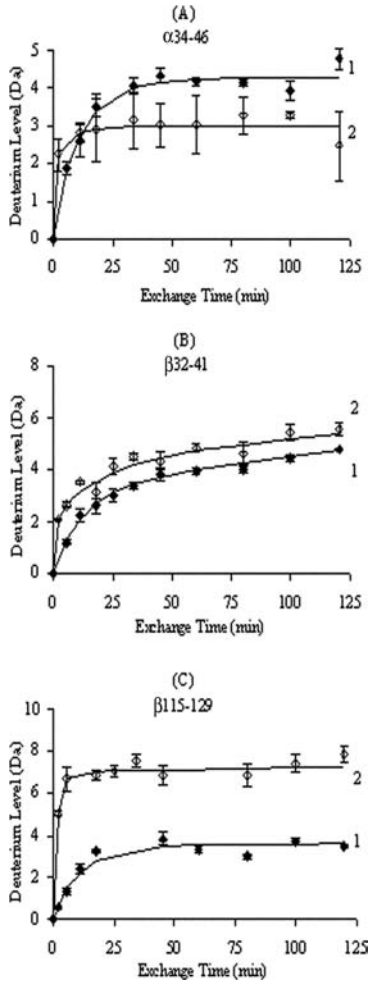

Figure 3. Representation of hydrogen/deuterium exchange kinetics of peptic peptides. The *Y*-axis is labeled with the number of deuterium incorporated and *X*-axis with the corresponding exchange time. Trace 1 in each panel (filled diamond) represents the best fit curve of the exchange kinetics for the corresponding peptide obtained from native hemoglobin and trace 2 in each panel (hollow diamond) represents the same for the peptide obtained from glutathionyl hemoglobin. Panel A represents peptide fragment 1585.8 m/z (α34−46). Panel B represents peptide fragment 1308.6 m/z (β32−41). Panel C represents peptide fragment 1635.8 m/z (β115−129).

residues of peptide 1585.8 belong to the αβ interface of the tetramer, a portion where inter-subunit interactions play an important role in the deoxy to oxy transition of the hemoglobin molecule. According to Hashimoto et al., αThr38 was found to undergo considerable displacement on deoxy to oxy (T to R) transition and reported to be an important residue in the oxygen binding of hemoglobin.[28] In the deoxy state of hemoglobin, βHis97 is positioned between residues αThr41 and αPro44. T to R transition results in the migration of the βHis97 residue between αThr38 and αThr41 and the formation of a hydrogen bond with αThr38.[16,29] Perutz MF reported that there is an increase in the number of van der Waals interactions on the T to R transition at the αβ interface of tetramer.[15] Hence, the observed decrease in the conformational flexibility associated with oxygenation of hemoglobin might be due to the appearance of the aforementioned noncovalent interactions at the αβ interface, which are important for the cooperativity of hemoglobin. Comparison of $GSHb_{oxy}$ and HbA_{oxy} data shows that, on glutathionylation of

dx.doi.org/10.1021/bc300291u | Bioconjugate Chem. 2012, 23, 2344−2353

HbA_{oxy}, the rate constant for the fast exchange step decreased by 1.6-fold whereas that of the intermediate exchange step increased by 1.7-fold with a large decrease in the rate for the slow exchange step. The fast and slow exchanging hydrogen populations increased by 18.14% and 11.52%, respectively. The above increase in population was compensated by a decrease in the same for intermediate exchanging hydrogens. The observed change in kinetic parameters indicated that the conformational flexibility in $GSHb_{oxy}$ was comparatively higher than that of HbA_{oxy}. Previously, we reported that glutathionylation of HbA_{deoxy} resulted in an increase in the fast exchanging population by 31.6% with a decrease in population for the intermediate and slow exchanging hydrogens.[10] The slow and the intermediate H/DX exchange rates increased and decreased, respectively, while the fast exchanging rate remained unaltered.[10] On the basis of NMR data, Craescu et al. showed that three inter-subunit ($\alpha\beta$) interactions were perturbed on glutathionylation of deoxy hemoglobin, *viz.*, αLys40-βHis146, αTyr42-βAsp99, and αPro44-βHis97.[9] Garel et al. reported a change in the conformation of four α globin residues, αLys40, αThr41, αTyr42, and αPro44, on glutathione binding to βCys93 of HbA_{deoxy}.[14] Comparing the kinetic parameters obtained in present study and previously reported data, we observed that the conformational perturbation associated with glutathionylation was relatively higher in $GSHb_{deoxy}$ than in $GSHb_{oxy}$.[10] As inter-subunit interactions are crucial for cooperativity of hemoglobin, the decrease in conformational rigidity caused by the disappearance of a number of noncovalent interactions might have contributed significantly to the reduction in the cooperativity of glutathionyl hemoglobin.

Sequence analysis of peptic fragments showed that peptide with m/z 1308.6 originated from the β globin subunit of hemoglobin. The fragment 1308.6 consists of eight exchangeable peptide amide hydrogens spanning residues β32 to β41 (LVVYPWTQRF). Figure 3B represents the best fit curve of H/DX data for the fragment in HbA_{oxy} (trace 1) and $GSHb_{oxy}$ (trace 2). Oxygenation of HbA_{deoxy} resulted in an increase in the rate constants for the fast and slow exchange steps and a decrease in the rate for intermediate exchange step. The changes in population of exchangeable amide hydrogens across all the groups were small. Thus, differentially populated hydrogens rearranged among the groups (Table 1). In HbA_{deoxy}, βTrp37 remained buried in the hinge region of the $\alpha\beta$ interface.[30] A hydrogen bond is formed between the indole NH group of βTrp37 and the carboxylate side chain of αAsp94.[30] Ligand binding induces expulsion of the C-terminus αTyr140 resulting in disruption of the quaternary structural constraints associated with βTrp37.[31] Hemoglobin with the following mutation, βW37S, resulted in an increased oxygen affinity and reduced cooperativity, thus indicating involvement of βTrp37 residue in oxygen binding.[32] In HbA_{deoxy}, the carbonyl group of βVal34 is bonded to the side chain of αArg141, whereas in HbA_{oxy}, αArg141 appears to be free.[16] It was also reported that in HbA_{oxy} βArg40 forms a hydrogen bond with αThr41.[16] Therefore, the differential behavior of the rate constants and populations in deoxy to oxy transition of hemoglobin might be due to the proximity of this region to the $\alpha\beta$ interface along with disappearance and appearance of several quaternary interactions. On glutathionylation of HbA_{oxy}, rate constants for all exchange steps increased with a decrease in the population of the fast and intermediate exchange group and an increase in the slow exchanging group. Though sufficient information regarding structural changes in this region of hemoglobin associated with glutathionylation is lacking, the observed H/DX data indicated that glutathionylation of the oxy state of hemoglobin resulted in an increase in the conformational flexibility in this region of the molecule.

The peptic peptide 1635.8 m/z was found to be a β globin chain fragment containing residues 115−129 (AHHFGKEFTPPVQAA) with 12 exchangeable peptide amide hydrogens. Traces 1 and 2 in Figure 3C represent fitted curves of H/DX kinetics data for peptide 1635.8 in HbA_{oxy} and $GSHb_{oxy}$, respectively. Comparison of the observed H/DX data for HbA_{oxy} and previously reported data for HbA_{deoxy} showed that oxygenation of hemoglobin led to an increase in the rate constants for the fast and the slow exchange steps and a decrease in the intermediate exchange step (Table 1). The population of the fast and slow exchanging protons decreased by 6.63% and 7.23%, respectively, whereas the population of the intermediate exchanging protons increased by 13.85% (Table 1). The above changes in the kinetic parameters on oxygenation of hemoglobin indicated that there was a change in the solvent exposure for the constituent residues in peptide 1635.8. Oxygen binding of hemoglobin was found to introduce a new salt bridge between βGlu121 and βLys17.[23] In another hemoglobin variant Hb Roma, mutation βA115V resulted in an increase in oxygen affinity.[33] Therefore, above constituent residues of the peptide 1635.8 are involved in the oxygen binding of hemoglobin. Hence, this region might be susceptible to an alteration in solvent exposure due to oxygenation. Glutathionylation of HbA_{oxy} showed a significant increase in the rate constants for all the exchange steps in the peptide 1635.8. A small increase in the fast and intermediate exchanging populations was balanced by the decrease in the same for the slow exchanging population. Previously, we reported that glutathionylation of HbA_{deoxy} resulted in a substantial increase in the fast and intermediate exchange rate constants with a significant increase in the respective population. There is not enough information available concerning the structural changes in this region of molecule associated with glutathionylation, but it is clear from the observed H/DX data, that glutathionylation had a more profound effect on the structural perturbation of the deoxy state than the oxy state of hemoglobin. Introduction of the new salt bridge (βGlu121-βLys17) on oxygenation might be the cause behind the relatively greater rigidity in the conformation in this region of $GSHb_{oxy}$ compared to $GSHb_{deoxy}$.

Pepsin digestion of hemoglobin generated a peptide fragment with m/z 2910.4, which corresponds to residues 1 to 29 in the α globin chain (VLSPADKTNVKAAWGKVGAHAGEYGAEAL) with 27 exchangeable amide hydrogens in it. The fitted curves of H/DX kinetics data for fragments 2910.4 in HbA_{oxy} (trace 1) and $GSHb_{oxy}$ (trace 2) molecules are shown in Figure 4A. On oxygenation of HbA_{deoxy}, there was an increase in the rate constants by 7.12-fold, 2.50-fold, and 1.44-fold for the fast, intermediate, and slow exchanging hydrogens, respectively. The fast exchanging population increased by 14.72%, which was compensated by the decrease in population for the intermediate and slow exchanging groups of hydrogens (Table 1). This indicated that on oxygenation there was an enhanced solvent exposure in this region of the molecule. It was reported that in deoxy hemoglobin, the α amino group of N-terminal αVal1 is involved in a salt bridge with the α carboxyl of arginine αArg141.[16] αVal1 contributes 20−30% in the alkaline Bohr effect and is also involved in the binding of allosteric

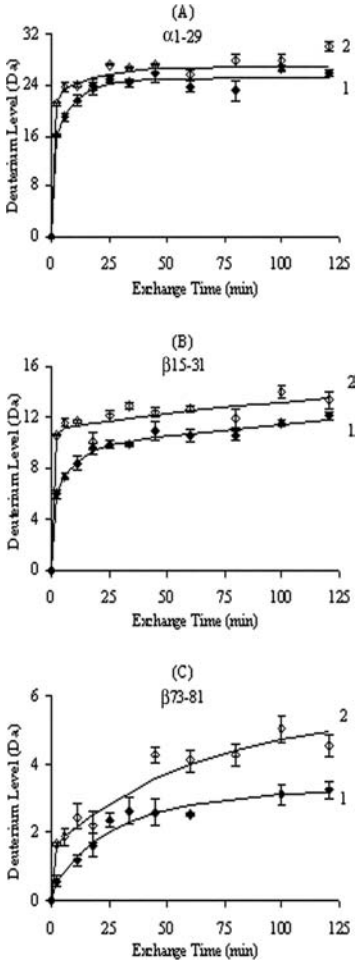

Figure 4. Representation of hydrogen/deuterium exchange kinetics of peptic peptides. The *Y*-axis is labeled with the number of deuterium incorporated and the *X*-axis with the corresponding exchange time. Trace 1 in each panel (filled diamond) represents the best fit curve of the exchange kinetics for the corresponding peptide obtained from native hemoglobin, and trace 2 in each panel (hollow diamond) represents the same for the peptide obtained from glutathionyl hemoglobin. Panel A represents peptide fragment 2910.4 *m*/*z* (*α*1−29). Panel B represents peptide fragment 1798.9 *m*/*z* (*β*15−31). Panel C represents peptide fragment 967.5 *m*/*z* (*β*73−81).

chloride.[34] *α*Asp6 interacts with other residues in the internal cavity between *α* chains and was found to contribute to the Bohr effect.[16] Disappearance of the above interactions on oxygenation might lead to an increase in the flexibility in conformation of the peptide 2910.4. Glutathionylation of HbA_{oxy} resulted in a decrease in the fast exchanging rate constants and an increase in the intermediate and slow exchanging rate constants. The fast and the slow exchanging hydrogen population increased on glutathionylation, whereas that of the intermediate one decreased (Table 1). Thus, glutathionylation caused significant conformational rearrangements among backbone amide hydrogens in this part of oxy hemoglobin.

The peptic peptide with *m*/*z* 1798.9 is a *β* globin chain fragment containing residues 15 to 31 with 16 exchangeable amide hydrogens (WGKVNVDEVGGEALGRL). Figure 4B illustrates the best fit curve of H/DX kinetics for both HbA_{oxy} (trace 1) and $GSHb_{oxy}$ (trace 2) molecules. Comparison of currently observed and previously reported H/DX kinetics data for HbA_{oxy} and HbA_{deoxy} showed that on oxygenation the rate constants for all exchange steps increased with a simultaneous increase in the number of the fast and slow exchanging population by 6% and 5.1%, respectively, and a decrease in the intermediate exchanging population by 11.1% (Table 1). The change in kinetic parameters suggested that the conformational flexibility in the region of this peptide in hemoglobin molecule increased on oxygenation. It was reported that recombinant hemoglobin with mutation *β*L28W and *β*L28F had very low oxygen affinity.[35] In the deoxy state of hemoglobin, *β*Leu28 is positioned in the B10 helix. On oxygenation of hemoglobin, proximity of the B10 helix to the ligand binding site makes it an important part of the molecule.[35] NMR data of the recombinant hemoglobin showed that the mutation affected the tertiary structure near the heme pocket, while there was no significant perturbation in the *αβ* interface.[35] On glutathionylation of the oxy state of hemoglobin, the rate constants for the fast and the intermediate exchanging step decreased. There was a small increase in the rate constant for the slow exchanging step. The increase in fast exchanging hydrogen population by 37.7% was balanced by the decrease in the same for the intermediate and slow exchanging hydrogens (Table 1). Though the changes in rate constant and in population of different groups of hydrogens were not unidirectional, but it is clear from H/DX kinetics data that, on glutathionylation,

Scheme 1

dx.doi.org/10.1021/bc300291u | *Bioconjugate Chem.* 2012, 23, 2344−2353

different groups of exchangeable hydrogen rearranged among themselves.

Sequence assignment from MS/MS spectra of the peptide fragment 967.5 m/z confirmed that it was a β globin chain fragment consisting of residues 73 to 81 (DGLAHLDNL) with eight exchangeable peptide amide hydrogens. Figure 4C illustrates the best fit curve of H/DX kinetics for both HbA_{oxy} (trace 1) and $GSHb_{oxy}$ (trace 2) molecules. On oxygenation, the fast exchanging population decreased by 27.2%, whereas the intermediate and the slow exchanging groups increased by 17.05% and 10.15%, respectively. The rate constants for the fast and intermediate exchange steps increased dramatically with a 2-fold increase for the slow exchange rate (Table 1). Therefore, on oxygenation of hemoglobin the fast exchanging amide hydrogens moved toward the intermediate group with a concomitant shift in the intermediate exchanging population to the slow exchanging group. It clearly indicated that oxygenation led to a decrease in the solvent accessibility in this region of peptide in the hemoglobin molecule. Glutathionylation of the oxy state resulted in an increase in the population of the fast and the intermediate exchanging hydrogen to a similar extent with a decrease in the population of the slow exchanging group. Rate constants for the intermediate group decreased, whereas that of the slow exchanging group increased while the fast exchange rate remained unchanged. Therefore, glutathionylation of HbA_{oxy} state induced an increase in the conformational flexibility for this peptide in hemoglobin to a small extent.

Both α and β globin subunits of hemoglobin have α-helical conformation. α chain comprises seven helices (lacks D helix), while the β chain consists of eight helices designated as A−H.[36] The amino acid sequences of those helices are marked in Scheme 1. The shaded area in the scheme denotes the nine experimental peptides where H/D exchange kinetics was monitored. The site of glutathionylation (βCys93) has been marked with an asterisk. On the basis of these nine peptides, sequence coverage for α and β were 29.7% and 67.8%, respectively.

CONCLUSION

The present study aimed to analyze the structural perturbation associated with glutathionylation of oxy hemoglobin using hydrogen/deuterium exchange based mass spectrometry. Using experimental H/DX-MS data of deoxy and oxy hemoglobin, we tried to understand the reported structure function correlation of normal hemoglobin. In the next step, we attempted to correlate the observed H/DX kinetics with structural perturbation of hemoglobin on glutathionylation and finally to its function. The isotope exchange parameters indicated that the glutathionylation of βCys93 induced conformational constraints in the region β86−102 causing glutathionyl hemoglobin to adopt oxy hemoglobin-like conformation. Analysis of H/DX kinetics of the peptide β1−14 showed that the enhanced solvent accessibility on oxygenation of hemoglobin might be due to the release of DPG, which was bonded through salt bridges prior to its release. Comparison of exchange kinetics indicated that the formation of $GSHb_{oxy}$ state is entropically more favored than the HbA_{oxy} state, which might be the probable rationale behind the higher oxygen affinity of GSHb compared to HbA. In general, glutathionylation caused an overall increase in the conformational flexibility of the molecule. The inter-subunit interactions that were reported to be crucial for the cooperativity of the molecule were perturbed. Isotope exchange kinetics showed significant conformational perturbations of the residues in the peptides α34−46 and β32−41, which are present at the $\alpha\beta$ interface of the protein and play an important role in the deoxy to oxy transition. The increased flexibility in GSHb might be caused by the disappearance of a number of noncovalent interactions at the $\alpha\beta$ interface which eventually manifests as reduced cooperativity. Significant structural perturbation was also observed in the peptides β130−146, β115−129, and β73−81. Among the peptides studied, the conformational rearrangement of residues occurred in the peptides α1−29 and β15−31.

Glutathionylation of proteins is emerging as an important post-translational modification because of its direct correlation with oxidative stress. The novelty in our approach lies in establishing the correlation between functional abnormality and structural perturbation of hemoglobin on glutathionylation using isotope exchange based mass spectrometry where the crystal structure of the molecule is not yet known. The H/DX-MS method has been found to be a simple technique to investigate structural perturbation and consequently structure function correlation of post-translationally modified proteins in solution phase. In addition, the requirement of picomoles of proteins and short time duration for the entire analysis makes the technique novel compared to other spectroscopic tools.

AUTHOR INFORMATION

Corresponding Author

*Phone: +91-80-25532037. Fax: +91-80-25501088. E-mail: amit@sjri.res.in.

Author Contributions

#The authors share equal contribution.

Notes

The authors declare no competing financial interest.

ACKNOWLEDGMENTS

We acknowledge Nano Science Mission DST, Govt. of India, for providing mass spectrometry facility in St John's Research Institute. We acknowledge all volunteers who provided sample in the study. We also acknowledge Dr. Anura V. Kurpad, Professor, St John's Research Institute, for helping us in data analysis.

REFERENCES

(1) Gilbert, H. F. (1995) Thiol/disulfide exchange equilibria and disulfide bond stability. *Methods Enzymol. 251*, 8−28.

(2) Niwa, T., Naito, C., Mawjood, A. H. M., and Imai, K. (2000) Increased glutathionyl hemoglobin in diabetes mellitus and hyperlipidemia demonstrated by liquid chromatography/electrospray ionization-mass spectrometry. *Clin. Chem. 46*, 82−88.

(3) Piemonte, F., Pastore, A., Tozzi, G., Tagliacozzi, D., Santorelli, F. M., Carrozzo, R., Casali, C., Damiano, M., Federici, G., and Bertini, E. (2001) Glutathione in blood of patients with Friedreich's ataxia. *Eur. J. Clin. Invest. 31*, 1007−1011.

(4) Nonaka, K., Kume, N., Urata, Y., Seto, S., Kohno, T., Honda, S., Ikeda, S., Muroya, T., Ikeda, Y., Ihara, Y., Kita, T., and Kondo, T. (2007) Serum levels of S-glutathionylated proteins as a risk-marker for arteriosclerosis obliterans. *Circ. J. 71*, 100−105.

(5) Mandal, A. K., Woodi, M., Sood, V., Krishnaswamy, P. R., Rao, A., Ballal, S., and Balaram, P. (2007) Quantitation and characterization of glutathionyl haemoglobin as an oxidative stress marker in chronic renal failure by mass spectrometry. *Clin. Biochem. 40*, 986−994.

(6) Lou, M. F. (2003) Redox regulation in the lens. *Prog. Retin. Eye Res. 22*, 657−682.

(7) Giustarini, D., Dalle-Donne, I., Colombo, R., Petralia, S., Giampaoletti, S., Milzani, A., and Rossi, R. (2003) Protein glutathionylation in erythrocytes. *Clin. Chem. 49*, 327−330.
(8) Murakami, K., and Mawatari, S. (2003) Oxidation of hemoglobin to methemoglobin in intact erythrocyte by a hydroperoxide induces formation of glutathionyl hemoglobin and binding of alpha-hemoglobin to membrane. *Arch. Biochem. Biophys. 417*, 244−250.
(9) Craescu, C. T., Poyart, C., Schaeffer, C., Garel, M. C., Kister, J., and Beuzard, Y. (1986) Covalent binding of glutathione to hemoglobin. II. Functional consequences and structural changes reflected in NMR spectra. *J. Biol. Chem. 261*, 14710−14716.
(10) Mitra, G., Muralidharan, M., Pinto, J., Srinivasan, K., and Mandal, A. K. (2011) Structural perturbation of human hemoglobin on glutathionylation probed by hydrogen-deuterium exchange and MALDI mass spectrometry. *Bioconjugate Chem. 22*, 785−793.
(11) Zhang, Z., and Smith, D. L. (1993) Determination of amide hydrogen exchange by mass spectrometry: a new tool for protein structure elucidation. *Protein Sci. 2*, 522−531.
(12) Hoofnagle, A. N., Resing, K. A., and Ahn, N. G. (2003) Protein analysis by hydrogen exchange mass spectrometry. *Annu. Rev. Biophys. Biomol. Struct. 32*, 1−25.
(13) Kemmer, G., and Keller, S. (2010) Nonlinear least-squares data fitting in Excel spreadsheets. *Nat. Protoc. 5*, 267−281.
(14) Garel, M. C., Domenget, C., Caburi-Martin, J., Prehu, C., Galacteros, F., and Beuzard, Y. (1986) Covalent binding of glutathione to hemoglobin. I. Inhibition of hemoglobin S polymerization. *J. Biol. Chem. 261*, 14704−14709.
(15) Perutz, M. F. (1970) Stereochemistry of cooperative effects in haemoglobin. *Nature 228*, 726−739.
(16) Baldwin, J., and Chothia, C. (1979) Haemoglobin: the structural changes related to ligand binding and its allosteric mechanism. *J. Mol. Biol. 129*, 175−220.
(17) Vallone, B., Bellelli, A., Miele, A. E., Brunori, M., and Fermi, G. (1996) Probing the alpha 1 beta 2 interface of human hemoglobin by mutagenesis. Role of the FG-C contact regions. *J. Biol. Chem. 27*, 12472−12480.
(18) Kavanaugh, J. S., Rogers, P. H., Arnone, A., Hui, H. L., Wierzba, A., DeYoung, A., Kwiatkowski, L. D., Noble, R. W., Juszczak, L. J., Peterson, E. S., and Friedman, J. M. (2005) Intersubunit interactions associated with Tyr42 alpha stabilize the quaternary-T tetramer but are not major quaternary constraints in deoxyhemoglobin. *Biochemistry 44*, 3806−3820.
(19) Kister, J., Kiger, L., Francina, A., Hanny, P., Szymanowicz, A., Blouquit, Y., Promé, D., Galactéros, F., Delaunay, J., and Wajcman, H. (1995) Hemoglobin Roanne [alpha 94(G1) Asp−>Glu]: a variant of the alpha 1 beta 2 interface with an unexpected high oxygen affinity. *Biochim. Biophys. Acta 1246*, 34−38.
(20) Shih, D. T., Jones, R. T., Imai, K., and Tyuma, I. (1985) Involvement of Glu G3 (101) beta in the function of hemoglobin. Comparative O_2 equilibrium studies of human mutant hemoglobins. *J. Biol. Chem. 260*, 5919−5924.
(21) Arnone, A., Thillet, J., and Rosa, J. (1981) The structure of hemoglobin Creteil (beta 89 Ser replaced by Asn) is similar to that of abnormal human hemoglobins having sequence changes at Tyr 145 beta. *J. Biol. Chem. 256*, 8545−8552.
(22) Shaanan, B. (1983) Structure of human oxyhaemoglobin at 2.1 A resolution. *J. Mol. Biol. 171*, 31−59.
(23) Kilmartin, J. V., Breen, J. J., Roberts, G. C., and Ho, C. (1973) Direct measurement of the pK values of an alkaline Bohr group in human hemoglobin. *Proc. Natl. Acad. Sci. U. S. A. 70*, 1246−1249.
(24) Louie, G., Tran, T., Englander, J. J., and Englander, S. W. (1988) Allosteric energy at the hemoglobin beta chain C terminus studied by hydrogen exchange. *J. Mol. Biol. 201*, 755−764.
(25) Arnone, A. (1974) Mechanism of action of hemoglobin. *Annu. Rev. Med. 25*, 123−130.
(26) Benesch, R., and Benesch, R. E. (1967) The effect of organic phosphates from the human erythrocyte on the allosteric properties of hemoglobin. *Biochem. Biophys. Res. Commun. 26*, 162−167.
(27) Chanutin, A., and Curnish, R. R. (1967) Effect of organic and inorganic phosphates on the oxygen equilibrium of human erythrocytes. *Arch. Biochem. Biophys. 121*, 96−102.
(28) Hashimoto, M., Ishimori, K., Imai, K., Miyazaki, G., Morimoto, H., Wada, Y., and Morishima, I. (1993) Site-directed mutagenesis in hemoglobin: functional and structural study of the intersubunit hydrogen bond of threonine-38(C3) alpha at the alpha 1-beta 2 interface in human hemoglobin. *Biochemistry 32*, 13688−13695.
(29) Safo, M. K., Burnett, J. C., Musayev, F. N., Nokuri, S., and Abraham, D. J. (2002) Structure of human carbonmonoxyhemoglobin at 2.16 Å: a snapshot of the allosteric transition. *Acta Crystallogr., Sect. D: Biol. Crystallogr. D58*, 2031−2037.
(30) Kavanaugh, J. S., Weydert, J. A., Rogers, P. H., and Arnone, A. (1998) High-resolution crystal structures of human hemoglobin with mutations at tryptophan 37beta: structural basis for a high-affinity T-state. *Biochemistry 37*, 4358−4373.
(31) Li, R., Nagai, Y., and Nagai, M. (2000) Contribution of alpha140Tyr and beta37Trp to the near-UV CD spectra on quaternary structure transition of human hemoglobin A. *Chirality 12*, 216−220.
(32) Sasaki, J., Imamura, T., Yanase, T., Atha, D. H., Riggs, A., Bonaventura, J., and Bonaventura, C. (1978) Hemoglobin Hirose, a human hemoglobin variant with a substitution at the alpha1beta2 interface. Subunit dissociation and the equilibria and kinetics of ligand binding. *J. Biol. Chem. 253*, 87−94.
(33) Manconi, B., De Rosa, M. C., Cappabianca, M. P., Olianas, A., Carelli, A. C., Mastropietro, F., Ponzini, D., Amato, A., and Pellegrini, M. (2010) A new beta-chain haemoglobin variant with increased oxygen affinity: Hb Roma [beta115(g17)Ala−>Val]. *Biochim. Biophys. Acta 1800*, 327−335.
(34) Kilmartin, J. V. (1977) The Bohr effect of human hemoglobin. *Trends Biochem. Sci. 2*, 247−250.
(35) Wiltrout, M. E., Giovannelli, J. L., Simplaceanu, V., Lukin, J. A., Ho, N. T., and Ho, C. (2005) A biophysical investigation of recombinant hemoglobins with aromatic B10 mutations in the distal heme pockets. *Biochemistry 44*, 7207−7217.
(36) Nichols, W. L., Zimm, B. H., and Ten Eyck, L. F. (1997) Conformation-invariant structures of the alpha1beta1 human hemoglobin dimer. *J. Mol. Biol. 270*, 598−615.

Bioconjugate Chemistry

Article

pubs.acs.org/bc

High-Affinity VEGF Antagonists by Oligomerization of a Minimal Sequence VEGF-Binding Domain

James E. Stefano,*[,†] Julie Bird,[†] Josephine Kyazike,[†] Anthony Wai-Ming Cheng,[∥] Ekaterina Boudanova,[†] Markryan Dwyer,[§] Lihui Hou,[†] Huawei Qiu,[†] Gloria Matthews,[‡] Michael O'Callaghan,[⊥] and Clark Q. Pan[†]

[†]Protein Engineering, [‡]Preclinical Orthopaedics, and [§]New Biologics, Genzyme Corporation (A Sanofi Company), Framingham, Massachusetts, United States

[∥]Department of Pathology, Duke University Medical Center, Durham, North Carolina, United States

[⊥]4s3Bioscience Inc., Medford, Massaschusetts, United States

Supporting Information

ABSTRACT: Vascular endothelial growth factor (VEGF) neutralizing antagonists including antibodies or receptor extracellular domain Fc fusions have been applied clinically to control angiogenesis in cancer, wet age-related macular degeneration, and edema. We report here the generation of high-affinity VEGF-binding domains by chemical linkage of the second domain of the VEGF receptor Flt-1 (D2) in several configurations. Recombinant D2 was expressed with a 13 a.a. C-terminal tag, including a C-terminal cysteine to enable its dimerization by disulfide bond formation or by attachment to divalent PEGs and oligomerization by coupling to multivalent PEGs. Disulfide-linked dimers produced by Cu^{2+} oxidation of the free-thiol form of the protein demonstrated picomolar affinity for VEGF in solution, comparable to that of a D2-Fc fusion (sFLT01) and ~50-fold higher than monomeric D2, suggesting the 26 a.a. tag length between the two D2 domains permits simultaneous interaction of both faces of the VEGF homodimer. Extending the separation between the D2 domains by short PEG spacers from 0.35 kD to 5 kD produced a modest ~2-fold increase in affinity over the disulfide, thus defining the optimal distance between the two D2 domains for maximum affinity. By surface plasmon resonance (SPR), a larger (~5-fold) increase in affinity was observed by conjugation of the D2 monomer to the termini of 4-arm PEG, and yielding a product with a larger hydrodynamic radius than sFLT01. The higher affinity displayed by these D2 PEG tetramers than either D2 dimer or sFLT01 was largely a consequence of a slower rate of dissociation, suggesting the simultaneous binding by these tetramers to neighboring surface-bound VEGF. Finally, disulfide-linked D2 dimers showed a greater resistance to autocatalytic fragmentation than sFLT01 under elevated temperature stress, indicating such minimum-sequence constructs may be better suited for sustained-release formulations. Therefore, these constructs represent novel Fc-independent VEGF antagonists with ultrahigh affinity, high stability, and a range of hydrodynamic radii for application to multiple therapeutic targets.

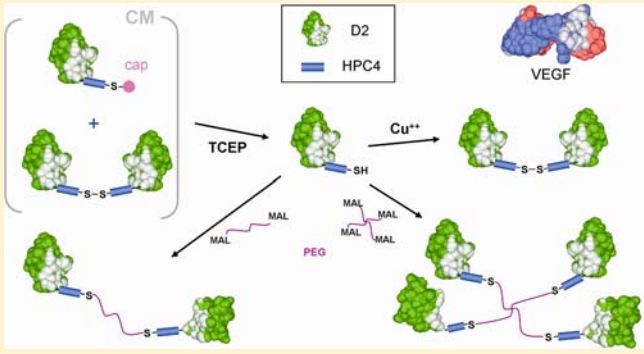

INTRODUCTION

Vascular endothelial growth factor (VEGF) serves the role as a potent angiogenic agent as well as having the capacity for increasing vascular permeability,[1,2] thereby increasing the perfusion of serum into tissue. It has been a primary therapeutic target for suppressing angiogenesis in cancer therapy, wet age-related macular degeneration (AMD), and diabetic retinopathy, conditions whose pathology is directly related to vessel growth. The most common form, VEGF A, is found in multiple splice variants, although the principal form is 165 amino acids in length (VEGF165).[3−5] VEGF165 has affinity for the heparin sulfate proteoglycan (HSPG) component of the extracellular matrix due to a heparin binding domain(s) in the C-terminal portion,[6,7] which is critical for its mitogenic potential.[8] The angiogenic activity of VEGF is associated with the binding of VEGF receptor 2 (VEGF R2, KDR, or Flk), a tyrosine kinase which induces endothelial cell growth with an EC_{50} in the sub-nanomolar range.[4,5] However, VEGF shows a higher (pM) affinity for a second receptor, VEGF R1 (or Flt-1), which is required for normal blood vessel formation during development, but whose tyrosine kinase activity is nonessential.[9] As a result, Flt-1 is thought to play a role in vivo largely in acting as a decoy to modulate VEGF availability. Two approved biotherapeutics (bevacizumab and ranibizumab) comprising

Received: June 7, 2012
Revised: November 6, 2012
Published: November 26, 2012

 © 2012 American Chemical Society

an IgG and its affinity-matured Fab fragment against VEGF have been approved for cancer and wet age-related macular degeneration (AMD), respectively.

Strategies to exploit the natural function of Flt-1 in regulating VEGF by the construction of soluble Flt-1 receptor decoys have focused on defining the minimal sequence required for high-affinity VEGF binding. Davis-Smyth demonstrated, through a series of deletions and swaps with other PDGF receptor family domains, that deletion of domain 2 (D2) obliterated binding to VEGF, but inclusion of Flt flanking domains 1 and 3 were required to replicate the high (pM) affinity of the full-length ectodomain.[10] While such constructs demonstrated efficacy in preclinical models, high doses were required,[11] and these constructs demonstrated poor pharmacokinetic profiles.[12] Moreover, continuous low-level expression of Flt(D1-D3) by adenoviral gene therapy was associated with morbidity and ascites formation.[13] The crystal structure of a VEGF fragment with a monomeric Flt-1 D2 fragment showed two D2 domains interacting with each of the outside faces of the VEGF homodimer, but monomeric D2 was reported to have ~100-fold lower binding than the complete receptor ectodomain. A low picomolar affinity was observed only with a monomeric D1-D3 fragment or a dimeric (D2-D3) Fc fusion.[14] An Fc fusion protein including the second domain of VEGF R1 and the homologous third domain of VEGF R2 (VEGF Trap, aflibercept) was subsequently found to circumvent the toxicity and PK issues with Flt(D1-D3)[12] and was approved for AMD and is currently in clinical trials for macular edema. More recently, the reported requirement for both D2 and D3 for full VEGF binding activity was challenged by the finding that a forced homodimer, containing only the D2 domain of Flt-1 fused to human IgG Fc through a 9Gly linker (sFLT01), demonstrated high-affinity binding comparable to two- and three-domain constructs.[15] A spacer sequence in addition to a CH3 domain which provided for formation of a noncovalent dimer were found to be required for high-affinity (pM) binding, suggesting that simultaneous binding to both chains of the VEGF homodimer is required for high affinity. A clinical trial of this molecule in gene therapy for AMD is in progress.

All VEGF antagonists currently in the clinic utilize an IgG Fc domain to provide for a long circulating half-life intended to ensure reasonable target exposure by systemic administration. However, systemic exposure to all antiVEGF agents is associated with a number of potentially mechanism-related side effects including hypertension, complications in wound healing, intestinal perforations, and nephrotic syndrome,[16,17] a subset of which may also have a component related to the Fc effector function. These side effects may restrict the use of these molecules from otherwise potentially treatable indications linked to VEGF activity, but which would require long-term administration. This class includes osteoarthritis, where subchondral bone damage may induce the expression of VEGF, which would elicit serum effusion into the joint, a possible direct source of pain. In addition, angiogenesis and growth of demyelinated nerve in the subchondral bone in the presence of VEGF also suggests VEGF may be a useful therapeutic target in this context.[18] The means to restrict potential side effects for this and other indications may benefit from the targeted delivery of the antiVEGF reagents to critical sites of action such as the tumor periphery or the joint. Here, we investigate the quaternary structure requirements for high-affinity VEGF binding for Flt-1 domain 2 (D2) through dimerization of the minimal sequence structure as well as conjugation to poly(ethylene glycol)s as a strategy for prolonging circulating half-life. Conjugation to multiarm PEGs was performed to assess possible avidity effects and to provide a potential platform for targeted delivery. Finally, the suitability of two compositions for sustained-release formulation was assessed by the resistance to thermal stress.

EXPERIMENTAL PROCEDURES

Expression and Purification of D2. Oligonucleotides corresponding to amino acids 133−226 of VEGF R1 (Flt-1) isoform 1 (SwissProt P17948) with a Kozak sequence (GCCACCATGG) and the Flt-1 signal peptide sequence were synthesized and Gateway-cloned into a modified commercially available vector containing a CMV immediate early enhancer-promoter (pCEP4, Invitrogen). HEK293-EBNA monolayers were transfected using Lipofectamine-2000 and conditioned medium harvested after 3 and 6 days, pooled, and stored at −80 °C. The medium was concentrated ~10-fold by centrifugal ultrafiltration (10 kDa MWCO) and applied to a 1 mL antiProtein C (HPC4) mAb affinity column (Roche 11815024001) equilibrated with 150 mM NaCl, 5 mM $CaCl_2$, 50 mM Tris pH 7.2 (EB) at 0.5 mL/min. The column was washed with 20CV EB and protein eluted with 10CV EB + 5 mM EDTA without $CaCl_2$. The eluate was concentrated by centrifugal ultrafiltration and stored at −80 °C.

Preparation of Conjugates. Homobifunctional and 4-arm maleimide PEGs were obtained commercially (Thermo Scientific, Rockfield, IL; Jenchem, Allen TX; NOF Corp., White Plains, NY). Purified D2 in 25 mM NaCl, 2 mM EDTA, and 25 mM Na phosphate pH7 was reduced for 1 h with 2 mM TCEP at 25 °C, desalted by a single dilution and centrifugal ultrafiltration on Vivaspin 4 5 kDa MWCO filters at 4 °C (Corning) prewashed with water. The product was reacted for 4 h in molar excess over PEG maleimide groups as described in the text and purified by SEC over a Superdex 200 column (G.E. Healthcare) using PBS as the mobile phase at 0.4 mL/min. Peaks were collected using A_{214}, concentrated by centrifugal ultrafiltration, and flash frozen at −80 °C. Concentrations were determined by an ultra micro BCA method using BSA as a standard, with the final A_{562} measured using a 720 nm reference wavelength on a Nanodrop 1000 spectrophotometer (Thermo Scientific). Assays were performed in triplicate. All values were within the standard curve and showed a c.v. of <10%.

Production of D2 Dimers through Forced Oxidation. For preparing D2 dimers by forced oxidation, the affinity column eluate was buffer exchanged into PBS, concentrated to 1 mg/mL, and treated with 2 mM TCEP (BondBreaker, Thermo Scientific) for 2 h at 25 °C. The product was buffer exchanged into 25 mM Tris HCl pH 7.5 using centrifugal diafiltration on Vivaspin 4 (5 kDa MWCO), adjusted to 0.5 mg/mL, and treated with 0.2 mM $CuCl_2$ for 1 h at 25 °C. EDTA was added to 2 mM and the product desalted with Tris buffer and then exchanged into PBS by centrifugal diafiltration. The concentration was determined by A_{280} using E = 0.91.

VEGF Binding by Surface Plasmon Resonance. Recombinant human VEGF165 (R&D Systems, Minneapolis, MN, USA) was covalently immobilized to the surface of a CM5 sensor chip using standard amine coupling chemistry on a Biacore 3000 instrument (GE Healthcare, Piscataway, NJ, USA). Human VEGF165 (293-CF, R&D Systems) was reconstituted at 50 μg/mL in 10 mM sodium acetate pH 4.5, then diluted to 10 or 20 μg/mL and injected over the activated chip surface at 5 μL/min to achieve the desired surface

densities. Three densities were achieved for VEGF (~130, ~500, and ~4000 RU). For a reference surface, the fourth flowcell was activated and quenched without protein. To follow kinetics, each sample was serially diluted 3-fold from 10 to 0.37 nM in 10 mM HEPES pH 7.4, 150 mM sodium chloride, 3 mM EDTA, 0.005% Surfactant P20 (HBS-EP, GE Healthcare, Piscataway, NJ), and flowed over the reference and VEGF-coupled surfaces for 4 min at 30 μL/min, followed by 5 min of buffer alone for dissociation. Samples were analyzed in duplicate. Each surface was regenerated with two 30 s injections of 10 mM glycine HCl pH 2.0 at 60 μL/min. Biosensor data were processed using *Scrubber2* software (BioLogic Software Pty Ltd., Campbell, AU). Kinetic constants were obtained by global fit to the sensorgram data using a 1:1 binding model based on the molar concentration of conjugate.

VEGF Binding by Competition ELISA. Briefly, human VEGF165 (293-VE, R&D Systems, Minneapolis, MN) was diluted to 20 pM in assay diluent (M199 Medium, 5% FBS, 1× penicillin/streptomycin) and mixed with an equal volume (150 μL) of serially diluted sample in assay diluent and incubated overnight with gentle shaking at room temperature. Unbound VEGF in the reaction was then determined by ELISA using an immobilized monoclonal antiVEGF for capture and a polyclonal antiVEGF-HRP conjugate for detection (Human VEGF Quantikine ELISA DVE00, R&D Systems) using the kit VEGF as standard and analysis using *SpectraMax* software. Sigmoidal fits to the free VEGF values were then derived using *Prism* (GraphPad Software, Inc., La Jolla, CA) to determine EC_{50} values. The reduction in free VEGF was assumed to reflect binding to conjugate in a 1:1 ratio.

RESULTS

Oligonucleotides encoding 107 amino acids including amino acids 9–109 of the D2 domain (a.a. 133–226 of Flt-1) with a HPC4 C-terminal appendage for affinity purification were synthesized and expressed in HEK293 cells. The resulting construct as shown in Figure 1a was isolated by affinity chromatography on an antiHPC4 tag antibody column. The product (expected 12304 Da) migrated as a band above the 22 kDa marker on the gel (Figure 1b). However, MALDI analysis (Figure 1c) showed a predominant peak at 16.6 kDa with a smaller amount of 32.8 kDa product, suggesting the 25 kDa (apparent MW) band represents glycosylated monomer. Consistent with this, treatment of the product with PNGase F resulted in a doublet migrating around the expected 12 kDa on SDS PAGE (data not shown). Edman degradation also showed a predominant amino terminal RPFV sequence consistent with cleavage of the signal at the expected site. The presence of a C-terminal cysteine was indicated by the ability of the purified product to dimerize by oxidation (see below). The molecular weight by MALDI (16.6 kDa) was consistent with the presence of glycans of approximately 2.1 kDa at each of the two potential N-linked glycosylation sites, comprising 26% of the total molecular weight of the expression product likely explaining the anomalous mobility by SDS PAGE. Initial results showed that the product was active in binding immobilized VEGF165, suggesting the C-terminal HPC4 tag did not strongly effect binding.

When expressed at larger scale, SDS PAGE showed the predominant product as a doublet near 21 kDa, but in addition, a significant amount of a second doublet migrating at ~40 kDa_{app} (Figure 2a). Upon reduction, the upper bands disappeared with an increase in intensity of the lower,

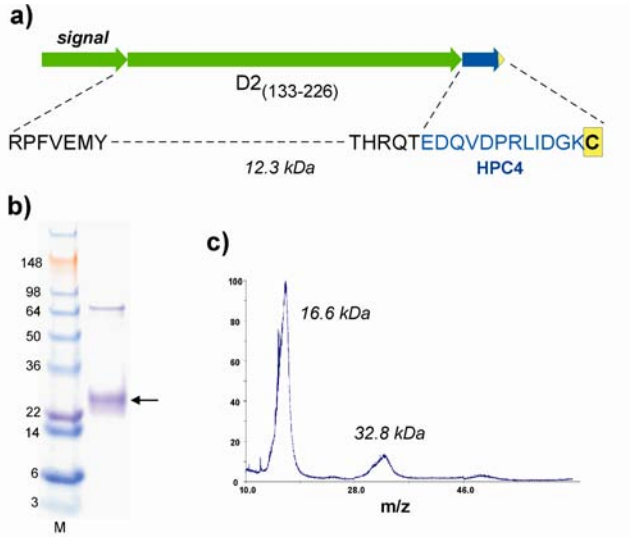

Figure 1. DNA construct and expression of the Flt-1 D2 domain (amino acids 133–226 of Flt-1) with a C-terminal HPC4 tag and cysteine. (a) Diagram of the expression construct and amino acid sequence. The expected amino terminal RPFV was confirmed by Edman sequencing (not shown). (b) Nonreducing SDS PAGE of the HPC4-purified product, which migrates as a broad band just above the 22 kDa marker. (c) MALDI analysis of the purified product showing a predominant species of 16.6 kDa with a second minor peak of ~33 kDa, likely reflecting glycosylation and the presence of some dimerized protein in conditioned medium.

suggesting the upper represent dimers coupled through disulfide bonds. The persistence of the doublet upon reduction may reflect heterogeneity in glycosylation. By SEC (Figure 2b, blue trace), two peaks (1, 2) were observed, corresponding to the upper and lower doublet. Reduction of the HPC4 eluate (red trace) yielded only peak 2, which contained the ~21 kDa_{app} doublet material by SDS PAGE (2b, right lane 2).

A fusion protein sFLT01, in which a D2 domain is separated from the IgG1 Fc by a Gly9 linker was found to bind VEGF165 with picomolar affinity.[15] The distance between the C-termini of two D2 domains in a crystal structure of D2 in complex with the VEGF165 homodimer[14] suggested that simultaneous binding to both VEGF subunits may be achieved by this linker. Thus, it seemed likely that D2 monomers linked through a comparably sized 13aa C-terminal HPC4 tag might also be able to bind the VEGF with high affinity. A preparation of dimer was purified by SEC of the affinity column eluate (Figure 2b) to yield dimer and monomer fractions (Figure 2b right). Alternatively, the dimer/monomer mixture in the eluate was converted to dimer through a reduction–oxidation approach. As found with other expressed proteins, the free cysteines were "capped" with disulfide-linked glutathione or cysteine and thus unable to dimerize directly by oxidation (not shown). The affinity-purified protein was therefore first reduced with low levels of TCEP followed by oxidation with Cu^{2+} to yield dimer in nearly pure form at high yield (Figure 2c). We reasoned that the 26 amino acid span provided by the two HPC4 tags and cysteines, if fully extended, would be sufficient to cover the ~55 Å distance between the C-termini of the D2 domains bound to VEGF as seen in the crystal structure. The effect of PEG linkers on the affinity for VEGF dimer was assessed, since PEGylation frequently affects target binding. Thus, dimers were prepared by coupling the D2 terminal thiols through bis-maleimide PEGs of varying lengths. A 0.4 kDa PEG only 3 ethylene oxide units

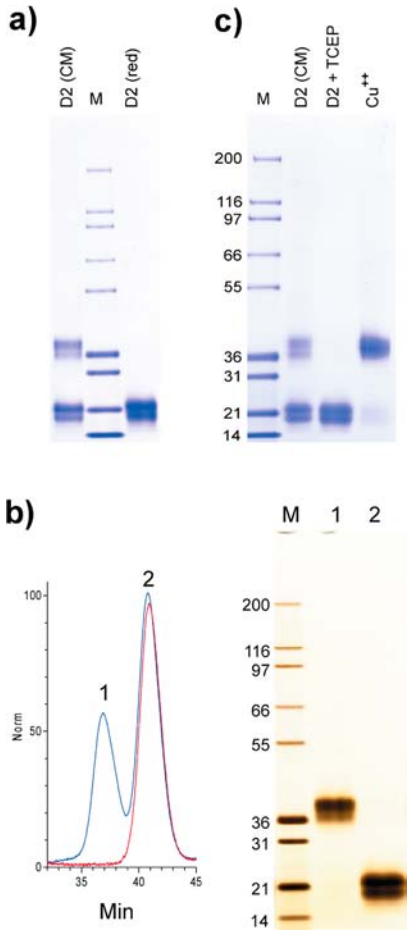

Figure 2. Identification and isolation of disulfide-linked dimers. (a) Nonreducing and reducing SDS PAGE of HPC4 affinity-purified D2. D2(CM), HPC4-purified protein from conditioned medium. (b) SEC profile of D2 from conditioned medium before (blue) and after (red) TCEP treatment. (Right) Silver-stained nonreducing SDS PAGE of peak fractions 1 and 2. (c) Preparation of disulfide-linked D2 dimer by copper oxidation of TCEP-reduced HPC4-affinity-purified protein. D2 (CM): HPC4-purified protein from conditioned medium. TCEP: reduced with TCEP and desalted. Cu^{++}: reduced, desalted, and oxidized with $CuCl_2$.

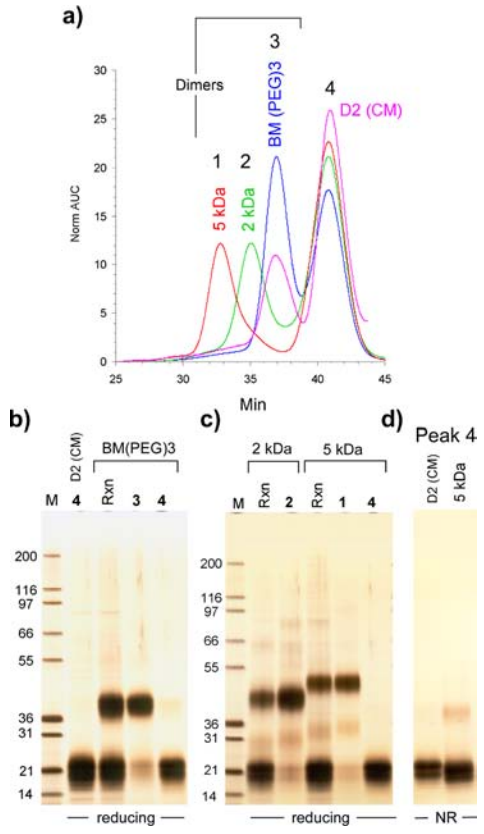

Figure 3. Preparation and characterization of PEG-linked D2 dimers. HPC4-purified D2 was reduced with TCEP and then reacted with molar excess of 2 kD or 5 kDa maleimide PEGs. (a) SEC profiles of PEGylation reaction products. Red, 5 kDa PEG linker conjugate; green, 2 kDa linker; blue, BM(PEG)3 linker; magenta, D2 from conditioned medium containing a mixture of disulfide-linked dimer and monomer. Peaks 1−3 are presumed dimers based on SDS PAGE analysis (see b,c,d). (b) Reducing SDS PAGE of SEC fractions from D2 conjugation to BM(PEG)3 linker. Numbers above the lanes refer to SEC peaks shown in (a). Note that only minor amounts of material from the dimer peak 3 ran as monomer upon reduction, indicating almost all was thioether linked through the PEG. (c) Reducing SDS PAGE of PEG conjugate peaks 1 (5 kDa PEG) and 2 (2 kDa PEG). Note that each of these dimer fractions also contained minor amounts migrating between monomer and the main PEGylated product whose gel mobility was PEG-dependent. These likely represent PEGylated molecules in which a single D2 is linked to each PEG. (d) Nonreducing SDS PAGE of peak 4 of the D2 monomer isolated from conditioned medium (C2 CM) or recovered from 5 kDa PEG conjugation reaction after coupling (5 kDa).

in length ("BM(PEG)3", 0.35 kDa), yielded an SEC profile (Figure 3a, blue trace) indistinguishable from that of the disulfide-linked dimer (purple). From the low abundance of monomer after reduction by SDS PAGE (Figure 3b), we concluded that this preparation largely contained dimers coupled through PEG rather than disulfide linkages. The similar SEC retention time (RT) for the shortPEG and disulfide-linked dimers also suggests the PEG does not produce a significant change in the solution conformation. In contrast, with larger bis-maleimide PEG linkers (2 kDa, 5 kDa), the increase in the linker MW resulted in a significant reduction in retention time (Figure 3a). For the 2 kDa PEG spacer, this RT shift was similar to that between the monomer and dimer (cf peaks 2 and 3 vs 3 and 4), suggesting the PEG conjugate is in an extended orientation in solution. Increasing the length of the spacer to 5 kDa resulted in a further RT shift (peak 1).

As a control, monomeric D2 was also obtained either directly from conditioned medium by SEC of HPC4 affinity column eluates (Figure 3a, peak 4 purple trace) or from the late-eluting SEC peak at the end of conjugation reactions run in D2 excess (Figure 3a peak 4 red, green, blue)). Similar to many proteins isolated from conditioned medium where solution-accessible cysteines are capped with a disulfide-linked glutathione or cysteine, monomer isolated from conditioned medium showed almost undetectable amounts of dimer (Figure 3d, "D2 (CM)") and migrated on nonreducing SDS PAGE as a doublet of slightly higher apparent MW than reduced monomer recovered from a PEGylation reaction such as shown for conjugation to 5 kDa PEG (Figure 3d, lane "5 kDa"), consistent with the presence of a cap preventing oxidative dimerization. As expected, monomer isolated from conjugation reactions showed a tendency toward dimerization (Figure 3d, "5 kDa").

Each of the SEC fractions was assayed for VEGF binding activity by surface plasmon resonance (SPR, Figure 4a), which showed very slow dissociation rates for the dimers but rapid

dx.doi.org/10.1021/bc300301m | Bioconjugate Chem. 2012, 23, 2354−2364

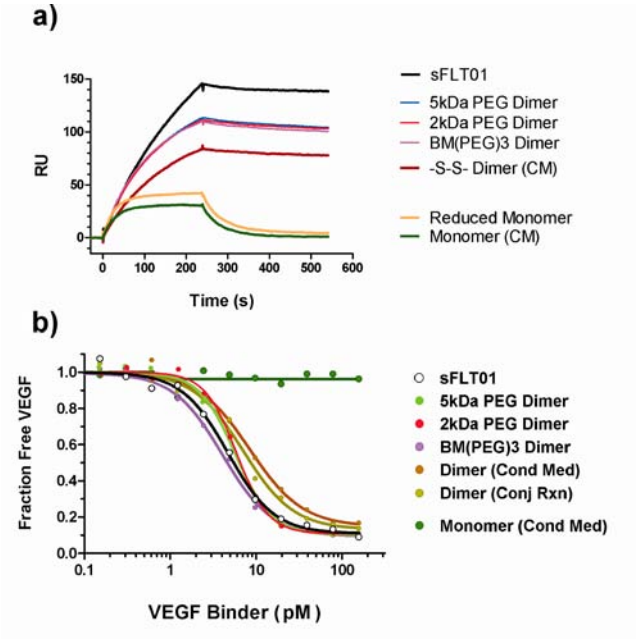

Figure 4. Binding of D2 dimers linked through disulfides or short PEG spacers to VEGF on a solid support (Biacore) and in solution. (a) Biacore sensorgrams. Samples were passed over a 500RU VEGF165 chip. Note that the response is directly related to the MW, which differs among the conjugates (sFLT01, 75 kDa; D2 dimers, 33−38 kDa). Tan: Reduced Monomer: unconjugated fraction of D2 monomer after coupling in excess to 5 kDa bis-maleimide PEG. (b) Solution phase binding to VEGF165. Conjugates were coincubated with 10 pM VEGF165 overnight followed by determination of the free (unbound) VEGF concentration by ELISA.

Table 1. Kinetic and Equilibrium Values for Binding VEGF on a Solid Support and in Solution

	Biacore			solution phase
sample	k_a ($\times 10^5$ M^{-1} s^{-1})	k_d ($\times 10^{-4}$ s^{-1})	k_D (nM)[a]	EC_{50} (pM)
D2 Monomer, CM[b]	10.2	202	19.8	ND[c]
D2 Monomer, CR[d]	15.5	171	11.1	[e]
-S−S-Linked D2 Dimer, CM[f]	6.0	2.5	0.42	8.4
-S−S-Linked D2 Dimer, CR[g]	6.9	3.7	0.53	7.1
-S−S-Linked D2 Dimer, Cu^{2+}[h]	-	-	-	8.3
BM(PEG)3-linked D2 Dimer	9.1	2.5	0.27	4.0
2 kDa PEG-linked D2 Dimer	7.6	2.8	0.37	5.8
5 kDa PEG-linked D2 Dimer	8.1	2.2	0.27	5.8
10 kDa 4-arm PEG-linked Tetramer	7.8	0.6	0.08	3.7
20 kDa 4-arm PEG-linked Tetramer	6.3	0.7	0.11	4.8
sFlt01	3.8	2.5	0.66	4.6

[a]Equilibrium values determined from binding kinetics on ∼500RU VEGF-loaded chips. The K_D values for dimer and multimeric conjugates were dependent on the VEGF density on the chip (see Figure 8 and text). [b]Monomer isolated from conditioned medium. [c]No binding detected within the range of the assay (≤0.15 nM). [d]Unconjugated monomer recovered from a conjugation reaction. [e]Weak and variable binding. This species is susceptible to spontaneous oxidative dimerization. [f]Disulfide-linked dimer isolated from conditioned medium. [g]Disulfide-linked dimer byproduct of a conjugation reaction. [h]Dimer generated by copper oxidation of monomer reduced with TCEP.

dissociation of monomers bound to immobilized VEGF. The results of these analyses are summarized in Table 1. All of the PEG-linked dimers showed slightly higher affinities than sFLT01 as a consequence of a 2- to 3-fold increase in the rate of binding VEGF on the chip (k_a). Of these, the BM(PEG)3-linked dimer showed the largest increase (2.4-fold). The off-rates (k_d) among all of the constructs as well as the fusion protein sFLT01 were very similar ($(2.5 \pm 0.21) \times 10^{-4}$ s^{-1}), suggesting that all of the complexes with VEGF on the chip involved an identical set of interactions. A minor loss in complex stability was observed for dimer recovered from the conjugation reaction ("-S-S-linked D2 dimer CR", Table 1), possibly reflecting partial reduction of the single internal D2 disulfide. The conjugates were also assayed for VEGF binding in solution by incubation with VEGF followed by ELISA to quantitate the amount of unbound VEGF.[12,15] Incubation of 10 pM VEGF with picomolar concentrations of either sFLT01 or any of the D2 dimers produced nearly quantitative depletion of free VEGF (Figure 4b). Surprisingly, the EC_{50} values in solution were about 20-fold lower than the K_D values obtained by SPR and close to those expected for an irreversible reaction with 1:1 stoichiometry. A similar result has been reported for expressed sFLT01 in conditioned medium.[15] Despite this extremely low EC_{50}, the sigmoidal shape and slopes of the curves were consistent with single-component equilibria with K_D values in the picomolar range (Table 1).

By SPR, monomers either isolated from conditioned medium or recovered from conjugation reactions showed a 2.5- to 4-fold faster on-rate than dimers, consistent with lower MW, but also showed a 70- to 80-fold faster rate of dissociation, consistent with a loss of half of the VEGF-binding determinants (Figure 4 and Table 1). Monomer isolated from conditioned medium showed the lowest affinity for VEGF (20 nM) but within 2-fold of excess monomer recovered from conjugation reactions (11 nM). Consistent with this result, no detectable binding in solution by ELISA was observed with up to 0.15 nM monomer obtained directly from conditioned medium. (Higher levels were not tested.) In those experiments, however, some binding was observed with unconjugated monomer recovered from coupling reactions at the end of incubation. However, since such preparations contain free thiols and frequently contain detectable dimer at low levels by nonreducing SDS PAGE (Figure 3d, 5 kDa; Figure 5a, lane 6:1), the possibility that dimer produced by air oxidation was responsible for the binding could not be excluded (data not shown).

The lack of a strong effect of PEG linker length on the affinity for VEGF suggested that higher MW multivalent polymers might show a still higher affinity through an avidity effect from the greater number of D2 domains. Thus, a pair of 4-arm maleimide-terminated PEGs of 10 kDa and 20 kDa were used as scaffolds to generate multivalent conjugates. As shown in Figure 5a, reaction of reduced D2 with a 4-arm 10 kDa PEG at a 1:1 molar D2/PEG ratio consumed virtually all of the monomer (at 21 kDa^{app}) and produced a somewhat complex set of products near 40 kDa and higher MW. As the D2/PEG molar ratio was increased to 6:1 (1.5:1 D2 to PEG maleimide groups), some remaining unconjugated D2 in both monomer and dimer forms (∼20 kDa^{app} and ∼40 kDa^{app}) were seen with

dx.doi.org/10.1021/bc300301m | Bioconjugate Chem. 2012, 23, 2354−2364

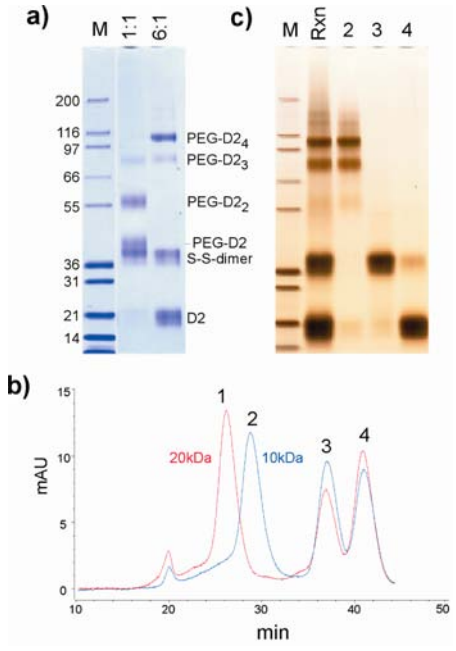

Figure 5. Conjugation of D2 to 4-arm PEGs. (a) SDS PAGE of reaction mixtures initiated with 1:1 and 6:1 (mol/mol) D2 monomer to 4-arm 10 kDa PEG. Assignments for the reaction products are shown. PEG bearing a single D2 (PEG-D2 dash in figure) migrates slightly more slowly than the disulfide-linked D2 dimer (S−S-dimer). This species in the reaction products at high D2 excess likely reflects reoxidation of unconjugated monomer during conjugation. (b) SEC profiles of conjugation products with 10 kDa and 20 kDa PEGs. (c) Silver-stained nonreducing SDS PAGEof peak SEC fractions from a 10 kDa PEG conjugation. Peak 2 comprises a mixture of two predominant PEGylated forms with apparent MW of ∼80 kDa and ∼100 kDa, likely corresponding to PEG coupled to three and four D2, respectively (see panel a). Peak 3 contained a predominant product of ∼38 kDa (disulfide-linked dimer), produced by oxidation, and peak 4, remaining unreacted D2 monomer added in excess to the reaction. Slight cross-contamination of dimer and monomer isolates is apparent.

a concomitant formation of a species with an apparent MW of ∼100 kDa. The appearance of similar ladder patterns for other PEG conjugates (not shown) led us to assign the band(s) formed at 1:1 D2/PEG as shown (Figure 5a): The broad band just above the 40 kDa disulfide dimer as the 4-arm PEG with a single D2 coupled, 60 kDa two, 80 kDa three, and 100 kDa four D2, respectively. These apparent MWs are reasonably close to that expected for the coupling of increasing numbers of D2 monomers of ∼20 kDa^{app} to a 10 kDa PEG with an apparent MW of 20 kDa. As expected from the 4 arms present on each PEG, products of higher MW were not observed. SEC of the 10 kDa PEG product at 6:1 mol/mol (Figure 5b) showed three major peaks with the earliest (1) containing mostly the 100 kDa$_{app}$ and 80 kDa$_{app}$ products by nonreducing SDS PAGE (Figure 5c, lane 2), peak 3 an ∼40 kDa product consistent with disulfide-linked dimer (Figure 5c, lane 3), and peak 4, an ∼20 kDa species consistent with reduced D2 monomer (Figure 5c, lane 4). The RT for peaks 3 and 4 were identical for conjugations with either PEG, whereas the RT of the leading peak varied with the PEG MW, consistent with 1 and 2 being the PEG conjugates and 3 and 4 as unconjugated D2 dimer and monomer, respectively. The background smear of peaks 1 and 2 fractions seen by silver staining (lane 2) but only weakly visible with Coomassie staining the reaction products (Figure 5a, lane "6:1") may reflect some MW and chain length heterogeneity in the PEG produced by random EtO polymerization on a tetravalent core, as well as possible D2$_{n=3}$ isomers. Note that SEC fractionation of the crude reaction mixture yielded material with reduced polydispersity (cf., Figure 5c, lanes 2 and Rxn). Similar results were obtained for the 20 kDa PEG conjugate (not shown). As shown in Figure 6, the SEC

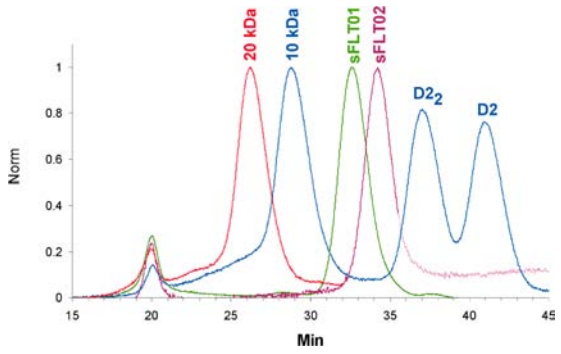

Figure 6. Comparison of tetrameric PEG conjugates to dimeric Ig Fc fusions by SEC. The profiles for all conjugates are of unpurified reaction end products. Annotations indicate the MW of the PEG linker. The flow rate was 0.5 mL/min with absorbance measured at 214 nm. Red and blue: tetrameric PEG conjugates. Green and gray: sFLT01, a D2-Gly$_9$-Fc fusion; and sFLT02, a D2-Gly$_9$-CH3 fusion.[15] The total MWs without glycosylation are as follows: 20 kDa PEG conjugate, 69 kDa; 10 kDa PEG conjugate, 59 kDa; sFLT01, 75 kDa; sFLT02: 47 kDa; D2$_2$ (dimer), 26.6 kDa; D2, 12.3 kDa. A portion of the 20 kDa PEG conjugate profile has been removed for clarity.

retention times of these conjugates were significantly shorter than the those of the PEG-linked dimers (Figure 3), as well as of two fusion proteins in which the D2 is linked either to the huIgG1 Fc (sFLT01) or the CH3 domain (sFLT02),[15] suggesting they will have substantially better PK than the dimer constructs.

Each of the SEC fractions was recovered and analyzed by SPR using immobilized VEGF165 (Figure S1, Table 1). With the 10 kDa PEG conjugate, binding to VEGF showed similar kinetics and final saturation levels as sFLT01 (Figure S1) and all of the conjugates demonstrated high-affinity binding (Table 1). However, although the 4-arm PEG tetramers with twice as many D2 showed a higher affinity of the magnitude expected by an increase in the number of D2 on the kinetics of binding, the increase was instead largely attributable to the ∼4-fold decrease in off-rate, suggesting a greater number of contacts with VEGF on the chip surface. The dimer with a 5 kDa PEG spacer showed a comparable rate of binding but a 3.6-fold faster off-rate than the 10 kDa 4-arm PEG tetramer in which 5 kDa of PEG separates each D2 pair. In contrast, in solution, the 4-arm 10 kDa PEG tetramer showed an only slightly higher affinity than sFLT01 (EC_{50} = 3.7 vs 4.7 pM) and the 20 kDa PEG conjugate was no different than sFLT01 (Table 1). As with the dimers, there was a large discrepancy between the K_D values by SPR and the EC_{50} values by solution-phase binding (80- to 200-fold).

Particularly with the multiarm PEG conjugates, the apparent affinity ($1/K_D$) by SPR was dependent upon the VEGF loading on the chip and increased with higher VEGF densities (Figure 7). With the 20 kDa PEG conjugate, a 5-fold increase of immobilized VEGF resulted in a 10-fold increase in the apparent affinity. The increase was less for the 10 kDa 4-arm

dx.doi.org/10.1021/bc300301m | Bioconjugate Chem. 2012, 23, 2354−2364

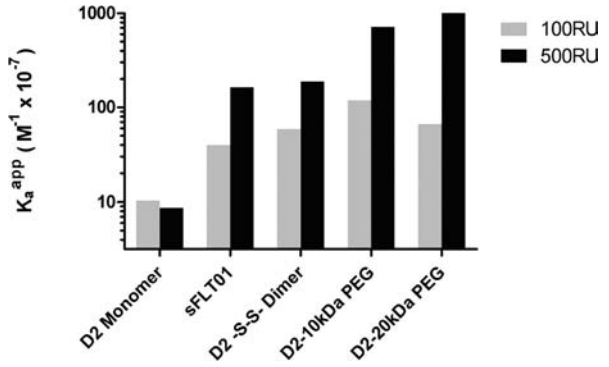

Figure 7. Effect of chip loading on apparent affinity by SPR. Binding affinities were assessed at three immobilized VEGF levels. The apparent affinity constants (K_a) of the constructs at two densities (100, 500 RU) are shown. The 20 kDa construct showed the greatest change in apparent K_a with chip loading. D2 monomer showed no significant change in K_a over the same range.

PEG conjugate and smallest with the disulfide-linked dimer. This effect resulted a change in rank order of affinity for the 4-arm conjugates. In contrast, D2 monomer showed no significant change in affinity with VEGF loading. For all of the PEG conjugates, the affinity increase with increasing VEGF density was entirely due to the reduction in off-rate. For sFLT01, the rate of association (k_a) increased only 16% and was not significantly different (<5%) than the dimer and PEG conjugates even with a 5-fold increase in VEGF. At very high loading, extremely slow off-rates and mass transport issues during binding, as suggested by a lack of curvature in the binding reaction profile, precluded an accurate determination of K_D values (data not shown). These results are consistent with avidity effects arising from simultaneous interaction of the conjugates with adjacent VEGF molecules on the chips, which would increase with decreasing distance between VEGF.

The high affinity for VEGF of the small dimer conjugates suggested the possibility of a broader application of these constructs to other applications such as localized delivery by incorporation into sustained-release depots. However, the formulation processes pose a significant challenge to protein stability, since most were designed for small molecule therapeutics and typically employ conditions and reagents which have a significant potential to induce protein denaturation. Consistent with this, internal efforts to formulate sFLT01 for sustained localized release were complicated by fragmentation and loss of VEGF binding activity. The minimal sequence D2 dimer (32 kDa) is within the MW range of proteins reported to be successfully incorporated into sustained-release depots. The higher yield of D2 dimer generated through a more direct process of reduction/oxidation enabled an assessment of the suitability by testing its thermal stability under comparable conditions. Thus, sFLT01 and the D2 dimer generated by copper oxidation were incubated in PBS pH 7.2 at 45 °C for extended periods in the presence of protease inhibitors and EDTA. As shown by reducing SDS PAGE (Figure 8a), sFLT01 showed a distinct cleavage product (arrowhead) and a diffuse band around 21 kDa (bracket), which accumulated over 36 days. In addition, higher MW covalent aggregates were also visible. By comparison, the D2 dimer showed no obvious fragmentation and only slight accumulation of a higher MW aggregate (Figure 8b). Since it was possible that an inhibitor-resistant protease in the sFLT01

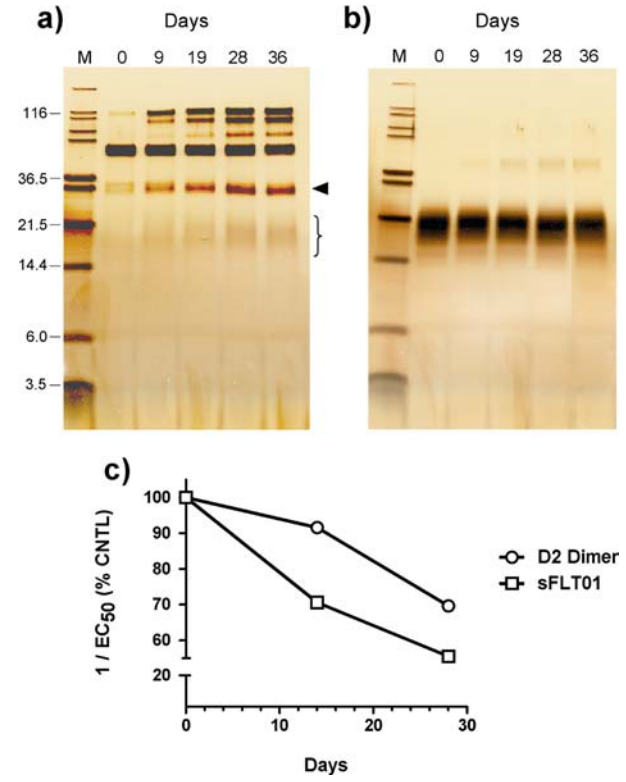

Figure 8. Forced degradation study of sFLT01 and D2 disulfide-linked dimer. Samples (0.25 mg/mL) were incubated in PBS + EDTA and protease inhibitors at 45 °C for up to 36 days; then, aliquots were withdrawn, stored at −80 °C, and analyzed by SDS PAGE. (a) Stability of sFLT01 to elevated temperature. Arrow: primary degradation product. (b) Stability of D2 dimer produced by Cu^{2+} oxidation. (c) Effect on VEGF-binding activity in solution. Binding assays were performed on samples from a different stability study but which showed a similar kinetics of degradation as in (a) and (b): (○) D2 Cu^{2+} Dimer; (□) sFLT01.

was responsible for degradation, dimer was also coincubated with the sFLT01 at elevated temperature. After 28 days, cleavage products corresponding to sFLT01 were still observed without detectable fragmentation of D2 (data not shown). The affinity of the molecules for VEGF was also assessed by solution-phase binding (Figure 8c). Both molecules showed loss of activity, but the initial rate of loss was significantly faster for sFLT01. After 14 days at 45 °C, sFLT01 had lost ~30% activity, while the D2 dimer showed less than 10% reduction.

■ DISCUSSION

These results demonstrate that D2 dimerization through a variety of linkages is sufficient and necessary for very high affinity binding to VEGF165 in the picomolar range, and that multimerization through conjugation to polymers yields molecules with comparable hydrodynamic radii as Fc fusions while retaining extremely high affinity. The different conjugate configurations explored in this study are shown diagrammatically in Scheme 1. These results demonstrate that the coupling of this minimal-sequence entity to such scaffolds provides a means to select the optimal hydrodynamic radius and represents a viable strategy for balancing the opposing requirements for prolonged PK and efficient tissue penetration for different therapeutic applications. The low MW of the disulfide-linked D2 dimer may be optimal for generating

dx.doi.org/10.1021/bc300301m | Bioconjugate Chem. 2012, 23, 2354−2364

Scheme 1. Diagrammatic Representation of the Molecules in the Study[a]

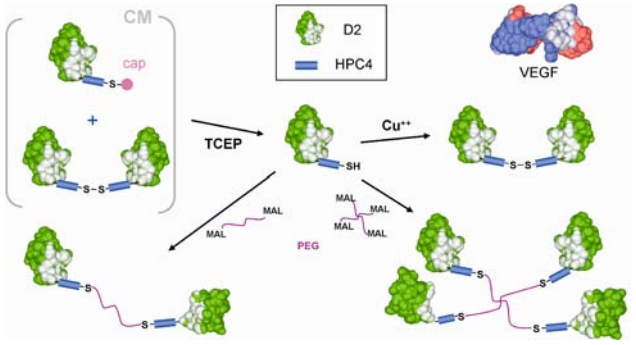

[a]CM: conditioned medium containing a mixture of capped monomer and disulfide-linked dimer forms. TCEP treatment reduces both the cap and linking disulfide to yield a free thiol form (center). Copper oxidizes the reduced product to produce a highly enriched dimer fraction without the use of SEC. Reaction of the free thiol form of the D2 with either 2-arm or 4-arm maleimide PEG yields PEG-linked dimers and tetramers, respectively. The structures of D2 and VEGF are taken from Weismann[14] and displayed at low resolution. The white patches indicate the interface residues identified in the crystal structure. The pink and blue portions of the VEGF indicate the two subunits. The structure of the HPC4 tag (blue rod) is unknown. The orientation of D2 bound to VEGF places the HPC4 tag linker structure on the bottom face of VEGF as shown. The size of the PEG is for representational purposes only.

sustained-release formulations for localized delivery, thus extending the application of these antiangiogenics to a broader range of indications such as osteoarthritis. In preliminary studies, we have found that these dimers demonstrate significantly greater stability than the sFLT01 Fc fusion to extended incubation, a stressor which mimics the effects of the depot formulation process (Li, unpublished results). In addition, conjugation to multivalent scaffolds may, through avidity effects, show superiority over dimeric constructs for neutralizing VEGF bound to extracellular matrix as illustrated by the higher-affinity binding to VEGF coupled to the dextran polymer on the chip surface. These multivalent scaffolds also provide a potential platform for the targeted delivery of VEGF antagonists through the co-conjugation of targeting moieties. A bispecific mAb with antiHer2 combined with an antiVEGF domain is currently in preclinical development.[20] However, the multiarm conjugation approach presented here could be superior by providing a second D2 domain to produce the high affinity of the bivalent interaction, and to more effectively sequester VEGF to a level below the EC_{50} for cell proliferation.

Requirement for Dimerization and the Effects of Spacers and the HPC4 Tag. Our results confirm previous indications[15] that the D2 sequence is sufficient to interact with VEGF165 with high affinity, but only in a dimer form that provides the ability to simultaneously interact with both binding faces in the VEGF homodimer. This conclusion was arrived at by the finding that both a linker element and a CH3 domain to provide for the formation of noncovalent dimers during expression of Fc fusion constructs were required for high-affinity binding to VEGF. By in vitro reconstruction, the present work directly demonstrates that physical linkage of two domains is required for a low picomolar EC_{50} interaction. Previously, the requirement for a linker element was inferred from molecules which lacked linkages showing either poor VEGF neutralizing activity or a substantial (~100-fold) reduction in binding.[15] We have extended these observations using synthetic spacers to examine the effect of increased distance between the D2. Only a modest effect of increasing the length of the spacer provided by the HPC4 tag to a 5 kDa PEG on VEGF binding was observed, suggesting that two disulfide-linked 13aa HPC4 tags in the dimer is sufficient to span the distance between the D2 C-termini when bound to VEGF and provide for a high-affinity interaction. The distance in the crystal structure between the C-termini of the two D2 in complex with a $VEGF_{8-109}$ homodimer (1flt) is ~55 Å [14] allowing for an additional unresolved terminal Thr in one chain, which could be easily spanned by the tag in fully extended form (80−90 Å at 3.4 Å/residue). The indistinguishable stability of VEGF complexes with sFLT01 and the HPC4 dimers as reflected in the rate of dissociation (Table 1) suggests that a significant interaction between either linker and VEGF is unlikely. However, the addition of a PEG spacer ($BM(PEG)_3$, 0.35 kDa) to the HPC4-dimer produced an increase in affinity by solution-phase assay or SPR, where the effect was seen due solely to a consequence of a faster rate of association. This is consistent with fewer degrees of freedom for binding VEGF for the molecule containing the disulfide bridge. Although only 55 Å separates the C-termini of D2 in the crystal structure, they are not in direct sight of each other. Thus, an increase in spacer length by PEG insertion may increase the probability of forming a bidentate complex when the linker is forced away from the VEGF surface. Model building to obtain a lowest-T_m-fold (Pep-Fold)[21] of the HPC4 tag suggests the peptide may form a relatively condensed structure and that its length may not be sufficient to permit the two D2 to simultaneously interact at their binding sites on the distal opposing faces of VEGF (not shown). However, the distance could be spanned by insertion of a small PEG (18 Å fully extended), even if the tag were partially folded. It is also worth noting that with the VEGF fragment the crystal structure, which lacked the C-terminal 56 amino acids of VEGF165, the C-terminus extends into the groove at the bottom face of the dimer and impinges on the path between the two D2 C-termini,[14] raising the possibility that this portion of VEGF165 could interfere with binding. A closer examination of the linker length dependence may be useful toward further understanding of the disposition of the two D2 in the complex.

Effect of PEG Size on Affinity. Surprisingly, an increase in the size of the PEG linker from 0.35 kDa to 5 kDa had a negligible further effect on binding as detected by SPR and only a slight decrease in the EC_{50} for solution binding (Table 1) in spite of a significant increase in the conjugate hydrodynamic radius (Figure 3). An increase in the spacer size beyond that necessary for high-affinity complex formation might also be expected to slow the rate of binding by lowering the probability of both D2 simultaneously interacting with the VEGF dimer, similar to the often-seen effect of PEGylation on binding other molecules. However, the stability of the initial complex of one D2 to a VEGF subunit, as seen with the D2 monomer−VEGF interaction (k_d = 0.02 s^{-1}; equivalent to $t_{1/2}$ = 35s; Table 1, Figure 4) is likely sufficient, as a consequence of the high local concentration of the second D2, to virtually guarantee the subsequent formation of the bidentate complex. Thus, even allowing for a substantial effect of PEG viscosity on the diffusion rate, the $t_{1/2}$ for binding of the second D2 could easily be so short as to produce a negligible effect of PEG size on either the observed rate of binding or EC_{50}. Alternatively, it is

dx.doi.org/10.1021/bc300301m | Bioconjugate Chem. 2012, 23, 2354−2364

possible that the D2 domains have a weak affinity for each other to form inactive complexes, for example, through a nonspecific interaction of their nearly flat hydrophobic VEGF-binding faces. PEG may solvate exposed hydrophobic residues, blocking the nonproductive interaction and thus effectively increasing the availability for binding VEGF. Longer PEGs would be more effective at this. However, since a longer PEG would also lower the availability for binding VEGF through steric hindrance, the combination of these factors may produce a negligible net effect with increasing PEG size. Of course, such a nonspecific interaction would be expected to strongly inhibit VEGF binding with shorter linkers such as BM(PEG)3 or the sFLT01 sequence, but below a certain size, the linkers may be too short to allow the D2 to freely interact in the most stable orientation. In the full receptors, Flt-1 and KDR, such interdomain interactions would be prevented by evolution of a higher-order structure for the receptor.

SPR vs Solution-Based Assays. The lack of an effect of PEG length in the dimers encouraged us to examine still larger PEG spacer, including HMW multiarm PEGs, which might also provide additional avidity effects. The increase in affinity for VEGF by the 4-arm PEG conjugates as measured by SPR (6- to 8-fold) was of the magnitude expected from the 6-fold increase in the number of pairs of D2 in the conjugate which are available for interaction with VEGF. However, all of the affinity increase was found to be due instead to a decrease in off-rate, unexpected for the binding of a single VEGF dimer by a pair of D2 domains since each VEGF homodimer can at most accommodate only two D2. It is likely that the higher affinity of these conjugates instead reflects the simultaneous binding of neighboring VEGF dimers on the chip. This is consistent with the observed drop in the apparent K_D with increasing VEGF density on the chip, which was more pronounced for conjugates with wider spacing between the D2 domains and completely absent for the D2 monomer. The largest effect was seen with the 20 kDa tetramer, where the stimulation was >10-fold with a 5-fold increase in VEGF density (Figure 7). As seen with the dimers, the affinities determined by SPR were typically ~100-fold lower than those measured by the solution-phase binding ELISA-based assay (Table 1). These data suggest that all of the contacts on the VEGF homodimer that are available in solution are not available when immobilized on a chip, perhaps due to interference of binding by the linkage to one of the two subunits. In this view, the much higher affinity in solution reflects the avidity associated with binding of both VEGF subunits by separate D2 domains in the conjugate, which is partially blocked in the case of immobilized VEGF. Consistent with this, in experiments where sFLT01 was bound to the chip surface and VEGF was in the mobile phase, a much higher affinity in the picomolar range was observed (data not shown). A similar effect on avidity as a consequence of ligand/receptor orientation has been reported for another dimeric molecule, TGFβ, where re-engineering the linkage to the chip replicated the high affinity associated with the naturally occurring binding to two separate receptor domains.[22] On the basis of the density of carboxylic acid groups on the dextran surface coating available for coupling D2, it is likely that a single bond links the VEGF dimer to the surface, leaving one unmodified subunit. Thus, binding of the monomeric D2 to VEGF by SPR may provide an accurate picture of the interaction of D2 with a single subunit of the VEGF dimer, and as expected, there was a complete absence of binding of monomer up to the highest concentration in the solution-phase assay (0.15 nM) consistent with the K_D observed by SPR (20nM). Thus, excluding the K_d values for the dimers and tetramers obtained by SPR as largely reflecting avidity for multiple surface-bound VEGF, the difference in affinities for the monomer vs the multimers is >4000-fold, strongly supporting the use of multimeric conjugates for the sequestration of low concentrations of VEGF.

Because of the restricted access to all of the VEGF contacts on the chip, SPR may be limited in its ability to detect any acceleration in binding compared to single VEGF homodimers as a consequence of the increase in D2 binding pairs such as in the 4-arm conjugates. However, the solution-phase assay also showed only a minor increase in affinity for these conjugates. It is likely that this assay significantly underestimates the actual affinity increase as a consequence of the extremely high affinities of the conjugates for VEGF. The limited sensitivity of the ELISA assay (~1 pM VEGF) required the use of VEGF concentrations close to and exceeding the EC_{50} of the VEGF binders. Under such conditions, the excess VEGF could deplete the available free binder to shift the equilibrium and observed EC_{50} upward from the actual K_D.[19] Consistent with this, preliminary results with a higher sensitivity assay permitting the use of lower VEGF concentrations yielded EC_{50} values for sFLT01 in the 1−2 pM range (data not shown).). Thus, the effect of multimerization on affinity may be underestimated by both assays. Nonetheless, for the purpose of reducing free VEGF levels, given the picomolar affinities of these constructs, binding of VEGF particularly by the PEG multimers may be considered to be nearly irreversible.

Thermal Stability of the Disulfide-linked Dimer. The similarly high affinity displayed by the low MW disulfide-linked dimer suggested a broader application of this synthetic approach to VEGF antagonism in applications such as localized delivery, where a reduction in systemic exposure would be desirable to minimize side effects. This issue would be particularly keen in the case of long-term administration of VEGF antagonists for indications such as OA pain. However, a major challenge for the development of sustained-release depot formulations has been protein stability, and success in the clinic has been reported only in a single instance of a low MW protein (<25 kDa),[23] but not with larger proteins. Indeed, our efforts to formulate the 80 kDa sFLT01 for sustained release have been complicated by fragmentation and loss of VEGF binding activity. A similar pattern of fragmentation was observed by extended incubation at elevated temperatures, that are similar to those used in forced degradation studies for biotherapeutics. Several lines of evidence indicate that this is not due to low-level protease contamination or deamidation, suggesting it may instead arise from stress on the D2 structure (Li et al., Genzyme Corporation, unpublished). It can be inferred from its greater thermal stability that the small disulfide-linked dimer may be better suited to these stresses of formulation as well as providing the long-term stability required for this application. This greater stability compared to sFLT01 is somewhat surprising considering the larger degrees of freedom expected for an unstructured glycine sequence as in sFLT01 compared to the HPC4 tag. The lesser effect of the VEGF surface density on binding the dimer by SPR (Figure 7) suggests that the D2 domains are effectively closer together than in sFLT01, even though this molecule shows a slightly lower apparent affinity for VEGF in solution. Thus, it is possible that the HPC4 tag partially interferes with the simultaneous binding of both D2 to the VEGF dimer subunits.

The tag may similarly constrain the hydrophobic D2 interfaces from interacting with each other in the absence of VEGF, an event which could distort the structure and make it prone to fragmentation. The site of fragmentation in D2 is close to the hydrophobic binding interface (not shown). Interestingly, PEGylation of sFLT01 was found to also increase its thermal stability (J.S., unpublished) suggesting that the PEG spacer elements such as employed in the multimeric conjugates described here may also provide additional benefit for the application of those molecules to such formulations.

CONCLUSIONS

These data demonstrate VEGF binders with equally high (pM) affinity as Fc receptor domain fusions can be obtained through disulfide linked dimerization and oligomerization of a minimal sequence Flt-1 D2 domain on PEG scaffolds. Higher affinities for binding VEGF bound to a biopolymer matrix were obtained through avidity effects achieved through multivalent conjugation of D2 to the termini of multiarm PEGs. These conjugates, particularly the 4-arm 20 kD PEG D2 tetramer with a total ~85 kDa, may possess sufficient hydrodynamic radius to display comparable PK/PD profile as existing VEGF antagonists that are Fc-based without the potential undesirable side effects associated with Fc-mediated effector function. The potential to co-conjugate targeting moieties may provide a means to generate targeted, high-affinity VEGF sequestering molecules to minimize possible side effects associated with systemic VEGF antagonism. In addition, the very small D2 homodimers (~35 kDa) linked through minimal-structure elements were shown to achieve similar high affinities but with greater thermal stability than the D2-Fc fusion (~80 kD). These novel conjugates may be more suitable for certain applications such as tissue penetration and sustained-release formulations.

ASSOCIATED CONTENT

Supporting Information

Additional figure. This material is available free of charge via the Internet at http://pubs.acs.org.

AUTHOR INFORMATION

Corresponding Author

*E-mail: jstefano@genzyme.com. Phone: 508-270-2271. Fax: 508-872-9080.

Notes

The authors declare the following competing financial interest(s): All authors except A.W.M.C and M.O. are employees of Genzyme Corporation.

ACKNOWLEDGMENTS

This study was in part supported by a scholarship to A.W.M.C. from the Osteoarthritis Research Society International. We would like to thank Dan Li and Jon Kingsbury for useful discussions and Bob Mattaliano for a critical reading of the manuscript.

ABBREVIATIONS

CV, column volume; PEG, poly(ethylene glycol); TCEP, *tris*-carboxyethylphosphine; PAGE, polyacrylamide gel electrophoresis; SPR, surface plasmon resonance

REFERENCES

(1) Connolly, D. T., Heuvelman, D. M., Nelson, R., Olander, J. V., Eppley, B. L., Delfino, J. J., Siegel, N. R., Leimgruber, R. M., and Feder, J. (1989) Tumor vascular permeability factor stimulates endothelial cell growth and angiogenesis. *J. Clin. Invest. 84*, 1470−8.

(2) Connolly, D. T., Olander, J. V., Heuvelman, D., Nelson, R., Monsell, R., Siegel, N., Haymore, B. L., Leimgruber, R., and Feder, J. (1989) Human vascular permeability factor. Isolation from U937 cells. *J. Biol. Chem. 264*, 20017−24.

(3) Harper, S. J., and Bates, D. O. (2008) VEGF-A splicing: the key to anti-angiogenic therapeutics? *Nat. Rev. Cancer 8*, 880−887.

(4) Robinson, C. J., and Stringer, S. E. (2001) The splice variants of vascular endothelial growth factor (VEGF) and their receptors. *J. Cell Sci. 114*, 853−65.

(5) Byrne, A. M., Bouchier-Hayes, D. J., and Harmey, J. H. (2005) Angiogenic and cell survival functions of vascular endothelial growth factor (VEGF). *J. Cell Mol. Med. 9*, 777−94.

(6) Gitay-Goren, H., Soker, S., Vlodavsky, I., and Neufeld, G. (1992) The binding of vascular endothelial growth factor to its receptors is dependent on cell surface-associated heparin-like molecules. *J. Biol. Chem. 267*, 6093−8.

(7) Fairbrother, W. J., Champe, M. A., Christinger, H. W., Keyt, B. A., and Starovasnik, M. A. (1998) Solution structure of the heparin-binding domain of vascular endothelial growth factor. *Structure 6*, 637−48.

(8) Keyt, B. A., Berleau, L. T., Nguyen, H. V., Chen, H., Heinsohn, H., Vandlen, R., and Ferrara, N. (1996) The carboxyl-terminal domain (111−165) of vascular endothelial growth factor is critical for its mitogenic potency. *J. Biol. Chem. 271*, 7788−95.

(9) Hiratsuka, S., Minowa, O., Kuno, J., Noda, T., and Shibuya, M. (1998) Flt-1 lacking the tyrosine kinase domain is sufficient for normal development and angiogenesis in mice. *Proc. Natl. Acad. Sci. U. S. A. 95*, 9349−54.

(10) Davis-Smyth, T., Chen, H., Park, J., Presta, L. G., and Ferrara, N. (1996) The second immunoglobulin-like domain of the VEGF tyrosine kinase receptor Flt-1 determines ligand binding and may initiate a signal transduction cascade. *EMBO J. 15*, 4919−27.

(11) Gerber, H. P., Kowalski, J., Sherman, D., Eberhard, D. A., and Ferrara, N. (2000) Complete inhibition of rhabdomyosarcoma xenograft growth and neovascularization requires blockade of both tumor and host vascular endothelial growth factor. *Cancer Res. 60*, 6253−8.

(12) Holash, J., Davis, S., Papadopoulos, N., Croll, S. D., Ho, L., Russell, M., Boland, P., Leidich, R., Hylton, D., Burova, E., Ioffe, E., Huang, T., Radziejewski, C., Bailey, K., Fandl, J. P., Daly, T., Wiegand, S. J., Yancopoulos, G. D., and Rudge, J. S. (2002) VEGF-Trap: a VEGF blocker with potent antitumor effects. *Proc. Natl. Acad. Sci. U. S. A. 99*, 11393−8.

(13) Ferrara, N., Chen, H., Davis-Smyth, T., Gerber, H. P., Nguyen, T. N., Peers, D., Chisholm, V., Hillan, K. J., and Schwall, R. H. (1998) Vascular endothelial growth factor is essential for corpus luteum angiogenesis. *Nat. Med. 4*, 336−40.

(14) Wiesmann, C., Fuh, G., Christinger, H. W., Eigenbrot, C., Wells, J. A., and de Vos, A. M. (1997) Crystal structure at 1.7 A resolution of VEGF in complex with domain 2 of the Flt-1 receptor. *Cell 91*, 695−704.

(15) Pechan, P., Rubin, H., Lukason, M., Ardinger, J., DuFresne, E., Hauswirth, W. W., Wadsworth, S. C., and Scaria, A. (2009) Novel anti-VEGF chimeric molecules delivered by AAV vectors for inhibition of retinal neovascularization. *Gene Ther. 16*, 10−6.

(16) Cohen, M. H., Gootenberg, J., Keegan, P., and Pazdur, R. (2007) FDA drug approval summary: bevacizumab (Avastin) plus Carboplatin and Paclitaxel as first-line treatment of advanced/metastatic recurrent nonsquamous non-small cell lung cancer. *Oncologist 12*, 713−8.

(17) Freeman, H. J. (2012) Colitis associated with biological agents. *World J. Gastroenterol. 18*, 1871−4.

(18) Walsh, D. A., McWilliams, D. F., Turley, M. J., Dixon, M. R., Franses, R. E., Mapp, P. I., and Wilson, D. (2010) Angiogenesis and

nerve growth factor at the osteochondral junction in rheumatoid arthritis and osteoarthritis. *Rheumatology (Oxford) 49*, 1852−61.
(19) Hulme, E. C., and Trevethick, M. A. (2010) Ligand binding assays at equilibrium: validation and interpretation. *Br. J. Pharmacol. 161*, 1219−37.
(20) Bostrom, J., Yu, S. F., Kan, D., Appleton, B. A., Lee, C. V., Billeci, K., Man, W., Peale, F., Ross, S., Wiesmann, C., and Fuh, G. (2009) Variants of the antibody herceptin that interact with HER2 and VEGF at the antigen binding site. *Science 323*, 1610−4.
(21) Maupetit, J., Derreumaux, P., and Tuffery, P. (2010) A fast method for large-scale de novo peptide and miniprotein structure prediction. *J. Comput. Chem. 31*, 726−38.
(22) De Crescenzo, G., Pham, P. L., Durocher, Y., and O'Connor-McCourt, M. D. (2003) Transforming growth factor-beta (TGF-beta) binding to the extracellular domain of the type II TGF-beta receptor: receptor capture on a biosensor surface using a new coiled-coil capture system demonstrates that avidity contributes significantly to high affinity binding. *J. Mol. Biol. 328*, 1173−83.
(23) Cleland, J. L., and Jones, A. J. (1996) Stable formulations of recombinant human growth hormone and interferon-gamma for microencapsulation in biodegradable microspheres. *Pharm. Res. 13*, 1464−75.

Supplemental Figures

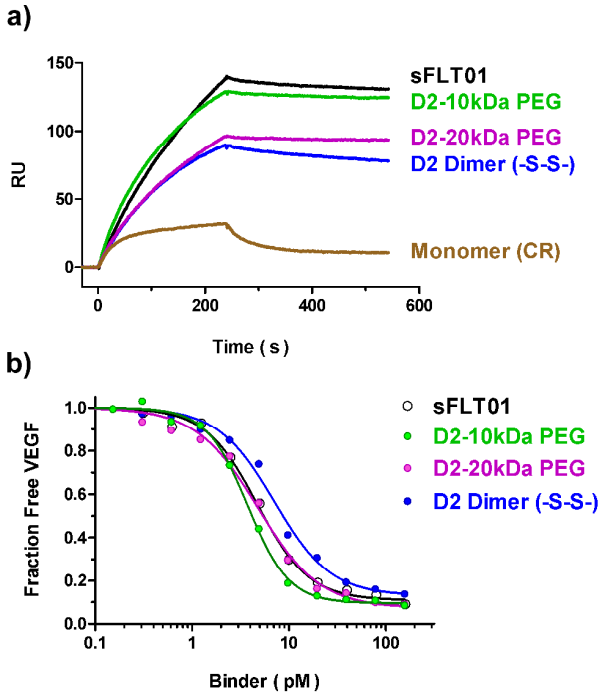

Fig. S1. Binding of 4-arm PEG conjugates to VEGF165. a) Biacore sensorgram of the binding reaction at 10nM ligand and 500RU VEGF coupled to the surface. b) VEGF ELISA of the same conjugates.

Bioconjugate Chemistry

Article

pubs.acs.org/bc

Modification of a Dioxygen Carrier, HemoCD, with PEGylated Dendrons for Extension of Circulation Time in the Bloodstream

Keiichi Karasugi, Hiroaki Kitagishi, and Koji Kano*

Department of Molecular Chemistry and Biochemistry, Doshisha University, Kyotanabe, Kyoto 610-0321, Japan

Supporting Information

ABSTRACT: A supramolecular diatomic receptor, hemoCD, was modified with PEGylated dendrons to extend its circulation time in the bloodstream. The core component was 4-oxo-4-[[4-(10,15,20-tris(4-sulfonatophenyl)-21*H*,23*H*-porphin-5-yl)phenyl]amino]butanoic acid (Por-COOH). The building block of the dendrons was Fmoc-4-amino-4-(2-carboxyethyl)heptanedioic acid (FmocTA), which was condensed with α-amino-ω-methoxy-poly(ethylene glycol) (PEG_{5000}-NH_2) to yield an FmocG1-dendron. After deprotection, the G1-dendron was condensed with Por-COOH to yield G1-Por. A precursor (FmocNA) of an FmocG2-dendron was prepared via a condensation reaction of 4-amino-4-(2-*t*-butoxycarbonylethyl)heptanedioic acid di-*t*-butyl ester (TA-E) with FmocTA followed by hydrolysis of the resultant nona-carboxylic acid nona-*t*-butyl ester. Condensation of FmocNA with PEG_{5000}-NH_2 yielded an FmocG2-dendron. After deprotection, the G2-dendron was condensed with Por-COOH to yield G2-Por. The ferrous complexes of G1- and G2-Pors formed stable 1:1 inclusion complexes with Py3CD, a per-*O*-methylated β-cyclodextrin dimer with a pyridine linker, in aqueous solution yielding supramolecular complexes designated as G1-hemoCD and G2-hemoCD, respectively. Both G1- and G2-hemoCDs bound molecular oxygen, with the O_2 affinities ($P_{1/2}$) of hemoCD, G1-, and G2-hemoCDs at pH 7.4 and 37 °C being 22, 20, and 20 Torr, respectively. The modification of hemoCD with the dendrons did not cause destabilization of the O_2 adducts via autoxidation, as indicated by their half-lives ($t_{1/2}$) of 6.8, 6.1, and 5.5 h for hemoCD, G1-, and G2-hemoCDs, respectively. The blood concentration−time curves of G1- and G2-hemoCDs injected into the bloodstream of rats exhibited two phases, with the half-lives of the fast and slow decays being 0.45 and 5.3 h, respectively, for G1-hemoCD, and 0.20 and 12.8 h, respectively, for G2-hemoCD. The half-lives of hemoCD were 0.02 and 0.50 h, respectively. The circulation time of hemoCD was markedly extended by its modification with the PEGylated dendrons, which was very effective in protecting hemoCD against opsonization for uptake by the reticuloendothelial system.

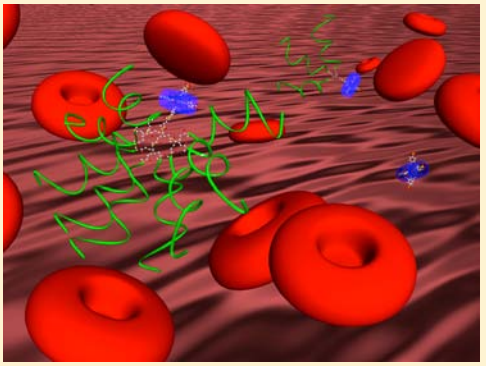

INTRODUCTION

The capturing of molecular oxygen (dioxygen) by metal complexes in aqueous solution is a fascinating research subject because of its functional similarity to hemoglobin (Hb), myoglobin (Mb), and hemocyanin.[1,2] Although many Hb/Mb model compounds have been prepared up to the present date, most receptors bind dioxygen only in organic solvents.[3] In aqueous solution, irreversible autoxidation of the O_2 adduct of a ferrous porphyrin occurs due to nucleophilic attack of H_2O to the Fe^{II}−O_2 bond, which makes it difficult to prepare a Hb/Mb model in aqueous solution.[4] This is the reason very few examples of Hb/Mb models in aqueous solution are known.[5] In the case of Hb or Mb, the Fe^{II}−O_2 bond is strengthened by electron donation from the proximal His residue coordinating to the Fe^{II} center of heme, and the O_2 adduct is stabilized by hydrogen bonding between the coordinated O_2 and the distal His residue. Such an O_2 binding phenomenon occurs in the heme pocket of the globin protein. It was previously predicted that an O_2 receptor that works in aqueous solution can be prepared if a ferrous porphyrin is placed in a hydrophobic environment to provide a nitrogenous ligand to the ferrous center. Such a prediction has been realized using a picket-fence porphyrin coordinated by 2-methylimidazole embedded in a phospholipid vesicle.[6] We also prepared a completely artificial dioxygen carrier, hemoCD, which is a 1:1 inclusion complex of 5,10,15,20-tetrakis(4-sulfonatophenyl)porphyrinatoiron(II) (Fe^{II}TPPS) with Py3CD (Figure 1).[7,8] Py3CD is a per-*O*-methylated β-cyclodextrin dimer whose cyclodextrin units are linked by a -SCH_2-Py-CH_2S- bond (-Py-: pyridine-3,5-diyl) at the 3- and 3′-positions of the cyclodextrin units. Py3CD is a substitute of the globin protein, and provides a hydrophobic environment around the ferrous center of Fe^{II}TPPS and an axial nitrogenous ligand (pyridine) to Fe^{II}. Moreover, Py3CD inhibits the formation of a μ-oxo-dimer of Fe^{III}TPPS, which is an undesirable species for O_2 adduct formation. The O_2 affinity ($P_{1/2}$) represented by the O_2 partial pressure at which half of the hemoCD molecules are oxygenated is 10 Torr at 25 °C.[9] Oxy-hemoCD is gradually autoxidized to ferric hemoCD (met-hemoCD) with a half-life ($t_{1/2}$) of 30 h.[7] If other factors such as the binding of biologically important diatomic molecules,

Received: June 8, 2012
Revised: October 17, 2012
Published: November 8, 2012

ACS Publications © 2012 American Chemical Society

dx.doi.org/10.1021/bc300303z | *Bioconjugate Chem.* 2012, 23, 2365−2376

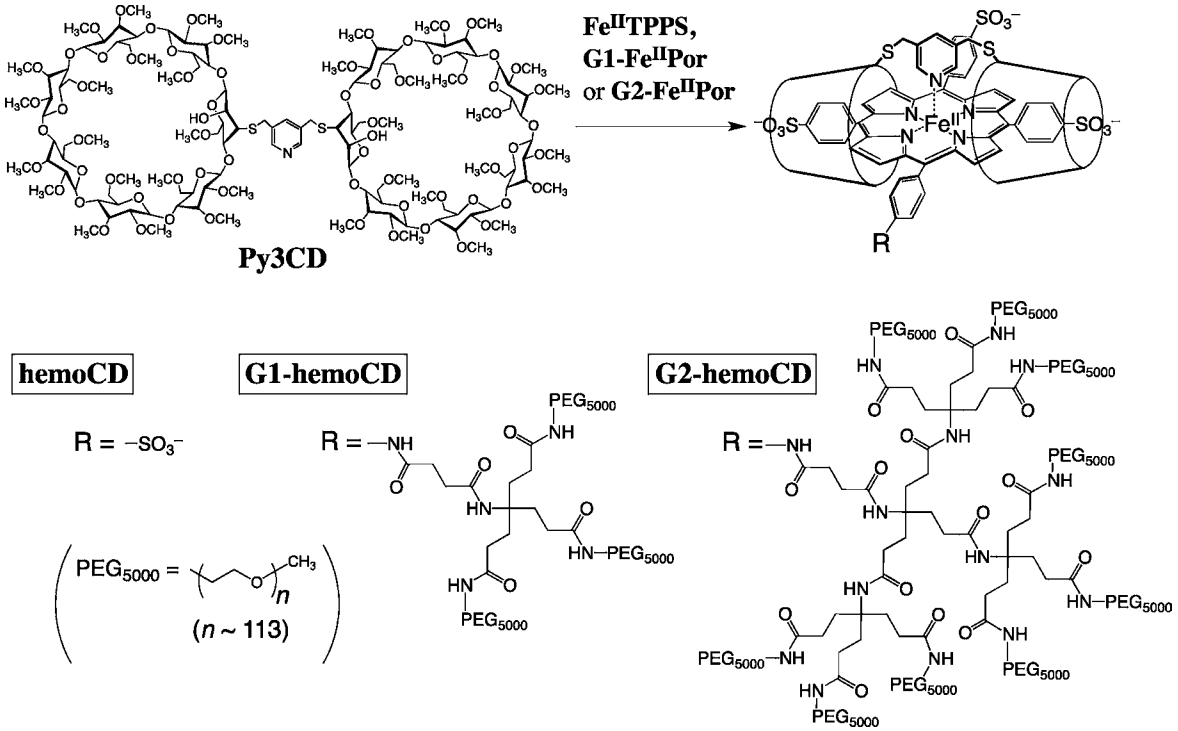

Figure 1. Structures of Py3CD, hemoCD, G1-hemoCD, and G2-hemoCD.

including carbon monoxide and nitric monoxide, to hemoCD are disregarded, hemoCD is a promising candidate for a red blood cell substitute. A previous study, however, revealed that hemoCD injected into the femoral vein of rats is rapidly excreted in the urine because of its small molecular size.[10] To prevent renal clearance, we attached hemoCD to poly(acrylic acid)[11] and on the surface of PEGylated gold nanoparticles.[12] Indeed, the macromolecularization of hemoCD makes its renal filtration unlikely. However, these hemoCD macromolecules are thought to accumulate in organs such as the liver and spleen. We confirmed that the hemoCD-embedded gold nanoparticles were trapped in the liver and spleen of rats.[12] It is known that polyanionic molecules are selectively taken up by nonparenchymal cells of the liver.[13] In the present study, we examined the effects of modification of hemoCD with PEGylated dendrons on the circulation of the O_2 carrier in the bloodstream of rats. Benefits of the modification with PEGylated dendrons are as follows:[14−16] (1) Structurally well-defined macromolecularization of hemoCD can be easily achieved. The size of the O_2 carrier can be controlled by changing the generation of the dendron. (2) Many poly(ethylene glycol) (PEG) chains can be simultaneously attached to a hemoCD molecule. The PEGylation is very important to protect hemoCD from interactions with proteins, uptake by organs such as the liver and spleen, and prevent antibody production.

Several studies on dendrimer-type O_2 receptors have been reported. Li and Aida used a fourth-generation (G4) poly(benzyl ether) dendrimer with an iron porphyrin core as an O_2 receptor.[17,18] The ferrous porphyrin dendrimer whose axial ligand is 1-methylimidazole reversibly binds O_2 in toluene and wet toluene. The half-life of the O_2 adduct is over 2 months, indicating a remarkable effect of the dendrimer on stabilization of the ferrous porphyrin-O_2 adduct. Unfortunately, however, this dendrimer is not soluble in water. Diederich et al. prepared G1 and G2 poly(ethylene glycol amide) dendrimers containing a ferrous porphyrin core.[19,20] The O_2 affinity of the G2 dendrimer in toluene is ca. 1500-fold higher than that of Hb in the T state. Such a high O_2 affinity and high stability of the O_2 adduct were explained in terms of tight packing of the dendrimer chains in toluene.[21] In the presence of H_2O, however, the chain packing becomes loose, leading to remarkable destabilization of the O_2 adduct. The preceding studies suggest that a water-soluble dendritic Hb/Mb model is very difficult to prepare. The present study revealed that such difficulty can be overcome by including a dendritic iron porphyrin with Py3CD. More importantly, macromolecularization of hemoCD with PEGylated dendrons extends the circulation time of the O_2 carrier in the bloodstream of rats.

■ EXPERIMENTAL PROCEDURES

Instruments. UV−vis spectra were recorded on Shimadzu UV-2100 and UV-2450 spectrophotometers equipped with thermostatic cell holders. Fluorescence spectra were recorded on a Shimadzu RF-5300PC spectrofluorometer. The pH values were measured with a Horiba pH meter M-12. ^{1}H NMR spectra were recorded on JEOL JNM-ECA 500 and JEOL JNM-A400 spectrometers using TMS as an internal standard. Matrix-assisted laser desorption-ionization time-of-flight mass (MALDI-TOF-MS) spectra were recorded on a Bruker Daltonics autoflex speed system. The mass scale was calibrated by linear regression using 2,3,6-tri-*O*-methyl-β-cyclodextrin (Nakalai, m/z = 1429.56 for monoisotropic mass of $[M+Na]^+$), cytochrome *c* (Sigma-Aldrich, m/z = 12361.96 for average mass of $[M+Na]^+$), and albumin from bovine serum (Sigma-Aldrich, m/z = 66430 for average mass of $[M+Na]^+$). Gel filtration chromatography (GFC) analyses were performed using a Superdex 200 10/300 GL column (1 × 30 cm) attached to an ÄKTA purifier FPLC system (GE Healthcare). Mixed O_2

dx.doi.org/10.1021/bc300303z | *Bioconjugate Chem.* 2012, 23, 2365−2376

gases with various partial pressures in N_2 were prepared with a KOFLOC GM-4B gas mixing apparatus.

Materials. α-Amino-ω-methoxy-poly(ethylene glycol) (PEG_{5000}-NH_2, average molecular weight = 5000),[22] 5-(4-aminophenyl)-10,15,20-tris(4-sulfonatophenyl)porphyrin tris(tetrabutylammonium) salt (NH_2-TPPS·TBA),[12,23] and Py3CD[7] (Figure 1) were synthesized according to the procedures described in the literature. Other chemicals were purchased and used as received. Water was purified using a Millipore Simpak 1. Pure O_2 (99.999%), N_2 (99.999%), and CO (99.9%) gases were purchased from Sumitomo Seika Chemicals.

Fmoc-4-amino-4-(2-carboxyethyl)heptanedioic acid (FmocTA). A mixture of 4-amino-4-(2-*t*-butoxycarbonylethyl)-heptanedioic acid di-*t*-butyl ester (TA-E, 500 mg, 1.20 mmol) and *N*,*N*-diisopropylethylamine (DIPEA, 0.70 mL, 3.97 mmol) in dichloromethane (2 mL) was cooled in an ice-bath, and then 9-fluorenylmethyl chloroformate (341 mg, 1.32 mmol) was added to the mixture. After stirring for 30 min, the ice bath was removed and the reaction mixture was warmed to room temperature. After 4 h, the reaction mixture was washed with saturated aqueous $NaHCO_3$ (3 × 100 mL). After drying over anhydrous Na_2SO_4, the solvent was evaporated and the residual crude product was purified by flash chromatography using a gradient elution of chloroform to 5% methanolic chloroform. FmocTA-E was obtained as a colorless solid (700 mg, 91%): ^{1}H NMR (500 MHz, $CDCl_3$) δ 1.42 (s, 27H, CH_3), 1.91 (m, 6H, CH_2), 2.20 (m, 6H, CH_2), 4.19 (t, J = 7.5 Hz, 1H, FmocCH), 4.36 (m, 2H, CH_2), 7.32 (t, J = 7.5 Hz, 2H, FmocArCH), 7.39 (t, J = 7.5 Hz, 2H, FmocArCH), 7.58 (d, J = 7.5 Hz, 2H, FmocArCH), 7.76 (d, J = 7.5 Hz, 2H, FmocArCH); MS (MALDI-TOF, α-CHCA) m/z calcd for $C_{37}H_{51}NNaO_8$ $[M + Na]^+$: 660.8, found: 660.5.

FmocTA-E (350 mg, 0.55 mmol) was dissolved in 6 mL of formic acid and stirred overnight to achieve deprotection of FmocTA-E and obtain FmocTA. Formic acid was removed by evaporation. The residue was transferred to toluene, followed by evaporation of toluene in vacuo to remove residual formic acid. The same procedure was repeated once, and the product (FmocTA) was finally dried under vacuum (253 mg, 98%): ^{1}H NMR (400 MHz, DMSO-d_6) δ 1.80 (m, 6H, CH_2), 2.21 (m, 6H, CH_2), 4.20 (m, 3H, CH_2 + FmocCH), 7.32 (t, J = 7.5 Hz, 2H, FmocArCH), 7.41 (t, J = 7.5 Hz, 2H, FmocArCH), 7.71 (d, J = 7.5 Hz, 2H, FmocArCH), 7.88 (d, J = 7.5 Hz, 2H, FmocArCH); MS (MALDI-TOF, α-CHCA) m/z calcd for $C_{25}H_{27}NNaO_8$ $[M + Na]^+$: 492.5, found: 492.3.

G1-dendron. FmocTA (150 mg, 0.32 mmol) and 1-[bis(dimethylamino)methylene]-1*H*-1,2,3-triazolo[4,5-*b*]-pyridinium 3-oxide hexafluorophosphate (HATU, 487 mg, 1.28 mmol) were dissolved in 50 mL of dry DMF. DIPEA (0.45 mL, 2.56 mmol) and PEG_{5000}-NH_2 (average molecular weight = 5000, 7.20 g, ca. 1.44 mmol) were successively added. The solution was stirred at room temperature for 24 h. Then, the reaction mixture was poured into 500 mL of diethyl ether and the precipitate was filtered. The resultant residue was dried under vacuum. The crude product was purified by flash chromatography using a gradient elution of chloroform to 10% methanolic chloroform. FmocG1-dendron was obtained as a colorless solid (3.96 g, 80%): ^{1}H NMR (500 MHz, $CDCl_3$) δ 1.91 (m, 6H, CH_2), 2.20 (m, 6H, CH_2), 3.38 (s, 9H, OCH_3), 3.51−3.83 (m, PEG backbone), 4.19 (t, J = 7.5 Hz, 1H, FmocCH), 4.37 (m, 2H, CH_2), 7.32 (t, J = 7.5 Hz, 2H, FmocArCH), 7.40 (t, J = 7.5 Hz, 2H, FmocArCH), 7.75 (d, J = 7.5 Hz, 2H, FmocArCH), 7.77 (d, J = 7.5 Hz, 2H, FmocArCH).

A solution of FmocG1-dendron (4.00 g, 0.26 mmol) in 20% (v/v) piperidine/dichloromethane (20 mL) was stirred at room temperature for 1 h. The reaction mixture was concentrated by evaporation to yield crude G1-dendron, which was purified by flash chromatography using a gradient elution of chloroform to 10% methanolic chloroform. G1-dendron was obtained as a colorless solid (3.64 g, 92%): ^{1}H NMR (400 MHz, $CDCl_3$) δ 1.91 (m, 6H, CH_2), 2.37 (m, 6H, CH_2), 3.38 (s, 9H, OCH_3), 3.51−3.83 (m, PEG backbone); MALDI-TOF-MS spectrum is shown in the Supporting Information (Figure S1a).

G1-Por. To a solution of 5-(4-aminophenyl)-10,15,20-tris(4-sulfonatophenyl)porphyrin tris(tetrabutylammonium) salt (NH_2-TPPS·TBA) (89.6 mg, 51.7 μmol) in CH_3CN (20 mL), succinic anhydride (7.76 mg, 77.5 μmol) was added, and the mixture was stirred for 12 h at 80 °C. The reaction mixture was evaporated in vacuo and the residue was diluted with MeOH. The methanolic solution was poured into 200 mL of diethyl ether (a poor solvent) and the precipitate was filtered. The resultant residue was dried under vacuum. An aqueous solution of the crude product was passed through an ion-exchange column with DOWEX MARATHON C-10 Cation Exchange Resin (Na-form). Water was evaporated from the eluate. The residual purple solid (Por-COOH) was dissolved in 10 mL of dry DMF. To the solution was added G1-dendron (524 mg, 34.4 μmol) and HATU (29.5 mg, 77.6 μmol); DIPEA (81.2 μL, 466 μmol) was successively added. The mixture was stirred at room temperature for 24 h. The reaction mixture was poured into 200 mL of diethyl ether and the precipitate was filtered. The resultant residue was dried under vacuum. Crude G1-Por was purified by gel filtration on Sephadex G-25 (fine). The title compound was obtained as a purple solid (504 mg, 90%): ^{1}H NMR (500 MHz, DMSO-d_6) δ 1.80−1.90 (m, 6H, CH_2), 2.08−2.10 (m, 6H, CH_2), 3.38 (s, 9H, OCH_3), 3.51−3.83 (m, PEG backbone), 8.03 (m, 8H, phenyl), 8.14 (m, 8H, phenyl), 8.88 (m, 8H, pyrrol); UV−vis (0.05 M phosphate buffer at pH 7.4) λ_{max} 418, 514, 550, 588, 643 nm; MALDI-TOF-MS spectrum is shown in the Supporting Information (Figure S1b).

4-Fmoc-amino-4-(3-oxo-3-((1,5-dicarboxy-3-(2-carboxyethyl)pentan-3-yl)amino)propyl)-*N*^{1},*N*^{7}-bis(1,5-dicarboxy-3-(2-carboxyethyl)pentan-3-yl)-heptanediamide (FmocNA). To a solution of FmocTA (150 mg, 0.32 mmol) in dry DMF (5 mL), 1-hydroxybenzotriazole (HOBt) monohydrate (147 mg, 0.96 mmol), *N*,*N*′-dicyclohexylcarbodiimide (DCC, 198 mg, 0.96 mmol), and TA-E (399 mg, 0.96 mmol) were added sequentially. The solution was stirred at room temperature for 48 h. The reaction mixture was filtered and the filtrate was evaporated in vacuo. The crude product was purified by flash column chromatography using a gradient elution of chloroform to chloroform containing 2.5% MeOH to yield the Fmoc-amino nona-acid-*t*-butyl ester (FmocNA-E, 484 mg, 91%): ^{1}H NMR (400 MHz, $CDCl_3$) δ 1.42 (s, 81H, CH_3), 1.91 (m, 24H, CH_2), 2.20 (m, 24H, CH_2), 4.19 (t, J = 7.5 Hz, 1H, FmocCH), 4.36 (m, 2H, CH_2), 7.32 (t, J = 7.5 Hz, 2H, FmocArCH), 7.39 (t, J = 7.5 Hz, 2H, FmocArCH), 7.58 (d, J = 7.5 Hz, 2H, FmocArCH), 7.76 (d, J = 7.5 Hz, 2H, FmocArCH); MS (MALDI-TOF, α-CHCA) m/z calcd for $C_{91}H_{144}N_4NaO_{23}$ $[M + Na]^+$: 1685.1, found: 1685.0.

FmocNA-E (216 mg, 0.13 mmol) was dissolved in 5 mL of formic acid and stirred for 12 h to obtain Fmoc-amino nona-acid (FmocNA). After completion of the reaction, formic acid

dx.doi.org/10.1021/bc300303z | *Bioconjugate Chem.* 2012, 23, 2365−2376

was removed in vacuo and the residue was dissolved in toluene. Toluene was evaporated to remove residual formic acid. The same procedure was repeated once, and the product (FmocNA) was finally dried under vacuum (150 mg, quant): ^{1}H NMR (400 MHz, DMSO-d_6) δ 1.84 (m, 24H, CH_2), 2.12 (m, 24H, CH_2), 4.18 (m, 3H, CH_2 + FmocCH), 7.00 (bs, 1H, NH), 7.38 (t, J = 7.5 Hz, 2H, FmocArCH), 7.40 (t, J = 7.5 Hz, 2H, FmocArCH), 7.76 (d, J = 7.5 Hz, 2H, FmocArCH), 7.85 (d, J = 7.5 Hz, 2H, FmocArCH); MS (MALDI-TOF, α-CHCA) m/z calcd for $C_{55}H_{72}N_4NaO_{23}$ $[M + Na]^+$: 1180.2, found: 1180.0.

G2-dendron. To a solution of FmocNA (174 mg, 0.15 mmol) in dry DMF (55 mL), HOBt monohydrate (414 mg, 2.70 mmol), DCC (557 mg, 2.70 mmol), and PEG-NH_2 (average molecular weight = 5000, 13.2 g, ca. 2.70 mmol) were added sequentially. The solution was stirred at room temperature for 72 h. The reaction mixture was filtered and concentrated in vacuo. The crude FmocG2 dendron was purified by flash column chromatography using a gradient elution of chloroform to 3.3% methanolic chloroform to yield FmocG2-dendron as a colorless solid (3.46 g, 50%): ^{1}H NMR (400 MHz, $CDCl_3$) δ 1.91 (m, 24H, CH_2), 2.20 (m, 24H, CH_2), 3.38 (s, 27H, OCH_3), 3.45−3.83 (m, PEG backbone), 4.19 (m, 1H, FmocCH), 4.37 (m, 2H, CH_2), 7.32−7.39 (m, 4H, FmocArCH), 7.58 (d, J = 7.5 Hz, 2H, FmocArCH), 7.74 (d, J = 7.5 Hz, 2H, FmocArCH).

A solution of FmocG2-dendron (2.68 g, 58.0 μmol) in 20% (v/v) piperidine/dichloromethane (20 mL) was stirred at room temperature for 1 h. The reaction mixture was concentrated in vacuo and the residue was purified by flash chromatography using a gradient elution of chloroform to 3.3% methanolic chloroform. G2-dendron was obtained as a colorless solid (2.61 g, 98%): ^{1}H NMR (400 MHz, $CDCl_3$) δ 2.40−2.80 (m, 48H, CH_2), 3.38 (s, 27H, OCH_3), 3.45−3.83 (m, PEG backbone); MALDI-TOF-MS spectrum is shown in the Supporting Information (Figure S2a).

G2-Por. To a solution of NH_2-TPPS·TBA (135 mg, 78 μmol) in CH_3CN (20 mL), succinic anhydride (11.7 mg, 117 μmol) was added and the solution was stirred for 12 h at 80 °C. The solvent of the reaction mixture was evaporated and the residue was diluted with MeOH. The methanolic solution was poured into 200 mL of diethyl ether and the precipitate was filtered. The resultant residue was dried under vacuum. An aqueous solution of the crude product was passed through an ion-exchange column with DOWEX MARATHON C-10 Cation Exchange Resin (Na-form). Water was evaporated from the eluate. The resultant purple solid (Por-COOH) was dried under high vacuum. Por-COOH was dissolved in 10 mL of dry DMF. G2-dendron (716 mg, 15.6 μmol) and HATU (45.0 mg, 117 μmol) were successively added to the solution, followed by the addition of DIPEA (104 μL, 597 μmol). The resultant solution was stirred at room temperature for 24 h. The reaction mixture was poured into 200 mL of diethyl ether and the precipitate was filtered. The resultant residue was dried under vacuum. Crude G2-Por was purified by gel-filtration on Sephadex G-25 (fine). G2-Por was obtained as a purple solid (652 mg, 89%): ^{1}H NMR (500 MHz, DMSO-d_6) δ 1.80−2.02 (m, 48H, CH_2), 3.25 (s, 27H, OCH_3), 3.51−3.83 (m, PEG backbone), 8.04 (m, 8H, phenyl), 8.15 (m, 8H, phenyl), 8.84 (m, 8H, pyrrol); UV−vis (0.05 M phosphate buffer at pH 7.4) λ_{max} 418, 514, 550, 588, 643 nm; MALDI-TOF-MS spectrum is shown in the Supporting Information (Figure S2b).

G1-Fe^{III}Por. G1-Por (440 mg, 26.8 μmol) was dissolved in 20 mL of dichloromethane and the solution was refluxed. A saturated methanolic solution of $FeCl_2·4H_2O$ (0.54 g, 2.7 mmol) was added to the G1-Por solution and refluxed for 1 h. The progress of the reaction was monitored by fluorescence spectroscopy. After the fluorescence originating from the free-base porphyrin completely disappeared, the solvent was removed under reduced pressure and the crude product was dissolved in distilled water. Aqueous ammonia (28%) was added to the crude product solution until the appearance of the inorganic salt precipitate, followed by filtration of the precipitate. Water was removed from the filtrate under reduced pressure and the residue was dissolved in distilled water. The aqueous solution was passed through a column of DOWEX MARATHON C-10 Cation Exchange Resin (Na-form). Evaporation of water from the eluate and high-vacuum drying of the resultant solid yielded a purple solid. The crude product was further purified by gel filtration on Sephadex G-25 (fine) followed by dialysis against water for 8 h. G1-Fe^{III}Por was obtained as a purple solid (400 mg, 91%): UV−vis (0.05 M phosphate buffer at pH 7.4) λ_{max} 314, 410, 570, 613 nm; MALDI-TOF-MS spectrum is shown in the Supporting Information (Figure S1c).

G2-Fe^{III}Por. G2-Por (705 mg, 15.0 μmol) was dissolved in 32 mL of dichloromethane and the solution was refluxed. A saturated methanolic solution (5 mL) of $FeCl_2·4H_2O$ (0.30 g, 1.5 mmol) was added to the G2-Por solution and refluxed for 1 h. The subsequent procedures were the same as those for the preparation of G1-Fe^{III}Por. The title compound was obtained as a purple solid (649 mg, 92%): UV−vis (0.05 M phosphate buffer at pH 7.4) λ_{max} 330, 417, 570 nm; MALDI-TOF-MS spectrum is shown in the Supporting Information (Figure S2c).

Animal Experiments. The animal experiments were performed in accordance with the Guidelines for Animal Experiments of Doshisha University. Male Wistar rats (SLC, Shizuoka, Japan) weighing 250−410 g were used. The rats were housed 3 per cage under controlled environmental conditions and fed commercial pelleted feed. All rats had free access to food and water.

Test solutions containing the O_2 adduct of hemoCD, G1-hemoCD, or G2-hemoCD in phosphate buffer saline (PBS) were prepared as follows. A met-hemoCD derivative (1:1 complex of Fe^{III}TPPS, G1-Fe^{III}Por, or G2-Fe^{III}Por with Py3CD) in PBS ([iron porphyrin]/[Py3CD] = 1/1.2) was reduced using $Na_2S_2O_4$ to form the ferrous state. The resultant solution was passed through a Sephadex G25 desalting column (GE Healthcare) to remove excess $Na_2S_2O_4$ and its oxidized derivatives. During this procedure, the hemoCD derivative bound O_2 from an aerobic source to form the O_2 adduct. The eluate was collected and appropriately diluted with PBS. The concentration was estimated from the extinction coefficient of oxy-hemoCD (ε = 1.64 × 10^5 M^{-1} cm^{-1} at 423 nm).[9]

Rats were placed under anesthesia with an intraperitoneal injection of urethane (1.0 g kg^{-1}). A cannula (tube) was surgically implanted in the urinary bladder of the rat to collect urine samples. The test solution ([oxy-hemoCD derivative] = 3.0 × 10^{-4} M, 1 mL) was infused into the femoral vein at a rate of 0.1 mL/min. Urine was collected at 30 min intervals from the initiation of infusion. At the end of each urine collection period, the bladder was flushed with approximately 1 mL of saline and the effluent was added to the urine collected over that interval. Urine samples containing the hemoCD derivative were mixed with $Na_2S_2O_4$ under a carbon monoxide (CO)

Scheme 1[a]

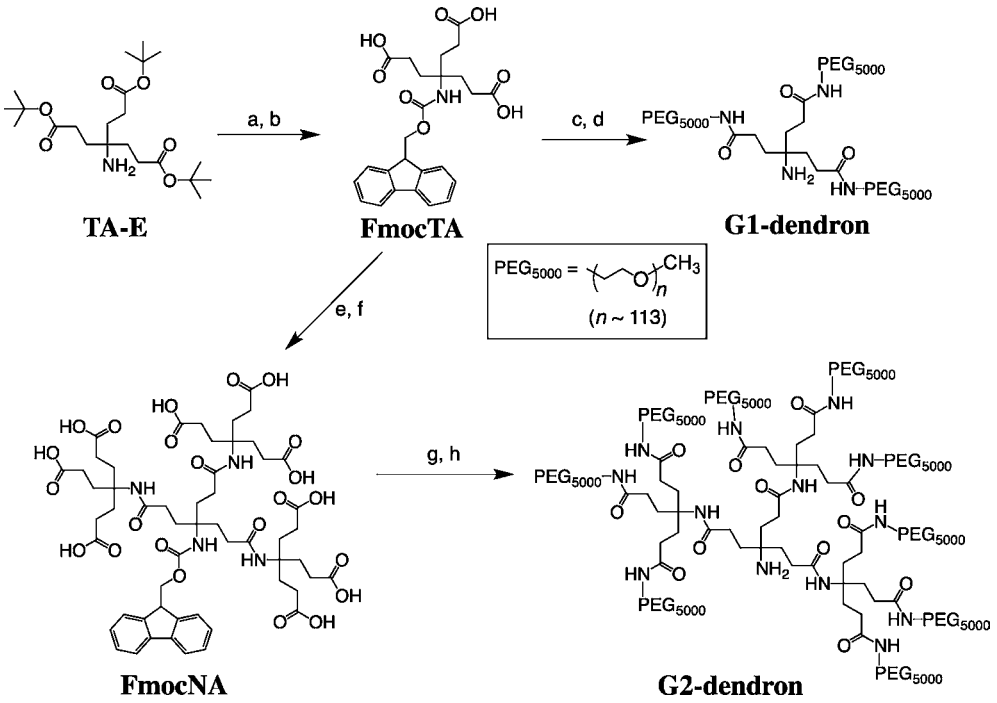

[a]Reaction conditions: (a) FmocCl, DIPEA, CH_2Cl_2, rt, 4 h (91%); (b) formic acid, rt, overnight (98%); (c) PEG_{5000}-NH_2, HATU, DIPEA, DMF, rt, 24 h (80%); (d) piperidine, CH_2Cl_2, rt, 1 h (92%); (e) TA-E, DCC, HOBt, DMF, rt, 48 h (91%); (f) formic acid, rt, overnight (quant); (g) PEG_{5000}-NH_2, DCC, HOBt, DMF, rt, 72 h (50%); (h) piperidine, CH_2Cl_2, rt, 1 h (98%).

atmosphere to convert all the iron porphyrins in the urine to the ferrous CO adduct. The samples were then analyzed by UV−vis spectroscopy and the total amount of hemoCD derivative in the urine samples was quantified using the extinction coefficient of CO-hemoCD (3.71×10^5 M^{-1} cm^{-1} at 422 nm).[9]

To determine the clearance rate of the infused hemoCD derivative, blood samples (250 μL each) were collected from the jugular vein of the rats using a silicon catheter with heparin at 0, 5, 10, 15, 30, 60, 180, and 360 min after the bolus injection of the O_2 adduct of hemoCD, G1-hemoCD, or G2-hemoCD in PBS (3.0×10^{-3} M, 1 mL) into the femoral vein. From each blood sample, 100 μL of plasma was separated by centrifugation. In the case of hemoCD, methanol (50 μL) was added to the plasma to precipitate serum proteins. After removal of the proteins by centrifugation, 100 μL of supernatant was diluted to 1 mL with PBS. In the cases of G1- and G2-hemoCDs, dichloromethane (100 μL) was added to the plasma. The mixture was vortexed well and then centrifuged. The organic layer containing Gn-FePor and Py3CD was evaporated to dryness using nitrogen flow. The residue was dissolved in 1 mL of PBS. The resultant PBS solution was mixed with $Na_2S_2O_4$ after introducing CO gas into the solution to transform all the iron porphyrins into ferrous CO complexes. The solution was analyzed by GFC. The results of the GFC were quantified using calibration curves for the CO adducts of the hemoCD derivatives. The total amount of hemoCD derivatives remaining in the bloodstream of rats was calculated based on the assumption that the circulation blood volume in rats is 50−70 mL/kg.[24]

Cytotoxicity. HeLa cells purchased from the RIKEN Cell Bank were maintained in D-MEM containing 10% fetal bovine serum (FBS) and 1% penicillin/streptomycin at 37 °C under a humidified atmosphere of 5% CO_2. A total of 10^4 cells in 100 μL of medium was transferred to a 96-well plate and allowed to grow overnight. The loading medium was replaced with the new medium containing met-hemoCD, G1-met-hemoCD, or G2-met-hemoCD ([iron porphyrin] = 5.0×10^{-5} M; [Py3CD] = 6.0×10^{-5} M). After 16 h incubation, the medium was removed and the cell viability was measured using MTT (3-[4,5-dimethylthiazol-2-yl]-2,5-diphenyltetrazolium bromide) Cell Proliferation Assay Kit (Cayman Chemical), according to the manufacturer's protocol. Cells incubated without met-hemoCD derivatives served as the control for 100% viability.

RESULTS AND DISCUSSION

Synthesis and Characterization of G1- and G2-Fe^{III}Pors. The synthetic routes to G1- and G2-Fe^{III}Pors are shown in Schemes 1 and 2. A key compound was Behera's amine (TA-E), whose amino group was protected by an Fmoc group. FmocTA-E was converted to free triacid (FmocTA) using Newkome's method.[25] FmocTA was condensed with PEG_{5000}-NH_2 (average molecular weight (MW) = 5000) using HATU as a coupling reagent and DIPEA as a base to obtain FmocG1-dendron.[26] Deprotection of FmocG1-dendron using a routine method yielded G1-dendron.

The reaction of TA-E with FmocTA was carried out according to a previously published method[27] to obtain Fmoc-protected nona-acid ester (FmocNA-E), whose ester groups were decomposed by formic acid[25] to yield Fmoc-protected nona-acid (FmocNA). FmocNA was reacted with PEG_{5000}-NH_2 using the same method as that for FmocTA to obtain FmocG2-dendron. Deprotection of FmocG2-dendron yielded G2-dendron.

Condensation reactions of G1- and G2-dendrons with Por-COOH in DMF in the presence of HATU and DIPEA yielded

dx.doi.org/10.1021/bc300303z | Bioconjugate Chem. 2012, 23, 2365−2376

Scheme 2[a]

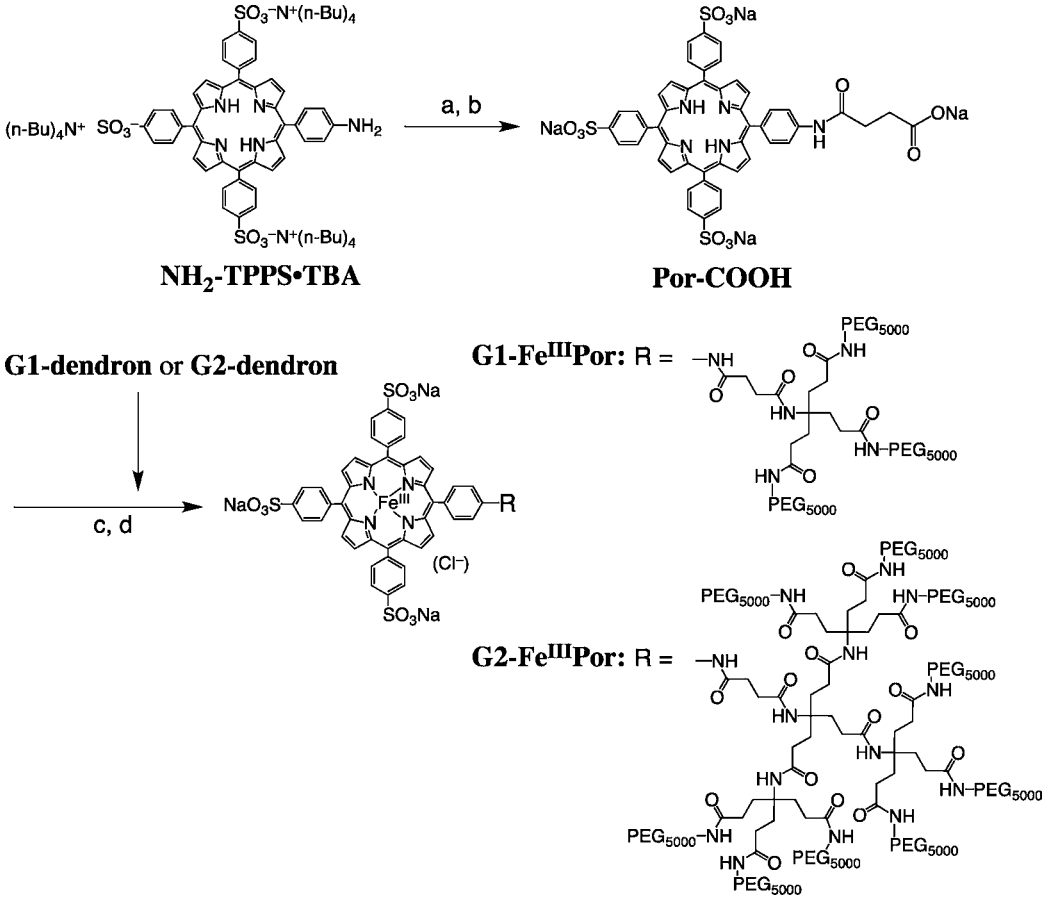

[a]Reaction conditions: (a) succinic anhydride, CH_3CN, 80 °C, 12 h; (b) ion exchange (Na-form); (c) G1- or G2-dendron, HATU, DIPEA, DMF, rt, 24 h (90% for G1, 89% for G2); (d) $FeCl_2{\cdot}4H_2O$, CH_2Cl_2/CH_3OH, reflux, 1 h (91% for G1, 92% for G2).

G1-Por and G2-Por, respectively. G1- and G2-Pors were purified by gel-filtration using Sephadex G25 column. The formation of G1- and G2-Pors was confirmed by ^{1}H NMR spectroscopy.[28] In the case of G1-Por, the signals attributed to the β-pyrrole protons were observed at around 8.9 ppm (8H). The singlet signal from the OCH_3 protons (9H) of the terminal groups of the PEG chains at 3.8 ppm was the best criterion to evaluate whether the 3 PEG chains were correctly attached to the porphyrin core. The area ratio of the signal of the OCH_3 protons to that of the β-pyrrole protons clearly indicated that the final product was the targeted material. The formation of G2-Por was similarly verified.

A ferric ion was introduced into G1- or G2-Por via an ordinary method using $FeCl_2{\cdot}4H_2O$ in chloroform/methanol. Purification was achieved by ion-exchange column chromatography, gel filtration using Sephadex G25 column, and dialysis. The results of analytical GFC of G1- and G2-Fe^{III}Pors are shown in Figure 2. The eluent was 0.05 M phosphate buffer at pH 7.4. A single component was detected for each dendrimer. The GFC samples were prepared by 10× dilution of the dendrimer stock solutions (1×10^{-3} M). The peak elution volumes (V_e) of the freshly prepared samples of G1- and G2-Fe^{III}Pors were 10.7 and 8.9 mL, respectively. However, the peak detected for the G2-Fe^{III}Por sample at 8.9 mL gradually moved to 9.8 mL, which corresponded to the V_e of the aged sample, while only one peak was detected for G1-Fe^{III}Por. The wavelength of maximum absorption (λ_{max}) of G1-Fe^{III}Por at

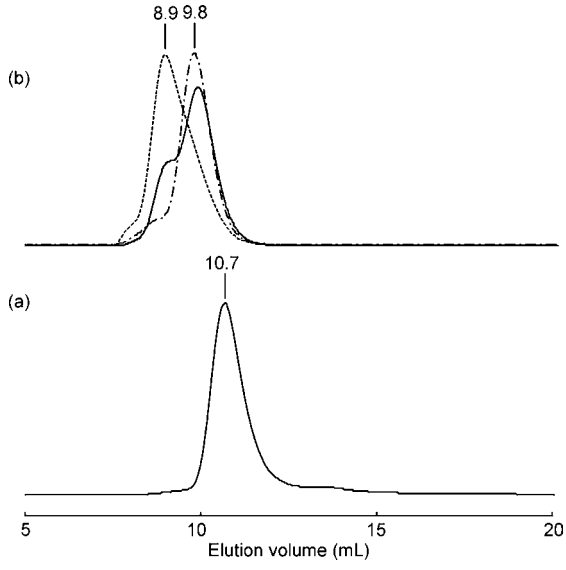

Figure 2. GFC profiles of G1-Fe^{III}Por (a) and G2-Fe^{III}Por (b) using a Superdex 200 10/300GL column at a flow rate of 0.5 mL/min with 0.05 M phosphate buffer at pH 7.4 and 4 °C. Elution was monitored at 410 nm. The dashed, solid, and dot−dashed lines in (b) indicate the GFC traces of G2-Fe^{III}Por samples that were diluted 10-fold from the G2-Fe^{III}Por stock solution (1.0×10^{-3} M) immediately, 2 h, and 16 h before the analysis.

dx.doi.org/10.1021/bc300303z | Bioconjugate Chem. 2012, 23, 2365−2376

pH 10 was 410 nm, which shifted to 398 nm at pH 4. The λ_{max} at pH 10 was the same as that of the μ-oxo dimer of Fe^{III}TPPS (410 nm), while that at pH 4 corresponded to that of the diaqua complex.[29] A pH titration curve of the UV−vis spectral changes of G1-Fe^{III}Por as a function of pH (Supporting Information, Figure S3) indicated that the apparent pK_a value for the equilibrium between the diaqua and μ-oxo dimer complexes of G1-Fe^{III}TPPS was 5.7. At pH 7.4, therefore, the main species of G1-Fe^{III}Por should be the μ-oxo dimer, which was detected at V_e = 10.7 mL by GFC. The Soret band for freshly prepared G2-Fe^{III}Por was observed at 410 nm, which gradually shifted to 418 nm within 6 h (Supporting Information, Figure S4). The absorption band with λ_{max} at 418 nm is ascribed to the monohydroxo complex of G2-Fe^{III}Por.[30] The results are explained as G2-Fe^{III}Por in a stock solution (1.0×10^{-3} M) predominantly existing as the μ-oxo dimer, which gradually changes to the monohydroxo complex upon dilution. Thus, the GFC results observed for G2-Fe^{III}Por can also be explained by slow conversion of the μ-oxo dimer (V_e = 8.9 mL) to the monohydroxo form (9.8 mL) after sample preparation. In general, ferric porphyrin predominantly exists in a μ-oxo dimer form in aqueous solutions at higher pH. However, formation of the μ-oxo dimer complex can be inhibited by steric hindrance, as observed with the picket-fence porphyrin.[31] In dilute solutions, the nine PEG chains appear to cling to a porphyrin ring causing steric hindrance during μ-oxo dimer formation. The pK_a value for the equilibrium between the diaqua-monohydroxo complexes of G2-Fe^{III}Por in the aged sample was determined to be 6.7 (Supporting Information, Figure S5). We previously determined the pK_a value for the same equilibrium of the 1:2 Fe^{III}TPPS/per-*O*-methylated β-cyclodextrin (TMe-β-CD) complex to be 4.3.[29] In the case of Fe^{III}TPPS/TMe-β-CD complex, the two sulfonatophenyl groups of Fe^{III}TPPS at the 5- and 15-positions are tightly incorporated into the two TMe-β-CD cavities resulting in preparation of a hydrophobic environment around the ferric center of the porphyrin. In such a case, the diaqua complex with one positive net charge should be unstable in the cyclodextrin capsule leading to easy exchange of the axial ligand from H_2O to OH^-. However, the positive charge at the iron center of the diaqua complex of G2-Fe^{III}Por is surrounded by many oxyethylene units, which provide a polar environment similar to that of crown ether resulting in the stabilization of the monocationic diaqua complex. This may explain the higher pK_a of G2-Fe^{III}Por compared to that of the Fe^{III}TPPS/TMe-β-CD complex.

Complexation of G1- and G2-Fe^{III}Pors with Py3CD. Figure 3 shows the absorption spectral changes of G2-Fe^{III}Por in phosphate buffer at pH 7.0 upon addition of Py3CD. Each spectrum was measured 2 h after sample preparation. The Py3CD-induced spectral changes of G2-Fe^{III}Por are quite similar to those observed for trisulfonatophenylporphyrinato-iron(III) covalently bound to poly(acrylic acid) (Fe^{III}TPPS-PAA),[11] suggesting that the two sulfonatophenyl groups of the porphyrin core are included in the two cyclodextrin units of the Py3CD molecule to form a *trans*-type 1:1 inclusion complex (Figure 1). Almost the same spectral changes were observed with G1-Fe^{III}Por. Because the spectral change was saturated at an equimolar concentration of Py3CD, the 1:1 inclusion complex must be as stable as the Fe^{III}TPPS/Py3CD system.[7] In this paper, the 1:1 inclusion complexes of G1- and G2-Fe^{III}Pors with Py3CD are abbreviated as G1-met-hemoCD and G2-met-hemoCD, respectively.

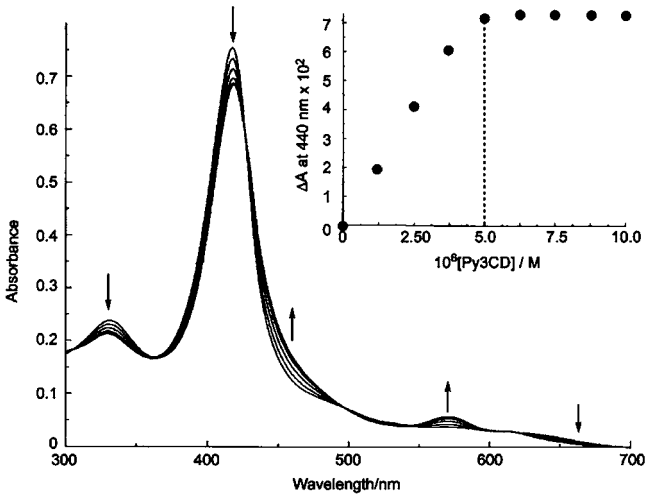

Figure 3. UV−vis spectral changes of G2-Fe^{III}Por (5.0×10^{-6} M) upon addition of Py3CD in 0.05 M phosphate buffer at pH 7.0 and 25 °C. The inset shows a plot of the changes in absorbance of G2-Fe^{III}Por versus [Py3CD].

Hydrodynamic Sizes of G1- and G2-met-hemoCDs. The hydrodynamic diameters (D_h) of G1- and G2-met-hemoCDs were estimated by GFC[32,33] (Supporting Information, Figure S6), and the results are listed in Table 1. Met-hemoCD is a 1:1 inclusion complex of Fe^{III}TPPS and Py3CD and its D_h was determined to be 3.1 nm. The MM3 calculation without considering the solvent provided a gyration diameter of 2.2 nm for met-hemoCD, which was smaller than the D_h determined from GFC. The determined D_h value of met-hemoCD appears if the presence of a hydration layer in this compound is assumed.[34] Modification of met-hemoCD with the dendrons increased the D_h values of G1-met-hemoCD and G2-met-hemoCD to 9.2 and 13.0 nm, respectively. It is well-known that neutral particles with a diameter less than 4 nm are easily filtered by the glomerulus, while those with a diameter

Table 1. Physicochemical Parameters of Artificial Dioxygen Carriers and Red Blood Cells (RBCs)

O_2 carrier	$t_{1/2}$ (h)[a]	$P_{1/2}$ (Torr)	D_h (nm)[b]	MW
hemoCD	6.8 (30)	22 ± 2 (10 ± 2)	3.1	3958
G1-hemoCD	6.1 (30)	20 ± 2 (8.8 ± 0.5)	9.2	19217[i]
G2-hemoCD	5.5 (27)	20 ± 2 (8.7 ± 0.7)	13.0	49893[i]
human HbA	8.9, 63[c]	26 (1.9 − 4.7)[d]		64500
horse heart Mb	5.7[c]	2.32 ± 0.02[e] (0.9)[f]		17800
PEG(HAS-FeP)[g]	12	32 (11)		
RBC[h]		28	(8000)	

[a]The half-lives ($t_{1/2}$) of the dioxygen adducts and the O_2 affinities were determined at pH 7.4 and 37 °C. The values in parentheses were determined at pH 7.4 and 25 °C. [b]The hydrodynamic diameters (D_h's) of the met-forms of the O_2 carriers were determined in phosphate buffer (0.05 M, pH 7.4) by GFC at 4 °C. [c]Two-exponential decay was observed for human HbA at pH 6.5 and 35 °C, whereas single exponential decay was measured for horse heart Mb (ref 41). [d]ref 37. [e]ref 39. [f]ref 38. [g]Nakagawa, A., Komatsu, T., Huang, Y., Lu, G., Tsuchida, E. (2007) O_2-binding albumin thin films: solid membranes of poly(ethylene glycol)-conjugated human serum albumin incorporating iron porphyrin. *Bioconjugate Chem. 18*, 1673−1677. [h]ref 40. [i]The molecular weights (MWs) were calculated based on the assumption that the MW of one PEG chain is 5000.

dx.doi.org/10.1021/bc300303z | *Bioconjugate Chem.* 2012, 23, 2365−2376

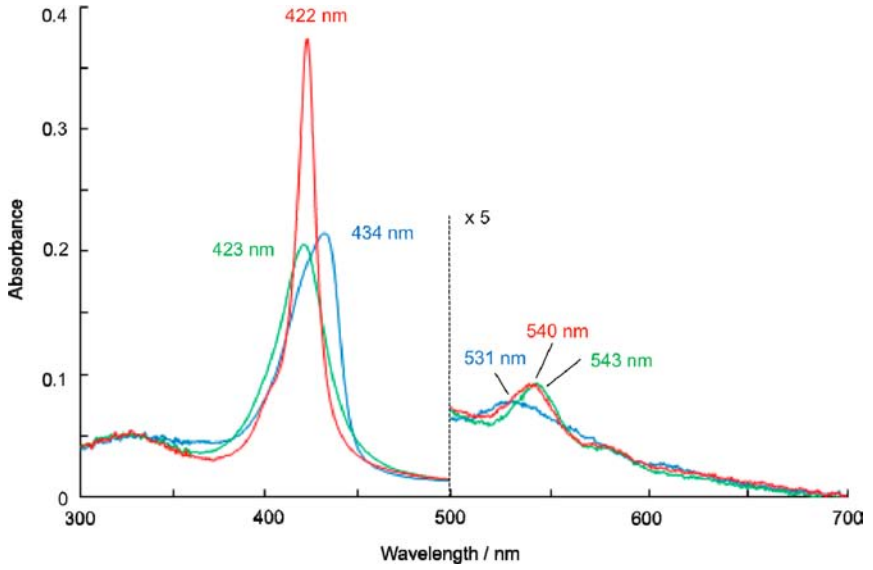

Figure 4. UV−vis spectra of G2-hemoCD ([G2-Fe^{II}Por] = 1.0×10^{-6} M, [Py3CD] = 1.2×10^{-6} M) under N_2 (a), O_2 (b), and CO (c) atmospheres in 0.05 M phosphate buffer at pH 7.4 and 25 °C.

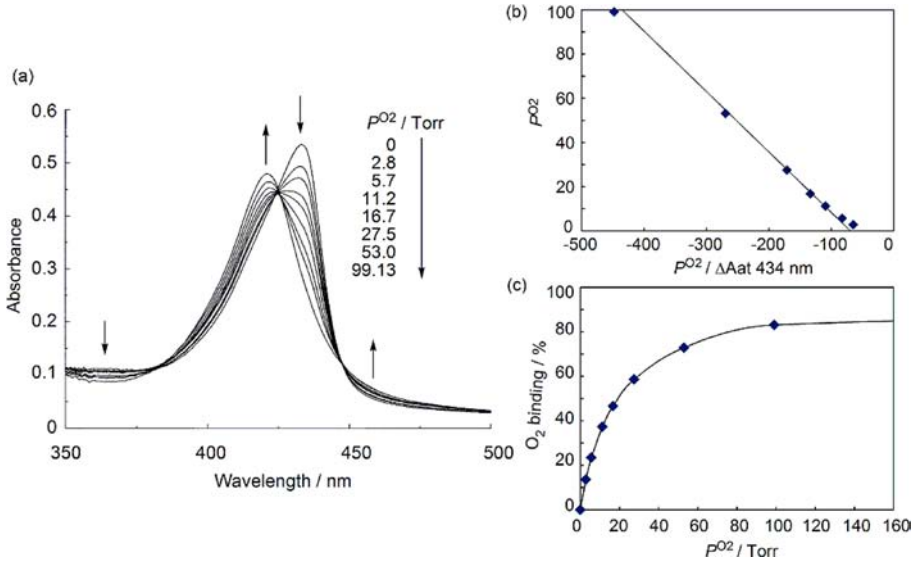

Figure 5. UV−vis spectral changes of G2-hemoCD (2.5×10^{-6} M) as a function of O_2 partial pressure (P^{O2}) in N_2 in 0.05 M phosphate buffer at pH 7.4 and 37 °C (a), plot of $P^{O2}/\Delta A$ versus P^{O2} for determining $P_{1/2}$ (b), and the saturation curve for the O_2 binding to G2-hemoCD (c).

larger than 8 nm are not. However, a transformable material may pass through the pore even if its apparent molecular size is larger than the pore size.[35] The hydrodynamic diameters predict that met-hemoCD is filtered by the glomerulus, while G2-met-hemoCD hardly passes through the glomerular membrane, resulting in extended circulation time in the bloodstream.

Dioxygen Binding to G1- and G2-hemoCDs. Formation of O_2 adducts of the ferrous porphyrin dendrimers could be followed by UV−vis spectroscopy. A G2-met-hemoCD stock solution was prepared by mixing 1.2 equiv of Py3CD with G2-Fe^{III}Por (1.0×10^{-3} M) in 1 mL of 0.05 M phosphate buffer at pH 7.4. After aging for 2 h, 10 equiv of $Na_2S_2O_4$ was added to the G2-met-hemoCD solution to reduce the ferric ion to the ferrous state, followed by gel filtration using a Sephadex G-25 desalting column at 4 °C. The solution thus obtained was arbitrarily diluted with the same buffer solution at 4 °C under aerobic conditions, and the UV−vis absorption spectrum was measured at 25 °C (Figure 4). Relatively broad absorption bands were observed at 423 and 543 nm. The absorption maxima shifted to 434 and 531 nm when the nitrogen gas was bubbled into the solution for 5 min. Upon changing the atmosphere from nitrogen to carbon monoxide, a new characteristically sharp absorption spectrum with λ_{max} at 422 and 540 nm was measured. These spectral changes have been used to confirm the O_2 binding phenomena of ferrous porphyrins.[7] The spectra observed under the air, N_2, and CO atmospheres are definitely ascribed to the oxy-, deoxy-, and CO-complexes of G2-hemoCD, respectively. The concentration of each species of G2-hemoCD was estimated from the extinction coefficient of oxy- ($\varepsilon = 1.64 \times 10^5$ M^{-1} cm^{-1} at 423 nm), deoxy- (2.13×10^5 M^{-1} cm^{-1} at 434 nm), or CO-coordinated hemoCD (3.71×10^5 M^{-1} cm^{-1} at 422 nm).[9] All calculations yielded the same value as the concentration of G2-hemoCD, suggesting that no autoxidation of oxy-G2-hemoCD occurred during conversion of oxy-G2-hemoCD to deoxy-G2-

dx.doi.org/10.1021/bc300303z | Bioconjugate Chem. 2012, 23, 2365−2376

hemoCD by bubbling of the N_2 gas. The same spectral changes were observed with ferrous G1-hemoCD (Supporting Information, Figure S7). It was found that both ferrous G1- and G2-hemoCDs reversibly bound dioxygen in aqueous solution as the case of hemoCD itself.

The dioxygen affinity of an O_2 receptor is evaluated by $P_{1/2}$ that corresponds to the partial dioxygen pressure (P^{O2}) at which half of the receptor molecules are oxygenated. The absorption spectra of the G1- and G2-hemoCD systems were measured as a function of P^{O2} in 0.05 M phosphate buffer at pH 7.4 and 37 and 25 °C (Figure 5 and Supporting Information, Figures S8–10). $P_{1/2}$ is correlated with P^{O2}, $\Delta\varepsilon$ (the difference between the extinction coefficients of the deoxy- and oxy-Gn-hemoCDs at a given wavelength), and ΔA (the change in the absorbance of Gn-hemoCD under various P^{O2}) by the following equation:[36]

$$P^{O_2} = (\Delta\varepsilon[\text{Gn-hemoCD}]_t P^{O_2})/\Delta A - P_{1/2} \quad (1)$$

The linear relationships between $P^{O2}/(\Delta A$ at 434 nm) and P^{O2} yield $P_{1/2}$. The results are shown in Table 1. The $P_{1/2}$ of hemoCD at pH 7.0 and 25 °C was previously reported to be 10 ± 0.5 Torr,[9] which increased to 22 ± 2 Torr at pH 7.4 and 37 °C. The $P_{1/2}$ values of G1- and G2-hemoCDs were 8.8 ± 0.5 and 8.7 ± 0.7 Torr, respectively, at 25 °C and 20 ± 2 Torr (for both) at 37 °C. Modification of hemoCD with PEGylated dendrons does not affect the dioxygen affinity of the receptor. The $P_{1/2}$ values of human HbA at pH 7.4 were reported to be 1.9–4.7 Torr at 25 °C and 26 Torr at 37 °C.[37] The reported $P_{1/2}$ values of horse heart Mb are 0.9 Torr at pH 7.2 and 25 °C[38] and 2.32 ± 0.02 Torr at pH 7.5 and 37 °C.[39] The $P_{1/2}$ of Hb in red blood cells under physiological conditions is 28 Torr,[40] which is very similar to the $P_{1/2}$ values of G1- and G2-hemoCDs. If the O_2 adducts of G1- and G2-hemoCDs are satisfactorily stable, these artificial O_2 receptors may become candidates for red blood cell substitutes.

Autoxidation Rates of Dioxygen Adducts. The O_2 adducts of G1- and G2-hemoCDs (λ_{max} 423 nm) were gradually oxidized to the monohydroxo met-hemoCD complexes (418 nm) (Supporting Information, Figures S11 and S12). In all cases, four isosbestic points were observed in the absorption spectral changes, indicating quantitative autoxidation of the ferrous porphyrins to the ferric forms. Progressive absorbance changes at 421 nm were analyzed by pseudo first-order reaction kinetics, and the half-lives of the O_2 adducts ($t_{1/2} = \ln 2/k_{obs}$) thus obtained are listed in Table 1. Autoxidation of the dioxygen adducts is greatly dependent on temperature. The O_2 adducts of hemoCD and G1- and G2-hemoCDs were scarcely autoxidized at 4 °C, whereas at 25 °C, they were gradually autoxidized with $t_{1/2}$ values of ca. 30 h. Relatively rapid oxidation occurred at 37 °C ($t_{1/2}$ = 6.8–5.5 h). The O_2 adduct of horse heart Mb is autoxidized with a k_{obs} of 0.122 h^{-1} ($t_{1/2}$ = 5.7 h) at pH 6.5 and 35 °C, while oxy-HbA (human) exhibits a biphasic decay with k_{obs} values of 0.078 ($t_{1/2}$ = 8.9 h) and 0.011 h^{-1} (63 h).[41] The dioxygen adducts of hemoCD and its dendrimer derivatives were as stable as that of Mb. It has been well established that the dioxygen adducts of Mb and Hb are stabilized by hydrogen bonding between the bound O_2 molecule and the distal His residue.[42] Despite the absence of a hydrogen donor, the O_2 adducts of hemoCD and its dendrimer derivatives were stable, indicating that hydrogen bonding is not essential, and placement of the ferrous center in a hydrophobic environment is important for stabilization of the dioxygen adduct of a ferrous porphyrin in the model system.

Pharmacokinetics of HemoCD Dendrimers. First, glomerular filtration rates of the dioxygen adducts of hemoCD and G1- and G2-hemoCDs were measured. An oxy-hemoCD derivative solution (3.0×10^{-4} M) in PBS (pH 7.4) was infused into the femoral vein of a rat at a rate of 0.1 mL/min for 10 min. Urine samples were collected every 30 min after the initiation of infusion. Each urine sample was appropriately diluted with PBS and a small amount of $Na_2S_2O_4$ was added under a CO atmosphere. The urine samples may contain deoxy, O_2-, and CO-coordinated ferrous porphyrins plus ferric porphyrin. These iron porphyrins can be converted to a CO-coordinated ferrous porphyrin by this treatment. Measurement of the UV–vis spectrum of the resultant CO-coordinated hemoCD derivatives informed the total amount of hemoCD derivatives excreted in the urine. The progressive changes in the ratios of the O_2 carriers (total) in the urine to the injection doses (% ID) are shown in Figure 6. As we previously

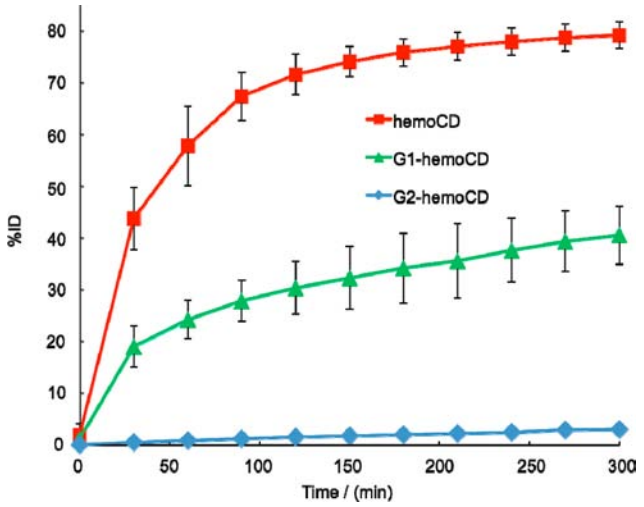

Figure 6. Time course of the amounts of urinary excreted hemoCD derivatives after the infusion of the O_2 adduct of hemoCD (red), G1-hemoCD (green), or G2-hemoCD (blue) into the femoral vein of rats (3.0×10^{-4} M solution in PBS infused at the rate of 0.1 mL/min for 10 min). The vertical axis shows the cumulative amounts of the excreted hemoCD derivatives (% Injection Dose, ID). Each point represents the mean ± SD of data obtained from three experiments using different analytes.

reported,[10] hemoCD in the oxy- and CO-coordinated forms was rapidly excreted in the urine. About 80% of the injected hemoCD molecules were filtered by the kidney within 5 h after injection. In the case of G1-hemoCD, elimination was markedly diminished and about 60% of the G1-hemoCD molecules remained in the body at 6 h. Almost no excretion was detected with G2-hemoCD, and over 97% of the G2-hemoCD molecules remained in the body at 5 h after injection. However, the problem is whether the O_2 carrier accumulates in organs such as the liver and spleen.

The rates of hemoCD derivative clearance from the rat bloodstream were followed by GFC. The progressive mass changes of the hemoCD derivatives in the plasma of rats are shown in Figure 7. Biphasic clearance of the O_2 carrier was observed in all cases. As is well-known, fast clearance (distribution phase) is due to the distribution of the carrier molecules to the various organs. The distribution phase (α-phase) was followed by a slower elimination phase (β-phase). HemoCD rapidly disappeared from the blood mainly due to

dx.doi.org/10.1021/bc300303z | Bioconjugate Chem. 2012, 23, 2365–2376

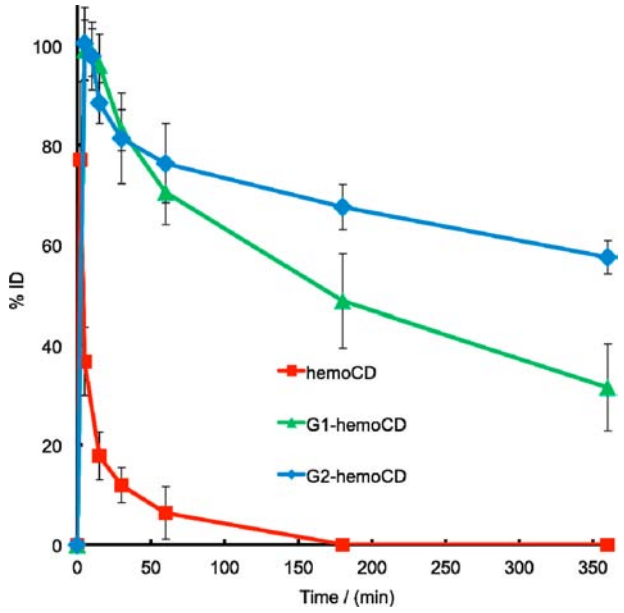

Figure 7. Time course of the amounts of hemoCD derivatives remaining in plasma (% ID) after the injection of the O_2 adduct of hemoCD (red), G1-hemoCD (green), or G2-hemoCD (blue) (3.0×10^{-3} M in PBS, 1 mL, bolus injection into the femoral vein of rats). Each point represents the mean ± SD of data obtained from three experiments using different analytes.

glomerular filtration. However, considerable amounts of G1- (32% ID) and G2-hemoCDs (58% ID) remained in the blood even at 6 h after injection. The half-lives of the fast and slow clearance processes of G2-hemoCD were 12 min (20%) and 13 h (80%), respectively (Table 2). Previously, we prepared a

Table 2. Half-Lives for the Blood Clearance of Artificial Dioxygen Carriers[a]

O_2 carrier	$t_{1/2\alpha}$ (min)	$t_{1/2\beta}$ (h)
hemoCD	1.40 ± 0.67 (76.9%)	0.54 ± 0.25 (23.1%)
G1-hemoCD	27.0 ± 19.3 (28.7%)	5.30 ± 0.91 (71.3%)
G2-hemoCD	11.9 ± 2.22 (19.0%)	12.8 ± 2.08 (81.0%)

[a]Half-lives are mean values obtained from three independent experiments. Abbreviations: $t_{1/2\alpha}$, half-life of distribution phase; $t_{1/2\beta}$, half-life of elimination phase. The values in parentheses indicate the ratios of α- and β-phases.

trisulfonatophenylporphyrinatoiron dimer (FeP-PEG20K) whose porphyrin units were linked with a PEG chain (MW = 20 000).[43] Each porphyrin unit of FeP-PEG20K was complexed with Py3CD to form PEG20K-hemoCD, whose D_h was determined to be 12 nm by GFC. Although the apparent D_h of PEG20K-hemoCD is almost the same as that of G2-hemoCD (13 nm), this hemoCD derivative with a single PEG chain is gradually excreted in the urine. The fact that G2-hemoCD is not excreted into the urine at all indicates the remarkable effect of branched PEG chains on renal filtration. Similar pharmacokinetics was previously observed with a bow-tie-type PEGylated dendrimer.[44] Long circulation times of PEGylated dendrimers in the bloodstream have been reported.[45−48] PEGylation of human serum albumin extends the circulation time of its inclusion complex with porphyrinatoiron.[49] These results strongly suggest that G2-hemoCD is a promising candidate for an artificial O_2 carrier if it does not show any cytotoxicity.

Cytotoxicity and Hemolytic Activity. It was reported that cytotoxic and hemolytic cationic dendrimers become nontoxic when masked with PEG chains.[50] A recent study revealed that the efficacy of antitumor activity and toxicity of doxorubicin are greatly improved by modification of this drug with PEGylated dendron.[16] The cytotoxicities of the hemoCD derivatives were examined using the MTT assay. The cell viability for each hemoCD derivative is shown in Figure 8. No cytotoxicity was observed with the hemoCD derivatives under the experimental conditions.

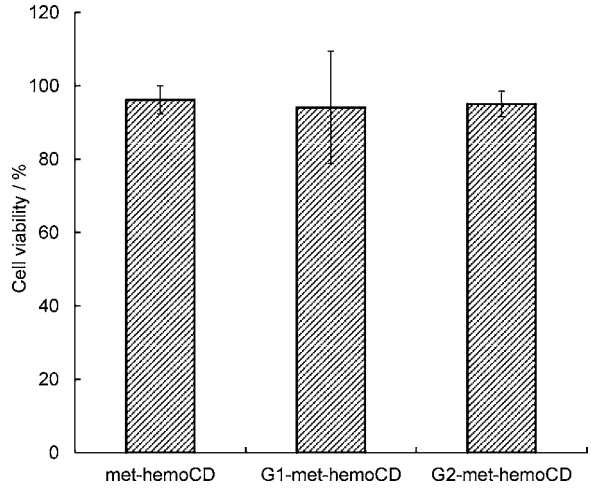

Figure 8. Cytotoxicity assay for met-hemoCD, G1-met-hemoCD, and G2-met-hemoCD. HeLa cells (10^4 cells) were assayed after incubation with medium (100 μL) containing met-hemoCD derivatives (5×10^{-5} M each) for 16 h at 37 °C. Viability is expressed as a percentage of untreated cells. Values represent the mean ± SD of data obtained from three experiments using different analytes.

In all cases, no free Hb extrusion from red blood cells was visually observed in the centrifuged blood samples of the hemoCD derivative-dosed rats, indicating that the hemoCD dendrimers as well as hemoCD itself do not exhibit hemolytic activity. In practical applications of G2-hemoCD as an artificial O_2 carrier, however, a more concentrated carrier solution might be used. In such a case, unexpected problems may be encountered, the investigation of which are outside the scope of the present study.

CONCLUSION

One of the serious problems in developing artificial red blood cells is the circulation time of the O_2 carrier in the bloodstream. Serum albumins and phospholipid vesicles, which are hardly filtered by the kidney and hardly accumulate in organs, have been used as platforms for O_2 carriers.[5] In the present study, we sought to extend the circulation time of hemoCD by modifying it with PEGylated dendrons. All physicochemical and pharmacokinetic data suggest that G2-hemoCD can be used as a completely artificial O_2 carrier in vivo. Serious problems that remain include the difficulty of G2-hemoCD mass production and binding of endogenous CO. We found that hemoCD itself exhibits an extremely high CO affinity,[10] whereas the CO affinity of a Fe^{II}TPPS complex of a per-*O*-methylated β-cyclodextrin dimer having an imidazole linker is significantly low.[51] On the basis of the present and previous

dx.doi.org/10.1021/bc300303z | Bioconjugate Chem. 2012, 23, 2365−2376

results, we will be able to design a new O_2 carrier that can be used for practical purposes.

■ ASSOCIATED CONTENT

Supporting Information

MALDI-TOF MS spectra of Gn-dendrons, Gn-Pors, and Gn-Fe^{III}Pors, UV−vis spectra of Gn-Fe^{III}Pors as a function of pH, time-course UV−vis spectral changes of G2-Fe^{III}Por upon dilution, GFC profiles of met-hemoCD, G1-met-hemoCD, and G2-met-hemoCD to estimate these hydrodynamic diameters, UV−vis spectra of deoxy-, oxy-, and CO-complexes of G1-hemoCD, determination of the O_2 affinities of G1- and G2-hemoCDs at 25 and 37 °C, autoxidation reactions of the O_2 complexes of G1- and G2 hemoCDs at 25 and 37 °C. This material is available free of charge via the Internet at http://pubs.acs.org.

■ AUTHOR INFORMATION

Corresponding Author

*E-mail: kkano@mail.doshisha.ac.jp; Tel: +81 774 65 6624; Fax: +81 774 65 6845.

Notes

The authors declare no competing financial interest.

■ ACKNOWLEDGMENTS

This work was supported by Grants-in-Aid on "Creating Research Center for Advanced Molecular Biochemistry", Strategic Development of Research Infrastructure for Private Universities from the Ministry of Education, Culture, Sports, Science and Technology.

■ REFERENCES

(1) Collman, J. P., Boulatov, R., Sunderland, C. J., and Fu, L. (2004) Functional analogues of cytochrome *c* oxidase, myoglobin, and hemoglobin. *Chem. Rev. 104*, 561−588.

(2) Magnus, K. A., Ton-That, H., and Carpenter, J. E. (1994) Recent structural work on the oxygen transport protein hemocyanin. *Chem. Rev. 94*, 727−735.

(3) Momenteau, M., and Reed, C. A. (1994) Synthetic heme-dioxygen complexes. *Chem. Rev. 94*, 659−698.

(4) Shikama, K. (1998) The molecular mechanism of autoxidation of myoglobin and haemoglobin: a venerable puzzle. *Chem. Rev. 98*, 1357−1373.

(5) Tsuchida, E., Sou, K., Nakagawa, A., Sakai, H., Komatsu, T., and Kobayashi, K. (2009) Artificial oxygen carriers, hemoglobin vesicles and albumin-hemes, based on bioconjugate chemistry. *Bioconjugate Chem. 20*, 1419−1440.

(6) Tsuchida, E. (1985) Liposome-embedded iron-porphyrins as an artificial oxygen carrier. *Ann. N.Y. Acad. Sci. 446*, 429−442.

(7) Kano, K., Kitagishi, H., Kodera, M., and Hirota, S. (2005) Dioxygen binding to a simple myoglobin model in aqueous solution. *Angew. Chem., Int. Ed. 44*, 435−438.

(8) Kano, K., Kitagishi, H., Dagallier, C., Kodera, M., Matsuo, T., Hayashi, T., Hisaeda, Y., and Hirota, S. (2006) Iron porphyrin-cyclodextrin supramolecular complex as a functional model of myoglobin in aqueous solution. *Inorg. Chem. 45*, 4448−4460.

(9) Kano, K., Chimoto, S., Tamaki, M., Itoh, Y., and Kitagishi, H. (2012) Supramolecular dioxygen receptors composed of an anionic water-soluble porphinatoiron(II) and cyclodextrin dimers. *Dalton Trans. 41*, 453−461.

(10) Kitagishi, H., Negi, S., Kiriyama, A., Honbo, A., Sugiura, Y., Kawaguchi, A. T., and Kano, K. (2010) A diatomic molecule receptor that removes CO in a living organism. *Angew. Chem., Int. Ed. 49*, 1312−1315.

(11) Kano, K., Ochi, T., Okunaka, S., Ota, Y., Karasugi, K., Ueda, T., and Kitagishi, H. (2011) Preparation and function of poly(acrylic acid)s modified by supramolecular complex composed of porphinatoiron and a cyclodextrin dimer that bind diatomic molecules (O_2 and CO) in aqueous solution. *Chem.−Asian J. 6*, 2946−2955.

(12) Karasugi, K., Kitagishi, H., and Kano, K. (2011) Gold nanoparticles carrying diatomic molecules (O_2 and CO) in aqueous solution. *Chem.−Asian J. 6*, 825−833.

(13) Wijagkanalan, W., Kawakami, S., and Hashida, M. (2011) Designing dendrimers for drug delivery and imaging: pharmacokinetic considerations. *Pharm. Rev. 28*, 1500−1519.

(14) Medina, S. H., and El-Sayed, M. E. H. (2009) Dendrimers as carriers for delivery of chemotherapeutic agents. *Chem. Rev. 109*, 3141−3157.

(15) Singh, P., Gupta, U., Asthana, A., and Jain, N. K. (2008) Folate and folate-PEG-PAMAM dendrimers: synthesis, characterization, and targeted anticancer drug derivery potential in tumor bearing mice. *Bioconjugate Chem. 19*, 2239−2252.

(16) Kaminskas, L. M., McLeod, V. M., Kelly, B. D., Sberna, G., Boyd, B. J., Williamson, M., Owen, D. J., and Porter, C. J. H. (2012) A comparison of charges to doxorubicin pharmacokinetics, antitumor activity, and toxicity mediated by PEGylated dendrimer and PEGylated liposome drug delivery systems. *Nanomedicine 8*, 103−111.

(17) Jiang, D.-L., and Aida, T. (1996) A dendritic iron porphyrin as a novel haemoprotein mimic: effects of the dendrimer cage on dioxygen-binding activity. *Chem. Commun.*, 1523−1524.

(18) Jiang, D.-L., and Aida, T. (1997) Dendrimer-encapsulated iron porphyrin as a novel hemoprotein mimic for dioxygen binding. *J. Macromol. Sci. A34*, 2047−2055.

(19) Collman, J. P., Fu, L., Zingg, A., and Diederich, F. (1997) Dioxygen and carbon monoxide binding in dendritic iron(II)-porphyrins. *Chem. Commun.*, 193−194.

(20) Zingg, A., Felber, B., Gramlich, V., Fu, L., Collman, J. P., and Diederich, F. (2002) Dendritic iron(II) porphyrins as models for hemoglobin and myoglobin: specific stabilization of O_2 complexes in dendrimers with H-bond-donor centers. *Helv. Chim. Acta 85*, 333−351.

(21) Van Doorslaer, S., Zingg, A., Schweiger, A., and Diederich, F. (2002) Effects of the dendrimer cage on O_2 binding of dendritic cobalt(II) porphyrins. *ChemPhysChem 3*, 659−667.

(22) Elbert, D, L., and Hubbell, J, A. (2001) Conjugate addition reactions combined with free-radical cross-linking for the design of materials for tissue engineering. *Biomacromolecules 2*, 430−441.

(23) Kruper, W. J., Jr., Chamberlin, T. A., and Kochanny, M. (1989) Regiospecific aryl nitration of meso-substituted tetraarylporphyrins: a simple route to bifunctional porphyrins. *J. Org. Chem. 54*, 2753−2756.

(24) Karim, N., and Ali, S. S. (2009) Jugular vein cannulation in rats − a mini review. *Can. J. Pure Appl. Sci. 3*, 929−935.

(25) Newkome, G. R., Behera, R. K., Moorefield, C. N., and Baker, G. R. (1991) Cascade polymers: syntheses and characterization of one-directional arborols based on adamantane. *J. Org. Chem. 56*, 7162−7167.

(26) Ornelas, C., Broichhagen, J., and Weck, M. (2010) Strain-promoted alkyne azide cycloaddition for the functionalization of poly(amide)-based dendrons and dendrimers. *J. Am. Chem. Soc. 132*, 3923−3931.

(27) Huang, K., Voss, B., Kumar, D., Hamm, H. E., and Harth, E. (2007) Dendritic molecular transporters provide control of delivery to intracellular compartments. *Bioconjugate Chem. 18*, 403−409.

(28) In the MALDI-TOF-MS measurements, these compounds could not be definitely confirmed because many fragmented peaks were observed as shown in the Supporting Information (Figures S1 and S2).

(29) Gandini, S. C. M., Yushmanov, V. E., and Tabak, M. (2001) Interaction of Fe(III)- and Zn(II)-tetra(4-sulfonatophenyl) porphyrins with ionic and nonionic surfactants: aggregation and binding. *J. Inorg. Biochem. 85*, 263−277.

(30) Kano, K., Kitagishi, H., Tamura, S., and Yamada, A. (2004) Anion binding to a ferric porphyrin complexed with per-*O*-methylated

β-cyclodextrin in aqueous solution. *J. Am. Chem. Soc. 126*, 15202−15210.
(31) Collman, J. P., Gagne, R. R., Halbert, T. R., Marchon, J.-C., and Reed, C. A. (1973) Reversible oxygen adduct formation in ferrous complexes derived from a "picket fence" porphyrin. A model for oxymyoglobin. *J. Am. Chem. Soc. 95*, 7868−7870.
(32) Laurent, T. C., and Killander, J. (1964) A theory of gel filtration and its experimental verification. *J. Chromatogr. 14*, 317−330.
(33) Kunji, E. R. S., Harding, M., Butler, P. J. G., and Akamine, P. (2008) Determination of the molecular mass and dimensions of membrane proteins by size exclusion chromatography. *Methods 46*, 62−72.
(34) Bagchi, B. (2005) Water dynamics in the hydration layer around proteins and micelles. *Chem. Rev. 105*, 3197−3219.
(35) Fox, M. E., Szoka, F. C., and Fréchet, J. M. J. (2009) Soluble polymer carriers for the treatment of cancer: the importance of molecular architecture. *Acc. Chem. Res. 42*, 1141−1151.
(36) Collman, J. P., Zhang, X., Wong, K., and Brauman, J. I. (1994) Dioxygen binding in iron and cobalt picnic basket porphyrins. *J. Am. Chem. Soc. 116*, 6245−6251.
(37) Niederhoffer, E. C., Timmons, J. H., and Martell, A. E. (1984) Thermodynamics of oxygen binding in natural and synthetic dioxygen complexes. *Chem. Rev. 84*, 137−203.
(38) Pedersen, C. L., Faggiano, S., Helbo, S., Gesser, H., and Fago, A. (2010) Roles of nitric oxide, nitrite and myoglobin on myocardial efficiency in trout (Oncorhynchus mykiss) and goldfish (Carassius auratus): implications for hypoxia tolerance. *J. Experimental Biol. 213*, 2711−2762.
(39) Schenkman, K. A., Marble, D. R., Burns, D. H., and Feigl, E. O. (1997) Myoglobin oxygen dissociation by multiwavelength spectroscopy. *J. Appl. Physiol. 82*, 86−92.
(40) Sakai, H., Yuasa, M., Onuma, H., Takeoka, S., and Tsuchida, E. (2000) Synthesis and physicochemical characterization of a series of hemoglobin-based oxygen carriers: objective comparison between cellular and acellular types. *Bioconjugate Chem. 11*, 56−64.
(41) Tsuruga, M., and Shikama, K. (1997) Biphasic nature in the autoxidation reaction of human oxyhemoglobin. *Biochim. Biophys. Acta 1337*, 96−104.
(42) Olson, J. S., and Phillips, G. N., Jr. (1997) Myoglobin discriminates between O_2, NO, and CO by electrostatic interactions with the bound ligand. *J. Biol. Inorg. Chem. 2*, 544−552.
(43) Ueda, T., Kitagishi, H., and Kano, K. (2012) PEGylation of an artificial O_2 and CO receptor: synthesis, characterization and pharmacokinetic study. *Org. Biomol. Chem. 10*, 4337−4347.
(44) Gillies, E. R., Dy, E., Fréchet, J. M. J., and Szoka, F. C. (2005) Biological evaluation of polyester dendrimer: poly(ethylene oxide) "bow-tie" hybrids with tunable molecular weight and architecture. *Mol. Pharmaceutics 2*, 129−138.
(45) Kaminskas, L. M., Boyd, B. J., Karellas, P., Krippner, G. Y., Lessene, R., Kelly, B., and Porter, C. J. H. (2008) The impact of molecular weight and PEG chain length on the systemic pharmacokinetics of PEGylated poly L-lysine dendrimers. *Mol. Pharmaceutics 5*, 449−463.
(46) Guillaudeu, S. J., Fox, M. E., Haidar, Y. M., Dy, E. E., Szoka, F. C., and Fréchet, J. M. J. (2008) PEGylated dendrimers with core functionality for biological applications. *Bioconjugate Chem. 19*, 461−469.
(47) Lim, J., Guo, Y., Rostollan, C. L., Stanfield, J., Hsieh, J.-T., Sun, X., and Simanek, E. E. (2008) The role of the size and number of polyethylene glycol chains in the biodistribution and tumor localization of triazine dendrimers. *Mol. Pharmaceutics 5*, 540−547.
(48) Kojima, C., Regino, C., Umeda, Y., Kobayashi, H., and Kono, K. (2010) Influence of dendrimer generation and polyethylene glycol length on the biodistribution of PEGylated dendrimers. *Int. J. Pharm. 383*, 293−296.
(49) Huang, Y., Komatsu, T., Wang, R.-M., Nakagawa, A., and Tsuchida, E. (2006) Poly(ethylene glycol)-conjugated human serum albumin including iron porphyrins: surface modification improves the O_2-transporting ability. *Bioconjugate Chem. 17*, 393−398.
(50) Chen, H.-T., Neerman, M. F., Parrish, A. R., and Simanek, E. E. (2004) Cytotoxicity, hemolysis, and acute in vivo toxicity of dendrimers based on melamine, candidate vehicles for drug delivery. *J. Am. Chem. Soc. 126*, 10044−10048.
(51) Kano, K., Kitagishi, H., Mabuchi, T., Kodera, M., and Hirota, S. (2006) A myoglobin functional model composed of a ferrous porphyrin and a cyclodextrin dimer with an imidazole linker. *Chem.−Asian J. 1*, 358−366.

Supporting Information:

Modification of a Dioxygen Carrier, HemoCD, with PEGylated Dendrons for Extension of Circulation Time in the Bloodstream

Keiichi Karasugi, Hiroaki Kitagishi, and Koji Kano*

Department of Molecular Chemistry and Biochemistry, Doshisha University, Kyotanabe, Kyoto 610-0321, Japan

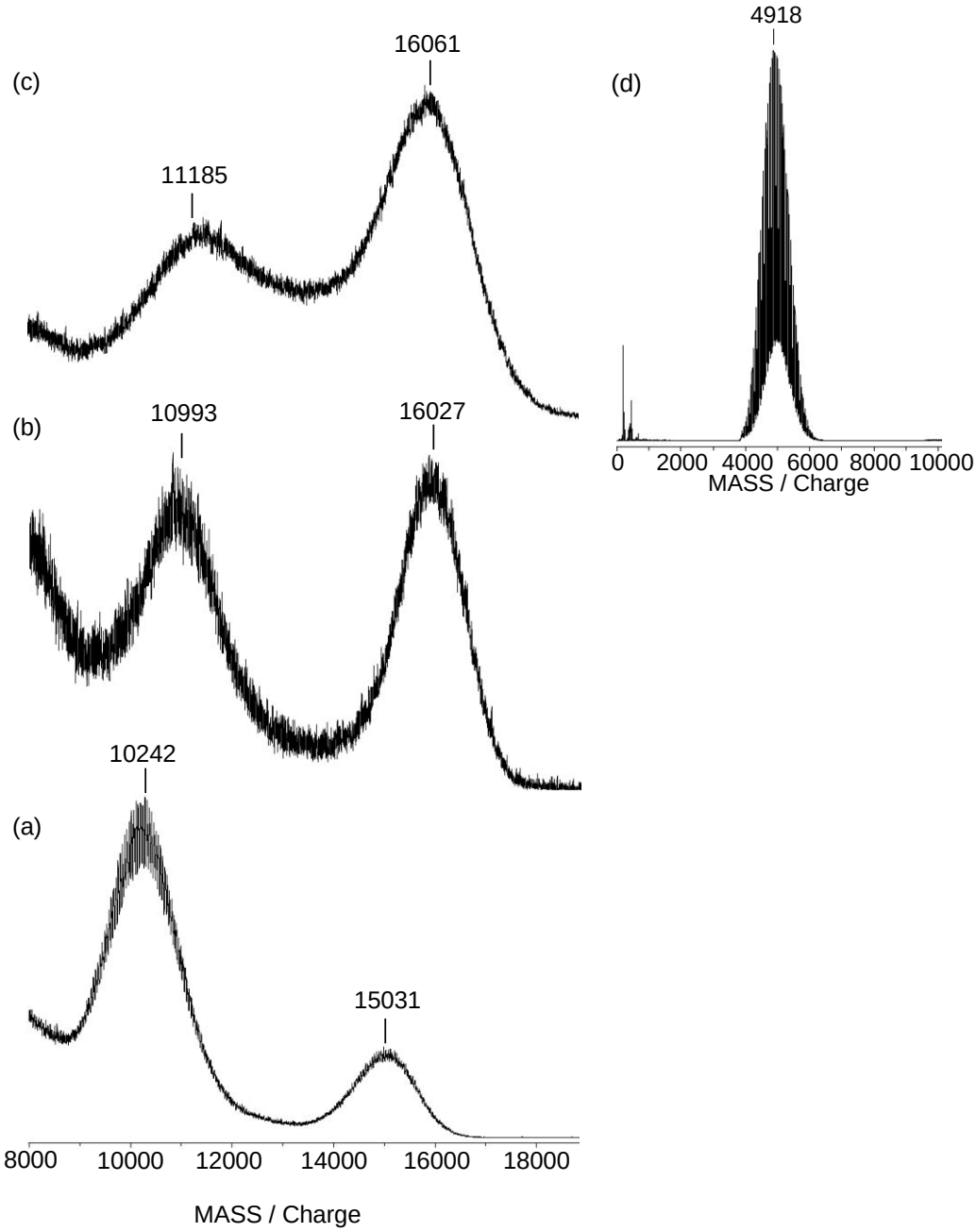

Figure S1. MALDI-TOF MS spectra (positive mode) of G1-dendron (a), G1-Por (b), and G1-Fe^{III}Por (c) with a subsequent addition of sinapinic acid. The spectra were recorded in a mass range of 8000－20000. (d) The MS spectrum of PEG_{5000}-NH_2 (positive mode, sinapinic acid matrix). The theoretical mass numbers were 14973, 16005, and 16036 for G1-dendron ($[M + Na]^+$), G1-Por ($[M + 4Na]^+$), and G1-Fe^{III}Por ($[M + 3Na - Cl]^+$), respectively, when the MW of one PEG chain (PEG_{5000}-NH-) was assumed to be 4917. The peaks due to fragmentation of the PEG_{5000} chain were detected. The full loadings of the three PEG_{5000} chains on the dendron were confirmed by ^1H NMR spectroscopy for G1-dendron and G1-Por.

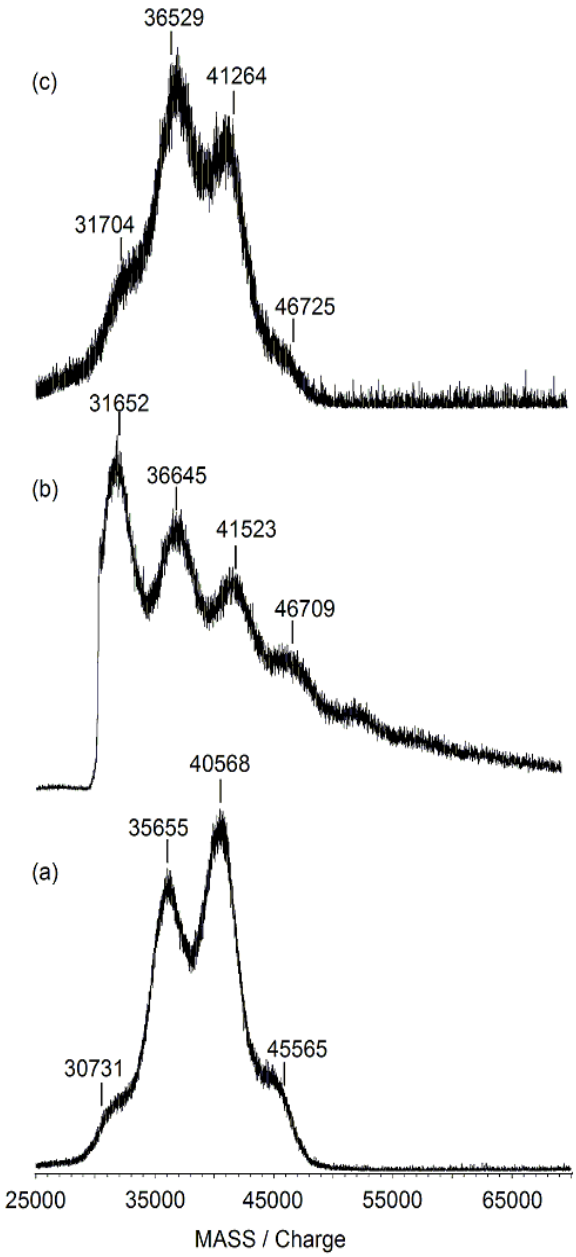

Figure S2. MALDI-TOF MS spectra (positive mode) of G2-dendron (a), G2-Por (b), and G2-Fe^{III}Por (c) with a subsequent addition of sinapinic acid. The spectra were recorded in a mass range of 25000—70000. The theoretical mass numbers were 45066, 46098, and 46129 for G2-dendron ($[M + Na]^+$), G2-Por ($[M + 4Na]^+$), and G2-Fe^{III}Por ($[M + 3Na – Cl]^+$), respectively, when the MW of one PEG chain (PEG_{5000}-NH-) was assumed to be 4917. The peaks due to fragmentation of the PEG_{5000} chain were detected. The full loadings of the nine PEG_{5000} chains on the dendron were confirmed by ^1H NMR spectroscopy for G2-dendron and G2-Por.

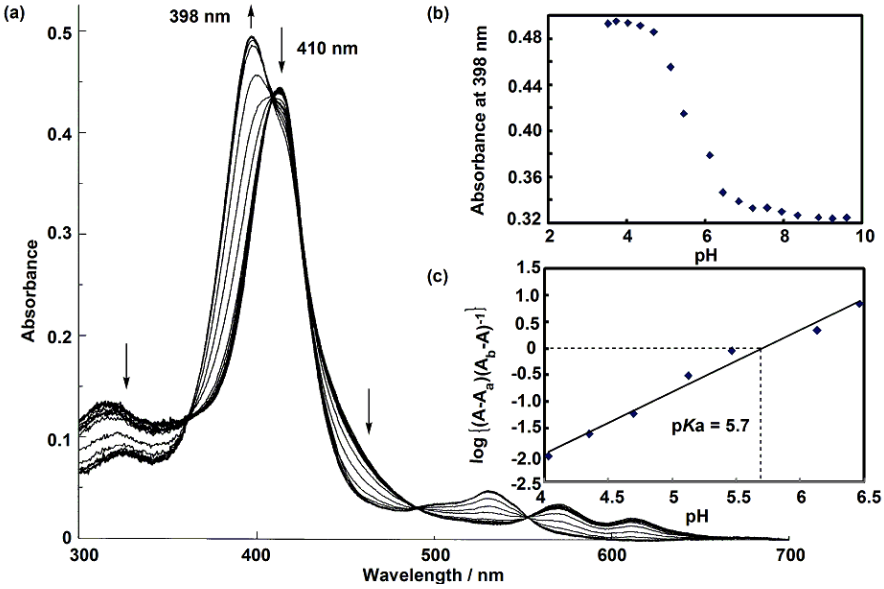

Figure S3. (a) UV-vis spectral changes of G1-Fe^{III}Por (5×10^{-6} M) as a function of pH in aqueous 0.1 M $NaClO_4$ at 25 °C. The pH values were adjusted by NaOH and $HClO_4$. (b) Changes in the absorbance at 398 nm as a function of pH. (c) Plot of $\log\{(A\text{-}A_a)(A_b\text{-}A)^{-1}\}$ at 398 nm versus pH for determining pK_a.

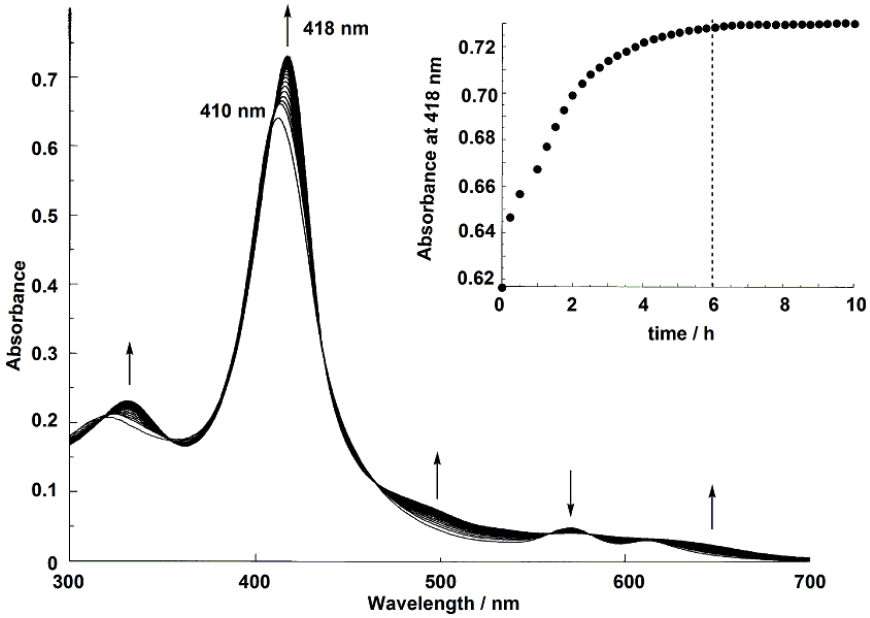

Figure S4. UV-vis spectral changes of G2-Fe^{III}Por after a freshly prepared G2-Fe^{III}Por stock solution (1 x 10^{-3} M) was diluted with a 0.05 M phosphate buffer (pH 7.4) to 4.56 $\times 10^{-6}$ M at 25 °C. The spectra were recorded at 15 min-intervals. Inset shows the time course of the absorbance at 418 nm.

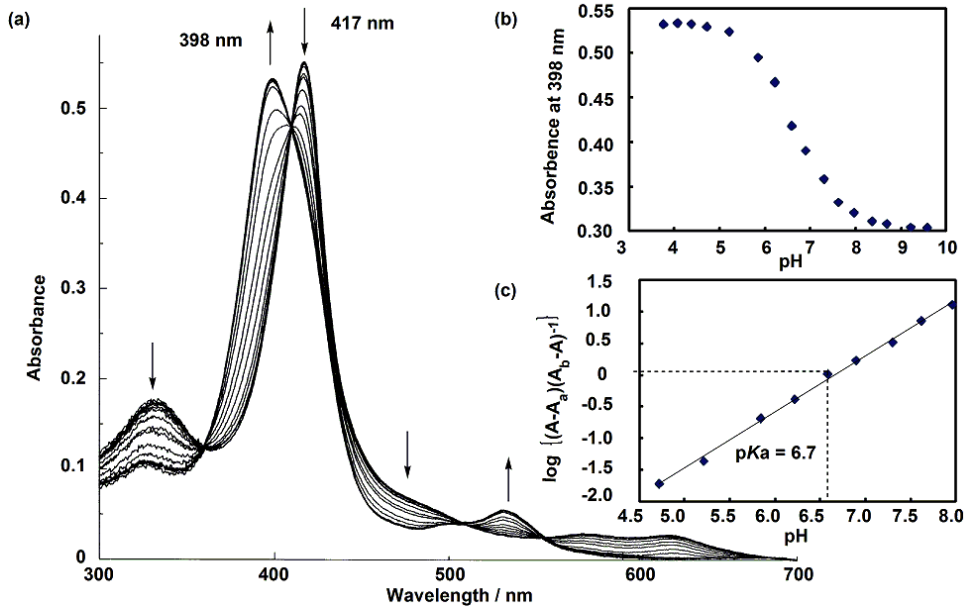

Figure S5. (a) UV-vis spectral changes of G2-Fe^{III}Por (5×10^{-6} M) as a function of pH in aqueous 0.1 M $NaClO_4$ at 25 °C. The pH values were adjusted by NaOH and $HClO_4$. (b) Changes in the absorbance at 398 nm as a function of pH. (c) Plot of $\log\{(A\text{-}A_a)(A_b\text{-}A)^{-1}\}$ at 398 nm versus pH for determining pK_a.

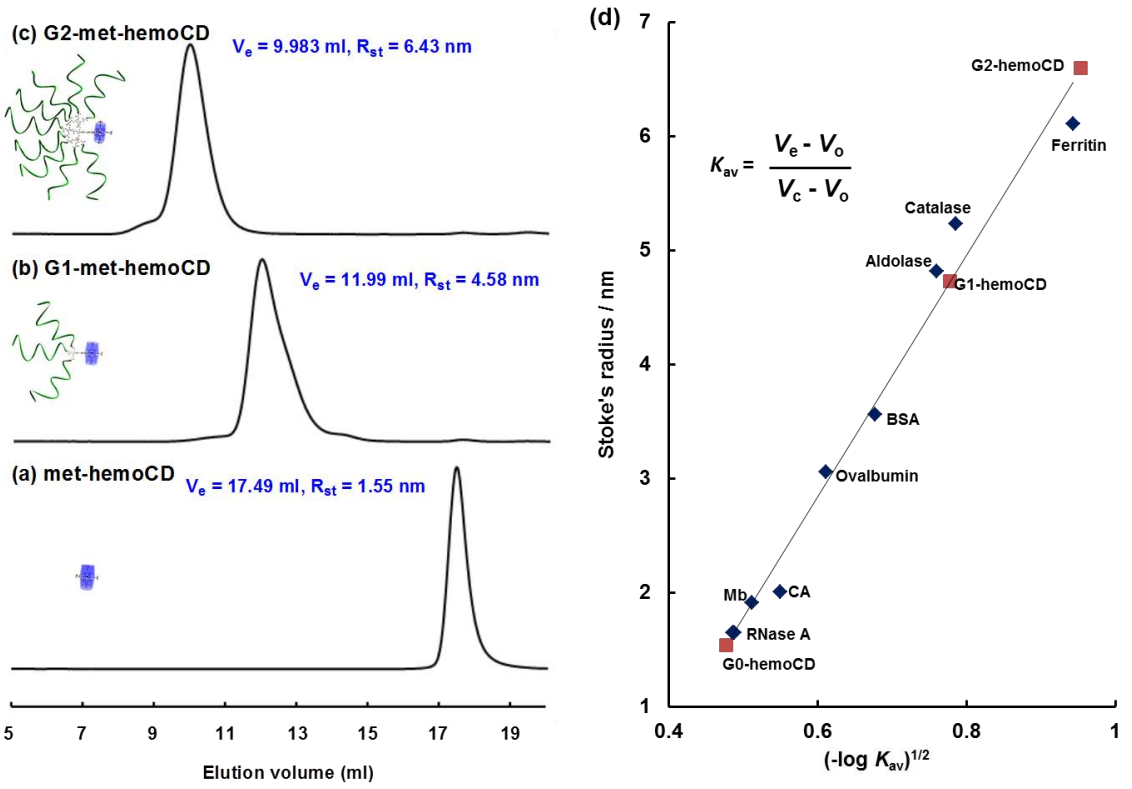

Figure S6. GFC profiles of met-hemoCD (a), G1-met-hemoCD (b), and G2-met-hemoCD (c). A Superdex 200 10/300GL column was used with a flow rate of 0.5 mL/min using 0.05 M phosphate buffer at pH 7.4 and 4 °C. Elution was monitored at 410 nm. (d) A calibration curve for estimating the Stokes radii (hydrodynamic radii) of met-hemoCD, G1-met-hemoCD, and G2-met-hemoCD (red squares) using standard samples (blue diamonds). Partition coefficients (K_{av}) were determined from the equation $K_{av} = (V_e - V_o)/(V_c - V_o)$, where V_e, V_o, and V_c denote the elution volume, the column void volume, and the total bed volume of the column, respectively. CA: carbonic anhydrase, RNase A: ribonuclease A, BSA: bovine serum albumin.

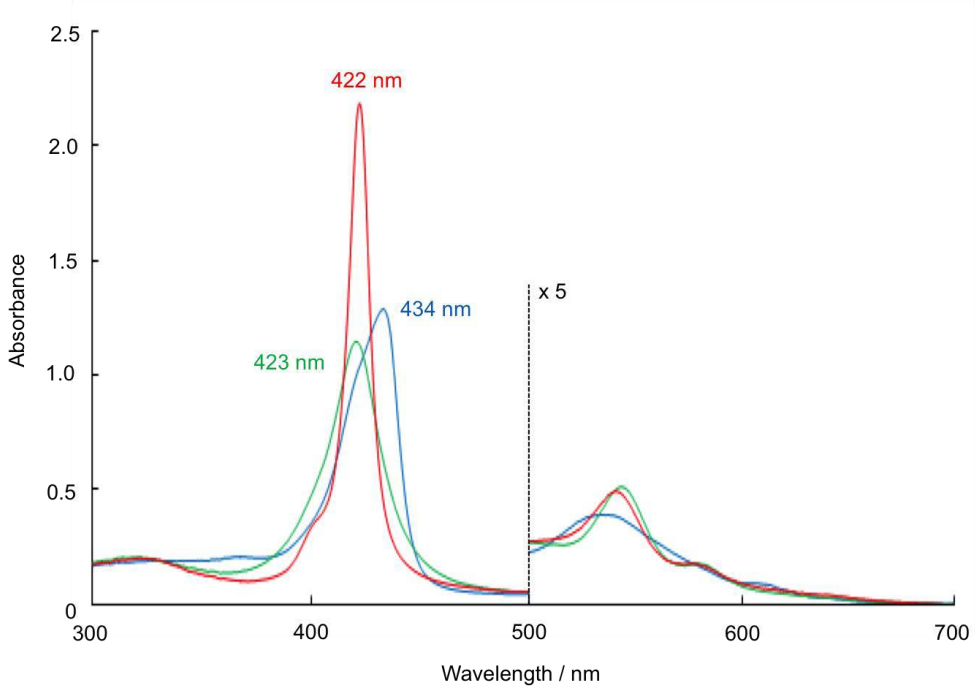

Figure S7. UV-vis spectra of G1-hemoCD ([G1-Fe^{II}Por] = 9.4 × 10^{-6} M, [Py3CD] = 1.1 × 10^{-5} M) under N_2 (blue), O_2 (green), and CO (red) atmospheres in 0.05 M phosphate buffer at pH 7.4 and 25 °C.

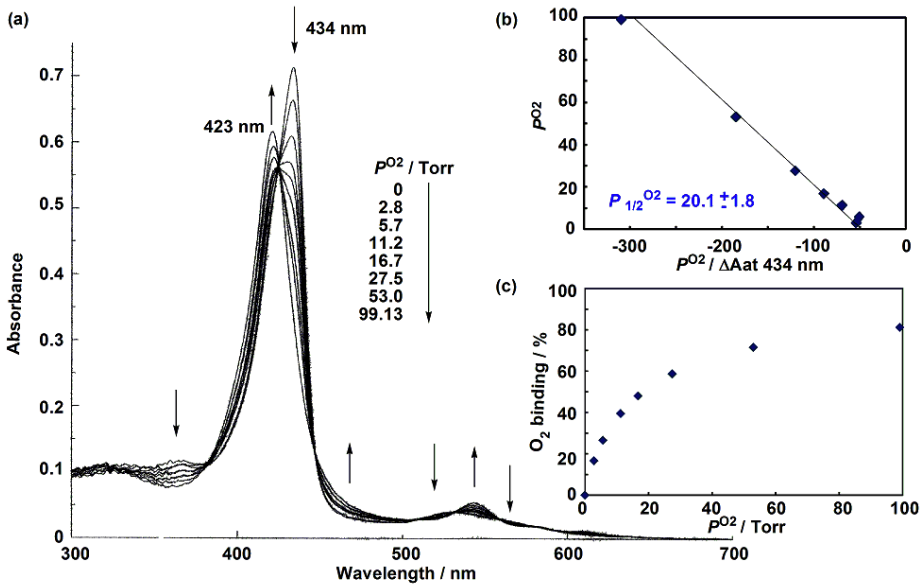

Figure S8. UV-vis spectral changes of G1-hemoCD (3.3 × 10^{-6} M) as a function of the O_2 partial pressure (P^{O2}) in N_2 in 0.05 M phosphate buffer at pH 7.4 and 37 °C (a), plot of P^{O2} / ΔA versus P^{O2} for determining $P_{1/2}$ (b), and the titration curve for O_2 binding to G1-hemoCD (c).

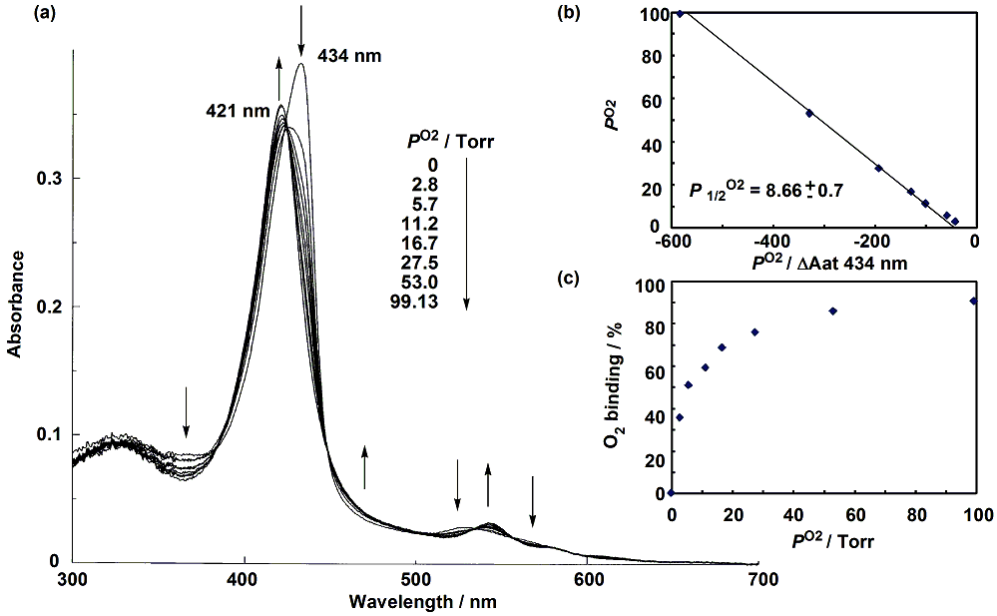

Figure S9. UV-vis spectral changes of G2-hemoCD (3.0×10^{-6} M) as a function of the O_2 partial pressure (P^{O2}) in N_2 in 0.05 M phosphate buffer at pH 7.4 and 25 °C (a), plot of P^{O2} / ΔA versus P^{O2} for determining $P_{1/2}$ (b), and the titration curve for O_2 binding to G2-hemoCD (c).

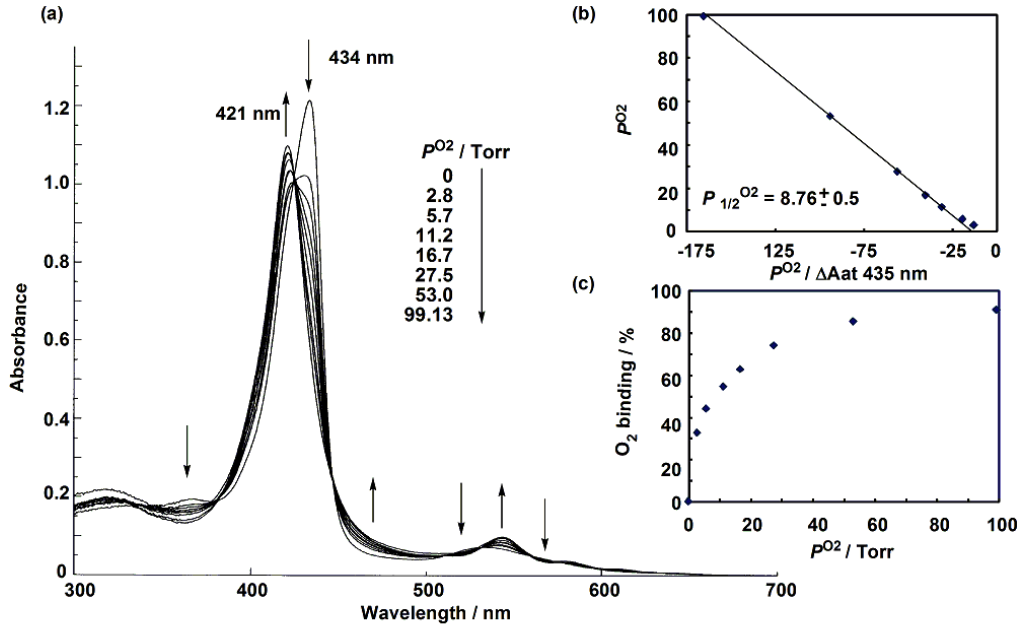

Figure S10.

Figure S10. UV-vis spectral changes of G1-hemoCD (9.5×10^{-6} M) as a function of the O_2 partial pressure (P^{O2}) in N_2 in 0.05 M phosphate buffer at pH 7.4 and 25 °C (a), plot of P^{O2} / ΔA versus P^{O2} for determining $P_{1/2}$ (b), and the titration curve for O_2 binding to G1-hemoCD (c).

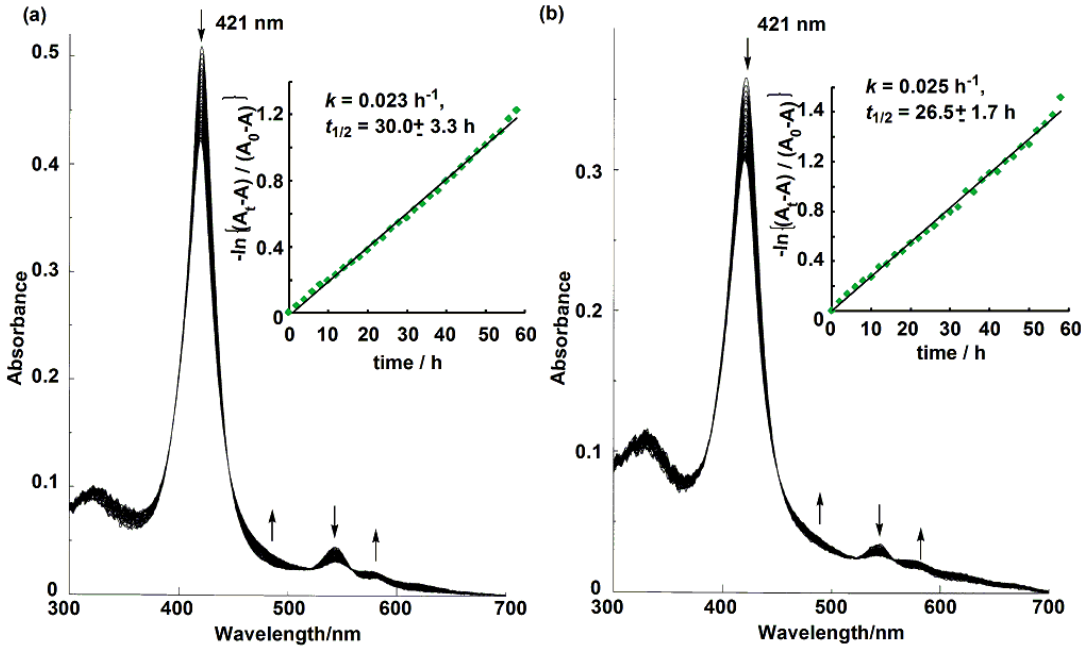

Figure S11. Autoxidation reactions of the O_2 adducts of G1-hemoCD (a, 4.6 x 10^{-6} M) and G2-hemoCD (b, 3.3 x 10^{-6} M) under air in 0.05 M phosphate buffer at pH 7.4 and 25 ^{o}C. The spectra were measured at 2 h-intervals. Inset: first-order plots based on the absorption changes at 421 nm.

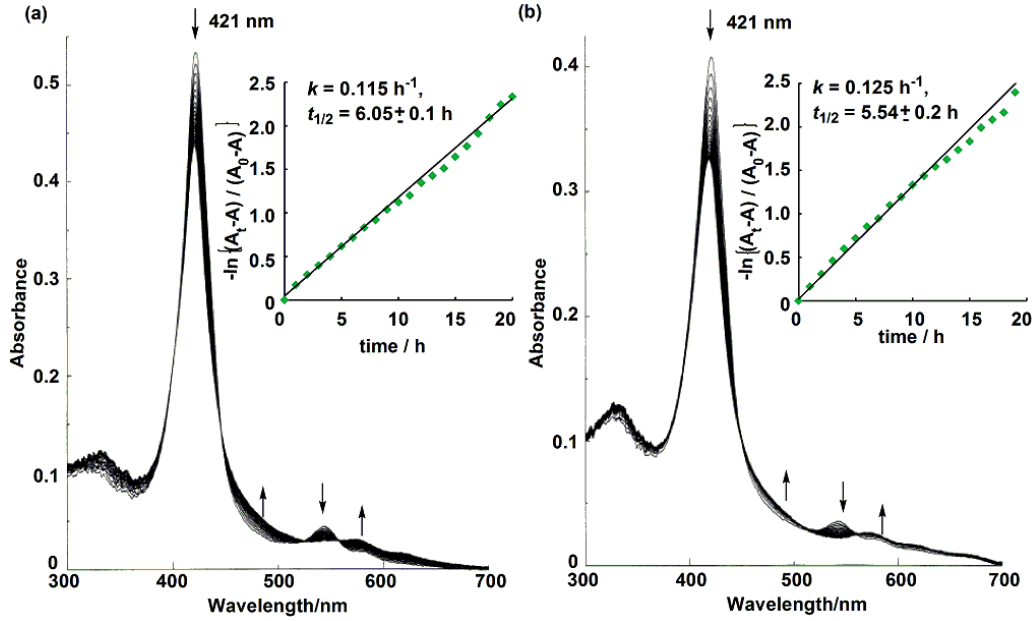

Figure S12. Autoxidation reactions of the O_2 adducts of G1-hemoCD (a, 3.4 x 10^{-6} M) and G2-hemoCD (b, 2.5 x 10^{-6} M) under air in 0.05 M phosphate buffer at pH 7.4 and 37 ^{o}C. The spectra were measured at 1 h-intervals. Inset: first-order plot based on the absorption changes at 421 nm.

Bioconjugate Chemistry

Article

pubs.acs.org/bc

Synthesis and Biological Evaluation of Low Molecular Weight Fluorescent Imaging Agents for the Prostate-Specific Membrane Antigen

Ying Chen,[†] Mrudula Pullambhatla,[†] Sangeeta R. Banerjee.,[†] Youngjoo Byun,[‡] Marigo Stathis,[§] Camilo Rojas,[§] Barbara S. Slusher,[§] Ronnie C. Mease,[†] and Martin G. Pomper*,[†]

[†]Russell H. Morgan Department of Radiology and [§]NeuroTranslational Drug Discovery Program, Brain Science Institute, Johns Hopkins Medical School, Baltimore, Maryland 21231, United States

[‡]College of Pharmacy, Korea University, 2511 Sejong-ro, Jochiwon-eup, Yeongi-gun, Chungnam 339-700, South Korea

Supporting Information

ABSTRACT: Targeted near-infrared (NIR) optical imaging can be used in vivo to detect specific tissues, including malignant cells. A series of NIR fluorescent ligands targeting the prostate-specific membrane antigen (PSMA) was synthesized and each compound was tested for its ability to image PSMA+ tissues in experimental models of prostate cancer. The agents were prepared by conjugating commercially available active esters of NIR dyes, including IRDye800CW, IRDye800RS, Cy5.5, Cy7, or a derivative of indocyanine green (ICG) to the terminal amine group of (*S*)-2-(3-((*S*)-5-amino-1-carboxypentyl)ureido)pentanedioic acid **1**, (14*S*,18*S*)-1-amino-8,16-dioxo-3,6-dioxa-9,15,17-triazaicosane-14,18,20-tricarboxylic acid **2** and (3*S*,7*S*)-26-amino-5,13,20-trioxo-4,6,12,21-tetraazahexacosane-1,3,7,22-tetracarboxylic acid **3**. The K_i values for the dye–inhibitor conjugates ranged from 1 to 700 pM. All compounds proved capable of imaging PSMA+ tumors selectively to varying degrees depending on the choice of fluorophore and linker. The highest tumor uptake was observed with IRDye800CW employing a poly(ethylene glycol) or lysine–suberate linker, as in 800CW-**2** and 800CW-**3**, while the highest tumor to nontarget tissue ratios were obtained for Cy7 with these same linkers, as in Cy7-**2** and Cy7-**3**. Compounds **2** and **3** provide useful scaffolds for targeting of PSMA+ tissues in vivo and should be useful for preparing NIR dye conjugates designed specifically for clinical intraoperative optical imaging devices.

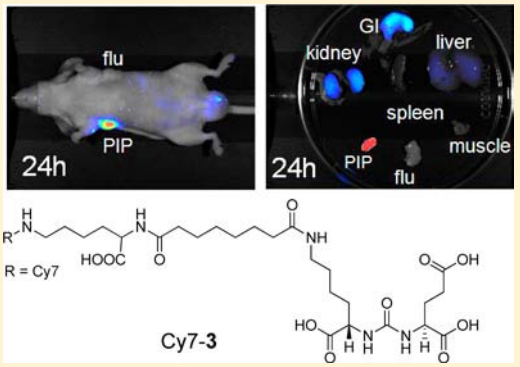

INTRODUCTION

The National Cancer Institute estimates 241 740 new cases and 28 170 new deaths from prostate cancer (PCa) in 2012.[1] PCa is the second leading cause of cancer-related death in men. Surgery is the most commonly used treatment for clinically localized PCa and provides a survival advantage compared to watchful waiting.[2] A pressing issue in surgery for PCa is the assurance of a complete resection of the tumor, namely, a negative surgical margin. A positive surgical margin necessitates adjuvant radiation therapy, which is required in up to 27.8% of patients[3] compared to 9.1% of men undergoing radical retropubic prostatectomy. Given that currently more than 50 000 radical prostatectomies are performed annually, these statistics would suggest that more than 9000 men are undergoing unnecessary adjuvant radiation therapy.[4] Given that such radiation therapy costs in excess of $25 000 per patient, the estimated cost of preventable positive margins is at least $225 M annually.

Local tumor invasion can be difficult to assess pre- and even intraoperatively, but its detection during surgery can be augmented through the use of fluorescent dyes that home to tumor in conjunction with an excitation laser and camera that are tuned to the excitation and emission wavelengths of the dye employed.[5−7] While such intraoperative tumor detection has been performed using nontargeted agents,[8] targeted agents are coming online.[9,10] Because of superior tissue penetration and less interference from the presence of blood in the surgical field, dyes with emission wavelengths in the near-infrared (NIR) region of the spectrum (650−900 nm) are generally employed for this purpose.[11] Because of its abundant expression on the surface of PCa[12,13] as well as within most solid tumor neovasculature,[14−17] we have developed a series of NIR-emitting dyes that target the prostate-specific membrane antigen (PSMA).

We and others have synthesized a variety of low-molecular-weight PSMA-targeting radiotracers to enable imaging of PCa, with several such agents currently in the clinic.[18−21] Optical agents have also been synthesized,[22−24] and we have previously tested one such compound in mice to good effect.[9] While a variety of radiolabeled PSMA-targeting antibodies have been

Received: July 16, 2012
Revised: November 12, 2012
Published: November 19, 2012

ACS Publications © 2012 American Chemical Society

used for tumor imaging,[25−27] we prefer agents of low molecular weight due to more tractable pharmacokinetics, namely, more rapid washout from nontarget sites enabling imaging within hours rather than days of administration.

NIR-emitting optical dyes are relatively large organic molecules with extended conjugation, which presents two potential difficulties for target acquisition in vivo: (1) steric hindrance when linked to small affinity agents, such as the ureas present in many of the above mentioned PSMA inhibitors; and (2) poor pharmacokinetics. Recently, we reported the preparation and evaluation in vivo of YC-27 (800CW-**3**), which contains a lysine−suberate linker between the dye (IRDye800CW, LI-COR Biosciences, Lincoln, NE) and the PSMA targeting urea.[9] With 800CW-**3** we were able to visualize a PSMA+ tumor xenograft by optical imaging, demonstrating that with a long lysine−suberate linking moiety, i.e., a long linker, PSMA inhibitors containing bulky groups will still bind to the target. Here, we extend this work by synthesizing and testing a series of PSMA-targeted NIR fluorescent agents, each containing either no linker, or one of two different linking groups that have different pharmacokinetic implications for imaging in vivo.

EXPERIMENTAL PROCEDURES

Chemistry. *General Methods.* All chemicals and solvents were purchased from either Sigma-Aldrich (Milwaukee, WI) or Fisher Scientific (Pittsburgh, PA). The *N*-hydroxysuccinimide (NHS) esters of IRDye800CW and IRDye800RS were purchased from LI-COR Biosciences. The *N*-hydroxysulfosuccinimide ester of ICG derivative (ICG-sulfo-OSu) was purchased from DOJINDO Molecular Technologies (Rockville, MD). The NHS esters of Cy7 and Cy5.5 were purchased from GE Healthcare (Piscataway, NJ). ^{1}H NMR spectra were obtained on a Bruker Avance 400 MHz Spectrometer (Billerica, MA). Mass spectra were obtained on a Bruker Esquire 3000 plus system (ESI) or an Applied Biosystems Voyager DE-FTR MALDI-TOF (Foster City, CA). High-performance liquid chromatography (HPLC) purifications were performed on a Waters 625 LC system (Milford, MA) or a Varian Prostar System (Varian Medical Systems, Palo Alto, CA). Optical images were obtained using the Pearl Impulse Imager (LI-COR Biosciences, Lincoln, NE) and a Xenogen IVIS Spectrum (Caliper Life Sciences, Hopkinton, MA). HPLC traces of all of the final compounds are available in the Supporting Information.

*Synthesis of (S)-2-(3-((S)-5-Amino-1-carboxypentyl)-ureido)pentanedioic Acid (**1**).* To a solution of (10*S*,14*S*)-tris(4-methoxybenzyl) 2,2-dimethyl-4,12-dioxo-3-oxa-5,11,13-triazahexadecane-10,14,16-tricarboxylate **4**[28] (0.264 g, 0.033 mmol) a solution of 3% anisole in TFA (1 mL) was added and the mixture was reacted at room temperature for 20 min, then concentrated on a rotary evaporator. The crude material was purified by HPLC [Econosphere C18, 10 μm, 250 × 10 mm, H_2O/CH_3CN/TFA (92/8/0.1), 4 mL/min] to afford 0.108 g (74%) of **1** (retention time = 4 min). ^{1}H NMR (400 MHz, D_2O) δ 4.17−4.25 (m, 2H), 2.94−2.98 (m, 2H), 2.46−2.50 (m, 2H), 2.11−2.19 (m, 1H), 1.80−1.98 (m, 2H), 1.61−1.73 (m, 3H), 1.40−1.49 (m, 2H). ^{13}C NMR (400 MHz, D_2O): δ 176.9, 176.8, 176.2, 163.0, 162.7, 162.3, 162.0, 158.8, 120.2, 117.3, 114.1, 111.5, 52.7, 52.4, 38.8, 30.0, 29.7, 25.8, 25.7, 21.5. ESI-Mass calcd for $C_{12}H_{22}N_3O_7$ $[M]^+$ 320.2, found 320.0.

*Synthesis of 800CW-**1**.* To a solution of **1** (0.5 mg, 1.15 μmol) in DMSO (0.1 mL) was added *N*,*N*-diisopropylethylamine (0.002 mL, 11.5 μmol), followed by the NHS ester of IRDye800CW (0.3 mg, 0.26 μmol). After 2 h at room temperature, the reaction mixture was purified by HPLC (Econosphere C18, 5 μm, 150 × 4.6 mm; mobile phase, A = 0.1% TFA in H_2O, B = 0.1% TFA in CH_3CN; gradient, 0 min = 5% B, 5 min = 5% B, 45 min = 100% B; flow rate, 1 mL/min) to afford 0.2 mg (60%) of 800CW-**1** (retention time = 15 min). ESI-Mass calcd for $C_{58}H_{74}N_5O_{21}S_4$ $[M]^+$ 1304.4, found 1303.8.

*Synthesis of 800RS-**1**.* To a solution of **1** (0.2 mg, 0.46 μmol) in DMSO (0.05 mL) was added *N*,*N*-diisopropylethylamine (0.002 mL, 11.5 μmol), followed by the NHS ester of IRDye800RS (0.2 mg, 0.21 μmol). After 2 h at room temperature, the reaction mixture was purified by HPLC as described for 800CW-**1** to afford 0.2 mg (84%) of 800RS-**1** (retention time = 23 min). ESI-Mass calcd for $C_{58}H_{73}N_5O_{15}S_2$ $[M]^+$ 1143.5, found 572.5 $[M+H]^{2+}$, 1144.0 $[M]^+$.

*Synthesis of ICG-**1**.* To a solution of **1** (0.2 mg, 0.46 μmol) in DMSO (0.1 mL) was added *N*,*N*-diisopropylethylamine (0.002 mL, 11.5 μmol), followed by ICG-sulfo-OSu (0.3 mg, 0.32 μmol). After 2 h at room temperature, the reaction mixture was purified by HPLC as described for 800CW-**1** to afford 0.2 mg (60%) of ICG-**1** (retention time = 24 min). ESI-Mass calcd for $C_{57}H_{69}N_5O_{11}S$ $[M]^+$ 1031.5, found 516.5 $[M+H]^{2+}$, 1032.0 $[M]^+$.

*Synthesis of Cy7-**1**.* To a solution of **1** (0.5 mg, 1.15 μmol) in DMSO (0.1 mL) was added *N*,*N*-diisopropylethylamine (0.002 mL, 11.5 μmol), followed by the NHS ester of Cy7 (0.3 mg, 0.37 μmol). After 2 h at room temperature, the reaction mixture was purified by HPLC as described for 800CW-**1** to afford 0.2 mg (55%) of Cy7-**1** (retention time = 16 min). ESI-Mass calcd for $C_{47}H_{61}N_5O_{14}S_2$ $[M]^+$ 983.4, found 492.5 $[M+H]^{2+}$, 984.0 $[M]^+$.

*Synthesis of Cy5.5-**1**.* To a solution of **1** (0.5 mg, 1.15 μmol) in DMSO (0.1 mL) was added *N*,*N*-diisopropylethylamine (0.002 mL, 11.5 μmol), followed by the NHS ester of Cy5.5 (0.3 mg, 0.27 μmol). After 2 h at room temperature, the reaction mixture was purified by HPLC as described for 800CW-**1** to afford 0.2 mg (62%) of Cy5.5-**1** (retention time = 14 min). ESI-Mass calcd for $C_{53}H_{63}N_5O_{20}S_4$ $[M]^+$ 1217.3, found 609.4 $[M+H]^{2+}$, 1217.7 $[M]^+$.

*Synthesis of (14S,18S)-1-Amino-8,16-dioxo-3,6-dioxa-9,15,17-triazaicosane-14,18,20-tricarboxylic Acid (**2**).* To the tosylate salt of (*S*)-5-(3-((*S*)-1,5-bis((4-methoxybenzyl)oxy)-1,5-dioxopentan-2-yl)ureido)-6-((4-methoxybenzyl)oxy)-6-oxohexan-1-aminium **5**[28,29] (0.103 g, 0.121 mmol) in DMF (2 mL) was added Boc-NH$(CH_2CH_2O)_2CH_2COOH$ (0.060 g, 0.135 mmol) and TBTU (0.040g, 0.125 mmol), followed by *N*,*N*-diisopropylethylamine (0.042 mL, 0.241 mmol). After stirring overnight at room temperature, the solvent was evaporated on a rotary evaporator. The crude material was purified by silica gel column chromatography using methanol/methylene chloride (5:95) to give 0.101 g of (14*S*,18*S*)-tris(4-methoxybenzyl) 1-amino-8,16-dioxo-3,6-dioxa-9,15,17-triazaicosane-14,18,20-tricarboxylate, **6** in 90% yield. MALDI-TOF Mass calcd for $C_{47}H_{64}N_4NaO_{15}$ $[M+Na]^+$ 947.4, found 947.1. Compound **6** was dissolved in a solution of 3% anisole in TFA (1 mL), allowed to react at room temperature for 10 min, and then concentrated. The crude material was purified by HPLC [Econosphere C18, 10 μm, 250 × 10 mm, H_2O/CH_3CN/TFA (92/8/0.1), 4 mL/min] to afford 0.035 g (57%) of **2** (retention time = 11 min). ^{1}H NMR (400 MHz, D_2O) δ 4.17−4.21 (m, 1H), 4.10−4.13 (m, 1H), 4.00 (s, 2H), 3.67−3.71 (m, 6H), 3.14−3.20 (m, 4H), 2.43−2.46 (m, 2H), 2.08−2.13 (m, 1H),

dx.doi.org/10.1021/bc3003919 | *Bioconjugate Chem.* 2012, 23, 2377−2385

1.87−1.93 (m, 1H), 1.76−1.79 (m, 1H), 1.63−1.67 (m, 1H), 1.45−1.50 (m, 2H), 1.33−1.40 (m, 2H). ^{13}C NMR (400 MHz, D_2O): δ 176.9, 176.8, 176.0, 171.7, 163.0, 162.7, 162.3, 162.0, 158.8, 117.3, 114.4, 69.8, 69.0, 65.9, 52.8, 52.2, 38.6, 38.1, 30.1, 29.6, 27.3, 25.8, 21.5. ESI-Mass calcd for $C_{18}H_{33}N_4O_{10}$ $[M]^+$ 465.2, found 465.2.

Synthesis of 800CW-2. To a solution of compound **2** (0.3 mg, 0.52 μmol) in DMSO (0.05 mL) was added *N,N*-diisopropylethylamine (0.002 mL, 11.5 μmol), followed by the NHS ester of IRDye800CW (0.2 mg, 0.17 μmol). After 2 h at room temperature, the reaction mixture was purified by HPLC (Econosphere C18, 5 μm, 150 × 4.6 mm mobile phase, A = 50 mM triethylamine acetate buffer (pH 6.0), B = CH_3CN; gradient, 0 min = 0% B, 5 min = 0% B, 45 min = 100% B; flow rate, 1 mL/min) to afford 0.2 mg (80%) of 800CW-**2** (retention time = 22 min). ESI-Mass calcd for $C_{64}H_{84}N_6O_{24}S_4$ $[M]^+$ 1448.4, found 1448.7.

Synthesis of 800RS-2. To a solution of **2** (0.3 mg, 0.52 μmol) in DMSO (0.05 mL) was added *N,N*-diisopropylethylamine (0.002 mL, 11.4 μmol), followed by the NHS ester of IRDye800RS (0.2 mg, 0.21 μmol). After 2 h at room temperature, the reaction mixture was purified by HPLC as in 800CW-**2** to afford 0.2 mg (75%) of 800RS-**2** (retention time = 28 min). ESI-Mass calcd for $C_{64}H_{84}N_6O_{18}S_2$ $[M]^+$ 1288.5, found 1288.9.

Synthesis of ICG-2. To a solution of **2** (0.5 mg, 0.86 μmol) in DMSO (0.1 mL) was added *N,N*-diisopropylethylamine (0.002 mL, 11.5 μmol), followed by ICG-sulfo-OSu (0.3 mg, 0.32 μmol). After 2 h at room temperature, the reaction mixture was purified by HPLC as described for 800CW-**1** to afford 0.2 mg (53%) of ICG-**2** (retention time = 26 min). ESI-Mass calcd for $C_{63}H_{80}N_6O_{14}S$ $[M]^+$ 1176.5, found 589.1 $[M+H]^{2+}$, 1177.1 $[M]^+$.

Synthesis of Cy7-2. To a solution of **2** (0.5 mg, 0.86 μmol) in DMSO (0.1 mL) was added *N,N*-diisopropylethylamine (0.002 mL, 11.5 μmol), followed by the NHS ester of Cy7 (0.2 mg, 0.24 μmol). After 2 h at room temperature, the reaction mixture was purified by HPLC as in 800CW-**1** to afford 0.2 mg (72%) of Cy7-**2** (retention time = 17 min). ESI-Mass calcd for $C_{53}H_{72}N_6O_{17}S_2$ $[M]^+$ 1128.4, found 565.0 $[M+H]^{2+}$, 1129.0 $[M]^+$.

Synthesis of Cy5.5-2. To a solution of **2** (0.5 mg, 0.86 μmol) in DMSO (0.1 mL) was added *N,N*-diisopropylethylamine (0.002 mL, 11.5 μmol), followed by the NHS ester of Cy5.5 (0.2 mg, 0.18 μmol). After 2 h at room temperature, the reaction mixture was purified by HPLC as in 800CW-**1** to afford 0.2 mg (83%) of Cy5.5-**2** (retention time = 13 min). ESI-Mass calcd for $C_{59}H_{74}N_6O_{23}S_4$ $[M]^+$ 1362.4, found 681.9 $[M+H]^{2+}$, 1362.7 $[M]^+$.

Synthesis of 800RS-3. To a solution of **3**[9] (0.3 mg, 0.42 μmol) in DMSO (0.1 mL) was added *N,N*-diisopropylethylamine (0.002 mL, 11.5 μmol), followed by the NHS ester of IRDye800RS (0.3 mg, 0.31 μmol). After 2 h at room temperature, the reaction mixture was purified by HPLC (column, Econosphere C18 5 μ, 150 × 4.6 mm; retention time, 27 min; mobile phase, A = 0.1% TFA in H_2O, B = 0.1% TFA in CH_3CN; gradient, 0 min = 0% B, 5 min = 0% B, 45 min = 100% B; flow rate, 1 mL/min) to afford 0.3 mg (67%) of 800RS-**3** (retention time = 27 min). ESI-Mass calcd for $C_{72}H_{97}N_7O_{19}S_2$ $[M]^+$ 1427.6, found 714.4 $[M+H]^{2+}$, 1427.8 $[M]^+$.

Synthesis of ICG-3. To a solution of **3** (0.5 mg, 0.71 μmol) in DMSO (0.1 mL) was added *N,N*-diisopropylethylamine (0.002 mL, 11.5 μmol), followed by ICG-Sulfo-OSu (0.3 mg, 0.32 μmol). After 2 h at room temperature, the reaction mixture was purified by HPLC as in 800RS-**3** to afford 0.3 mg (71%) of ICG-**3** (retention time = 32 min). ESI-Mass calcd for $C_{71}H_{93}N_7O_{15}S$ $[M]^+$ 1315.6, found 1316.0 $[M]^+$.

Synthesis of Cy7-3. To a solution of **3** (0.5 mg, 0.71 μmol) in DMSO (0.1 mL) was added *N,N*-diisopropylethylamine (0.002 mL, 11.5 μmol), followed by the NHS ester of Cy7 (0.5 mg, 0.61 μmol). After 2 h at room temperature, the reaction mixture was purified by HPLC as in 800RS-**3** to afford 0.5 mg (64%) of Cy7-**3** (retention time = 19 min). ESI-Mass calcd for $C_{61}H_{85}N_7O_{18}S_2$ $[M]^+$ 1267.5, found 634.5 $[M+H]^{2+}$, 1267.9 $[M]^+$.

Synthesis of Cy5.5-3. To a solution of **3** (0.5 mg, 0.71 μmol) in DMSO (0.1 mL) was added *N,N*-diisopropylethylamine (0.002 mL, 11.5 μmol), followed by the NHS ester of Cy5.5 (0.5 mg, 0.44 μmol). After 2 h at room temperature, the reaction mixture was purified by HPLC as in 800RS-**3** to afford 0.6 mg (90%) of Cy5.5-**3** (retention time = 18 min). ESI-Mass calcd for $C_{67}H_{87}N_7O_{24}S_4$ $[M]^+$ 1501.5, found 751.4 $[M+H]^{2+}$, 1501.6 $[M]^+$.

Biology. *In Vitro PSMA Inhibition Assay.* The PSMA binding affinities of the dye−urea conjugates for PSMA were measured using the *N*-acetylated-α-linked acidic dipeptidase (NAALADase) assay, as previously described.[30,31] PSMA is known also as glutamate carboxypeptidase II (GCPII), or NAALADase.[32,33] A reaction mixture (total volume of 50 μL) containing [^{3}H]*N*-acetyl-aspartylglutamate ([^{3}H]NAAG, 30 nM, 1850 GBq/mmol) and human recombinant GCPII (40 pM final) in Tris-HCl (pH 7.4, 40 mM) containing 1 mM $CoCl_2$ was used. The reaction was carried out at 37 °C for 15 min and stopped with ice-cold sodium phosphate buffer (pH 7.4, 0.1 M, 50 μL). Blanks were obtained by incubating the reaction mixture in the presence of 2-phosphonomethyl pentanedioic acid (2-PMPA, 1 μM final), a selective and potent inhibitor of PSMA.[32] Dye−urea conjugates and controls were tested at log-unit final concentrations that ranged from 100 μM to < fM. A 90 μL aliquot from each terminated reaction was transferred to a well in a 96-well spin column containing AG1 × 8 ion-exchange resin. The plate was centrifuged at 1500 rpm for 5 min using a Beckman GS-6R centrifuge (Beckman Coulter, Inc., Brea, CA) equipped with a PTS-2000 rotor. [^{3}H]NAAG bound to the resin and [^{3}H]-glutamate eluted in the flowthrough. Columns were then washed twice with formate (1 M, 90 μL) to ensure complete elution of [^{3}H]glutamate. The flowthrough and the washes were collected in a deep 96-well block. From each well with a total volume of 270 μL, a 200 μL aliquot was transferred to its respective well in a solid scintillator-coated 96-well plate (Packard, Meriden, CT) and dried to completion. The radioactivity corresponding to [^{3}H]glutamate was determined with a scintillation counter (Topcount NXT, Packard, counting efficiency 80%). IC_{50} curves were generated from CPM results, by use of both *Microsoft Office Excel 2007* and *GraphPad Prism 5* programs, with K_i values derived from the IC_{50} values.[34]

Cell Lines and Tumor Models. PSMA+ PC3 PIP and PSMA nonexpressing PC3 flu cell lines were originally a gift from Warren Heston (Cleveland Clinic Foundation[35]). Cells were cultured in RPMI 1640 medium (Mediatech, Manassas, VA) containing 10% FBS (Sigma) and 1% penicillin−streptomycin (Mediatech) in a humidified incubator under 5% CO_2 at 37 °C. Cells were cultured to 80% confluence and then trypsinized and collected. Two million cells each of PSMA+ PC3 PIP and

PSMA- PC3 flu were resuspended in 0.1 mL PBS (Mediatech) and injected subcutaneously (s.c.) into 4−6-week-old male athymic nude mice (NCI, Frederick, MD) in the upper right and left flanks. Mice were used in imaging studies when tumors reached 3−5 mm in diameter.

In Vivo Imaging and Ex Vivo Biodistribution. In vivo images with compounds Cy5.5-**1**, Cy5.5-**2**, and Cy5.5-**3** were acquired on the IVIS Spectrum using an excitation wavelength of 675 nm and detection of the emission wavelength at 720 nm. The exposure time for each image acquisition was 1 s. Images were scaled to the same maximum intensity using the supplier's software.

Compounds containing 800CW, 800RS, ICG derivative, and Cy7 as fluorophores were imaged using the Pearl Impulse Imager. The Pearl imager is a dedicated fluorescence imaging instrument for mice and has fixed excitation wavelengths of 685 and 785 nm and emission wavelengths of 700 and 800 nm, respectively, as well as a white-light overlay. For in vivo studies, stock solutions (∼1 mM) of dye−urea conjugates were prepared in H_2O (compounds containing 800CW, 800RS, Cy5.5, and Cy7) or DMSO (compounds containing the ICG derivative) and were diluted with PBS for injection. After image acquisition at baseline (preinjection), each mouse was injected intravenously with 1 nmol of dye−urea conjugate and images were acquired at 5 min, 1 h, 4 h, and 24 h time points. Following the 24 h image, each mouse was sacrificed by cervical dislocation and tumor, muscle, liver, spleen, kidneys, and intestine were collected and assembled on a Petri dish for image acquisition. All images were scaled to the same maximum intensity for direct comparison. For quantification, regions of interest (ROI) were drawn over the organs displayed in ex vivo images (n = 4) and fluorescence signal intensity of the organs was calculated using the supplier's software. Signal intensity of the muscle was set as background for all calculations. For binding specificity (blocking) studies, Cy7-**3** was coinjected with 1 μmol of (*S*)-2-(3-((*S*)-1-carboxy-5-(4-iodobenzamido)-pentyl)ureido)pentanedioic acid (DCIBzL, a known high-affinity PSMA inhibitor[29]) and images were acquired at 1, 4, and 24 h postinjection.

RESULTS AND DISCUSSION

Chemical Synthesis. Compound **1** is urea containing both lysine and glutamate substituents (a lysine−glutamate urea). It was obtained after deprotection of the *tert*-butyloxycarbonyl (Boc) and the *p*-methoxybenzyl (PMB) groups from compound **4**[28] as outlined in Scheme 1. Compound **2** has a short poly(ethylene glycol) (PEG) linker. Compound **5**[28] was conjugated to Boc-NH$(CH_2CH_2O)_2CH_2COOH$ to give compound **6**, which was then deprotected to provide compound **2**. Compound **3** has a lysine−suberate linker attached to the lysine−glutamate urea, and it was prepared as previously reported.[9]

The commercially available amine-reactive active esters of IRDye800CW, IRDye800RS, the indocyanine green (ICG) derivative, Cy7, or Cy5.5 with principal excitation/emission wavelengths at 774/789, 767/786, 768/804, 743/767, and 675/694 nm, respectively, were conjugated with **1**, **2**, and **3** to produce the dye−PSMA inhibitors shown in Figure 1. Conjugation of activated esters of the NIR dyes to **1**−**3** were completed at room temperature within 2 h. The yields for these conjugates ranged from 53% to 90%.

In Vitro PSMA Inhibition. The IC_{50} values of the conjugates were measured using the NAALADase assay[30,31]

Scheme 1[a]

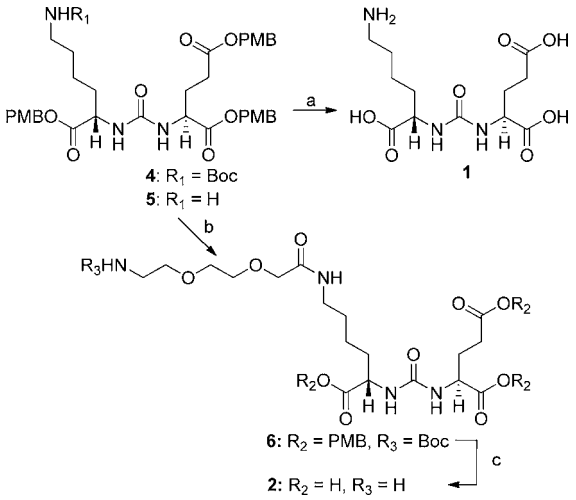

[a](a) TFA/anisole; (b) Boc-NH$(CH_2CH_2O)_2CH_2COOH$, TBTU, *N*,*N*-diisopropylethylamine; (c) TFA/anisole.

with results presented as K_i values in Table 1. The K_i values range from 1 to 700 pM, which is similar to other compounds of this class.[9,28,29,36] We observed a trend whereby agents with linkers, such as 800CW-**2**, ICG-**2**, Cy5.5-**2**, 800CW-**3**, ICG-**3**, and Cy5.5-**3**, had lower K_i values than their counterparts with no linkers (800CW-**1**, ICG-**1**, and Cy5.5-**1**). However, Cy7 conjugates did not follow this trend and exhibited similar high affinities independent of the linker. This may be due to the smaller size of Cy7 compared to Cy5.5 and ICG derivative and the greater flexibility of the polyene moiety in Cy7 compared to the cyclohexene containing polyene in 800CW and 800RS dyes. Both effects could increase the accessibility of the urea to the PSMA binding site.

NIR Imaging and Biodistribution. Among the five dyes tested in this study, only the Cy5.5−urea conjugates have excitation and emission wavelengths below 700 nm. Accordingly, imaging studies with Cy5.5-**1**, Cy5.5-**2**, and Cy5.5-**3** were undertaken on the Xenogen IVIS 200 system with excitation at 675 nm and emission at 720 nm. Figure 2 shows images at 24 h after injection of 1 nmol of Cy5.5-**1**, Cy5.5-**2**, and Cy5.5-**3** in mice with PSMA+ PC3 PIP and PSMA- PC3 flu tumors. All three compounds demonstrated high uptake within PSMA+ PC3 PIP tumors and little uptake in PSMA- PC3 flu tumors. The relative degree of observed PSMA+ PC3 PIP tumor uptake was in the order: Cy5.5-**3** > Cy5.5-**2** > Cy5.5-**1**. Renal uptake is due to high expression of PSMA within proximal renal tubules as well as to excretion, as previously shown.[37−39] Imaging of compounds containing 800CW, 800RS, the ICG derivative, and Cy7 as fluorophores were conducted using the Pearl Imager, which has a set excitation wavelength at 785 nm and emission at 800 nm. These dye−urea conjugates have excitation and emission wavelengths above 700 nm, which allow for better depth of light penetration than compounds that emit at lower wavelengths and minimal autofluorescence. Figure 3 shows typical whole body and excised organ imaging of mice with PSMA+ PC3 PIP and PSMA- PC3 flu tumors at 24 h after injection of 1 nmol of the 800CW, 800RS, the ICG derivative or Cy7-urea conjugates. All compounds demonstrated PSMA+ PC3 PIP tumor uptake with little PSMA- PC3 flu tumor uptake, indicating target selectivity in vivo.

dx.doi.org/10.1021/bc3003919 | *Bioconjugate Chem.* 2012, 23, 2377−2385

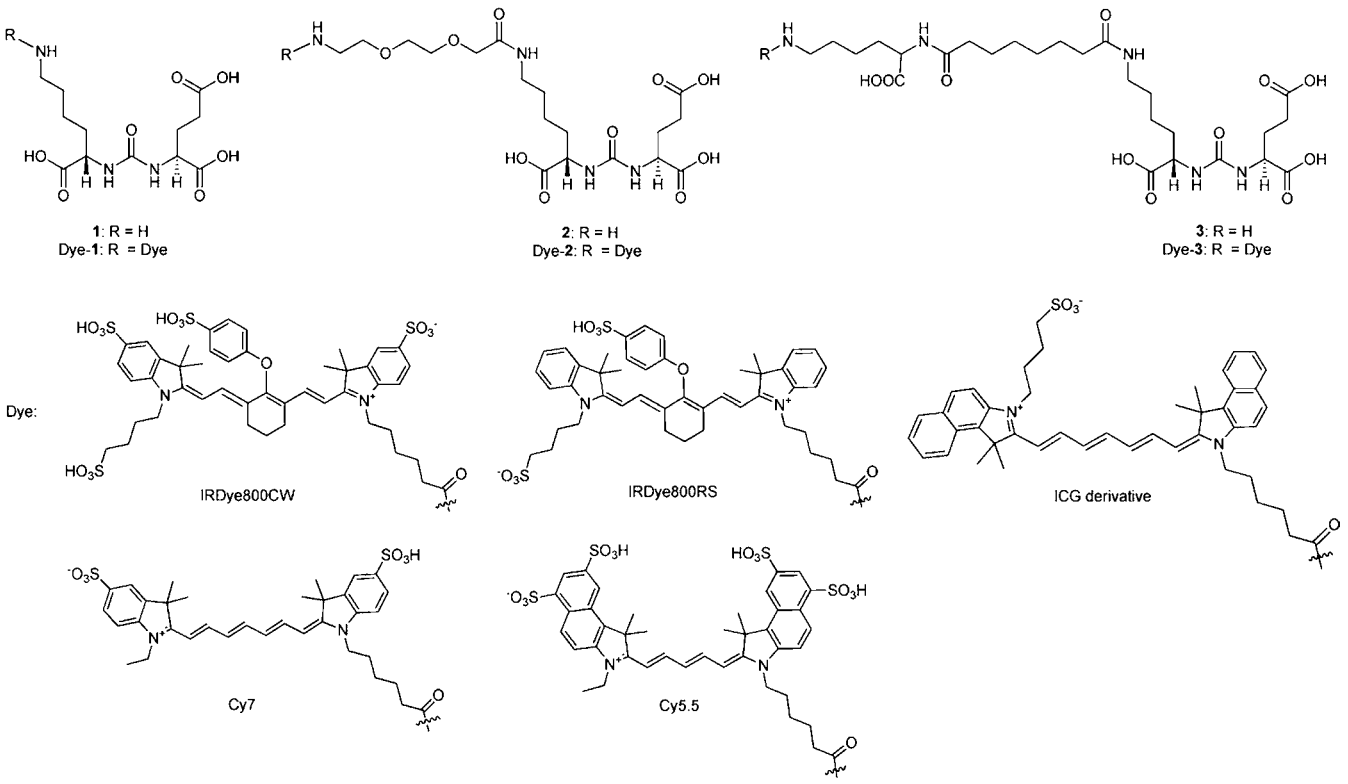

Figure 1. Structures of PSMA-based near-infrared fluorescent imaging agents.

Table 1. PSMA in Vitro Inhibitory Activities[a]

compound	K_i (pM)
800CW-**1**	70 ± 5[b]
800CW-**2**	40 ± 10[b]
800CW-**3**	20 ± 5[b]
800RS-**1**	100 ± 10[cd]
800RS-**2**	200 ± 50[b]
800RS-**3**	4 ± 0.5[c]
ICG-**1**	700 ± 10[cd]
ICG-**2**	400 ± 60[cd]
ICG-**3**	200 ± 5[cd]
Cy7-**1**	1 ± 0.5[c]
Cy7-**2**	7 ± 0.4[b]
Cy7-**3**	5 ± 0.2[c]
Cy5.5-**1**	90 ± 40[b]
Cy5.5-**2**	50 ± 20[b]
Cy5.5-**3**	50 ± 2[c]

[a]Values are in K_i ± SEM. [b]n = 4. [c]n = 2. [d]Measured in DMSO; all others in water.

These images also demonstrate that the choice of dye and linking group have significant effects on biodistribution. Intense fluorescence signals were observed in both tumor and kidneys for all three IRDye800CW conjugates (800CW-**1**, 800CW-**2**, and 800CW-**3**) with 800CW-**3** having much lower normal tissue uptake than the other two compounds. IRDye800RS has a similar structure, but with two less sulfonate groups compared to IRDye800CW. PSMA+ PIP tumor uptake was observed in all three 800RS−urea conjugates. However, the fluorescence intensities were significantly lower than for the corresponding 800CW conjugates. Among those three 800RS−urea conjugates, 800RS-**3**, which has a lysine suberate linker, showed the highest PSMA+ PIP tumor uptake. Similarly, among the three ICG−urea conjugates, ICG-**3** gave the highest PSMA+ PIP tumor uptake. ICG-**3** also demonstrated higher PSMA+ PIP tumor uptake compared to kidney, which differs from 800CW-**3** and 800RS-**3**, which had roughly equivalent tumor and kidney uptake. Cy7-**2** and Cy7-**3** had significantly higher PSMA + PIP tumor uptake than uptake in kidneys. They also demonstrated the lowest normal tissue uptake comparing to the other compounds with the same linker. From this preliminary evaluation, we chose 800CW and Cy7 conjugates for further study, where the organs of 4 mice/agent were harvested and imaged at 24 h postadministration of imaging agent. Fluorescence intensity per organ is shown in Figure 4. In both the Cy7 series and the IRDye800CW series, the degree of PSMA+ PIP tumor uptake was 800CW-**3** or Cy7-**3** ≈ 800CW-**2** or Cy7-**2** > 800CW-**1** or Cy7-**1**, confirming the importance of the linker moiety for modifying pharmacokinetics. Tumor to kidney ratios for Cy7-**2** and Cy7-**3** were higher than for 800CW-**2** and 800CW-**3**. The fluorescence intensities of all organs except the gastrointestinal tract for Cy7 conjugates were lower than for the corresponding 800CW conjugates. This is most likely because the Pearl Imager has a fixed excitation maximum at 785 nm and collects emission at 820 nm, which is further from the excitation and emission maxima of Cy7 (743/767) than those for IRDye800CW (774/789).

In order to demonstrate the PSMA-binding specificity of the PSMA inhibitor−dye conjugates, DCIBzL was coadministered with Cy7-**3**. As shown in Figure 5, all emission from the PSMA + target tumor was blocked with concurrent DCIBzL administration, indicating specific binding. The excised organ imaging results are consistent with the in vivo images.

The active site of PSMA possesses two binding sites, comprising a pharmacophore (S1′) site and an amphiphilic, nonpharmacophore (S1) site.[40] The S1′ site is generated by amino acid residues highly sensitive to structural modification

dx.doi.org/10.1021/bc3003919 | Bioconjugate Chem. 2012, 23, 2377−2385

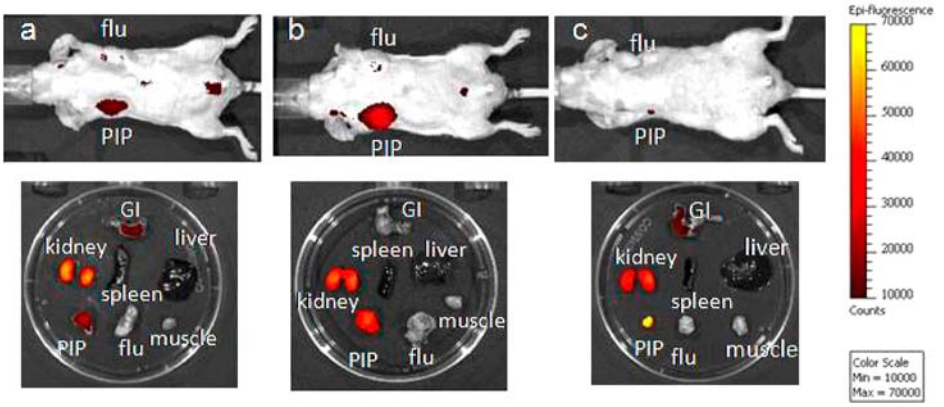

Figure 2. Whole body and ex vivo organ imaging of mice with PSMA+ PC3 PIP and PSMA- PC3 flu tumors at 24 h postinjection of 1 nmol of (a) Cy5.5-**1**, (b) Cy5.5-**2**, and (c) Cy5.5-**3**.

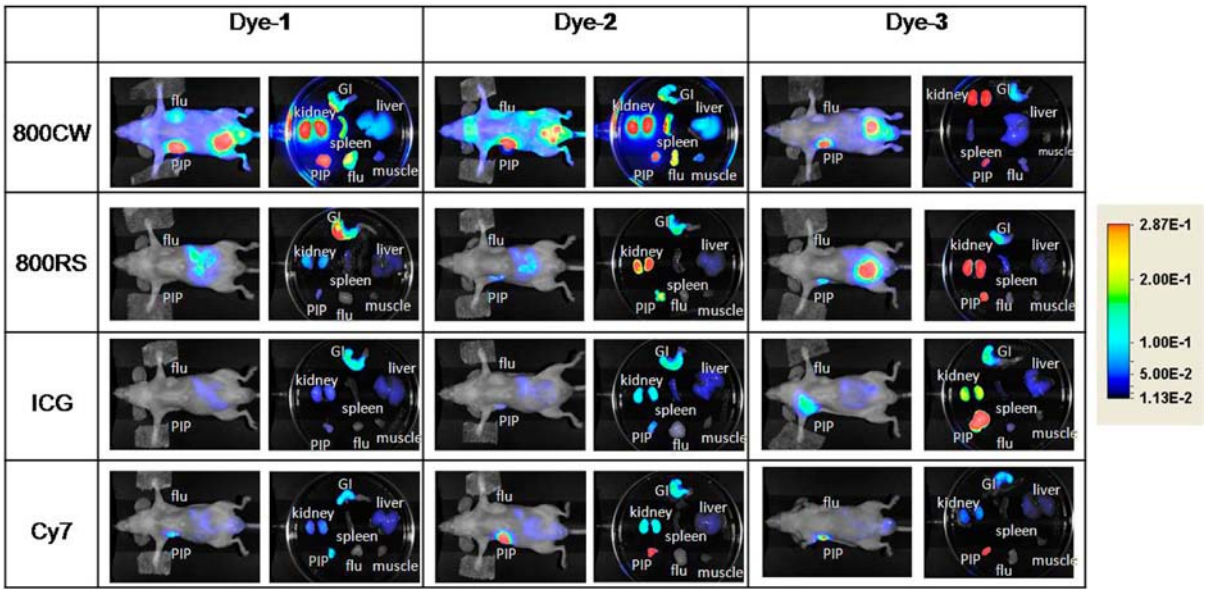

Figure 3. Whole body and ex vivo organ imaging of mice with PSMA+ PC3 PIP and PSMA- PC3 flu tumors at 24 h postinjection of 1 nmol of the indicated dye−urea conjugates.

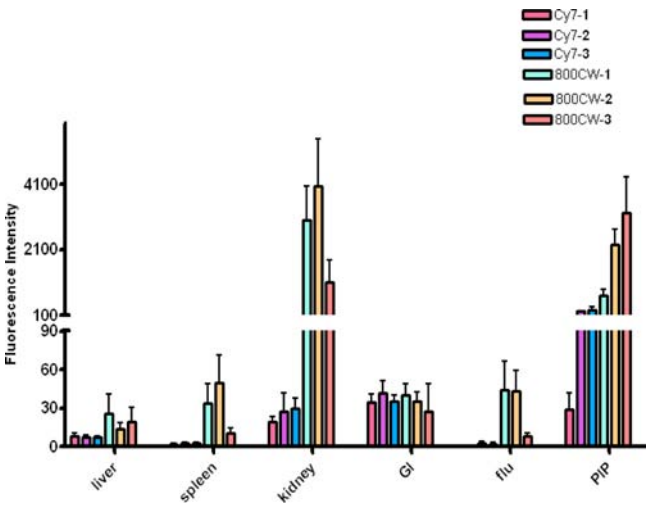

Figure 4. Biodistribution data at 24 h postinjection from regions of interest (ROI) drawn over organs displayed in ex vivo images and normalized to muscle. Four animals were imaged per agent. Values are represented as mean ± SEM.

of potential ligands, demonstrating a strong preference for glutamate or glutamate-like residues. Compared to the S1′ site, the S1 site is more promiscuous. A tunnel-like region (~20 Å) linked to the S1 site is projected toward the surface of the enzyme. Utilizing the tunnel region, we have attached bulky chelated metals to the urea-based specificity-conferring moiety through a long linker to maintain the chelated metal entirely outside the protein. In so doing, we have produced a small array of PSMA-targeted radiotracers capable of imaging PSMA in experimental models of prostate cancer.[28,36,41] Similarly, by attaching bulky fluorophores to the urea inhibitors through a linker, such as in dye-**2** or dye-**3** conjugates, the fluorophores can be situated outside of the active site, allowing maximum interaction with the urea-based specificity conferring portion of the agent. This effect is most noticeable in the higher tumor uptake demonstrated by 800RS-**2**, 800RS-**3**, ICG-**2**, ICG-**3**, and Cy5.5-**3** compared to dye−**1** conjugates 800RS-**1**, ICG-**1**, and Cy5.5-**1**.

Recently, Nakajima et al. used the anti-PSMA antibody J591 conjugated to ICG to visualize PSMA+ tumors in whole mice at up to 10 days after administration.[10] We and others have focused on developing low-molecular-weight optical imaging

dx.doi.org/10.1021/bc3003919 | *Bioconjugate Chem.* 2012, 23, 2377−2385

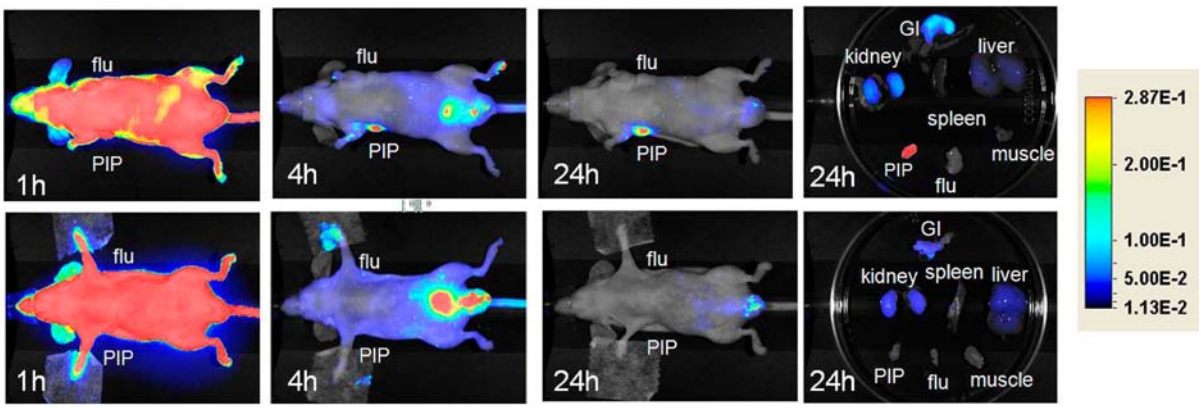

Figure 5. Top row: Images after administration of 1 nmol Cy7-**3** at (left to right) 1, 4, and 24 h postinjection, as well as images of the excised organs at 24 h postinjection. Bottom row: Image after administration of 1 nmol Cy7-**3** + 1 mmol DCIBzL, a high-affinity ligand for PSMA (blocker) at same time points as above. Note lack of uptake in the mice treated with DCIBzL, indicating binding specificity.

agents for PSMA, in part to avoid the longer biological half-lives of antibody-based methods, to enable imaging at shorter times after administration.[9,23,24,42−44] However, to date most such low-molecular-weight agents have only been used in vitro. Humblet et al. reported in vivo imaging of PSMA-binding NIR-emitting phosphonate derivatives; however, at 20 s, the time of maximum PSMA-positive tumor uptake, the tumor to background ratio was less than 2.[24] Previously, we were able to image PSMA+ tissues in experimental models of prostate cancer using the targeted, IRDye800CW-based agent, YC-27 (800CW-**3**).[9] Here, we used the same urea-based targeting moiety but expanded to the small series reported, investigating the pharmacokinetic effects of different linkers and fluorophores.

CONCLUSION

Compounds **2** and **3**, which contain PEG and lysine−suberate linkers, respectively, provide useful scaffolds for optical imaging of PSMA. Although IRDye800CW and Cy7 conjugates 800CW-**2**, 800CW-**3**, Cy7-**2**, and Cy7-**3** demonstrated high, PSMA-specific uptake in vivo at 24 h postinjection, the exact choice of dye for intraoperative imaging will depend upon the specifications of the camera used for detection in the operating suite. Nevertheless, this small series demonstrates that a variety of dyes with different absorption and emission spectra can be accommodated.

ASSOCIATED CONTENT

Supporting Information

HPLC conditions and traces for the final compounds, ligated to the commercial and previously reported NIR dyes used herein, are provided: 800CW-**1**; 800CW-**2**; 800CW-**3**; 800RS-**1**; 800RS-**2**; 800RS-**3**; ICG-**1**; ICG-**2**; ICG-**3**; Cy7-**1**; Cy7-**2**; Cy7-**3**; Cy5.5-**1**; Cy5.5-**2**; Cy5.5-**3**. This material is available free of charge via the Internet at http://pubs.acs.org.

AUTHOR INFORMATION

Corresponding Author

*Phone: 410-955-2789. Fax: 443-817-0990. E-mail: mpomper@jhmi.edu.

Notes

The authors declare no competing financial interest.

ACKNOWLEDGMENTS

We thank CA134675 and the AdMeTech Foundation for financial support and Dr. Ron Rodriguez for helpful discussions.

ABBREVIATIONS

NIR, near-infrared; ICG, indocyanine green; PSMA, prostate-specific membrane antigen; NAAG, *N*-acetylaspartyl glutamate; NAALADase, *N*-acetylated-α-linked-acidic dipeptidase; Boc, *tert*-butyloxycarbonyl; PMB, *p*-methoxybenzyl; PEG, poly(ethylene glycol); NHS, *N*-hydroxysuccinimide; DCIBzL, (*S*)-2-(3-((*S*)-1-carboxy-5-(4-iodobenzamido)pentyl)ureido)-pentanedioic acid.

REFERENCES

(1) Siegel, R., Naishadham, D., and Jemal, A. (2012) Cancer statistics, 2012. *Ca— Cancer J. Clin. 62*, 10−29.

(2) Bill-Axelson, A., Holmberg, L., Ruutu, M., Garmo, H., Stark, J. R., Busch, C., Nordling, S., Haggman, M., Andersson, S. O., Bratell, S., Spangberg, A., Palmgren, J., Steineck, G., Adami, H. O., and Johansson, J. E. (2011) Radical prostatectomy versus watchful waiting in early prostate cancer. *N. Engl. J. Med. 364*, 1708−17.

(3) National Cancer Institute (2008) Surveillance Epidemiology and End Results (SEER). http://seer.cancer.gov/data/.

(4) Hu, J. C., Wang, Q., Pashos, C. L., Lipsitz, S. R., and Keating, N. L. (2008) Utilization and outcomes of minimally invasive radical prostatectomy. *J. Clin. Oncol. 26*, 2278−84.

(5) Gioux, S., Choi, H. S., and Frangioni, J. V. (2010) Image-guided surgery using invisible near-infrared light: fundamentals of clinical translation. *Mol. Imaging 9*, 237−55.

(6) Frangioni, J. V. (2008) New technologies for human cancer imaging. *J. Clin. Oncol. 26*, 4012−21.

(7) Ye, Y., Bloch, S., Xu, B., and Achilefu, S. (2006) Design, synthesis, and evaluation of near infrared fluorescent multimeric RGD peptides for targeting tumors. *J. Med. Chem. 49*, 2268−75.

(8) Schaafsma, B. E., Mieog, J. S., Hutteman, M., van der Vorst, J. R., Kuppen, P. J., Lowik, C. W., Frangioni, J. V., van de Velde, C. J., and Vahrmeijer, A. L. (2011) The clinical use of indocyanine green as a near-infrared fluorescent contrast agent for image-guided oncologic surgery. *J. Surg. Oncol. 104*, 323−32.

(9) Chen, Y., Dhara, S., Banerjee, S. R., Byun, Y., Pullambhatla, M., Mease, R. C., and Pomper, M. G. (2009) A low molecular weight PSMA-based fluorescent imaging agent for cancer. *Biochem. Biophys. Res. Commun. 390*, 624−9.

(10) Nakajima, T., Mitsunaga, M., Bander, N. H., Heston, W. D., Choyke, P. L., and Kobayashi, H. (2011) Targeted, activatable, in vivo fluorescence imaging of prostate-specific membrane antigen (PSMA)

positive tumors using the quenched humanized J591 antibody-indocyanine green (ICG) conjugate. *Bioconjugate Chem. 22*, 1700−5.
(11) Solomon, M., Liu, Y., Berezin, M. Y., and Achilefu, S. (2011) Optical imaging in cancer research: basic principles, tumor detection, and therapeutic monitoring. *Medical Principles and Practice: International Journal of the Kuwait University, Health Science Centre 20*, 397−415.
(12) Silver, D. A., Pellicer, I., Fair, W. R., Heston, W. D., and Cordon-Cardo, C. (1997) Prostate-specific membrane antigen expression in normal and malignant human tissues. *Clin. Cancer Res. 3*, 81−5.
(13) Ghosh, A., and Heston, W. D. (2004) Tumor target prostate specific membrane antigen (PSMA) and its regulation in prostate cancer. *J. Cell. Biochem. 91*, 528−39.
(14) Baccala, A., Sercia, L., Li, J., Heston, W., and Zhou, M. (2007) Expression of prostate-specific membrane antigen in tumor-associated neovasculature of renal neoplasms. *Urology 70*, 385−90.
(15) Chang, S. S., O'Keefe, D. S., Bacich, D. J., Reuter, V. E., Heston, W. D., and Gaudin, P. B. (1999) Prostate-specific membrane antigen is produced in tumor-associated neovasculature. *Clin. Cancer Res. 5*, 2674−81.
(16) Haffner, M. C., Kronberger, I. E., Ross, J. S., Sheehan, C. E., Zitt, M., Muhlmann, G., Ofner, D., Zelger, B., Ensinger, C., Yang, X. J., Geley, S., Margreiter, R., and Bander, N. H. (2009) Prostate-specific membrane antigen expression in the neovasculature of gastric and colorectal cancers. *Hum. Pathol. 40*, 1754−61.
(17) Milowsky, M. I., Nanus, D. M., Kostakoglu, L., Sheehan, C. E., Vallabhajosula, S., Goldsmith, S. J., Ross, J. S., and Bander, N. H. (2007) Vascular targeted therapy with anti-prostate-specific membrane antigen monoclonal antibody J591 in advanced solid tumors. *J. Clin. Oncol. 25*, 540−7.
(18) Cho, S. Y., Gage, K. L., Mease, R. C., Senthamizhchelvan, S., Holt, D. P., Kwanisai-Jeffrey, A., Endres, C. J., Dannals, R. F., Sgouros, G., Lodge, M. A., Eisenberger, M. A., Rodriguez, R., Carducci, M. A., Rojas, C., Slusher, B. S., Kozikowski, A. P., and Pomper, M. G. (2012) Biodistribution, tumor detection and radiation dosimetry of N-[N-[(S)-1,3-Dicarboxypropyl]carbamoyl]-4-18F-fluorobenzyl-L-cysteine (18F-DCFBC), a low molecular weight inhibitor of PSMA, in patients with metastatic prostate cancer. *J. Nucl. Med. 53*, 1883−91.
(19) Barrett, J. S., LaFrance, N., Coleman, R. E., Goldsmith, S. J., Stubbs, J. B., Petry, N. A., Vallabhajosula, S., Maresca, K. P., Femia, F. J., and Babich, J. W. (2009) Targeting metastatic prostate cancer [PCa] in patients with 123I-MIP1072 & 123I-MIP1095. *J. Nucl. Med. 50 (Suppl)*, 136.
(20) Babich, J., Coleman, R. E., Van Heertum, R., Vallabahajosula, S., Goldsmith, S., Osborne, J., Slawin, K., and Joyal, J. (2012) Small molecule inhibitors of prostate specific membrane antigen (PSMA) for SPECT: Summary of phase I studies in patients with prostate cancer (PCa). *J. Nucl. Med. 53 (Suppl)*, 55.
(21) Afshar-Oromieh, A., Haberkorn, U., Eder, M., Eisenhut, M., and Zechmann, C. M. (2012) [68Ga]Gallium-labelled PSMA ligand as superior PET tracer for the diagnosis of prostate cancer: comparison with 18F-FECH. *Eur. J. Nucl. Med. Mol. Imaging 39*, 1085−6.
(22) Kularatne, S. A., Wang, K., Santhapuram, H. K., and Low, P. S. (2009) Prostate-specific membrane antigen targeted imaging and therapy of prostate cancer using a PSMA inhibitor as a homing ligand. *Mol. Pharm. 6*, 780−9.
(23) Liu, T., Wu, L. Y., Hopkins, M. R., Choi, J. K., and Berkman, C. E. (2010) A targeted low molecular weight near-infrared fluorescent probe for prostate cancer. *Bioorg. Med. Chem. Lett. 20*, 7124−6.
(24) Humblet, V., Lapidus, R., Williams, L. R., Tsukamoto, T., Rojas, C., Majer, P., Hin, B., Ohnishi, S., De Grand, A. M., Zaheer, A., Renze, J. T., Nakayama, A., Slusher, B. S., and Frangioni, J. V. (2005) High-affinity near-infrared fluorescent small-molecule contrast agents for in vivo imaging of prostate-specific membrane antigen. *Mol. Imaging 4*, 448−62.
(25) Elsasser-Beile, U., Reischl, G., Wiehr, S., Buhler, P., Wolf, P., Alt, K., Shively, J., Judenhofer, M. S., Machulla, H. J., and Pichler, B. J. (2009) PET imaging of prostate cancer xenografts with a highly specific antibody against the prostate-specific membrane antigen. *J. Nucl. Med. 50*, 606−11.
(26) Bander, N. H., Trabulsi, E. J., Kostakoglu, L., Yao, D., Vallabhajosula, S., Smith-Jones, P., Joyce, M. A., Milowsky, M., Nanus, D. M., and Goldsmith, S. J. (2003) Targeting metastatic prostate cancer with radiolabeled monoclonal antibody J591 to the extracellular domain of prostate specific membrane antigen. *J. Urol. 170*, 1717−21.
(27) Yao, D., Trabulsi, E. J., Kostakoglu, L., Vallabhajosula, S., Joyce, M. A., Nanus, D. M., Milowsky, M., Liu, H., and Goldsmith, S. J. (2002) The utility of monoclonal antibodies in the imaging of prostate cancer. *Semin. Urol. Oncol. 20*, 211−8.
(28) Banerjee, S. R., Foss, C. A., Castanares, M., Mease, R. C., Byun, Y., Fox, J. J., Hilton, J., Lupold, S. E., Kozikowski, A. P., and Pomper, M. G. (2008) Synthesis and evaluation of technetium-99m- and rhenium-labeled inhibitors of the prostate-specific membrane antigen (PSMA). *J. Med. Chem. 51*, 4504−17.
(29) Chen, Y., Foss, C. A., Byun, Y., Nimmagadda, S., Pullambahatla, M., Fox, J. J., Castanares, M., Lupold, S. E., Babich, J. W., Mease, R. C., and Pomper, M. G. (2008) Radiohalogenated prostate-specific membrane antigen (PSMA)-based ureas as imaging agents for prostate cancer. *J. Med. Chem. 51*, 7933−7943.
(30) Robinson, M. B., Blakely, R. D., Couto, R., and Coyle, J. T. (1987) Hydrolysis of the brain dipeptide N-acetyl-L-aspartyl-L-glutamate. Identification and characterization of a novel N-acetylated alpha-linked acidic dipeptidase activity from rat brain. *J. Biol. Chem. 262*, 14498−506.
(31) Rojas, C., Frazier, S. T., Flanary, J., and Slusher, B. S. (2002) Kinetics and inhibition of glutamate carboxypeptidase II using a microplate assay. *Anal. Biochem. 310*, 50−4.
(32) Jackson, P. F., Cole, D. C., Slusher, B. S., Stetz, S. L., Ross, L. E., Donzanti, B. A., and Trainor, D. A. (1996) Design, synthesis, and biological activity of a potent inhibitor of the neuropeptidase N-acetylated alpha-linked acidic dipeptidase. *J. Med. Chem. 39*, 619−22.
(33) Foss, C. A., Mease, R. C., Cho, S. Y., Kim, H. J., and Pomper, M. G. (2012) GCPII imaging and cancer. *Curr. Med. Chem. 19*, 1346−59.
(34) Cheng, Y., and Prusoff, W. H. (1973) Relationship between the inhibition constate (K1) and the concentration of inhibitor which causes 50% inhibition (I50) of an enzymatic reaction. *Biochem. Pharmacol. 22*, 3099−3108.
(35) Ghosh, A., Wang, X., Klein, E., and Heston, W. D. (2005) Novel role of prostate-specific membrane antigen in suppressing prostate cancer invasiveness. *Cancer Res. 65*, 727−31.
(36) Banerjee, S. R., Pullambhatla, M., Byun, Y., Nimmagadda, S., Foss, C. A., Green, G., Fox, J. J., Lupold, S. E., Mease, R. C., and Pomper, M. G. (2011) Sequential SPECT and optical imaging of experimental models of prostate cancer with a dual modality inhibitor of the prostate-specific membrane antigen. *Angew. Chem., Int. Ed. 50*, 9167−70.
(37) Silver, D. A., Pellicer, I., Fair, W. R., Heston, W. D., and Cordon-Cardo, C. (1997) Prostate-specific membrane antigen expression in normal and malignant human tissues. *Clin. Cancer Res. 3*, 81−5.
(38) de la Taille, A., Cao, Y., Sawczuk, I. S., Nozemu, T., d'Agati, V., McKiernan, J. M., Bagiella, E., Buttyan, R., Burchardt, M., Olsson, C. A., Bander, N., and Katz, A. E. (2000) Detection of prostate-specific membrane antigen expressing cells in blood obtained from renal cancer patients: a potential biomarker of vascular invasion. *Cancer Detect. Prev. 24*, 579−88.
(39) Kinoshita, Y., Kuratsukuri, K., Landas, S., Imaida, K., Rovito, P. M., Jr., Wang, C. Y., and Haas, G. P. (2006) Expression of prostate-specific membrane antigen in normal and malignant human tissues. *World J. Surg. 30*, 628−36.
(40) Mesters, J. R., Barinka, C., Li, W., Tsukamoto, T., Majer, P., Slusher, B. S., Konvalinka, J., and Hilgenfeld, R. (2006) Structure of glutamate carboxypeptidase II, a drug target in neuronal damage and prostate cancer. *Embo J. 25*, 1375−84.
(41) Banerjee, S. R., Pullambhatla, M., Byun, Y., Nimmagadda, S., Green, G., Fox, J. J., Horti, A., Mease, R. C., and Pomper, M. G. (2010) 68Ga-labeled inhibitors of prostate-specific membrane antigen (PSMA) for imaging prostate cancer. *J. Med. Chem. 53*, 5333−41.

(42) Liu, T., Wu, L. Y., Kazak, M., and Berkman, C. E. (2008) Cell-Surface labeling and internalization by a fluorescent inhibitor of prostate-specific membrane antigen. *Prostate 68*, 955−64.
(43) Kularatne, S. A., Venkatesh, C., Santhapuram, H. K., Wang, K., Vaitilingam, B., Henne, W. A., and Low, P. S. (2010) Synthesis and biological analysis of prostate-specific membrane antigen-targeted anticancer prodrugs. *J. Med. Chem. 53*, 7767−77.
(44) Humblet, V., Misra, P., Bhushan, K. R., Nasr, K., Ko, Y. S., Tsukamoto, T., Pannier, N., Frangioni, J. V., and Maison, W. (2009) Multivalent scaffolds for affinity maturation of small molecule cell surface binders and their application to prostate tumor targeting. *J. Med. Chem. 52*, 544−50.

SUPPLEMENTARY INFORMATION

Synthesis and Biological Evaluation of Low Molecular Weight Fluorescent Imaging Agents for the Prostate-Specific Membrane Antigen

Ying Chen,[1] Mrudula Pullambhatla,[1] Sangeeta R. Banerjee.[1]Youngjoo Byun,[2] Marigo Stathis,[3] Camilo Rojas,[3] Barbara S. Slusher,[3] Ronnie C. Mease,[1] Martin G. Pomper[1]

HPLC Analysis of Final Compounds.

Column: phenomenex Luna C18 10μ, 250 × 4.6 mm.

Method I: mobile phase, A = 0.1% TFA in H_2O, B = 0.1% TFA in CH_3CN; gradient, 0 min = 15% B, 30 min = 35% B; flow rate, 2 mL/min.

Method II: mobile phase, A = 0.1% TFA in H_2O, B = 0.1% TFA in CH_3CN; gradient, 0 min = 25% B, 30 min = 45% B; flow rate, 2 mL/min.

Method III: mobile phase, A = 0.1% TFA in H_2O, B = 0.1% TFA in CH_3CN; gradient, 0 min = 40% B, 30 min = 60% B; flow rate, 2 mL/min.

Method IV: mobile phase, A = 0.1% TFA in H_2O, B = 0.1% TFA in CH_3CN; gradient, 0 min = 10% B, 30 min = 40% B; flow rate, 2 mL/min.

800CW-**1** (method I)

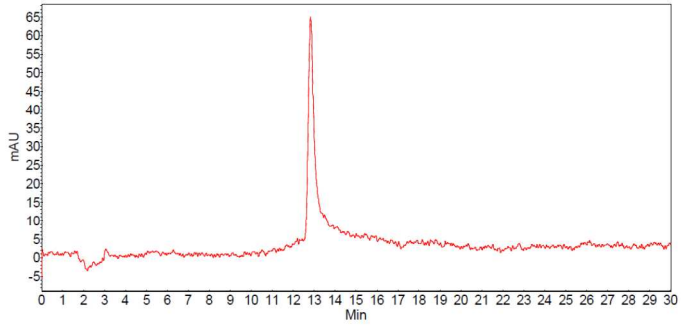

800CW-**2** (method I)

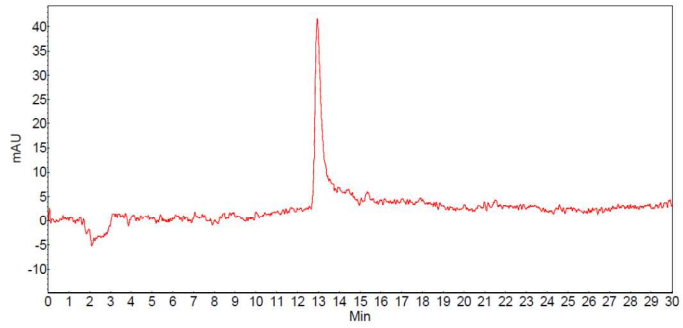

800CW-**3** (method I)

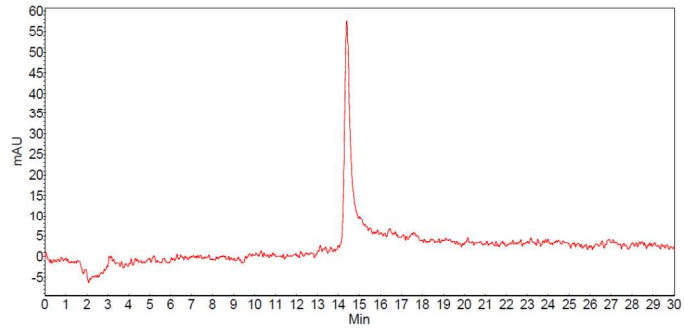

800RS-**1** (method II)

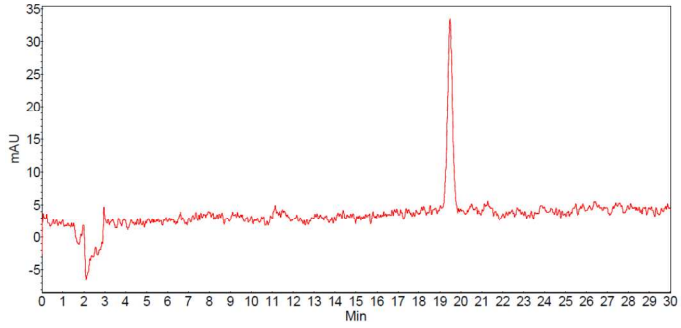

800RS-**2** (method II)

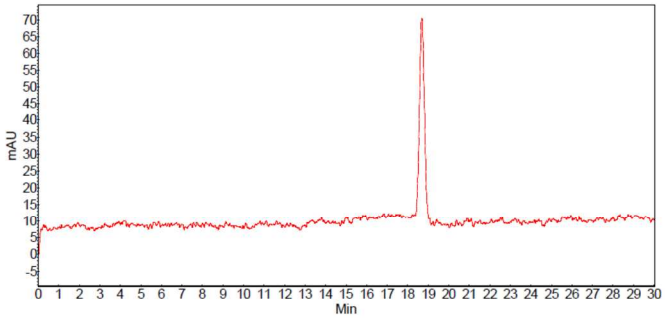

800RS-**3** (method II)

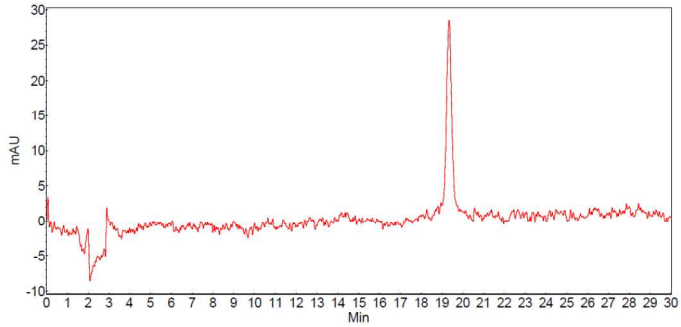

ICG-**1** (method III)

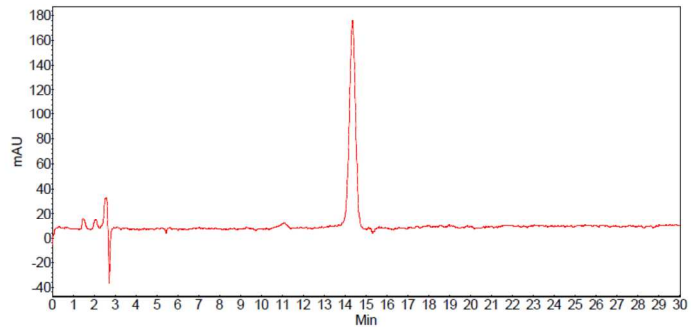

ICG-**2** (method III)

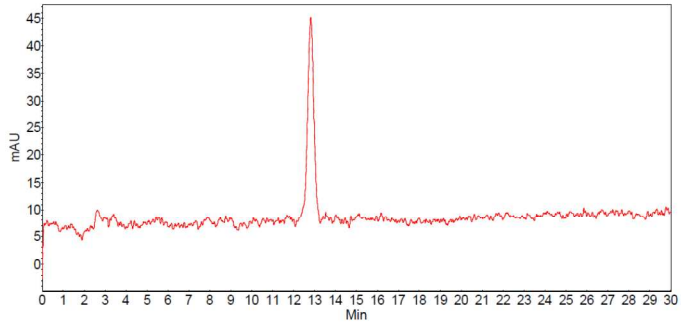

ICG-**3** (method III)

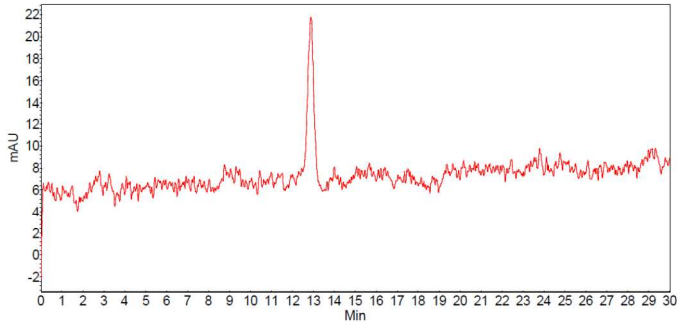

Cy7-**1** (method I)

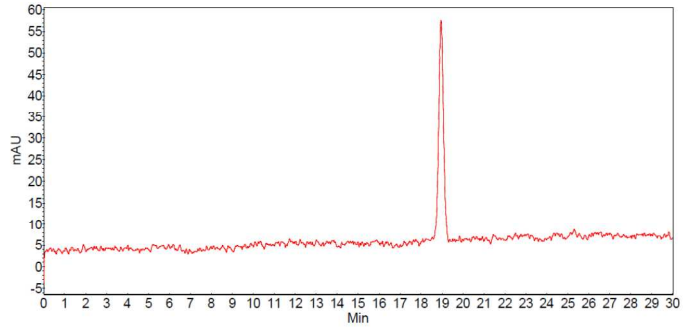

Cy7-**2** (method I)

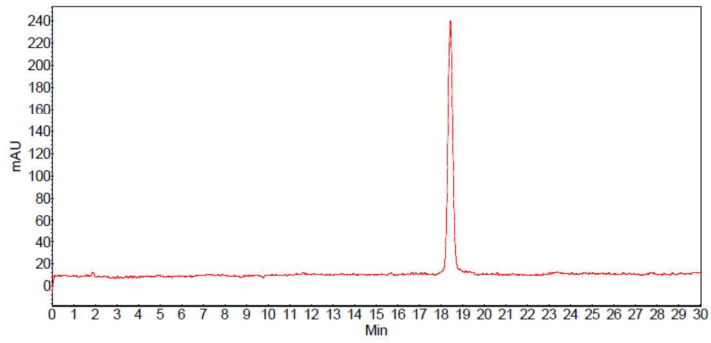

Cy7-**3** (method I)

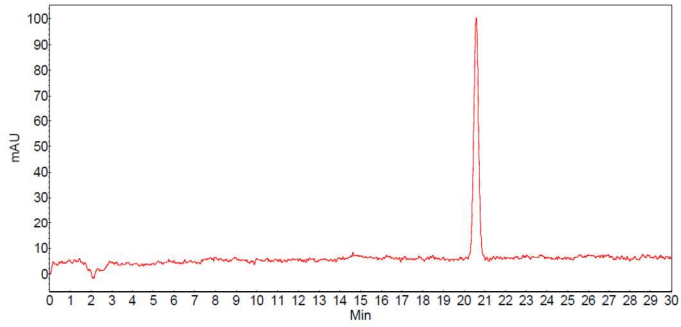

Cy5.5-**1** (method IV)

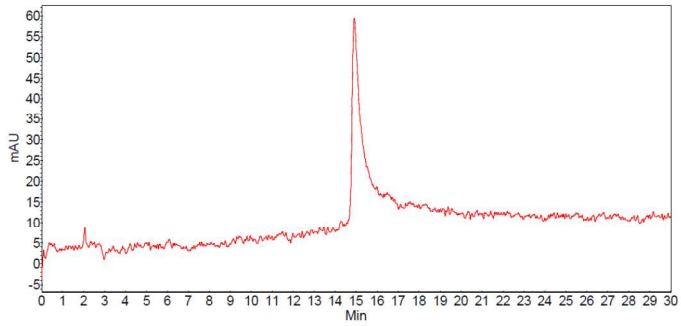

Cy5.5-**2** (method IV)

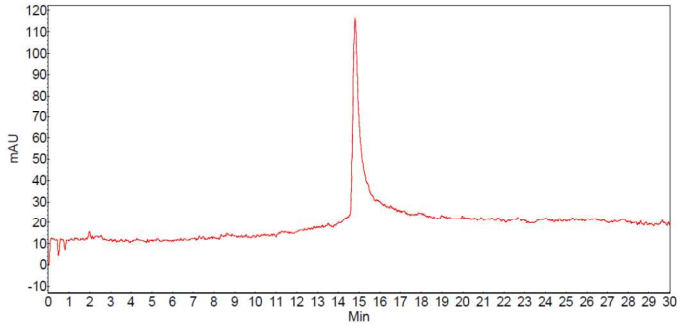

Cy5.5-**3** (method IV)

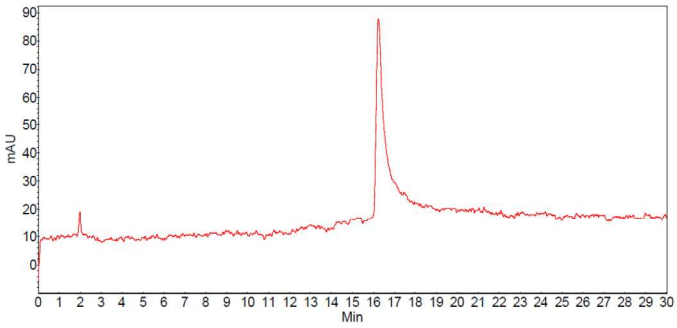

Bioconjugate Chemistry

Article

pubs.acs.org/bc

Structural Analysis of ATP Analogues Compatible with Kinase-Catalyzed Labeling

Sujit Suwal,[†] Chamara Senevirathne, Satish Garre, and Mary Kay H. Pflum*

Department of Chemistry, Wayne State University, Detroit, Michigan 48202, United States

Supporting Information

ABSTRACT: Kinase-catalyzed protein phosphorylation is an important biochemical process involved in cellular functions. We recently discovered that kinases promiscuously accept γ-modified ATP analogues as cosubstrates and used several ATP analogues as tools for studying protein phosphorylation. Herein, we explore the structural requirements of γ-modified ATP analogues for kinase compatibility. To understand the influence of linker length and composition, a series of ATP analogues was synthesized, and the efficiency of kinase-catalyzed labeling was determined by quantitative mass spectrometry. This study on factors influencing kinase cosubstrate promiscuity will enable design of ATP analogues for a variety of kinase-catalyzed labeling reactions.

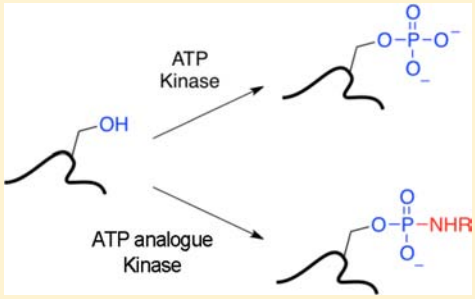

INTRODUCTION

Protein phosphorylation is mediated by kinase enzymes in a highly regulated manner to influence a variety of biological processes, including cell signaling, diseases, cancer, and immunosuppression.[4] Over 500 different kinases containing a conserved catalytic domain have been characterized. Kinases phosphorylate using adenosine 5′-triphosphate (ATP) as a cosubstrate.[5] On the basis of crystal structures of various kinases, the adenine moiety of ATP binds in the hydrophobic pocket of the active site, while the triphosphate chain of ATP protrudes out toward the solvent-exposed, substrate binding region. The proximity of the protein substrate and ATP facilitates transfer of the γ-phosphate of ATP to the hydroxyl of serine, threonine, or tyrosine residues. When the neutral hydroxyl group is replaced with a negatively charged phosphate group, the activity of the protein may change, which influences cell biology. With a significant role in biochemical functions, it is important to identify and characterize phosphorylation events.

Techniques to monitor phosphorylation involve ^{32}P radiolabeling, immobilized metal affinity chromatography, covalent modification of the phosphate, and gel-based visualization using specific antibodies or phosphate stains (for example, Pro-Q Diamond).[6−11] In addition to these methods, γ-phosphate modified ATP analogues have been developed for kinase-catalyzed labeling of phosphoproteins and phosphopeptides (Table 1). Specifically, ATP analogues containing biotin, dansyl, azide, and ferrocene groups at the γ-phosphate have highlighted the diversity of functional tags that can be enzymatically attached to phosphoprotein/peptide substrates.[1−3,12,13] However, a systematic study of the tolerance of kinases to γ-phosphate modified ATP analogues has yet to be reported.

Quantitative mass spectrometric (QMS) analysis was performed with ATP analogues containing biotin, dansyl, or arylazide groups (Table 1).[1−3] In these studies, three different kinases (PKA, CK2, and Abl) showed the highest conversions with the ATP-dansyl derivative (81−91%) compared with the ATP-biotin or ATP-arylazide analogues (51−86%). Distinguishing features of the ATP-dansyl derivative that may account for its high conversions are the all carbon diamine linker and sulfonamide group. To understand the role of the linker and amide/sulfonamide groups in kinase-catalyzed labeling, we explored the relationship between ATP analogue structure and

Table 1. Kinase-Catalyzed Labeling with Previously Reported ATP Analogues[a]

ATP analogue	PKA	CK2	Abl
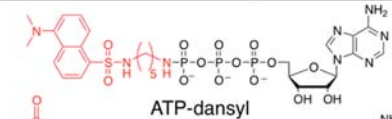 ATP-dansyl	91%	81%	87%
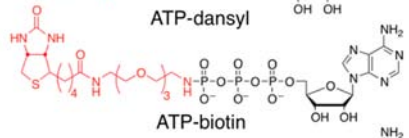 ATP-biotin	79%	56%	80%
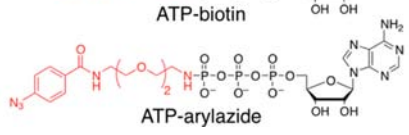 ATP-arylazide	86%	51%	78%

[a]Percentage conversions were determined using QMS, as previously reported.[1−3]

Received: July 20, 2012
Revised: October 17, 2012
Published: November 1, 2012

 © 2012 American Chemical Society

Scheme 1. Synthesis of ATP Analogues 2a–b, 6a–f, 9a–b, and 13

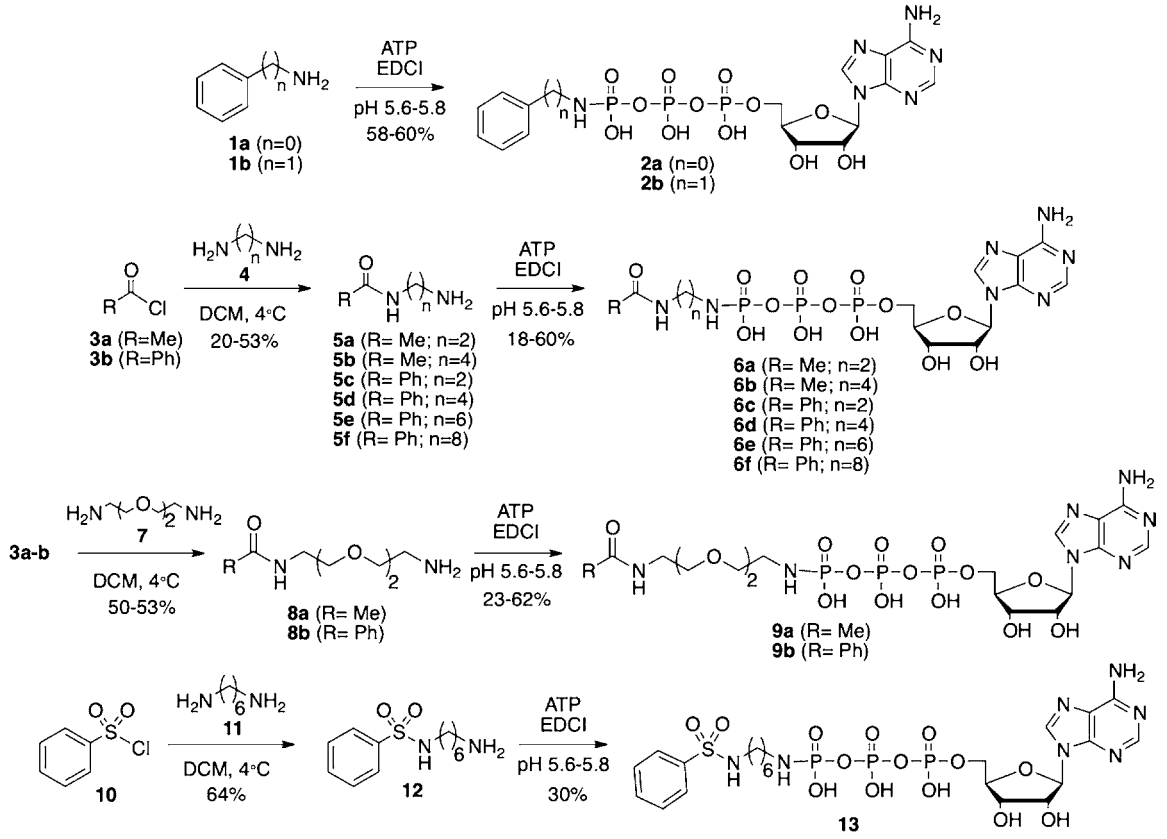

kinase reaction efficiency. Herein, we report the synthesis and kinase compatibility of a variety of γ-phosphate modified ATP analogues related to ATP-dansyl, ATP-biotin, and ATP-arylazide.

EXPERIMENTAL PROCEDURES

General Protocol for Synthesis of Amines 5a–f, 8a–b, and 12. To an ice-cooled solution of diamine **4**, **7**, or **11** (1–5 equiv) in dichloromethane (250 mL), a solution of acetyl, benzoyl, or benzenesulfonyl chloride (1 equiv) in dichloromethane (100 mL) was added dropwise. The resultant mixture was allowed to stand at room temperature overnight under argon. The organic solution was concentrated *in vacuo*. The crude mixture was purified using flash chromatography on silica gel (ethanol, dichloromethane, and ammonium hydroxide, 3:1:0.05) to afford the amine. Specific reagent amounts and spectra characterization for all amines are reported as Supporting Information.

General Protocol for Synthesis of ATP-analogues 2a–b, 6a–f, 9a–b, and 13. ATP·2Na (0.05 mmol, 1 equiv) was dissolved into 3 mL of water and the pH was adjusted to 7.0 with 1 M sodium hydroxide, as assessed with a pH meter. EDCI (2 mmol, 40 equiv) was added and the pH was adjusted to 5.6–5.8 followed by addition of 1 mL water. An aqueous solution of amine linker (1.5–3 mmol in 1 mL water, 30–60 equiv) was added to the ATP mixture and the reaction was incubated for 2 h under a controlled pH of 5.6–5.8. Progress of the reaction was monitored by TLC (6:3:1, isopropanol/NH_4OH/H_2O). The reaction mixture was brought to pH 8.5 using 1 M triethyl amine (TEA) and purified using an A-25 Sephadex anion exchange column with 0.1–1 M triethyl ammonium bicarbonate (TEAB) buffer solution (pH 8.5) as eluent. The purified product was lyophilized to dryness to obtain the ATP analogue as a white TEA salt. The product thus obtained was dissolved in methanol and stored at −20 °C for several months. Specific reagent amounts and spectra characterization for all ATP analogues are reported as Supporting Information.

Kinase Reactions with Peptides. Each reaction contained either PKA (26.6 U/μL) or CK2 (9 U/μL), along with either the PKA substrate peptide (LRRTSIIGT or LRRASLG, 33 μM) or CK2 substrate peptide (RRREEETEEE, 33.3 μM). A phosphopeptide was generated using ATP (1.3 mM), while a phosphoramidate peptide was created using the ATP analogue (1.3 mM). The ATP analogue storage solvent methanol was evaporated using a ThermoSavant speedvac concentrator and the ATP analogue was resuspended in a reaction buffer prior to reaction. For PKA reactions, the final concentration of buffer components was 39 mM Tris–HCl, 7.5 mM $MgCl_2$, 3.7 mM NaCl, 3.7 mM KCl, 3.75% glycerol, 0.15 mM DTT, and 0.25 mM EDTA, at pH 7.5 @ 25 °C. For the CK2 reaction, the final concentration of buffer components was 11.3 mM Tris–HCl, 4.5 mM $MgCl_2$, 15.75 mM NaCl, 22.5 mM KCl, 0.09 mM DTT, 0.09 mM EDTA, and 0.005% Triton X-100, at pH 7.5 @ 25 °C. The reaction mixtures were incubated at 30 °C for 2 h without shaking. The final volume for the PKA reaction was 7.5 μL, while that for the CK2 was 4.5 μL.

Quantitative Mass Spectrometric Analysis. The phosphopeptides and phosphoramidate-peptides generated in kinase reactions were analyzed by QMS, as previously described.[14] To each of the peptides, 300 μL of anhydrous D_0-MeOH or D_4-MeOH was added, followed by 50 μL of acetyl chloride to generate 2 N HCl *in situ*. The phosphopeptide was incubated with D_4-MeOH while the phosphoramidate peptide was

dx.doi.org/10.1021/bc300404s | *Bioconjugate Chem.* 2012, 23, 2386–2391

incubated with D_0-MeOH. The reaction mixture was allowed to shake at 700 rpm at 16 °C for 3 h to afford acid esterification. Since the conditions of esterification were acidic, the phosphoramidate bond linking the substituent to the peptide was cleaved, producing the two differentially labeled phosphopeptides required for QMS analysis. The acidic methanol solution was evaporated in a ThermoSavant Speedvac (~2 h). The peptide was further subjected to MALDI-TOF MS analysis after equal volumes of the two isotopically differentiated phosphopeptides were combined. The sample was prepared as follows: One of the differentially labeled peptide reactions was dissolved in a minimum amount of water (~2 μL) and combined with the second vial. The first vial was washed (2 μL) and the resulting solution (4 μL) was mixed with 10 μL of a saturated solution of 4-hydroxy-α-cyanocinnamic acid in 1:1 acetonitrile/0.1% TFA in water. The mixture (1 μL) was spotted onto a MALDI plate (Standard 384 MTP, Bruker) and analyzed using a MALDI-TOF instrument.

Autodocking Analysis. The Autodock Vina program was designed by Dr. Oleg Trott of the Molecular Graphics Lab at The Scripps Research Institute (http://vina.scripps.edu/index.html). Crystal structures were downloaded from the RCSB Protein Data Bank (PKA: 1ATP and CK2: 1DAW). The *PyMOL* program was used to delete the ATP analogue in the active site of the structures. The ATP analogues structures were drawn in *Chem 3D Pro* and MM2 was used for energy minimization. The grid dimensions used for the autodock analysis and the output file with all binding modes are shown as Supporting Information.

RESULTS

Synthesis of the ATP Analogues. ATP analogues with a variety of linker lengths and terminal functional groups were prepared using a two-step synthetic strategy (Scheme 1), as previously described.[2] First, various amines were generated by reacting acetyl, benzoyl, or benezenesulfonyl chlorides (**3** or **10**) with diamine linkers (**4**, **7**, or **11**). In some cases, the amine group was obtained from commercial sources (aniline **1a** and benzylamine **1b**). Syntheses of the ATP analogues were accomplished by activating the terminal phosphate of ATP using 1-ethyl-3-(3-dimethylaminopropyl)-carbodiimide hydrochloride (EDCI), followed by coupling with the desired amines (Scheme 1).

Acetyl Series of ATP Analogues. The initial series of ATP analogues was generated with an acetyl group to test whether an amide functionality would be tolerated. Three different types of linkers were employed. Ethylenediamine (**4**, n = 2) and butylenediamine (**4**, n = 4) were used because they are relatively short and hydrophobic, similar to the linker of ATP-dansyl. The third linker, 2,2′-ethylenedioxybis-(ethylamine) (**7**), was relatively long and hydrophilic, similar to the linker in ATP-biotin or ATP-arylazide.

To perform a systematic study of kinase-catalyzed labeling, we chose CK2 as the model kinase due to its relatively variable conversion efficiencies with ATP-dansyl, ATP-biotin, and ATP-arylazide (Table 1). The efficiency of phosphorylation by CK2 and the ATP analogues was assessed by QMS analysis, as previously described.[14] The QMS data showed that the acetyl analogues were accepted by CK2, although with variable conversion efficiencies (Table 2). The analogues containing the all-carbon linkers ethylenediamine (**6a**) and butylenediamine (**6b**) demonstrated 72% and 27% conversion, respectively (Table 2). Given the high conversion of ATP-dansyl with its all-carbon linker (Table 1), these analogues suggest that the sulfonamide group of ATP-dansyl is important for its high efficiency. The analogue containing a relatively long and hydrophilic poly(ethylene glycol) linker **9a**, similar to that in ATP-biotin or ATP-arylazide, displayed 62% conversion (Table 2). The slightly augmented conversion with a methyl group in place of the larger and more polar biotin or arylazide groups (compare CK2 conversions with **9a**, 62%, to that with ATP-biotin and ATP-arylazide, 51−56%) suggests that the terminal group influences the efficiency. The QMS data from the acetyl series of ATP analogues provide our first evidence that the linker length and polarity play significant roles in dictating kinase compatibility.

Table 2. Efficiency of Phosphorylation with CK2 and the Acetyl Series of ATP Analogues

Analogue	γ-phosphate group	Conversion[a]
6a	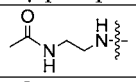	72%
6b	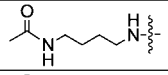	27%
9a	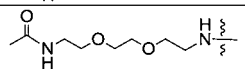	62%

[a]Percentage conversion was determined using QMS by comparing to ATP phosphorylation (set to 100%). See Figures S45−S47 in Supporting Information.

Aryl Series of ATP Analogues. To further explore the role of the linker and terminal group on kinase-catalyzed labeling, an aryl analogue series was created. Both the ATP-dansyl and ATP-arylazide derivatives (Table 1) contain aromatic terminal groups. In addition, aryl substituents are relatively hydrophobic, which will test the influence of polarity on the kinase reaction. To expand our study, the efficiency of phosphorylation with the aryl series of ATP analogues was determined with both CK2 and PKA using QMS. The percentage conversion of the aryl series ranged from <5% (the detection minimum of the MS technique) to 54% (Table 3). Given the high efficiencies observed with the acetyl series (up to 72%), the data initially suggest that the presence of an aryl group reduces conversion efficiency.

The conversion efficiency with the aryl series was dependent on length and composition of the linker. Analogues lacking a linker, created with aniline (**1a**) or benzyl amine (**1b**) groups, showed undetectable or low levels of phosphorylation (Table 3, **2a** and **2b**), indicating that PKA and CK2 do not tolerate the presence of a bulky group directly attached to the terminal phosphate. The presence of an all-carbon linker between the ATP and aryl substituent (**6c**, **6d**, and **6f**) resulted in low to moderate percentage conversions ranging from <5% to 38% (Table 3). Similarly, the acetyl analogue containing an all-carbon butylene diamine linker (Table 2, **6b**) displayed 27% conversion. The low percentage conversion for analogues containing all-carbon linkers suggests that hydrophobicity reduces kinase compatibility. However, as the linker length increased, there was an increase in the percent conversion with both PKA and CK2. Presumably, the increased linker length positions the hydrophobic aryl substituent away from the kinase active site to augment conversion.

The most efficient enzymatic conversion among the aryl series of ATP analogues was observed with compound **9b**,

Table 3. Efficiency of Phosphorylation with PKA and CK2 and the Aryl Series of ATP Analogues

Analogue	γ-phosphate group	Conversion[a] PKA	CK2
2a		<5%	<5%
2b	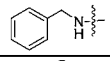	<5%	6%
6c	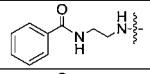	5%	27%
6d	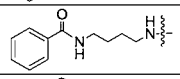	<5%	33%
6f	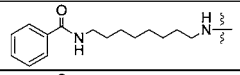	22%	38%
9b	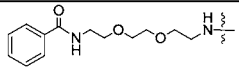	54%	54%

[a]Percentage conversion was determined using QMS by comparing to ATP phosphorylation (set to 100%). See Figures S48–S59 in Supporting Information.

which contains an ethylene glycol linker (Table 3). Unlike the all-carbon linkers, the hydrophilic ethylene glycol may counter balance the hydrophobic aryl substituent, while also positioning the aryl group away from the active site area. It is notable that compound **9a** is identical to ATP-arylazide (Table 1), except for the absence of the terminal azide group. The relatively similar conversions of the two analogues with CK2 (54% versus 51%) suggest that the presence of the azide group does not significantly influence kinase compatibility. In contrast, the presence of the azide group significantly enhanced conversion with PKA (54% versus 86%), suggesting that polarity in the linker and terminal group are critical for high conversion with PKA. Overall, the data with the aryl series suggests that the composition and length of the linker are factors that influence cosubstrate tolerance.

Role of the Sulfonamide Group. Earlier reports indicated that ATP-dansyl displays the highest kinase conversion efficiency of the analogues tested (Table 1). One of the distinguishing features of ATP-dansyl compared to ATP-biotin or ATP-arylazide is the presence of a sulfonamide group. To study the influence of the sulfonamide group on kinase-catalyzed labeling, ATP analogues containing a six-carbon linker, similar to ATP-dansyl, but displaying either a benzoyl (**6e**) or benzene sulfonyl (**13**) group were synthesized and subjected to kinase-catalyzed phosphorylation (Table 4). While

Table 4. Efficiency of Phosphorylation with PKA and CK2 and the ATP-Dansyl-Like Analogues

Analogue	γ-phosphate group	Conversion[a] PKA	CK2
6e	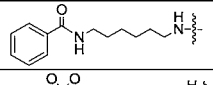	61%	36%
13	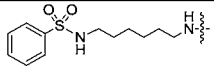	94%	83%

[a]Percentage conversion was determined using quantitative MS by comparing to ATP phosphorylation (set to 100%). See Figures S60–S63 in Supporting Information.

the ATP-benzoyl analogue **6e** demonstrated 61% and 36% conversion, the ATP-benzenesulfonamide derivative **13** displayed 94% and 83% conversion (Table 4) with PKA and CK2, respectively. Given the similar percentage conversions observed with **13** and ATP-dansyl (91%/81% and 94%/83%; Tables 1 and 4), the data suggest that a sulfonamide group promotes high conversion.

Docking Studies. To rationalize the high conversion with the dansyl analogue, we docked ATP-dansyl into the active site of PKA (GenBank ID 6755076, PDB: 1ATP)[15] using the Autodock Vina program (http://vina.scripps.edu/).[16] The most favorable binding mode (−9.5 kcal/mol, SI Table S1) positioned the diamine linker and dansyl modification wrapped around the peptide inhibitor (Figure 1A). Although the dansyl modification protrudes from the active site, it is within 3.5–4.5 Å of several residues—G53 and S54 near the carbon chain and P203 and P244 near the dansyl group. G53 is well-conserved among the kinases (conservation of 83%), while S54, P203, and P244 are not (conservation of 16%, 18%, and 9%, respectively) (http://sequoia.ucsf.edu/ksd/).[17]

Similarly, docking of ATP-dansyl into the active site of CK2 (GenBank ID 7766821, PDB: 1DAW)[18] resulted in a favorable binding mode (−8.9 kcal/mol, SI Table S2) where the phosphate groups are positioned close to G48 and the dansyl group is near S194 (Figure 1B). Comparison of the favorable binding modes of ATP-dansyl with CK2 and PKA shows that both contain a GXGX sequence (X being a hydrogen bond donor or acceptor) near the ATP binding site (SI Table S7). These docking results suggest that the conserved glycine creates an open active site to accommodate the enlarged ATP analogue. Nonconserved S54 and S194 may create a polar environment where the phosphate diesters and ethylene glycol or sulfonamide linker bind favorably. In addition, the preference of PKA for an eight atom linker (Table 3, compounds **6f** and **9b**, and Table 4) may be due to optimal positioning of the aromatic group near a binding pocket comprising nonconserved P203 and P244.

To understand the influence of the linker and terminal groups on binding interactions, we also docked analogues **2b** and **13** into the active sites of CKII and PKA. With **2b**, higher energy binding energies were observed with CKII (−6.3 kcal/mol) and PKA (−6.7 kcal/mol) compared to ATP-dansyl, which suggests that the shorter benzyl group of **2b** does not maintain the favorable binding interactions of the dansyl group (SI Tables S3–S4 and Figures S64–S65). The high energy binding is consistent with the low conversions observed in kinase reactions (Table 3, <5% and 6%). In contrast, comparable binding energies were observed with ATP-dansyl and compound **13** with CKII (−8.6 kcal/mol) and PKA (−8.4 kcal/mol) (SI Tables S5–S6 and Figures S66–S67), which is consistent with the high conversion data (Tables 1 and 4, 81–94%) and strongly suggests that the sulfonamide group leads to favorable interactions. In total, the docking analysis confirms the need for long linkers and polar groups to enhance binding interactions between the ATP analogues and kinases.

■ DISCUSSION

The data reported here provide guiding principles for the design of new ATP analogues for kinase-catalyzed labeling. First, the data suggest that the functional tag attached at the γ-phosphate of ATP should be positioned sufficiently distant from the kinase active site to allow high conversions. With the aryl series of ATP analogues, compounds with an eight atom

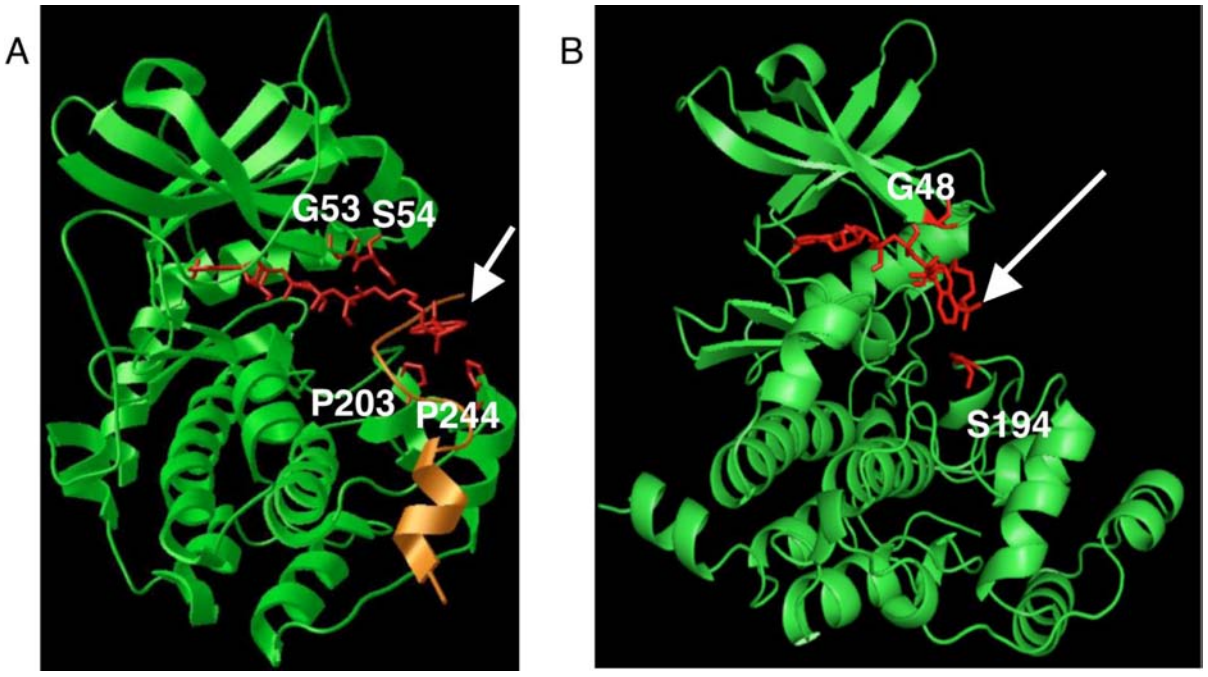

Figure 1. Docking of ATP-dansyl (red) into the active sites of PKA (A, green) complexed with peptide substrate inhibitor (yellow) or CK2 (B, green). The dansyl group protrudes from both active sites (arrows), but within close proximity to G53, S54, P203, and P244 of PKA (A, red) and G48 and S194 of CK2 (B, red).

diamine linker demonstrated the highest conversion efficiencies (Table 3, compounds **6f** and **9b**). Docking studies were consistent with the conversion data, showing that compounds with eight-atom linkers (ATP-dansyl and compound **13**) showed more favorable binding energies than a compound lacking a linker (compound **2b**). In addition, a previous report using ATP-ferrocene derivatives indicated that an eight- to twelve-atom all-carbon linker gave optimal electrochemical signal.[19] Interestingly, when the terminal group is relatively small, like with the acetyl analogue series, a four-atom diamine linker was sufficient to observe high conversions (Table 2, compound **6a**). The linker distance required to obtain high kinase-catalyzed labeling is dependent on the size of the functional tag.

In addition to linker length, the data also suggest that the composition of the linker is important for kinase compatibility. With both the acetyl and aryl series of ATP analogues, the percentage conversion increased with analogues containing an ethylene glycol linker compared to a similar all carbon linker (Table 2, compounds **6b** and **9a** and Table 3, compounds **6f** and **9b**). The data suggest that a polar linker promotes high conversions. Interestingly, the ATP-benzenesulfonamide analogue **13** displayed excellent conversion despite containing an all-carbon linker (Table 4). Perhaps the sulfonyl group provides sufficient polarity to promote high-efficiency labeling. In total, the data indicate that the linker connecting the γ-phosphate of ATP to the functional tag should contain polar groups, whether within the diamine linker itself or the presence of a sulfonamide group.

Prior work with ATP-ferrocene analogues and surface-mobilized substrates reported higher electrochemical signal with an all-carbon linker compared to poly(ethylene glycol) linkers.[20] However, when the substrate was in solution, poly(ethylene glycol) and all-carbon linkers performed similarly. Combined with the work reported here showing preference for polar linkers, the optimal linker composition and polarity may depend on the environment of the substrate.

To characterize the efficiency of ATP-dansyl as a kinase cosubstrate, kinetics measurements were previously reported using an enzyme-coupled or FRET-based assay.[21] With PKA and Abl, ATP-dansyl showed similar K_M values but significantly reduced k_{cat} values compared to the natural ATP.[3] Therefore, prior data suggest that the reduced conversion with the ATP analogues compared to ATP is primarily due to a change in V_{max}. A more complete kinetics analysis is currently ongoing and will be published in due course. We note, however, that dansylation with ATP-dansyl displayed similar catalytic efficiency (k_{cat}/K_M) to thiophosphorylation with ATP-γS,[3] which is well-documented for phosphoprotein labeling.[22] Hence, ATP-dansyl and the other ATP analogues maintain appropriate catalytic efficiency for a variety of applications.

In conclusion, efficient kinase-catalyzed labeling requires ATP analogues with a polar linker containing at least eight atoms. However, the size of the functional tag can influence linker length, while the substrate environment can influence the linker composition. These linker guidelines will aid in the development of additional analogues for phosphopeptide and phosphoprotein labeling. Given the role of kinases and their phosphoprotein products in cell biology, new biochemical tools based on kinase-catalyzed labeling have the potential to augment cell signaling research.

■ ASSOCIATED CONTENT

Supporting Information

Information on materials and instrumentation, compound synthesis and characterization, ATP analogue spectral data, QMS analysis, docking studies, and sequence alignment. This material is available free of charge via the Internet at http://pubs.acs.org.

AUTHOR INFORMATION

Corresponding Author

*Phone: 313-577-1515. E-mail: pflum@chem.wayne.edu.

Present Address

†The Scripps Research Institute, 130 Scripps Way, Jupiter, FL 33458.

Notes

The authors declare no competing financial interest.

ACKNOWLEDGMENTS

Research reported in this publication was supported by the National Institute of General Medical Sciences of the National Institutes of Health under award number R01GM079529. The content is solely the responsibility of the authors and does not necessarily represent the official views of the National Institutes of Health. We thank T. Anthony and A. Fouda for comments on the manuscript.

REFERENCES

(1) Green, K. D., and Pflum, M. H. (2007) Kinase-catalyzed biotinylation for phosphoprotein detection. *J. Am. Chem. Soc. 129*, 10−11.

(2) Suwal, S., and Pflum, M. H. (2010) Phosphorylation-dependent kinase-substrate cross-linking. *Angew. Chem., Int. Ed. Engl. 49*, 1627−30.

(3) Green, K. D., and Pflum, M. H. (2009) Exploring kinase cosubstrate promiscuity: monitoring kinase activity through dansylation. *ChemBioChem 10*, 234−237.

(4) Hunter, T. (2000) Signaling-2000 and beyond. *Cell 100*, 113−127.

(5) Adams, J. A. (2001) Kinetic and catalytic mechanisms of protein kinases. *Chem. Rev. 101*, 2271−2290.

(6) Kalume, D. E., Molina, H., and Pandey, A. (2003) Tackling the phosphoproteome: tools and strategies. *Curr. Opin. Chem. Biol. 7*, 64−69.

(7) Garcia, B. A., Shabanowitz, J., and Hunt, D. F. (2005) Analysis of protein phosphorylation by mass spectrometry. *Methods 35*, 256−64.

(8) Steinberg, T. H., Agnew, B. J., Gee, K. R., Leung, W.-Y., Goodman, T., Schulenberg, B., Hendrickson, J., Beechem, J. M., Haugland, R. P., and Patton, W. F. (2003) Global quantitative phosphoprotein analysis using multiplexed proteomics technology. *Proteomics 3*, 1128−1144.

(9) Mann, M., Ong, S. E., Gronborg, M., Steen, H., Jensen, O. N., and Pandey, A. (2002) Analysis of protein phosphorylation using mass spectrometry: deciphering the phosphoproteome. *Trends Biotechnol 20*, 261−8.

(10) Posewitz, M. C., and Tempst, P. (1999) Immobilized gallium(III) affinity chromatography of phosphopeptides. *Anal. Chem. 71*, 2883−92.

(11) Sun, T., Campbell, M., Gordon, W., and Arlinghaus, R. B. (2001) Preparation and application of antibodies to phosphoamino acid sequences. *Biopolymers 60*, 61−75.

(12) Song, H., Kerman, K., and Kraatz, H. B. (2008) Electrochemical detection of kinase-catalyzed phosphorylation using ferrocene-conjugated ATP. *Chem. Commun. (Camb.)*, 502−4.

(13) Lee, S. E., Elphick, L. M., Anderson, A. A., Bonnac, L., Child, E. S., Mann, D. J., and Gouverneur, V. (2009) Synthesis and reactivity of novel gamma-phosphate modified ATP analogues. *Bioorg. Med. Chem. Lett. 19*, 3804−7.

(14) Senevirathne, C., Green, K. D., and Pflum, M. K. H. (2009) Kinase-Catalyzed Biotinylation of Peptides, Proteins, and Lysates, in *Current Protocols in Chemical Biology*, John Wiley & Sons, Inc.

(15) Zheng, J., Knighton, D. R., Ten Eyck, L. F., Karlsson, R., Xuong, N., Taylor, S. S., and Sowadski, J. M. (1993) Crystal structure of the catalytic subunit of cAMP-dependent protein kinase complexed with magnesium-ATP and peptide inhibitor. *Biochemistry 32*, 2154−2161.

(16) Trott, O., and Olson, A. J. (2010) AutoDock Vina: improving the speed and accuracy of docking with a new scoring function, efficient optimization, and multithreading. *J. Comput. Chem. 31*, 455−61.

(17) Buzko, O., and Shokat, K. M. (2002) A kinase sequence database: sequence alignments and family assignment. *Bioinformatics 18*, 1274−1275.

(18) Niefind, K., Putter, M., Guerra, B., Issinger, O.-G., and Schomburg, D. (1999) GTP plus water mimic ATP in the active site of protein kinase CK2. *Nat. Struct. Mol. Biol. 6*, 1100−1103.

(19) Martić, S., Labib, M., Freeman, D., and Kraatz, H.-B. (2011) Probing the role of the linker in ferrocene−ATP conjugates: monitoring protein kinase catalyzed phosphorylations electrochemically. *Chem.—Eur. J. 17*, 6744−6752.

(20) Martić, S., Rains, M. K., Freeman, D., and Kraatz, H.-B. (2011) Use of 5′-γ-ferrocenyl adenosine triphosphate (Fc-ATP) bioconjugates having poly(ethylene glycol) spacers in kinase-catalyzed phosphorylations. *Bioconjugate Chem. 22*, 1663−1672.

(21) Cook, P. F., Neville, M. E., Jr., Vrana, K. E., Hartl, F. T., and Roskoski, R., Jr. (1982) Adenosine cyclic 3′,5′-monophosphate dependent protein kinase: kinetic mechanism for the bovine skeletal muscle catalytic subunit. *Biochemistry 21*, 5794−9.

(22) Kwon, S. W., Kim, S. C., Jaunbergs, J., Falck, J. R., and Zhao, Y. (2003) Selective enrichment of thiophosphorylated polypeptides as a tool for the analysis of protein phosphorylation. *Mol. Cell. Proteomics 2*, 242−7.

Supporting Information

Structural Analysis of γ-phosphate modified ATP analogs Compatible with Kinase-Catalyzed Labeling

Sujit Suwal, Chamara Senevirathne, Satish Garre and Mary Kay H. Pflum

Department of Chemistry, Wayne State University, Detroit, MI, 48202

Table of Contents:

I. Materials and instrumentation S2

II. Synthesis and characterization of all compounds S2

III. ATP analog characterization S9

IV. Quantitative mass spectrometric (QMS) analysis of kinase activity S31

V. Autodocking analysis S50

VI. Sequence alignment of 15 representative kinases showing the GXGX motif S55

I. Materials and Instrumentation

Materials.

ATP was purchased from Calbiochem. CKII and PKA were bought from New England Biolabs. CKII and PKA peptide substrates were purchased from Promega. Acetyl chloride, benzoyl chloride, benzenesulfonyl chloride, benzylamine, 1,4- diaminobutane, 1,6-diaminohexane, 1,8 diaminooctane, 2,2'-ethylenedioxy bis-(ethylamine), 4-hydroxy-α-cyanocinnamic acid (4-HCCA), 1-(3-Dimethylaminopropyl)-3-ethylcarbodiimide hydrochloride (EDCI) and N,N-diisopropyl-ethylamine (DIPEA) were purchased from Acros. Ethylene diamine was bought from Fisher. Aniline was obtained from Sigma. D_4-MeOH was purchased from Cambridge isotope lab., Inc. Dichloromethane (DCM) and liquid ammonia were purchased from Mallinchkrodt chem. Ethanol was obtained from Decon lab. All the other solvents were purchased from Fisher. Flash chromatography was performed on silica gel, 200-400 mesh (Merck). A-25 Sephadex was purchased from Aldrich.

Instrumentation

IR spectra were recorded on an FT/IR-460 plus (JASCO Co. Ltd.) spectrometer. Absorbance of intermediate compounds and the ATP-analog were measured on UV-Vis spectrophotometer (HP 8452A Diode array spectrophotometer). ^{1}H NMR, ^{13}C NMR and ^{31}P NMR were measured in Varian's Mercury-400. The peaks around δ 4.95 and 3.3 in the ^{1}H NMR and δ 58.0 in ^{13}C NMR are due to CD_3OD solvent. Likewise, the peaks at δ 1.3 and 3.2 in the ^{1}H NMR are due to ethanol solvent. The triethyl amine counter ion in the ATP-analogs is observed near δ 1.18 and 3.2 in the ^{1}H NMR and δ 8.7 and 46.0 in ^{13}C NMR. ESI MS (Waters' ZQ2000) were used to authenticate the linker amines as well as all the ATP analogs. High resolution mass spectra were obtained using LCT Premier XT, Waters. The ATP analogs were purified with the aid of a diaphragm pump manufactured from Fluid Metering Inc. lab pump (Model RPSY) and concentrated using benchtop lyophilizer SP industries (V55C). Kinase reactions were performed in a thermomixer purchased from Eppendorf. Quantitative mass spectrometric analyses of phosphopeptides resulting from the kinase reactions were performed using a MALDI-TOF MS (Bruker Ultraflex) with matrix, 4-hydroxy- α-cyanocinnamic acid (4-HCCA).

II. Synthesis and characterization of all compounds

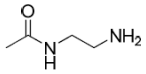

Synthesis of N-acetyl 1, 2-ethylene diamine 5a. The general protocol for synthesis of amines was followed using ethylene diamine (4.4 g, 73 mmol) and acetyl chloride **3a** (1.2 mL, 15 mmol) and purification affording amine **5a** (305.8 mg, 3 mmol, 20% yield). IR (neat, cm^{-1}) 3406, 3084, 1641, 1558, 1441, 1373, 1300, 1176, 1098, 1041, 993, 911; ^{1}H NMR (400 MHz, CD_3OD): 1.99 (s, 3H), 3.05 (t, 2H), 3.45 (t, 2H); ^{13}C NMR (100 MHz, CD_3OD): 21.4, 37.0, 39.7, 173.5; LRMS (ESI) calculated for $C_4H_{10}N_2O$ [M+H]: 103.0, found: 103.0.

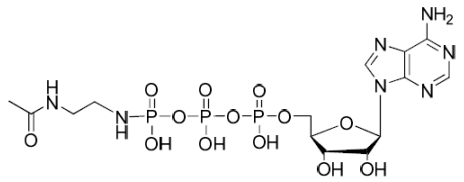

Synthesis of ATP-γ-N-acetyl-1, 2 diaminoethane 6a. The general protocol for synthesis of ATP analogs was followed using ATP•2Na (27 mg, 0.05 mmol) and N-acetyl-1, 2-ethylene diamine **5a** (204 mg, 2 mmol) and purification affording the triethyl ammonium salt of **6a** (26 mg, 0.03 mmol, 60% yield). UV (MeOH): λ 259.0 nm; ^{1}H NMR (400 MHz, CD_3OD): 1.99 (s, 3H), 3.05 (t, 2H), 3.45 (t, 2H), 4.33 (m, 3H), 4.57 (t, 1H), 4.72 (t, 1H), 6.05 (d, 1H), 8.20 (s, 1H), 8.60 (s, 1H); ^{31}P NMR (400 MHz, CD_3OD) -0.87 (d, γ-P), -10.33 (d, α-P), -21.28 (t, β-P); LRMS (MALDI-TOF) calculated for $C_{14}H_{24}N_7O_{13}P_3$ [M-H]: 590.06, found: 589.56.

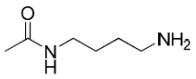

Synthesis of N-acetyl-1,4-diaminobutane 5b. The general protocol for synthesis of amines was followed using butylene diamine (880.2 mg, 10 mmol) and acetyl chloride **3a** (440 mg, 5.6 mmol) and purification affording amine **5b** (218.4 g, 1.68 mmol, 30% yield). IR (neat, cm^{-1}): 3403, 3084, 1629, 1566, 1445, 1378, 1305, 675; ^{1}H NMR (400 MHz, CD_3OD): 1.58 (m, 2H), 1.69 (m, 2H), 1.94 (s, 3H), 2.95 (t, 2H), 3.20 (t, 2H); ^{13}C NMR (100MHz, CD_3OD): 21.4, 24.6, 26.1, 38.4, 39.2, 172.2; LRMS (ESI) calculated for $C_6H_{14}N_2O$ [M+H]: 131.11, found: 131.28.

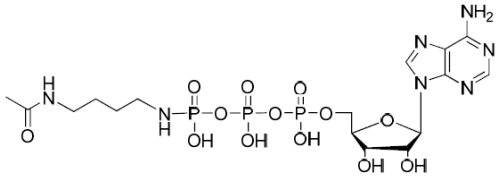

Synthesis of ATP-γ-N-acetyl-1,4-diaminobutane 6b. The general protocol for synthesis of ATP analogs was followed using ATP•2Na (15 mg, 0.027 mmol) and N-acetyl-1, 4 diaminobutane **5b** (131 mg, 1 mmol) and purification affording the triethyl ammonium salt of **6b** (7.4 mg, 0.008 mmol, 30% yield). UV (MeOH): λ 263.0 nm; ^{1}H NMR (400 MHz, CD_3OD): 1.53 (m, 4H), 1.92 (s, 3H), 3.00 (m, 4H), 4.28 (m, 3H) 4.57 (t, 1H), 4.72 (t, 1H) 6.08 (d, 1H), 8.18 (s, 1H) 8.59 (s, 1H); ^{31}P NMR (400 MHz, CD_3OD) -0.18 (d γ -P), -10.40 (d, α -P), -21.41 (t, β -P); LRMS (MALDI-TOF) calculated for $C_{16}H_{28}N_7O_{13}P_3$ [M-H]: 618.09, found: 617.63.

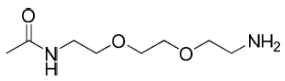

Synthesis of N-acetyl-2, 2'-ethylenedioxy bis-(ethylamine) 8a. The general protocol for synthesis of amines was followed using 2, 2'-ethylenedioxy bis-(ethylamine) **7** (4.1 mL, 28 mmol) and acetyl chloride **3a** (440 mg, 5.6 mmol) and purification affording amine **8a** (533 mg, 2.8 mmol, 50% yield). IR (neat, cm-

[1]) 3367, 2878, 1640, 1566, 1480, 1378, 1312, 1095, 812; ^{1}H NMR (400 MHz, CD_3OD): 1.95 (s, 3H), 2.83 (t, 2H), 3.35 (t, 2H), 3.54 (m, 4H), 3.62 (m, 4H); ^{13}C NMR (100MHz, CD_3OD): 21.37, 39.23, 40.70, 69.37, 70.08, 70.13, 71.59, 172.20; LRMS (MALDI-TOF) calculated for $C_8H_{18}N_2O_3$ [M+H]: 191.13, found: 191.3.

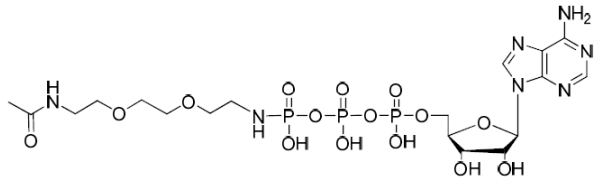

Synthesis of ATP-γ-N-acetyl-2, 2'-ethylenedioxy bis-(ethylamine) 9a. The general protocol for synthesis of ATP analogs was followed using ATP•2Na (27 mg, 0.05 mmol) and N-acetyl-2, 2'-ethylenedioxy bis-(ethylamine) **8a** (385 mg, 2 mmol) and purification affording the triethyl ammonium salt of **9a** (29 mg, 0.03 mmol, 62% yield). UV (MeOH):λ 259.0 nm; ^{1}H NMR (400 MHz, CD_3OD): 1.94 (s, 3H), 3.34 (m, 4H), 3.60 (m, 8H), 4.25 (m, 3H), 4.47 (t, 1H), 4.57 (t, 1H), 6.09 (d, 1H), 8.18 (s, 1H), 8.63 (s, 1H); ^{31}P NMR (400 MHz, CD_3OD) -0.58 (d, γ -P), -10.37 (d, α -P), -21.38 (t, β -P); LRMS (MALDI-TOF) calculated for $C_{18}H_{32}N_7O_{15}P_3$ [M-H]: 678.12, found: 677.74.

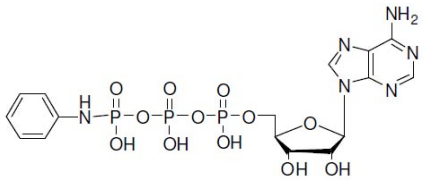

Synthesis of ATP-γ-aniline 2a. The general protocol for synthesis of ATP analogs was followed using ATP•2Na (27 mg, 0.05 mmol) and aniline **1a** hydrochloride salt (260 mg, 2 mmol) and purification affording the triethyl ammonium salt of **2a** (26.7 mg, 0.03 mmol, 60% yield). UV (MeOH): λ 259.0 nm; ^{1}H NMR (400MHz, D_2O): 4.18-4.29 (m, 3H), 4.52 (t, 1H), 4.63 (t, 1H), 6.07 (d, 1H), 6.69 (t, 1H), 7.08 (m, 4H), 8.18 (s, 1H), 8.58 (s, 1H). ^{31}P NMR (400 MHz, D_2O): -9.41 (d, γ-P), -10.08 (d, α-P), -21.68 (d, β-P); LRMS (MALDI-TOF) calculated for $C_{16}H_{21}N_6O_{12}P_3$ [M+Li-H]: 587.05, found: 587.47.

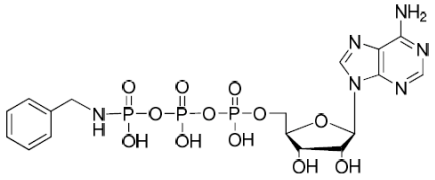

Synthesis of ATP-γ-benzylamine 2b. The general protocol for synthesis of ATP analogs was followed using ATP•2Na (27 mg, 0.05 mmol) and benzylamine hydrochloride salt (0.28 g, 2 mmol) and purification affording the triethyl ammonium salt of **2b** (26 mg, 0.029 mmol, 58% yield). UV (MeOH): λ 258.0 nm; ^{1}H NMR (400 MHz, CD_3OD): 4.24 (m, 5H), 4.55 (t, 1H), 4.67 (t, 1H), 6.07 (d, 1H), 7.20 (m, 3H), 7.37 (d, 2H), 8.17 (s, 1H), 8.60(s, 1H) ^{31}P NMR (400 MHz, CD_3OD) -0.47 (d, γ-P),-10.02 (d, α-P), -20.59 (t, β-P); LRMS (MALDI-TOF) calculated for $C_{17}H_{23}N_6O_{12}P_3$ [M-H]: 595.06, found: 594.59.

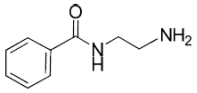

Synthesis of N-benzoyl-1,2-diaminoethane 5c. The general protocol for synthesis of amines (pg S2) was followed using ethylene diamine (0.4 g, 6 mmol) and benzoyl chloride **3b** (0.83 g, 5.9 mmol) and purification affording amine **5c** (0.35 g, 2.5 mmol, 43% yield). IR (neat, cm^{-1}) 3288, 3063, 2937, 2874, 1636, 1540, 1485, 1305, 1183, 1071, 1031, 932, 853, 808, 698; ^{1}H NMR (400 MHz, CD_3OD): 2.85 (t, 2H), 3.45 (t, 2H), 7.45 (t, 2H), 7.52 (t, 1H), 7.83 (d, 2H); ^{13}C NMR (100MHz, CD_3OD): 40.8, 42.2, 127.1, 128.3, 131.4, 134.4, 169.4; LRMS (ESI) calculated for $C_9H_{12}N_2O$ [M+H]: 165.09, found: 165.3.

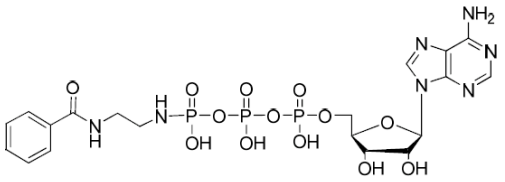

Synthesis of ATP-γ-N-benzoyl-1,2-diaminoethane 6c. The general protocol for synthesis of ATP analogs (pg S2-3) was followed using ATP•2Na (27 mg, 0.05 mmol) and N-benzoyl-1, 2-diaminoethane **5c** (0.25 g, 1.5 mmol) and purification affording the triethyl ammonium salt of **6c** (21.51 mg, 0.022 mmol, 45% yield). UV (MeOH): λ 257.0 nm; ^{1}H NMR (400 MHz, CD_3OD): 3.33 (t, 2H), 3.50 (t, 2H), 4.28 (m, 3H), 4.57(s, 1H), 4.71(s, 1H), 6.08 (d, 1H), 7.42 (m, 3H), 7.92 (d, 2H), 8.18 (s, 1H), 8.59 (s, 1H); ^{31}P NMR (400 MHz, CD_3OD) -0.58 (d, γ-P), -10.58 (d, α-P), -21.30 (t, β-P); LRMS (MALDI-TOF) calculated for $C_{19}H_{26}N_7O_{13}P_3$ [M-H]: 652.08, found: 651.72.

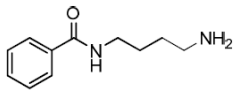

Synthesis of N-benzoyl-1,4-diaminobutane 5d. The general protocol for synthesis of amines (pg S2) was followed using 1,4-diaminobutane (0.76 g, 10 mmol) and benzoyl chloride **3b** (1.68 g, 10mmol) and purification affording amine **5d** (0.86 g, 4.5 mmol, 45%). IR (neat, cm^{-1}) 3319, 3034, 2934, 2645, 1633, 1537, 1484, 1309, 1160, 801, 714, 697; ^{1}H NMR (400 MHz, CD_3OD): 1.70 (s, 4H), 2.93 (m, 2H), 3.42 (m, 2H), 7.45 (t, 2H), 7.53 (t, 1H), 7.82 (d, 2H); ^{13}C NMR (100MHz, CD_3OD): 25.5, 26.4, 38.9, 39.5, 127.1, 128.4, 131.5, 134.4, 169.1; LRMS (ESI) calculated for $C_{11}H_{16}N_2O$ [M+H]: 193.12, found: 193.1.

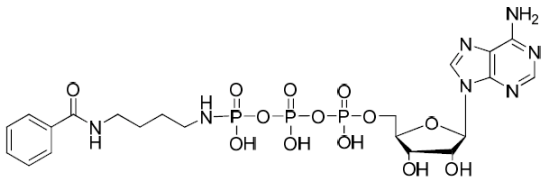

Synthesis of ATP-γ-N-benzoyl-1, 4-diaminobutane 6d. The general protocol for synthesis of ATP analogs was followed using ATP•2Na (27 mg, 0.05 mmol) and N-benzoyl-1, 4-diaminobutane **5d** (0.5 g, 3 mmol) and purification affording the triethyl ammonium salt of **6d** (13.77 mg, 0.014 mmol, 28% yield). UV (MeOH): λ 258.0 nm; ^{1}H NMR (400 MHz, CD_3OD): 1.59 (m, 4H), 3.35 (m, 4H), 4.23 (m, 3H), 4.53

(s, 1H), 4.80 (s, 1H), 6.09 (d, 1H) 7.44 (m, 3H), 7.81 (d, 2H), 8.16 (s, 1H), 8.63 (s, 1H); ^{31}P NMR (400 MHz, CD_3OD) 1.16 (d, γ -P), -8.96 (d, α -P), -18.75 (t, β -P); LRMS (MALDI-TOF) calculated for $C_{21}H_{30}N_7O_{13}P_3$ [M-H]: 680.11, found: 679.78.

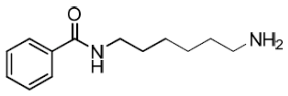

Synthesis of N-benzoyl-1, 6-diamino hexane 5e. The general protocol for synthesis of amines was followed using 1,6-diaminohexane (5.6 gm, 50 mmol) and benzoyl chloride **3b** (1.68 g, 10 mmol) and purification affording amine **5e** (1.16 gm, 5.3 mmol, 53%). IR (neat, cm^{-1}) 3310, 3061, 2934, 2860, 1634, 1540, 1482, 1446, 1302, 710; ^{1}H NMR (400 MHz, CD_3OD): 1.39 (m, 4H), 1.49 (m, 2H), 1.63 (m, 2H), 2.64 (t, 2H), 3.36 (t, 2H), 7.44 (t, 2H), 7.51 (t, 1H), 7.79 (d, 2H); ^{13}C NMR (100MHz, CD_3OD): 26.4, 26.6, 29.2, 32.2, 39.7, 41.1, 127.0, 128.3, 131.3, 134.7, 169.0; LRMS (ESI) calculated for $C_{13}H_{20}N_2O$ [M+H]: 221.15, found: 221.35.

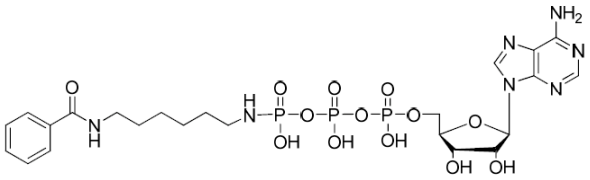

Synthesis of ATP-γ-N-benzoyl-1,6-diaminohexane 6e. The general protocol for synthesis of ATP analogs was followed using ATP•2Na (27 mg, 0.05 mmol) and N-benzoyl-1, 6-diaminohexane **5e** (0.44 g, 2 mmol) and purification affording the triethyl ammonium salt of **6e** (20.24 mg, 0.02 mmol, 40% yield). UV (MeOH): λ 268.0 nm; ^{1}H NMR (400 MHz, CD_3OD): 1.36 (m, 4H), 1.49 (m, 2H), 1.59 (m, 2H), 3.34 (m, 4H), 4.2 (m, 3H), 4.5 (s, 1H), 4.7 (s, 1H), 6.08 (d, 1H), 7.47 (m, 3H), 7.81 (d, 2H), 8.18 (s, 1H), 8.62 (s, 1H); ^{31}P NMR (400MHz, CD_3OD): 0.68 (d, γ -P), -9.59 (d, α -P), -19.70 (t, β -P); LRMS (MALDI-TOF) calculated for $C_{23}H_{34}N_7O_{13}P_3$ [M-H]: 708.14, found: 707.82.

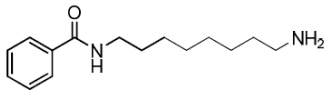

Synthesis of N-benzoyl-1,8-diaminooctane 5f. The general protocol for synthesis of amines was followed using 1,8-diaminooctane (7.2 gm, 50 mmol) and benzoyl chloride **3b** (1.68 g, 10 mmol) and purification affording amine **5f** (620.47 mg, 2.5 mmol, 25% yield). IR (neat, cm^{-1}) 3312, 3065, 2928, 2853, 1632,1603, 1577, 1540, 1490, 1473, 1440, 1131, 713; ^{1}H NMR (400 MHz, CD_3OD): 1.36 (m, 8H), 1.49 (m, 2H), 1.62 (m, 2H), 2.66 (t, 2H), 3.36 (t, 2H), 7.44 (t, 2H), 7.51 (t, 1H), 7.79 (d, 2H); ^{13}C NMR (100MHz, CD_3OD): 26.1, 26.7, 27.3, 28.9, 29.2, 39.5, 39.7, 39.8, 127.0, 128.3, 131.3, 134.6, 169.1; LRMS (ESI) calculated for $C_{15}H_{24}N_2O$ [M+H]: 249.18, found: 249.4.

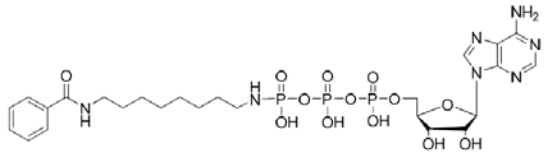

ATP-γ-N-benzoyl-1,8-diaminooctane 6f

The general protocol for synthesis of ATP analogs was followed using ATP•2Na (27 mg, 0.05 mmol) and N-benzoyl-1, 8 -diaminooctane (0.496 g, 2 mmol) and purification affording the triethyl ammonium salt of **6f** (9.35 mg, 0.09 mmole, 18% yield). UV (MeOH): λ 259.0 nm; ^{1}H NMR (400 MHz, CD_3OD): 1.30 (m, 8H), 1.45 (m, 2H), 1.58 (m, 2H), 3.34 (m, 4H), 4.25 (m, 3H), 4.58 (s, 1H), 4.72 (s, 1H), 6.09 (d, 1H), 7.44 (m, 3H), 7.50 (t, 2H), 8.18 (s, 1H), 8.60 (s, 1H); ^{31}PNMR (400MHz, CD_3OD): 0.51 (d, γ-P), -9.74 (d, α-P), -19.99 (t, β -P); LRMS (MALDI-TOF) calculated for $C_{23}H_{34}N_7O_{13}P_3$ [M-H]: calculated: 736.17, found: 735.86.

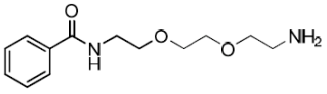

Synthesis of N-benzoyl-2,2'-ethylenedioxy bis-(ethylamine) 8b. The general protocol for synthesis of amines was followed using 2,2'-ethylenedioxy bis-(ethylamine) **7** (4.4 mL, 28.7 mmol) and benzoyl chloride **3b** (0.8 gm, 5.74 mmol) and purification affording amine **8b** (0.76 gm, 3.04 mmol, 53% yield). IR (neat, cm^{-1}) 3355, 3066, 2874, 1642, 1547, 1485, 1309, 1249, 1105, 936, 868, 808, 708; ^{1}H NMR (400 MHz, CD_3OD): 2.78 (t, 2H), 3.52 (t, 2H), 3.56-3.68 (m, 8H), 7.44 (t, 2H), 7.52 (t, 1H), 7.81 (d, 2H); ^{13}C NMR (100MHz, CD_3OD): 39.7, 40.7, 69.3, 70.1, 71.7, 127.1, 128.3, 131.5, 134.4, 169.1; LRMS (ESI) calculated for $C_{13}H_{20}N_2O_3$ [M+H]: 253.14, found: 253.3.

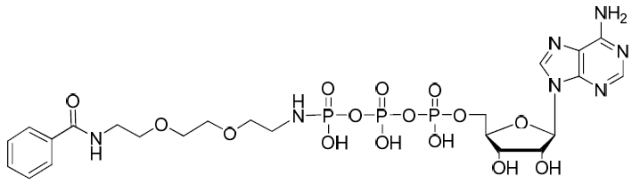

Synthesis of ATP-γ- N-benzoyl-2,2'-ethylenedioxy bis-(ethylamine) 9b. The general protocol for synthesis of ATP analogs was followed using ATP•2Na (27 mg, 0.05 mmol) and N-benzoyl-2, 2'-ethylenedioxy bis-(ethylamine) **8b** (0.51 g, 2 mmol) and purification affording the triethyl ammonium salt of **9b** (11.49 mg, 0.011 mmol, 23% yield). UV (MeOH): λ 257.0 nm; ^{1}H NMR (400 MHz, CD_3OD): 3.55-3.70 (m, 12H), 4.27 (t, 3H), 4.57 (m, 1H), 4.70 (t, 1H) 6.08 (d, 1H), 7.44 (t, 2H), 7.50 (t, 1H), 7.81 (d, 2H), 8.18 (s, 1H), 8.59 (s, 1H); ^{31}P NMR (400 MHz, CD_3OD): 1.32 (d, γ-P), -8.81 (d, α-P), -18.48 (t, β-P); LRMS (MALDI-TOF) calculated for $C_{23}H_{34}N_7O_{15}P_3$ [M+H]: 740.13, found: 739.82.

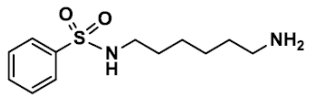

Synthesis of N-benzenesulfonyl-1,6-diaminohexane 12. The general protocol for synthesis of amines was followed using 1,6-diaminohexane **11** (5.8 g, 50 mmol) and benzenesulfonyl chloride **10** (1.8 g, 7.8 mmol) and purification affording amine **12** (1.28 g, 5.0 mmol, 64% yield). IR (neat, cm^{-1}) 3291, 2938, 1603, 1439, 1317, 1154, 1085, 745, 690; ^{1}H NMR (400 MHz, CD_3OD): 0.99-1.06 (m, 4H), 1.18-1.23 (m, 4H), 2.37 (t, 2H, J=7.2 Hz), 2.61 (t, 2H, J=7.0 Hz), 7.31-7.40 (m, 3H), 7.61 (d, 2H, J=7.2 Hz); ^{13}C NMR (100MHz, $CDCl_3$): 26.4, 26.5, 29.7, 33.4, 42.0, 43.3, 127.2, 129.3, 132.7, 140.3; HRMS (ESI) calculated for $C_{12}H_{21}N_2O_2S$ [M+H]: 257.1324, found: 257.1334.

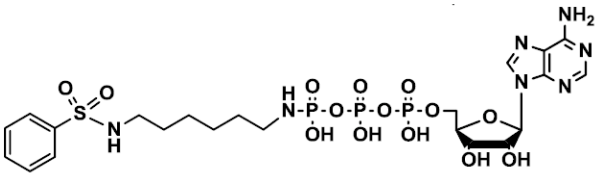

Synthesis of ATP- γ-N- benzenesulfonyl -1,6-diaminohexane 13. The general protocol for synthesis of ATP analogs was followed using ATP•2Na (27 mg, 0.05 mmol) and N-benzenesulfonyl-1, 6-diaminohexane **12** (0.512 g, 2 mmol) and purification affording the triethyl ammonium salt of **13** (11.18 mg, 0.015 mmol, 30% yield). UV (MeOH): λ 259.0 nm ^{1}H NMR (400 MHz, CD_3OD): 1.38-1.60 (m, 4H), 2.79-3.01 (m, 8H), 4.23-4.29 (m, 3H), 4.46-4.49 (m, 1H), 4.53-4.56 (m, 1H), 4.67-4.75 (m, 1H), 6.09 (dd, 1H, J=2.4 Hz and 5.6 Hz), 7.57 (m, 3H), 7.84 (d, 2H, J=8Hz), 8.11(d, 1H, J=6Hz), 8.60 (s, 1H); $^{31}PNMR$ (400MHz, CD_3OD): -1.21(d, γ -P), -11.54 (d, α -P), -23.07 (t, β -P); HRMS (ESI) calculated for $C_{22}H_{33}N_7O_{14}P_3$ [M-H]: 744.1019, found: 744.1019.

III. Compound characterization

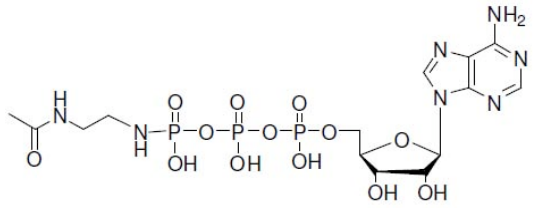

ATP-γ-N-acetyl-1, 2 diaminoethane **6a**

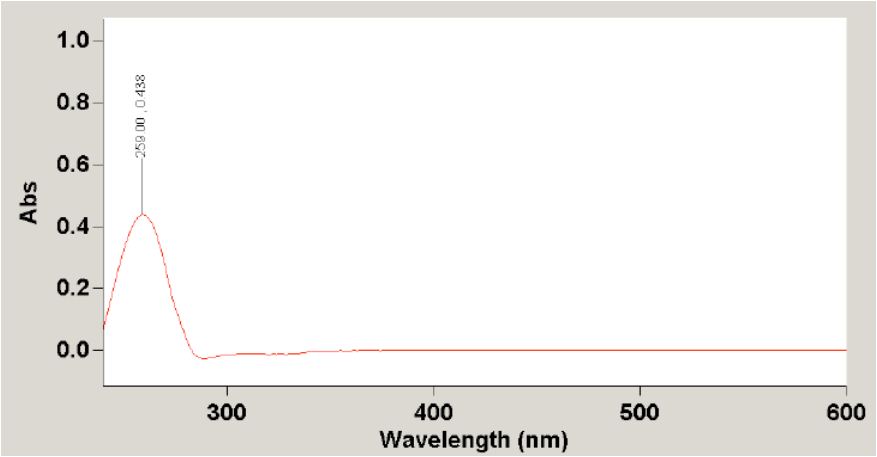

Figure S1: UV of ATP-γ-N-acetyl-1, 2 diaminoethane **6a**.

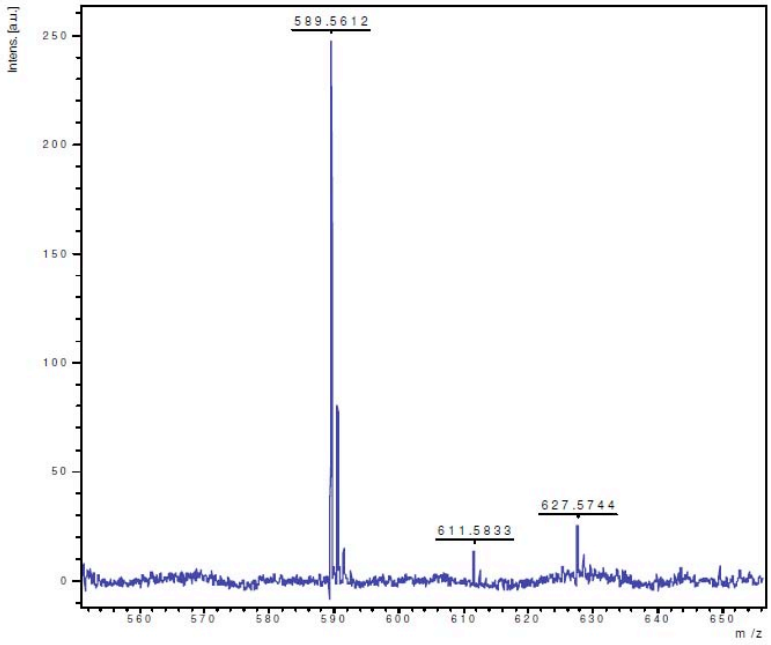

Figure S2: MALDI-TOF MS of ATP-γ-N-acetyl-1, 2 diaminoethane **6a**.

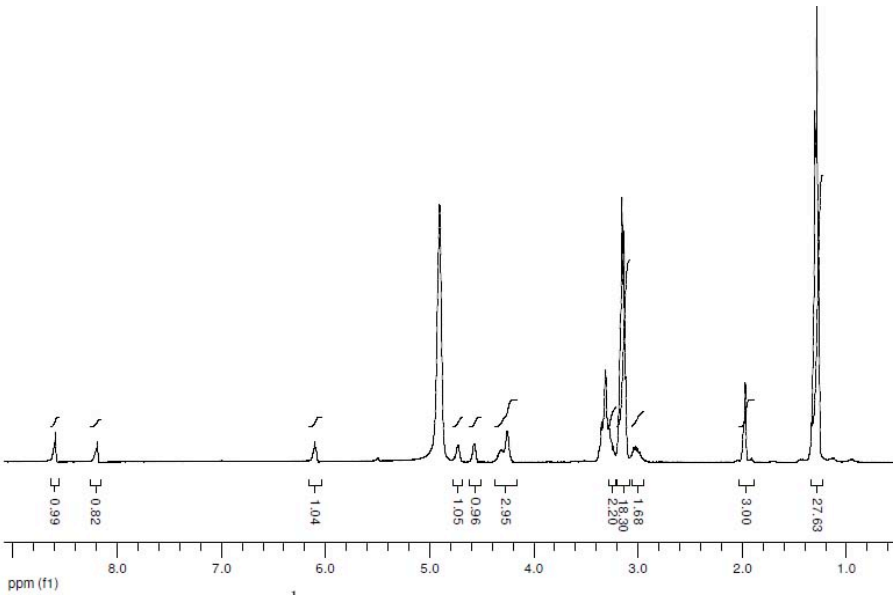

Figure S3: ^{1}H-NMR of ATP-γ-N-acetyl-1, 2 diaminoethane **6a**.

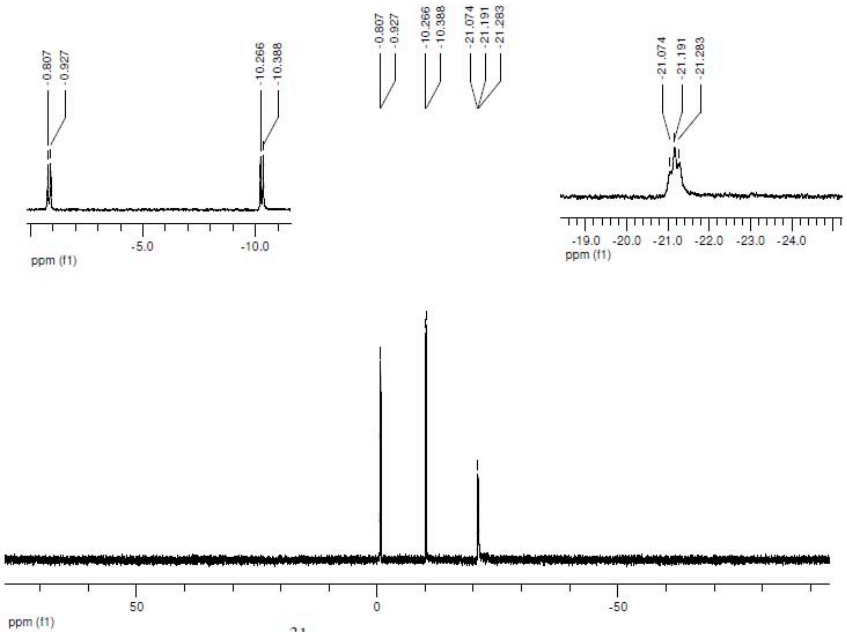

Figure S4: ^{31}PNMR of ATP-γ-N-acetyl-1, 2 diaminoethane **6a**.

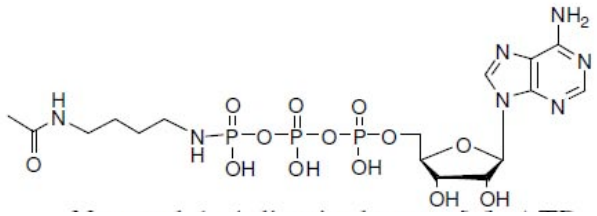

ATP-γ-N-acetyl-1, 4 diaminobutane **6b**

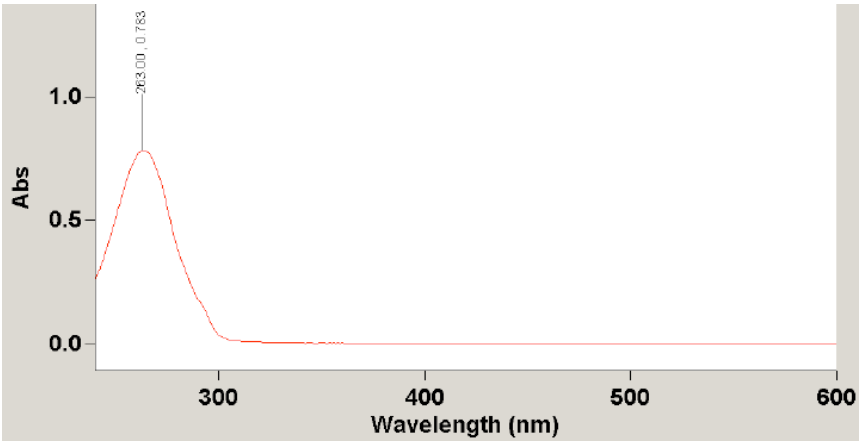

Figure S5: UV of ATP-γ-N-acetyl-1, 4 diaminobutane **6b**.

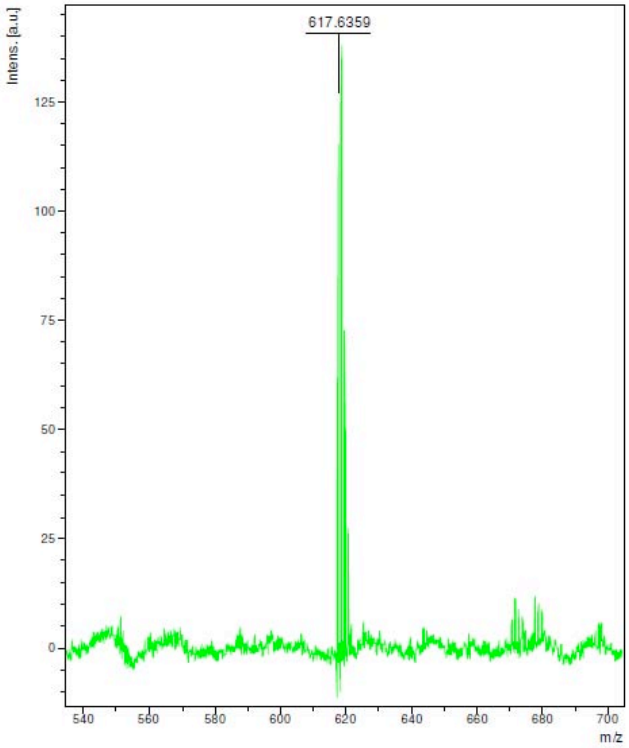

Figure S6: MALDI-TOF-MS of ATP-γ-N-acetyl-1, 4 diaminobutane **6b**.

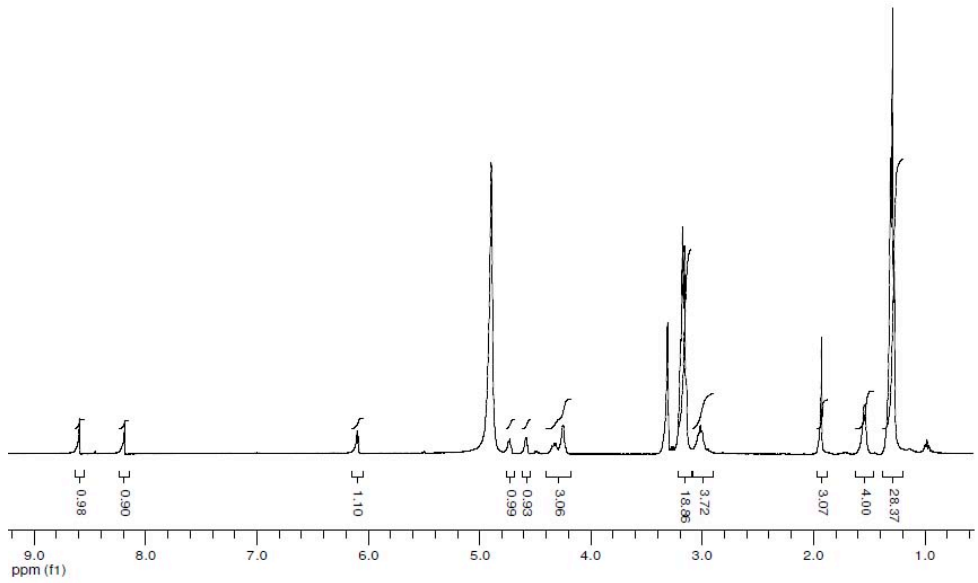

Figure S7: ^{1}H NMR of ATP-γ-N-acetyl-1, 4 diaminobutane **6b**.

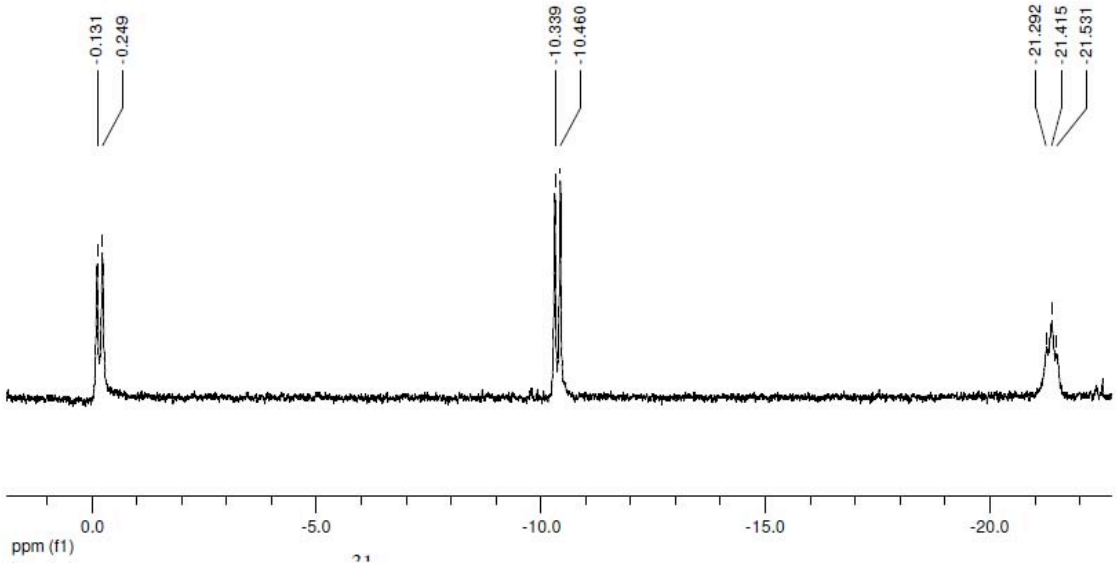

Figure S8: 31P NMR of ATP-γ-N-acetyl-1, 4 diaminobutane **6b**.

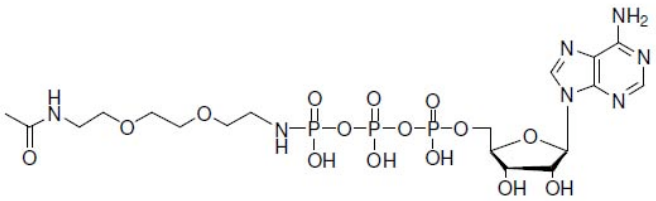

ATP-γ-N-acetyl-2, 2’-ethylenedioxy bis-(ethylamine) **9a**

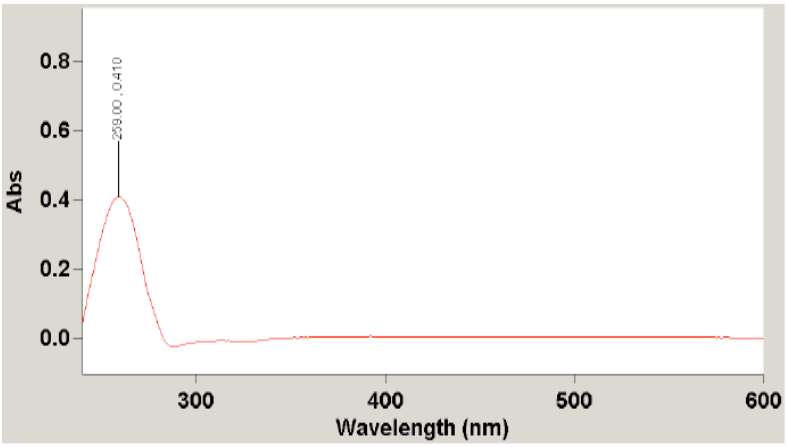

Figure S9: UV spectra of ATP-γ-N-acetyl-2, 2’-ethylenedioxy bis-(ethylamine) **9a**.

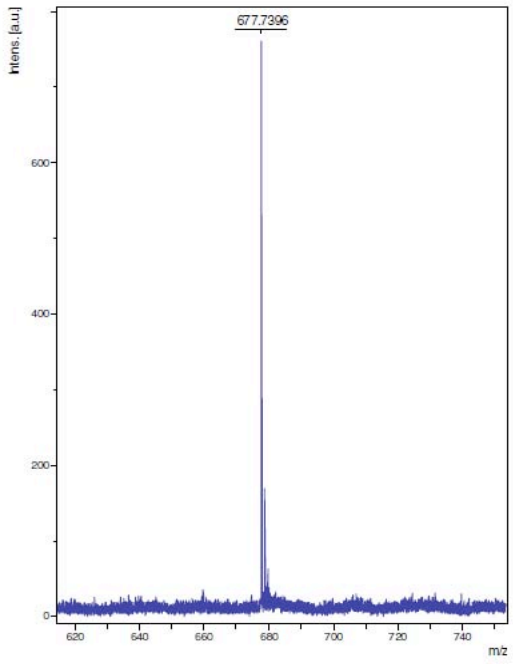

Figure S10: MALDI-TOF of ATP-γ-N-acetyl-2, 2’-ethylenedioxy bis-(ethylamine) **9a**

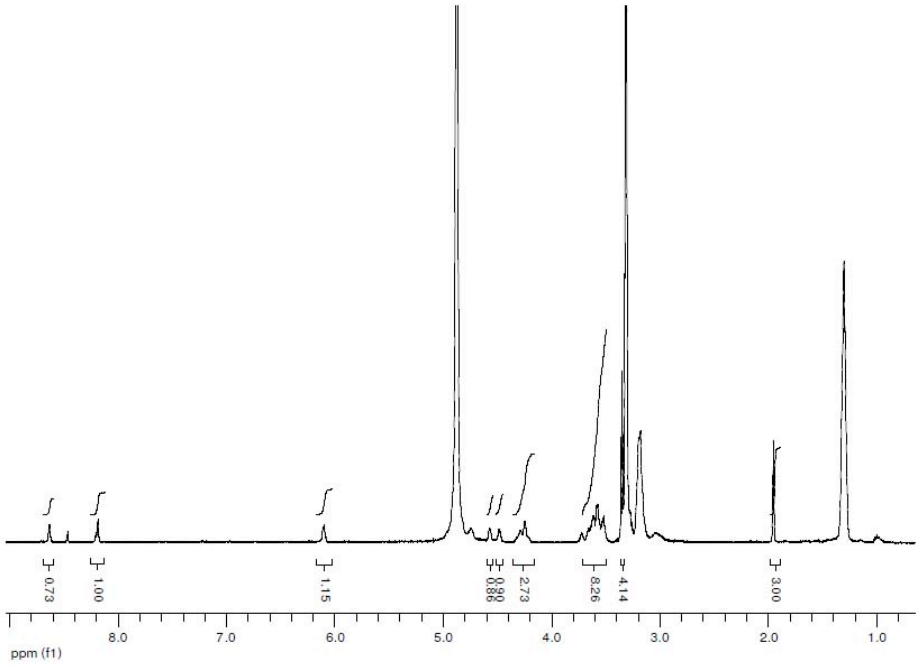

Figure S11: ^{1}H-NMR of ATP-γ-N-acetyl-2, 2'-ethylenedioxy bis-(ethylamine) **9a**

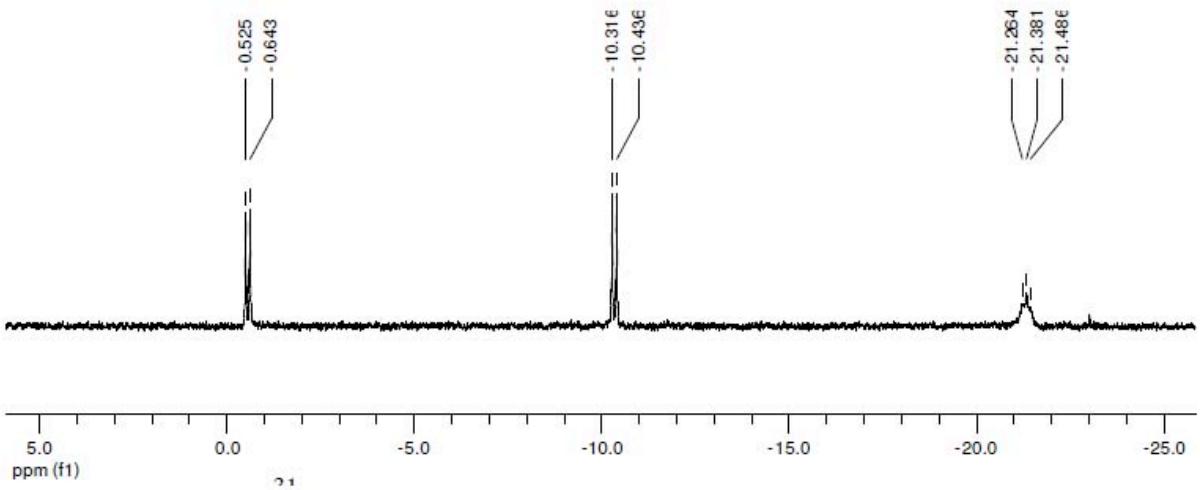

Figure S12: ^{31}PNMR of ATP-γ-N-acetyl-2, 2'-ethylenedioxy bis-(ethylamine) **9a**

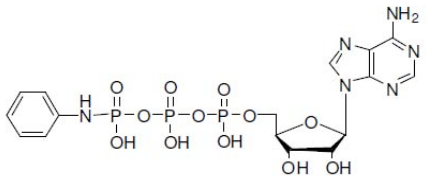

ATP-γ-aniline **2a**

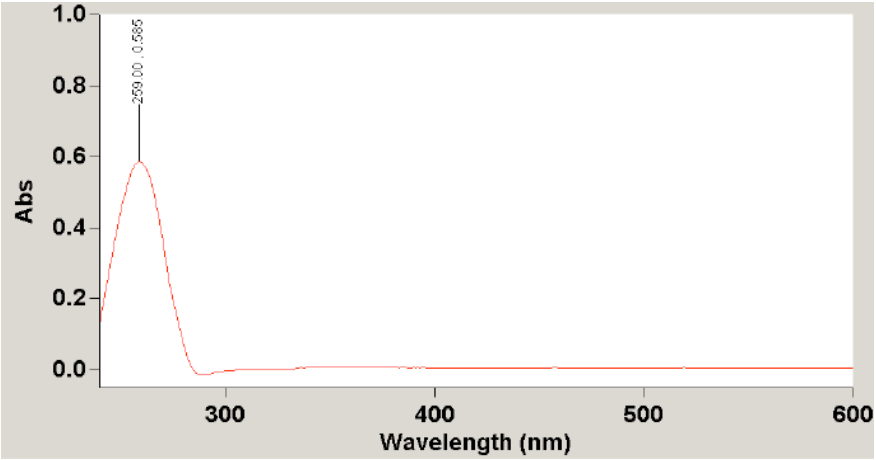

Figure S13: UV of ATP-γ-aniline **2a**

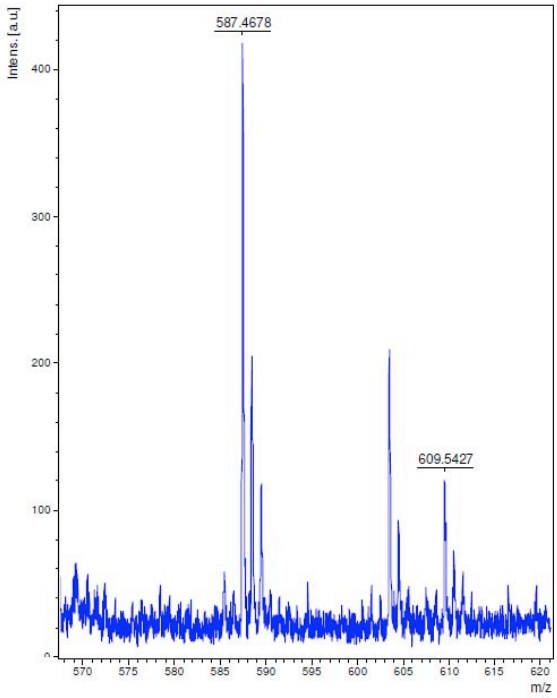

Figure S14: MALDI-TOF MS of ATP-γ-aniline **2a**

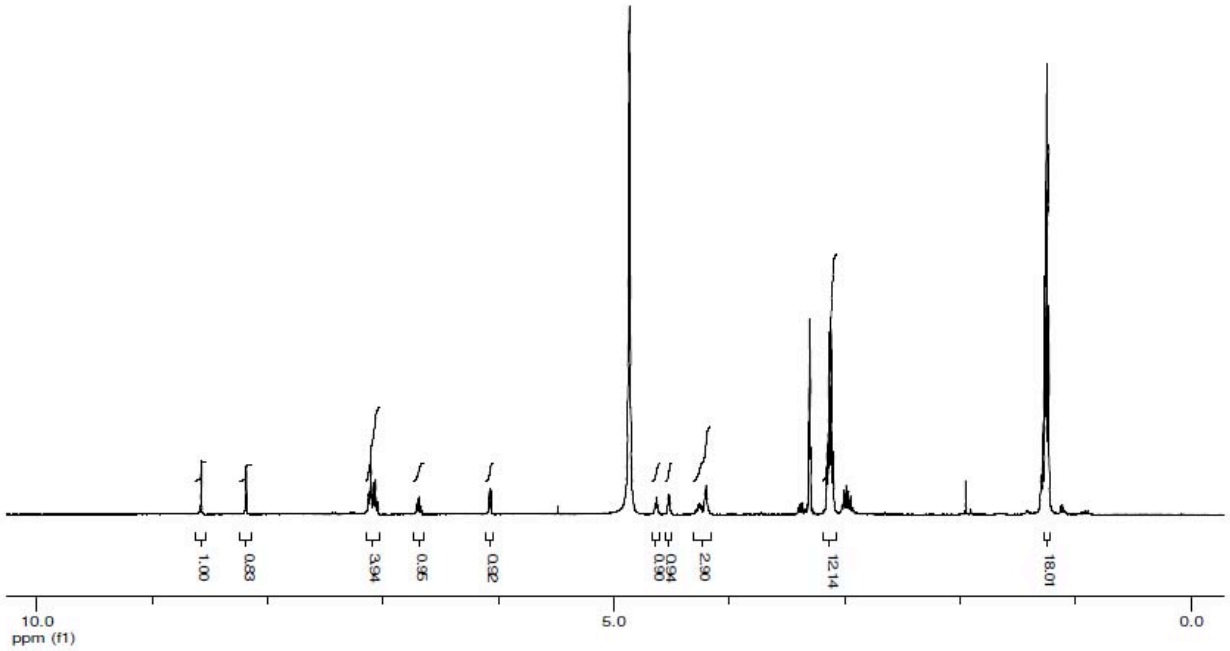

Figure S15: ^{1}H-NMR of ATP-γ-aniline **2a**

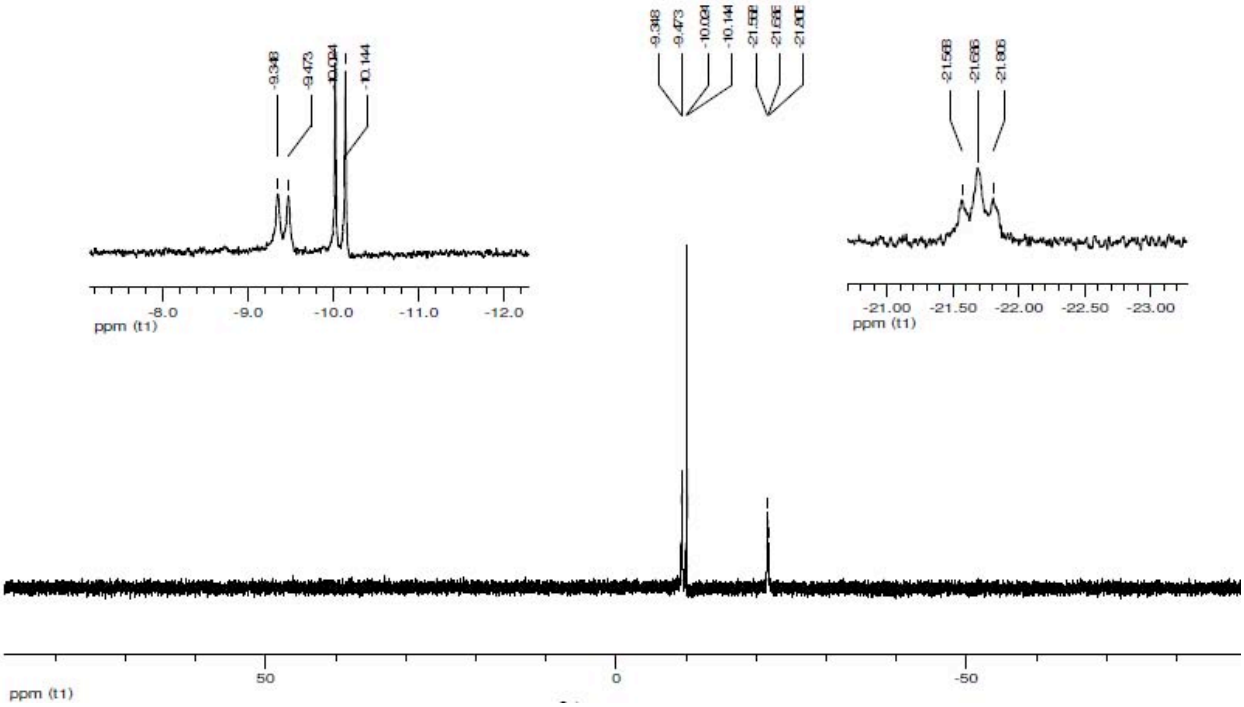

Figure S16: ^{31}P NMR of ATP-γ-aniline **2a**

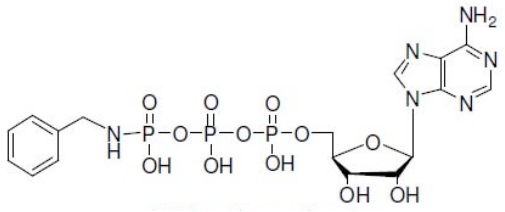

ATP-γ-benzylamine **2b**

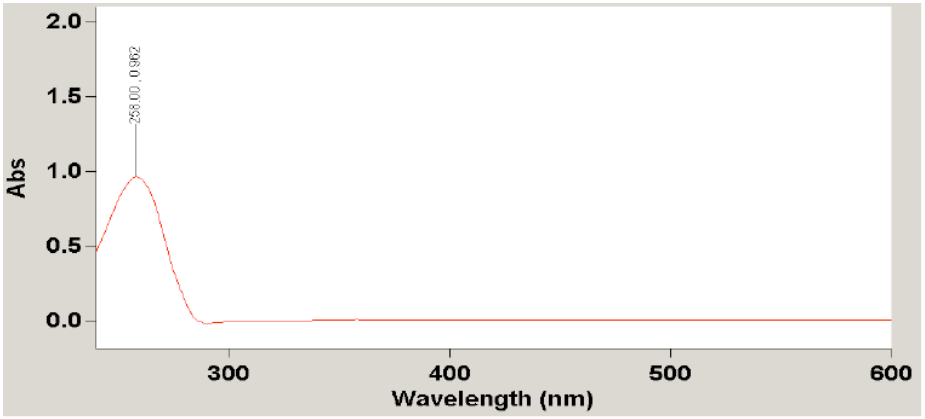

Figure S17: UV of ATP-γ-benzylamine **2b**

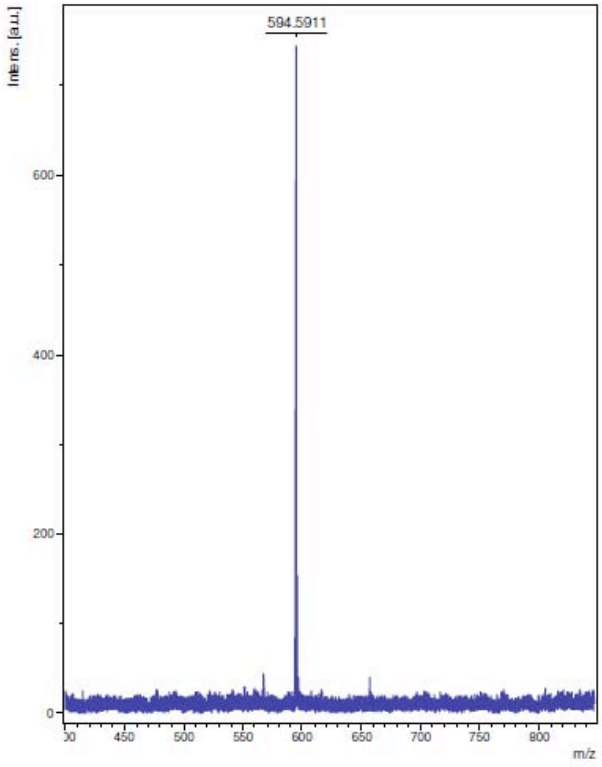

Figure S18: MALDI-TOF MS of ATP-γ-benzylamine **2b**

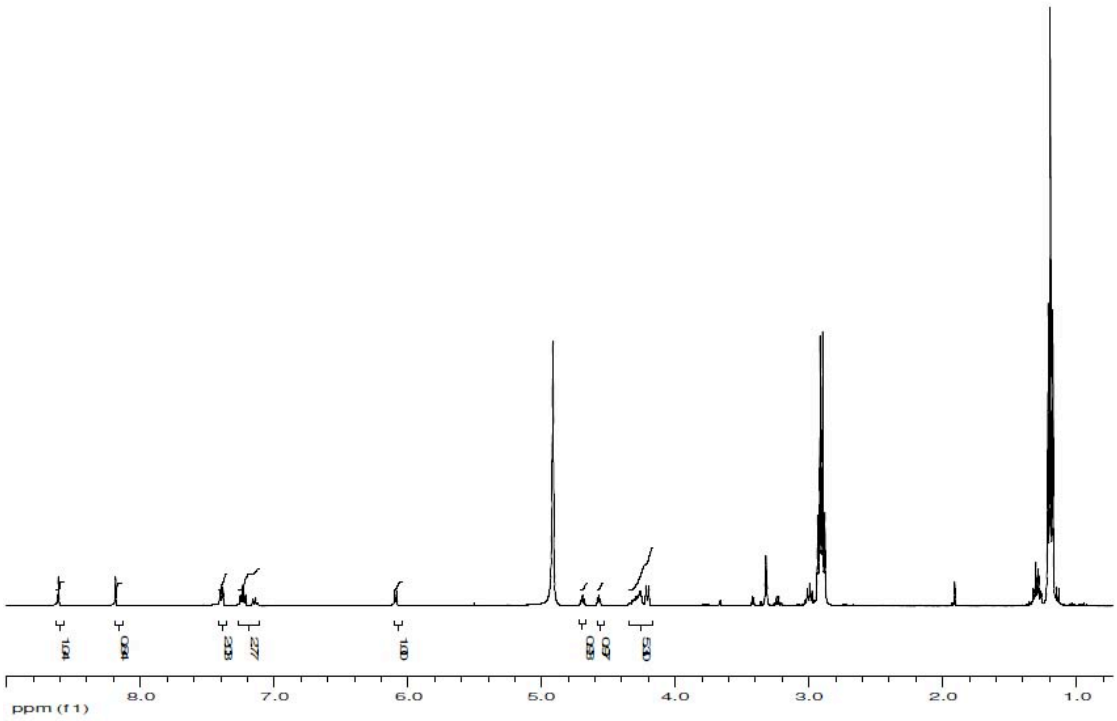

Figure S19: ^{1}H-NMR of ATP-γ-benzylamine **2b**

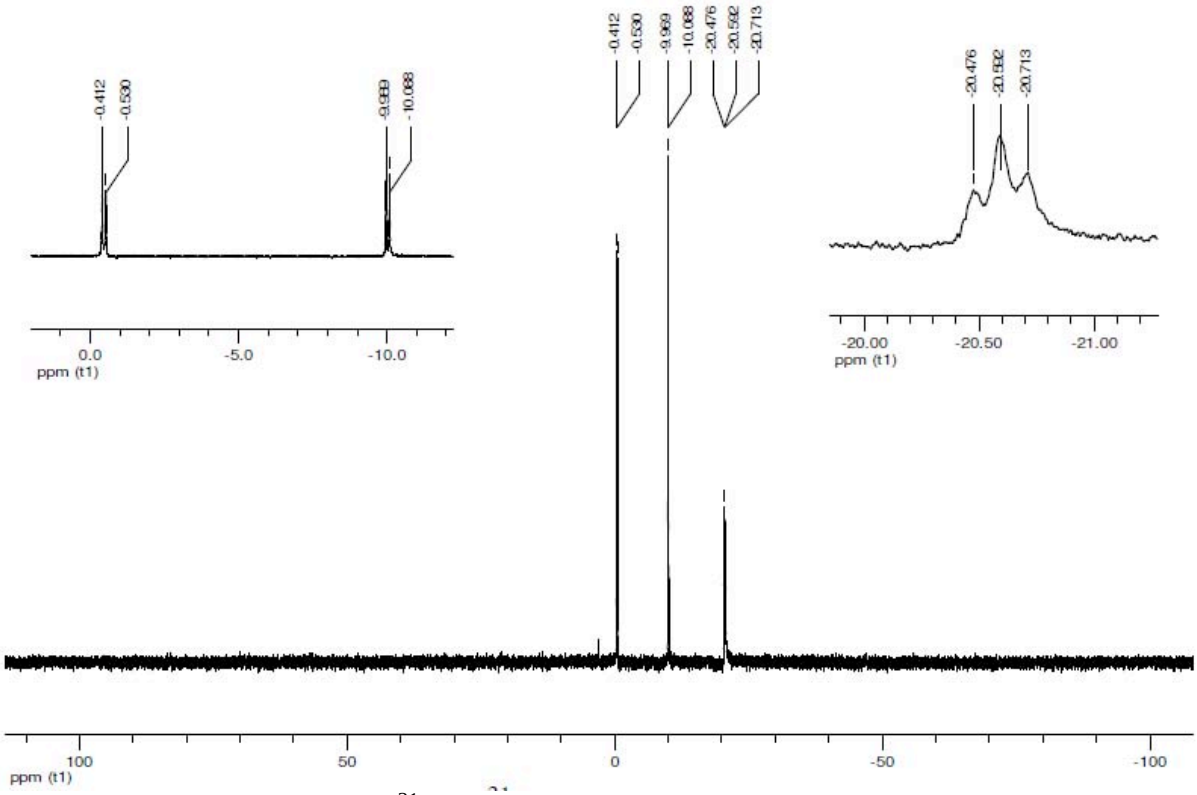

Figure S20: ^{31}PNMR of ATP-γ-benzylamine **2b**

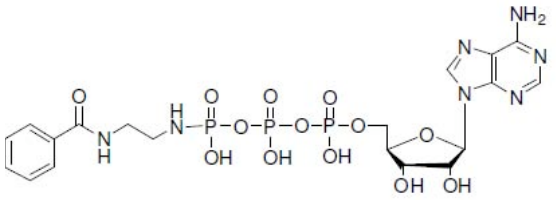

ATP-γ-N-benzoyl-1, 2 diaminoethane **6c**

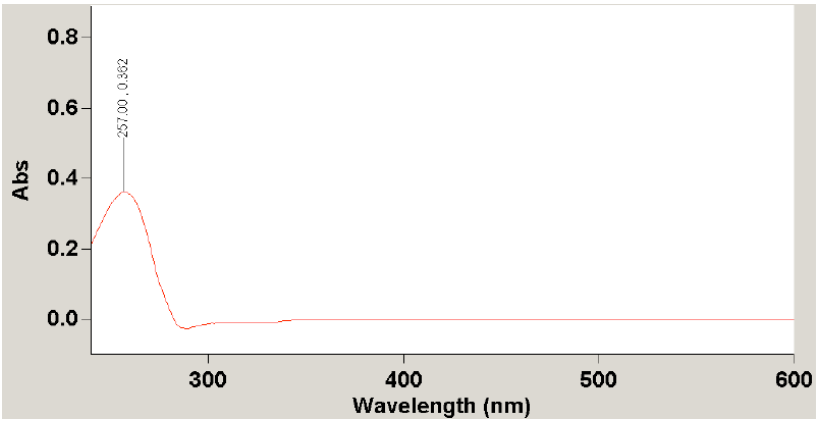

Figure S21: UV of ATP-γ-N-benzoyl-1, 2 diaminoethane **6c**

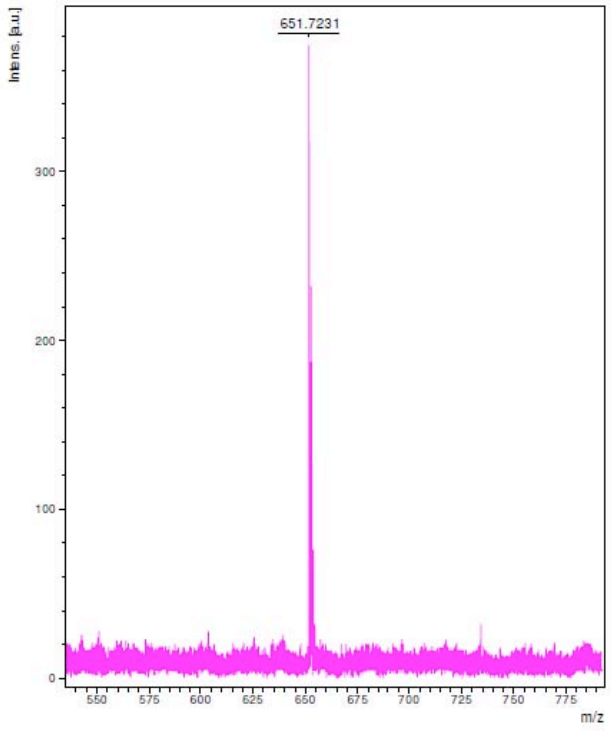

Figure S22: MALDI-TOF MS of ATP-γ-N-benzoyl-1, 2 diaminoethane **6c**

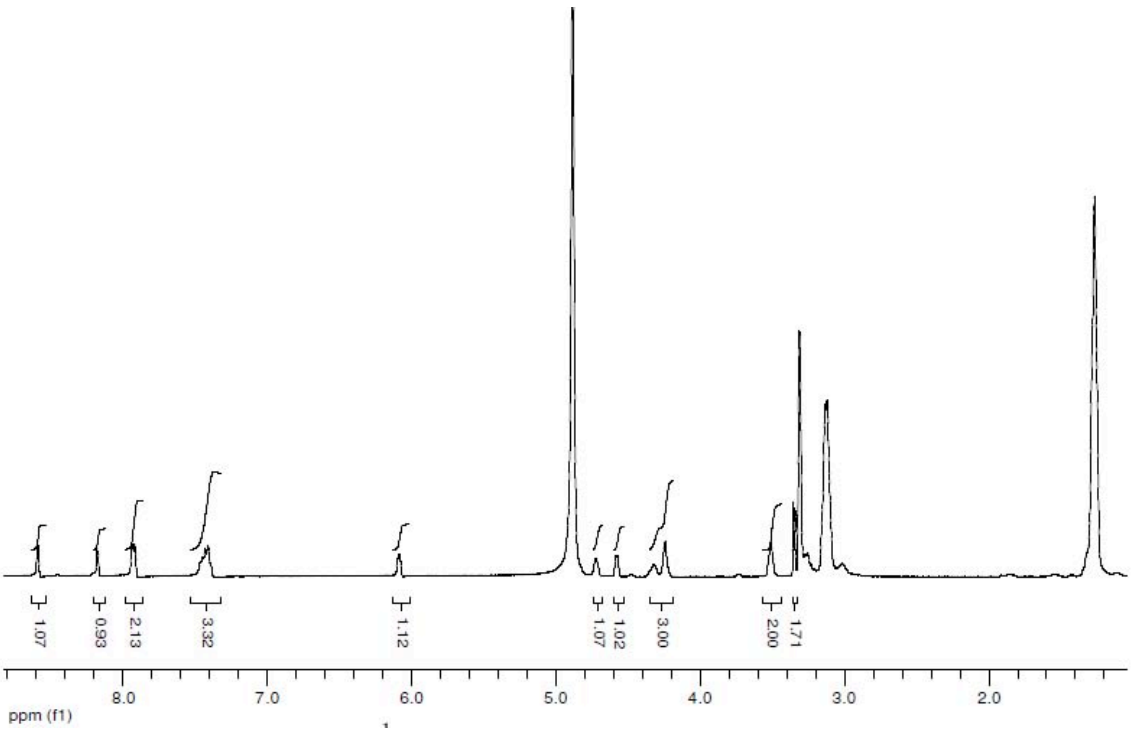

Figure S23: ^{1}H NMR of ATP-γ-N-benzoyl-1, 2 diaminoethane **6c**

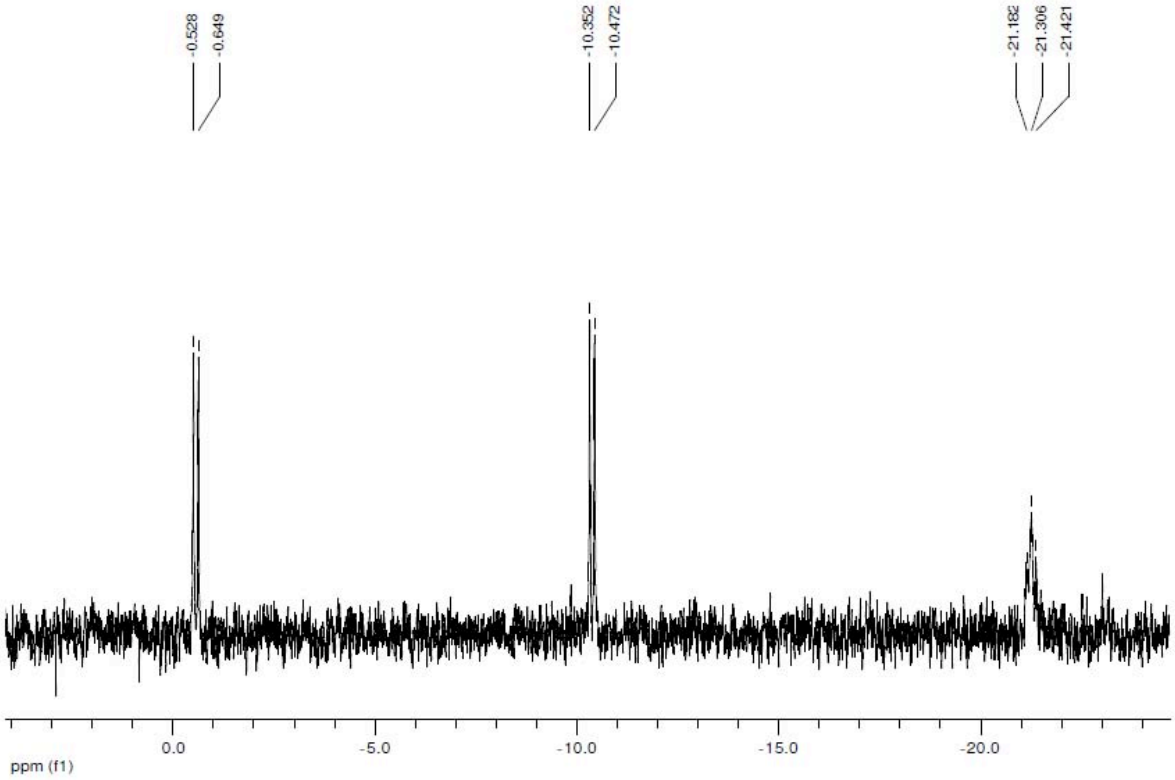

Figure S24: ^{31}P NMR of ATP-γ-N-benzoyl-1, 2 diaminoethane **6c**

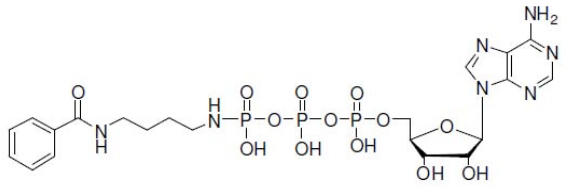

ATP-γ-N-benzoyl-1, 4-diaminobutane **6d**

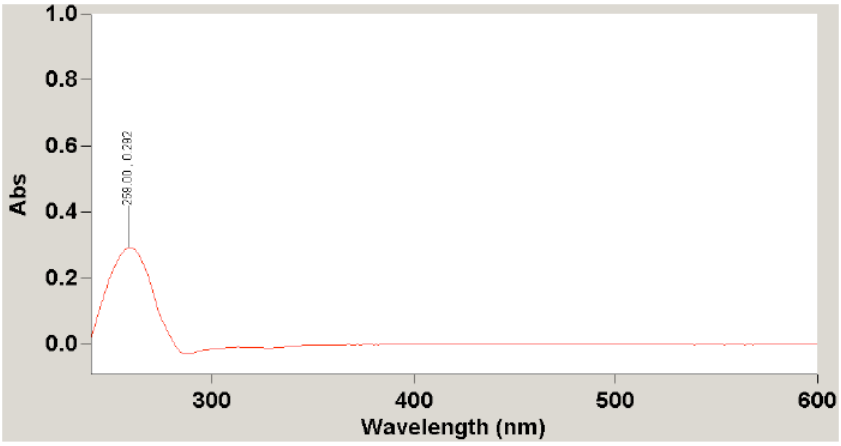

Figure S25: UV of ATP-γ-N-benzoyl-1, 4-diaminobutane **6d**

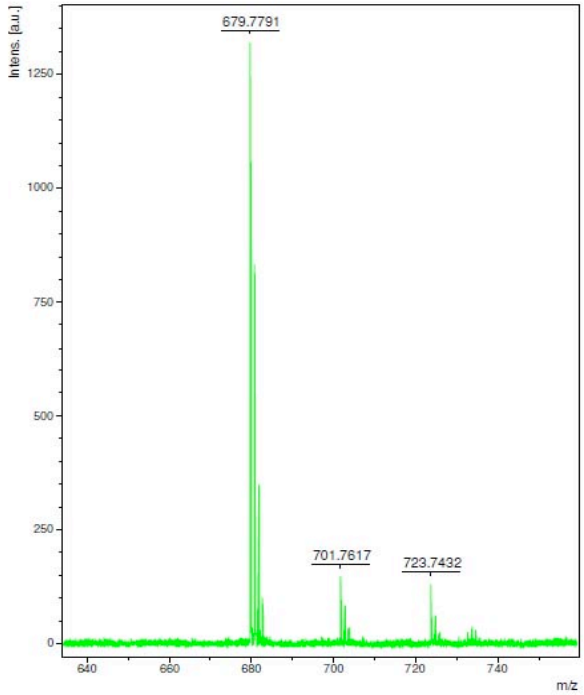

Figure S26: MALDI-TOF MS of ATP-γ-N-benzoyl-1, 4-diaminobutane **6d**

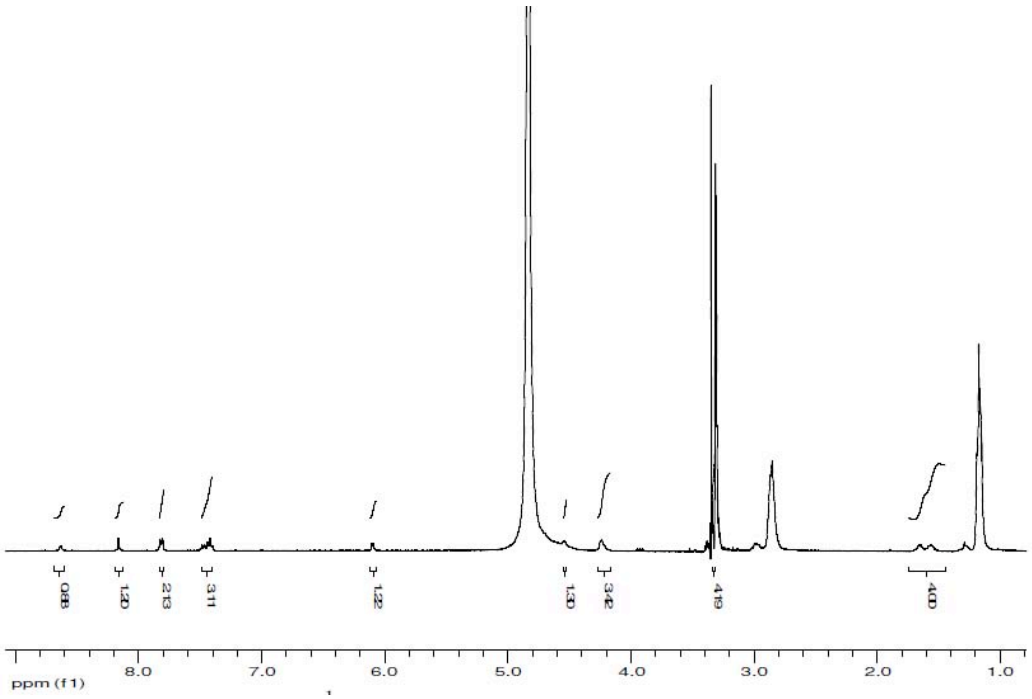

Figure S27: ^{1}H NMR of ATP-γ-N-benzoyl-1, 4-diaminobutane **6d**

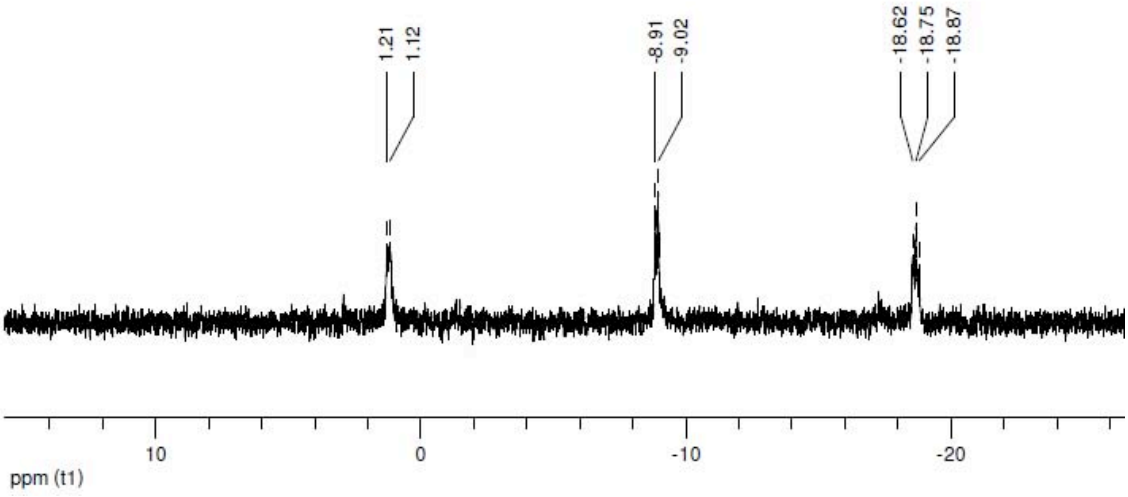

Figure S28: ^{31}P NMR of ATP-γ-N-benzoyl-1, 4-diaminobutane **6d**

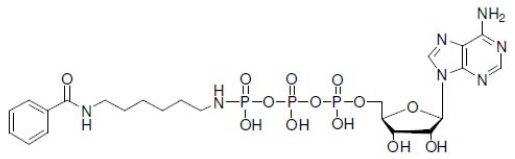

ATP-γ-N-benzoyl-1,6-diaminohexane **6e**

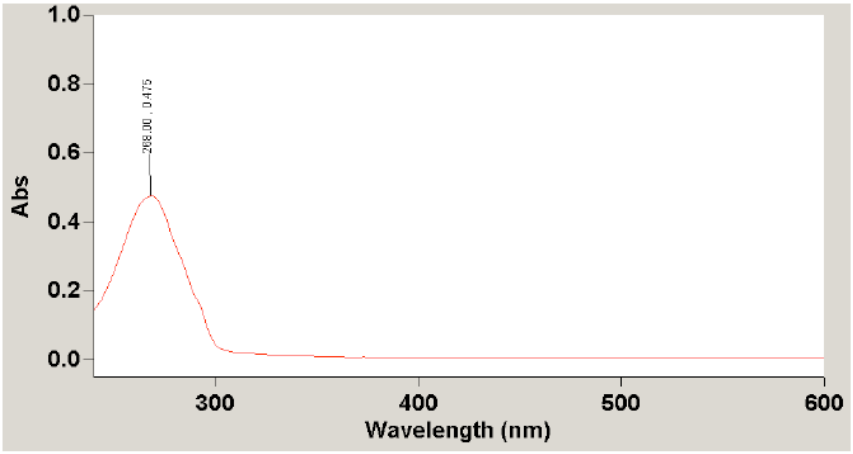

Figure S29: UV of ATP-γ-N-benzoyl-1, 6-diaminohexane **6e**

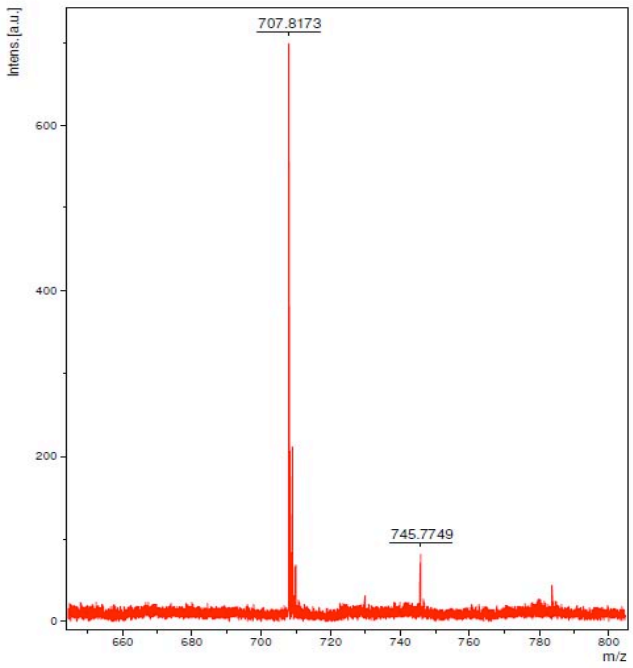

Figure S30: MALDI-TOF MS of ATP-γ-N-benzoyl-1, 6-diaminohexane **6e**

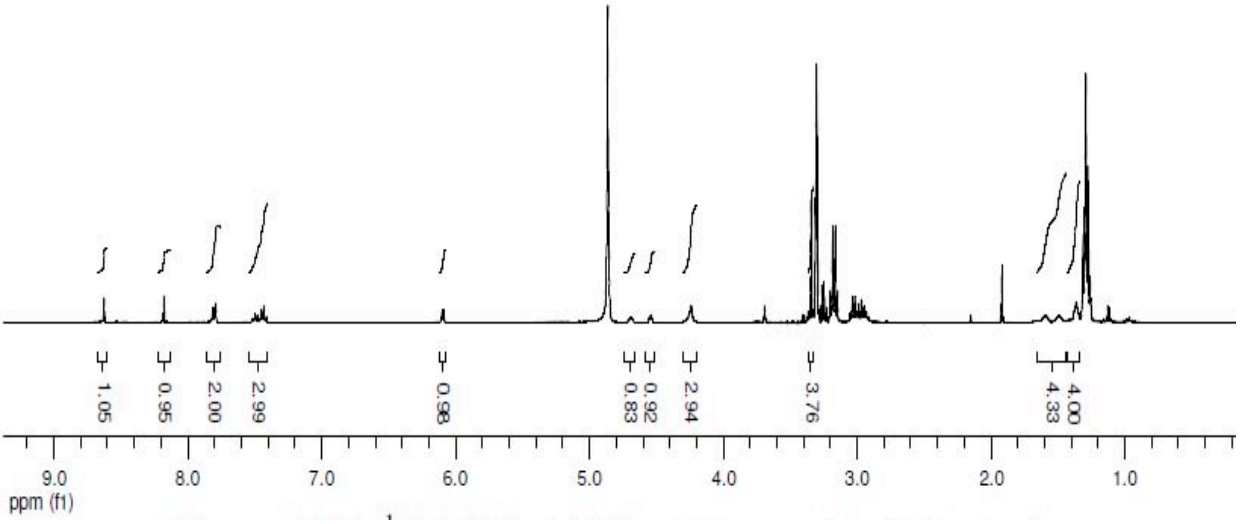

Figure S31: ^{1}H NMR of ATP-γ-N-benzoyl-1, 6-diaminohexane **6e**

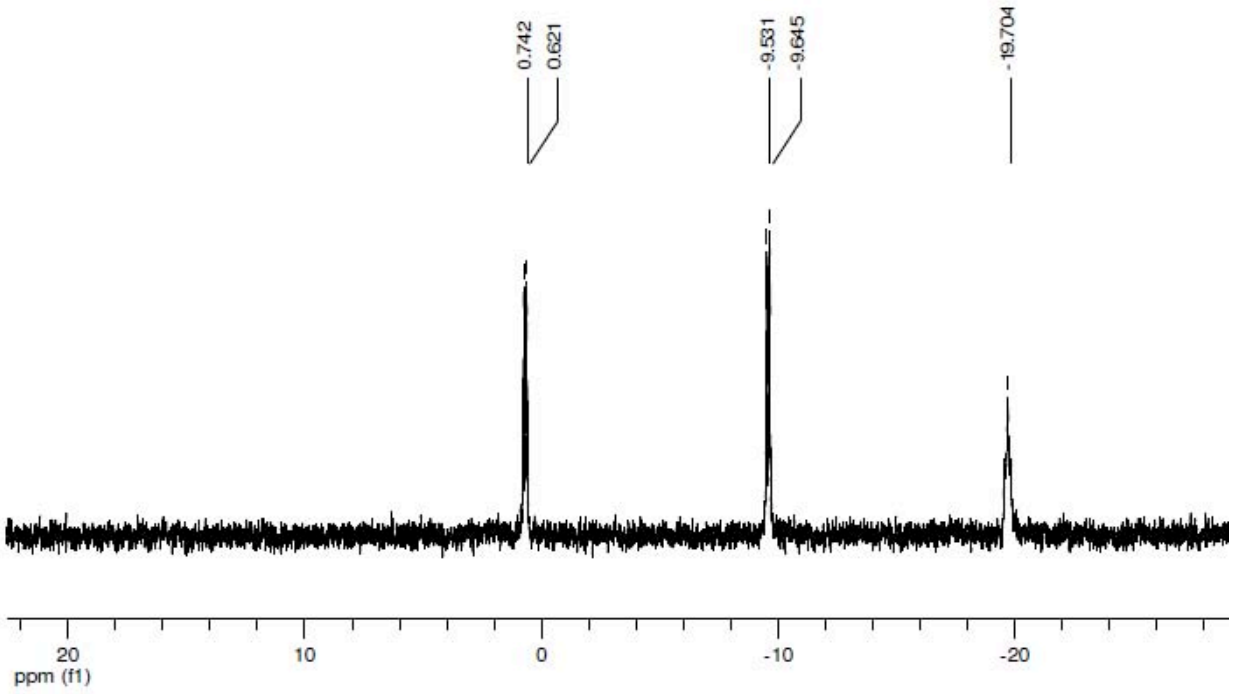

Figure S32: ^{31}P NMR of ATP-γ-N-benzoyl-1, 6-diaminohexane **6e**

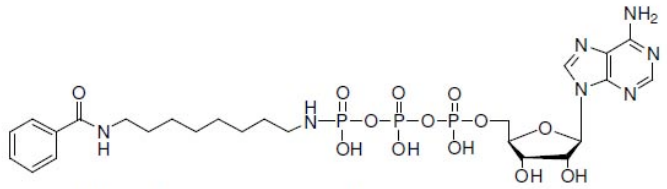

ATP-γ-N-benzoyl-1,8 diaminooctane **6f**

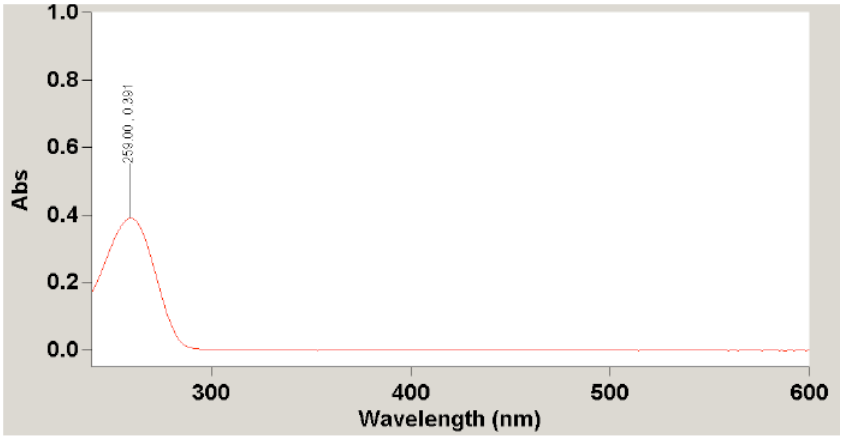

Figure S33: UV of ATP-γ-N-benzoyl-1, 8 diaminooctane **6f**

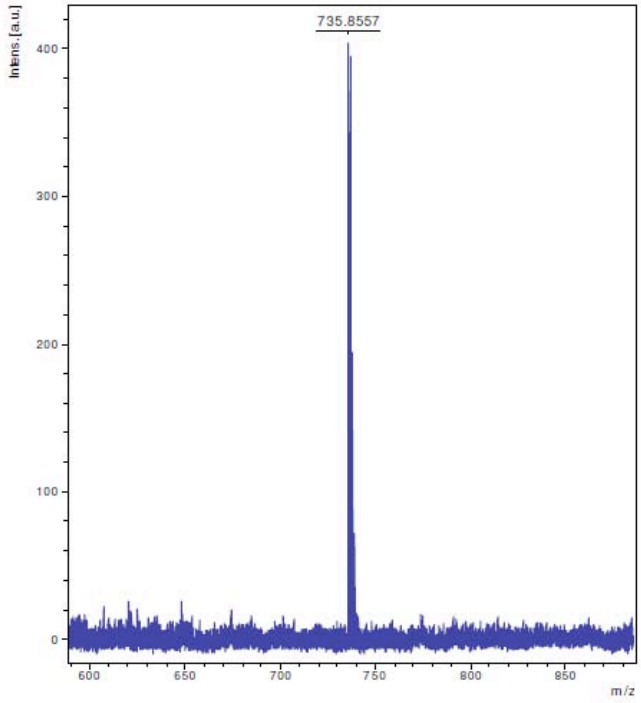

Figure S34: MALDI-TOF of ATP-γ-N-benzoyl-1, 8 diaminooctane **6f**

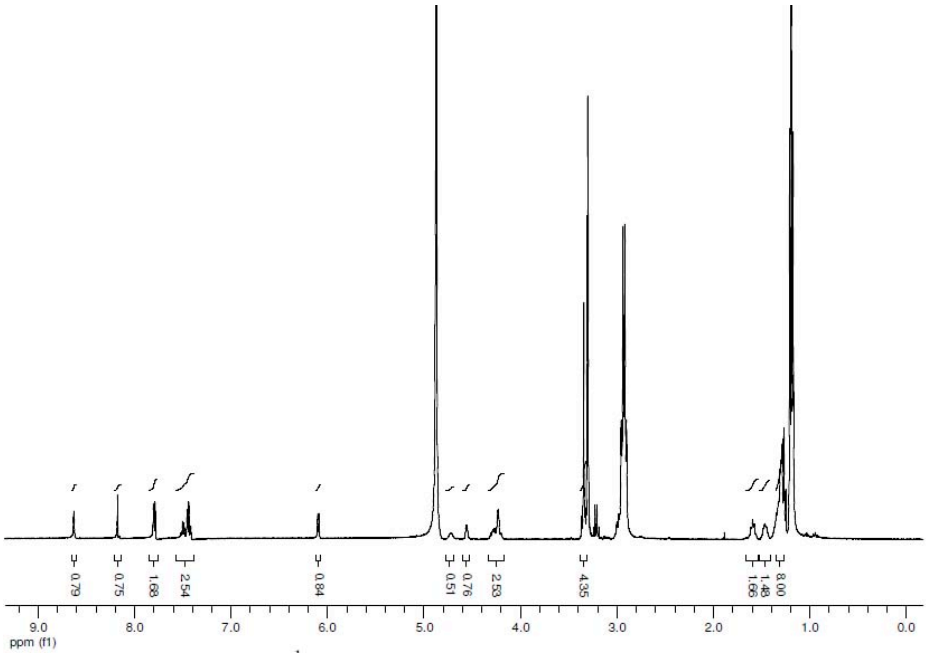

Figure S35: ^{1}H NMR of ATP-γ-N-benzoyl-1, 8 diaminooctane **6f**

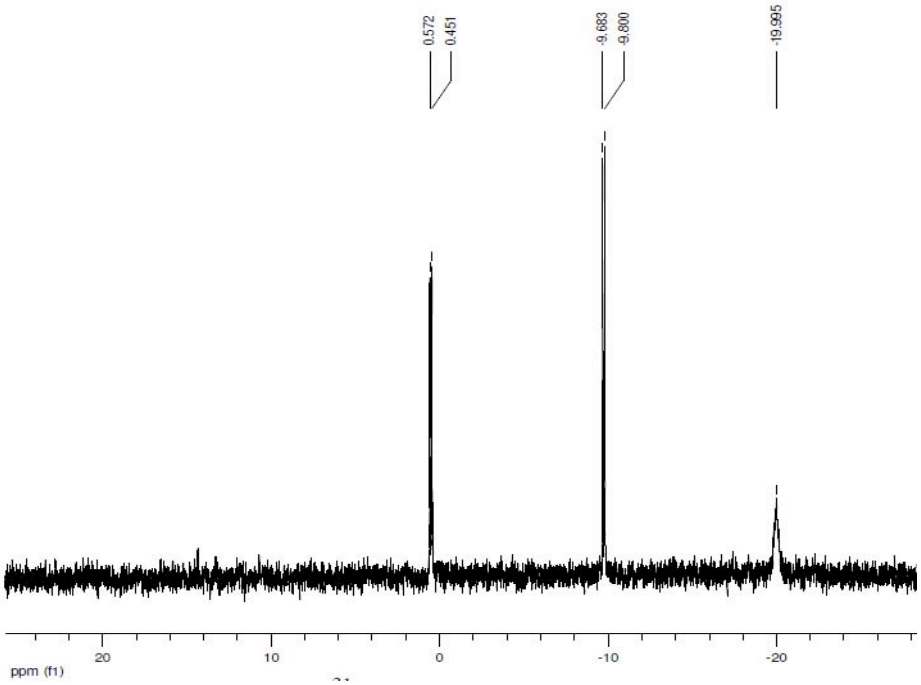

Figure S36: 31P NMR of ATP-γ-N-benzoyl-1, 8 diaminooctane **6f**

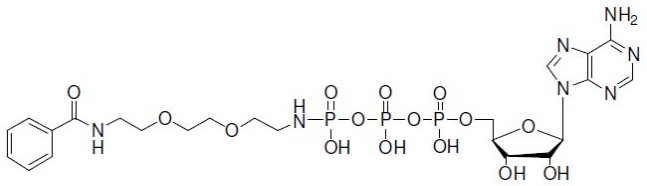

ATP-γ- N-benzoyl-2, 2’-ethylenedioxy bis-(ethylamine) **9b**

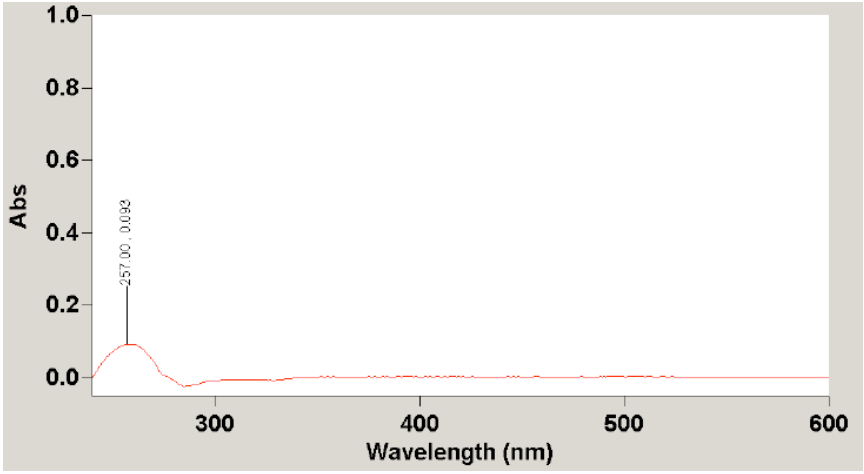

Figure S37: UV of ATP-γ- N-benzoyl-2, 2’-ethylenedioxy bis-(ethylamine) **9b**

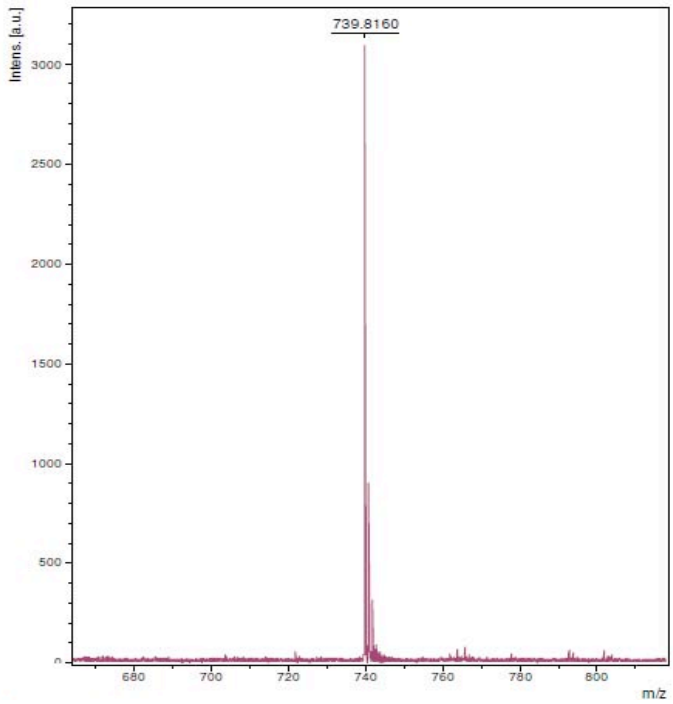

Figure S38: MALDI-TOF of ATP-γ- N-benzoyl-2, 2’-ethylenedioxy bis-(ethylamine) **9b**

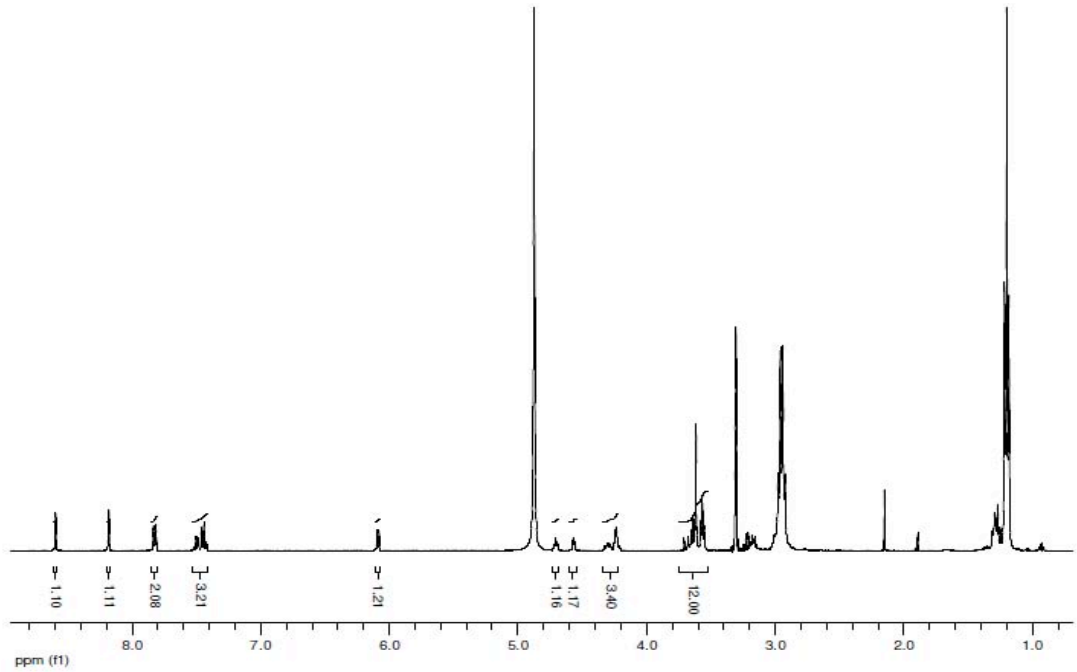

Figure S39: ^{1}H NMR of ATP-γ- N-benzoyl-2, 2'-ethylenedioxy bis-(ethylamine) **9b**

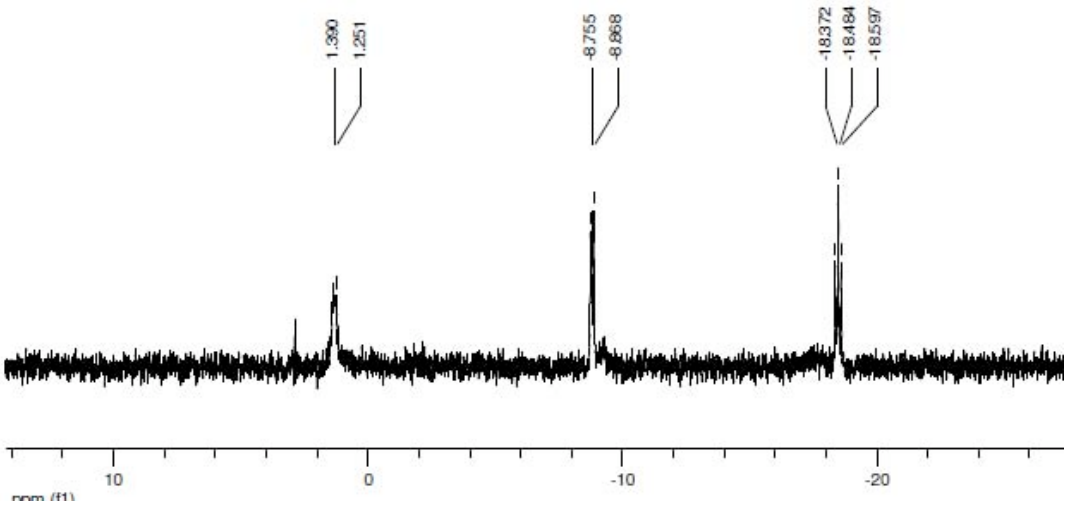

Figure S40: ^{31}PNMR of ATP-γ- N-benzoyl-2, 2'-ethylenedioxy bis-(ethylamine) **9b**

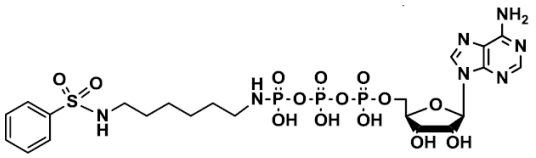

ATP-γ-N-benzenesulfonyl-1,6-diaminohexane **13**

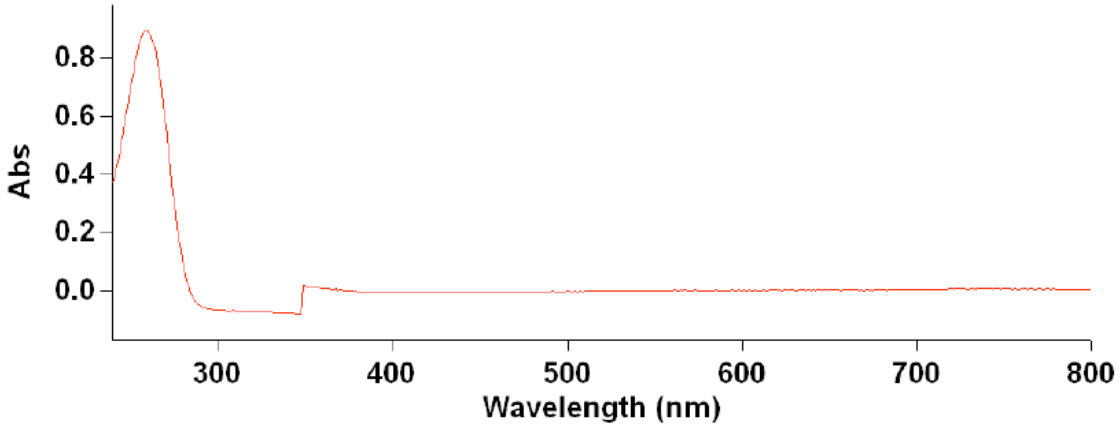

Figure S41: UV of ATP-γ-N- benzenesulfonyl-1, 6-diaminohexane **13**

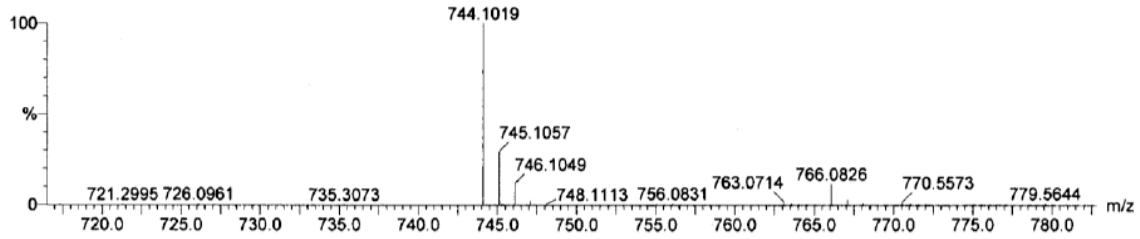

Minimum:				-1.5			
Maximum:		5.0	8.0	50.0			
Mass	Calc. Mass	mDa	PPM	DBE	i-FIT	i-FIT (Norm)	Formula
744.1019	744.1022	-0.3	-0.4	7.5	120.5	0.4	C24 H38 N O16 23Na S P3
	744.1019	0.0	0.0	11.5	121.1	1.1	C22 H33 N7 O14 S P3

Figure S42: HRMS of ATP-γ-N- benzenesulfonyl-1, 6-diaminohexane **13**

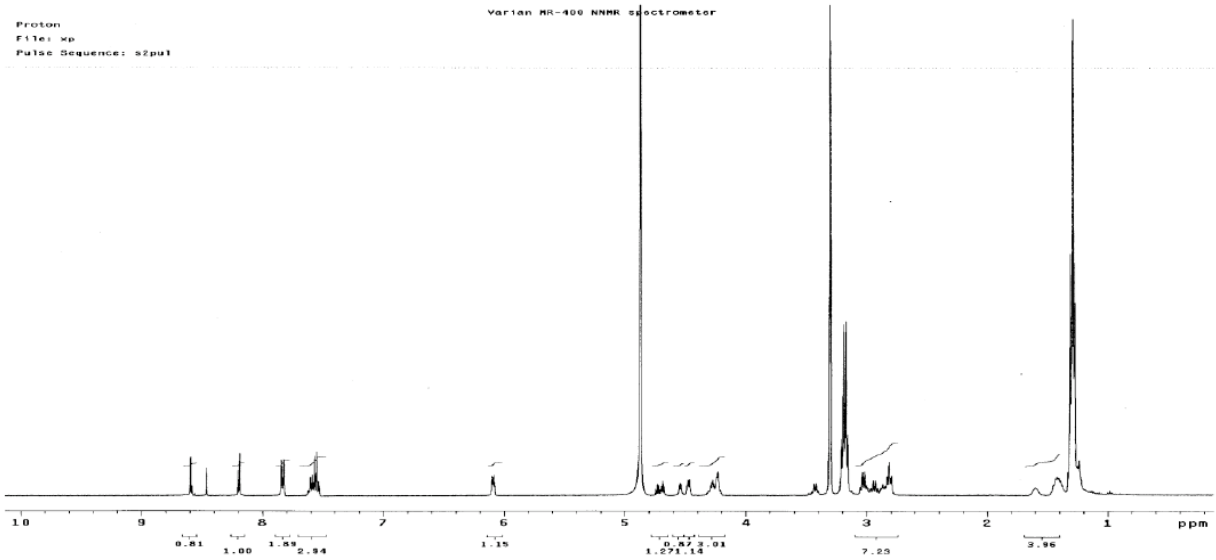

Figure S43: ^{1}H NMR of ATP-γ-N- benzenesulfonyl-1, 6-diaminohexane **13**

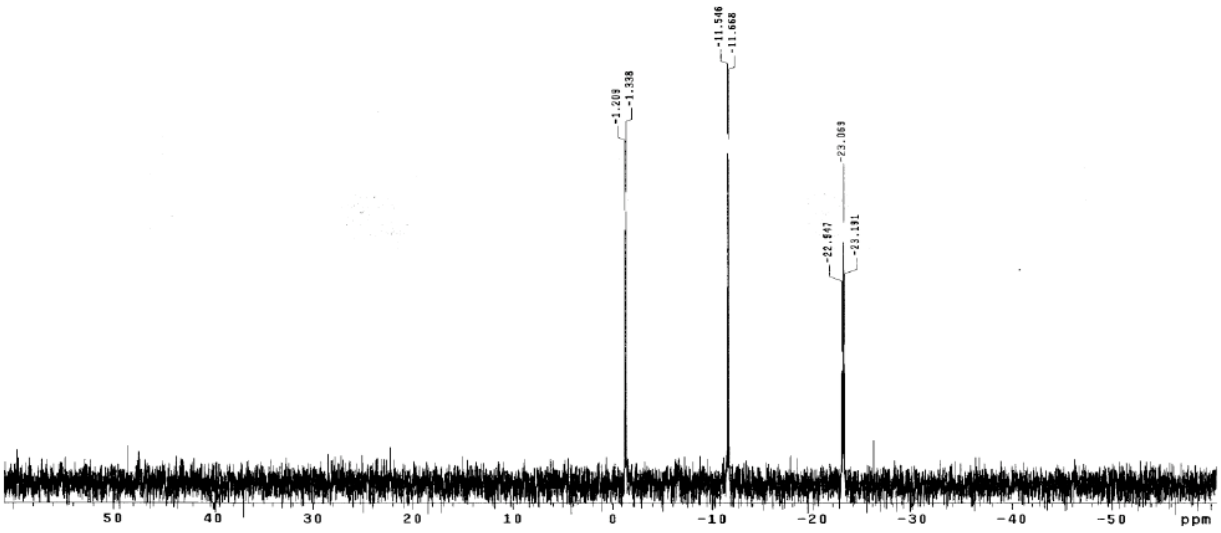

Figure S44: ^{31}P NMR of ATP-γ-N- benzenesulfonyl-1, 6-diaminohexane **13**

IV. Quantitative mass spectrometric (QMS) analysis of kinase activity

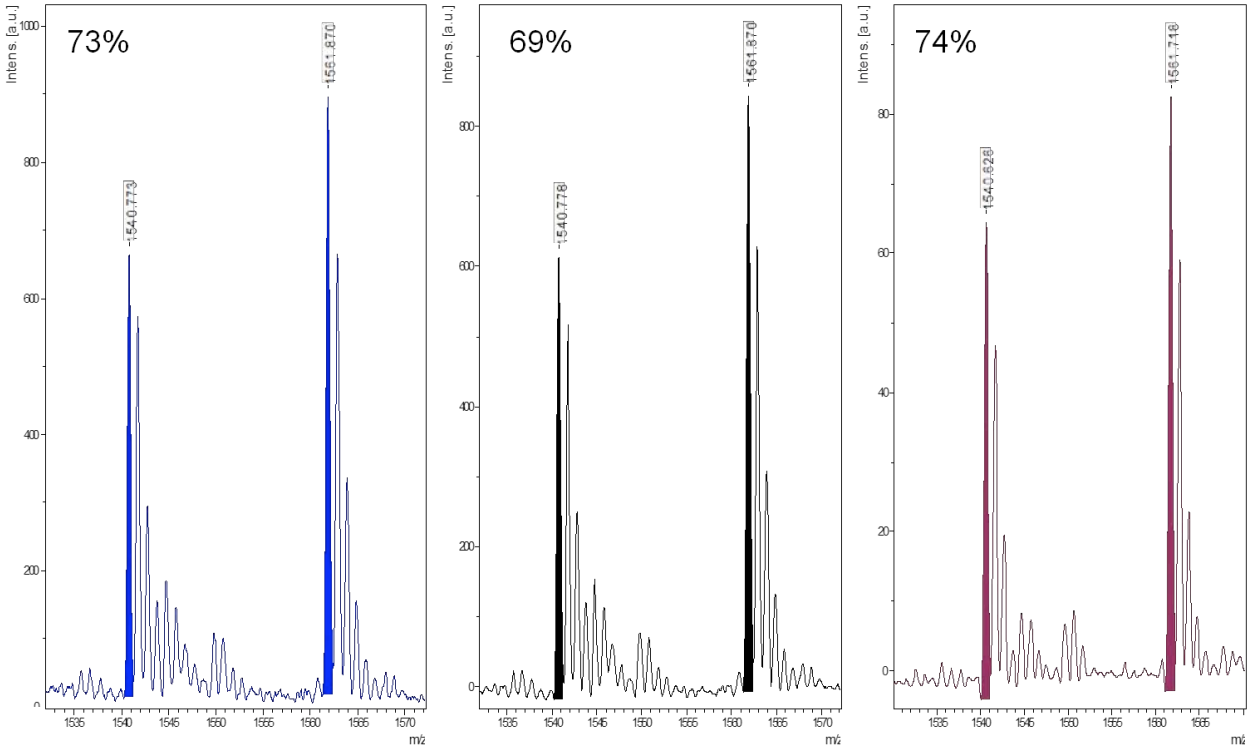

m/z	Area
1540.773	299
1561.870	410

m/z	Area
1540.778	266
1561.870	386

m/z	Area
1540.626	32
1561.718	43

Figure S45: QMS analysis for ATP-γ-N-acetyl-1,2-diaminoethane **6a** with CK2 and the CK2 substrate peptide. The peak at ~1540 corresponds to the hepta-methylated phosphopeptide ester after phosphorylation with **6a** and acid-mediated phosphoramidate bond cleavage. The ~1561 m/z corresponds to the deuterated phosphopeptide esters from the reaction with ATP. The percent conversion in each experiment is calculated from the areas under each peak and is shown in each panel. The percent conversion reported in the Table 2 of the manuscript is the average of these three independent trials (72%).

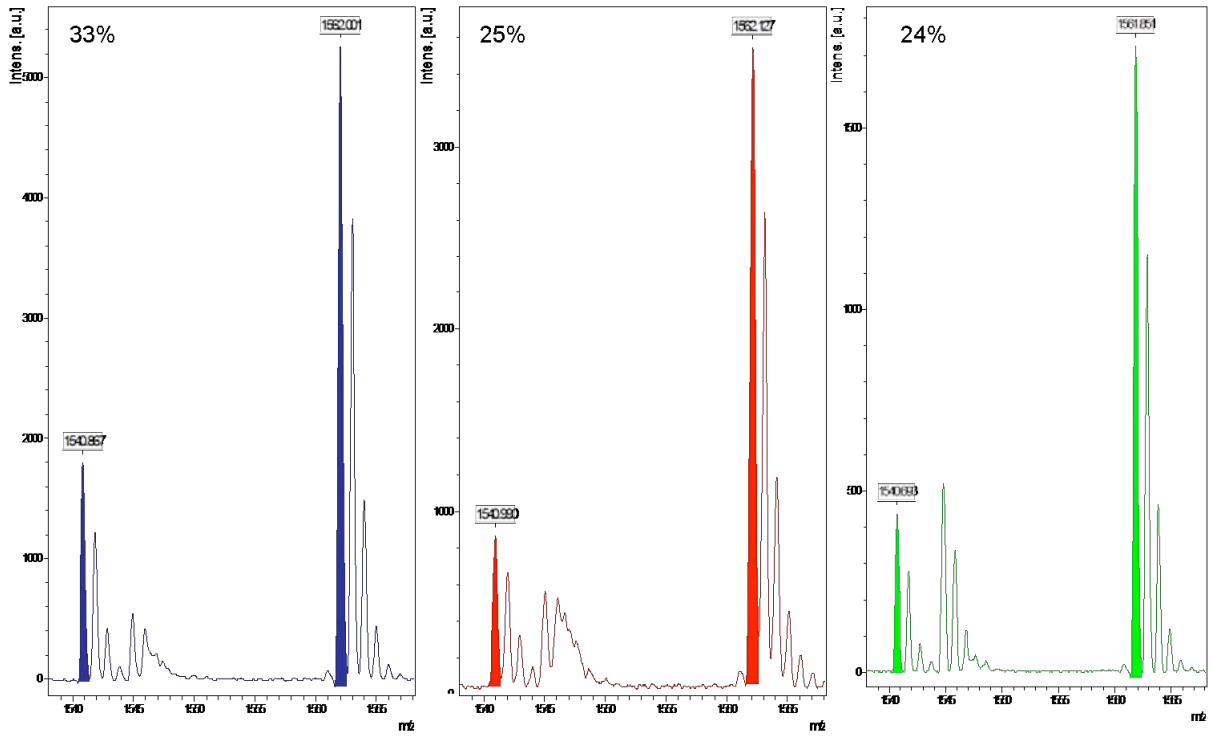

Figure S46: QMS analysis for ATP-γ-N-acetyl-1, 4-diaminobutane **6b** with CK2 wi and the CK2 substrate peptide. The peak at ~1540 corresponds to the hepta-methylated phosphopeptide ester after phosphorylation with **6b** and acid-mediated phosphoramidate bond cleavage. The ~1561 m/z corresponds to the hepta-methylated, deuterated phosphopeptide ester from the reaction with ATP. The percent conversion in each experiment is calculated from the areas under each peak and is shown in each panel. The percent conversion reported in the Table 2 of the manuscript is the average of these three independent trials (27%).

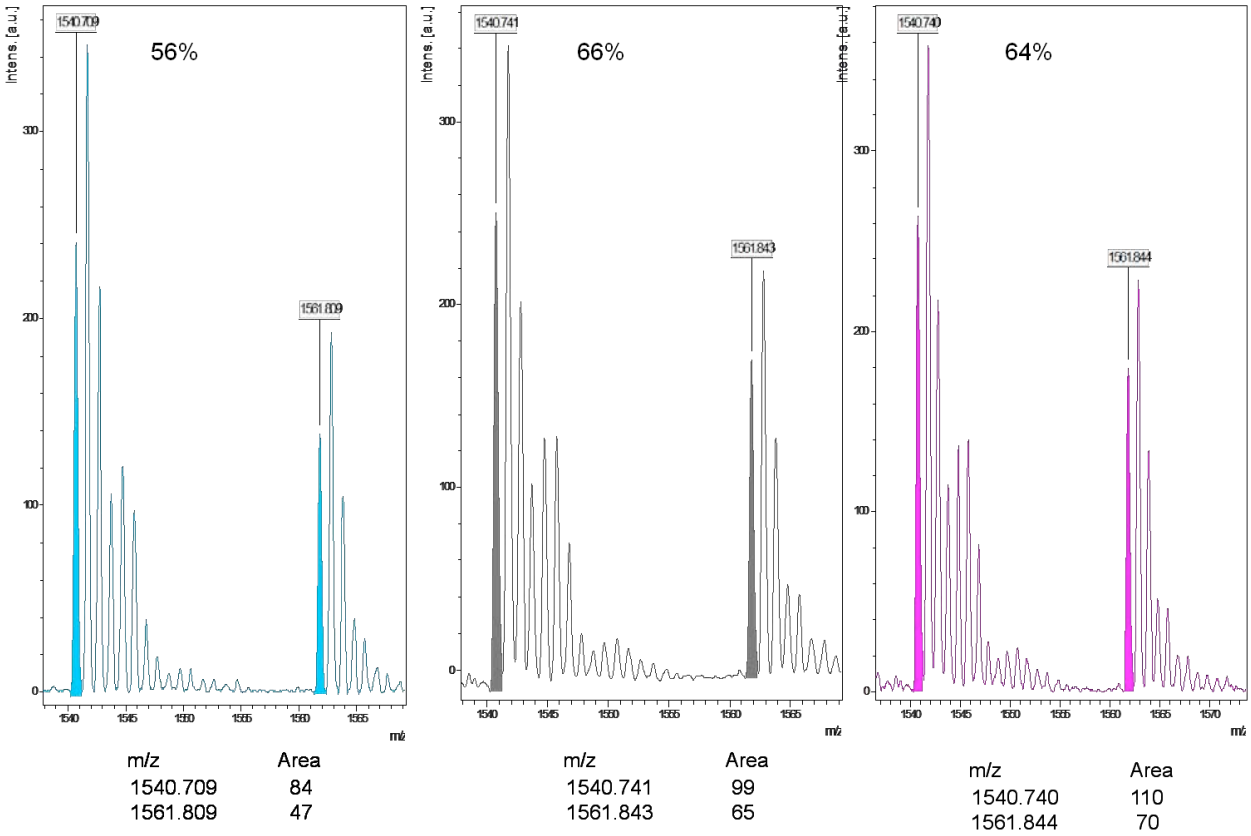

Figure S47: QMS analysis for ATP-γ-N-acetyl-2, 2'-ethylenedioxy bis-(ethylamine) **9a** with CK2 with CK2 and the CK2 substrate peptide. The peak at ~1540 corresponds to the hepta-methylated, deuterated phosphopeptide ester from the reaction with ATP. The ~1561 m/z corresponds to the hepta-methylated phosphopeptide ester after phosphorylation with **9a** and acid-mediated phosphoramidate bond cleavage. The percent conversion in each experiment is calculated from the areas under each peak and is shown in each panel. The percent conversion reported in the Table 2 is the average of these three independent trials (62%).

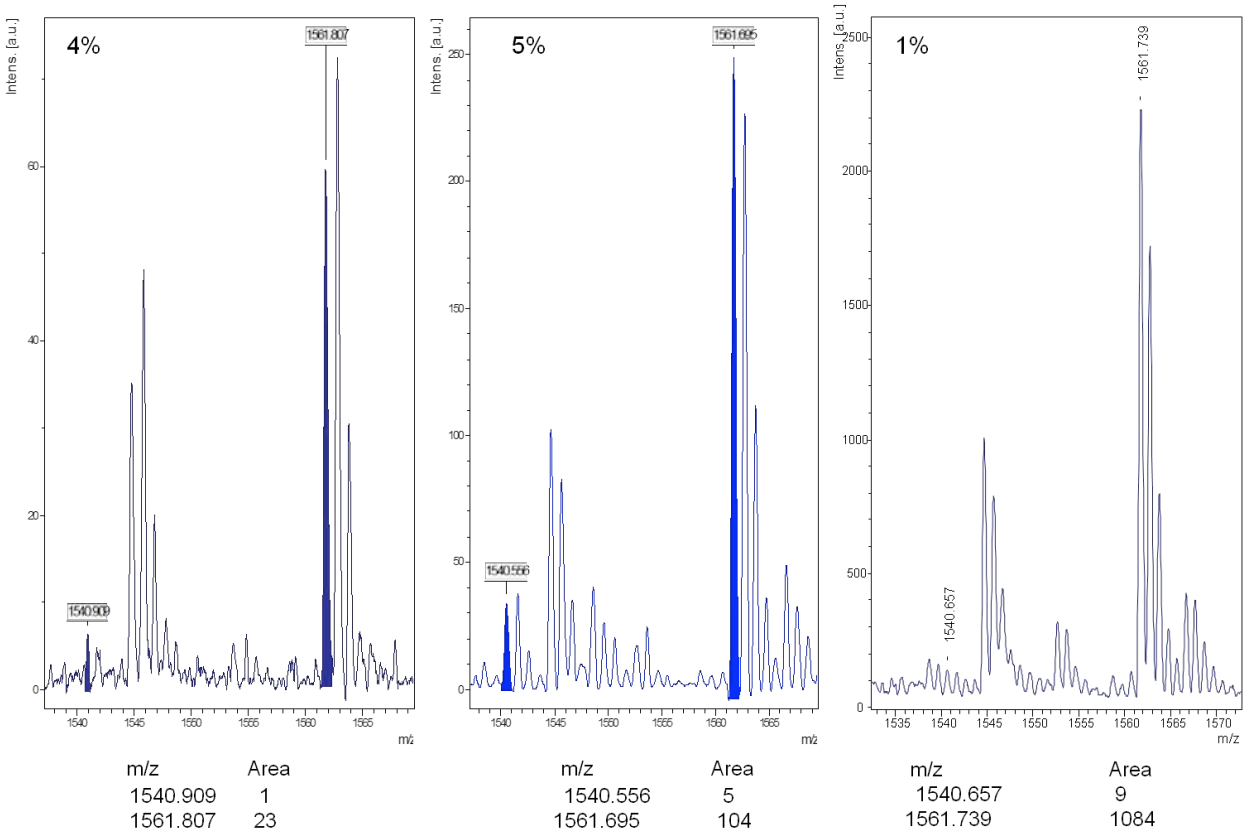

m/z	Area
1540.909	1
1561.807	23

m/z	Area
1540.556	5
1561.695	104

m/z	Area
1540.657	9
1561.739	1084

Figure S48: QMS analysis for ATP-γ-aniline **2a** with CK2 and the CK2 substrate peptide. The peak at ~1540 corresponds to the hepta-methylated phosphopeptide ester after phosphorylation with **2a** and acid-mediated phosphoramidate bond cleavage. The ~1561 m/z corresponds to the hepta-methylated, deuterated phosphopeptide ester from the reaction with ATP. The percent conversion in each experiment is calculated from the areas under each peak and is shown in each panel. The percent conversion reported in Table 3 of the manuscript is the average of these three independent trials (<5%).

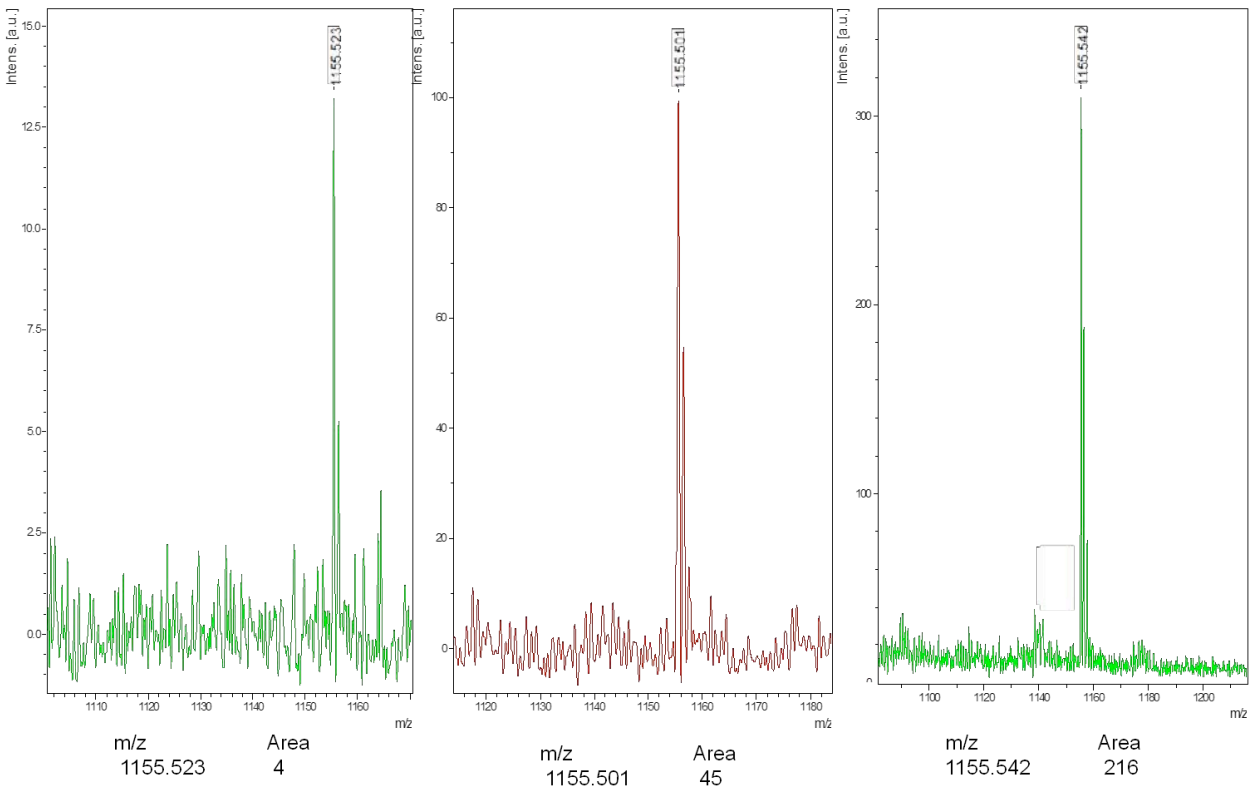

Figure S49: QMS analysis for ATP-γ-aniline **2a** with PKA and the PKA substrate peptide. No peak at ~1152 is observed corresponding to the mono-methylated phosphopeptide ester after phosphorylation with **2a** and acid-mediated phosphoramidate bond cleavage, indicating no conversion in any trial. The ~1555 m/z corresponds to the hepta-methylated, deuterated phosphopeptide ester from the reaction with ATP. Because no conversion is observed in the trials, >5% is reported in Table 3 of the manuscript.

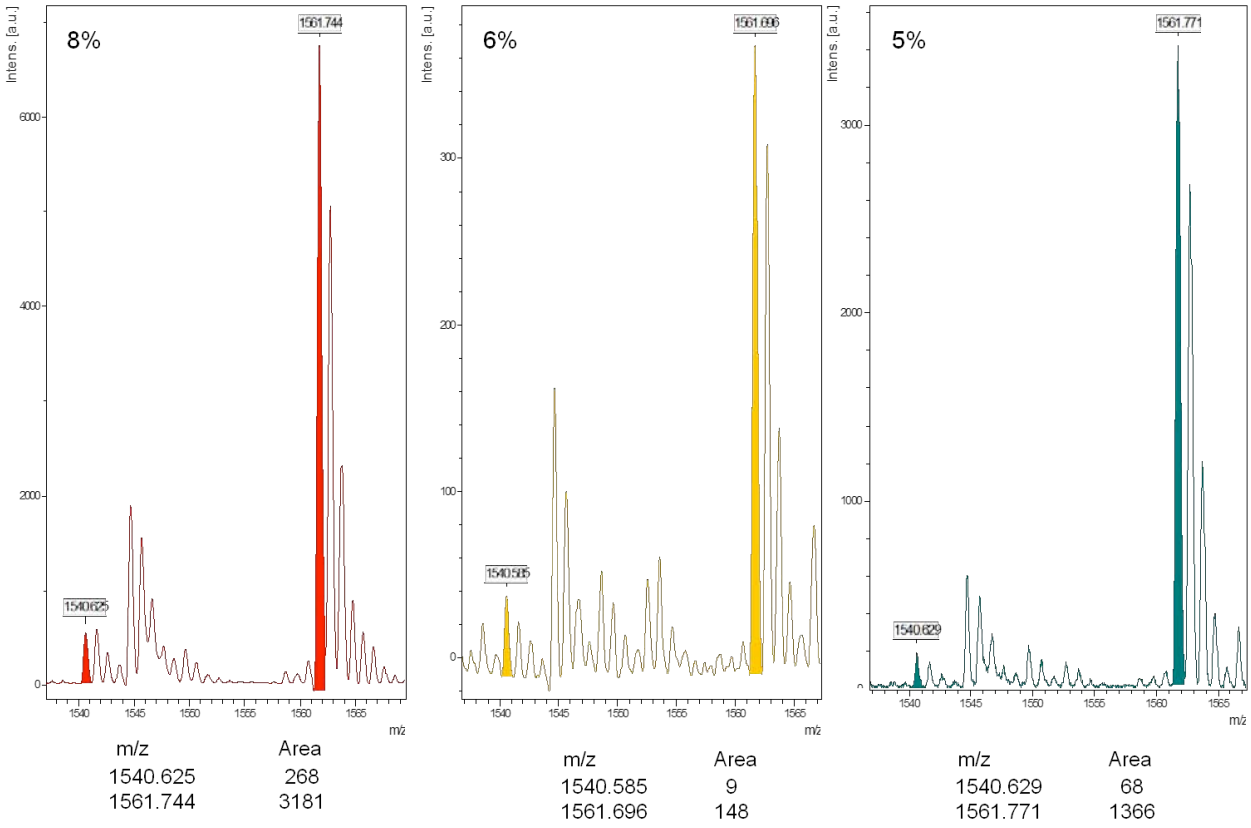

Figure S50: QMS analysis for ATP-γ-benzylamine **2b** with CK2 and the CK2 substrate peptide. The peak at ~1540 corresponds to the hepta-methylated phosphopeptide ester after phosphorylation with **2b** and acid-mediated phosphoramidate bond cleavage. The ~1561 m/z corresponds to the hepta-methylated, deuterated phosphopeptide ester from the reaction with ATP. The percent conversion in each experiment is calculated from the areas under each peak and is shown in each panel. The percent conversion reported in Table 3 of the manuscript is the average of these three independent trials (6%).

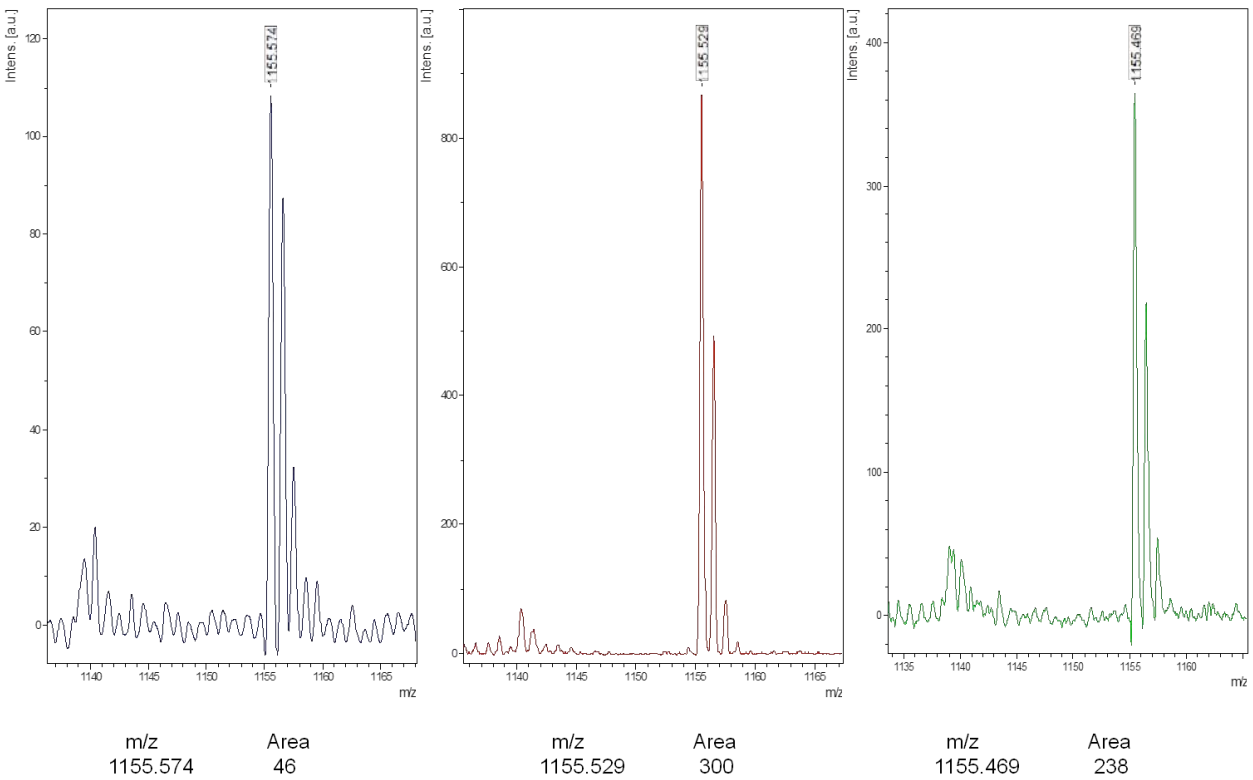

m/z	Area
1155.574	46

m/z	Area
1155.529	300

m/z	Area
1155.469	238

Figure S51: QMS analysis for ATP-γ-benzylamine **2b** with PKA and the PKA substrate peptide. No peak at ~1152 corresponding to the mono-methylated phosphopeptide ester after phosphorylation with **2b** and acid-mediated phosphoramidate bond cleavage is observed, indicating no conversion in any trial. The ~1155 m/z corresponds to the mono-methylated, deuterated phosphopeptide ester from the reaction with ATP. Because no conversion is observed, >5% is reported in Table 3 of the manuscript.

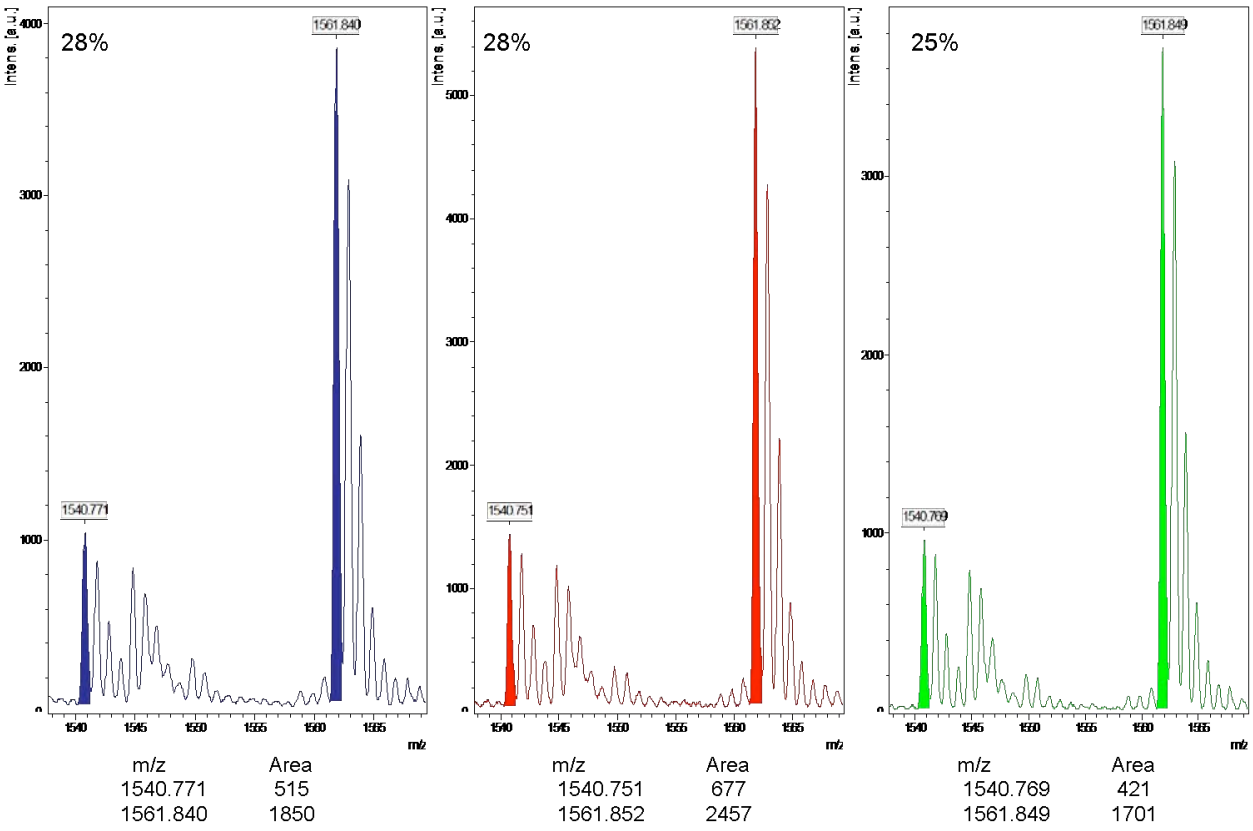

Figure S52: QMS analysis for ATP-γ-N-benzoyl-1,2-diaminoethane **6c** with CK2 and the CK2 substrate peptide. The peak at ~1540 corresponds to the hepta-methylated phosphopeptide ester after phosphorylation with **6c** and acid-mediated phosphoramidate bond cleavage. The ~1561 m/z corresponds to the hepta-methylated, deuterated phosphopeptide ester from the reaction with ATP. The percent conversion in each experiment is calculated from the areas under each peak. and is shown in each panel. The percentage conversion reported in Table 3 of the manuscript is the average of these three independent trials (27%).

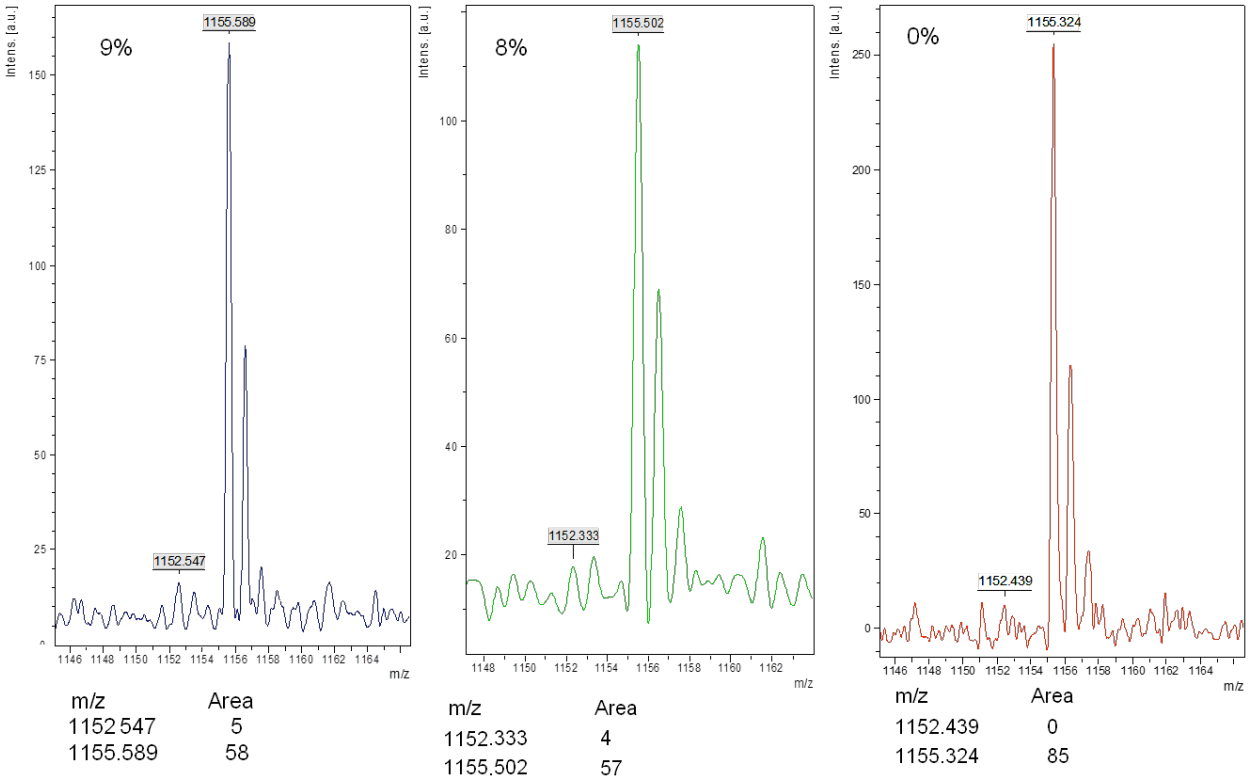

Figure S53: QMS analysis for ATP-γ-N-benzoyl-1,2-diaminoethane **6c** with PKA and the PKA substrate peptide. The peak at ~1152 corresponds to the mono-methylated phosphopeptide ester after phosphorylation with **6c** and acid-mediated phosphoramidate bond cleavage. The ~1155 m/z corresponds to the mono-methylated, deuterated phosphopeptide ester from the reaction with ATP. The percent conversion in each experiment is calculated from the areas under each peak and is shown in each panel. The percent conversion reported in the Table 3 of the manuscript is the average of these three independent trials (5%).

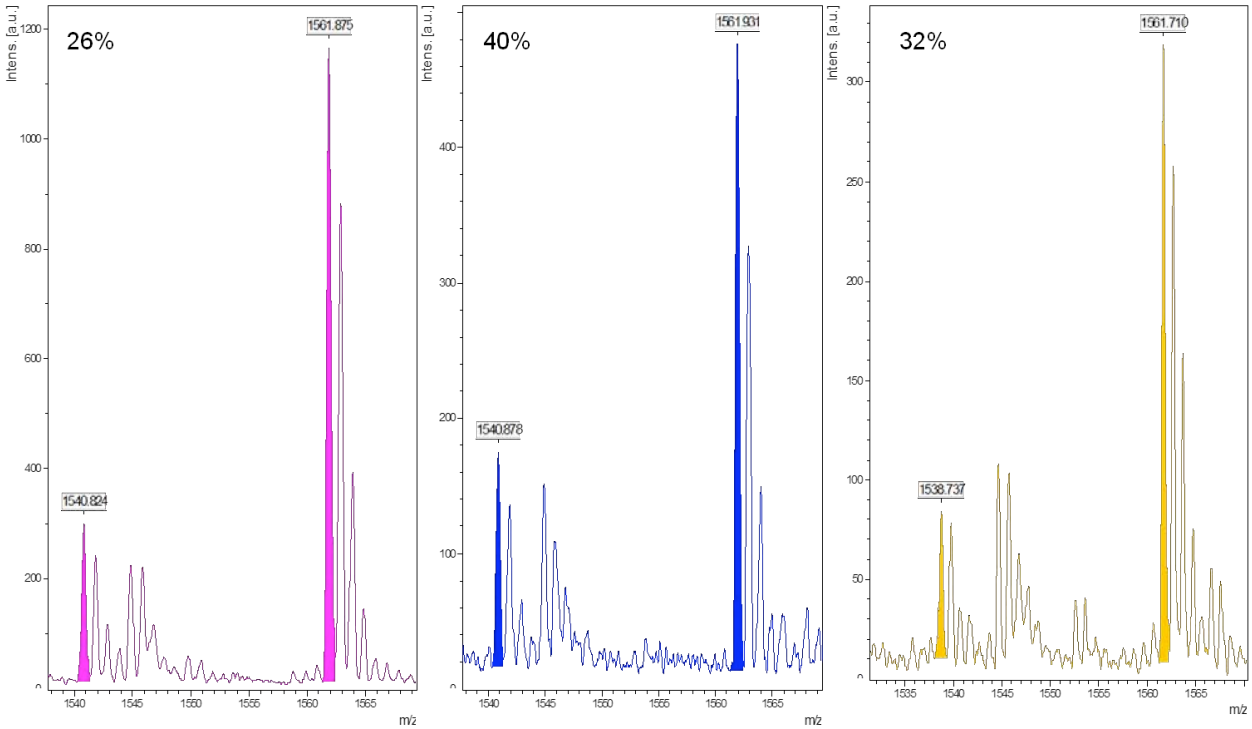

m/z	Area
1540.824	142
1561.875	547

m/z	Area
1540.878	85
1561.931	215

m/z	Area
1538.737	45
1561.710	141

Figure S54: QMS analysis for ATP-γ-N-benzoyl-1,4-diaminobutane **6d** with CK2 and the CK2 substrate peptide. The peak at ~1540 corresponds to the hepta-methylated phosphopeptide ester after phosphorylation with **6d** and acid-mediated phosphoramidate bond cleavage. The ~1561 m/z corresponds to the hepta-methylated, deuterated phosphopeptide ester from the reaction with ATP. The percent conversion in each experiment is calculated from the areas under each peak and is shown in each panel. The percent conversion reported in Table 3 of the manuscript is the average of these three independent trials (33%).

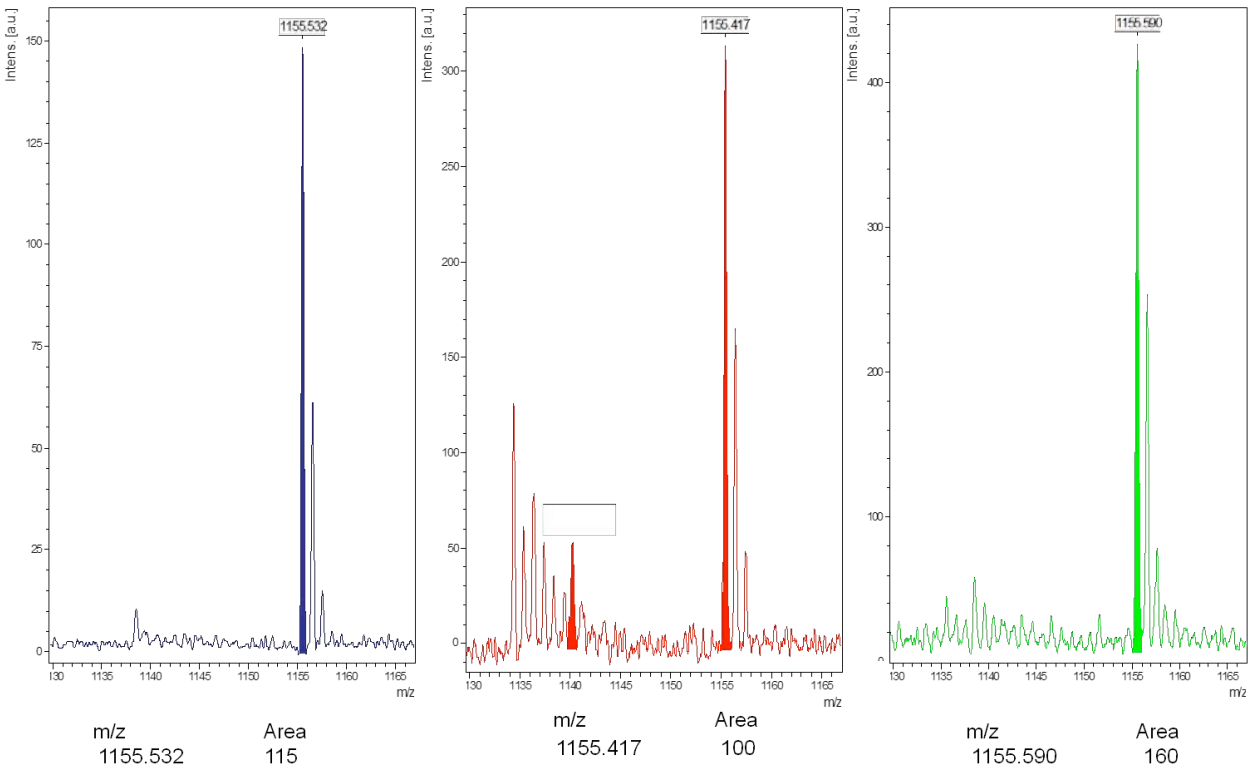

Figure S55: QMS analysis for ATP-γ-N-benzoyl-1,4-diaminobutane **6d** with PKA and the PKA substrate peptide. No peak is observed at ~1152 corresponding to the mono-methylated phosphopeptide ester after phosphorylation with **6d** and acid-mediated phosphoramidate bond cleavage, indicating no conversion in any trial. The ~1155 m/z corresponds to the mono-methylated, deuterated phosphopeptide ester from the reaction with ATP. Because no conversion is observed, >5% is reported in Table 3 of the manuscript.

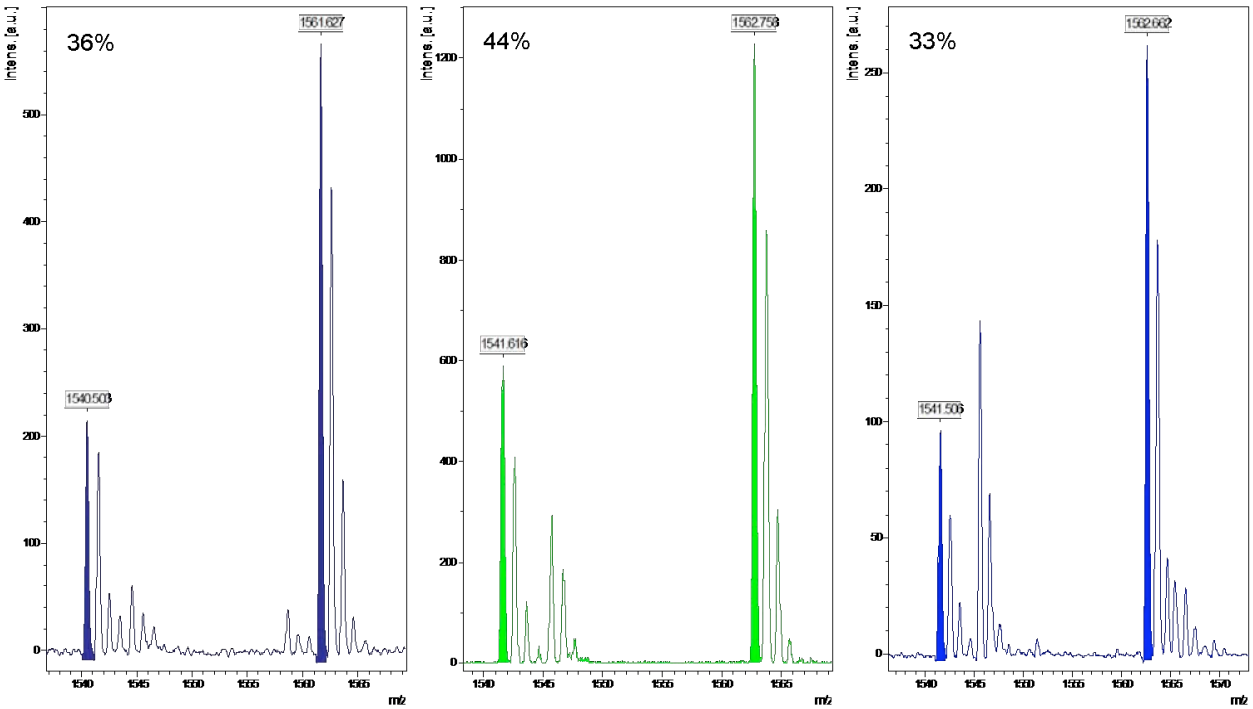

m/z	Area
1540.503	68
1561.627	188

m/z	Area
1541.616	194
1562.758	444

m/z	Area
1541.506	33
1562.662	100

Figure S56: QMS analysis for ATP-γ-N-benzoyl-1, 8-diaminooctane **6f** with CK2 and the CK2 substrate peptide. The peak at ~1540 corresponds to the hepta-methylated phosphopeptide ester after phosphorylation with **6f** and acid-mediated phosphoramidate bond cleavage. The ~1561 m/z corresponds to the hepta-methylated, deuterated phosphopeptide ester from the reaction with ATP. The percent conversion in each experiment is calculated from the areas under each peak and is shown in each panel. The percent conversion reported in Table 3 of the manuscript is the average of these three independent trials (38%).

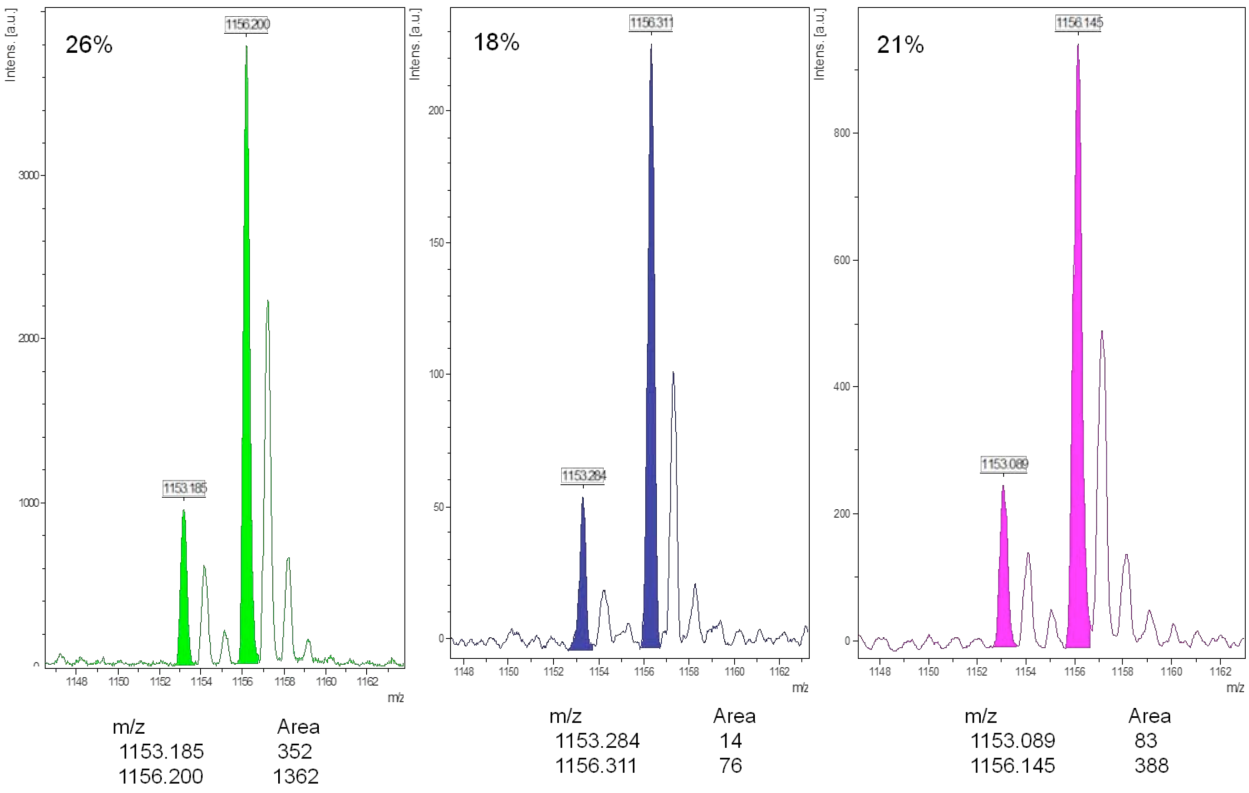

Figure S57: QMS analysis for ATP-γ-N-benzoyl-1,8-diaminooctane **6f** with PKA and the PKA substrate peptide. The peak at ~1153 corresponds to the mono-methylated phosphopeptide ester after phosphorylation with **6f** and acid-mediated phosphoramidate bond cleavage. The ~1156 m/z corresponds to the mono-methylated, deuterated phosphopeptide ester from the reaction with ATP. The percent conversion in each experiment is calculated from the areas under each peak and is shown in each panel. The percent conversion reported in the Table 3 of the manuscript is the average of these three independent trials (22%).

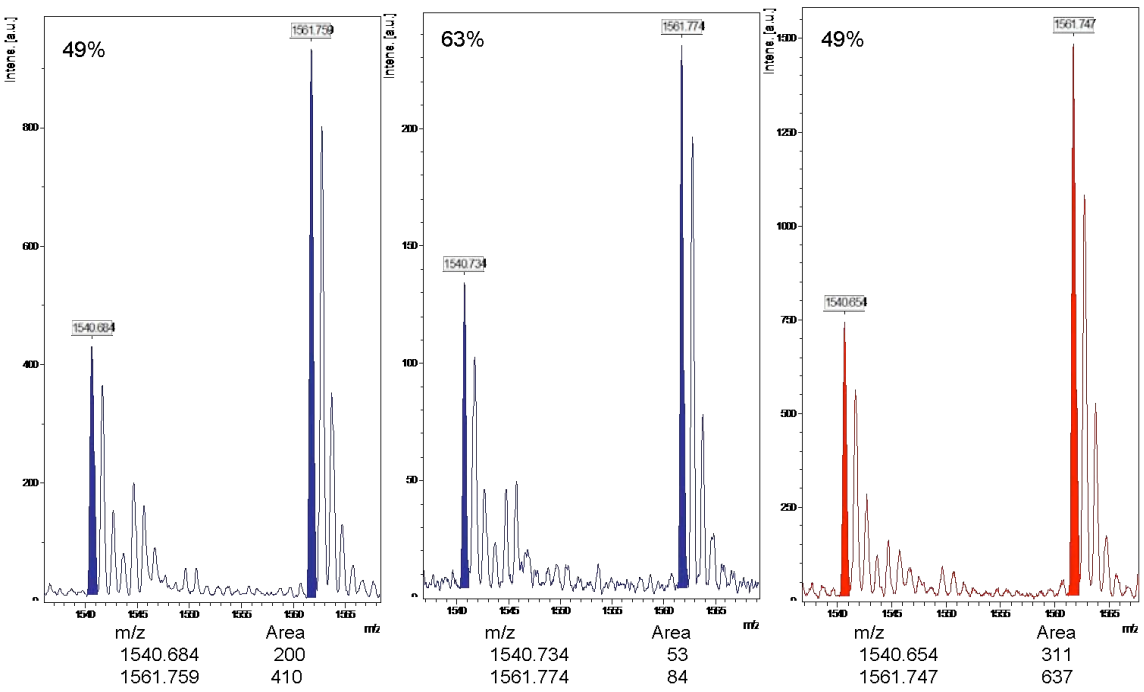

Figure S58: QMS analysis for ATP-γ- N-benzoyl-2,2'-ethylenedioxy bis-(ethylamine) **9b** with CK2 and the CK2 substrate peptide. The peak at ~1540 corresponds to the hepta-methylated phosphopeptide ester after phosphorylation with **9b** and acid-mediated phosphoramidate bond cleavage. The ~1561 m/z corresponds to the hepta-methylated, deuterated phosphopeptide ester from the reaction with ATP. The percent conversion in each experiment is calculated from the areas under each peak and is shown in each panel. The percent conversion reported in Table 3 is the average of these three independent trials (54%).

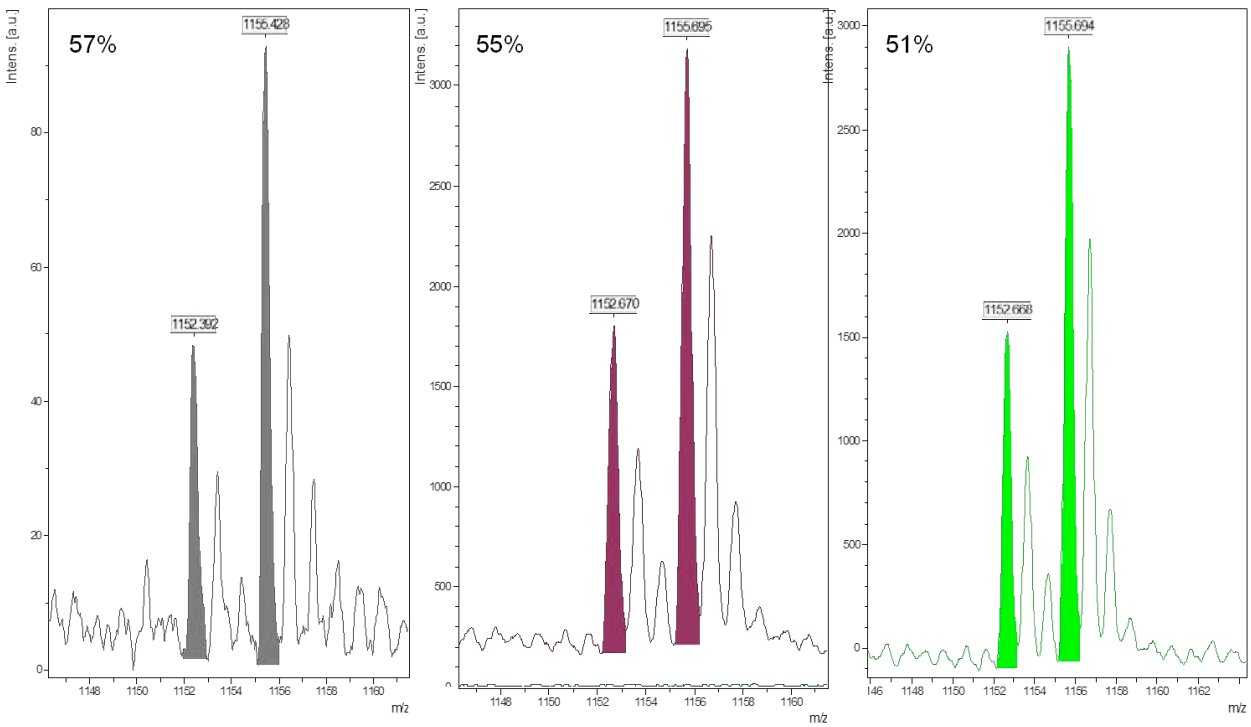

m/z	Area
1152.392	20
1155.428	35

m/z	Area
1152.670	17
1155.695	31

m/z	Area
1152.668	673
1155.694	1328

Figure S59: QMS analysis for ATP-γ-N-benzoyl-2,2'-ethylenedioxy bis-(ethylamine) **9b** with PKA and the PKA substrate peptide. The peak at ~1153 corresponds to the mono-methylated phosphopeptide ester after phosphorylation with **9b** and acid-mediated phosphoramidate bond cleavage. The ~1156 m/z corresponds to the mono-methylated, deuterated phosphopeptide ester from the reaction with ATP. The percent conversion in each experiment is calculated from the areas under each peak. The percent conversion shown in each panel and reported in Table 3 is the average of these three independent trials (54%).

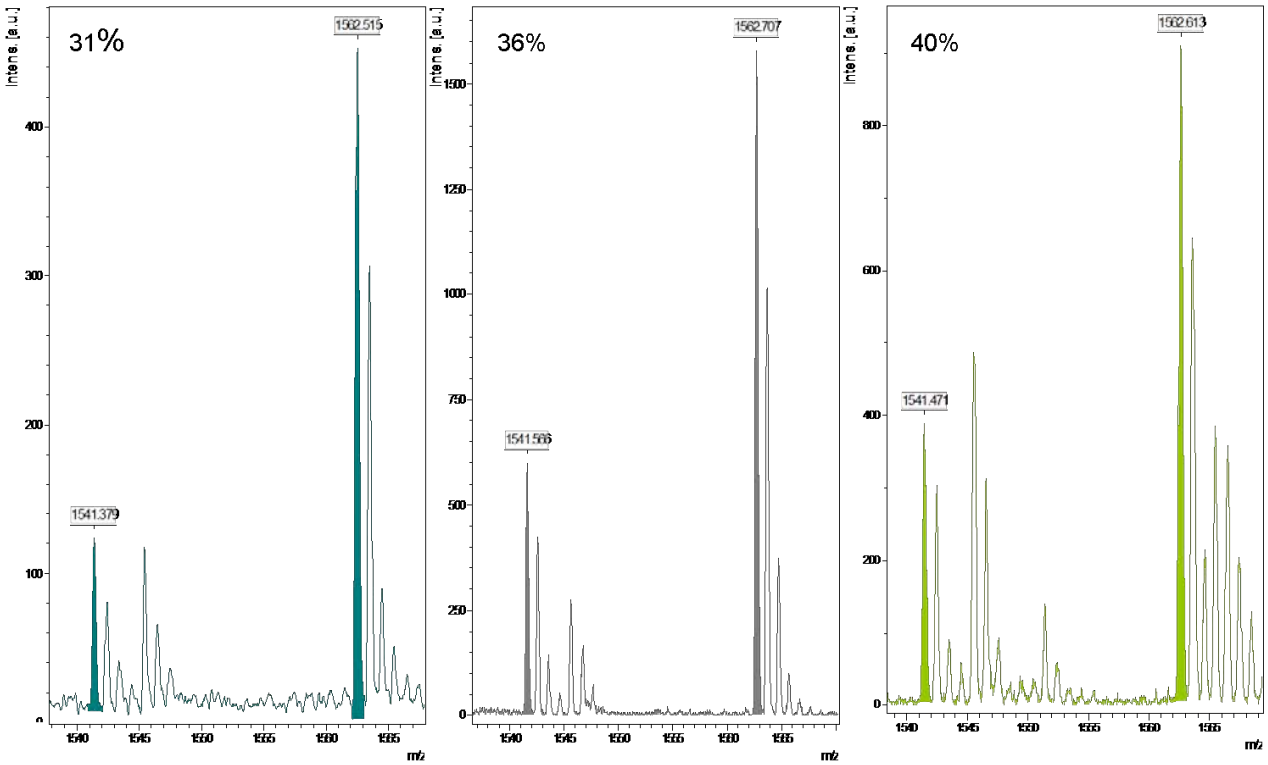

m/z	Area
1541.379	49
1562.515	158

m/z	Area
1541.566	178
1562.707	497

m/z	Area
1541.471	130
1562.613	328

Figure S60: QMS analysis for ATP-γ-N-benzoyl-1, 6-diaminohexane **6e** with CK2 and the CK2 substrate peptide. The peak at ~1541 corresponds to the hepta-methylated phosphopeptide ester after phosphorylation with **6e** and acid-mediated phosphoramidate bond cleavage. The ~1562 m/z corresponds to the hepta-methylated, deuterated phosphopeptide ester from the reaction with ATP. The percent conversion in each experiment is calculated from the areas under each peak and is shown in each panel. The percent conversion reported in Table 4 of the manuscript is the average of these three independent trials (36%).

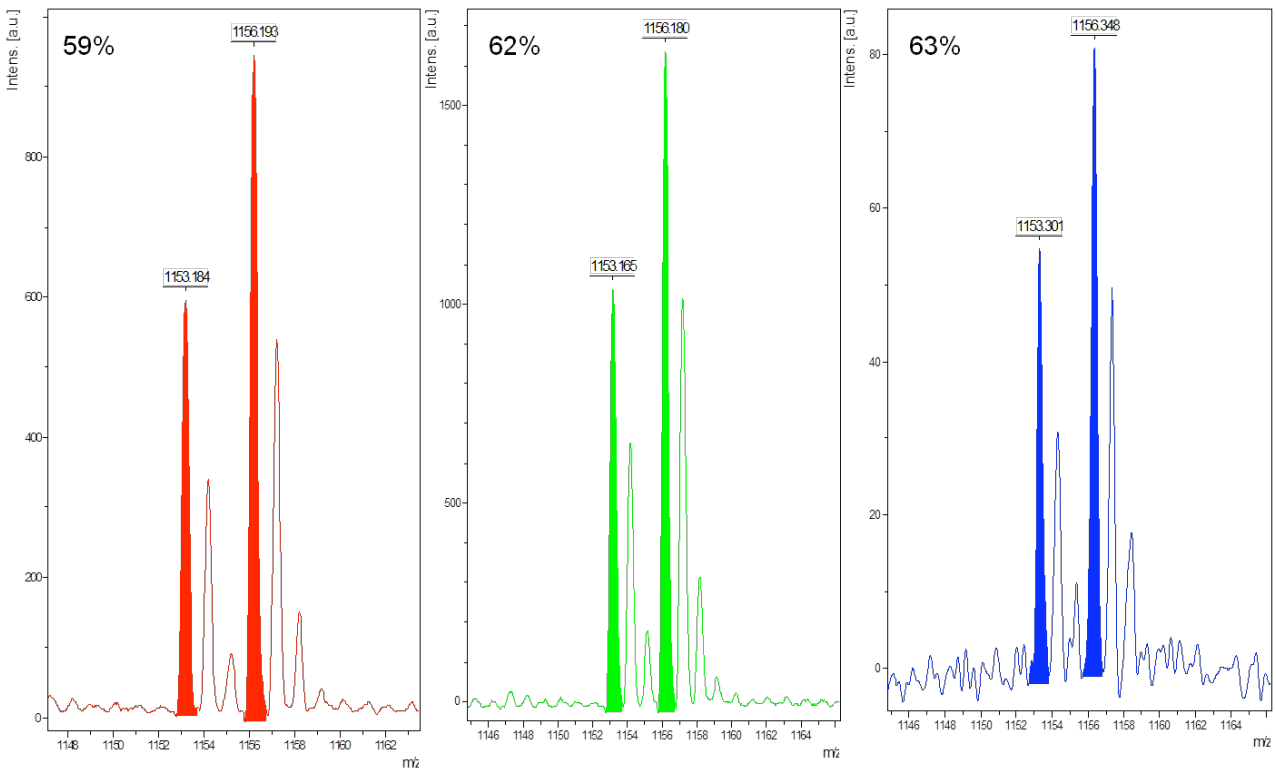

m/z	Area
1153.184	209
1156.193	355

m/z	Area
1153.165	392
1156.180	636

m/z	Area
1153.301	19
1156.348	30

Figure S61: QMS analysis for ATP-γ-N-benzoyl-1, 6-diaminohexane **6e** with PKA and the PKA substrate peptide. The peak at ~1153 corresponds to the mono-methylated phosphopeptide ester after phosphorylation with **6e** and acid-mediated phosphoramidate bond cleavage. The ~1156 m/z corresponds to the mono-methylated, deuterated phosphopeptide ester from the reaction with ATP. The percent conversion in each experiment is calculated from the areas under each peak and is shown in each panel. The percent conversion reported in Table 4 in the manuscript is the average of these three independent trials (61%).

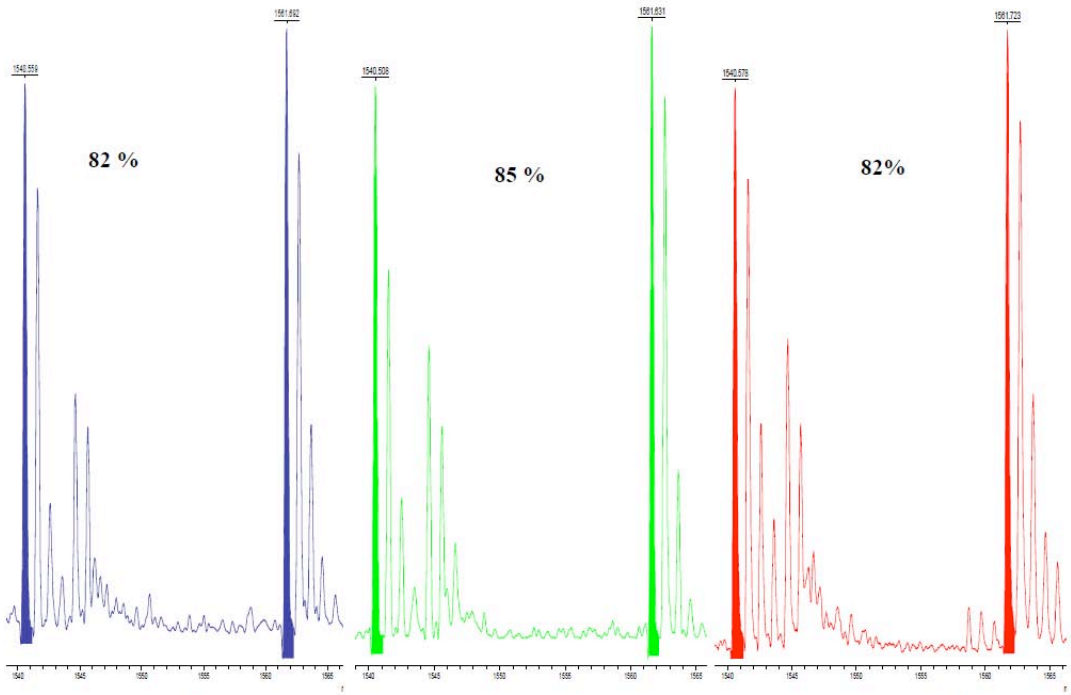

Figure S62: QMS analysis for ATP-γ-N-benzenesulfonyl-1, 6-diaminohexane **13** with CK2 and the CK2 substrate peptide. The peak at ~1540 corresponds to the hepta-methylated phosphopeptide ester after phosphorylation with **13** and acid-mediated phosphoramidate bond cleavage. The ~1561 m/z corresponds to the hepta-methylated, deuterated phosphopeptide ester from the reaction with ATP. The percent conversion in each experiment is calculated from the areas under each peak and is shown in each panel. The percent conversion reported in the Table 2 is the average of these three independent trials.

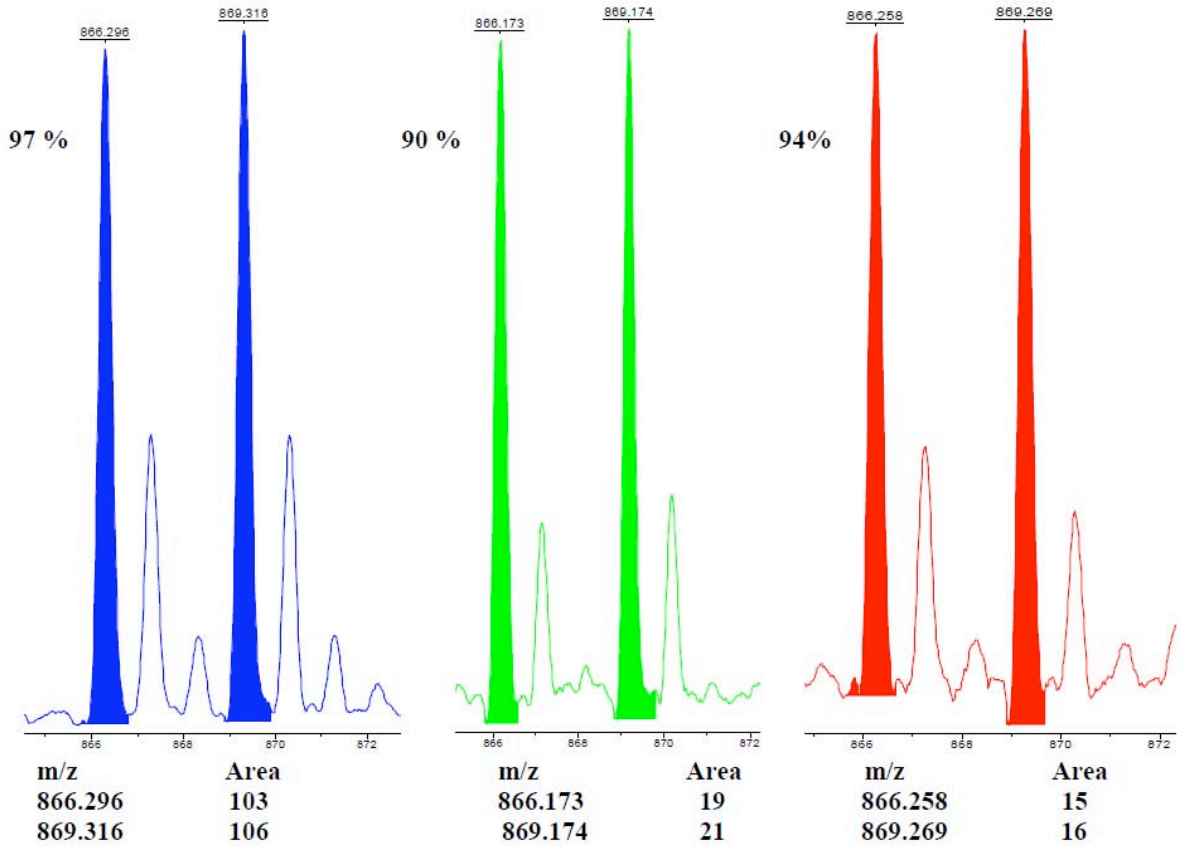

Figure S63: QMS analysis for ATP-γ-N-benzenesulfonyl-1, 6-diaminohexane **13** with PKA and the PKA substrate peptide. The peak at ~866 corresponds to the mono-methylated phosphopeptide ester after phosphorylation with **6e** and acid-mediated phosphoramidate bond cleavage. The ~869 m/z corresponds to the mono-methylated, deuterated phosphopeptide ester from the reaction with ATP. The percent conversion in each experiment is calculated from the areas under each peak and is shown in each panel. The percent conversion reported in the Table 2 is the average of these three independent trials.

V. Autodocking analysis
(The lowest energy binding mode with correct orientation is in bold font)

Table S1. The grid dimensions and output file with all the different binding modes obtained from docking of ATP-dansyl and PKA.

center_x = 12.689, size_x = 38
center_y = 5.654 size_y = 24
center_z = -2.28 size_z = 26 exhaustiveness = 8

Mode	affinity (kcal/mol)	dist from best mode rmsd l.b.	rmsd u.b.
1	-10.1	0.000	0.000
2	-9.7	1.215	1.868
3	**-9.5**	**3.652**	**15.660**
4	-9.4	1.862	3.326
5	-9.4	3.239	15.147
6	-9.3	3.733	15.332
7	-9.2	1.753	3.006
8	-9.1	1.772	3.065
9	-8.8	3.744	15.678

The most favorable binding mode has an affinity of -9.5 kcal/mole, as indicated in the manuscript, because the -10.1 and -9.7 kcal/mole modes position the dansyl group, not the ATP, in the kinase active site, which is inconsistent with the crystal structure of the PKA/ATP complex and is not compatible with the phosphorylation reaction.

Table S2. The grid dimensions and output file with all the different binding modes obtained from docking of ATP-dansyl and CK2.

center_x = 21.579 size_x = 22
center_y = 5.811 size_y = 30
center_z = 19.517 size_z = 18 exhaustiveness = 8

Mode	affinity (kcal/mol)	dist from best mode rmsd l.b.	rmsd u.b.
1	**-8.9**	**0.000**	**0.000**
2	-7.9	1.796	2.347
3	-7.3	3.173	4.890
4	-7.2	1.769	2.467
5	-7.1	1.997	2.880
6	-7.0	3.533	11.895
7	-6.7	2.345	3.680
8	-6.5	2.184	2.860
9	-6.5	3.957	5.223

Table S3. The grid dimensions and output file with all the different binding modes obtained from docking of ATP-analog **2b** and PKA

center_x = 12.669 size_x = 38
center_y = 5.687 size_y = 24
center_z = -2.286 size_z = 26 exhaustiveness = 8

mode	affinity (kcal/mol)	dist from best mode rmsd l.b.	rmsd u.b.
1	**-6.7**	**0.000**	**0.000**
2	-6.7	1.919	3.359
3	-6.7	2.082	3.175
4	-6.4	10.945	14.066
5	-6.4	11.463	14.819
6	-6.2	11.061	14.191
7	-6.2	9.017	11.150
8	-6.2	2.129	3.449
9	-6.2	7.696	13.212

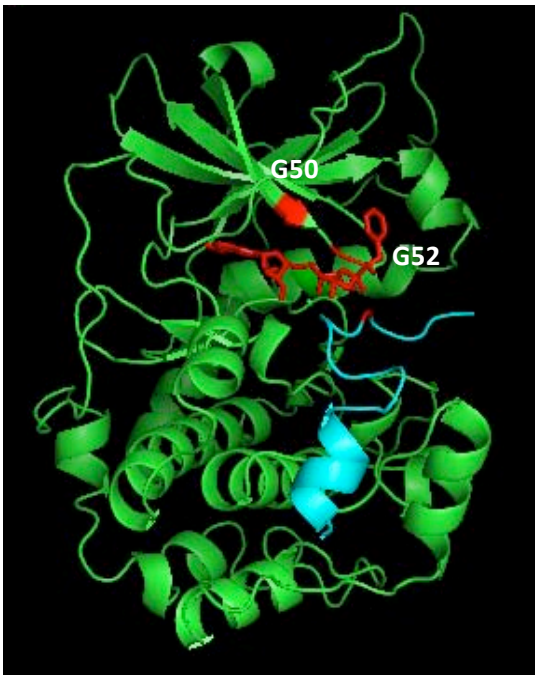

Figure S64: Docking of ATP-analog **2b** (red) into the active site of PKA (green) in complex with peptide substrate inhibitor (blue). The benzyl protrudes from the active site, but within close proximity to G52 (red). Compared to ATP-dansyl (Figure 1A), fewer binding interactions are possible with this analog.

Table S4. The grid dimensions and output file with all the different binding modes obtained from docking of ATP-analog **2b** and CKII

center_x = 22.159 size_x = 18
center_y = 5.479 size_y = 30
center_z = 17.635 size_z = 18 exhaustiveness = 8

mode	affinity (kcal/mol)	dist from best mode rmsd l.b.	rmsd u.b.
1	-8.6	0.000	0.000
2	-8.3	1.481	2.085
3	-7.9	2.371	3.716
4	-7.8	4.007	6.106
5	-7.6	1.963	3.217
6	-7.5	3.322	5.371
7	-7.1	4.765	7.050
8	-6.5	2.900	4.532
9	**-6.3**	**3.285**	**10.979**

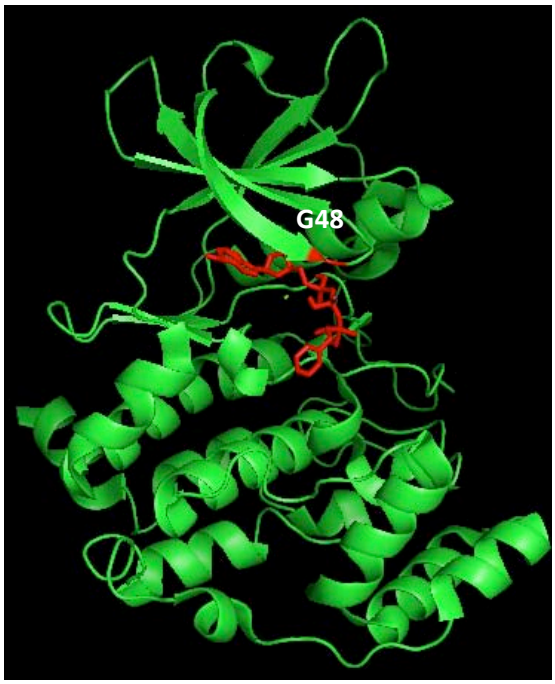

Figure S65: Docking of ATP-analog **2b** (red) into the active site of CKII (green). The phosphate groups interact with G48 (red) amino acid residues, and the linker part does not have any interactions.

Table S5. The grid dimensions and output file with all the different binding modes obtained from docking of ATP-analog **13** and PKA

center_x = 12.891 size_x = 28
center_y = 8.681 size_y = 20
center_z = 2.591 size_z = 18 exhaustiveness = 8

mode	affinity (kcal/mol)	dist from best mode rmsd l.b.	rmsd u.b.
1	-8.9	0.000	0.000
2	-8.8	1.533	2.338
3	**-8.4**	**3.745**	**14.135**
4	-8.2	5.218	13.337
5	-8.1	3.617	14.256
6	-8.1	2.114	3.572
7	-8.0	4.882	13.073
8	-7.9	1.514	1.982
9	-7.7	4.488	6.174

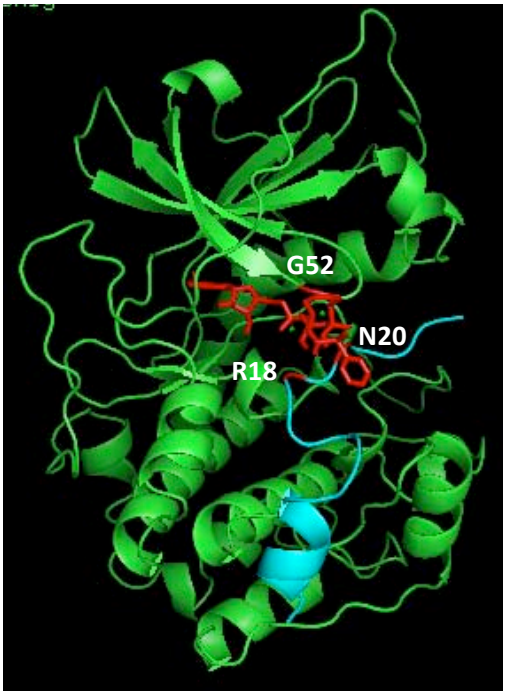

Figure S66: Docking of ATP-analog **13** (red) into the active site of PKA (green) in complex with peptide substrate inhibitor (blue). The linker protrudes from the active site, but within close proximity to G52 and peptide's R18 and N20 (red), making contacts with the residues present in the entrance of the active site.

Table S6. The grid dimensions and output file with all the different binding modes obtained from docking of ATP-analog **13** and CKII

center_x = 24.489 size_x = 20
center_y = 4.524 size_y = 34
center_z = 17.41 size_z = 16 exhaustiveness = 8

mode	affinity (kcal/mol)	dist from best mode rmsd l.b.	rmsd u.b.
1	**-8.6**	**0.000**	**0.000**
2	-7.9	3.031	4.451
3	-7.8	3.968	13.413
4	-7.7	2.307	2.983
5	-7.7	3.908	13.485
6	-7.7	4.231	13.143
7	-7.6	4.615	13.326
8	-7.5	4.141	13.411
9	-7.5	4.067	13.806

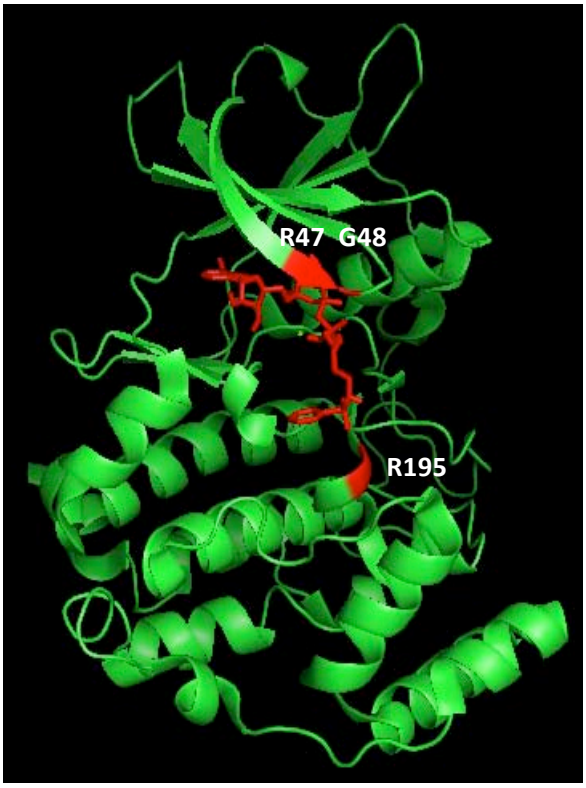

Figure S67: Docking of ATP-analog **13** (red) into the active site of CKII (green). The phosphate groups interact with R47 and G48 (red) amino acid residues, and the sulfonyl group interacts with R195.

Table S7. Sequence alignment of 15 different kinases representing various branches throughout the kinome.

Entry[a]	Kinase[b]	Sequence[c]
P00519	Abl	242---ITMKHKLGGGQYGEVYEG---259
P31749	AKT1	150---FEYLKLLGKGTFGKVILVK--168
Q99683	ASK	680---NGDRVVLGKGTYGIVYAGRD-699
Q16566	CAMK4	046---FEVESELGRGATSIVYRC---063
O14757	CHK1	009---WDLVQTLGEGAYGEVQLAV--027
P48729	CK1	017---YKLVRKIGSGSFGDIYLA---034
P68400	CK2	039---YQLVRKLGRGKYSEVFEAIN-058
P34947	GRK5	186---FRQYRVLGKGGFGEVCACQ--204
P49840	GSK3	119---YTDIKVIGNGSFGVVYQARL-138
P52333	JAK3	822---LKYISQLGKGNFGSVELCR--840
Q9P0L2	MARK1	060---YRLQKTIGKGNFAKVKLA---077
P80192	MLK1	144---LTLEEIIGIGGFGKVYRA---160
P17612	PKA	044---FERIKTLGTGSFGRVMLV---061
P04049	Raf	349---VMLSTRIGSGSFGTVYKG---366
P12931	Src	270---LRLEVKLGQGCFGEVWMG---287

[a] Primary Accession number for each kinase; [b] Kinase name; [c] region of the kinase containing the GXGX sequence near the ATP binding site (highlighted), with the amino acid numbers indicated.

Bioconjugate Chemistry

Article

pubs.acs.org/bc

Efficient Biofunctionalization of Polysilicon Barcodes for Adhesion to the Zona Pellucida of Mouse Embryos

Oriol Penon,[†] Sergi Novo,[‡] Sara Durán,[§] Elena Ibañez,[‡] Carme Nogués,[‡] Josep Samitier,[∥,⊥] Marta Duch,[§] José Antonio Plaza,[§] and Lluïsa Pérez-García*[,†]

[†]Department of Pharmacology and Therapeutical Chemistry and Institute of Nanoscience and Nanotechnology UB (IN2UB), Universitat de Barcelona, Avda. Joan XXIII s/n, 08028 Barcelona, Spain

[‡]Department of Cellular Biology, Physiology and Immunology, Universitat Autònoma de Barcelona, 08193 Bellaterra, Barcelona, Spain

[§]Institute of Microelectronics of Barcelona, IMB-CNM (CSIC), Campus UAB, 08193 Bellaterra, Barcelona, Spain

[∥]Institute for Bioengineering of Catalonia (IBEC), Baldiri Reixac 10-12, 08028 Barcelona, Spain

[⊥]Department of Electronics, Universitat de Barcelona, c/Martí i Franquès 1, 08028 Barcelona, Spain

Supporting Information

ABSTRACT: Cell tracking is an emergent area in nanobiotechnology, promising the study of individual cells or the identification of populations of cultured cells. In our approach, microtools designed for extracellular tagging are prepared, because using biofunctionalized polysilicon barcodes to tag cell membranes externally avoids the inconveniences of cell internalization. The crucial covalent biofunctionalization process determining the ultimate functionality was studied in order to find the optimum conditions to link a biomolecule to a polysilicon barcode surface using a self-assembled monolayer (SAM) as the connector. Specifically, a lectin (wheat germ agglutinin, WGA) was used because of its capacity to recognize some specific carbohydrates present on the surface of most mammalian cells. Self-assembled monolayers were prepared on polysilicon surfaces including aldehyde groups as terminal functions to study the suitability of their covalent chemical bonding to WGA. Some parameters, such as the polysilicon surface roughness or the concentration of WGA, proved to be crucial for successful biofunctionalization and bioactivity. The SAMs were characterized by contact angle measurements, time-of-flight secondary ion mass spectrometry (TOF-SIMS), laser desorption/ionization time-of-flight mass spectrometry (LDI-TOF MS), and atomic force microscopy (AFM). The biofunctionalization step was also characterized by fluorescence microscopy and, in the case of barcodes, by adhesion experiments to the zona pellucida of mouse embryos. These experiments showed high barcode retention rates after 96 h of culture as well as high embryo viability to the blastocyst stage, indicating the robustness of the biofunctionalization and, therefore, the potential of these new microtools to be used for cell tagging.

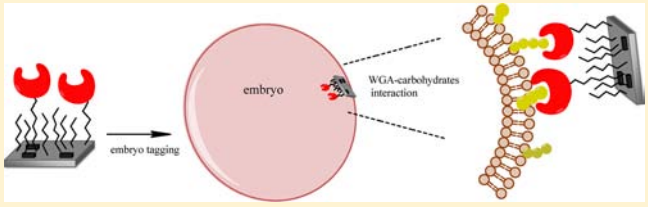

INTRODUCTION

Immobilization of biomolecules or synthetic bioactive molecules onto solid supports is a key step in the assembly of biosensors.[1−4] Since molecular recognition between protein receptors and their ligands is a central event in a wide variety of important biological processes, protein immobilization has become a fundamental tool to aid understanding of these interactions and in the search for applications of the phenomenon in many fields from bioanalytical chemistry to drug discovery.[5−11] One of the most currently used methods to immobilize biomolecules to substrates is the formation of an organic monolayer that will act as a linker, the so-called self-assembled monolayer (SAM). This organized layer of molecules induced by the chemisorption between the substrate and a functional headgroup provides one of the most elegant approaches to making stable ultrathin organic films spontaneously.[12−18] SAMs are also used as model substrates in biological studies because of their well-defined structure, controlled surface properties, and biocompatibility. SAM formation allows the possibility to change surface properties or add new characteristics to the materials. Different materials have been employed as substrates for the formation of monolayers, but gold and silicon are the most widely used and studied because of the ease of using thiol and silane chains, respectively, to be attached onto the corresponding surfaces; they form well-organized SAMs and they are biocompatible materials. Biofunctionalization of SAMs, i.e., modification of the SAM surface with different biomolecules, is of great interest and gives selective biological properties to the substrate, the preparation of biosensors being one of the main applications of the biofunctionalized SAMs. Chemical immobilization methodologies are of determinant importance in preserving

Received: July 30, 2012
Revised: October 22, 2012
Published: November 27, 2012

ACS Publications © 2012 American Chemical Society

dx.doi.org/10.1021/bc3004205 | *Bioconjugate Chem.* 2012, 23, 2392−2402

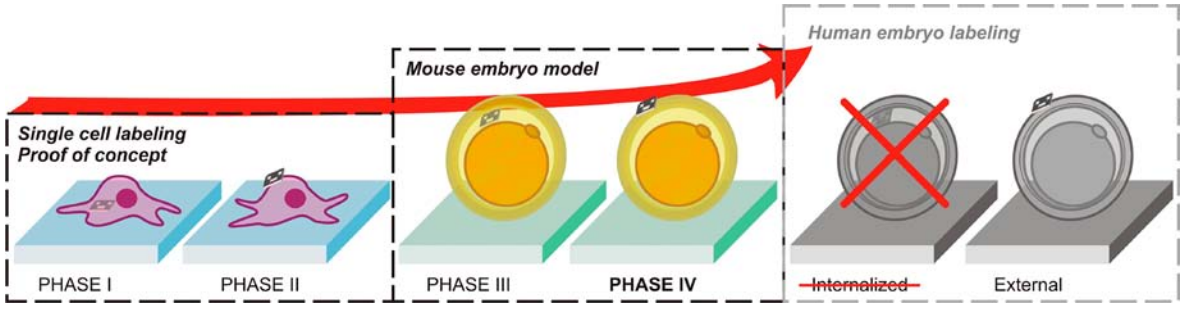

Figure 1. Toward human embryo labeling.

the activity of biomolecules,[5−18] and covalent binding renders the most robust and reliable devices. Unfortunately, characterization of the monolayers is often not sufficiently thorough, which does not allow a direct relationship between chemical functionality and bioactivity.

On the other hand, individual cell tagging[19,20] is a topic of interest in nanomedicine as a tool to track cells and to evaluate their behavior individually. Different nanomaterials, such as quantum dots or metallic particles, introduced inside cells have been envisaged as codes to discriminate different cell populations mixed in the same culture or to identify a subpopulation of cells in vivo,[21−25] but in general, these materials are complex and could be harmful for living cells.

Microfabrication opens up huge opportunities to obtain new materials for tracking and studying living cells.[26] For instance, silicon barcodes could offer the possibility to follow an individual cell over the course of a few days, provided that the codes are sufficiently small to be introduced into it or attached to the cell surface. The evolution of our research in this topic, toward human embryo labeling, is depicted in Figure 1. To this end, silicon barcodes have been phagocyted by macrophages,[27] whose locomotion was followed for 10 days (Phase I in Figure 1). Also, it has been possible to track Vero cells for up to seven days,[28] through attachment of biofunctionalized materials to their plasma membranes (Phase II in Figure 1). Tagging of mouse embryos by the microinjection of unfunctionalized barcodes in the perivitelline space has also been achieved recently (Phase III in Figure 1),[29] but the direct contact between the embryo membrane and the barcode implicit for an internalized tagging is a limitation. As a step forward, in the present work tag externalization is targeted in order to avoid possible damage to the processes occurring inside the cell and simplifying the attachment protocol (microinjection is not needed); mouse embryos were used to establish the proof of concept. To achieve it, specific adhesion of biofunctionalized barcodes to the zona pellucida (ZP), the cover that surrounds oocytes and embryos, is aimed for (Phase IV in Figure 1), and for this purpose, covalent biofunctionalization of polysilicon barcodes will become a decisive process to create selective, robust, and nontoxic microtools for external cell tagging. In fact, microtool preparation for cell applications requires an extremely cautious and demanding selection of the components of the microtools to be used, especially for setting up protocols applicable to human embryo labeling. Therefore, an accurate methodology to produce them, at the level of both microfabrication and chemical biofunctionalization, must be established.

To achieve our goal, lectins are regarded as optimal tools to link a biofunctionalized SAM with the cell surface, because of their ability to recognize saccharide structures.[30,31] Specific interactions between lectins and their complementary carbohydrates on cell surfaces have been thoroughly studied because of their importance in processes like cell−cell recognition or cellular adhesion. Wheat germ agglutinin (WGA) is one of the most widely characterized and least immunogenic lectins, the structure of which is that of a dimer consisting of two identical subunits and four carbohydrate binding sites.[32] WGA recognizes specifically *N*-acetylglucosamine (GlcNAc) and sialic acid, carbohydrates that are abundant on the surface of the plasma membrane and the zona pellucida of oocytes and embryos.[33] Only a few examples are known of studies exploiting the interaction between the lectin and carbohydrates for cell recognition,[28,34] including the use of AFM to characterize and measure the carbohydrate−protein binding.[35−37]

In this context, the present interdisciplinary research involves the covalent biofunctionalization of polysilicon surfaces through synthetic organic moieties to obtain microtools designed to interact with and tag biological material. In particular, in this work we aimed to use lectins such as WGA as the key element for adhesion to the ZP of mouse embryos, once they have been covalently immobilized through SAMs to polysilicon substrates, to build up a device destined for embryo tagging. These microtools consist of three main components (Figure 2): (i) a barcode made of polysilicon, with a structural codification easily identifiable using an optical microscope, (ii) a SAM which acts as the linker to the surface as well as the point of the biomolecule attachment, conferring strength and stability to the microtool, and (iii) a biomolecule (WGA) that, covalently attached to the SAM, will perform the recognition function on the embryo ZP. Following this design, we report here (a) the selection for the components of the device, (b) the microfabrication of the polysilicon surface supports, (c) the synthesis of the an appropriate SAMs linker, (d) the chemical and

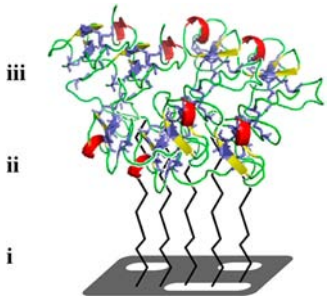

Figure 2. Schematic representation of the microtools for embryo tagging with their components: (i) polysilicon barcode, (ii) SAM linker, and (iii) immobilized WGA.

dx.doi.org/10.1021/bc3004205 | *Bioconjugate Chem.* 2012, 23, 2392−2402

physical characterization of every intermediate step in the SAMs formation obtained by a variety of techniques including atomic force microscopy (AFM), time-of-flight secondary ion mass spectrometry (TOF-SIMS), laser desorption/ionization time-of-flight mass spectrometry (LDI-TOF MS), fluorescence microscopy and contact angle measurements, and (e) the ability of the so prepared microtools to recognize and adhere to the ZP area of mouse preimplantation embryos.

EXPERIMENTAL SECTION

Fabrication of Polysilicon Barcodes and Microparticles. *Microparticle and Barcode Fabrication.* The barcodes were manufactured using semiconductor microtechnologies based on photolithographic processes to obtain reproducible devices. The polysilicon barcodes were fabricated on 4" p-type silicon wafers (Figure 3a). A 1-μm-thick silicon oxide layer was thermally grown to be used as sacrificial layer (Figure 3b). Next, a 1-μm-thick low-pressure chemical vapor deposition (LPCVD) polysilicon layer was deposited as the device layer (Figure 3c). The devices were patterned by a photolithographic step (Figure 3d,e) and by a posterior polysilicon dry etching process at the front side (Figure 3f). Polysilicon etching stopped at the silicon oxide layer. Vertical profile and uniformity of the etching were required due to the small dimensions of the devices. Afterward, the photoresist was removed by plasma etching (Figure 3g). The barcodes were released by 40 min etching in vapors of HF (49%) of the silicon oxide sacrificial layer (Figure 3h), and finally, the barcodes were suspended by ultrasound (with a MiniSpin Plus instrument) in absolute ethanol, centrifuged, and collected at 14 000 rpm for 5 min (Figure 3i). Microparticles were fabricated using a similar microtechnology.

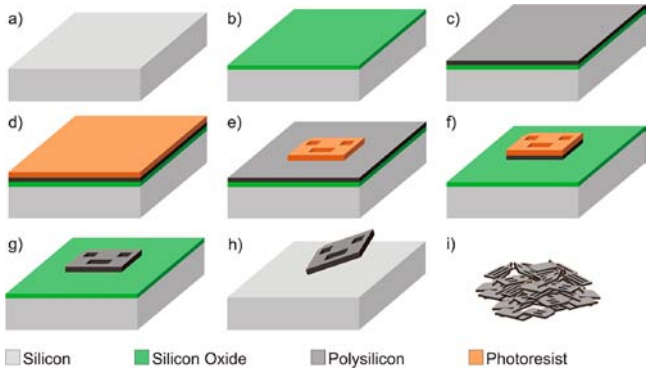

Figure 3. Schematic view of the fabrication process: (a) Silicon wafer as initial substrate, (b) thermal growth of a silicon oxide sacrificial layer, (c) deposition of a polysilicon device layer, (d) covering of the wafer with photoresist by spin coating, (e) photolitographic step, (f) polysilicon patterning by dry etching, (g) photoresist removed by plasma etching, (h) devices released by HF etching of the sacrificial layer, and finally, (i) centrifugation and collection of the barcodes inside an Eppendorf (not showed in the figure).

Chemical (Bio)Functionalization of Barcodes and Microparticles. *General Methods.* Particle counter analysis was carried out using a Multisizer II (MSZ) electronic particle analyzer (Coulter Corporation) with the capacity to process 2 mL of the material suspension in PBS, from Centres Cientifics i Tècnològics de la Universitat de Barcelona (CCiT-UB). A 0.5 mL aliquot of the sample was diluted in 10 mL of PBS. Data were analyzed with Coulter *MultisizerAccuComp* software v 1.15 (Coulter Corporation). Counting experiments on at least two equivalent samples were measured to give statistical significance.

Static contact angles were measured in air inside a clean room with high-purity deionized water by a 3 μL drop using a contact angle goniometer (OCA 15Plus with the software SCA20 Dataphysics, Germany), from Nanotechnology platform of the Parc Científic de Barcelona (PCB) to determine the hydrophobicity of the modified surfaces. Values of the contact angle on at least three samples were measured to give statistical significance.

The TOF-SIMS analyses were performed using a TOF-SIMS IV (IONTOF, Munster, Germany), from Nanotechnology platform (PCB), operated at a pressure of 5×10^{-9} mbar. Samples were bombarded with a pulsed bismuth liquid metal ion source (Bi^{3+}), at energy of 25 keV. The gun was operated with a 20 ns pulse width, 0.3 pA pulsed ion current for a dosage lower than 5×10^{11} ions/cm^2, well below the threshold level of 1×10^{13} ions/cm^2 generally accepted for static SIMS conditions. Secondary ions were detected with a reflection time-of-flight analyzer, a multichannel plate (MCPs), and a time-to-digital converter (TDC). Measurements were performed with a typical acquisition time of 20 s, at a TDC time resolution of 200 ps. Charge neutralization was achieved with a low energy (20 eV) electron flood gun. Secondary ion spectra and images in both positive and negative modes were acquired from a randomly rastered surface areas of 500 μm $\times$ 500 μm along the sample's surface. Secondary ions are extracted with 2 kV voltages and are postaccelerated to 10 keV kinetic energy just before hitting the detector. The maximum mass resolution, $R = m/\mathrm{Dm}$, was around 9.000, where m is the target ion mass and Dm is the resolved mass difference at the peak half-width.

LDI-TOF-MS analyses were performed using a Voyager-DE-RP (Applied Biosystems, Framingham, USA) mass spectrometer, from CCiT-UB. The substrates were allowed to dry and attached directly onto the stainless steel LDI sample plate with double-sided tape and loaded into the spectrometer. MS analysis was operated in the delayed extraction mode. A 3 ns pulse nitrogen laser (337 nm) was used for desorption and ionization with an accelerating voltage of 20 kV. Ions were detected as negative on a time-of-flight mass detector in the reflector. All the measurements were performed without matrix.

Topographic and phase images were acquired using a multimode atomic force microscope attached to a Nanoscope IV electronics (Veeco, Santa Barbara, CA), from CCiT-UB. Images were acquired in intermittent contact mode using silicon single-beam cantilevers with a nominal spring constant of 40 nN/nm (ACT-W, AppNano, Santa Clara, CA). In order to minimize sample damage, images were acquired at minimum vertical force and thermal piezo drift was minimized by scanning the sample for several minutes before acquiring the first image. For the surface roughness evaluation, topographic and amplitude images were acquired from a Dimension 3100 atomic force microscope with a NanoScope IV controller (Veeco, Santa Barbara, CA) from IMB-CNM (Scientific and Technical Installation). Images were acquired in a tapping mode using silicon single-beam cantilevers with a nominal spring constant of 12−103 N/m. A drop of the released barcodes in absolute ethanol (2 μL) was deposited on a 1 cm^2 polysilicon wafer, and the absolute ethanol was completely evaporated before the selected barcodes were observed on an optical microscope (Leica Microsystems, DM LM) and their roughness was measured on the AFM.

dx.doi.org/10.1021/bc3004205 | *Bioconjugate Chem.* 2012, 23, 2392−2402

SEM characterization was performed on scanning electron microscope Carl Zeiss Auriga (Carl Zeiss Microscopy GmbH, Germany). The electron high tension (EHT) value was fixed at 3 kV and the images were acquired with 5 mm of working distance and the secondary electron detector. The released devices were observed after depositing a 2 μL absolute ethanol drop on a 1 cm^2 polysilicon wafer, with it being necessary that absolute ethanol was totally evaporated before the silicon wafer was introduced inside the sample chamber.

Fluorescence images were obtained with a Leica TCS-SP2 confocal microscope from CCiT-UB equipped with an inverted fluorescence microscope. The samples were observed through a water immersion objective in fluorescence and transmission light simultaneously. Transmitted light images were performed using differential interference contrast at 488 nm. The Texas Red conjugated lectin was visualized by excitation of the fluorochrome with a 541 nm laser diode and the emitted fluorescence was detected between 576 and 654 nm.

UV absorption spectra were obtained on UV-1800 Shimadzu UV spectrophotometer. Absorption spectra were determined in perchloric acid/water (1:1) mixture.

Materials. Solvents and reagents were absolute ethanol, deionized water, sulfuric acid (96%), hydrogen peroxide, ammonium hydroxide (20%), acetic acid, and perchloric acid (70%). Water used in the experiments was HPLC grade produced by a Milli-Q plus system from Millipore (Milli-Q water).

Commercial compounds 2-(2-aminoethoxy)ethanol, ethylenediamine, sodium cyanoborohydride, sterile phosphate buffered saline (PBS), and sodium bicarbonate were purchased from Sigma-Aldrich. 11-(Triethoxysilyl)undecanal (TESUD) was purchased from ABCR. Sulfo-succinimidyl-4-*O*-(4,4′-dimethoxytrityl) butyrate (s-SDTB) was purchased from Apollo Scientific, and Texas Red-X conjugated WGA was purchased from Invitrogen.

Synthesis. Silicon Surface Activation. The silicon surface (polysilicon wafer, particle, or barcode) was treated with (1) piranha solution H_2SO_4/H_2O_2 (7:3) for 1 h and then with (2) basic solution $NH_4OH/H_2O_2/H_2O$ (1:1:5) for 30 min to activate the surface hydroxyl groups. Finally, the surface was rinsed thoroughly in deionized water.

WGA-SAM. The formation of the WGA-SAM was achieved in two steps: (1) 0.1 mL of acetic buffer pH = 5.2 were added to absolute ethanol (1.8 mL) and triethoxysilaneundecanal (TESUD) (0.1 mL), corresponding to a final TESUD concentration of 135 mM. The silicon surface was immersed for 3 h at room temperature in this solution. Next, it was rinsed with absolute ethanol (3 × 2 mL), and placed into an oven at 90 °C for 1 h. (2) Protein immobilization. The terminal aldehyde groups reacted with the WGA amine groups under reductive conditions by adding a solution of WGA in PBS (either 15, 25, or 35 μg/mL) to the previously aldehyde covered surfaces, in the presence of a PBS solution of sodium cianoborohydride (5 mM, 0.5 mL), and the mixture was kept at 4 °C overnight. To cover the unreacted aldehyde groups on the surface, a PBS solution of 2-(2-aminoethoxy)ethanol (15 mM, 0.5 mL) was added. After 20 min, the surface was rinsed with PBS abundantly (5 × 2 mL), to eliminate unspecific protein adsorption.

The volumes of the different solutions used for the surface functionalization and rinsing were 2 mL for the wafers, and 0.5 mL for the particles or barcodes. The same protocol for functionalizing wafers was used for the biofunctionalization of the polysilicon particles and barcodes, although particles were centrifuged (2 min at 13 000 rpm) in every step. For the embryo adhesion experiments, autoclaved PBS was used.

Surface Coverage Determination. A dry polysilicon wafer functionalized as CHO-SAM was placed in a capped vial, and a PBS solution of sodium cianoborohydride (5 mM, 2 mL) and ethylenediamine (30 μL) were added. The vial was incubated for 3 h at room temperature, and then the wafer was removed, rinsed thoroughly with Milli-Q water, placed in a precleaned glass vial containing of freshly prepared solution of sulfo-succinimidyl-4-*O*-(4,4′-dimethoxytrityl)butyrate (s-SDTB) (0.1 mM, 2 mL), and left at room temperature for 30 min. At this point, the wafer was rinsed thoroughly with Milli-Q water, placed in a precleaned vial containing a perchloric acid aqueous solution (35%, 2 mL), and ultrasonicated for 15 min. The absorbance of the solution in each vial was then directly measured at 502 nm with a UV−visible absorption spectrometer. All the measurements were done by duplicate.

Barcode Adhesion to the Zona Pellucida of Mouse Embryos. *Mouse Embryo Collection.* Animal care and procedures used in this study were conducted according to the protocols approved by the Ethics Committee on Animal and Human Research of the Universitat Autònoma de Barcelona and by the Departament d'Agricultura, Ramaderia i Pesca of the Generalitat de Catalunya.

Hybrid B6CBAF1 (C57BL/6J x CBA/J) female mice (age, 8−12 weeks) were used as pronuclear (PN) embryo donors. Females were superovulated by intraperitoneal injection of 5 IU of pregnant mare serum gonadotropin (Intervet, Spain) followed 48 h later by a second injection of 5 IU of human chorionic gonadotropin (hCG; Farma-Lepori, Spain), and mated with males of the same strain. PN embryos were collected from the oviducts 25 h after hCG administration and incubated for 5−10 min at 37 °C in Hepes-buffered potassium simplex optimized medium (H-KSOM)[38] supplemented with 150 U/mL of hyaluronidase (Sigma, Spain) for the dispersion of cumulus cells. Denuded PN embryos were then washed twice in fresh H-KSOM, prepared without bovine serum albumin (BSA).

Barcode Attachment to the Zona Pellucida. Biofunctionalized barcodes were placed in groups of ten in a drop of KSOM-H by micromanipulation techniques. Then, PN embryos were individually rolled over each group of biofunctionalized barcodes under a stereoscopic microscope using a mouth-controlled glass capillary with 150 μm of inner diameter, until all ten barcodes were attached. Contact between the ZP and the biofunctionalized barcode surfaces was enough to attach the barcodes to the ZP.

Embryo Culture and Evaluation. Embryos with ten barcodes attached to their ZP were individually cultured for 96 h (blastocyst stage) in standard conditions (37 °C and 5% CO_2) in drops of 20 μL KSOM culture medium prepared without BSA. Embryo development was assessed every 24 h and compared with a control group of embryos without barcodes attached to their ZP.

To quantify the efficiency of barcode attachment, the number of barcodes that remained attached to each embryo at the blastocyst stage was recorded (retention rate).

Statistical Analysis. Blastocysts and barcode retention rates were analyzed by the Fisher's exact test. Probability values lower than 0.05 were considered statistically significant.

RESULTS AND DISCUSSION

The microtools developed in this work consist of three components: a surface acting as substrate to be chemically modified with a linker (SAM), in turn functionalized with a biomolecule performing a function. Therefore, the first point to be addressed is the selection of these components.

Silicon Substrates Selection. Devices were made of polysilicon, which is robust, biocompatible, and a common material in the semiconductor industry. The polysilicon surfaces used in this work for different purposes belong to three kinds (Figure 4): (a) Wafers (Figure 4a,d). The pieces of

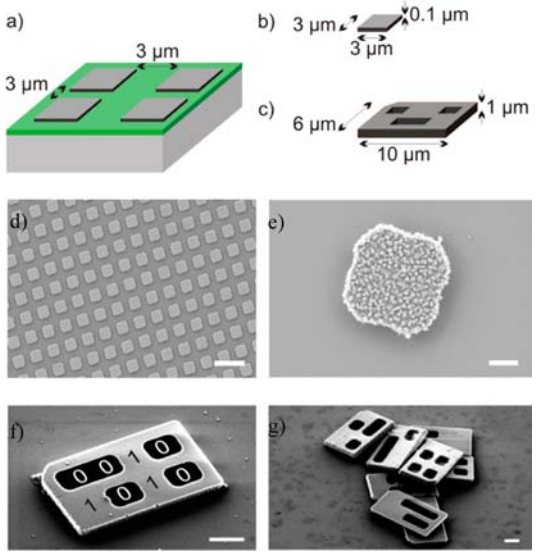

Figure 4. Different polysilicon substrates used in this work: Ideal representation of (a) 1 cm^2 polysilicon microparticles wafer, (b) 3 μm × 3 μm polysilicon particle, and (b) 10 μm × 6 μm polysilicon barcode; SEM images of the polysilicon microparticles (d) before and (e) after release. Left scale bar = 10 μm and right scale bar = 1 μm; SEM images of the polysilicon barcodes (f) after release; bits values are indicated on the picture Code 0010 1010 = 42 (binary numeral system = decimal numeral system), and (g) a view of different barcodes. Scale bar = 2 μm.

wafer used have an area of approximately 1 cm^2, cut from the 4 in. wafer samples using a diamond scribe, and present a pattern of polysilicon particles with lateral dimensions 3.0 μm × 3.0 μm and 0.1 μm thickness on the thermal silicon oxide layer. Biofunctionalization was always attempted first using wafers, mainly because they are easier to manipulate and characterize, and the synthetic methodology was then adapted to microparticle functionalization. (b) Particles (Figure 4b,e). The released 3.0 × 3.0 μm^2 and 0.1 μm thickness particles were obtained by treating the silicon wafer as described before (see Experimental Section), using hydrogen fluoride solution to detach the polysilicon particles from the thermal oxide layer, and in this work, they were used as models for the functionalization process at the microscale, in order to find the optimum experimental conditions for this process. (c) Barcodes (Figure 4c,f,g). The external dimensions of the barcode devices were fixed to 10.0 μm length, 6.0 μm width, and 1.0 μm thickness, in order to make them easily identifiable under an optical microscope,[29] when code reading will be necessary. The barcodes consist of a matrix of 2 rows and 4 columns of individual bits. Thus, the total 8 bits represent 256 combinations (codes) of different values in a base-2 number system (Figure S1 in Supporting Information). Bits lateral dimensions were fixed to 2.0 μm length, 1.5 μm width, and 1.0 μm thickness. A solid-bit represents symbol 1 (Bit = 1) and a hole-bit represents symbol 0 (Bit = 0). A start mark was designed in order to expedite the correct reading of data. Barcodes were obtained using a similar methodology to that previously reported (see Experimental Section).[27−29] The barcodes do not break during fabrication or collection, thus ruling out false identification. Scanning electron microscopy (SEM) images of fabricated barcodes after their release are shown in Figure 4.

Chemical (Bio)functionalization. Synthesis of self-assembled monolayers (SAMs) on polysilicon surfaces. Among the various types of immobilization procedures existing to link biomolecules to solid substrates,[5−18] in our work we have chosen covalent bonding, because of their strength and stability, and the formation of SAMs relies on silicon chemistry procedures, based on the formation of covalent Si−O bonds. The silane reagent incorporates the desired alkyl chain with a functional group appropriate for the posterior modification and linkage to the protein WGA via its *N*-terminal amino groups. The selected spacer consisted of an eleven carbon atom alkyl chain, and an aldehyde was chosen as the terminal group to form secondary amine bonds ($-CH_2-NH-$),[39−41] stable in biological conditions. A fluorescent labeled lectin, Texas Red WGA, was used as the protein in order to characterize the formation of the biolayer using fluorescence microscopy.

As mentioned before, polysilicon structured wafers were tested first. Before the formation of the monolayer, the polysilicon surfaces were first hydroxylated with piranha solution (H_2SO_4/H_2O_2 (7:3)) and then treated with basic solution ($NH_4OH/H_2O_2/H_2O$ (1:1:5)) to ensure a complete surface hydroxylation. The synthesis of WGA-SAM, as reflected in Scheme 1, was based on the formation of a SAM using the

Scheme 1. Stepwise Formation of the WGA-SAM on Polysilicon Surfaces

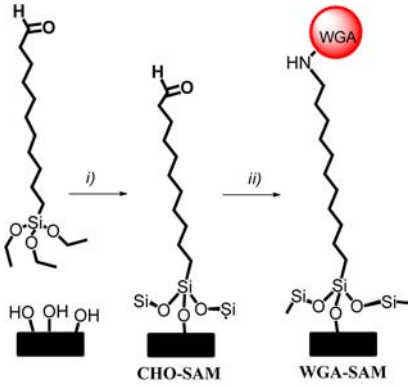

i) EtOH, ii) WGA/PBS with $NaBH_3CN$.

aldehyde 11-(triethoxysilyl)undecanal (TESUD). Following Scheme 1, only two steps were needed: (1) chemisorption of TESUD on the hydroxylated silicon surface to give CHO-SAM and (2) immobilization of the WGA through a reductive amination process, by formation of an imine between the aldehyde covered surface and the amino groups in WGA, and its subsequent reduction to form a secondary amine, to afford WGA-SAM.

Two synthetic aspects are worth mentioning. First, a key experimental variable is the concentration of WGA: three

dx.doi.org/10.1021/bc3004205 | Bioconjugate Chem. 2012, 23, 2392−2402

different concentrations have been used on the barcode functionalization (15 μg/mL, 25 μg/mL, and 35 μg/mL), and the best results were obtained when the concentration was 35 μg/mL (see later, barcode adhesion to the zona pellucida of mouse embryos). Second, chemical blocking of unreacted aldehyde groups after WGA bonding was proven to be essential for the reproducibility of results, in order to avoid incomplete surface coverage as well to give additional structuring to the WGA SAM. In this case, 2-(2-aminoethoxy)ethanol was used as a chemical blocker, which also reduced unspecific protein adsorption.[42] Although polysilicon wafers were tested first, the same synthetic protocols were used with polysilicon particles and barcodes as the substrates, in similar experimental conditions (see Experimental Section).

Characterization of the (Bio)functionalized Surfaces. *Contact Angle Measurements.* Contact angle determination is a simple method to assess qualitatively the hydrophobicity of differently functionalized surfaces, a property which is related to the chemical nature of the terminal group of a given SAM, and the quality of the packing of the monolayer.[43] Thus, this technique was used for the monitoring of the formation of the monolayers as well as their different chemical transformations. Contact angle measurements were estimated by the deposition of a water drop (3 μL) onto the silicon wafers, and the obtained contact angles are shown in Table 1.

Table 1. Contact Angle Measurements, θ (°), for the Different Chemically Modified Polysilicon Surfaces (SAMs)

terminal functional group in SAM	contact angle[a] θ (deg)
none (clean surface)	58 ± 2
−OH	30 ± 6
CHO-SAM	98 ± 5
WGA-SAM	34 ± 5
WGA-SAM[b]	24 ± 1

[a]All the experiments were performed using milliQ water. [b]After chemical blockage of the unreacted terminal groups.

The as-received polysilicon wafers have a contact angle of θ = 58°, in good agreement with values previously described,[44] which after treatment with piranha is reduced to θ = 30°, indicating a good level of surface hydroxylation. When the SAM formed on polysilicon had a terminal aldehyde functional group (CHO-SAM) the material became extremely hydrophobic (θ = 98°, Table 1). After WGA immobilization, surfaces again become very hydrophilic, as reflected by contact angles of θ = 34° for WGA-SAM, a value that experiences further reduction after chemical blocking has taken place (blocked-WGA-SAM θ = 24°, Table 1), indicating full surface coverage.

Time-of-Flight Secondary Ion Mass Spectrometry (TOF-SIMS). TOF-SIMS is useful for the characterization of monolayers distinguishing different compounds on a surface due to its chemical specificity and surface sensitivity, and thus we used this technique to monitor the SAMs formed using wafers. The peak interpretation in the TOF-SIMS positive ion spectrum of the CHO-SAM was difficult due to the presence of many unspecific peaks. However, in the negative ion spectrum, a significant increase in the m/z = 197 peak was observed, corresponding to the whole molecule of the silane on the SAM (-Si-$(CH_2)_{10}$-CHO). We also analyzed WGA-SAM, of special interest taking into consideration that there are only a few examples in the literature where immobilized proteins have been characterized by TOF-SIMS using the protein amino acid peak patterns as the probe.[45] The positive ion spectrum of WGA-SAM is shown in Figure 5a, corresponding to the protein

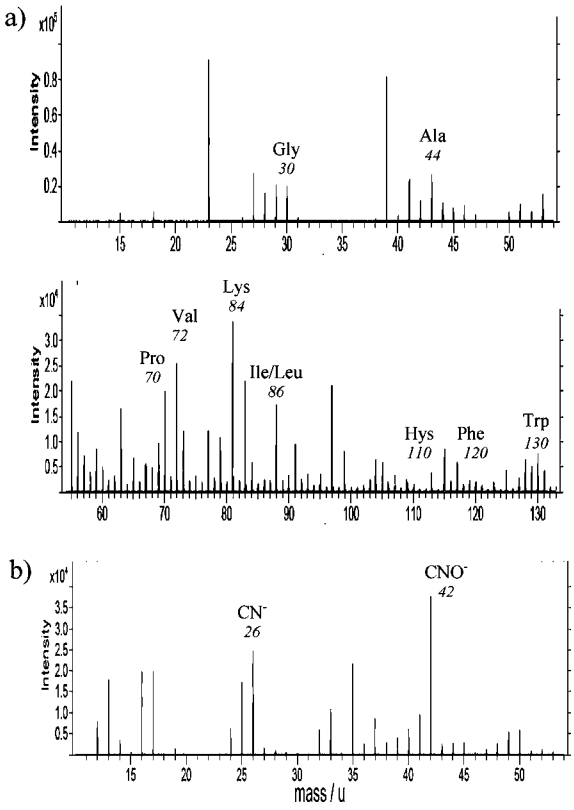

Figure 5. (a) Positive ion TOF SIMS spectrum of WGA-SAM.The amino acids that correspond to the peaks are indicated. (b) Negative ion TOF-SIMS spectrum of WGA-SAM.

amino acid fragments, and the most abundant secondary ions from the fragmentation of the protein are labeled on the diagram. As has been reported in the literature,[46] several amino acid moieties were identified on the spectrum related to Gly (m/z = 30), Ala (m/z = 44), Pro (m/z = 70), Val (m/z = 72), and Lys (m/z = 84) among others. Instead, in the spectrum of WGA-SAM recorded in negative mode, only unspecific peaks at m/z = 26 and m/z = 42 were detected with a significant intensity, corresponding to the peptide backbone (Figure 5b).

Laser Desorption/Ionization Time-of-Flight Mass Spectrometry (LDI-TOF MS). MALDI-TOF MS is a soft ionization mass spectrometry technique, allowing the analysis of biomolecules and large organic molecules, which uses a matrix to ionize the target molecules. Some examples of this technique to analyze SAMs are reported, either on gold[47] or silicon surfaces.[48] In our case, the first experiments to analyze the functionalized surfaces using MALDI-TOF MS were performed using several ionizing agents and matrices as trifluoroacetic acid (TFA) and dithranol, but the results were not conclusive. Consequently, we explored the use of LDI-TOF MS (where the surface is expected to act as the absorbing material) for the characterization of CHO-SAM on polysilicon wafers. All the spectra were recorded in the negative mode and the analysis was performed without using a matrix. In the spectrum of CHO-SAM, shown in Figure S2 in Supporting Information, several fragments of the molecule attached to the surface could be identified, and the highest-intensity peak at m/z 188 shows the fragment corresponding to the rupture of the β–γ bond of

dx.doi.org/10.1021/bc3004205 | Bioconjugate Chem. 2012, 23, 2392–2402

the complete chemisorbed silane. Some other fragments could be detected, corresponding to the complete silane without an oxygen atom and linked with an extra silicon atom, and also the total molecule with two extra silicon atoms. These results indicate the adequate functionalization of the polysilicon surfaces with CHO-SAM.

Atomic Force Microscopy (AFM). AFM images were recorded to demonstrate the formation of the organic monolayer on the silicon substrates, using functionalized wafers which were dried in nitrogen before analyzing and were tested in air. Figure S3 in Supporting Information shows AFM topographic images of a polysilicon structured wafer (Figure S3a) and of a polysilicon microparticle located on the wafer with 0.1 μm thickness (Figure S3b), all taken before any chemical treatment was done. The microparticle profile (Figure S3c) allows the estimation of a the roughness of the polysilicon surface (ca. 10 nm).

Figure S4a and S4b in Supporting Information show AFM phase and 3D images of a neat polysilicon wafer microparticle before and after functionalization as the CHO-SAM, respectively. Figure S4a shows the surface morphology of the starting silicon wafer, and Figure S4b shows the CHO-SAM on the silicon surface which is significantly different from the phase image in Figure S4a, as a qualitative indication of the formation of the SAM.

Also, 3D images (see Figure S4)[49] were recorded to confirm the differences between the functionalized surfaces, evidencing the increase in the roughness of the functionalized material CHO-SAM, as a proof of the layer formation. It can be seen that the terminal aldehyde functionalization film on the silicon surface is complete, dense, and homogeneous with only a few aggregates. An additional aspect studied using AFM was the influence of the etching process duration, needed to release barcodes from their wafers, on the roughness of the polysilicon barcodes and subsequently in the functionalization process, as seen in Figure S5 in Supporting Information. This aspect was assessed by measuring first the maximum roughness of unreleased barcodes on a wafer (Figure S5a) and comparing this value with the roughness of released barcodes that had been exposed to 49% HF vapors for either 15 or 40 min. This was achieved when a drop of released barcodes was deposited in the AFM equipment and the roughness of a selected barcode was estimated. Roughness of the released barcodes was measured before chemical treatment (Figure S5b), after hydroxylation (Figure S5c), as well as after aldehyde treatment (CHO-SAM) (Figure S5d). The results of the study are included in the graph in Figure S5e, and indicate that roughness increases proportionally with etching time (time of exposure to HF vapors), with values of ca. 8.5 nm when etching took 15 min, and of ca. 15 nm when etching was 40 min. Figure S5f and S5g show images of barcodes released after 15 or 40 min etching, respectively. However, this difference is not significant after hydroxylation or functionalization of the barcodes, for which roughness has smaller values, indicating a dense packing of functional groups on the polysilicon barcode surface after chemical treatment. Furthermore, the best functionality results on ZP adhesion were obtained using barcodes of the higher roughness (see later, barcode adhesion to mouse embryos).

Surface Coverage Determination. In order to quantify the monolayer density, a protocol reported in the literature[50] was adapted to measure the aldehyde concentration in CHO-SAM. This method consists of three chemical steps (Scheme S1 in Supporting Information) and is based on the derivatization of the aldehyde groups with ethylenediamine in the presence of sodium cyanoborohydride, followed by treatment with SDTB and then release of the 4,4′-dimethoxytrityl cation and its detection by UV−visible absorption spectroscopy. Following this protocol, and considering a substrate area of 1 cm^2 for the wafer, a density area of 4×10^{-10} mol/cm^2 of the aldehyde-terminated SAM (CHO-SAM) was obtained, in accordance with the value reported for a similar quantification process.[50]

Particle Counting Experiments. Prior to the functionalization process of microparticles and barcodes, counter equipment was used in order to quantify the number that was used in the biofunctionalization process. Counting of microparticle samples gave an average value of 5×10^4 particles/mL, whereas the barcode samples contained 1.3×10^6 barcodes/mL. After biofunctionalization as WGA-SAM, barcode samples (see Figure S6 in Supporting Information) contained 6.3×10^5 barcodes/mL, meaning a loss of ca. 50% of the barcodes during biofunctionalization, partly because of them breaking during the chemical protocol. Despite the significant loss, the biofunctionalized sample contains enough barcodes to do reproducible and trustworthy adhesion experiments.

Fluorescence Microscopy. The presence of the immobilized protein on the surfaces was well-characterized by fluorescence microscopy. Furthermore, this technique allows the characterization of all the types of biofunctionalized surfaces used in this study, wafers, particles, and barcodes, whereas mass spectrometry or contact angle techniques were not suitable for the characterization at the microscale of particles and barcodes. For this purpose, a fluorescently labeled WGA was used, using Texas Red as the marker. Figure 6a gives an overview image of a biofunctionalized polysilicon structured wafer, whereas Figure 6b includes an enlarged area, and the relative fluorescence intensity, indicating the uniformity in the degree of WGA coverage on the polysilicon particles for WGA-SAM. The relative fluorescence intensity images were represented on a scale from 0 to 255 (according to the maximum intensity in

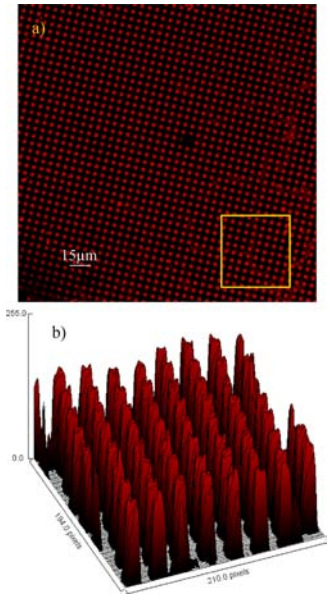

Figure 6. Fluorescence microscopy images of a polysilicon structured wafer functionalized as WGA-SAM: (a) general view, and (b) 3D diagram showing the relative fluorescence intensity.

pixels), after subtracting the background fluorescence making the same contrast enhancement.[51]

The extent of formation of WGA-SAM on released polysilicon microparticles was also analyzed by fluorescence microscopy. Figure 7 shows the relative fluorescence exhibited

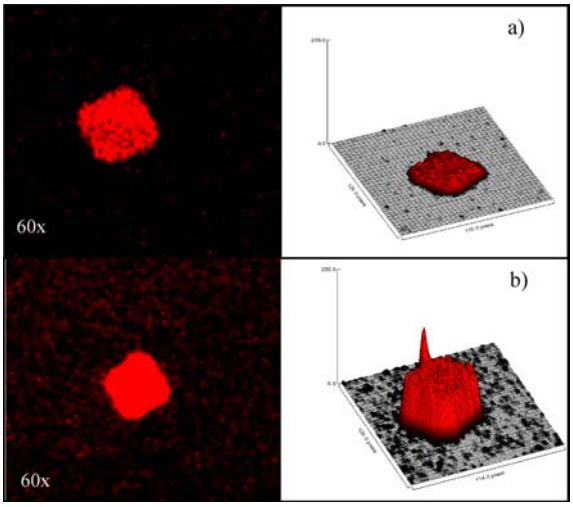

Figure 7. Fluorescence microscopy images of a released polysilicon microparticle: (a) unfunctionalized and (b) after functionalization as WGA-SAM. For each sample, a general view and a 3D diagram showing relative fluorescence intensity are shown.

by a representative selected microparticle before (Figure 7a) and after biofunctionalization (Figure 7b), indicating the occurrence of residual fluorescence on the nontreated polysilicon surface, which value was subtracted from the obtained for functionalized particles.

Biofunctionalized barcodes for WGA-SAM were also visualized by fluorescence imaging using a confocal microscope. Figure 8a shows the low level of red fluorescence of several nonbiofunctionalized barcodes, an enlarged view of a selected barcode and its 3D representation, whereas Figure 8b shows some of the WGA functionalized barcodes (WGA-SAM), which are homogeneous and intensely fluorescent. Figure 8 also includes several parameters evaluated to assess the degree and uniformity of WGA immobilization, such as maximum fluorescence intensity, square area of the fluorescence measurement, total fluorescence intensity, intensity mean value, and mean average, recorded for representative selected unfunctionalized barcodes, and WGA-SAM functionalized barcodes. Some of the differences observed between the values obtained for a given barcode could be attributed to the spatial location, with changes in the area exposed to light, of the particular barcode in the fluorescence microscope. Nevertheless, the relative fluorescence of the biofunctionalized barcodes shows intensity 54 times higher than that observed in the control barcodes, indicating the extent and uniformity of the WGA biofuncionalization (Figure 8).

Barcode Adhesion to the Zona Pellucida of Mouse Embryos. Adhesion capacity of WGA-biofunctionalized microparticles and barcodes to the cell surface was studied using mouse embryos. The ZP is rich in carbohydrates that are specifically recognized by the WGA lectin. Barcodes were preferred for the study rather than microparticles for various reasons: their surface area is bigger, which strengthens the contact with the ZP, they are also much easier to manipulate

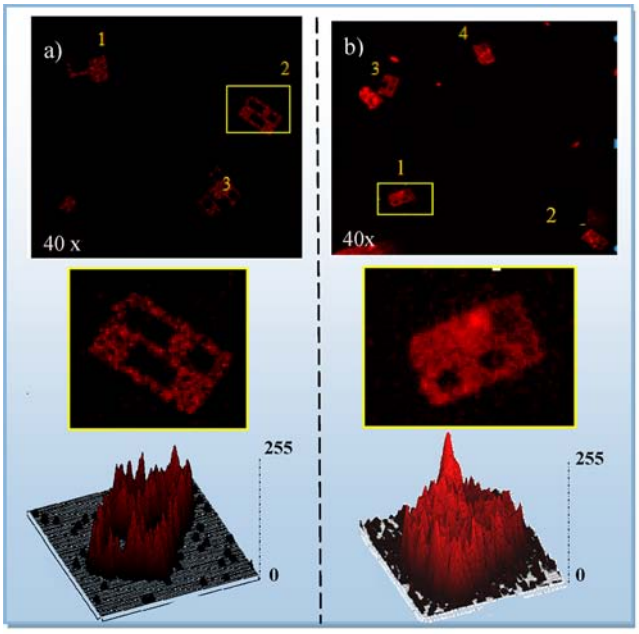

Barcode	Max[a]	Area[b]	Int[c]	Mean[d]	Average[e]
1 [f]	6	15960	3209	0.201	
2 [f]	5	12600	2095	0.166	0.17
3 [f]	5	14616	2102	0.143	
1 [g]	235	10496	92214	8.786	
2 [g]	248	10780	92170	8.550	
3 [g]	100	10208	73716	7.221	9.15
4 [g]	189	11328	13657	12.057	

Figure 8. Fluorescence microscopy images of released polysilicon barcodes: (a) unfunctionalized and (b) after functionalization as WGA-SAM. For each sample, a general view, an enlarged view of a selected barcode, and a 3D diagram showing relative fluorescence intensity are shown. Values related to the fluorescence of different barcodes are included.

than microparticles, and most important, their unique codification will allow a direct and easy identification using an optical microscope.

Biofunctionalized barcodes were adhered to the ZP PN embryos (10 barcodes per embryo), and the number of barcodes that remained attached at the end of the culture (96 h), when embryos reach the blastocyst stage, was counted in order to determine the barcode retention rate, indicative of the efficiency of barcode biofunctionalization. Figure 9 shows three different focal planes of embryos at one-cell, two-cell, morula, and blastocyst development stages: Figure 9 A1−3, B, C, and D, respectively.

Biofunctionalized WGA-SAM was tested using barcodes, and the embryo adhesion was highly increased as chemical biofunctionalization was improved, as shown by the high retention rates obtained (at 96 h of culture) as shown in Figure 10. Various factors were crucial to optimize both the synthetic procedure of formation of WGA-SAM and the experimental conditions for the adhesion experiments. For instance, the adhesion was probed in the presence and the absence of bovine

dx.doi.org/10.1021/bc3004205 | *Bioconjugate Chem.* 2012, 23, 2392−2402

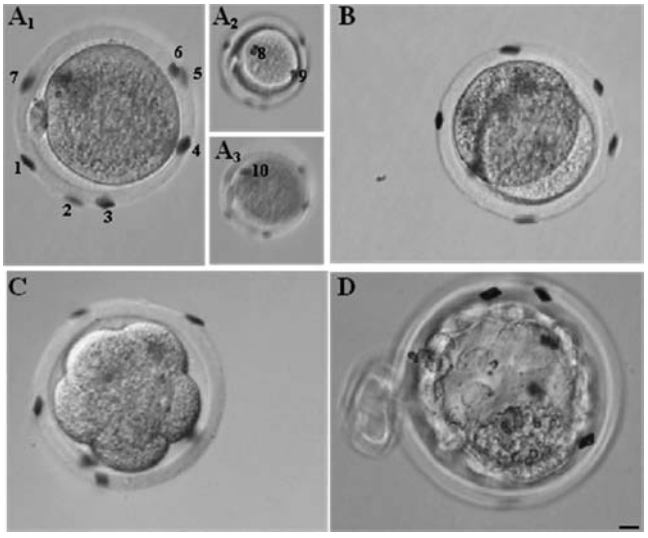

Figure 9. Mouse embryos at different development stages tagged with polysilicon barcodes biofunctionalized as WGA-SAM: one-cell (A1–3), two-cell (B), morula (C), and blastocyst (D) stages. Three different focal planes are shown for each embryo, and the numbers in the images indicate the total number of barcodes attached to the ZP.

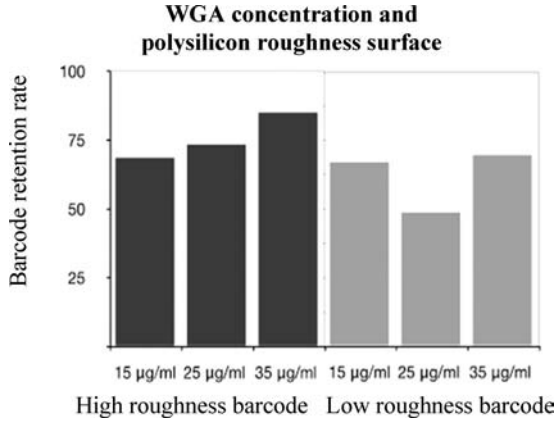

Figure 10. Influence of WGA concentration and surface roughness of polysilicon barcodes biofunctionalized as WGA-SAM on their retention rates after adhesion to mouse embryos and culture for 96 h.

serum albumin (BSA) in the embryo manipulation and culture medium. The barcode's adhesion improves notably in the absence of BSA, since BSA could interact with the active areas of WGA and minimize its interaction with the carbohydrates at the ZP.

More importantly, protein concentration and polysilicon surface roughness also proved to be crucial for successful adhesion, as shown in Table S1 (in Supporting Information) and Figure 10. Higher roughness barcodes (after 40 min etching) functionalized as CHO-SAM, were used to assess whether protein concentration influenced the biofunctionalization efficiency. At least 6 experiments for each concentration were done. Embryo development was not affected when WGA concentration was increased (see Table S1 in Supporting Information), as for all concentrations tested, blastocyst rates were equivalent to that of the control group (88.5%). These results are extremely important, because they proved the efficiency of the biofunctionality, since WGA would be toxic for the embryos in solution in the culture medium.[52] Regarding adhesion rates, it was observed that the greater the WGA concentration used for barcode biofunctionalization, the higher the barcode retention rate achieved. Thus, the highest retention rate after 96 h of culture was obtained with a WGA concentration of 35 μg/mL (84.9%), which was significantly higher than for 25 μg/mL (73.4%) and 15 μg/mL (68.6%) concentrations (Figure 10, and Table S1 in Supporting Information).

Lower roughness barcodes (after 15 min etching) were functionalized with the same concentrations of WGA as higher roughness barcodes. In this case, at least two experiments were performed for each concentration. Again, no significant differences in embryo development were observed at any concentration when compared with the embryo control group (90.0%) (see Table S1 in Supporting Information). In contrast to the results with higher roughness barcodes, no differences were observed in barcode retention rates among the three WGA concentrations used. Thus, the same retention rate was achieved with the lowest (15 μg/mL: 67.2%) and the highest (35 μg/mL: 69.8%) WGA concentration used. The comparison between higher roughness and lower roughness barcodes showed that retention rates of higher roughness barcodes biofunctionalized with 25 and 35 μg/mL of WGA were significantly higher than those of lower roughness barcodes biofunctionalized at the same concentrations (Figure 10 and Table S1 in Supporting Information), i.e., higher surface roughness is a positive factor influencing biofunctionalization.

Finally, once these chemically and biologically different experimental conditions had been explored, optimization of the biofunctionalization protocol—using higher roughness WGA-SAM barcodes biofunctionalized with a concentration of WGA of 35 μg/mL in sterile PBS followed by chemical blocking—leads to improved adhesion of these microtools, showing excellent retention rates (95.6%) on mouse embryos (n = 126) and higher viability up to the blastocyst stage (94%), proving the efficiency of the biofunctionalization process.

■ CONCLUSION

Microtools selected for cell tagging have been successfully prepared. These microtools are based on polysilicon surfaces, microfabricated enclosing a characteristic pattern code, enabling individual external cell identification. A cell adhesion related protein (WGA) was covalently immobilized on these surfaces using a SAM as a linker between the WGA and the silicon material. Different chemical parameters have been explored to optimize both the chemical functionalization and relate it to the level of cell adhesion, and factors like the material roughness and protein concentration probed to be relevant for embryo ZP adhesion. The best conditions were found to be using high roughness barcodes functionalized with an aldehyde terminated silane (TESUD) in absolute ethanol for 3 h, followed by treatment with 35 μg/mL of WGA in PBS, which lead to microtools showing adhesion to mouse embryos, with a retention rate of ca. 96% after 96 h of embryo culture, and viability of ca. 94% for a total of 126 embryos. Avoiding unspecific protein binding to the surface was also crucial, and it was achieved by using chemical blockers. All the chemical steps were characterized by contact angle measurements, TOF-SIMS, LDI-TOF MS, and AFM, and also, the immobilization of the WGA was characterized by fluorescence microscopy in the silicon barcodes and microparticles, showing a good homogeneous biofunctionalization. We can conclude that the biofunctionalization of the silicon microtools proceeds with good surface coverage, and all the characterization techniques

dx.doi.org/10.1021/bc3004205 | Bioconjugate Chem. 2012, 23, 2392–2402

used confirm the viability of the process. Furthermore, biofunctionalization of these polysilicon barcodes has driven their excellent adhesion ability to the embryo ZP, with extremely successful retention rates and high embryo survival.

The highly demanding requirements of these microtools destined to tag cells and embryos—such as reproducibility of results, efficacy of adhesion, nontoxicity, stability, and ease of readability—emerge in our design, which proves successful thanks to the careful selection of their components, and to a combination of precise microfabrication and chemical biofunctionalization methodologies, and a thorough chemical and biological characterization. With our work, we set up the biofunctionalization methodology to develop an embryo tagging procedure potentially useful in assisted reproduction protocols.

■ ASSOCIATED CONTENT

Supporting Information

(1) Schematic symbology of the 256 different barcodes (Figure S1); (2) LDI-TOF MS spectrum of CHO-SAM (Figure S2); (3) AFM topographic images of (a) a polysilicon structured wafer; and 3D images representing polysilicon microparticles on the wafer: (b) 0.1 μm thickness; (c) profile diagram of a 0.1 μm thickness polysilicon microparticle on the wafer (Figure S3); (4) AFM phase and 3D images of a polysilicon particle on a wafer: (a) unfunctionalized and (b) after functionalization as CHO-SAM (Figure S4); (5) AFM measurements of roughness of (a) a barcode on a silicon wafer, (b) a released barcode, (c) a released hydroxylated barcode, and (d) a released hydroxylated and biofunctionalized barcode. The graphic (e) corresponds to the roughness value tendency vs exposure time of the devices in vapors of HF 49%. Finally, barcode SEM images correspond to (f) 15 min etching time and (g) 40 min etching time (Figure S5); (6) A representative barcode counting diagram (a) before and (b) after biofunctionalization process on WGA-SAM. Counting includes particles with a diameter size between 2 and 10 μm (Figure S6); (7) Protocol for quantification of the aldehyde residues on CHO-SAM (Scheme S1); (8) WGA concentration and surface roughness influence on the adhesion of biofunctionalized WGA-SAM barcodes to the ZP of mouse embryos (Table S1). This material is available free of charge via the Internet at http://pubs.acs.org.

■ AUTHOR INFORMATION

Corresponding Author

*E-mail: mlperez@ub.edu. Telephone: (+34) 934035849. Fax: (+34) 934024539.

Notes

The authors declare no competing financial interest.

■ ACKNOWLEDGMENTS

Financial support from the Ministerio de Ciencia e Innovación (MICINN) (projects TEC2008-06883 and TEC2011-29140) and the Generalitat de Catalunya (2009SGR158, 2009SGR00282) is acknowledged. O.P. and S.D. thank the MICINN for predoctoral grants. S.N. thanks the Universitat Autònoma de Barcelona for a predoctoral grant.

■ DEDICATION

Dedicated to Prof. Fraser Stoddart, on the occasion of his 70th birthday.

■ REFERENCES

(1) Siqueira, J. R., Jr., Caseli, L., Crespilho, F. N., Zucolotto, V., and Oliveira, O. N., Jr. (2010) Immobilization of biomolecules on nanostructured films for biosensing. *Biosens. Bioelectron. 25*, 1254–1263.

(2) Samanta, D., and Sarkar, A. (2011) Immobilization of bio-macromolecules on self-assembled monolayers: methods and sensors applications. *Chem. Soc. Rev. 40*, 2567–2592.

(3) Cheng, F., Shang, J., and Ratner, D. (2011) A versatile method for functionalizing surfaces with bioactive glycans. *Bioconjugate Chem. 22*, 50–57.

(4) Wang, H., Zhang, Y., Yuan, X., Chen, Y., and Yan, M. (2011) A universal protocol for photochemical covalent immobilization of intact carbohydrates for the preparation of carbohydrate microarrays. *Bioconjugate Chem. 22*, 26–32.

(5) Wong, L. S., Khan, F., and Micklefield, J. (2009) Selective covalent protein immobilization: strategies and applications. *Chem. Rev. 109*, 4025–4053.

(6) Köhn, M. J. (2009) Immobilization strategies for small molecule, peptide and protein microarrays. *Pept. Sci. 15*, 393–397.

(7) Soloducho, J., Cabaj, J., and Swist, A. (2009) Structure and sensor properties of thin ordered solid films. *Sensors 9*, 7733–7752.

(8) Frasconi, M., Mazzei, F., and Ferri, T. (2010) Protein immobilization at gold-thiol surfaces and potential for biosensing. *Anal. Bioanal. Chem. 398*, 1545–1564.

(9) Ekblad, T., and Liedberg, B. (2010) Protein adsorption and surface patterning. *Curr. Opin. Colloid Interface Sci. 15*, 499–509.

(10) Früh, V., Ijzerman, A. P., and Siegal, G. (2011) How to catch a membrane protein in action: a review of functional membrane protein immobilization strategies and their application. *Chem. Rev. 111*, 640–656.

(11) Dettin, M., Muncan, N., Bugatti, A., Grezzo, F., Danesin, R., and Rusnati, M. (2011) Chemoselective surface immobilization of proteins through a cleavable peptide. *Bioconjugate Chem. 22*, 1753–1757.

(12) Ulman, A. (1996) Formation and structure of self-assembled monolayers. *Chem. Rev. 96*, 1533–1554.

(13) Wink, T., van Zuilen, S. J., Bult, A., and van Bennekom, W. P. (1997) Self-asembled monolayers for biosensors. *Analyst 122*, 43–50.

(14) Hodneland, C. D., Lee, Y., Min, D., and Mrksich, M. (2002) Selective immobilization of proteins to self-assembled monolayers presenting active site-directed capture ligands. *Proc. Natl. Acad. Sci. U.S.A. 99*, 5048–5052.

(15) Chaki, N. K., and Vijayamohanan, K. (2002) Self-assembled monolayers as a tunable platform for biosensors applications. *Biosens. Bioelectron 17*, 1–12.

(16) Love, J. C., Estroff, L. A., Kriebel, J. K., Nuzzo, R., and Whitesides, G. M. (2005) Self-assembled monolayers of thiolates on metals as a form of nanotechnology. *Chem. Rev. 105*, 1103–1170.

(17) Haensch, C., Hoeppener, S., and Schubert, U. (2010) Chemical modification of self-assembled silane based monolayers by surfaces reactions. *Chem. Soc. Rev. 39*, 2323–2334.

(18) Gooding, J. J., and Ciampi, S. (2011) The molecular level modification of surfaces: from self-assembled monolayers to complex molecular assemblies. *Chem. Soc. Rev. 40*, 2704–2718.

(19) George, N., Pick, H., Vogel, H., Johnsson, N., and Johnsson, K. (2004) Specific labeling of cell surface proteins with chemically diverse compounds. *J. Am. Chem. Soc. 126*, 8896–8897.

(20) Rogers, W. J., Meyer, C. H., and Kramer, C. M. (2006) Technology insight: in vivo cell tracking by use of MRI. *Nat. Clin. Pract. Card. 3*, 554–562.

(21) Gao, J., and Xu, B. (2009) Applications of nanomaterials inside cells. *Nano Today 4*, 37–51.

(22) Han, M., Gao, X., Su, J. Z., and Nie, S. (2001) Quantum-dot-tagged microbeads for multiplexed optical coding of biomolecules. *Nat. Biotechnol. 19*, 631–635.

(23) Nicewarrner-Peña, S., Griffith-Freeman, R., Reiss, B. D., He, L., Peña, D. J., Walton, I. D., Cromer, R., Keating, C. D., and Natan, M. J. (2001) Submicrometer metallic barcodes. *Science 294*, 137–141.

(24) Wilhelm, C., and Gazeau, F. (2008) Universal cell labelling with anionic magnetic nanoparticles. *Biomaterials 29*, 3161−3174.
(25) Faklaris, O., Garrot, D., Joshi, V., Druon, F., Boudou, J., Sauvage, T., Georges, P., Curmi, P. A., and Treussart, F. (2008) Detection of single photoluminescent diamond nanoparticles in cells study of the internalization pathway. *Small 4*, 2236−2239.
(26) Weibel, D. B., DiLuzio, W. R., and Whitesides, G. M. (2007) Microfabrication meets microbiology. *Nat. Rev. Microbiol. 5*, 209−218.
(27) Fernández-Rosas, E., Gómez, R., Ibáñez, E., Barrios, L., Duch, M., Esteve, J., Nogués, C., and Plaza, J. A. (2009) Intracellular polysilicon barcodes for cell tracking. *Small 5*, 2433−2439.
(28) Fernández-Rosas, E., Baldi, A., Ibáñez, E., Barrios, L., Novo, S., Esteve, J., Plaza, J. A., Duch, M., Gómez, R., Castell, O., Nogués, C., and Fernández-Sánchez, C. (2011) Chemical functionalization of polysilicon microparticles for single cells. *Langmuir 27*, 8302−8308.
(29) Novo, S., Barrios, L., Santaló, J., Gómez-Martínez, R., Duch, M., Esteve, J., Plaza, J. A., Nogués, C., and Ibáñez, E. (2011) A novel embryo identification system by direct tagging of mouse embryos using silicon-based barcodes. *Hum. Reprod. 26*, 96−105.
(30) Nilsson, C. L. (2003) Lectins: Proteins that interpret the sugar code. *Anal. Chem. 75*, 348−352.
(31) Sharon, N., and Lis, H. (2004) History of lectins: from hemagglutinins to biological recognition. *Glycobiology 14*, 53R−62R.
(32) Nagata, Y., and Burguer, M. M. (1974) Wheat germ agglutinin: molecular characteristics and specificity for sugar binding. *J. Biol. Chem. 249*, 3116−3122.
(33) Lee, J. E., Mirza, S. P., Didier, D. N., Scalf, M., Olivier, M., Greene, A. S., and Smith, L. M. (2008) Identification of cell surface markers to differentiate rat endothelial and fibroblasts cells using lectin arrays and LC-ESI-MS/MS. *Anal. Chem. 80*, 8269−8275.
(34) Xie, H., Xie, M., Zhang, Z., Long, Y., Liu, X., Tang, M., Pang, D., Tan, Z., Dickinson, C., and Zhou, W. (2007) Wheat germ agglutinin-modified trifunctional nanospheres for cell recognition. *Bioconjugate Chem. 18*, 1749−1755.
(35) Touhami, A., Hoffman, B., Vasella, A., Denis, F. A., and Dufrêne, Y. F. (2003) Probing specific lectin-carbohydrate interactions using atomic force microscopy imaging and force measurements. *Langmuir 19*, 1745−1751.
(36) Lienemann, M., Paananen, A., Boer, H., de la Fuente, J. M., García, I., Penadés, S., and Koivula, A. (2009) *Glycobiology 19*, 633−643.
(37) Zhang, X., and Yadavalli, V. K. (2009) Functionalized self-assembled monolayers for measuring single molecule lectin carbohydrate interactions. *Anal. Chim. Acta 649*, 1−7.
(38) Biggers, J. D., McGinnis, L. K., and Raffin, M. (2000) Amino acids and preimplantation development of the mouse in protein-free potassium simplex optimized medium. *Biol. Reprod. 63*, 281−293.
(39) Rozkiewicz, D. I., Kraan, Y., Werten, M., de Wolf, F. A., Subramaniam, V., Ravoo, B. J., and Reinhoudt, D. N. (2006) Covalent microcontact printing of proteins for cell patterning. *Chem.—Eur. J. 12*, 6290−6297.
(40) Lee, J. E., Didier, D. N., Lockett, M. R., Scalf, M., Green, A. S., Olivier, M., and Smith, L. M. (2007) Characterization of vascular endothelial growth factor receptors on the endothelial cell surface during hypoxia using whole cell binding arrays. *Anal. Biochem. 369*, 241−247.
(41) Hozumi, A., Taoda, H., Saito, T., and Shirahata, N. (2008) Formation of aldehyde- and carboxy- terminated self-assembled monolayer on SiO_2 surfaces. *Surf. Interface Anal. 40*, 408−411.
(42) Arima, Y., and Iwata, H. (2007) Effects of surface functional groups on protein adsorption and subsequent cell adhesion using self-assembled monolayers. *J. Mater. Chem 17*, 4079−4087.
(43) Förch, R., Schönherr, H., and Jenkins, A. T. A. (Eds) (2009) Contact Angle Goniometry, *Surface Design: Applications in Bioscience and Nanotechnology*, pp 471−473, Appendix C, Wiley-VCH Verlag GmbH & Co. KGaA, Weinheim, Germany.
(44) Park, J. G., Prasad, Y. N., Kang, Y., Kim, I., Hong, Y., Han, S., Yun, S., Yoon, B., and Busnaina, N. (2009) Effects of polysilicon wettability on polishing and organic defects during CMP. *J. Electrochem. Soc. 156*, 869−873.
(45) Wagner, M. S., and Castner, D. G. (2001) Characterization of adsorbed proteins films by Time-of-flight secondary ion mass spectrometry with principal components analysis. *Langmuir 17*, 4649−4660.
(46) Wang, P., Hadjar, O., Gassman, P. L., and Laskin, J. (2008) Reactive landing of peptide ions on self-assembled monolayer surfaces: an alternative approach for covalent immobilization of peptides on surfaces. *Phys. Chem. Chem. Phys. 10*, 1512−1522.
(47) Su, J., and Mrksich, M. (2003) Using MALDI-TOF mass spectrometry to characterize interfacial reactions on self-assembled monolayers. *Langmuir 19*, 4867−4870.
(48) Hsieh, S., Ku, H. Y., Ke, Y. T., and Wu, H. F. (2007) Self-assembled monolayer-modified silicon substrate to enhance the sensitivity of peptide detection for AP-MALDI mass spectrometry. *J. Mass Spectrom. 42*, 1628−1636.
(49) AFM observation was attempted on WGA-SAM formed in situ under liquid conditions, but the results were unclear.
(50) Wei, S., Vaidya, B., Patel, A. B., Soper, A., and McCarley, R. L. (2005) Photochemically patterned poly(methyl methacrylate) surfaces used in the fabrication of microanalytical devices. *J. Phys. Chem. B 109*, 16988−16996.
(51) All the images were treated with the *Image J* program (http://rsbweb.nih.gov/ij).
(52) Menino, A. R., Wiliams, J. S., and Gardiner, C. S. (1989) Development of mouse embryos in media containing lectins. *Theriogenology 31*, 821−834.

Supporting Information

Efficient biofunctionalization of polysilicon barcodes for adhesion to the zona pellucida of mouse embryos[a]

Oriol Penon,[†] Sergi Novo,[‡] Sara Durán,[§] Elena Ibañez,[‡] Carme Nogués,[‡] Josep Samitier,[□] Marta Duch,[§] José Antonio Plaza,[§] and Lluïsa Pérez-García[†]*

[†] Department of Pharmacology and Therapeutical Chemistry and Institute of Nanoscience and Nanotechnology UB (IN2UB), Universitat de Barcelona, Avda. Joan XXIII s/n, 08028 Barcelona, Spain

[‡] Department of Cellular Biology, Physiology and Immunology, Universitat Autònoma de Barcelona, 08193 Bellaterra, Barcelona, Spain

[§] Institute of Microelectronics of Barcelona, IMB-CNM (CSIC), Campus UAB, 08193 Bellaterra, Barcelona, Spain

[□]Institute for Bioengineering of Catalonia (IBEC), Baldiri Reixac 10-12, 08028 Barcelona, Spain and Department of Electronics, Universitat de Barcelona, c/ Martí i Franquès 1, 08028 Barcelona, Spain

[a]Dedicated to Prof. Fraser Stoddart, in the occasion of his 70th birthday

Corresponding Author

*E-mail: mlperez@ub.edu. Telephone: (+34) 934035849. Fax: (+34) 934024539

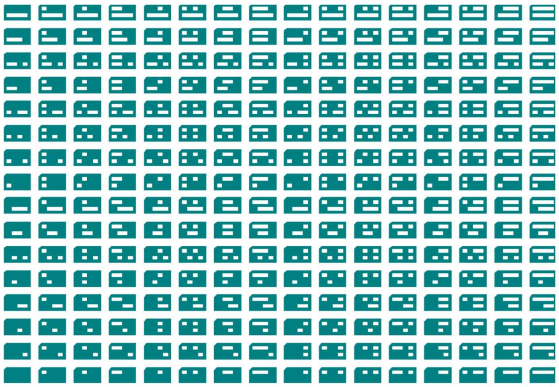

Figure S1. Schematic symbology of the 256 different barcodes.

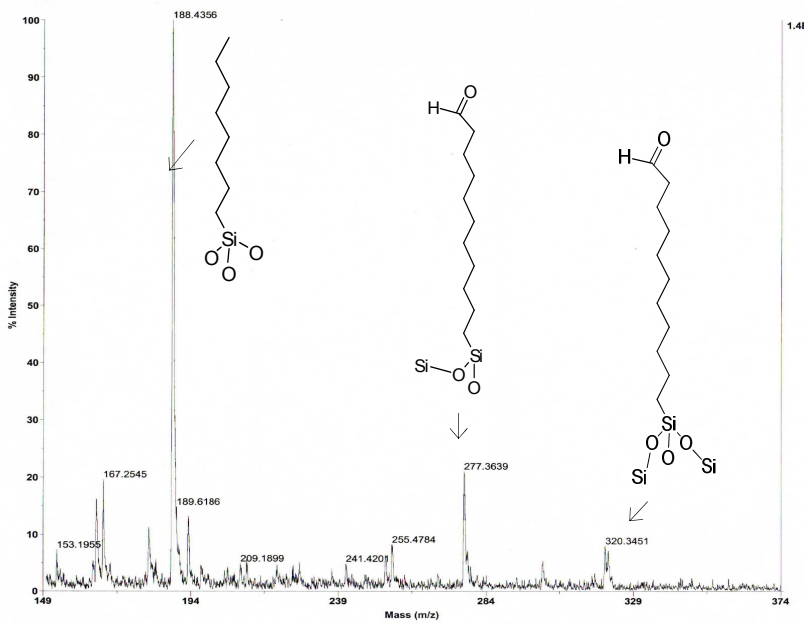

Figure S2. LDI-TOF MS spectrum of CHO-SAM.

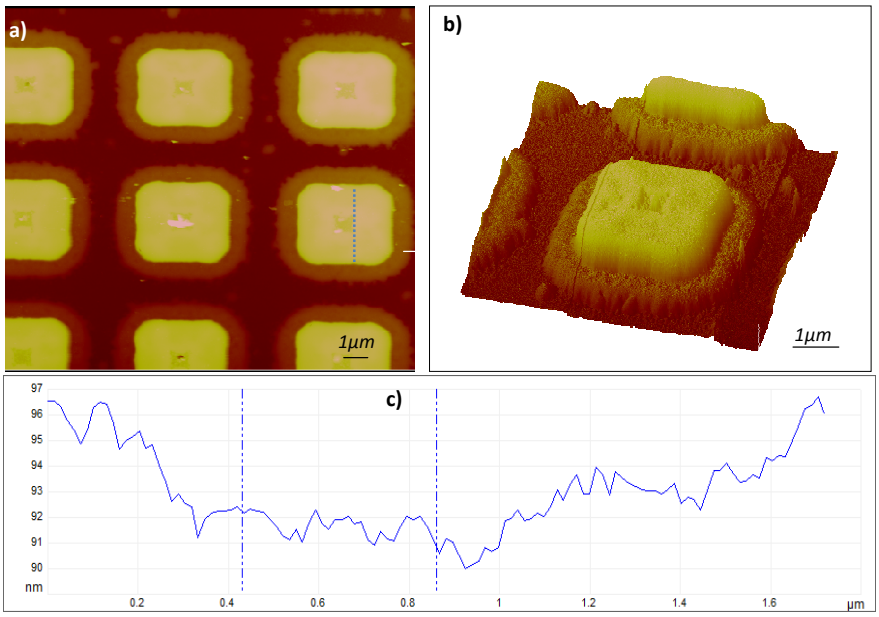

Figure S3. AFM topographic images of a) a polysilicon structured wafer; and b) 3D images representing polysilicon microparticles on the wafer; c) profile diagram of a 0.1 µm thickness polysilicon microparticle on the wafer.

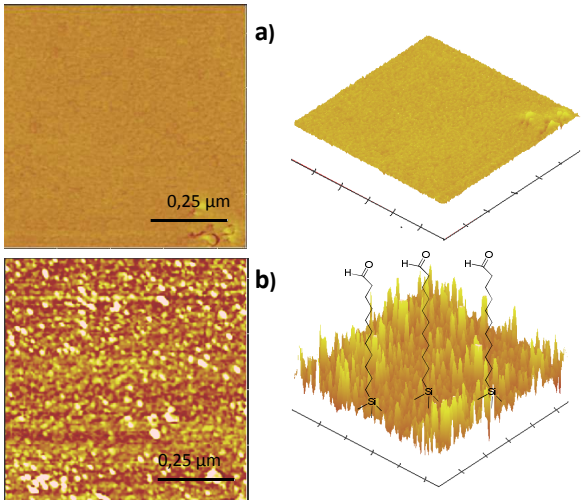

Figure S4. AFM phase and 3D images of a polysilicon particle on a wafer: a) unfunctionalized and b) after functionalization as CHO-SAM.

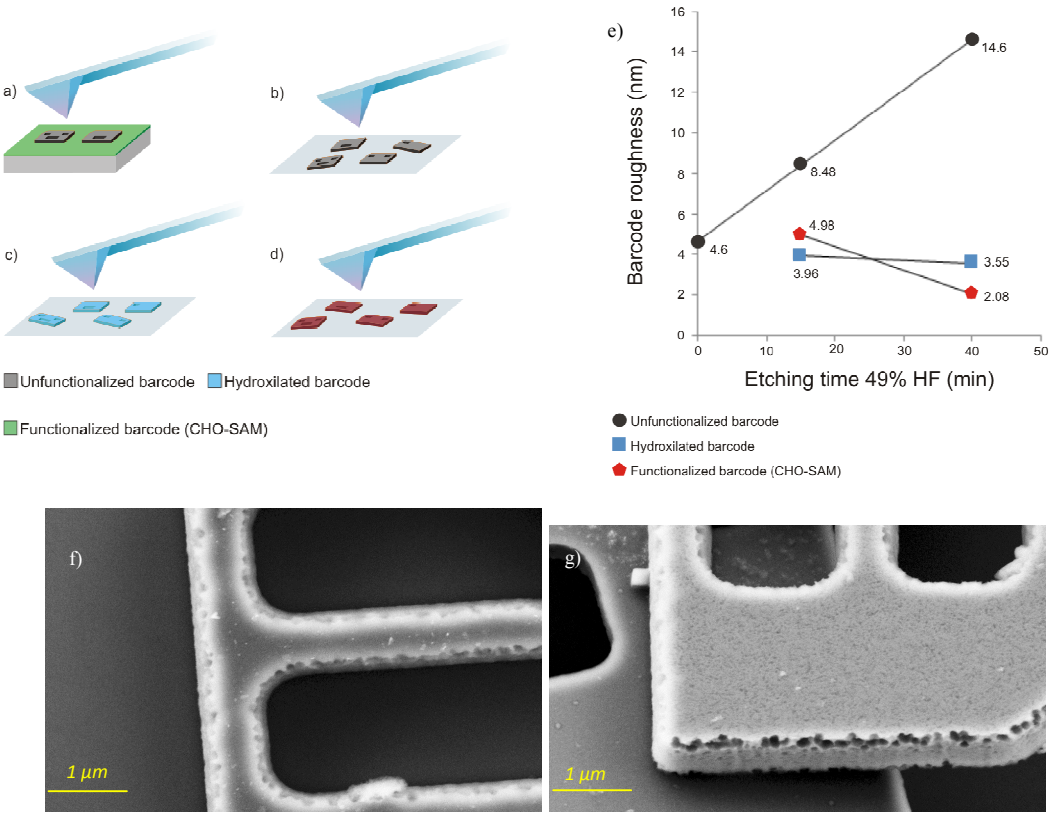

Figure S5. AFM measurements of roughness of a) a barcode on a silicon wafer, b) a released barcode, c) a released hydroxylated barcode and a d) released hydroxylated and biofunctionalized barcode. The graphic e) corresponds to the roughness values tendence vs. exposure time of the devices in vapors of HF 49%. Finally, barcode SEM images correspond to f) 15 min etching time and g) 40 min etching time.

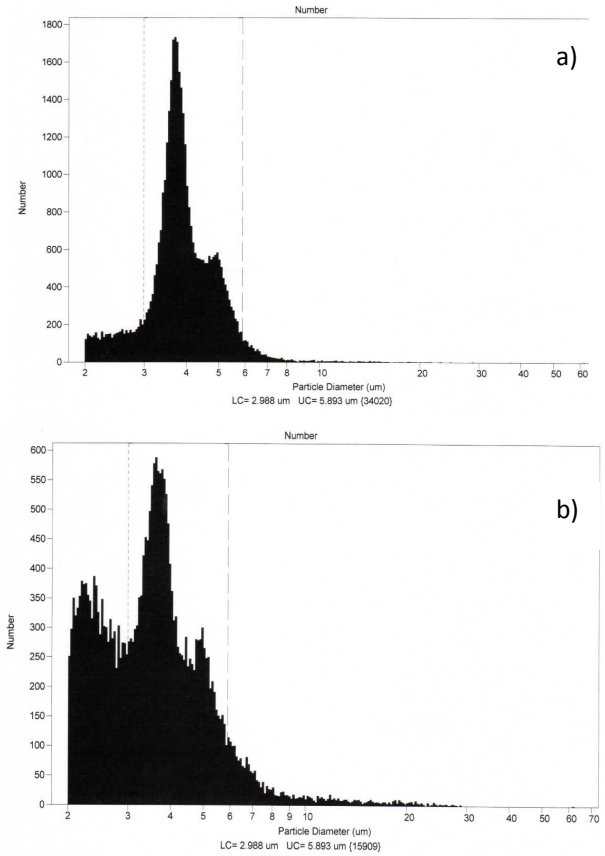

Figure S6. A representative barcode counting diagram a) before and b) after biofunctionalization process on WGA-SAM. Counting includes particles with a diameter size between 2 and 10 μm.

Scheme S1. Protocol for quantification of the aldehyde residues on CHO-SAM.

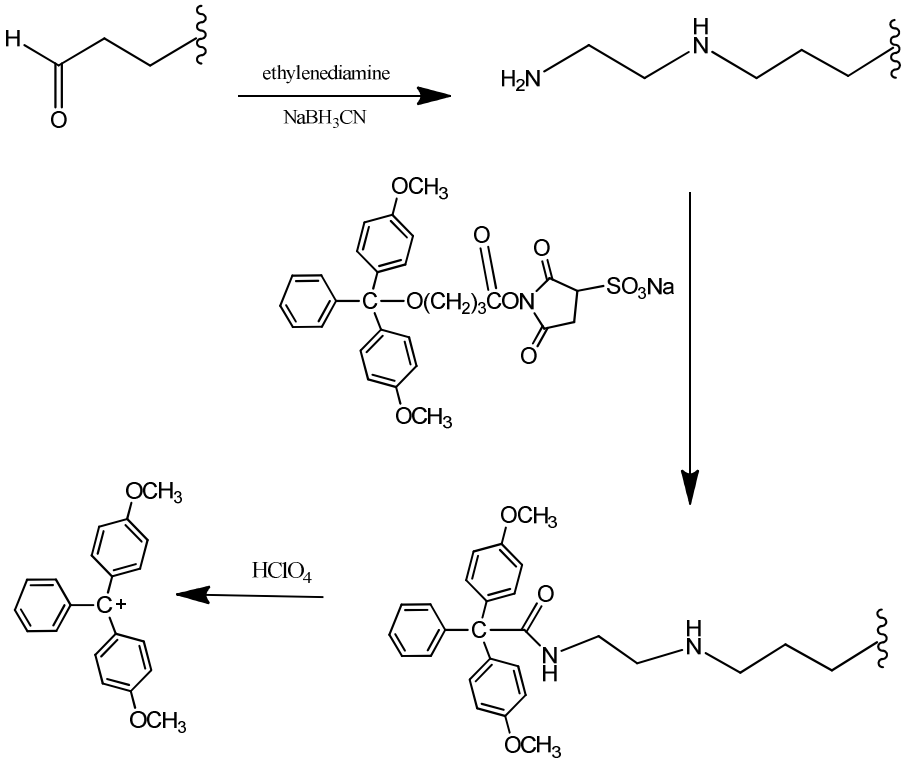

Table S1. WGA concentration and surface roughness influence on the adhesion of biofunctionalized WGA-SAM barcodes to the ZP of mouse embryos.

WGA concentration (μg/mL)	Barcode Roughness	Number of Experiments	Number of embryos (n)	Blastocyst rate (%)	Retention rate (%)
None (Control)		14	130	88.5%	
15	high	6	140	88.6%	68.6%[a]
25	high	8	150	92.0%	73.4%[a]
35	high	13	265	89.1%	84.9%[b]
None (Control)		6	60	90.0%	
15	low	2	40	86.0%	67.2%[a]
25	low	2	40	80.0%	48.8%[c]
35	low	6	90	92.2%	69.8%[a]

[a-c] Different superscript denote significant differences between rows of the same column ($P < 0.05$).

Bioconjugate Chemistry

Article

pubs.acs.org/bc

Design, Synthesis, and X-ray Analysis of a Glycoconjugate Bound to *Mycobacterium tuberculosis* Antigen 85C

Diaa A. Ibrahim,[†] Julie Boucau,[‡] Daniel H. Lajiness,[‡] Sri Kumar Veleti,[‡] Kevin R. Trabbic,[‡] Samuel S. Adams,[‡] Donald R. Ronning,*[,‡] and Steven J. Sucheck*[,‡]

[†]National Organization for Drug Control & Research, Cairo, Gizaa, Egypt

[‡]Department of Chemistry, The University of Toledo, 2801 W. Bancroft Street, Toledo, Ohio 43606, United States

Supporting Information

ABSTRACT: Tuberculosis (TB) is a global health threat with nearly 500 000 new cases of multidrug-resistant TB estimated to occur every year, so new drugs are desperately needed. A number of current antimycobacterial drugs work by interfering with the biosynthesis of key components of the mycolylarabinogalactan (mAG). In light of this observation, other enzymes involved in the synthesis of the mAG should also serve as targets for antimycobacterial drug development. One potential target is the Antigen 85 (Ag85) complex, a family of mycolyltransferases that are responsible for the transfer of mycolic acids from trehalose monomycolate (TMM) to the arabinogalactan. Virtual thiophenyl−arabinoside conjugates were docked to antigen Ag85C (PDB code: 1va5) using Glide. Compounds with good docking scores were synthesized by a Gewald synthesis followed by linking to 5-thioarabinofuranosides. The resulting thiophenyl-thioarabinofuranosides were assayed for inhibition of mycoyltransferase activity using a 4-methylumbelliferyl butyrate fluorescence assay. The conjugates showed K_i values ranging from 18.2 to 71.0 μM. The most potent inhibitor was soaked into crystals of *Mycobacterium tuberculosis* antigen 85C and the structure of the complex determined. The X-ray structure shows the compound bound within the active site of the enzyme with the thiophene moiety positioned in the putative α-chain binding site of TMM and the arabinofuranoside moiety within the known carbohydrate-binding site as exhibited for the Ag85B-trehalose crystal structure. Unexpectedly, no specific hydrogen bonding interactions are being formed between the arabinofuranoside and the carbohydrate-binding site of the active site suggesting that the binding of the arabinoside within this structure is driven by shape complementarily between the arabinosyl moiety and the carbohydrate binding site.

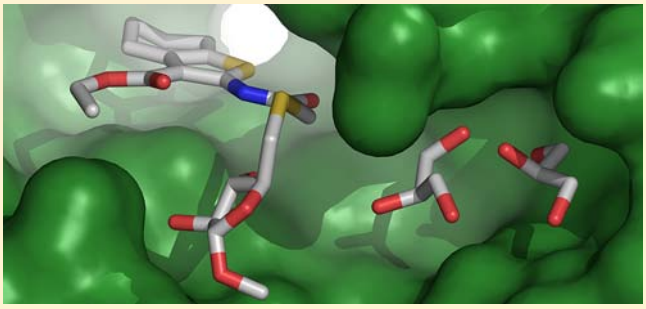

INTRODUCTION

Tuberculosis (TB) is a global health threat with nearly 500 000 new cases of multidrug-resistant TB (MDF-TB) estimated to occur every year. More concerning is that, since 2006, strains of extensively drug-resistant TB (XDR-TB), estimated to be 4% of MDR-TB, have been reported in over 50 countries. It is also estimated that 30−40% of XDR-TB is untreatable with the current antitubercular drug repertoire.[1] On this basis, it is clear that new approaches to treating the disease are needed. Several of the current drugs used to treat TB work by interfering with mycobacterial cell wall synthesis.[2] Contained within the structure of the cell is a unique macromolecular structure called the mycolylarabinogalactan (mAG), which is composed of the arabinogalactan (AG) and mycolic acids.[3] The structure serves as a protective barrier for the organism and limits the diffusion of hydrophobic and hydrophilic drugs.[4]

A number of antimycobacterial drugs, e.g., ethambutol,[5,6] isoniazid,[7] and ethionamide,[8] work by interfering with the biosynthesis of key components of the mAG. In light of this observation, other enzymes involved in the synthesis of the mAG may also serve as targets for antimycobacterial drug development. One potential target that has attracted some attention is the Antigen 85 complex (Ag85). Ag85 represents a family (Ag85A, Ag85B, and Ag85C) of homologous mycolyltransferases that are responsible for the synthesis of trehalose-6,6′-dimycolate (TDM) from trehalose-6-monomycolate (TMM)[9−12] and for transfer of mycolic acids from TMM to the arabinogalactan (AG).[13,14] Results from inhibitor studies suggest that Ag85 is essential for bacterial viability. For example, 6-azido-6-deoxytrehalose, a known inhibitor of Ag85s, has been shown to completely inhibit the growth of *Mycobacterium aurum* a surrogate for *Mycobacterium tuberculosis*.[15] Other studies which support the essentiality of Ag85 include the use of Ag85-specific antisense oligonucleotides, which were shown to reduce *Mycobacterium tuberculosis* growth as well significantly enhance bacterial sensitivity to isoniazid.[16,17] Similarly, an Ag85A knockout strain of *Mycobacterium smegmatis* exhibits increased sensitivity to drugs that target peptidoglycan biosynthesis, i.e., vancomycin and imipenem.[18]

Received: August 7, 2012
Revised: November 7, 2012
Published: November 29, 2012

ACS Publications © 2012 American Chemical Society

dx.doi.org/10.1021/bc3004342 | *Bioconjugate Chem.* 2012, 23, 2403−2416

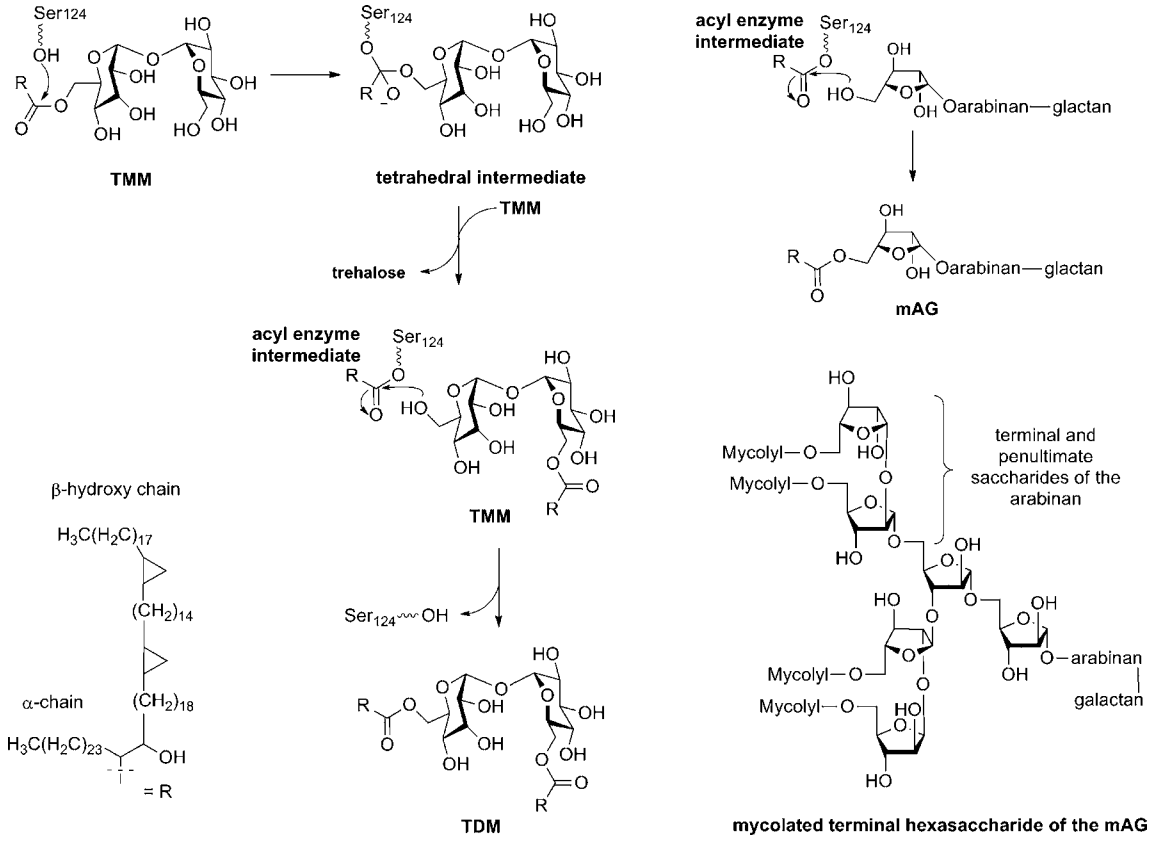

Figure 1. Proposed mechanism for Ag85-mediated mycolyl transfer resulting in the formation of mAG and TDM.

A variety of putative Ag85 inhibitors have been described. For example, alkyl phosphonates[19] expected to mimic the tetrahedral intermediate of Ag85s were shown to be active against *Mycobacterium avium* and inhibited mycolyltransferase activity.[20] Other examples include trehalose-based substrate analogues that contain aliphatic chains which showed activity against *Mycobacterium smegmatis*,[21] and related compounds consisting of 6,6′-bis(sulfonamido) and *N*,*N*′-dialkylamino derivatives active against *Mycobacterium tuberculosis* and *Mycobacterium avium*.[22] Further, a fluorophosphonate derivative of trehalose was shown to form a covalent adduct with the active site serine of *M. tuberculosis* Ag85C.[23] More recently, we have found arabinofuranoside-based substrate analogues containing *S*-alkyl chains (Figure 2) that inhibited the growth of *Mycobacterium smegmatis*;[24−26] however, the latter compounds did not inhibit acyltransferase activity using our recently developed colorimetric acyltransferase assay.[27] On the other hand, α-ketoester derivatives of arabinofuranosides showed weak (mM) inhibitory activity against Ag85C but were inactive in cell-based assays.[28] In light of this data, we thought it was necessary to identify more potent Ag85 inhibitors.

The crystal structures of secreted forms of Ag85A,[29] Ag85B,[30,31] and Ag85C[29,32,33] from *Mycobacterium tuberculosis* have all been determined. The structures reveal an α/β-hydrolase fold, with a catalytic triad formed by Ser124, Glu228, and His260 (Ag85C numbering). The carbohydrate binding site is highly conserved between the three acyltransferases. Near the catalytic triad is a binding site for the carbohydrate moiety with a negative electrostatic potential, as well as a hydrophobic tunnel, well-suited to accommodate the shorter α-branch of the mycolyl moiety. Additionally, a nearby shallow cleft possessing hydrophobic character may bind the longer β-branch of the mycolyl moiety. However, it seems more likely that the β-branch of the mycolyl moiety will remain embedded in the mycobacterial outer membrane during the mycolyltransfer reaction. According to the proposed mechanism of the catalytic mycolyl transfer reaction, Ser124 attacks the carboxyl carbon of TMM to give a mycolyl-enzyme intermediate and free trehalose. In the next step, the 6-OH group of a second TMM molecule attacks the carboxylate carbon of the acyl-enzyme intermediate to produce TDM. Both the acylation and deacylation steps proceed via a high-energy tetrahedral transition state.[33] In the case of the formation of the mAG, the terminal and penultimate primary hydroxyl groups of arabinan serve as acyl acceptors (Figure 1). Recombinant Ag85C has been shown to catalyze this reaction in vitro.[34] On the basis of this model and the available crystallographic data, we envisioned conjugates that would contain both a rigid, drug-like moiety, that could mimic the affinity of the mycolyl moiety and could also be conjugated to a fragment of the arabinan for selectivity (Figure 2). We reasoned that the carbohydrate component of compounds could occupy the carbohydrate binding site on Ag85s and provide specificity, while a hydrophobic component could occupy the pocket leading into the tunnel proposed to accommodate the α-branch of the mycolyl moiety. The main difficulty in this endeavor would be to select an appropriate motif that could accommodate at least a portion of the putative mycolyl moiety binding site. Our interests were drawn toward 2-amino-4,5,6,7-tetrahydrobenzo-[*b*]thiopenes due to their structural similarity with ebselen (Figure 2). We have identified the latter compound as a nanomolar inhibitor of Ag85s via the screening of the NIH Clinical Collection.[35] The ability of this motif to accommodate the putative binding pocket of mycolyl moiety was confirmed

dx.doi.org/10.1021/bc3004342 | *Bioconjugate Chem.* 2012, 23, 2403−2416

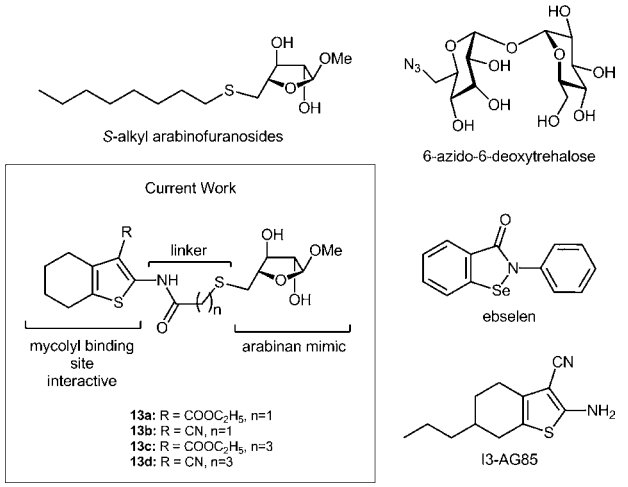

Figure 2. Design of arabinose−thiophene conjugates designed to act as inhibitors of Ag85s. Structures of an *S*-alkyl arabinofuranoside, ebselen, and I3-AG85.

by a docking strategy. Once identified, we noted that the 2-amino-4,5,6,7-tetrahydrobenzo[*b*]thiophene had been used extensively as a scaffold for enzyme inhibitor development.[36−40]

We have previously disclosed the structure of **1a** (Scheme 1).[41,42] We also note, 2-amino-4,5,6,7-tetrahydrobenzo[*b*]-thiophene-3-carbonitrile (**1b**, Scheme 1) has been independently identified as a binder of Ag85C using an ^{15}N-HSQC NMR spectroscopy-based fragment screening protocol.[43,44] The resulting thiophene was found to selectively inhibit the growth of *M. smegmatis* with an MIC of 50−100 μg/mL.[39] More recently, 2-amino-6-propyl-4,5,6,7-tetrahydro-1-benzo-thiophene-3-carbonitrile (I3-AG85, Figure 2) was identified as a second-generation inhibiter with MICs of 100 μg/mL against *M. tuberculosis*. The I3-AG85 reduced survival of *M. tuberculosis* inside macrophages and at a 100 μM concentration. The compound inhibited the growth of 7 MDR and 3 XDR *M. tuberculosis* strains at 200 μM or lower. Finally, I3-AG85 was shown to inhibit the synthesis of TDM. The generalized structures, which we explored in docking studies, are shown in Figure 2.

EXPERIMENTAL PROCEDURES

Biological Methods. *K_M Determination for 4-MUB.* Ag85C was purified as described previously.[27] All assays were performed under atmospheric pressure at 37 °C in a 384-well format on a Synergy H4 Hybrid Multi-Mode Microplate Reader (Biotek). All 4-methylumbelliferyl butyrate (4-MUB) stock solutions were made and stored in 100% DMSO at −20 °C. Excitation and emission wavelengths, 365 and 450 nm, respectively, were used to monitor the production of the 4-methylumbelliferone (4-MU) at 20 s intervals for 30 min. For each reaction, a master mix was made consisting of 600 nM Ag85C, 10 mM trehalose, and an appropriate volume of 20 mM bis(2-hydroxyethyl)amino-tris(hydroxymethyl)methane (Acros Organics) for an overall reaction volume of 50 μL. 0.5 μL of 4-MUB was added from each corresponding stock solution to reach the desired substrate concentration (25−400 μM). The data were normalized using negative controls where no Ag85C

Scheme 1. Synthesis of Tetrahydrobenzo[*b*]thiophenes[a]

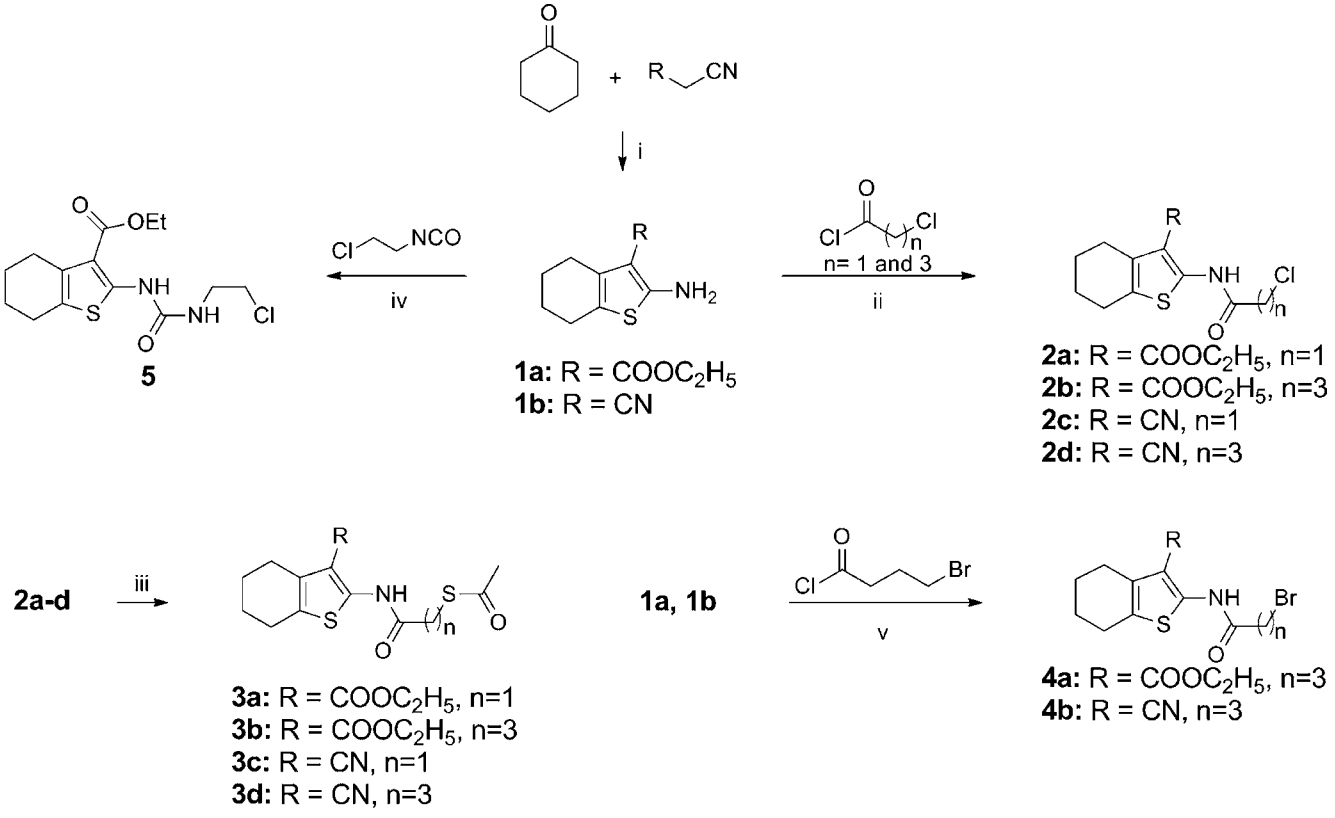

[a]Reagent and conditions: (i) sulfur, *N*-ethylmorpholine, EtOH, **1a** (27%), **1b** (33%); (ii) Et_3N, CH_2Cl_2, rt, **2a** (11%), **2b** (9%), **2c** (15%), **2d** (29%); (iii) $KSCOCH_3$, DMF, rt, **3a** (62%), **3b** (66%), **3c** (96%), **3d** (78%); (iv) toluene, 112 °C, 3 h (53%); (v) CH_2Cl_2, rt, **4a** (39%), **4b** (67%).

dx.doi.org/10.1021/bc3004342 | *Bioconjugate Chem.* 2012, 23, 2403−2416

was added. The background fluorescence from the negative control was subtracted from the intensities measured from the enzyme-catalyzed reaction. To correlate relative fluorescence intensity with the amount of product, the fluorescence of 4-MU (1−1000 nM) was determined using reaction conditions. RFU/min rates from the enzyme-catalyzed reaction were directly correlated to the amount of 4-MU produced per minute using the equation for the line of best fit, using *Microsoft Excel*. *GraphPad Prism 5* software was used to determine Michelis-Menten parameters via nonlinear regression analysis.

Inhibition Assays. All stock solutions for each compound were made and stored in 100% DMSO. Excitation and emission scans of each compound to be tested were conducted to avoid regions of overlap with 4-methylumbelliferone. The excitation and emission wavelengths used for each compound were as follows: SA-1, λ_{ex} = 320 nm, λ_{em} = 500 nm; KT-1-189, λ_{ex} = 380 nm, λ_{em} = 500 nm; DI-1, λ_{ex} = 380 nm, λ_{em} = 500 nm; DI-2, λ_{ex} = 320 nm, λ_{em} = 450 nm. All fluorescence intensities were determined at 20 s intervals over 30 min. The identities and concentrations of the reaction components used for determining the K_M were employed in these reactions as well; however, the 4-MUB concentration was held constant at 100 μM. 0.5 μL of each tested inhibitor was added from its corresponding stock solution to give final concentrations ranging from 20 μM to 320 μM. Inhibition was determined by comparing the relative rate of the reaction performed with inhibitor against a reaction that contained no inhibitor (v_i'/v_i, where v_i' and v_i are steady-state rates with and without inhibitor, respectively). The equilibrium dissociation constant (K_i) for each inhibitor was obtained by fitting the data into the equation below using *Prism*:

$$\frac{v_i'}{v_i} = \frac{K_M + [S]}{K_M + [S] + \frac{K_M[I]}{K_i}}$$

K_M is the Michelis-Menten constant for 4-MUB; [S] and [I] are the concentrations of 4-MUB and inhibitor, respectively.

Protein Crystallization, Diffraction, and Model Building. The Ag85C crystals were obtained using the hanging drop method where 1 μL of purified Ag85C was combined with 1 μL of the well solution containing 0.3 M ammonium sulfate and 0.1 M sodium acetate. These crystals were prepared for X-ray diffraction studies by adding 1 μL of a 10.7 mM solution of **13a** dissolved in an 80% v/v solution of DMSO to the 2 μL crystallization drop. These crystals were incubated at 16 °C for 2 days prior to data collection. Crystals were cryoprotected by adding glycerol directly to the drop containing the Ag85C crystal and **13a**. Diffraction data were collected at the LS-CAT beamline at the Advanced Photon Source using a wavelength of 0.978 56 Å. Data were reduced using HKL2000.[45] Molecular replacement was performed using EPMR.[46] Manual model building was performed using Coot.[47] Refinement, building inhibitor **13a**, and addition of glycerol and water molecules was performed using Phenix.[48,49] Glycerol molecules were manually fit to $F_o - F_c$ density using Coot.

Kirby-Bauer Disk Diffusion Assay. Disk diffusion assays were adapted from methods outlined by the NCCLS and Wang et al.[21,50] *Mycobacterium smegmatis* ATCC 14468 was inoculated into Middlebrook 7H9 containing 0.2% glycerol and ADC enrichment, respectively. The inocula were incubated for approximately 48 h at 37.5 °C at 160 rpm. The bacteria were plated on agar (Lennox or Middlebrook 7H10 containing 0.5% glycerol and OADC Enrichment) using sterile cotton-tipped applicators. Aliquots (10 μL) of arabinose derivatives dissolved in DMSO (20 mg/mL) and INH (500 μg/mL) were applied to 6-mm-diameter sterile paper disks. The plates were incubated at 37 °C for 24 h and then analyzed.

Synthetic Methods. *Ethyl 2-Amino-4,5,6,7-tetrahydrobenzo[b]thiophene-3-carboxylate (**1a**).* Cyclohexanone (30.0 mL, 290 mmol), sulfur (9.30 g, 290 mmol), *N*-ethylmorpholine (25.2 mL, 200 mmol), ethyl cyanoacetate (51.5 mL, 290 mmol) and ethanol (320 mL) were combined in a round-bottom flask and stirred at room temperature. After 3 h of continuous stirring, the reaction was complete and filtered to remove sulfur. The solvent was evaporated under reduced pressure. The product was extracted with 200 mL of methanol and crystallized by adding 100 mL of water to the methanol solution. The crystals were filtered and rinsed with cold 1:1 methanol−water: yield = 17.6 g (27%); mp = 117−119 °C (Lit:[51] 113−117 °C); R_f = 0.55 (4:1 hexanes−ethyl acetate); mass spectrum (ESIMS), m/z = 226 $(M+H)^+$, $C_{11}H_{106}NO_2S$ requires 226.

*2-Amino-4,5,6,7-tetrahydrobenzo[b]thiophene-3-carbonitrile (**1b**).* Cyclohexanone (30.0 mL, 290 mmol), malonitrile (19.8 g, 290 mmol), sulfur (9.30 g, 290 mmol), and 25.2 mL of *N*-ethylmorpholine (25.2 mL, 200 mmol) were combined in a round-bottom flask and stirred at room temperature. After 3 h of continuous stirring, the reaction was complete and filtered to remove sulfur. The solvent was evaporated under reduced pressure, and the product was extracted by 200 mL of methanol. The product was crystallized by adding 100 mL of water to the methanol solution. The crystals were filtered and rinsed with a solution of cold 4:1 methanol−water: yield = 17.0 g (33%); mp = 147−149 °C (Lit:[52] 147 °C); R_f = 0.35 (9:1 hexane−ethyl acetate); mass spectrum (ESIMS), m/z = 179 $(M+H)^+$, $C_9H_{11}N_2S$ requires 179.

*Ethyl 2-[(2-Chloroacetyl)amino]-4,5,6,7-tetrahydrobenzo-[b]thiophene-3-carboxylate (**2a**).*[53] Compound (**1a**) (0.500 mg, 2.2 mmol) was treated with chloroacetyl chloride (0.35 mL, 4.4 mmol) in chloroform (5 mL) and reaction was refluxed for 3 h. The reaction was analyzed for completion by TLC with 9:1 hexanes−ethyl acetate. The reaction solution was concentrated under reduced pressure and the residue crystallized from chloroform−hexanes: yield 0.231 g (34%); mp = 118−121 °C (Lit:[54] 115−117 °C); R_f = 0.49 (9:1 hexanes−ethyl acetate); ^{1}H NMR ($CDCl_3$, 400 MHz): δ1.39 (t, J = 7.2 Hz, 3H), 1.79−1.81 (m, 4H), 2.66 (t, J = 4.4 Hz, 2H), 2.79 (t, J = 5.2 Hz, 2H), 4.26 (s, 2H), 4.36 (q, J = 7.2 Hz, 2H), 12.14 (br. s, 1H, NH); mass spectrum (ESIMS), m/z = 324 $(M+Na)^+$, $C_{13}H_{16}ClNO_3S$ requires 324.

*Ethyl 2-[(4-Chlorobutanoyl)amino]-4,5,6,7-tetrahydrobenzo[b]thiophene-3-carboxylate (**2b**).* Compound **1a** (1.13 g, 5.00 mmol), triethyl amine (2.10 mL, 15.0 mmol), and dry dichloromethane (20.0 mL) were combined in a round-bottom flask. 4-Chlorobutyryl chloride (1.20 mL, 15.0 mmol) was added and the reaction stirred at room temperature for 6 h. The solution was washed with 30.0 mL of 1 M HCl followed by 30.0 mL of saturated sodium bicarbonate solution. The organic layer was dried using anhydrous sodium sulfate, filtered, and rinsed with dichloromethane. The filtrate was evaporated to dryness, and the product was purified by flash column chromatography on silica gel (30 mm × 150 mm). The column was eluted with 3:1 chloroform−hexanes and concentrated to dryness under reduced pressure. The residue was crystallized from ethyl acetate−hexanes. After cooling to room temperature, the crystals were filtered and rinsed with 20.0 mL of cold 10:1 hexanes−ethyl acetate: yield = 0.47 g

(9.4%); mp = 70−72 °C; R_f = 0.63 (3:1 chloroform−hexanes); ^{1}H NMR (DMSO-d_6, 600 MHz): δ 1.39 (t, J = 6.8 Hz, 3H), 1.54−1.57 (m, 2H), 1.79−1.80 (m, 4H), 2.23 (p, J = 7.2 Hz, 2H), 2.65−2.69 (m, 2H), 2.78 (t, J = 6 Hz, 2H), 3.65 (t, J = 6 Hz, 2H), 4.33 (q, J = 7.2 Hz, 2H), 11.35 (s, 1H); ^{13}C NMR (DMSO-d_6, 150 MHz) δ: 14.5, 23.0, 23.1, 24.5, 26.5, 27.9, 33.6, 44.3, 60.7, 111.7, 126.9, 130.9, 147.6, 166.8, 168.8; mass spectrum (HRMS), m/z = 330.0910 (M+H)$^+$, $C_{15}H_{21}ClNO_3S$ requires 330.0931.

*2-Chloro-N-(3-cyano-4,5,6,7-tetrahydrobenzo[b]thien-2-yl)acetamide (**2c**).* Compound (**1b**) (0.500 g, 2.8 mmol) was treated with chloroacetyl chloride (0.44 mL, 5.61 mmol) in chloroform (5 mL). The reaction was refluxed for 3 h. The reaction was analyzed for completion by TLC with 9:1 hexanes−ethyl acetate. The reaction solution was concentrated under reduced pressure. The residue is crystallized from chloroform−hexanes: yield 0.418 g (59%); mp = 180−183 °C (Lit:[24] 171−173 °C); R_f = 0.3 (9:1 hexanes−ethyl acetate); ^{1}H NMR ($CDCl_3$, 400 MHz); δ 1.85 (m, 4H), 2.62 (t, J = 5.6 Hz, 2H), 2.66 (t, J = 4.4 Hz, 2H), 4.28 (s, 2H), 9.38 (s, 1H); mass spectrum (ESIMS), m/z = 277 (M+Na)$^+$, $C_{11}H_{11}ClN_2OS$ requires 277.

*4-Chloro-N-(3-cyano-4,5,6,7-tetrahydrobenzo[b]thien-2-yl)butanamide (**2d**).* Compound **1b** (1.07 g, 6.00 mmol), triethyl amine (2.50 mL, 18.0 mmol), and dry dichloromethane (20 mL) were combined in a round-bottom flask. The reaction occurred under dry nitrogen and 4-chlorobutyryl chloride (2.03 mL, 18.0 mmol) was added. The reaction was analyzed for completion by TLC using 3:1 hexanes−ethyl acetate. The solution was washed with 30 mL of 1 M HCl in a separatory funnel; the organic layer was then washed with 30 mL saturated sodium bicarbonate solution. The organic layer was dried using anhydrous sodium sulfate, filtered, and rinsed with dichloromethane. The product was concentrated to dryness under reduced pressure. The product was decolorized using carbon decolorizing charcoal in ethyl acetate solution. The solution was filtered, concentrated, and crystallized by chloroform and hexanes. Crystals were rinsed and filtered with cold 1:1 chloroform−hexanes: yield = 1.48 g (29%); mp = 158−161 °C (Lit:[54] mp = 186−187 °C, Lit:[55] mp = 143−146 °C); R_f = 0.5 (3:1 hexanes−ethyl acetate); ^{1}H NMR ($CDCl_3$, 400 MHz): δ 1.92−1.87 (m, 2H), 2.15 (p, J = 6.4 Hz, 2H), 2.70 (t, J = 5.6 Hz, 1H), 2.77 (t, J = 4.4 Hz, 1H), 2.89 (t, J = 7.2 Hz, 2H), 3.63 (t, J = 6.0 Hz, 2H) 9.08 (s, 1H); ^{13}C NMR ($CDCl_3$, 100 MHz): δ 22.3, 23.3, 24.1(2), 32.8, 27.9, 44.4, 92.5, 115.0, 128.2, 130.9, 147.7, 169.6; mass spectrum (ESIMS), m/z = 283 (M+H)$^+$, $C_{13}H_{16}ClN_2OS$ requires 283.

*2-(Acetylthio)alkanamido-4,5,6,7-tetrahydrobenzo[b]-thiophene derivatives **3a−d**.* Potassium thioacetate (0.423 mg, 3.78 mmol) was added to a solution of 2-(chloroalkyl) aminothiophene derivatives **2a−d** (3.15 mmol) in anhydrous DMF (25 mL) under nitrogen. The reaction mixture was stirred overnight, and the solvent was removed under reduced pressure. The residue was dissolved in ethyl acetate (15 mL), and the resulting solution was washed with water. The combined organic extracts were dried over anhydrous Na_2SO_4, filtered, and the solvent was removed under reduced pressure. The residue was purified by flash chromatography to give the acetylthio derivatives **3a−d.**

*Ethyl 2-(2-(Acetylthio)acetamido)-4,5,6,7-tetrahydrobenzo[b]thiophene-3-carboxylate (**3a**).* Potassium thioacetate (43.9 mg, 0.385 mmol) was added to a conical vial containing a solution of 2-(chloroalkyl) aminothiophene derivative **2a** (100 mg, 0.332 mmol) in anhydrous DMF (5.0 mL) under nitrogen. The reaction mixture was stirred at room temperature for 20 h and diluted with ethyl acetate (10.0 mL). The resulting solution was washed with water and the combined organic extracts were dried with anhydrous sodium sulfate, filtered, and concentrated under reduced pressure. The crude product was purified by flash column chromatography on silica gel (30 mm × 150 mm) eluting with 1:4 ethyl acetate−hexanes. The solid could be crystallized from ethyl acetate−hexanes to generate yellow microcrystals: yield = 68.9 mg (62%); mp = 115−116 °C; R_f = 0.48 (1:4 ethyl acetate−hexanes); ^{1}H NMR ($CDCl_3$, 400 MHz): δ 1.38 (t, J = 7.2 Hz, 3H) 1.77−1.78 (m, 4H), 2.46 (s, 3H), 2.63−2.64 (m, 2H), 2.76−2.77 (m, 2H), 3.82 (s, 2H), 4.36 (q, J = 6.8 Hz, 2H), 11.68 (s, 1H); ^{13}C NMR ($CDCl_3$, 150 MHz): δ 14.3, 22.8, 22.9, 24.3, 26.3, 30.2, 33.0, 60.5, 112.3, 127.1, 131.0, 146.6, 164.8, 166.2, 194.0; mass spectrum (HRMS), m/z = 364.0630 (M+Na)$^+$, $C_{15}H_{19}NNaO_4S_2$ requires 364.0653.

*Ethyl 2-(4-(Acetylthio)butanamido)-4,5,6,7-tetrahydrobenzo[b]thiophene-3-carboxylate (**3b**).* The solid could be crystallized from ethyl acetate−hexanes to generate yellow needles: yield 0.78g (66%); mp = 74.0−74.5 °C; ^{1}H NMR ($CDCl_3$, 600 MHz): δ 1.38 (t, J = 7.2 Hz, 3H), 1.78 (m, 4H), 2.03 (m, 2H), 2.33 (s, 3H), 2.54 (m, 2H), 2.63 (m, 2H), 2.76 (m, 2H), 2.97 (m, 2H), 4.37 (q, J = 6.8 Hz, 2H), 11.28 (s, 1H); ^{13}C NMR ($CDCl_3$, 600 MHz): δ 14.3, 22.8, 22.9, 24.3, 25.0, 26.3, 28.3, 30.6, 35.2, 60.5, 111.4, 126.6, 130.6, 147.3, 166.6, 195.5; mass spectrum (HRMS), m/z = 392.0938 (M+Na)$^+$, $C_{17}H_{23}NNaO_4S_2$ requires 392.0966.

*4-(3-Cyano-4,5,6,7-tetrahydrobenzo[b]thiophen-2-ylamino)-4-oxoethyl ethanethioate (**3c**).* The solid could be crystallized from ethyl acetate−hexanes to generate yellow needles: yield 0.89g (96%); mp = 170.0−170.5 °C; ^{1}H NMR ($CDCl_3$, 600 MHz): δ 1.83−1.79 (m, 4H), 2.47 (s, 3H), 2.58−2.57 (m, 2H), 2.63−2.59 (m, 2H), 3.78 (s, 2H), 9.48 (s, 1H); ^{13}C NMR ($CDCl_3$, 600 MHz): δ 22.0, 23.0, 23.9, 23.9, 30.2, 32.8, 94.1, 113.9, 128.6, 131.1, 146.1, 165.1, 196.5; mass spectrum (ESIMS), m/z = 295 (M+H)$^+$, $C_{13}H_{15}N_2O_2S_2$ requires 295.

*4-(3-Cyano-4,5,6,7-tetrahydrobenzo[b]thiophen-2-ylamino)-4-oxobutyl ethanethioate (**3d**).* Yield 0.79g (78%); ^{1}H NMR ($CDCl_3$, 600 MHz): δ 1.85 (m, 4H), 2.03 (m, 2H), 2.33 (m, 2H), 2.34 (s, 3H), 2.55 (m, 4H), 2.95 (m, 2H), 9.40 (s, 1H); ^{13}C NMR ($CDCl_3$, 600 MHz): δ 22.8, 22.9, 24.3, 25.0, 26.3, 29.3, 32.6, 34.2, 91.5, 114.4, 128.6, 132.6, 148.3, 170.8, 196.5; mass spectrum (HRMS), m/z = 322.0527 (M+Na)$^+$, requires 322.0548.

*Ethyl 2-[(4-Bromobutanoyl)amino]-4,5,6,7-tetrahydrobenzo[b]thiophene-3-carboxylate (**4a**).* Compound **1a** (0.600 g, 2.66 mmol) was dissolved in dichloromethane (15 mL) and cooled to 0 °C. 4-Bromobutyryl chloride (0.366 mL, 3.16 mmol) was added dropwise under nitrogen atmosphere. The reaction was stirred continuously for 1.5 h and analyzed for completion by TLC using 3:1 (hexanes−ethyl acetate). Upon completion, the reaction mixture was washed with brine (3 × 20 mL), satd $NaHCO_3$ (3 × 20 mL), and 1 N HCl (3 × 20 mL). The organic layer was dried using anhydrous sodium sulfate, filtered, and rinsed with dichloromethane. The crude product was purified by flash column chromatography on silica gel (30 mm × 150 mm) using 1:3 hexanes−ethyl acetate as the eluent. The product was concentrated to dryness and recrystallized from hot hexanes: yield = 0.392 g (39%); mp = 80−81 °C; R_f = 0.5 (3:1 hexanes−ethyl acetate); ^{1}H NMR

($CDCl_3$, 400 MHz): δ 1.39 (t, J = 6.8 Hz, 2H, 3H), 1.77−1.79 (m, 4H), 2.31 (p, J = 6.4 Hz, 2H), 2.62−2.67 (m, 4H), 2.69−2.77 (m, 2H), 3.52 (t, J = 6.4 Hz, 2H), 4.33 (p, J = 7.2 Hz, 2 H), 11.34 (s,1H); ^{13}C NMR ($CDCl_3$, 400 MHz) δ 14.5, 23.0, 23.1, 24.5, 26.5, 28.0, 33.0, 34.9, 60.7, 111.6, 126.9, 131.0, 147.4, 166.3, 168.7; mass spectrum (HRMS), m/z = 396.0253 $(M+H)^+$ $C_{15}H_{2o}BrNO_3SNa$ requires 396.0245; Anal. Calcd for $C_{15}H_{20}BrNO_3S$: C, 48.13; H, 5.39; N, 3.74. Found: C, 48.78; H, 5.41; N, 3.77.

*4-Bromo-N-(3-cyano-4,5,6,7-tetrahydrobenzo[b]-thiophen-2-yl)butanamide (**4b**).* Compound **1b** (1.00 g, 5.61 mmol) was dissolved in dichloromethane (25 mL) and cooled to 0 °C. 4-Bromobutyryl chloride (0.773 mL, 6.68 mmol) was added dropwise under nitrogen atmosphere and the reaction was stirred continuously for 1.5 h. The reaction was analyzed for completion by TLC using 3:1 hexanes−ethyl acetate. Upon completion, the reaction mixture was washed with brine (3 × 20 mL), satd $NaHCO_3$ (3 × 20 mL), and 1 N HCl (3 × 20 mL). The organic layer was dried using anhydrous sodium sulfate, filtered, and concentrated under reduced pressure. The crude product was purified by flash column chromatography on silica gel (30 mm × 150 mm) using 1:3 hexanes−ethyl acetate as the eluent. The product was concentrated to dryness and recrystallized using dichloromethane−hexanes: yield = 1.23 g (67%); mp = 173−174 °C; R_f = 0.5 (3:1 hexanes−ethyl acetate); ^{1}H NMR ($CDCl_3$, 600 MHz): δ 1.53−1.59 (m, 1H), 1.83−1.84 (m, 4H), 2.31 (p, J = 6.6 Hz, 2H), 2.60−2.64 (m, 4H), 2.69 (t, J = 7.2 Hz, 2H), 3.53 (t, J = 6.0 Hz, 2H), 8.57 (m,1H, NH); ^{13}C NMR ($CDCl_3$, 600 MHz): δ 22.3, 23.3, 24.1, 24.2, 27.9, 33.1, 34.1, 92.8, 114.9, 128.4, 131.0, 147.3, 169.2; mass spectrum (ESIMS), m/z = 349 $(M+Na)^+$ $C_{13}H_{15}BrN_2NaOS$ requires 349; Anal. Calcd for $C_{13}H_{15}BrN_2OS$: C, 47.71; H, 4.62; N, 8.56. Found: C, 47.82; H, 4.44; N, 8.53.

*Ethyl 2-(3-(2-Chloroethyl)ureido)-4,5,6,7-tetrahydrobenzo-[b]thiophene-3-carboxylate (**5**).* A solution of ethyl 2-amino-4,5,6,7-tetrahydrobenzo[b]thiophene-3-carboxylate **1a** (1.125 g, 5.00 mmol) in toluene (5 mL) was treated with 2-chloroethyl isocyanate (0.636 mL, 7.50 mmol). The resulting solution was refluxed at 112 °C for 3 h under dry nitrogen. The solution was allowed to cool to room temperature and was then concentrated under reduced pressure. The crude product was purified by flash column chromatography on silica gel (75 mm × 50 mm) eluting with 1:9 ethyl acetate−hexanes. The product was concentrated to dryness and crystallized from 2:2:6 dichloromethane−diethyl ether−hexanes): yield 867 mg (53%); R_f = 0.56 (3:7 ethyl acetate−hexanes); mp = 119−123 °C (Lit:[56] 123−125 °C); ^{1}H NMR (600 MHz, $CDCl_3$): δ 1.37−1.35 (t, J = 7.2 Hz, 3H), 1.78−1.77 (m, 4H), 2.60−2.58 (d, J = 6 Hz, 2H), 2.74−2.73 (d, J = 6 Hz, 2H), 3.68−3.65 (m, 4H), 4.31−4.27 (q, J = 7.2, Hz, 2H), 5.52 (s, 1H); ^{13}C NMR (600 MHz, $CDCl_3$): δ 14.4, 23.0, 24.4, 26.5, 42.5, 44.2, 60.4, 77.2, 109.4, 125.1, 130.6, 150.8, 153.7, 167.1; mass spectrum (ESIMS), m/z = 332 $(M+H)^+$, $C_{14}H_{20}ClN_2O_3S$ requires 332.

*Methyl 5-O-p-Toluenesulfonyl-α-D-arabinofuranoside (**6**).*[24] Methyl α-D-arabinofuranoside[24] (3.05 mmol) was dissolved in 20 mL of pyridine. Tosyl chloride was then added in slight excess (3.25 mmol) and the solution stirred at 37 °C for 24 h under dry nitrogen. The heat was removed and the reaction was allowed to progress at room temperature for an additional 5 days. Ice was used to quench the reaction and an additional 60 mL of water was added along with 15 mL of brine. The solution was extracted with ethyl acetate (3 × 35 mL). The organic layers were combined and back extracted with water and brine. Anhydrous sodium sulfate was used to dry the solution, which was then filtered and concentrated. The crude product was purified by flash column chromatography on silica gel (50 mm × 150 mm) eluting with 3:3:14 acetone−chloroform−hexanes (500 mL), followed by 1:1:3 acetone−chloroform−hexanes (250 mL), and finally followed by 1:1:2 acetone−chloroform−hexanes (200 mL). The product fractions were pooled and concentrated: yield 633 mg (65%); R_f = 0.45 (1:9 methanol−chloroform).

*Methyl 5-O-p-Toluenesulfonyl-2,3-di-O-acetyl-α-D-arabinofuranoside (**7**)..*[57,58] Compound **7** (1.28 g, 3.88 mmol) was dissolved in 30 mL of 1:1 pyridine−acetic anhydride in a round-bottom flask. The solution was allowed to stir at room temperature under dry nitrogen for 24 h. The reaction was quenched with ice (30.0 g) and extracted using dichloromethane and back-extracted with brine. The solution was dried with anhydrous sodium sulfate, filtered, and concentrated under reduced pressure. The crude product was purified by flash column chromatography on silica gel (30 mm × 150 mm). The product was eluted with 1:3 ethyl acetate−hexanes, followed by 1:1 ethyl acetate−hexanes (100 mL). The product fractions were pooled and concentrated under reduced pressure: yield 1.15 g (73%); R_f = 0.16 (1:3 ethyl acetate−hexanes); ^{1}H NMR ($CDCl_3$, 600 MHz): δ 2.08 (s, 6H), 2.45 (s, 3H), 3.36 (s, 3H), 4.16−4.18 (m, 1H), 4.26 (dd, 1H, J = 5.4, 10.8 Hz), 4.32 (dd, 1H, J = 3, 10.8 Hz), 4.87 (m, 1H), 4.89 (s, 1H), 5.02 (s, 1H), 7.35 (d, 2H, 6.6 Hz), 7.81 (d, 1H, J = 6.6 Hz); ^{13}C NMR (600 MHz, $CDCl_3$): δ 20.9, 21.9, 55.6, 68.9, 71.4, 75.9, 78.8, 80.7, 81.1, 81.1, 107.0, 128.1, 128.2, 128.3, 130.1, 130.1, 133.0, 145.2, 170.1, 170.5, 170.7.

*Methyl 2,3-Tri-O-acetyl-5-S-acetyl-5-thio-α-D-arabinofuranoside (**8**).*[21] Compound **7** (1.15 g, 2.86 mmol) was dissolved in 10 mL of anhydrous DMF in a round-bottom flask. An additional 10 mL of anhydrous DMF was used to dissolve $KSCOCH_3$ (0.40 g, 3.50 mmol). The $KSCOCH_3$ solution was then added dropwise to the starting material and allowed to stir at room temperature under nitrogen for 24 h. The solution was diluted with 50 mL of water and extracted with three 30 mL portions of ether. The ether layers were combined and washed with saturated sodium chloride solution. The ether was dried with anhydrous sodium sulfate, filtered, and concentrated under reduced pressure. The crude product was purified by flash column chromatography on silica gel (30 mm × 150 mm). The product was eluted with 1:1:5 acetone−chloroform−hexanes and concentrated to dryness under reduced pressure: yield = 525 mg (60%); R_f = 0.39 (2:3 ethyl acetate−hexanes); ^{1}H NMR ($CDCl_3$, 600 MHz): δ 2.03 (s, 6H), 2.33 (s, 3H), 3.12−3.17 (m, 1H), 3.32−3.37 (m, 4H), 4.14 (dd, 1H, J = 5.2, 12 Hz), 4.84 (s, 1H), 4.86 (d, 1H, J = 6.0), 4.98 (s, 1H). ^{13}C NMR (600 MHz, $CDCl_3$): 21.0, 30.7, 31.3, 55.2, 78.2, 79.7, 81.9, 106.8, 170.0, 170.3, 194.9; mass spectrum (HRMS), m/z = 329.0646 $(M+Na)^+$, $C_{12}H_{18}NaO_7S$ requires 329.0671.

*Methyl α-D-Arabinofuranoside-5-thiol (**9**).* A solution of **8** (3.37 g, 11.0 mmol) in 0.1 M methanolic NaOMe (40 mL) was stirred for 4 h at 50 °C under nitrogen and neutralized with Amberlite IR120 (H+ form). The resin was filtered off, and the filtrate was concentrated under reduced pressure. The residue was extracted with ethyl acetate to provide thiol **9** after concentration: yield 1.21 g (61%); ^{1}H NMR ($CDCl_3$, 600 MHz): δ 1.68−1.65 (t, ^{1}H, J = 6.0 Hz), 2.81−2.77 (m, 1H), 2.89−2.81 (m, 1H), 3.39 (s, 3H), 3.92−3.91 (m, 2H), 4.09−4.06 (m, 3H), 4.85 (s, 1H); ^{13}C NMR ($CDCl_3$, 600 MHz): δ

26.9, 55.8, 79.9, 81.7, 84.4, 108.3; mass spectrum (HRMS), m/z = 203.0337 $(M+Na)^+$, $C_6H_{12}NaO_4S$ requires 203.0354.

5-Iodo-α-D-arabinofuranoside (11). Methyl α-D-arabinofuranoside (**10**) (1.00 g, 6.66 mmol) was dissolved in dry THF (10 mL) and placed on ice. The reaction was cool to 0 °C in an ice bath and imidazole (1.07 g, 15.8 mmol), iodine (2.01 g, 7.92 mmol), and triphenylphosphine (2.00 g, 7.92 mmol) were added. The solution was warmed to 65 °C and allowed to stir for 1.5 h. The solution was diluted with 50 mL of water and extracted with dichloromethane (3 × 30 mL). The organic layers were combined, dried with anhydrous sodium sulfate, filtered, and concentrated under reduced pressure. The crude product was purified by flash column chromatography on silica gel (30 mm × 150 mm). The product was eluted with 8:1 chloroform−acetone and concentrated to dryness under reduced pressure: yield = 1.13 g (65%); R_f = 0.50 (3:1 chloroform−acetone); ^{1}H NMR (DMSO, 400 MHz) δ 3.25 (s, 2H), 3.35 (s, 3H), 3.46−3.59 (m, 2H), 3.83 (s, 1H), 4.64 (s, 1H), 5.39−5.40 (m,1H), 5.49−5.50 (m,1H); ^{13}C NMR (DMSO, 100 MHz) δ 09.1, 54.5, 80.6, 81.2, 82.0, 108.8; mass spectrum (ESIMS), m/z = 297 $(M+Na)^+$. Anal. Calcd for $C_6H_{11}IO_4$: C, 26.30; H, 4.05; N, 0.00; Found: C, 26.04; H, 4.02; N, 0.03.

Ethyl 2-(Methyl 5-thio-α-D-arabinofuranoside-5-S-yl)-acetamido-4,5,6,7-tetrahydrobenzo[b]thiophene-3-carboxylate (13a). Step 1: Compound (**2a**) (0.100 g, 0.33 mmol) and thiourea (0.504 g, 0.66 mmol) were suspended in 2 mL of absolute ethanol and stirred for 3 h at 65 °C. The reaction was analyzed for completion by TLC 3:1 hexanes−ethyl acetate. The reaction was cooled and filtered. The filtrate was rinsed with absolute ethanol and concentrated to dryness under reduced pressure. Compound **12a** was obtained as yellow color residue: yield 0.100 g (80%); mass spectrum (ESIMS), m/z = 342 $(M)^+$, $C_{14}H_{20}N_3O_3S_2^+$ requires 342. Step 2: Compound (**12a**) (0.100 g, 0.29 mmol) was combined with compound **11** (0.040 g, 0.14 mmol), cesium carbonate (0.19 g, 0.584 mmol) in dry DMF (2 mL). The solution was stirred for 16 h at 85 °C under nitrogen atmosphere. The reaction was monitored by using TLC (2:1 toluene−acetone). On completion, the crude reaction mixture was loaded onto silica gel and the residual solvent evaporated under reduced pressure. The sample was loaded on silica gel column (30 mm × 150 mm) and eluted with hexanes followed by 4:1 toluene−acetone to afford the product. The product fractions were combined, concentrated under reduced pressure. The product was pink amorphous solid: yield 0.018 g (28%); R_f = 0.37 (2:1 toluene−acetone); ^{1}H NMR ($CDCl_3$, 600 MHz); δ 1.39 (t, J = 7.2 Hz, 3H), 1.79 (m, 4H), 2.65 (m, 2H), 2.76 (m, 2H), 2.98 (m, 2H), 3.36 (s, OCH_3), 3.53 (d, J = 16.2 Hz, 1H), 3.64 (d, J = 16.2 Hz, 1H), 3.98 (m, 1H), 4.0 (m, 1H), 4.23 (m, 1H), 4.34 (q, J = 7.2 Hz, 2H), 4.89 (s, 1H). ^{13}C NMR (CD_3OD, 400 MHz); δ 12.4, 20.2, 20.4, 20.6, 30.4, 30.6, 50.4, 60.0, 80.0, 80.2, 80.3, 100.9, 112.0, 126.0, 129.0, 146.0, 165.0,167.0; mass spectrum (HRMS), m/z = 468.1089 $(M+Na)^+$, $C_{19}H_{27}NNaO_7S_2$ requires 468.1127.

N-(3-Cyano-4,5,6,7-tetrahydrobenzo[b]thiophen-2-yl)-2-(methyl 5-thio-α-D-arabinofurano-side-5-S-yl)acetamide (13b). Step 1: Compound (**2c**) (0.200 g, 0.78 mmol) and thiourea (0.119 g, 1.57 mmol) were suspended in 4 mL absolute ethanol and stirred for 3 h at 65 °C. The reaction was analyzed for completion by TLC using 3:1 hexanes−ethyl acetate. The reaction was cooled and filtered. The filtrate was rinsed with a minimal amount of absolute ethanol and concentrated to dryness under reduced pressure. Compound **12b** was obtained as brown color residue: yield 0.216 g (83%); mass spectrum (ESIMS), m/z = 295 $(M)^+$, $C_{12}H_{15}N_4OS_2^+$ requires 295. Step 2: Compound **12b** (0.118 g, 0.36 mmol) was combined with Compound **11** (0.05 mg, 0.18 mmol) and cesium carbonate (0.234 g, 0.72 mmol) in dry DMF (2 mL). The solution was stirred for 16 h at 85 °C under nitrogen atmosphere. The reaction was monitored in thin layer chromatography using (2:1 toluene−acetone). On completion, the crude reaction mixture was loaded onto silica gel and the residual solvent evaporated under reduced pressure. The sample was loaded on silica gel column (30 mm × 150 mm) and eluted with hexanes followed by 4:1 toluene−acetone to afford the product. The product was orange amorphous solid: yield 0.040 g (56%); R_f = 0.39 (2:1 toulene−acetone); mp = 160−163 °C. ^{1}H NMR (CD_3OD, 600 MHz): δ 1.8 (m, 4H), 2.51 (m, 2H), 2.59 (m, 2H), 2.85 (dd, J = 24.6 Hz, 7.2 Hz, 1H), 2.93 (dd, J = 18.6 Hz, 4.2 Hz, 1H), 3.26 (s, OCH_3), 3.52 (d, J = 15 Hz, 1H), 3.54 (d, J = 15 Hz, 1H), 3.76 (m, 1H), 3.86 (m, 1H), 3.98 (m, 1H), 4.68 (d, J = 1.8 Hz, 1H). ^{13}C NMR (CD_3OD, 400 MHz): δ 23.4, 24.3, 24.9, 25.1, 35.9, 36.5, 55.4, 81.7, 83.6, 84.5, 110.5, 114.9, 129.9, 132.6, 169.9; mass spectrum (HRMS), m/z = 421.0873 $(M+Na)^+$, $C_{17}H_{22}N_2O_5S_2$ requires 421.0868.

Ethyl 2-(Methyl 5-thio-α-D-arabinofuranoside-5-S-yl)-butamido-4,5,6,7-tetrahydrobenzo[b]thiophene-3-carboxylate (13c). Step 1: Compound **4a** (0.275 g, 0.725 mmol) and thiourea (0.110 g, 1.45 mmol) were suspended in 2 mL of absolute ethanol and stirred at reflux for 4 h. The reaction was analyzed for completion by TLC using 3:1 hexanes−ethyl acetate. The reaction was cooled on ice and filtered. The filtrate was rinsed with a minimal amount of absolute ethanol and concentrated to dryness under reduced pressure. Compound **12c** was obtained as colorless crystals. yield = 0.170 g (52%); mp = 212−213 °C; ^{1}H NMR (DMSO, 400 MHz) δ 1.25 (t, J = 7.2 Hz, 3H), 1.63 (br. s, 4H), 1.85−1.92 (m, 2H), 2.59−2.62 (m, 4H), 3.18 (t, J = 7.2 Hz, 2H), 3.37−3.41 (m, 1H), 4.22 (p, J = 6.8 Hz, 2H), 9.00−9.11 (m, 4H), 10.95 (s, 1H); ^{13}C NMR (DMSO, 400 MHz) δ 14.1, 22.3, 22.5, 23.7, 24.3, 25.8, 29.4, 34.1, 60.3, 111.2, 125.9, 130.3, 145.9, 165.0, 168.9, 169.7; Anal. Calcd for $C_{16}H_{24}BrN_3O_3S_2$: C, 42.67; H, 5.37; N, 9.33; Found: C, 42.46; H, 5.17; N, 9.34. Step 2: Compound **12c** was combined with compound **11** (0.110 g, 0.244 mmol) and cesium carbonate (0.268 g, 0.825 mmol) in dry DMF (4 mL). The solution was stirred for 16 h at 85 °C under nitrogen atmosphere. The reaction was monitored by TLC using (2:1 toluene−acetone). Upon completion, the crude reaction mixture was loaded onto silica gel and DMF was evaporated under reduced pressure. The dry slurry was purified by flash column chromatography on silica gel (30 mm × 150 mm). Elution with 4:1 toluene−acetone affords a partially purified product. The compound was further purified on a second silica gel column to remove residual DMF, eluting with (4:1 ethyl acetate−hexanes). The product fractions were combined, concentrated, and dried in vacuum where the product crystallized upon standing: yield = 0.080 g (77%); R_f = 0.53 (2:1 toulene−acetone); mp = 92−93 °C; ^{1}H NMR ($CDCl_3$, 400 MHz) δ 1.39 (t, J = 6.8 Hz, 3H), 1.78−1.79 (m, 4H), 2.04 (t, J = 7.2 Hz, 3H), 2.59−2.64 (m, 2H), 2.70−2.77 (m, 3H), 2.83−2.90 (m, 2H), 3.38 (s,3H), 3.90−3.93 (m,1H), 4.06 (d, J = 6.8 Hz, 1H), 4.20−4.22 (m, 1H), 4.34 (q, J = 7.2 Hz, 2H), 4.90 (s, 1H), 5.39 (d, J = 6.0 Hz, 1H), 11.32 (s, 1H) ppm; ^{13}C NMR ($CDCl_3$, 400 MHz) δ 14.5, 23.0, 23.2, 24.5, 25.0, 26.6,

dx.doi.org/10.1021/bc3004342 | Bioconjugate Chem. 2012, 23, 2403−2416

32.8, 34.5, 55.1, 60.8, 80.5, 80.7, 85.7, 109.1, 111.7, 127.0, 131.0, 147.5, 167.0, 169.4 ppm; mass spectrum (ESIMS), m/z = 496.2 $(M+Na)^+$ Anal. Calcd for $C_{21}H_{31}NO_7S_2$: C, 53.26; H, 6.60; N, 2.96; O, 23.65; S, 13.54. Found: C, 53.32; H, 6.51; N, 2.93.

*N-(3-Cyano-4,5,6,7-tetrahydrobenzo[b]thiophen-2-yl)-2-(methyl-5-thio-α-D-arabinofuranoside-5-S-yl)butamide (**13d**).* Step 1: Compound **4b** (0.300 g, 0.916 mmol) and thiourea (0.139g, 1.83 mmol) were suspended in 2 mL of absolute EtOH and stirred at reflux for 4 h. The reaction was analyzed for completion by using TLC 3:1 (hexanes−ethyl acetate). The reaction mixture was cooled on ice and filtered with minimal amount of abs EtOH and dried in vacuo. Compound **12d** was obtained as colorless crystals: yield = 0.262 g (71%); mp = 205−207 °C. ^{1}H NMR (DMSO, 600 MHz): δ 1.67 (m, 4H), 1.83−1.85 (m, 3H), 2.01 (s, 2H), 2.40−2.44 (m, 2H), 2.55−2.58 (m, 2H), 3.12−3.132 (m, 2H), 8.98 (m, 1H) ppm; ^{13}C NMR (DMSO, 600 MHz): δ 21.7, 22.6, 23.3, 23.5, 24.0, 29.5, 30.7, 33.1, 114.3, 127.1, 130.6, 146.4, 169.6, 170.1 ppm; Anal. Calcd for $C_{14}H_{19}BrN_4OS_2$: C, 41.69; H, 4.75; Br, 19.81; N, 13.89; O, 3.97; S, 15.90. Found: C, 40.88; H, 4.57; N, 14.20. Step 2: Compound **12d** was combined to compound **11** (0.210 g, 0.520 mmol), cesium carbonate (0.268 g, 0.825 mmol) were dissolved in dry DMF (5 mL). The solution was stirred for 24 h at 85 °C under nitrogen atmosphere. The reaction was monitored by thin layer chromatography using (1:1 acetone−hexanes). Upon completion, the crude reaction mixture was loaded onto silica gel and the DMF was evaporated under reduced pressure. The dry slurry was purified by flash column chromatography on silica gel (30 mm × 150 mm). Elution was with 2:1 acetone−hexanes. The product fractions were combined and concentrated to dryness. The crude product was crystallized using ethanol and filtered with cold ethanol: yield = 0.110 g (49%); R_f = 0.3 (1:1 acetone−hexanes); mp = 183−184 °C; ^{1}H NMR (DMSO, 600 MHz) δ 1.69 (s, 4H), 1.80 (p, J = 6.0 Hz, 4H), 2.42 (br. s, 2H), 2.51−2.62 (m, 4H), 2.73 (s, 1H), 3.18 (s, 3H), 3.56−3.58 (m, 1H), 3.71−3.72 (m, 1H), 3.74−3.76 (m, 1H), 4.55 (s, 1H), 5.25 (d, J = 6, 1H), 5.39 (d, J = 6.0 Hz, 1H), 11.51 (br. s, 1H) ppm; ^{13}C NMR (DMSO, 400 MHz) δ 21.8, 22.7, 23.3, 23.5, 24.8, 31.6, 33.8, 33.9, 54.4, 79.9, 80.1, 81.9, 82.6, 92.2, 109.0, 114.4, 127.04, 130.6, 146.67, 170.66 ppm; mass spectrum (HRMS), m/z = 449.1199 $(M+Na)^+$ $C_{19}H_{26}N_2O_5S_2Na$ requires 449.1181; Anal. Calcd for $C_{19}H_{26}N_2O_5S_2$: C, 53.50; H, 6.14; N, 6.57; O, 18.75; S, 15.03. Found: C, 48.78; H, 5.41; N, 3.71.

*Methyl 5-S-[2-(2,4-Dioxo-1,4,5,6,7,8-hexahydro[1]-benzothieno[2,3-d]-pyrimidin-3(2H)-yl)ethyl]-5-thioarabino-furanoside (**14**).* Compound **10** (0.194 g, 0.634 mmol) and compound **5** (0.289 g, 0.868 mmol) were combined in 3 mL NaOMe (3.06 mmol Na metal in 3 mL NaOH). The solution was stirred at room temperature for 24 h then quenched using 20 mL 1 N HCl. The solution was diluted with water and extracted with chloroform (3 × 20 mL). The chloroform was dried with anhydrous sodium sulfate, filtered, and dried under reduced pressure. The product was purified by flash column chromatography on silica gel (30 mm × 150 mm) eluting with 50:50 hexanes−acetone. The product fractions were concentrated to afford **14**, a colorless waxy solid: yield = 36 mg (13%); R_f = 0.46 (1:1 hexanes−acetone); ^{1}H NMR ($CDCl_3$, 600 MHz): δ 1.78 (m, 4H), 2.60 (s, 2H), 2.83−3.04 (m, 6H), 3.37 (s, 3H), 4.03 (br. s, 2H), 4.13 (br. s, 1H), 4.19 (m, 4H), 4.88 (s, 1H), 10.91 (br. s, 1H); ^{13}C NMR ($CDCl_3$, 600 MHz): δ 22.2, 23.2, 24.7, 25.5, 30.3, 34.3, 39.8, 55.4, 80.0, 81.5, 83.9, 108.8, 114.0, 127.3, 132.2, 148.7, 152.2, 159.1; mass spectrum (HRMS), m/z = 451.0969 $(M+Na)^+$, $C_{18}H_{25}N_2O_6S_2$ requires 429.1154.

RESULTS AND DISCUSSION

Molecular Modeling. The substrate analogues shown in Figure 2 all contain the 2-amino-4,5,6,7-tetrahydrobenzo[b]-thiophene scaffold. Different linker lengths and the arabinose moiety were converted to three-dimensional structures (MDL mol file format) using *Chem3D* (CambridgeSoft). The compound data sets were then imported into *Maestro* v 8.0 (Schrodinger, Inc.) and were prepared for docking using *MacroModel* (Schrodinger, Inc.) by using conformational analysis and minimization methods to obtain the lowest energy conformer. The crystallographic coordinates for the Ag85C-octylthioglucoside complex (PDB code: 1va5)[29] was obtained from the Protein Data Bank (www.rcsb.org) and prepared by removing all the solvent and adding hydrogen atoms and minimal minimization in the presence of bound ligand using protein preparation. Grids for molecular docking with *Glide* v 4.5 (Schrodinger, Inc.) were calculated without any constraint to the protein.[59] Compounds were docked using *Glide* in extra-precision mode, with up to five poses saved per molecule. The docked poses were then minimized using the local optimization feature in *MacroModel*,[60] and the energies were calculated using the OPLS force field[61] and the GBSA continuum model[62] in *Maestro*. The binding free energy ΔG_{bind} is estimated as

$$\Delta G_{bind} = \Delta E_{MM} + \Delta G_{solv} + \Delta G_{SA}$$

where ΔE_{MM} is the difference in energy between the complex structure and the sum of the energies of the ligand and the unliganded protein, using the OPLS force field, ΔG_{solv} is the difference in the GBSA solvation energy of the complex and the sum of the solvation energies for the ligand and unliganded protein, and ΔG_{SA} is the difference in the surface area energy for the complex and the sum of the surface area energies for the ligand and uncomplexed protein. Corrections for entropic changes were not applied. Finally, according to the docking score and binding energy we selected the candidate structures for preparing and testing as inhibitors for Ag85C. Structures with good docking scores included compounds containing a 2-amino-4,5,6,7-tetrahydro-1-benzothiophene-3-carbonitrile or an ethyl 2-amino-4,5,6,7-tetrahydro-3-carboxylate linked through the 2-amino moiety to a methyl 5-thio-α-D-arabinofuranoside. The docking scores are shown in Table 1 and include **13a−d** and compound **14**. Of these compounds, **13a** showed the highest binding energy of −62 kJ/mol.

Potential intermolecular hydrogen-bonded interactions between compound **13a** and the Ag85C protein showed four

Table 1. Docking Scores, Binding Energies, and Measured K_i of Compounds 13a−d and Compound 14

compound	docking score	binding energy	K_i (μM)[a]
native ligand	−11.3	−53	N.D.
13a	−12	−62	18.2 ± 1.8
13b	−12.88	−19	34.8 ± 3.8
13c	−11.4	−6	71.0 ± 5.3
13d	−10.9	−29	N.D.
14	−11.85	−15	47.1 ± 3.9

[a]N.D. = no data.

Table 2. X-ray Diffraction and Crystallographic Refinement Data

diffraction statistics	
resolution range (å) (highest shell)	35−2.15 (2.20−2.15)
space group	$P2_12_12_1$
unit cell parameters	a = 67.5,b = 80.2, c = 136.6, $\alpha = \beta = \gamma$ = 90°
total reflections (unique reflections)	246 157 (40 674)
completeness (%) (highest shell)	99.0 (99.9)
average $I/\sigma I$	7.0
R_{sym} (%) (highest shell)	8.8 (40.4)
refinement statistics	
protein molecules/atoms (per A.S.U.)	2/4695
R_{work}/R_{free} (%)	15.86/19.66
average B-factor (Å^2) (protein/ligand/solvent)	25.66/43.58/36.17
ligand occupancy (%)	100
r.m.s.d. bonds/angles (Å/°)	0.007/1.041
Ramachanran (favored/disallowed) (%)	96.2/0.0

hydrogen bonds (OH-3 of the arabinose with NH of Arg41 and HOH 2037, OH-4 of the arabinose with NH of Trp262, and S of the linker with HOH 2242) (Figure 3). In addition, the

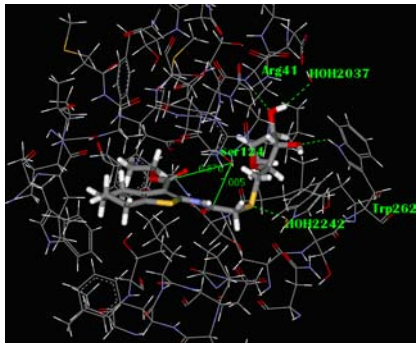

Figure 3. Hypothetical binding mode of inhibitor **13a** in the Ag85C active site predicted using *Glide 4.5*. The arabinofuranoside substituent is located in the trehalose binding pocket, and the ester moiety is oriented in the vicinity of Ser124. The tetrahydrobenzo[*b*]thiophene is accommodated in the mycolate α-chain binding channel extending through the core of Ag85C.

calculated distance between the OH of Ser124 and the carbon of carbonyl carbon of the ester was found to be 6.876 Å. Finally, we calculated the electrostatic interactions between compound **13a** and the Ag85C protein (Figure 4). According to the hydrogen bond and electrostatic interactions, compound **13a** was expected to be a good template for occupying the active site of the enzyme.

Synthesis of Glycoconjugates. Both the 2-amino-4,5,6,7-tetrahydro-1-benzothiophene-3-carbonitrile and ethyl 2-amino-4,5,6,7-tetrahydro-1-benzothiophene-3-carboxylate classes of thiophenes could be accessed through a classic Gewald synthesis[52] followed by amine functionalization with an appropriate linker. The Gewald synthesis was performed by treating cyclohexanone with malononitrile or ethyl cyanoacetate and sulfur in the presence of *N*-ethylmorpholine to yield 3-carboxylate thiophene **1a**[51] and 3-carbonitrile thiophene **1b**, respectively, in a modest yield. Thiophenes **1a** and **1b** were then reacted with either chloroacetyl chloride or 4-chlorobutyrl chloride to prepare amides **2a−d** (Scheme 1) in modest yield. Alternatively, **1a** was reacted with 2-chloroethyl isocyanate to form urea **5**[56] in 53% yield. With key intermediates in hand, we explored different approaches to form a thioether linkage between the thiophenes and the C-5 position of a methyl α-D-arabinofuranoside. In the first approach, the chloro substituent of thiophenes **2a−d** was displaced with potassium thioacetate in anhydrous DMF to afford the thioesters **3a−d** in yields of 62−92%. The resulting thiophenes were treated with NaOEt, concentrated, and directly reacted with the known methyl 5-*O*-*p*-toluenesulfonyl-α-D-arabinofuranoside (**6**) (Scheme 3).[24−26] Unfortunately, we failed to isolate an identifiable product using this protocol. We then chose to reverse the polarity of the electrophile by converting the tosylate to a sulfhydryl. This required peracetylation of arabinofuranoside **6** with acetic anhydride to afford the diacetylated compound **7** in 73% yield (Scheme 2). Acetylated sulfonate **7** was then treated with potassium thioacetate to afford the thioester **8** in 60% yield. Arabinofuranoside **8** was then treated with NaOMe at 50 °C for 2 h. The reaction was neutralized with Amberlite IR120 (H + form), filtered and dried. The resulting methyl 5-deoxy-5-thio-α-D-arabinofuranoside **9** was resuspended in THF and combined with an equivalent of alkyl chlorides **2a−d** and triethyl amine to afford glycoconjugates **13a−d** (Scheme 3). In our hands, only the α-chloroamides **2a** and **2c** reacted with the mercaptan **9** to produce thioethers **13a** and **13b**, respectively, in unacceptable yield. Modification of bases and solvents and addition of disulfide reducing agents failed to generate the longer-chain thioethers.

Unsatisfied with failure of the reaction between halides **2b** and **2d** and mercaptan **9**, as well as poor coupling yields to this point, we began to explore alternate options for synthesizing the desired thioether linkages. There are numerous examples of alkyl halides reacting with isothiourionium salts to form thioethers.[63] Therefore, we converted methyl α-D-arabinofuranoside (**10**)[24−26] to the known methyl 5-deoxy-5-iodo-α-D-arabinofuranoside (**11**) using I_2-P(Ph)$_3$-imidizole in 65% yield (Scheme 2).[64] Compounds **1a** and **1b** were then acylated with 4-chlorobutyryl chloride to provide amides **4a** and **4b**, respectively (Scheme 1). Amides **2a**, **2c**, **4a**, and **4b** were then treated with thiourea in refluxing ethanol to afford the respective isothiourionium salts **12a−d**, in good yield (Scheme 3). The isothiourionium salts reacted cleanly with iodide **11** in the presence of cesium carbonate in *N*,*N*-dimethylformamide to form thioethers **13a−d**, respectively.

We also found it noteworthy that chloride **5** and methyl 5-thio-α-D-arabinofuranoside **8** in methanol-NaOMe, afforded the 3-substituted pyrimidinedione **14** linked to a methyl 5-thio-α-D-arabinofuranoside moiety (Scheme 4). The resulting materials were then used to evaluate the structural class as inhibitors of the Ag85C acyltransferase activity.

Enzyme Inhibition Studies. To determine if any compounds from this library inhibit the Ag85C enzyme, assays measuring the enzymatic activity were performed. These assays employed 4-methylumbelliferyl butyrate (4MUB) as the acyl donor and trehalose as the acyl acceptor. Binding of 4MUB within the enzyme active site allows nucleophilic attack on the substrate to produce an acyl-Ag85C intermediate and release of the fluorescent molecule 4-methylumbelliferone (4-MU). Subsequent binding of trehalose in the active site allows nucleophilic attack by trehalose on the acyl-Ag85C intermediate to form trehalose-6-butyrate. Measuring the fluorescence emission of 4-MU at 500 nm affords an accurate determination of the initial rate of the enzymatic reaction.

dx.doi.org/10.1021/bc3004342 | *Bioconjugate Chem.* 2012, 23, 2403−2416

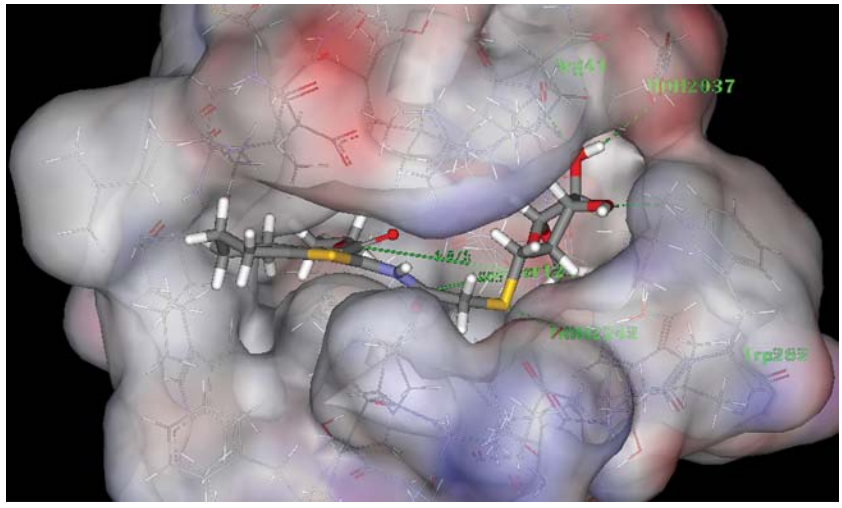

Figure 4. Electrostatic potential and hydrogen bonding interaction between compound **13a** and Ag85C. The distances between the OH of Ser124 and the ester and amide C═O moieties of **13a** is indicated by green lines.

Scheme 2. Synthesis of Arabinofuranosides[a]

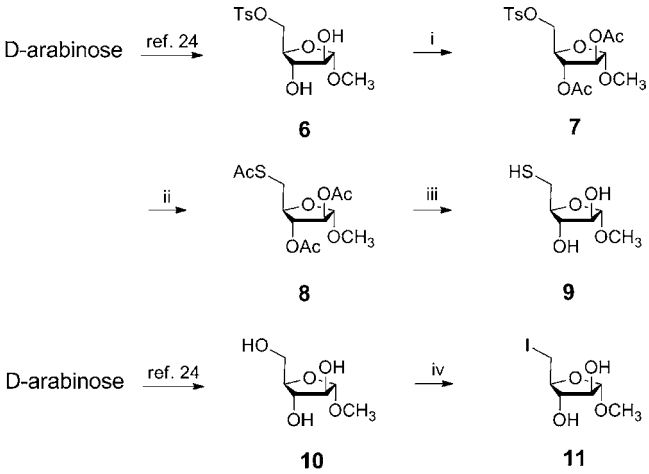

[a]Reagent and conditions: (i) Ac_2O, pyridine, 24 h, rt (73%); (ii) $KSCOCH_3$, DMF, 24 h, rt (60%); (iii) 0.1 M methanolic NaOMe 2 h, 50 °C then Amberlite IR120; (iv) imidazole, I_2, PPh_3, THF, 0 to 65 °C, (65%).

To determine the K_i values for the library of inhibitors, the initial reaction rate using this fluorescence-based assay was performed in the presence of varying concentrations of each inhibitor. The ratio of the rates of the inhibited reaction versus the uninhibited reaction plotted as a function of inhibitor concentration exhibits a clear dose-dependent decrease in enzymatic activity. Fitting these data allowed the calculation of K_i values for each of the inhibitors, which ranged from 18.2 to 71.0 μM (Table 1 and Figure 5A).

While the K_i values of the inhibitors do not vary significantly, a general trend is observed that offers insight for the design of second-generation compounds with improved affinity for the Ag85C enzyme and better inhibitory activity. Because of the choices of arabinofuranosides tested, the importance of two structural variables can be related to inhibitory activity. First, of the thiophene containing compounds, those elaborated with the ethyl ester moiety on the thiophene, have slightly better inhibitory activity than compounds with a corresponding nitrile moiety as seen when comparing the K_i values of **13a** and **13b**.

Scheme 3. Isothiourionium Salt-Based Synthesis of Thioethers[a]

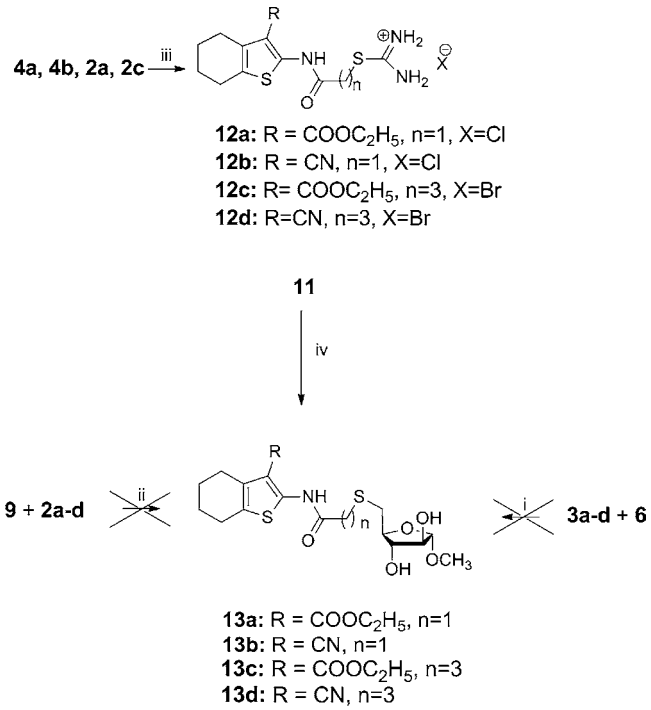

[a]Reagent and conditions: (i) NaOEt, MeOH, rt, no reaction; (ii) THF, TEA, 6 h, rt, no reaction; (iii) $CS(NH_2)_2$, EtOH, 4 h, reflux, **12a** (83%), **12b** (80%), **12c** (52%), **12d** (71%); (iv) **12a**–**12d**, Cs_2CO_3, DMF, 16 h, 85 °C, **13a** (28%), **13b** (56%), **13c** (77%), **13d** (49%).

Scheme 4. Synthesis of Pyrimidinedione 14[a]

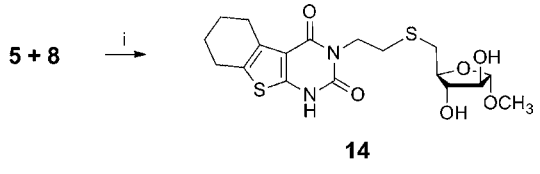

[a]Reagents and conditions: (i) NaOMe, MeOH, 24 h, rt (13%).

dx.doi.org/10.1021/bc3004342 | Bioconjugate Chem. 2012, 23, 2403–2416

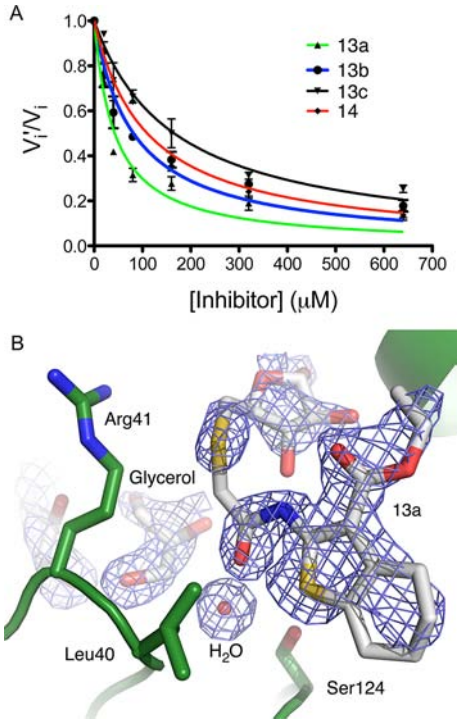

Figure 5. Inhibition of Ag85C. (A) v_i' represents the initial velocity of the inhibited enzymatic reaction at the respective inhibitor concentration. v_i represents the initial velocity of the uninhibited enzymatic reaction. (B) The enzyme active site is shown (with green carbon atoms) with one molecule of **13a**, one water molecule, and two molecules of glycerol (molecules with gray carbon atoms). The placement of these compounds was based on the F_o-F_c omit maps (light blue difference density) shown contoured at 3σ. Colors for the atoms other than carbon are blue, red, and yellow for nitrogen, oxygen, and sulfur, respectively.

Second, the length of the linker between the thioether and the aromatic fused ring system affects inhibitory activity. Compound **13a**, which contains a methylene linker, exhibits stronger inhibition than **13c**, which possesses a propylene linker. The single three-ringed compound tested is difficult to analyze in isolation. The K_i is near the middle of the range observed in the inhibition studies. Synthesis of similar compounds and further testing will be required to determine if there is a benefit to having the third ring. The compounds were screened for growth inhibition activity against *M. smegmatis*; however, no growth inhibition was observed.

Crystal Structure of the Ag85C-Inhibitor Complex. To gain insight into the mechanism of inhibition and information necessary to develop better inhibitors, specific structural information is needed. To this end, crystals of recombinant Ag85C were soaked with compound **13a**. Compound **13a** was chosen because it possesses the lowest K_i value. The difference map calculated with these data show four strong regions of electron density within the Ag85C active site. These are consistent with one compound of **13a**, a single water molecule, and two molecules of glycerol. The binding of **13a** within the active site indicates that it functions as a competitive inhibitor of Ag85C (Figure 5B).

The orientation of **13a** within the active site of the crystal structure (Figure 6) is different with respect to the predicted structure from the inhibitor modeling data. The thiophene moiety is positioned in roughly the same location, but is flipped 180° along the major axis of the two-ringed system to position the ethyl ester pointing away from the enzyme rather than into the hydrophobic tunnel. The arabinofuranoside moiety binds within the known carbohydrate-binding site as exhibited for the Ag85B-trehalose crystal structure.[30] However, the arabinosyl moiety of **13a** overlaps with the glucosyl moiety of trehalose that is distal to Ser124 of Ag85B rather than binding in the proximal carbohydrate binding pocket that accommodates the sugar to be acylated by the enzyme.

Unexpectedly, no specific hydrogen bonding interactions are being formed between the arabinofuranoside and the carbohydrate-binding site of the active site. This would suggest that the binding is driven by hydrophobic interactions between the thiophene moiety and the mycolyl binding site, and that linker length as well as shape complementarity between the arabinosyl moiety and the carbohydrate binding site ultimately

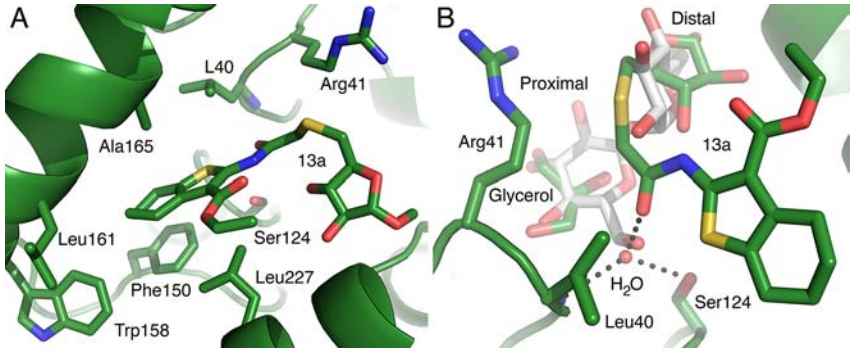

Figure 6. Interactions between **13a** and the Ag85C active site. Two views of the Ag85C active site are shown from different orientations. (A) Nonspecific interactions. The Ag85C protein backbone is shown as the green ribbon. The carbon atoms are in green, nitrogen atoms are in blue, oxygen in red, and sulfur in yellow. The location of the serine nucleophile is shown as a reference. All of the hydrophobic residues within 4 Å of the thiophene moiety are shown, as well as the R41 side chain that interacts with the thioether linker. (B) The superposition of the trehalose-bound Ag85B and the **13a**-bound Ag85C structures shows overlap of the trehalose and **13a** binding sites. The trehalose from the Ag85B structure is shown with gray carbon atoms. All other atom types are colored as in panel A. The distal glucosyl moiety of trehalose and the methylarabinoside of **13a** are clearly occupying the same region within the active site. The proximal glucosyl and an ordered glycerol molecule also superimpose well and form similar hydrogen bonding interactions with Ag85. The ordered water molecule near O6 of the Ag85b-bound trehalose is shown. The dashed lines represent hydrogen bonds between this water molecule and the **13a** amide carbonyl, the side chain of Ser124, and the backbone amide of Leu40, which forms part of the oxyanion hole. The length of these hydrogen bonds range from 2.6 to 3.0 Å.

dx.doi.org/10.1021/bc3004342 | *Bioconjugate Chem.* 2012, 23, 2403−2416

determine the location of the arabinosyl binding. The interaction between Ag85C and the arabinofuranosyl moiety is rather dissimilar to the interactions observed in the Ag85B-trehalose crystal structure, where O2 and O3 of the distal glucosyl moiety of trehalose are hydrogen-bonded to the side chain of Arg41 and O6 is hydrogen-bonded to the backbone carbonyl of His260.[30]

The fused, two-ring system of **13a** is positioned in the proposed mycolic acid-binding pocket and forms van der Waals interactions with the side chains of Phe150, Trp158, Leu161, Ala165, and Leu227.[29,33] In addition, the linker connecting the thiophene to the arabinofuranosides moiety forms van der Waals interactions with the side chain of Arg41. The carbonyl oxygen of the amide moiety appears to be poised to form a hydrogen bond with the backbone amide of Leu40, although the 4.5 Å distance between these is too long for a bonafide hydrogen bond. The approach of **13a** to the oxyanion hole is blocked by an ordered water molecule that forms hydrogen bonds with both the oxyanion hole and the amide carbonyl of **13a**. One key to improving binding and inhibitory activity of a second-generation inhibitor would be to displace this water molecule with a hydrogen bond acceptor to promote a direct interaction between the inhibitor and the oxyanion hole.

Another important piece of information from this structure can be used for future design efforts to improve both strength and specificity of binding. The pocket initially assumed to be important for binding the trehalose still has an undefined role.[33] To date, no structure has revealed binding of any substrate or product analogues within this site even though the residues forming this site (Asp38, Asp45, and Trp262) are conserved in all Ag85 complex mycolyltransferases. The only compounds observed in any structures within this site are glycerol and water, which implies that it may accommodate additional carbohydrate moieties exposed on the surface of the mycobacterial outer membrane.[28,29,33] One potential substrate accommodated by this conserved site would be a neighboring subunit of the arabinan. As the conserved sequence and structure in this region implies an important role, the Ag85C-**13a** complex structure gives very specific information regarding the future design of inhibitors that could bind within this site. Specifically, the methyl group on the methyl-arabinofuranoside can be replaced with a much bulkier moiety such as another arabinofuranosyl moiety, capable of forming a complex hydrogen-bonded network with the conserved residues in this site. Alternatives other than carbohydrates could also be used. Ideally, these groups would possess a large number of both hydrogen bond donors and acceptors to maximize the interaction potential within this site.

CONCLUSION

Virtual thiophene−arabinoside conjugates were docked to antigen Ag85C using *Glide*. Compounds with good docking scores were synthesized by a Gewald synthesis followed by linking to 5-thioarabinofuranosides. The resulting thiophenyl-thioarabinofuranosides were assayed for inhibition of mycoyl-transferase activity using a 4-methylumbelliferyl butyrate fluorescence assay. The conjugates showed K_i values that ranged from 18.2 to 71.0 μM. The inhibitor with the lowest K_i value, **13a**, was used to obtain a crystal structure of the inhibitor bound within the active site of Ag85C. Closely related thiophene derivatives have recently been shown to inhibit the synthesis of TDM, a mycobacterial virulence factor, and inhibit the growth of *M. tuberculosis* particularly in macrophages. The limited set of structures we identified showed no activity against *M. smegmatis*, a model organism, in a disk diffusion assay; however, the structures we identified are very similar to thiophenes which show activity in macrophages infected with drug resistant strains *M. tuberculosis*. On the basis of this observation, we plan to evaluate these compounds and others in a macrophage infection model. The crystal structure highlights interactions between both the thiophene and arabinofuranosides moieties and will be leveraged to design improved inhibitors of Ag85s.

ASSOCIATED CONTENT

Supporting Information

^{1}H and ^{13}C spectra for compounds **2a−2d**, **3a−3d**, **4a**, **4b**, **5**, **7−9**, **11**, **12c**, **12d**, **13a−d**, **14**, HRMS for compound **14**. The material is available free of charge via Internet at http://pubs.acs.org.

AUTHOR INFORMATION

Corresponding Author

*S.J.S.: phone, 419-530-1054; fax, 419-530-1190; e-mail, steve.sucheck@utoledo.edu. D.R.R.: phone, 419-530-1585; e-mail, donald.ronning@utoledo.edu.

Notes

The authors declare no competing financial interest.

ACKNOWLEDGMENTS

Use of the Advanced Photon Source was supported by the U.S. Department of Energy, Office of Science, Office of Basic Energy Sciences, under Contract No. DE-AC02-06CH11357. Use of the LS-CAT Sector 21 was supported by the Michigan Economic Development Corporation and the Michigan Technology Tri-Corridor for the support of this research program (Grant 085P1000817). This was supported by an NIH grants to D. R. Ronning (AI089653) and S. J. Sucheck (GM094734). We also thank students Shen Zhang and Shuangqianzi Li for assistance with the resynthesis and characterization of key intermediates.

REFERENCES

(1) Institute of Medicine of the National Academies (2009) *Addressing the Threat of Drug-Resistant Tuberculosis: A Realistic Assessment of the Challenge. Workshop Summary*, The National Academies Press, Washington, DC.

(2) Zhang, Y., and Amzel, L. M. (2002) Tuberculosis drug targets. *Curr. Drug Targets 3*, 131−54.

(3) Chatterjee, D., and Brennan, P. J. (2009) Glycosylated Components of the Mycobacterial Cell Wall: Structure and Function, In *Microbial Glycobiology* (Moran, A. P., Ed) pp 147−167, Elsevier, London.

(4) Brennan, P. J., and Nikaido, H. (1995) The envelope of mycobacteria. *Annu. Rev. Biochem. 64*, 29−63.

(5) Belanger, A. E., Besra, G. S., Ford, M. E., Mikusova, K., Belisle, J. T., Brennan, P. J., and Inamine, J. M. (1996) The *embAB* genes of *Mycobacterium avium* encode an arabinosyl transferase involved in cell wall arabinan biosynthesis that is the target for the antimycobacterial drug ethambutol. *Proc. Natl. Acad. Sci. U.S.A. 93*, 11919−11924.

(6) Telenti, A., Philipp, W. J., Sreevatsan, S., Bernasconi, C., Stockbauer, K. E., Wieles, B., Musser, J. M., and Jacobs, W. R., Jr. (1997) The *emb* operon, a gene cluster of *Mycobacterium tuberculosis* involved in resistance to ethambutol. *Nat. Med. 3*, 567−570.

(7) Takayama, K., Wang, L., and David, H. L. (1972) Effect of isoniazid on the in vivo mycolic acid synthesis, cell growth, and

viability of *Mycobacterium tuberculosis*. *Antimicrob. Agents Chemother. 2*, 29−35.
(8) Schroeder, E. K., de Souza, O. N., Santos, D. S., Blanchard, J. S., and Basso, L. A. (2002) Drugs that inhibit mycolic acid biosynthesis in *Mycobacterium tuberculosis*. *Curr. Pharm. Biotechnol. 3*, 197−225.
(9) Takayama, K., Wang, C., and Besra, G. S. (2005) Pathway to synthesis and processing of mycolic acids in *Mycobacterium tuberculosis*. *Clin. Microbiol. Rev. 18*, 81−101.
(10) Fukui, Y., Hirai, T., Uchida, T., and Yoneda, M. (1965) Extracellular proteins of tubercle bacilli. IV. Alpha and beta antigens as major extracellular protein products and as cellular components of a strain (H37Rv) of *Mycobacterium tuberculosis*. *Biken J. 8*, 189−199.
(11) Kilburn, J. O., Takayama, K., and Armstrong, E. L. (1982) Synthesis of trehalose dimycolate (cord factor) by a cell-free system of *Mycobacterium smegmatis*. *Biochem. Biophys. Res. Commun. 108*, 132−139.
(12) Sathyamoorthy, N., and Takayama, K. (1987) Purification and characterization of a novel mycolic acid exchange enzyme from *Mycobacterium tuberculosis*. *J. Biol. Chem. 262*, 13417−13423.
(13) Jackson, M., Raynaud, C., Lanéelle, M.-A., Guilhot, C., Laurent-Winter, C., Ensergueix, D., Gicquel, B., and Daffé, M. (1999) Inactivation of the antigen 85C gene profoundly affects the mycolate content and alters the permeability of the *Mycobacterium tuberculosis* cell envelop. *Mol. Microbiol. 31*, 1573−1587.
(14) Puech, V., Bayan, N., Salim, K., Leblon, G., and Daffé, M. (2000) Characterization of the in vivo acceptors of the mycoloyl residues transferred by the corynebacterial PS1 and the related mycobacterial antigens 85. *Mol. Microbiol. 35*, 1026−1041.
(15) Belisle, J. T., Vissa, V. D., Sievert, T., Takayama, K., Brennan, P. J., and Besra, G. S. (1997) Role of the major antigen of *Mycobacterium tuberculosis* in cell wall biogenesis. *Science 276*, 1420−1422.
(16) Harth, G., Horwitz, M. A., Tabatadze, D., and Zamecnik, P. C. (2002) Targeting the *Mycobacterium tuberculosis* 30/32 kDa mycolyl transferase complex as a therapeutic strategy against tuberculosis: Proof of principle using antisense technology. *Proc. Natl. Acad. Sci. U.S.A. 99*, 15614−15619.
(17) Harth, G., Zamecnik, P. C., Tabatadze, D., Pierson, K., and Horwitz, M. A. (2007) Hairpin extensions enhance the efficacy of mycolyl transferase-specific antisense oligonucleotides targeting *Mycobacterium tuberculosis*. *Proc. Natl. Acad. Sci. U.S.A. 104*, 7199−204.
(18) Nguyen, L., and Pieters, J. (2009) Mycobacterial subversion of chemotherapeutic reagents and host defense tactics: challenges in tuberculosis drug development. *Annu. Rev. Pharmacol. Toxicol. 49*, 427−53.
(19) Gobec, S., Plantan, I., Mravljak, J., Ŝavajger, U., Wilson, R. A., Besra, G. S., Soares, S. L., Appelberg, R., and Kikelj, D. (2007) Design, synthesis, biochemical evaluation and antimycobacterial action of phosphonate inhibitors of antigen 85C, a crucial enzyme involved in biosynthesis of the mycobacterial cell wall. *Eur. J. Med. Chem. 42*, 54−63.
(20) Kremer, L., Maughan, W. N., Wilson, R. A., Dover, L. G., and Besra, G. S. (2002) The *M. tuberculosis* antigen 85 complex and mycolyltransferase activity. *Lett. Appl. Microbiol. 34*, 233−237.
(21) Wang, J., Elchert, B., Hui, Y., Takemoto, J. Y., Bensaci, M., Wennergren, J., Chang, H., Rai, R., and Chang, C.-W. T. (2004) Synthesis of trehalose-based compounds and study of their antibacterial activity against *Mycobacterium smegmatis*. *Bioorg. Med. Chem. 12*, 6397−6413.
(22) Rose, J. D., Maddry, J. A., Comber, R. N., Suling, W. J., Wilson, L. N., and Reynolds, R. C. (2002) Synthesis and biological evaluation of trehalose analogs as potential inhibitors of mycobacterial cell wall biosynthesis. *Carbohydr. Res. 337*, 105−120.
(23) Barry, C. S., Backus, K. M., Barry, C. E., III, and Davis, B. G. (2011) ESI-MS Assay of *M. tuberculosis* cell wall Antigen 85 enzymes permits substrate profiling and design of a mechanism-based inhibitor. *J. Am. Chem. Soc. 133*, 13232−13235.
(24) Kam, B. L., Barascut, J.-L., and Imbach, J.-L. (1979) A general method of synthesis and isolation, and an NMR spectroscopic study, of tetra-*O*-acetyl-D-aldopentofuranose. *Carbohydr. Res. 69*, 135−142.
(25) Ayers, J. D., Lowary, T. L., Morehouse, C. B., and Besra, G. S. (1998) Synthetic arabinofuranosyl oligosaccharides as mycobacterial arabinosyltransferase substrates. *Bioorg. Med. Chem. Lett. 8*, 437−442.
(26) Sanki, A. K., Boucau, J., Srivastava, P., Adams, S. S., Ronning, D. R., and Sucheck, S. J. (2008) Synthesis of methyl 5-*S*-alkyl-5-thio-arabinofuranosides and evaluation of their antimycobacterial activity. *Bioorg. Med. Chem. 16*, 5672−5682.
(27) Boucau, J., Sanki, A. K., Voss, B. J., Sucheck, S. J., and Ronning, D. R. (2009) A coupled assay measuring *Mycobacterium tuberculosis* antigen 85C enzymatic activity. *Anal. Biochem. 385*, 120−127.
(28) Sanki, A. K., Boucau, J., Umesiri, F. E., Ronning, D. R., and Sucheck, S. J. (2009) Design, synthesis and biological evaluation of sugar-derived esters, alpha-ketoesters and alpha-ketoamides as inhibitors for Mycobacterium tuberculosis antigen 85C. *Mol. BioSyst. 5*, 945−956.
(29) Ronning, D. R., Vissa, V., Besra, G. S., Belisle, J. T., and Sacchettini, J. C. (2004) *Mycobacterium tuberculosis* antigen 85A and 85C structures confirm binding orientation and conserved substrate specificity. *J. Biol. Chem. 279*, 36771−36777.
(30) Anderson, D. H., Harth, G., Horwitz, M. A., and Eisenberg, D. (2001) An interfacial mechanism and a class of inhibitors inferred from two crystal structures of the *Mycobacterium tuberculosis* 30 kDa major secretory protein (Antigen 85B), a mycolyl transferase. *J. Mol. Biol. 307*, 671−681.
(31) Goulding, C. W., Perry, L. J., Anderson, D., Sawaya, M. R., Cascio, D., Apostol, M. I., Chan, S., Parseghian, A., Wang, S.-S., Wu, Y., Cassano, V., Gill, H. S., and Eisenberg, D. (2003) Structural genomics of *Mycobacterium tuberculosis*: a preliminary report of progress at UCLA. *Biophys. Chem. 105*, 361−370.
(32) Tonge, P. J. (2000) Another brick in the wall. *Nat. Struct. Biol. 7*, 94−96.
(33) Ronning, D. R., Klabunde, T., Besra, G. S., Vissa, V. D., Belisle, J. T., and Sacchettini, J. C. (2000) Crystal structure of the secreted form of antigen 85C reveals potential targets for mycobacterial drugs and vaccines. *Nat. Struct. Biol. 7*, 141−146.
(34) Sanki, A. K., Boucau, J., Ronning, D. R., and Sucheck, S. J. (2009) Antigen 85C-mediated acyl transfer between synthetic acyl donors and fragments of the arabinan. *Glycoconj. J. 5*, 589−596.
(35) Umesiri, F. E., Sanki, A. K., Boucau, J., Ronning, D. R., and Sucheck, S. J. (2010) Recent advances toward the inhibition of mAG and LAM synthesis in *Mycobacterium tuberculosis*. *Med. Res. Rev. 30*, 290−326.
(36) Amemiya, Y., Terada, A., Wachi, K., Miyazawa, H., Hatakeyama, N., Matsuda, K., and Oshima, T. (1989) Synthesis and thromboxane synthetase inhibitory activity of di- or tetrahydrobenzo[*b*]-thiophenecarboxylic acid derivatives. *J. Med. Chem. 32*, 1265−1272.
(37) Bilokin, Y. V., Vasylyev, M. V., Branytska, O. V., Kovalenko, S. M., and Chernykh, V. P. (1999) A novel and expedient approach to new heterocycles containing benzothiophene, benzothieno[2,3-d]-pyrimidine and coumarin moieties. *Tetrahedron 55*, 13757−13766.
(38) Baraldi, P. G., Romagnoli, R., Pavani, M. G., Nunez, M. C., Tabrizi, M. Ag., Shryock, J. C., Leung, E., Moorman, A. R., Uluoglu, C., Iannotta, V., Merighi, S., and Borea, P. A. (2003) Synthesis and biological effects of novel 2-amino-3-naphthoylthiophenes as allosteric enhancers of the A_1 adenosine receptor. *J. Med. Chem. 46*, 794−809.
(39) Bishop, A. C., and Blair, E. R. (2006) A gatekeeper residue for inhibitor sensitization of protein tyrosine phosphatases. *Bioorg. Med. Chem. Lett. 16*, 4002−4006.
(40) Kaila, N., Janz, K., Huang, A., Moretto, A., DeBernardo, S., Bedard, P. W., Tam, S., Clerin, V., Keith, J. C., Jr., Tsao, D. H. H., Sushkova, N., Shaw, G. D., Camphausen, R. T., Schaub, R. G., and Wang, Q. (2007) 2-(4-Chlorobenzyl)-3-hydroxy-7,8,9,10-tetrahydrobenzo[H]quinoline-4-carboxylic acid (PSI-697): Identification of a clinical candidate from the quinoline salicylic acid series of P-selectin antagonists. *J. Med. Chem. 50*, 40−64.
(41) Sanki, A. K., Sucheck, S. J., Ronning, D. R., Boucau, J., Umesiri, F. E., and Ibrahim, D. A. (2010) Inhibitors of Antigen 85 from Mycobacterium tuberculosis, *Abstracts of Papers, 239th ACS National Meeting*, March 21−25, San Francisco, CA, United States, ORGN-118.

(42) Ibrahim, D. A., Adams, S. S., Sucheck, S. J., Trabbic, K. R., Ronning, D. R., Sanki, A. K., and Boucau, J. (2010) Inhibitors of *Mycobacterium tuberculosis* Antigen 85, *Abstracts, 41st Central Regional Meeting of the ACS*, June 16−19, Dayton, OH, United States, CERMACS-307.
(43) Scheich, C., Puetter, V., and Schade, M. (2010) Novel small molecule inhibitors of MDR *Mycobacterium tuberculosis* by NMR fragment screening of antigen 85C. *J. Med. Chem. 53*, 8362−8367.
(44) Warrier, T., Tropis, M., Werngren, J., Diehl, A., Gengenbacher, M., Schlegel, B., Schade, M., Oschkinat, H., Daffe, M., Hoffner, S., Eddine, A. N., and Kaufmann, S. H. E. (2012) Antigen 85C inhibition restricts *Mycobacterium tuberculosis* growth through disruption of Cord Factor biosynthesis. *Antimicrob. Agents Chemother. 56*, 1735−1743.
(45) Otwinowski, Z., and Minor, W. (1997) Processing of X-ray diffraction data collected in oscillation mode. *Methods Enzymol. 276*, 307−26.
(46) Kissinger, C. R., Gehlhaar, D. K., and Fogel, D. B. (1999) Rapid automated molecular replacement by evolutionary search. *Acta Crystallogr., Sect. D: Biol. Crystallogr. 55*, 484−91.
(47) Emsley, P., Lohkamp, B., Scott, W. G., and Cowtan, K. (2010) Features and development of Coot. *Acta Crystallogr., Sect. D: Biol. Crystallogr. 66*, 486−501.
(48) Adams, P. D., Gopal, K., Grosse-Kunstleve, R. W., Hung, L. W., Ioerger, T. R., McCoy, A. J., Moriarty, N. W., Pai, R. K., Read, R. J., Romo, T. D., Sacchettini, J. C., Sauter, N. K., Storoni, L. C., and Terwilliger, T. C. (2004) Recent developments in the PHENIX software for automated crystallographic structure determination. *J. Synchrotron Radiat. 11*, 53−5.
(49) Adams, P. D., Grosse-Kunstleve, R. W., Hung, L. W., Ioerger, T. R., McCoy, A. J., Moriarty, N. W., Read, R. J., Sacchettini, J. C., Sauter, N. K., and Terwilliger, T. C. (2002) PHENIX: building new software for automated crystallographic structure determination. *Acta Crystallogr., Sect. D: Biol. Crystallogr. 58*, 1948−54.
(50) National Committee for Clinical Laboratory Standards (2000) Approved Standard: M2-A7, *Performance standards for antimicrobial disk susceptibility tests*, 7th ed., National Committee for Clinical Laboratory Standards, Wayne, PA.
(51) Peet, N. P., Sunder, S., Barbuch, R. J., and Vinogradoff, A. P. (1986) Mechanistic observations in the Gewald syntheses of 2-aminothiophene. *J. Heterocycl. Chem. 23*, 129−134.
(52) Gewald, K., Schinke, E., and Böttcher, H. (1966) Heterocyclen aus CH-aciden nitrilen, VIII. 2-Amino-thiophene aus methylenaktiven nitrilen, carbonylverbindungen und schwefel. *Chem. Ber. 99*, 94−100.
(53) Khan, K. M., Nullah, Z., Lodhi, M. A., Jalil, S., Choudhary, M. I., and Rahman, A. U. (2006) Synthesis and anti-inflammatory activity of some selected aminothiophene analogs. *J. Enzym. Inhib. Med. Chem. 21*, 139−143.
(54) Manhas, M. S., Rao, V. V., and Amin, S. G. J. (1976) Heterocyclic compounds. VII. Synthesis of thiadiazasteroid analogs. *Heterocycl. Chem. 13*, 821−824.
(55) Hagen, H., Nilz, G., Walter, H., and Landes, A. (1995) Preparation of 2-aminothiophene derivatives as herbicide antidotes. U. S. Patent 5,442,335, June 6, 1995.
(56) Sugiyama, M., Sakamoto, T., Tabata, K., Endo, K., Ito, K., Kobayashi, M., and Fukumi, H. (1989) Condensed thienopyrimidines. I. Synthesis and gastric antisecretory activity of 2,3-dihydro-5H-oxazolothienopyrimidin-5-one derivatives. *Chem. Pharm. Bull. 37*, 2091−2102.
(57) Yoshimura, Y., Kuze, T., Ueno, M., Komiya, F., Haraguchi, K., Tanaka, H., Kano, F., Yamada, K., Asami, K., Kaneko, N., and Takahata, H. (2006) A Practical synthesis of 4′-thioribonucleosides. *Tetrahedron Lett. 47*, 591−594.
(58) Hughes, N. A., Kuhajda, K.-M., and Miljkovic, D. A. (1994) New syntheses of methyl 5-thio-β-D-arabinopyranoside and (+) biotin. *Carbohydr. Res. 257*, 299−304.
(59) Friesner, R. A., Banks, J. L., Murphy, R. B., Halgren, T. A., Klicic, J. J., Mainz, D. T., Repasky, M. P., Knoll, E. H., Shelley, M., Perry, J. K., Shaw, D. E., Francis, P., and Shenkin, P. S. (2004) Glide: A new approach for rapid, accurate docking and scoring. 1. Method and assessment of docking accuracy. *J. Med. Chem. 47*, 11729−1749.
(60) Jacobson, M. P., Pincus, D. L., Rapp, C. S., Day, T. J., Honig, B., Shaw, D. E., and Friesner, R. A. (2004) A hierarchical approach to all-atom protein loop prediction. *Proteins 55*, 351−367.
(61) Kaminski, G. A., Friesner, R. A., Tirado-Rives, J., and Jorgensen, W. L. J. (2001) Evaluation and reparametrization of the OPLS-AA force field for proteins via comparison with accurate quantum chemical calculations on peptides. *Phys. Chem. B 105*, 6474−6487.
(62) Yu, Z., Jacobson, M. P., and Friesner, R. A. (2006) What role do surfaces play in GB models? A new-generation of surface-generalized born model based on a novel Gaussian surface for biomolecules. *J. Comput. Chem. 27*, 72−89.
(63) García-lópez, J., Hernández-Mateo, F., Isac-García, J., Kim, J., Roy, R., Santoyo-González, F., and Vergas-Berengeul, A. (1999) Synthesis of per-glycosylated β-cyclodextrines having enhanced lectin binding affinity. *J. Org. Chem. 64*, 522−531.
(64) Skaanderup, P. R., Poulsen, C. S., Hyldtoft, L., Jorgensen, M. R., and Madsen, R. (2002) Regioselective conversion of primary alcohols into iodides in unprotected methyl furanosides and pyranosides. *Synthesis 12*, 1721−1727.

NOTE ADDED AFTER ASAP PUBLICATION

This paper was published on the Web on Dec 10, 2012, with errors in Scheme 3. The corrected version was reposted on Dec 19, 2012.

Supporting Information for

Design, synthesis and X-ray analysis of a glycoconjugate bound to *Mycobacterium tuberculosis* Antigen 85C

Diaa A. Ibrahim[1], Julie Boucau[2], Daniel Lajiness[2], Sri Kumar Veleti[2], Kevin R. Trabbic[2], Samuel S. Adams[2], Donald R. Ronning[2] and Steven J. Sucheck[2]**

[1]National Organization for Drug Control & Research, Cairo, Gizaa, Egypt.

[2]Department of Chemistry, The University of Toledo, 2801 W. Bancroft Street, Toledo, Ohio 43606, USA.

Donald.Ronning@UToledo.edu; Steve.Sucheck@UToledo.edu

^{1}H NMR of Ethyl 2-[(2-chloroacetyl) amino]-4,5,6,7-tetrahydrobenzo[*b*]thiophene-3-carboxylate (2a).

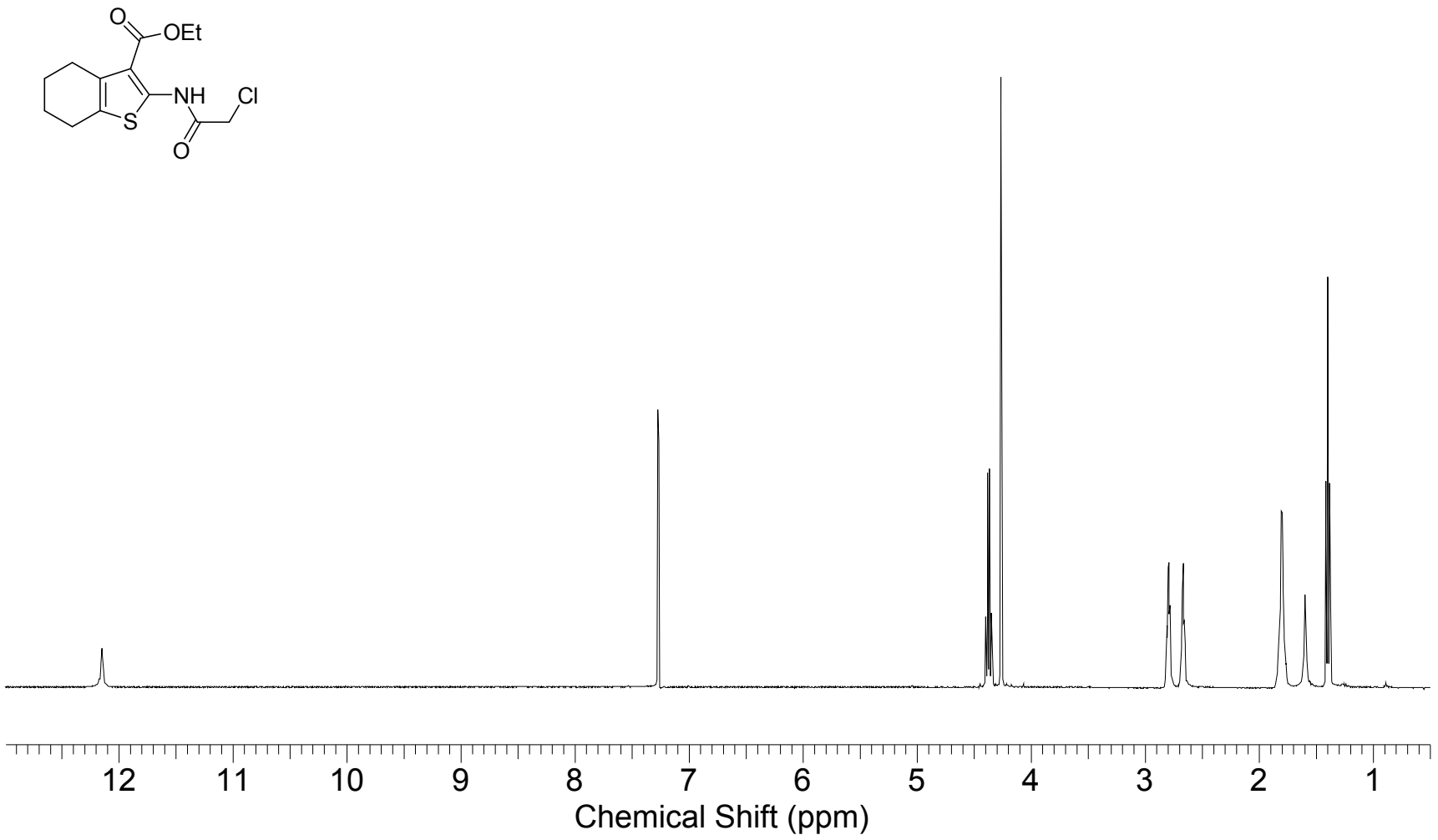

^{1}H NMR of Ethyl 2-[(4-chlorobutanoyl) amino]-4,5,6,7-tetrahydrobenzo[*b*]thiophene-3-carboxylate (2b).

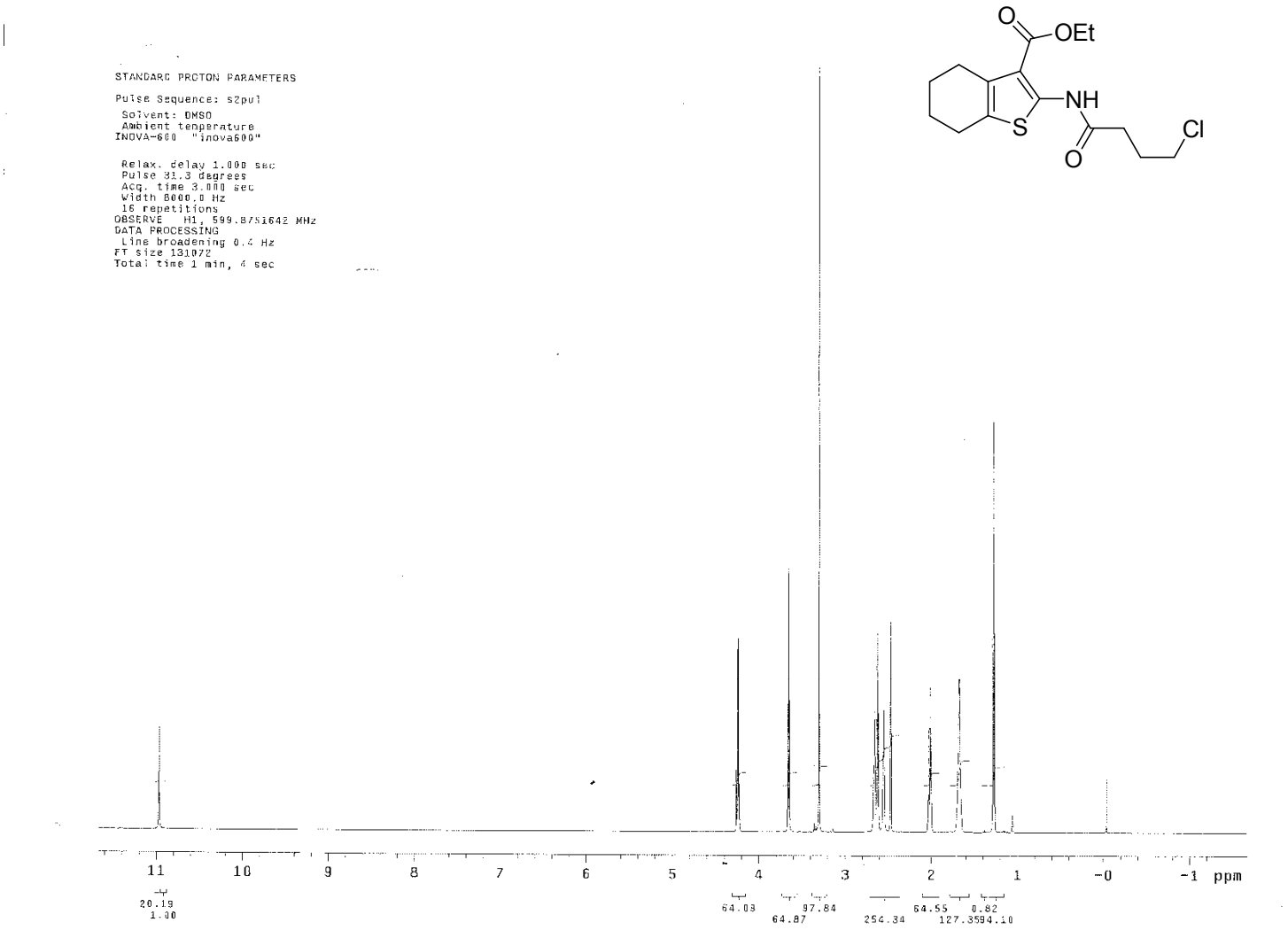

^{13}C NMR of Ethyl 2-[(4-chlorobutanoyl) amino]-4,5,6,7-tetrahydrobenzo[*b*]thiophene-3-carboxylate (2b).

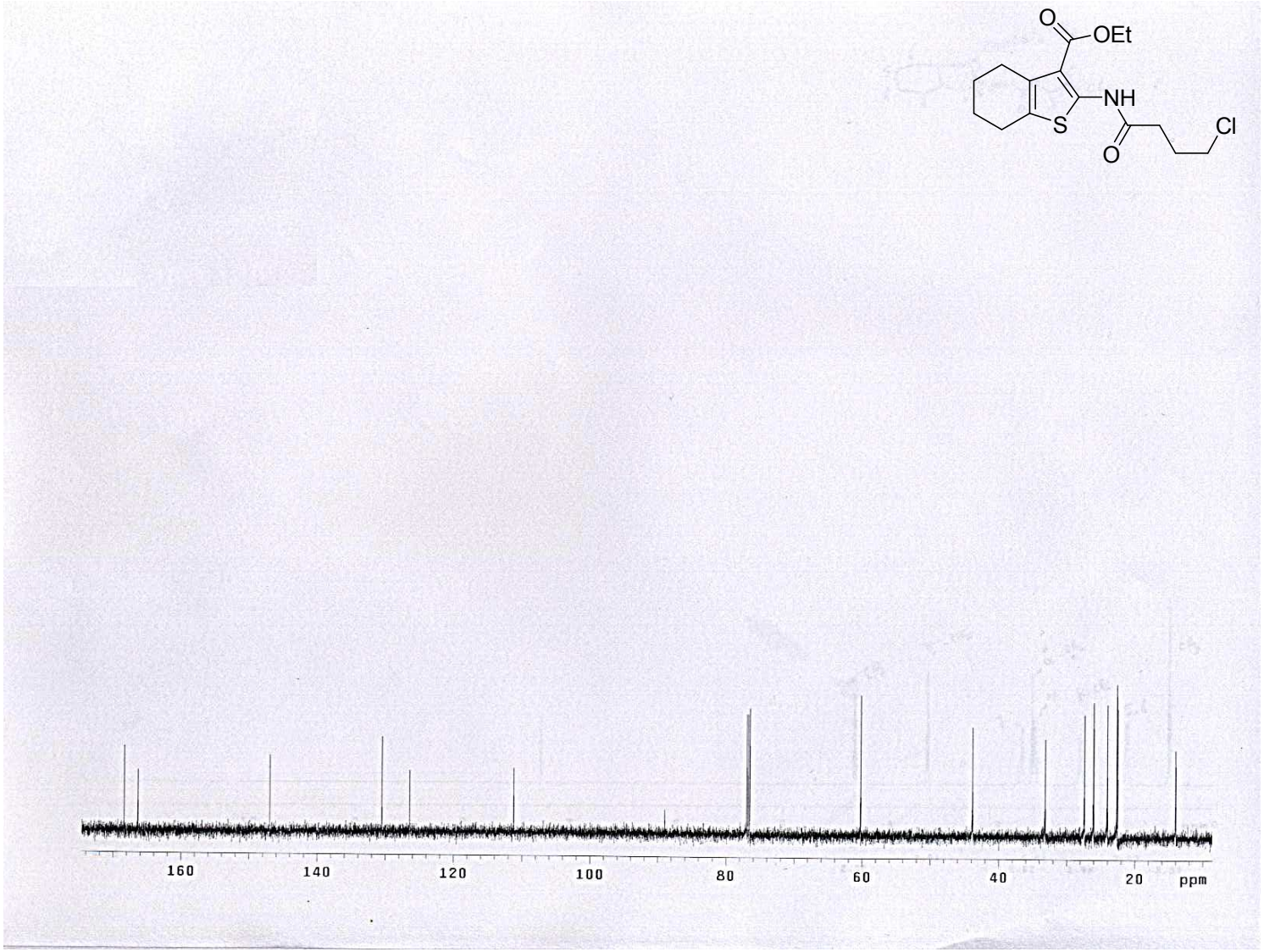

^{1}H NMR of 2-Chloro-*N*-(3-cyano-4,5,6,7-tetrahydrobenzo[*b*]thien-2-yl)acetamide (2c).

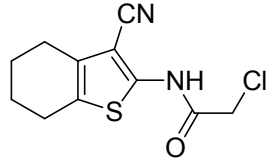

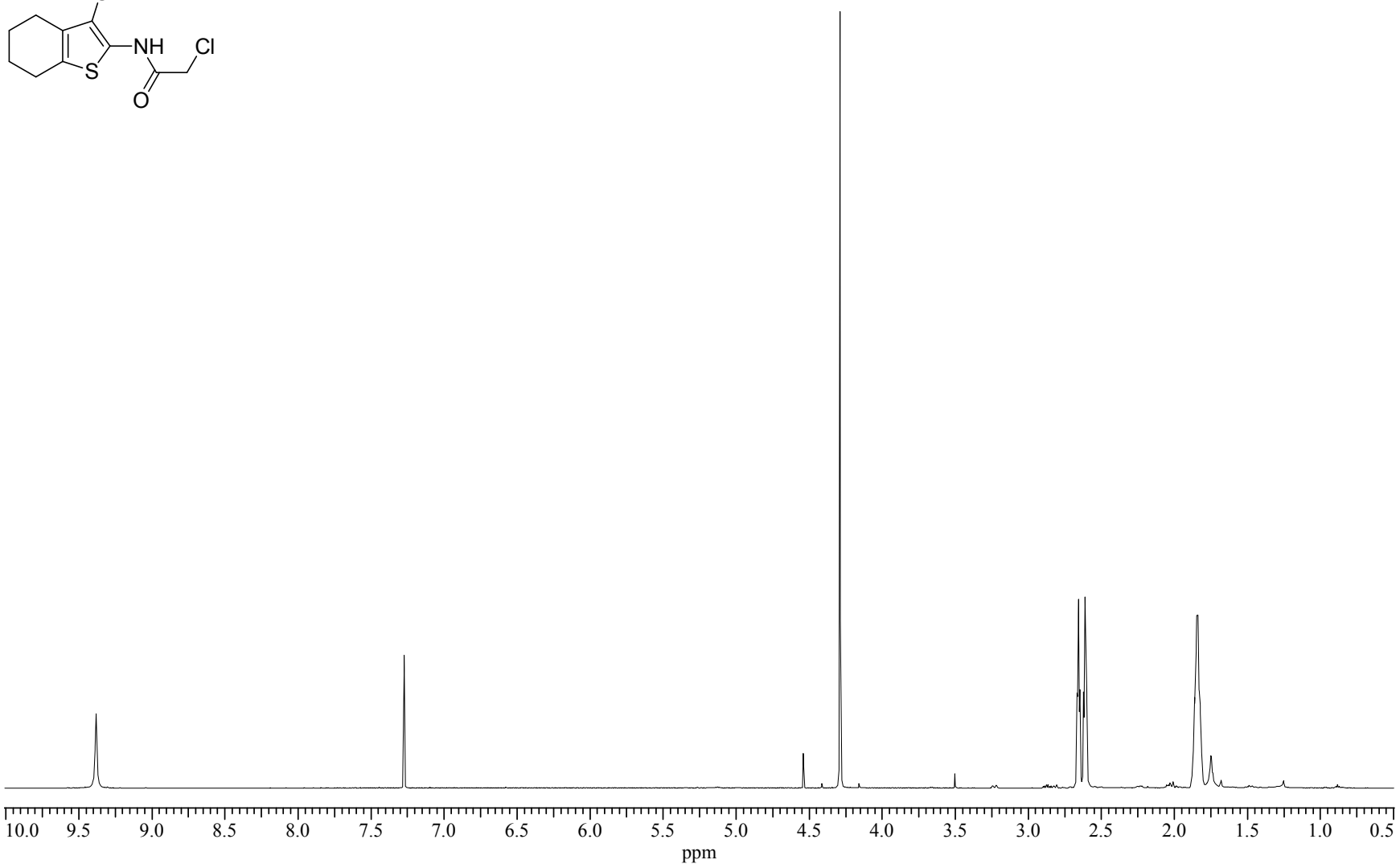

^{13}C NMR of 2-Chloro-*N*-(3-cyano-4,5,6,7-tetrahydrobenzo[*b*]thien-2-yl)acetamide (2c).

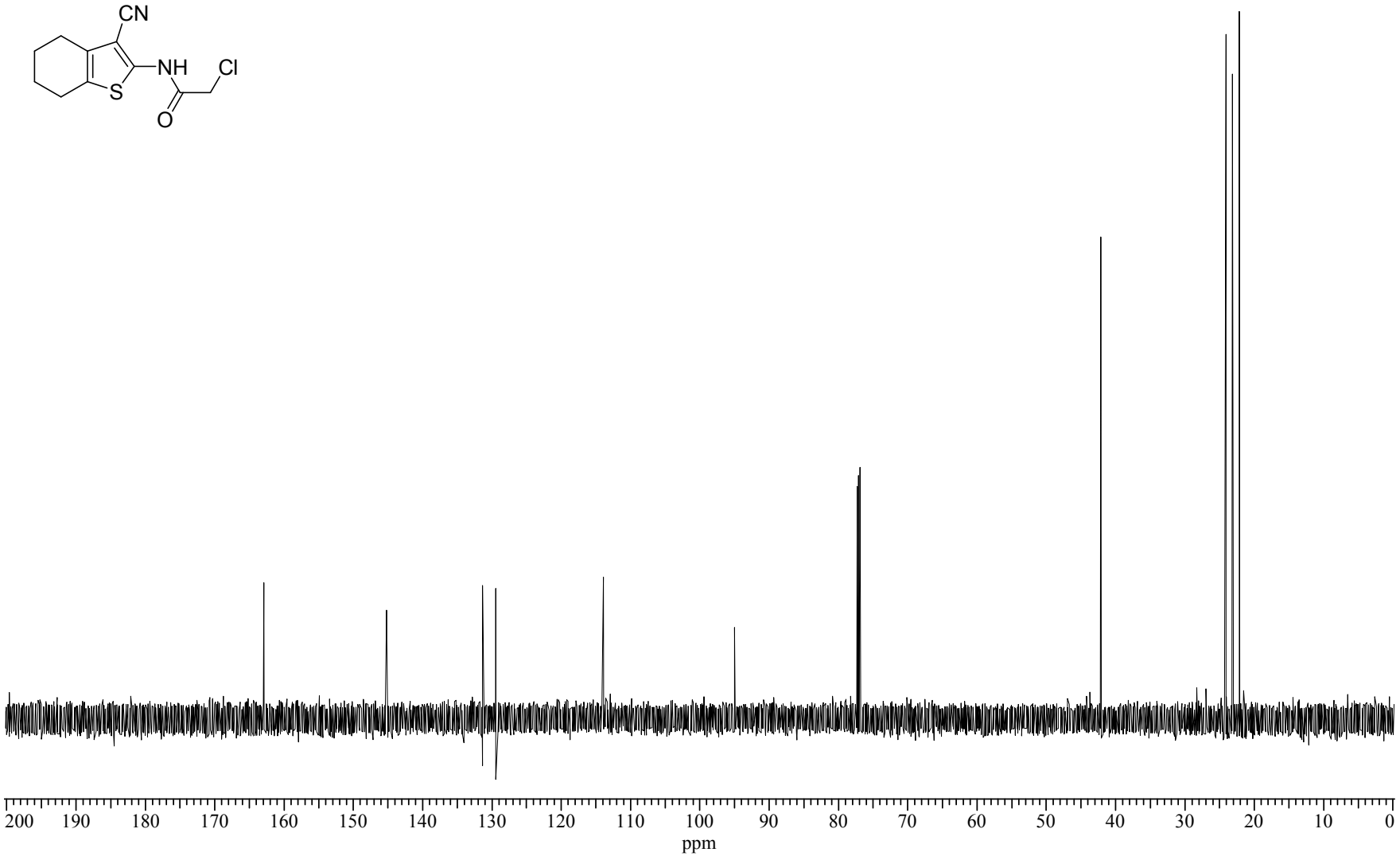

^{1}H NMR of 4-Chloro-*N*-(3-cyano-4,5,6,7-tetrahydrobenzo[*b*]thien-2-yl)butanamide (2d).

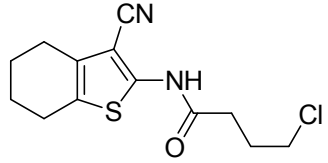

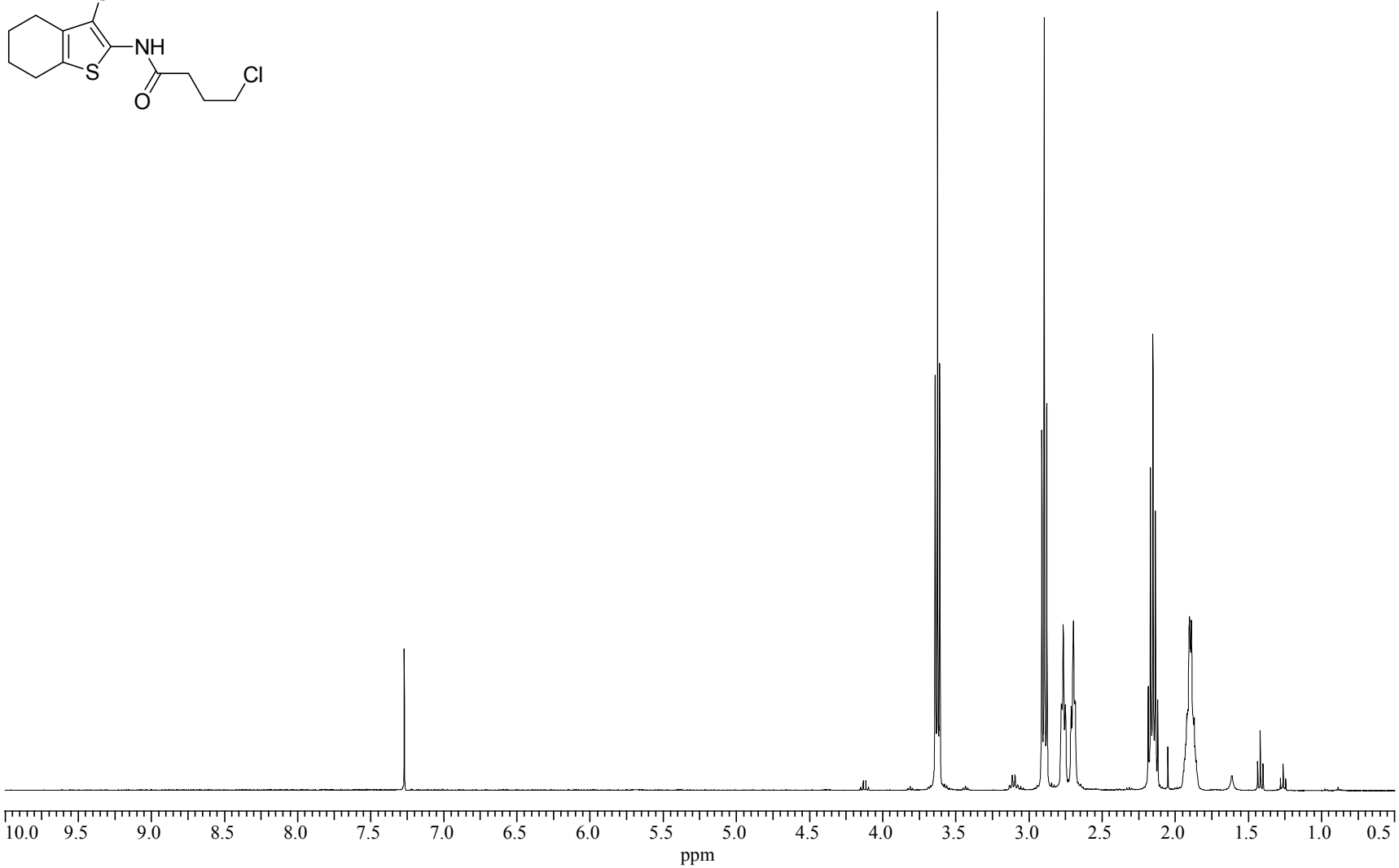

^{13}C NMR of 4-Chloro-*N*-(3-cyano-4,5,6,7-tetrahydrobenzo[*b*]thien-2-yl)butanamide (2d).

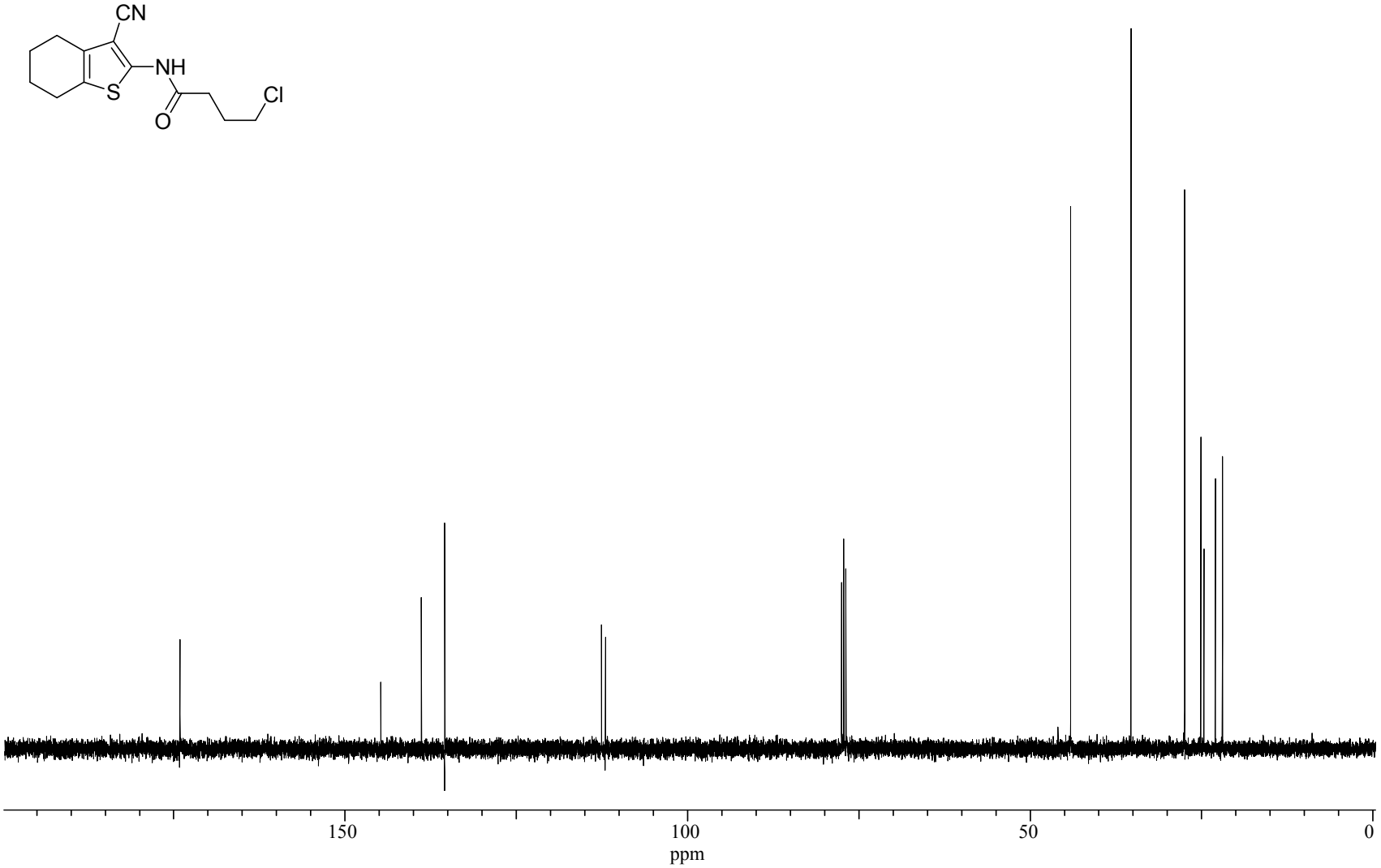

^{1}H NMR of Ethyl 2-(2-(acetylthio)acetamido)-4,5,6,7-tetrahydrobenzo[*b*]thiophene-3-carboxylate (3a).

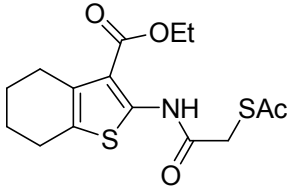

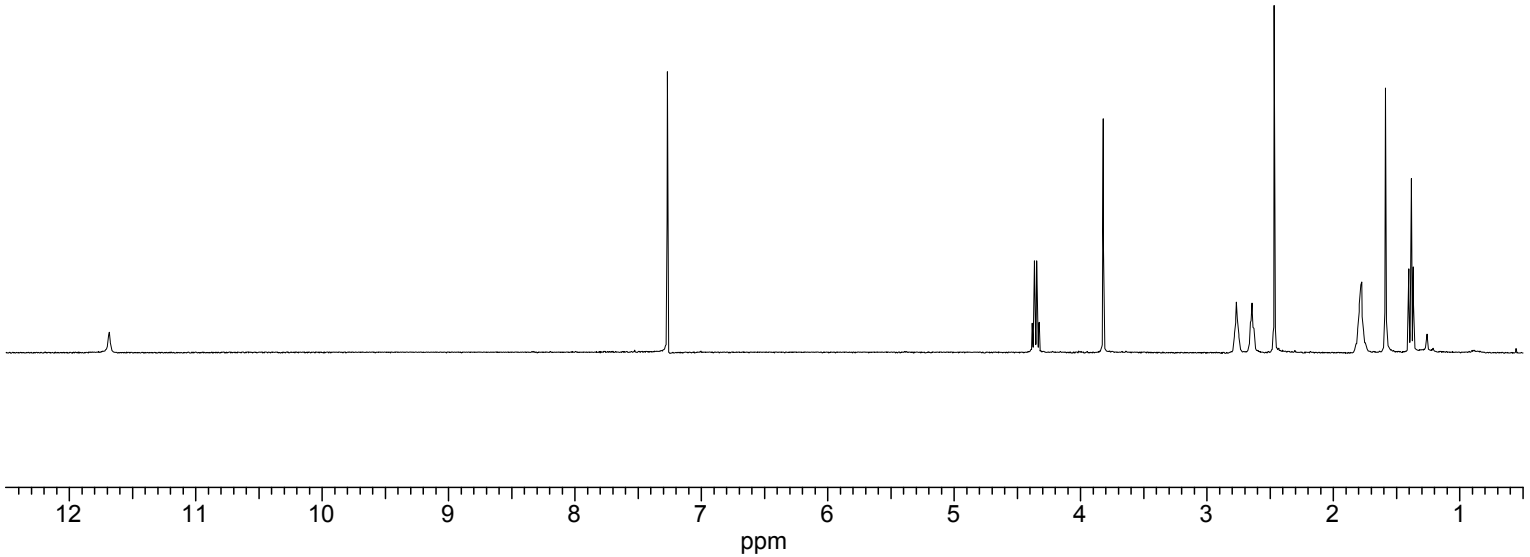

^{13}C NMR Ethyl 2-(2-(acetylthio)acetamido)-4,5,6,7-tetrahydrobenzo[*b*]thiophene-3-carboxylate (3a).

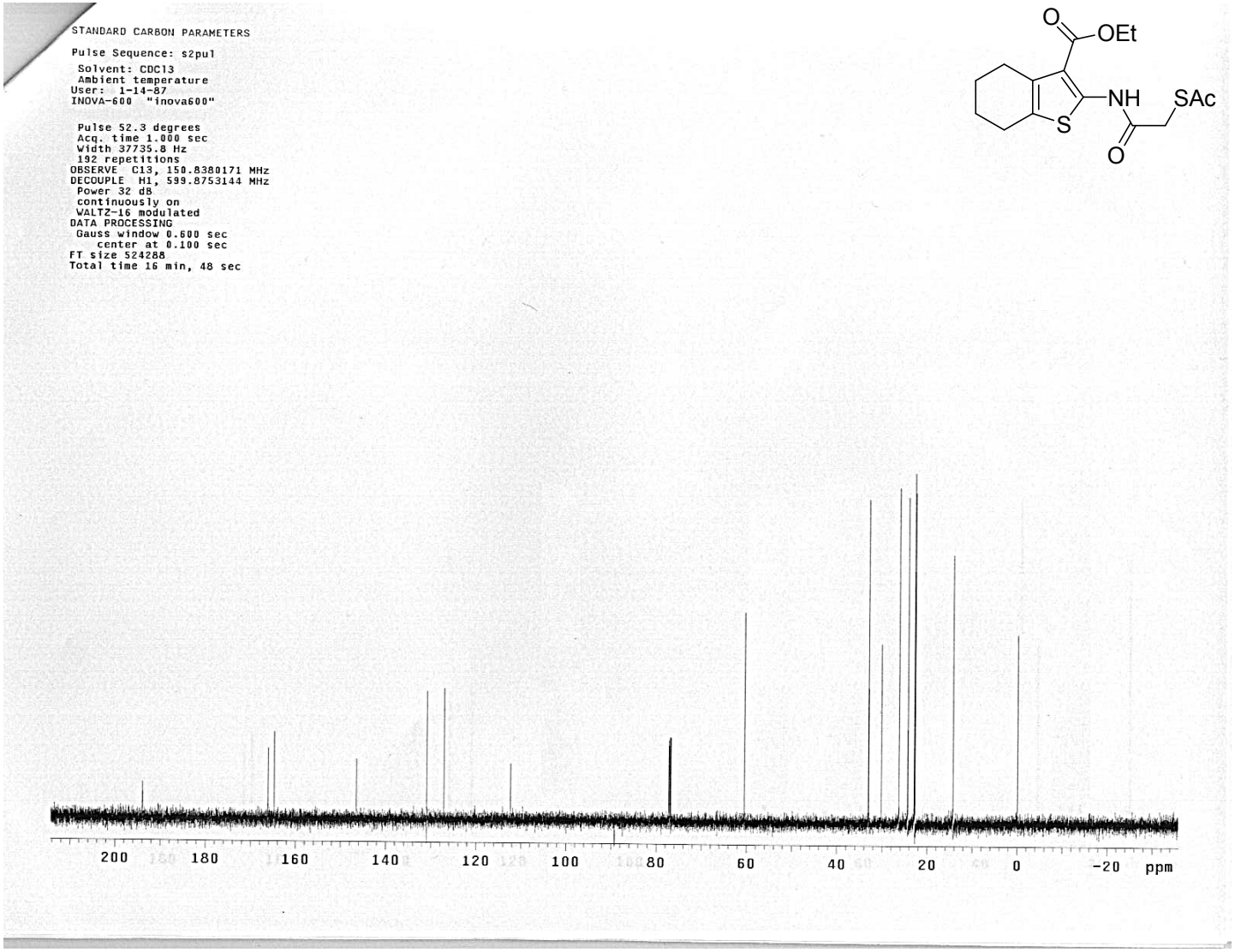

^{1}H NMR of Ethyl 2-(4-(acetylthio)butanamido)-4,5,6,7-tetrahydrobenzo[*b*]thiophene-3-carboxylate (3b).

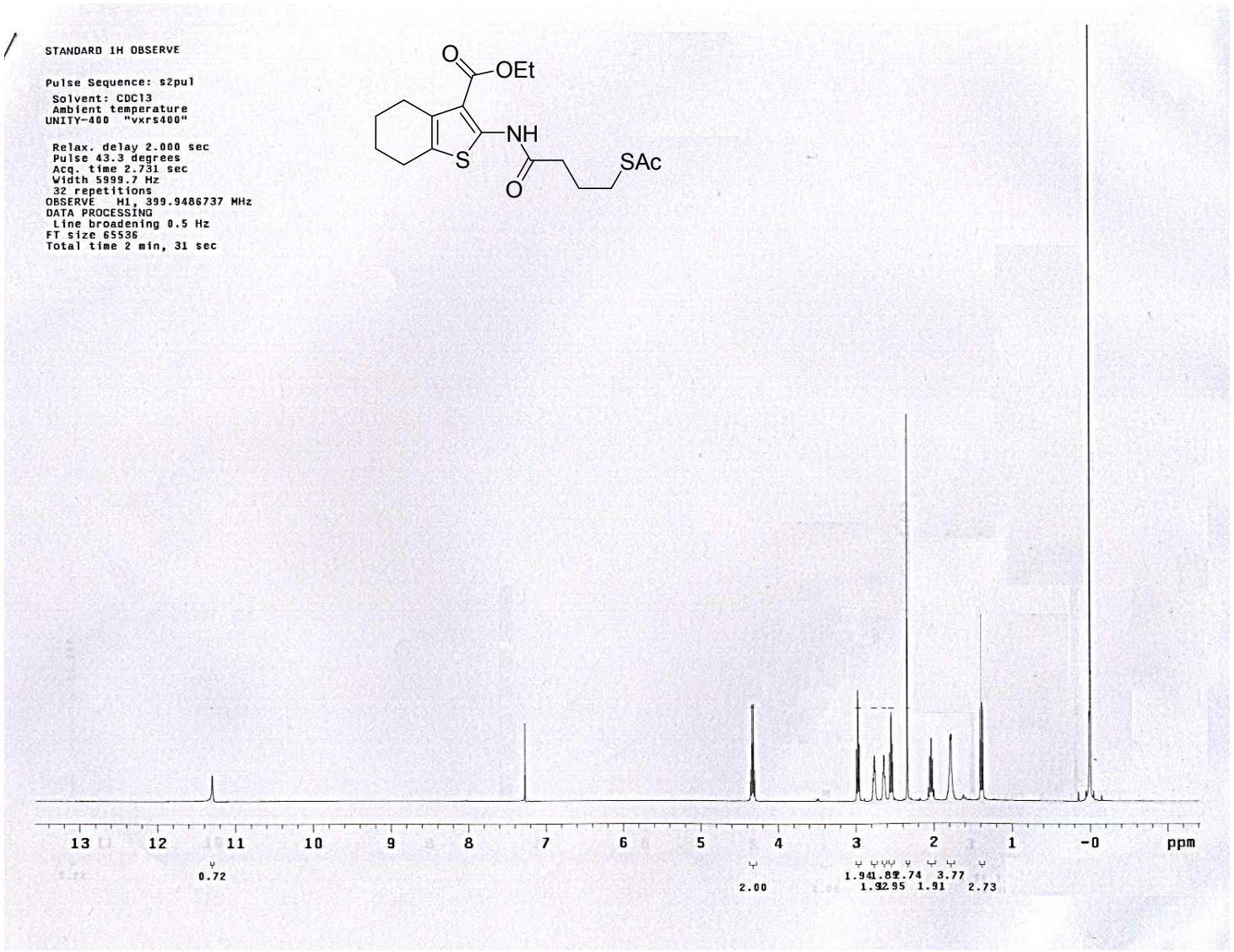

^{13}C NMR of Ethyl 2-(4-(acetylthio)butanamido)-4,5,6,7-tetrahydrobenzo[*b*]thiophene-3-carboxylate (3b).

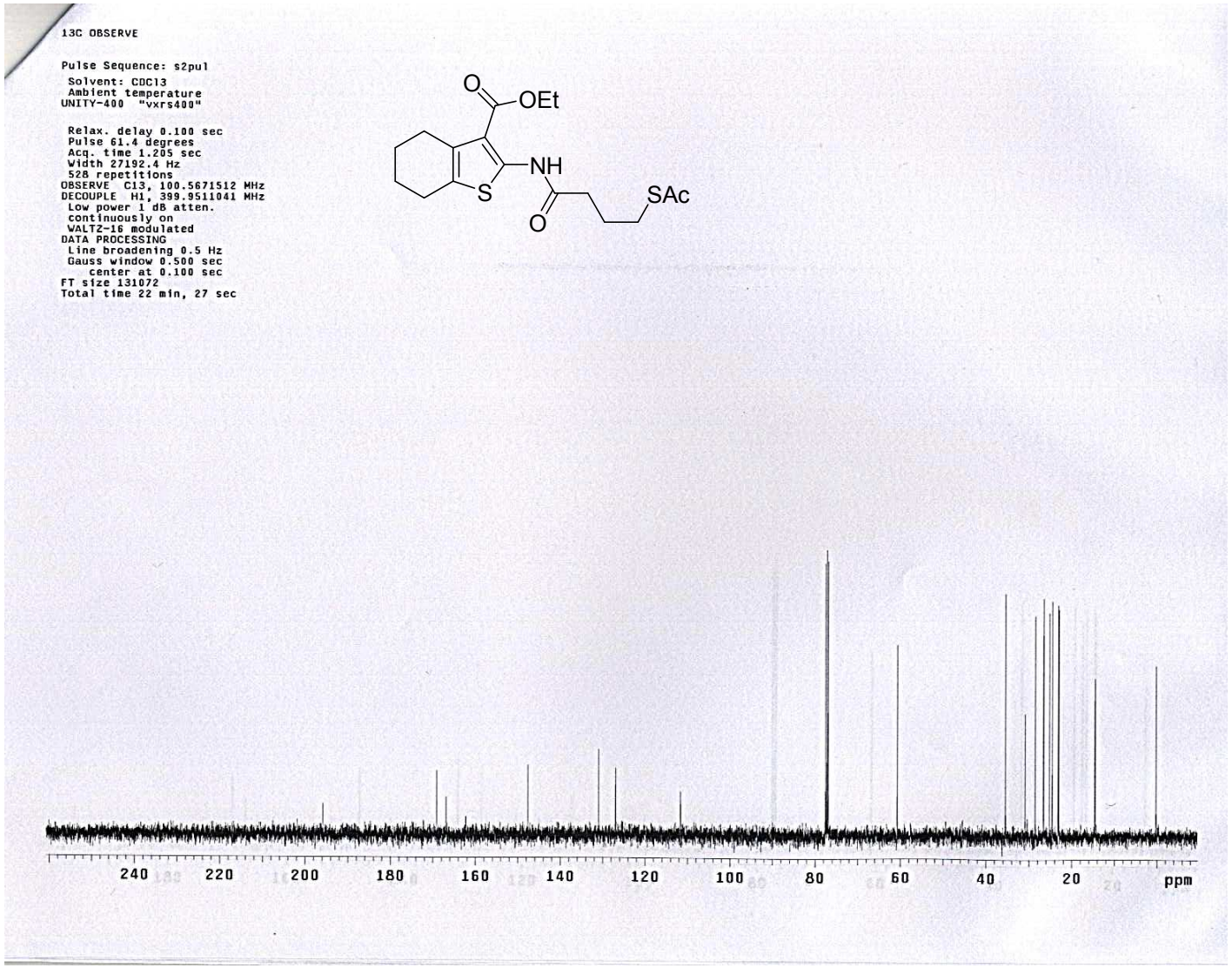

^{1}H NMR of 4-(3-Cyano-4,5,6,7-tetrahydrobenzo[*b*]thiophen-2-ylamino)-4-oxoethyl ethanethioate (3c).

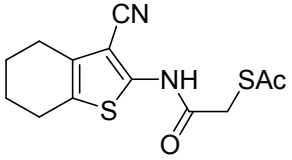

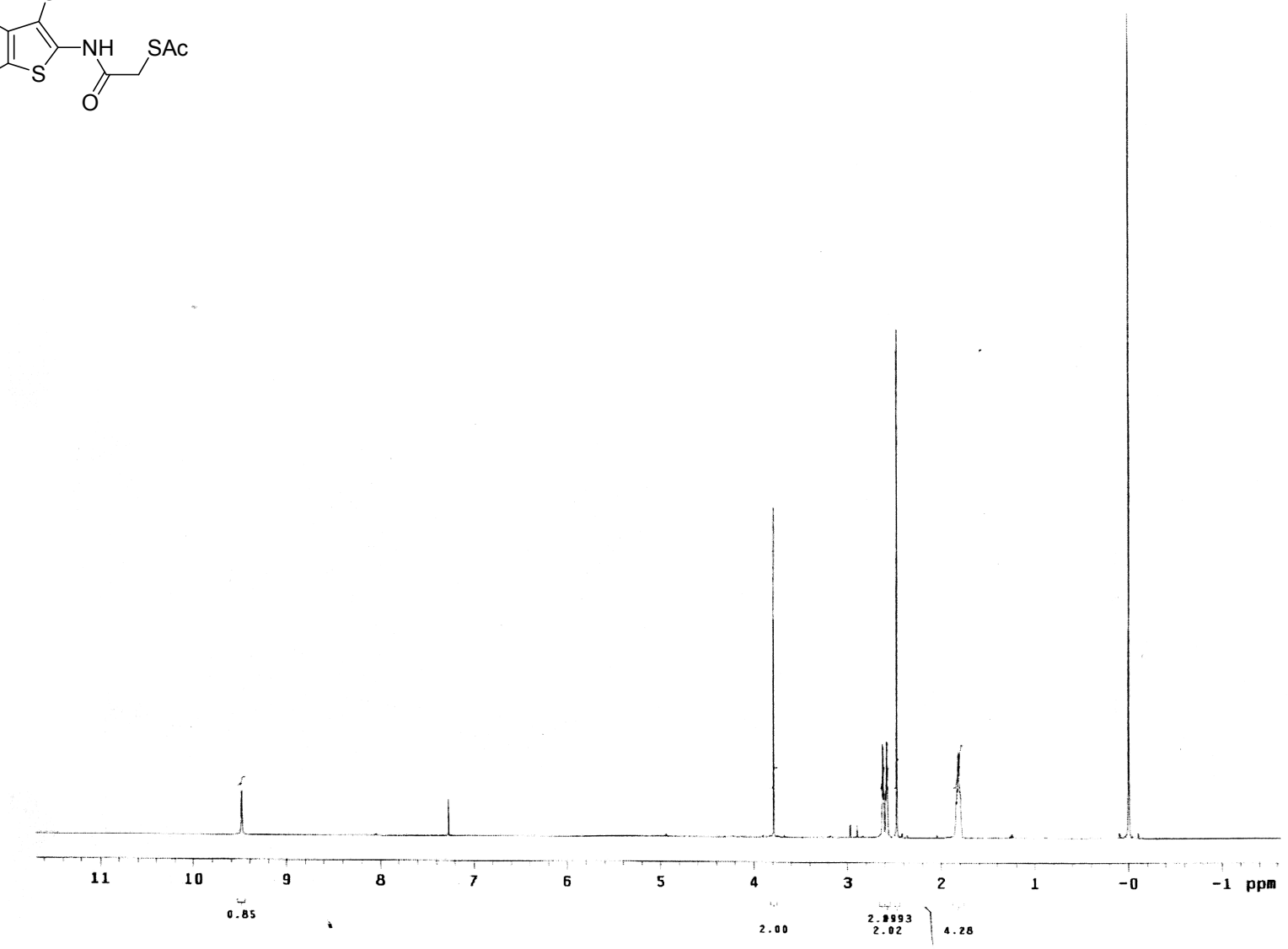

^{13}C NMR of 4-(3-Cyano-4,5,6,7-tetrahydrobenzo[*b*]thiophen-2-ylamino)-4-oxoethyl ethanethioate (3c).

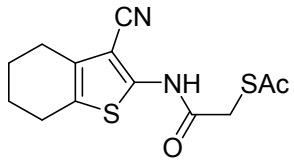

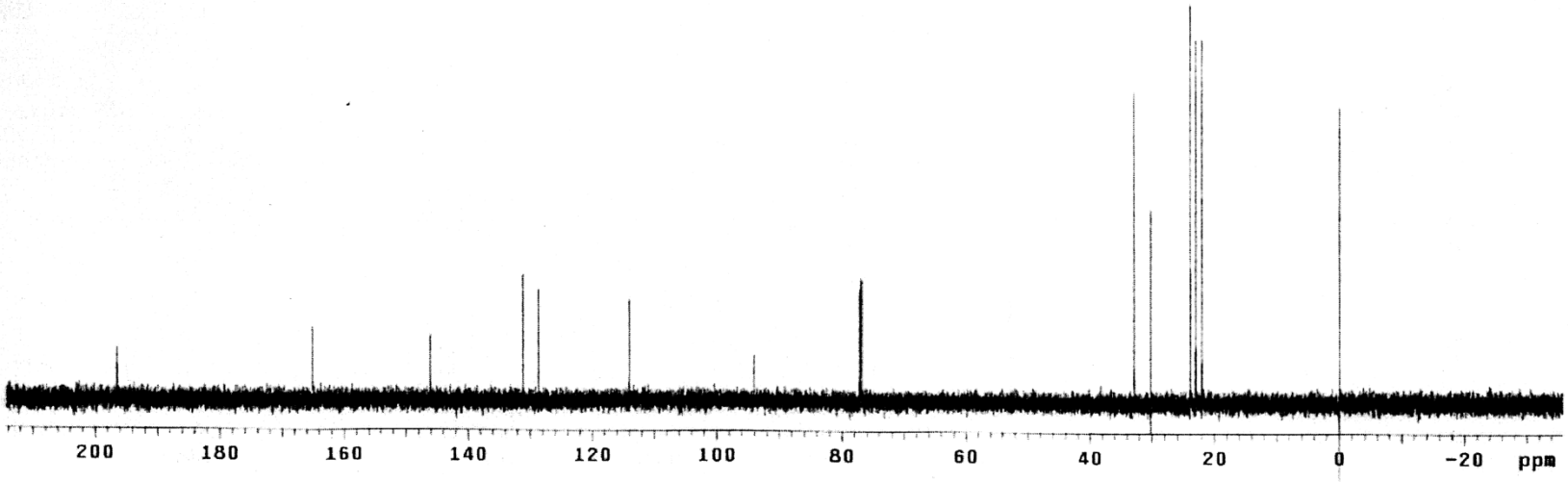

^{1}H NMR of 4-(3-Cyano-4,5,6,7-tetrahydrobenzo[*b*]thiophen-2-ylamino)-4-oxobutyl ethanethioate (3d).

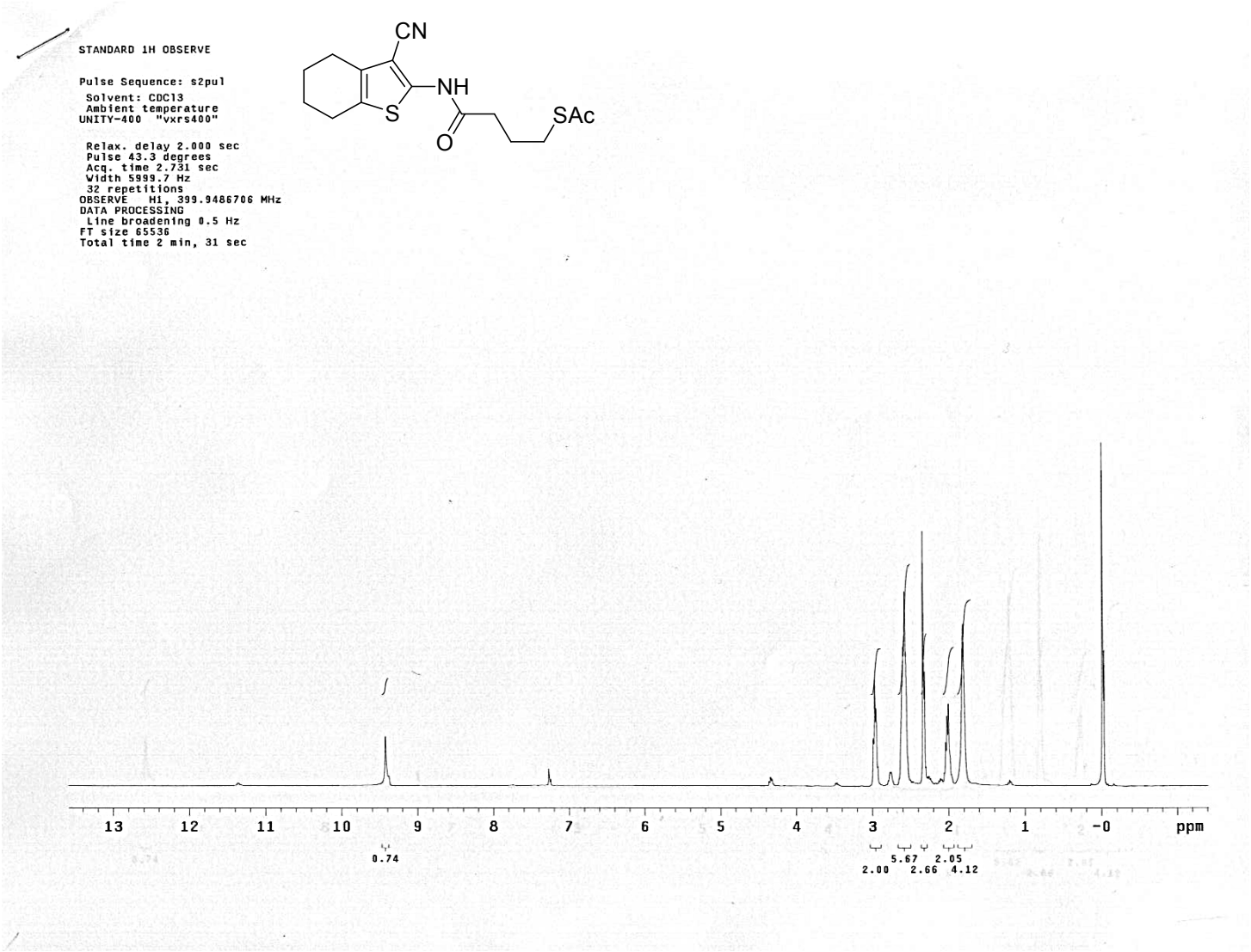

^{13}C NMR of 4-(3-Cyano-4,5,6,7-tetrahydrobenzo[*b*]thiophen-2-ylamino)-4-oxobutyl ethanethioate (3d).

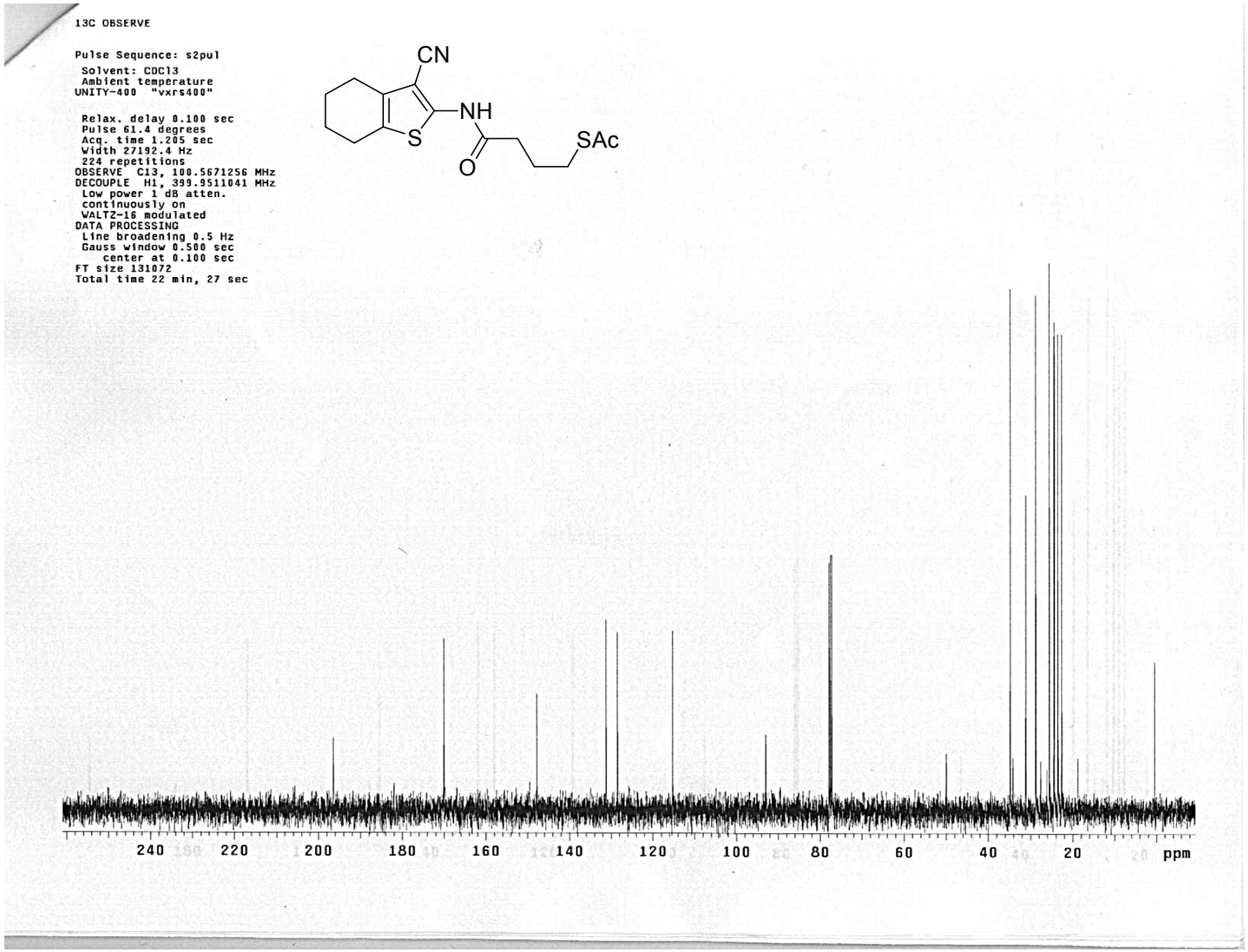

^{1}H NMR of Ethyl 2-[(4-bromobutanoyl)amino]-4,5,6,7-tetrahydrobenzo[*b*]thiophene-3-carboxylate (4a)

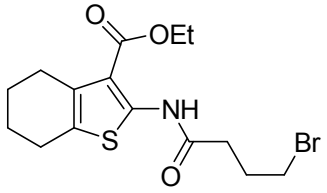

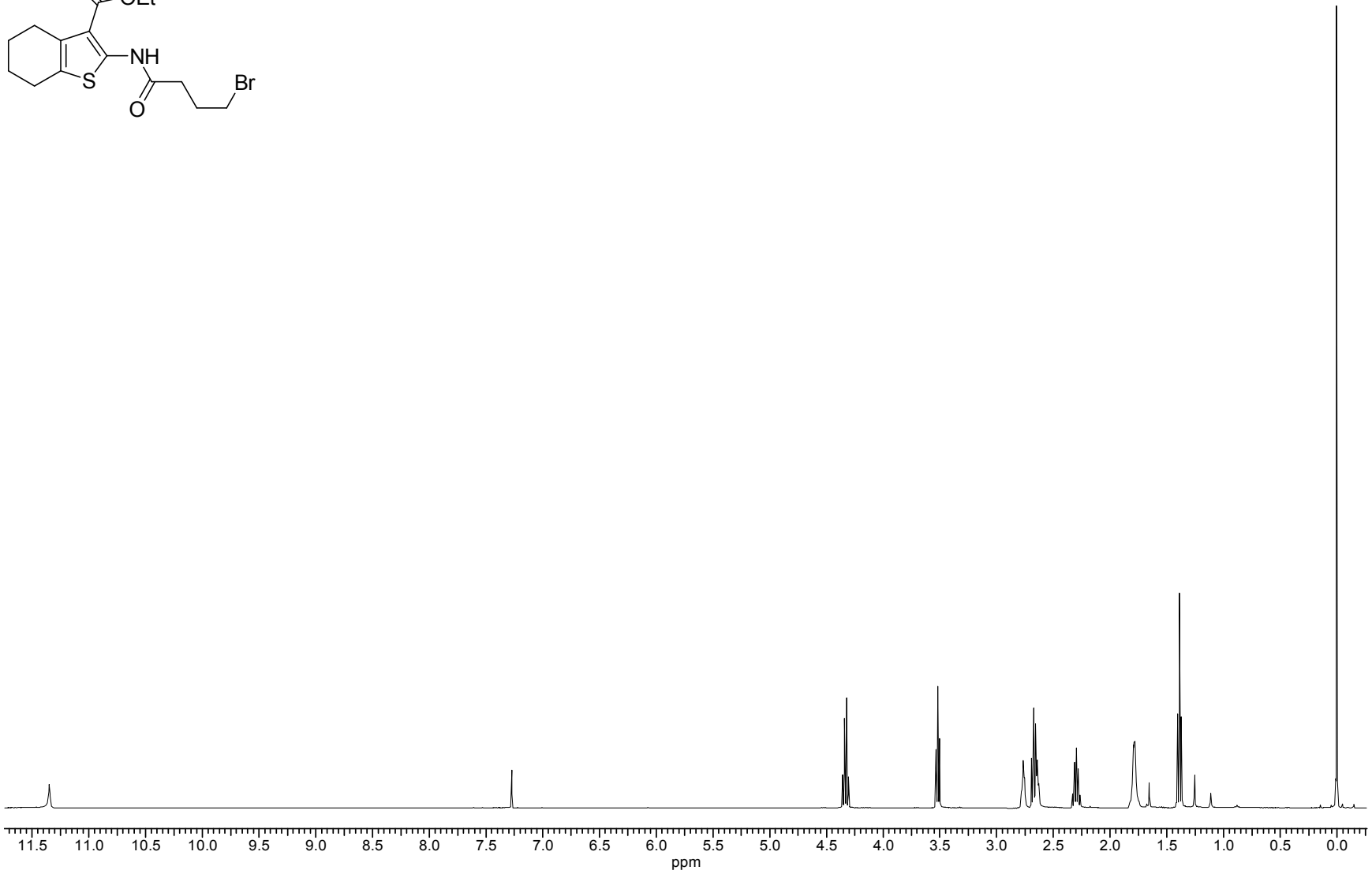

^{13}C NMR of Ethyl 2-[(4-bromobutanoyl)amino]-4,5,6,7-tetrahydrobenzo[*b*]thiophene-3-carboxylate (4a)

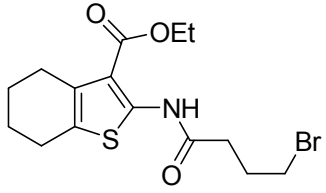

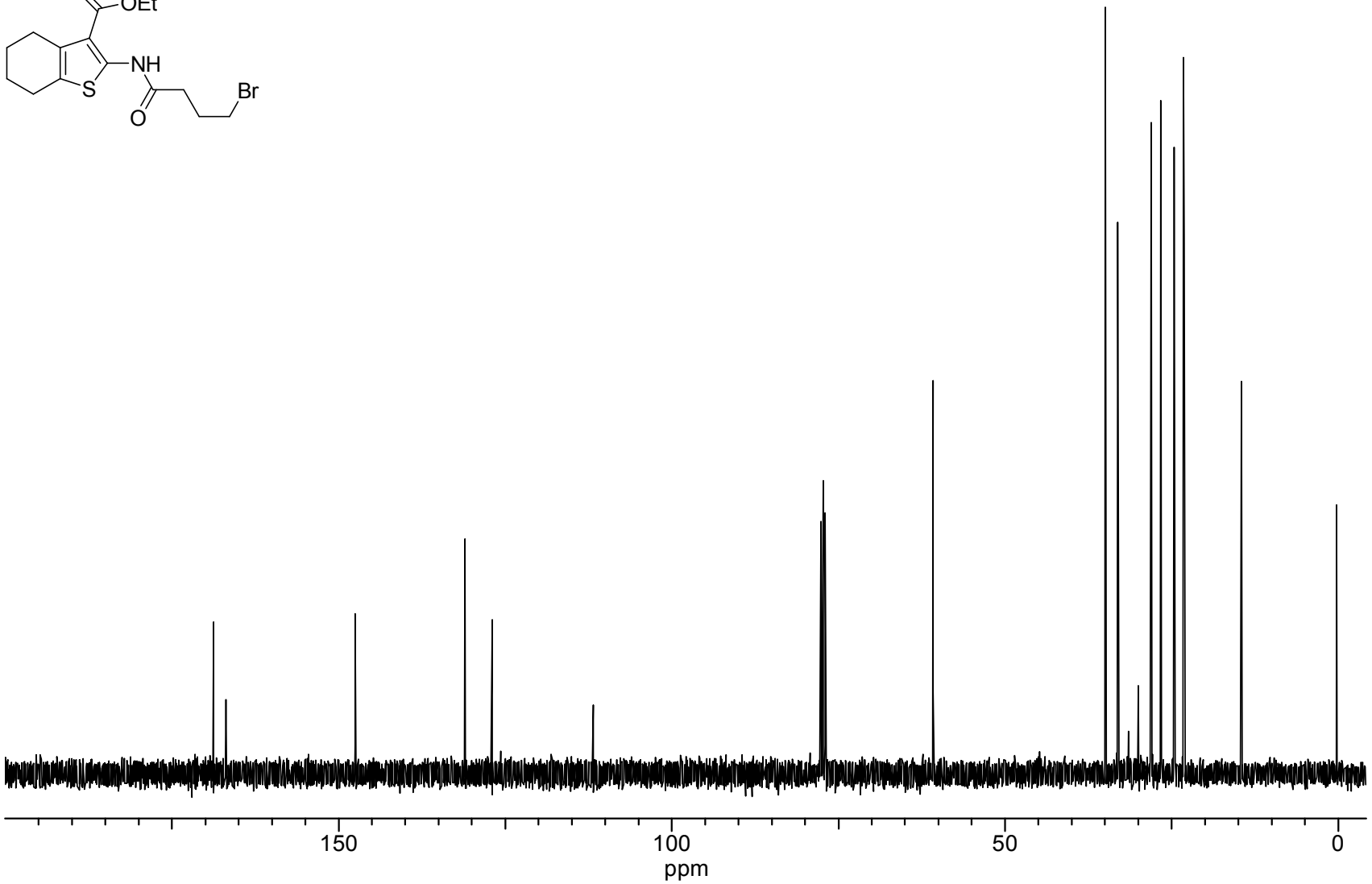

^{1}H NMR of 4-Bromo-*N*-(3-cyano-4,5,6,7-tetrahydrobenzo[*b*]thiophen-2-yl)butanamide (4b)

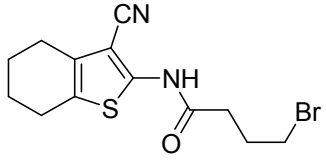

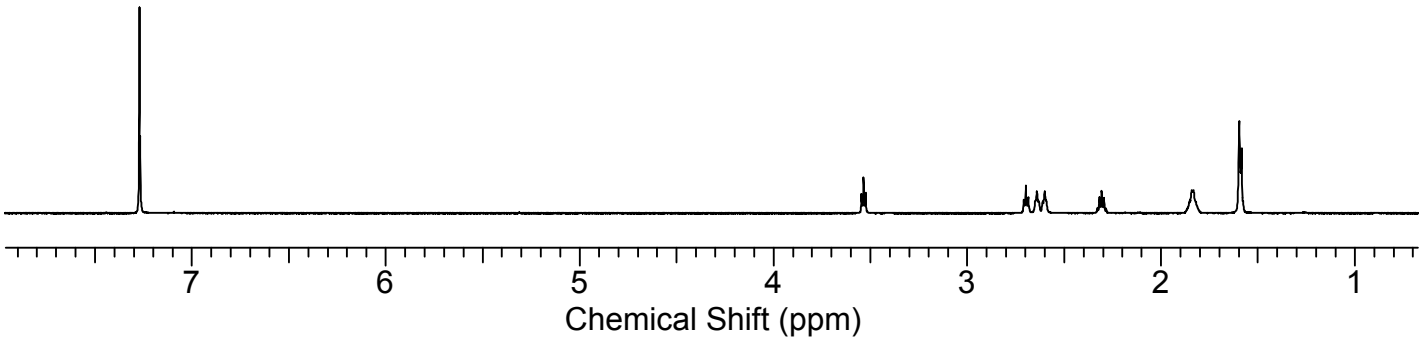

^{13}C NMR of 4-Bromo-*N*-(3-cyano-4,5,6,7-tetrahydrobenzo[*b*]thiophen-2-yl)butanamide (4b)

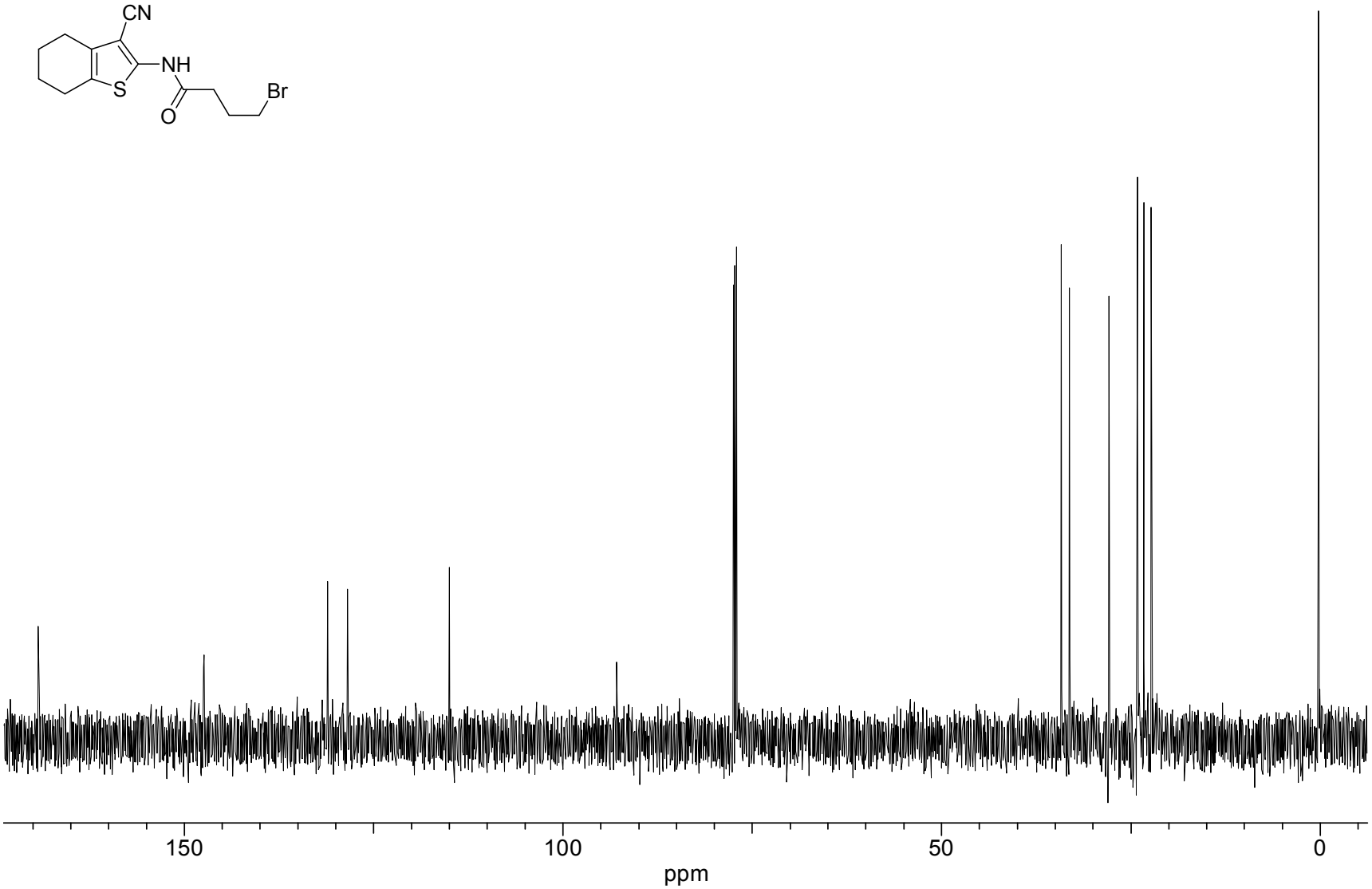

^{1}H NMR of Ethyl 2-(3-(2-chloroethyl)ureido)-4,5,6,7-tetrahydrobenzo[*b*]thiophene-3-carboxylate (5).

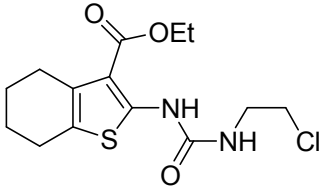

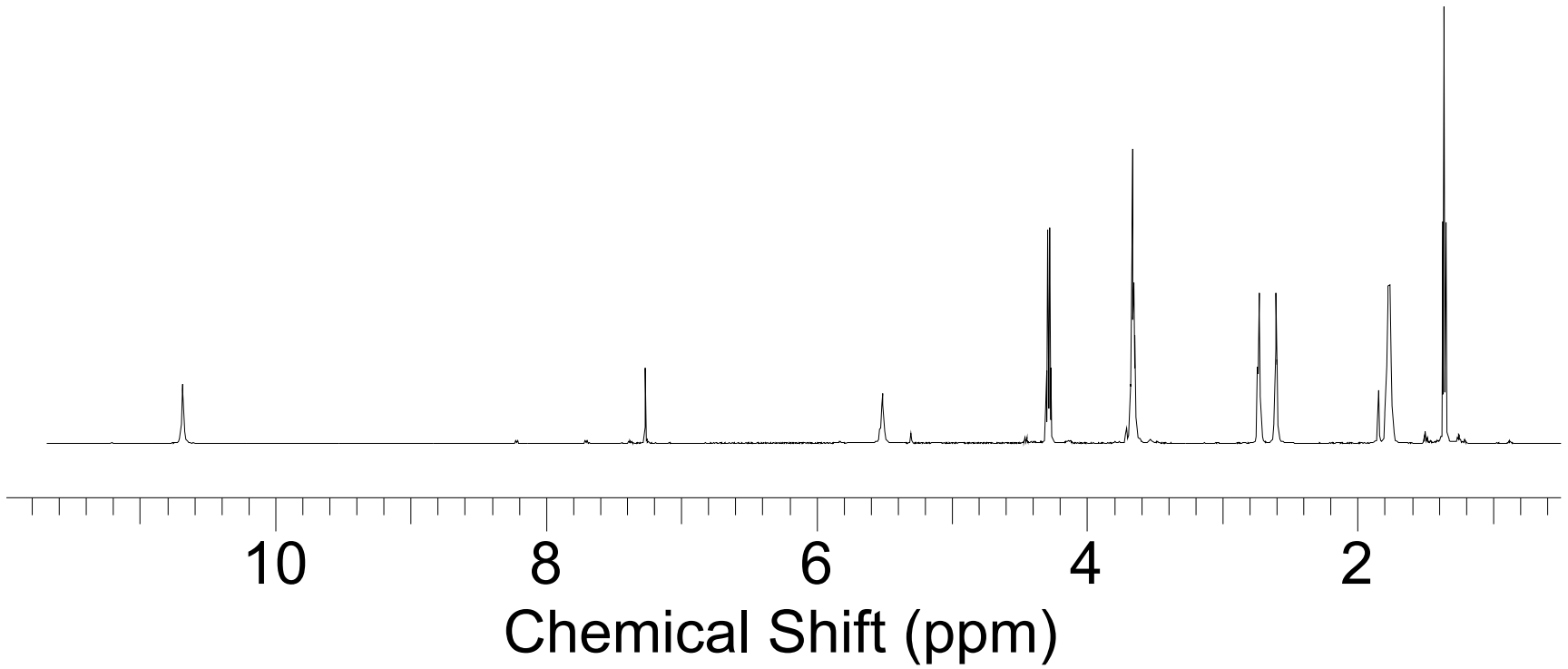

^{13}C NMR of Ethyl 2-(3-(2-chloroethyl)ureido)-4,5,6,7-tetrahydrobenzo[*b*]thiophene-3-carboxylate (5).

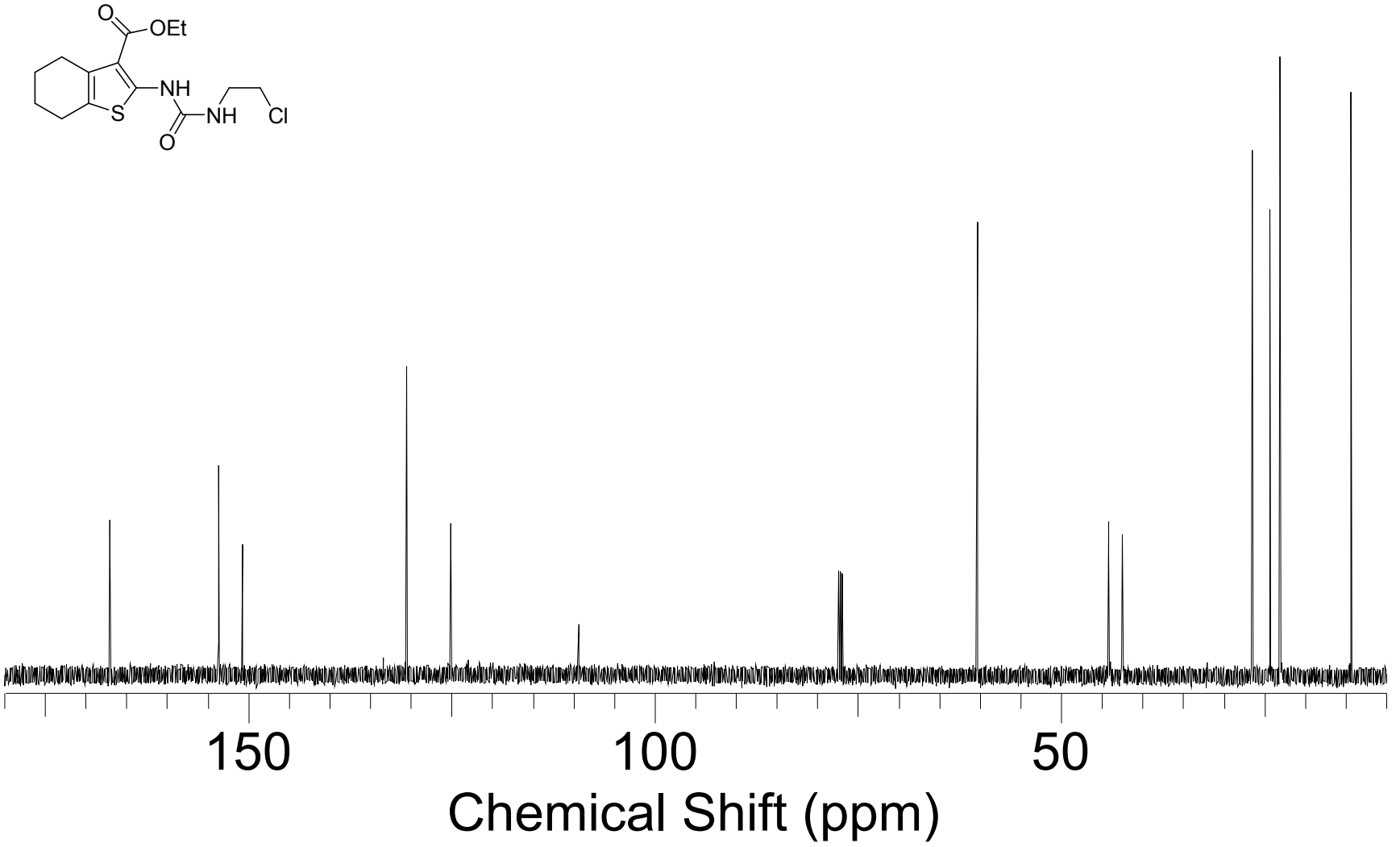

^{1}H NMR of Methyl 5-*O*-*p*-Toluenesulfonyl-2,3-di-*O*-acetyl-α-D-arabinofuranoside (7).

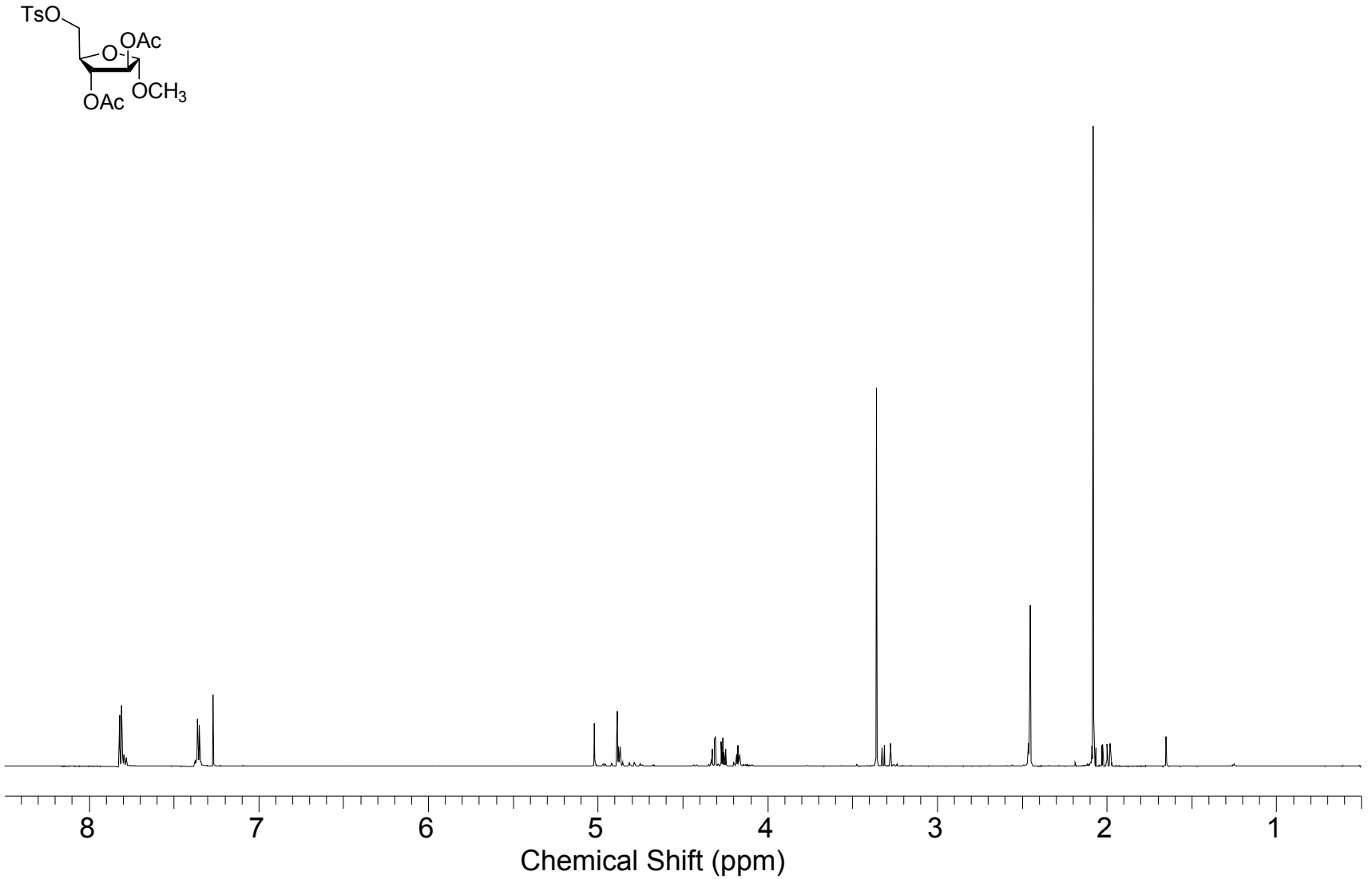

^{13}C NMR of Methyl 5-*O*-*p*-Toluenesulfonyl-2,3-di-*O*-acetyl-α-D-arabinofuranoside (7).

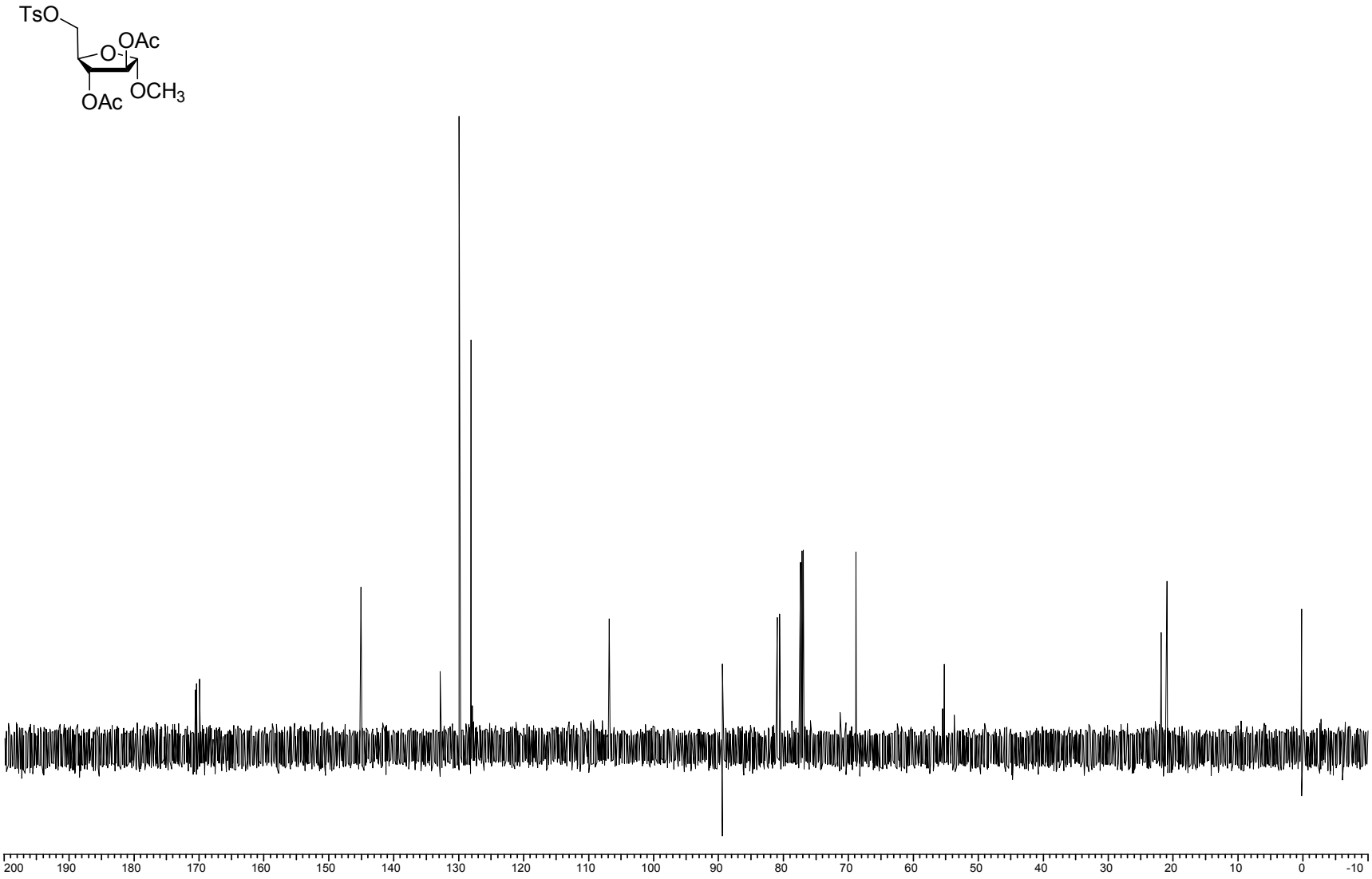

^{1}H NMR of Methyl 2,3-tri-*O*-acetyl-5-*S*-acetyl-5-thio-α-D-arabinofuranoside (8).

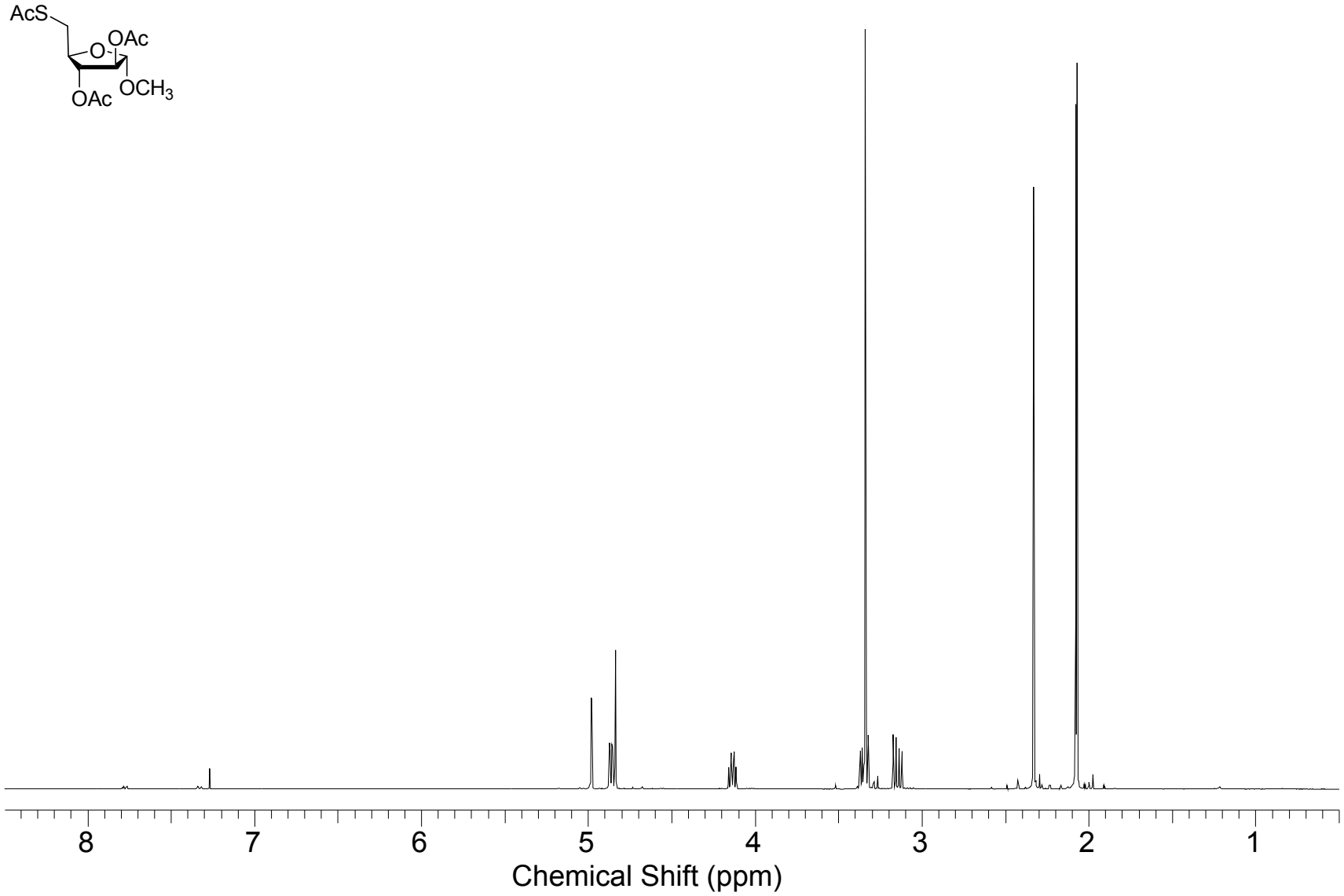

^{13}C NMR of Methyl 2,3-tri-*O*-acetyl-5-*S*-acetyl-5-thio-α-D-arabinofuranoside (8).

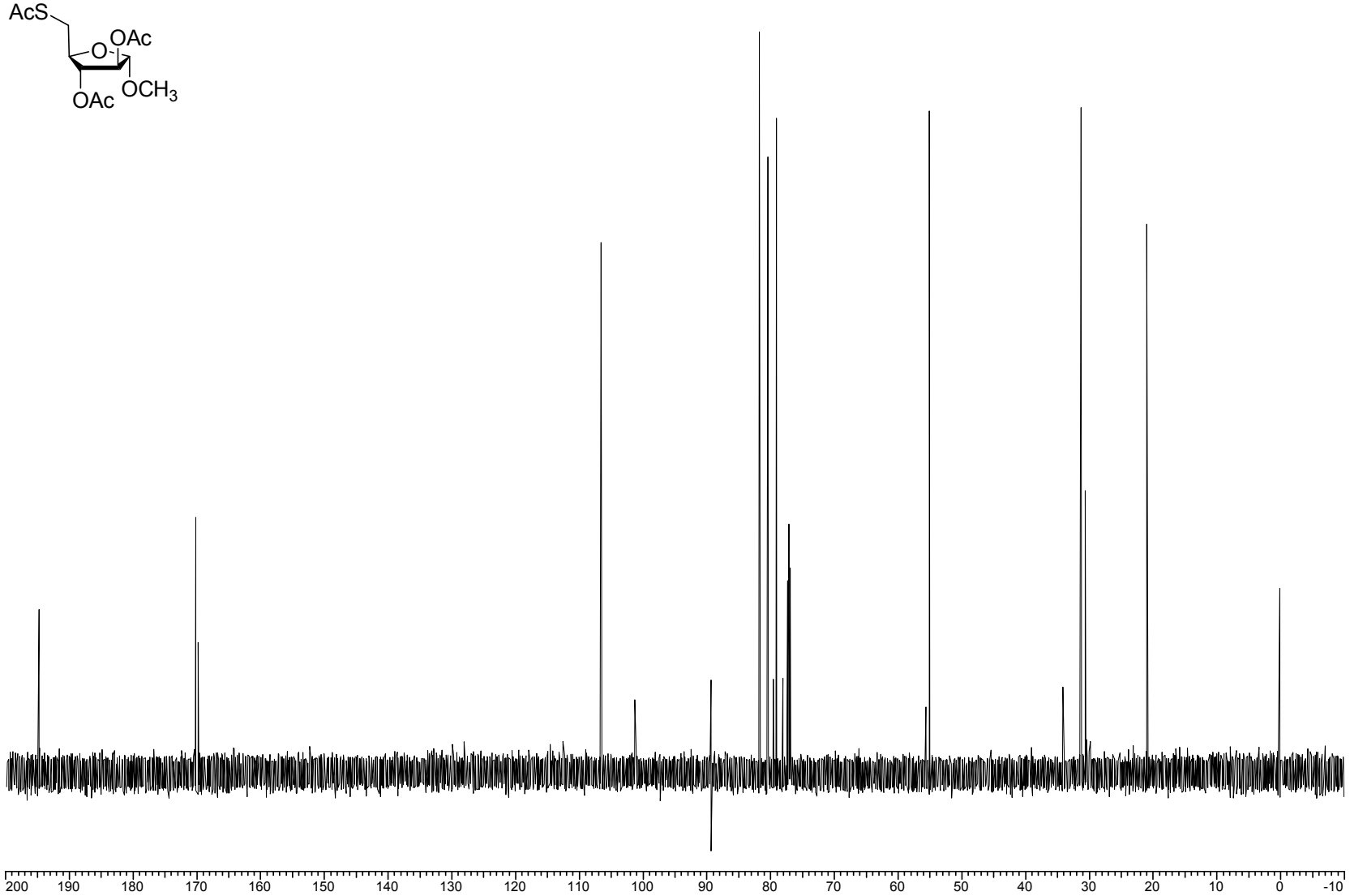

^{1}H NMR of Methyl α-D-arabinofuranoside-5-thiol (9).

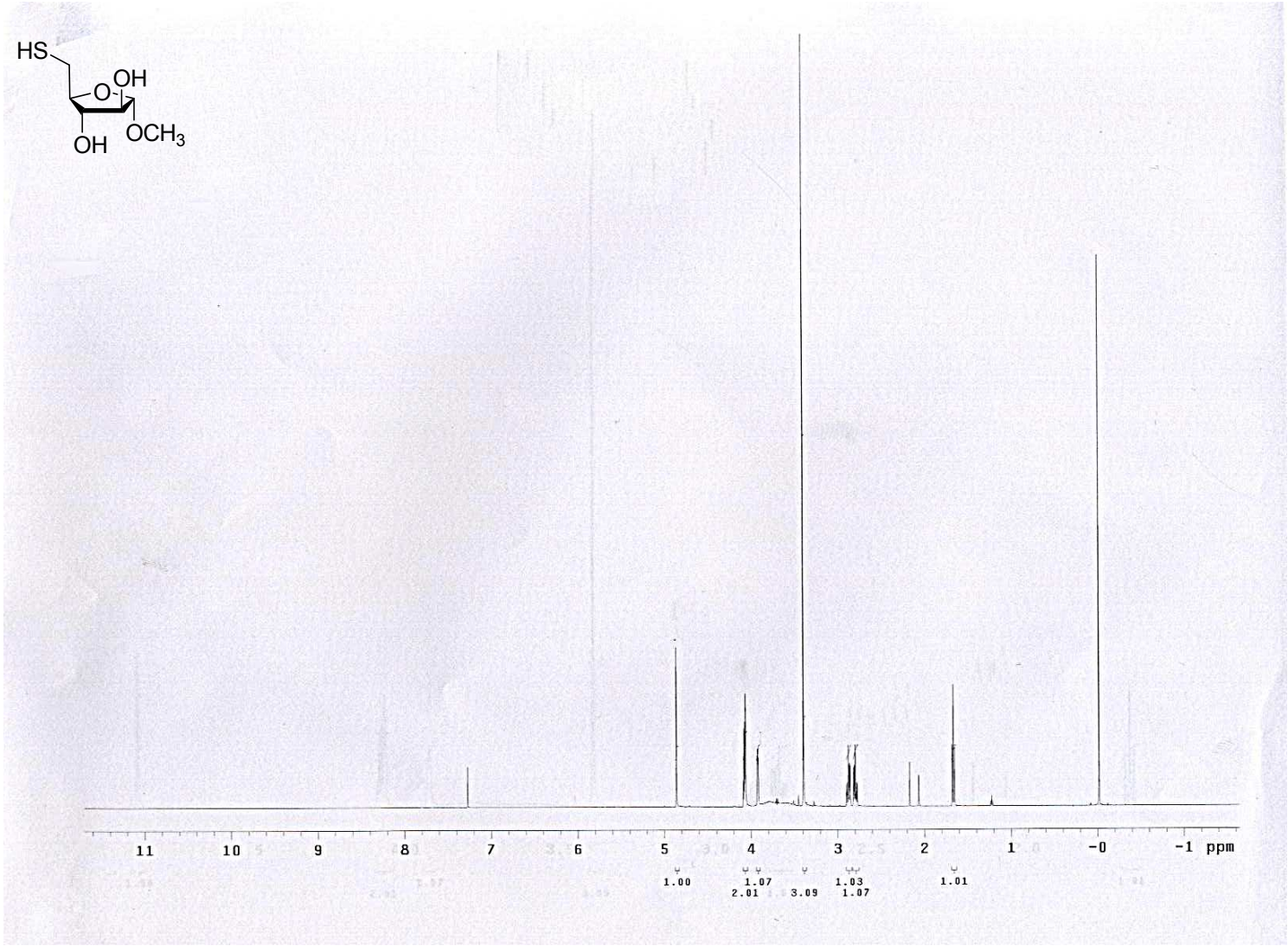

^{13}C NMR of Methyl α-D-arabinofuranoside-5-thiol (9).

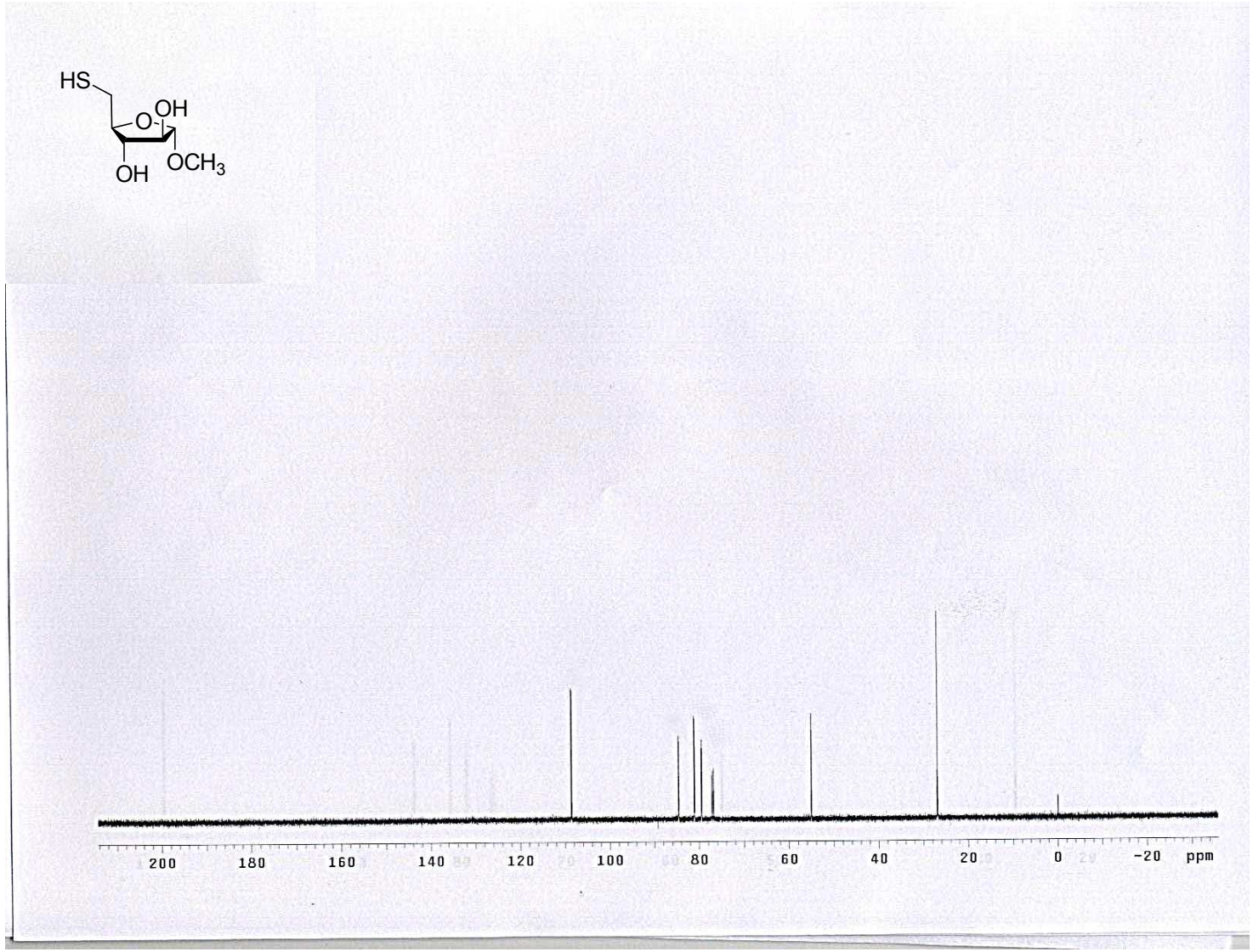

^{1}H NMR of 5-Iodo-α-D-arabinofuranoside (11).

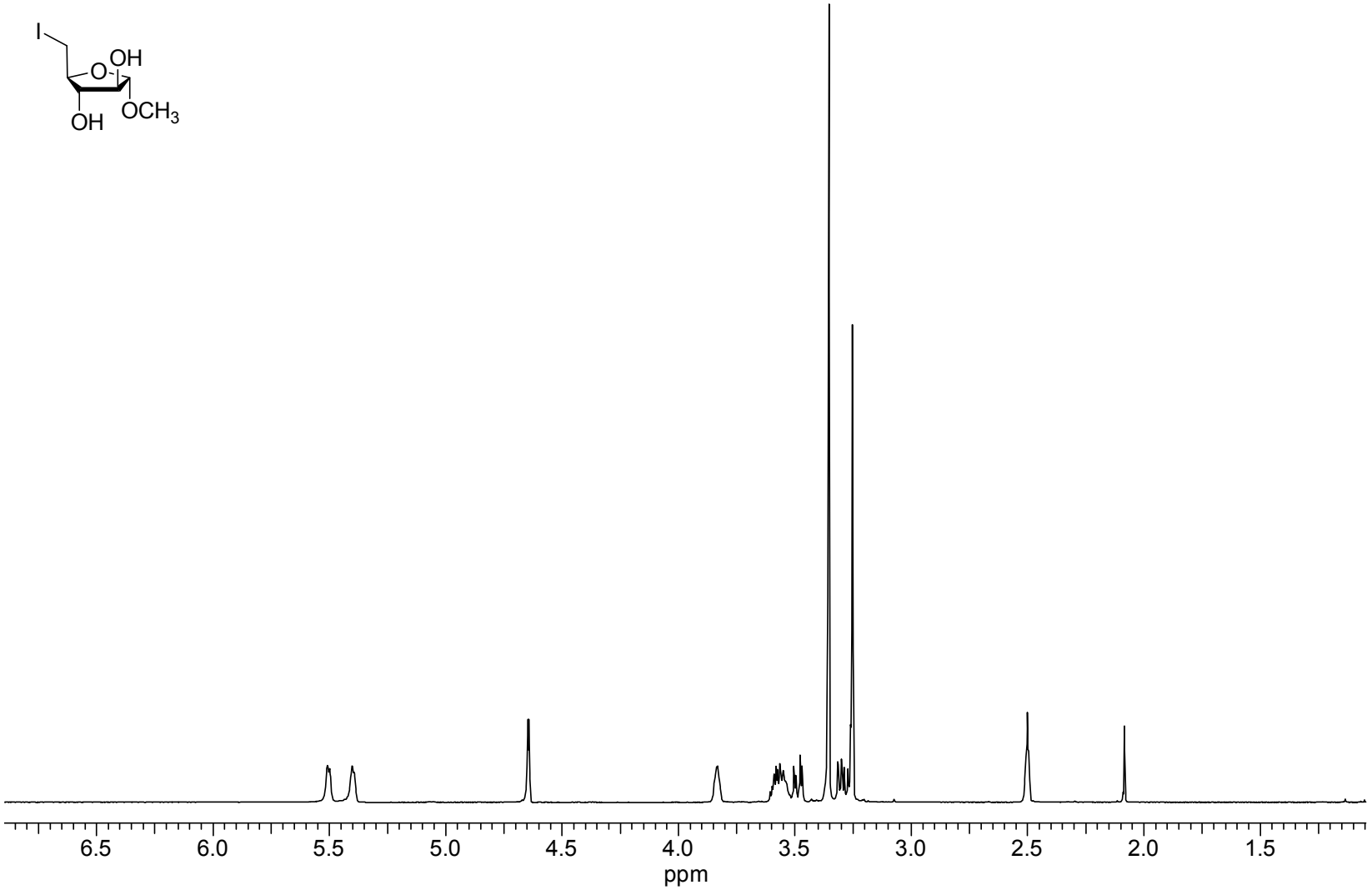

^{13}C NMR of 5-Iodo-α-D-arabinofuranoside (11).

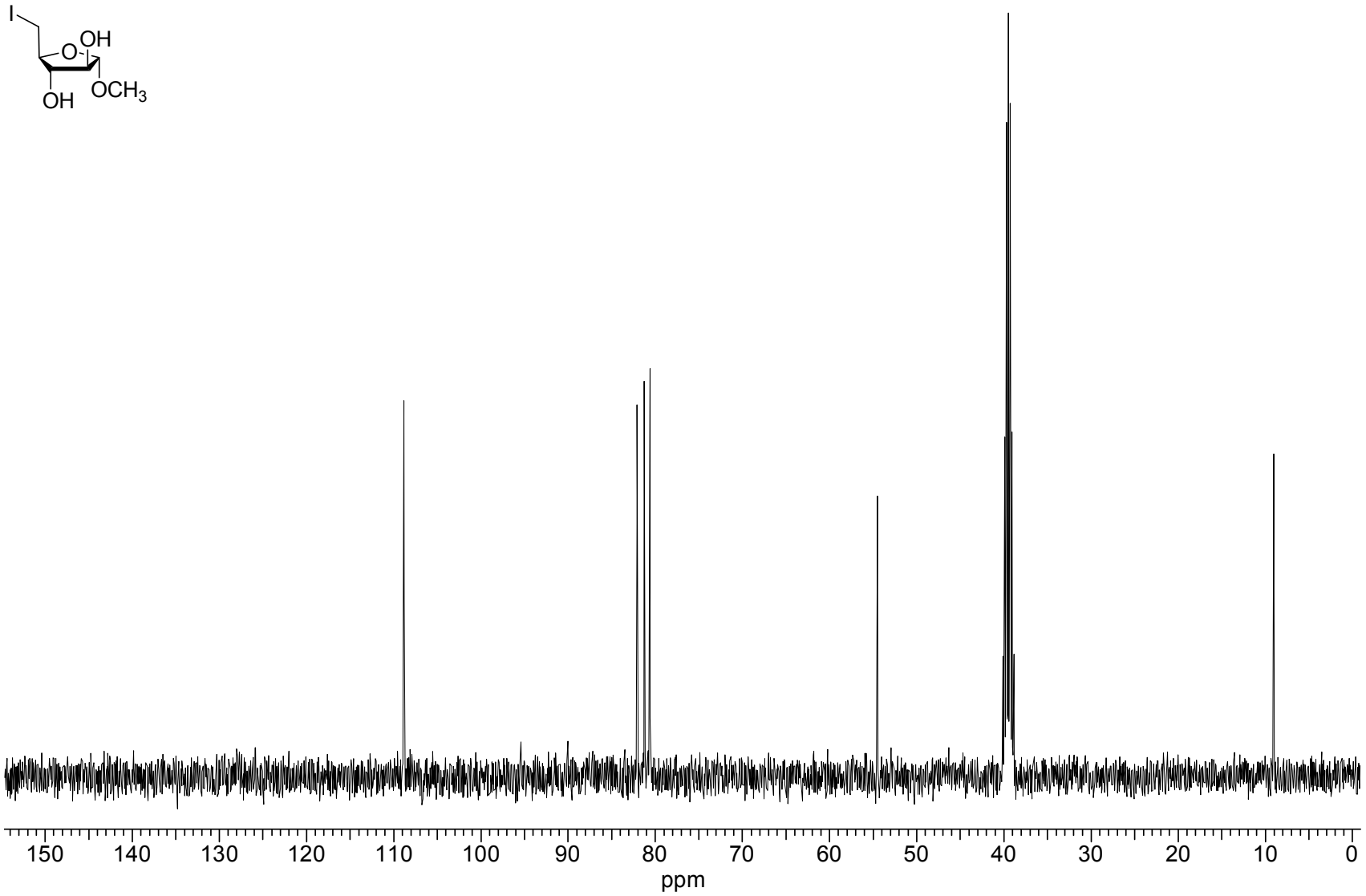

^{1}H NMR of 2-(4-(3-(Ethoxycarbonyl)-4,5,6,7-tetrahydrobenzo[*b*]thiophen-2-ylamino)-4-oxobutyl)isothiouronium bromide (12c).

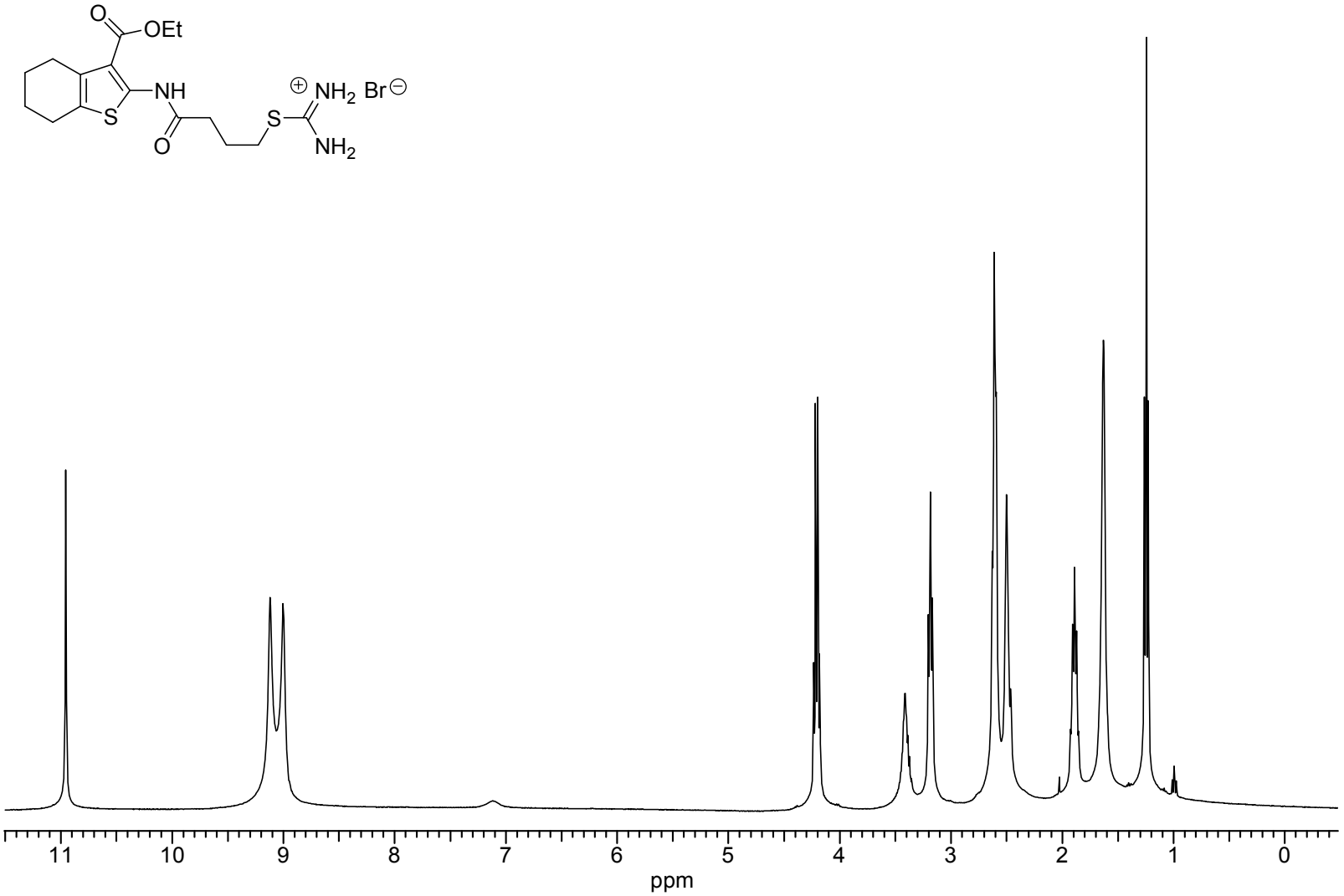

^{13}C NMR of 2-(4-(3-(Ethoxycarbonyl)-4,5,6,7-tetrahydrobenzo[*b*]thiophen-2-ylamino)-4-oxobutyl)isothiouronium bromide (12c).

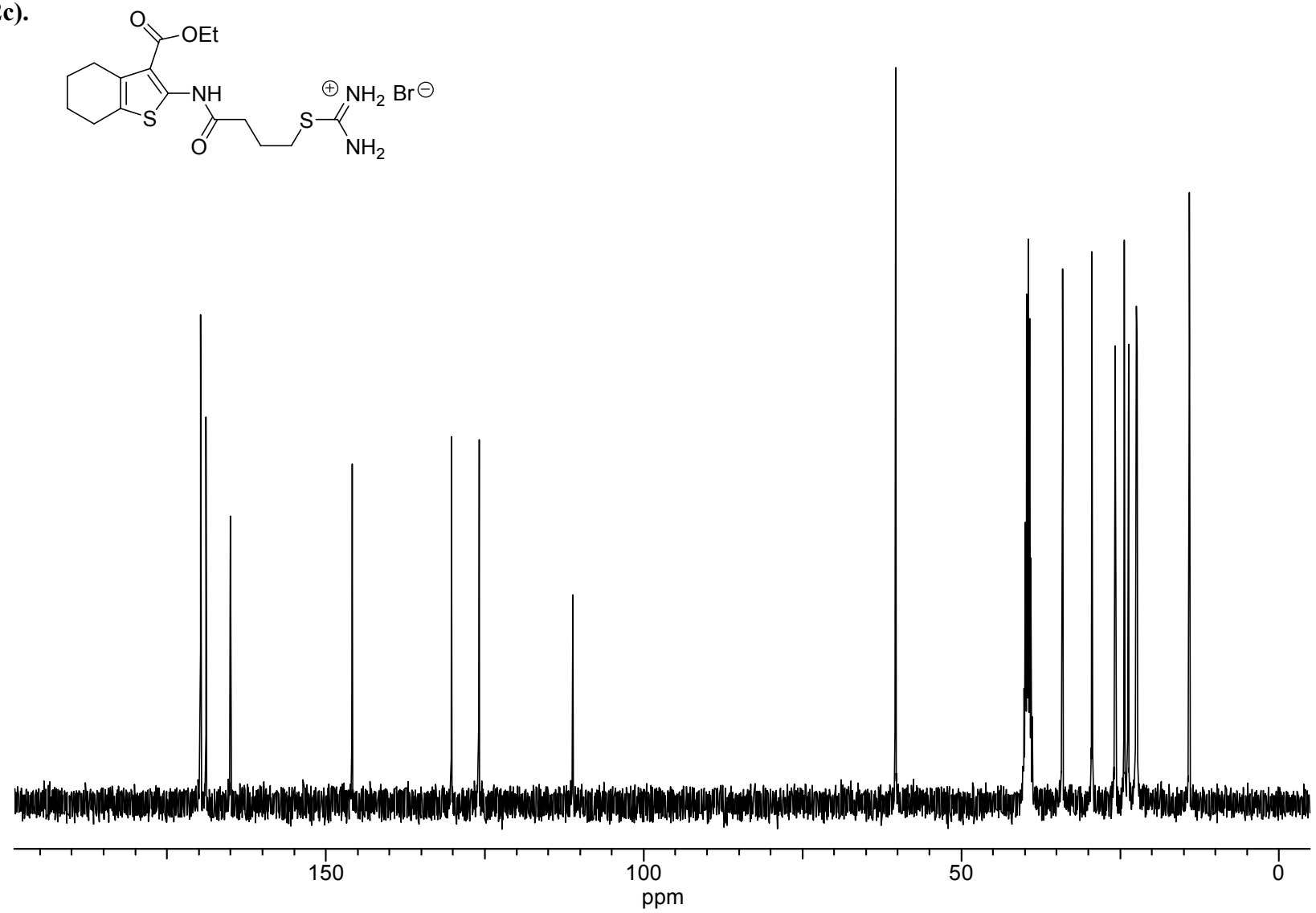

^{1}H NMR 2-(4-(3-Cyano-4,5,6,7-tetrahydrobenzo[*b*]thiophen-2-ylamino)-4-oxobutyl)isothiouronium bromide (12d).

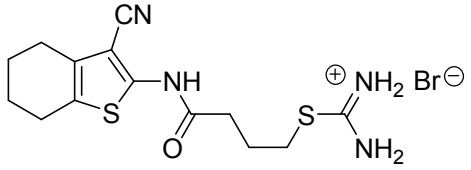

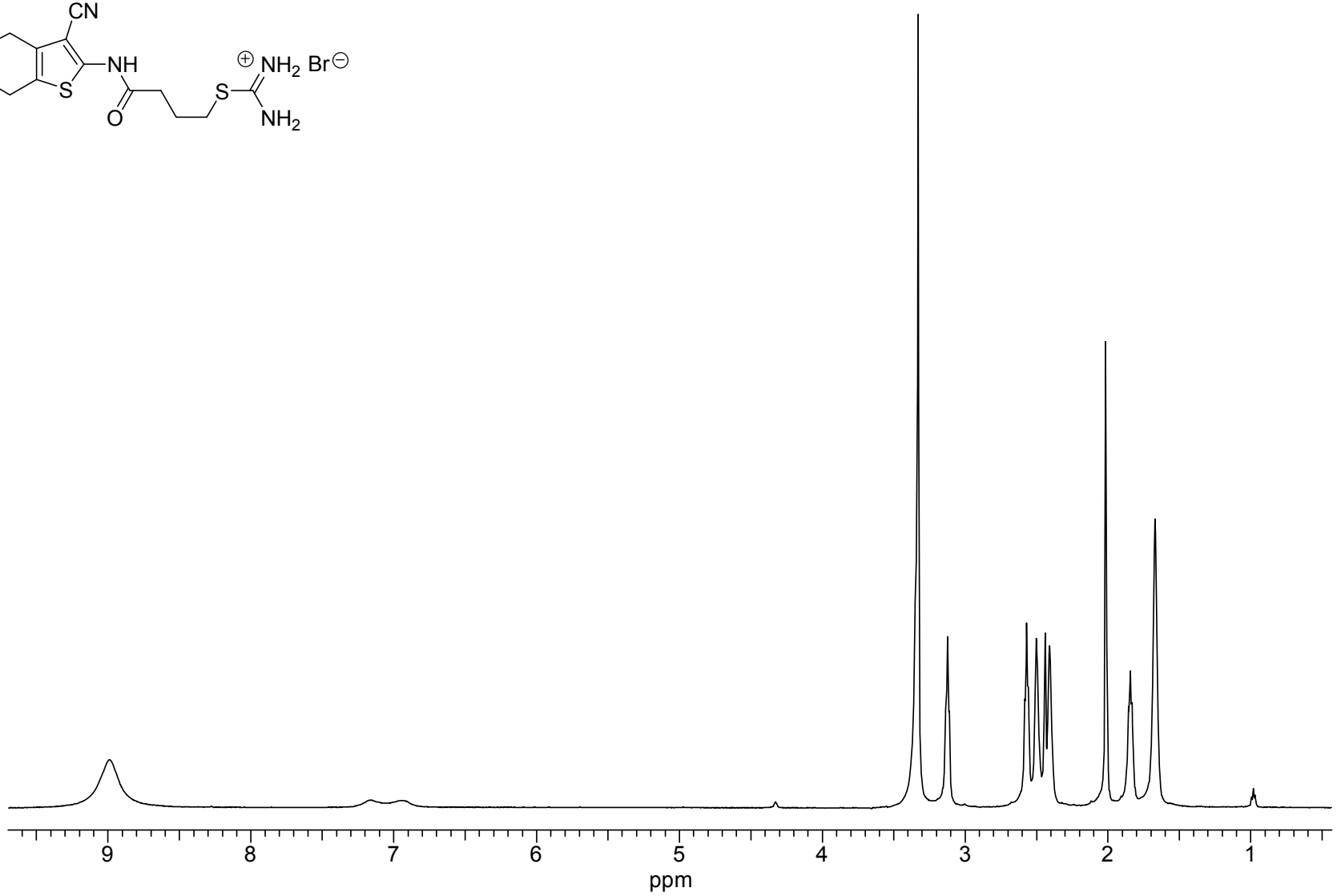

2-(4-(3-Cyano-4,5,6,7-tetrahydrobenzo[*b*]thiophen-2-ylamino)-4-oxobutyl)isothiouronium bromide (12d).

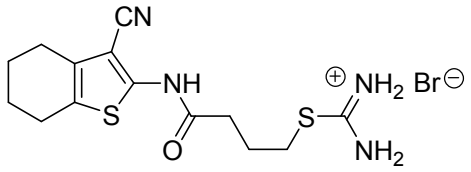

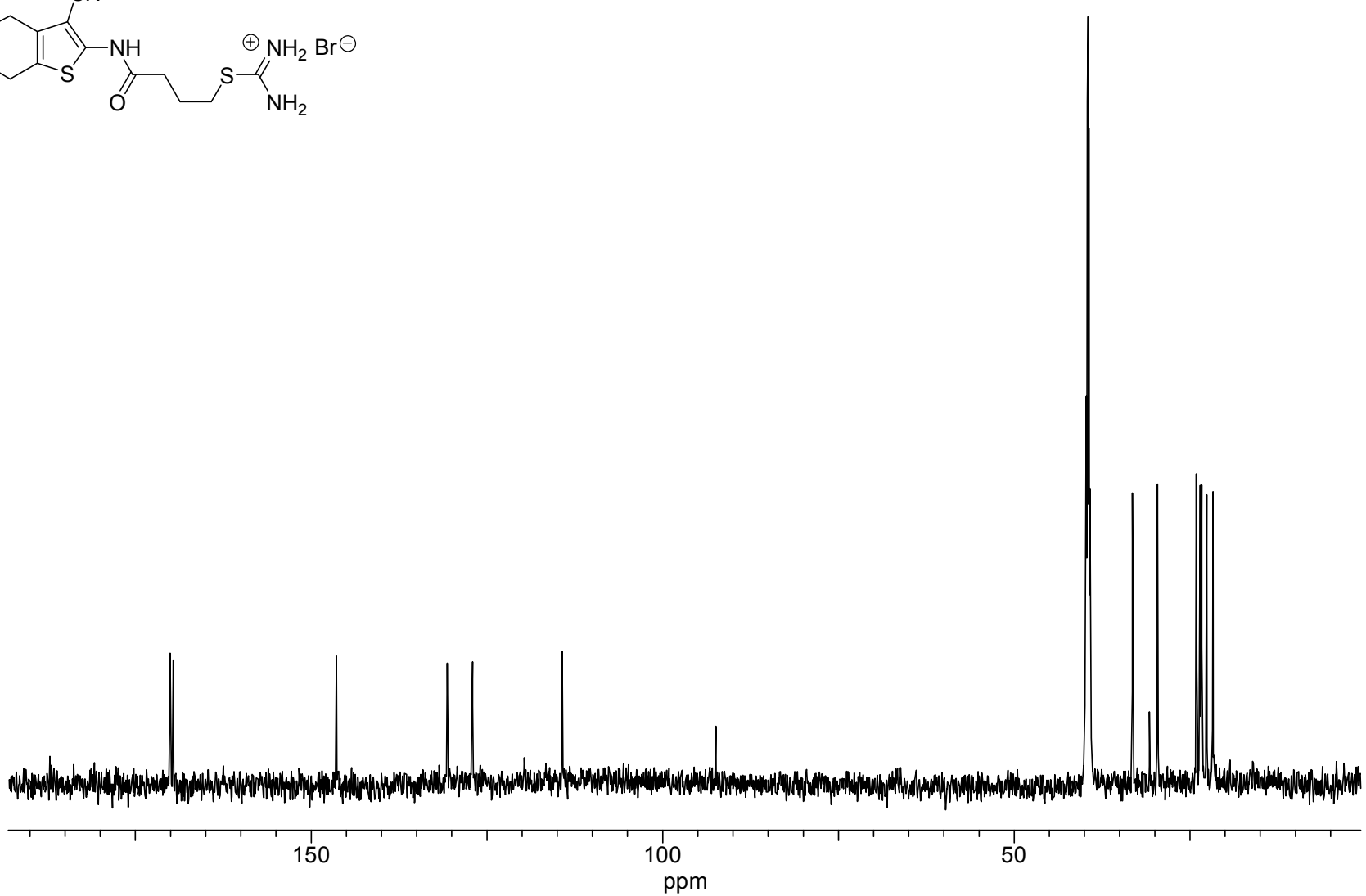

^{1}H NMR of Ethyl 2-(methyl 5-thio-*α*-D-arabinofuranoside-5-*S*-yl)acetamido-4,5,6,7-tetrahydrobenzo[*b*]thiopene-3-carboxylate (13a).

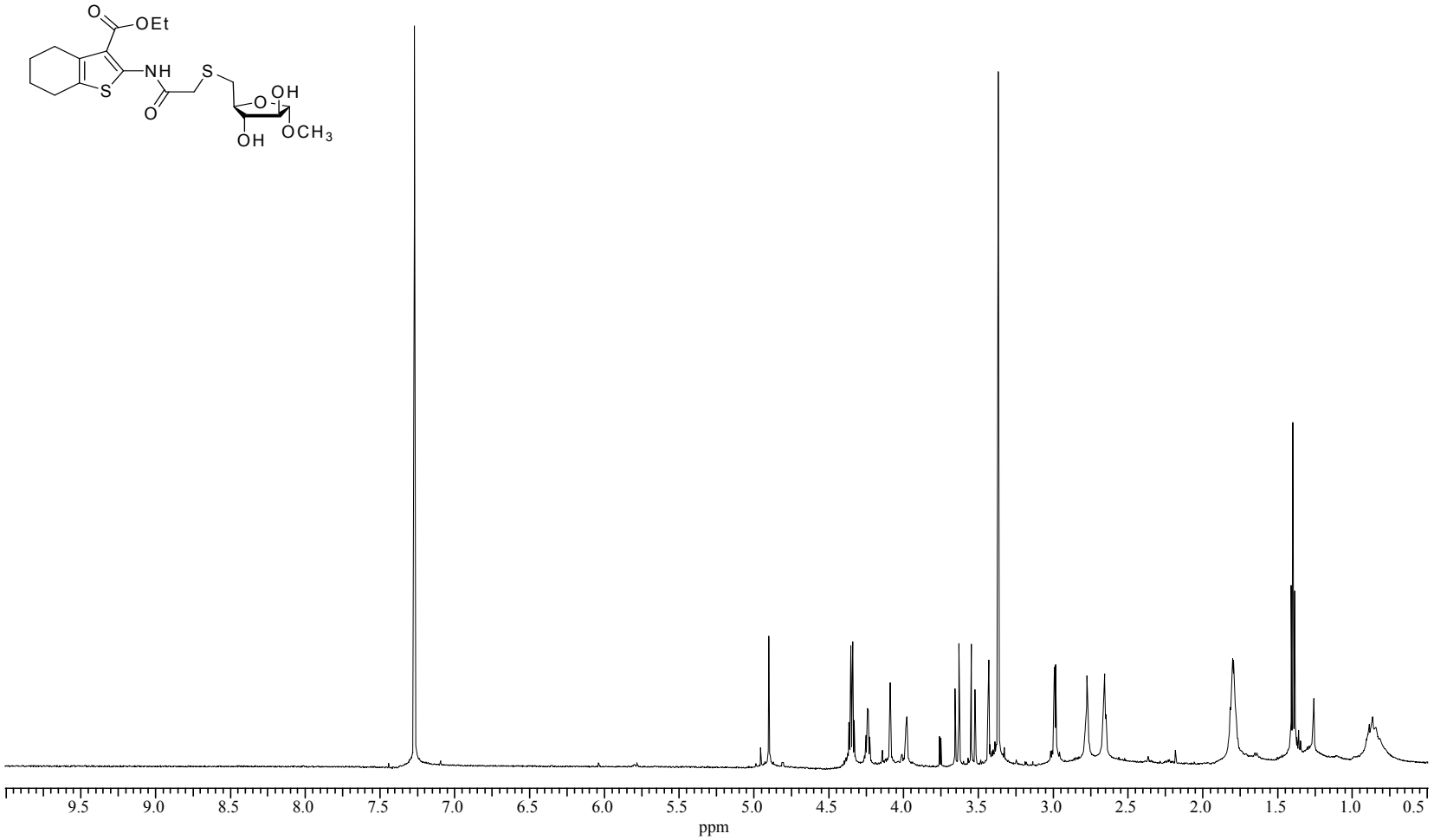

^{13}C NMR of Ethyl 2-(methyl 5-thio-α-D-arabinofuranoside-5-*S*-yl)acetamido-4,5,6,7-tetrahydrobenzo[*b*]thiopene-3-carboxylate (13a).

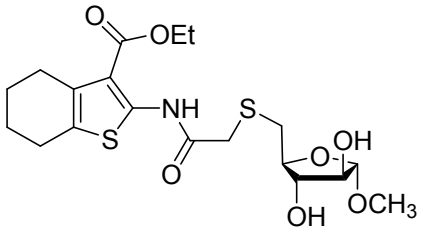

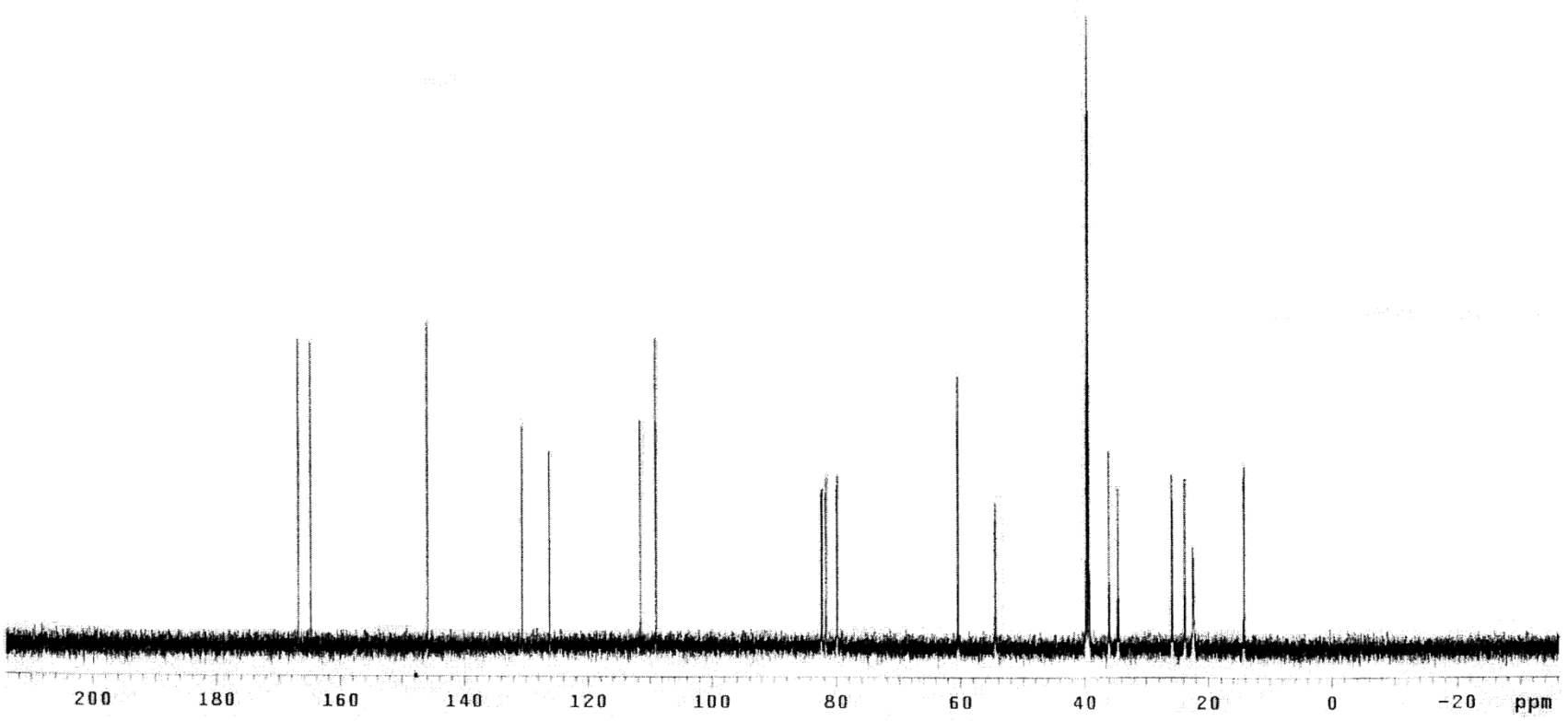

^{1}H NMR *N*-(3-cyano-4, 5, 6, 7-tetrahydrobenzo[*b*]thiophen-2-yl)-2-(methyl 5-thio-α-D-arabinoside-5-*S*-yl) acetamide (13b).

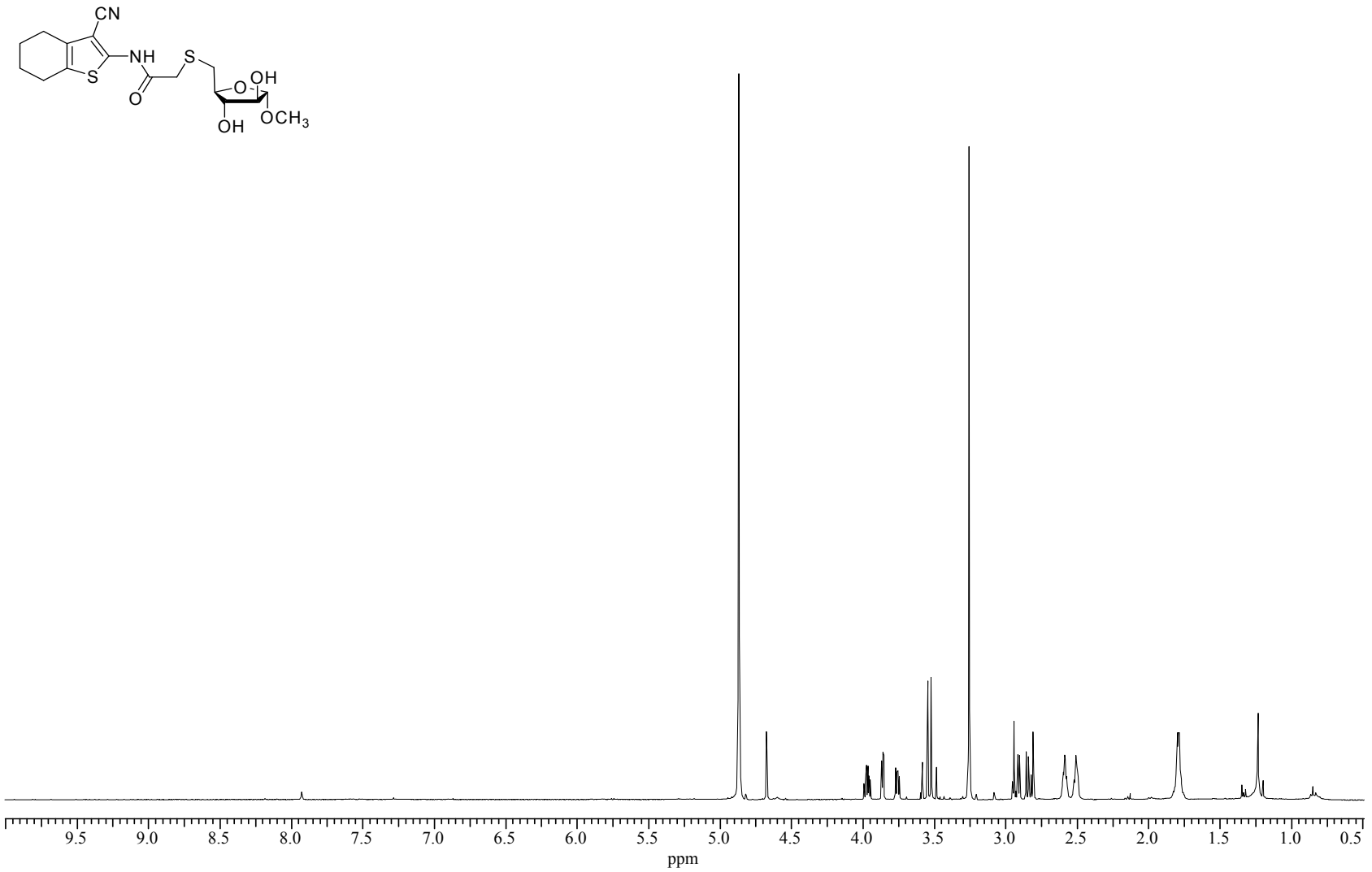

^{13}C NMR *N*-(3-cyano-4, 5, 6, 7-tetrahydrobenzo[*b*]thiophen-2-yl)-2-(methyl 5-thio-α-D-arabinoside-5-*S*-yl) acetamide (13b).

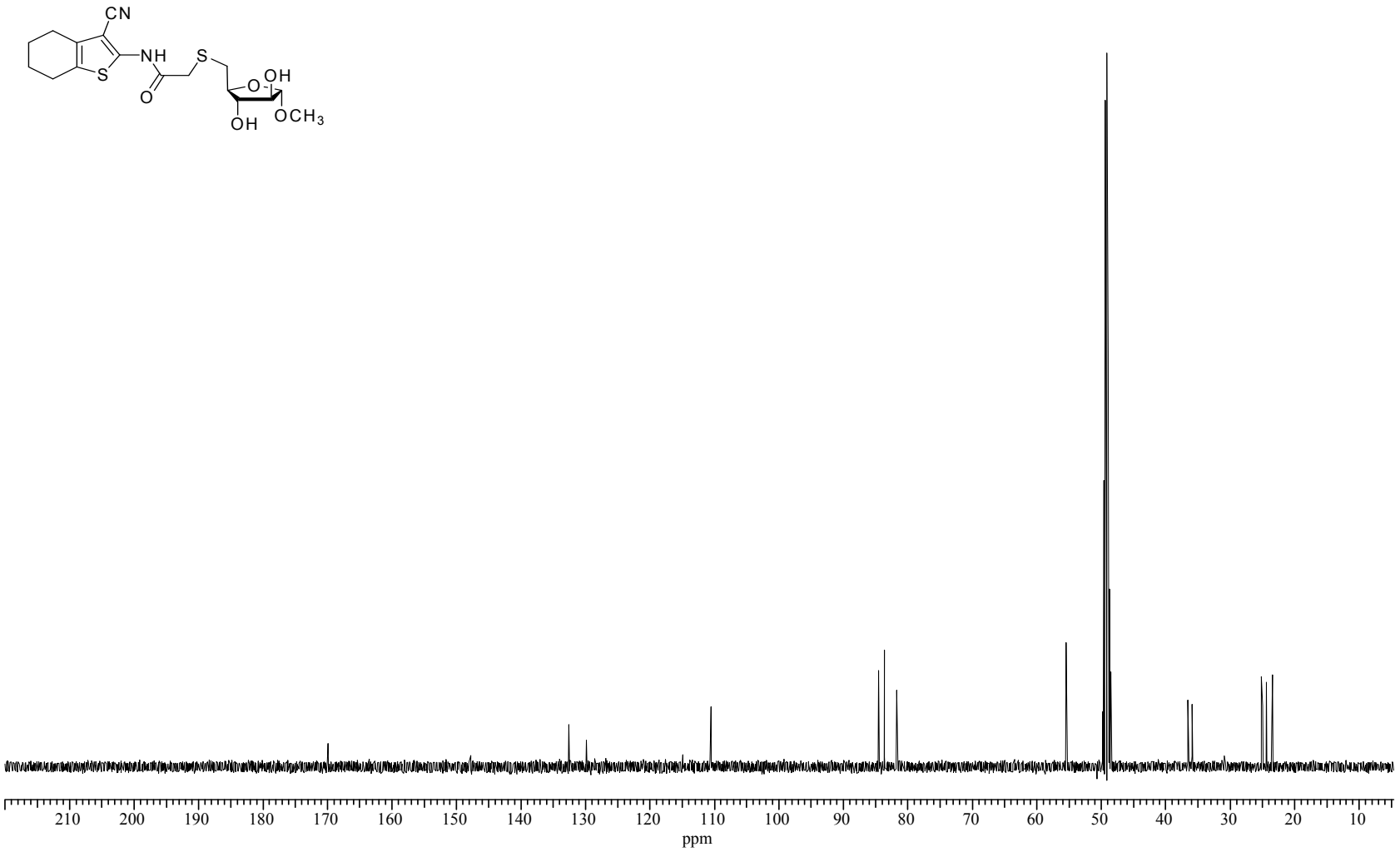
CN
NH
S
S
O
O
OH
OH
OCH3
210
200
190
180
170
160
150
140
130
120
110
100
90
80
70
60
50
40
30
20
10
ppm

^{1}H NMR of Ethyl 2-(methyl 5-thio-α-D-arabinofuranoside-5-*S*-yl)butamido-4,5,6,7-tetrahydrobenzo[*b*]thiopene-3-carboxylate (13c).

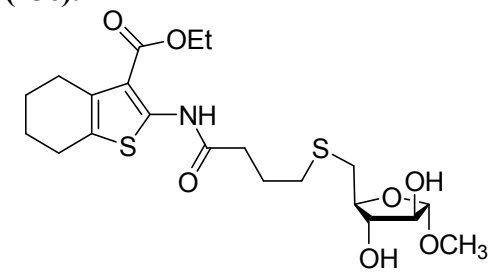

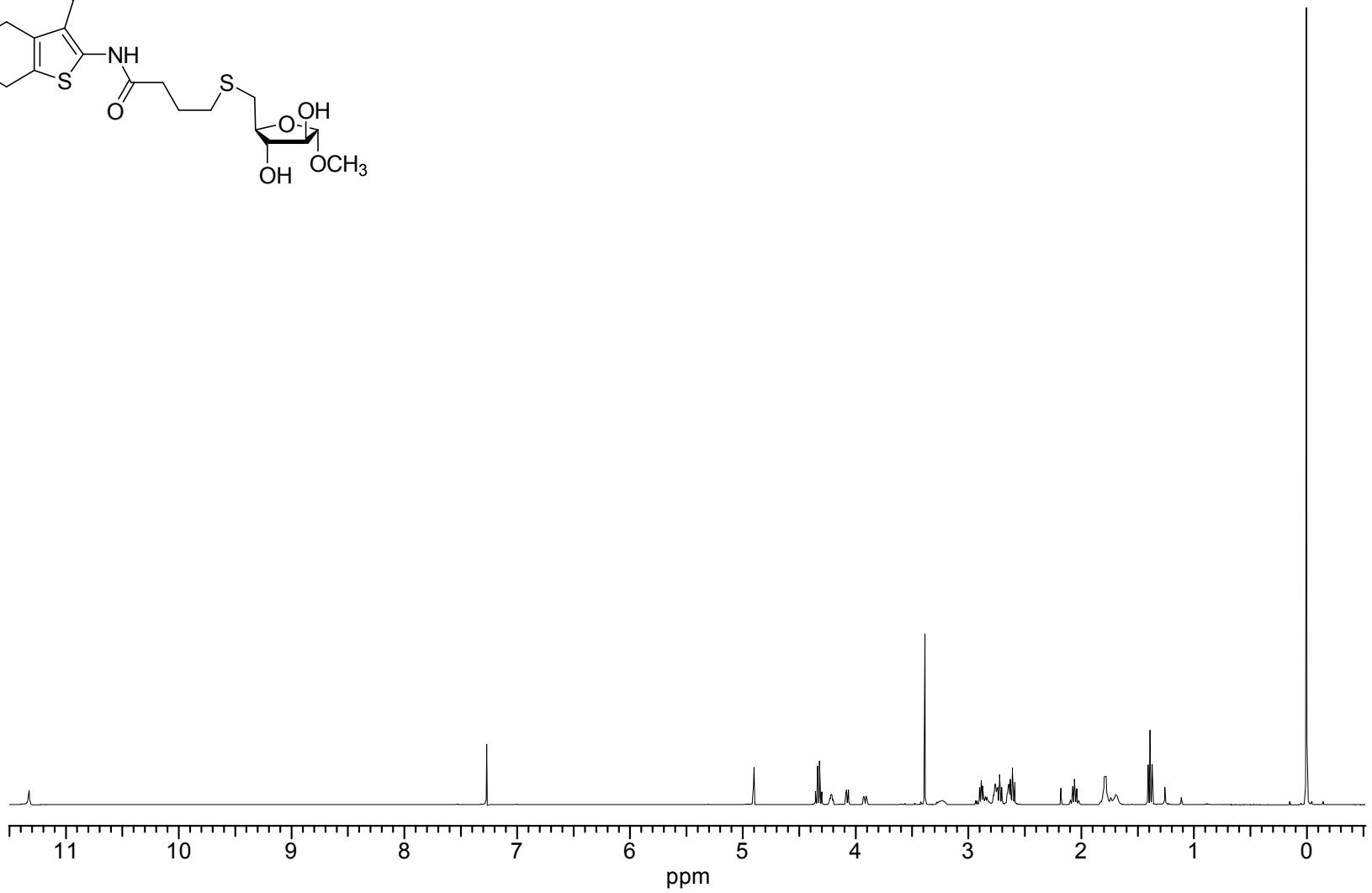

^{13}C NMR of Ethyl 2-(methyl 5-thio-α-D-arabinofuranoside-5-*S*-yl)butamido-4,5,6,7-tetrahydrobenzo[*b*]thiopene-3-carboxylate (13c).

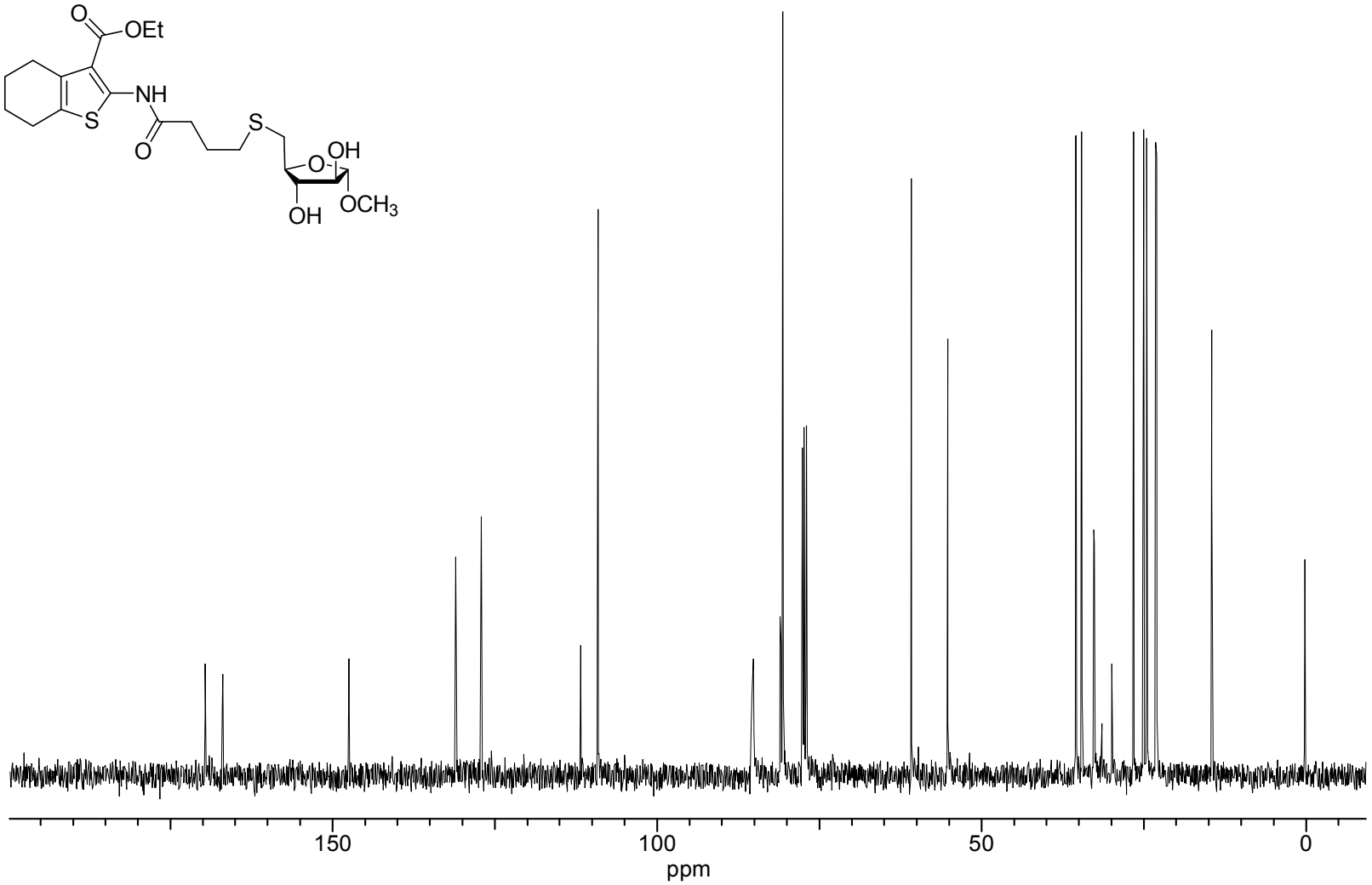

^{1}H NMR of compound *N*-(3-cyano-4,5,6,7-tetrahydrobenzo[*b*]thiophen-2-yl)-2-(methyl 5-thio-α-D-arabinofuranoside-5-*S*-yl)butamide (13d).

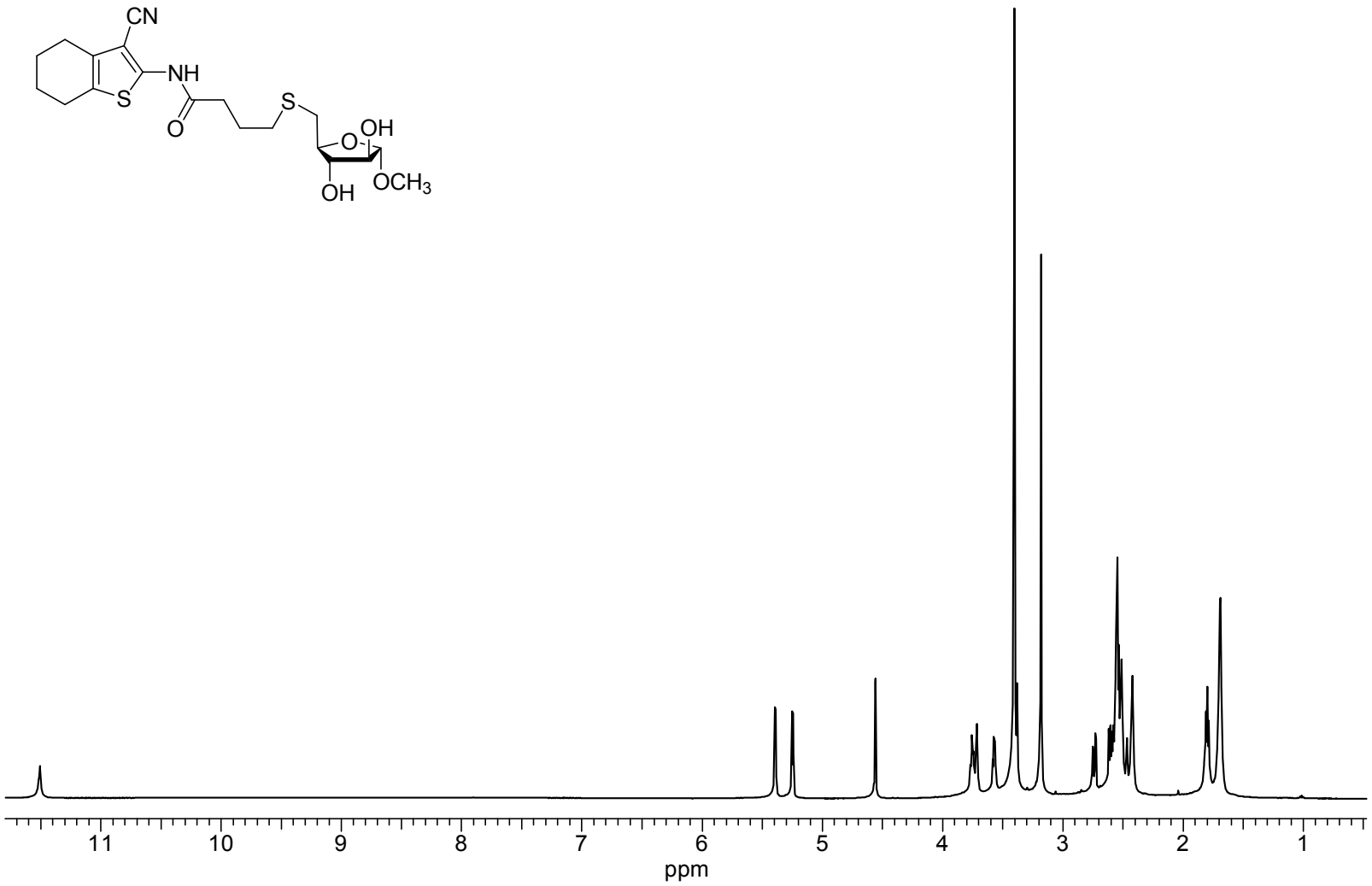

^{13}C NMR of compound *N*-(3-cyano-4,5,6,7-tetrahydrobenzo[*b*]thiophen-2-yl)-2-(methyl 5-thio-α-D-arabinofuranoside-5-*S*-yl)butamide (13d).

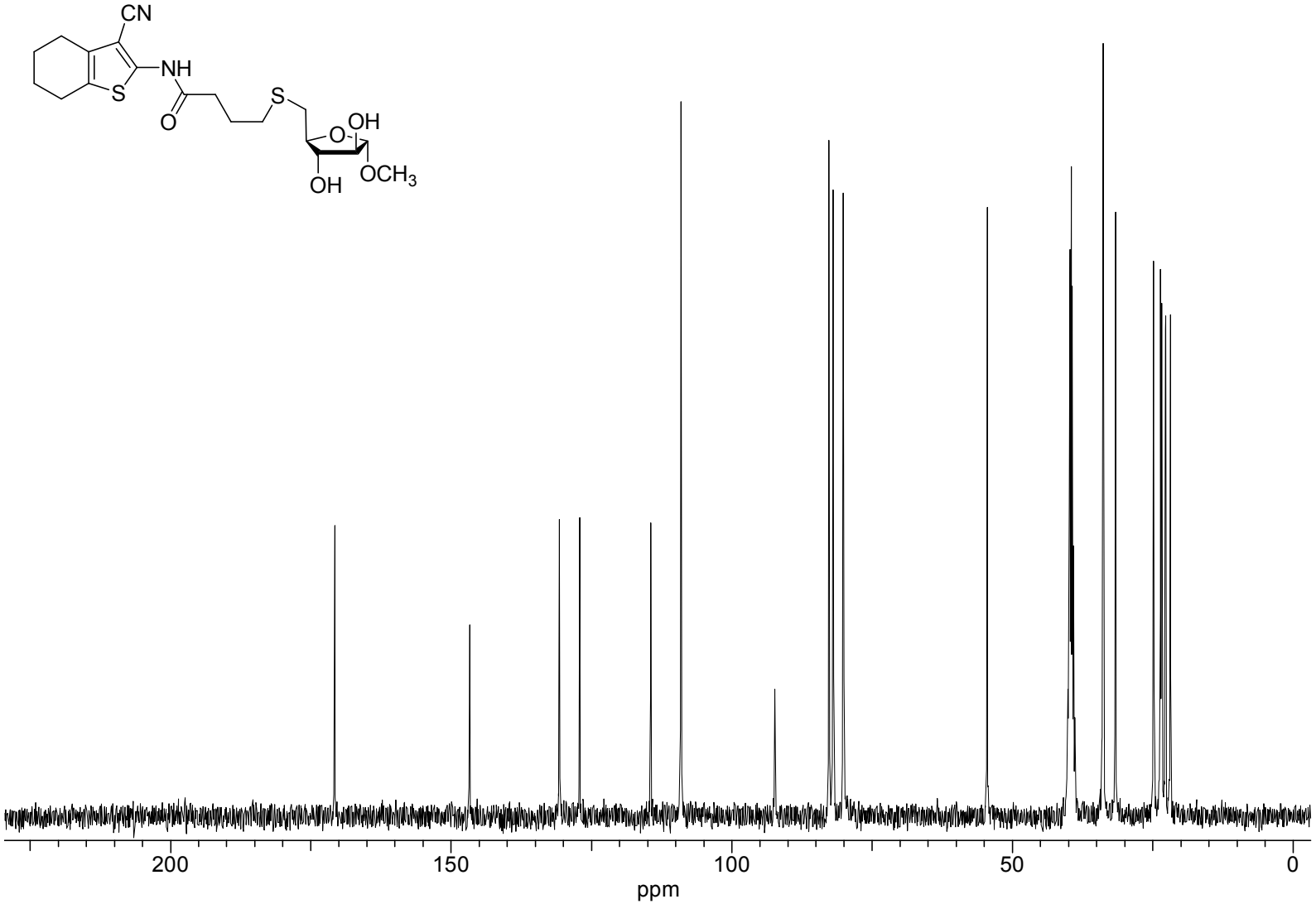

^{1}H NMR of compound Methyl 5-*S*-[2-(2,4-dioxo-1,4,5,6,7,8-hexahydro[1]benzothieno[2,3-d]-pyrimidin-3(2H)-yl)ethyl]-5-thioarabinofuranoside (14).

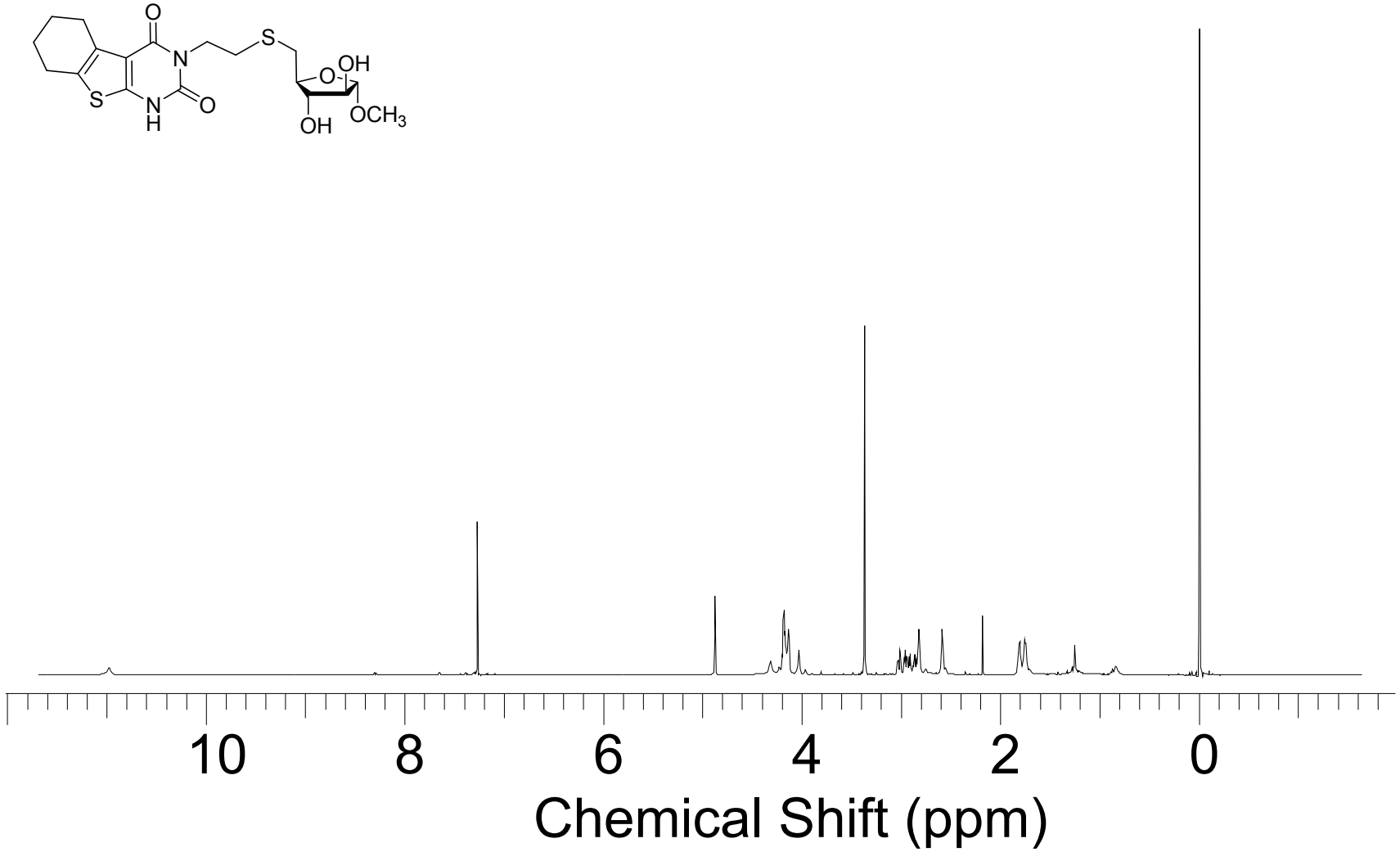

^{13}C NMR of compound Methyl 5-*S*-[2-(2,4-dioxo-1,4,5,6,7,8-hexahydro[1]benzothieno[2,3-d]-pyrimidin-3(2H)-yl)ethyl]-5-thioarabinofuranoside (14).

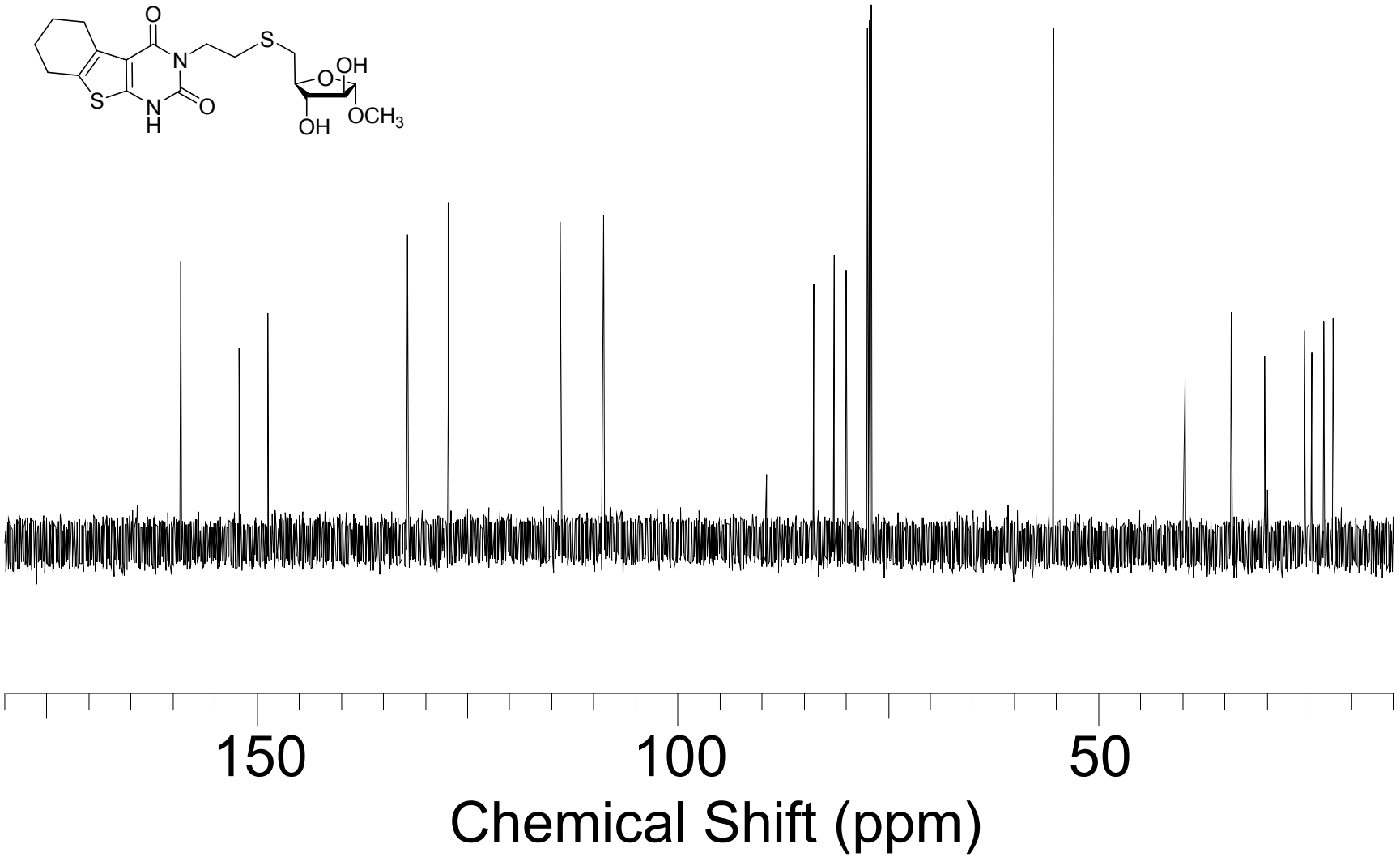

HRMS of Methyl 5-*S*-[2-(2,4-dioxo-1,4,5,6,7,8-hexahydro[1]benzothieno[2,3-d]-pyrimidin-3(2H)-yl)ethyl]-5-thioarabinofuranoside (14).

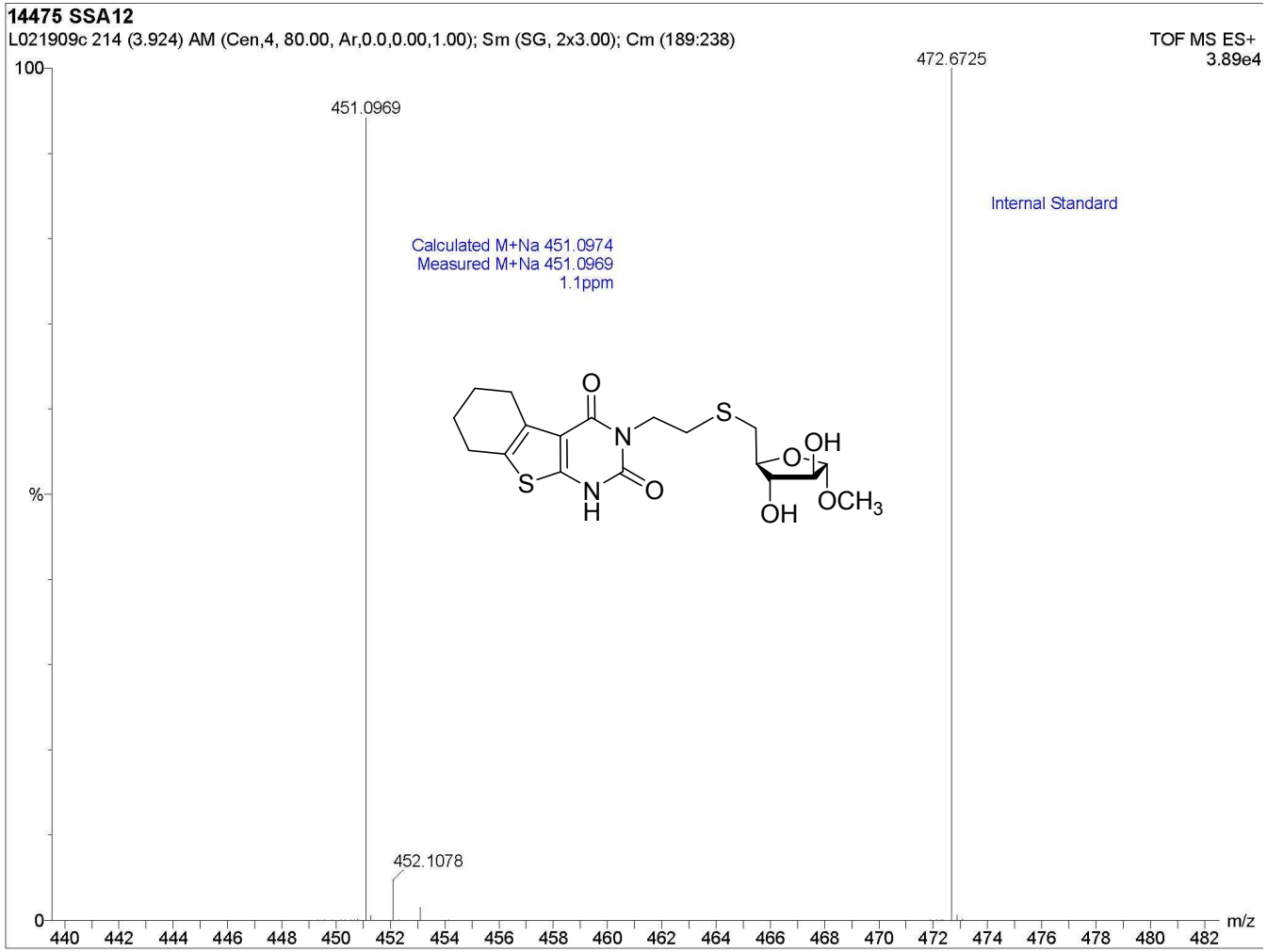

Bioconjugate Chemistry

Article

pubs.acs.org/bc

Advanced Aqueous-Phase Phosphoramidation Reactions for Effectively Synthesizing Peptide–Oligonucleotide Conjugates Trafficked into a Human Cell Line

Tzu-Pin Wang,*[,†] Ni Chien Ko,[†] Yu-Chih Su,[†] Eng-Chi Wang,[†] Scott Severance,[‡] Chi-Ching Hwang,[§] Ying Ting Shih,[⊥] Min Hui Wu,[†] and Yen-Hsu Chen*[,⊥,∥]

[†]Department of Medicinal and Applied Chemistry, [§]Department of Biochemistry, Faculty of Medicine, [⊥]School of Medicine, Graduate Institute of Medicine, College of Medicine, and [∥]Division of Infectious Diseases, Department of Internal Medicine, Kaohsiung Medical University Hospital, Kaohsiung Medical University, Kaohsiung, 80708, Taiwan

[‡]Department of Science and Mathematics, Baptist Bible College, S. Abington Township, Pennsylvania 18411, United States

Supporting Information

ABSTRACT: Peptide–oligonucleotide conjugates (POCs) have held promise as effective therapeutic agents in treating microbial infections and human genetic diseases including cancers. In clinical applications, POCs are especially useful to circumvent cellular delivery and specificity problems of oligonucleotides. We previously reported that nucleic acid phosphoramidation reactions performed in aqueous solutions have the potential for facile POC synthesis. Here, we carried out further studies to significantly improve aqueous-phase two-step phosphoramidation reaction yield. Optimized reactions were employed to effectively synthesize POCs for delivery into human A549 cells. We achieved optimization of aqueous-phase two-step phosphoramidation reaction and improved reaction yield by (1) determining appropriate co-solutes and co-solute concentrations to acquire higher reaction yields, (2) exploring a different nucleophilicity of imidazole and its derivatives to stabilize essential nucleic acid phosphorimidazolide intermediates prior to POC formation, and (3) enhancing POC synthesis by increasing reactant nucleophilicity. The advanced two-step phosphoramidation reaction was exploited to effectively conjugate a well-studied cell penetrating peptide, the Tat_{48-57} peptide, with oligonucleotides, bridged by either no linkers or a disulfide-containing linker, to have the corresponding POC yields of 47–75%. Phosphoramidation-synthesized POCs showed no cytotoxicity to human A549 cells at studied POC concentrations after 24 h inoculation and were successfully trafficked into the human A549 cell line as demonstrated by flow cytometry, fluorescent microscopy, and confocal laser scanning microscopy study. The current report provides insight into aqueous-phase phosphoramidation reactions, the knowledge of which was used to develop effective strategies for synthesizing POCs with crucial applications including therapeutic agents for medicine.

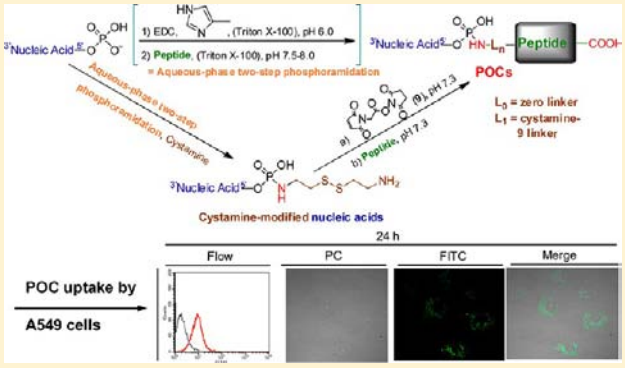

INTRODUCTION

Extensive research endeavors have been devoted to exploring the therapeutic potential of nucleic acids, including siRNA, miRNA, catalytic RNA (ribozymes), aptamer oligonucleotides (oligonucleotides with exquisite roles similar to protein receptors), and antisense oligonucleotides.[1−7] Theoretically, when designed appropriately, nucleic acids delivered into biological systems will participate in cellular activities, such as RNA interference or gene silencing, to abolish specific gene expression in cells and to attain more precise therapeutic targeting than typical small molecule drugs. Nucleic acid-based therapeutics have shown promise for treating a variety of human genetic diseases and microbial infections. Recent progress has resulted in some antisense oligonucleotides and aptamer RNA reaching clinical applications, while a significant number of clinical trials for siRNA are underway.[1,3,5,6]

The direct use of nucleic acids for treating diseases, however, faces serious hurdles. Difficulties include cell specificity, inefficient cellular uptake of nucleic acids, and inaccessibility of nucleic acids to cell nuclei, due primarily to ineffective translocation of nucleic acids across biological barriers after administration.[6,7] Consequently, successful use of nucleic acids in clinical practice will not be achieved until there are better strategies for targeted and efficient delivery of nucleic acids to cells and tissues.[4−7] The critical issue of efficient target delivery for nucleic acids has been studied by many laboratories through chemical modification of nucleic acids to improve stability and cellular delivery properties of nucleic acids in vivo. Developed

Received: August 14, 2012
Revised: November 3, 2012
Published: November 30, 2012

 © 2012 American Chemical Society

methods include conjugating cellular surface receptor-specific ligands with various nucleic acid-containing nanocarriers or covalently linking cellular surface receptor-specific ligands with nucleic acids directly.[7−11]

The use of peptides as ligands to traffic nucleic acids across the plasma membrane has been extensively investigated in the development of effective nucleic acid-based therapeutic agents.[7,8,11,12] Conjugating nucleic acids such as oligonucleotides with cell-penetrating peptides (CPPs) or cell-targeting peptides (CTPs) to acquire peptide−oligonucleotide conjugates (POCs) has created appropriate designs to circumvent cellular delivery or cell specificity problems inherited from administrating only oligonucleotides in clinics.[7,11,12] CPPs, including the Tat, the Antennapedia, the CyLoP-1, and the $(KFF)_3K$ peptides, are either protein-derived or artificially developed short sequences (10−16 amino acids), and they are able to spontaneously cross cellular barriers when provided in extracellular media.[8,12−18] The unique cell permeability properties of CPPs significantly improve the uptake efficiency of oligonucleotides in POCs by cells and facilitate broader uses of POCs in science and medicine.

POCs are primarily prepared by coupling peptides with oligonucleotides after solid-phase synthesis (fragment coupling strategy) or directly synthesized through stepwise solid-phase reactions (online solid-phase synthesis).[19] To achieve peptide−oligonucleotide conjugations, current POC synthesis methods typically require previous incorporations of additional functionalities in peptides, oligonucleotides, or both. The requirement to have additional functional groups renders these methods inefficient, inconvenient, and not cost-effective for academia or industry. The development of a facile approach to exploit readily available functionalities, such as hydroxyl or phosphate groups, in standard oligonucleotides in order to synthesize POCs with high purity and yields is crucial to the advancement of POC applications.

We previously demonstrated that aqueous-phase two-step phosphoramidation reactions are an ideal strategy to synthesize POCs without compromising oligonucleotide base-pairing specificity, an essential criterion when administrating oligonucleotides as therapeutic agents.[20] The original two-step phosphoramidation reaction easily accommodates multiple active functionalities in peptides for POC synthesis; however, it suffers from a drawback of relatively low POC yield, typically ranging from 27% to 44%. Low POC yield in the original two-step phosphoramidation reaction was ascribed to the interfering presence of the co-solute urea, the instability of nucleic acid phosphorimidazolide intermediates in aqueous solutions during reactions, and peptide nucleophilicity.[20]

Here, we report further study of the two-step phosphoramidation reaction to glean essential information for improving product yield and synthesizing POCs more effectively. We successfully employed the optimized two-step phosphoramidation reaction to effectively conjugate a well-studied CPP, the TAT_{48-57} peptide,[12,18] with DNA or RNA to produce corresponding POC yields of 47−75%. Phosphoramidation-synthesized POCs showed no cytotoxicity to human A549 cells at studied POC concentrations after 24 h inoculation and were successfully trafficked into the human A549 cell line as demonstrated by flow cytometry, fluorescent microscopy, and confocal laser scanning microscopy study. The following report confirms that the optimized two-step aqueous-phase phosphoramidation reaction is a facile and effective approach to synthesize bioactive POCs which can stimulate broader applications of POCs in research and clinics.

MATERIALS AND METHODS

All reagent-grade chemicals were purchased from commercial sources (Sigma-Aldrich, Acros, Alfa Aesar, Mallinckrodt Baker, and Merck KGaA) except where noted, and were further purified if necessary. Synthesis of **1** was reported previously.[20] Procedures modified from a published method were used to synthesize H_2N-Gly-Gly-Gly-Gly-OH (tetraglycine; **3**).[21] Compound **3** was also obtained from commercial sources (Acros and TCI) to avoid the time-consuming organic synthesis. Five peptides (Tat_{48-57}, H_2N-GRKKRRQRRR-$CONH_2$; Tat_{47-57}, H_2N-YGRKKRRQRRR-$CONH_2$; $(KFF)_3K$, H_2N-KFFKFFKFFK-$CONH_2$; $G(KFF)_3K$, H_2N-GKFFKFFKFFK-$CONH_2$; $C(KFF)_3K$, H_2N-CKFFKFFKFFK-$CONH_2$) were purchased from Peptide 2.0 (Chantilly, VA, USA) and used without further purification. ^1H and ^{13}C NMR spectra were recorded using either a Varian 200 or 400 MHz spectrometer (Varian, Inc., Palo Alto, CA, USA) at Kaohsiung Medical University, Taiwan. NMR samples were prepared in CD_3OD, DMSO-d_6, or $CDCl_3$, and the chemical shifts of ^1H signals were given in parts per million downfield from TMS. ^{13}C signals were given in parts per million based on the internal standard of each deuteriated solvent. ESI high-resolution mass spectra were acquired from Department of Chemistry, National Sun Yat-Sen University, Taiwan, on a Bruker APEX II Fourier-transfer mass spectrometry (FT-MS; Bruker Daltonics Inc., Taiwan). FAB high-resolution mass spectra were obtained from Department of Chemistry, National Cheng Kung University, Taiwan, on a JEOL JMS-700 instrument (JEOL Ltd., Tokyo, Japan). Radiolabeled nucleic acid conjugates were analyzed by urea polyacrylamide gel electrophoresis (urea-PAGE) or streptavidin (SAv) gel shift assay in urea-PAGE, visualized and quantified by an Amersham Typhoon PhosphorImager (GE Healthcare Bio-Sciences AB, Uppsala, Sweden) at Kaohsiung Medical University, Taiwan. Molecular mass of POCs was measured by using an Autoflex III TOF/TOF analyzer (Bruker Daltonics, Taiwan) available at Kaohsiung Medical University, Taiwan. POC uptake by human A549 cells was analyzed by a BD FACSCalibur cytometer (BD, Franklin Lakes, NJ, USA), a Nikon ECLIPSE Ti−U Inverted microscope (Nikon, Shinjuku, Tokyo, Japan) and a FluoView 1000 confocal laser scanning microscope (Olympus, Tokyo, Japan). These instruments were located at Kaohsiung Medical University, Taiwan.

Synthesis of the Diamino Derivatives of Tetraglycine (7). *{2-[2-(2-tert-Butoxycarbonylamino-acetylamino)-acetylamino]-acetylamino}-acetic Acid (4).* Tetraglycine (**3**; 50 mg, 0.2 mmol) was dissolved in 16 mL of a dioxane/NaOH/water (4:2:2) solution to which was slowly added di-*tert*-butyldicarbonate (355 mg, 1.6 mmol) within 3 min and reacted at rt for 2 h. The final reaction mixture was concentrated under reduced pressure to give the white-colored solid **4** (70 mg, 95%). ^1H NMR (400 MHz) (DMSO-d_6) δ: 8.32 (t, 1H, GIy^4-NH), 8.26 (t, 1H, Gly^3-NH), 7.33 (t, 1H, GIy^2-NH), 7.05 (t, 1H, Gly^1-NH), 3.74 (d, 2H, $Gly^{4\alpha}$-H), 3.68 (d, 2H, $Gly^{3\alpha}$-H), 3.59 (d, 2H, $Gly^{2\alpha}$-H), 3.32 (d, 2H, $Gly^{1\alpha}$-H), 1.37 [s, 9H, $CO_2C(CH_3)_3$]. ^{13}C NMR (DMSO-d_6) δ: 171.2, 169.9, 169.3, 167.7, 155.9, 79.2, 78.2, 43.8, 43.4, 42.3, 42.1, 28.2. HRMS (ESI) calculated for $C_{13}H_{22}N_4O_7$ Na, $[M+Na]^+$ 369.1386 (calcd.), 369.1388 (found).

[({[({[(2-tert-Butoxycarbonylamino-ethylcarbamoyl)-methyl]-carbamoyl}-methyl)-carbamoyl]-methyl}-carbamo-

*yl)-methyl]-carbamic Acid tert-Butyl Ester (**6a**).* {2-[2-(2-*tert*-Butoxycarbonylamino-acetylamino)-acetylamino]-acetylamino}-acetic acid (**4**; 70 mg, 0.20 mmol) was first sonicated to completely dissolve in 20 mL DMF, followed by submerging the reaction mix in an ice−water bath. EDC (40 mg, 0.40 mmol) and HOBt (65 mg, 0.4 mmol) were then added to the reaction mixture to activate **4** for 15 min, followed by addition of a solution of mono-*t*-Boc-ethylenediamine (**5a**; 80 mg, 0.50 mmol) and DIPEA (0.035 mL, 0.40 mmol) in 5 mL of DMF to initiate the coupling reaction at rt for 6 h. Compound **5a** was previously synthesized according to similar reported procedures for **5b** synthesis.[20] The final reaction solution was filtrated, evaporated in vacuo, resuspended in 25% MeOH in DCM, and loaded to a silica column for further purification. The products were separated by eluting with mobile phases of 25% MeOH in DCM to afford **6a** (50 mg; 50%) as light yellowish solid. ^{1}H NMR (400 MHz) (DMSO-d_6) δ: 8.17 (t, 1H, CON*H*CH_2CH_2), 8.10−8.04 (m, 2H, Gly^1-N*H*, CH_2CH_2N*H* CO_2 $C(CH_3)_3$), 7.80 (t, 1H, Gly^4-NH), 6.99 (t, 1H, GIy^3-NH), 6.80 (t, 1H, Gly^2-NH), 3.74 (t, 4H, Gly$^{4\alpha}$-H, Gly$^{1\alpha}$-H), 3.66 (d, 2H, Gly$^{3\alpha}$-H), 3.58 (d, 2H, Gly$^{2\alpha}$-H), 3.08 (q, 2H,NHCH_2), 2.98 (q, 2H, CH_2NH), 1.37 [d, 18H, $CO_2C(CH_3)_3$]. ^{13}C NMR (DMSO-d_6) δ: 169.9, 169.4, 169.0, 168.8, 155.8, 155.6, 78.2, 77.7, 48.6, 43.3., 42.1, 42.1, 42.0, 40.1, 28.2, 28.2. HRMS (ESI) calculated for $C_{20}H_{36}N_6O_8$ Na, $[M+Na]^+$ 511.2492 (calcd.), 511.2490 (found).

*[6-(2-{2-[2-(2-tert-Butoxycarbonylamino-acetylamino)-acetylamino]-acetylamino}-acetylamino)-hexyl]-carbamic Acid tert-Butyl Ester (**6b**).* {2-[2-(2-*tert*-Butoxycarbonylamino-acetylamino)-acetylamino]-acetylamino}-acetic acid (**4**; 100 mg, 0.29 mmol) was first sonicated to completely dissolve in 20 mL DMF, followed by immersing the reaction mix in an ice−water bath. EDC (110 mg, 0.58 mmol) and HOBt (78 mg) were initially added to the reaction mix to activate **4** for 15 min, followed by addition of a solution of mono-*t*-Boc-hexanediamine (**5b**; 63 mg, 0.29 mmol)[20] and DIPEA (0.1 mL, 0.29 mmol) in 5 mL of DMF to commence the coupling reaction at rt for 6 h. The final reaction mixture was filtrated, evaporated in vacuo, redissolved in 10% MeOH in DCM, and loaded to a silica column for further purification. The products were separated by eluting with mobile phases of 10% MeOH in DCM to afford **6b** (85 mg; 54%) as a yellowish solid. ^{1}H NMR (400 MHz) (DMSO-d_6) δ: 8.16 (t, 1H, CON*H*CH_2CH_2), 8.04−8.08 [m, 2H, Gly^4-N*H*, N*H* $CO_2C(CH_3)_3$], 7.70 (t, 1H, Gly^3-NH), 7.00 (t, 1H, Gly^1-NH), 6.75 (t, 1H, GIy^2-NH),, 3.75 (d, 2H, Gly$^{1\alpha}$-H), 3.72 (d, 2H, Gly$^{4\alpha}$-H), 3.65 (d, 2H, Gly$^{3\alpha}$-H), 3.58 (d, 2H, Gly$^{2\alpha}$-H), 3.03 (q, 2H, NHCH_2), 2.88 (q, 2H, CH_2NH), 1.37 [d, 22H, $CO_2C(CH_3)_3$, NHCH_2CH_2], 1.21−1.23 (m, 4H, CH_2). ^{13}C NMR (DMSO-d_6) δ: 169.9, 169.4, 169.0, 168.4, 155.9, 155.6, 78.2, 77.3, 43.3, 42.2., 42.1, 42.0, 38.9, 38.5, 29.5, 29.1, 28.3, 28.2, 26.1, 26.0. HRMS (ESI) calculated for $C_{24}H_{44}N_6O_8$ Na, $[M+Na]^+$ 567.3118 (calcd.), 567.3115 (found).

*2-Amino-N-{[({[(2-amino-ethylcarbamoyl)-methyl]-carbamoyl}-methyl)-carbamoyl]-methyl}-acetamide (**7a**).* [({{[({[(2-*tert*-Butoxycarbonylamino-ethylcarbamoyl)-methyl]-carbamoyl}-methyl)-carbamoyl]-methyl}-carbamoyl)-methyl]-carbamic acid *tert*-butyl ester (**6a**; 50 mg, 0.12 mmol) was dissolved in a TFA/DCM solution (1:1; 4 mL), stirred at 0 °C for 1 h, and then reacted at rt for 1 h. The product was evaporated under reduced pressure, washed by ether and chloroform, sequentially, and again concentrated under reduced pressure to remove ether and chloroform to give the yellow-colored oil-like TFA salt of **7a**. The obtained TFA salt of **7a** was further dissolved in 5 mL of a DCM/MeOH mixture (DCM/MeOH = 1:1) and mixed with 10 equiv of Amberlyst A-21 (0.14 mg, 1.1 mmol) while rocking for 30 min.[20] After filtering to remove Amberlyst A-21, the filtrate of the reaction products was concentrated under reduced pressure to give white solid **7a** (30 mg, 95%). ^{1}H NMR (400 MHz) (DMSO-d_6) δ: 8.65 (t, 1H, N*H*CH_2CH_2), 8.32 (t, 1H, Gly^4-NH), 8.17 (t, 1H, GIy^3-NH), 8.06 (t, 1H, Gly^2-NH), 7.80−8.02 (br, 4H, Gly^1-NH_2, $CH_2CH_2NH_2$), 3.85 (d, 2H, Gly$^{4\alpha}$-H), 3.77 (d, 2H, Gly$^{3\alpha}$-H), 3.71 (d, 2H, Gly$^{2\alpha}$-H), 3.62 (s, 2H, Gly$^{1\alpha}$-H), 3.30 (q, 2H, CH_2NH), 2.85 (q, 2H, NHCH_2). ^{13}C NMR (DMSO-d_6) δ: 169.6, 169.1, 168.8, 166.4, 42.0, 42.0., 42.0, 39.0, 38.5, 36.3. HRMS (ESI) calculated for $C_{10}H_{21}N_6O_4$, $[M+H]^+$ 289.1624 (calcd.), 289.1626 (found).

*2-Amino-N-{[({[(6-amino-hexylcarbamoyl)-methyl]-carbamoyl}-methyl)-carbamoyl]-methyl}-acetamide (**7b**).* [6-(2-{2-[2-(2-*tert*-Butoxycarbonylamino-acetylamino)-acetylamino]-acetylamino}-acetylamino)-hexyl]-carbamic acid *tert*-butyl ester (**6b**; 60 mg, 0.11 mmol) was dissolved in a TFA/DCM solution (1:1; 4 mL), stirred at 0 °C for 1 h, and then reacted at rt for 1 h. The product was evaporated under reduced pressure, washed by ether and chloroform, sequentially, and again concentrated under reduced pressure to remove ether and chloroform to obtain the brown oil-like TFA salt of **7b**. The acquired TFA salt of **7b** (0.52 g, 0.88 mmol) was further dissolved in 5 mL of DCM/MeOH mixture (DCM/MeOH = 1:1) and mixed with 10 equiv of Amberlyst A-21 (0.14 mg, 1.1 mmol) while rocking for 30 min.[20] After filtering to remove Amberlyst A-21, the filtrate of the reaction products was concentrated under reduced pressure to afford white solid **7b** (50 mg, 95%). ^{1}H NMR (400 MHz) (DMSO-d_6) δ: 8.68 (t, 1H, N*H*CH_2CH_2), 8.33 (t, 1H, Gly^4-NH), 8.13 (t, 1H, Gly^3-NH), 7.84−8.08 (br, 4H, GIy^1-NH_2, $CH_2CH_2NH_2$), 7.79 (t, 1H, Gly^2-NH), 3.84 (d, 2H, Gly$^{4\alpha}$-H), 3.75 (d, 2H, Gly$^{3\alpha}$-H), 3.66 (d, 2H, Gly$^{2\alpha}$-H), 3.62 (s, 2H, Gly$^{1\alpha}$-H), 3.04 (q, 2H, CH_2NH), 2.76 (t, 2H, CH_2NH_2), 1.18−1.60 (m, 8H, CH_2). ^{13}C NMR (DMSO-d_6) δ: 169.0, 168.9, 168.5, 166.5, 42.1, 42.5, 42.0, 40.2, 38.8, 38.4, 28.9, 27.0,25.8,25.5. HRMS (ESI) calculated for $C_{14}H_{29}N_6O_4$, $[M+H]^+$ 345.2250 (calcd.), 345.2251 (found).

Synthesis of a *N*-Maleoyl Amino Acid Succinimidyl Ester, AMAS (9). (2,5-Dioxo-2,5-dihydro-pyrrol-1-yl)-acetic acid 2,5-dioxo-pyrrolidin-1-yl ester (**9**) was synthesized from (2,5-dioxo-2,5-dihydro-pyrrol-1-yl)-acetic acid (**8**) which was prepared by a previously reported method.[22] The acquired **8** (69 mg, 0.45 mmol) and NHS (103 mg, 0.89 mmol) were first dissolved in THF (10 mL), followed by dropwise addition of DCC (184 mg, 0.89 mmol) in THF (10 mL) while stirring. After overnight reaction at rt, the mixture was quenched by addition of three drops of glacial acetic acid and stirring for 1 h and filtered to remove suspension. The acquired filtrate was concentrated under reduced pressure, washed by EtOH twice, resuspended in 2-propanol (30 mL) while stirring for 1 h, and filtered to separate the suspension from its filtrate. The final solid was washed by 2-propanol and dried to afford a white-colored **9** (96 mg; 86%). ^{1}H NMR (400 MHz) (DMSO-d_6) δ: 7.20 (s, 2H, CHCH), 4.73 (s, 2H, CH_2), 2.81 (s 4H, CH_2CH_2) ^{13}C NMR (DMSO-d_6) δ: 169.7, 169.7, 164.4, 135.1, 36.3, 25.4. HRMS (ESI) calculated for $C_{10}H_8N_2O_6$Na, $[M+Na]^+$ 275.0280 (calcd.), 275.0279 (found).

Synthesis of the Thiol-Containing Biotin Derivative (13). *5-(2-Oxo-hexahydro-thieno[3,4-d]imidazol-4-yl)-pentanoic acid (2-{2-[5-(2-oxo-hexahydro-thieno[3,4-d]imidazol-*

*4-yl)-pentanoylamino]-ethyldisulfanyl}-ethyl)-amide (**12**).* 5-(2-Oxo-hexahydro-thieno[3,4-*d*]imidazol-4-yl)-pentanoic acid 2,5-dioxo-pyrrolidin-1-yl ester (**11**; 0.19 g, 0.55 mmol) was synthesized from **10** according to our previously published method[20] and was completely dissolved in DMF (7 mL) with gentle warming. After slowly cooling the **11** solution to rt without recurring precipitation, it was mixed with an aqueous solution (1 mL) containing cystamine dihydrochloride (0.068 g, 0.30 mmol) and Et_3N (0.14 g, 1.38 mmol) with stirring. The reaction proceeded at rt overnight with stirring and the reaction products were concentrated in vacuo. The remaining solid was redissolved in 2-propanol (20 mL) with gentle heating, cooled down to room temperature, and reprecipitated at 4 °C overnight. The obtained white solid was recovered from the glassware, washed with cold 2-propanol and air-dried to give **12** (0.14 g; 82.1%). ^{1}H NMR (400 MHz) (DMSO) δ: 8.01 (s, 2H, CONH), 6.54 (s, 2H, CONH), 6.39 (s, 2H, CONH), 4.31 (t, 2H, CHN), 4.15 (t, 2H, CHN), 3.11 (dd, 2H, CHS), 2.85 (d, 2H, C*H*HS), 2.78 (t, 4H, CH_2S), 2.58 (d, 2H, C*H*HS), 2.09 (t, 4H, CH_2CO), 1.31−1.61 (m, 12H). ^{13}C NMR (100.67 MHz) (DMSO) δ: 172.26, 162.74, 61.04, 59.21, 55.43, 41.10, 37.88, 37.31, 35.15, 28.11, 25.23. HRMS (ESI) calculated for $C_{24}H_{40}N_6O_4S_4Na$, $[M+Na]^+$ 627.1891 (calcd.), 627.1893 (found).

*5-(2-Oxo-hexahydro-thieno[3,4-d]imidazol-4-yl)-pentanoic acid (2-mercapto-ethyl)-amide (**13**).* 5-(2-Oxo-hexahydro-thieno[3,4-*d*]imidazol-4-yl)-pentanoic acid (2-{2-[5-(2-oxo-hexahydro-thieno[3,4-*d*]imidazol-4-yl)-pentanoylamino]-ethyldisulfanyl}-ethyl)-amide (**12**; 0.14 g, 0.23 mmol) was completely dissolved in DMF (8 mL) with gentle warming. After cooling, the **12** solution to rt without recurring precipitation, DL-dithiothreitol (DTT; 0.11 g, 0.68 mmol) and Et_3N (0.002 g, 0.02 mmol) were added to the solution with stirring. Additional DTT (0.11 g, 0.68 mmol) was replenished to the reaction mixture 1 h later. The reaction proceeded at rt for 2 more hours, followed by evaporation in vacuo. The remaining solid was washed by DCM (10 mL) three times and concentrated under reduced pressure to give white-colored **13** (0.07 g; 52.7%). ^{1}H NMR (400 MHz) (DMSO) δ: 7.98 (s, 1H, CONH), 6.45 (s, 1H, CONH), 6.38 (s, 1H, CONH), 4.32 (t, 1H, CHN), 4.14 (t, 1H, CHN), 3.19 (t, 2H, CH_2SH), 3.11 (dd, 1H, CHS), 2.83 (d, 1H, C*H*HS), 2.58 (d, 1H, C*H*HS), 2.37 (t, 1H, SH), 1.32−1.61 (m, 6H). ^{13}C NMR (100.67 MHz) (DMSO) δ: 172.38, 162.81, 61.07, 59.23, 55.44, 42.04, 35.14, 28.21, 28.03, 25.25, 23.52. HRMS (FAB) calculated for $C_{17}H_{30}O_5N_5SNa$, $[M+Na]^+$ 439.5112 (calcd.), 439.1865 (found).

Nucleic Acid Preparation and Radiolabeling. The 3′ primer (5′-TACCCCTTGGGGATACCACC-3′), a single-stranded DNA, was purchased from Purigo Biotech, Inc., Taiwan, and used without purification. The $TW17_{1-17}$ RNA (5′-GGGAUCGUCAGUGCAUU-3′) was purchased from Bioneer (Daejeon, South Korea) and also used without purification. The 5′ GMP-primed TW17 RNA (87-mer; 5′-GGGAUCGUCAGUGCAUUGAGAAGUGCAGUGUCUUG-CGCUGGGUUCGAGCGGUCCGUGGUGCUGGC-CCGGUGGUAUCCCCAAGGGGUA-3′) was prepared as previously described.[23] The TW17 RNA body-labeled with ^{32}P and the 3′ primer DNA ^{32}P-labeled at the 5′-end were prepared according to the previously reported procedures.[20,23]

Optimization of Two-Step Nucleic Acid Phosphoramidation Reactions. The optimized two-step phosphoramidation reaction for RNA was carried out by dissolving the GMP-primed TW17 RNA (0.32 nmol) and EDC (4.17 μmol) in 4 μL 4(5)-methylimidazole-Triton X-100 buffer [0.1 M 4(5)-methylimidazole, 15% Triton X-100, pH 6.0] and activating at rt for 90 min. The resulting 5′-phosphorimidazolide RNA was purified by ethanol precipitation and resuspended in 5.5 μL of EPPS-Triton X-100 buffer (100 mM EPPS, 15% Triton X-100, 2 mM EDTA, pH 7.5). One microliter of **1** (187.2 mM in DMF) was then added to the 5′-phosphorimidazolide RNA solution to allow a phosphoramidation reaction at 41 °C for 3 h.

For the single-stranded 3′-primer DNA, the optimized two-step phosphoramidation reaction was performed by dissolving the single-stranded DNA (0.32 nmol) and EDC (4.17 μmol) in 4 μL of 4(5)-methylimidazole buffer [0.1 M 4(5)-methylimidazole, pH 6.0] and activating at rt for 90 min. Similarly, the resulting 5′-phosphorimidazolide DNA was purified by ethanol precipitation and redissolved in 5.5 μL of EPPS buffer (100 mM EPPS, 2 mM EDTA, pH 7.5). A solution of **1** (1 μL; 187.2 mM in DMF) was later added to the 5′-phosphorimidazolide DNA solution to allow a phosphoramidation reaction at 55 °C for 3 h. No co-solute was used in the two-step phosphoramidation reaction of the single-stranded DNA to attain higher reaction yield.

All resulting nucleic acid−substrate conjugates were purified twice by ethanol precipitation, analyzed by urea-PAGE and SAv gel shift assay (8% urea-PAGE for the TW17 RNA, and 20% urea-PAGE for single-stranded DNA), visualized, and quantified by an Amersham Typhoon PhosphorImager to determine reaction yield.

Nucleic Acid-Tetraglycine Derivative Conjugate Preparation. The phosphoramidation reactions between the TW17 RNA and **6a**/**6b** adhered to the optimized two-step phosphoramidation reaction stated above but with **1** replaced by the same concentration of **6a**/**6b**. The phosphoramidation reactions between the 3′ primer DNA and **6a**/**6b** was also carried out by following the previously optimized two-step phosphoramidation reaction for single-stranded DNA but with the same concentration of **6a**/**6b** substituting for **1**. The synthesized nucleic acid-tetraglycine derivative conjugates were purified twice by ethanol precipitation, analyzed by 8% (the TW17 RNA) or 20% (the 3′ primer DNA) urea-PAGE to separate reaction products, visualized and quantified by an Amersham Typhoon PhosphorImager.

Two-Step Phosphoramidation Reactions for Synthesis of Nucleic Acid−Tat_{48-57} Peptide Conjugates. The single-stranded 3′-primer DNA was conjugated with the Tat_{48-57} peptide according to the optimized two-step phosphoramidation reaction described previously but with the following modifications. First, the scale of the reaction was increased five times to acquire the sufficient conjugates for subsequent ex vivo studies. In addition, the pH of the conjugation reaction between the 5′-phosphorimidazolide DNA and the Tat_{48-57} peptide was increased to 8.0 achieved by addition of concentrated EPPS buffer (600 mM EPPS, 5 mM EDTA, pH 8.0) to attain higher yield. Finally, only 20 mM of the Tat_{48-57} peptide was required in the coupling reaction to have the best yield.

For RNA-Tat_{48-57} conjugates, preparation also followed the optimized two-step RNA phosphoramidation reaction but with following modifications: (1) Only 20 mM of the Tat_{48-57} peptide was required in conjugation reactions, and (2) concentrated EPPS-Triton X-100 buffer (600 mM EPPS, 15% Triton X-100, 5 mM EDTA, pH 7.5) was added to the

conjugation reaction between the 5′-phosphorimidazolide RNA and the Tat_{48-57} peptide to retain the buffering capacity.

The synthesized nucleic acid-Tat_{48-57} conjugates were also purified twice by ethanol precipitation, analyzed by 8% (the TW17 RNA) or 20% (the 3′ primer DNA and the $TW17_{1-17}$ RNA) urea-PAGE, visualized and quantified by an Amersham Typhoon PhosphorImager.

Two-Step Phosphoramidation Reactions for Synthesis of Nucleic Acid−Cystamine Conjugates. Similar optimized two-step phosphoramidation reactions were applied when preparing nucleic acid−cystamine conjugates and are described below. The RNA−cystamine conjugate synthesis was carried out by dissolving the GMP-primed $TW17_{1-17}$ RNA (0.32 nmol) and EDC (4.17 μmol) in 4 μL of 4(5)-methylimidazole-Triton X-100 buffer and activating at rt for 90 min. The resulting 5′-phosphorimidazolide RNA was purified by ethanol precipitation and then resuspended in 5.5 μL of concentrated EPPS-Triton X-100 buffer with the addition of 1 μL of cystamine (187.2 mM in water) to allow a reaction at 41 °C for 3 h.

For the single-stranded 3′-primer DNA, the cystamine conjugate was prepared by dissolving the DNA (1.59 nmol) and EDC (26 μmol) in 20 μL 4(5)-methylimidazole buffer and activating at rt for 90 min. The resulting 5′-phosphorimidazolide DNA was purified by ethanol precipitation, redissolved in 27.5 μL of concentrated EPPS buffer. Five microliters of cystamine (187.2 mM in DEPC water) was then added to the 5′-phosphorimidazolide DNA solution to allow reaction at 55 °C for 3 h. Again, no co-solute was used in the two-step phosphoramidation reaction of the single-stranded DNA to attain higher reaction yield.

The products of the conjugation reactions between cystamine and nucleic acids were separated by 20% urea-PAGE, visualized and quantified by an Amersham Typhoon PhosphorImager to determine reaction yield.

Optimization of AMAS (9) Reactions to Effectively Conjugate Nucleic Acids with the $C(KFF)_3K$ Peptide. The heterobifunctional **9** served as the linker to conjugate cystamine-modified nucleic acids with peptides (Scheme S1). Before having **9** react with cystamine-modified nucleic acids and peptides, each reaction was optimized by using one of the model compounds **11** and **13** to attain the highest yield. The optimization reactions are briefly described below.

For the reaction between a cystamine-modified nucleic acid and **9**, **11** with an activated carboxyl group was substituted for **9**. The substitution simplified the acylation reaction allowing the determination of the appropriate condition to provide the highest yield as stated below. The cystamine-modified 3′ primer DNA (900 pmol) was dissolved in 22.5 μL of concentrated EPPS-7.3 buffer (600 mM EPPS, pH 7.3) to produce 40 μM of the DNA solution in a microfuge tube. After addition of **11** solution (9 μL; 0.01−1 M in DMF), the microfuge tube was wrapped with aluminum foil, and reacted at rt with rocking for 1.5 h. The resulting 3′ primer DNA-**11** conjugates were purified twice by ethanol precipitation, analyzed by 20% urea-PAGE, visualized and quantified by an Amersham Typhoon PhosphorImager to determine reaction yield.

The conjugation of the **9**-modified 3′ primer DNA with **13** was studied to determine optimal conditions for the Michael addition reaction between the **9**-modified nucleic acids and cysteine-containing peptides and to attain high yield (Scheme S1; Supporting Information). The reaction optimization is briefly described below. Assuming no DNA loss during ethanol precipitation, the acquired **9**-modified 3′ primer DNA reaction mixture (0.9 nmol) was dissolved in 50 μL of concentrated EPPS-7.3 buffer, followed by the slow addition of 50 μL of **13** solution (36−3600 μM in DMF), and reacted at rt with rocking for 16 h. The acquired 3′ primer DNA-**13** conjugates were purified twice by ethanol precipitation, analyzed by 20% urea-PAGE, visualized and quantified by an Amersham Typhoon PhosphorImager to determine reaction yield.

Synthesis of Nucleic Acid−$C(KFF)_3K$ Peptide Conjugates Using the Cystamine-9 Linker. All nucleic acid−$C(KFF)_3K$ peptide conjugates were prepared by following the optimized AMAS (**9**) reactions described previously and briefly stated below. The $TW17_{1-17}$ RNA- $C(KFF)_3K$ peptide conjugate synthesis was initiated by dissolving the previously prepared cystamine-modified $TW17_{1-17}$ RNA (0.22 nmol) in 5.55 μL of concentrated EPPS-7.3 buffer to yield a 40 μM RNA solution. After addition of 22 μL of **9** (10 mM in DMSO) to the RNA solution, the microfuge tube containing the RNA reaction mixture was wrapped with aluminum foil and reacted at rt with rocking for 1.5 h. The **9**-modified RNA was purified by standard ethanol precipitation to remove excess **9**, and was redissolved in 50 μL of concentrated EPPS-7.3 buffer. A solution of $C(KFF)_3K$ solution (50 μL; 4.4 nmol) was then slowly added to the **9**-modified RNA solution and reacted at rt with rocking for 16 h (Scheme S1).

For DNA conjugates, the cystamine-modified 3′ primer DNA (0.9 nmol) was dissolved in 22.5 μL of concentrated EPPS-7.3 buffer to produce a 40 μM DNA solution in a microfuge tube. A solution of **9** (90 μL; 10 mM in DMSO) was added to the DNA solution and followed by wrapping the reaction mixture-containing microfuge tube with aluminum foil and rocking the reaction mixture at rt for 1.5 h. The reaction products were purified twice by ethanol precipitation to remove excess **9**. The obtained **9**-modified 3′ primer DNA (∼0.9 nmol) was redissolved in 50 μL of concentrated EPPS-7.3 buffer, followed by slow addition of 50 μL of the $C(KFF)_3K$ peptide solution (18 nmol in DEPC water), and reacted at rt with rocking for 16 h (Scheme S1). The obtained nucleic acid−$C(KFF)_3K$ peptide conjugate was purified twice by ethanol precipitation, analyzed by 20% urea-PAGE, visualized and quantified by an Amersham Typhoon PhosphorImager to obtain reaction yield.

MALDI-TOF MS for POC Characterizations. Prior to MALDI-TOF analysis, each POC sample was purified by urea-PAGE and desalted by passing through a Sephadex G-10 (GE Healthcare Life Sciences, Taipei, Taiwan). MALDI-TOF mass spectra were recorded on an Autoflex III TOF/TOF analyzer (Bruker Daltonics, Taiwan). Each MALDI-TOF sample was prepared by mixing a purified POC (100 pmol in 0.5 μL water) with the MALDI-TOF matrix solution (0.5 μL), deposited on a target plate and allowed to dry before the POC mass measurement. A fresh MALDI-TOF matrix solution was prepared daily by adopting a volume ratio of 1:2:1 for 2,3,4-trihydroxyacetophenone (0.2 M in 50% acetonitrile), 2,4,6-trihydroxyacetophenone (0.2 M in 50% acetonitrile), and ammonium citrate (0.3 M), respectively.

Cell Culture. Cells of A549, a human lung carcinoma cell line, were maintained in Ham's F12K (Biowest, France) and supplemented with 10% fetal bovine serum (FBS; Hyclone, USA), 1% penicillin−streptomycin−amphotercin (PSA; Biological Industries, Israel), and 1% L-glutamine solution (Biological Industries, Israel).

Cytotoxicity Assays. The viability of mammalian cells in the presence of POCs was determined by the methylthiazolete-

trazolium (MTT) conversion assay described previously.[24] A549 cells were cultured in 96 well plates (2×10^4 cells/well; 0.1 mL medium/well), washed, and maintained in medium containing serum overnight prior to assay. After inoculation with 0−10 μM of the 3′ primer, DNA- Tat_{48-57} peptide conjugate, cells were maintained at 37 °C for 24 h and further incubated with MTT (0.5 mg/mL) at 37 °C for 4 h. By the end of MTT incubation, the medium was removed and the insoluble formazan product was dissolved by adding DMSO (100 μL/well) with thoroughly mixing. MTT conversion was determined by colorimetric analysis at 570 nm. Each experiment was performed in triplicate; the reported result was mean of triplicate experiments ± SD.

Fluorescent Labeling of DNA and Its Conjugation with the Tat_{48-57} Peptide. In order to detect the uptake of DNA in POCs by mammalian cells using flow cytometry, fluorescent microscopy, and confocal laser scanning microscopy, the DNA was required to be labeled with fluorophores before conjugating with the Tat_{48-57} peptide for POC synthesis. Fluorescent labeling of DNA was achieved by a DNA depurination method[25] and briefly described below. DNA depurination was accomplished by resuspension of the 3′ primer DNA (1−10 mg) in 0.2 N HCl (10 mL) and allowed to react at 37 °C for 90 min. The depurinated DNA solution was diluted with 40 mL of ethylenediamine buffer (650 mM, pH 7.6) and reacted at 37 °C for 3 h. The solution of the imine-containing DNA was further reacted with freshly prepared $NaBH_4$ (0.1 M in water, 4 mL) at rt for 30 min. The acquired diamino-derivatized DNA sample was purified by adding 1 mL of lithium perchlorate (2% in acetone) to precipitate the DNA, washing the DNA with acetone twice and air−drying. After redissolving the diamino-derivatized DNA in carbonate buffer (0.1 M, pH 9.0; 20 μL), a solution of fluorescein isothiocyanate (FITC; 2.57 mM in DMSO, 20 μL) was slowly added to the DNA solution and reacted in the dark for 12 h. The reaction products were precipitated by ethanol and further purified by 20% urea-PAGE to obtain the FITC-labeled 3′ primer DNA. The FITC-labeled DNA was conjugated with the Tat_{48-57} peptide according to the optimized zero-linker two-step phosphoramidation reaction described in this study. The POC, the FITC-labeled 3′ primer DNA- Tat_{48-57} peptide conjugate, was again purified by 20% urea-PAGE in which the migration of the FITC-labeled POC was visualized by an Amersham Typhoon PhosphorImager with the settings of the excitation wavelength at 488 nm and the emission wavelength at 525 nm for fluorescein detection. It is noted that the FITC-labeled Tat_{48-57} peptide was also prepared according to a previously described method.[20]

Flow Cytometry. A549 cells were seeded into a 12-well plate (2×10^5 cells in 1 mL medium per well) and cultured overnight. The medium in the overnight cultures was removed, replenished with a fresh medium containing 0 or 5 μM of the FITC-labeled Tat_{48-57} peptide or 3′ primer DNA−Tat_{48-57} peptide conjugate, and further maintained at 37 °C for 24 h. The peptide/POC-containing medium was discarded after incubation in which the cells were washed by PBS once and detached from the plate surface by treating with trypsin (trypsin−EDTA 1×, 0.5 mL per well; Biowest, France) for 3−5 min. The trypsinized cells were resuspended in the medium (0.5 mL) and centrifuged at 700 rcf for 4 min. After removal of the supernatants, the cells were resuspended in ice-cold PBS (1 mL) and subjected to another round of centrifugation (700 rcf for 4 min). The final cell pellets were again resuspended in ice-cold PBS (1 mL), transferred to Falcon tubes (BD Bioscience, San Jose, CA, USA) and placed on ice in the dark before each analysis. Each experiment was performed in triplicate; in each case, the fluorescence of at least 10 000 viable cells was measured by using a BD FACSCalibur cytometer (BD, Franklin Lakes, NJ, USA).

Confocal Laser Scanning Microscopy and Fluorescent Microscopy. A549 cells were seeded in an 8-well Lab-Tek coverglass chamber (0.3 mL medium per well; Nalge Nunc, Rochester, NY, USA) with an appropriate density of 1×10^4 cells per well and incubated for 24 h before the experiment. The medium in the overnight cultures was removed, replenished with a fresh medium containing 0 or 5 μM of the FITC-labeled Tat_{48-57} peptide or 3′ primer DNA−Tat_{48-57} peptide conjugate, and further maintained at 37 °C for 24 h. The peptide/POC-containing medium was discarded after incubation, followed by washing the cells with PBS three times before confocal imaging analysis. The pictures were obtained using a FluoView 1000 confocal laser scanning microscope (Olympus, Tokyo, Japan). All images were acquired using living and nonfixed cells. Each experiment was performed in triplicate. Experimental procedures similar to those described above were used in fluorescent microscopy analysis.

RESULTS

General Considerations in Optimizing the Aqueous-Phase Two-Step Phosphoramidation Reactions for POC Synthesis. We envisioned that three aspects of two-step nucleic acid phosphoramidation reactions critical to POC synthesis could be modified to increase product yields (Scheme 1). First, inert co-solutes such as Tween 20 and Triton X-100 were substituted for urea (8 M in the original reactions)[20] in phosphoramidation reactions to ensure co-solutes would carry out their proposed roles of denaturing nucleic acids without participating in nucleophilic substitution reactions. Our previous study has revealed that using urea as a co-solute could lead to less than optimal reaction yield. Second, we sought to attain higher POC yields by modestly increasing the nucleophilicity of the imidazole moiety. Appropriately stabilizing phosphorimidazolide intermediates would extend their half-lives in aqueous solutions while not deterring subsequent nucleophilic substitution reaction with peptides. Third, POC yields could be further improved by chemically modifying peptides to increase peptide nucleophilicity. We adopted these three strategies to improve the aqueous-phase two-step phosphoramidation reactions and present the results in the following sections.

Identification of an Appropriate Co-Solute and Concentration to Facilitate POC Synthesis. We exploited previously synthesized **1** (Scheme 1) as the nucleophile in aqueous-phase two-step phosphoramidation reactions to optimize conjugation with nucleic acids. First, we substituted one of five different co-solutes (Triton X-100, Tween 20, PEG-6000, PEG-8000, and glycerol) for urea in the phosphoramidation reactions while varying co-solute concentrations from 0% to 33% (w/v) to identify appropriate co-solutes and concentrations for DNA and RNA conjugation with the nucleophile **1**. These co-solutes were chosen because each of their structures only contains the hydroxyl functionality, which is unlikely to deprotonate and participate in phosphoramidation reactions as nucleophiles at neutral pH. The TW17 RNA (87-mer nt) clearly favored 15% Triton X-100 in the phosphoramidation reactions to have the best yield (Figure 1A). The 3′

Scheme 1. Strategies to Optimize Aqueous-Phase Two-Step Phosphoramidation Reactions for Conjugating Nucleic Acid with Nucleophiles, Such as Peptides, to Synthesize Peptide–Oligonucleotide Conjugates (POCs)[a]

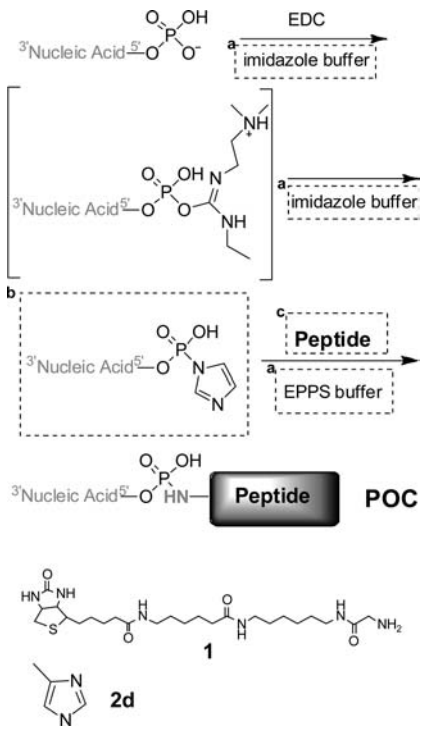

[a]Dashed boxes indicate the approaches to improve the reaction yields. Each bold, superscripted, lower-case letter represents the specific method to explore reaction conditions to achieve best reaction yields. These methods include the following: **a**, identifying an appropriate co-solute and concentration; **b**, investigating imidazole derivatives to stabilize phosphorimidazolide intermediates and facilitate subsequent phosphoramidation reactions; **c**, increasing numbers of nucleophilic functionalities in nucleophiles which were peptides in this study. Compound **1** was one of the model nucleophiles in this study. Compound **2d** was identified as the best imidazole derivative for POC synthesis revealed by the results noted in the text.

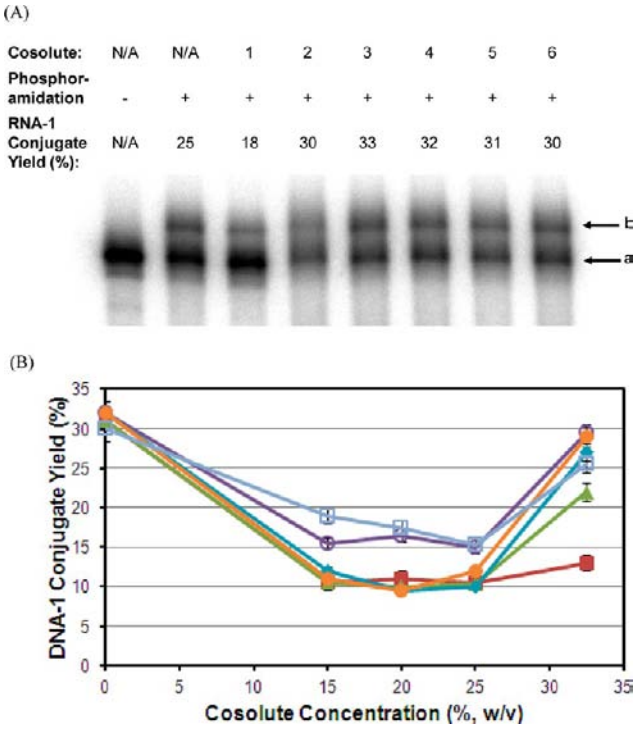

Figure 1. Effects of co-solutes on yields of aqueous-phase two-step phosphoramidation reactions when conjugating **1** with (A) the ^{32}P-labeled TW17 RNA or (B) the ^{32}P-labeled single-stranded 3′ primer DNA. (A) The studied co-solutes included the following: 1, urea; 2, Tween 20; 3, Triton X-100; 4, PEG 6000; 5, PEG 8000; 6, glycerol. Each co-solute had a concentration of 15% (w/v) in both buffers for the phosphoramidation reactions. The reaction products were purified by ethanol precipitation, analyzed by 8% urea-PAGE, visualized and quantified by an Amersham Typhoon PhosphorImager. **a**, unreacted TW17 RNA; **b**, TW17 RNA-**1** conjugate. (B) The relationship of co-solute concentrations and DNA-**1** conjugate yields for each studied co-solute. The data were quantified by results from several urea-PAGE analyses similar to that in (A). Each data point is determined by calculating the average of the yields from triplicate experiments accompanied with the standard deviation represented as a vertical bar. The studied co-solutes in the phosphoramidation reactions were urea (closed square, ■), Tween 20 (closed triangle, ▲), Triton X-100 (open circle, ○), PEG 6000 (closed diamond, ♦), PEG 8000 (closed circle, ●), and glycerol (open square, □).

primer DNA (20-mer nt), however, had the best yield when no co-solutes were included in the phosphoramidation reactions (Figure 1B). Acquiring better yield with no co-solutes in DNA phosphoramidation reactions is consistent with previous findings[20] and likely reflects short single-stranded DNA, such as the 3′ primer DNA, having less of a tendency to fold into secondary structures which would interfere in phosphoramidation reactions. Having co-solute concentrations higher than 32.5% in two-step phosphoramidation reactions might promote product formation as implicated in Figure 1B, but this is an impractical approach as reaction mixtures became too thick to handle.

Survey of Imidazole Derivatives with Potential to Enhancing POC Formation. After determining optimal co-solute conditions in the two-step phosphoramidation reactions for nucleic acids, we substituted one of six imidazole derivatives (**2a–f**; Figure S1) for imidazole in reactions. All the imidazole derivatives have electron-donating substitutions in the aromatic ring which presumably strengthens phosphoramidate bonds and improves stability of the key phosphorimidazolide intermediates in water (boxed in **b** in Scheme 1). Results of the studied two-step phosphoramidation reactions in the presence of these imidazole derivatives, however, indicated that only **2d** [4(5)-methylimidazole); Scheme 1] could substantially increase product yields for both DNA and RNA conjugation (Figure 2). The ability of compound **2d** as the only imidazole derivative to enhance product formation suggests that not only the nucleophilicity in the imidazole ring but also the steric hindrance imposed on the nucleophilic N in the imidazole moiety determine product yield in phosphoramidation reactions. Increasing nucleophilicity in the imidazole ring is a double-edged sword approach; it could stabilize the phosphoramidate bond in a phosphorimidazolide intermediate so effectively as to deter subsequent nucleophilic substitution required to attain desired products. We are currently synthesizing imidazole derivatives based on **2d** to further improve two-step phosphoramidation reaction yield.

Increase of Peptide Nucleophilicity to Promote POC Synthesis. We explored the relationship between peptide nucleophilicity and phosphoramidation yield. We previously demonstrated that diamino nucleophiles provided higher

dx.doi.org/10.1021/bc300444y | Bioconjugate Chem. 2012, 23, 2417–2433

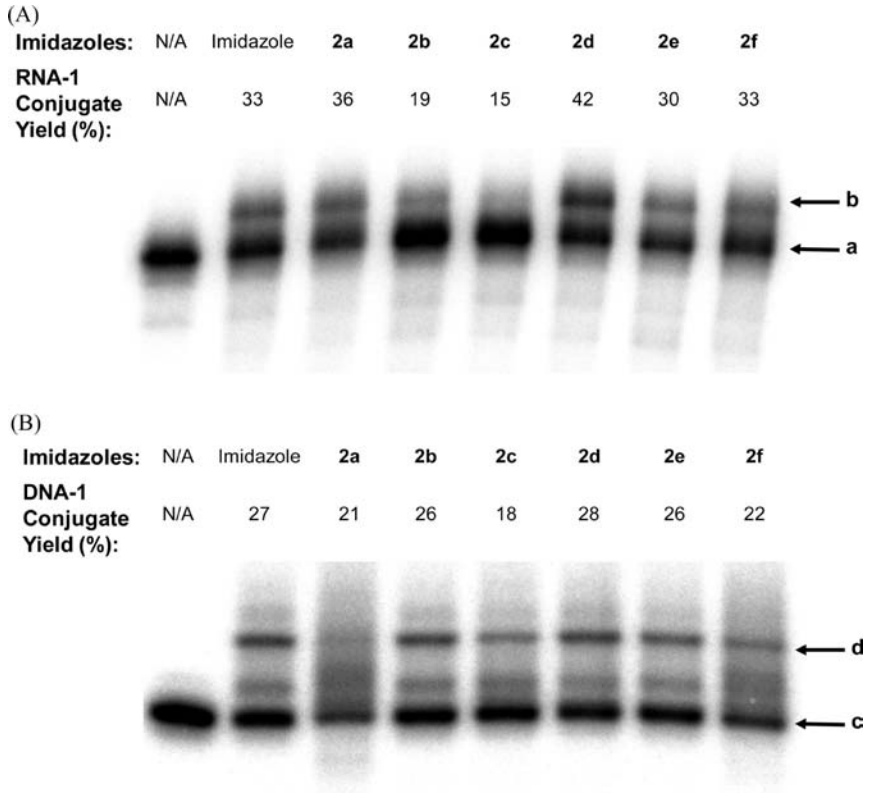

Figure 2. Influence of imidazole nucleophilicity on yields of two-step phosphoramidation reactions when conjugating **1** with (A) the ^{32}P-labeled TW17 RNA or (B) the ^{32}P-labeled single-stranded 3′ primer DNA. Either imidazole or one of its derivatives (**2a**–**f**, Figure S1) was individually incorporated into a phosphoramidation reaction. The reaction product was purified by ethanol precipitation, analyzed by 8% urea-PAGE for the RNA-**1** conjugate and 20% urea-PAGE for the DNA-**1** conjugate, visualized and quantified by an Amersham Typhoon PhosphorImager. **a**, unreacted TW17 RNA; **b**, TW17 RNA-**1** conjugate; **c**, unreacted 3′ primer DNA; **d**, 3′ primer DNA-**1** conjugate.

product yield in significantly shorter reaction time than monoamino nucleophile **1** in phosphoramidation reaction.[20] We thus reasoned that using modified peptides carrying additional amino groups would improve peptide nucleophilicity and further increase phosphoramidation reaction yields. Since we previously synthesized tetraglycine (**3**)[20] and it is also commercially available, we decided to use **3** as the starting material to yield two of its amino derivatives, the novel peptides **7a** and **7b**, each carrying an additional amino group appended on two or six carbon linkers (Scheme 2).

Synthesis of **7a** and **7b** started with Boc protection of **3** to give **4**. The Boc-protected **4** was initially acylated with **5a**/**5b** following our previous method for similar reactions in synthesis of **3** (EDC and Et_3N in DMF). Unexpectedly, the desired **6a**/**6b** was not produced after the reactions and their formations were not improved when DMAP was included in the reactions. We eventually adopted standard peptide coupling conditions[26] using EDC, HOBt, and DIPEA as reagents for the reactions and successfully synthesized **6a** and **6b**. Boc deprotection of **6a** and **6b** (TFA in DCM) and subsequent TFA removal by Amberlyst A-21[20] finally led to effective synthesis of the required **7a** and **7b**.

The successful synthesis of **7a** and **7b** allowed study of the two-step phosphoramidation reaction using **7a** and **7b** as the nucleophiles in the optimized reaction conditions. As expected, **7a** and **7b** were better nucleophiles than **1** and **3** when coupled with either the 3′ primer DNA or the TW17 RNA to give higher reaction yield (Figure 3). Increasing the extent of amino functionality in the nucleophiles could contribute to higher yields in two-step phosphoramidation reactions. The results

Scheme 2. Synthesis of the Tetraglycine Derivatives 7[a]

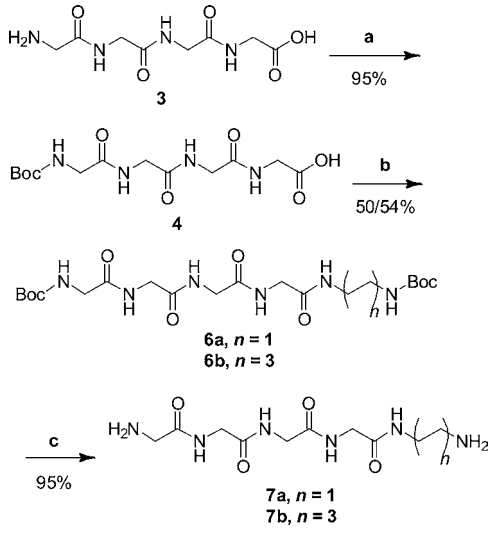

[a]Reaction conditions: **a**, Di-*t*-Boc, NaOH/H_2O/dioxane; **b**, (1) EDC, HOBt, (2) **5a**/**5b**, DIPEA, DMF; **c**, (1) TFA, DCM, (2) Amberlyst A-21, MeOH/DCM.

encouraged us to exploit the optimized two-step phosphoramidation reaction to synthesize POCs other than nucleic acid-**3** conjugates because typical peptides usually have more amino groups than **7a** and **7b**. However, before employing the optimized two-step phosphoramidation reactions for synthesis

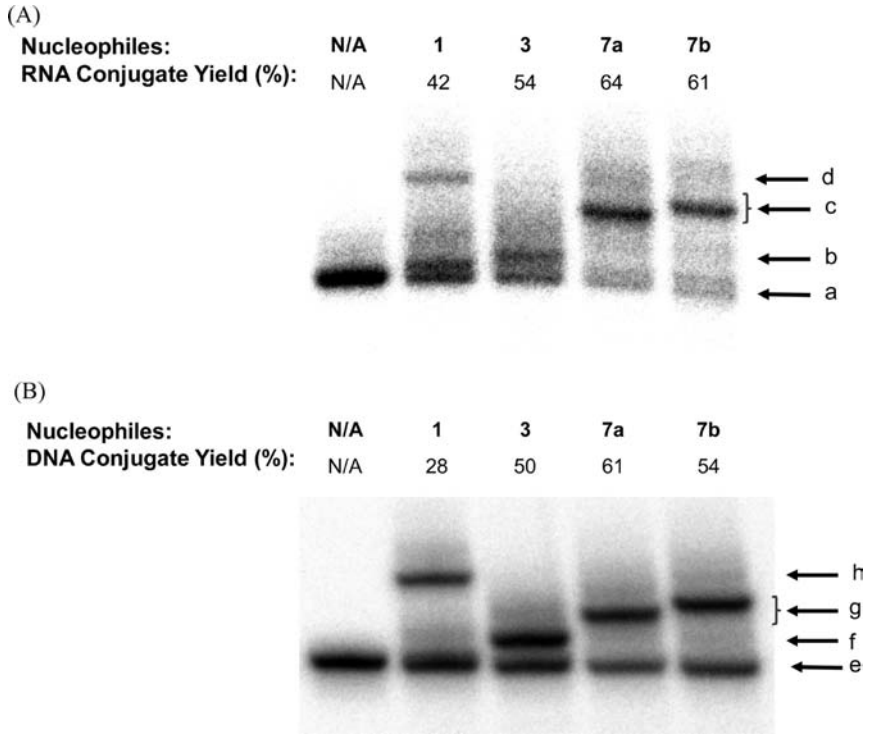

Figure 3. Phosphoramidation yield influenced by the nucleophilicity of nucleophiles when reacting with (A) the ^{32}P-labeled 17-mer TW17$_{1-17}$ RNA and (B) the ^{32}P-labeled single-stranded 3′ primer DNA. Each nucleophile (**1**, **3**, **7a**, or **7b**) was conjugated with the nucleic acids according to the two-step phosphoramidation reactions optimized in this study. The reaction products were purified by ethanol precipitation, analyzed by 20% urea-PAGE, visualized and quantified by an Amersham Typhoon PhosphorImager. **a**, unreacted TW17$_{1-17}$ RNA; **b**, TW17$_{1-17}$ RNA-**3** conjugate; **c**, TW17$_{1-17}$ RNA-**7a** (or **7b**) conjugate; **d**, TW17$_{1-17}$ RNA-**1** conjugate; **e**, unreacted 3′ primer DNA; **f**, 3′ primer DNA-**3** conjugate; **g**, 3′ primer DNA-**7a** (or **7b**) conjugate; **h**, 3′ primer DNA-**1** conjugate.

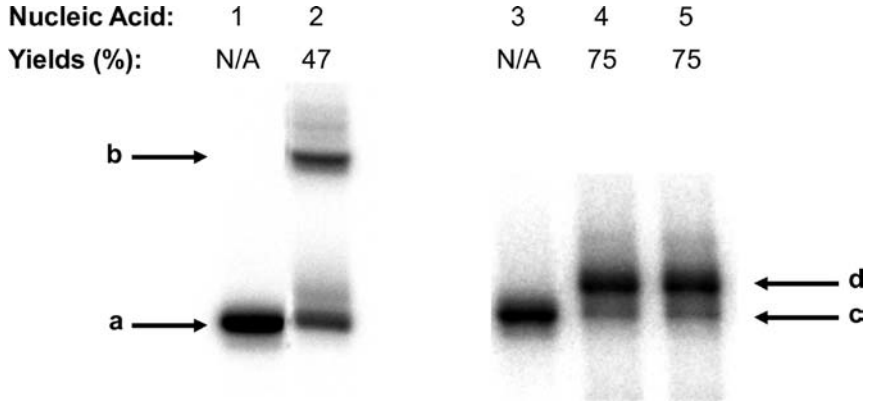

Figure 4. Autoradiogram of nucleic acids **1** (3′ primer DNA), **2** (two-step phosphoramidation reaction between the 3′ primer DNA and the Tat$_{48-57}$ peptide), **3** (TW17 RNA), **4** (two-step phosphoramidation reaction between the TW17 RNA and 200 mM of the Tat$_{48-57}$ peptide), and **5** (two-step phosphoramidation reaction between the TW17 RNA and 20 mM of the Tat$_{48-57}$ peptide) analyzed by 8% urea−PAGE for the TW17 RNA samples and 20% urea−PAGE for the 3′ primer DNA samples, visualized and quantified by an Amersham Typhoon PhosphorImager. The arrows indicate migrations of **a**, 3′ primer DNA; **b**, 3′ primer DNA−Tat$_{48-57}$ peptide conjugate; **c**, TW17 RNA; **d**, TW17 RNA−Tat$_{48-57}$ peptide conjugate.

of bioactive POCs, we desired to further increase POC yields by carrying out the reactions for DNA at higher temperatures.

Effects of Higher Temperatures on DNA Phosphoramidation Reactions. We previously concluded that RNA phosphoramidation reactions at 41 °C is the optimal reaction temperature because it balances reaction yield and RNA degradation at higher temperatures.[20] DNA, on the other hand, is far more chemically stable than RNA. Therefore, we investigated whether we could substantially improve yields of two-step DNA phosphoramidation reactions when performed above 41 °C (Figure S2). Indeed, we observed a steady increase of product yields when having two-step phosphoramidation reactions at temperatures higher than 45 °C. DNA in the two-step phosphoramidation reactions, however, suffered from significant degradation at reaction temperatures above 55 °C. We, therefore, determined that 55 °C was the optimal temperature for two-step DNA phosphoramidation reactions and was used subsequently.

POC Synthesis by the Optimized Two-Step Phosphoramidation Reactions Using the Zero Linker Approach. We first employed the developed two-step phosphoramidation reactions to directly conjugate nucleic acids with a well-studied

dx.doi.org/10.1021/bc300444y | *Bioconjugate Chem.* 2012, 23, 2417−2433

Table 1. Survey of Aqueous-Phase Two-Step Nucleic Acid Phosphoramidation Reactions for Identifying the Optimal Reaction Condition to Give the Best Reaction Yields and to Be Exploited for POC Synthesis[a]

DNA[b]/RNA[c,d]	co-solute	imidazole and derivatives	nucleophile	temperature (°C)	yield (%)
RNA[c]	N/A	imidazole	**1**	41	25%
RNA[c]	urea, 15% (w/v)	imidazole	**1**	41	18%
RNA[c]	Tween 20, 15% (w/v)	imidazole	**1**	41	30%
RNA[c]	Triton X-100, 15% (w/v)	imidazole	**1**	41	33%
RNA[c]	PEG 6000, 15% (w/v)	imidazole	**1**	41	32%
RNA[c]	PEG 8000, 15% (w/v)	imidazole	**1**	41	31%
RNA[c]	glycerol, 15% (w/v)	imidazole	**1**	41	30%
DNA[b]	N/A	imidazole	**1**	41	27%
DNA[b]	N/A	**2a**	**1**	41	21%
DNA[b]	N/A	**2b**	**1**	41	26%
DNA[b]	N/A	**2c**	**1**	41	18%
DNA[b]	N/A	**2d**	**1**	41	28%
DNA[b]	N/A	**2e**	**1**	41	26%
DNA[b]	N/A	**2f**	**1**	41	22%
RNA[c]	Triton X-100, 15% (w/v)	**2a**	**1**	41	36%
RNA[c]	Triton X-100, 15% (w/v)	**2b**	**1**	41	19%
RNA[c]	Triton X-100, 15% (w/v)	**2c**	**1**	41	15%
RNA[c]	Triton X-100, 15% (w/v)	**2d**	**1**	41	42%
RNA[c]	Triton X-100, 15% (w/v)	**2e**	**1**	41	30%
RNA[c]	Triton X-100, 15% (w/v)	**2f**	**1**	41	33%
RNA[c]	Triton X-100, 15% (w/v)	**2d**	**3**	41	**54%**
RNA[c]	Triton X-100, 15% (w/v)	**2d**	**7a**	41	**64%**
RNA[c]	Triton X-100, 15% (w/v)	**2d**	**7b**	41	**61%**
DNA[b]	N/A	**2d**	**3**	41	50%
DNA[b]	N/A	**2d**	**7a**	41	61%
DNA[b]	N/A	**2d**	**7b**	41	54%
DNA[b]	N/A	**2d**	**1**	45	31%
DNA[b]	N/A	**2d**	**1**	50	33%
DNA[b]	N/A	**2d**	**1**	55	**37%**
DNA[b]	N/A	**2d**	**1**	60	37%
DNA[b]	N/A	**2d**	Tat_{48-57} peptide	55	**47%**
RNA[c]	Triton X-100, 15% (w/v)	**2d**	Tat_{48-57} peptide	41	**75%**
DNA[b]	N/A	**2d**	cystamine	55	**72%**
RNA[c]	Triton X-100, 15% (w/v)	**2d**	cystamine	41	**60%**
DNA[b]	N/A	**2d**	cystamine, $C(KFF)_3K$ peptide[e]	55	**59%**
RNA[d]	Triton X-100, 15% (w/v)	**2d**	cystamine, the $C(KFF)_3K$ peptide[e]	41	**75%**

[a]It is noted that only the most important results from the co-solute effect study have been provided. The yields for the optimized two-step phosphoramidation reactions and for POC synthesis are bolded. [b]3′ primer DNA. [c]TW17 RNA. [d]$TW17_{1-17}$ RNA. [e]Conjugated to the nucleic acids by Michael addition.

CPP, the Tat_{48-57} peptide,[12,18] in the presence of no linking molecules between them, the zero linker approach. The Tat_{48-57} peptide was used to serve the purpose of a vector to traffic DNA into mammalian cells validated by subsequent biological analysis. The Tat_{48-57} peptide has 9 nucleophilic amino groups (3 primary amino and 6 secondary amino groups) in each molecule. Since increasing numbers of nucleophilic functionalities in nucleophiles was likely to enhance POC yields (Figure 3), we reasoned that using the Tat_{48-57} peptide as the nucleophile could decrease the molar ratios of nucleophiles to nucleic acids well below 585, the required ratio for **1** and **3** as the nucleophiles, while retaining similar reaction yields in the optimized two-step phosphoramidation reactions.

As expected, the optimized two-step phosphoramidation reactions by the zero linker approach only required 62.5 as ratio of Tat_{48-57} peptide to nucleic acids to achieve a 47% yield for the 3′ primer DNA−Tat_{48-57} peptide conjugate and a 75% yield for the TW 17 RNA−Tat_{48-57} peptide conjugate (Figure 4 and Table 1). Figure 4 also clearly indicates that only a nucleic acid molecule was covalently linked to the Tat_{48-57} peptide even though the Tat_{48-57} peptide has 9 nucleophilic functionalities for phosphoramidation reactions. In addition, multiple nucleophilic functionalities in the Tat_{48-57} peptide suggested that each amino group in the Tat_{48-57} peptide has the potential to engage in a phosphoramidation reaction to contribute to the observed POC in Figure 4. Interestingly, the product complexity did not seem to be an issue, because we observed significantly lower POC yields in the same phosphoramidation reactions when replacing the Tat_{48-57} peptide, which has glycine in the N-terminus, with the Tat_{47-57} peptide, which has tyrosine in the N-terminus (Figure S3). Similar preference for glycine in the N terminus was also observed when an *E. coli* CPP, the $(KFF)_3K$ peptide, and its derivatives were phosphoramidated with the 3′ primer DNA (Figure S3). These results implicated the N-terminus amino group in a peptide as the primary nucleophile in phosphoramidation reactions and its reactivity strongly affected by steric hindrance

dx.doi.org/10.1021/bc300444y | *Bioconjugate Chem.* 2012, 23, 2417−2433

imposed by the side chain of the N-terminus amino acid residue. The N-terminus glycine in a peptide emerges as the best nucleophile in phosphoramidation reactions because very limited steric hindrance would be enacted by the hydrogen atom, the side chain of glycine. The preference of glycine over other amino acids in the N-terminus of peptides for phosphoramidation-prepared POC formation is also consistent with the properties of **2d** [4(5)-methylimidazole)] to give the best phosphoramidation yield (Figure 2). Consequently, despite the presence of primary and secondary amino groups in typical peptides, the N-terminus amino group is clearly the best nucleophile to participate in nucleophilic substitution reactions with nucleic acid phosphorimidazolides. The N-terminus amino group of a peptide as the favorite nucleophile in nucleic acid phosphoramidation attains more specific reactions and produces relatively structurally uniform POC conjugates. Moreover, glycine in the N-terminus of peptides should be the choice for synthesis of phosphoramidation-prepared POCs because it has the least steric hindrance among amino acids.

We characterized the acquired POCs by MALDI-TOF MS to determine the molecular mass. We initially wondered whether the molecular mass of a phosphoramidation-prepared POC could be measured by more sensitive positive-mode MALDI-TOF MS. Adopting positive-mode MALDI-TOF MS required the use of acidic MALDI-TOF matrices, reported to be detrimental to phosphoramidate bonds in DNA during analysis and lead to DNA degradation.[27] Therefore, we performed a control experiment prior to positive-mode MALDI-TOF MS analysis by incubating the gel-purified 3′ primer DNA−Tat_{48-57} peptide conjugate in an acidic MALDI-TOF matrix solution composed of 2,3,4-trihydroxyacetophenone, 2,4,6-trihydroxyacetophenone, and ammonium citrate for 3 h. We were pleased to observe that the phosphoramidate bond linking the 3′ primer DNA and the Tat_{48-57} peptide was significantly inert in the MALDI-TOF matrix solution because only 5% of the phosphoramidation-prepared POC were hydrolyzed at the end of incubation (Figure S4).

The molecular mass of the 3′ DNA primer−Tat_{48-57} peptide conjugate was ultimately confirmed by MALDI-TOF MS ($[M+H]^+$ = 7416.096; Table 1 and Supporting Information). We, however, were not able to determine the molecular mass of the TW17 RNA−Tat_{48-57} peptide conjugate because the TW17 RNA was synthesized by in vitro transcription of T7 RNA polymerase to render a heterogeneous molecular mass of the RNA.[28] In addition, the size of the TW17 RNA−Tat_{48-57} peptide conjugate (~30 kD) prevents an accurate measurement of the molecular mass by MALDI-TOF MS.

Optimizing the Two-Step Phosphoramidation Reactions for Synthesis of POCs Containing the Cystamine-9 Linker. We synthesized POCs by using cystamine in two-step phosphoramidation reactions in order to introduce a cystamine-**9** linker in nucleic acids for subsequent peptide coupling reactions. The cystamine-**9** linker was harnessed for two purposes: (1) the disulfide linkage in cystamine potentially reduced in vivo to release oligonucleotides from POCs which could be essential for oligonucleotides to more specifically silence target genes in biological systems, and (2) the maleimide group in **9** to perform the more effective Michael addition reaction which would lower ratios of peptides to nucleic acids in POC synthesis. Reducing ratios of peptide to nucleic acids in synthesis of phosphoramidation-prepared POCs has important economic significance, as fewer peptides will be wasted during POC synthesis. We were thus motivated to pursue the cystamine-**9** linker strategy for more effective POC synthesis.

To achieve synthesis of the cystamine-**9** linker-included POCs, we decided to synthesize **9**, a *N*-maleoyl amino acid succinimidyl ester. In addition, we desired to develop a method for general synthesis of *N*-maleoyl amino acid succinimidyl esters for POC synthesis in the future. We succeeded in synthesizing **9** (Scheme 3) by adopting a reported procedure to

Scheme 3. Synthesis of the *N*-Maleoyl Amino Acid Succinimidyl Ester 9[a]

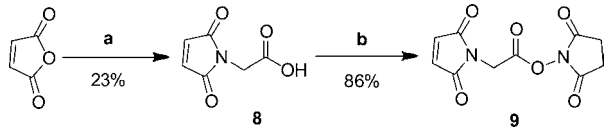

[a]Reaction conditions: **a**, (1) glycine, glacial AcOH, 16 h (2) reflux, 8 h; **b**, NHS, DCC, THF, 16 h.

acquire **8**[22] and following up a NHS ester formation reaction to give the desired **9** with good yield. We are improving the method for synthesis of **9** and developing a more universal approach to synthesize other useful *N*-maleoyl amino acid succinimidyl esters.

When applying **9** for POC synthesis, we soon realized the importance of optimizing the conjugation reactions involving both functionalities in **9**, i.e., acylation and Michael addition reactions to relieve the cost burden when purchasing peptides from commercial vendors. Therefore, we synthesized **11** and **13** (Scheme 4) as model compounds to optimize the reactions of **9**

Scheme 4. Synthesis of 13, a Thiol Derivative of Biotin[a]

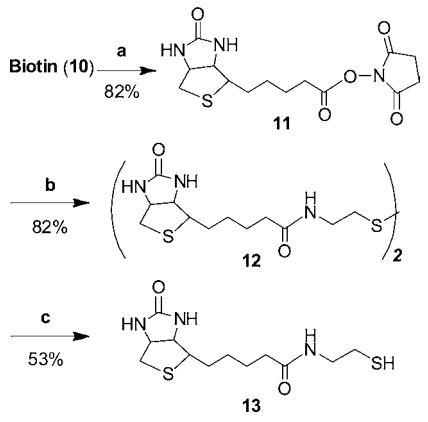

[a]Reaction conditions: **a**, NHS, DCC, pyridine, DMF, 24 h; **b**, cystamine, Et_3N, DMF/H_2O, 16 h; **c**, DTT, Et_3N, DMF, 3 h.

for more effective conjugation of nucleic acids with peptides. The reasons for using **11** and **13** to determine optimal reaction conditions of **9** for POC synthesis were that these compounds have appropriate functionalities to engage in one of the conjugation reactions. In addition, both compounds have biotin tags to separate reaction products from reactants by SAv gel shift assay[23] in case of an inability to separate nucleic acid samples by urea-PAGE. Synthesis of **11** was reported by us previously.[20] Starting from **11**, a facile acylation reaction successfully produced **12** (82%), which was subsequently reduced in the presence of DTT to give the desired **13** (53%).

dx.doi.org/10.1021/bc300444y | *Bioconjugate Chem.* 2012, 23, 2417−2433

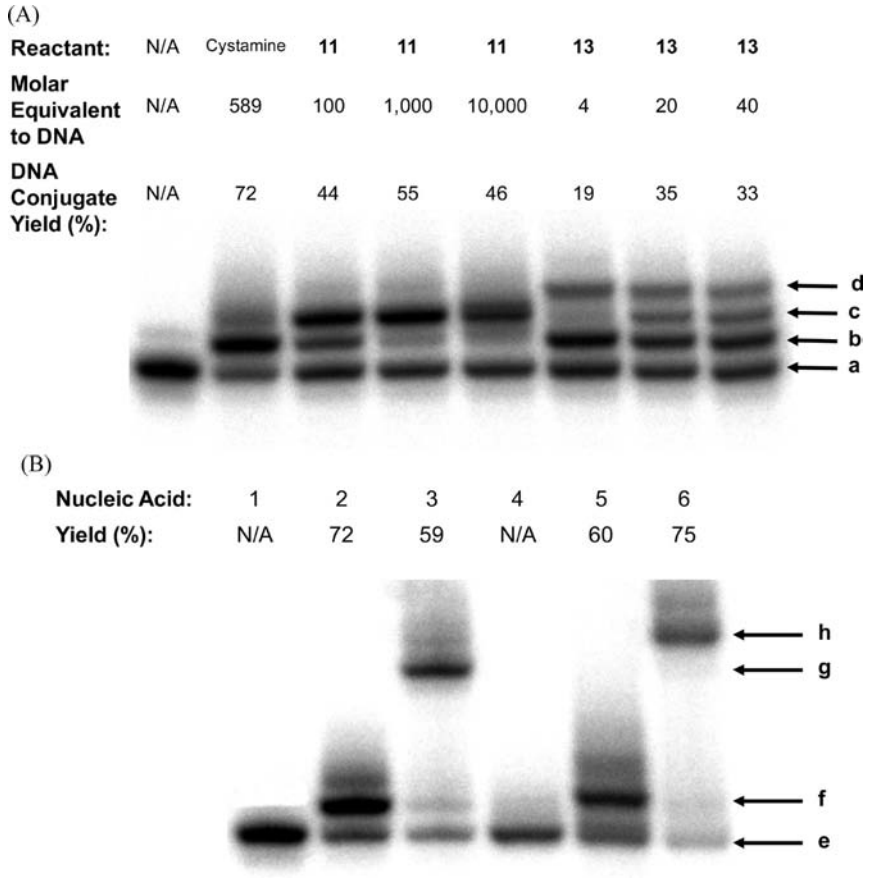

Figure 5. Optimization of the reactions involving AMAS (**9**) and synthesis of POCs in the presence of the cystamine-**9** linker. (A) The reactions of **9** were optimized by using **11** and **13**. The ^{32}P-labeled single-stranded 3′ primer DNA (**a**) was first coupled with cystamine to acquire the DNA−cystamine conjugate (Chart S1; Supporting Information) (**b**). The DNA−cystamine conjugate was subsequently reacted with various molar equivalents of **11** to determine the appropriate molar equivalent able to give the best yield of the DNA−cystamine−**11** conjugate (Chart S1; Supporting Information) (**c**). A molar equivalent of 1000 was adopted to react the DNA−cystamine conjugate with **9** to yield the DNA−cystamine−**9** conjugate (Chart S1; Supporting Information) (**c**), which was later coupled with various molar equivalents of **13**. It was determined that the molar equivalent of 20 was sufficient to have the best yield of the DNA−cystamine−**9**−**13** conjugate (Chart S1; Supporting Information) (**d**). Each reaction product was purified by ethanol precipitation, analyzed by 20% urea−PAGE, visualized, and quantified by an Amersham Typhoon PhosphorImager. **a**, the unreacted 3′ primer DNA; **b**, the 3′ primer DNA−cystamine conjugate; **c**, the 3′ primer DNA-cystamine-**11** (or -**9**) conjugate; **d**, the 3′ primer DNA-**9**-**13** conjugate. (B) The cystamine-**9** linker-prepared POCs were synthesized by the optimized reaction conditions developed in Figure 5A. The nucleic acids in the autoradiogram contains **1** (the 3′ primer DNA), **2** (the cystamine-modified 3′ primer DNA preparation reaction), **3** (the 3′ primer DNA-C$(KFF)_3$K peptide conjugate preparation reaction), **4** (the 17-mer $TW17_{1-17}$ RNA), **5** (the cystamine-modified $TW17_{1-17}$ RNA preparation reaction), and **6** (the $TW17_{1-17}$ RNA−C$(KFF)_3$K peptide conjugate preparation reaction). The arrows indicate migrations of **e**, the 3′ primer DNA or $TW17_{1-17}$ RNA; **f**, the cystamine-modified oligonucleotides; **g**, the 3′ primer DNA−C$(KFF)_3$K peptide conjugate; **h**, the $TW17_{1-17}$ RNA−C$(KFF)_3$K peptide conjugate.

We first used **11** to optimize the acylation reaction between the cystamine-modified 3′ primer DNA and **9**. The 3′ primer DNA was initially conjugated with cystamine according to the optimized two-step phosphoramidation reaction reported in this study with a yield of 72% (Figure 5A and Table 1). When reacting the cystamine-modified 3′ primer DNA with **11**, we were delighted to observe that the ^{32}P-labeled 3′ primer DNA and its structure-modified derivatives were well separated in urea-PAGE so that the potentially ambiguous SAv gel shift assay was not required. Moreover, the results from the reactions of cystamine-modified 3′ primer DNA with various concentrations of **11** clearly indicated that a value of 1000 for the molar ratio of **11** to the 3′ primer DNA gave the best yield for the acylation reaction and was adopted for the similar reaction between the cystamine-modified 3′ primer DNA and **9**. The acquired **9**-cystamine-modified 3′ primer DNA was employed to react with a series of **13** concentrations and to identify the appropriate molar ratio of **13** to nucleic acids for attaining the best yield in the Michael addition reaction (Figure 5A). A value of 20 for the molar ratio of **13** to the **9**-cystamine-modified 3′ primer DNA was sufficient to provide the best yield for the studied Michael addition reaction and was determined to be the optimal condition for POC synthesis.

The optimized reactions for **9** were successfully applied to conjugating nucleic acids with the C$(KFF)_3$K peptide, the derivative of a previously reported synthetic CPP $(KFF)_3$K peptide,[17] to obtain the corresponding POCs with excellent yields (59−75%; Figure 5B and Table 1). It is noted that we used a shorter version of TW17 RNA, $TW17_{1-17}$ RNA, in order to measure the molecular mass of the desired RNA POC, $TW17_{1-17}$ RNA−C$(KFF)_3$K peptide conjugate, subsequently by MALDI-TOF MS. As expected, the identity of each synthesized POCs was successfully characterized by MALDI-TOF MS to determine the molecular mass (Table 1 and

Supporting Information). The two-step phosphoramidation reactions for POC synthesis in the presence of the cystamine-**9** linker demonstrated advantages over POC synthesis by the phosphoramidation reactions performed with the zero linker approach. The incorporation of the cystamine-**9** linker in POC synthesis offers both higher reaction yields (Figures 4 and 5B) and a lower demand for peptides in POC synthesis (20 as the molar ratio of peptide to oligonucleotide in this reaction) than the zero linker strategy for POC synthesis. We expect that the use of linkers similar to the cystamine-**9** bridge will have more leverage for future POC synthesis.

Cytotoxicity of Phosphoramidation-Prepared POCs to a Human Cell Line. We understood that the phosphoramidate linkage has to exhibit low to no toxicity to human beings before phosphoramidation-prepared POCs would be administrated in clinical applications. Therefore, we exploited the two-step phosphoramidation reactions using the zero linker approach to synthesize more of the POC, the 3′ primer DNA−Tat_{48-57} peptide conjugate (Figure 4), and to study toxicity of the POC to human A549 cells. We chose the zero linker approach rather than using the cystamine-**9** linker strategy to synthesize POC for the toxicity study because we want to focus only on the toxic effects of the introduced phosphoramidate bond in the 3′ primer DNA−Tat_{48-57} peptide conjugate. We were satisfied to find that the inoculated 3′ primer DNA−Tat_{48-57} peptide conjugate with concentrations up to 10 μM showed no toxicity to human A549 cells after 24 h inoculation (Figure 6).

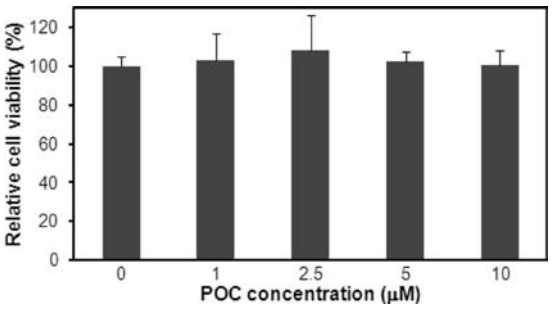

Figure 6. Undetectable cytotoxicity of phosphoramidation-prepared POCs to human A549 cells after 24 h inoculation. Human A549 cells were incubated with increased concentrations of the phosphoramidation-prepared POC, the 3′ primer DNA−Tat_{48-57} peptide conjugate (0−10 μM). After 24 h inoculation, cell viability for each sample containing a specified POC concentration was determined by the MTT assay.

Therefore, there is no detectable toxicity of phosphoramidate linkages in POCs to human cells in these studied concentrations after 24 h inoculation, and we validated the potentially safe use of phosphoramidation-prepared POC as therapeutic agents for treating human diseases.

Uptake of Phosphoramidation-Prepared POCs by a Human Cell Line. We had already shown that phosphoramidate bonds in POCs had no toxicity to human A549 cells after 24 h inoculation (Figure 6). The potential evidence of human safety of phosphoramidate linkages in POCs encouraged us to carry out additional studies to explicate effects of phosphoramidate bonds on the cellular permeability ability of CPPs in phosphoramidation-prepared POCs. We again used the 3′ primer DNA−Tat_{48-57} peptide conjugate as the model POC to study the uptake of POCs by human A549 cells. To unambiguously demonstrate uptake of the 3′ primer DNA by human A549 cells, we labeled the 3′ primer DNA with the fluorophore FITC by a depurination method[25] before the DNA was conjugated with the Tat_{48-57} peptide by the two-step phosphoramidation reaction developed in this study. Acquisition of the FITC-labeled 3′ primer DNA−Tat_{48-57} peptide conjugate allowed us to study permeability of the POC into human A549 cells by flow cytometry, fluorescent microscopy, and confocal laser scanning microscopy.

The results from flow cytometry analysis clearly showed that the FITC-labeled 3′ primer DNA−Tat_{48-57} peptide conjugate was significantly taken up by human A549 cells after 24 h inoculation of the POC (Figure 7). In addition, the association of the FITC-labeled 3′ primer DNA−Tat_{48-57} peptide conjugate with A549 cells was revealed by fluorescent microscopy studies which indicated colocalization of fluorescence signals with intact A549 cells (Figure S5). Finally, we performed confocal laser scanning microscopy to determine whether the observed fluorescence signals were contributed by the FITC-labeled 3′ primer DNA−Tat_{48-57} peptide conjugate trafficked inside A549 cells or by the FITC-labeled POC adsorbed on the cell membrane. Consistent with our expectation, the results from the confocal laser scanning microscopy study unequivocally demonstrated that the FITC-labeled 3′ primer DNA−Tat_{48-57} peptide conjugate was taken up by A549 cells rather than merely adsorbed on the cell membrane after 24 h inoculation (Figure 7). The results of these biological uptake studies support the premise that a phosphoramidate bond does not alter cellular permeability activity of CPPs in phosphoramidation-prepared POCs and would not have a negative impact on cellular delivery and targeting of phosphoramidation-prepared POCs when administrated as therapeutic agents in the clinic.

■ DISCUSSION

We have significantly improved reaction yields of two-step nucleic acid phosphoramidation by studying the contribution of three crucial factors, co-solute effect, imidazole nucleophilicity and structure, and the advantage of multiple nucleophilic functionalities in nucleophiles (Figures 1−3, Scheme 1, and Table 1). Moreover, we successfully employed the zero linker strategy of the optimized two-step phosphoramidation reactions to effectively conjugate a well-studied CPP TAT_{48-57} peptide with DNA or RNA with corresponding POC yields of 47−75% (Figure 4, Table 1, and Scheme 5). We also developed a more effective phosphoramidation method for DNA/RNA POC synthesis by exploiting a cystamine-**9** linker to acquire corresponding POC yields of 59−75% (Figure 5, Table 1, and Scheme 5). The phosphoramidation-synthesized DNA POC, 3′ primer DNA−Tat_{48-57} peptide conjugate, showed no cytotoxicity to human A549 cells at POC concentrations up to 10 μM after 24 h inoculation and established the potentially safe use of phosphoramidation-synthesized POCs in clinical applications (Figure 6). In addition, the FITC-labeled 3′ primer DNA−Tat_{48-57} peptide conjugate was successfully trafficked into the human A549 cell line as demonstrated by studies of flow cytometry, fluorescent microscopy, and confocal laser scanning microscopy (Figures 7 and S5). These results provide evidence that the presence of phosphoramidate bonds in CPP-containing POCs will not impair the cell permeability of CPPs in POCs and suggests the potential development of target-delivered therapeutic reagents based on nucleic acid phosphoramidation reactions. The current study corroborates the assertion that the advanced

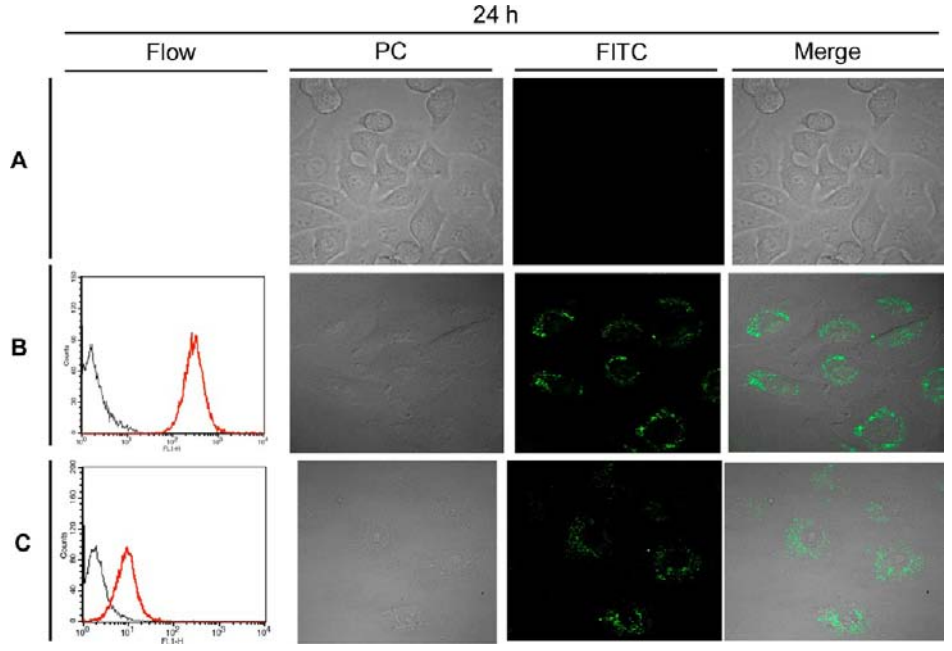

Figure 7. Uptake of phosphoramidation-prepared POCs by human A549 cells. Human A549 cells were inoculated with 5 μM of the FITC-labeled Tat_{48-57} peptide or the phosphoramidation-prepared POC, the FITC-labeled 3′ primer DNA−Tat_{48-57} peptide conjugate, for 24 h and followed by analysis with flow cytometry and confocal laser scanning microscopy. For flow cytometry, cells were washed and harvested with trypsin/EDTA before analysis. A549 cells for the confocal laser scanning microscopy study were washed three times with PBS and analyzed immediately. The studied A549 cell samples included: **A**, cells not treated with either the Tat_{48-57} peptide or the 3′ primer DNA−Tat_{48-57} peptide conjugate; **B**, cells incubated with the FITC-labeled Tat_{48-57} peptide for 24 h; **C**, cells incubated with the FITC-labeled 3′ primer DNA−Tat_{48-57} peptide conjugate for 24 h. PC, phase contrast.

Scheme 5. Optimized Aqueous-Phase Two-Step Phosphoramidation Reactions for POC Synthesis

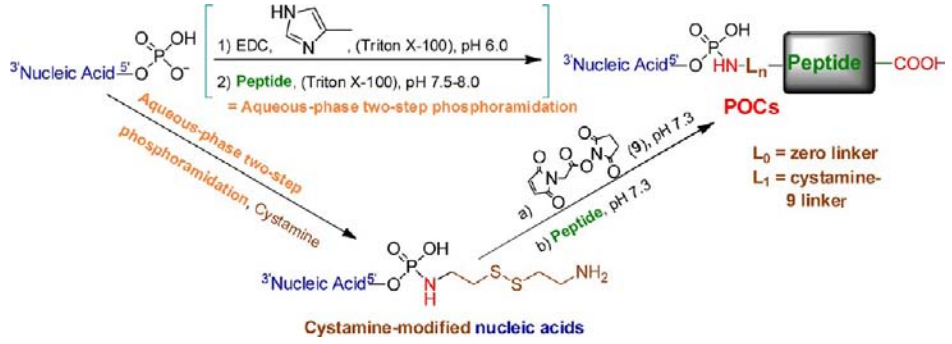

aqueous-phase two-step phosphoramidation reactions are an efficient and effective approach to synthesize bioactive POCs.

The use of urea and other co-solutes in phosphoramidation reactions deserves additional discussion to explicate their roles. The current study clearly demonstrates that urea could not carry out its expected function of denaturing nucleic acids to confer higher product yields for phosphoramidation reactions. Instead, urea caused reduction of reaction yield because of direct participation of urea in nucleophilic substitution preventing the desired product formation (Figure 1).[20] We had reached a similar conclusion on DNA phosphoramidation reactions but had observed the beneficial presence of urea in RNA phosphoramidation reactions previously.[20] The discrepancy of the effect of urea in RNA phosphoramidation reactions is attributed to the shortcomings of the SAv gel shift assay used in the previous study. A standard SAv gel shift assay relies on strong interaction between biotin and SAv to separate biotin-tagged from non-biotin-tagged biomacromolecules. Unfortunately, in previously studied nucleic acid phosphoramidation reactions, SAv-retarded nucleic acids co-migrated with polymerized nucleic acids, byproducts of the phosphoramidation reactions,[29] and were indistinguishable in the standard SAv gel shift assay. The co-migration resulted in an overestimation of the desired RNA reaction products (Ko and Wang, unpublished results). We had carefully optimized the concentrations and ratios of EDC to nucleic acids to significantly suppress the unwanted polymerization of nucleic acids (less than 5%) in not only the two-step phosphoramidation reactions reported in this study, but also the one-step phosphoramidation versions (Wang et al., manuscript in preparation). The more accurate determination of the phosphoramidation reaction yield was attained by analysis of urea-PAGE, which depends solely on the size and the charge of nucleic acids to achieve separation and unambiguously resolved the molecular difference of reactants and phosphoramidation products, resulting in more faithful calculations of product formation. Therefore, urea-PAGE was a major analytical method employed in the current study. Consequently, inclusion of urea as co-solute in any nucleic

acid phosphoramidation reactions should be avoided, as urea has a negative impact on the reactions by reducing the yield of the desired product. On the contrary, more inert and hydroxyl group-based co-solutes such as Triton X-100 will perform the anticipated function of RNA denaturation and deliver higher product yield in phosphoramidation reactions (Figure 1A).

In addition to the effects of co-solutes in phosphoramidation reactions, the chemoselectivity of nucleic acids toward specific primary amino groups of peptides in the zero linker approach of the phosphoramidation reactions is significant (Figure S3). Specifically, we observed that nucleic acids in zero-linker two-step phosphoramidation reactions primarily reacted with the α-amino group in N-terminus glycine residue of a peptide and only one nucleic acid was conjugated to each peptide molecule. This phenomenon came as a pleasant surprise, as we were initially concerned about the multiple nucleophilic functionalities in a typical peptide and their potential to engage in phosphoramidation reactions. We anticipated that it would be unlikely to have specific phosphoramidation reactions for controllable POC synthesis and expected undesirable complicated structures of POC products which might impede the use of phosphoramidation reactions for synthesis of POCs as therapeutic agents or scientific tools. Therefore, it was very exciting to find that the phosphorimidazolide intermediates of nucleic acids had chemoselectivity and preferred to react with the N-terminal α-amino group and with glycine in the N-terminus of a peptide.

The chemoselective property of the phosphoramidation reactions between nucleic acids and peptides is intriguing because the basicity of the primary amino group in the side chain of lysine (pK_a = 10.54),[30] which is one of the major components in the peptides in this study, is higher than that of the α-amino group in glycine (pK_a = 9.78).[30] When considering the basicity and nucleophilicity of the primary amino groups in glycine and lysine, we would predict that the phosphorimidazolide intermediates of nucleic acids are more likely to react with the ε-amino group of lysine than with the α-amino group of glycine in these peptides. In addition, multiple primary amino groups in the peptides would also implicate that conjugations of nucleic acids with a peptide by zero-linker two-step phosphoramidation reactions should produce complicated structural variations of POC products because of the likelihood of multiple nucleic acid conjugations with each peptide.

Fortunately, the ε-amino groups of lysine in the peptides did not demonstrate appreciably reactivity with the phosphorimidazolide intermediates of nucleic acids, and each peptide was only conjugated with one molecule of nucleic acid (Figure 4). We speculate that the ε-amino groups of lysine in the peptides might have been buried in the interior of three-dimensional peptide structures and were unavailable for phosphoramidation reactions. NMR analysis and computational studies of these peptide structures in water are required to provide essential information on the steric environments of these primary amino groups in the peptides and their relationship to the chemoselectivity of nucleic acid phosphoramidation reactions.

The achievement of only one nucleic acid unit conjugated with each peptide molecule in zero-linker two-step phosphoramidation reactions provided relatively uniform and predictable POC structures and could be explained by a strong electrostatic attraction between nucleic acids and peptides. Nucleic acids are well-known polyelectrolytes laden with negatively charged phosphate groups at a physiological pH. On the other hand, the CPPs studied here all have ample lysine or lysine and arginine residues in their structures to contribute high positive charge density in the peptides at neutral pH. Consequently, when the α-amino group in the N-terminal glycine of a CPP underwent a phosphoramidation reaction with a nucleic acid, the phosphoramidate bond brought these oppositely charged components in close proximity to enact strong electrostatic forces between the CPP and the nucleic acid. Extensive electrostatic forces from CPP−nucleic acid interactions would immediately shield other primary amino groups in the CPP from having further phosphoramidation reactions and attain a single nucleic acid conjugation in each CPP. In fact, the electrostatic attractive forces between nucleic acids and CPPs were so strong that even boiling the nucleic acid−CPP complexes for minutes in the presence of 8 M urea did not completely remove CPPs from nucleic acids as revealed by standard urea-PAGE (Su and Wang, unpublished results). Moreover, the sizes of nucleic acids (6037 amu for the 3′ primer DNA, 5440 amu for the $TW17_{1-17}$ RNA, and ∼28 000 amu for the TW17 RNA) are far larger than those of CPPs (1396 amu for the Tat_{48-57} peptide and 1517 amu for the $C(KFF)_3K$ peptide) so that a nucleic acid molecule could adsorb and exclude each CPP from contacting a second nucleic acid. Similarly, strong electrostatic attraction between the Tat_{48-57} peptide and nucleic acids could play a prominent role to enhance POC formation observed in Figure 4.

Using a nucleic acid-CPP bridge similar to the cystamine-**9** linker further alleviates the potential complexity problem of POC products synthesized by phosphoramidation reactions. The use of molecular bridges such as the cystamine-**9** linker for POCs synthesized by phosphoramidation reactions took advantage of a more defined conjugation reaction between nucleic acids and CPPs, which was achieved by the more specific Michael addition reaction between the thiol group in CPPs and the maleimide moiety in phosphoramidation-modified nucleic acids. Maleimides have specific reactivity for thiol groups in the pH range 6.5−7.5.[31] The other benefit of introducing molecular bridges analogous to the cystamine-**9** linker is a significantly reduced requirement for the amount of CPP for effective POC synthesis (Figure 5B), which again could be attributed to effectiveness of the Michael addition reaction. The outstanding properties of Michael addition to convey more effective and chemospecific reactions and to deliver more structure-defined POC products justify the preferred choice of adopting the maleimide-containing bridges for POCs synthesized by aqueous-phase two-step phosphoramidation reactions.

In summary, this study significantly improved the aqueous-phase two-step phosphoramidation reactions and demonstrated the potential of either zero linker or linkers containing maleimide moieties of phosphoramidation reactions for effective and efficient POC synthesis. In addition, chemoselectivity of the advanced two-step nucleic acid phosphoramidation reactions supports the synthesis of POCs with expected structures, which is essential to evaluating POC functions in clinical applications. Furthermore, the versatility of phosphoramidation reactions enables us to append diverse functional groups to nucleic acids for subsequent reactions and further facilitate POC synthesis. Finally, the advanced nucleic acid phosphoramidation reaction is not restricted to POC synthesis for acquiring nucleic acid-based therapeutic agents useful in clinic. It can be exploited to conjugate nucleic acids with various tag molecules invaluable in research. For example,

we had developed a facile and low-cost universal fluorescent labeling method for DNA and RNA based on the advanced two-step phosphoramidation reaction (Wang et al., manuscript in preparation). We expect broader applications of nucleic acid phosphoramidation reactions in research and in clinic in the future.

■ ASSOCIATED CONTENT

Supporting Information

Full details of supporting figures, scheme and chart referenced in the text, NMR and MS spectra for new compounds (**4**, **6a**, **6b**, **7a**, **7b**, **9**, **12**, and **13**) and MALDI-TOF spectra for three POCs. This material is available free of charge via the Internet at http://pubs.acs.org.

■ AUTHOR INFORMATION

Corresponding Author

*Department of Medicinal and Applied Chemistry, Kaohsiung Medical University, Kaohsiung, 80708, Taiwan; E-mail: tzupinw@cc.kmu.edu.tw; Tel: +886-07-312-1101, ext. 2756; Fax: +886-07-312-5339 (T.-P. Wang). School of Medicine, Graduate Institute of Medicine, College of Medicine, Kaohsiung Medical University, Kaohsiung, 80708, Taiwan; Division of Infectious Diseases, Department of Internal Medicine, Kaohsiung Medical University Hospital, Kaohsiung Medical University, Kaohsiung, 80708, Taiwan; E-mail: infchen@gmail.com (Y.-H. Chen).

Notes

The authors declare no competing financial interest.

■ ACKNOWLEDGMENTS

We thank Dr. Susan Fetzer for critical reading of the manuscript. We also thank Drs. Shih-Shin Liang and Chi-Yu Lu for providing expertise in MALDI-TOF MS analysis. This work was supported with grants from the National Science Council of Taiwan awarded to T.-P. W. (99-2113-M-037-008- and 100-2113-M-037-008-). M. H. W. is supported by the undergraduate research program funded by National Science Council of Taiwan (101CFD2100044).

■ ABBREVIATIONS

POCs, peptide−oligonucleotide conjugates; Tat_{48-57} peptide, amino acid residues 48 to 57 of the HIV Tat protein; siRNA, small interference RNA; miRNA, microRNA; CPPs, cell-penetrating peptides; CTPs, cell-targeting peptides; urea-PAGE, urea polyacrylamide gel electrophoresis; SAv, streptavidin; HOBt, 1-hydroxybenzotriazole; DIPEA, *N*,*N*-diisopropylethylamine; EDC, 1-ethyl-3-(3-dimethylaminopropyl)-carbodiimide; TFA, trifluoroacetic acid; AMAS, *N*-(α-maleimidoacetoxy) succinimide ester; NHS, *N*-hydroxysuccinimide; DCC, *N*,*N*′-dicyclohexylcarbodiimide; Et_3N, triethylamine; DTT, DL-dithiothreitol; EPPS, 3-[4-(2-hydroxyethyl)-1-piperazinyl]propanesulfonic acid; DEPC, diethylpyrocarbonate; MTT, methylthiazoletetrazolium; FITC, fluorescein isothiocyanate; PBS, phosphate buffer saline; DMAP, 4-dimethylaminopyridine.

■ REFERENCES

(1) Bennett, C. F., and Swayze, E. E. (2010) RNA targeting therapeutics: molecular mechanisms of antisense oligonucleotides as a therapeutic platform. *Annu. Rev. Pharmacol. Toxicol. 50*, 259−293.

(2) Douglas, S. M., Bachelet, I., and Church, G. M. (2012) A logic-gated nanorobot for targeted transport of molecular payloads. *Science 335*, 831−834.

(3) Juliano, R., Bauman, J., Kang, H., and Ming, X. (2009) Biological barriers to therapy with antisense and siRNA oligonucleotides. *Mol. Pharmaceutics 6*, 686−695.

(4) Whitehead, K. A., Langer, R., and Anderson, D. G. (2009) Knocking down barriers: advances in siRNA delivery. *Nat. Rev. Drug Discovery 8*, 129−138.

(5) Watts, J. K., and Corey, D. R. (2012) Silencing disease genes in the laboratory and the clinic. *J. Pathol. 226*, 365−379.

(6) Burnett, J. C., and Rossi, J. J. (2012) RNA-based therapeutics: current progress and future prospects. *Chem. Biol. 19*, 60−71.

(7) Juliano, R. L., Ming, X., and Nakagawa, O. (2012) The chemistry and biology of oligonucleotide conjugates. *Acc. Chem. Res. 45*, 1067−1076.

(8) Ivanova, G. D., Arzumanov, A., Abes, R., Yin, H., Wood, M. J. A., Lebleu, B., and Gait, M. J. (2008) Improved cell-penetrating peptide-PNA conjugates for splicing redirection in HeLa cells and exon skipping in mdx mouse muscle. *Nucleic Acids Res. 36*, 6418−6428.

(9) Ming, X., Alam, M. R., Fisher, M., Yan, Y., Chen, X., and Juliano, R. L. (2010) Intracellular delivery of an antisense oligonucleotide via endocytosis of a G protein-coupled receptor. *Nucleic Acids Res. 38*, 6567−6576.

(10) Nakagawa, O., Ming, X., Huang, L., and Juliano, R. L. (2010) Targeted intracellular delivery of antisense oligonucleotides via conjugation with small-molecule ligands. *J. Am. Chem. Soc. 132*, 8848−8849.

(11) Said Hassane, F., Saleh, A., Abes, R., Gait, M., and Lebleu, B. (2010) Cell penetrating peptides: overview and applications to the delivery of oligonucleotides. *Cell. Mol. Life Sci. 67*, 715−726.

(12) Vives, E., Schmidt, J., and Pelegrin, A. (2008) Cell-penetrating and cell-targeting peptides in drug delivery. *Biochim. Biophys. Acta 1786*, 126−138.

(13) Derossi, D., Calvet, S., Trembleau, A., Brunissen, A., Chassaing, G., and Prochiantz, A. (1996) Cell internalization of the third helix of the antennapedia homeodomain is receptor-independent. *J. Biol. Chem. 271*, 18188−18193.

(14) Good, L., Awasthi, S. K., Dryselius, R., Larsson, O., and Nielsen, P. E. (2001) Bactericidal antisense effects of peptide-PNA conjugates. *Nat. Biotechnol. 19*, 360−364.

(15) Jha, D., Mishra, R., Gottschalk, S., Wiesmüller, K.-H., Ugurbil, K., Maier, M. E., and Engelmann, J. (2011) CyLoP-1: A novel cysteine-rich cell-penetrating peptide for cytosolic delivery of cargoes. *Bioconjugate Chem. 22*, 319−328.

(16) Saleh, A. F., Arzumanov, A., Abes, R., Owen, D., Lebleu, B., and Gait, M. J. (2010) Synthesis and splice-redirecting activity of branched, arginine-rich peptide dendrimer conjugates of peptide nucleic acid oligonucleotides. *Bioconjugate Chem. 21*, 1902−1911.

(17) Vaara, M., and Porro, M. (1996) Group of peptides that act synergistically with hydrophobic antibiotics against gram-negative enteric bacteria. *Antimicrob. Agents Chemother. 40*, 1801−1805.

(18) Vivès, E., Brodin, P., and Lebleu, B. (1997) A truncated HIV-1 Tat protein basic domain rapidly translocates through the plasma membrane and accumulates in the cell nucleus. *J. Biol. Chem. 272*, 16010−16017.

(19) Lu, K., Duan, Q.-P., Ma, L., and Zhao, D.-X. (2010) Chemical strategies for the synthesis of peptide-oligonucleotide conjugates. *Bioconjugate Chem. 21*, 187−202.

(20) Wang, T.-P., Chiou, Y.-J., Chen, Y., Wang, E.-C., Hwang, L.-C., Chen, B.-H., Chen, Y.-H., and Ko, C.-H. (2010) Versatile phosphoramidation reactions for nucleic acid conjugations with peptides, proteins, chromophores, and biotin derivatives. *Bioconjugate Chem. 21*, 1642−1655.

(21) Boger, D. L., Zhou, J., Winter, B., and Kitos, P. A. (1995) Key analogs of the tetrapeptide subunit of RA-VII and deoxybouvardin. *Bioorg. Med. Chem. 3*, 1579−1593.

(22) Allen, V. C., Robertson, C. C., Turega, S. M., and Philp, D. (2010) A simple network of synthetic replicators can perform the logical OR operation. *Org. Lett. 12*, 1920−1923.
(23) Wang, T.-P., Su, Y.-C., Chen, Y., Liou, Y.-M., Lin, K.-L., Wang, E.-C., Hwang, L.-C., Wang, Y.-M., and Chen, Y.-H. (2012) In vitro selection and characterization of a novel Zn(II)-dependent phosphorothiolate thiolesterase ribozyme. *Biochemistry 51*, 496−510.
(24) Lin, C.-M., Chiu, J.-H., Wu, I. H., Wang, B.-W., Pan, C.-M., and Chen, Y.-H. (2010) Ferulic acid augments angiogenesis via VEGF, PDGF and HIF-1α. *J. Nutr. Biochem. 21*, 627−633.
(25) Proudnikov, D., and Mirzabekov, A. (1996) Chemical methods of DNA and RNA fluorescent labeling. *Nucleic Acids Res. 24*, 4535−4542.
(26) Grauer, A., Riechers, A., Ritter, S., and König, B. (2008) Synthetic receptors for the differentiation of phosphorylated peptides with nanomolar affinities. *Chem.—Eur. J. 14*, 8922−8927.
(27) Shchepinov, M. S., Denissenko, M. F., Smylie, K. J., Wörl, R. J., Leppin, A. L., Cantor, C. R., and Rodi, C. P. (2001) Matrix-induced fragmentation of P3′-N5′ phosphoramidate-containing DNA: high-throughput MALDI-TOF analysis of genomic sequence polymorphisms. *Nucleic Acids Res. 29*, 3864−3872.
(28) Milligan, J. F., Groebe, D. R., Witherell, G. W., and Uhlenbeck, O. C. (1987) Oligoribonucleotide synthesis using T7 RNA polymerase and synthetic DNA templates. *Nucleic Acids Res. 15*, 8783−8798.
(29) Ho, N. W. Y., Duncan, R. E., and Gilham, P. T. (1981) Esterification of terminal phosphate groups in nucleic acids with sorbitol and its application to the isolation of terminal polynucleotide fragments. *Biochemistry 20*, 64−67.
(30) Dawson, R. M. C., Elliott, D. C., Elliott, W. H., and Jones, K. M. (1986) *Data for Biochemical Research*, 3rd ed.; Oxford Science Publication.
(31) Hermanson, G. T. (1996) *Bioconjugate techniques*, Academic Press, San Diego, USA.

Supporting Information

Advanced aqueous-phase phosphoramidation reactions for effectively synthesizing peptide-oligonucleotide conjugates trafficked into a human cell line

Tzu-Pin Wang[*, †], Ni Chien Ko[†], Yu-Chih Su[†], Eng-Chi Wang[†], Scott Severance[§], Chi-Ching Hwang[⊥], Ying Ting Shih[‡], Min Hui Wu[†] and Yen-Hsu Chen[*, ‡, ǁ]

Running title: Effective synthesis of bioactive peptide-oligonucleotide conjugates by phosphoramidation reactions

*Corresponding author: tzupinw@cc.kmu.edu.tw (T.-P. Wang); infchen@gmail.com (Y.-H. Chen)

*Contact address: Department of Medicinal and Applied Chemistry, Kaohsiung Medical University, Kaohsiung, 80708, Taiwan (T.-P. Wang); School of Medicine, Graduate Institute of Medicine, College of Medicine, Kaohsiung Medical University, Kaohsiung, 80708, Taiwan; Division of Infectious Diseases, Department of Internal Medicine, Kaohsiung Medical University Hospital, Kaohsiung Medical University, Kaohsiung, 80708, Taiwan (Y.-H. Chen)

Contents

1. Scheme S1 …….. S2
2. Figures S1-S5 ..... S3-S6
2. Chart S1 ……..… S7
3. ^{1}H and ^{13}C NMR, and HRMS Spectra of New Compounds..... S8-S32
4. MALDI-TOF Spectra of three POCs S33-S35

(A)

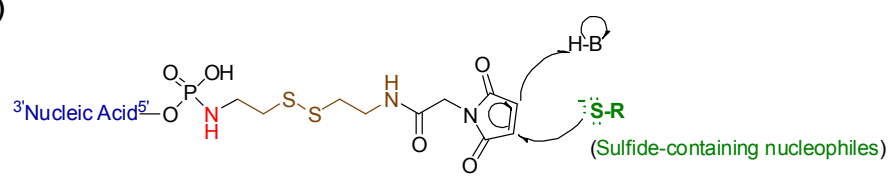

Nucleic acid-cystamine-9 conjugate

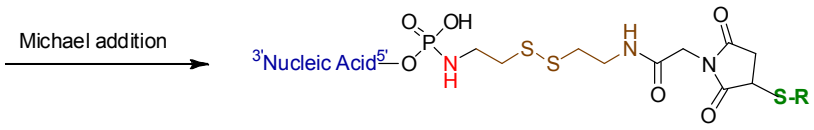

Michael addition adduct

(B) When the sulfide-containing nucleophile is **13**

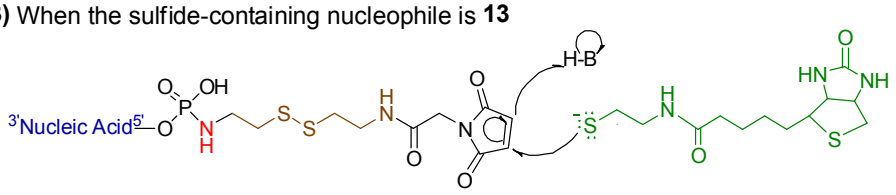

Nucleic acid-cystamine-9 conjugate

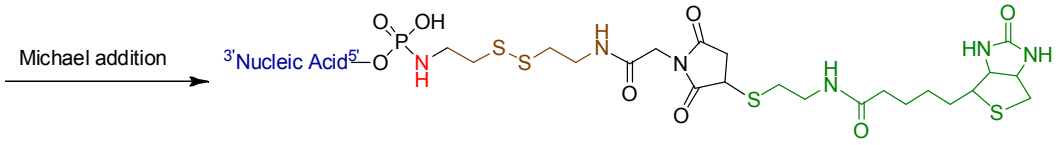

Nucleic acid-cystamine-9-13 conjugate

(C) When the sufide-containing nucleophile is a cysteine-included peptide

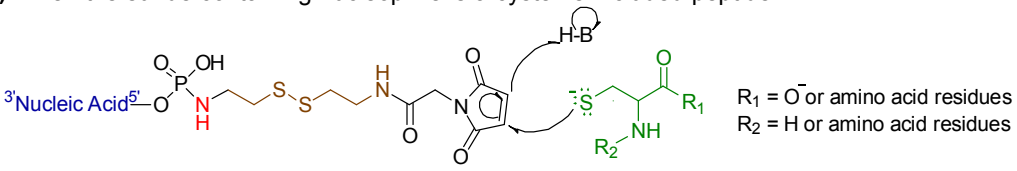

Nucleic acid-cystamine-9 conjugate

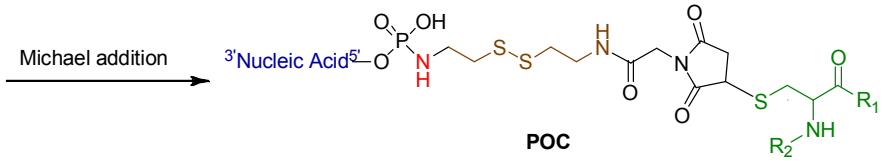

POC

Scheme S1. Michael addition through nucleophilic addition of a maleimide moiety in nucleic acid-cystamine-**9** conjugate by a sulfide-containing nucleophile. (A) The general reaction mechanism for this type of Michael addition. (B) The Michael addition reaction when the nucleophile is **13**. (C) The Michael addition reaction when the nucleophile is a cysteine-containing peptide such as the $C(KFF)_3K$ peptide used in this study, to give a POC.

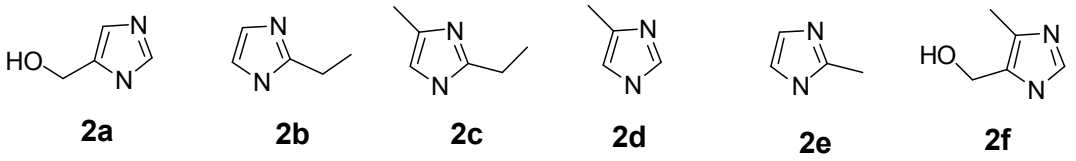

Figure S1. The six imidazole derivatives studied to evaluate their potential to stabilizing phosphorimidazolide intermediates and to increasing product yields in aqueous-phase two-step phosphoramidation reactions.

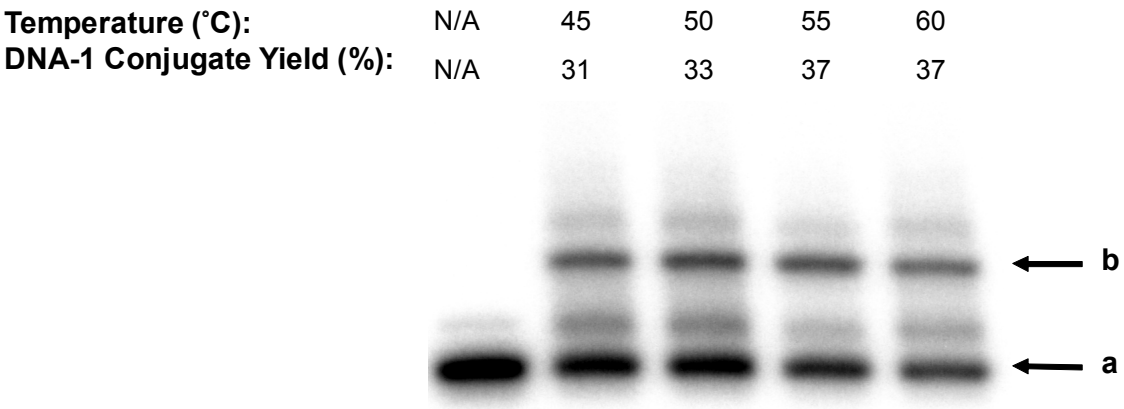

Figure S2. Increasing temperatures of phosphoramidation reactions to improve yields of the ^{32}P-labeled 3' primer DNA-**1** conjugate. The optimized reaction condition for single-stranded DNA conjugation was exploited while varying reaction temperatures as specified. The reaction products were purified by ethanol precipitation, analyzed by 20% urea-PAGE for the DNA-**1** conjugate, visualized and quantified by an Amersham Typhoon PhosphorImager. **a**, the unreacted 3' primer DNA; **b**, the 3' primer DNA-**1** conjugate.

CPPs:	N/A	1	2	3	4	5
Yields (%):	N/A	11	27	5	35	12

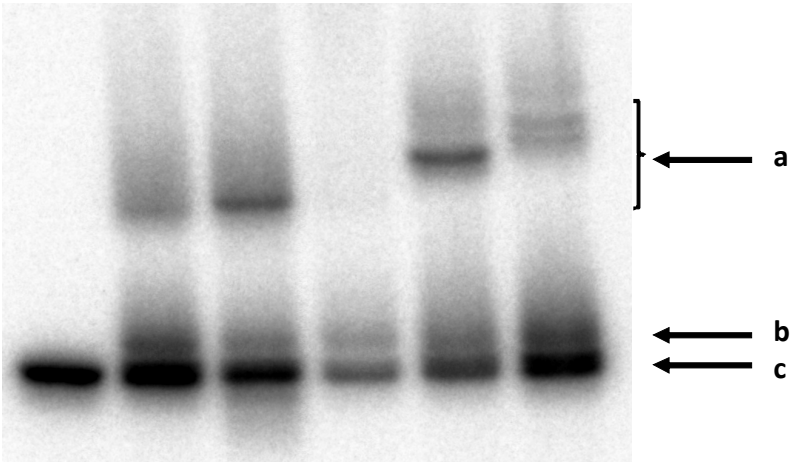

Figure S3. Formation of POC affected by structures of N-terminus amino acids in CPPs. The optimized reaction condition for single-stranded DNA was employed for conjugating the 3' primer DNA with a specific CPP. The reaction products were purified by ethanol precipitation, separated by 20% urea-PAGE, visualized and quantified by an Amersham Typhoon PhosphorImager. The studied CPPs included: 1, the $(KFF)_3K$ peptide (H_2N-**K**FFKFFKFFK-$CONH_2$); 2, the $G(KFF)_3K$ peptide (H_2N-**G**KFFKFFKFFK-$CONH_2$); 3, the $C(KFF)_3K$ peptide (H_2N-**C**KFFKFFKFFK-$CONH_2$); 4, the $Tat_{48\text{-}57}$ peptide (H_2N-**G**RKKRRQRRR-$CONH_2$); 5, the $Tat_{47\text{-}57}$ peptide (H_2N-**Y**GRKKRRQRRR-$CONH_2$). N-terminus amino acid residues of peptides in parentheses are bolded and underlined. **a**, the 3' primer DNA-peptide conjugates; **b**, proposed to be the phosphorimidazolide intermediate of the 3' primer DNA; **c**, the unreacted 3' primer DNA.

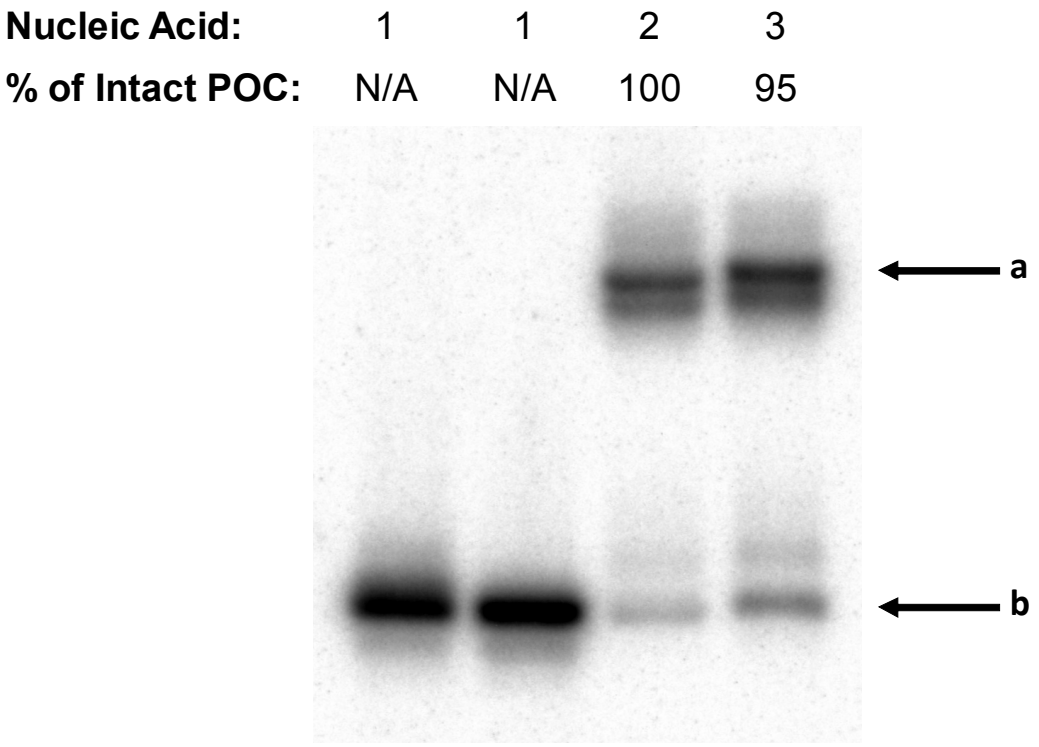

Figure S4. Stability of a phosphoramidation-prepared POC in the acidic MALDI-TOF matrix solution used for positive-mode MALDI-TOF MS analysis. The ^{32}P-labeled DNA samples analyzed by the 20% urea-PAGE included: 1, the 3' primer DNA; 2, the gel-purified 3' primer DNA-the Tat_{48-57} peptide conjugate; 3, the 3-h incubation products of the gel-purified 3' primer DNA-the Tat_{48-57} peptide conjugate in the acidic MALDI-TOF matrix solution required for positive-mode MALDI-TOF MS analysis. The DNA samples were visualized and quantified by an Amersham Typhoon PhosphorImager. **a**, the 3' primer DNA-the Tat_{48-57} peptide conjugate; **b**, the unreacted 3' primer DNA.

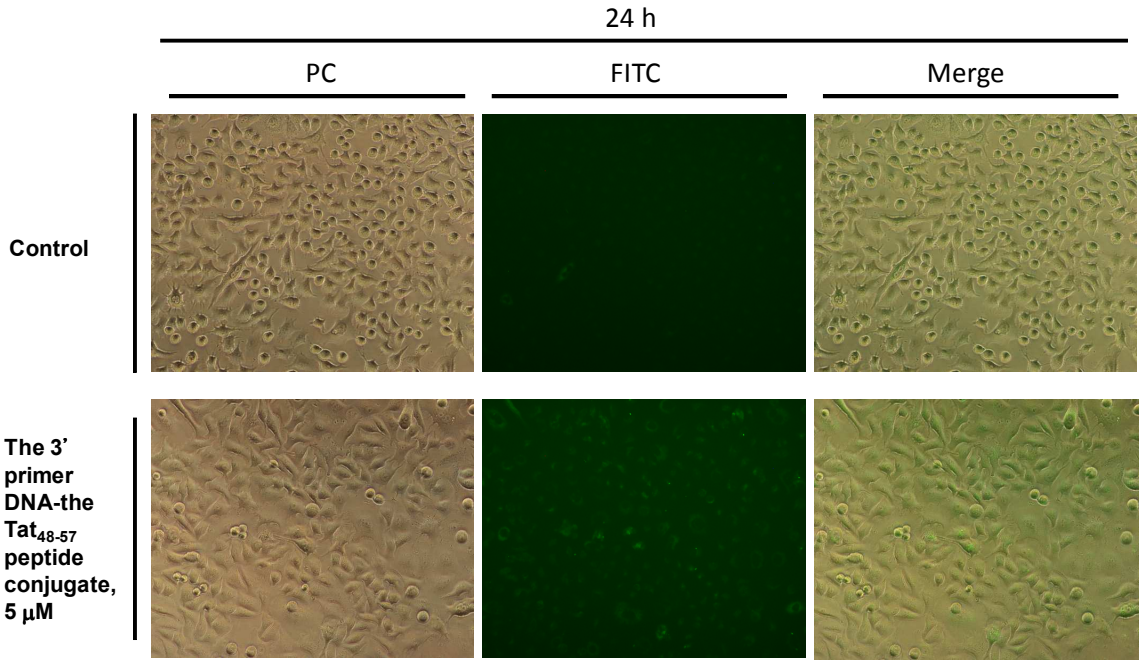

Figure S5. Fluorescent microscopy study to demonstrate association of phosphoramidation-prepared POCs with human A549 cells. The A549 cells for fluorescent microscopy were prepared according to the same procedures for confocal laser scanning microscopy experiments. Cells were inoculated with 5 μM of the FITC-labeled and phosphoramidation-prepared POC, the FITC-labeled 3' primer DNA-the Tat_{48-57} peptide conjugate, for 24 h, followed by washing three times with PBS and immediately analyzed by a fluorescent microscope (Nikon ECLIPSE Ti-U Inverted microscope; Nikon, Shinjuku, Tokyo, Japan) located at Kaohsiung Medical University, Taiwan. In the control sample, the A549 cells were incubated for 24 h in the absence of the FITC-labeled 3' primer DNA-the Tat_{48-57} peptide conjugate before fluorescent microscopy analysis. PC, phase contrast.

(A) Nucleic acid-cystamine conjugate

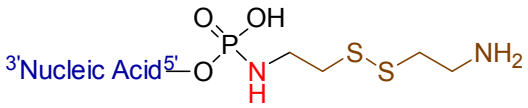

(B) Nucleic acid-cystamine-11 conjugate

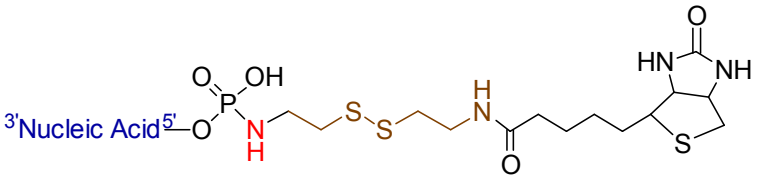

(C) Nucleic acid-cystamine-9 conjugate

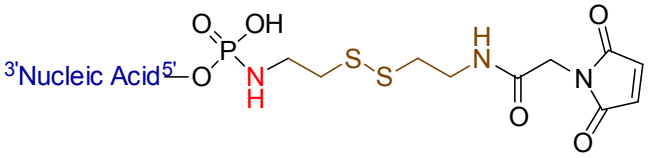

(D) Nucleic acid-cystamine-9-13 conjugate

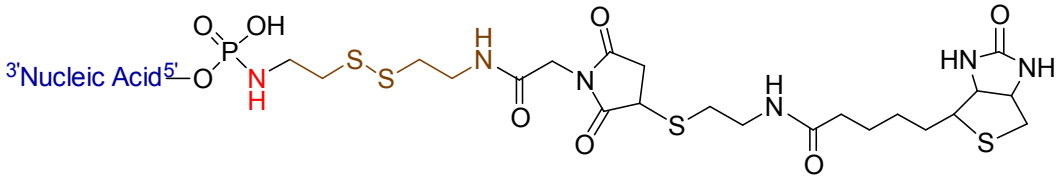

Chart S1. The major structures for four nucleic acid conjugates described in the figure legend for Figure 5.

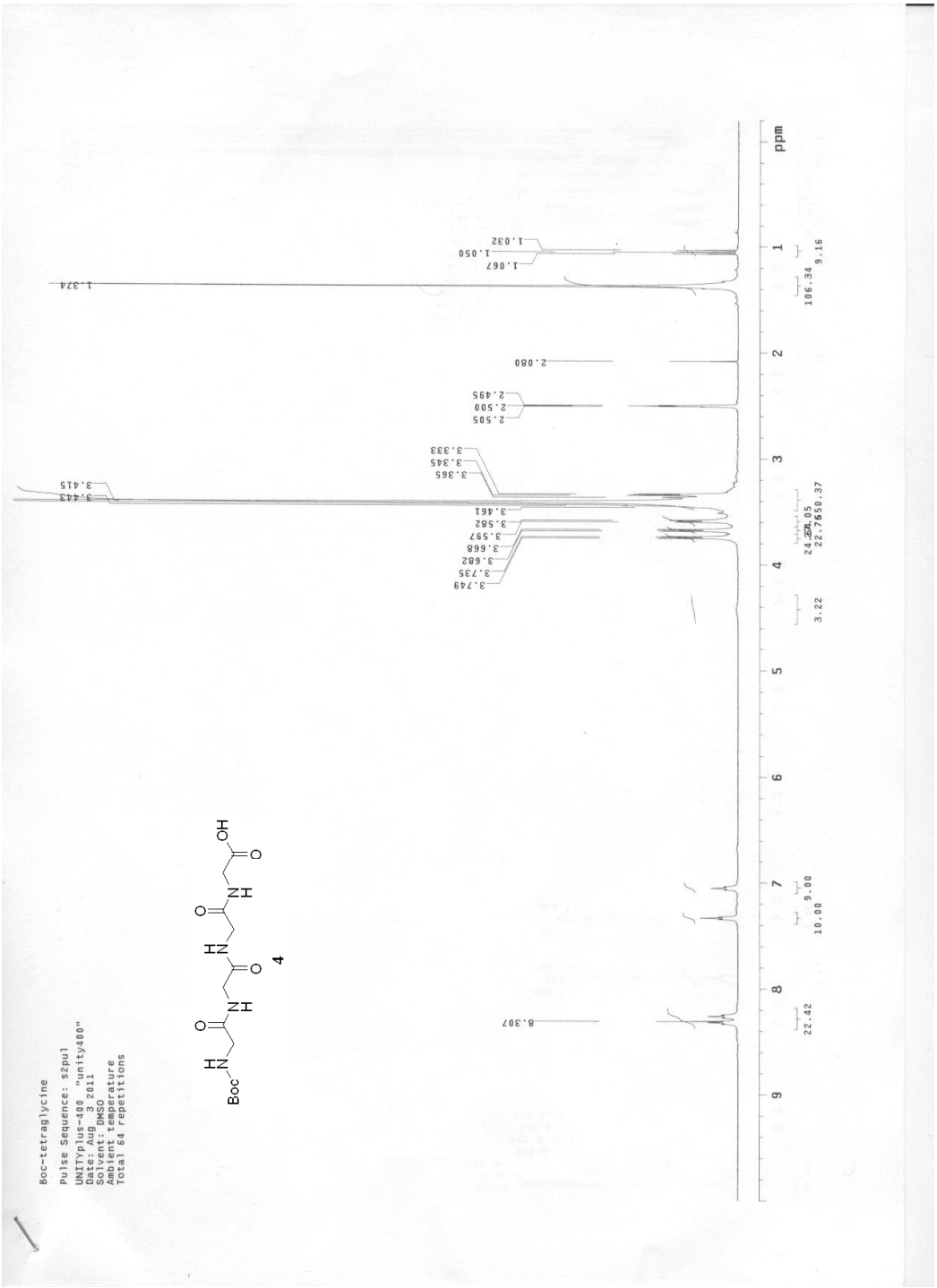
Boc-tetraglycine
Pulse Sequence: s2pul
UNITYplus-400 "unity400"
Date 4 Aug 2011
Solvent: DMSO
Ambient temperature
Total 64 repetitions
Boc
4
ppm

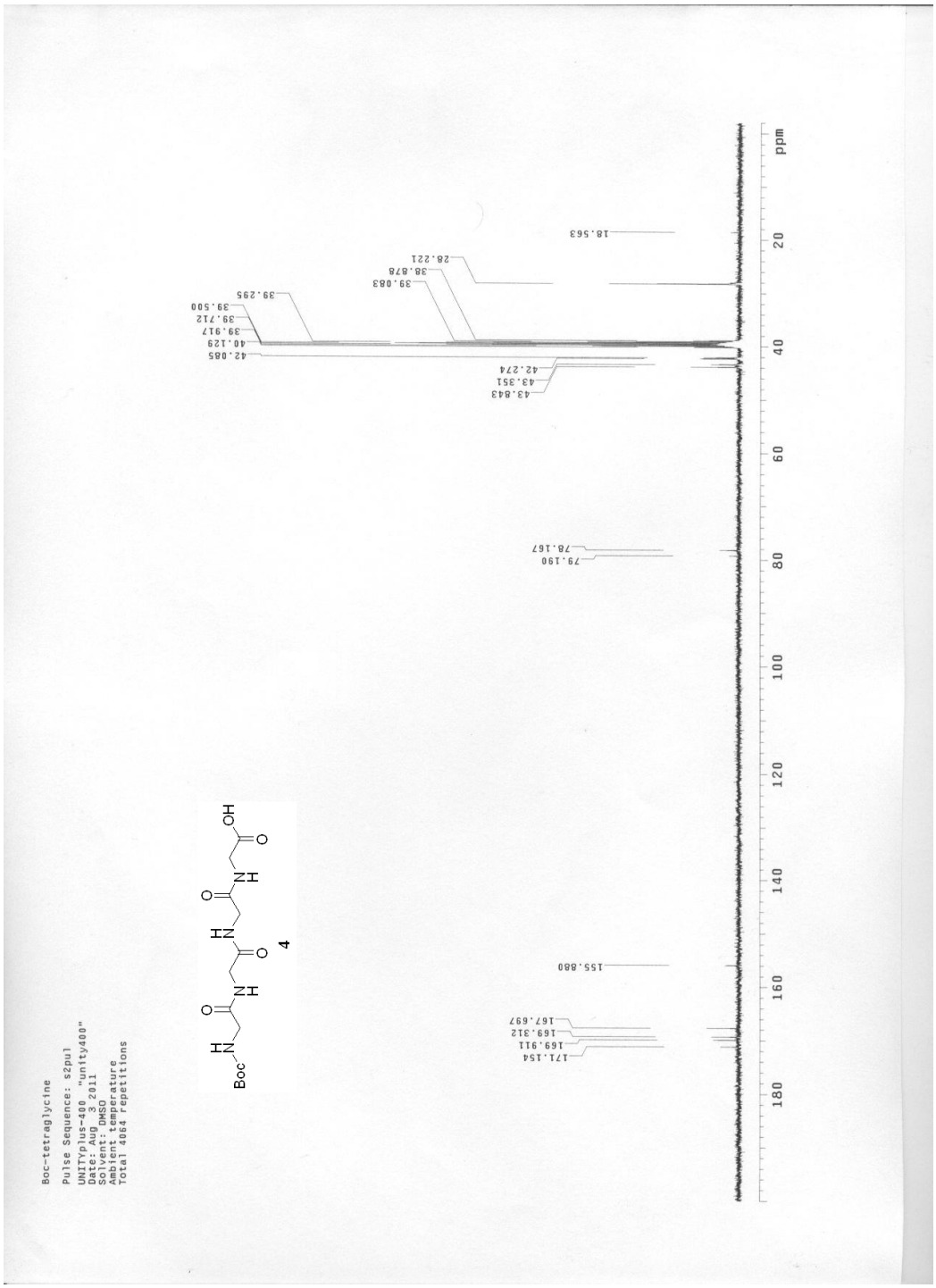
Boc-tetraglycine
Pulse Sequence: s2pul
UNITYplus-400 "unity400"
Date: Aug 2 2011
Solvent: DMSO
Ambient temperature
Total 4064 repetitions
4
Boc
ppm
18.563
28.221
38.878
39.083
39.295
39.500
39.712
39.917
40.129
42.085
42.274
43.351
43.843
78.167
79.190
155.880
167.697
169.312
169.911
171.154

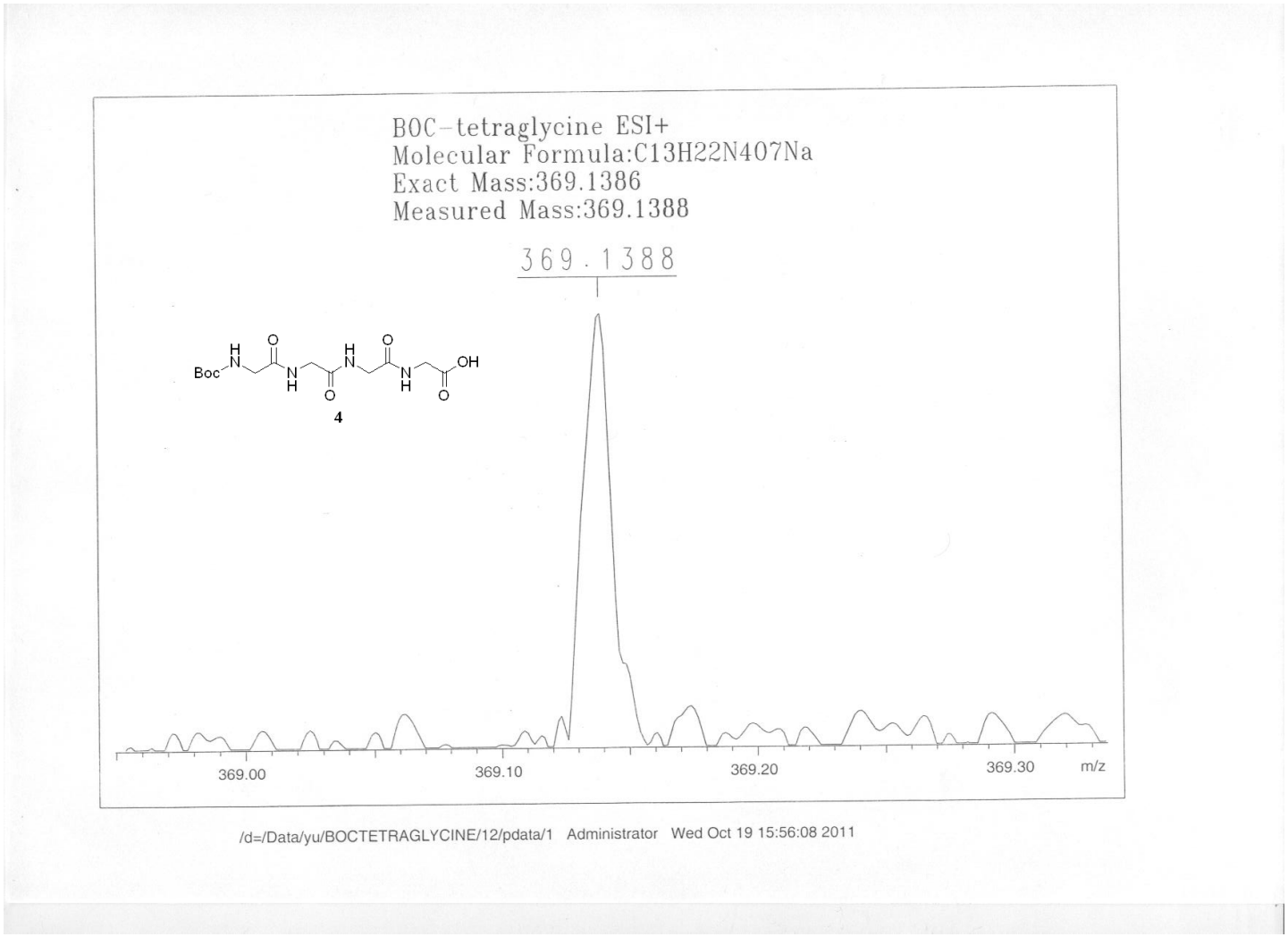
BOC-tetraglycine ESI+
Molecular Formula:C13H22N4O7Na
Exact Mass:369.1386
Measured Mass:369.1388
369.1388
Boc
OH
4
369.00
369.10
369.20
369.30
m/z
/d=/Data/yu/BOCTETRAGLYCINE/12/pdata/1 Administrator Wed Oct 19 15:56:08 2011

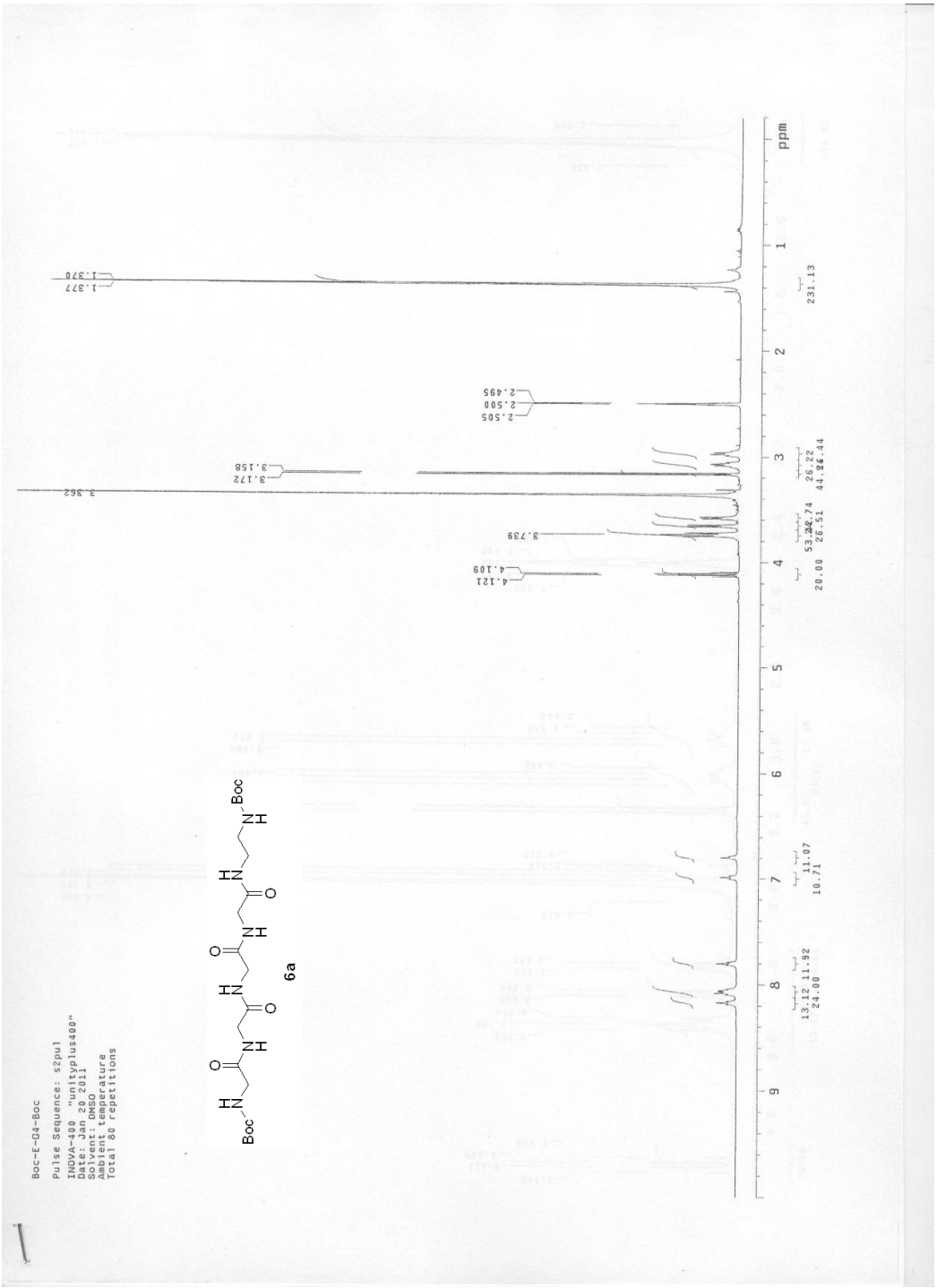
Boc-E-O4-Boc
Pulse Sequence: s2pul
INOVA-400 "unityplus400"
Date: Jan 20 2011
Solvent: DMSO
Ambient temperature
Total 80 repetitions
6a
Boc
NH
O
ppm
1.377
1.370
2.505
2.500
2.495
3.172
3.158
3.362
3.739
4.121
4.109
231.13
53.22
26.51
26.22
44.44
20.00
11.07
10.71
11.92
24.00

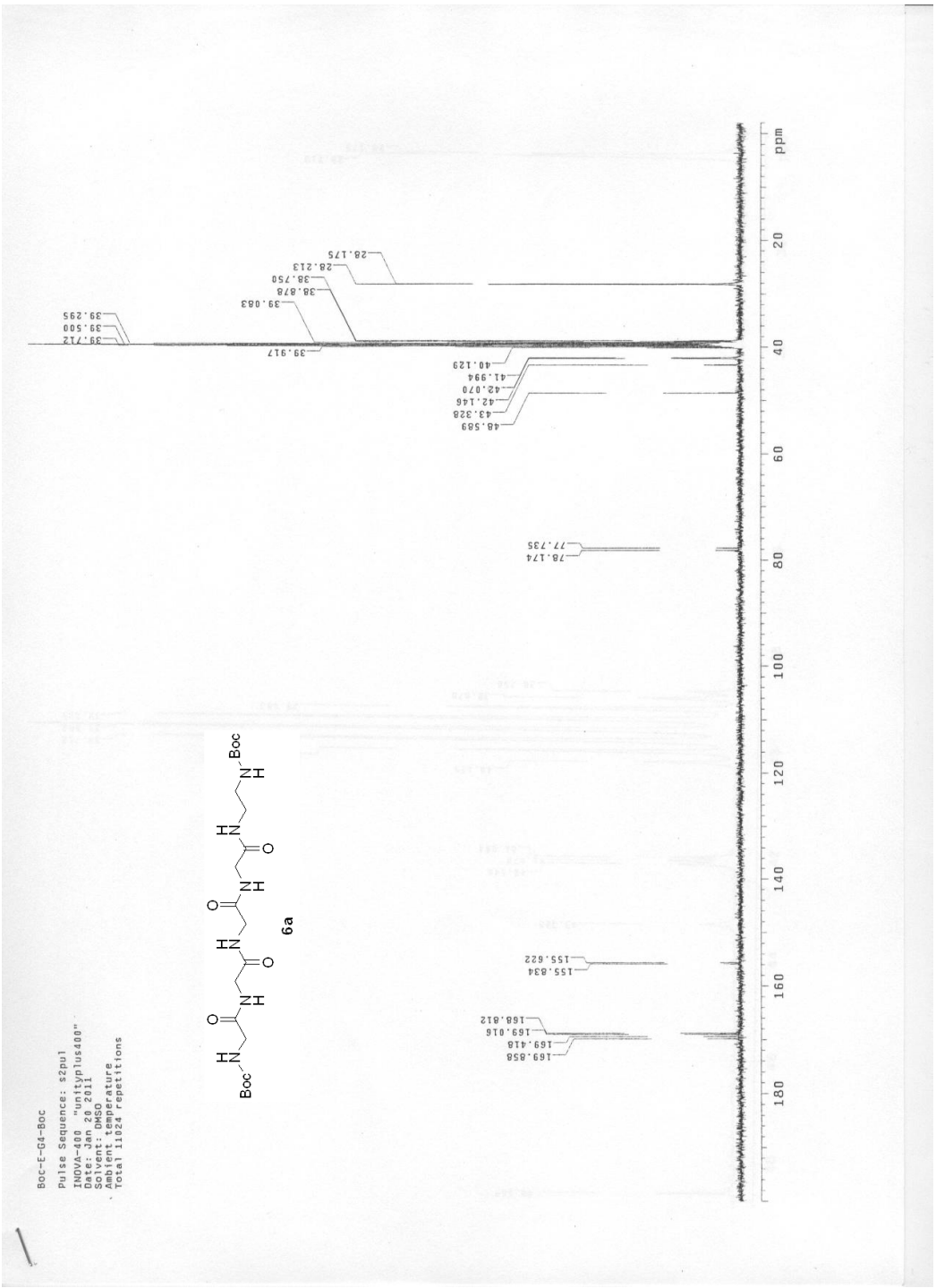
Boc-E-G4-Boc
Pulse Sequence: s2pul
INOVA-400 "unityplus400"
Date: Jan 20 2011
Solvent: DMSO
Ambient temperature
Total 11024 repetitions
6a
Boc
Boc
ppm
28.175
28.213
38.750
38.878
39.083
39.295
39.500
39.712
39.917
40.129
41.994
42.070
42.146
43.328
48.589
77.735
78.174
155.622
155.834
168.812
169.016
169.418
169.858

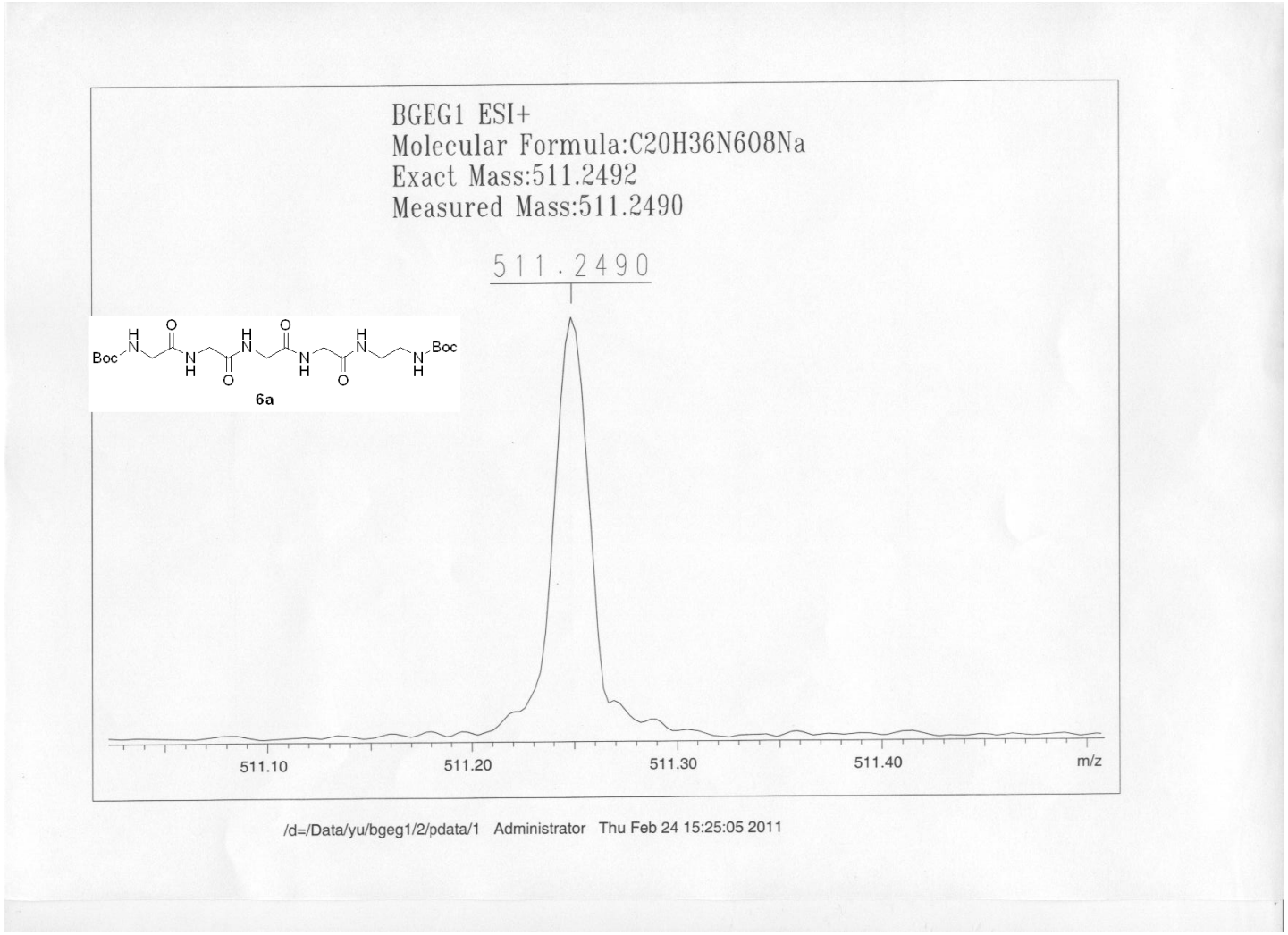
BGEG1 ESI+
Molecular Formula:C20H36N6O8Na
Exact Mass:511.2492
Measured Mass:511.2490
511.2490
Boc
Boc
6a
511.10
511.20
511.30
511.40
m/z
/d=/Data/yu/bgeg1/2/pdata/1 Administrator Thu Feb 24 15:25:05 2011

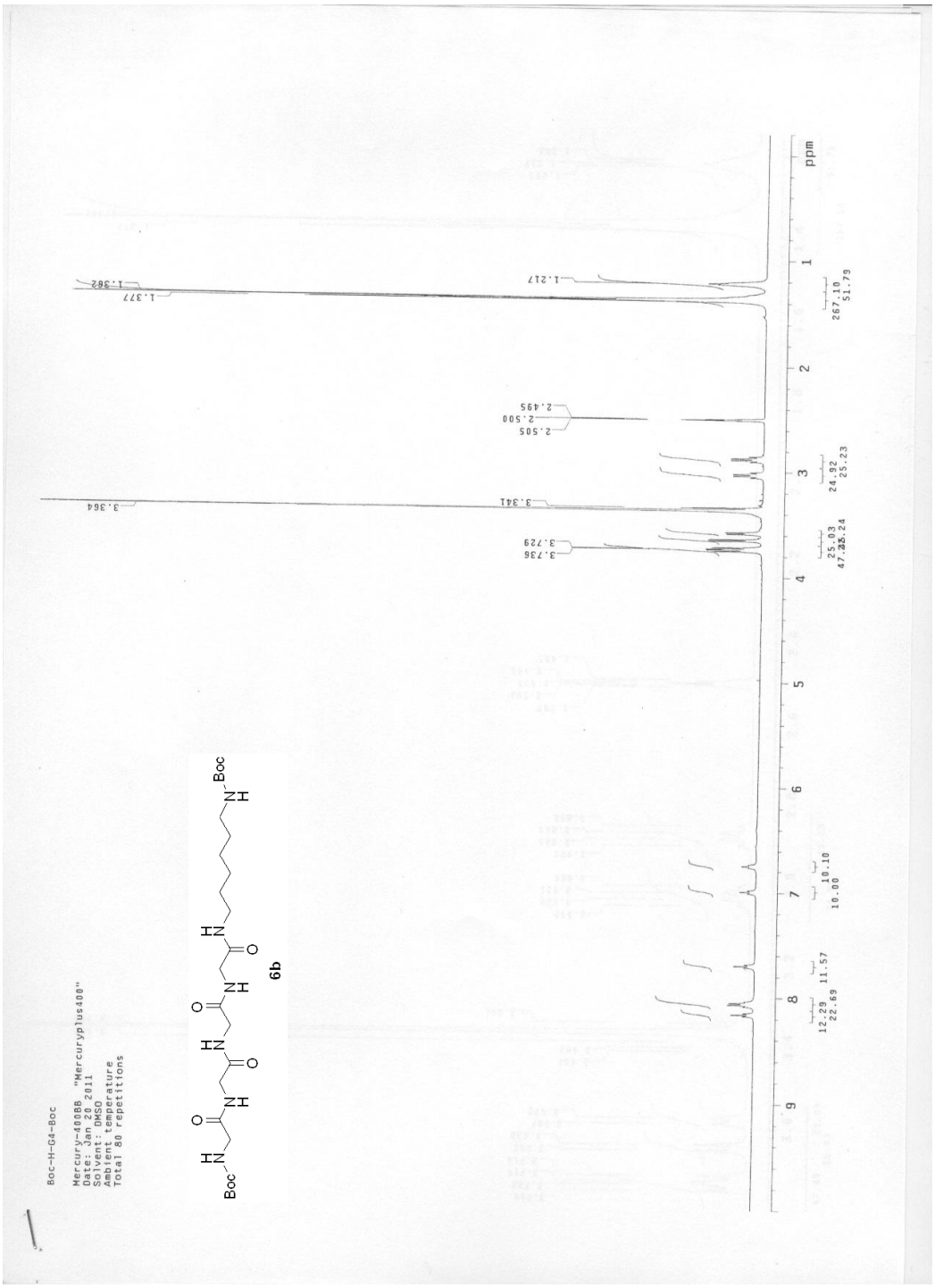
Boc-H-G4-Boc
Mercury-400BB "Mercuryplus400"
Date: Jan 20 2011
Solvent: DMSO
Ambient temperature
Total 80 repetitions
Boc
Boc
6b
ppm
1.217
1.377
1.382
2.495
2.500
2.505
3.341
3.364
3.729
3.736

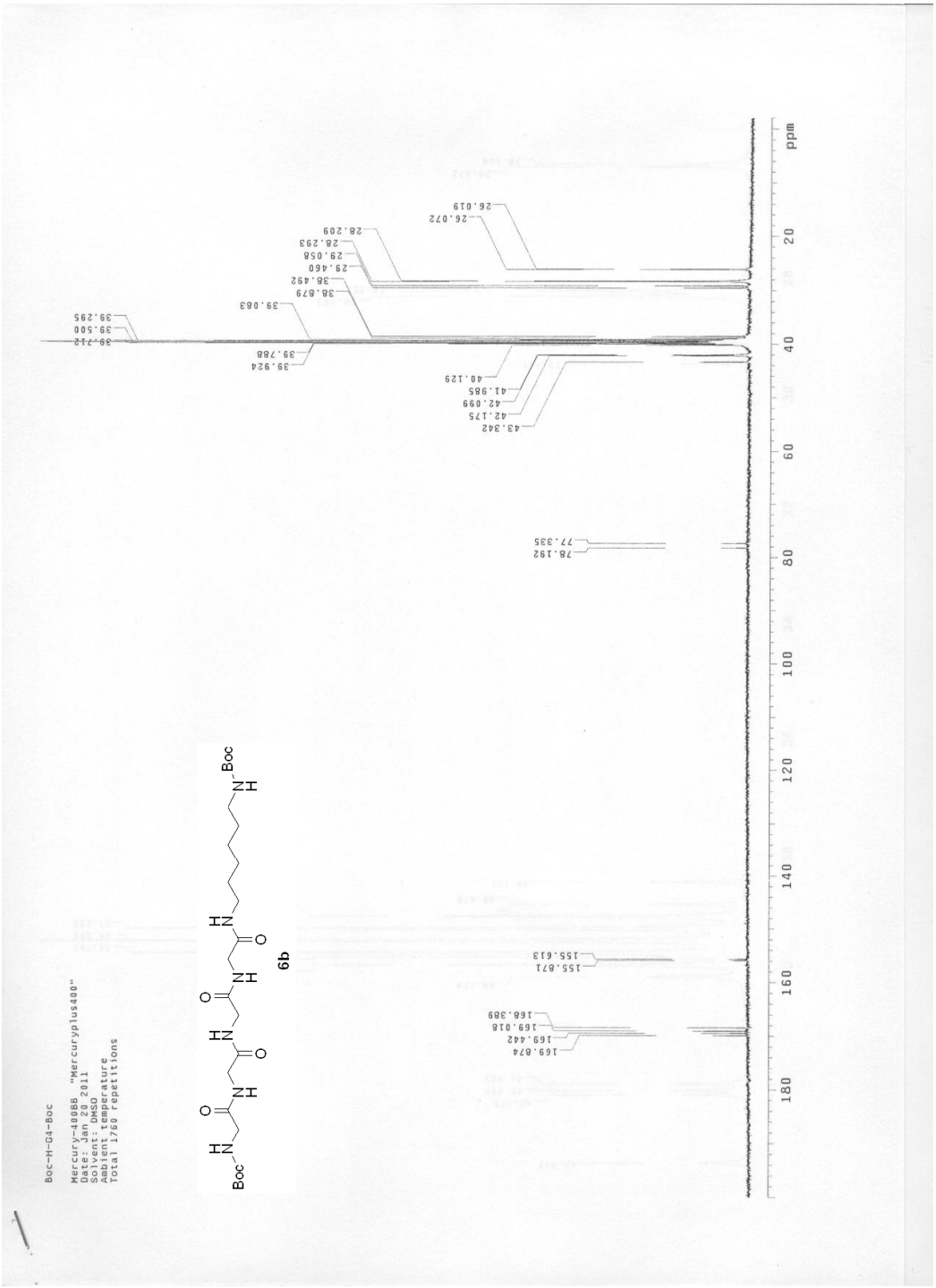
Boc-H-G4-Boc
Mercury-400BB "Mercuryplus400"
Date: Jan 20 2011
Solvent: DMSO
Ambient temperature
Total 1760 repetitions
Boc
Boc
6b
ppm
20
40
60
80
100
120
140
160
180
26.019
26.072
28.209
28.293
29.058
29.460
38.492
38.879
39.063
39.295
39.500
39.712
39.768
39.924
40.129
41.985
42.099
42.175
43.342
77.335
78.192
155.613
155.871
166.389
169.018
169.442
169.874

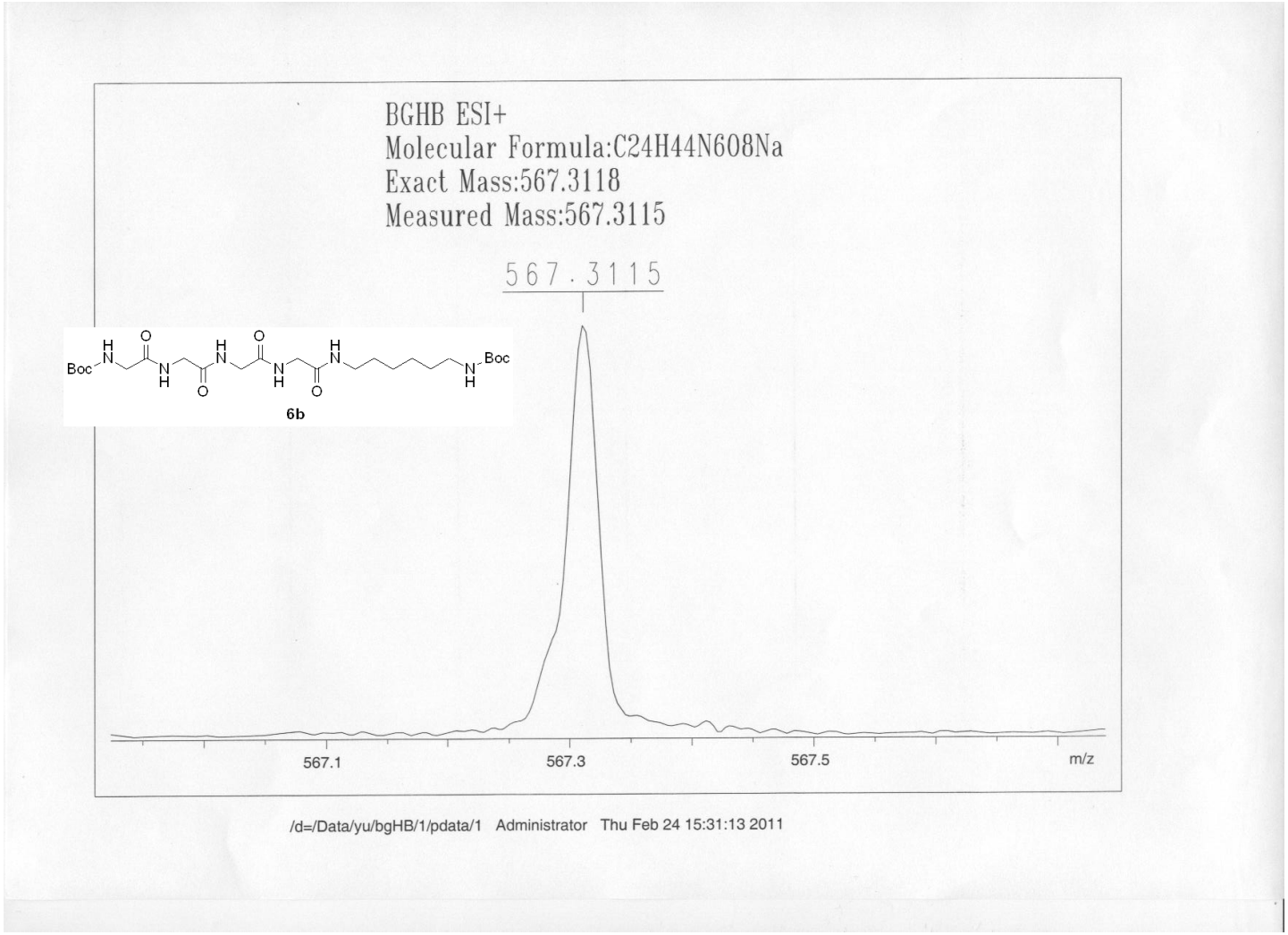
BGHB ESI+
Molecular Formula:C24H44N6O8Na
Exact Mass:567.3118
Measured Mass:567.3115
567.3115
Boc
Boc
6b
567.1
567.3
567.5
m/z
/d=/Data/yu/bgHB/1/pdata/1 Administrator Thu Feb 24 15:31:13 2011

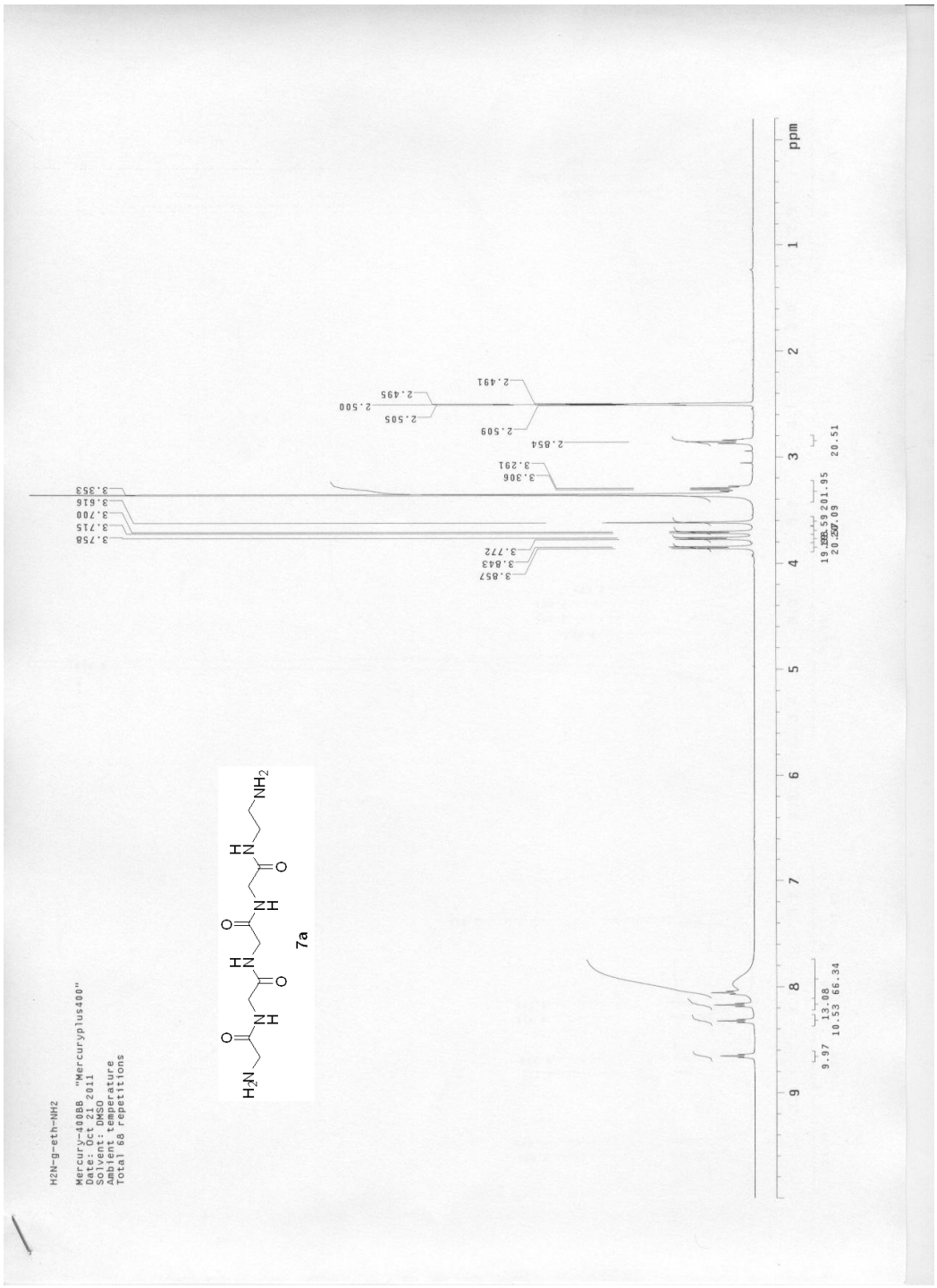
H2N-g-eth-NH2
Mercury-400BB "Mercuryplus400"
Date: Oct 2 2011
Solvent: DMSO
Ambient temperature
Total 68 repetitions
7a
3.857
3.843
3.772
3.758
3.715
3.700
3.616
3.353
3.306
3.291
2.854
2.509
2.505
2.500
2.495
2.491
ppm
9.97
13.08
10.53
66.34
19.59
20.25
201.95
207.09
20.51

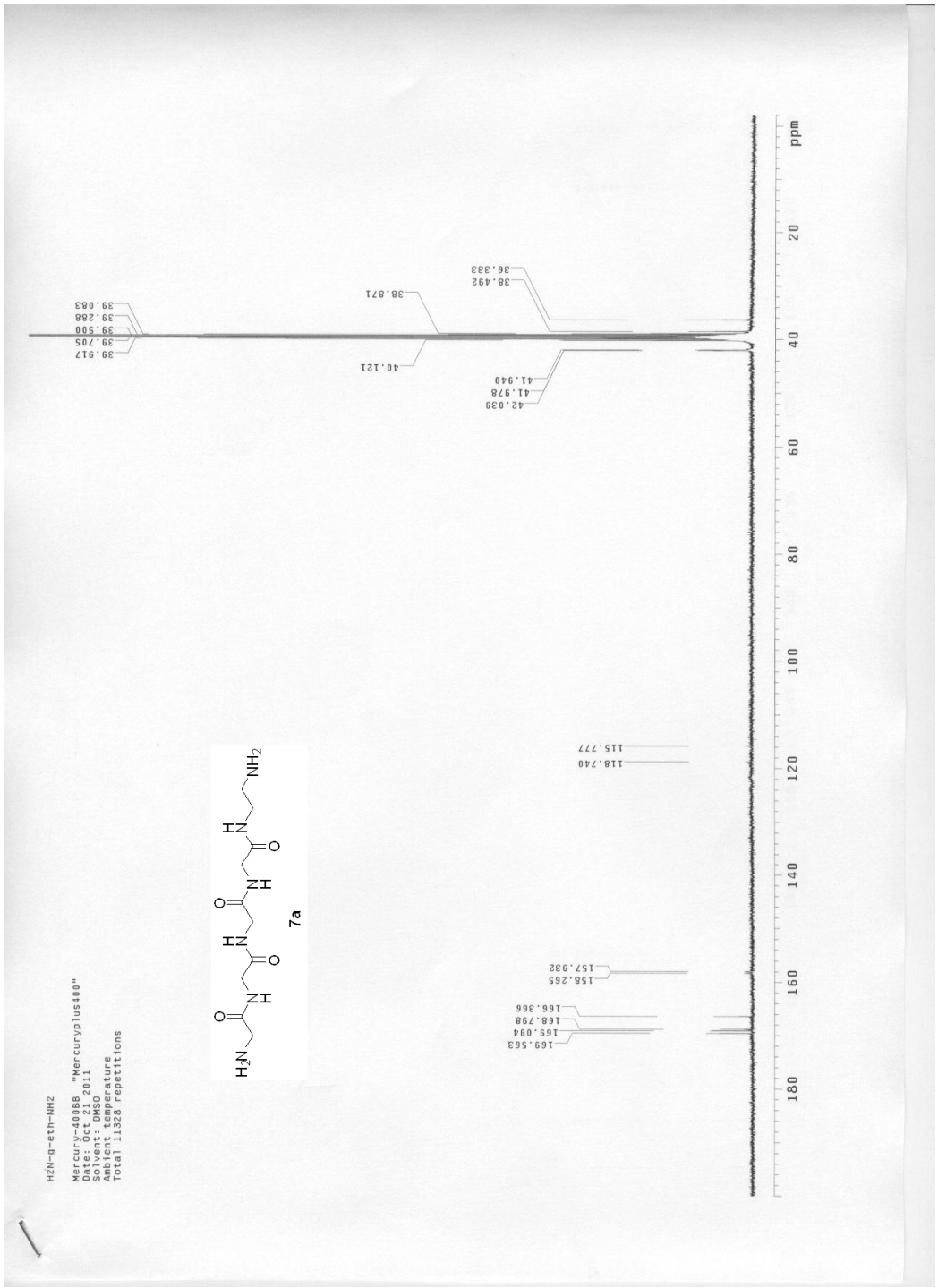
H2N-g-eth-NH2
Mercury-400BB "Mercuryplus400"
Date: Oct 21 2011
Solvent: DMSO
Ambient temperature
Total 11328 repetitions
7a
ppm
20
40
60
80
100
120
140
160
180
39.917
39.705
39.500
39.288
39.083
40.121
38.871
38.492
36.333
42.039
41.978
41.940
118.740
115.777
158.265
157.932
169.563
168.798
169.094
166.366

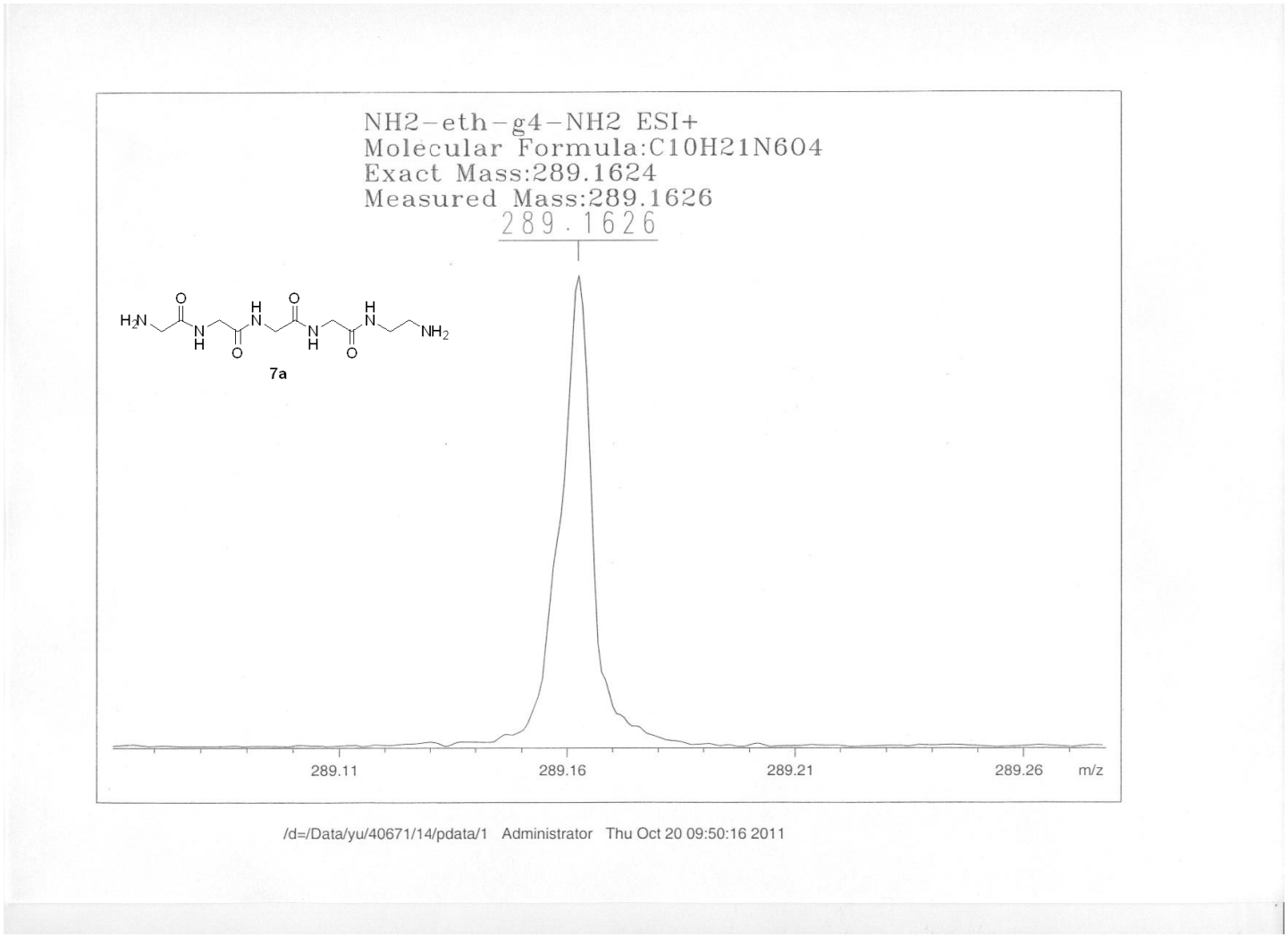
NH2-eth-g4-NH2 ESI+
Molecular Formula:C10H21N6O4
Exact Mass:289.1624
Measured Mass:289.1626
289.1626
7a
289.11
289.16
289.21
289.26
m/z
/d=/Data/yu/40671/14/pdata/1 Administrator Thu Oct 20 09:50:16 2011

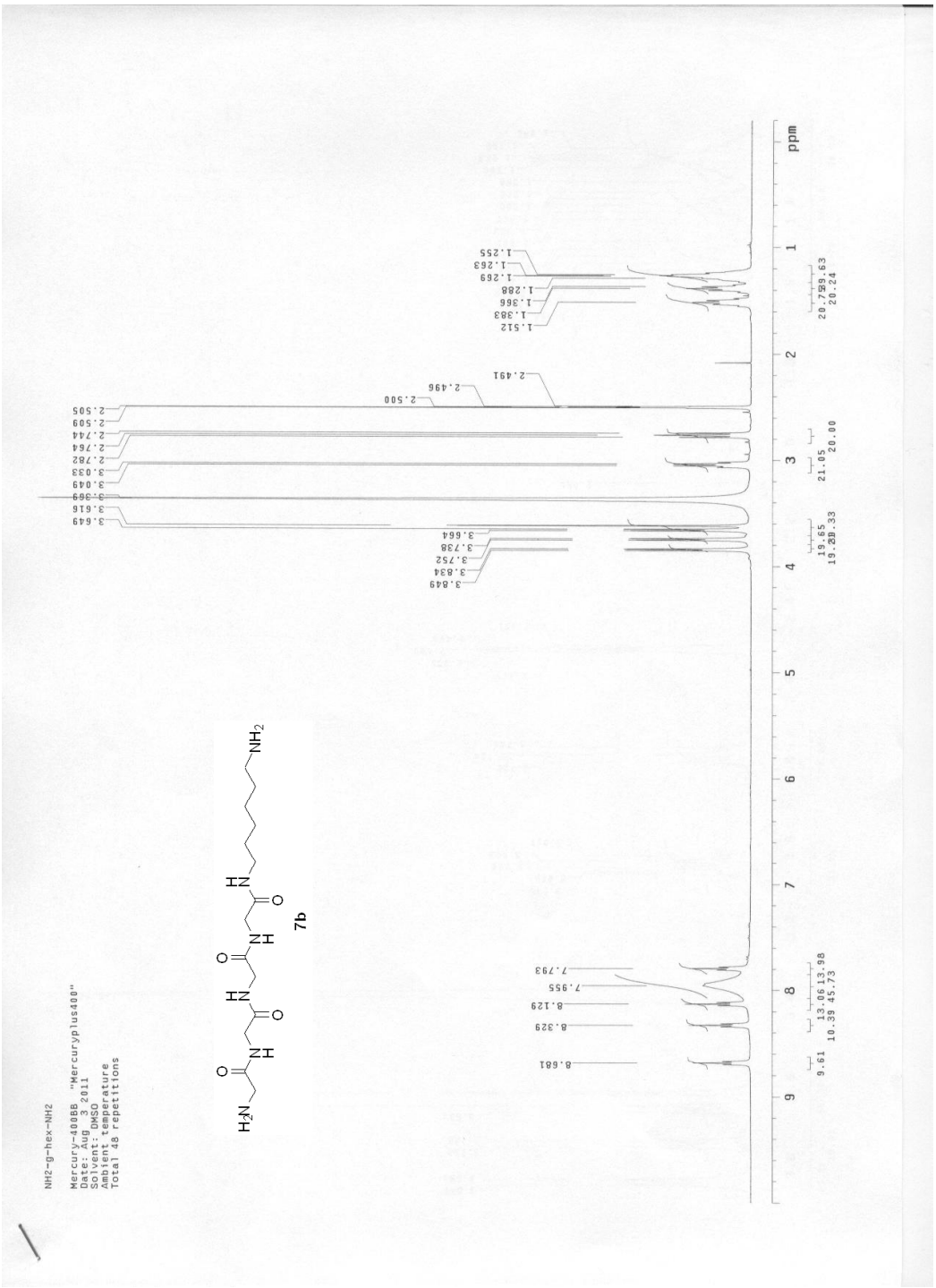
NH2-g-hex-NH2
Mercury-400BB "Mercuryplus400"
Date: Aug 3 2011
Solvent: DMSO
Ambient temperature
Total 48 repetitions
7b
ppm

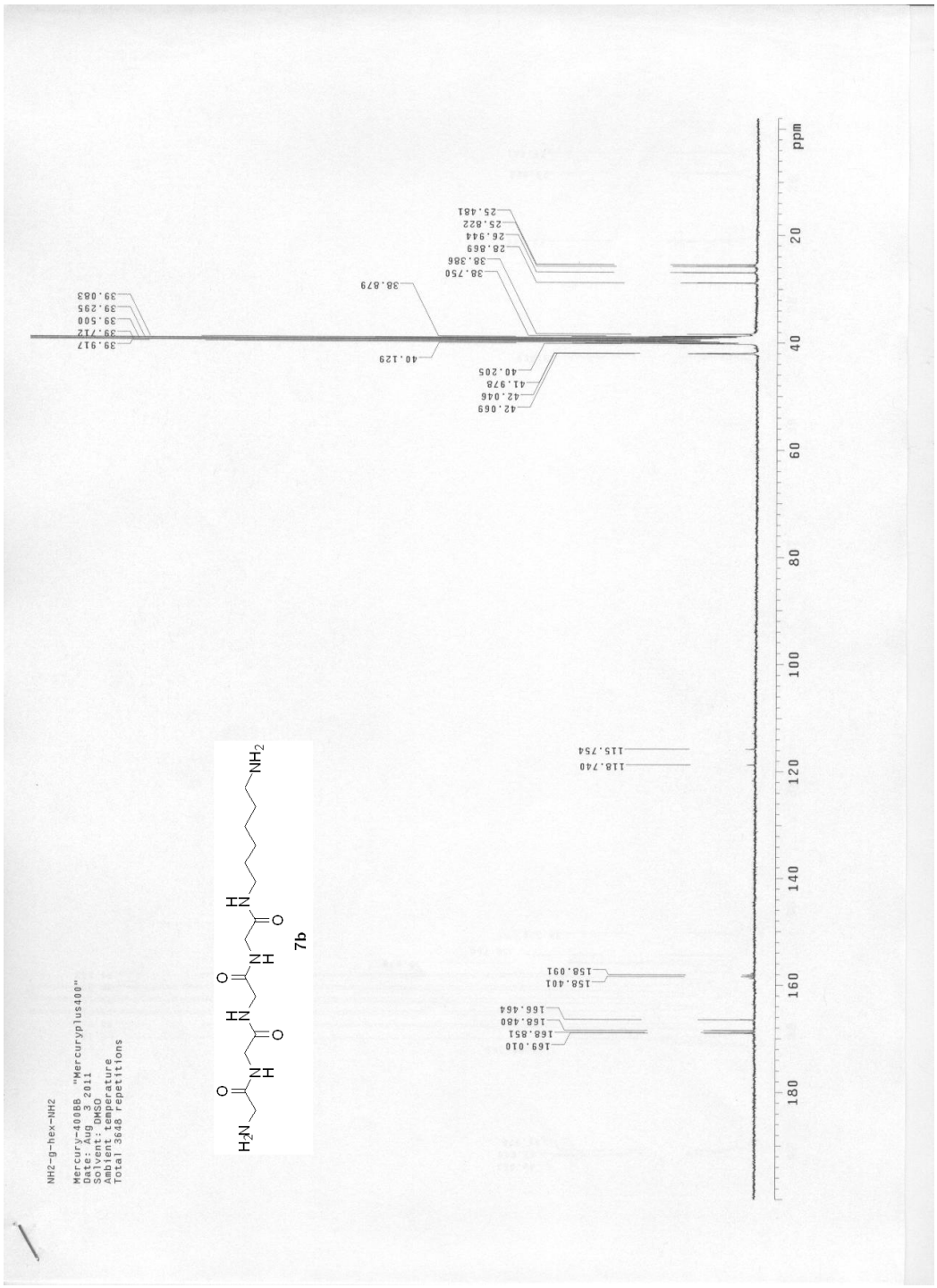
NH2-g-hex-NH2
Mercury-400BB "Mercuryplus400"
Date: Aug 3 2011
Solvent: DMSO
Ambient temperature
Total 3648 repetitions
7b
ppm
20
40
60
80
100
120
140
160
180
39.917
39.712
39.500
39.295
39.083
38.879
40.129
38.750
38.386
28.869
26.944
25.822
25.481
42.069
42.046
41.978
40.205
118.740
115.754
158.401
158.091
169.010
168.851
168.480
166.464

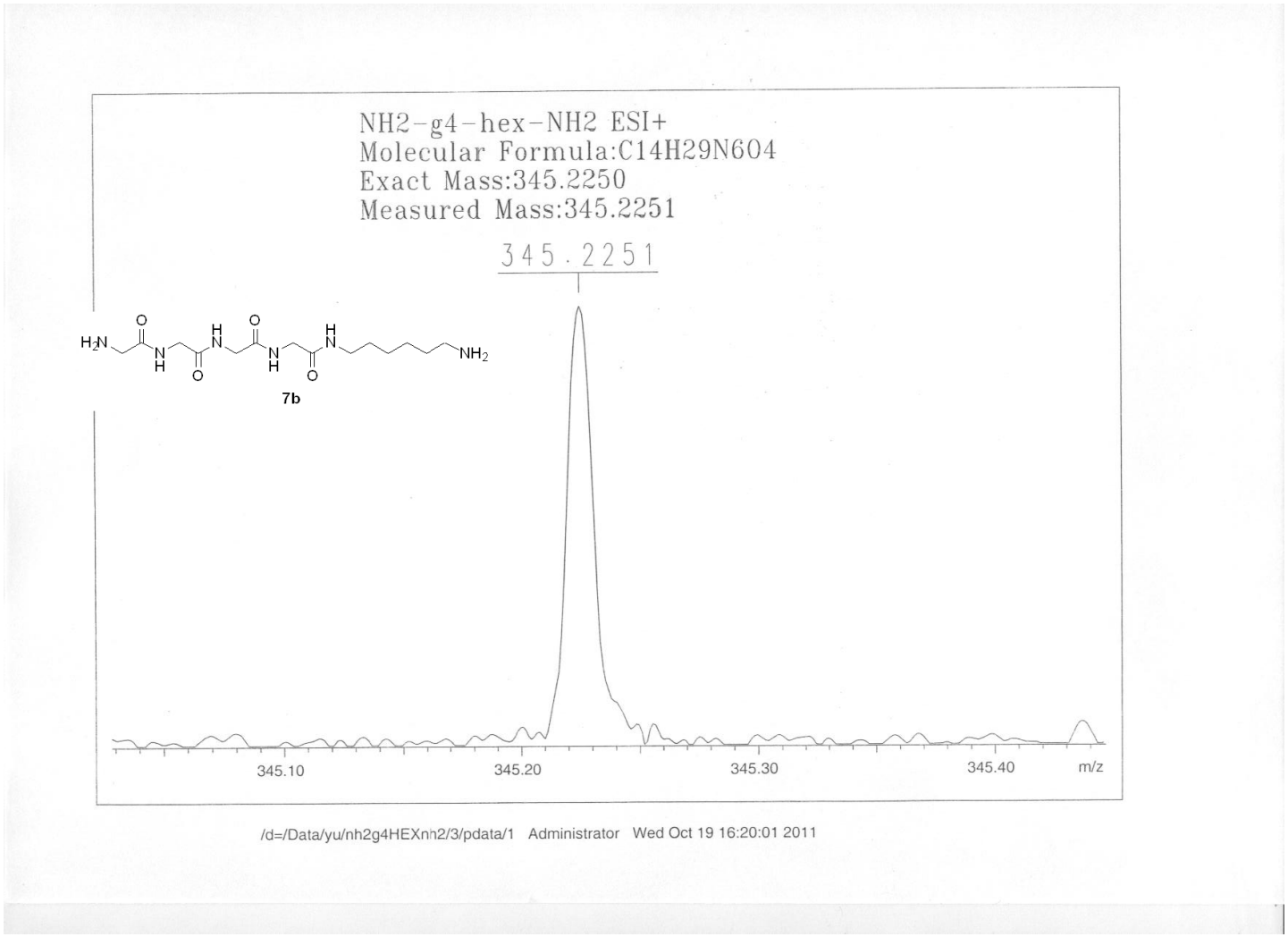
NH2-g4-hex-NH2 ESI+
Molecular Formula:C14H29N6O4
Exact Mass:345.2250
Measured Mass:345.2251
345.2251
7b
345.10
345.20
345.30
345.40
m/z
/d=/Data/yu/nh2g4HEXnh2/3/pdata/1 Administrator Wed Oct 19 16:20:01 2011

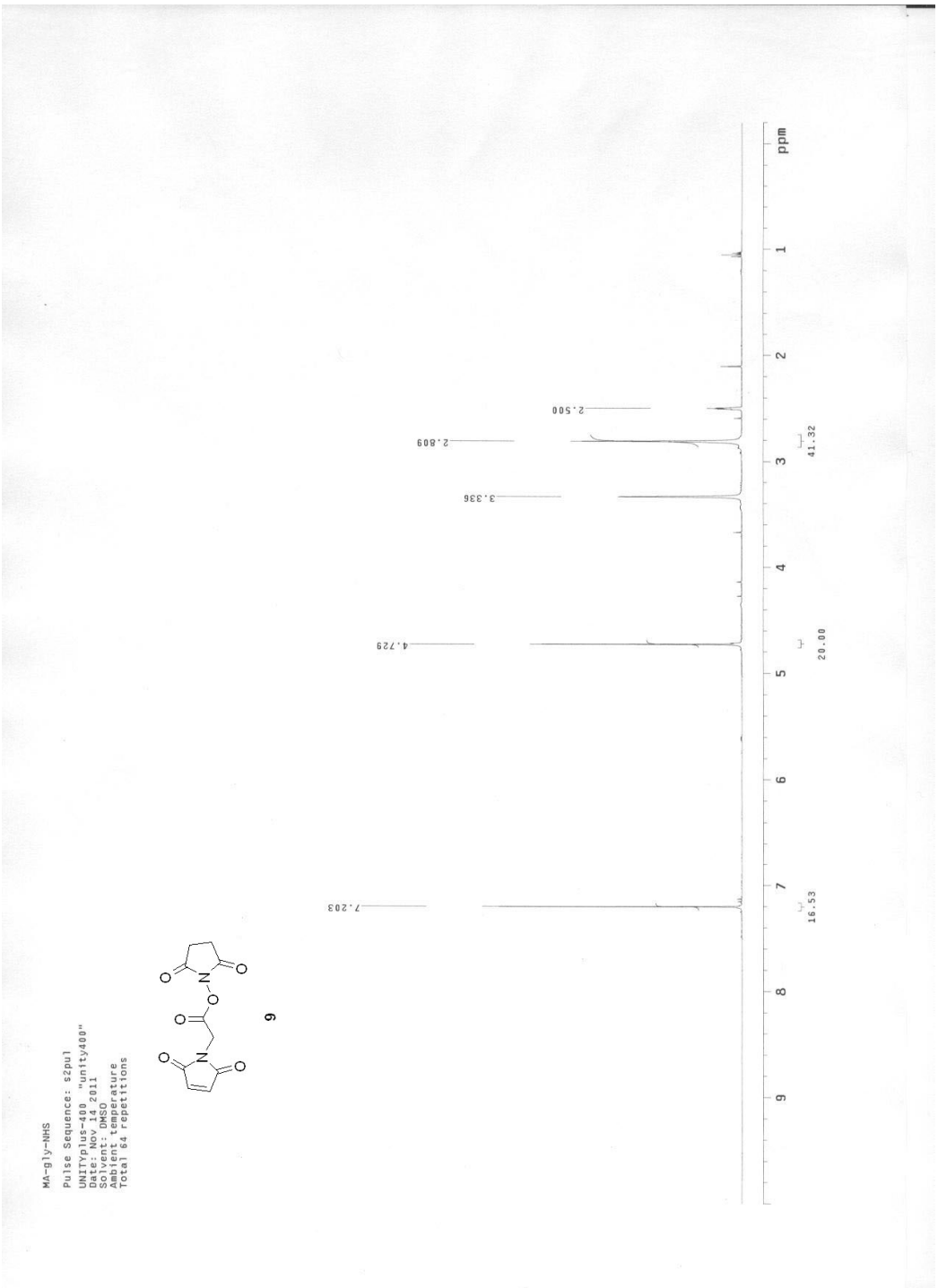
MA-gly-NHS
Pulse Sequence: s2pul
UNITYplus-400 "unity400"
Date: Nov 14 2011
Solvent: DMSO
Ambient temperature
Total 64 repetitions
9
7.203
4.729
3.336
2.809
2.500
16.53
20.00
41.32
ppm

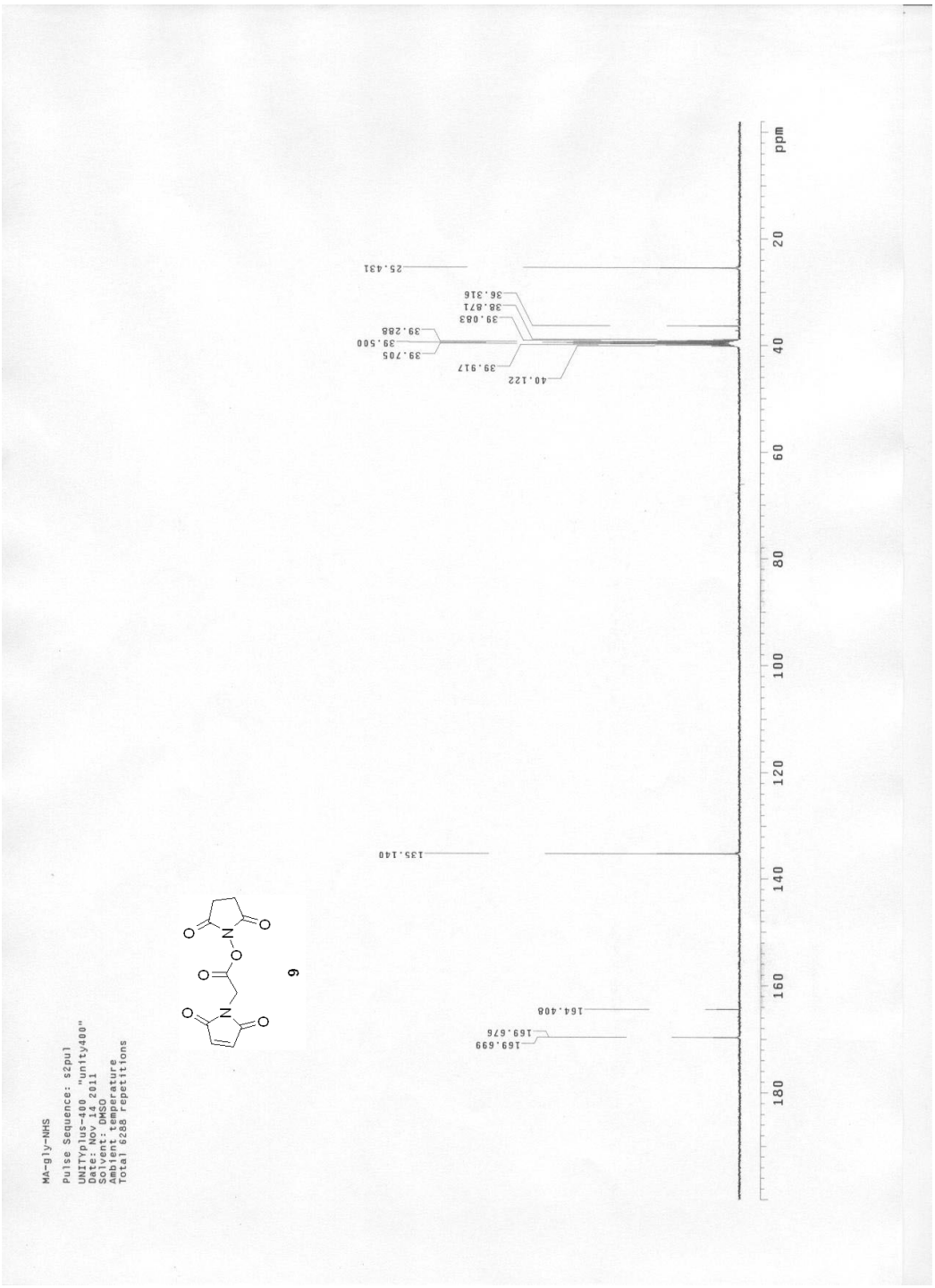
MA-gly-NHS
Pulse Sequence: s2pul
UNITYplus-400 "unity400"
Date: Nov 14 2011
Solvent: DMSO
Ambient temperature
Total 628 repetitions
ppm
20
40
60
80
100
120
140
160
180
25.431
36.316
38.871
39.083
39.288
39.500
39.705
39.917
40.122
135.140
164.408
169.676
169.699
6

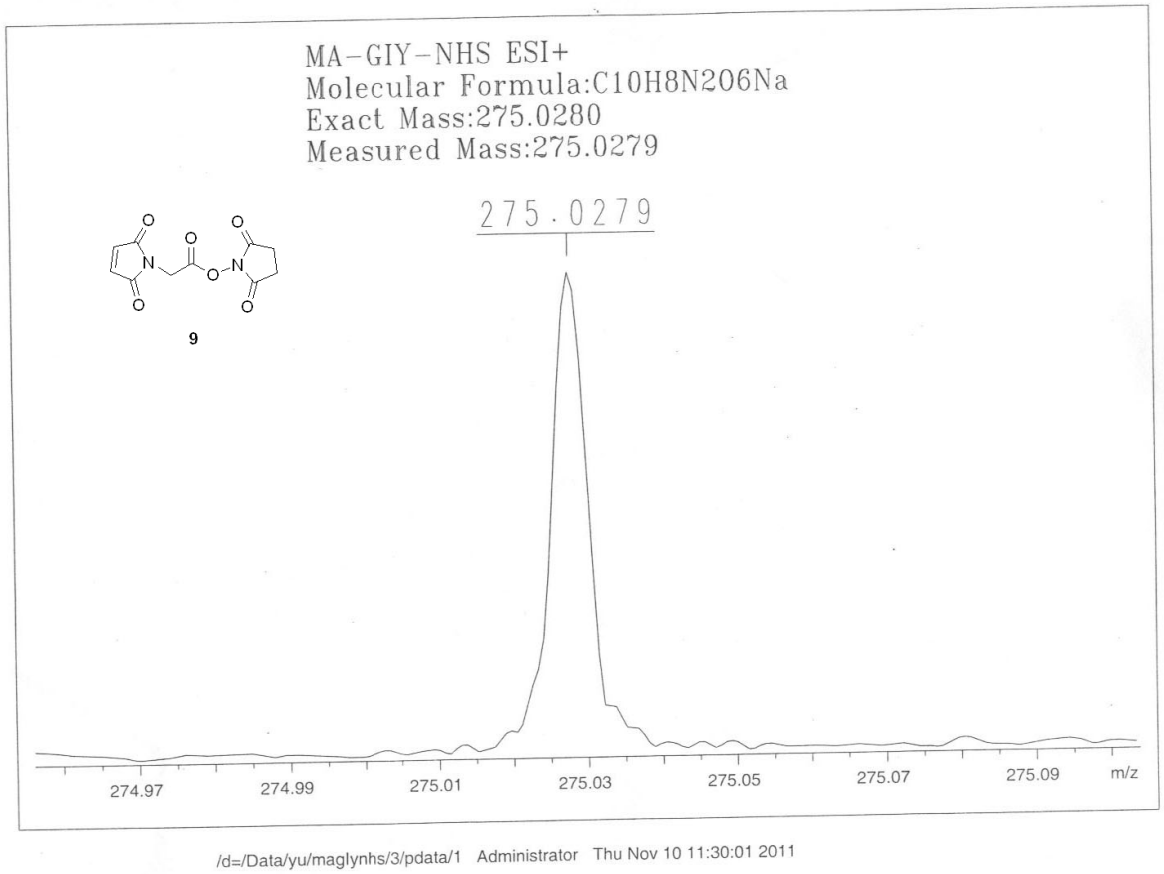
MA-GIY-NHS ESI+
Molecular Formula:C10H8N2O6Na
Exact Mass:275.0280
Measured Mass:275.0279
275.0279
9
274.97
274.99
275.01
275.03
275.05
275.07
275.09
m/z
/d=/Data/yu/maglynhs/3/pdata/1 Administrator Thu Nov 10 11:30:01 2011

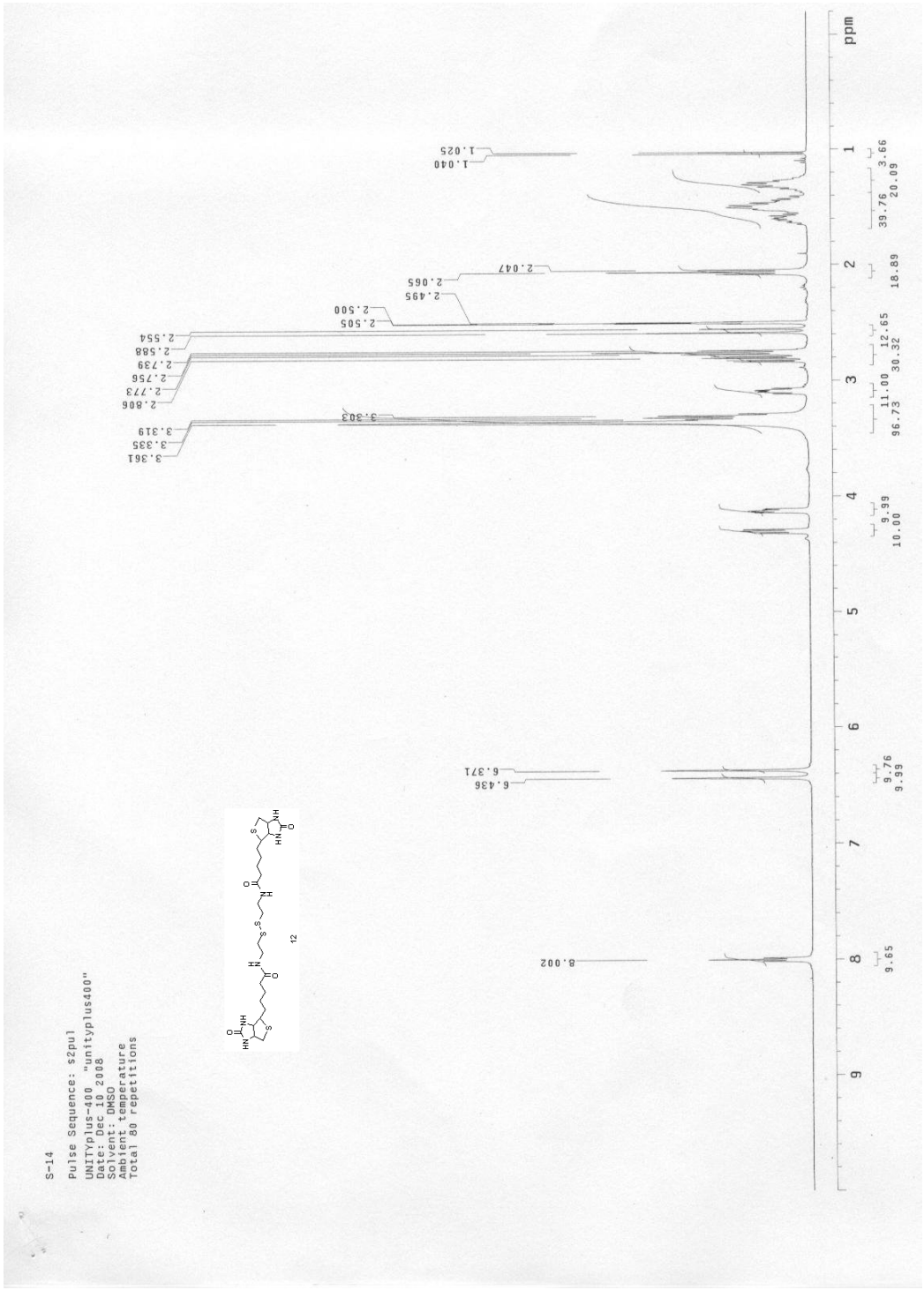
S-14
Pulse Sequence: s2pul
UNITYplus-400 "unityplus400"
Date: Dec 10 2008
Solvent: DMSO
Ambient temperature
Total 80 repetitions
12
ppm
8.002
6.436
6.371
3.361
3.335
3.319
3.303
2.806
2.773
2.756
2.739
2.588
2.554
2.505
2.500
2.495
2.065
2.047
1.040
1.025

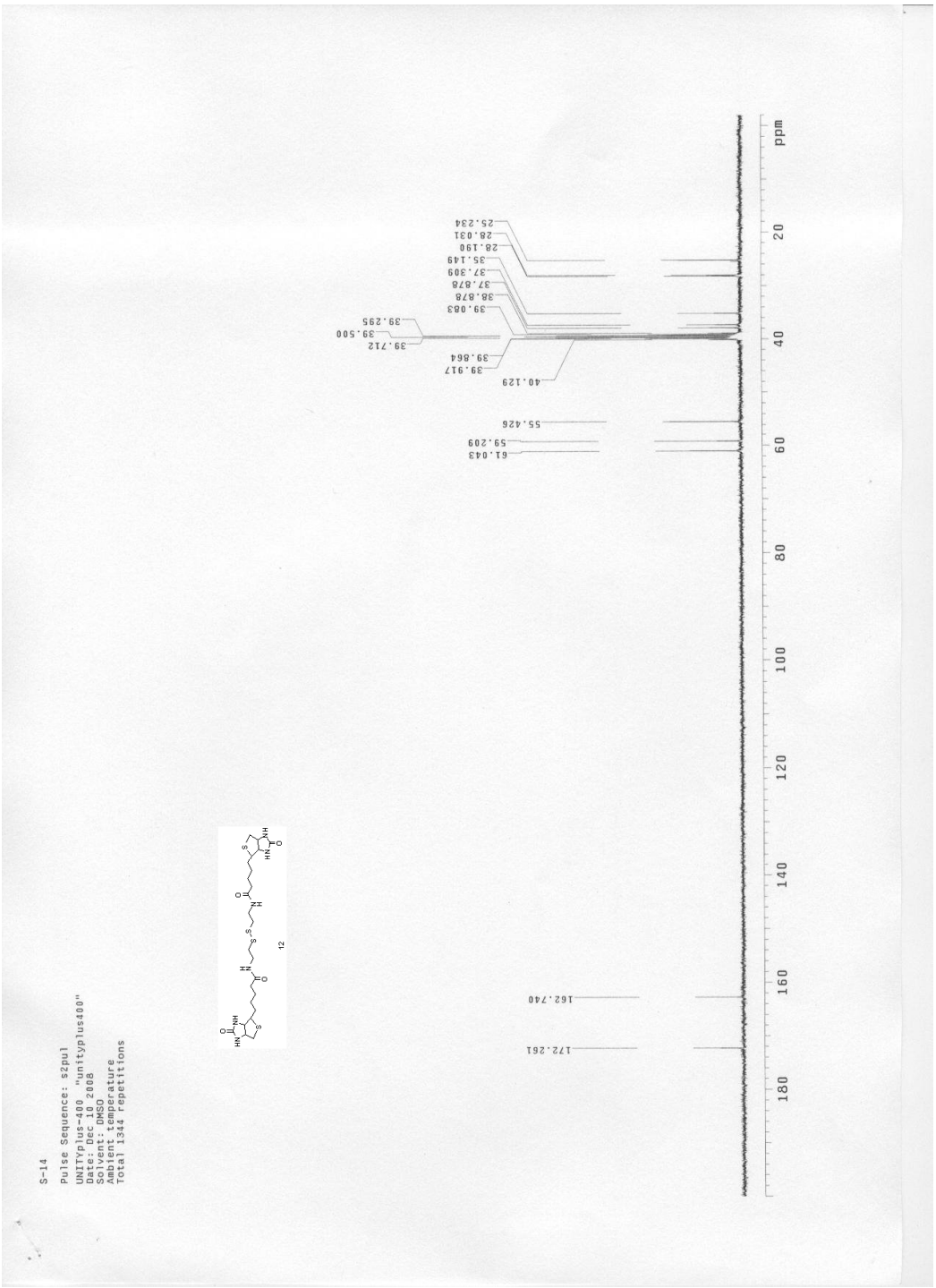
S-14
Pulse Sequence: s2pul
UNITYplus-400 "unityplus400"
Date_ 10 Dec 2008
Solvent: DMSO
Ambient temperature
Total 1344 repetitions
172.261
162.740
61.043
59.209
55.426
40.129
39.917
39.664
39.712
39.500
39.295
39.083
38.878
37.878
37.309
35.149
28.190
28.031
25.234
ppm

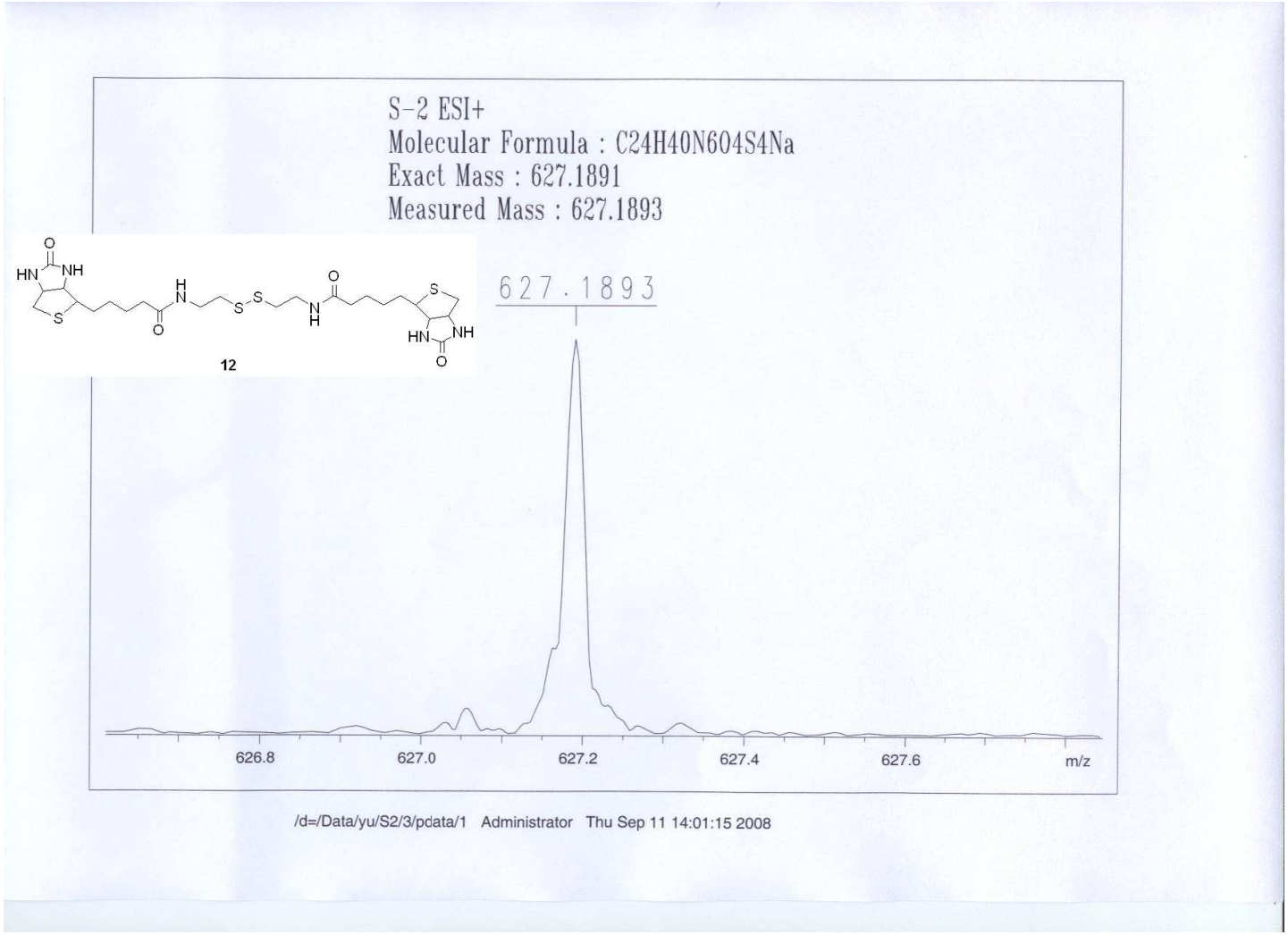
S-2 ESI+
Molecular Formula : C24H40N6O4S4Na
Exact Mass : 627.1891
Measured Mass : 627.1893
627.1893
12
626.8
627.0
627.2
627.4
627.6
m/z
/d=/Data/yu/S2/3/pdata/1 Administrator Thu Sep 11 14:01:15 2008

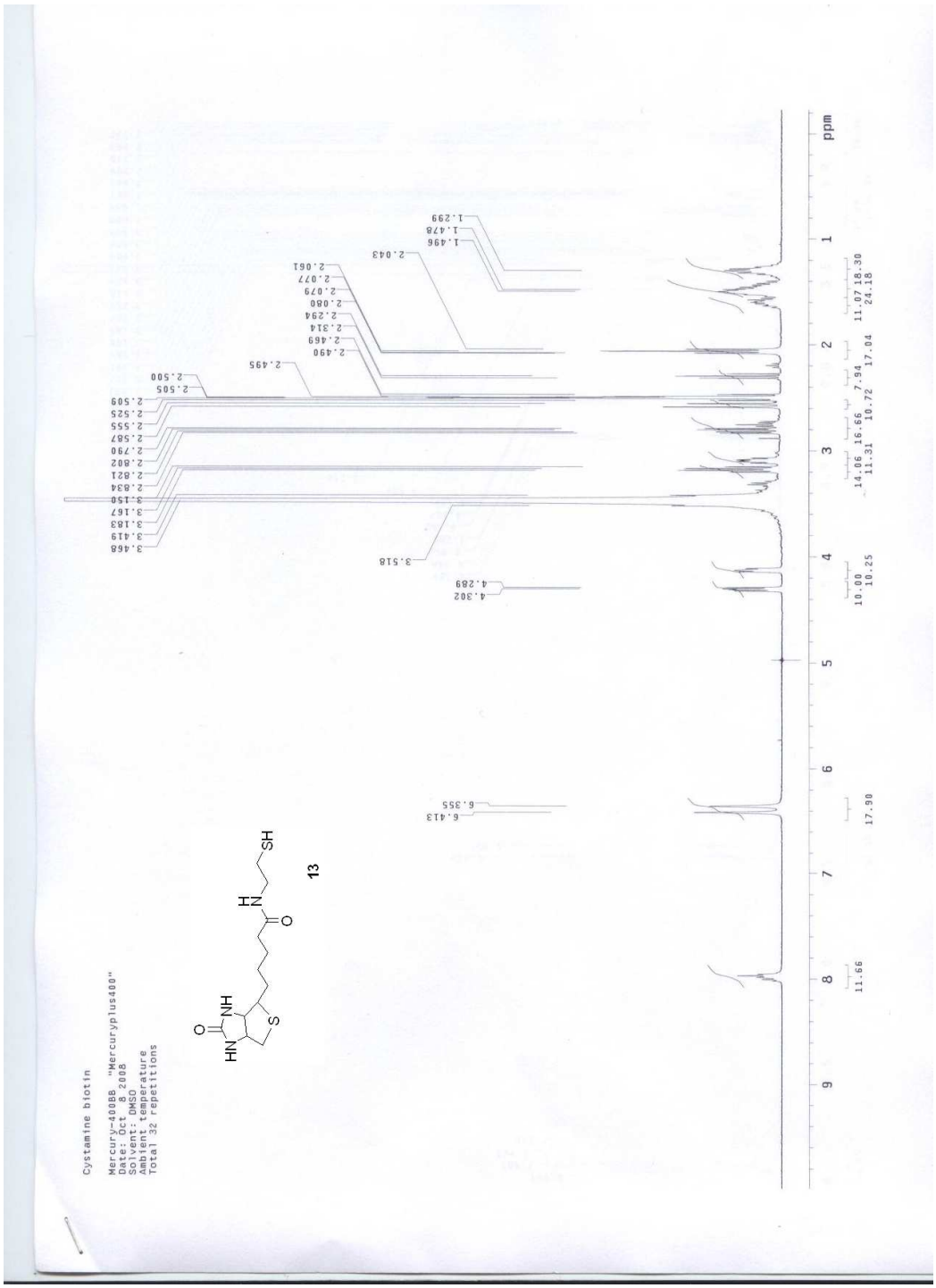
Cystamine biotin
Mercury-400BB "Mercuryplus400"
Date: Oct 8 2008
Solvent: DMSO
Ambient temperature
Total 32 repetitions
13
ppm

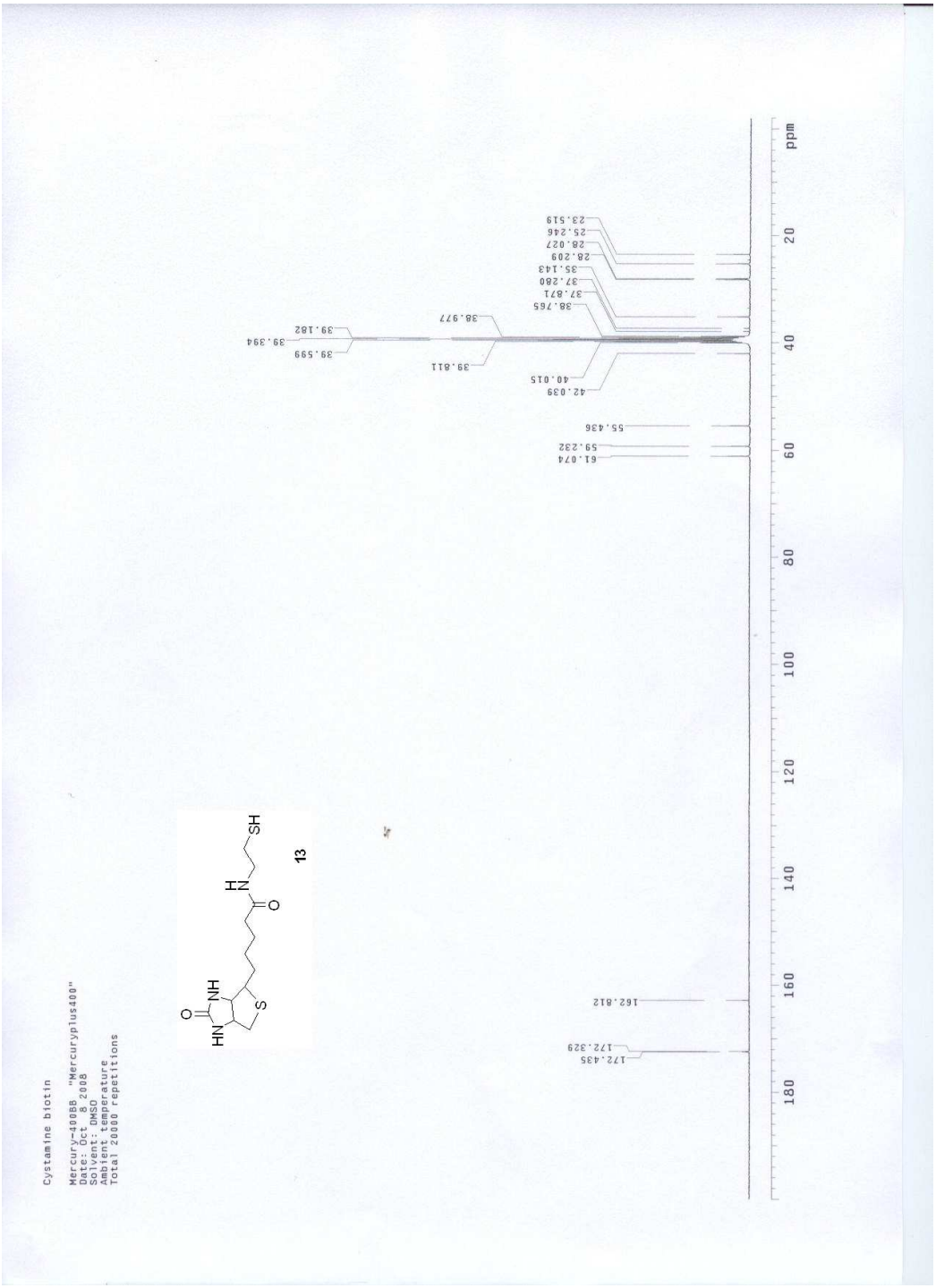
Cystamine biotin
Mercury-400BB "Mercuryplus400"
Date: Oct 8 2008
Solvent: DMSO
Ambient temperature
Total 20000 repetitions
13
ppm
20
40
60
80
100
120
140
160
180
23.519
25.246
28.027
28.209
35.143
37.260
37.671
38.765
38.977
39.182
39.394
39.599
39.811
40.015
42.039
55.436
59.232
61.074
162.812
172.329
172.435

Page: 1

[Theoretical Ion Distribution]
Molecular Formula : C17 H30 O5 N5 S Na
(m/z 439.1865, MW 439.5115, U.S. 6.0)
Base Peak : 439.1865, Averaged MW : 439.5112(a), 439.5122(w)

m/z	INT.	
439.1865	100.0000	**********
440.1893	22.1745	**********
441.1863	7.7799	*****
442.1877	1.3272	*
443.1885	0.1970	
444.1900	0.0229	
445.1915	0.0023	
446.1931	0.0002	

[Elemental Composition] Page: 1

Data : EIHR075 Date : 14-Jan-2009 16:37
Sample: S-15
Note : NBA
Inlet : Direct Ion Mode : FAB+
RT : 0.34 min Scan#: 3
Elements : C 18/0, H 33/0, O 5/0, N 5/0, S 3/0, Na 1/0
Mass Tolerance : 5mmu
Unsaturation (U.S.) : 0.5 - 30.0

Observed m/z	Int%	Err[ppm / mmu]	U.S.	Composition
439.1864	4.6	-0.3 / -0.1	6.0	C 17 H 30 O 5 N 5 S Na

[Theoretical Ion Distribution] Page: 1

Molecular Formula : C17 H30 O5 N5 S Na
(m/z 439.1865, MW 439.5115, U.S. 6.0)
Base Peak : 439.1865, Averaged MW : 439.5112(a), 439.5122(w)

m/z	INT.	
439.1865	100.0000	**********
440.1893	22.1745	**********
441.1863	7.7799	*****
442.1877	1.3272	*
443.1885	0.1970	
444.1900	0.0229	
445.1915	0.0023	
446.1931	0.0002	

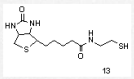

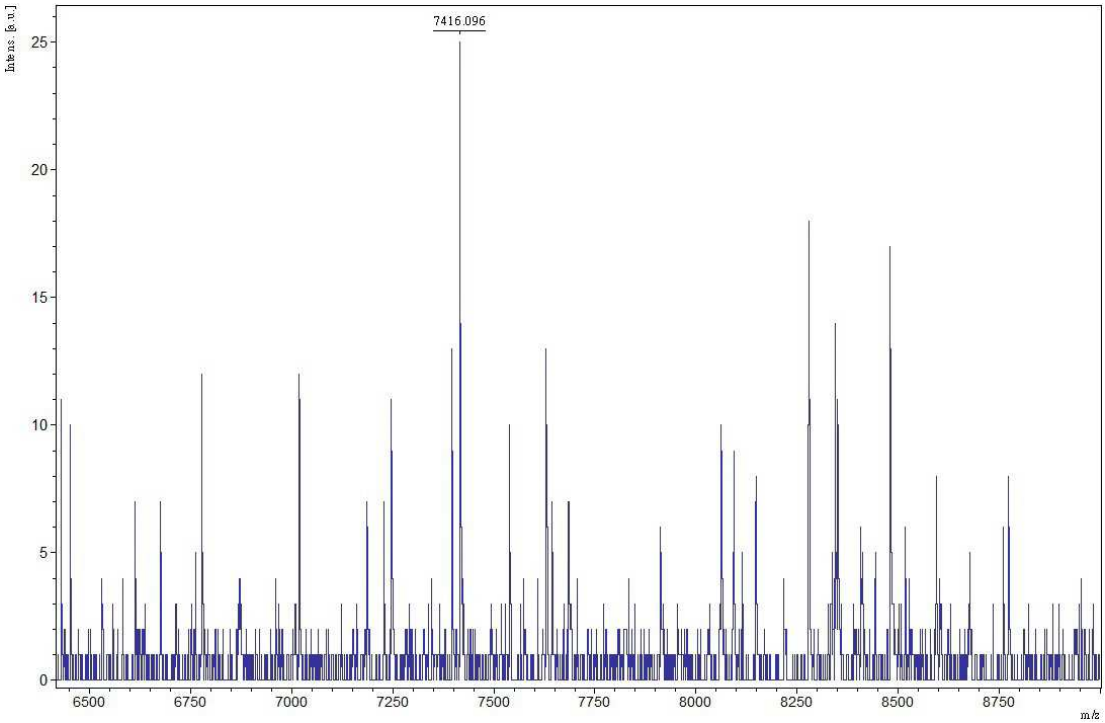

The MALDI-TOF MS spectrum of the 3' primer DNA-the Tat_{48-57} peptide conjugate, $[M+H]^+$ = 7416.096

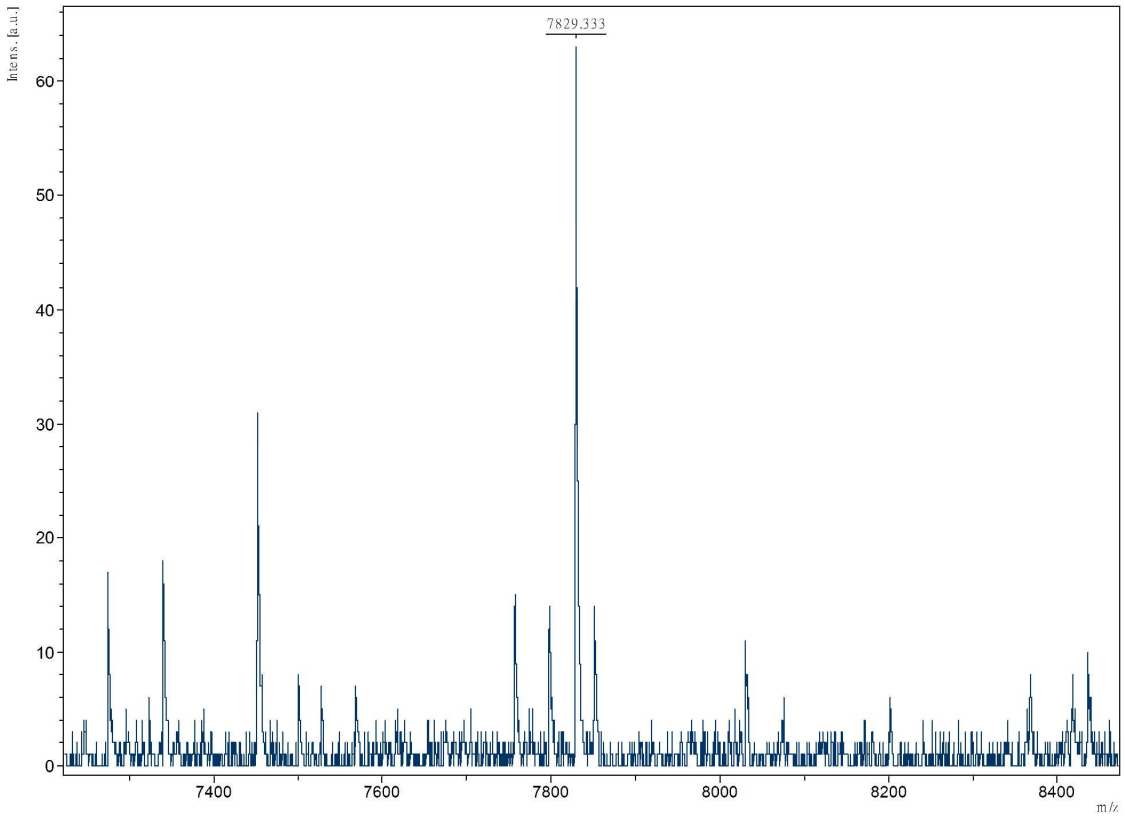

The MALDI-TOF MS spectrum of the 3' primer DNA-the $C(KFF)_3K$ peptide conjugate, $[M+Na]^+ = 7829.333$

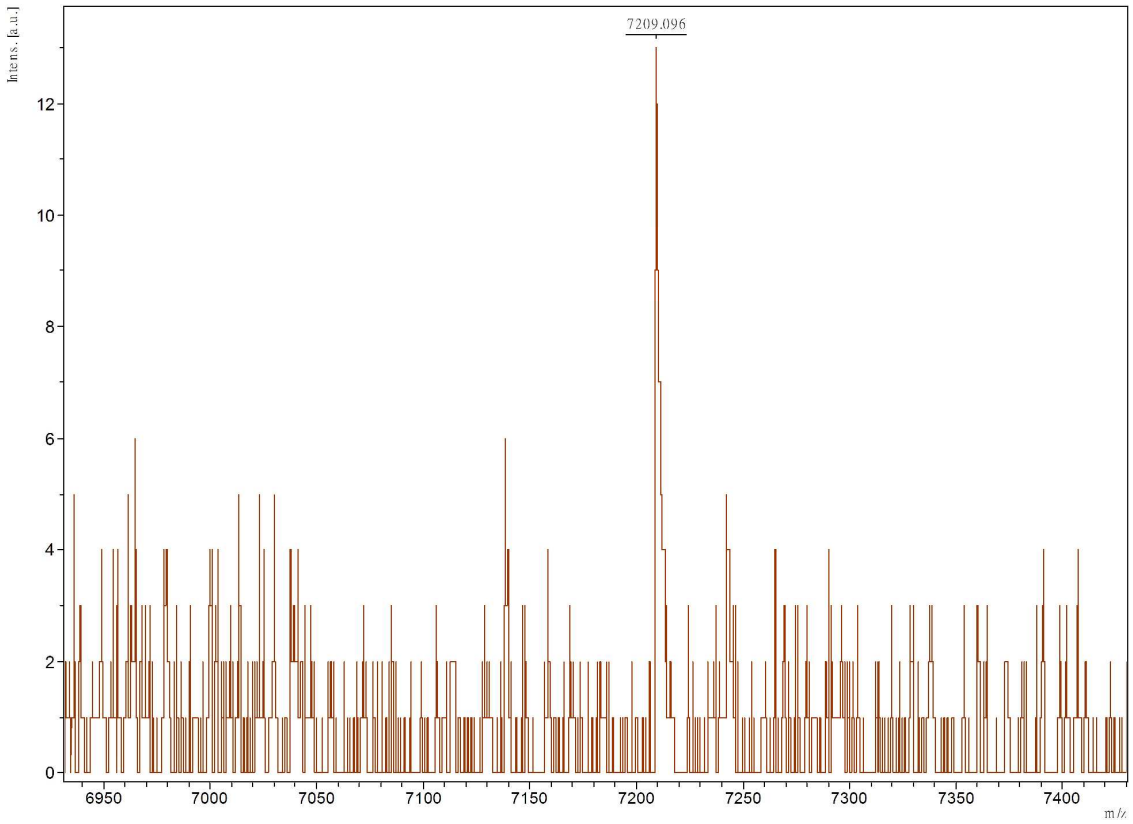

The MALDI-TOF MS spectrum of the $TW17_{1\text{-}17}$ RNA-the $C(KFF)_3K$ peptide conjugate, $[M+Na]^+ = 7209.096$

Bioconjugate Chemistry

Article

pubs.acs.org/bc

Two-Color Fluorescent L-Amino Acid Mimic of Tryptophan for Probing Peptide–Nucleic Acid Complexes

Aleksandr V. Strizhak,[‡,§,†] Viktoriia Y. Postupalenko,[‡,§] Volodymyr V. Shvadchak,[§] Nelly Morellet,[⊥] Eric Guittet,[⊥] Vasyl G. Pivovarenko,[†,§] Andrey S. Klymchenko,*[,§] and Yves Mély*[,§]

[§]Laboratoire de Biophotonique et Pharmacologie, UMR 7213 CNRS, Université de Strasbourg, Faculté de Pharmacie, 67401 Illkirch, France

[†]Department of Chemistry, National Taras Shevchenko University of Kyiv, 01601 Kyiv, Ukraine

[⊥]CNRS UPR 2301, Chimie et biochimie structurales, Institut de Chimie des Substances Naturelles, Centre de recherche de Gif-sur-Yvette, 91190 Gif-sur-Yvette, France

Supporting Information

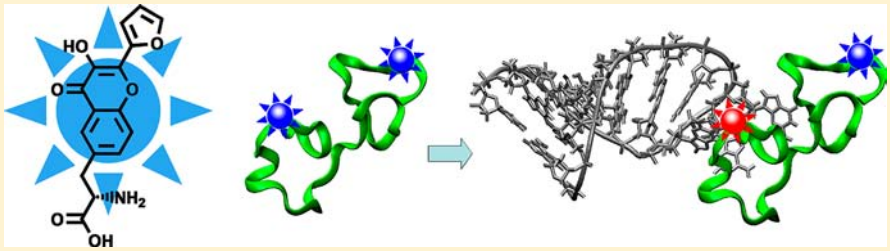

ABSTRACT: Non-natural amino acids are important tools for site-selective probing of peptide properties and interactions. Here, for the first time a fluorescent L-amino acid, exhibiting excited-state intramolecular proton transfer (ESIPT) and hydration-sensitive dual emission, was synthesized. It is an analogue of L-tryptophan bearing a slightly larger 2-(2-furyl)-3-hydroxychromone aromatic moiety instead of indole. This new amino acid was incorporated through solid-phase synthesis into NC(11−55), the zinc finger domain of the HIV-1 nucleocapsid protein, that exhibits potent nucleic acid chaperone properties. It was substituted for the Trp37 and Ala30 residues, located in the distal finger motif and the linker between the fingers of NC(11−55), respectively. Though the highly conserved Trp37 residue plays a key role in NC(11−55) structure and activity, its substitution for the new fluorescent analogue preserved the folding, the nucleic acid binding and chaperone activity of the peptide, indicating that the new amino acid can conservatively substitute Trp residues. In the presence of oligonucleotides, the Trp37-substituted peptide, but not the Ala30 variant, showed strong changes of the dual emission corresponding to local dehydration. The results are in line with NMR data, suggesting that the fluorescent amino acid interacts similarly to Trp37 with the nucleobases and is thus screened from water. Due to the exceptional sensitivity of its ESIPT fluorophore to hydration in highly polar environment, the new amino acid appears as a promising tool for substituting Trp residues and site-selectively investigating peptide−nucleic acid complexes.

INTRODUCTION

Non-natural amino acids are important tools to investigate peptides and proteins, since they can be incorporated at any position, and thus serve as local probes for site-selective monitoring of protein properties and functions. Probably, the most popular ones are those bearing fluorine[1−4] and dyes[5−7] used with NMR and fluorescence techniques, respectively. Fluorescent amino acids are particularly attractive, due to the ultimate sensitivity of fluorescence-based methods. Since the natural fluorescent amino acid tryptophan suffers from poor fluorescence properties, continuous efforts have been made to design amino acids with improved fluorophores.[5−7] Of special interest in this respect are environmentally sensitive (or solvatochromic) fluorophores, which change their emission properties in response to changes in their environment.[7,8] Biomolecular interactions commonly decrease the polarity at the labeling site due to screening from water and, thus, can be readily monitored by environmentally sensitive fluorescent amino acids.[7] For instance, a Prodan-based amino acid was used for monitoring the interaction of S-peptide with ribonuclease S[9] and δ-opioid receptor with antagonists[10] and to estimate the local dielectric constant of the B1 domain of the staphylococcal protein G.[5] Moreover, an amino acid based on 4-dimethylaminophthalimide (4-DMAP) fluorophore was applied to sense binding of labeled octapeptides to the 14−3−3bp protein.[11] Finally, improved analogues of 4-DMAP, such as 6-dimethylaminonaphthalimide, were recently applied to investigate the SH2 phosphotyrosine binding domains,[12] major histocompatibility complexes (MHC) at the cell surface,[7] and peptide−calmodulin interactions.[13] Despite the importance of

Received: August 24, 2012
Revised: October 20, 2012
Published: November 16, 2012

 © 2012 American Chemical Society

environmentally sensitive fluorescent amino acids in biomolecular research, their examples are limited.

Moreover, most examples are focused on protein−protein interactions,[7] while applications of fluorescent amino acids for sensing peptide−oligonucleotide (ODNs) interactions have been poorly explored (Figure 1A). To address this problem, we

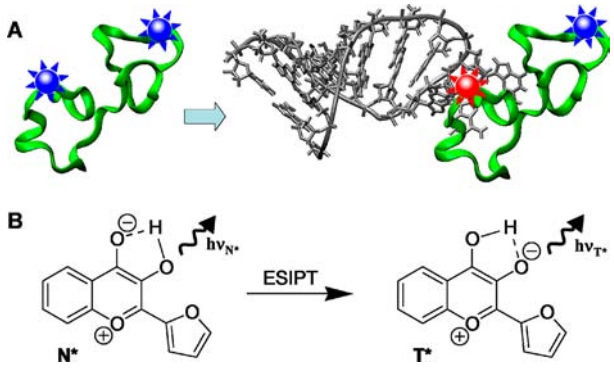

Figure 1. Monitoring of peptide/oligonucleotide interaction using solvatochromic fluorescent amino acid. (A) Principle: the interaction of the labeled peptide (in green) with oligonucleotides changes the fluorescence intensity and color of the label. (B) ESIPT reaction in 2-(2-furyl)-3-hydroxychromone dye.

selected 3-hydroxychromone (3HC) fluorophores which undergo excited-state intramolecular proton transfer (ESIPT),[14] resulting in the emission of both a normal (N*) excited state and an ESIPT product tautomer (T*) (Figure 1B). The dual emission of 3HC dyes is highly sensitive to polarity and H-bonding interactions.[8,15−23] The 2-(2-furyl)-3-hydroxychromone (FHC) label is particularly interesting due to the high sensitivity of its dual emission to polar environments.[15,17,24,25] Being attached to the N-terminus of peptides and oligocations, it shows strong changes in its dual emission upon interaction with ODNs,[26,27] and allows quantification of water content in its surrounding.[28] This prompted us to develop an L-amino acid based on the FHC fluorophore.

As a target protein for labeling, we selected the nucleocapsid protein (NC) of the human immunodeficiency virus, type 1 (HIV-1), which plays a crucial role in the viral life cycle.[29,30] NC is a small (55 amino acids) basic protein, characterized by two rigid zinc fingers connected by a flexible basic linker and flanked by poorly folded N- and C-terminal basic domains.[31,32] NC binds both specifically[33−38] and nonspecifically,[35,39−41] to a large range of nucleic acid sequences. Specific binding is mainly mediated through the folded finger motifs, with a key role being played by the hydrophobic residues forming a hydrophobic platform at the top of the folded fingers.[34,36,38] This hydrophobic plateau also plays a key role in the nucleic acid chaperone properties of NC, which direct the structural rearrangement of ODNs into their most stable conformation and promote the annealing of complementary ODN sequences through specific pathways.[42−44] Within this hydrophobic plateau, the Trp37 residue plays a particularly important role, since its substitution by a nonaromatic residue leads to a dramatic decrease in ODN affinity,[35,40,45] a complete loss in the highly specific ODN destabilization component of the NC chaperone properties,[40,42] as well as a complete loss of HIV-1 infectivity.[46] In the present work, we synthesized an L-amino acid analogue based on 2-(2-furyl)-3-hydroxychromone dye through an original route from L-tyrosine. It was then incorporated at two different positions of the NC(11−55), inside and outside of its fingers, which allowed us to site-selectively investigate its interaction with ODNs. Remarkably, substitution of Trp residue for the new amino acid marginally alters the folding as well as the nucleic acid binding and chaperone activity of the peptide, indicating that this new amino acid could be used as a Trp mimic. The ODNs selected for binding (Figure S1, Supporting Information) to the labeled peptides were SL2 and SL3, two stem-loops of the HIV-1 RNA encapsidation sequence[33,35,38] and ΔP(-)PBS, the cDNA copy of the primer binding site, deleted of its 5′ overhang.[36] These three ODNs bind NC with high affinity and 1:1 stoichiometry, and their structures in complex with NC are known.[34,36,38] The results showed that this amino acid allows probing of protein sites responsible for DNA binding.

MATERIALS AND METHODS

All the solvents and chemicals were purchased from Sigma-Aldrich Chemical Co. For absorption and fluorescence studies, the solvents were of spectroscopic grade. ΔP(-)PBS DNA, SL2, and SL3 RNAs were synthesized and HPLC-purified by IBA GmbH (Germany). Concentrations of the ODNs were calculated from their absorbance using the molar extinction coefficients at 260 nm provided by the supplier.

NMR spectra were recorded on a 400 and 500 MHz BrukerAvance III, BBFO+ at room temperature. Mass spectra were obtained on a Bruker HCT Ultra and Agilent Technologies Accurate-Mass Q-TOF LC/MS 6520 mass spectrometers.

Synthesis of Fmoc-3HCaa. The synthesis of compounds **1** and **2** (Scheme S1) was performed as described previously.[47,48]

*N-(tert-Butoxycarbonyl)-3-[(2E)-3-(2-furyl)prop-2-enoyl]-L-tyrosine (**3**).* 6.425 g (19.89 mmol) of 3-acetyl-*N*-(*tert*-butoxycarbonyl)-L-tyrosine **2** was dissolved in 48 mL of ethanol upon stirring under Ar atmosphere. To the reaction mixture, 48 mL of degassed 25% solution of sodium hydroxide was added upon cooling in a cold water bath. Then, 2.409 g of furfural (25.09 mmol, 1.26 equiv) was added and the mixture was stirred for 12 h at RT under Ar. Additional 0.5 g of furfural was added and the mixture was stirred overnight. The reaction mixture was acidified with HCl and diluted twice with water. The formed precipitate was filtered and washed with diluted ethanol and water, dried, and used in the next step without further purification. Yield 7.62 g (95%) of chalcone **3** as a yellow powder. ^{1}H NMR (500 MHz, MeOD) δ 1.33 (s, 9H), 2.87−2.92 (dd, J = 13.9 Hz, J = 8.85 Hz, 1H), 3.16−3.19 (dd, J = 13.9 Hz, J = 4.43 Hz, 1H), 4.31−4.34 (dd, J = 8.85 Hz, J = 4.43 Hz, 1H), 6.61−6.62 (dd, J = 3.16 Hz, J = 1.89 Hz, 1H), 6.87−6.89 (d, J = 8.21 Hz, 1H), 6.94 (d, J = 3.8 Hz, 1H), 7.39−7.41 (dd, J = 8.22 Hz, J = 1.9 Hz, 1H), 7.64−7.71 (dd, J = 15.16 Hz, J = 4.42 Hz, 2H), 7.71 (d, J = 1.9 Hz, 1H), 7.86−7.87 (d, J = 1.9 Hz, 1H). ^{13}C NMR (500 MHz, MeOD) δ 28.66, 38.11, 55.49, 80.47, 114.01, 118.33, 118.84, 119.02, 120.97, 129.45, 131.65, 132.31, 138.58, 147.17, 152.98, 157.68, 163.09, 175.69, 194.74 (two carbon signals are absent due to incidental equivalence). HRMS (EI) m/z calcd for $C_{21}H_{23}NO_7$ 401.14745, found: 401.147.

*N-(tert-Butoxycarbonyl)-3-[2-(2-furyl)-3-hydroxy-4-oxo-4H-chromen-6-yl]-L-alanine (**4**).* 7.62 g (19 mmol) of chalcone **3** was dissolved in 75 mL of ethanol, cooled in an ice bath. Then, 75 mL of 1 M solution of sodium hydroxide was added with stirring. Next, 4.73 mL (41.8 mmol) of 30% hydrogen peroxide was added and the mixture was stirred in ice bath for 4

h. The reaction was monitored by TLC (silica, EtOAc/MeOH 9:1). After completing the reaction, the mixture was acidified and the formed precipitate was filtered. Yield of the crude 3-hydroxychromone **4** was 3.56 g (45%). It was purified to about 95% purity by crystallization several times from toluene and then from acetonitrile. Final yield ~1.5 g (20%) of yellow crystals. ^{1}H NMR (500 MHz, MeOD) δ 1.33 (s, 9H), 2.98−3.03 (dd, J = 13.9 Hz, J = 9.48 Hz, 1H), 3.26−3.30 (m, J = 5.05 Hz, 1H), 4.36−4.39 (dd, J = 9.48 Hz, J = 5.05 Hz, 1H), 6.67 (m, 1H), 7.33 (d, J = 3.16 Hz, 1H), 7.51−7.53 (d, J = 8.85 Hz, 1H), 7.60−7.62 (d, J = 8.85 Hz, 1H), 7.78 (s, 1H), 7.97 (d, J = 1.27 Hz, 1H). ^{13}C NMR (500 MHz, MeOD) δ 28.6, 38.27, 56.26, 80.52, 113.58, 116.91, 119.29, 122.83, 126.26, 135.77, 135.97, 138.44, 141.29, 145.86, 146.08, 155.09, 157.77, 173.81, 175.11 (two carbon signals are absent due to incidental equivalence). HRMS (EI) m/z calcd for $C_{21}H_{21}NO_8$ 415.12672, found: 415.12659.

*3-[2-(2-Furyl)-3-hydroxy-4-oxo-4H-chromen-6-yl]-L-alanine Hydrochloride (**5**).* 944 mg of 3-hydroxychromone **4** was dissolved in 10 mL of dioxane. Then, 10 mL of conc. HCl was added to the reaction mixture in cold water bath. After 5−10 min, the bath was removed and the mixture was stirred for 2−3 h. The reaction mixture was concentrated under reduced pressure to give the desired product **5** as a dark yellow powder, yield 0.769 g (96%). ^{1}H NMR (500 MHz, MeOD) δ 3.28−3.34 (dd, J = 14.56 Hz, J = 7.78 Hz, 1H), 3.42−3.48 (dd, J = 14.56 Hz, J = 5.77 Hz, 1H), 4.34−4.37 (dd, J = 7.53 Hz, J = 5.77 Hz, 1H), 6.7−6.72 (dd, J = 3.52 Hz, J = 1.76 Hz, 1H), 7.37−7.38 (d, J = 3.51 Hz, 1H), 7.63−7.65 (d, J = 8.79 Hz, 1H), 7.68−7.71 (dd, J = 8.79 Hz, J = 2.26 Hz, 1H), 7.81−7.82 (d, J = 1.00 Hz, 1H), 8.05−8.06 (d, J = 1.76 Hz, 1H). ^{13}C NMR (500 MHz, MeOD) δ 36.74, 54.95, 113.70, 117.23, 120.29, 123.34, 126.81, 132.56, 135.79, 138.64, 141.67, 145.83, 146.33, 155.71, 171.00, 173.74. HRMS (EI) m/z calcd for $C_{16}H_{13}NO_6$ 315.07429, found: 315.07419.

*N-[(9H-Fluoren-9-ylmethoxy)carbonyl]-3-[2-(2-furyl)-3-hydroxy-4-oxo-4H-chromen-6-yl]-L-alanine (**6**).* 614 mg (1.744 mmol) of amino acid hydrochloride **5** was dissolved in a solution of 500 mg (5.95 mmol) of sodium bicarbonate in 10 mL of water. Then, 30 mL of acetonitrile and 588 mg (1 equiv) of FmocOSu were added and the mixture was stirred for 24 h. The reaction mixture was filtered and the precipitate was dissolved in hot water (about 100 mL per 1 g) with further acidification with HCl. Yield: 900 mg (96%) of yellow powder. ^{1}H NMR (500 MHz, DMSO-d_6) δ 3.00−3.05 (m, 1H), 3.22−3.26 (dd, J = 14.04 Hz, J = 4.27 Hz, 1H), 4.12−4.19 (m, 3H), 4.26−4.30 (m, 1H), 6.77−6.78 (dd, J = 3.05 Hz, J = 1.83 Hz,1H), 7.21−7.25 (m, 2H), 7.27−7.28 (d, J = 3.05 Hz, 1H), 7.34−7.37 (t, J = 7.32 Hz, 2H), 7.57−7.58 (d, J = 7.32 Hz, 2H), 7.59−7.61 (d, J = 8.55 Hz, 1H), 7.68−7.70 (d, J = 8.55 Hz, 1H), 7.75−7.76 (d, J = 8.55 Hz, 1H), 7.82−7.83 (d, J = 7.32 Hz, 2H), 8.01 (s, 1H), 8.04 (s, 1H), 9.88 (s, 1H), 12.76 (br s, 1H). ^{13}C NMR (500 MHz, DMSO-d_6) δ 35.80, 46.54, 55.39, 65.64, 112.82, 115.27, 118.03, 120.04, 121.56, 124.95, 125.11, 125.18, 126.98, 127.55, 134.68, 137.20, 139.19, 140.63, 143.67, 144.09, 145.17, 152.96, 156.01, 171.78, 173.07 (six carbon signals are absent due to incidental equivalence). HRMS (EI) m/z calcd for $C_{31}H_{23}NO_8$ 537.14237, found: 537.14187.

Proof of Optical Purity. To test the enantiomeric purity of the obtained chromone-amino acid derivative, we prepared the dibenzyl ether ester of the amino acid, which was acylated by two enantiomers of Mosher's acid chloride to give compounds **9** and **10** (Scheme S1). The NMR spectra of the diastereomeric Mosher amides were then compared. No signal of the second diastereomer was found in each spectrum.

*Benzyl 3-[3-(Benzyloxy)-2-(2-furyl)-4-oxo-4H-chromen-6-yl]-N-[(2S)-3,3,3-trifluoro-2-methoxy-2-phenylpropanoyl]-L-alaninate (**9**).* ^{1}H NMR (400 MHz, $CDCl_3$) δ 3.14−3.19 (dd, J = 14.24 Hz, J = 7.12 Hz, 1H), 3.20 (s, 3H), 3.24−3.29 (dd, J = 14.24 Hz, J = 5.60 Hz, 1H), 4.89−4.94 (dd, J = 14.25 Hz, J = 6.62 Hz, 1H), 5.05−5.08 (d, J = 12.21 Hz, 1H), 5.11−5.14 (d, J = 12.21 Hz, 1H), 5.24 (s, 2H), 6.48−6.49 (dd, J = 3.56 Hz, J = 1.52 Hz,1H), 7.18−7.44 (m, 17H), 7.59 (d, J = 1.01 Hz, 1H), 7.96 (d, J = 1.53 Hz, 1H). ^{19}F-NMR (376 MHz, $CDCl_3$) δ −69.5 (9), −72.03 (Mosher acid).

*Benzyl 3-[3-(Benzyloxy)-2-(2-furyl)-4-oxo-4H-chromen-6-yl]-N-[(2R)-3,3,3-trifluoro-2-methoxy-2-phenylpropanoyl]-L-alaninate (**10**).* ^{1}H NMR (400 MHz, $CDCl_3$) δ 3.02−3.07 (dd, J = 14.05 Hz, J = 7.53 Hz, 1H), 3.16−3.21 (dd, J = 14.05 Hz, J = 5.52 Hz, 1H), 3.35 (d, J = 1.50 Hz, 3H), 4.94−5.00 (m, J = 5.52 Hz, J = 7.28 Hz,1H), 5.07−5.10 (d, J = 12.05 Hz, 1H), 5.14−5.17 (d, J = 12.05 Hz, 1H), 5.20−5.23 (d, J = 10.54 Hz, 1H), 5.23−5.26 (d, J = 10.54 Hz, 1H), 6.49−6.51 (dd, J = 3.52 Hz, J = 1.76 Hz,1H), 7.01−7.04 (dd, J = 8.79 Hz, J = 2.26 Hz, 1H), 7.05−7.07 (d, J = 8.53 Hz, 1H), 7.17−7.32 (m, 15H), 7.42−7.45 (dd, J = 8.29 Hz, J = 1.76 Hz, 1H), 7.60 (dd, J = 1.76 Hz J = 0.75 Hz,, 1H), 7.84 (d, J = 2.26 Hz, 1H). ^{19}F-NMR (376 MHz, $CDCl_3$) δ −69.41(10), −72.03 (Mosher acid).

Peptide Synthesis. The labeled NC(11−55) peptides were synthesized by solid-phase peptide synthesis on a 433A synthesizer (ABI, Foster City, CA), according to a previously established protocol.[49] The synthesis was performed at a 0.1 mmol scale using the standard fluorenylmethoxycarbonyl (Fmoc)-amino acid-coupling protocol starting from 0.44 mmol/g Wang LL resin. At selected positions of the peptide, the fluorescent amino acid analogue was incorporated by the following procedure. In a flask, 2−4 mol equiv of the Fmoc-3HCaa were mixed with 4 equiv of HBTU/HOBt coupling solution (in DMF) and 5 equiv of DIEA. This mixture was immediately added to the peptidyl resin and shaken at 37 °C for 12 h. Then, the resin was washed with 1-methyl-2-pyrrolidone (NMP) and peptide synthesis was continued on the synthesizer. At the end of the synthesis, the Fmoc-deprotected peptidyl resin was isolated and washed with NMP, methanol, and dichloromethane.

Cleavage of the peptidyl resin and deprotection were performed for 2 h using a 10 mL trifluoroacetic acid (TFA) solution containing water (5%, v/v), phenol (2%, w/v), thioanisole (5%, v/v), triisopropylsilane (2.5%, v/v), and ethanedithiol (2.5%, v/v). The peptide was precipitated using ice-cold diethyl ether and pelleted by centrifugation. The pellet was air-dried for approximately 15 min, solubilized with aqueous TFA (0.05%, v/v), and lyophilized. Purification by HPLC was carried out on a C8 column (uptisphere 300 Å, 5 μm; 250 × 10, Interchim, France) in water/acetonitrile mixture containing 0.05% TFA with a linear gradient 10−35% of acetonitrile for 30 min and monitored at 210 and 360 nm (3HC dye absorption). Obtained peptides were characterized by ESI-MS analysis. NC(11−55)-W37-3HCaa peptide: calculated M = 5245.40, found $[M+7H]^{7+}$ = 750.64 corresponding to M = 5245.38 after deconvolution; NC(11−55)-A30-3HCaa peptide: calculated M = 5360.43, found $[M+7H]^{7+}$ = 767.06 corresponding to M = 5360.37 after deconvolution.

Preparation of Zn-Bound Peptides. Lyophilized labeled peptides were dissolved in water (~0.5 mg in 500 μL). Then, about 10 μL of this solution was used to determine the peptide

Scheme 1. Synthesis of the Fluorescent Amino Acid and the Labeled Peptides[a]

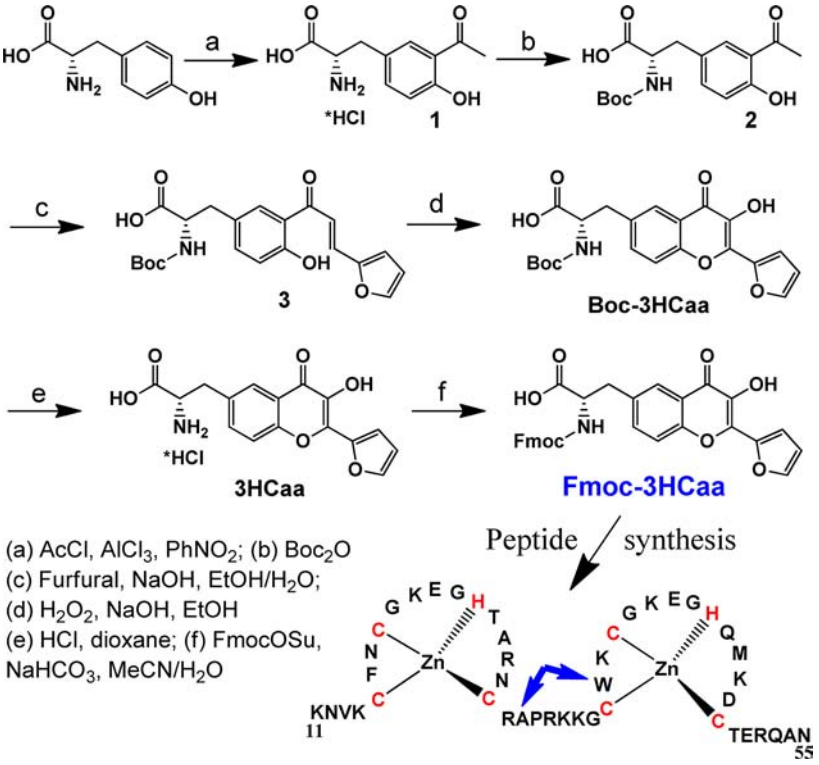

[a]The substituted positions of the NC(11-55) peptide are shown by blue arrows.

concentration using an extinction coefficient of 15 000 $M^{-1} \times cm^{-1}$ at 350 nm. Next, 2 mol equiv of $ZnSO_4$ was added to the peptide and pH was raised to its final value, by adding buffer. This last step was done only at the end to prevent peptide oxidization. Noticeably, a large excess of Zn^{2+} ions should be avoided since this ion could affect the 3HC fluorescence.

NMR Structural Studies. The two NC(11−55) conjugates at 0.5 mM concentration in neat water, pH 6.5 at 293 K, were studied on an Avance Bruker spectrometer operating at 600.13 MHz equipped with a cryoprobe. A mixing time of 200 ms and a water gate pulse program for water signal suppression in NOESY experiments were used.

Spectroscopic Measurements. Unless otherwise indicated, the experiments were performed in 10 mM phosphate buffer, pH 6.5, 30 mM NaCl, at 20 °C. This low pH was used to prevent deprotonation of the 3-hydroxy group of the 3HC amino acid. Absorption spectra were recorded with a Cary 4000 UV−visible spectrophotometer (Varian). Fluorescence spectra were recorded on FluoroMax3 and FluoroLog spectrofluorimeters (Jobin Yvon) equipped with thermostatted cell compartments. Fluorescence spectra were corrected for Raman scattering. Quantum yields were calculated using quinine sulfate in 0.5 M sulfuric acid (quantum yield, φ = 0.577) as a reference.[50] Excitation wavelength was 350 nm for 3HCaa.

To determine the affinity of the labeled peptides for the ODNs, fixed amounts of the ODN were titrated with peptides by monitoring the two-band fluorescence of the labeled peptides. For each data point, the emission of the same concentration of labeled peptide in buffer was subtracted from the signal measured in the presence of the ODN. Affinity constants were determined from direct fitting of the corrected signal to the rewritten Scatchard equation

$$I = I_0 - \frac{(I_0 - I_t)}{N_t} \times \left\{ [1 + (P_t + nN_t)K_a] - \sqrt{[1 + (P_t + nN_t)K_a]^2 - 4P_t nN_t K_a^2} \right\} / 2K_a \quad (1)$$

where I and I_t are the signal at a given and a saturating peptide concentration, respectively, I_0 is the signal in the absence of peptide, N_t is the total ODN concentration, P_t is the total concentration of peptide, K_a is the apparent affinity constant, and n is the number of binding sites. The parameters were recovered from nonlinear fits of eq 1 to experimental data sets using the *MicrocalOrigin 6.0* software.

Peptide Activity Tests. The ability of the labeled peptides to destabilize the secondary structure of ODNs was tested using cTAR DNA, the complementary sequence of the trans-activation response element, involved in the minus strand DNA transfer during reverse transcription. To this end, we used a cTAR sequence labeled at its 3′ and 5′ ends by 5(6)-carboxytetramethylrhodamine (TMR) and 4-(4′- methylaminophenylazo) benzoic acid (Dabcyl), respectively. In the absence of NC, cTAR is mainly in a nonfluorescent closed form where the TMR and Dabcyl labels are close together, giving excitonic coupling.[51] The destabilization was measured through the fluorescence intensity increase of TMR in the labeled cTAR as a function of NC(11−55) concentration.[43,52]

The ability of the labeled peptides to promote the annealing of cTAR (55 base hairpin DNA) with its complementary dTAR sequence was compared to that of the unlabeled NC peptide.[53] The kinetic measurements were performed under pseudo-first-order conditions by using unlabeled dTAR at a concentration which was 30-fold higher than the concentration of cTAR labeled with carboxytetramethylrhodamine (TMR) at the 5′

dx.doi.org/10.1021/bc300464u | *Bioconjugate Chem.* 2012, 23, 2434−2443

end and with 5/6-carboxyfluorescein (Fl) at the 3′ end.[53] Excitation and emission wavelengths were 480 and 520 nm, respectively, for monitoring the Fl fluorescence. All reported concentrations correspond to those after mixing. To avoid high local concentrations during mixing, both reactants were mixed at the same volume. Peptides were added to each reactant separately at a peptide/ODN ratio of 3:1, and then, the reaction was initiated by mixing the peptide-coated ODNs together. Experiments were performed in 25 mM Tris, 30 mM NaCl, 0.2 mM $MgCl_2$, pH 7.5 at 20 °C.

RESULTS AND DISCUSSION

To obtain the L-amino acid bearing the 3HC fluorophore, we started with L-tyrosine that was converted into corresponding acetophenone **1** using a described procedure[47,48] based on Fries reaction (Scheme 1). Then, the amino group was protected with the Boc group, and the product **2** was condensed with furaldehyde in the presence of a base. The obtained chalcone **3** was further converted into a 3HC derivative (Boc-3HCaa) using the Algar-Flynn-Oyamada reaction. Then, the Boc group was removed to obtain the desired amino acid (3HCaa). Finally, it was protected with the Fmoc group, which is required for solid-phase peptide synthesis. We checked that the basic conditions used in the synthesis do not alter the optical purity of the obtained amino acid. For this purpose, the obtained Boc-protected amino acid was first benzylated, and then the amino group was deprotected and finally modified with (R)- and (S)-Mosher agents (Scheme S2, Supporting Information). The ^{19}F-NMR spectra of the two products **9** and **10** showed only one fluorine peak corresponding to pure diastereomers, indicating that the synthesis did not produce any racemization. This conclusion was confirmed by ^{1}H NMR spectra of these two diastereomers.

Then, the spectroscopic properties of the new amino acid (Boc-3HCaa) were characterized in different solvents (Figure 2, Table S1, Supporting Information). The absorption and emission maxima of Boc-3HCaa were remarkably close to those reported previously for the basic fluorophore FHC (Table S1),[24] indicating that 6-substitution in this fluorophore did not change its spectroscopic properties. The dual emission of Boc-3HCaa was found to depend strongly on solvent polarity, showing an increase of the relative intensity of the N* band in more polar solvents (Figure 2A) due to an inhibition of the ESIPT reaction.[8] However, it should be noted that the ratio of the two emission bands of Boc-3HCaa in polar protic solvents is considerably lower than that of the parent fluorophore, indicating that the Boc-protected amino acid group partially screens the fluorophore from polar solvents. Therefore, to estimate the local water concentration, we used the calibration curve log(N*/T*) vs water concentration previously reported for the parent FHC dye (Figure 2B).[28]

Using the Fmoc-protected 3HCaa, we then synthesized two labeled NC(11−55) peptides: NC(11−55)-A30-3HCaa and NC(11−55)-W37-3HCaa, where the fluorescent amino acid substituted Ala30 and Trp37 residues, located in the linker and the distal zinc finger, respectively (Scheme 1). Importantly, the 3HCaa was compatible with the standard protocols of peptide synthesis and purification. The NOESY spectra show that the folding of the zinc fingers is maintained in the two labeled NC(11−55) peptides (Figure S2, Supporting Information), since similar medium- and long-distance NOEs were found as for the native peptide. Thus, the incorporated amino acid analogue 3HCaa does not significantly affect the native folding in the two labeled peptides.

Next, we compared the chaperone activity of the labeled peptides with that of the native peptide. First, we checked the ability of the peptides to promote destabilization of DNA stem-loops, such as, for instance, the cTAR sequence involved in the first strand transfer of reverse transcription.[40] This test is particularly important, because substitution of Trp37 in NC(11−55) for a nonaromatic amino acid results in the loss of this component of NC chaperone activity.[40] Remarkably, NC(11−55)-W37-3HCaa showed high destabilization activity, nearly identical to that of the native peptide, while NC(11−55)-A30-3HCaa was less active (Figure 3). Second, we tested the ability of the labeled peptides to promote the annealing of two complementary sequences. Both labeled peptides exhibited similar activities comparable to that of the native peptide (Figure S3, Supporting Information), indicating that this

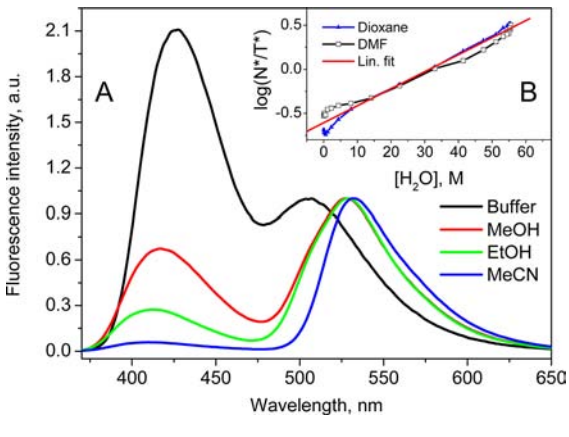

Figure 2. Fluorescence spectra of the Boc-3HCaa derivative in different solvents (A) and dependence of log(N*/T*) of 2-(2-furyl)-3HC (FHC) on water concentration in organic solvents based on previous data[28] (B). In (A), 10 mM phosphate buffer, 30 mM NaCl, pH 6.5 was used. All the spectra were normalized at the T* band. Excitation wavelength was 350 nm. Concentration of Boc-3HCaa was 1 μM.

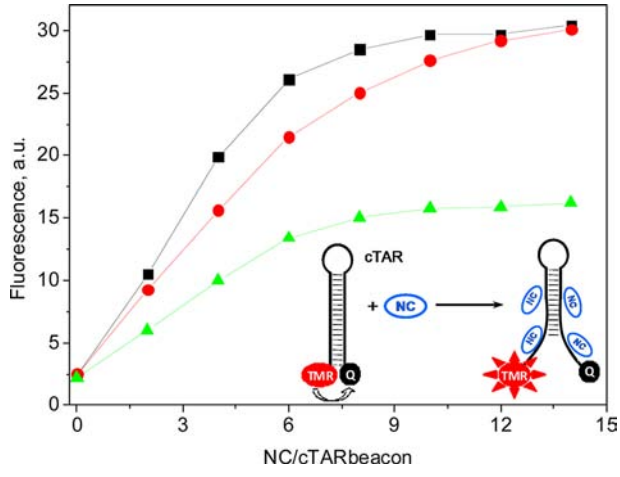

Figure 3. Destabilization of doubly labeled cTAR DNA by NC(11−55) (squares), NC(11−55)-W37-3HCaa (disks), and NC(11−55)-A30-3HCaa (triangles). Titration of 100 nM Dabcyl-5′-cTAR-3′-TMR (cTAR beacon) by NC peptides was performed in 25 mM TRIS (pH 7.5), 30 mM NaCl, and 0.2 mM $MgCl_2$. To monitor TMR fluorescence, excitation wavelength was set at 520 nm.

component of NC chaperone activity is also preserved. The preserved chaperone activity of NC(11−55)-W37-3HCaa shows that the new amino acid does not affect the peptide folding and can functionally substitute the Trp37 residue. We could explain this outstanding feature of the new amino acid by two factors. First, similarly to Trp, 3HCaa bears a flat and relatively small aromatic moiety. Second, the 3HC moiety, due to its compact structure, can easily intercalate within the nucleobases, as was shown in different recent reports.[26,27,54] This property allows the 3HC moiety to mimic the interaction of the Trp37 indole moiety with nucleobases in the complexes of the peptide with nucleic acid sequences.[34−36,38]

Labeled peptides in aqueous solutions (Figure 4) showed dual emission, characteristic of 3HC dyes, where the short- and

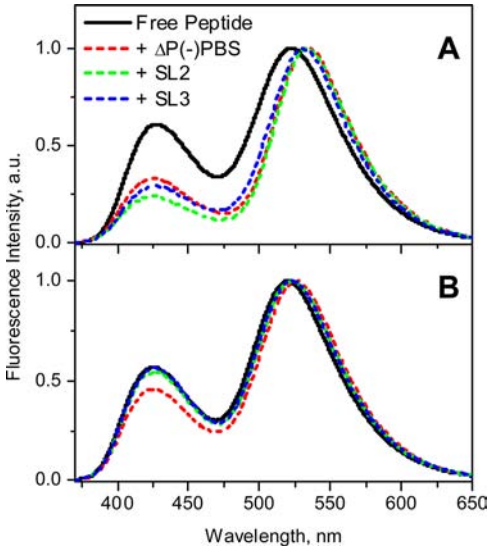

Figure 4. Effect of ODN interaction on the fluorescence spectra of the 3HCaa-labeled NC(11−55) peptides. Fluorescence spectra of NC(11−55)-W37-3HCaa (A) and NC(11−55)-A30-3HCaa (B) were normalized at the T* band. Peptide and ODN concentrations were 1 μM. Measurements were done in 10 mM phosphate buffer, 30 mM NaCl, pH 6.5. Excitation wavelength was 350 nm.

long-wavelength bands can be assigned to N* and T* forms, respectively. The observed intensity ratio of the two emission bands, N*/T*, is close to that for the FHC fluorophore in ethanol (Tables 1 and S1, Supporting Information), indicating that the 3HCaa fluorophore is partially screened from water by the peptide in its folded form. Using a recently developed method,[28] the local water concentration $[H_2O]_L$ of the 3HCaa solvation shell in both peptides was estimated around 31−32 M (Table 1), which corresponds to a water access coefficient W_A for the probe of 0.57 ($W_A = [H_2O]_L/[H_2O]$, where $[H_2O]$ = 55.56 M is the concentration of neat water). This estimation indicates that almost half of the space around the 3HC fluorophore is screened from the bulk water by the peptide backbone.

On interaction with ODNs SL2, SL3, and ΔP(-)PBS, a strong change in the NC(11−55)-W37-3HCaa fluorescence spectrum was observed, with notably a large drop in the N*/T* ratio, a shift of the T* emission maximum to the red (Figures 4 and 5) and a decrease in the fluorescence quantum yield (Table

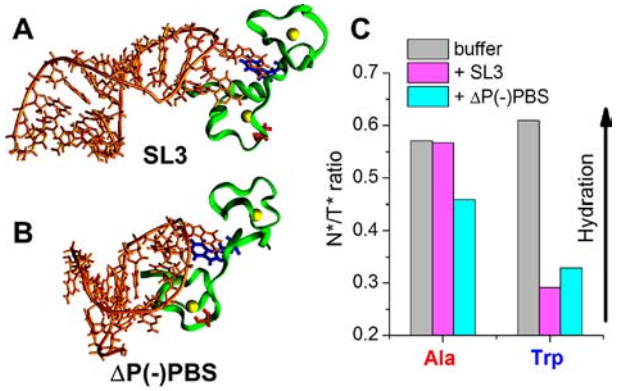

Figure 5. Correlation between the 3D structures of NC-ODN complexes and the response of the 3HCaa-labeled peptides on ODN binding. 3D structures of NC complexes with SL3 (A) and ΔP(-)PBS (B) drawn based on NMR data.[34,36] Only the NC(11−55) part is shown. Zn atoms are represented as yellow spheres; Ala30 and Trp37 residues are in red, and blue, respectively. Fluorescence intensity ratio N*/T* for NC(11−55)-A30-3HCaa (Ala) and NC(11−55)-W37-3HCaa (Trp) peptides in buffer and bound to SL3 or ΔP(-)PBS (C).

1). The drop in the N*/T* ratio can be assigned to a decrease in the local hydration of the 3HCaa environment, with a water access coefficient W_A of the probe dropping to 0.32−0.41 for the three ODNs (Table 1). The observed dehydration is likely connected to the interaction of the 3HC fluorophore with the nucleobases, which leads to an efficient screening of this fluorophore from water.[26,27] Moreover, this conclusion is substantiated by the observed red shift of the T* band[26,27] and is in line with the NMR-derived 3D structures of the NC-ODN complexes (Figure 5), showing that the Trp37 residue strongly

Table 1. Spectroscopic Properties of the 3HCaa-Labeled NC(11-55) Peptides in Complexes with ODNs[a]

peptide	oligo-nucleotide	λ_{ABS} nm	λ_{N*} nm	λ_{T*} nm	N*/T*	$[H_2O]$, M	W_A	QY, %
NC(11−55)-A30−3HCaa	-	364	426	520	0.57	31	0.56	3.7
	ΔP(-) PBS	364	425	526	0.46	27	0.49	2.5
	SL3	363	426	523	0.57	30	0.54	2.5
	SL2	363	426	523	0.54	30	0.54	2.5
NC(11−55)-W37−3HCaa	-	366	427	522	0.61	32	0.58	9.0
	ΔP(-) PBS	367	425	534	0.33	23	0.41	5.1
	SL3	368	427	531	0.29	21	0.38	4.0
	SL2	368	425	533	0.24	18	0.32	4.8

[a] λ_{ABS}, λ_{N*}, and λ_{T*} are the maxima of absorption, N* and T* emission bands, respectively; N*/T* is the intensity ratio of the two emission bands measured at the peak maxima (error ±5%); $[H_2O]$ is the water concentration estimated using a method reported elsewhere (error ±1M);[28] W_A is water access coefficient;[28] QY is the fluorescence quantum yield. Excitation wavelength was 350 nm. Measurements were done in 10 mM phosphate buffer, 30 mM NaCl, pH 6.5. Peptide and ODN concentrations were 1 μM.

dx.doi.org/10.1021/bc300464u | Bioconjugate Chem. 2012, 23, 2434−2443

Table 2. Spectroscopic Properties and Response to Environment of the New 3HC Amino Acid in Comparison to Other Amino Acid Analogues[a]

Amino acid	Fluoro-phore	λ_{abs} (nm) EtOH	ε ($M^{-1}cm^{-1}$)	λ_{em} (nm) EtOH	λ_{em} (nm) Water	Δλ (nm)	Refs
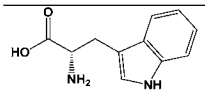	Indole	280	5500	342	355	13	(*56*)
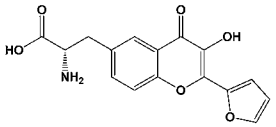	FHC	360	15000	531	427	-104	-
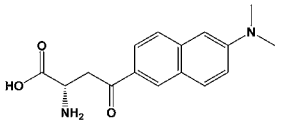	Prodan	360	18400	496	531	35	(*5, 9, 57*)
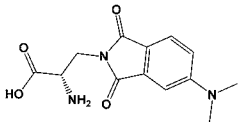	4-DMAP	408	6500	534[b]	562	28	(*11, 58*)

[a] λ_{abs} and λ_{em} − absorption and emission maxima of the fluorophores in the corresponding solvent; ε − absorption coefficient of the fluorophore in ethanol; $\Delta\lambda$ − shift of the emission maximum in response to changes in the solvent polarity (water vs ethanol). [b] Data in methanol.

interacts with the nucleobases.[34−36,38] Therefore, this observation further confirms that the 3HCaa can mimic the Trp residue at position 37. In contrast, binding of NC(11−55)-A30-3HCaa to the three ODNs led to either no change (with SL2 and SL3) or a limited decrease (with ΔP(-)PBS) in the N*/T* ratio with a slight decrease in its quantum yield (Table 1) and almost negligible spectral shifts of the absorption and emission maxima (Table 1). The absence of changes in the N*/T* ratio observed with the SL2 and SL3 sequences can be rationalized by the large distance between the A30 residue and the nucleobases in the NC-ODN complexes (Figure 5). As a consequence, the 3HCaa at position 30 in the complexes with SL2 and SL3 cannot interact with the ODN and remains highly exposed to water, as in the free peptide. Finally, the moderate change in the N*/T* ratio observed when NC(11−55)-A30-3HCaa was complexed with ΔP(-)PBS is fully consistent with the closer proximity of the Ala30 residue to the ΔP(-)PBS nucleobases, as compared to that in the complexes with SL2 and SL3.[34,36,38]

Finally, using the changes in the N*/T* ratio or the quantum yield of 3HCaa as an analytical signal of interaction, we further measured the binding constant of the three labeled peptides to SL3. The obtained binding constants matched closely that obtained with the native peptide (Table S2, Supporting Information),[35,37] indicating that the incorporated 3HCaa probe did not change the binding affinity of the peptides and could thus be also used for quantification of the peptide−ODN interaction. Since Trp37 was shown to be critical for the high affinity of NC to its target ODNs,[40,42,45] this indicates that the substitution of Trp37 by 3HCaa does not alter the ability of NC to recognize its ODN targets. The results are in line with the peptide activity tests and NMR structural data, providing a clear background for considering 3HCaa as a new amino acid analogue that can readily substitute Trp even at the places where it plays a crucial role in the peptide.

Though the N*/T* ratio of 3HCaa is mostly controlled by the environment polarity and hydration, we could not exclude possible quenching effects, which are frequently observed for dyes interacting with nucleobases.[35,41] Indeed, the N*/T* ratio could decrease, for instance, due to a more efficient quenching of the N* state compared to the T* state, as a consequence of static or dynamic quenching by the neighbor nucleobases. However, we expect this effect to be minor in the probe response, because the red shift of the T* band produced by the peptide−DNA interaction correlates well with the changes in the N*/T* ratio (Table 1). As this red shift is directly linked to the dehydration of the dye environment[26,27,55] and not to quenching, the ratio changes appear mainly driven by the dehydration within the peptide−DNA complex. Moreover, as the N* and T* states are coupled by the ESIPT reaction, the quenching of the N* state should influence the N*/T* ratio to a less significant extent, compared to the case where the two states are independent.

Compared to Trp, the new fluorophore features strongly red-shifted absorption and emission (Table 2), allowing more convenient spectroscopic studies in biological samples with less background noise and photodamage. Moreover, it preserves its fluorescence on peptide binding to nucleic acids, while Trp is frequently quenched.[35,41] Moreover, due to ESIPT, it presents much higher sensitivity to the environment in high-polarity range, so that it almost switches its fluorescence from dominant T* emission in ethanol (at 531 nm) to dominant N* emission in water (at 427 nm), while Trp in these conditions changes its emission maximum only by a few nm.[56] This exclusive environmental sensitivity places it in front of all other existing fluorescent amino acid analogues of similar small size, based on Prodan and 4-DMAP (Table 2). Indeed, for highly polar environments (alcohols and water), the fluorophore of the new amino acid (FHC) is about 3-fold more sensitive to solvent polarity (hydration) as compared to Prodan and 4-DMAP. Moreover, the FHC provides an opportunity to quantitatively evaluate the hydration in the site of interaction between the two biomolecules. These exclusive properties originate from the strong effect of H-bonding solvents on the ESIPT reaction in

these derivatives.[15] As peptides and nucleic acids present rather highly polar microenvironments, the new amino acid constitutes a unique tool for probing interactions of these biomolecules in a site-specific manner.

CONCLUSION

For the first time, a fluorescent L-amino acid, exhibiting ESIPT and hydration-sensitive dual emission, was synthesized. This amino acid bears, as a side chain, the 2-(2-furyl)-3-hydroxychromone fluorophore, which is flat and close in size to the indole moiety of L-tryptophan. It was incorporated at two different positions of the NC(11−55) peptide. Remarkably, substitution of the highly conserved Trp37 residue by this fluorescent amino acid was found to preserve both the native folding and the chaperone activity of the peptide. Interaction of the labeled peptides with target ODNs dramatically changed the dual emission of the incorporated amino acid, and these changes depended on its position in the peptide and on the ODN sequence. The obtained results established a correlation between the fluorescence response of the amino acid probe and its proximity to the interacting ODN bases. This amino acid appears as an attractive tool for probing the binding sites in peptide−nucleic acid complexes, being particularly suitable for substitution of tryptophan residues. Compared to tryptophan and its close fluorescent analogues, this new amino acid presents superior environment sensitivity.

ASSOCIATED CONTENT

Supporting Information

Additional characterization data on the fluorescent amino acid and its peptide conjugates and the studied ODN sequences. This material is available free of charge via the Internet at http://pubs.acs.org.

AUTHOR INFORMATION

Corresponding Author

*E-mail addresses: andrey.klymchenko@unistra.fr; yves.mely@unistra.fr. Tel: +33 368 854255, +33 368 854263. Fax: +33 368 854313.

Author Contributions

‡A.V.S. and V.Y.P. equally contributed to this work.

Notes

The authors declare no competing financial interest.

ACKNOWLEDGMENTS

V.Y.P. and V.G.P. were supported by ANR (ANR-07-BLAN-0287), ANR Femtostack, ANRS, CNRS, and Université de Strasbourg. O.V.S. was supported by ARCUS Alsace. We thank Cyril Antheaume and Patrick Wehrung for NMR and mass measurements, respectively.

REFERENCES

(1) Mikhailiuk, P. K., Afonin, S., Chernega, A. N., Rusanov, E. B., Platonov, M. O., Dubinina, G. G., Berditsch, M., Uirich, A. S., and Komarov, I. V. (2006) Conformationally rigid trifluoromethyl-substituted alpha-amino acid designed for peptide structure analysis by solid-state F-19 NMR spectroscopy. *Angew. Chem., Int. Ed. 45*, 5659−5661.

(2) Mizukami, S., Takikawa, R., Sugihara, F., Shirakawa, M., and Kikuchi, K. (2009) Dual-function probe to detect protease activity for fluorescence measurement and F-19 MRI. *Angew. Chem., Int. Ed. 48*, 3641−3643.

(3) Ieronimo, M., Afonin, S., Koch, K., Berditsch, M., Wadhwani, P., and Ulrich, A. S. (2010) F-19 NMR analysis of the antimicrobial peptide PGLa bound to native cell membranes from bacterial protoplasts and human erythrocytes. *J. Am. Chem. Soc. 132*, 8822−8824.

(4) de Villiers, J., Koekemoer, L., and Strauss, E. (2010) 3-Fluoroaspartate and pyruvoyl-dependant aspartate decarboxylase: exploiting the unique characteristics of fluorine to probe reactivity and binding. *Chem.—Eur. J. 16*, 10030−10041.

(5) Cohen, B. E., McAnaney, T. B., Park, E. S., Jan, Y. N., Boxer, S. G., and Jan, L. Y. (2002) Probing protein electrostatics with a synthetic fluorescent amino acid. *Science 296*, 1700−1703.

(6) Brun, M. P., Bischoff, L., and Garbay, C. (2004) A very short route to enantiomerically pure coumarin-bearing fluorescent amino acids. *Angew. Chem., Int. Ed. 43*, 3432−3436.

(7) Venkatraman, P., Nguyen, T. T., Sainlos, M., Bilsel, O., Chitta, S., Imperiali, B., and Stern, L. J. (2007) Fluorogenic probes for monitoring peptide binding to class II MHC proteins in living cells. *Nat. Chem. Biol. 3*, 222−228.

(8) Demchenko, A. P., Mely, Y., Duportail, G., and Klymchenko, A. S. (2009) Monitoring biophysical properties of lipid membranes by environment-sensitive fluorescent probes. *Biophys. J. 96*, 3461−3470.

(9) Nitz, M., Mezo, A. R., Ali, M. H., and Imperiali, B. (2002) Enantioselective synthesis and application of the highly fluorescent and environment-sensitive amino acid 6-(2-dimethylaminonaphthoyl) alanine (DANA). *Chem. Commun. (Camb.)*, 1912−1913.

(10) Chen, H., Chung, N. N., Lemieux, C., Zelent, B., Vanderkooi, J. M., Gryczynski, I., Wilkes, B. C., and Schiller, P. W. (2005) [Aladan3]TIPP: a fluorescent delta-opioid antagonist with high delta-receptor binding affinity and delta selectivity. *Biopolymers 80*, 325−331.

(11) Vazquez, M. E., Rothman, D. M., and Imperiali, B. (2004) A new environment-sensitive fluorescent amino acid for Fmoc-based solid phase peptide synthesis. *Org. Biomol. Chem. 2*, 1965−1966.

(12) Vazquez, M. E., Blanco, J. B., and Imperiali, B. (2005) Photophysics and biological applications of the environment-sensitive fluorophore 6-N,N-dimethylamino-2,3-naphthalimide. *J. Am. Chem. Soc. 127*, 1300−1306.

(13) Loving, G., and Imperiali, B. (2008) A versatile amino acid analogue of the solvatochromic fluorophore 4-N,N-dimethylamino-1,8-naphthalimide: a powerful tool for the study of dynamic protein interactions. *J. Am. Chem. Soc. 130*, 13630−13638.

(14) Sengupta, P. K., and Kasha, M. (1979) Excited state proton-transfer spectroscopy of 3-hytdroxyflavone and quercetin. *Chem. Phys. Lett. 68*, 382−385.

(15) Das, R., Klymchenko, A. S., Duportail, G., and Mely, Y. (2009) Unusually slow proton transfer dynamics of a 3-hydroxychromone dye in protic solvents. *Photochem. Photobiol. Sci. 8*, 1583−1589.

(16) Shynkar, V. V., Klymchenko, A. S., Piemont, E., Demchenko, A. P., and Mely, Y. (2004) Dynamics of intermolecular hydrogen bonds in the excited states of 4′-dialkylamino-3-hydroxyflavones. On the pathway to an ideal fluorescent hydrogen bonding sensor. *J. Phys. Chem. A 108*, 8151−8159.

(17) Enander, K., Choulier, L., Olsson, A. L., Yushchenko, D. A., Kanmert, D., Klymchenko, A. S., Demchenko, A. P., Mely, Y., and Altschuh, D. (2008) A peptide-based, ratiometric biosensor construct for direct fluorescence detection of a protein analyte. *Bioconjugate Chem. 19*, 1864−1870.

(18) Chou, P.-T., Martinez, M. L., and Clements, H. (1993) Reversal of excitation behavior of proton-transfer vs. charge-transfer by dielectric perturbation of electronic manifolds. *J. Phys. Chem. 97*, 2618−2622.

(19) Ormson, S. M., Brown, R. G., Vollmer, F., and Rettig, W. (1994) Switching between charge- and proton-transfer emission in the excited state of a substituted 3-hydroxyflavone. *J. Photochem. Photobiol., A 81*, 65−72.

(20) Swinney, T. C., and Kelley, D. F. (1993) Proton transfer dynamics in substituted 3-hydroxyflavones: Solvent polarization effects. *J. Chem. Phys. 99*, 211−221.

(21) Klymchenko, A. S., and Demchenko, A. P. (2003) Multiparametric probing of intermolecular interactions with fluorescent dye exhibiting excited state intramolecular proton transfer. *Phys. Chem. Chem. Phys. 5*, 461−468.
(22) Strandjord, A. J. G., and Barbara, P. F. (1985) Proton-transfer kinetics of 3-hydroxyflavone: Solvent effects. *J. Phys. Chem. 89*, 2355−2361.
(23) McMorrow, D., and Kasha, M. (1984) Intramolecular excited-state proton transfer in 3-hydroxyflavone. Hydrogen-bonding solvent perturbations. *J. Phys. Chem. 88*, 2235−2243.
(24) Klymchenko, A. S., and Demchenko, A. P. (2004) 3-Hydroxychromone dyes exhibiting excited-state intramolecular proton transfer in water with efficient two-band fluorescence. *New J. Chem. 28*, 687−692.
(25) Yushchenko, D. A., Fauerbach, J. A., Thirunavukkuarasu, S., Jares-Erijman, E. A., and Jovin, T. M. (2010) Fluorescent ratiometric MFC probe sensitive to early stages of alpha-synuclein aggregation. *J. Am. Chem. Soc. 132*, 7860−7861.
(26) Klymchenko, A. S., Shvadchak, V. V., Yushchenko, D. A., Jain, N., and Mely, Y. (2008) Excited-state intramolecular proton transfer distinguishes microenvironments in single-and double-stranded DNA. *J. Phys. Chem. B 112*, 12050−12055.
(27) Shvadchak, V. V., Klymchenko, A. S., De Rocquigny, H., and Mely, Y. (2009) Sensing peptide - Oligonucleotide interactions by a two-color fluorescence label: Application to the HIV-1 nucleocapsid protein. *Nucleic Acids Res. 37*, e25.
(28) Pivovarenko, V. G., Zamotaiev, O. M., Shvadchak, V. V., Postupalenko, V. Y., Klymchenko, A. S., and Mély, Y. (2012) Quantification of local hydration at the surface of biomolecules using dual-fluorescence labels. *J. Phys. Chem. A 116*, 3103−3109.
(29) Thomas, J. A., and Gorelick, R. J. (2008) Nucleocapsid protein function in early infection processes. *Virus Res. 134*, 39−63.
(30) Darlix, J. L., Godet, J., Ivanyi-Nagy, R., Fosse, P., Mauffret, O., and Mely, Y. (2011) Flexible nature and specific functions of the HIV-1 Nucleocapsid protein. *J. Mol. Biol. 410*, 565−581.
(31) Summers, M. F., Henderson, L. E., Chance, M. R., Bess, J. W., Jr, South, T. L., Blake, P. R., Sagi, I., Perez-Alvarado, G., Sowder, R. C., III, Hare, D. R., and Arthur, L. O. (1992) Nucleocapsid zinc fingers detected in retroviruses: EXAFS studies of intact viruses and the solution-state structure of the nucleocapsid protein from HIV-1. *Protein Sci. 1*, 563−574.
(32) Morellet, N., Jullian, N., De Rocquigny, H., Maigret, B., Darlix, J. L., and Roques, B. P. (1992) Determination of the structure of the nucleocapsid protein NCp7 from the human immunodeficiency virus type 1 by 1H NMR. *EMBO J. 11*, 3059−3065.
(33) Clever, J., Sassetti, C., and Parslow, T. G. (1995) RNA secondary structure and binding sites for gag gene products in the 5′ packaging signal of human immunodeficiency virus type 1. *J. Virol. 69*, 2101−2109.
(34) de Guzman, R. N., Wu, Z. R., Stalling, C. C., Pappalardo, L., Borer, P. N., and Summers, M. F. (1998) Structure of the HIV-1 nucleocapsid protein bound to the SL3 Ψ-RNA recognition element. *Science 279*, 384−388.
(35) Vuilleumier, C., Bombarda, E., Morellet, N., Gerard, D., Roques, B. P., and Mely, Y. (1999) Nucleic acid sequence discrimination by the HIV-1 nucleocapsid protein NCp7: a fluorescence study. *Biochemistry 38*, 16816−16825.
(36) Bourbigot, S., Ramalanjaona, N., Boudier, C., Salgado, G. F. J., Roques, B. P., Mely, Y., Bouaziz, S., and Morellet, N. (2008) How the HIV-1 nucleocapsid protein binds and destabilises the (-)primer binding site during reverse transcription. *J. Mol. Biol. 383*, 1112−1128.
(37) Shubsda, M. F., Paoletti, A. C., Hudson, B. S., and Borer, P. N. (2002) Affinities of packaging domain loops in HIV-1 RNA for the nucleocapsid protein. *Biochemistry 41*, 5276−5282.
(38) Amarasinghe, G. K., De Guzman, R. N., Turner, R. B., Chancellor, K. J., Wu, Z. R., and Summers, M. F. (2000) NMR structure of the HIV-1 nucleocapsid protein bound to stem-loop SL2 of the Psi-RNA packaging signal. Implications for genome recognition. *J. Mol. Biol. 301*, 491−511.
(39) Fisher, R. J., Rein, A., Fivash, M., Urbaneja, M. A., Casas-Finet, J. R., Medaglia, M., and Henderson, L. E. (1998) Sequence-specific binding of human immunodeficiency virus type 1 nucleocapsid protein to short oligonucleotides. *J. Virol. 72*, 1902−1909.
(40) Beltz, H., Clauss, C., Piemont, E., Ficheux, D., Gorelick, R. J., Roques, B., Gabus, C., Darlix, J. L., de Rocquigny, H., and Mely, Y. (2005) Structural determinants of HIV-1 nucleocapsid protein for cTAR DNA binding and destabilization, and correlation with inhibition of self-primed DNA synthesis. *J. Mol. Biol. 348*, 1113−1126.
(41) Mely, Y., de Rocquigny, H., Sorinasjimeno, M., Keith, G., Roques, B. P., Marquet, R., and Gerard, D. (1995) Binding of the HIV-1 nucleocapsid protein to the primer tRNA(3)(Lys), in-vitro, is essentially not specific. *J. Biol. Chem. 270*, 1650−1656.
(42) Godet, J., Ramalanjaona, N., Sharma, K. K., Richert, L., De Rocquigny, H., Darlix, J. L., Duportail, G., and Mély, Y. (2011) Specific implications of the HIV-1 nucleocapsid zinc fingers in the annealing of the primer binding site complementary sequences during the obligatory plus strand transfer. *Nucleic Acids Res. 39*, 6633−6645.
(43) Bernacchi, S., Stoylov, S., Piemont, E., Ficheux, D., Roques, B. P., Darlix, J. L., and Mely, Y. (2002) HIV-1 nucleocapsid protein activates transient melting of least stable parts of the secondary structure of TAR and its complementary sequence. *J. Mol. Biol. 317*, 385−399.
(44) Post, K., Kankia, B., Gopalakrishnan, S., Yang, V., Cramer, E., Saladores, P., Gorelick, R. J., Guo, J. H., Musier-Forsyth, K., and Levin, J. G. (2009) Fidelity of plus-strand priming requires the nucleic acid chaperone activity of HIV-1 nucleocapsid protein. *Nucleic Acids Res. 37*, 1755−1766.
(45) Avilov, S. V., Piemont, E., Shvadchak, V., de Rocquigny, H., and Mely, Y. (2008) Probing dynamics of HIV-1 nucleocapsid protein/target hexanucleotide complexes by 2-aminopurine. *Nucleic Acids Res. 36*, 885−896.
(46) Dorfman, T., Luban, J., Goff, S. P., Haseltine, W. A., and Gottlinger, H. G. (1993) Mapping of functionally important residues of a cysteine-histidine box in the human immunodeficiency virus type 1 nucleocapsid protein. *J. Virol. 67*, 6159−6169.
(47) Hufford, C. D., Oguntimein, B. O., and Shoolery, J. N. (1987) Angoluvarin, an antimicrobial dihydrochalcone from Uvaria angolensis. *J. Org. Chem. 52*, 5286−5288.
(48) Chen, C., Zhu, Y. F., and Wilcoxen, K. (2000) An improved synthesis of selectively protected L-Dopa derivatives from L-tyrosine. *J. Org. Chem. 65*, 2574−2576.
(49) De Rocquigny, H., Ficheux, D., Gabus, C., Fournie-Zaluski, M. C., Darlix, J. L., and Roques, B. P. (1991) First large scale chemical synthesis of the 72 amino acid HIV-1 nucleocapsid protein NCp7 in an active form. *Biochem. Biophys. Res. Commun. 180*, 1010−1018.
(50) Eastman, J. W. (1967) Quantitative spectrofluorimetry-the fluorescence quantum yield of quinine sulfate. *Photochem. Photobiol. 6*, 55−72.
(51) Bernacchi, S., Piémont, E., Potier, N., Van Dorsselaer, A., and Mély, Y. (2003) Excitonic heterodimer formation in an HIV-1 oligonucleotide labeled with a donor-acceptor pair used for fluorescence resonance energy transfer. *Biophys. J. 84*, 643−654.
(52) Beltz, H., Azoulay, J., Bernacchi, S., Clamme, J. P., Ficheux, D., Roques, B., Darlix, J. L., and Mely, Y. (2003) Impact of the terminal bulges of HIV-1 cTAR DNA on its stability and the destabilizing activity of the nucleocapsid protein NCp7. *J. Mol. Biol. 328*, 95−108.
(53) Godet, J., de Rocquigny, H., Raja, C., Glasser, N., Ficheux, D., Darlix, J. L., and Mely, Y. (2006) During the early phase of HIV-1 DNA synthesis, nucleocapsid protein directs hybridization of the TAR complementary sequences via the ends of their double-stranded stem. *J. Mol. Biol. 356*, 1180−1192.
(54) Dziuba, D., Postupalenko, V. Y., Spadafora, M., Klymchenko, A. S., Guérineau, V., Mély, Y., Benhida, R., and Burger, A. (2012) A universal nucleoside with strong two-band switchable fluorescence and sensitivity to environment for investigating DNA interactions. *J. Am. Chem. Soc. 134*, 10209−10213.
(55) Kenfack, C. A., Klymchenko, A. S., Duportail, G., Burger, A., and Mély, Y. (2012) Ab initio study of the solvent H-bonding effect on

ESIPT reaction and electronic transitions of 3-hydroxychromone derivatives. *Phys. Chem. Chem. Phys. 14*, 8910−8918.
(56) Lakowicz, J. R. (2006) *Principles of Fluorescence Spectroscopy*, Kluwer Academic, New York.
(57) Weber, G., and Farris, F. J. (1979) Synthesis and spectral properties of a hydrophobic fluorescent probe: 6-propionyl-2-(dimethylamino)naphthalene. *Biochemistry 18*, 3075−3078.
(58) Soujanya, T., Fessenden, R. W., and Samanta, A. (1996) Role of nonfluorescent twisted intramolecular charge transfer state on the photophysical behavior of aminophthalimide dyes. *J. Phys. Chem. 100*, 3507−3512.

Supporting information

Two-color fluorescent L-amino acid mimic of tryptophan for probing peptide-nucleic acid complexes

Aleksandr V. Strizhak, Viktoriia Y. Postupalenko, Volodymyr V. Shvadchak, Nelly Morellet, Eric Guittet, Vasyl G. Pivovarenko, Andrey S. Klymchenko, Yves Mély

Table of contents

Material and methods 2
Proof of optical purity 2
Supporting figures 4
Supporting tables 6
References 6

Materials and methods

Proof of optical purity: synthesis of 9 and 10.
To test the enantiomeric purity of the obtained chromone-amino acid derivative, we prepared the dibenzyl ether-ester of the amino acid (step A, B). Then, the obtained aminoester was acylated by two enantiomers of Mosher's acid chloride (step C). The NMR spectra of the diastereomeric Mosher amides were then compared. No signal of the opposite diastereomer was found in each spectrum.

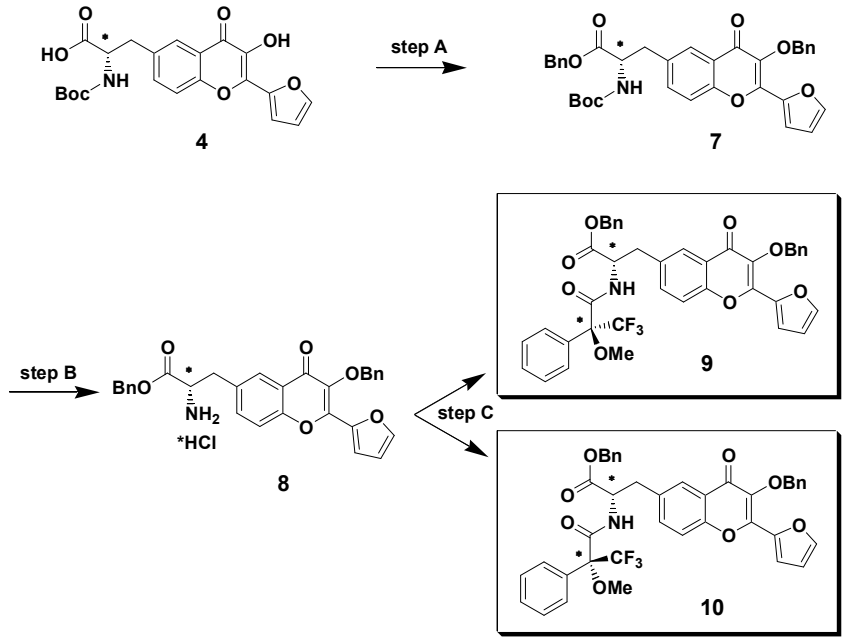

A) BnBr, K_2CO_3, $(C_4H_9)_4NI$, DMF; B) conc. HCl, dioxane; C) Mosher, $EtN(i\text{-}Pr)_2$, THF

Scheme S1. Scheme of synthesis of the diastereomeric Mosher amides to prove the optical purity of the synthesized fluorescent amino acid.

Benzyl 3-[3-(benzyloxy)-2-(2-furyl)-4-oxo-4H-chromen-6-yl]-N-(tert-butoxycarbonyl)-L-alaninate (7). Benzylation was performed in soft conditions to prevent possible racemisation.[1b] 600 mg of Boc-protected amino acid **4** was dissolved in 8 mL of DMF, followed by the addition of 500 mg of benzyl bromide, 438 mg of anhydrous potassium carbonate and 54 mg of tetrabutylammonium iodide. The mixture was stirred at RT for 4 h, and controlled by TLC (EtOAc or EtOAc:heptane 1:1). The mixture was diluted with water and the product was extracted 3 times with EtOAc. The combined organic layers were dried with Na_2SO_4 and concentrated under reduced pressure. The resulting residue was purified by column chromatography (EtOAc:heptane 1:1) to give the desired product **7** as a yellow oil.

*Benzyl 3-[3-(benzyloxy)-2-(2-furyl)-4-oxo-4H-chromen-6-yl]-L-alaninate (**8**).*Boc-deprotection was performed by dissolving Boc-dibenzylderivate**7** indioxane (1 mL per 100 mg), adding conc. HCl (1mL per 100 mg) and stirring during ~ 2 h. The reaction was controlled by TLC (EtOAc:Heptane 1:1). The solution was concentrated under reduced pressure and the residue was recrystallized from MeOH/ether. Pale yellow solid, yield ~ 90%.

*Mosher conjugates (**9, 10**).* 33 mg of dried chlorohydrate **8** was suspended in 1 mL of THF. Then, 26 mg of Hunig's base and ~ 20 mg of Mosher's chloride were added. The mixture was stirred for 24 h, diluted with water, and stirred for 1 h to hydrolyze the excess of Mosher's chloride. The

reaction mixture was then extracted with dichloromethane. The organic layer was washed with bicarbonate solution followed by 1M HCl, brine, dried with Na_2SO_4 and concentrated under reduced pressure to give the desired products **9** and **10** as yellow oil.

Benzyl 3-[3-(benzyloxy)-2-(2-furyl)-4-oxo-4H-chromen-6-yl]-N-[(2S)-3,3,3-trifluoro-2-methoxy-2-phenylpropanoyl]-L-alaninate (9).**^{1}H-NMR** (400 MHz, $CDCl_3$) δ 3.14-3.19 (dd, *J* = 14.24 Hz, *J* = 7.12 Hz, 1H), 3.20 (s, 3H), 3.24-3.29 (dd, *J* = 14.24 Hz, *J* = 5.60 Hz, 1H), 4.89-4.94 (dd, *J* = 14.25 Hz, *J* = 6.62 Hz, 1H), 5.05-5.08 (d, *J* = 12.21 Hz, 1H), 5.11-5.14 (d, *J* = 12.21 Hz, 1H), 5.24 (s, 2H), 6.48-6.49 (dd, *J* = 3.56 Hz, *J* = 1.52 Hz,1H), 7.18-7.44 (m, 17H), 7.59 (d, *J* = 1.01 Hz, 1H), 7.96 (d, *J* = 1.53 Hz, 1H).**^{19}F-NMR** (376 MHz, $CDCl_3$) δ -69.5 (**9**), -72.03 (Mosher acid).
*Benzyl 3-[3-(benzyloxy)-2-(2-furyl)-4-oxo-4H-chromen-6-yl]-N-[(2R)-3,3,3-trifluoro-2-methoxy-2-phenylpropanoyl]-L-alaninate (10).***^{1}H-NMR** (400 MHz, $CDCl_3$) δ 3.02-3.07 (dd, *J* = 14.05 Hz, *J* = 7.53 Hz, 1H), 3.16-3.21 (dd, *J* = 14.05 Hz, *J* = 5.52 Hz, 1H), 3.35 (d, *J* = 1.50 Hz, 3H), 4.94-5.00 (m, *J* = 5.52 Hz, *J* = 7.28 Hz,1H), 5.07-5.10 (d, *J* = 12.05 Hz, 1H), 5.14-5.17 (d, *J* = 12.05 Hz, 1H), 5.20-5.23 (d, *J* = 10.54 Hz, 1H), 5.23-5.26 (d, *J* = 10.54 Hz, 1H), 6.49-6.51 (dd, *J* = 3.52 Hz, *J* = 1.76 Hz,1H), 7.01-7.04 (dd, *J* = 8.79 Hz, *J* = 2.26 Hz, 1H), 7.05-7.07 (d, *J* = 8.53 Hz, 1H), 7.17-7.32 (m, 15H), 7.42-7.45 (dd, *J* = 8.29 Hz, *J* = 1.76 Hz, 1H), 7.60 (dd, *J* = 1.76 Hz *J* = 0.75 Hz, , 1H), 7.84 (d, *J* = 2.26 Hz, 1H). **^{19}F-NMR** (376 MHz, $CDCl_3$) δ -69.41(**10**), -72.03 (Mosher acid).

Supporting figures

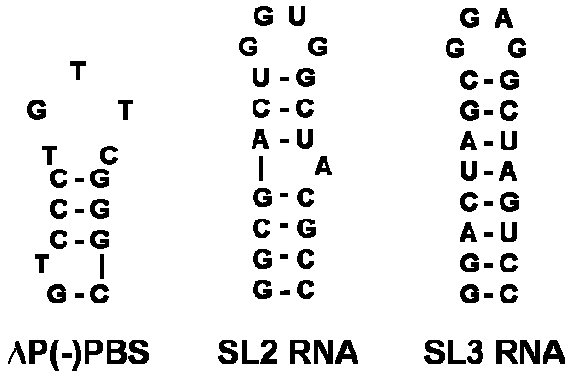

Figure S1. Sequences of the ΔP(-)PBS DNA, SL2 and SL3 RNAs used in this study.

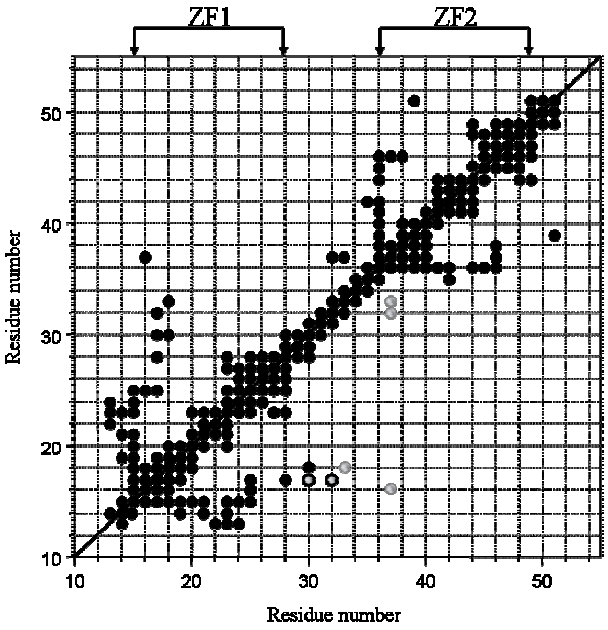

Figure S2. Diagonal plot of side-chain/side-chain Nuclear Overhauser Effects (NOEs) comparing the (13-51) domain of native NC (upper part) and the labeled NC(11-55) derivatives (lower part). ● NOEs seen for both labeled peptides; ◍ NOEs seen for none of the two labeled peptides; ◎ NOEs seen only for the NC(11-55)-W37-3HCaa peptide. Analysis of NOEs shows that the internal structure is preserved for each zinc finger (residues 15 to 28 and 36 to 49 for ZF1 and ZF2, respectively) in the two labeled peptides, since the same NOEs as for the native protein are found in the spectra, resulting in a perfect symmetry for these residues on both sides of the diagonal (black discs). The differences observed for the labeled peptides compared to the native NC (grey disks) are marginal. The data were obtained at 600 MHz, mixing time of 200 ms, and 293 K. Concentration of NC(11-55) conjugates was 0.5 mM in water, pH 6.5.

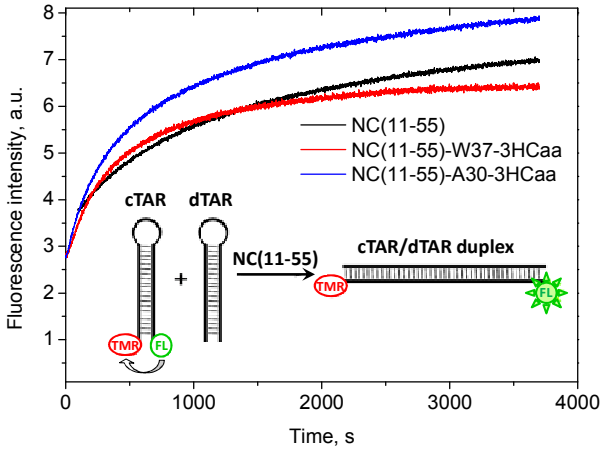

Figure S3. Nucleic acid chaperone activity of the 3HCaa-labeled NC(11-55) peptides. The annealing kinetics of 10 nM TMR-5'-cTAR-3'-Fl with 300 nM dTAR in the presence of the unlabeled and labeled NC(11-55) peptides added at a protein:ODN ratio of 3 :1 were monitored in 25 mM Tris (pH 7.5), 30 mM NaCl and 0.2 mM $MgCl_2$. Excitation and emission wavelengths were 480 and 520 nm, respectively.

Supporting tables

Table S1. Spectroscopic properties of the Boc-3HCaa and the basic fluorophore 2-(2-furyl)-3-hydroxychromone (FHC).[a]

Solvent	Dye	λ_{ABS}	λ_{N^*}	λ_{T^*}	N*/T*	QY, %
Buffer	Boc-3HCaa	358	427	505	2.2	1.9
	FHC	358	427	513	3.2	5.0
MeOH	Boc-3HCaa	355	419	529	0.75	3.9
	FHC	356	421	530	1.7	8.0
EtOH	Boc-3HCaa	356	415	531	0.33	4.6
	FHC	348	414	534	0.64	8.0
MeCN	Boc-3HCaa	350	412	534	0.07	3.0
	FHC	409	409	533	0.10	6.0

[a] λ_{ABS} – position of absorption maxima, λ_{N^*} and λ_{T^*} - position of the fluorescence maxima of N* and T* forms, respectively. N*/T* - ratio of the intensities of the two emission bands at their peak maxima. QY – fluorescence quantum yield. 10 mM phosphate buffer, 30 mM NaCl, pH = 6.5 was used. Excitation wavelength was 350 nm. Quinine sulfate in H_2SO_4 pH=1 (QY = 57.7%) was used as a reference for quantum yield calculation. All data on FHC dye are from Ref. [1].

Table S2. Binding constants of NC(12-53) and 3HCaa-labeled NC(11-55) peptides with SL3.

Peptide	K_{bind}, M^{-1}
NC(12-53)[a]	$1(\pm0.2)\times10^6$
NC(11-55)-W37-3HCaa	$1(\pm0.3)\times10^6$
NC(11-55)-A30-3HCaa	$1(\pm0.8)\times10^6$

[a] value taken from literature.[2] Binding constants of the 3HCaa-labeled NC(11-55) peptides with SL3 were obtained by monitoring the 3HC fluorescence. Excitation wavelength was 350 nm. Measurements were done in 50 mM Hepes buffer, 100 mM NaCl, pH 6.5. Concentration of SL3 was 0.5 μM. The results are expressed as mean +/- standard error for three experiments.

References:

[1] A. S. Klymchenko, A. P. Demchenko, New J. Chem. 2004, 28, 687

[2] C. Vuilleumier, E. Bombarda, N. Morellet, D. Gerard, B. P. Roques, Y. Mely, *Biochemistry* **1999**, *38*, 16816.

Bioconjugate Chemistry

Article

pubs.acs.org/bc

Quantitative Evaluation of Bioorthogonal Chemistries for Surface Functionalization of Nanoparticles

Lise N. Feldborg,[†] Rasmus I. Jølck,[†] and Thomas L. Andresen*

DTU Nanotech, Department of Micro- and Nanotechnology, Technical University of Denmark, Building 423 2800 Lyngby, Denmark

Supporting Information

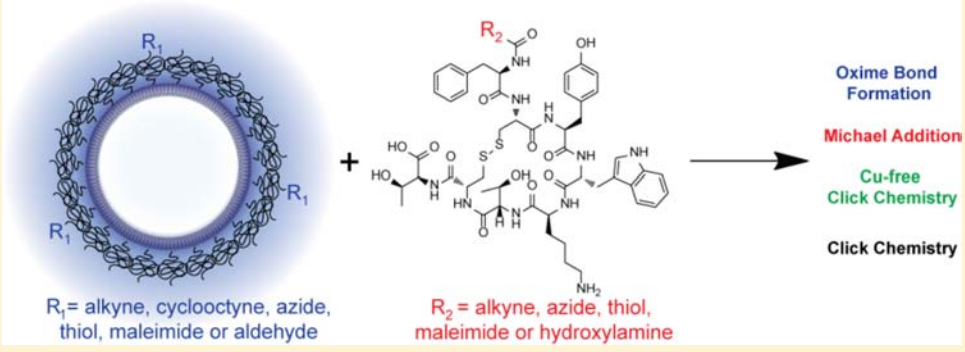

ABSTRACT: We present here a highly efficient and chemoselective liposome functionalization method based on oxime bond formation between a hydroxylamine and an aldehyde-modified lipid component. We have conducted a systematic and quantitative comparison of this new approach with other state-of-the-art conjugation reactions in the field. Targeted liposomes that recognize overexpressed receptors or antigens on diseased cells have great potential in therapeutic and diagnostic applications. However, chemical modifications of nanoparticle surfaces by postfunctionalization approaches are less effective than in solution and often not high-yielding. In addition, the conjugation efficiency is often challenging to characterize and therefore not addressed in many reports. We present here an investigation of PEGylated liposomes functionalized with a neuroendocrine tumor targeting peptide (TATE), synthesized with a variety of functionalities that have been used for surface conjugation of nanoparticles. The reaction kinetics and overall yield were quantified by HPLC. Reactions were conducted in solution as well as by postfunctionalization of liposomes in order to study the effects of steric hindrance and possible affinity between the peptide and the liposome surface. These studies demonstrate the importance of choosing the correct chemistry in order to obtain a quantitative surface functionalization of liposomes.

INTRODUCTION

Functional nanomaterials have attracted considerable attention due to their highly interesting properties in relation to diagnostic,[1−3] sensor,[4,5] imaging,[6,7] vaccine,[8] and drug delivery applications.[9,10] Within the drug delivery field, liposomes have particularly advantageous properties.[11] However, despite positive results obtained by exploiting the EPR-effect,[12] numerous methods to improve drug bioavailability in the diseased tissue, while maintaining stable liposomes during circulation, is currently being investigated. By coating the liposome surfaces with targeting ligands such as antibodies,[13,14] peptides,[15] proteins,[16] polysaccharides,[17] lectins,[18] and vitamin analogues,[19,20] which are recognized by antigens or receptors selectively, or overexpressed in, e.g., tumor tissue, increased drug accumulation in tumors can be achieved. Numerous bioconjugation methods have been established to surface-modify liposomes with targeting ligands to enhance tissue specificity. To ensure correct orientation of the targeting ligand, bioorthogonal and site-specific surface reactions are required. By the incorporation of unnatural amino acids in peptide or protein sequences,[21] introduction of unnatural functional groups such as maleimides for Michael addition, azides for copper(I)-catalyzed Huisgen 1,3-dipolar cycloaddition[22−24] (CuAAC) or Staudinger ligation using triphosphines,[25,26] controlled display of surface ligands can be obtained. Unfortunately, ligand conjugation to the surface of nanoparticles can suffer from low reproducibility and highly varying yields; e.g., we have previously found that it can be very difficult to control the Michael addition of a somatostatin receptor targeting peptide (TATE) to a lipid moiety, even though the maleimide-based Michael addition is one of the most utilized conjugation chemistries for peptides and proteins.[27,28] As a consequence hereof, we have conducted a systematic study on a variety of generally applied conjugation reactions using HPLC as a method to follow and quantify the reactions both in solution and by direct conjugation to the liposomal surface. Reactions conducted directly on liposome surfaces are likely not to show the same reaction kinetics as ones preformed in

Received: September 8, 2012
Revised: October 24, 2012
Published: November 16, 2012

 © 2012 American Chemical Society

solution, and the yield of functionalization will not necessarily be quantitative and has to be determined case by case.

In this study, we furthermore introduce a novel highly selective and bioorthogonal conjugation reaction relevant for the surface functionalization of liposomes. We show a fast and quantitative coupling of a hydroxylamine functionalized peptide to an aldehyde-modified liposome, a strategy for coating liposomes, which to our knowledge has not previously been reported. In addition, we show a large dependency on the relative position of the conjugation functionalities. A knowledge which we believe is highly useful when designing new functionalized liposomal systems or other functional nanomaterials.

EXPERIMENTAL PROCEDURES

Synthesis of Functionalized TATE Peptides. The functionalized TATE peptides **1a−e** were synthesized manually by using a Wang Resin preloaded with NH_2-Thr(*t*Bu)-OH by standard Fmoc methodology. Each coupling was performed by activating the Fmoc protected amino acid with *O*-(7-azabenzotriazol-1-yl)-*N*,*N*,*N*′,*N*′-tetramethyluronium hexafluorophosphate (HATU) in the presence of 2,4,6-collidine in DMF. Cleavage of the Fmoc group was carried out using piperidine in DMF. Completion of each coupling and deprotection step was monitored by the Kaiser test. Removal of the acetamidomethyl (Acm) protection groups on the two cysteines and simultaneous disulfide bond formation was achieved by addition of $Tl(CF_3COO)_3$ in DMF. The resin containing the cyclized peptide was extensively washed with DMF and subsequently divided into five solid-phase peptide synthesis (SPPS) reaction vials in which the N-terminal was acylated with the desired functionality, cleaved from the solid support, and purified by HPLC. Full experimental details and peptide characterization are available as Supporting Information.

Synthesis of Functionalized DSPE-PEG_{2000} Phospholipids. Functionalized DSPE-PEG_{2000} phospholipids **2a−d** were synthesized in a single step from DSPE-PEG_{2000}-NH_2 by acylation of the amino group with the desired functionality in the presence of either HATU or EDC·HCl. Phospholipid **3** was synthesized in a single step from DSPE-PEG_{2000}-PDP by reduction by dithiothreitol (DTT). Full experimental details and lipid characterization are available as Supporting Information.

Liposome Formulation. Lipids were dissolved in CH_3Cl/MeOH (9:1) and mixed in the ratio 95:4:1 DSPC/DSPE-PEG_{2000}/DSPE-PEG_{2000}-R (R being the different functional groups illustrated in Schemes 2 and 3). The solvent was removed under a stream of nitrogen and the films placed under vacuum overnight to remove remaining traces of organic solvent. The obtained films were hydrated in a Hepes buffer, (10 mM Hepes, pH 6.5, 145 mM NaCl) at 65 °C for 1 h; followed by 10 freeze−thaw cycles and extrusion at 65 °C through a 100 nm polycarbonate filter using an Avanti Polar Lipids mini-extruder. The size distribution of the liposomes was analyzed using dynamic light scattering, as well as their zeta potential using a Brookhaven Zeta PALS analyzer. All sizes were 100−120 nm and all zeta potentials were slightly negative (approximately −5 mV).

Conjugation in Solution. DSPE-PEG_{2000} functionalized lipid (0.2 mM, 0.55 mL, 1.1 equiv.) was dissolved in MeOH and mixed with the corresponding functionalized TATE in MeOH (0.2 mM, 0.50 mL, 1.0 equiv.). The reaction was stirred at room temperature and aliquots (50 μL) were removed at the indicated times and analyzed by analytical HPLC. A linear gradient was used from 100% A (aqueous solution containing 5% MeCN and 0.1% TFA) to 100% B (MeCN containing 0.1% TFA) over 15 min with a flow rate of 1 mL/min and AUC for the free TATE was measured relative to AUC for the coupled product at 280 nm. For the reaction between the maleimide and thiol functionalities Et_3N (50 mM, 6.0 μL, 3.0 equiv.) was added to facilitate the coupling, while for the copper catalyzed click reactions $CuSO_4·5H_2O$ (1.0 M, 2.5 μL, 25 equiv.) and sodium ascorbate (1.0 M, 5.0 μL, 50 equiv.) were added. Before injecting the aliquots from the copper catalyzed click reactions onto the analytical HPLC column 20 μL of a 10% NH_4OH solution was added to ensure the copper ions were in solution and not interfering with the HPLC signals.[29]

Conjugation by Post-Functionalization of Liposomes. Preformed functionalized liposomes ((25 mM, 0.50 mL, 1.1 equiv.) - normalized according to a 45:55 distribution ratio between the inner- and outer liposomal membrane) were mixed with the corresponding TATE peptide (4.2 mM, 15 μL, 1.0 equiv.) dissolved in MeOH. The reactions were shaken (not stirred; to avoid foaming) at room temperature and aliquots (40 μL) removed for analysis by analytical HPLC. A linear gradient was used from 100% A (aqueous solution containing 5% MeCN and 0.1% TFA) to 100% B (MeCN containing 0.1% TFA) over 15 min with a flow rate of 1 mL/min. The AUC for the free TATE was calculated relative to the AUC of the phospholipid coupled product at 280 nm to monitor the conjugation efficiency. For the copper catalyzed click reactions $CuSO_4·5H_2O$ (1.0 M, 1.6 μL, 25 equiv.) and sodium ascorbate (1.0 M, 3.1 μL, 50 equiv.) were added. As for the conjugations done in solution 20 μL of a 10% NH_4OH solution was added to the copper catalyzed click aliquots prior to HPLC analysis.

RESULTS AND DISCUSSION

Synthesis and Characterization. The model peptides **1a−1e** for somatostatin receptor targeting[30] were prepared using a SPPS strategy as shown in Scheme 1.[31] The N-terminal functionalized TATE peptides **1a−e** were synthesized by SPPS on H-Thr(*t*Bu)-OH preloaded Wang Resin. Acylation of the N-terminal of the peptide was achieved by activating the Fmoc-protected amino acid with HATU to ensure high conversion with minimum epimerization. After assembly of the resin immobilized octapeptide, H-D-Phe-Cys(Acm)-Tyr(*t*Bu)-D-Trp-(Boc)-Lys(Boc)-Thr(*t*Bu)-Cys(Acm)-Thr(*t*Bu)-resin, the peptide was treated with $Tl(CF_3COO)_3$, which in a single step removed the two Acm-protection groups present on the cysteine residues and formed the intramolecular disulfide bond. The reaction was followed by cleavage of a small amount of peptide from the resin with TFA and analyzing the crude peptide by MALDI-TOF MS. Complete Acm-removal and disulfide formation were observed after 75 min with no sign of dimerization. After extensive washing of the resin, the N-terminal was acylated with the desired carboxylic acid functionalized linker derivatives and cleaved from the solid support by treatment with a mixture of TFA/H_2O/TIS (95:2.5:2.5) to give the desired functionalized TATE peptides **1a−e**. Final purification of the peptides was accomplished by HPLC and the obtained products **1a−e** characterized by MALDI-TOF MS (Table 1). In order to formulate liposomes exposing the appropriate chemical functionalities at the distal end of the PEG-corona, PEGylated phospholipids with the desired functionalities were synthesized from either DSPE-

dx.doi.org/10.1021/bc3005057 | Bioconjugate Chem. 2012, 23, 2444−2450

Scheme 1. Synthesis of the TATE-Derivatives 1a−1e

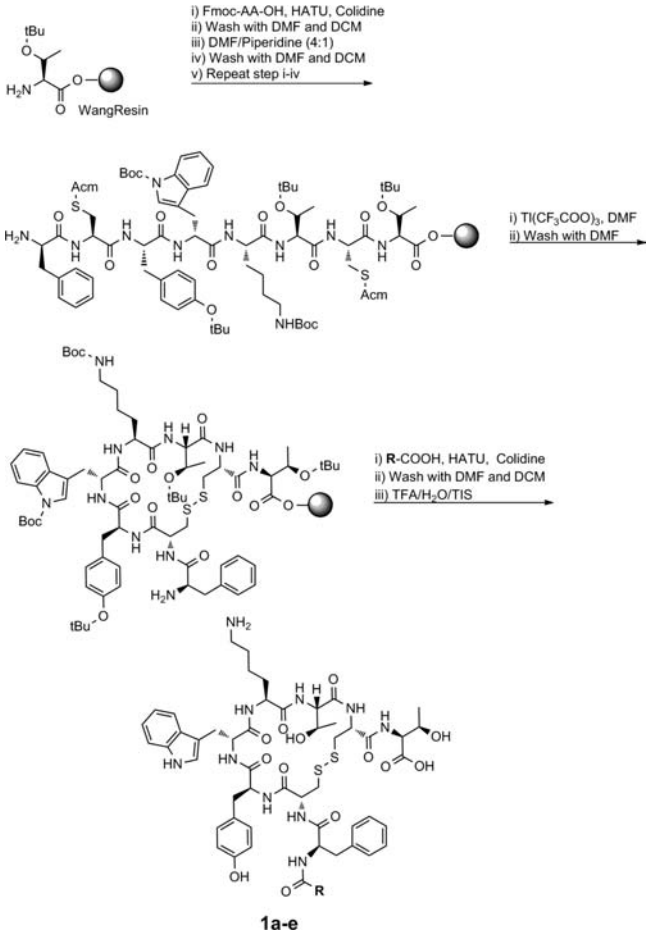

Table 1. Chemical Structure of R-COOH Used for Synthesis of TATE Derivatives 1a−1e and Corresponding Characterization by MALDI TOF MS

Compound #	R_1	MS $(M+Na)^+$ (cald.)	MS $(M+Na)^+$ (found)
1a	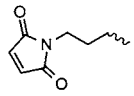	1236.35	1236.39
1b		1159.33	1159.57
1c		1196.33	1196.60
1d		1129.31	1129.47
1e	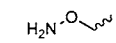	1144.25	1144.41

PEG_{2000}-NH_2 or DSPE-PEG_{2000}-PDP as illustrated in Schemes 2 and 3. PEGylated phospholipids exposing a terminal alkyne, a cyclic alkyne, an aldehyde, or an azide functionality at the distal end of the polymer (**2a−d**) were synthesized by acylating DSPE-PEG_{2000}-NH_2 with 4-pentynoic acid, 1-fluorocyclooct-2-ynecarboxylic acid, 4-carboxybenzaldehyde, or 5-azidopentanoic acid, respectively. 1-Fluorocyclooct-2-ynecarboxylic acid was synthesized as described elsewhere.[32] DSPE-PEG_{2000}-SH (**3**) was synthesized in a single step from DSPE-PEG_{2000}-PDP by reduction of the pyridyldithiopropionate (PDP) group by DTT applying standard conditions[33] which resulted in the desired free thiol (Scheme 3). The DSPE-PEG_{2000}-maleimide (**4**) functionalized phospholipid was purchased from Avanti Polar Lipids, Inc., Alabama.

Scheme 2. Synthesis of the DSPE-PEG_{2000}-NH_2 Modified Phospholipids 2a−d

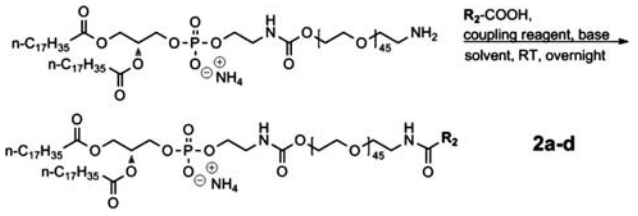

Compound #	R_2	Coupling reagent	Base	Solvent
2a		EDC·HCl	DMAP	CH_2Cl_2
2b		HATU	Et_3N	DMF
2c	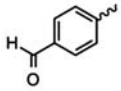	HATU	Et_3N	DMF
2d		HATU	Et_3N	DMF

Scheme 3. Synthesis of the DSPE-PEG_{2000}-SH (3) Functionalized Phospholipid

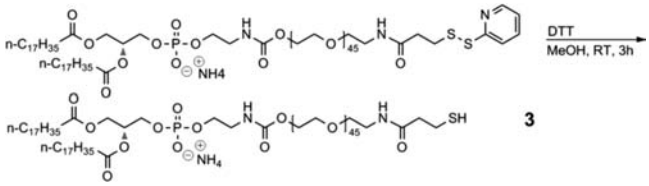

In order to evaluate the efficiency of the different coupling strategies and make a valid comparison, a standardized protocol was used to minimize the influence of other parameters. Functionalized liposomes composed of DSPC/DSPE-PEG_{2000}/DSPE-PEG_{2000}-R (95:4:1) (R = alkyne (**2a**), cycloalkyne (**2b**), aldehyde (**2c**), azide (**2d**), thiol (**3**), or maleimide (**4**)) were prepared by the method described by Bangham and co-workers.[34] The lipid components were dissolved in a mixture of $CHCl_3$/MeOH (9:1), and the solvent was removed to form a transparent lipid film. The lipid film was hydrated in HEPES-buffer (pH 6.5) at 65 °C and extruded through 100 nm polycarbonate filters to form liposomes in the 100 nm range. The liposomes were characterized by dynamic light scattering (DLS), and the ζ-potentials were measured to ensure that liposomes were formed. All liposomes had a diameter of approximately 100 nm and slightly negative ζ-potential due to the presence of the DSPE-PEG_{2000} lipids. Postfunctionalization was carried out by adding the required components for the individual reactions (e.g., $CuSO_4 \cdot 5H_2O$ and sodium ascorbate for the CuAAC reaction), followed by addition of the required functionalized TATE peptide **1a−e** (1 equiv peptide to 1.1 equiv of the functionalized lipid component) in MeOH. Postfunctionalization reactions were carried out at room temperature and carefully mixed using a plate shaker.

dx.doi.org/10.1021/bc3005057 | Bioconjugate Chem. 2012, 23, 2444−2450

For the conjugation reactions in solution, functionalized phospholipids (1.1 equiv) and functionalized TATE peptides (1 equiv) were dissolved in methanol, mixed with the required additives to facilitate reaction, as described in the Experimental Procedures, and stirred at room temperature. Triplicates of all reactions were carried out to ensure reproducibility and elucidate the heterogeneity of liposomal postfunctionalization. The amount of functionalized TATE added in the two conjugation approaches was carefully controlled by measuring the concentration of the peptide stock solution by UV−vis, thus ensuring exactly the same peptide concentration in all reactions. To ensure the same total concentration of phospholipids in all reactions, phosphorus content measurement was carried out by ICP-AES. All reactions were monitored for 24 h by HPLC using UV-detection (λ = 280 nm), and up to 72 h in selected cases, by removing small aliquots from the reaction vial, and the conjugation efficiency was calculated based on the area under the curve (AUC) for the free peptide and the DSPE-PEG_{2000}-TATE conjugate, respectively (Figure 1). MALDI-TOF MS was used to verify that an excess of the functionalized phospholipids reagent existed in all reactions that did not go to completion within 72 h.

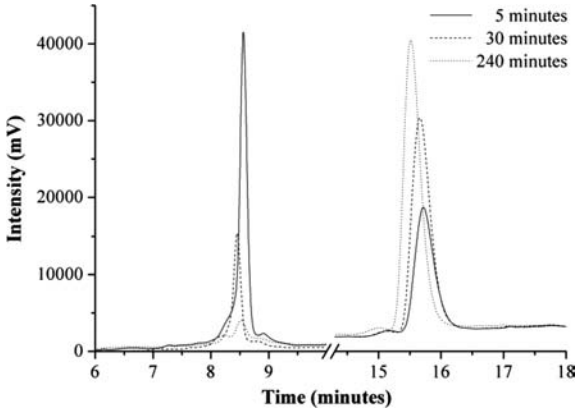

Figure 1. Example of the monitoring of a conjugation reaction by HPLC over time at 280 nm. The decreasing peak at 8.5 min belongs to the free TATE-maleimide (**1a**), while the peak increasing at 15.6 min is the product from the Michael addition between TATE-maleimide (**1a**) and DSPE-PEG_{2000}-SH (**3**).

Conjugation of TATE and DSPE-PEG_{2000} by Oxime Formation. This method, which has not previously been reported for the surface functionalization of liposomes, is chemoselective and bioorthogonal to functional groups in most natural occurring ligands and could serve as an excellent alternative to existing liposome postfunctionalization methods.[35] TATE-hydroxylamine (**1e**) and DSPE-PEG_{2000}-benzaldehyde (**2c**) were conjugated, both in solution and on the liposome surface, by simply mixing the two components without any additives. Oxime bond formation in solution was found to be quantitative within one hour, whereas eight hours of incubation was needed once performed directly on the liposome surface (Figure 2). Both procedures resulted in complete conversion to the phospholipid coupled TATE within 24 h under mild conditions.

Oxime bond formation is known to be accelerated by the presence of aniline,[36] acetic acid,[37] or Lewis acids.[38] In order to verify this, acetic acid (0.1% v/v) was added to a liposome batch containing TATE-hydroxylamine (**1e**). Under these

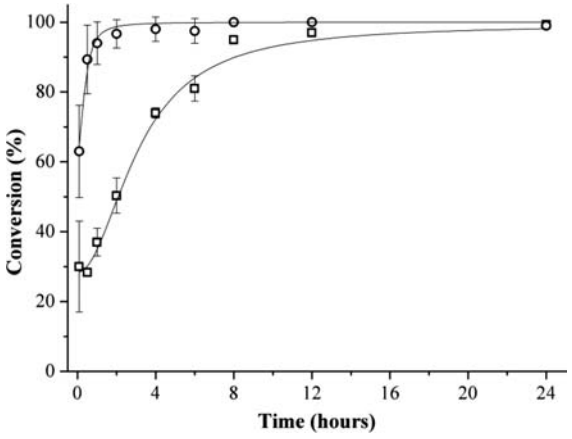

Figure 2. Conjugation of DSPE-PEG_{2000} and TATE by oxime bond formation. Reactions carried out in solution and directly on the liposome surface. TATE-hydroxylamine (**1e**) + DSPE-PEG_{2000}-benzaldehyde (**2c**) in solution (○), TATE-hydroxylamine (**1e**) + DSPE-PEG_{2000}-benzaldehyde (**2c**) on liposomes (□). All values are means ± SEM (n = 3).

conditions, the conjugation yield reached 78% within 5 min. Without the presence of the catalyst, 30% conversion was observed within the same time frame. The oxime bond formation is a reversible process; however, HPLC and MALDI TOF MS did not show any reversible formation of the starting materials within one week in aqueous medium, which supports the reporting of oxime bonds to be more hydrolytically stable than, e.g., its analogous hydrazine bond at physiologically relevant pH.[39] The position of these two functional groups is not interchangeable, as placing the aldehyde functionality on TATE will induce the risk of intramolecular imine formation.

Conjugation of TATE and DSPE-PEG_{2000} by CuAAC. An often applied procedure for nanoparticle functionalization is the CuAAC reaction—commonly referred to as the Click Reaction.[22−24] Conjugation of TATE and DSPE-PEG_{2000} by the CuAAC reaction was carried out using sodium ascorbate to generate Cu^{I} from $CuSO_4 \cdot 5H_2O$ in situ. Reactions were carried out with the azide present on the TATE peptide, the alkyne at the PEG terminal of DSPE-PEG_{2000}, and vice versa. The relative position of the functional moieties was found to have no significant effect on the reaction efficacy under the solution conditions, as both orientations result in approximately 98% yield after 12 h (Figure 3). A different result was obtained when monitoring the postfunctionalization reaction on the liposome surface. The cycloaddition between the azide-functionalized TATE (**1c**) and the alkyne-modified phospholipid (**2a**) resulted in about 75% yield after 2 h, while the opposite position having the azide functionality present on the liposomes and the alkyne at the N-terminal of the peptides leveled out at 43% (Figure 3).

Functionalization of azide-modified liposomes by the CuAAC reaction has not previously been reported elsewhere to our knowledge. Functionalization of liposomes by the CuAAC reaction has consistently been carried out with alkyne-modified liposomes and azide-functionalized ligands; thus, these reports have not observed the clear negative trend observed here with the azide-functionalized liposomes. Furthermore, removing the copper fully from the final product to avoid copper induced cytotoxicity can be challenging, which

dx.doi.org/10.1021/bc3005057 | Bioconjugate Chem. 2012, 23, 2444−2450

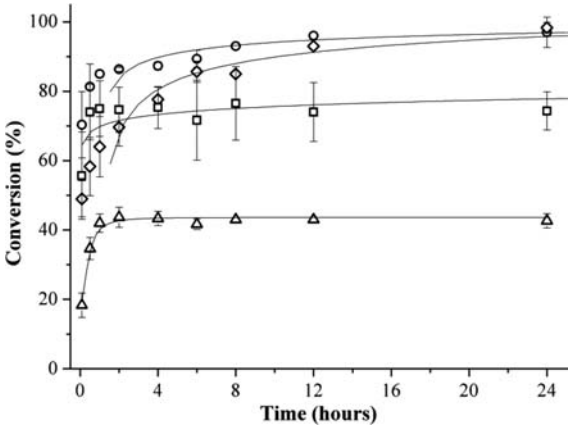

Figure 3. Conjugation of DSPE-PEG$_{2000}$ and TATE by the CuAAC reaction. Reactions carried out in solution and directly on the liposome surface. TATE-azide (**1c**) + DSPE-PEG$_{2000}$-alkyne (**2a**) in solution (○), TATE-azide (**1c**) + DSPE-PEG$_{2000}$-alkyne (**2a**) on liposomes (□), TATE-alkyne (**1d**) + DSPE-PEG$_{2000}$-azide (**2d**) in solution (◊), TATE-alkyne (**1d**) + DSPE-PEG$_{2000}$-azide (**2d**) on liposomes (Δ). All values are means ± SEM (n = 3).

to some degree reduces the usability of this reaction for biological purposes.

Conjugation of TATE and DSPE-PEG$_{2000}$ by Cu-Free Click Chemistry. A method to avoid addition of toxic copper salts as catalyst in the triazole formation is to use strained or electron-deficient alkynes.[40,41] This strategy was studied using the DSPE-PEG$_{2000}$-cyclooctyne (**2b**) and azide-functionalized TATE (**1c**). In solution, the conjugation was remarkably slow, yet highly reliable and reproducible with no form of decomposition or side product formation. As the reaction was terminated after 50 days, a product yield of 86% was obtained without reaching a plateau. Applying the post-functionalization protocol resulted in a remarkably faster initial reaction (Figure 4), and a level of 84% yield was reached after 72 h.

Interestingly, triazole formation was significantly faster when performed on liposome surfaces compared to the reaction in solution. This is presumably due to favorable interactions between the liposome surface and TATE-azide (**1c**). As TATE-azide (**1c**) is not highly soluble in the buffer, it prefers to bind to the PEG layer, bringing it closer to the reaction sites on the surface, which leads to a faster reaction. Choosing a more reactive cyclooctyne could not only increase the reaction rate in solution, but also increase the risk of side product formation.[42,43] However, a relatively long synthetic procedure to obtain the cyclooctyne moiety limits the use of this type of copper-free click reaction. Furthermore, it has been shown that thiols can add spontaneously to cyclooctynes limiting the bioorthogonality, as some degree of nonspecific reactions can occur.[44]

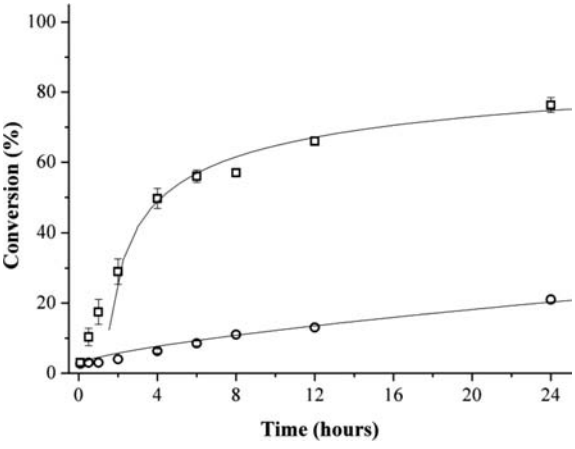

Figure 4. Conjugation of DSPE-PEG$_{2000}$ and TATE by strain-promoted Click reaction. Reactions were carried out in solution and directly on the liposome surface. TATE-azide (**1c**) + DSPE-PEG$_{2000}$-cyclooctyne (**2b**) in solution (○), TATE-azide (**1c**) + DSPE-PEG$_{2000}$-cyclooctyne (**2b**) on liposomes (□). All values are means ± SEM (n = 3).

Conjugation of TATE and DSPE-PEG$_{2000}$ by Michael Addition. The final approach tested to conjugate TATE and DSPE-PEG$_{2000}$ was using the Michael addition procedure. In general, the Michael addition proceeded rapidly within the first four hours until reaching a plateau, and reactions carried out in solution were slightly faster compared to the liposomal counterpart. The orientation of the maleimide and the thiol was found to have a decisive impact on the conjugation efficiency. Michael addition in solution between DSPE-PEG$_{2000}$-SH (**3**) and TATE-maleimide (**1a**) resulted in 97% conversion, whereas when performed on the liposome surface, 92% conversion was observed. The opposite orientation of functionalities expressed in the form of DSPE-PEG$_{2000}$-maleimide (**4**) and TATE-thiol (**1b**) only resulted in 53% product formation when performed in solution and 40% for the postfunctionalization of liposomes (Figure 5), which was surprising. The origin for this observation is not clear, however; multiple factors could have caused this drop in conversion. Hydrolysis of the maleimide moiety to the nonreactive maleamic acid at pH > 8.5 has been reported in the literature,[45] but at pH 6.5 where our reactions are carried out, this should be minimized.[46,47] This was confirmed by MALDI-TOF MS where intact DSPE-PEG$_{2000}$-maleimide as well as unreacted TATE-SH was observed. However, a minor amount of methoxy-substituted maleimide was also observed by MALDI-TOF MS indicating that the oxa-Michael addition is a competing side

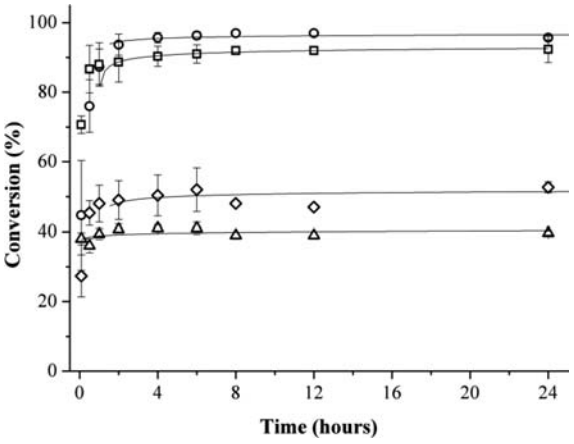

Figure 5. Conjugation of DSPE-PEG$_{2000}$ and TATE by Michael addition. Reactions carried out in solution and directly on the liposome surface. TATE-maleimide (**1a**) + DSPE-PEG$_{2000}$-SH (**3**) in solution (○), TATE-maleimide (**1a**) + DSPE-PEG$_{2000}$-SH (**3**) on liposomes (□), TATE-thiol (**1b**) + DSPE-PEG$_{2000}$-maleimide (**4**) in solution (◊), TATE-thiol (**1b**) + DSPE-PEG$_{2000}$-maleimide (**4**) on liposomes (Δ). All values are means ± SEM (n = 3).

dx.doi.org/10.1021/bc3005057 | Bioconjugate Chem. 2012, 23, 2444−2450

reaction.[48] As poor conversion was observed for the reaction carried out in solution as well as on the surface, we speculated that the TATE-thiol (**1b**) peptide was the limiting factor in this reaction. TATE-thiol (**1b**) is highly prone to oxidation resulting in nonreactive TATE-dimers; however, dimerization was not observed by HPLC or by MALDI-TOF MS. As a positive control of the reactivity of the commercial DSPE-PEG_{2000}-maleimide (**4**), a test reaction using 2-mercaptoethanol was conducted. Using this small and highly reactive thiol, complete product formation was observed within two hours as confirmed by MALDI-TOF MS, confirming excellent reactivity of DSPE-PEG_{2000}-maleimide (**4**). Hence, the reason for the low coupling efficiency between DSPE-PEG_{2000}-maleimide (**4**) and TATE-SH (**1b**) is not clear.

CONCLUSION

In conclusion, a novel highly effective method to functionalize liposomes by postfunctionalization as well as under solution conditions has been introduced in the form of an oxime bond formation between an aldehyde and a hydroxylamine. This conjugation is chemoselective and bioorthogonal to functional groups in most naturally occurring relevant ligands, and based on our investigations, it could serve as an excellent alternative to existing liposome postfunctionalization methods.

In addition, a systematic study has been conducted to elucidate the optimal postfunctionalization chemistry with focus on the relative position of the reactive functionalities. In general, the reactions carried out directly on the surface of the functionalized liposomes were slower than the solution-phase counterpart, except for the strain-promoted Click reaction, which surprisingly showed the opposite trend. Despite of possible heterogeneities of liposomal formulations, surface conjugation reactions were, in general, highly reproducible. The relative position of the reactive functionalities was found to have a significant impact on the degree of conversion for the Michael addition and the CuAAC reaction. The Michael addition was found to be most effective when the nucleophilic thiol was present at the distal end of the PEG polymer compared to the N-terminal of TATE. A similar observation was observed for the CuAAC reaction. The relative positions of the azide and the alkyne did not influence the degree of conversion in solution; however, once performed on the liposome surface it had a decisive impact. Having the alkyne functionality present at the liposome surface resulted in 75% conversion, whereas the azide functionalized liposomes only resulted in 43% product formation.

The findings described above will be useful for future postfunctionalization designs and clearly illustrate that care should be taken to select the most appropriate chemistry for the desired chemical manipulation. Furthermore, it is also evident that postfunctionalized nanoparticles in general should always be analyzed in order to ensure the desired composition of the nanoparticle constructs.

ASSOCIATED CONTENT

Supporting Information

Detailed description of the synthetic approach to compounds **1a–e**, **2a–d**, **3** and their characterization (^{1}H NMR, FT-IR, HPLC, and MALDI-TOF MS). This material is available free of charge via the Internet at http://pubs.acs.org.

AUTHOR INFORMATION

Corresponding Author

*E-mail: Thomas.andresen@nanotech.dtu.dk.

Author Contributions

†Authors contributed equally.

Notes

The authors declare no competing financial interest.

ACKNOWLEDGMENTS

The Danish Strategic Research Council (NABIIT) grant 2106-07-0033 and 2106-08-0081 is gratefully acknowledged for funding.

ABBREVIATIONS

EPR, enhanced permeability and retention effect; CuAAC, copper catalyzed azide–alkyne cycloaddition; TATE, [Tyr^3,Thr^8]-octreotate; DSPC, 1,2-distearoyl-*sn*-glycero-3-phosphocholine; DSPE, 1,2-distearoyl-*sn*-glycero-3-phosphoethanolamine; HPLC, high-performance liquid chromatography; SPPS, solid-phase peptide synthesis; MALDI TOF MS, matrix-assisted laser desorption/ionization time-of-flight mass spectroscopy; DLS, dynamic light scattering; ICP-AES, inductively coupled plasma atomic emission spectroscopy.

REFERENCES

(1) Petersen, A. L., Hansen, A. E., Gabizon, A., and Andresen, T. L. (2012) Liposome imaging agents in personalized medicine. *Adv. Drug Delivery Rev. 64*, 1417–1435.

(2) Phillips, M. A., Gran, M. L., and Peppas, N. A. (2010) Targeted nanodelivery of drugs and diagnostics. *Nano Today 5*, 143–159.

(3) Petersen, A. L., Binderup, T., Jølck, R. I., Rasmussen, P., Henriksen, J. R., Pfeifer, A. K., Kjaer, A., and Andresen, T. L. (2012) Positron emission tomography evaluation of somatostatin receptor targeted 64Cu-TATE-liposomes in a human neuroendocrine carcinoma mouse model. *J. Controlled Release 160*, 254–263.

(4) Pavlov, V., Xiao, Y., Shlyahovsky, B., and Willner, I. (2004) Aptamer-functionalized Au nanoparticles for the amplified optical detection of thrombin. *J. Am. Chem. Soc. 126*, 11768–11769.

(5) Liu, J., and Lu, Y. (2006) Preparation of aptamer-linked gold nanoparticle purple aggregates for colorimetric sensing of analytes. *Nat. Protoc. 1*, 246–252.

(6) Taylor, K. M. L., Kim, J. S., Rieter, W. J., An, H., Lin, W., and Lin, W. (2008) Mesoporous silica nanospheres as highly efficient MRI contrast agents. *J. Am. Chem. Soc. 130*, 2154–2155.

(7) Sun, I. C., Eun, D. K., Koo, H., Ko, C. Y., Kim, H. S., Yi, D. K., Choi, K., Kwon, I. C., Kim, K., and Ahn, C. H. (2011) Tumor-targeting gold particles for dual computed tomography/optical cancer imaging. *Angew. Chem., Int. Ed. 50*, 9348–9351.

(8) Muhs, A., Hickman, D. T., Pihlgren, M., Chuard, N., Giriens, V., Meerschman, C., van der Auwera, I., van Leuven, F., Sugawara, M., Weingertner, M. C., Bechinger, B., Greferath, R., Kolonko, N., Nagel-Steger, L., Reisner, D., Brady, R. O., Pfeifer, A., and Nicolau, C. (2007) Liposomal vaccines with conformation-specific amyloid peptide antigens define immune response and efficacy in APP transgenic mice. *Proc. Natl. Acad. Sci. U.S.A. 104*, 9810–9815.

(9) Davis, M. E., Chen, Z. G., and Shin, D. M. (2008) Nanoparticle therapeutics: An emerging treatment modality for cancer. *Nat. Rev. Drug Discovery 7*, 771–782.

(10) Petros, R. A., and DeSimone, J. M. (2010) Strategies in the design of nanoparticles for therapeutic applications. *Nat. Rev. Drug Discovery 9*, 615–627.

(11) Gregoriadis, G., Wills, E. J., Swain, C. P., and Tavill, A. S. (1974) Drug-carrier potential of liposomes in cancer chemotherapy. *Lancet 1*, 1313–1316.

(12) Maeda, H., Wu, J., Sawa, T., Matsumura, Y., and Hori, K. (2000) Tumor vascular permeability and the EPR effect in macromolecular therapeutics. A review. *J. Controlled Release 65*, 271−284.
(13) Koning, G. A., Gorter, A., Scherphof, G. L., and Kamps, J. A. (1999) Antiproliferative effect of immunoliposomes containing 5-fluorodeoxyuridine dipalmitate on colon cancer cells. *Br. J. Cancer 80*, 1718−1725.
(14) Koning, G. A., Morselt, H. W., Gorter, A., Allen, T. M., Zalipsky, S., Scherphof, G. L., and Kamps, J. A. (2003) Interaction of differently designed immunoliposomes with colon cancer cells and Kupffer cells. An in vitro comparison. *Pharm. Res. 20*, 1249−1257.
(15) Nardin, A., Lefebvre, M. L., Labroquère, K., Faure, O., and Abastado., J. P. (2006) Liposomal muramyl tripeptide phosphatidylethanolamine: Targeting and activating macrophages for adjuvant treatment of osteosarcoma. *Curr. Cancer Drug Targets 6*, 123−133.
(16) Chiu, S. J., Liu, S., Perrotti, D., Marcucci, G., and Lee, R. J. (2006) Efficient delivery of a Bcl-2-specific antisense oligodeoxyribonucleotide (G3139) via transferrin receptor-targeted liposomes. *J. Controlled Release 112*, 199−207.
(17) Zhu, J., Xue, J., Guo, Z., Zhang, L., and Marchant, R. E. (2007) Biomimetic glycoliposomes as nanocarries for targeting P-selectin on activated platelets. *Bioconjugate Chem. 18*, 1366−1369.
(18) Matsui, M., Shimizu, Y., Kodera, Y., Kondo, E., Ikehara, Y., and Nakanishi, H. (2010) Targeted delivery of oligomannose-coated liposome to the omental micrometastasis by peritoneal macrophages from patients with gastric cancer. *Cancer Sci. 101*, 1670−1677.
(19) Lee, R. J., and Low, P. S. (1994) Delivery of liposomes into cultured KB cells via folate receptor-mediated endocytosis. *J. Biol. Chem. 269*, 3198−3204.
(20) Sudimack, J., and Lee, R. J. (2000) Targeted drug delivery via the folate receptor. *Adv. Drug Delivery Rev. 41*, 147−162.
(21) O'Donnell, M. J., Zhou, C., and Scott, W. L. (1996) Solid-phase unnatural peptide synthesis. *J. Am. Chem. Soc. 118*, 6070−6071.
(22) Tornøe, C. W., Christensen, C., and Meldal, M. (2002) Peptidotriazoles on solid phase: [1,2,3]-triazoles by regiospecific copper(I)-catalyzed 1,3-dipolar cycloadditions of terminal alkynes to azides. *J. Org. Chem. 67*, 3057−3064.
(23) Meldal, M., and Tornøe, C. W. (2008) Cu-catalyzed azide-alkyne cycloaddition. *Chem. Rev. 108*, 2952−3015.
(24) Rostovtsev, V. V., Green, L. G., Fokin, V. V., and Sharpless, K. B. (2002) A stepwise huisgen cycloaddition process: Copper(I)-catalyzed regioselective "ligation" of azides and terminal alkynes. *Angew. Chem., Int. Ed. 41*, 2596−2599.
(25) Staudinger, H., and Meyer, J. (1919) New organic compounds of phosphorus. III. phosphinemethylene derivatives and phosphinimines. *Helv. Chim. Acta 2*, 635−646.
(26) Saxon, E., and Bertozzi, C. R. (2000) Cell surface engineering by a modified Staudinger reaction. *Science 287*, 2007−2010.
(27) Reubi, J. C., and Maecke, H. R. (2008) Peptide-based probes for cancer imaging. *J. Nucl. Med. 49*, 1735−1738.
(28) Jølck, R. I., Feldborg, L. N., Andersen, S., Moghimi, S. M., and Andresen, T. L. (2011) Engineering liposomes and nanoparticles for biological targeting. *Adv. Biochem. Eng. Biotechnol. 125*, 251−280.
(29) Sharpless, W. D., Wu, P., Hansen, T. V., and Lindberg, J. G. (2005) Just click it: Undergraduate procedures for the copper(I)-catalyzed formation of 1,2,3-triazoles from azides and terminal acetylenes. *J. Chem. Educ. 82*, 1833−1836.
(30) Bauer, W., Briner, U., Doepfner, W., Haller, R., Huguenin, R., Marbach, P., Petcher, T. J., and Pless, J. (1982) SMS 201−995: A very potent and selective octapeptide analog of somatostatin with prolonged action. *Life Sci. 31*, 1133−1140.
(31) Merrifield, R. B. (1963) Solid phase peptide synthesis. I. The synthesis of a tetrapeptide. *J. Am. Chem. Soc. 85*, 2149−2154.
(32) Schultz, M. K., Parameswarappa, S. G., and Pigge, F. C. (2010) Synthesis of a DOTA-biotin conjugate for radionuclide chelation via Cu-free click chemistry. *Org. Lett. 12*, 2398−2401.
(33) Cleland, W. W. (1964) Dithiothreitol, a new protective reagent for SH groups. *Biochemistry 3*, 480−482.
(34) Bangham, A. D., and Horne, R. W. (1964) Negative staining of phospholipids and their structural modification by surface-active agents as observed in the electron microscope. *J. Mol. Biol. 8*, 660−668.
(35) Richard, A., and Bourel-Bonnet, L. (2005) Internalization of a peptide into multilamellar vesicles assisted by the formation of an alpha-oxo oxime bond. *Chem.—Eur. J. 11*, 7315−7321.
(36) Dirksen, A., and Dawson, P. E. (2008) Rapid oxime and hydrazone ligations with aromatic aldehydes for biomolecular labeling. *Bioconjugate Chem. 19*, 2543−2548.
(37) Gustafsson, M., Olsson, R., and Andersson, C.-M. (2001) General combinatorial synthesis of tertiary amines on solid support. A novel conditional release strategy based on traceless linking at nitrogen. *Tetrahedron Lett. 42*, 133−136.
(38) Sridhar, M., Narsaiah, C., Raveendra, J., Reddy, G. K., Reddy, M., Reddy, M. K. K., and Ramanaiah, B. C. (2011) Efficient microwave-assisted synthesis of oximes from acetohydroxamic acid and carbonyl compounds using $BF_3{\cdot}OEt_2$ as the catalyst. *Tetrahedron Lett. 52*, 4701−4704.
(39) Rose, K., Zeng, W., Regamey, P. O., Chernushevich, I. V., Standing, K. G., and Gaertner, H. F. (1996) Natural peptides as building blocks for the synthesis of large protein-like molecules with hydrazone and oxime linkages. *Bioconjugate Chem. 7*, 552−556.
(40) Agard, N. J., Prescher, J. A., and Bertozzi, C. R. (2004) A strain-promoted [3 + 2] azide-alkyne cycloaddition for covalent modification of biomolecules in living systems. *J. Am. Chem. Soc. 126*, 15046−15047.
(41) Li, Z., Seo, T. S., and Ju, J. (2004) 1,3-dipolar cycloaddition of azides with electron-deficient alkynes under mild condition in water. *Tetrahedron Lett. 45*, 3143−3146.
(42) Chenoweth, K., Chenoweth, D., and Goddard, W. A., III. (2009) Cyclooctyne-based reagents for uncatalyzed click chemistry: A computational survey. *Org. Biomol. Chem. 7*, 5255−5258.
(43) Codelli, J. A., Baskin, J. M., Agard, N. J., and Bertozzi, C. R. (2008) Second-generation difluorinated cyclooctynes for copper-free click chemistry. *J. Am. Chem. Soc. 130*, 11486−11493.
(44) Fairbanks, B. D., Sims, E. A., Anseth, K. S., and Bowman, C. N. (2010) Reaction rates and mechanisms for radical, photoinitated addition of thiols to alkynes, and implications for thiol-yne photopolymerizations and click reactions. *Macromolecules 43*, 4113−4119.
(45) Gregory, J. D. (1955) The stability of N-ethylmaleimide and its reaction with sulfhydryl groups. *J. Am. Chem. Soc. 77*, 3922−3923.
(46) Barradas, R. G., Fletcher, S., and Porter, J. D. (1976) The hydrolysis of maleimide in alkaline solution. *Can. J. Chem. 54*, 1400−1404.
(47) Matsui, S., and Aida, H. (1978) Hydrolysis of some N-alkylmaleimides. *J. Chem. Soc., Perkin Trans. 2*, 1277−1280.
(48) Finnegan, R. A., and Mueller, W. H. (1965) Base-catalyzed addition and solvolysis reactions of N-phenyl-maleimide in methanol. *J. Pharm. Sci. 54*, 1257−1260.

Supporting Information

Quantitative Evaluation of Bioorthogonal Chemistries for Surface Functionalization of Nanoparticles

Lise N. Feldborg[1], Rasmus I. Jølck[1] and Thomas L. Andresen*

DTU Nanotech, Department of Micro-and Nanotechnology
Technical University of Denmark, Building 423
2800 Lyngby, Denmark

[*] T. L. Andresen, E-mail: Thomas.andresen@nanotech.dtu.dk.
[1] Authors contributed equally

Materials

1,2-Distearoyl-*sn*-glycero-3-phosphocholine (DSPC), 1,2-distearoyl-*sn*-glycero-3-phosphoethanolamine-(polyethylene glycol)$_{2000}$ (DSPE-PEG$_{2000}$), 1,2-distearoyl-*sn*-glycero-3-phosphoethanolamine-N-[amino(polyethylene glycol)$_{2000}$] (DSPE-PEG$_{2000}$-NH$_2$), 1,2-distearoyl-*sn*-glycero-3-phosphoethanolamine-N-[maleimide(polyethylene glycol)$_{2000}$] (DSPE-PEG$_{2000}$-Mal), and 1,2-distearoyl-*sn*-glycero-3-phosphoethanolamine-N-[PDP(polyethylene glycol)$_{2000}$] (DSPE-PEG$_{2000}$-PDP) were purchased from Avanti Polar Lipids Inc. (Alabaster, USA). Dithiothreitol (DTT), 5-azidopentanoic acid, 4-formyl benzoic acid, 4-pentynoic acid, N-(3-dimethylaminopropyl)-N′-ethylcarbodiimide hydrochloride (EDC·HCl), thallium(III) trifluoroacetate, trifluoroacetic acid (TFA), and triisopropylsilane (TIS) were purchased from Sigma Aldrich (Schnelldorf, Germany). The coupling reagent *O*-(7-Azabenzotriazol-1-yl)-*N,N,N′,N′*-tetramethyluronium hexafluorophosphate (HATU), Wang Resin and all Fmoc protected amino acids used for the solid phase peptide synthesis were purchased from GL Biochem (Shanghai, China). All chemicals and reagents were of analytical grade and used without further purification.

Instrumentation

FT-IR was recorded on a Perkin Elmer Spectrum 100 FT-IR Spectrometer. Dynamic light scattering (DLS) and zeta-potential measurements were performed on a Brookhaven Instruments Corporation ZetaPALS zeta potential analyzer**.** Analytical reversed-phase high-performance liquid chromatography (RP-HPLC) was carried out on a Shimadzu LC-2010 analytical HPLC by employing a Waters XTerra® C_8 5 µm (4.6 x 150 mm) column. Semi-preparative HPLC was performed on a Waters Semi-preparative HPLC equipped with a Waters 600 Pump & Controller and a Waters 2489 UV/Visible Detector using a a Waters XTerra® C_8 5µm (19 x 150 mm) column. HPLC Eluent A consisted of a 5% MeCN aqueous solution with 0.1% TFA; HPLC Eluent B consisted of 0.1% TFA in MeCN. HPLC analysis was monitored using dual channel UV detection at 254 nm and 280 nm. Pre-packed Strata C_8 solid phase extraction (SPE) (55 µm, 70 Å) Giga Tubes from Phenomenex (Torrance, USA) were used for the purification of functionalized phospholipids. Mass spectra were recorded using a Bruker Daltonics Reflex IV MALDI-TOF Spectrometer using 2,5-dihydroxybenzoic acid (DHB) spiked with sodium trifluoroacetate in MeOH as matrix. NMR spectra were recorded either on a Bruker Avance DPS 250 MHz or a Varian Mercury 300 MHz Spectrometer using the solvent peak as an internal reference.

Synthesis of functionalized TATE peptides

General SPPS protocol: The linear TATE octapeptide NH_2-D-Phe-Cys(Acm)-Tyr(*t*Bu)-D-Trp(Boc)-Lys(Boc)-Thr(*t*Bu)-Cys(Acm)-Thr(*t*Bu)-Resin was synthesized manually by SPPS on a Wang Resin preloaded with NH_2-Thr(*t*Bu)-OH (0.50 g, 0.50 mmol/g) by standard Fmoc methodology. Each coupling was performed by 4.0 equiv. Fmoc protected amino acid, 3.95 equiv. HATU and 8.0 equiv. 2,4,6-collidine in DMF (5.0 mL). Cleavage of the Fmoc group was carried out using piperidine in DMF (1:4) for 2 x 5 minutes. Completion of each coupling and deprotection step were monitored by the Kaiser test. Removal of the Acm protection groups on the two cysteines and simultaneous disulfide bond formation was achieved by addition of $Tl(CF_3COO)_3$ (0.27 g, 0.50 mmol, 2.0 equiv.) in DMF (5.0 mL) for 75 min.. The resin containing the cyclized peptide was extensively washed with DMF (10 × 5.0 mL) and subsequently divided into five SPPS reaction vials (5 × 0.10 g) in which the N-terminal was acylated with the desired functionality as described below.

TATE-maleimide (1a). 4-Maleimidobutyric acid (38 mg, 0.20 mmol, 4.0 equiv.), HATU (75 mg, 0.198 mmol, 3.95 equiv.) and 2,4,6-colidine (53 uL, 0.40 mmol, 8.0 equiv.) in DMF (2.0 mL) were added to the resin immobilized cyclic octapeptide for 2 hours at room temperature followed by washing with DMF (4 × 5.0 mL). The peptide was cleaved from the solid support by addition of TFA/H_2O/TIS (95:2.5:2.5) for 2 hours. Final purification was achieved by semi-preparative HPLC employing a Waters Xterra® C_8 5µm (19 x 150 mm) column. Eluent: (A) 5% CH_3CN + 0.1% TFA in H_2O, (B) 0.1% TFA in CH_3CN. Gradient profile; linear gradient from 0% B to 100% B over 15 min. Flow rate; 15 mL/min. Maleimido-TATE (**1a**) was isolated as a homogenous peak with retention time of 7.99 min. The solvent was removed *in vacuo* and the product lyophilized from a mixture of water and acetonitrile to give a white fluffy powder (27 mg, 45%). The purity of the product was monitored by analytical HPLC, using the same gradient profile and solvent mixtures as above, but with a Waters XTerra® C_8 5µm (4.6 x 150 mm) column, flow rate 1 mL/min. Purity >98%. MALDI-TOF MS (m/z) (DHB+Na): Calcd. For $C_{57}H_{71}N_{11}O_{15}S_2$ $(M+Na)^+$ 1236.45. Found: 1236.39.

TATE-SH (1b). 3-(tritylthio)-propionoic acid (70 mg, 0.20 mmol, 4.0 equiv.), HATU (75 mg, 0.198 mmol, 3.95 equiv.) and 2,4,6-colidine (53 µL, 0.40 mmol, 8.0 equiv.) in DMF (2.0 mL) were added to the resin immobilized cyclic octapeptide for 2 hours at room temperature followed by washing with DMF (4 × 5.0 mL). The peptide was cleaved from the solid support by addition of TFA/H_2O/TIS (95:2.5:2.5) for 2 hours. Final purification was achieved by semi-preparative HPLC employing a Waters Xterra® C_8 5µm (19 x 150 mm) column. Eluent: (A) 5% CH_3CN + 0.1% TFA in H_2O, (B) 0.1% TFA in CH_3CN. Gradient profile; linear gradient from 0% B to 40% B over 15 min. Flow rate; 15 mL/min. TATE-thiol (**1b**) was isolated as a homogenous peak with retention time of 13.83 min. The solvent was removed *in vacuo* and the product lyophilized from a mixture of water and acetonitrile to give a white fluffy powder (2.8 mg, 6.0%). The purity of the product was monitored by analytical HPLC using the same gradient profile and solvent mixtures as above, but with a Waters XTerra® C_8 5µm (4.6 x 150 mm) column, flow rate 1 mL/min. Purity >98%. MALDI-TOF MS (m/z) (DHB+Na): Calcd. For $C_{52}H_{68}N_{10}O_{13}S_3$ $(M+Na)^+$ 1159.33. Found: 1159.57.

TATE-azide (1c). 5-azidopentonoic acid (29 mg, 0.20 mmol, 4.0 equiv.), HATU (75 mg, 0.198 mmol, 3.95 equiv.) and 2,4,6-colidine (53 µL, 0.40 mmol, 8.0 equiv.) in DMF (2.0 mL) were added to the resin immobilized cyclic octapeptide for 2 hours at room temperature followed by washing with DMF (4 × 5.0 mL). The peptide was cleaved from the solid support by addition of TFA/H_2O/TIS (95:2.5:2.5) for 2 hours. Final purification was achieved by semi-preparative HPLC employing a Waters Xterra® C_8 5µm (19 x 150 mm) column. Eluent: (A) 5% CH_3CN + 0.1% TFA in H_2O, (B) 0.1% TFA in CH_3CN. Gradient profile; linear gradient from 0% B to 40% B over 15 min. Flow rate; 15 mL/min. TATE-azide (**16b**) was isolated as a homogenous peak with retention time of 16.22 min. The solvent was removed *in vacuo* and the product lyophilized from a mixture of water and acetonitrile to give a white fluffy powder (9.6 mg, 17%). The purity of the product was monitored by analytical HPLC using the same gradient profile and solvent mixtures as above but with a Waters XTerra® C_8 5µm (4.6 x 150 mm) column, flow rate 1

mL/min. Purity >98%. MALDI-TOF MS (m/z) (DHB+Na): Calcd. For $C_{54}H_{71}N_{13}O_{13}S_2$ $(M+Na)^+$ 1196.33. Found: 1236.39.

TATE-alkyne (1d). 4-pentynoic acid (20 mg, 0.20 mmol, 4.0 equiv.), HATU (75 mg, 0.198 mmol, 3.95 equiv.) and 2,4,6-colidine (53 µL, 0.40 mmol, 8.0 equiv.) in DMF (2.0 mL) were added to the resin immobilized cyclic octapeptide for 2 hours at room temperature followed by washing with DMF (4 × 5.0 mL). The peptide was cleaved from the solid support by addition of TFA/H_2O/TIS (95:2.5:2.5) for 2 hours. Final purification was achieved by semi-preparative HPLC employing a Waters Xterra® C_8 5µm (19 x 150 mm) column. Eluent: (A) 5% CH_3CN + 0.1% TFA in H_2O, (B) 0.1% TFA in CH_3CN. Gradient profile; linear gradient from 0% B to 30% B over 15 min. Flow rate; 15 mL/min. TATE-alkyne (**16c**) was isolated as a homogenous peak with retention time of 18.32 min. The solvent was removed *in vacuo* and the product lyophilized from a mixture of water and acetonitrile to give a white fluffy powder (7.2 mg, 13%). The purity of the product was monitored by analytical HPLC using the same gradient profile and solvent mixtures as above, but with a Waters XTerra® C_8 5µm (4.6 x 150 mm) column, flow rate 1 mL/min. Purity >98%. MALDI-TOF MS (m/z) (DHB+Na): Calcd. For $C_{54}H_{68}N_{10}O_{13}S_2$ $(M+Na)^+$ 1151.29. Found: 1151.51.

TATE-hydroxylamine (1e). Bis-Boc-amino-oxyacetic acid (47 mg, 0.15 mmol, 3 equiv.), HATU (56 mg, 0.146 mmol, 2.95 equiv.) and 2,4,6-colidine (41 µL, 0.30 mmol, 6.0 equiv.) in DMF (2.0 mL) were added to the resin immobilized cyclic octapeptide for 2 hours at room temperature, followed by washing with DMF (4 × 5.0 mL). The peptide was cleaved from the solid support by addition of TFA/H_2O/TIS (95:2.5:2.5) for 2 hours. Final purification was achieved by semi-preparative HPLC employing a Waters Xterra® C_8 5µm (19 x 150 mm) column. Eluent: (A) 5% CH_3CN + 0.1% TFA in H_2O, (B) 0.1% TFA in CH_3CN. Gradient profile; linear gradient from 0% B to 30% B over 15 min. Flow rate; 15 mL/min. TATE-hydroxylamine (**16d**) was isolated as a homogenous peak with retention time of 14.17 min. The solvent was removed *in vacuo* and the product lyophilized from a mixture of water and acetonitrile to give a white fluffy powder (15 mg, 27%). The purity of the product was monitored by analytical HPLC using the same gradient profile and solvent mixtures as above, but with a Waters XTerra® C_8 5µm (4.6 x 150 mm) column, flow rate 1 mL/min. Purity >98%. MALDI-TOF MS (m/z) (DHB+Na): Calcd. For $C_{51}H_{67}N_{11}O_{14}S_2$ $(M+Na)^+$ 1144.25. Found: 1144.41.

Synthesis of functionalized DSPE-PEG$_{2000}$ phospholipids

DSPE-PEG$_{2000}$-alkyne (2a). DSPE-PEG$_{2000}$-NH_2 (40 mg, 14 µmol, 1.0 equiv.) was dissolved in dry CH_2Cl_2 (5.0 mL) in a pre-dried flask under a nitrogen atmosphere. A mixture of 4-pentynoic acid (6.4 mg, 66 µmol, 4.7 equiv.) , EDC·HCl (12.2 mg, 64 µmol, 4.6 equiv.) and DMAP (16.2 mg, 0.13 mmol, 9.3 equiv.) in dry CH_2Cl_2 (1.0 mL) were added and the reaction stirred overnight under nitrogen at room temperature. The solvent was removed *in vacuo* and the product purified on a Strata-C_8 SPE column using a 10% stepwise gradient from 0-100% MeOH in water. Fractions with the desired compound was combined, reduced *in vacuo* and lyophilized from a mixture of water and acetonitrile to give the title compound as a white powder (25 mg, 61%). ^{1}H-NMR (250MHz, $CDCl_3$): δ 8.20 (bs, 1H), 6.57 (bs, 1H), 5.87 (bs, 1H), 5.27-5.18 (m, 1H), 4.36 (dd, *J* = 11.7, 3.4Hz, 1H), 4.25-3.90 (m, 7H), 3.64 (bs, 164H), 2.35-2.25 (m, 8H), 2.02 (t, *J* = 2.5Hz, 2H), 1.67-1.51 (m, 4H), 1.25 (bs, 56H), 0.88 (t, *J* = 6.6Hz). MALDI-TOF MS (m/z) (DHB+Na): 2807.1 ± n×44.0. IR (KBr): ν(cm^{-1}) 3435.9, 2918.3, 2851.4, 1697.5, 1112.9.

DSPE-PEG$_{2000}$-cyclooctyne (2b). DSPE-PEG$_{2000}$-NH_2 (75 mg, 27 µmol, 1.0 equiv.) was dissolved in dry DMF (3.0 mL) in a pre-dried flask under a nitrogen atmosphere. A mixture of 1-fluorocyclooct-2-ynecarboxylic acid (Schultz et al.[1]) (9.2 mg, 54 µmol, 2.0 equiv.), Et_3N (7.5 µL, 54 µmol, 2 equiv.) and HATU (20 mg, 53 µmol, 1.96 equiv.) in dry DMF (3.0 mL) were added and the reaction stirred overnight under nitrogen at room temperature. The solvent was removed *in vacuo* and the product purified on a Strata-C_8 SPE column using a 10% stepwise gradient from 0-100% MeOH in water. Fractions with the desired compound was combined, reduced *in vacuo* and lyophilized from a mixture of water and acetonitrile to give the title compound as a white powder (56 mg,

71%). ^{1}H-NMR (250MHz, $CDCl_3$): δ 6.89 (bs, 1H), 5.83 (bs, 1H), 5.25-5.19 (m, 1H) , 4.40-4.04 (m, 10H), 3.95-3.89 (m, 2H), 3.64 (bs, 164H), 3.53-3.33 (m, 6H), 2.37-2.29 (m, 6H), 1.67-1.55 (m, 6H), 1.25 (bs, 56H), 0.88 (t, *J* = 6.6 Hz, 6H). MALDI-TOF MS (m/z) (DHB+Na): 2968.3 ± n×44.0. IR (KBr): ν(cm^{-1}) 3445.3, 2918.2, 2851.4, 1741.6, 1648.9, 1104.6.

DSPE-PEG$_{2000}$-benzaldehyde (2c). DSPE-PEG$_{2000}$-NH_2 (100 mg, 36 µmol, 1.0 equiv.) was dissolved in dry DMF (1.0 mL) in a pre-dried flask under a nitrogen atmosphere. A mixture of 4-formyl benzoic acid (22 mg, 0.14 mmol, 4.0 equiv.), Et_3N (40 µL, 0.29 mmol, 8 equiv.) and HATU (54 mg, 0.14 mmol, 3.95 equiv.), in dry DMF (0.40 mL) were added and the reaction was stirred under nitrogen over night at room temperature. The solvent was removed *in vacuo* and the product purified on a Strata-C_8 SPE column using a 10% stepwise gradient from 50-100% MeOH in water. Fractions with the desired compound was combined, reduced *in vacuo* and lyophilized from a mixture of water and acetonitrile to give the title compound as a white powder (62 mg, 59%). ^{1}H-NMR (300MHz, $CDCl_3$): δ 10.08 (s, 1H), 8.01 (d, *J* = 8.4Hz, 2H), 7.94 (d, *J* = 8.4Hz, 2H), 6.00 (bs, 1H), 5.21 (bs, 1H), 4.37-3.31 (m, 1H), 4.22-4.03 (m, 10H), 3.89-3.85 (m, 2H), 3.64 (bs, 164H), 3.51-3.39 (m, 4H), 2.37-2.29 (m, 6H), 1.67-1.55 (m, 6H), 1.25 (bs, 56H), 0.88 (t, *J* = 6.6 Hz, 6H). MALDI-TOF MS (m/z) (DHB+Na): 2904.6 ± n×44.0. IR (*neat*): ν(cm^{-1}) 2917.0, 2850.8, 1744.5, 1702.1, 1466.5, 1343.5, 1102.5.

DSPE-PEG$_{2000}$-azide (2d). DSPE-PEG$_{2000}$-NH_2 (100 mg, 36 µmol, 1.0 equiv.) was dissolved in dry DMF (1.0 mL) in a pre-dried flask. A mixture of 5-azidopentanoic acid (21 mg, 0.14 mmol, 4.0 equiv.), Et_3N (40 µL, 0.29 mmol, 8.0 equiv.) and HATU (54 mg, 0.14 mmol, 3.95 equiv.) in dry DMF (0.50 mL) were added and the reaction stirred overnight under nitrogen at room temperature. The solvent was removed *in vacuo* and the product purified on a Strata-C_8 SPE column using a 10% stepwise gradient from 50-100% MeOH in water. Fractions with the desired compound was combined, reduced *in vacuo* and lyophilized from a mixture of water and acetonitrile to give the title compound as a white powder (79 mg, 79%). ^{1}H-NMR (300MHz, $CDCl_3$): δ 6.37 (bs, 1H), 5.20 (bs, 1H), 5.83 (bs, 1H), 4.38-4.32 (m, 1H) , 4.23-3.99 (m, 8H), 3.89-3.84 (m, 4H), 3.64 (bs, 164H), 3.54-3.27 (m, 4H), 2.33-2.16 (m, 8H), 1.75-1.55 (m, 8H), 1.25 (bs, 58H), 0.88 (t, *J* = 6.6 Hz, 6H). MALDI-TOF MS (m/z) (DHB+Na): 2898.4 ± n×44.0. IR (*neat*): ν(cm^{-1}) 2917.2, 2851.0, 2097.7, 1739.3, 1343.2, 1102.3.

DSPE-PEG$_{2000}$-SH (3). DTT (10 mg, 66 µmol, 3.9 equiv.) was added to a pre-dried flask under a nitrogen atmosphere containing DSPE-PEG$_{2000}$-PDP (50 mg, 17 µmol, 1.0 equiv.) in dry MeOH (1.0 mL). The reaction was stirred under nitrogen over night at room temperature after which the solvent was removed and the product purified on a Strata-C_8 SPE column, using a 10% stepwise gradient from 50-100% MeOH in water. Fractions with the desired compound were combined, reduced *in vacuo and* lyophilized from a mixture of water and acetonitrile to give a white fluffy powder (34 mg, 71%). ^{1}H-NMR (300MHz, $CDCl_3$): δ 6.99 (bs, 1H), 6.59 (bs, 1H), 5.20 (bs, 1H), 4.39-4.34 (m, 1H) , 4.23-4.13 (m, 4H), 4.08-3.99 (m, 4H), 3.89-3.85 (m, 2H), 3.64 (bs, 166H), 3.57-3.38 (m, 4H), 2.81 (dt, *J* = 8.3, 6.8 Hz, 2H), 2.51 (t, *J* = 6.8 Hz, 2H), 2.33-2.26 (m, 4H), 2.07 (s, 1H), 1.67-1.56 (m, 6H), 1.25 (bs, 56H), 0.88 (t, *J* = 6.6 Hz, 6H). MALDI-TOF MS (m/z) (DHB+Na): 2904.4 ± n×44.0. IR (*neat*): ν(cm^{-1}) 2917.1, 2850.9, 1739.0, 1466.6, 1343.0, 1101.6.

[1] Schultz, M. K., Parameswarappa, S. G. and Pigge, F. C. (2010) Synthesis of a DOTA-biotin conjugate for radionuclide chelation via Cu-free click chemistry. *Org. Lett. 12*, 2398-2401.

Bioconjugate Chemistry

Article

pubs.acs.org/bc

Synthesis and Characterization of a Melanoma-Targeted Fluorescence Imaging Probe by Conjugation of a Melanocortin 1 Receptor (MC1R) Specific Ligand

Narges K. Tafreshi,[†] Xuan Huang,[†] Valerie E. Moberg,[†] Natalie M. Barkey,[†] Vernon K. Sondak,[‡] Haibin Tian,[†] David L. Morse,*[,†] and Josef Vagner*[,§]

[†]Department of Cancer Imaging and Metabolism, [‡]Department of Cutaneous Oncology, H. Lee Moffitt Cancer Center & Research Institute, Tampa, Florida, United States

[§]BIO5 Institute, University of Arizona, Tucson, Arizona, United States

Supporting Information

ABSTRACT: The incidence of malignant melanoma is rising more rapidly than that of any other cancer in the United States. The melanocortin 1 receptor (MC1R) is overexpressed in most human melanoma metastases, thus making it a promising target for imaging and therapy of melanomas. We have previously reported the development of a peptidomimetic ligand with high specificity and affinity for MC1R. Here, we have conjugated near-infrared fluorescent dyes to the C-terminus of this ligand via lysine-mercaptopropionic acid linkers to generate MC1R specific optical probes (MC1RL-800, 0.4 nM K_i; and MC1RL-Cy5, 0.3 nM K_i). Internalization of the imaging probe was studied in vitro by fluorescence microscopy using engineered A375/MC1R cells and B16F10 cells with endogenous MC1R expression. The in vivo tumor targeting of MC1RL-800 was evaluated by intravenous injection of probe into nude mice bearing bilateral subcutaneous A375 xenograft tumors with low MC1R expression and engineered A375/MC1R tumors with high receptor expression. Melanotic B16F10 xenografts were also studied. Fluorescence imaging showed that the agent has higher uptake values in tumors with high expression compared to low ($p < 0.05$), demonstrating the effect of expression levels on image contrast-to-noise. In addition, tumor uptake was significantly blocked by coinjection of excess NDP-α-MSH peptide ($p < 0.05$). In conclusion, the MC1R-specific imaging probe developed in this study displays excellent potential for the intraoperative detection of regional node involvement and for margin detection during melanoma metastasis resection.

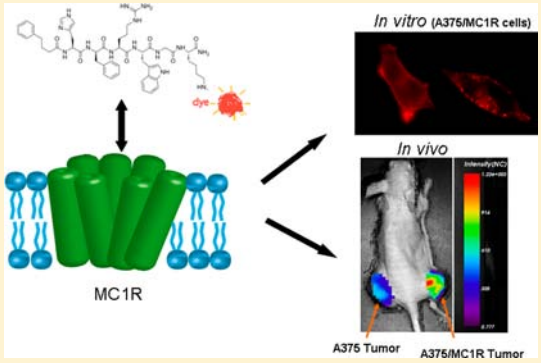

INTRODUCTION

Malignant melanoma is the most lethal form of skin cancer and one of the fastest-increasing cancers in the U.S.[1,2] About 16% of patients develop metastases over time.[3,4] The most common metastatic sites are regional lymph nodes, lung, liver, and brain.[5] Surgery remains the mainstay of melanoma therapy at all sites, if it is technically feasible and risk of morbidity and mortality is low and the patient is likely to live long enough to accrue benefit.[5,6]

The complete removal of tumor during surgery is dependent on the surgeon's ability to differentiate tumor from normal tissue using subjective criteria that are not easily quantifiable. A real-time visualization of cancer cells with high resolution during surgery in patients would be of great value and there is great interest in approaches that can optimize surgical margins at the initial surgery.[7,8]

Currently, ultrasound and X-ray fluoroscopy are the two imaging techniques that are most utilized during human surgery. However, ultrasound requires direct contact with tissue and only sees a thin "slice" of the surgical field-of-view. When X-ray fluoroscopy is used, the patient and caregivers are exposed to ionizing radiation. Importantly, neither of these methods are tumor-specific, since targeted contrast agents are not available (reviewed in ref 9). In contrast, near-infrared real-time fluorescence imaging (700−900 nm), as an optical technique, offers the possibility of actively imaging the resection cavity in real time as the surgery progresses, providing superior resolution and sensitivity,[8] high tissue penetration up to several millimeters deep, and low autofluorescence, providing a favorable signal-to-noise ratio. In addition, several near-infrared fluorescent (NIRF) dyes are available for chemical conjugation to molecules that can target tumors, e.g., antibodies or peptides (reviewed in ref 10).

Intraoperative sentinel lymph node biopsy (SLNB) is widely used for staging of melanoma, and the pathologic status of the sentinel lymph node is reported to be one of the most important prognostic indicators.[11,12] However, SLNB is associated with morbidity.[13,14] SLNB typically involves the

Received: October 5, 2012
Revised: November 1, 2012
Published: November 1, 2012

 © 2012 American Chemical Society

use of blue dye and/or radiocolloid to detect the sentinel nodes followed by removal and histologic examination to determine pathologic status. The radiocolloid and dyes currently used for SLNB are not tumor specific and, hence, cannot directly detect lymph node involvement. Indocyanine green (ICG) NIRF dye has been used intraoperatively for SLNB,[15] although it is not tumor specific. Therefore, NIRF-labeled melanoma targeted imaging agents would allow the intraoperative detection of regional metastasis in lymph nodes, directing the biopsy of only lymph nodes with suspected involvement, and potentially decreasing SLNB associated morbidities.

The amount of the surrounding normal skin that needs to be excised around a primary cutaneous melanoma has been a controversial issue among surgeons[6] and development of melanoma targeted imaging probes for intraoperative evaluation of margin status of melanoma lesions as well as melanoma metastasis resection has the potential to improve the outcome of the surgery. Such a probe would also allow for intraoperative detection of regional lymph nodes bearing metastases. In addition, there is increasing interest in the use of novel targeted therapies for treatment of malignant melanomas that are resistant to most systemic therapies.[16]

Melanoma progression is associated with altered expression of cell surface proteins, including adhesion proteins and receptors.[17−19] It has been estimated that over 80% of malignant melanomas express high levels of the MC1R,[20] making it one of the very few specific targets potentially useful for diagnosis and therapy of metastatic melanoma.[21−23] MC1R is a member of a family of five G protein-coupled receptors (MC1R−MC5R) for melanocortins.[24−26] Melanocortin receptors are expressed in a wide range of tissues and organs throughout the body, ranging from the hair and skin (MC1R), kidneys and lungs (MC5R), adrenal glands (MC2R), and hypothalamus (MC3R/MC4R) (see ref 27 for review). Peptide ligands have been developed, e.g., [Nle^4,D-Phe^7]-α-MSH (NDP-α-MSH), that have high binding affinities for MC1R, MC3R, MC4R, and MC5R, and these ligands have been investigated extensively.[28−31] However, these ligands are not selective for MC1R, and such off-target binding is undesirable given the presence of these receptors in clearance organs such as the kidney.

To discover a ligand with high affinity and specificity for MC1R, we have previously screened eight ligands against cell lines engineered to overexpress MC1R, MC4R, or MC5R.[32] MC3R was excluded from these analyses, as these peptide ligands are not expected to cross the blood-brain barrier. One of the compounds (4-phenylbutyryl-His-DPhe-Arg-Trp-Gly-Lys) exhibited high (0.2 nM) binding affinity for MC1R and low (high nanomolar) affinities for MC4R and MC5R. In the current study, by conjugating a near-infrared fluorescent dye (IRDye800CW from Li-Cor), as well as Cy5 to this ligand, we have developed MC1R-specific molecular imaging probes and characterized their tumor cell specificity, binding, and uptake in vitro. In addition, the probe was used to image MC1R expression in vivo following intravenous injection into nude mice bearing bilateral high- and low-MC1R expressing xenograft tumors.

The NIRF molecular imaging probe developed in this study has potential for real-time intraoperative detection of regional melanoma lymph node metastases and margin detection of melanoma metastasis to lung, liver, brain, and other sites during surgery.

EXPERIMENTAL PROCEDURES

Cell Culture. A375 human malignant melanoma cells and melanotic B16F10-Luc mouse melanoma cells were grown in Dulbecco's Modified Eagle's Medium (DMEM) containing 10% fetal bovine serum, 100 units/mL penicillin, and 100 μg/mL streptomycin in 5% CO_2 at 37 °C. The A375 and B16F10-Luc were obtained from American Type Culture Collection (ATCC) and Caliper Life Sciences, respectively, expanded for two passages and cryopreserved. All experiments were performed with cells of passage number less than 25 for A375 cells and 50 for B16F10-Luc cells. Cells were authenticated as negative for mycoplasma by testing at the ATCC and were monitored by microscopy and confirmed to maintain morphological traits over subsequent passages.

Generation of Stably Transfected A375 Cells Bearing the MC1R Gene. Vector pCMV6 containing *Homo sapiens* MC1R and neomycin as a selection marker was purchased (Origene). To identify the optimal concentration for selection, a range (100−1000 μg/mL) of G418 was tested on cells. A375 cells were transfected with 5 μg of the vector. In response to G418, massive cell death was observed after ∼5 days. After 2 weeks, resistant colonies appeared. Large colonies were selected and transferred to individual plates. The clone with the highest expression of *MC1R* was determined using qRT-PCR as previously described.[33] *MC1R* specific primer sets were designed using *Gene Runner* software for Windows v 3.05: forward, 5′-AATGTCATTGACGTGATCACCTG-3′ and reverse, 5′-GCAGTGCGTAGAAGATGGAGAT-3′. β-actin was used for normalization.[33] A clone with the highest expression was selected and maintained in medium containing 300 μg/mL of G418.

Characterization of hMC1R Expression on A375 Cells by Immunocytochemistry (ICC). To verify the cell surface expression of hMC1R, two sets of A375 (parental) and A375/hMC1R cells were plated at a cell density of 1×10^4 cells/well on glass coverslips placed at the bottom of culture wells and incubated for 16 h. Cells were then treated with 30 μg/mL MC1R antibody (Almone Laboratories) and 5.0 μg/mL of WGA (Invitrogen) at 4 °C for 10 min, washed 3 times with PBS, fixed with cold methanol/acetone (1:1), and air-dried for 20 min. Plates were washed 3 times with warm PBS and incubated with 1:2000 secondary antibody (Alexa-Fluor 555 goat antimouse IgG, Invitrogen). After three washes with PBS, coverslips were mounted with mounting medium and DAPI. Samples were viewed in the Moffitt Analytical Microscopy Core Facility using an automated Zeiss Observer Z.1 inverted microscope using 40×/1.3NA oil immersion objectives through narrow bandpass DAPI and FITC/A488 Chroma filter cubes and Nomarski Differential Interference Contrast polarizing and analyzing prisms. Images were produced using the AxioCam MRm CCD camera and *Axiovision* v 4.6 software suite (Carl Zeiss Inc., Germany). *Image Pro Plus 6.2* software (Mediacybernetics Inc.) was used to measure the probe-related fluorescence intensity per image.

Probe Synthesis, Purification, and Characterization. *Materials.* N$^{\alpha}$-Fmoc protected amino acids, HBTU, and HOBt were purchased from SynPep (Dublin, CA) or from Novabiochem (San Diego, CA). Rink amide Tentagel S resin was acquired from Rapp Polymere (Tubingen, Germany). The following side chain protecting groups were used for the amino acids: Arg(N^{g}-Pbf); His(N^{im}-Trt); Trp(N^{in}-Trt); and Lys(N$^{\varepsilon}$-Aloc).

IRDye800CW maleimide dye was purchased from Li-Cor (Lincoln, NE). Cy5 maleimide dye was purchased from Li-Cor (Lincoln, NE). Peptide synthesis solvents, dry solvents, and solvents for HPLC (reagent grade), and 4-phenylbutyric acid, were acquired from VWR (West Chester, PA) or Sigma-Aldrich, and were used without further purification unless otherwise noted. Compounds were manually assembled using 5 to 50 mL plastic syringe reactors equipped with a frit and Domino manual synthesizer obtained from Torviq (Niles, MI). The C-18 Sep-Pak Vac RC cartridges for solid-phase extraction were purchased from Waters (Milford, MA).

Peptide Synthesis. Ligands were synthesized on Tentagel Rink amide resin (initial loading: 0.2 mmol/g) using N^{α}-Fmoc protecting groups and a standard DIC/HOBt or HBTU/HOBt activation strategy. The resin was swollen in THF for an hour, washed with DMF, and Fmoc protecting group removed with 20% piperidine in DMF (2 min + 20 min). The resin was washed with DMF, DCM, 0.2 M HOBt in DMF, and finally with DMF, and the first amino acid coupled using preactivated 0.3 M HOBt ester in DMF (3 equiv of N^{α}-Fmoc amino acid, 3 equiv of HOBt, and 6 equiv of DIC). An on-resin test using Bromophenol Blue was used for qualitative and continuous monitoring of reaction progress. To avoid deletion sequences and slower coupling rate in longer sequences, the double coupling was performed at all steps with 3 equiv of amino acid, 3 equiv of HBTU, and 6 equiv of DIEA in DMF. Any unreacted NH_2 groups on the resin thereafter were capped using an excess of 50% acetic anhydride in pyridine for 5 min. When the coupling reaction was finished, the resin was washed with DMF, and the same procedure was repeated for the next amino acid until all residues were coupled.

Aloc Cleavage. The orthogonal protecting Aloc group of C-terminal Lys was cleaved as follows. The resin was washed with DCM, then flushed with argon for 10 min. A cleavage mixture of dimethylbarbituric acid (5 equiv) and $Pd(TPP)_4$ (0.2 equiv) in DCM (0.5 M solution) was flushed with argon and injected into the syringe. The reaction mixture was stirred for 30 min then repeated. The resin was washed with DMF, 10% DIEA in DMF, DMF, 2% sodium diethyldithiocarbamate trihydride, 10% DIEA in DMF, DCM, and DMF. The Trt-Mpr was attached to the free amine via HBTU coupling as described above.

Cleavage of Ligand from the Resin. A cleavage cocktail (10 mL per 1 g of resin) of TFA (91%), water (3%), triisopropylsilane (3%), and 1,2-ethylenedithiol (3%) was injected into the resin and stirred for 4 h at room temperature. The crude ligand was isolated from the resin by filtration, the filtrate was reduced to low volume by evaporation using a stream of nitrogen, and the ligand was precipitated in ice-cold diethyl ether, washed several times with ether, dried, dissolved in water, and lyophilized to give off-white solid powders that were stored at −20 °C until purified. The crude compound was purified by size-exclusion chromatography.

Labeling Procedure. The purified thiol compound (1 μmol) was dissolved in 1 mL DMF and reacted with 1 equiv of IRDye800CW or Cy5 maleimide under argon atmosphere. The reaction was monitored by HPLC and additional aliquots (0.1 equiv) of dye were added until completion of the reaction. The compound was purified by HPLC.

Purification and Analysis. Purity of the peptides was ensured using analytical HPLC (Waters Alliance 2695 separation model with a dual wavelength detector Waters 2487) with a reverse-phase column (Waters Symmetry, 3.0 75 mm, 3.5 μm; flow rate = 0.3 mL/min) (Conditions: HPLC, linear gradient from 10% to 90% B over 30 min, where A is 0.1% TFA and B is acetonitrile). The HPLC traces for compounds are shown in Supporting Information as proof of purity (Figure S1 and S2). Size exclusion chromatography was performed on a borosilicate glass column (2.6 × 250 mm) filled with medium-sized Sephadex G-25 or G-10. The compounds were eluted with an isocratic flow of 1.0 M aqueous acetic acid. Solid-phase extraction (SPE) was employed where simple isolation of final compound was needed from excess salts and buffers. For this purpose, C-18 Sep-Pak cartridges (100 mg or 500 mg) were used and preconditioned initially with 5 column volumes (5 times the volume of packed column bed) each of acetonitrile, methanol, and water, in that order. After loading the compound, the column was washed several times with water, and then gradually with 5%, 10%, 20%, 30%, 50%, and 70% of aqueous acetonitrile to elute the peptide. Structures were characterized by ESI (Finnigan, Thermoquest LCQ ion trap instrument), MALDI-TOF, or FT-ICR mass spectrometry. An appropriate mixture of standard peptides was used for internal calibrations. For compound MC1RL-800, MS calculated and measured (M+2)/2 was 1127.7 and 1127.9, respectively, and for MC1RL-Cy5, MS calculated and measured (M+2)/2 was 921.9 and 922.0, respectively.

Binding Assays. A375 melanoma cells engineered to express MC1R were used to assess ligand binding in a competitive binding assay as described before.[32]

The receptor number of A375/MC1R (engineered cells to express MC1R) was determined using saturation binding assay following a previously described method,[34] except that Eu-DTPA labeled NDP-α-MSH was used as a test ligand and 5 μM of NDP-α-MSH was used as a blocking ligand. These cells were used as a MC1R high expressing line, while the parental (A375) cells were used as a low expressing line with 400 ± 93 MC1R/cell.[35]

In Vitro MC1R Probe Uptake Study. To study the uptake of the MC1R probe in vitro, A375 (parental), A375/hMC1R (engineered cells for MC1R expression), and B16F10 cells (melanotic MC1R endogenous expressing cells) were plated at a cell density of 1×10^4 cells/well on glass coverslips placed at the bottom of culture wells and incubated for 16 h. Cells were incubated in media containing 15 nM probe and uptake evaluated by fluorescence microscopy at different time points from 40 s to 15 min. To determine specificity, MC1R receptors were blocked by a 10 min preincubation with 2 μM of NDP-α-MSH prior to addition of MC1R probe and images acquired 1 min after addition of labeled probe. Samples were viewed using an Axio Observer Z1 inverted fluorescence microscope (Carl Zeiss, Inc., Germany) using 40×/1.3 NA oil immersion objectives through a narrow band Cy5 filter. Cy5 fluorescence images were prepared with a DIC overlay image using *Axiovision 4.6* software (Carl Zeiss, Inc., Germany).

Log D. The log of the octanol−water partition coefficient at pH 7.4 ($\log D_{7.4}$) was determined by miniaturized shake flask assay. Briefly, (200 μL to 1 mL) *n*-octanol (Sigma) was added to a solution of the test compound prepared in PBS (25 mM NaH_2PO_4/Na_2HPO_4 buffer, pH 7.4, Sigma, HPLC grade). Then, three different ratios of octanol to PBS buffer were prepared. The mixture was stirred in a vortex mixer at room temperature for 1 min and then two layers were separated by centrifuge. The concentration of compound in each layer was determined by HPLC (Poroshell 120 EC-C18 column) using (26% acetonitrile in water, 0.1% TFA) in 280 nm channel. All

sample injections were performed 3 times, and the results were averaged to yield the final values.

Tumor Xenograft Studies and Fluorescence Imaging. Male *nu/nu* mice 6−8 weeks old (Harlan Sprague−Dawley, Inc., Indianapolis, IN) were injected subcutaneously (s.c.) with 1×10^6 MC1R expressing A375 cells in the right flank and the same number of parental cells in the left flank. Tumor volume was determined with calipers using the formula: volume = (length × width^2)/2. Once tumors reached 500−800 mm^3, 3 nmol/kg of either MC1RL-800 or MC1RL-Cy5 in 100 μL sterile saline was injected into the tail vein. In vivo fluorescence images were acquired using the Optix-MX3 (Advanced Research Technologies, Inc., a subsidiary of SoftScan Healthcare Group, Montreal, Canada). For the blocking study, 3 nmol/kg of probe was coinjected with 0.25 μg of the melanocortin receptor-specific ligand, NDP-α-MSH (Sigma), and animals were imaged similarly. Animals were positioned on a heating pad and anesthetized using isoflurane (flow 2−2.5 l/min). Fluorescence images were acquired using a scan resolution of 1.5 mm and a 790 nm pulsed laser diode with 40 MHz frequency and 12 ns time window. Images were analyzed using Optix-MX3 *Optiview* software (v 3.01). Autofluorescence background was subtracted by determining the mean tumor fluorescence signal prior to injection; then, mean normalized intensity values were obtained within a ROI on these images.

For B16F10 xenografts, 1×10^6 cells were injected s.c. into the right flank and allowed to grow to a volume of 500−800 mm^3, 3 nmol/kg of MC1R targeted imaging probe was injected into the tail vein and mice were then imaged using the Optix MX3 and FMT 2500 LX quantitative fluorescence tomography in vivo imaging system (PerkinElmer), which acquires both 2D surface fluorescence reflectance images (FRI) and 3D fluorescence molecular tomographic (FMT) imaging data sets. Using image data from phantoms containing known concentrations of the imaging probe and *TrueQuant* software v 3.0 (PerkinElmer), the in vivo fluorescence data were quantitatively reconstructed to provide three-dimensional fluorescence tomography images and probe concentrations within the tumors.

MC1R IHC staining of xenograft tumors was performed in the Moffitt Tissue Core facility. Tumors were excised and fixed in formalin and embedded in paraffin for histology and fine sectioning. Formalin-fixed sections (5 μm) were IHC stained with rabbit MC1R polyclonal antibody (GTX70735, GeneTex), 1:200 dilution. The slides were scanned in the Moffitt Analytical Microscopy Core Facility using a ScanScope XT digital slide scanner (Aperio, CA). Positivity (number of positive pixels/total pixels number) of each slide was determined using *Positive Pixel Count* v 9 Aperio Toolbox software.

Statistics. Data are represented as mean ± s.d. All statistical analyses were performed with GraphPad *Prism* v 5.01. Unpaired Student's *t* test was used to determine the statistical significance of differences between two independent groups of variables. For all tests, $p \leq 0.05$ was considered significant.

RESULTS AND DISCUSSION

Characterization of MC1R Expression in A375/MC1R Cells. A375 malignant melanoma cells were transfected to stably overexpress MC1R for evaluation of the MC1R imaging probes both in vitro and in vivo. The A375 malignant melanoma cell line was chosen due to its very low endogenous expression of MC1R,[35,36] providing both low- and high-expressing cells for the in vitro as well as in vivo selectivity studies. qRT-PCR of A375 and A375/MC1R cells revealed the level of MC1R mRNA expression to be ~100-fold higher in the engineered cells compared to the parental cell line. For further confirmation, hMC1R expression on the cell surface of the cells was characterized through ICC (Figure 1). Both engineered

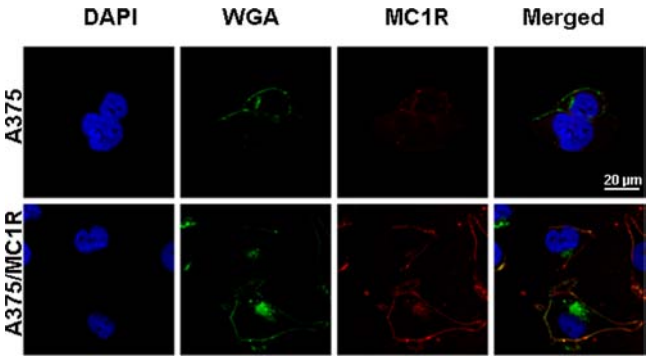

Figure 1. ICC of MC1R expression on the surface of A375 parental and engineered cells. Confocal micrographs of cells incubated with the nuclear marker DAPI (blue), the plasma- and plasma-membrane marker, WGA (green) and an MC1R primary antibody labeled with an Alexa Fluor 555 secondary antibody (red). To inhibit cellular uptake, cells were incubated with WGA and MC1R antibody at 4 °C for 10 min. The merged image shows colocalization of MC1R (red) with membrane marker (green) indicating accumulation of the receptor on the cell-surface (yellow).

A375/hMC1R and parental A375 cells were incubated with the nuclear marker DAPI, the plasma membrane marker WGA, and an MC1R primary antibody labeled with an Alexa Fluor 555 secondary antibody. The merged images illustrate colocalization of MC1R (red) with membrane marker (WGA, green) indicating accumulation of the receptor on the cell-surface (yellow). Notably, the parental A375 line does appear to have a detectable amount of MC1R antibody binding to the cell surface and the MC1R-related (red) fluorescence intensity was 8.5-fold higher in the engineered A375/MC1R cells compared to the A375 cells.

To determine MC1R receptor number on the cell surface, saturation binding assays were performed using Eu-NDP-α-MSH. Increasing amounts of Eu-NDP-α-MSH were added to A375/MC1R cells. Binding specificity was determined in the presence of melanocortin-receptor specific blocking ligand, 5 μM unlabeled NDP-α-MSH (Figure 2A). Results indicate that the K_d, B_{max}, and receptor number were 1.8 nM, 668 046 ± 67 108, and 75 000, respectively.

Synthesis and Characterization of MC1R Targeted Probes. It has been known that MC1R ligands also show cross-reactivity with other melanocortin receptors. Since MC5R is expressed in kidney and lung, MC1R ligands with off-target binding to MC5R are not ideal for targeting of melanoma in patients. Recently, our group described a high-affinity peptidomimetic ligand against MC1R. K_i values for this ligand against MC1R, MC4R, and MC5R were 0.24 nM, 254 nM, and 46 nM, correspondingly, demonstrating very low interaction against MC4R and MC5R, 1000 and 200 times lower affinity compared with MC1R, respectively.[32] The use of small peptidomimetics as carriers for the delivery of imaging or therapeutic moieties to diseased tissues offers several advantages such as high biostability, ease of synthesis and

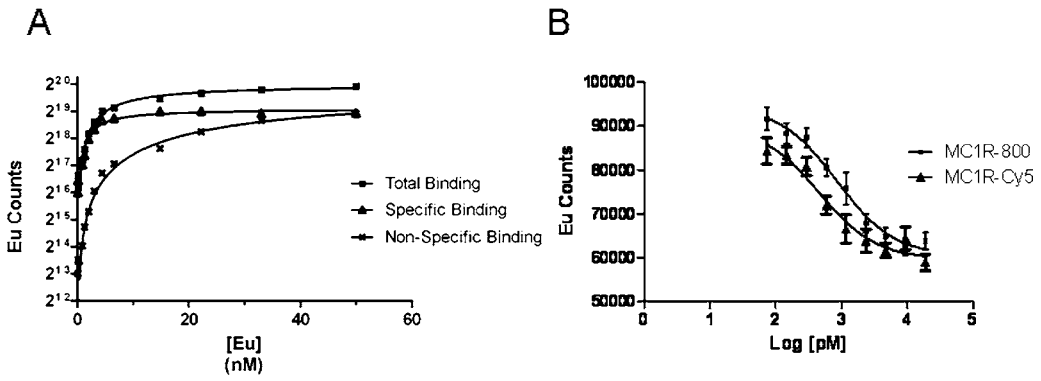

Figure 2. (A) Representative saturation binding assays for A375/hMC1R cells. (B) Representative competition binding plot of MC1RL-800 and MC1RL-Cy5 imaging probes to A375/hMC1R cells.

Scheme 1. Synthetic Route for Cy5 and IRDye800CW Ligands[a]

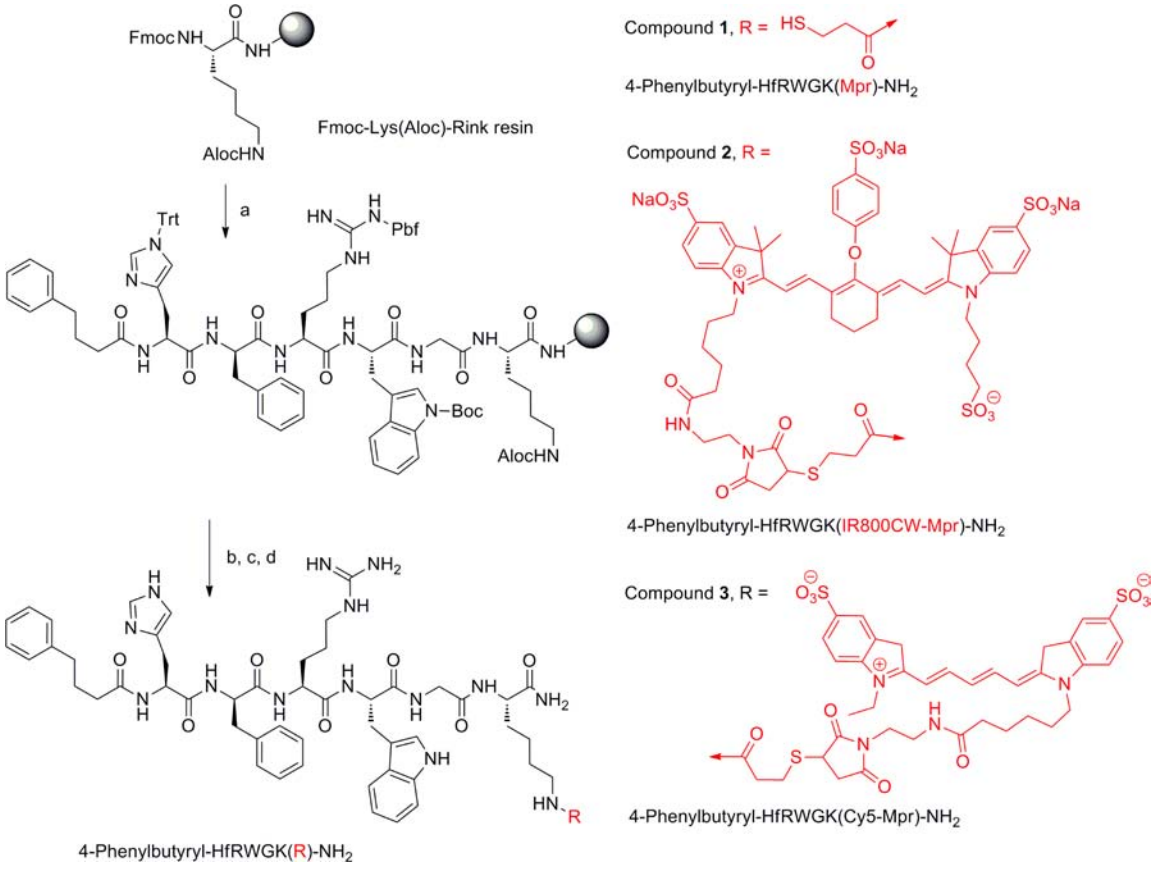

[a](a) Fmoc/*t*Bu synthesis continued as follows: (i) Fmoc-aa-OH (3 equiv), HOBt (3 equiv), DIEA (6 equiv), and HBTU (3 equiv) in DMF for amino acid coupling; (ii) Piperidine/DMF (1:4) for Fmoc deprotection. (b) Aloc deprotection: (i) Pd(0)TPP_4 (0.2 equiv), dimethylbarbituric acid (5.0 equiv) in DCM (0.5 M) for 30 min; (ii) Trt-OH (3 equiv), DIEA (6 equiv), and HBTU (3 equiv) in DMF; (c) TFA-scavengers cocktail (91% trifluoroacetic acid, 3% water, 3% triisopropylsilane, and 1,2-ethylenedithiol (3%) for 4 h; (d) IRDye800CW maleimide or Cy5 maleimide (1 equiv) in DMF.

modification, faster blood clearance, high-affinity and high-specificity, and low toxicity and immunogenicity.[37−41]

Here, we describe the attachment of a NIRF dye IRDye800CW as well as Cy5 to the C-terminus of the MC1R-specific ligand via lysine-mercaptopropionic acid linker (4-phenylbutyryl-His-DPhe-Arg-Trp-Gly-Lys(Mpr-IRDye800CW)-NH_2, LiCor IRDye800CW Maleimide) to generate MC1RL-800 and MC1RL-Cy5 (Scheme 1). The sequence of this ligand was reported previously to have a high affinity and selectivity for MC1R[22,42] and it was consequently chosen as a template for the design of the novel ligands.[32]

To evaluate the binding affinity of the MC1RL-800 and MC1RL-Cy5 probes, competition binding assays were preformed on A375/hMC1R cells with Eu-NDP-α-MSH as the competed ligand (Figure 2B). The MC1RL-800 and MC1RL-Cy5 probes retained high affinity for MC1R, with a K_i of 0.4 ± 0.1 nM and 0.3 ± 0.05 nM, respectively, which is comparable to the K_i for the unlabeled ligand of 0.24 nM K_i.[32]

dx.doi.org/10.1021/bc300549s | *Bioconjugate Chem.* 2012, 23, 2451−2459

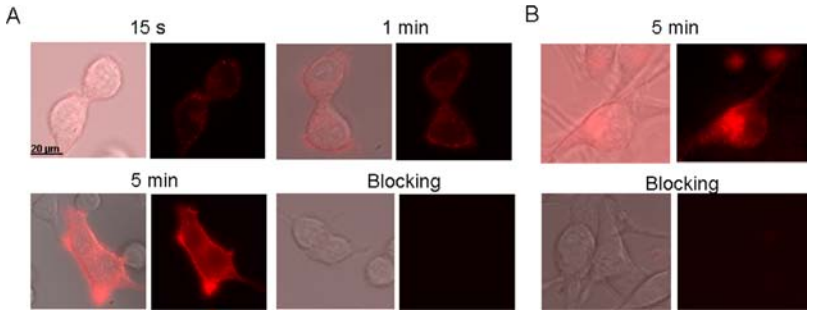

Figure 3. In vitro uptake studies of the MC1RL-Cy5 targeted imaging probe. (A) Fluorescence microscopy images at 15 s, 1 min, and 5 min following addition of probe to an incubation chamber containing A375/MC1R cells grown on a coverslip. Probe binding is observed by 15 s and internalization by 5 min. (B) Fluorescence microscopy images of probe uptake by B16 cells at the 5 min time-point showing internalization of probe into the cells. For both panels A and B, images are included for blocking studies at the 5 min time-point, where cells were preincubated with the unlabeled melanocortin-receptor ligand, NDP-α-MSH, prior to addition of probe. Preincubation with unlabeled ligand completely blocked binding and uptake of probe. For both panels A and B, the image on the left of each pair shows the overlay of the fluorescence image on the visible light (differential interference contrast) image of the corresponding cells and the right panel shows only the fluorescence.

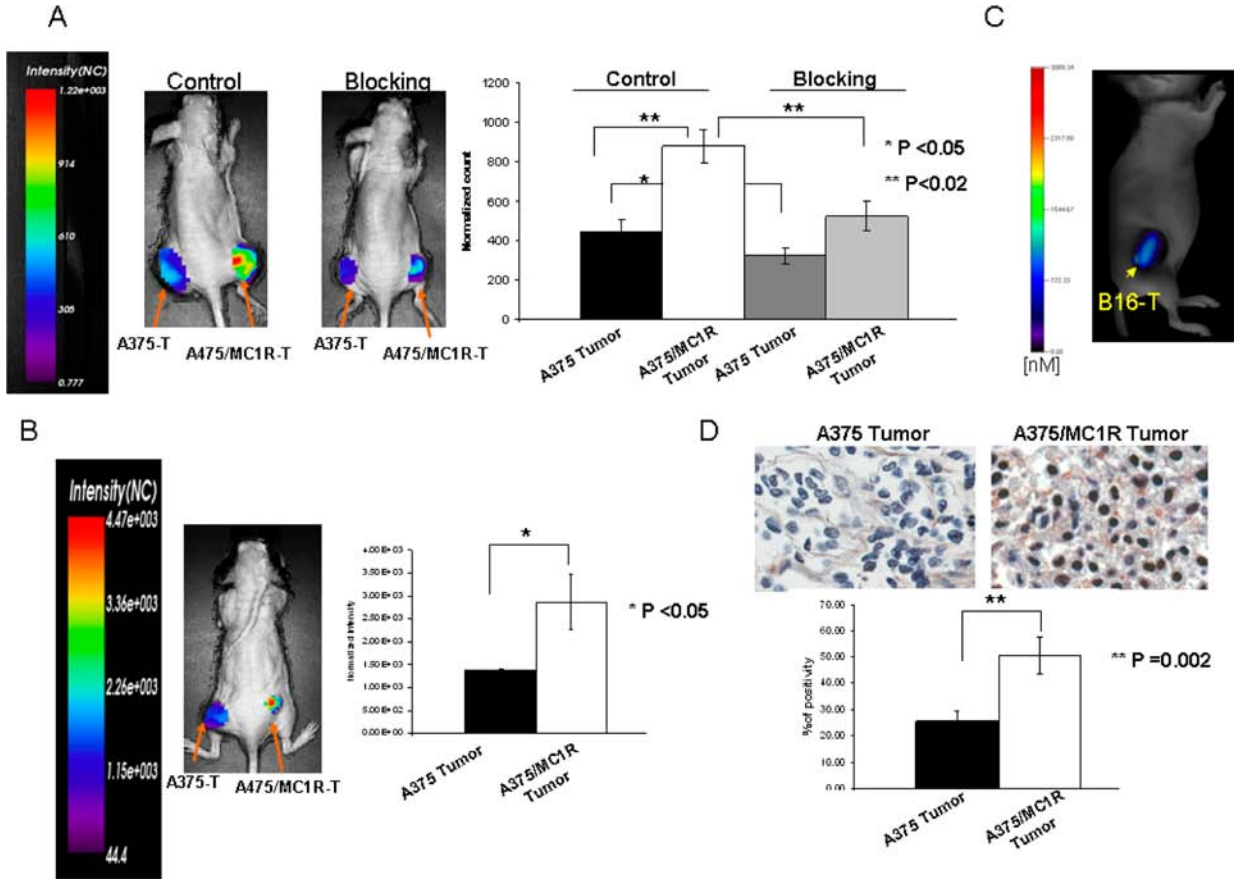

Figure 4. In vivo targeting of MC1R specific probe. (A) Representative images of normalized fluorescence intensity maps overlaid on mice bearing xenograft tumors. A375 cells that constitutively express low levels of MC1R were used to form the low-expressing tumor (left flank), and A375/MC1R cells were used to form the high-expressing tumor (right flank). The control image (left mouse) shows lower fluorescence signal in the left flank tumor relative to the right flank tumor 4 h after intravenous injection of 3 nmol/kg of the MC1RL-800 probe. A blocking experiment (right mouse) was performed by coinjection of 0.25 μg unlabeled NDP-α-MSH and 3 nmol/kg of the MC1RL-800 probe to demonstrate specific binding. Inset on the far right graphs normalized fluorescence counts that significantly vary among low- and high-expressing tumors, and among tumors in control experiments compared to blocking experiments. (B) Representative image at 4 h after injection of 3 nmol/kg of the MC1RL-Cy5 probe. Graph shows relative quantification of fluorescence in low- and high-expressing tumors. For panels A & B, images were acquired using the Optix-MX3 imaging system (Advanced Research Technologies, Inc.), graphed data represent the mean ± s.d., and NC = Normalized Counts. (C) Representative tomographic image of a mouse bearing a B16F10 xenograft tumor at 4 h after injection of 3 nmol/kg of the MC1RL-800 imaging probe using the FMT 2500 LX quantitative fluorescence tomography in vivo imaging system (PerkinElmer). (D) MC1R IHC staining of A375 and A375/MC1R xenograft tumors. The bar graph shows the quantification of MC1R staining. Data represent mean ± s.d.

Cellular Uptake Studies. To study uptake of the MC1R probe by cells, MC1RL-Cy5 was incubated with live cells and images were acquired at different time-points after incubation using an inverted fluorescence microscope. Binding of probe to

the surface of A375/MC1R cells was observed as early as 15 s after incubation and intracellular accumulation was observed within 5 min (Figure 3A). Therefore, the ligand could also be used in the clinic as a MC1R targeted delivery vehicle for radionuclides, toxins, and chemotherapeutic molecules. No binding or uptake of probe was observed when 2 μM NDP-α-MSH was used as a blocking agent before adding the probe to the cells (Figure 3A). Probe uptake was also observed (Figure 3B) by melanotic B16F10 cells that endogenously express MC1R (~22 000 ± 4200 MC1R/cell[35]) and blocking of probe-uptake was also observed in these cells. The blocking studies demonstrate the specificity of the probes for melanocortin receptor.

Determination of Log D of MC1RL-800. To measure lipophilicity of the probe, log D (distribution coefficient) was determined. Lipophilicity is a key determinant of the pharmacokinetic behavior of drugs and can influence distribution into tissues, absorption, and the binding characteristics of a drug, as well as determination of the solubility of a compound (reviewed in ref 43). The log D of MC1RL-800 probe was calculated to be −3.10 ± 0.13, suggesting that the probe is highly soluble in aqueous buffer and the probe would have low permeability across the gastrointestinal tract or blood brain barrier.

In Vivo Tumor Targeting. To investigate tumor targeting of the probe in vivo, bilateral subcutaneous xenograft tumors were established with A375/MC1R engineered cells in the right flank and A375 parental cells with relatively low MC1R expression in the left flank. After tumor growth to approximately 500−800 mm^3, MC1RL-800 or MC1RL-Cy5 probe was injected intravenously and fluorescence accumulation was monitored over time. For both probes, the A375 tumors with low MC1R expression had significantly lower normalized fluorescence signal compared to A375/MC1R tumors 4 h postinjection ($P \leq 0.05$, $n = 3$) (Figure 4A,B). In vivo blocking studies were performed to determine that probe retention in the tumor was due to specific binding. MC1RL-800 probe (3 nmol/kg) was coinjected with 0.25 μg of the melanocortin receptor-specific ligand, NDP-α-MSH. After blocking, the probe-related fluorescence signal decreased 1.7-fold in the A375/MC1R tumors ($p \leq 0.02$, $n = 3$) and 1.4-fold in A375 tumors ($p \leq 0.05$, $n = 3$) relative to the unblocked tumor at 4 h after injection (Figure 4A).

MC1R expression ranges from several hundred to around 10 000 receptors per cell in different human cell lines.[20] Therefore, development of a noninvasive imaging method for visualizing and quantifying MC1R expression will be useful for monitoring alterations in MC1R expression as an indicator of treatment response.[44] Our in vivo results indicate that the MC1RL-800 imaging probe related fluorescence was 2.0 ± 0.4-fold higher in the high-expressing tumor relative to the low-expressing tumor. This increase is lower than expected based on the receptor number per cell as determined in vitro in cultured cells by saturation binding assay, i.e., the level of MC1R expression in A375 melanoma cells is 400 ± 93 sites/cell[35] compared to 75 000 sites/cell in the A375/MC1R cells which is a 190-fold difference. However, by comparing the same cell lines using ICC fluorescence, MC1R expression was determined to be only 8.5-fold higher. Also, proteins expressed in cultured cell lines are known to differ from that of tumor xenografts using the same cell line. Such discrepancies are common throughout the literature and undoubtedly play a role in the increased sensitivity of cancer cell lines to chemotherapy relative to solid tumors.[45] IHC staining of A375/MC1R xenograft tumors for MC1R was 2.0 ± 0.2-fold higher compared to A375 tumors, which is nearly identical to the in vivo fluorescence imaging results (Figure 4D).

Since a large percentage of melanoma metastases express melanin, we used the mouse B16F10 tumor xenograft model with endogenous expression of MC1R to determine the feasibility of using the NIRF probes for detection of melanotic lesions by fluorescence imaging. Fluorescence from the MC1RL-800 probe was not detectable at the 3 nmol/kg dosage using the Optix MX3 imaging system, but was detected using the FMT 2500 tomographic imaging instrument (Figure 4C). The probe concentration within the B16F10 tumors was determined to be 2120 ± 710 pmol. Hence, detection of fluorescence is possible in melanotic tumors but may be diminished as fluorescence was detected in the amelanotic A375 tumors with lower expression of MC1R using the same low dosage of probe and the Optix MX3 instrument. However, the use of higher dosages of probe or instrumental optimization could improve detection. Furthermore, detection of NIRF probes by a different imaging modality, such as multispectral optoacoustic tomography, may have superior detection compared to fluorescence imaging.[46]

CONCLUSION

The MC1R specific fluorescent imaging probe with high affinity for the MC1R was successfully synthesized and characterized, and binding and uptake studies were performed. We have demonstrated that the probe can differentiate high- from low-MC1R expressing tumors in vivo. Therefore, MC1RL-800 is a promising molecular imaging probe for detection of MC1R-positive melanoma tumors and metastases in patients.

Targeted near-infrared fluorescence can be used for real-time intraoperative image-guidance with high resolution and sensitivity.[8] Therefore, our probe could be used to evaluate surgical margins of melanoma lesions and to detect regional lymph node metastasis in real time during surgery. This capability could improve the rate of complete surgical resection of melanoma metastasis to a number of organ sites in melanoma patients whose tumors overexpress MC1R, thereby decreasing the amount of tumor left behind and increasing tumor-free survival. Detection and removal of only lymph nodes that contain metastases would decrease morbidities associated with the nonspecific removal of regional lymph nodes that do not have metastases during standard SLNB. Detection of fluorescence was possibly decreased in melanotic lesions relative to amelanotic lesions. Hence, the use of fluorescence for detection of melanoma may require optimization of the dosages administered and fluorescence instrumentation used, or use of a more sensitive modality, such as multispectral optoacoustic tomography may be required. In the future, the targeting ligand could be used to develop targeted radiolabeled PET or SPECT probes for the specific detection of melanoma metastases in the clinic, or as a MC1R targeted delivery vehicle for therapeutic agents.

ASSOCIATED CONTENT

Supporting Information

Additional data and figures. This material is available free of charge via the Internet at http://pubs.acs.org.

AUTHOR INFORMATION

Corresponding Author

*J.V.: phone 520-626-4179, fax 520-626-4824, e-mail vagner@email.arizona.edu. D.L.M.: e-mail David.Morse@moffitt.org.

Notes

The authors declare no competing financial interest.

ACKNOWLEDGMENTS

The authors wish to acknowledge the Analytic Microscopy and Small Animal Modeling and Imaging Shared Resources at the H. Lee Moffitt Cancer Center & Research Institute, and the Comparative Biomedicine Department at the University of South Florida for their technical support. We also thank Michael Olive and LI-COR Biosciences for providing IRDye800CW. This work was supported by NIH/NCI R01CA097360, Morse PI.

ABBREVIATIONS

MC1R, Melanocortin 1 receptor.

REFERENCES

(1) Siegel, R., Naishadham, D., and Jemal, A. (2012) Cancer statistics, 2012. *CA Cancer J. Clin. 62*, 10−29.

(2) Thompson, J. F., and Uren, R. F. (2005) Lymphatic mapping in management of patients with primary cutaneous melanoma. *Lancet Oncol. 6*, 877−85.

(3) Balch, C. M., Soong, S. J., Gershenwald, J. E., Thompson, J. F., Reintgen, D. S., Cascinelli, N., Urist, M., McMasters, K. M., Ross, M. I., Kirkwood, J. M., Atkins, M. B., Thompson, J. A., Coit, D. G., Byrd, D., Desmond, R., Zhang, Y., Liu, P. Y., Lyman, G. H., and Morabito, A. (2001) Prognostic factors analysis of 17,600 melanoma patients: validation of the American Joint Committee on Cancer melanoma staging system. *J. Clin. Oncol. 19*, 3622−34.

(4) Kalady, M. F., White, R. R., Johnson, J. L., Tyler, D. S., and Seigler, H. F. (2003) Thin melanomas: predictive lethal characteristics from a 30-year clinical experience. *Ann. Surg. 238*, 528−35 discussion 535−7..

(5) Caudle, A. S., and Ross, M. I. (2011) Metastasectomy for stage IV melanoma: for whom and how much? *Surg. Oncol. Clin. N. Am. 20*, 133−44.

(6) Ott, P. A., and Berman, R. S. (2011) Surgical approach to primary cutaneous melanoma. *Surg. Oncol. Clin. N. Am. 20*, 39−56.

(7) Nguyen, Q. T., Olson, E. S., Aguilera, T. A., Jiang, T., Scadeng, M., Ellies, L. G., and Tsien, R. Y. (2010) Surgery with molecular fluorescence imaging using activatable cell-penetrating peptides decreases residual cancer and improves survival. *Proc. Natl. Acad. Sci. U. S. A. 107*, 4317−22.

(8) van Dam, G. M., Themelis, G., Crane, L. M., Harlaar, N. J., Pleijhuis, R. G., Kelder, W., Sarantopoulos, A., de Jong, J. S., Arts, H. J., van der Zee, A. G., Bart, J., Low, P. S., and Ntziachristos, V. (2011) Intraoperative tumor-specific fluorescence imaging in ovarian cancer by folate receptor-alpha targeting: first in-human results. *Nat. Med. 17*, 1315−9.

(9) Frangioni, J. V. (2008) New technologies for human cancer imaging. *J. Clin. Oncol. 26*, 4012−21.

(10) Keereweer, S., Kerrebijn, J. D., van Driel, P. B., Xie, B., Kaijzel, E. L., Snoeks, T. J., Que, I., Hutteman, M., van der Vorst, J. R., Mieog, J. S., Vahrmeijer, A. L., van de Velde, C. J., Baatenburg de Jong, R. J., and Lowik, C. W. (2011) Optical image-guided surgery–where do we stand? *Mol. Imaging Biol. 13*, 199−207.

(11) Balch, C. M. (1985) [Diagnosis and prognosis of malignant melanoma]. *Dtsch. Med. Wochenschr. 110*, 1783−6.

(12) Hinz, T., Ahmadzadehfar, H., Wierzbicki, A., Hoeller, T., Wenzel, J., Biersack, H. J., Bieber, T., and Schmid-Wendtner, M. H. (2012) Sentinel lymph node status as most important prognostic factor in patients with high-risk cutaneous melanomas (tumour thickness >4.00 mm): outcome analysis from a single institution. *Eur. J. Nucl. Med. Mol. Imaging 39*, 1316−25.

(13) Hettiaratchy, S. P., Kang, N., O'Toole, G., Allan, R., Cook, M. G., and Powell, B. W. (2000) Sentinel lymph node biopsy in malignant melanoma: a series of 100 consecutive patients. *Br. J. Plast. Surg. 53*, 559−62.

(14) Cigna, E., Gradilone, A., Ribuffo, D., Gazzaniga, P., Fino, P., Sorvillo, V., and Scuderi, N. (2012) Morbidity of selective lymph node biopsy for melanoma: meta-analysis of complications. *Tumori 98*, 94−8.

(15) Crane, L. M., Themelis, G., Buddingh, K., Harlaar, N. J., Pleijhuis, R. G., Sarantopoulos, A., van der Zee, A. G., Ntziachristos, V., and van Dam, G. M. (2010) Multispectral real-time fluorescence imaging for intraoperative detection of the sentinel lymph node in gynecologic oncology. *J. Vis. Exp. 44*, 2225.

(16) Wagner, J. D. (2004) A role for FDG-PET in the surgical management of stage IV melanoma. *Ann. Surg. Oncol. 11*, 721−2.

(17) Hsu, M., Andl, T., Li, G., Meinkoth, J. L., and Herlyn, M. (2000) Cadherin repertoire determines partner-specific gap junctional communication during melanoma progression. *J. Cell Sci. 113* (Pt 9), 1535−42.

(18) Wang, R., Kobayashi, R., and Bishop, J. M. (1996) Cellular adherence elicits ligand-independent activation of the Met cell-surface receptor. *Proc. Natl. Acad. Sci. U. S. A. 93*, 8425−30.

(19) Yang, P., Farkas, D. L., Kirkwood, J. M., Abernethy, J. L., Edington, H. D., and Becker, D. (1999) Macroscopic spectral imaging and gene expression analysis of the early stages of melanoma. *Mol. Med. 5*, 785−94.

(20) Siegrist, W., Solca, F., Stutz, S., Giuffre, L., Carrel, S., Girard, J., and Eberle, A. N. (1989) Characterization of receptors for alpha-melanocyte-stimulating hormone on human melanoma cells. *Cancer Res. 49*, 6352−8.

(21) Cai, M., Varga, E. V., Stankova, M., Mayorov, A., Perry, J. W., Yamamura, H. I., Trivedi, D., and Hruby, V. J. (2006) Cell signaling and trafficking of human melanocortin receptors in real time using two-photon fluorescence and confocal laser microscopy: differentiation of agonists and antagonists. *Chem. Biol. Drug Des. 68*, 183−93.

(22) Koikov, L. N., Ebetino, F. H., Solinsky, M. G., Cross-Doersen, D., and Knittel, J. J. (2003) Sub-nanomolar hMC1R agonists by end-capping of the melanocortin tetrapeptide His-D-Phe-Arg-Trp-NH(2). *Bioorg. Med. Chem. Lett. 13*, 2647−50.

(23) Mayorov, A. V., Han, S. Y., Cai, M., Hammer, M. R., Trivedi, D., and Hruby, V. J. (2006) Effects of macrocycle size and rigidity on melanocortin receptor-1 and −5 selectivity in cyclic lactam alpha-melanocyte-stimulating hormone analogs. *Chem. Biol. Drug Des. 67*, 329−35.

(24) Geschwind, I. I., Huseby, R. A., and Nishioka, R. (1972) The effect of melanocyte-stimulating hormone on coat color in the mouse. *Recent Prog. Horm. Res. 28*, 91−130.

(25) Hunt, G., Kyne, S., Wakamatsu, K., Ito, S., and Thody, A. J. (1995) Nle4DPhe7 alpha-melanocyte-stimulating hormone increases the eumelanin:phaeomelanin ratio in cultured human melanocytes. *J. Invest. Dermatol. 104*, 83−5.

(26) Tamate, H. B., and Takeuchi, T. (1984) Action of the e locus of mice in the response of phaeomelanic hair follicles to alpha-melanocyte-stimulating hormone in vitro. *Science 224*, 1241−2.

(27) Gong, R. (2012) The renaissance of corticotropin therapy in proteinuric nephropathies. *Nat. Rev. Nephrol. 8*, 122−8.

(28) Chen, J., Giblin, M. F., Wang, N., Jurisson, S. S., and Quinn, T. P. (1999) In vivo evaluation of 99mTc/188Re-labeled linear alpha-melanocyte stimulating hormone analogs for specific melanoma targeting. *Nucl. Med. Biol. 26*, 687−93.

(29) Cai, M., Mayorov, A. V., Cabello, C., Stankova, M., Trivedi, D., and Hruby, V. J. (2005) Novel 3D pharmacophore of alpha-MSH/gamma-MSH hybrids leads to selective human MC1R and MC3R analogues. *J. Med. Chem. 48*, 1839−48.

(30) Handl, H. L., Vagner, J., Yamamura, H. I., Hruby, V. J., and Gillies, R. J. (2004) Lanthanide-based time-resolved fluorescence of in cyto ligand-receptor interactions. *Anal. Biochem. 330*, 242−50.
(31) Yang, Y., Hruby, V. J., Chen, M., Crasto, C., Cai, M., and Harmon, C. M. (2009) Novel binding motif of ACTH analogues at the melanocortin receptors. *Biochemistry 48*, 9775−84.
(32) Barkey, N. M., Tafreshi, N. K., Josan, J. S., De Silva, C. R., Sill, K. N., Hruby, V. J., Gillies, R. J., Morse, D. L., and Vagner, J. (2011) Development of melanoma-targeted polymer micelles by conjugation of a melanocortin 1 receptor (MC1R) specific ligand. *J. Med. Chem. 54*, 8078−84.
(33) Morse, D. L., Carroll, D., Weberg, L., Borgstrom, M. C., Ranger-Moore, J., and Gillies, R. J. (2005) Determining suitable internal standards for mRNA quantification of increasing cancer progression in human breast cells by real-time reverse transcriptase polymerase chain reaction. *Anal. Biochem. 342*, 69−77.
(34) Xu, L., Vagner, J., Alleti, R., Rao, V., Jagadish, B., Morse, D. L., Hruby, V. J., Gillies, R. J., and Mash, E. A. (2010) Synthesis and characterization of a Eu-DTPA-PEGO-MSH(4) derivative for evaluation of binding of multivalent molecules to melanocortin receptors. *Bioorg. Med. Chem. Lett. 20*, 2489−92.
(35) Cheng, Z., Xiong, Z., Subbarayan, M., Chen, X., and Gambhir, S. S. (2007) 64Cu-labeled alpha-melanocyte-stimulating hormone analog for microPET imaging of melanocortin 1 receptor expression. *Bioconjugate Chem. 18*, 765−72.
(36) Baumann, J. B., Bagutti, C., Siegrist, W., Christen, E., Zumsteg, U., and Eberle, A. N. (1997) MSH receptors and the response of human A375 melanoma cells to interleukin-1 beta. *J. Recept. Signal Transduct. Res. 17*, 199−210.
(37) Abell, A. (1997) *Advances in Amino Acid Mimetics and Peptidomimetics*, 1st ed.; Vol. 1, JAI Press, Greenwich, CT.
(38) Bullok, K. E., Gammon, S. T., Violini, S., Prantner, A. M., Villalobos, V. M., Sharma, V., and Piwnica-Worms, D. (2006) Permeation peptide conjugates for in vivo molecular imaging applications. *Mol. Imaging 5*, 1−15.
(39) Knight, L. C. (2003) Non-oncologic applications of radiolabeled peptides in nuclear medicine. *Q. J. Nucl. Med. 47*, 279−91.
(40) Okarvi, S. M. (2001) Recent progress in fluorine-18 labelled peptide radiopharmaceuticals. *Eur. J. Nucl. Med. 28*, 929−38.
(41) Okarvi, S. M. (2004) Peptide-based radiopharmaceuticals: future tools for diagnostic imaging of cancers and other diseases. *Med. Res. Rev. 24*, 357−97.
(42) Koikov, L. N., Ebetino, F. H., Solinsky, M. G., Cross-Doersen, D., and Knittel, J. J. (2004) Analogs of sub-nanomolar hMC1R agonist LK-184 [Ph(CH2)3CO-His-D-Phe-Arg-Trp-NH2]. An additional binding site within the human melanocortin receptor 1? *Bioorg. Med. Chem. Lett. 14*, 3997−4000.
(43) Di, L., and Kerns, E. H. (2003) Profiling drug-like properties in discovery research. *Curr. Opin. Chem. Biol. 7*, 402−8.
(44) Cheng, Z., Zhang, L., Graves, E., Xiong, Z., Dandekar, M., Chen, X., and Gambhir, S. S. (2007) Small-animal PET of melanocortin 1 receptor expression using a 18F-labeled alpha-melanocyte-stimulating hormone analog. *J. Nucl. Med. 48*, 987−94.
(45) Stein, W. D., Litman, T., Fojo, T., and Bates, S. E. (2004) A Serial Analysis of Gene Expression (SAGE) database analysis of chemosensitivity: comparing solid tumors with cell lines and comparing solid tumors from different tissue origins. *Cancer Res. 64*, 2805−16.
(46) Razansky, D., Deliolanis, N. C., Vinegoni, C., and Ntziachristos, V. (2012) Deep tissue optical and optoacoustic molecular imaging technologies for pre-clinical research and drug discovery. *Curr. Pharm. Biotechnol. 13*, 504−22.

Synthesis and Characterization of a Melanoma-Targeted Fluorescence Imaging Probe by Conjugation of a Melanocortin 1 Receptor (MC1R) Specific Ligand

Narges K Tafreshi [†], Xuan Huang[†], Valerie E Moberg [†], Natalie M. Barkey[†], Vernon K. Sondak [‡], Haibin Tian[†], David L Morse[†*] and Josef Vagner [§*]

Authors' Affiliations: [†]Dept. Cancer Imaging and Metabolism, [‡]Department of Cutaneous Oncology, H. Lee Moffitt Cancer Center & Research Institute, Tampa, FL; [§]BIO5 Institute, University of Arizona, Tucson, AZ

*Corresponding Authors: J. V., The BIO5 Institute, University of Arizona, 1657 E Helen Street, Tucson, Arizona 85721, Phone 520-626-4179, fax 520-626-4824; e-mail vagner@email.arizona.edu; and D.L.M., H. Lee Moffitt Cancer Center and Research Institute, 12902 Magnolia Drive, Tampa, FL 33612; David.Morse@moffitt.org

Supporting Information:

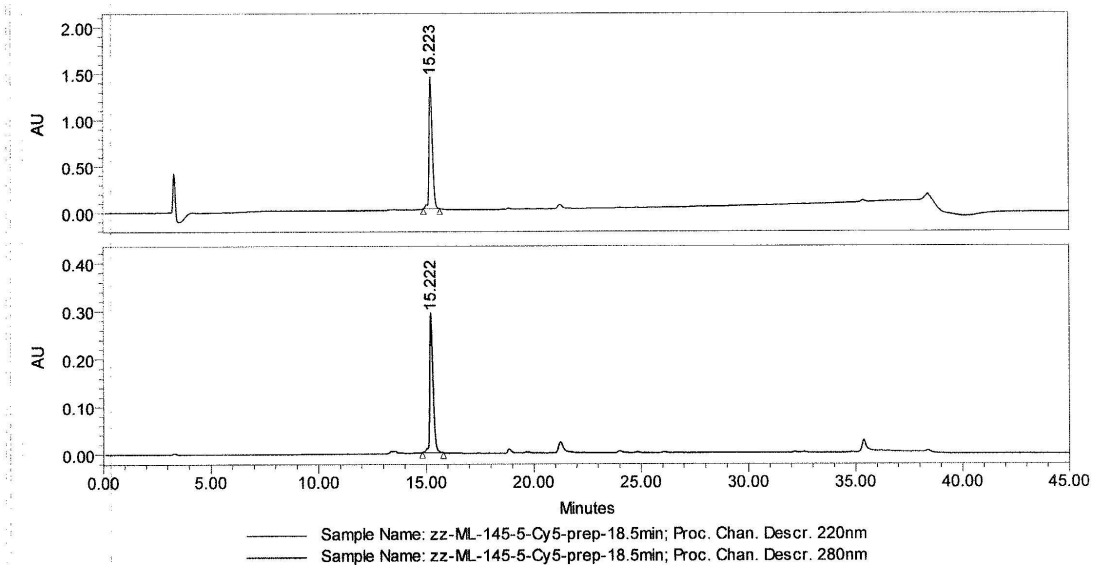

Channel 220 nm
Channel: 2487Channel 1

	RT	Area (µV*sec)	% Area	Channel
1	15.223	1.50e+007	100.00	2487Channel 1

Channel 280 nm
Channel: 2487Channel 2

	RT	Area (µV*sec)	% Area	Channel
1	15.222	3.15e+006	100.00	2487Channel 2

Figure S1. HPLC of the MC1RL-Cy5 compound.

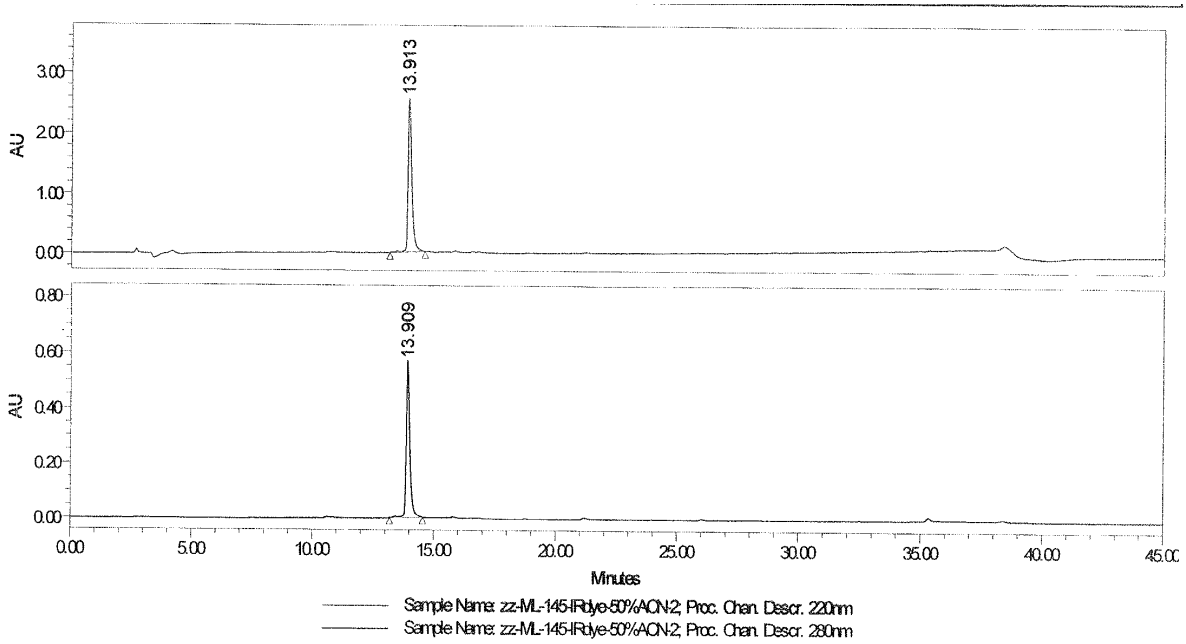

Channel 220 nm
Channel: 2487Channel 1

	RT	Area (µV*sec)	%Area	Channel
1	13.913	2.90e+007	100.00	2487Channel 1

Channel 280 nm
Channel: 2487Channel 2

	RT	Area (µV*sec)	%Area	Channel
1	13.909	6.18e+006	100.00	2487Channel 2

Figure S2. HPLC of the MC1RL-800 compound.